

Lecture Notes in Electrical Engineering 417

Pengfei Zhao

Yun Ouyang

Min Xu

Li Yang

Yujie Ouyang

*Editors*

# Advanced Graphic Communications and Media Technologies

# Lecture Notes in Electrical Engineering

Volume 417

## Board of Series editors

Leopoldo Angrisani, Napoli, Italy  
Marco Arteaga, Coyoacán, México  
Samarjit Chakraborty, München, Germany  
Jiming Chen, Hangzhou, P.R. China  
Tan Kay Chen, Singapore, Singapore  
Rüdiger Dillmann, Karlsruhe, Germany  
Haibin Duan, Beijing, China  
Gianluigi Ferrari, Parma, Italy  
Manuel Ferre, Madrid, Spain  
Sandra Hirche, München, Germany  
Faryar Jabbari, Irvine, USA  
Janusz Kacprzyk, Warsaw, Poland  
Alaa Khamis, New Cairo City, Egypt  
Torsten Kroeger, Stanford, USA  
Tan Cher Ming, Singapore, Singapore  
Wolfgang Minker, Ulm, Germany  
Pradeep Misra, Dayton, USA  
Sebastian Möller, Berlin, Germany  
Subhas Mukhopadhyay, Palmerston, New Zealand  
Cun-Zheng Ning, Tempe, USA  
Toyoaki Nishida, Sakyo-ku, Japan  
Bijaya Ketan Panigrahi, New Delhi, India  
Federica Pascucci, Roma, Italy  
Tariq Samad, Minneapolis, USA  
Gan Woon Seng, Nanyang Avenue, Singapore  
Germano Veiga, Porto, Portugal  
Haitao Wu, Beijing, China  
Junjie James Zhang, Charlotte, USA



### *About this Series*

“Lecture Notes in Electrical Engineering (LNEE)” is a book series which reports the latest research and developments in Electrical Engineering, namely:

- Communication, Networks, and Information Theory
- Computer Engineering
- Signal, Image, Speech and Information Processing
- Circuits and Systems
- Bioengineering

LNEE publishes authored monographs and contributed volumes which present cutting edge research information as well as new perspectives on classical fields, while maintaining Springer’s high standards of academic excellence. Also considered for publication are lecture materials, proceedings, and other related materials of exceptionally high quality and interest. The subject matter should be original and timely, reporting the latest research and developments in all areas of electrical engineering.

The audience for the books in LNEE consists of advanced level students, researchers, and industry professionals working at the forefront of their fields. Much like Springer’s other Lecture Notes series, LNEE will be distributed through Springer’s print and electronic publishing channels.

More information about this series at <http://www.springer.com/series/7818>

Pengfei Zhao · Yun Ouyang  
Min Xu · Li Yang · Yujie Ouyang  
Editors

# Advanced Graphic Communications and Media Technologies

 Springer

*Editors*

Pengfei Zhao  
China Academy of Printing Technology  
Beijing  
China

Li Yang  
China Academy of Printing Technology  
Beijing  
China

Yun Ouyang  
China Academy of Printing Technology  
Beijing  
China

Yujie Ouyang  
China Academy of Printing Technology  
Beijing  
China

Min Xu  
China Academy of Printing Technology  
Beijing  
China

ISSN 1876-1100

ISSN 1876-1119 (electronic)

Lecture Notes in Electrical Engineering

ISBN 978-981-10-3529-6

ISBN 978-981-10-3530-2 (eBook)

DOI 10.1007/978-981-10-3530-2

Library of Congress Control Number: 2016963181

© Springer Nature Singapore Pte Ltd. 2017

This work is subject to copyright. All rights are reserved by the Publisher, whether the whole or part of the material is concerned, specifically the rights of translation, reprinting, reuse of illustrations, recitation, broadcasting, reproduction on microfilms or in any other physical way, and transmission or information storage and retrieval, electronic adaptation, computer software, or by similar or dissimilar methodology now known or hereafter developed.

The use of general descriptive names, registered names, trademarks, service marks, etc. in this publication does not imply, even in the absence of a specific statement, that such names are exempt from the relevant protective laws and regulations and therefore free for general use.

The publisher, the authors and the editors are safe to assume that the advice and information in this book are believed to be true and accurate at the date of publication. Neither the publisher nor the authors or the editors give a warranty, express or implied, with respect to the material contained herein or for any errors or omissions that may have been made. The publisher remains neutral with regard to jurisdictional claims in published maps and institutional affiliations.

Printed on acid-free paper

This Springer imprint is published by Springer Nature

The registered company is Springer Nature Singapore Pte Ltd.

The registered company address is: 152 Beach Road, #21-01/04 Gateway East, Singapore 189721, Singapore

# Preface

As one of the series of academic activities which are launched by China Academy Printing Technology, “2016 China Academic Conference on Printing, Packaging Engineering & Media Technology” is co-hosted by China Academy of Printing Technology, Xi’an University of Technology and Stuttgart Media University, and co-organized by Beijing Key Laboratory of Printing and Packaging New Technology of China Academy of Printing Technology, Faculty of Printing, Packaging Engineering and Digital Media Technology of Xi’an University of Technology and Printing Technology Professional Committee of Chinese Society for Imaging Science and Technology. It will be held on November 25–27, 2016 in Xi’an, China.

By far, “China Academic Conference on Printing and Packaging” and its series of events have been held for seven sessions since the first session in 2010. Due to the influence of the sponsors, academic foresight in the keynotes and the active participation among scholars, the conference has become the most influential academic exchange activity in printing and packing field in China, aiming at promoting the exchange and innovation of academic research in the field of international printing and packaging, and improving, merging as well as elevating the printing technology, which is the traditional technology of recording the development of human culture, into the information age.

As China economic development has entered a new norm period, the printing and packaging industry of China has been keeping a stable growth. In 2015, the total output value of China printing industry has topped to RMB 1124.62 billion, increasing by 3.6% and the main business revenue of packaging industry has reached RMB 1136.55 billion, increasing by 4.08%. Research innovation is becoming more and more important in the enterprise development of printing and packaging industry, and technology is becoming the key factor for enterprises to win in the fierce market competition. In the meantime, with the deep application of IT technology and the Internet in printing and packaging technology innovation and product development, product form of printing and packaging industry has been extended from traditional media to digital media.

In accordance with the purpose of the conference, “2016 China Academic Conference on Printing, Packaging Engineering & Media Technology” focused on digital technology, environmental technology and advanced materials technology in printing and packaging fields. We invited Prof. Jon Yngve Hardeberg from Norwegian University of Science and Technology, Prof. Mathias Hinkelmann from Stuttgart Media University, Prof. Patrick Gane from Aalto University, and other internal famous scholars to make keynote speeches on key techniques of multi-spectral color imaging, new digital media technology and new business models in the printing industry, and surface pore network structure and fluid interaction. At the same time, all the participants shared the latest research trends and achievements on color science, image processing, digital media, printing engineering, packaging engineering, mechanical engineering and intelligence, information materials and detection technology on nine panel discussion meetings.

The conference received 245 papers this year, including 3 keynote speeches and 242 oral presentations, among which 143 were selected to be published on *Lecture Notes in Electrical Engineering* (LNEE) (ISSN: 1876-1100) by Springer.

Here we greatly acknowledge all the organizations that offered great support for the conference and they are: China Printing Technology Association, Chinese Society for Imaging Science and Technology, Beijing Institute of Graphic Communication, School of Printing and Packaging of Wuhan University, College of Communication and Art Design of University of Shanghai for Science and Technology, School of Media and Design of Hangzhou Dianzi University, College of Light Industry and Engineering of South China University of Technology, Zhengzhou Institute of Surveying and Mapping, Light Industry College of Harbin University of Commerce, College of Packaging and Printing Engineering of Tianjin University of Science and Technology, School of Mechanical Engineering of Jiangnan University, School of Light Industry & Chemical Engineering of Dalian Polytechnic University, School of Packaging & Material Engineering of Hunan University of Technology, School of Biological and Chemical Engineering/School of Light Industry of Zhejiang University of Science and Technology, College of Engineering of Qufu Normal University, College of Light Industry Science and Engineering of Nanjing Forestry University, College of Light Industry and Energy of Shaanxi University of Science & Technology, College of Printing and Packaging Engineering of Qilu University of Technology, College of Materials Science and Engineering of Beijing University of Chemical Technology, College of Material Science & Engineering of Zhengzhou University, School of Food and Chemical Engineering of Beijing Technology and Business University, School of Media and Communication of Shenzhen Polytechnic, Shanghai Publishing and Printing College, State Key Laboratory of Modern Optical Instrumentation, Zhejiang University, National Taiwan University of Arts, Norwegian University of Science and Technology, Stuttgart Media University, Aalto University, and Beijing Keyin Media & Culture Co., Ltd.

We would like to express our gratitude to the 55 experts from China, Germany, Britain, American and Japan for reviewing and recommending papers for the conference with strict standards.

We also thank Springer for offering us an international platform for publishing.  
We look forward to our reunion at the next China Academic Conference on  
Printing and Packaging.

November 2016

Edited by  
China Academy of Printing Technology

# **2016 China Academic Conference on Printing, Packaging Engineering & Media Technology**

**Date** November 25–27, 2016

**Location** Jianguo Hotel, Xi'an, China

## **Sponsors**

China Academy of Printing Technology

Xi'an University of Technology

Stuttgart Media University

## **Supports**

China Printing Technology Association

Chinese Society for Imaging Science and Technology

## **Organizers**

Beijing Key Laboratory of Packaging and Printing New Technology, China Academy of Printing Technology

Faculty of Printing, Packaging Engineering and Digital Media Technology, Xi'an University of Technology

Printing Technology Professional Committee, Chinese Society for Imaging Science and Technology

## **Co-Sponsors**

School of Printing and Packaging Engineering, Beijing Institute of Graphic Communication

School of Printing and Packaging, Wuhan University

College of Communication and Art Design, University of Shanghai for Science and Technology  
 Light Industry College, Harbin University of Commerce  
 School of Light Industry & Chemical Engineering, Dalian Polytechnic University  
 College of Light Industry Science and Engineering, Nanjing Forestry University  
 College of Engineering, Qufu Normal University  
 College of Printing and Packaging Engineering, Qilu University of Technology  
 College of Packaging and Printing Engineering, Tianjin University of Science and Technology  
 College of Light Industry and Engineering, South China University of Technology  
 Zhengzhou Institute of Surveying and Mapping  
 School of Media and Design, Hangzhou Dianzi University  
 School of Mechanical Engineering, Jiangnan University  
 State Key Laboratory of Modern Optical Instrumentation, Zhejiang University  
 School of Biological and Chemical Engineering/School of Light Industry, Zhejiang University of Science and Technology  
 College of Light Industry and Energy, Shaanxi University of Science & Technology  
 College of Materials Science and Engineering, Beijing University of Chemical Technology  
 School of Packaging & Material Engineering, Hunan University of Technology  
 College of Material Science & Engineering, Zhengzhou University  
 Shanghai Publishing and Printing College  
 School of Food and Chemical Engineering, Beijing Technology and Business University  
 School of Media and Communication, Shenzhen Polytechnic  
 Department of Graphic Communication Arts, College of Communications, National Taiwan University of Arts

## **Conference Executive Committee**

### **Chairman**

Xiaolian Li (President of Xi'an University of Technology)  
 Tingliang Chu (President of China Academy of Printing Technology)  
 Alexander Roos (President of Stuttgart Media University)

### **Vice Chairman**

Congjun Cao (Dean of Faculty of Printing, Packaging Engineering and Digital Media Technology, Xi'an University of Technology)  
 Pengfei Zhao (Vice President of China Academy of Printing Technology)  
 Mathias Hinkelmann (Vice President of Stuttgart Media University)

### **Secretary-general**

Yun Ouyang (Chief Engineer of China Academy of Printing Technology)  
 Yuanlin Zheng (Vice Dean of Faculty of Printing, Packaging Engineering and Digital Media Technology, Xi'an University of Technology)



## **Conference Academic Committee**

### **Chairman**

Deren Li (Academician of Chinese Academy of Sciences, Academician of China Engineering Academy, Professor of Wuhan University, Director of State Key Laboratory of Information Engineering in Surveying, Mapping and Remote)

### **Vice Chairman**

Guangan Ni (Academician of China Engineering Academy, Researcher of Institute of Computing Technology Chinese Academy of Sciences, Board Chairperson of Chinese Information Processing Society of China)

Kefu Chen (Academician of China Engineering Academy, Professor of South China University of Technology, Director of Academic Committee of State Key Laboratory of Pulp and Paper Engineering)

Songlin Zhuang (Academician of China Engineering Academy, Director and Professor of School of Optical-Electrical and Computer Engineering of University of Shanghai for Science and Technology, Optical Expert)

Bingheng Lu (Academician of Chinese Academy of Engineering, Professor of Xi'an Jiaotong University, Director of the National Engineering Research Center of Rapid Manufacturing)

### **Commissioners**

Yuri Andreev (Head of Moscow State University of Printing Arts)

Stephen W. Bigger (Doctor, Professor, Vice President of Faculty of Engineering and Science of Victoria University)

Congjun Cao (Doctor, Professor of Xi'an University of Technology, Master student supervisor)

Guorong Cao (Professor of Beijing Institute of Graphic Communication, Master student supervisor)

Ping Chen (Doctor, Doctoral supervisor)

Guangxue Chen (Doctor, Professor of South China University of Technology, Doctoral supervisor)

Yunzhi Chen (Doctor, Professor of Tianjin University of Science and Technology, Doctoral supervisor)

Tingliang Chu (Professor of China Academy of Printing Technology, Master student supervisor)

Fuqiang Chu (Doctor, Professor of Qilu University of Technology, Master student supervisor)

De Gao (Professor of Ningbo Institute of Technology, Zhejiang University, Master student supervisor)

Patrick Gane (Doctor, Professor of Printing Technology at the School of Chemical Technology, Aalto University)

Phil Green (Professor of Colour Imaging, London College of Communication)

Jon Yngve Hardeberg (Doctor, Professor of Norwegian University of Science and Technology)

Roger D. Hersch (Doctor, Professor of Computer Science and Head of the Peripheral Systems Laboratory at the Ecole Polytechnique Fédérale de Lausanne (EPFL))

Mathias Hinkelmann (Doctor, Professor of Stuttgart Media University)

Yungcheng Hsieh (Professor of National Taiwan University of Arts)

Thomas Hoffmann-Walbeck (Professor of the Faculty of Print and Media Technology, Stuttgart University of Media)

Guobin Jin (Professor of Shanghai University, Vice Director of China Packaging Education Committee)

Takashi Kitamura (Doctor, Professor of Graduate School of Advanced Integration Science, Chiba University)

Shijun Kuang (Consultant Engineer of China National Pulp and Paper Research Institute, Chief Engineer)

Jose Maria Lagaron (Doctor, Professor, Leader and Founder of the Group Novel Materials and Nanotechnology for Food Related Applications at the Institute of Agrochemistry and Food Technology of the Spanish Council for Scientific Research)

Benjamin Lee (Professor, Director of Department of Technology, California State University)

Houbin Li (Doctor, Professor of Wuhan University, Doctoral supervisor)

Luhai Li (Doctor, Professor of Beijing Institute of Graphic Communication, Master student supervisor)

Zhijian Li (Doctor, Professor of Shaanxi University of Science & Technology, Doctoral supervisor)

Haoxue Liu (Doctor, Professor of Beijing Institute of Graphic Communication, Master student supervisor)

Zhen Liu (Professor of University of Shanghai for Science and Technology, Doctoral supervisor)

Dongming Lu (Doctor, Professor of Zhejiang University, Doctoral supervisor)

M. Ronnier Luo (Professor, Director of the Department of Color Science, University of Leeds)

Xiufeng Ma (Professor of Qufu Normal University, Master student supervisor)

Luciano Piergiovanni (Professor of the Department of Food, Environmental and Nutritional Sciences, Faculty of Agricultural and Food Sciences, University of Milan)

Ngamtip Poovarodom (Doctor, Associate Professor of Department of Packaging and Materials Technology of Faculty of Agro-Industry, Kasertart University)

Jialing Pu (Doctor, Professor of Beijing Institute of Graphic Communication, Doctoral supervisor)

Penggang Ren (Doctor, Professor of Xi'an University of Technology, Master student supervisor)

Ruizhi Shi (Doctor, Professor of Zhengzhou Institute of Surveying and Mapping, Doctoral supervisor)

Zhihui Sun (Professor of Harbin University of Commerce, Doctoral supervisor)

Shaoyan Tang (Professor of Hunan University of Technology, Master student supervisor)

Zhengning Tang (Doctor, Professor of Jiangnan University, Master student supervisor)

Anita Teleman (Doctor, Research Manager of Printing Solutions at the Research Institute Innventia, Sweden)

Yuemin Teng (Professor of Shanghai Publishing and Printing College)

Philipp Urban (Head of Emmy-Noether Research Group, Institute of Printing Science and Technology, Technische Universität Darmstadt)

Howard E. Vogl (Visiting Professor of Rochester Institute of Technology)

Xiaoxia Wan (Doctor, Professor of Wuhan University, Doctoral supervisor)

Haiqiao Wang (Doctor, Professor of Beijing University of Chemical Technology, Doctoral supervisor)

Jianqing Wang (Professor of Tianjin University of Science and Technology, Doctoral supervisor)

Lijie Wang (Professor of Shenzhen Polytechnic)

Qiang Wang (Doctor, Professor of Hangzhou Dianzi University, Doctoral supervisor)

Yiqing Wang (Doctor, Professor of Xi'an Jiaotong University)

Yuhchang Wei (Professor of Chinese Culture University)

Xianfu Wei (Doctor, Professor of Beijing Institute of Graphic Communication, Doctoral supervisor)

Punan Xie (Professor of Beijing Institute of Graphic Communication)

Xiulan Xin (Doctor, Professor of Beijing Technology and Business University, Master student supervisor)

Jinlin Xu (Professor of Xi'an University of Technology)

Wencai Xu (Professor of Beijing Institute of Graphic Communication, Doctoral supervisor)

Haigen Yao (Professor of Shanghai Publishing and Printing College)

Bin Yang (Doctor, Researcher of Peking University)

Yadong Yin (Doctor, Professor of University of California, Riverside)

Shisheng Zhou (Doctor, Professor of Xi'an University of Technology, Doctoral supervisor)

Xiuping Zhao (Professor of Tianjin University of Science and Technology, Master student supervisor)

Haiyan Zhang (Professor of Xi'an University of Technology, Master student supervisor)

Yingquan Zou (Doctor, Professor of Beijing Normal University, Doctoral supervisor)

### **Reviewers**

Congjun Cao (Doctor, Professor of Xi'an University of Technology)

Shaozhong Cao (Doctor, Professor of Beijing Institute of Graphic Communication)

Guangxue Chen (Doctor, Professor of South China University of Technology)

Jinzhou Chen (Professor of Zhengzhou University)

Yunzhi Chen (Doctor, Professor of Tianjin University of Science and Technology)

Fuqiang Chu (Doctor, Professor of Qilu University of Technology)  
Tingliang Chu (Professor, President of China Academy of Printing Technology)  
Yi Fang (Doctor, Teacher of Beijing Institute of Graphic Communication)  
Yabo Fu (Doctor, Associate Professor of Beijing Institute of Graphic Communication)  
Huan Gu (Associate Professor of Xi'an University of Technology)  
Yanfeng Guo (Professor of Xi'an University of Technology)  
Minghui He (Doctor of South China University of Technology)  
Junyan Huang (Associate Professor of Dalian Polytechnic University)  
Peiqing Huang (Associate Professor of Beijing Institute of Graphic Communication)  
Zhen Huang (Doctor, Professor of Tianjin University of Commerce)  
Lijiang Huo (Professor of Dalian Polytechnic University)  
Yang Jin (Doctor, Professor of Beijing Institute of Graphic Communication)  
Xiaoshan Jiang (Doctor, Vice Professor of Beijing Institute of Graphic Communication)  
Houbin Li (Doctor, Professor of Wuhan University)  
Luhai Li (Professor of Beijing Institute of Graphic Communication)  
Xiaozhou Li (Associate Professor of Qilu University of Technology)  
Zhijian Li (Doctor, Professor of Shaanxi University of Science & Technology)  
Zhijiang Li (Doctor, Associate Professor of Wuhan University)  
Jing Liang (Doctor, Teacher of Dalian Polytechnic University)  
Haixue Liu (Doctor, Professor of Beijing Institute of Graphic Communication)  
Yanan Liu (Doctor, Engineer of China Academy of Printing Technology)  
Zhuang Liu (Doctor, Teacher of Harbin University of Commerce)  
Maohai Lin (Associate Professor of Qilu University of Technology)  
Lixin Lu (Doctor, Professor of Jiangnan University)  
Rubai Luo (Doctor, Associate Professor of Xi'an University of Technology)  
M. Ronnier Luo (Doctor, Professor of University of Leeds)  
Yongjun Ma (Doctor, Professor of School of Computer Science and Information Engineering (SCSIE), Tianjin University of Science and Technology)  
Yalin Miu (Associate Professor of Xi'an University of Technology)  
Lixin Mo (Associate Professor of Beijing Institute of Graphic Communication)  
Yun Ouyang (Chief Engineer of China Academy of Printing Technology)  
Wenfa Qi (Engineer of Institute of Computer Science and Technology, Peking University)  
Ruizhi Shi (Doctor, Professor of Zhengzhou Institute of Surveying and Mapping)  
Zhengning Tang (Doctor, Professor of Jiangnan University)  
Haiqiao Wang (Doctor, Professor of Beijing University of Chemical Technology)  
Qiang Wang (Doctor, Professor of Hangzhou Dianzi University)  
Xianfu Wei (Doctor, Professor of Beijing Institute of Graphic Communication)  
Dehong Xie (Doctor, Teacher of Nanjing Forestry University)  
Xiulan Xin (Doctor, Professor of Beijing Technology and Business University)  
Hongwei Xu (Doctor, Professor of Xi'an University of Technology)  
Zhuofei Xu (Doctor, Teacher of Xi'an University of Technology)

Yaohua Yi (Doctor, Professor of Wuhan University)  
Pengfei Zhao (Vice President of China Academy of Printing Technology)  
Erhu Zhang (Doctor, Professor of Xi'an University of Technology)  
Fazhong Zhang (Doctor, Engineer of China Academy of Printing Technology)  
Hanyue Zhang (Professor of Tianjin University of Science and Technology)  
Ruijing Zhang (Doctor, Teacher of Hangzhou Dianzi University)  
Zhigang Zhang (Associate Professor of Xi'an University of Technology)  
Yuanlin Zheng (Doctor, Vice Professor of Xi'an University of Technology)  
Ming Zhu (Doctor, Vice Professor of Henan Institute of Engineering)

# Contents

## Part I Color Science and Technology

<b>Test Criteria and Investigation of Uniform Color Spaces to Meet the Requirements of Future Imagery</b> . . . . .	3
Muhammad Safdar and Ming Ronnier Luo	
<b>Image Colorization Method Using Texture Descriptors and ISLIC Segmentation</b> . . . . .	9
Liqin Cao, Lei Jiao and Zhijiang Li	
<b>Study on Spectral Reconstruction Based on Sample Optimization Method of Color Digital Camera</b> . . . . .	17
Zhaoyang Jia and Guangxue Chen	
<b>What Do We Need for Assessing Whiteness?</b> . . . . .	25
Shining Ma, Minchen Wei, Jing Liang and Ming Ronnier Luo	
<b>Regional Culture Preferences to LED Light Color Rendering</b> . . . . .	33
Ran Wei, Xiaoxia Wan, Qiang Liu, Guo Cao and Haiwen Wang	
<b>Gamut Testing of EPSON Stylus Photo R270 Color Ink-Jet Printer by ICC 3D</b> . . . . .	41
Xiaochun Li, Ming Zhu and Mingming Yin	
<b>Research on Spectral Reflection Characteristics of Overprinted Color Inks and the Numeric Compensation to the Theoretical Model</b> . . . . .	49
Ji Qi, Yang Jin, Xinggen Qian and Yusheng Lian	
<b>Dual Attributes of Color</b> . . . . .	55
Yechi Pang, Zhijie Li, Pengfei Zhao, Min Xu and Wensi Liang	
<b>Extracting the Representative Colors in Facial Image Based on the Eye Tracking</b> . . . . .	65
Pei Deng	

**Study on Color Model on Green Gamut Part for High Fidelity Printing** . . . . . 75  
Xiaoyan She, Shisheng Zhou and Guanjun Zhu

**Polynomial Fitting Approach for Colorimetric Values Transform Based on Large Scale Spectral Dataset.** . . . . . 83  
Yijing Xun, Qiang Liu, Xiaoxia Wan, Zheng Huang, Guo Cao and Haiwen Wang

**Study on Color Matching Technology of Flexographic Printing Ink.** . . . . . 91  
Ben Liu, Maohai Lin, Guichun Hu and Meiqi Lin

**Study on Gamut Mapping Algorithm Based on GRNN.** . . . . . 99  
Pukang Yuan, Qiang Wang, Lingjun Kong and Quanhui Tian

**Performance Test of Liquid Crystal Display Parameters.** . . . . . 105  
Hongyan Chen, Li Cheng and Xiao Jin

**Simulation and Rejuvenation for Chinese Fading Paint Under Ultraviolet** . . . . . 117  
Zhen Liu, Fang Cai, ShuangShuang Chen and Chong Sun

**Study on Observers’ Categories Based on Color Matching Experiments.** . . . . . 123  
Chunjie Shi, Min Huang, Yu Liu, Zeyang Li and Haoxue Liu

**Measurement and Analysis of Colorimetric Values for Holographic Paper with Light Pillars** . . . . . 131  
Zeyang Li, Min Huang, Yu Liu, Chunjie Shi, Haoxue Liu and Guihua Cui

**A Brief Review of Colour Quality Assessments of LED Lightings for Museums.** . . . . . 139  
Qiyang Zhai and Ming Ronnier Luo

**Testing the Performance of Color Difference Formulae Using Two Distinct Glossiness of Color Printing Atlas.** . . . . . 145  
Jing Liang, Buyun Yao, Siyu Ning and Liang Sun

**Color Restoration Method of Underwater Multispectral Images.** . . . . . 153  
Ping Yang, Yilu Guo, Hong Song, Jingnan Sun, Yong Wang, Xiandou Zhang and Qiang Wang

**Research on the Conversion Algorithms of Monitor Color Management Based on WCS** . . . . . 161  
Rui Zhang, Congjun Cao, Nana Liu and Jingshang Fan

**Presumption Evaluation of Color Reproduction Based on Multi-feature Model in Digital Printing** . . . . . 171  
Yang Zhao, Xiaozhou Li, Xuelin Li, Qian Cao and Jingqiang Jia

**Part II Image Processing Technology**

**A New Parallel Hierarchical K-Means Clustering Algorithm for Video Retrieval** . . . . . 179  
 Kaiyang Liao, Ziwei Tang, Congjun Cao, Fan Zhao and Yuanlin Zheng

**Comprehensive Imaging Quality Assessment Method for Laser Printer Based on SVM** . . . . . 187  
 Yaohua Yi, Luolan Zhou, Yuan Yuan and Rui Li

**An Efficient Approach of Color Image Matching by Combining Color Invariant and ORB Feature.** . . . . . 195  
 Shenghui Li, Ruizhi Shi and Hui Ye

**Color Printing Image Quality Evaluation Method Based on Full Quaternion Matrix.** . . . . . 205  
 Yunfei Zhong, Ruoqing Wang, Lujing Fu, Yaojian Hu and Lu Chen

**An Output of Oil Painting Stylized Digital Image from Photographs with Optimum Tone Reproduction** . . . . . 213  
 Jing Geng, Congjun Cao, Jingshang Fan, Hirokatsu Shimizu, Naokazu Aoki and Hiroyuki Kobayashi

**Contrastive Analysis on Emotional Cognition of Skeuomorphic and Flat Icon.** . . . . . 225  
 Xiaoming Zhang, Qiang Wang and Yan Shi

**Reproduction of HDR Image Based on Multiple Bilateral Filtering** . . . . . 233  
 Yang Zhao, Xiaozhou Li, Jingqiang Jia and Qian Cao

**BOF Image/Video Retrieval Model with Global Feature** . . . . . 241  
 Mingzhu Zhang, Kaiyang Liao, Congjun Cao, Fan Zhao and Yuanlin Zheng

**Applications of Personalized QR Code on Packaging Design** . . . . . 249  
 Xianjing Bao, Yunfei Zhong, Pengcheng Su and Ruoqing Wang

**Research on Augmented Reality of Printed Matter Based on Random Ferns and Orientation Gradient with Integral Graph.** . . . . . 257  
 Da Li, Ruizhi Shi, Xuhui Zhao and Hui Ye

**BM3D Image Denoising Algorithm Based on K-Means Clustering** . . . . . 265  
 Jinru Gao and Qiang Wang

**Person Re-identification Based on Fusing Appearance Features in Perceptual Color Space.** . . . . . 273  
 Caixia Fan, Yajun Chen and Lei Cao

**A Night Image Enhancement Algorithm Based on Guided Filtering.** . . . . . 283  
 Xuxin Tang, Zhijiang Li and Yuhang Chen



**Three-Dimensional Color Gamut Visualization and Interaction for Digital Images** . . . . . 289  
 Zhijin Li, Maohai Lin, Guangyuan Wu, Yehong Chen and Meiqi Lin

**Application of Multi-spectral Technology in Presswork Forgery Prevention** . . . . . 297  
 Yan Li and Dongsheng Jiang

**Scene Text Segmentation Method Based on MSER and MLBP** . . . . . 305  
 Miaomiao Guo, Yaohua Yi, Juhua Liu and Ying Li

**Research on Stereo Image Rendering Based on Micro Lens Array** . . . . . 311  
 Wei Liu, Guangxue Chen and Mengyu Li

**Research on Reading Recognition Technology of Gas Meter Based on Key Feature Matching** . . . . . 317  
 Wenfa Qi, Bowen Xue and Yuxin Liu

**Image Quality Assessment Scheme Based on Structural Contrast Index and Gradient Similarity** . . . . . 325  
 Li Liu, Yuanlin Zheng and Wei Wang

**Study on Memory Color Extraction Method of Image Processing** . . . . . 333  
 Jingnan Sun, Ping Yang and Qiang Wang

**Part III Digital Media Technology**

**Semantic Based Text Similarity Computation** . . . . . 343  
 Yaqi Liu and Zhijiang Li

**Design and Manufacture of 3D Printers of Virtual Assembly Display Platform** . . . . . 349  
 Haiyue Zhang and Zhanjun Si

**Research on the Application Process of Mobile Augmented Reality in Printed Product** . . . . . 357  
 Hui Ye, Ruizhi Shi, Shenghui Li and Da Li

**Research and Application of Online Image Processing Technology Based on HTML5** . . . . . 367  
 Chunxia Dong and Zhanjun Si

**Information Publishing System Based on the Framework of Django** . . . . . 375  
 Shenliang Li and Zhanjun Si

**Trends of Digital Publishing: A Case Study of Taiwan’s Tourist Press** . . . . . 383  
 Yungcheng Hsieh, Mingchw Wei and Yungchao Ting

**Design and Implementation of Interactive Courseware Based on Mobile Terminal** . . . . . 393  
 Ying Wang, Zhanjun Si and Lu Zhang

**Generating Customized PDF Document Based XML Source Data** . . . . . 401  
 Rubai Luo, Meng Wang and Shisheng Zhou

**Research on Presswork to eBook Conversion Method** . . . . . 409  
 Ying Hu and Huiqiang Lu

**Interactive Design of Mobile Game Interfaces Based on UCD** . . . . . 415  
 Jing Zhao, Lei Guo and Chunhong Zhang

**Research and Implement of HTML5 Game Based on WebSocket** . . . . . 423  
 Ke Shen, Zhanjun Si and Lu Zhang

**Part IV Printing Engineering Technology**

**Research on a New Reflectance Model for Printing Based on Dot Shape** . . . . . 431  
 Qi Wang, Xi Yang and Honghao Liu

**Impact of Screening Parameters for Electrostatic Imaging Quality** . . . . . 441  
 Kaili Zhang and Guangxue Chen

**Effect of Paper Optical Properties on the Color Reproduction in Ink Jet Printing** . . . . . 447  
 Guichun Hu, Haoran Fang, Maohai Lin and Fuqiang Chu

**Study on Fidelity of Inkjet Dots Based on Multiple Linear Regression Analysis** . . . . . 453  
 Fangfang Lu, Zhitao Zhang, Yang Zou and Yanfen Zhang

**Study on the Mode of the Printing Industry in Cloud Computing** . . . . . 461  
 Yunzhi Chen, Yongkai Wang and Chong Gu

**A Pre-actuation Method for Initial Droplets Accurateness of Inkjet Printing with Volatile Materials** . . . . . 467  
 Zhiqiang Gao, Cheng Sun, Liqiang Huang and Xing Yin

**Analysis of Print Quality of UV Flatbed Inkjet Printer** . . . . . 475  
 Ying Wu and Ang Xu

**Process Analysis of Seamless Adhesion for Cutting Model Printed by Color Paper-Based 3D Printing** . . . . . 483  
 Jiangping Yuan, Yimin Liu, Guangxue Chen and Liuxi He

<b>Study of Printing Process of Creative Prints Based on TFEL Technology</b> . . . . .	489
Rubai Luo, Ming Lu and Shisheng Zhou	
<b>Study on the Influence of Paper Surface Efficiency on Ink Color Effect</b> . . . . .	497
Li Cheng, Xuejun Tian and Xi Xiong	
<b>Effect of Different Basic Weight of Paper on Microfluidic Devices Fabricated by UV Inkjet Printing</b> . . . . .	509
Yingzhe He, Guangxue Chen and Junfei Tian	
<b>Performance Study of Flexible Capacitive Pressure Sensor Based on Dielectric Structures</b> . . . . .	515
Qichao Hou, Mengmeng Liang, Ruping Liu and Wei Wang	
<b>Paper Suitable Analysis Based on Printed Electronics</b> . . . . .	525
Zhongmin Jiang and Yingmei Zhou	
<b>Water Washing Improving the Conductivity of Flexography Printed ITO-Free Transparent Electrode for Polymer Solar Cells</b> . . . . .	531
Yi Fang, Lu Fu, Yuanyuan Li, Yafang Feng, Shiqi Zhu, Yanfang Xu, Li Yang and Luhai Li	
<b>Study of the Screen Printing Technology on RFID Tag Antenna</b> . . . . .	539
Wei Liu, Guangxue Chen and Yusi Zhang	
<b>Research on the Covering Property of White Ink Applied on Transfer Paperboard</b> . . . . .	547
Xinting Wang, Guorong Cao, Ling Cheng and Xu Wang	
<b>Research on Theory and Application of Computer Ink Color Matching</b> . . . . .	555
Guhong Liu, Qifeng Chen and Guangxue Chen	
<b>PTC Effect of Conductive Composites Based on Resin Mixed with Carbon Nanoparticle</b> . . . . .	561
Mengmeng Liang, Qichao Hou, Ruping Liu, Xudong Wu, Wei Wang and Luhai Li	
<b>Part V Packaging Engineering Technology</b>	
<b>Preservation Effect of Thymol Active Packaging Films on Sugar Oranges</b> . . . . .	571
Xiaowen Liu, Yabo Fu, Dongli Li and Wencai Xu	
<b>Experimental Investigation of Influence Factors for Compression Strength of Thin Honeycomb Paperboard Box</b> . . . . .	581
Shibao Wen, Xiaoke Chu and Jujie Sun	

**Research on Application of WSN in Cold Chain Logistics’  
Warehousing and Transportation** . . . . . 589  
Hanyue Zhang and Shijuan Yang

**Effect of Pressure Sensitive Adhesive Polypropylene Tape  
on Performance of Corrugated Box**. . . . . 599  
Bingjie Shi and Xiaohui He

**Finite Element Analysis of Moisture Diffusion  
in Damp-Proof Packing** . . . . . 607  
Hongtao Miao

**Analysis of the Dynamic Performance of the Cushion Material  
Composed of EPE and EPS Based on Finite Element Method** . . . . . 617  
Xiaoli Song, Gaimei Zhang, Jiandong Lu and Fanjun Meng

**Modal Analysis on Laptop and Its Packaging System Based  
on Finite Element Method** . . . . . 627  
Gaimei Zhang, Xiaoli Song, Xiongbin Zhao, Jingting Zhang, Yue Shi  
and Fan Su

**Analysis of Mechanical Properties of Glass Packaging**. . . . . 635  
Jiang Chang, Xue Gong and Zhihui Sun

**Investigation of Active MAP Film with Menthol  
on Sugar Orange Preservation**. . . . . 643  
Hui Liu, Yabo Fu, Dongli Li and Wencai Xu

**Effect of Oxygen Permeability and Water Vapor Permeability  
of Fresh-Keeping Bags on the Preservation Effect of Nectarine** . . . . . 651  
Juanping Li and Dongli Li

**Identification Method of Egg Freshness by Principal Component  
and Discriminant Analysis** . . . . . 659  
Yinghao Xing, Qigen Tong, Xiujuan Zhi and Bin Du

**Application of Ultra-High Pressure Technology  
in the Processing of Shellfish Shell**. . . . . 667  
Xue Gong, Jiang Chang and Zhihui Sun

**Research on Storage Location Technology Based on RFID**. . . . . 673  
Hanyue Zhang, Xixi Feng and Jiao Wen

**Simulation Research About the Influence of Particle Characteristics  
on Transition of Particles in the Horizontal Screw Conveyor** . . . . . 683  
Jiandong Lu, Tianshu Zhao, Lizheng Zhang and Xiaoli Song

**Design and Material Selection of Shopping Malls  
Point-of-Purchase Displays**. . . . . 689  
Deqing Chen and Miaomiao Zhong

<b>Present Situation and Ideas of Express Packaging Greenization</b> . . . . .	697
Ling Cheng and Guorong Cao	
<b>Problems and Solutions for Express Logistic Packaging</b> . . . . .	705
Chenyang Liu and Lijiang Huo	
<b>Research on Packaging Evaluation System of Fast Moving Consumer Goods Based on Analytical Hierarchy Process Method</b> . . . . .	711
Lizheng Zhang, Jiandong Lu, Guorong Cao and Hongtao Miao	
<b>Research on the Embedding of Brocade Pattern of Li Nationality in Tourism Product Packaging</b> . . . . .	719
Wenjia Liu, Junwei Hu and Jinmin Gao	
<b>Part VI Mechanical Engineering &amp; Numerical Control Technology</b>	
<b>Research on Warpage Deformation Mechanism &amp; Control Method of Fused Deposition Parts</b> . . . . .	729
Linlin Liu, Chuliang Wan, Kaikai Li and Jimei Wu	
<b>Incomplete 3D Model's Repair Based on AFPF Technology</b> . . . . .	739
Shun Pan, Jiong Liang, Kun Hu and Yonghao Xiao	
<b>Object Tracking Algorithm Based on Adaptive Learning Parameter by Online Loss Detection</b> . . . . .	745
Yehong Chen, Pil Seong Park, Pingli Lv and Maohai Lin	
<b>Structure Design of Front-Edge Paper Feeder in the Production Line of Corrugated Carton</b> . . . . .	753
Jin Wang, Rongyu Ge and Jiatai Wang	
<b>Traction Characteristics of Guide Roller with the Air Entrainment</b> . . . . .	759
Mingyue Shao, Jimei Wu, Li'e Ma and Zhen Tian	
<b>Virtual Design of Web-Fed Typed Paper—Feeding Mechanism with Virtual Prototyping Technology</b> . . . . .	767
Hongqiang Wan, Minru Yao and You Li	
<b>Transducer Torque Control System of the Web Wind-up Tension in Gravure Press</b> . . . . .	775
Qiumin Wu, Hanxiao Zhang and Jimei Wu	
<b>Study on the Flow Mixing Results of Revolving Static Mixer Used in Solventless Laminator</b> . . . . .	783
Hongwei Xu, Wei Li, Xusheng Wang, Hang Zhang and Donghong Liu	

**Effect of High Temperature on Morphology and Structure of a New Composite as Raw Material of Filament for Fused Deposition Modeling Processes** . . . . . 791  
 Yonghao Xiao, Jia Yan, Kun Hu, Lin Zhu, Shun Pan, Luhai Li and Yen Wei

**Mechanical Property and Structure Improvement of Sleeve Mandrel in Central Impression Flexographic Press** . . . . . 797  
 Li'e Ma, Jierui Li, Jimei Wu, Shuaichao Huang and Shanhui Liu

**Digital Stamping Control System Design Based on the STM32 SCM** . . . . . 803  
 Ming Mu and Yujie Ouyang

**Print-Defect Detection Method Based on the Modified Artificial Immune Algorithm** . . . . . 813  
 Guanjun Zhu, Shisheng Zhou and Xiaoyan She

**Design of the Remote Fault Diagnosis System for the Printing Machines Based on the Internet of Things and Fuzzy Inference** . . . . . 825  
 Hongbo Liang, Shaozhong Cao, Xinpei Li and Hongfeng Xiang

**A Method of Printing Press Fault Diagnosis Based on Image Texture Information** . . . . . 837  
 Xueqian Bai, Haiyan Zhang, Weibo Chun, Zhuofei Xu and Qianqian Xu

**A Method of Diagnosis for Printing Press Ink Roller Bearing Based on Acoustic Signal and Spectrum Analysis** . . . . . 845  
 Yanyan Li, Haiyan Zhang, Qianqian Xu and Zhuofei Xu

**Part VII Ink and Related Technology**

**Study of Factors on Ethanol Resistance Stability of Water-Based Acrylic Resin Emulsion** . . . . . 857  
 Changming Yin, Xiaoyu Li and Haiqiao Wang

**Research of Water-Based Graphene Conductive Screen Printing Ink and Its Property** . . . . . 865  
 Minghui Zhang, Xianfu Wei, Beiqing Huang and Bin Long

**Effect of the Polyols Content on the Properties of the Waterborne Polyurethane** . . . . . 875  
 Xin Wang and Fuqiang Chu

**Study of Dispersion of the Yellow UV-LED Inkjet Ink** . . . . . 883  
 Yiran Li, Xianfu Wei and Beiqing Huang

**Double-Layer Corrosion Protection of Aluminium Pigments Applied in Water-Based Silver Ink** . . . . . 893  
 Wenlong Zhao, Shisheng Zhou and Zhengneng Wu

<b>Wettability and Dispersion of Phthalocyanine Blue Pigment and Evaluation of Its Effect on Printing Quality</b> . . . . .	903
Ruichun Cao, Xianfu Wei, Qi Wang and Hui Zhang	
<b>Preparation and Characterization of Nano Silver Applied in UV-Curing Conductive Ink</b> . . . . .	911
Ting Mi, Qifeng Chen and Guangxue Chen	
<b>Effect of Ketone and Hydrazine Self-Crosslinking Reaction on Polyurethane Emulsion</b> . . . . .	917
Yunlong Huang, Zhigang Hu, Ying Chen, Xiaoyu Li and Haiqiao Wang	
<b>Luminescent Properties of Rhodamine 6G Doped with DNA-CTMA and Its Application in Fluorescent Ink-Jet Ink</b> . . . . .	925
Hui Hao, Xia Li, XiaoYu Zhu, Huan Zheng, Beiqing Huang, Xianfu Wei and Lijuan Liang	
<b>Luminescence Properties of Eu(TTA)<sub>3</sub>(H<sub>2</sub>O)<sub>2</sub> Doped with DNA-CTMA and Its Application in Fluorescent Inkjet Ink</b> . . . . .	933
Tong Zhao, Chunrui Lin, Xiaoyu Zhu, Huan Zheng, Lianfang Li, Beiqing Huang, Xianfu Wei and Lijuan Liang	
<b>Influence of Coalescent on the Gloss of Plastic Water-Based Flexographic Ink</b> . . . . .	941
Xue Gao, Zhiyong Sun, Yun Ouyang, Xiaofang Wang, Xiaoli Liu, Li Yang and Xiaojuan Feng	
<b>Study on Properties of Magenta Water-Based Flexo Ink Used on BOPP Film</b> . . . . .	949
Yang Liu, Beiqing Huang, Xianfu Wei and Ying Shen	
<b>Preparation of Acrylate Latex via RAFT Soap-Free Emulsion Polymerization</b> . . . . .	959
Weiwei Liu, Zhi Qiao, Jinqiang Tu, Xiaoyu Li and Haiqiao Wang	
<b>Effect of Defoamer on the Performance of Plastic Water-Based Flexographic Ink</b> . . . . .	967
Xiaoli Liu, Yun Ouyang, Xiaofang Wang, Zhiyong Sun, Xue Gao and Yanchao Yu	
<b>Research on the Performance Optimization of Silver Water-Based Gravure Ink</b> . . . . .	975
Tengfei Zhou, Beiqing Huang, Xihao Li and Xianfu Wei	

## Part VIII Paper and Related Technology

- Revealing the Components at Work in Classical Liquid Imbibition Models: Inertial, Bosanquet and Viscous Lucas-Washburn Applied to Printing** . . . . . 987  
Guodong Liu, Xinya Zhang, Meiyun Zhang and Patrick Gane
- Effect of Main Composition of Dissolving Pulp on Its Reactivity** . . . . . 997  
Wei Liu, Guangxue Chen and Siwang Li
- Study on the Antistatic Coating Technology and Coated Paperboard Performance** . . . . . 1005  
Qinghua Gao, Junyan Huang, Shangjie Jiang and Huizhong Zhang
- Influence of Silica Pigments with Different Sizes on the Performances of Coated Ink-Jet Printing Paper** . . . . . 1015  
Xu Liu, Yunzhi Chen and Zhengjian Zhang
- Study on the Neutral Deinking Technology of Old Digital Printing Paper (ODP)** . . . . . 1021  
Longkang Cong, Xiaolin Zhang, Liu Shi and Xiangsheng Deng

## Part IX Film and Related Material Technology

- Preparation and Properties of Nano Zinc Oxide/Poly Lactic Acid Antibacterial Packaging Films** . . . . . 1029  
Xing Yin, Cheng Sun, Zhiqiang Gao and Li Xue
- Barrier Mechanism Analysis of Silicon Oxide Film by SEM** . . . . . 1039  
Lihua Zhu, Yan Li, Wensi Liang, Jun Wu, Yunjin Sun and Yun Ouyang
- Preparation and Characterization of Cellulose Gel Films** . . . . . 1045  
Junran Li, Xiaojun Ma, Yunfei Wang and Xuejiao Zhang
- Preparation and Research of POSS Modified PLLA Films: Mechanical Properties** . . . . . 1053  
Xiaohui Zhang and Feiyan Zheng
- Preparation and DSC Analysis of  $\gamma$ -Poly Glutamic Acid Ester** . . . . . 1061  
Wei Xiao, Zhihui Sun, Fengqing Wang and Jing Dong
- Application of Anti-static Release Coating in Packaging Film** . . . . . 1067  
Jichao Huang, Shenghong Chen, Chengzhi Li, Chunxiu He and Yun Xiang
- Edible Coating Packaging and Its Preservation Effect to Cherry Tomatoes** . . . . . 1075  
Liya Zhou, Junyan Huang, Hao Xing, Qinghua Gao, Yaoqi Li and Xiaomin Li



## **Part X Novel Functional Material Technology**

<b>Highly Sensitive Flexible Pressure Sensor with Microstructural Dielectric Layer</b> . . . . .	1087
Zhengbo Li, Lianfang Li, Lixin Mo, Zhenguo Wang, Wei Yang, Hui Zhou, Haichao Zhang and Luhai Li	
<b>Hydrophilic Modification and Characterization of Bagasse Cellulose</b> . . . . .	1095
Tingli Liu and Guangxue Chen	
<b>Synthesis of 2-Allyloxy-3, 6, 7, 10, 11-Pentabutoxytriphenylene and Its Mesophases Study</b> . . . . .	1103
Wanying Zhang, Xingtian Hao, Feng Hong, Jianchuang Wang, Shuaifeng Zhang, Chunxiu Zhang and Jialing Pu	
<b>Research on the Preparation of Silver Nanoparticles by Chemical Reduction Method</b> . . . . .	1109
Yanxiang Li and Fuqiang Chu	
<b>Optical Emission Spectroscopy Diagnostics of HMDSO/O<sub>2</sub> Magnetized Plasma</b> . . . . .	1115
Zhonghua Bian, Xinyue Wang, Yunjin Sun and Qiang Chen	
<b>Experimental Analysis of the Effect of Vacuum Degassing Technology on the Solventless Laminating Adhesive Performance</b> . . . . .	1123
Hongwei Xu, Xusheng Wang, Ruining Lei, Xuhong Chen and Donghong Liu	
<b>Effect of Monomer and Promoter on UV-LED Varnish Performance</b> . . . . .	1131
Xiaoli Li, Shiyong Luo and Wencai Xu	
<b>Study of Printability of Hybrid Light Curable Material Used in 3D Printing—Product Flexographic Plate</b> . . . . .	1139
Beiqing Huang, Xiaoyue Shang, Yiran Li, Xianfu Wei and Changlong Guo	
<b>Discussing the Preparation Conditions of Graphene</b> . . . . .	1155
Xiaotong Xiong, Beiqing Huang and Xianfu Wei	
<b>Study on the UV Curing Molding Material in 3D Printing Modification of Expanding Monomer</b> . . . . .	1163
Lu Zhang, Beiqing Huang and Xianfu Wei	
<b>Preparation of Branched Polymers Using a Polymerizable RAFT Agent</b> . . . . .	1171
Guiyu Ma, Zhongxiao Li, Yingqun Qi and Ti Wu	

**Part I**  
**Color Science and Technology**

# Test Criteria and Investigation of Uniform Color Spaces to Meet the Requirements of Future Imagery

Muhammad Safdar and Ming Ronnier Luo

**Abstract** The television and cinema industry has grown very rapidly during last few years and future displays will likely be able to cover high dynamic range (HDR) and wide color gamut (WCG). A uniform color space is desired that is suitable not only for efficient quantization but also for color volume mapping in HDR and WCG environment. A design goal for the next generation display is Rec.2020 which is the minimum requirement for future video encoding. There are a number of aspects which must be considered while developing a color space in order to meet the requirements of future imagery. Current study lists eight different criterions to test the ability of a color space to meet these requirements. After defining the testing criteria, this study investigated four different color spaces including CIELAB, CAM16-UCS, ICaCb, and recently proposed zICaCb. Results showed that zICaCb outperformed other spaces tested for most of the measures and gave similar performance for others.

**Keywords** Color spaces · CIELAB · CAM16-UCS · ICaCb · zICaCb

## 1 Introduction

Many researchers have proposed different perceptually uniform color spaces for color image encoding. Such approaches target image encoding using a minimum number of code values without introducing visible quantization artifacts or loss of

---

M. Safdar · M.R. Luo (✉)  
State Key Laboratory of Modern Optical Instrumentation, Zhejiang University,  
Hangzhou, China  
e-mail: m.r.luo@zju.edu.cn

M. Safdar  
Department of Computer Science, COMSATS Institute of Information Technology,  
Sahiwal, Pakistan

M.R. Luo  
School of Design, University of Leeds, Leeds, UK

image details. To encode high quality images, a color space is needed which can cover high dynamic range (HDR) and wide color gamut (WCG), and should at least meet requirements of Rec.2020 [1, 2]. The selected color space should be suitable for color image processing such as blending, fading, chroma sub-sampling, and resizing quickly, and with minimal error. It is desirable to transmit video signals in an encoding color space that is not only suitable for efficient image encoding but also for tone and gamut mapping often referred to as color volume mapping. As the volume of color essence increases, color transformations become more costly. This paper defines comprehensive testing criteria for a color space to meet the requirements of future imagery and offers minimal computational cost.

Current study considered four perceptually uniform color spaces including CIELAB, CAM16-UCS (a revision of CAM02-UCS) [3, 4], ICaCb [5], and zICaCb [6]. All these color spaces are based on device independent CIE XYZ tristimulus space. The CIELAB is a CIE recommended uniform color space and CAM16-UCS is uniform color space based on CAM16 color appearance model (a revision of CIECAM02 with similar performance) [3, 4]. The CIELAB and CAM02-UCS (previous version of CAM16-UCS) have been tested for typical dynamic range [7, 8]. They need to be further investigated to investigate how good they meet the requirements for high dynamic range and wide color gamut imagery. Froehlich et al. [5] proposed a color space with simple structure named ICaCb for HDR and WCG color difference signals. Safdar and Luo [6] refined ICaCb and proposed new zICaCb (optimized using more reliable datasets). Current study compared the performance of the mentioned four color spaces after defining comprehensive test criteria.

The next section of this paper will explain the criteria for testing a color space in different aspects. Then the test results for selected four color spaces will be presented. Conclusions will be drawn in the end.

## 2 Defining Test Criteria

In this section we define the criteria for testing a color space if it meets the requirements of HDR and WCG color difference applications and is suitable for image processing work flows. Following criterions should be met by the selected model for future imagery.

- I. **Local Uniformity:** The major goal of image encoding is to assign least number of digital code words required to prevent visible quantization artifacts or distortions in an image. The best encoding performance is typically achieved when quantization error is distributed perceptually evenly over the color space. Ideally, the color discrimination ellipses should turn out to be circles for a locally uniform color space.
- II. **Global Uniformity:** For a globally uniform color space, all the color discrimination ellipses should appear to be of equal size.

- III. **High Dynamic Range:** Selected color space should support large variance of luminance according to requirements of high dynamic range imagery. A consumer study using an HDR display in a dark viewing environment identified that a dynamic range of 0.005–10,000 cd/m<sup>2</sup> is required to satisfy 90% of the total number of viewers [1].
- IV. **Wide Color Gamut:** Selected color space should support wide color gamut representing specifications of future displays. A design goal for the gamut of next generation displays is Rec.2020.
- V. **Hue Linearity:** The selected color space should be hue-linear i.e. the iso-hue colors should fit in a linear line.
- VI. **Neutral Point Convergence:** The unique hue (red, green, yellow, blue) lines should converge at a single neutral point (locus).
- VII. **Neutral Point (Locus) Error:** A neutral color should remain neutral while mapping the color volume. The locus should be at the origin of red-green and yellow-blue planes otherwise hue calculations in that color space will be erroneous.
- VIII. **Computational Cost:** Finally, the transformation complexity should be as minimum as possible to allow mass deployment of the selected color space in a wide range of applications.

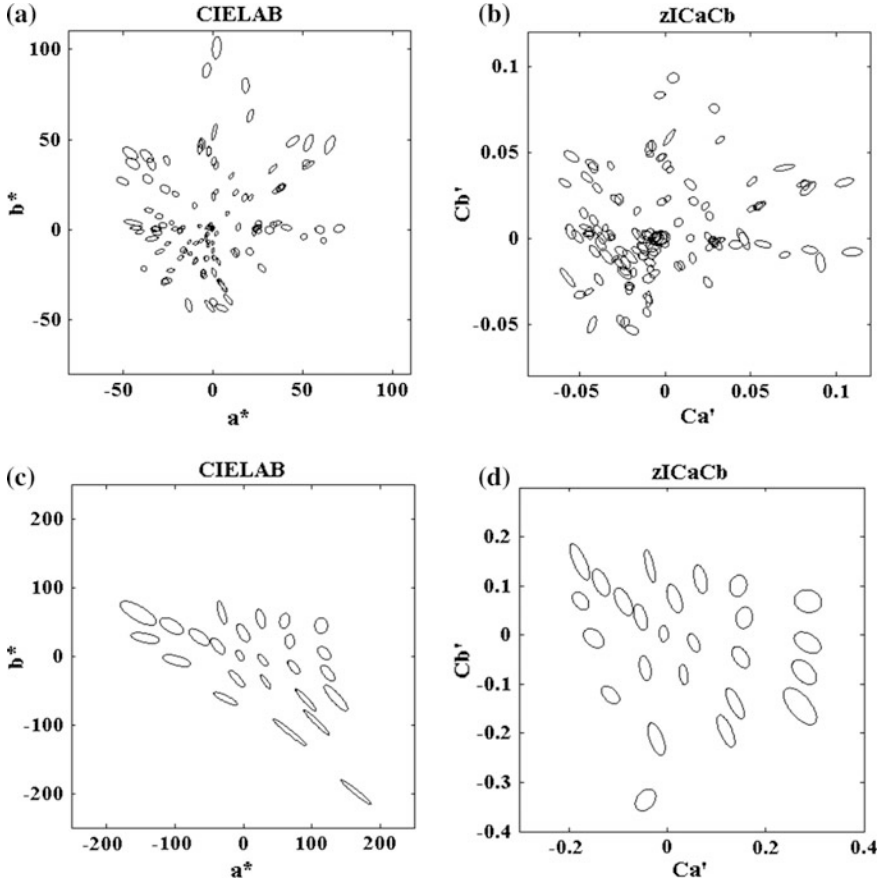
### 3 Test Results

Color space uniformity was tested using BFD and RIT-DuPont color discrimination data (previously used to develop CIEDE2000 color difference formula [9]) for surface colors and MacAdam just-noticeable-difference (JND) data [10]. Hung and Berns [11] collected iso-hue data with 12 different hues and constant luminance. This data was used for hue linearity test and will hereafter be called H&B-CL data. Xiao et al. [12] conducted visual experiments to judge unique hues (unique red (UR), unique green (UG), unique yellow (UY), and unique blue (UB)) for various different values of luminance, and chroma assessed by 185 observers and each observer repeated three times. This data set was used to test hue linearity, neutral point convergence, and neutral point error, and will hereafter be called Xiao-UH data. The uniformity, hue linearity, and neutral point (locus) error were tested using measures including standardized residual sum of squares (STRESS), hue linearity coefficient (HLC) [6], and color difference (in units of CIEDE2000) between origin (0,0) and locus, respectively as given in Table 1 (best values are underlined). The neutral point convergence can be observed from plots of hue linear lines (see later).

To test color spaces for encoding capability of high dynamic range and wide gamut signals, and computational cost, a gamut hull was generated for Rec.2020 with a dynamic range of 0.005–10,000 cd/m<sup>2</sup> and gamma of 2.8. The Rec.2020 RGB space was transformed to each test color space and CPU time was recorded. It was found that all the selected color spaces can encode Rec.2020 signals with HDR

**Table 1** Test results of four color spaces for uniformity (average of local and global), average hue linearity, neutral point (locus) error, and computational cost

Color spaces	Uniformity (STRESS)	Hue Lin. (HLC)	Locus error ( $\Delta E_{00}$ )	CPU time (millisecond)
CIELAB	50	9.2	2.3	<u>30</u>
CAM16-UCS	39	12.5	6.6	122
ICaCb	42	9.2	6.8	35
zICaCb	<u>36</u>	<u>8.3</u>	<u>1.2</u>	36

**Fig. 1** Color discrimination ellipses plotted using BFD&RIT-DuPont data; **a** CIELAB and **b** zICaCb, and MacAdam data (10 times amplified ellipses); **c** CIELAB and **d** zICaCb

and WCG color differences. The total computational cost for ten conversions is also given in Table 1. Table 1 shows that CIELAB costs minimum computational complexity while ICaCb and zICaCb have similar complexity and not significantly different compared with CIELAB. The CAM16-UCS proved to be significantly expensive in terms of computational cost.

The color discrimination ellipses were plotted for color spaces which gave either best or worst performance to visually observe uniformity. Ellipse plots using BFD&RIT-DuPont data for CIELAB (worst) and zICaCb (best) are shown in Fig. 1a, b, respectively. While ellipse plots using MacAdam data for CIELAB and zICaCb are shown in Fig. 1c, d, respectively.

The unique hue lines plotted using Xiao-UH data for CAM16-UCS (worst) and zICaCb (best) are shown in Fig. 2a, b, respectively. While the iso-hue lines plotted using H&B-CL data for CAM16-UCS and zICaCb are shown in Fig. 2c, d, respectively. Figure 2b also shows that, for zICaCb color space, four unique hue lines converge at single point and very close to origin [with color difference of 1.2 in CIEDE2000 units (see Table 1)].

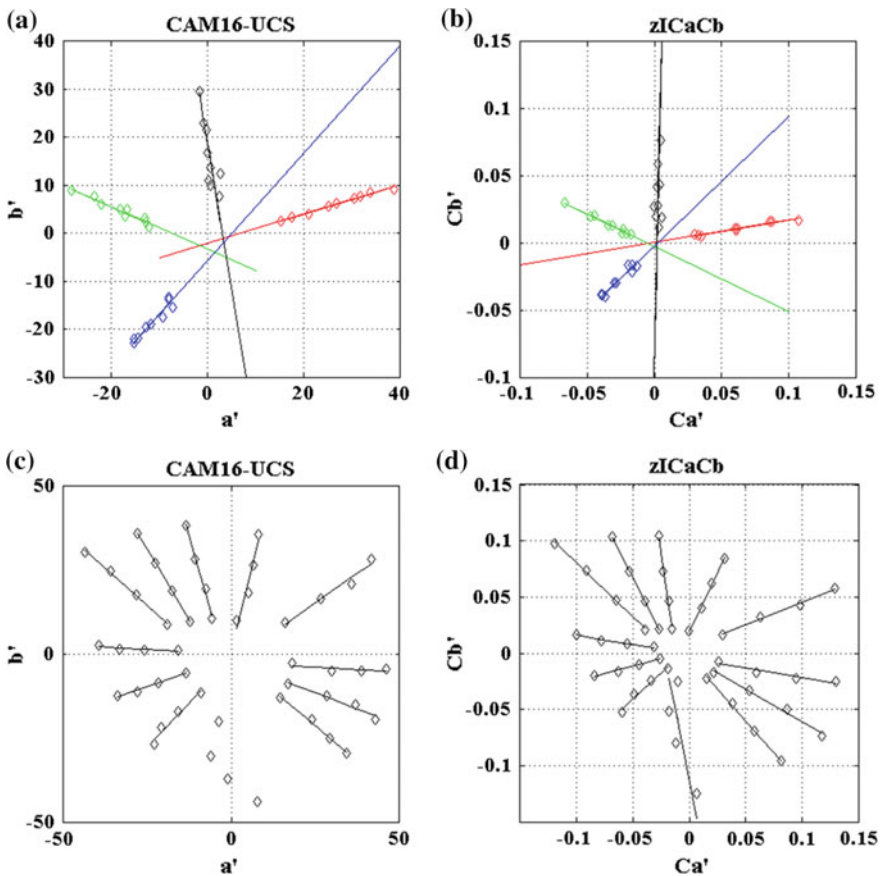


Fig. 2 Iso-hue lines plotted using Xiao-UH data; a CAM16-UCS and b zICaCb, and using H&B-CL data; c CAM16-UCS and d zICaCb

## 4 Conclusions

Four different uniform color spaces including CIELAB, CAM16-UCS, ICaCb, and zICaCb were tested for high dynamic range and wide color gamut imagery. Results showed that all selected color spaces can encode HDR and WCG signals and zICaCb outperformed other color spaces for uniformity, hue linearity, and neutral point error. The computational cost of CIELAB was found minimum and very similar values were found for ICaCb and zICaCb. The CAM16-UCS was ranked second for uniformity but performed worst for hue linearity and computational cost. Hence, zICaCb could be recommended as an encoding space for high dynamic range and wide gamut color difference applications.

## References

1. Daly, S., Kunkel, T., Sun, X., Farrell, S., Crum, P. (2013). Preference limits of the visual dynamic range for ultra-high quality and aesthetic conveyance. In *Proceeding of Electronic Imaging*, Burlingame, CA, USA, (IS&T/SPIE 2013).
2. International Telecommunication Union (ITU), Recommendation ITU-R BT.2020-1. Parameter values for ultra-high definition television systems for production and international programme exchange. Geneva, Switzerland, 2014.
3. Li, C. J., Li, Z., Wang, Z., Xu, Y., Luo, M. R., Cui, G., Melgosa, M., Pointer, M. (2016). A Revision of CIECAM02 and its CAT and UCS. In *Proceedings of 24th Color and Imaging Conference*, San Diego, USA (IS&T 2016).
4. Luo, M. R., Cui, G., & Li, C. (2006). Uniform Colour Spaces based on CIECAM02 Colour Appearance Model. *Col. Res. App.* 31(4), 320–330.
5. Froehlich, J., Kunkel, T., Atkins, R., Pytlarz, J., Daly, S., Schilling, A., Eberhardt, B. (2015). Encoding Color Difference Signals for High Dynamic Range and Wide Gamut Imagery. In *Proceedings of 23rd Color and Imaging Conference*, Darmstadt, Germany (IS&T 2015).
6. Safdar, M., Luo, M. R. (2016). Investigating Performance of Uniform Color Spaces for High Dynamic Range and Wide Gamut Color Difference Applications. In *Proceedings of 24th Color and Imaging Conference*, San Diego, USA (IS&T 2016).
7. Safdar, M., Luo, M. R., & Liu, X. Y. (2015). Improvement of JPEG for the Color Images by Incorporation of CAM02-UCS and Cubic Spline Interpolation. *App. Mech. and Mater.* 70, 7–12.
8. Safdar, M., Luo, M. R., & Liu, X. Y. (2015). Performance Evaluation of JPEG, JPEG2000 and New CSI-JPEG Algorithms by Incorporating Different Color Spaces. In *Proceedings of 23rd Color and Imaging Conference*, Darmstadt, Germany (IS&T 2015).
9. Luo, M. R., Cui, G., Rigg, B. (2000). Development of CIE 2000 Color Difference Formula: CIEDE2000. *Col. Res. App.* 53(1), 340–350.
10. MacAdam, D. L. (1942). Visual Sensitivities to Color Differences in Daylight. *J. of the Opt. Soc. of Am.* 32(5), 247–273.
11. Hung, P. C., Berns, R. S. (1995). Determination of Constant Hue Loci for a CRT Gamut and Their Predictions using Color Appearance spaces. *Col. Res. App.* 20(5), 285–295.
12. Xiao, K., Wuerger, S., Fu, C., & Karatzas, D. (2011). Unique hue colour appearance models. Part I: Loci of unique hues and hue uniformity. *Col. Res. App.* 16(5), 316–323.



# Image Colorization Method Using Texture Descriptors and ISLIC Segmentation

Liqin Cao, Lei Jiao and Zhijiang Li

**Abstract** We present a new colorization method to assign color to a grayscale image based on a reference color image using texture descriptors and Improved Simple Linear Iterative Clustering (ISLIC). Firstly, the pixels of images are classified using Support Vector Machine (SVM) according to texture descriptors, mean luminance, entropy, homogeneity, correlation, and local binary pattern (LBP) features. Then, the grayscale image and the color image are segmented into superpixels, which are obtained by ISLIC to produce more uniform and regularly shaped superpixels than those obtained by SLIC, and the classified images are further post-processed combined with superpixels for removing erroneous classifications. Thereafter, each pixel of the grayscale image is assigned with a color obtained from the color image following a predefined matching metric based on the superpixels and the classes. Experimental results show that our proposed approach is effective and has a better colorization in naturalness compared with Welsh algorithm and unimproved SLIC strategy method.

**Keywords** Color transfer · Improved SLIC · Texture descriptors

## 1 Introduction

Colorization is a crucial technique by adding color to grayscale content. It is very useful for obtaining rich information from classic movies and monochrome photographs and images. A traditional category of colorization methods requires manually operation to add colors to grayscale images. On the contrary, another

---

L. Cao (✉) · Z. Li  
School of Printing and Packaging, Wuhan University, Wuhan, Hubei, China  
e-mail: clq@whu.edu.cn

L. Jiao  
Department of Information and Communication Technology,  
University of Agder, Grimstad, Norway

colorization approaches consist in transferring color from a pre-selected color image as a reference, which are called Exemplar-Based Methods [1].

Most of exemplar-based colorization approaches assume that the target grayscale pixels should be assigned to the color from reference color pixels which have similar intensities or similar neighborhood. Welsh et al. proposed a colorization technique, which relies only on matching the luminance values that is calculated by averaging its neighborhood pixels in the target image to those in the reference image, and transferring color accordingly [2]. However, mismatching may appear in difference region of the color image though the correspondences are with the same luminance value and similar neighborhood statistical characteristics. Therefore, some methods take account to the higher-level content of each pixel in addition to luminance. For, example, Irony et al. used a classification image obtained by supervised classifier and texture features to achieve convincing colorization [3]. Charpiat et al. exploited feature descriptors using Speeded Up Robust Features (SURF) incorporated into a probability estimation model to achieve colorization [4]. Gupta et al. presented a method that is employed a cascade feature matching scheme to seek matching pixels between grayscale and color images [5]. To summarize, the main underlying idea of these exemplar-based approaches is to find the best corresponding pixel (region) between the reference image and the target image, and to transfer the color accurately.

In this paper, we propose a new approach for example-based image colorization. To determine correspondences between reference image and target image, a series of statistical descriptors and a segmentation algorithm are employed. The main stages include classification and color transfer. The closest scheme of classification to our method is the approach of Irony et al. [3], which exploits K-nearest-neighbor (Knn) and linear discriminant analysis (LDA) with manually marked segmentation regions of reference images. In contrast to [3], we use SVM classifier based on statistical texture descriptors and SLIC segmentation to achieve classification images without manually marked regions. Meanwhile, we take the advantage of ISLIC to obtain the classification with more accuracy and more spatial consistency than that of SLIC.

The remaining of this paper is organized as follows. Section 2 describes the related techniques of our colorization solution in detail. Experimental results and analysis are shown in Sect. 3 before conclusions are given in Sect. 4.

## 2 Colorization by Example

### 2.1 Feature Space and Classifier

**Luminance:** Luminance is useful feature to provide information to guide correspondences, which has been demonstrated by Welsh et al. [2]. In this paper, the mean luminance of the grayscale image and that of the color image are utilized as a descriptor.

Entropy, homogeneity, correlation: the Gray Level Co-occurrence Matrix (GLCM) is an effective method to extract second order statistical texture features which can help to characterise the local structure in the scene. There are 14 features computed based on GLCM. According to them, entropy, homogeneity, correlation are uncorrelated and can be available for obtaining high classification accuracy. Entropy reflects the homogeneity for scenes. Homogeneity, called Angular Second Moment (ASM), is to describe homogeneity of an image. Correlation is to measure dependence between the pixels at the specified position relative to each other. Those three features are employed in our work.

LBP feature: Different from the GLCM method that is greatly restricted by image scale, “uniform” LBP is an operator which is defined by invariant against any monotonic transformation for arbitrary quantization of angular space and spatial of the gray scale. It is a very formidable tool to analyze rotation invariant texture [6], and is also effectively used for image classification.

SVM: Once the feature space has been computed by label vectors, the supervised learning models are used for classification and regression analysis. SVM is an efficient and robust classifier with associated learning algorithms that analyze data to classify. It can perform linear and non-linear classification. The latter category, called kernel trick, can implicitly map the inputs into high dimensional feature spaces using kernel trick and achieve good classifications. In this paper, the SVM classifier is employed for naive classification and a radial basis kernel function is utilized.

## 2.2 Superpixels Extraction

Applying the SVM classifier for pixel-level may still lead to many non-discriminating and erroneous classifications. To avoid those misclassified pixels and to improve the efficiency of the classifier, the segmentation images are employed. Image segments are computed by superpixels that maintain strong spatial coherency to ensure the consistency of adjacent classification pixels.

SLIC is a simple and efficient segmentation approach, which produces a relatively regular lattice and possesses low computational complexity [7, 8]. In the SLIC method, the local K-means clustering based on the color and spatial distances is performed to extract superpixels. However, some small and isolated segments are generated because the number of superpixels is fixed.

To obtain relatively coherent superpixels and avoid over-segmentation of large homogeneous regions, the Sigma filter is employed to update the cluster centers which are calculated by only the pixels with the similar luminance values at the original center [8]:

$$\varphi_j = \frac{1}{N} \sum_{i \in \Omega_j} \begin{bmatrix} C_i \\ S_i \end{bmatrix}, \quad (1)$$

$$\mathbf{\Omega}_j = (\|L_i - L_j\| < \alpha * \sigma_j) \cap \mathbf{G}_j, \quad (2)$$

where  $C_i$  and  $S_i$  represent the value of the  $j$ th cluster's color space and the centred location respectively.  $N$  is the number of pixels in  $\mathbf{\Omega}_j$ , which is a subset of the  $j$ th cluster and can be calculated in (2).  $L_i$  and  $L_j$  are the luminance value of pixel  $i$  and the mean luminance value of the  $j$ th cluster respectively.  $\sigma_j$  is the standard deviation of the luminance of all the pixels in the  $j$ th cluster  $\mathbf{G}_j$  and  $\alpha$  is a constant.

After iterative clustering, the obtained superpixels are further processed to produce a set of homogeneous segments  $S_{seg}$ . The neighbour superpixels with similar statistical characteristics are merged to form larger segments as follow:

$$s_i = s_i \cup s_j \mid \varepsilon < T, \quad (3)$$

$$\varepsilon = \sqrt{(\mu_i - \mu_j)^2 + (\sigma_i - \sigma_j)^2}, \quad (4)$$

$$T = \beta * \sigma_i, \quad (5)$$

where  $\mu_i$  and  $\mu_j$ , represent the mean luminance of the segments  $s_i$  and  $s_j$  respectively.  $\beta$  is a defined threshold.

In our work, we use the  $\alpha\beta$  color space to segment image. Then, post-classifying is processed based on a small neighbourhood around each pixel in superpixels. It is assumed that (1) the centre pixel belongs to the class that all of the adjacent pixels belong to; (2) all the pixels in a superpixel are in the same class if 85% of the pixels in this superpixel belong to the same class.

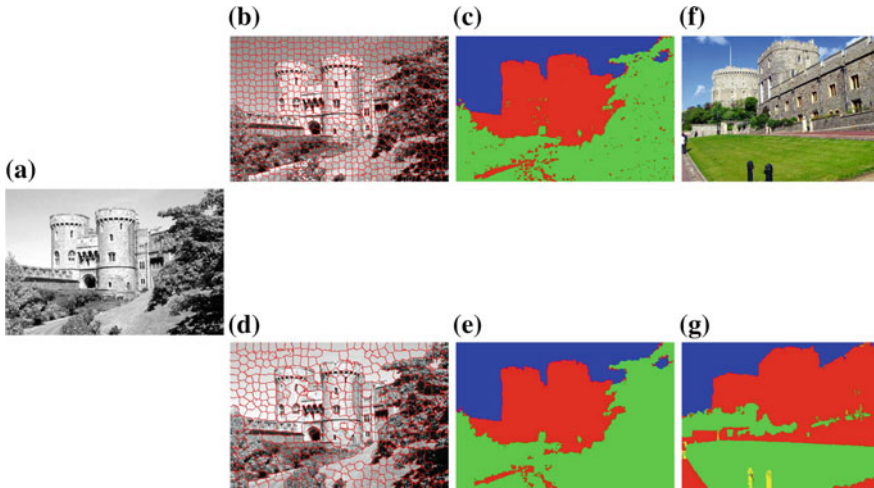
### 2.3 Feature Matching and Color Mapping

For each target superpixel, we can seek a cross all reference superpixels combined with all features to find the corresponding superpixel which is most similar to the target one. Here, the candidate pixels in the matching superpixels must be in the same class according to the result of classification.

By this constricted condition, the most appropriate matching pixel can be found in the reference image. Using the matching pixel, color can be borrowed from the reference to the target image. The color mapping processing is the same as the method proposed by Welsh et al. [2].

## 3 Colorization Evaluations

Figure 1 illustrates the process of classification. The number of initialization superpixels is configured as 800, and  $\alpha = 0.8$ ,  $\beta = 0.8$  in our implementation.

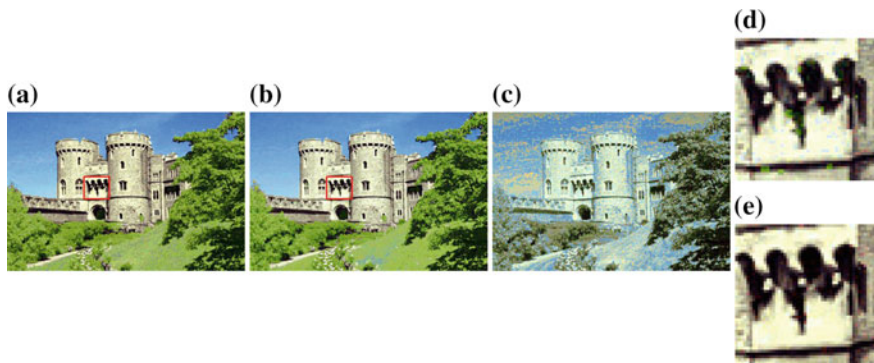


**Fig. 1** Classification on **a** target image and **f** reference image; **b** and **d** superpixels by SLIC and ISLIC; **c** and **e** classifications combined with SVM classifier and superpixels based on SLIC and ISLIC; **g** classification of reference image based on our method

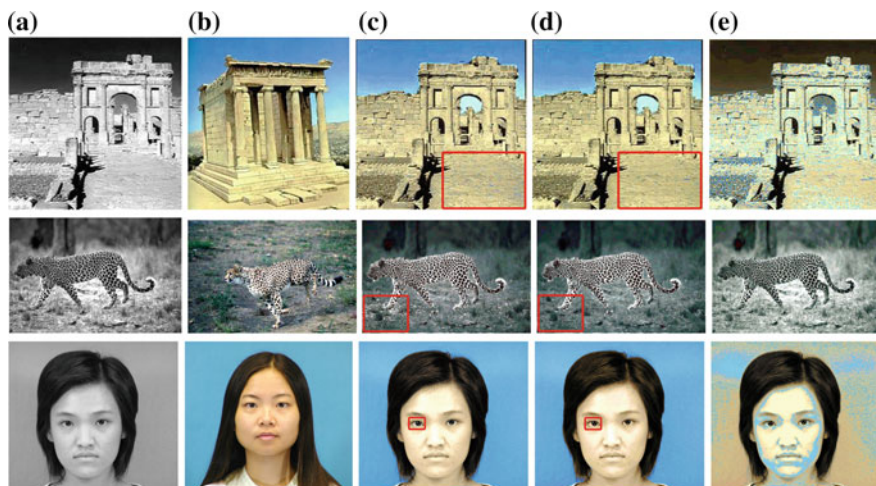
Clearly the naive SVM classifier combined with SLIC segmentation still leads to many erroneous classifications as shown in Fig. 1c. For example, some vegetation and building pixels are failed to discriminate. Classification through post-processing by ISLIC segmentation in Fig. 1e demonstrates a greatly improved result since most of the adjacent pixels in each superpixel are labeled to the same class. Figure 1g also shows a satisfactory classification result of the reference image based on our technique. Those results can provide accurate matching superpixels and classes between target and reference images.

After seeking colors using above segmentations and classifications, the final results after color transferring are obtain as shown in Fig. 2. We compare the colorization results of our method with that of the unimproved SLIC strategy and that of the approach proposed by Welsh et al. Due to the complexity of the image, the method by Welsh et al. yield uncorrected color in most regions shown in Fig. 2c since it is based only on direct luminance intensity matching. The methods for Fig. 2a, b produce comparable good results with successful mapping and colorization. However, there are some mistakes colorization in Fig. 2d which is based on unimproved method because of misclassification and mismatching. Improved colorization result in spatially continuity and consistency achieved by our approach is shown in Fig. 2e. It implies that our method has an advantage in creating spatially coherent color.

Figure 3 shows more results of colorization for different scenes. The human images are downloaded from the website for FDDB [9] (<http://tamaraberg.com/faceDataset/>). It can be observed that combining both texture descriptors and superpixels results in good performance on colorization. Compared with post-processing classification based on SLIC, our approach produces more robust

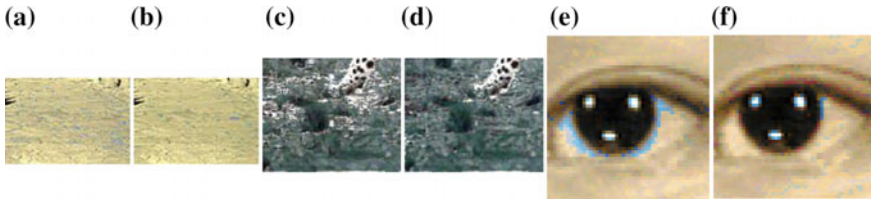


**Fig. 2** Colorization results obtained by **a** texture descriptors + SLIC classification and **b** texture descriptors classification + ISLIC, **c** Welsh et al. method. **d** and **e** are the details information of *red rectangle* in **a** and **b**



**Fig. 3** Comparison with different colorization methods. **a** Grayscale images; **b** color images; **c**, **d** colorization obtained by texture descriptors + SLIC and texture descriptors + ISLIC; **e** colorization obtained based on Welsh et al. method

colorization. The details in red rectangle in Fig. 3c, d are demonstrated in Fig. 4. They clearly show that the resulted colorization of our method explicitly enforces spatial coherency. However, in some complex regions, our method also fails to transfer exact color information, such as the right forefeet of the tiger in Fig. 3d. The pixels are inaccurate at object boundaries or at thin image structures, which also result in incorrectly assigning colors. For example, the boundaries of the woman's eye in Fig. 4f take color from the background of the picture. The reason is that the categories of these pixels are difficult to discriminate based on the space features that we choose.



**Fig. 4** Details of colorization results in *red rectangle area*. **a, c and e** Colorization obtained by texture descriptors + SLIC; **b, d and f** colorization obtained by texture descriptors + ISLIC

## 4 Conclusions

In this paper, we presented a new method for colorization grayscale images. This method exploits texture descriptors and segments images based on ISLIC to seek correspondences and to achieve colorize. Experimental results illustrate that our method develop perceptually appealing colorizations. Additionally, comparisons among unimproved SLIC method and Welsh et al's method demonstrate that our method is more effective in colorization.

**Acknowledgements** This study is funded by National Natural Science Foundation of China (41201449).

## References

1. Bugeau, A., Ta, V. T., Papadakis, N. (2014): Variational exemplar-based image colorization. *IEEE Transactions on Image Processing*, 23(1), 298–307
2. Welsh, T., Ashikhmin, M., Mueller, K. (2002): Transferring color to greyscale images. *ACM Transactions on Graphics (TOG)*, 21(3), 277–280
3. Irony, R., Cohen-Or, D., Lischinski, D. (2005): Colorization by example. In: *Proceedings of the 16th Eurographics Conference on Rendering Techniques*, pp. 201–210. Eurographics Association Aire-la-Ville Press, Switzerland
4. Charpiat, G., Hofmann, M., Schölkopf, B. (2008): Automatic image colorization via multi-modal predictions. In: *10th European Conference on Computer Vision*, pp. 126–139. Springer Berlin Heidelberg Marseille, Marseille, France
5. Gupta, R.K., Chia, A.Y.S., Rajan, D., Ng, E.S., Huang, Z.Y. (2012): Image colorization using similar images. In: *Proceedings of the 20th ACM International Conference on Multimedia*, pp. 369–378. ACM New York Press, Nara, Japan
6. Ojala, T., Pietikäinen, M. Mäenpää, T. (2002): Multiresolution gray-scale and rotation invariant texture classification with local binary patterns. *IEEE Transactions on Pattern Analysis and Machine Intelligence*, 24(7), 971–987
7. Achanta, R., Shaji, A., Smith, K., Lucchi, A., Süsstrunk, S. (2012): Slic superpixels compared to state-of-the-art superpixel methods. *IEEE Transactions on Pattern Analysis and Machine Intelligence*, 34(11), 2274–2281
8. Kim, K.S., Zhang, D., Kang, M.C., Ko, S.J. (2013): Improved simple linear iterative clustering superpixels. In: *IEEE International Symposium on Consumer Electron*, pp. 259–260. Hsinchu, Taiwan
9. Jain, V., Learned-Miller, E. (2010): Fddb: A benchmark for face detection in unconstrained settings. Technical Report UMCS-2010–009. University of Massachusetts, Amherst

# Study on Spectral Reconstruction Based on Sample Optimization Method of Color Digital Camera

Zhaoyang Jia and Guangxue Chen

**Abstract** According to the nonlinear characteristics of color digital camera imaging system, spectral reflectance reconstruction by the response values of color digital camera had been studied through the method of combining principal component analysis method with polynomial model under given conditions of illumination and observation environment. Sample optimization method selected standard color card sample as training sample which was similar to reconstruction of chroma space and broad representativeness in spectral space. It could avoid usual “over-fitting” problem brought by excessive samples in regression and could reconstruct spectral reflectance of object surface accurately. The results showed that polynomial model can simulate the nonlinear relationship accurately between the camera response and the coefficient vector obtained from the principal component analysis and the sample optimization could make full use of sample information so that the accuracy and stability of the regression function improved. The mean of RMSE of ColorChecker SG was 0.0247 and the average CIE DE2000 was 2.5123, the spectral and chroma accuracy have improved greatly compared with traditional algorithm.

**Keywords** Sample optimization · Spectral reconstruction · Multispectral image · Polynomial model

---

Z. Jia · G. Chen (✉)  
State Key Laboratory of Pulp and Paper Engineering, South China  
University of Technology, Guangzhou, China  
e-mail: chengx@scut.edu.cn

Z. Jia  
e-mail: fire\_y@tust.edu.cn

Z. Jia  
College of Packaging and Printing Engineering, Tianjin University of  
Science and Technology, Tianjin, China



## 1 Introduction

With the development of the color reproduction technology, people demand more and more accuracy on reproduction of color; broadband multispectral image acquisition technology can record the spectral reflectance of objects accurately and achieve the true color reproduction. Achieving the digital image through color digital camera is the most direct and effective way currently, and it can shoot the surface of the object of non-contact under the complex light. Therefore, it is the research hotspot based on digital camera multispectral image acquisition and spectral reflectance reconstruction in the field of color science currently.

Predecessors' studies on the spectral reconstruction have put forward many shaping algorithms, such as Wiener estimation [1], the pseudo inverse method [2, 3], the finite dimension model [2, 4] and polynomial regression algorithm [4]. The selection methods of training samples include mainly Hardeberg method [5] and Cheung and Westland method [6], etc. Some of training samples are based on high dimensional spectral reflectance space, and others are based on chroma space. But each method only considered the spatial of spectral reflectance or chroma space, and has no comprehensive characteristics of both spectral reflectance space and chroma space. Therefore, spectral reconstruction precision is limited.

A method for combining principal component analysis with polynomial model was presented. The reconstruction results improved in removal of noise interference and improving the linearity. A method for spectral reflectance reconstruction based on sample optimization was also put forward. Sample optimization considers comprehensively the similarity of chroma space and broad representativeness of spectral spatial, and improves the accuracy of spectral reconstruction and chroma.

## 2 Basic Theory

### 2.1 *Spectral Reconstruction Model Based on Principal Component Analysis and Polynomial Model*

Spectral reflectance of natural object surface is continuous and can be represented as a linear combination of several basic vectors. Therefore, the spectral reflectance of the color can be reconstructed by a finite dimensional linear model, which can reduce the dimension of the prediction space effectively and reduce the complexity of the reconstruction process. The principal component analysis method can fully extract the spectral reflectance characteristics of the color samples, and it is typical representative of these methods and is applied to the reconstruction of the color spectrum of a variety of imaging devices successfully.

In practical application, it is generally believed that the spectral reflectance curve is smooth and spectral reflectance data set  $R_0$  of sample optimization can be expressed of linear combination of several main feature vectors  $F_0$  [7]. So the sample optimization spectral reflectance  $R_0$  can be expressed as:

$$R_0 = \sum_{i=1}^l e_i \alpha_i = F_0 \alpha_0 \quad (1)$$

where  $e_i$  is the feature vector,  $F_0$  is  $i$ -dimensional base vector of sample optimization,  $\alpha_0$  is the corresponding coefficient vector.

The relationship between response value of the camera and the coefficient vector  $\alpha_0$  can be obtained according to the polynomial principle [8]. Assuming that  $g_0$  represents a polynomial matrix which is consisting of  $N$  vectors  $[R_0 \ G_0 \ B_0]$ , then there is a matrix  $M$  that meets the following relationship:

$$\alpha_0 = M g_0 \quad (2)$$

The transformation matrix  $M$  can be obtained by the following formula based on the least square method:

$$M = \alpha_0 (g_0^T g_0)^{-1} g_0^T \quad (3)$$

$g_0$  is a polynomial model of the sample optimization camera response value. The transformation matrix will change when the number increasing of  $g_0$  items. Precision and items of polynomial model are closely related to its extension type.

Then the reconstructed spectral reflectance is:

$$\widehat{R} = \widehat{R}_0 g_0^+ g \quad (4)$$

where  $\widehat{R}$  is the spectral reflectance of sample to be reconstructed;  $\widehat{R}_0$  is the spectral reflectance estimation of sample optimization;  $g_0^+$  and  $g$  are pseudo inverse matrix of polynomial model of sample optimization camera response value and polynomial model of reconstructed sample camera response value.

## 2.2 Theory and Method on Sample Optimization

Spectral reflectance reconstruction by training samples is also known as the reconstruction method based on learning, which can make full use of sample optimization information, improve the accuracy and stability of the regression function, have better generalization performance, and avoid usual “over-fitting” problem in regression analysis brought by too many samples. So the training sample is an important factor to affect spectral reflectance reconstruction. Literature [9] demonstrated when training samples reach a certain amount for color order system with numerous samples. It will produce redundancy and the reconstruction results decrease if the color sample continues increasing. Therefore, we need optimize sample from all the samples, and make them present spectral spatial and chroma space characteristics.

In this paper, the principle of sample optimization is responding of characteristics of color order system by fewer samples, and has broad representativeness of spectral reflectance space and the similarity of chroma space. The optimized method and steps are as follows:

- (1) In Spectral reflectance space, training samples are correlated with one another as small as possible and we define them as the set of samples  $A = (\alpha_1, \alpha_2 \dots \alpha_n)$ . The first sample of set  $A$  selects modulus maximum of spectral reflectance vector and standard of selecting is minimum correlation matrix between the accession of each training vector spectral reflectance vector and the original set from second samples, then the  $n$ th selection of training sample satisfies the Eq. (5):

$$\frac{\omega_{\max}([R_{a_1}, R_{a_2}, \dots, R_{a_n}])}{\omega_{\min}([R_{a_1}, R_{a_2}, \dots, R_{a_n}])} \leq \frac{\omega_{\max}([R_{a_1}, R_{a_2}, \dots, R_{a_{n-1}}, R_i])}{\omega_{\min}([R_{a_1}, R_{a_2}, \dots, R_{a_{n-1}}, R_i])} \quad (5)$$

$$1 \leq i \leq T, \quad i \notin \{a_1, a_2, \dots, a_{n-1}\}$$

- (2) We do cluster according to the K-means clustering method in chroma space of *CIELAB* with the  $i$  classification initial point of condensation which is chroma coordinate  $(L^*, a^*, b^*)$  of  $\alpha_i$  in set  $A$ , because difference between samples could be distinguished with Euclidean distance in uniform chroma space. After clustering, each subset is clustering samples with similar characteristics, and could reflect the specific chroma space features.
- (3) Clustering center was calculated for each class, and then sample optimization set is the nearest cluster center sample of each cluster in color order system according to the clustering results.

Sample optimization according to above-mentioned method is clustering result for color order system samples in chroma space. Clustering center can represent the main characteristics information of such class according to the similarity theory, so it has the maximum effect on spectral reflection reconstruction if the sample is the nearest to cluster center.

### 3 Experiments and Result Analysis

In the experiment, we used GTI MiniMatcher standard light box and D65 standard light source; Nikon D7000 digital camera, ColorChecker SG standard color card (abbreviation for SG card) 140 colors; RAW format; recorded RGB value of SG card. It shot the dark current image after obtaining the each image through closing the shutter. Spectral reflectance of SG color card has been measured under the field of  $2^\circ$  view, D65 light source by the Spectrolino.

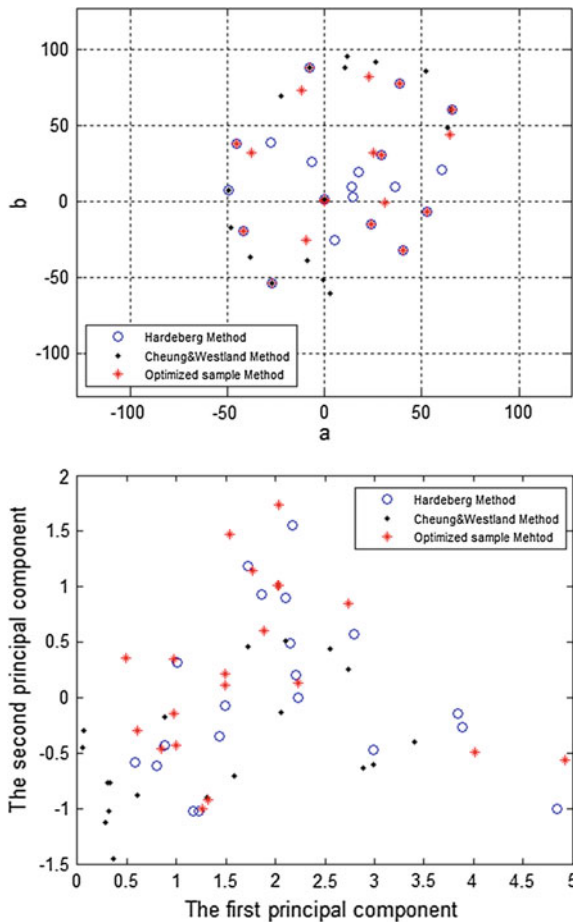
As mentioned above, the spectral reconstruction process is divided into the following steps: (1) the color card was optimized and got 20 optimized samples after obtaining experimental data; (2) the principal component analysis was

performed on the spectral reflectance of sample optimization, base vector matrix  $F_0$  was obtained and the corresponding coefficient vector  $\alpha_0$ . (3) Polynomial model was used to determine the relationship between the response value  $R_0 G_0 B_0$  of the camera and coefficient vector  $\alpha_0$  of the sample optimization; (4) Spectral reflectance was reconstructed according to the formula (4).

### 3.1 Optimized Sample and Its Characteristics

We obtained optimization sample sets in SG color card adopting above-mentioned method. Figure 1 is distribution chart in chroma space and principal component space. As can be seen from Fig. 1, sample optimization distribution is more well-distributed in chroma space, and its distribution of Hardeberg method is more

**Fig. 1** Sample distribution chart of chroma space and principal component space for sample optimization, Hardeberg method and Cheung and Westland method



centralized relatively, and Cheung and Westland method are mostly distributed on the edge. In the principal component space, Hardeberg method distributes well and Cheung & Westland method are more centralized relatively. So the spectral reflection reconstruction is prone to “over-fitting” phenomenon. Overall distribution of sample optimization is more well-distributed although there are near samples, so the spectral reflection reconstruction can achieve good effect.

### 3.2 *Determination of Sample Optimization Base Vector*

In order to determine the relationship between the polynomial model of the camera response value and the coefficient vector  $\alpha_0$ , the principal component analysis is performed on the spectral reflectance of sample optimization. As shown in Table 1, the cumulative contribution rate reached 98.85% when the number of principal components is 9. So we selected 9 basis vectors and its corresponding coefficient vectors considering the calculation and other factors.

### 3.3 *Establishment of the Relationship Matrix Between the Camera Response Value of Sample Optimization and the Principal Component Coefficients Vector According to Polynomial Model*

The polynomial model could generate high-dimensional input data through selecting the combination item of camera response value  $g_0 = [R_0 G_0 B_0]$  with a group of equations. These data through linear combination are fitting for coefficient vector  $\alpha_0$  of sample optimization and then the coefficient of equation group is obtained. After many experiments, the final polynomial model of sample optimization  $g_0$  is:

$$g_0 = [R_0^2 G_0^2 B_0^2 R_0 G_0 G_0 B_0 R_0 B_0 R_0 G_0 B_0]. \quad (6)$$

### 3.4 *Spectral Reflectance Reconstruction and Its Evaluation*

Spectral reflectance of SG color card was reconstructed on different sample selection method according to the principal component analysis, polynomial model (6) and formula (4). Experimental results were shown in Table 2.

**Table 1** The number of principal components and their cumulative contribution rate

Number of principal components	5	6	7	8	9	10
Cumulative contribution rate(%)	95.26	96.67	97.54	98.3	98.85	99.25

**Table 2** Reconstruction results comparison of mean of RMSE, mean of GFC and average CIE DE2000 for SG color card on Hardeberg, Cheung and Westland and optimized methods

	Mean of RMSE	Mean of GFC	Average CIE DE2000
Hardeberg	0.0288	0.9686	3.5228
Cheung and Westland	0.0306	0.9612	7.1960
Optimized method	0.0247	0.9779	2.5123

**Fig. 2** Reconstruction spectral reflectance curve of the best sample and worst sample for SG color card

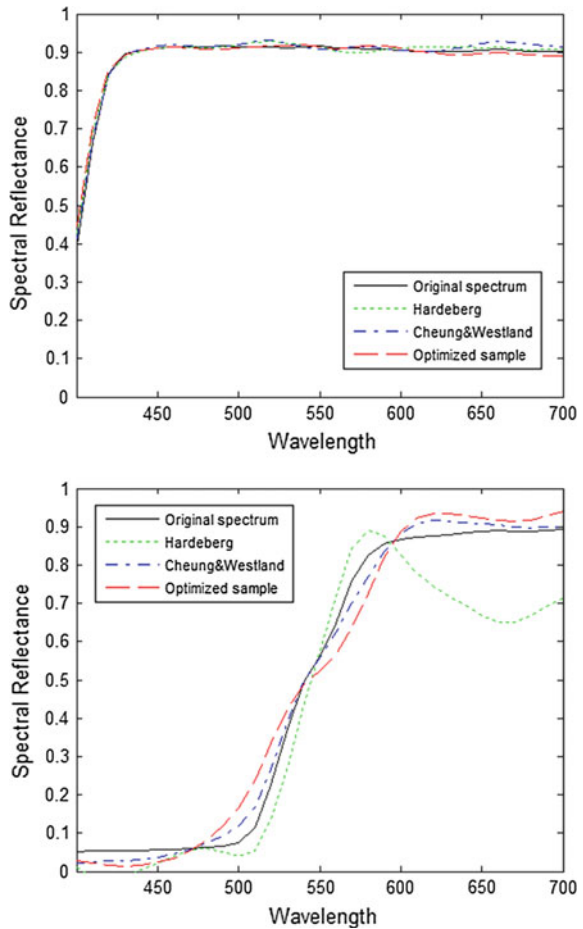


Table 2 shows that principal component analysis combined with polynomial model and sample optimization method are better than literature method on effect on spectral reflection reconstruction for SG color card and spectral accuracy and chroma accuracy are improved.

Figure 2 is the spectral reflectance curve of the best sample and worst sample for spectral reconstruction effect.

## 4 Conclusions

It can accurately simulate the nonlinear relationship between camera response value and coefficient vectors by using principal component analysis combined with the polynomial model method and the spectral reflectance of the object surface can be reconstructed accurately. Sample optimization method has not only broad representatives of spectral space, but also the similarity of chroma space, avoiding “over-fitting” phenomenon brought by excessive samples. The accuracy of spectral reconstruction is good. The mean of RMSE and the average color difference are improved obviously in spectral reflection reconstruction through sample optimization. The mean of GFC is increased which are better than selection methods of traditional sample. It could better meet the requirements of high precision color duplication of production and life, art digital collection, color multimedia display and color quality evaluation etc.

**Acknowledgements** This research was financially supported by the Guangdong Provincial Science and Technology Project, 2013B090600060. The work was supported by the Tianjin Natural Science Foundation Program of China, Grant No. 13JCYBJC41800. This work is also supported by the College Students Innovation and Entrepreneurship Training Program of Tianjin University of Science and Technology, 201610057093.

## References

1. Shimano N. (2006). Recovery of spectral reflectances of objects being imaged without prior knowledge. *IEEE Transactions on Image Processing*, 15(7), 1848–1856.
2. Zhang Zhe-chao. (2010). Reconstructions of spectral reflectance in imaging system. *Zhejiang University*.
3. N. Shimano, K. Terai, M. Hironaga. (2007). Recovery of spectral reflectances of objects being imaged by multi-spectral cameras. *Journal of the Optical Society of America A*, 24, 3211–3219.
4. LONG Yong-hong. (2009). Color Image Segmentation Approaches for Printing Quality Inspection. *Central South University*.
5. J. Y. Hardeberg. (2001). Acquisition and reproduction of color images: colorimetric and multispectral approaches.
6. V. Cheung, S. Westland. (2006). Method for optimal color selection. *Journal of imaging science and technology*, 50, 481–488.
7. REN Peng-yuan, LIAO Ning-fang. (2005). Spectral reflectance recovery based on multispectral imaging. *Optical Technique*, 31(3), 427–433.
8. D.R. Connah, J.Y.Hardeberg. (2005). Spectral recovery using polynomial models, *in proc. of SPIE-IS&T Electronic Imaging*, SPIE 5667, 66–75.
9. Yang S H. (2000). Watershed river pollution sources separation using independent component analysis. *Taiwan, National Taiwan University*.

# What Do We Need for Assessing Whiteness?

Shining Ma, Minchen Wei, Jing Liang and Ming Ronnier Luo

**Abstract** Whiteness is an important quality parameter for surface colour industries. The CIE whiteness metric has been widely used but is known for shortcomings. For example, it cannot cover sufficient ‘white’ region in colour space and it should only be used for illuminant D65. In a psychophysical experiment, fifty samples were assessed using 2 scales. We investigated the influence of the spectral power distribution (SPD) of LED sources on whiteness perception. The results showed that the SPD can strongly affect the performance of whiteness metrics. Three versions based on CIE whiteness index were derived and they all gave similar degree of accuracy in predicting experimental data. The one with CAT02 performed quite well and is simple to use by applying the original CIE whiteness index under D65. The boundary limit can also be extended based on these data.

**Keywords** Whiteness perception · CIE whiteness · LED

## 1 Introduction

Whiteness is an important quality parameter for many products in the surface colour industries, e.g. paper substrates, textile materials such as wool, cotton, detergents or washing power determines the value of a product. Optical Brightening Agents

---

S. Ma · J. Liang · M.R. Luo (✉)  
State Key Laboratory of Modern Optical Instrumentation, Zhejiang University,  
Hangzhou, China  
e-mail: m.r.luo@zju.edu.cn

M.R. Luo  
School of Design, University of Leeds, Leeds, UK

M. Wei  
Department of Building Services Engineering, The Hong Kong Polytechnic  
University, Kowloon, Hong Kong

J. Liang  
School of Light Industry and Chemical Engineering, Dalian Polytechnic  
University, Dalian, China



(OBAs), also called Fluorescent Whitening Agents (FWAs), have been widely used in these manufacturing industries as part of the chemical process to achieve the required bluish-white brightness that consumers have grown to expect of white products.

In 1986, a formula [1] was recommended by the CIE and is denoted as  $W_{CIE}$ . It is defined by the formula given in Eq. (1). It is only defined for use with the D65/10° and D65/2° illuminant/observer combination.

$$W_{CIE} = Y + 800(x_n - x) + 1700(y_n - y) \quad (1)$$

where  $Y$  is the CIE1964 or 1931  $Y$  tristimulus value and  $x$ ,  $y$  and  $x_n$ ,  $y_n$  are the chromaticity coordinates, in the CIE1964 or 1931  $x$ ,  $y$  chromaticity diagram, of the sample and the perfect diffuser illuminated by illuminant D65 respectively. The application of  $W_{CIE}$  is limited to the range  $40 < W_{CIE} < (5Y - 280)$ .

For the CIE whiteness index, there is a common restriction— $T_w$ . The green/red tint value  $T_w$  can be calculated using Eqs. (2) and (3) corresponding to CIE 1964 10° Observer and 1931 2° Observer respectively:

$$T_{w,10} = 900(x_{n,10} - x_{10}) - 650(y_{n,10} - y_{10}) \quad (2)$$

$$T_w = 1000(x_n - x) - 650(y_n - y) \quad (3)$$

A sample assessed as greenish has a positive value of  $T_w$  where as a sample assessed as reddish has a negative value:  $T_w$  is equal to zero if the tint does not significantly deviate from that of the white reference sample. For CIE 1964 10° Observer, an object is white when the value of  $T_w$  lies within the range +3 to -3. While for CIE 1931 2° Observer,  $T_w$  lies within the range +2 to -4. So the application of CIE Whiteness is restricted to samples that can be called commercially ‘white’ [1].

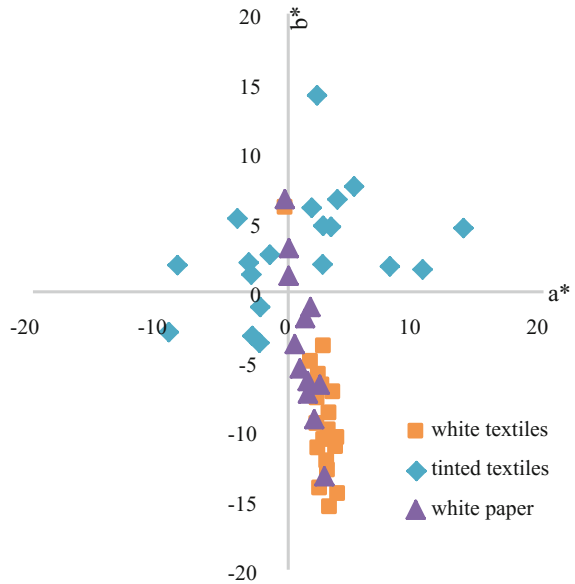
With the above in mind, CIE TC1-95, *the validity of the CIE Whiteness and Tint equation*, was formed with an aim to accumulate new data to recommend modifications to the existing CIE whiteness and tint equations to extend their application to illuminants other than D65 and verify the limits defined by the tint equation. The current work closely follows the aims of this technical committee.

## 2 Experimental

### 2.1 Lighting Conditions and Apparatus

A light booth coated with a mid-grey matte paint was used for visual assessment. The light settings were created using a 14-channel LED lighting system whose peak wavelength covered from 360 to 660 nm. The lighting system was controlled by software to produce the desired lighting quality.

**Fig. 1** Sample distribution plotted in  $a^*b^*$  plane in CIELAB colour space



**Fig. 2** Experimental condition



In this experiment, 12 lighting conditions comprised 4 correlated colour temperature (CCT) levels (3000, 4000, 5000 and 6500 K) with 3 UV levels (designated zero, medium and high) for each CCT value.

Fifty 'nominally white' samples were selected for the experiment. Figure 1 shows the chromatic distribution of all the samples plotted in CIE  $a^*b^*$  plane under D65/10°. It can be observed that some samples covered a relatively wide range of hues close to the neutral axis.

Figure 2 shows the experimental condition. Samples were placed in the central part of the lighting booth with uniform illuminance distribution. The observers viewed the samples at an illumination viewing geometry of 0°:45° approximately.

## 2.2 Procedure

Eight observers with normal vision were recruited from Zhejiang University. They have an average age of 23.2 with a standard deviation of 1.5. Before commencing the experiment, observers adapted to the viewing conditions for two minutes. They were then asked to rate the whiteness, whiteness percentage. The experiment under each lighting condition took approximately 30 min.

Whiteness has six categories: No trace of white (-3), little white (-2), unacceptable white (-1), acceptable white (1), white (2), pure white (3).

Observers were instructed to scale the appearance of each sample in terms of a whiteness percentage scale. It included two components, white and colour, when added together equaled to 100. Thus the whiteness percentage of a pure white sample would be 100 and that of no trace of white would be 0.

Two instruments were used to make spectral measurements in this experiment: a Datacolor Spectraflash SF600TM spectrophotometer and JETI specbos1211TM tele-spectroradiometer (TSR). All measurements were made using the SF600 under CIE Whiteness calibrated UV conditions. The lighting inside SF600 was a Xenon D65 simulator. As for JETI, it was used to measure the samples under all the lighting conditions with  $0^\circ:45^\circ$  geometry. Under the 6500 K with high UV level, the whiteness measured using SF600 agreed best with those measured using the TSR, which implies that UV energy of the illumination is essential for assessing whiteness.

## 3 Results

### 3.1 Performance of CIE Whiteness Metrics

In this section, various versions of CIE whiteness metrics were derived and tested using the visual data. To test the CIE whiteness metric, the visual results of whiteness-percentage were used because it was found that whiteness percentage attribute to be more consistent than that of whiteness. The correlation coefficient ( $r$ ) was used to indicate the agreement between the metric's predictions and visual results.

$W_{SF-65}$  and  $W_{TSR-65}$ : CIE whiteness index was proposed to evaluate the whiteness only under illuminant D65. So, the whiteness predictions were calculated from both the SF600 and TSR measurement data under 6500 K with high UV level because this phase gave the best agreement to predict CIE whiteness from the SF600 data. By limiting the samples to be within the tint boundary (i.e.  $\pm 3$  units), only 30 samples were considered. These metrics are denoted as  $W_{SF-65}$  and  $W_{TSR-65}$ , respectively. It can be seen in Table 1 that the two metrics gave similar performance, for which they predicted well for the visual results of medium level UV, followed by those of the high UV level and zero UV level. This implies that

**Table 1** The performance of various whiteness metrics base on CIE whiteness metric in terms of the correlation coefficient,  $r$  (between calculated whiteness and visual whiteness)

Lighting condition	$W_{SF-65}$	$W_{TSR-65}$	$W_{TSR}$	$W_{CAT02}$
3000 K zero UV	0.27	0.29	0.63	0.66
3000 K medium UV	0.92	0.92	0.87	0.88
3000 K high UV	0.85	0.85	0.84	0.85
4000 K zero UV	0.31	0.33	0.84	0.87
4000 K medium UV	0.88	0.88	0.85	0.85
4000 K high UV	0.81	0.81	0.78	0.78
5000 K zero UV	0.49	0.53	0.84	0.85
5000 K medium UV	0.69	0.70	0.84	0.84
5000 K high UV	0.85	0.85	0.87	0.88
6500 K zero UV	0.58	0.60	0.84	0.84
6500 K medium UV	0.83	0.83	0.86	0.86
6500 K high UV	0.70	0.70	0.70	0.70
Mean	0.68	0.69	0.81	0.82

regardless how precise the calibration of a spectrophotometer, a source with suitable UV content is highly desired for assessing whiteness.

$W_{TSR}$ : This version calculates the CIE whiteness from Eq. (2), having the  $x_n, y_n$  values corresponding to the reference white measured under the 12 sources used. This formula is denoted as  $W_{TSR}$ . The results in Table 1 showed that  $W_{TSR}$  outperformed those original whiteness metrics in most of the cases, with a mean  $r$  value of 0.81.

$W_{CAT02}$ : This version was derived to use a chromatic adaptation transform, CAT02 [2], to transform from the data to D65 from the other illuminants. Subsequently, the original CIE whiteness from Eq. (2), having the  $x_n, y_n$  values corresponding to 6500 K, is used. As shown in Table 1, it is encouraging that  $W_{CAT02}$  had the performance equal to or better than  $W_{TSR}$  for all phases, although the improvement is small (mean  $r$  value increased of 0.01).

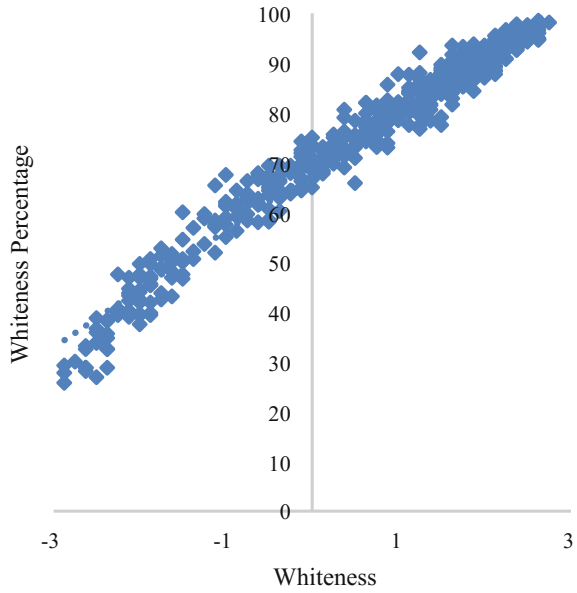
In conclusion, two indices were developed by modifying the whiteness formula  $W_{TSR-D65}$ . It is obvious that  $W_{CAT02}$  has the best performance. The use of  $W_{CAT02}$  would be simple to transform all colorimetric values from other illuminants to the D65/10 condition, to calculate the whiteness value using the original CIE whiteness metric.

### 3.2 Whiteness Boundary

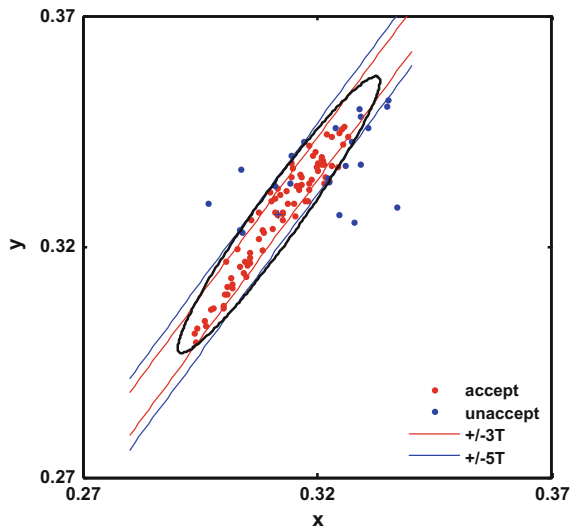
The tint tolerance of CIE whiteness metric is  $-3 < T_w < 3$  for CIE 1964 10° Observer which was used in the performance test. In Fig. 4, to cover a larger ‘white’ gamut, all the present data together with 55 additional samples [3] are plotted in CIE 1964 chromaticity diagram. The two parallel red lines and blue lines are also plotted to represent the tint limits  $\pm 3 T$  and  $\pm 5 T$  of whiteness respectively. The red and

blue points represented samples with whiteness percentage larger and less than 70% respectively, corresponding to acceptable white and unacceptable white respectively. Note that 70% whiteness percentage under D65 can be regarded as the visual whiteness boundary according to Fig. 3. Figure 4 also shows an ellipse which was fitted to acceptable white data (red points) with 95% confidence interval. The wrong decision percentage (WD%) [4] measure was used to determine the white limits. It

**Fig. 3** Comparison between whiteness and whiteness percentage



**Fig. 4** Plot of the data points, the white tolerance ellipse together with the white limits corresponding to  $\pm 3$  and  $\pm 5$



can be seen that the white limits can be extended to  $\pm 5$  T to encompass the white tolerance ellipse. Also, the WD% can be reduced from 18 to 6%.

## 4 Conclusions

An experiment was conducted to investigate the whiteness perception under sources having different correlated colour temperature and UV content. The results were used to test and derive various versions of CIE whiteness metrics. Comparing the two versions of original CIE metrics ( $W_{SF-65}$  and  $W_{TSR-65}$ ), they gave the similar performance and fit all data not badly except for those under real sources having no UV contents. Comparing the CIE whiteness metric using the variant reference white ( $W_{TSR}$ ), in general, it outperformed the two original versions.

A new metrics were derived by either using the CAT02 chromatic adaptation transform (named  $W_{CAT02}$ ). The results demonstrated that the performance was improved compared to original CIE whiteness.

As for the tint limit, there is a strong evidence to suggest that the white limit could be expanded to  $\pm 5$  T. The present finding supports the work of CIETC1-95.

## References

1. CIE, (2004) Colorimetry, in CIE15:2004, Vienna, Austria.
2. C. Li, M. R. Luo, B. Rigg, et al (2002) CMC 2000 chromatic adaptation transform: CMCCAT2000. Color Res. & Appl., 27(1):49–58.
3. Y. Chen, (2013) Measurement of White Colour Containing Fluorescent Whitening Agent, (PhD Thesis, The University of Leeds, School of Colour Chemistry, Leeds).
4. McLAREN. K., (1976) An introduction to instrumental shade passing and sorting and a review of recent developments. Journal of the Society of Dyers and Colourists. 92(9): 317–326.

# Regional Culture Preferences to LED Light Color Rendering

Ran Wei, Xiaoxia Wan, Qiang Liu, Guo Cao and Haiwen Wang

**Abstract** Different geographical environment affects the forming and development of several aspects of race, customs and culture, which directly lead to the diverse preferences to colors and LED light color rendering. Chinese people's cognition features of colors and LED light color rendering, share great similarity, and meanwhile bear many differences that vary according to regional distribution. This article demonstrates the result of a comparative research that focuses on 5 different LED light color rendering of correlative color temperatures. In order to explore the relations between the subjective assessment and various factors, such as gender and regional culture, the researchers conducted psychophysical experiments to 60 observers from different regions, and collected their subjective assessment to both regular objectives and two kinds of painting. Then, comparing the preferences of the observers to LED light color rendering, the researchers come to how the different regional cultures influence over people's preference to different LED light color rendering. According to the research result, the observers generally prefer the color temperature range of 4000–6000 K; appears the regional divergence in the 3 regions selected in the research.

---

R. Wei · X. Wan (✉) · Q. Liu (✉)

School of Printing and Packaging, Wuhan University, Wuhan 430079, China  
e-mail: wan@whu.edu.cn

Q. Liu

e-mail: liuqiang@whu.edu.cn

Q. Liu

Shen Zhen Institute, Wuhan University, Shenzhen 518000, China

Q. Liu

State Key Laboratory of Pulp and Paper Engineering, South China University of Technology, Guangzhou 510640, China

G. Cao

Shen Zhen Fu Tian N1 Digital Building Studio, Shenzhen 518000, China

H. Wang

School of Biological and Chemical Engineering/School of Light Industry, Zhejiang University of Science and Technology, Hangzhou 310023, China

© Springer Nature Singapore Pte Ltd. 2017

P. Zhao et al. (eds.), *Advanced Graphic Communications*

and *Media Technologies*, Lecture Notes in Electrical Engineering 417,

DOI 10.1007/978-981-10-3530-2\_5

**Keywords** Regional culture preferences · Subjective assessment · LED · Color rendering

## 1 Introduction

With the improvement of people's living level and continuous development of LED lighting technology, people have increasingly high quality requirements for indoor decoration lighting. Luis Cheskin, the United States color experts considers that the impact of color preferences is mainly about three factors: First, self-intervention (personal habits, accounting for 20%) [1]; second, a decent maintenance (reconciling oneself and the environment, accounting for 40%), the third is the pursuit of happiness. It has concluded that the environmental factors have great influence on it. People's preferences of color is not only due to the physical properties, but also depends on some cultural elements [2]. The preference and the taboo of color are extremely complex, and have a close connection with religion, geography, politics and social customs [3]. The differences of geographical environment have created a special aesthetic of people in different regions, which also has contributed to local color psychology [4].

Different urban residents have a unique color preference. For example, Nurakomat Abaek shows that, in Uygur traditional art, blue, green, white and red are displayed comparing with each other in hue and brightness. Among them, green and blue is the main colors of Uygur [5]. Yandong Sun shows that people of loess plateau prefer red and green, and people of Jiangnan region choose black, white, and grey for the best [6]. Meanwhile people of the Tibetan nationality are partial to gorgeous colors for sharp contrast [7]. Therefore, the North and the South have different living habits. The different topography and climate form a wide variety of customs, which affect the color preference and living habits of urban residents in our country (showed both common and personalized) [8].

Vision sense tends to give people a different psychological impact, especially when the different color temperature of light illuminates the typical object, the observers would feel apparent differences. This article aims to grasp the demands of residents in different regions accurately, provide more forward-looking and targeted guidance to the relevant institutions and different regional residents with different design scheme of production by exploring the differences in lighting and color preference among residents in different regions and analyzing the possible reasons for the preference. All in all, these conclusions will be applied to the practical life to improve people's quality of life.

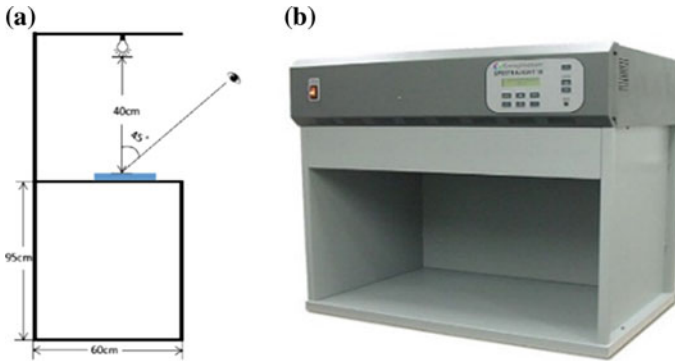
## 2 Visual Psychology Experiment

This experiment uses Philips Hue dimmable LED light as light sources, which can adjust the CCT with invariant illuminance. The CCT of 5 different light sources in following experiment is 2500, 3500, 4500, 5500 and 6500 K, which could be referred



**Table 1** Relevant information of 5 kinds of light sources in the experiment

Light source number	Standard color temperature (K)	Measured color temperature (K)	Illumination (lux)	x	y
1	2500	2442	200	0.4778	0.4070
2	3500(3496)	3437	200	0.4047	0.3826
3	4500(4504)	4453	200	0.3600	0.3537
4	5500(5496)	5524	202	0.3315	0.3307
5	6500(6493)	6627	200	0.3129	0.3126



**Fig. 1** Schematic diagram of the experiment and the X-Rite Spectra-Light III standard light box

to the following details in Table 1. The illuminometer in this experiment is testo545 illuminometer. Figure 1a illustrates the observation condition by 0°/45° lighting.

The observers sit in front of the lamp house (Size: 60 cm \* 66 cm \* 89 cm), as Fig. 1b shows that the light source sets on the top of it. During the experiment, the color of the surrounding and the bottom should be maintained grey.

60 observers are selected from three different regions(Tibet-Xinjiang region, Jiangsu-Zhejiang-Shanghai region and the mid-China region, following called T-X region, J-Z-S region and M-C region),each region has 10 males and 10 females, whose age ranges roughly 18–27 years old. Every observer should be visual normal. Before the experiment, the observer needs to put on the neutral color jacket to avoid the interference caused by the color of the clothes.

The subjective experiment is divided into three parts: in the first part, the observers should be preconditioned into the 5 different light sources and have been in the darkroom conditions for 3 min. After that, the staff would adjust the light sources for the observers to make a preliminary intuitive feeling of each light source. For different light source, the observers have 1 min to adapt. The second part is to observe two different styles of art paintings, such as Fig. 2. Considering about the regional characteristics of the observers, single-colored and simple art painting 1 (like Fig. 2a), as well as rich-colored and complex-composed art painting 2 (like Fig. 2b) are particular selected as the object of observation of this experiment. The 5 different light sources are incriminated as A (6500 K), B (5500 K),

C (4500 K), D (3500 K), E (2500 K), the observers watch art painting 1 with one stable light source. The observers grade the art painting 1 on a scale of one to five about naturalness and preference in 5 different light sources. There are 5 levels, in which 5 means the highest score. There are 3–5 min for the observers to rest before scoring the art painting 2. The same steps like above would be done after the rest. The third part is to score the light source, that is, the observers would score the 5 different light sources directly by preference. The steps are the same like second part.

### 3 Results and Analysis

In the visual experiment, the subjective evaluation results are shown in Figs. 3, 4, 5, 6, 7, 8.

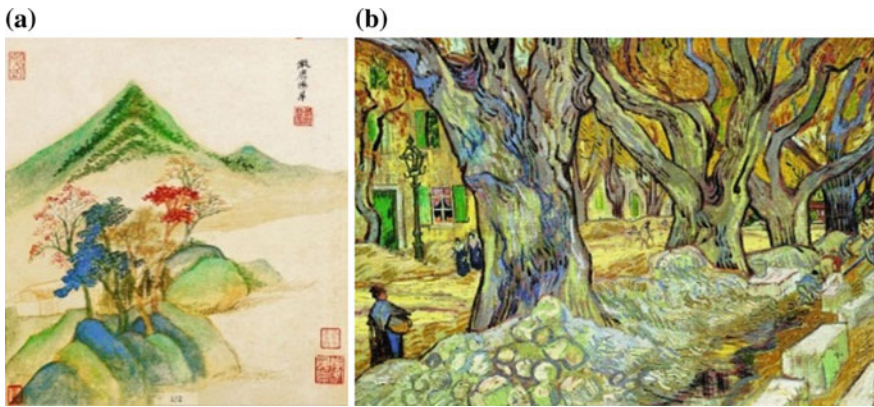


Fig. 2 Object: art painting 1 (a) and art painting 2 (b)

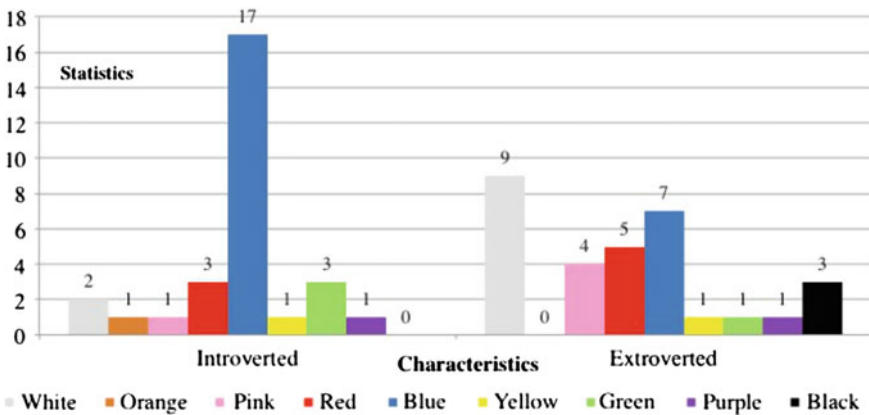


Fig. 3 The impact of personality factors on the most favorite color

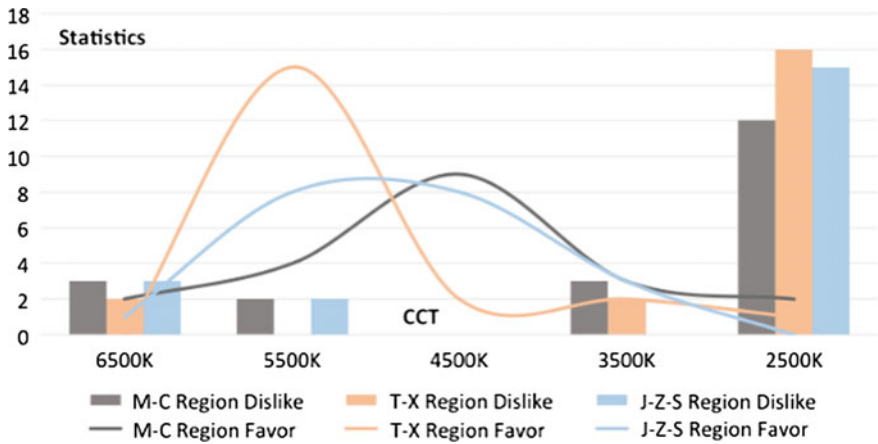


Fig. 4 The statistic of the evaluations about chosen light sources in different regions

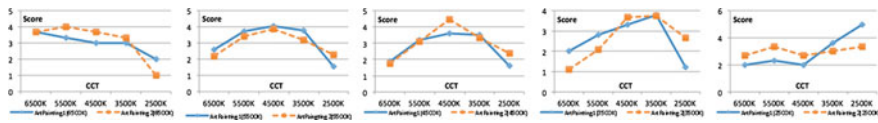


Fig. 5 The statistics of the evaluation for the score of the different art paintings assessed by the observers who choose certain light source (which in the brackets) as the most favorite

Figure 3 shows the data comparison chart of people with different personalities when choosing people’s favorite colors. Referring to the questionnaire filled by the 60 observers, 29 of them are introverted, the rest of them are extroverted. Among the introverted, 17 of them prefer to the color of blue, which confirms the opinion of Psychology Professor Marx Lucia, that is, people who favor the color of blue are introverted.

Figure 4 is an evaluation of 5 different light sources of different observers from different regions. Column bar represents the quantity statistics about a kind of color temperature that 60 people do not like the least. After combining the both to draw a conclusion that observers of different regions are the people who dislike the color temperature of 2500 K the most. People select the most favorite light source to show regional differences in different regions. By observing the line chart compared to other regions, the observers of the T-X region show that the consistency of subjective evaluation is stronger. Consistent with the conclusions of the study on the subjective preference caused by the differences between Chinese and western cultures in the study of Anqing Liu, that is, the culture of the M-C region and J-Z-S region is more open than that of Tibet and Xinjiang where people pursuit more of personality. While the people of T-X region prefer to pursue the commonness.

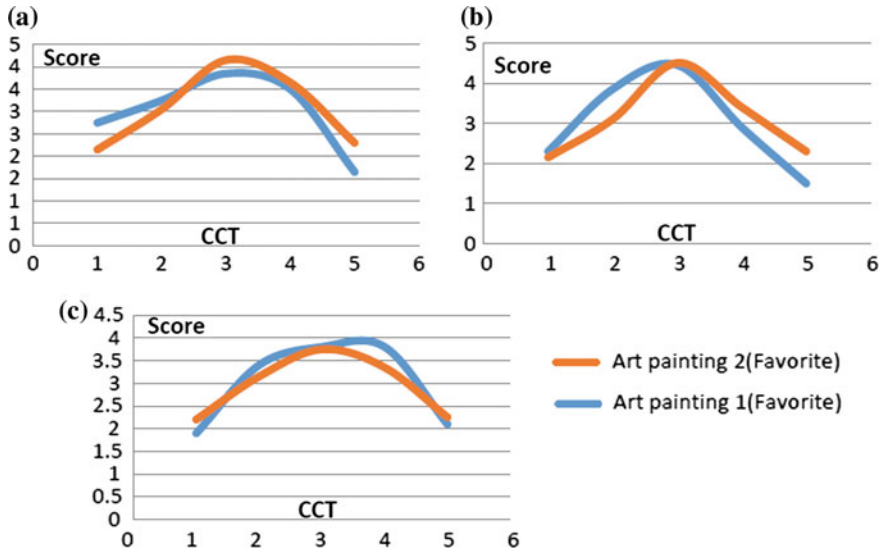


Fig. 6 Subjective evaluation results of different regions observers on two art paintings (From the left M-C region, T-X region and J-Z-S region)

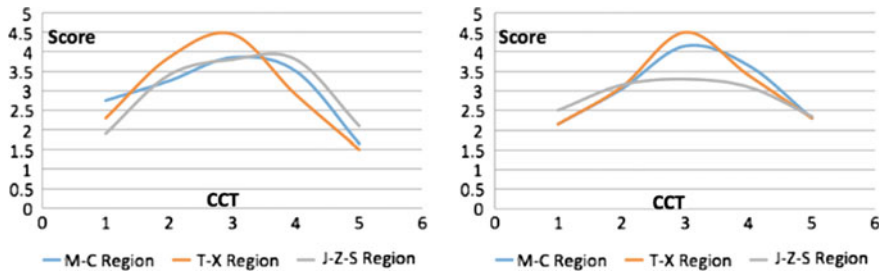


Fig. 7 The subjective evaluation results of the same art painting by the observers from different regions (Left art painting 1, Right art painting 2)

Figure 5 represents the independent analysis on regarding different light source as the most comfortable light source. Through the score results of the different art paintings and the light source itself, the researchers can see that the score of the light itself is familiar with that of art painting 1, which is vastly different with the score of art painting 2. In other words, observers who choose the CCT of 2500 K as the most comfortable light source also select the same CCT as the most favorite light source when evaluate the art painting 1. In subjective evaluation of art painting 1, it also follows the above conclusion when other four CCTs are chosen as the most comfortable light source. The reason is that the author believes the art painting 2 is more colorful and with higher color saturation, so the observer have much more diverse subjective evaluation.

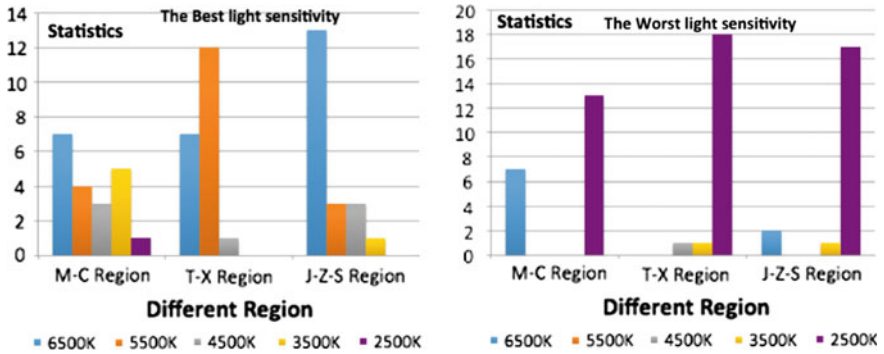


Fig. 8 The sensitivity to the 5 different light sources of the observers in different regions

The 1, 2, 3, 4, 5 of horizontal axis in Fig. 6 represents the light source with CCT of 6500, 5500, 4500, 3500 and 2500 K. Through the comparative analysis of the experiment, it can be seen that the subjective evaluation fractional curve of observers from the M-C and the J-Z-S region on two different styles of Art painting is basically the same, while there is an obvious deviation in the score curve of subjective evaluation in T-X region on two different styles of art painting. The evaluation curve of the favorite light source people choose the most of the art painting 2 is deviated rightly from that of art painting 1. This shows that the most favorite light source about the art painting 1 of the observers in this region is ranged from 4500 to 6500 K, which is closer to 2500–4500 K about art painting 2.

Figure 7 is the subjective evaluation results of the same art painting for the observers in different regions. It can be concluded that the subjective evaluation about the art painting 1 of the observers in J-Z-S region shows obvious consistency, where people would prefer low-color-temperature light source, while the observers of T-X region prefer high-color-temperature light source. What the researchers can infer through the right part of Fig. 7 is that among the subjective evaluations of art painting 2, the observers from T-X region would prefer the CCT of 3500–5500 K. In particular, the preference of the observers from J-Z-S region for the art painting 2 is not obviously changed.

During the Experiment, 20 observers from M-C region, T-X region and J-Z-S region were selected to do the subjective evaluation of 5 different light sources, including the sensitivity, the comfort, the preference and the naturalness. When it comes to the subjective evaluation of the sensitivity, the method is to let the observers observe a group of hue chess and change the color of that in 5 different light source. The scores of each test can infer the most sensitive light source.

From the Fig. 8, the researchers know that more people from the M-C region and J-Z-S region acknowledge that the most sensitive light source is the CCT of 6500 K, especially observers from J-Z-S region. While most people from T-X region consider that is the CCT of 5500 K, that is, the difference about the most sensitive light source among the three regions is great. But the most insensitive light source that most people think is the CCT of 2500 K, which is with consistence.

## 4 Conclusions

The experiment gets subjective evaluation of light source in diverse situations of the observers in different regions through a psychophysical experiment, it also conclude the subjective evaluation about two art paintings. Then by combining with the different geographical and cultural characteristics the experiment infers the preference of different people. In the process of multi angle analysis of the original data of the experiment, the researchers find that the observer's sex, native place, character, the different object of observation and other factors would influence the subjective preference. Among which, the difference of regional cultural background has great influence, especially the T-X region, compare with the M-C region and the J-Z-S region has significant differences in subjective evaluation because of its particular regionality.

To sum up, this paper, combining with the intelligent LED adjustable lamp analyze the influence of regional culture on the color preference of LED light source from subjective perception, which is based on psychophysical experiment. The results would provide the corresponding theoretical data for different local residents to choose different production design and to develop personalized lighting for different groups of people. All of these have great significance in practical production.

**Acknowledgements** The authors acknowledge the support of the Nature Science Foundation of Hubei Province in China (grant No. 2015CFB204), Shenzhen basic research project (grant No. JCYJ20150422150029093), the Open Fund of the State Key Laboratory of Pulp and Paper Engineering (grant No. 201528) and National Natural Science Foundation of China (grant No. 61505149).

## References

1. Y. Mizokami, C. Kamesaki, N. Ito, S. Sakaibara, and H. Yaguchi (2012). Effect of spatial structure on colorfulness adaptation for natural images. *Opt. Soc. Amer. A.* 29, 118–127.
2. Meng Liu (2014). Comparative analysis on color preference of the Bai, Naxi and Tibetan buildings in Yunnan area. *Journal of Panzhihua University.* 31(6): 66–70.
3. Guan Chen, Wenzhi Zheng (2013). A comprehensive empirical study on the color psychology preference of the young men and women through whole country. *Academic forum of China commodity society.* 144–151.
4. Harold Linton (2009). *Color in Architecture: Design Methods for Architectures, Interiors, And Urban Spaces.* New York: McGraw-Hill.
5. Nurakomat Abaek (2014). The influence of regional color characteristics on contemporary Xinjiang oil painting creation in Xinjiang. Xinjiang Normal University.
6. Dongyan Sun (2012). Application of color in urban landscape design. Chongqing University.
7. Berns RS (2011). Designing white-light LED lighting for the display of art: a feasibility study. *Color Research and Application.* 36:324–334.
8. Boyce PR. Editorial (2013). LEDs are the answer, now what's the question? *Lighting Research and Technology.* 45:265.

# Gamut Testing of EPSON Stylus Photo R270 Color Ink-Jet Printer by ICC 3D

Xiaochun Li, Ming Zhu and Mingming Yin

**Abstract** “ICC 3D” software is a very useful tool for color engineering. It can be used for testing gamut boundary description, gamut visualization and gamut mapping. In this paper, the printing gamuts of EPSON Stylus Photo R270 color ink-jet printer were tested and analyzed by “ICC 3D” software. The gamuts that different “Printing Quality” options in printing driver, different media and different color output models can reproduce were respectively tested, compared and analyzed. For most of the current color ink-jet printers, no matter whether the functions of their printing drivers are complex or not, their printing functions and controlling parameters are similar. Therefore, it is hoped that the research methods and results of this paper can have great realistic significance to application of color ink-jet printers.

**Keywords** Gamut · Ink-jet printer · Color model · ICC 3D

## 1 Introduction

With the rapid development of digital ink-jet printing technology, the printing quality and color reproduction capacity of the current color ink-jet printing equipment have been improved greatly [1, 2]. Generally, the printing driver is the last color-controlling step before printing output, so it is necessary to research and comprehend the influences of output-controlling parameters in printer’s driver on color reproduction accuracy. In this paper, EPSON Stylus Photo R270 Color Ink-jet Printer was taken as a case, the influences of output-controlling parameters in printer’s driver on color reproduction accuracy of printer were studied. “ICC 3D” software is a very useful tool for color engineering. So the gamuts that different “Printing Quality” options, different media and different color output models can

---

X. Li · M. Zhu (✉) · M. Yin  
College of Materials and Chemical Engineering,  
Henan University of Engineering, Zhengzhou, Henan, China  
e-mail: zhuming\_printing@haue.edu.cn

reproduce were respectively tested, compared and analyzed by “ICC 3D” software in this paper.

## 2 The Gamuts Corresponding to Different Printing Quality

Most color ink-jet printers provide several “Printing Quality” options in their printing driver. Under different quality options, the printing quality and speed are different. We can find three “Printing Quality” options in “Printing Quality” list box of the driver. They are “Economic” (the third grade option), “Photo” (the second grade option) and “Photo RPM” (the first grade option) respectively, as shown in Fig. 1. The printing quality corresponding to the first grade option “Photo RPM” is the highest, and the printing quality of “Text” option is the lowest [3].

Designing test color target: EPSON R270 printer is RGB driving printer, this printer can receive RGB image directly, and the printing driver is in charge of transforming the RGB input image into color output values for six ink channels C, M, Y, K, Lc, Lm before printing. So the test color target was designed around the boundary of RGB color space (RGB color cube): the color samples of the target were designed within the six planes of RGB color cube to ensure all the color samples are located on the printing gamut boundary. This not only ensures accuracy of the gamut boundary description, but also reduces the number of sampling points effectively. Note that the “black (0, 0, 0)” is assumed to be the coordinated origin of the RGB three-dimensional color cube. Taken the plane “black-blue-green-cyan” as an example, in the case, R = 0, and the sampling for the G, B channel are (0, 10, 30, 55, 80, 105, 130, 155, 180, 205, 235, 255). So there are 144(12 × 12) color samples totally in the plane “black-blue-green-cyan”. The color target within each plane is designed and saved as target image in RGB model. We can get six target images corresponding to six planes of RGB color cube. Correspondingly, there are 864 color samples totally within the six planes.

Printing test color target: the target images were printed by “Photoshop CS4” software in this paper. In “Print” dialogue, “Printer Manages Colors” option was selected in “Color Handling” list box of the “Color Management” setting

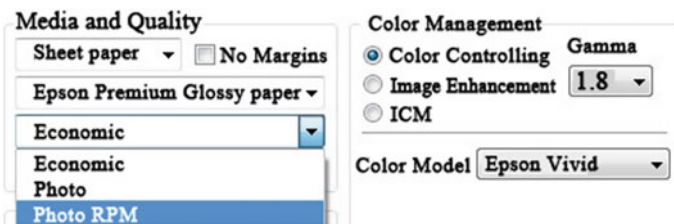


Fig. 1 The “Printing Quality” options in printing driver



group. This can ensure that the target images are printed by controlling parameters of the printing driver. We used “Epson Premium Matt Photo Paper (255 g/m<sup>2</sup>)” as actual media, and select “Epson Premium Matt Paper” option in the “Media Type” list box of the printing driver. Then, these target images were printed by the above three “Printing Quality” options respectively. And other printing parameters were set as default.

Target measurement and Gamut description: After printing target images, Lab chromatic values of each color samples in the six target images were measured by the spectrophotometer “i1 pro” and “Gretag Macbeth Measure Tool” software. The measuring condition was set to “2°” visual field and “D50” light source. The measured Lab values were used to plot the 3D gamut boundary of the printer. The “SMGBD” method is selected as gamut boundary descriptor, where the number of segment is “10” [4]. Figure 2 shows that 3D printing gamuts drawn by “ICC 3D” software [5] corresponding to different “Printing Quality” options.

In order to facilitate observation and comparison, the gamut of each “Printing Quality” option was observed respectively from three visual angles in CIELab color space: (“ab” plane, “La” plane, “Lb” plane). After comparing these gamuts relevant to different visual angles, we can find clearly that the volume of gamut corresponding to high “Printing Quality” option(for example, “Photo RPM”) is

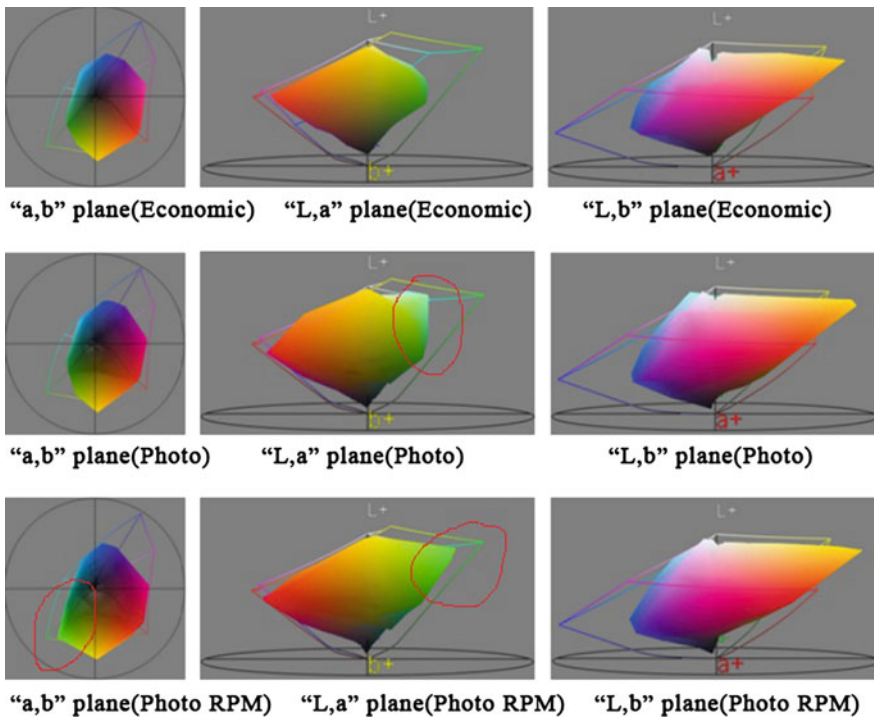


Fig. 2 Printing gamuts corresponding to the different “Printing Quality” options

significantly larger than that corresponding to low “Printing Quality” option (for example, “Economic”), especially for the gamut part for green color. Under the high “Printing Quality” option, printer can print green color with higher brightness and saturation. And these colors are different to print out under low “Printing Quality” option. This is the reason why the printing brightness and saturation are very high when printing images with green tone (for example, “grass”, “tree”, and “forest” and so on) with high “Printing Quality” option.

### 3 The Gamuts Corresponding to Different Printing Media

In order to test and analyze the influences of different printing medias on actual printing gamuts, we used the method of Sect. 2 to test the printing gamuts of three type of printing media “Ordinary glossy photo paper (No Epson brand, 230 g/m<sup>2</sup>)”, “Epson Glossy Photo Paper (200 g/m<sup>2</sup>)” and “Epson Premium Matt Photo Paper (255 g/m<sup>2</sup>)”. When printing gamut test targets, “Printing Quality” was set to “Photo” option and other printing parameters were set as default. “Media Type” list box of the printing driver should be set to “Epson Premium Glossy paper” option, if “Ordinary Glossy Photo Paper (230 g/m<sup>2</sup>)” or “Epson Glossy Photo Paper (200 g/m<sup>2</sup>)” is used. And “Media Type” list box should be set to “Epson Premium Matt paper” option, if “Epson Premium Matt Photo Paper (255 g/m<sup>2</sup>)” is used. Printing gamuts that the three types of printing media can reproduce were shown in Fig. 3. It can be seen that the volume of gamuts that “Epson Glossy Photo Paper” and “Epson Premium Matt Photo Paper” can reproduce are similar, no matter from which angle of view. The former is superior to the latter in printing quality, but they both have similar performance on gamut reproduction. This also demonstrates that there is no correlation between the influences of different media on actual printing quality and on printing gamuts under the same printing controlling parameters. In addition, as shown in Fig. 3, “Epson Premium Matt Photo Paper” has a better performance than the former two types of media, especially in red-yellow-green gamut parts. Generally, the best printing quality and printing gamuts can be obtained by Epson printer with Epson brand printing media [6].

### 4 The Gamuts Corresponding to Different Color Output Models

In the “Color Management” setting group of the printing driver, we can also use “Color Control” function to control the color output effect of printing images. In the dialogue of the printing driver as shown in Fig. 1, only when the “Color Control” box is checked, we can set the parameters relevant to printing color controlling. “Gamma” list box is used to control the contrast of printing image. Its default value

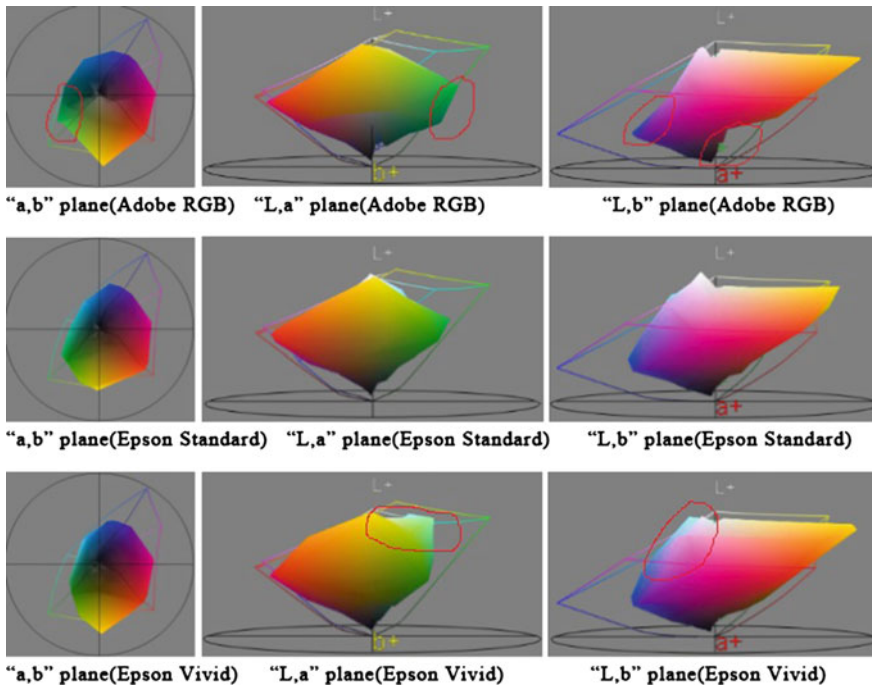
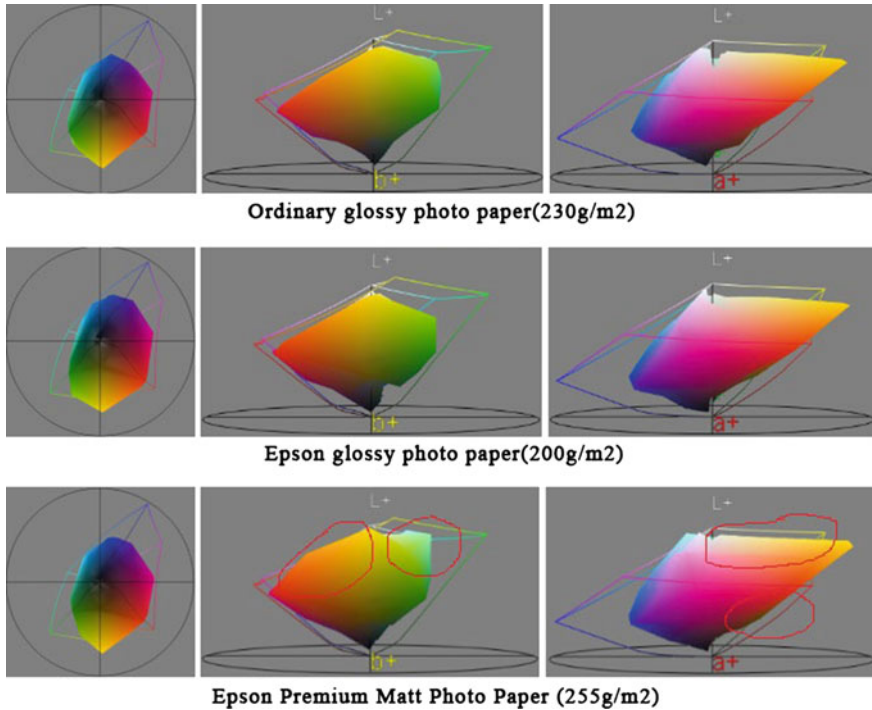


Fig. 3 Printing gamuts that the three type of printing media can reproduce

is "1.8". There are three color output models listed in "Color Model" list box, i.e. "Epson Vivid", "Epson Standard" and "Adobe RGB" [7]. In parameter setting of the driver, the three color output models were used respectively to printed the gamut test targets, "Printing Quality" option was set to "Photo" option, "Media Type" list box was set to "Epson Premium Matt Paper" option, and the "Epson Premium Matt Photo paper (200 g/m<sup>2</sup>)" was used as actual media.

The printing gamuts corresponding to different color output models were tested by the same method as Sect. 2. As shown in Fig. 4, we can find that the volume of green gamut part that the "Adobe RGB" model can reproduce is larger than that of "Epson Standard" model and "Epson Vivid" model. Compared with the latter two models, "Adobe RGB" can print many more green colors with higher saturation. In addition, we can find also that the volume of red-blue gamut part that the "Epson Standard" model and "Epson Vivid" model can reproduce are larger than that of "Adobe RGB" model. And compared with "Epson Standard", "Epson Vivid" has a better ability to reproduce the red-blue gamut part. So in order to obtain the desired printing results, we can select the proper color output model according to the color characteristic of printing image.



**Fig. 4** Printing gamuts that the different color output models can reproduce

## 5 Conclusions

The function of parameter setting in the EPSON R270 printing driver were researched and analyzed. The influences of different “Printing Quality” options, image enhancement setting and different media on actual printing quality were evaluated and analyzed. Through a series of gamut test experiments, we can find that the printer can print out green color with higher brightness and saturation under the high “Printing Quality” option. And these colors are different to print out under low “Printing Quality” option. The gamuts that different media can reproduce are different, but there is no correlation between the influences of different media on actual printing quality and on printing gamuts. Generally, the best printing quality and printing gamuts can be obtained by Epson printer with Epson brand paper. The gamuts that different color output models can reproduce are also different. The volume of green gamut part that the “Adobe RGB” model can reproduce is larger than that of “Epson Standard” model and “Epson Vivid” model, but the latter two models have a better ability to reproduce the red-blue gamut part. So in order to obtain the desired printing results, we can select the proper color output model according to the color characteristic of printing images. For most of the current color ink-jet printers, no matter whether the functions of their printing drivers are

complex or not, their printing functions and controlling parameters are similar. Therefore, the research methods and results of this paper have great realistic significance to application of color ink-jet printers.

**Acknowledgements** This paper is founded by National Natural Science Foundation of China (project number: 61301231) and Digital Printing Color Research Center of Henan Institute of Engineering (project number: YJJJ2013003).

## References

1. ZHU Ming. The Research on High-Fidelity Reproduction of High Dynamic Range Images[D]. Nanjing: Nanjing Forestry University, 2011.
2. LIU Shi-wei. The Algorithm of Light Color and Primary Color Ink Mapping for Multi-color Printer[J]. Packaging Engineering, 2014, 35(19):109–113.
3. YAO Hai-gen, KONG Ling-jun. Digital Printing[M]. China Light Industry Press, 2013.
4. J Morovic, M R Luo. Calculating Medium and Image Gamut Boundaries for Gamut Mapping [J]. Color research and application, 2000, 25(6):394–401.
5. I Farup, JY Hardeberg, AM Bakke, S Kopperud, A Rindal. Visualization and Interactive Manipulation of Color Gamuts[C]. Tenth Color Imaging Conference: Color Science & Engineering System, 2002:250–255.
6. ZHU Zhi-wei, CHEN Guang-xue, CHEN Qi-feng, CHEN Shuang-lian. The Influences of Surface Properties of Ink-jet Print Paper on Color Reproduction. Packaging Engineering, 2012 (3):109–112.
7. M Inui. Why is Color Gamut of Red Region of Adobe RGB Also Wider Than That of sRGB? [J]. Journal of the Society of Photographic Science & Technology of Japan, 2011, 72(2): 85–87.

# Research on Spectral Reflection Characteristics of Overprinted Color Inks and the Numeric Compensation to the Theoretical Model

Ji Qi, Yang Jin, Xinggen Qian and Yusheng Lian

**Abstract** The trapping of several color inks on substrate is a general phenomenon in multicolor printing. As fundament of color reproduction, the spectral characteristics of mono-color ink and of overprinted color inks are close related with the color reproduction. Theoretically, the spectral reflectance of overprinted color inks can be obtained from spectral reflectance of inks and of substrate. But the error appears, because some influences from ink, paper and other external conditions exist. Based on the measured spectral reflectance of Cyan/Magenta/Yellow/Black ink, of paper and of the overprinted inks, the spectral difference between measured and the theoretical data is compared and analyzed. The spectral difference data is transformed to DCT coefficients and filtered. Applying the compensation data from inverse DCT curve, the corresponding color errors ( $\Delta E$ ) are very small.

**Keywords** Spectrum characteristics · Ink trapping · Color reproduction · Numerical compensation

## 1 Introduction

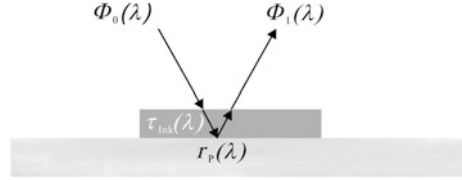
In color reproduction of printing, a color can be reproduced and apperceived rely on its light spectrum, which comes from the printed paper or other substrates. The spectrum of the light from the paper is related closely to the spectrums of light source, of the reflection/transmission/absorption rates of inks and of the paper. As showed in Fig. 1, the spectral reflectance of a ink film on paper,  $r_1(\lambda)$  depends on spectral reflectance of paper  $r_P(\lambda)$  and spectral transmission rate of ink film  $\tau_{\text{Ink}}(\lambda)$ :

$$r_1(\lambda) = \frac{\Phi_0(\lambda) \times \tau_{\text{Ink}}(\lambda) \times r_P(\lambda) \times \tau_{\text{Ink}}(\lambda)}{\Phi_0(\lambda)} = \tau_{\text{Ink}}(\lambda)^2 \times r_P(\lambda) \quad (1)$$

---

J. Qi · Y. Jin (✉) · X. Qian · Y. Lian  
School of Printing and Packaging Engineering, Beijing Institute of  
Graphic Communication, Beijing, China  
e-mail: jinyang@bigc.edu.cn

**Fig. 1** Light transmission path of a single ink film on paper



If the spectral reflectance of a single ink film on paper  $r_1(\lambda)$  and the spectral reflectance of the paper  $r_p(\lambda)$  are measured, the transmission ratio of the ink  $\tau_{ink}(\lambda)$  can be obtained:

$$\tau_{ink}(\lambda) = \sqrt{\frac{r_1(\lambda)}{r_p(\lambda)}} \quad (2)$$

Formula 3 describes the relationship among spectral reflectance ratio of  $n$  layers of ink films on paper and the spectral transmission ratios of every ink layers and the spectral reflectance of paper, the transmission ratios can be computed out from the ratios of single layer of inks and of paper:

$$r_n(\lambda) = \tau_{ink1}(\lambda)^{2 \times n} \times \tau_{ink2}(\lambda)^{2 \times n} \times \cdots \times \tau_{inkn}(\lambda)^{2 \times n} \times r_p(\lambda) \quad (3)$$

But the influences from ink, paper and others lead to errors in the predicted spectral reflectance of trapped inks. Researchers have made efforts to construction models for more accurate results [1–3].

## 2 The Measured and Theoretical Spectral Data of Single- and Multi-layers of Ink

On a printability tester (IGT AIC2-2000), applying process color inks of CMYK (“New Caps”/DIC), samples are printed on coated paper (128 g/m<sup>2</sup>). The thickness of the ink films are 1.2  $\mu$ m. The samples are printed with only one ink on paper (K/C/M/Y), or more layers of ink on paper (M + Y/C + Y/C + M/K + C/K + M/K + Y, K + M + Y/K + C + Y/K + C + M/C + M + Y, K + C + M + Y). The sequence of the printed color ink is K  $\rightarrow$  C  $\rightarrow$  M  $\rightarrow$  Y. The spectral reflectance of every 15 samples and of paper is measured with an X-Rite 530 spectral photometer. Every sample is measured at 5 positions and the average values are applied. The measured spectral curves are showed as Fig. 2.

Based on the measured spectral reflectance of single-layer of CMYK inks and of paper, the spectral transmission rates of the inks  $\tau_{ink, i}(\lambda)$  can be obtained, wherein  $i = 1/2/3/4$  correspond separately to C/M/Y/K. According to Formula 3,

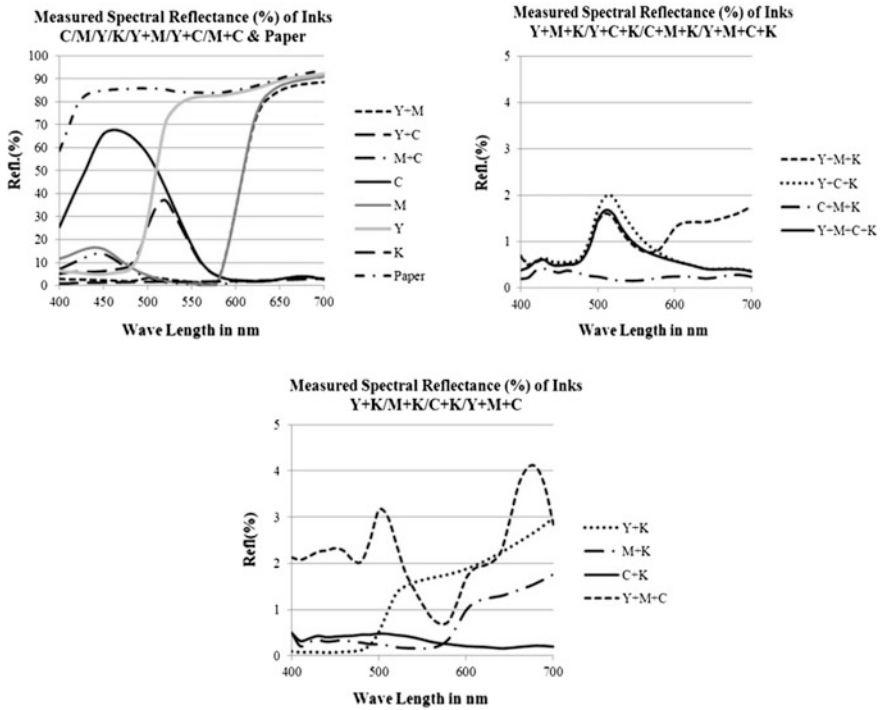


Fig. 2 Measured spectral reflectance of paper and of single or multi-layers of CMYK inks

the spectral reflectance of trapped ink  $r(\lambda)$  can be computed out. These theoretical spectral data are showed in Fig. 3.

### 3 The Error of Spectral Data and Its Numeric Compensation

According to the measured and theoretical data of spectral reflectance, error data can be obtained, which comes from the subtraction of the theoretical from the measured reflectance data. The curves of error (Difference) data are showed in Fig. 4.

As we have analyzed, the wrong spectral reflection and absorption of inks, i.e. the insufficiency or excess of spectral reflection (or absorption) ratio of the ink in relevant spectral ranges, the spectral influence of the first ink layer, the spectral reflectance of paper, all of these factors lead to the spectral differences. The color error  $\Delta E$  under CIE 1976  $L^*a^*b^*$  system of theoretical and measured spectral data are listed in Table 1. The average color error is 10.11, while the maximal value reaches 17.47 and the minimal one is 1.74.



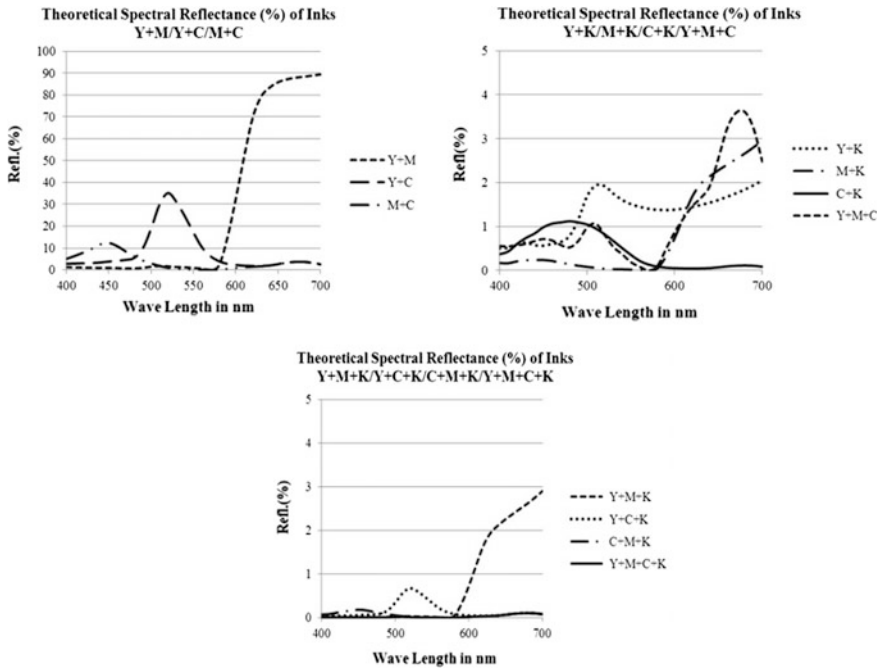


Fig. 3 Theoretical spectral reflectance of multi-layers of CMYK inks

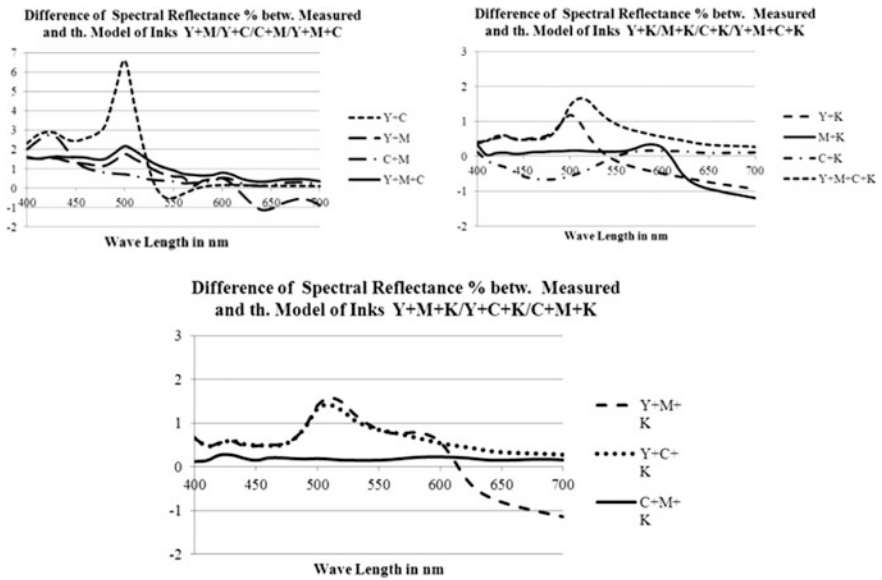


Fig. 4 Difference of the measured and theoretical data of spectral reflectance

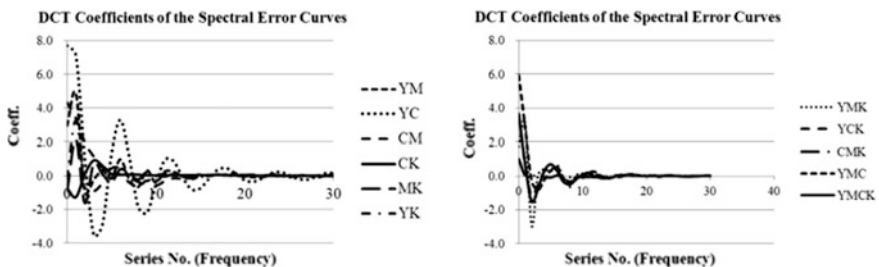
**Table 1** Color error of theoretical and measured spectral data

Color	Y + M	Y + C	M + C	Y + K	M + K	C + K
$\Delta E$	13.40	9.86	4.22	11.69	5.38	8.01
Color	Y + M + K	Y + C + K	C + M + K	C + M + Y	C + M + Y + K	$\Delta E_{Av}$
$\Delta E$	17.47	11.51	1.74	13.51	14.46	10.11

In application of Neugebauer Equation for the prediction of printing color, the predictive precision depends on the color accuracy of the “color elements”, i.e. the solid printed color. If the colors of elements are with errors as listed in Table 1, the computing of reproduced color is also incorrect. For the precise computing of colors, either the curves of spectral error serve as compensation curves or the measured spectral curves are directly applied in color computing. The spectral error curves or the measured spectral curves can be fitted as mathematical functions.

Because the interval of the wave length ( $\lambda$  as argument) is constant, the spectral reflectance or spectral error (difference) data can be transformed in frequency domain. The spatial data can be described as a series of coefficients in frequency. The original data can be complete restored through the inverse transform. The usage of frequency data have their advantages, such as can be filtered, smoothed etc. To avoid complex data (like in FFT), 1 dimensional Discrete Cosine Transformation (DCT) is applied. After DCT, every spectral error curve has 31 coefficients; they are showed in Fig. 5. It can be seen, that most of the coefficients in the high frequency range are very small, so they can be filtered and set to zero. Through the inverse DCT, the unfiltered coefficients are transformed back to the original data. If unfiltered DCT coefficients are applied, the absolute error values of the restored data are smaller than  $5 \times 10^{-10}$ ; if the DCT coefficients whose absolute values less than 0.05 are filtered, the maximal errors of absolute values are less than 0.071, the curves can be high precisely recovered.

Applying the data which from filtered coefficients and inverse DCT, add them with the spectral data from model, the model-based spectral data are corrected. The color error ( $\Delta E$ ) based on corrected spectral data and the original measured data are less than 1.89 and are listed in Table 2.



**Fig. 5** DCT coefficients of the spectral error curves

**Table 2** Color error based on corrected and measured spectral data

Color	Y + M	Y + C	M + C	Y + K	M + K	C + K
$\Delta E$	0.00047	0.00043	0.00059	0.02916	0.0156	1.8939
Color	Y + M + K	Y + C + K	C + M + K	C + M + Y	C + M + Y + K	$\Delta E_{Av}$
$\Delta E$	0.2027	0.6342	0.0606	1.1897	1.2252	0.4775

## 4 Conclusions

Under the influences of some factors, the spectral reflectance of solid printed ink and overprinted inks has more or less difference with the ideal theoretical value. Based on the measured and theoretical spectral data, the spectral characteristics of trapped printing color are analyzed. According to the difference between measured and theoretical data (spectral error data), compensation-curves are fitted in frequency domain. The curves can be applied to improve the accuracy of prediction of color.

## References

1. Wang Hai-wen et al. (2008). Research on the Printing Color Reproduction Technology Based on Spectral Imaging. *Packaging Engineering*, 29(4), 40–42.
2. Guan Li-Ming et al. (2011). Method of Printing Rebuild Based on Color Spectrum Reproducing. *Journal of Central South University (Science and Technology)*, 42(8), 2345–2350.
3. Liu Pan et al. (2015). Spectral Dimension Reduction Methods for Color Reproduction. *Packaging Engineering*, 37(3), 119–122.

# Dual Attributes of Color

Yechi Pang, Zhijie Li, Pengfei Zhao, Min Xu and Wensi Liang

**Abstract** Color is the light visual effect by the human eye, brain, life experience generated. Our eyes have seen the light, by a very narrow wavelength range of electromagnetic waves generated by the electromagnetic performance of different wavelength different colors. In this paper, the author based complex spectrum color theory, from a number of color characteristics, summarized the dual color attributes, namely: light is an electromagnetic wave energy and vector nature. People in color signal processing are divided into two phases, the first stage is feeling stage, and the second stage is perception. Compared with the wavelength domain, in the frequency domain the color is evenly distributed. The color of the physical attributes and mental attributes are interdependent and complementary, it will only combined together to form a unified color science.

**Keywords** Light · Electromagnetic wave · Amplitude · Color vector · Evenly distributed

## 1 Light Energy and Color Vector

WANG Daheng, the academician and the founder of color optics in China, said that color science is an interdisciplinary subject integrating optics, biophysics and psychology. Despite generating from the brain, color is the result of photo stimulation after all. In the natural world, the light with wavelength being 380–780 nm is named as compound light. Based on the Trichromatic Theory, any compound light can be deemed as the color generated by pyramidal cells of RGB through their photo stimulation in different wavelength zones. In other words, the proportion of

---

Y. Pang (✉) · Z. Li · P. Zhao · M. Xu  
Packaging and Printing Technology, Beijing Key Laboratory, China Academy of Printing  
Technology, Beijing, China  
e-mail: pangyechi@keyin.cn

W. Liang  
Food Science and Engineering College, Beijing University of Agriculture, Beijing, China

RGB determines the generated colors. “In terms of the retinal pyramidal cells of human beings, it’s still a controversial issue to describe the exact curve shape of the spectral sensitivity.” [1] With regard to how the light becomes colors, we float a new idea: the Complex Frequency Spectrum Theory (hereinafter referred as CFS) [2]. Light is the electromagnetic wave with dual attributes of energy and vector. Once entering the eyes, light stimulates pyramidal cells to generate nerve pulses. Moreover, there is considerable evidence that the intensity of output signal of pyramidal cells and the absorbed light energy are not in direct proportion, but much closer to square root [3]. Also, the wave-particle dualism of light tells that light energy is determined by both frequency and amplitude intensity [4]. The square root of light energy is proportional to the light amplitude. The undulatory property of light lies in its periodicity. The phase of amplitude varies from 0 phase to  $2\pi$  phase in each cycle, repeating the process again and again. Amplitude at different phases has different characteristics in direction, revealing that amplitude at phase is a time domain dynamic phasor, namely the vector of light. This also explains why the amplitude of light is called as complex amplitude.

In the formula of complex amplitude of light  $E = E_0 \cdot e^{i\omega t}$ ,  $t$  means time domain variable and  $\omega$  means angular frequency. Under the condition of visual timing,  $t$  becomes  $T$ ,  $\omega t$  becomes  $\omega T$ . For  $\omega = 2\pi\nu$  ( $\nu$  means the frequency of light), thus  $\omega T = 2\pi\nu T = \theta$ ,  $\theta$  means phase. Again such background, phase  $\theta$  has nothing to do with time  $T$ , instead, it’s just proportional to frequency  $\nu$ . On the other hand, under the same condition, the time domain dynamic phasor of light maps on the CFS and then becomes the static frequency domain phasor, namely the CFS phasor, and the formula is  $Z = re^{i\theta}$ . At this time, the output signal of pyramidal cells is neither light energy nor light phasor, but the CFS Color Vector.

The area surrounded by the CFS extremity is directly proportional to light energy, which is presented in the formula  $L = \frac{1}{2\pi} \int_0^{2\pi} r^2 d\theta$ .  $L$  means Luminance;  $r$  means the module of color vector, also named as radius vector.  $\theta$  means that the phase of  $0-2\pi$  radian ( $0^\circ-360^\circ$ ) corresponds to the frequency of 384–768 MMHz. This formula clearly presents the square relations between light energy  $I$  and amplitude  $E$ . Meanwhile, it also tells the square relations between Luminance  $L$  and radius vector  $r$  of color vector with mapping on the CFS, and Luminance  $L$  is the integral of square of radius vector  $r$  in full frequency domain  $0-2\pi$ .

## 2 Sensations and Perception

Human beings’ optic nerve signal consists of color and space signals, and the mixed signals make the processing mechanism more complicated. Just in terms of color signal, there’re still many unfathomable enigma up to now. Here, we might as well divide the color signal processing into two stages: Sensation stage and Perception stage. At Sensation stage, light transfers light vector into color vector by stimulating pyramidal cells, and then conducts integrated processing of color vector, in which perception isn’t generated.

Visible amplitude mapping each frequency in the spectrum is complex micro color vector. Moreover, an infinite number of color vectors of CFS will spontaneously seek for the balance in accordance with the natural law of thermodynamic entropy equilibrium. The so-called balance means that the sum of all the vectors equals zero. In the daylight, the sunlight looks colorless (white), for the color vectors of all frequencies reach white balance. The bronze red ink takes on bright red color, for the light in its complementary color—cyan zone is absorbed by ink. Once the cyan vector is lost, the original white balance of white light will be destroyed and the color vector in red zone will make printing ink turn red. The CFS chromaticity diagram of bronze red ink is as follows (Fig. 1).

At Sensation stage, the integration result of color vectors identifies the hue, whiteness, luminance and saturation of color. Furthermore, this stage doesn't mix any psychological factors of human beings but just follows the natural law, thus reflecting the pure physical property of color. With the help of vector features of the physical property of color, the original complex color changes can be dealt with

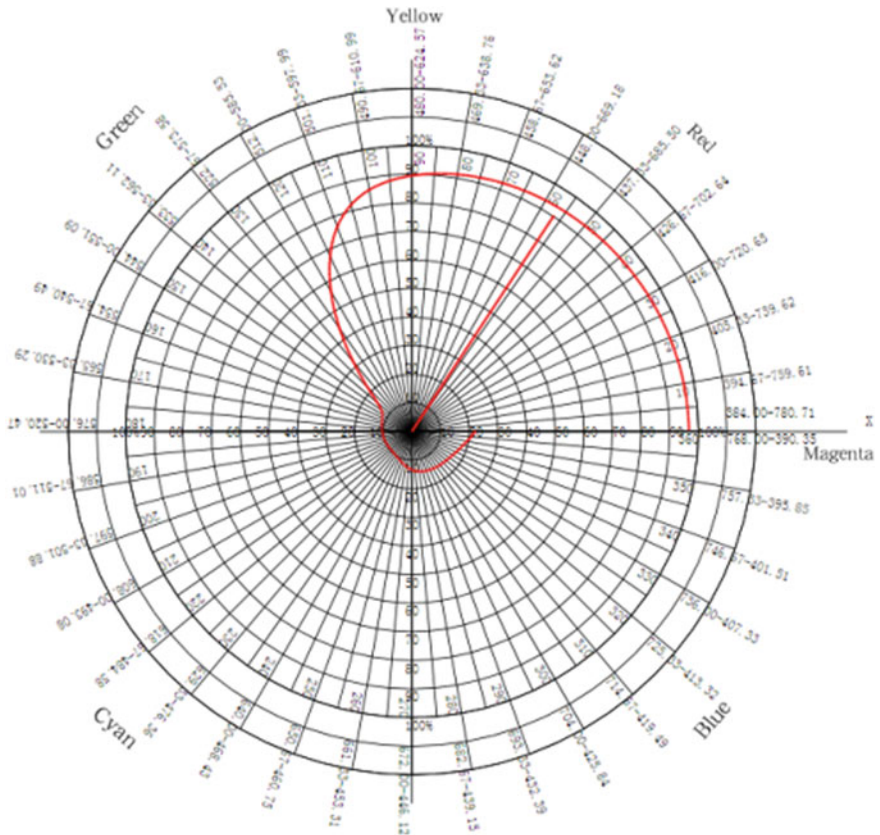


Fig. 1 Complex frequency spectrum chromaticity diagram of bronze red ink

simplified mathematical treatment by use of plane vector characteristics of color vector. For instance, the color composition of polychromatic light, the color decomposition (color separation) in printing technology as well as the white balance or the light-absorbed grey balance, all these are applicable to such treatment.

In light of the pure physical property of color in natural world revealing the basic element of light color changes—color vector, we can say that the basic physical properties of color are generated in the course of vector balance. After integrating and balancing color vectors, as long as the balance vector  $X_c$  and  $Y_c$  on the CFS chromaticity coordinates are known, the CFS luminance  $L$ , the CFS hue  $H$ , the CFS color intensity  $C$  and CFS whiteness  $W$  can all be calculated, which are just the quantitative representations of the physical property of color. With these numerical values of CFS color characteristics, we can conveniently make calculation of adding, subtracting, decomposition and composition of colored light [5].

### 3 The Distribution of Hue in Wavelength Domain and Frequency Domain

Hue is the phase of color on the plane coordinates ( $0^\circ$ – $360^\circ$ ). For a long time, people habitually correspond the hue of color to the wavelength of light, and call it dominant wavelength. According to wave optics, the wavelength of light is related to both the natural attribute of light itself and the nature of conduction medium. That is to say, even at the same frequency, the light wavelength also varies with the different conduction medium. Under the certain condition of velocity of light, the wavelength is inversely proportional to frequency. In other words, there is correlation between wavelength and frequency. Thus, it's better to match hue and frequency rather than the wavelength. It's known that frequency is the eigen—main factor of light property. In the CFS analysis formula, the exponential factor  $\theta = 2\pi\nu T$ ,  $\theta$  (phase) and  $\nu$  (frequency) are in linear relation. On the CFS chromaticity coordinates,  $H$  (hue) is evenly distributed in the frequency domain (384–768  $MM_H$ ), which is conducive to the calculation of color vector.

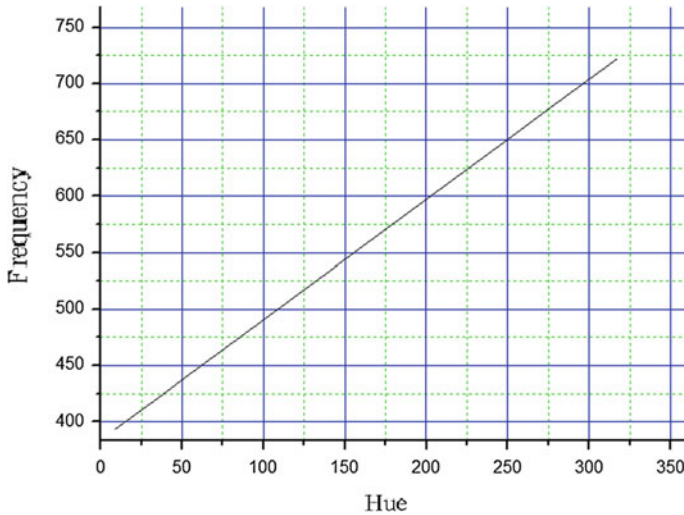
Now, we take the distribution of commonly-used ten printing ink colors (namely the hue values of CFS) in wavelength and frequency domains as example to expound further. The hue values of CFS, the corresponding dominant wavelength and the dominant frequency are shown as the following Table 1.

The distribution of above ten printing ink colors in frequency domain and wavelength domain is respectively shown as Figs. 2 and 3

The Fig. 2 shows that the phase of color is linearly distributed in frequency domain and the same frequency difference equals to its corresponding phase difference. The Fig. 3 shows that the phase of color is curvilinear distributed in wavelength domain and any same wavelength difference matches different phase difference. For example, in Fig. 3, from 650 to 750 mm, the wavelength difference is 100 mm, and its corresponding phase difference is 57.7. However, from 400 to 500 mm, despite the wavelength difference being still 100 mm, the corresponding

**Table 1** The correspondence between hue values of ten printing ink colors and wavelength and frequency

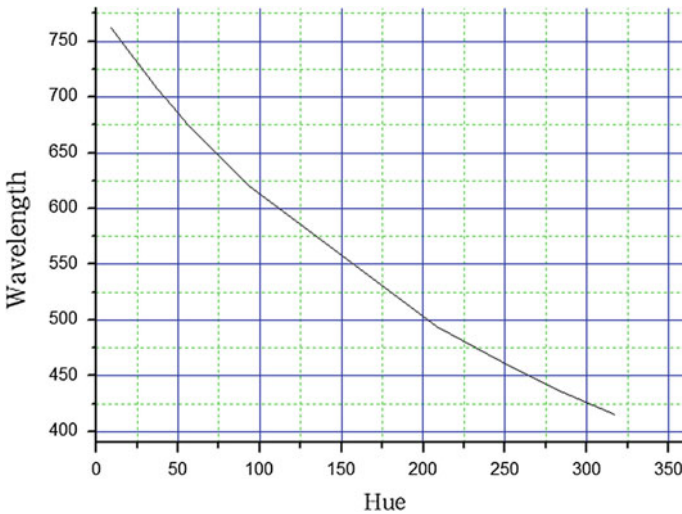
Serial no.	Printing ink	H (°)	Dominant frequency (MM <sub>H</sub> )	Dominant wavelength (nm)
1	Rose bengal	8.915	393.51	761.84
2	Magenta	37.717	424.23	706.67
3	Scarlet	45.92	432.981	692.39
4	Bronze red	56.692	444.472	674.49
5	Medium yellow	93.62	483.861	619.58
6	Green	208.124	605.999	494.71
7	Azure	254.704	655.684	457.22
8	Dark blue	273.16	675.371	443.892
9	Reflex blue	281.333	684.088	438.236
10	Pale purple	317.29	722.442	414.942



**Fig. 2** The phase distribution in frequency domain

phase difference increases to 140.5, which is almost two and a half fold of the former. Thus, it follows that the phase of color is not evenly distributed in wavelength domain. In the red zone with longer wavelength, the phase changes slowly and the color tolerance changes more. But in the blue zone with short wavelength, it was quite the contrary, namely the phase changes fast and the color tolerance changes less.





**Fig. 3** The phase distribution in wavelength domain

**Table 2** The numerical symbols of color features in CFS-xy chromaticity system

$X_C$	The comprehensive color vectors of all integrated and balanced color vectors on X-axis in CFS-xy coordinate systems
$Y_C$	The comprehensive color vectors of all integrated and balanced color vectors on Y-axis in CFS-xy coordinate systems
$C$	Color intensity $C = \sqrt{X_C^2 + Y_C^2}$ . $C$ and $H$ constitute a color vector and $C$ is the module of color vector
$H$	Hue is the phase position of color intensity $C$ . $H$ and $C$ constitute a color vector
$L$	Luminance. It corresponds to the relative energy of light and is related to the area surrounded by the function curve of CFS extremity
$S$	Color saturation (be short of saturation). It refers to the percent of the monochromatic light in the total energy of relative light
$W$	Whiteness. It refers to the percent of white light in the luminance
Dominant frequency	It refers to the frequency corresponding to hues on the CFS

## 4 The Comparison Between CFS Chromaticity System and CIE Color Space

The numerical symbols of color features in CFS-xy chromaticity system is shown in Table 2, and the numerical symbols of color features in CIE L\*a\*b\* uniform color space is shown in Table 3.

From the Tables 2 and 3, it can be seen that the CFS-xy chromaticity system describes and analyzes color in two-dimensional coordinate system and the

**Table 3** The numerical symbols of color features in CIEL\*a\*b\* uniform color space

<i>X, Y, Z</i>	The tristimulus values of CIE
<i>L</i>	Psychological luminance, namely the luminance value of CIE. It's the value of vertical axis in the CIE three-dimensional color space within 0–100
<i>a</i>	<i>a</i> is the colorimetric value of red and green on the abscissa-axis in the plane-coordinate system. Green (−120), Neutral (0), Red (+120)
<i>b</i>	<i>b</i> is the colorimetric value of yellow and blue on the vertical axis in the plane-coordinate system. Blue (−120), Neutral (0), Yellow (+120).
<i>h</i>	Hue angle. $h = \arctg(b/a)$ . It refers to the intersection angle between <i>a</i> and <i>b</i> diagonal and a-axis in the a-b plane-coordinate system
<i>c</i>	Color intensity. $c = \sqrt{a^2 + b^2}$ . It refers to the length from <i>a</i> and <i>b</i> diagonal apex to the origin of coordinate in the a-b plane-coordinate system

**Table 4** The comparison of two color systems

Chromaticity systems	CFS-xy chromaticity system	CIEL*a*b* uniform color space
Theoretical basis	Photochromic transformation CFS chromaticity theory	CIE chromaticity theory
Operation mechanism	Balance and integration of photochromic transformation color vector	Light energy stimulating pyramidal cells
Property	Visual physical property	Visual psychological property
Expression formula	CFS: $Z = re^{i\theta}$	CIE-xyz tristimulus values
Corresponding domain values	Frequency domain: 384–768 MM <sub>H</sub>	Wavelength domain: 380–780 mm
Coordinate systems	CFS plane-coordinate system: x-y complex number plane	CIE three-dimensional color space: lab three-dimensional uniform color space
Dominant frequency	Frequency corresponding to hue H	N/A
Uniformity	Hue is in proportion to frequency and is distributed uniformly	The red zone and cyan zone both have the tendency to deviate to blue zone

numerical value of the color feature is with both size and direction, namely the vector. Whereas, the CIEL\*a\*b\* uniform color space describes and analyzes color in three-dimensional color space and the numerical value of the color feature is only with size, namely the scalar.

The analysis and description of color in natural world between CFS-xy chromaticity system and CIEL\*a\*b\* uniform color space is presented as the Table 4.

## 5 Complementation and Uniformity of Color Science

As the most sensations of human beings, color sense and auditory sense are different by nature, but there still shares the similarity: duality. “In terms of the duality of sound, it can be defined from two aspects. From the perspective of physics, sound is regarded as the transmission of air particles vibration from the near to the distant, in other words, sound is the sound wave. From the perspective of psychology, sound is regarded as the subjective sensation acoustically produced by sound wave. When making an evaluation of sound quality, sound should be discerned from the viewpoint of psychophysics.” [6] Take music as an example. Music is the acoustically subjective sensation of sound wave, however, when people make an assessment of sound quality of music, they naturally connect the psychological feeling of music with the physical property of sound. The volume has something to do with the strength of vibration amplitude of sound wave, the pitch of tone with the dominant frequency of sound wave vibration, and the tone with the harmonic frequency of sound wave.

Sound is generated by mechanical vibration on auditory organ, and color is generated by electromagnetic wave on visual organ. In this sense, sound and color shares something in common: duality. Thus, the assessment of color should also be made from the perspective of psychophysics. In terms of physics viewpoint, the vector characteristics of color is related to that of light, the hue of color to the dominant frequency of light, the luminance of color to the relative value of energy of light, as well as the saturability of color to the energy proportion of monochromatic light among the relative total energy of light.

It is usually said that seeing is believing, but that isn't really the case. Sometimes people turn a blind eye to the things which objectively exist. In spite of the color vector being invisible to human beings, it's the decomposition, composition and balance of color vector that makes color change and determines the change results. In the integration process of optic nerve sensation, color vector as the key factor presents the physical properties including hue, color intensity and luminance by integration. Then, perception stage follows. Under the influence of psychological factors, human beings can see the hue, luminance and purity of color which are the psychological properties of color. The numerical values of hue, luminance and intensity deduced from CFS chromaticity theory represent the physical properties of color vector. Despite the color vector being invisible to human eyes, it still plays a decisive role in all the photochromic changes.

The visual process of human being is divided into Sensation Stage and Perception Stage, which respectively reflects the physical and the psychological property of color (namely, the color features being visible to human eyes). That's also why color science belongs to psychophysics. The above-mentioned two stages are applicable to different situations. When it comes to the problems such as the photochromic measurement, the decomposition and composition of color as well as the color balance, the color vector should be employed as the effective means to solve them, for the physical property of color is easier to calculate. Meanwhile,

in terms of the aesthetics and artistic vision fields which involve in the color temperature, fashion trend and emotions and so on, it's more appropriate to apply the psychological property of color.

From the above exposition, it can be proved that the physical and psychological properties of color are interdependent and mutual supplementary. Only their combination can generate into an integral color science.

## References

1. TENG Jinxiu, QIU Jiayi & ZENG Xiaodong, Color Measuring Technique [M]. Beijing: China Metrology Press, Jan. 2008:4
2. PANG Duoyi & PANG Yechi, Analysis of Complex Frequency Spectrum Physical Color of Photochromic Change [J]. Beijing Institute of Graphic Communication Journal, 2007, 15 (04):8–11
3. TENG Jinxiu, QIU Jiayi & ZENG Xiaodong, Color Measuring Technique [M]. Beijing: China Metrology Press, Jan. 2008: 15
4. PANG Duoyi & PANG Yechi, Color is the Mapping of Wave-Particle Dualism of Light in Complex Frequency Spectrum [J]. China Printing and Packaging Study, 2010, 2(05):19–23
5. PANG Duoyi & PANG Yechi, The Calculation Method of Complex Frequency Spectrum and Numerical Values of Color Features [P]. China Patent for Invention, CN200710130676.2.2008:1–4
6. CHEN Xiaoping, Sound and Hearing Perception [M]. Beijing: China Radio and Television Publishing House, Sept. 2006: 45

# Extracting the Representative Colors in Facial Image Based on the Eye Tracking

Pei Deng

**Abstract** Within the printing industry, human skin is one of the most important and difficult color to reproduce. In order to reproduce a better skin color, the printing industry, cosmetic industry and other related industries study invested significantly on facial skin colors. With the increasing of experimental data and facial color recognition technologies, managing these data is now particularly important. But the facial colors are not uniform. Many different experiments were carried out in relation to this topic in hope to extract the facial color. In this study, the observer's sight and eye movements were tracked by an eye tracking device, the experimental data were analyzed and a better solution was suggested to extract the representative value of each facial images.

**Keywords** Eye tracking · Facial images · Representative value

## 1 Introduction

The research of skin color provides a great convenience by digitalizing skin tones. However, it poses challenges due to the imbalance in colors, thus making it difficult to have specific skin tone to represent a color group. At the present time, there are three techniques to measure the skin tones: colorimetry, colorimetric method and color image measurement [1]. Colorimetry method compares color chart and facial tone to determine its similarity with human eye. It uses one of human body's most precise instruments for color comparison, but it also greatly depends on the person's degree of proficiency. Colorimetric method uses color measurement instrument by having a direct skin contact. It takes much less time comparing to Colorimetry method, and it is easy to operate. However the drawback to this method is that the result from this instrument differs from human eye's intuition [2]. With the

---

P. Deng (✉)

College of Packaging and Printing Engineering,  
Tianjin University of Science and Technology, Tianjin, China  
e-mail: dengpei@tust.edu.cn

development of optical and computer processing technology, researchers are now beginning to use images to measure complexion. The advantages include faster processing speed and small burden for color measurement, however the acquisition of hardware, and lighting conditions are more difficult to achieve.

For determining the skin tone, the absolute value comparison between experiments becomes difficult due to the purpose of each experiment, as well as the differences in location of skin. In earlier researches, Yamamoto [3] used the average value of all parts of facial skin as the representative color in the research between the favorable skin tones in China, Japan, and South Korea. Aoki [4] took account of people's impression as well as this matching experiments, he took the representative value of facial skin tones, and then found out the same value from the original images. He statistically analyzed 10 frontal images, and proposed that using the tone underneath eyelid as the color representation. However, the human visual system has a complex structure [5], and there is a great difference in the perception of human eye and the camera imaging system [6, 7].

This research used eye tracking device to observe and record the focal point and eye movement trajectory when observe a facial image, to understand human's subconscious. Then this research proposed a new method to extract the representative value of facial images.

## 2 Eye-Tracking Experiment

This study examines participant's ocular behavior in response to different facial images, and its correlation with evaluations of each result.

### 2.1 *Sample Images*

In this study, 10 frontal view photos of university students were adopted in order to meet the need of eye tracking experiments. Photo background must only have one simple achromatic color, and it must be a frontal facial view. In order to ensure the details of the facial photos can be seen clearly, the shadow on the face has to be minimal. To linearize the result, the gender ratio (male to female) was set to 1:1. The sample images were shown in the Fig. 1.

### 2.2 *Instruments*

Measurement of eye movement data was recorded using an Ems-8 eye tracking device. A fixed frequency for tracking eye movement on a computer screen on both eyes was set to 60 Hz and it has an accuracy range of between  $0.5^\circ$  and  $1^\circ$ , which was sufficient for the purpose of this study.

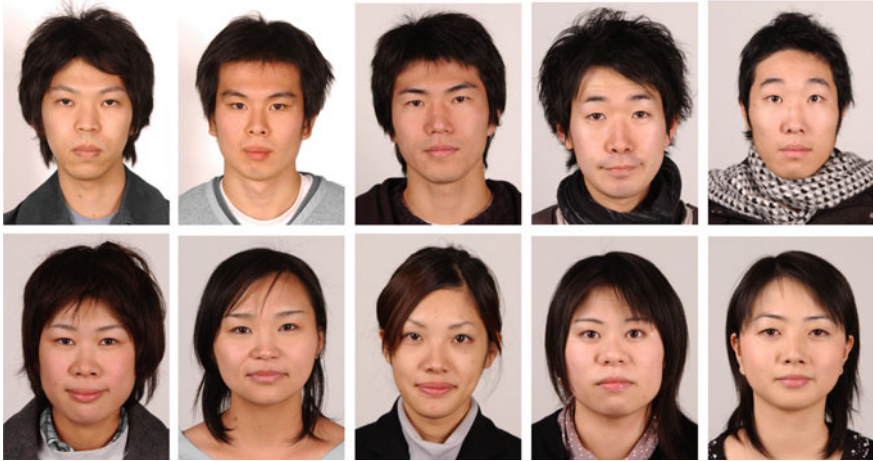


Fig. 1 Sample images

### 2.3 Participants

Participants are 3 students (mean age = 20.35 years) with regular vision. Participants are all majored in information science.

### 2.4 Experimental Procedure

Participants sat on the chair with a 17-inch. display monitor (length 33.5 cm \* height 26 cm) was placed in front of participants about 60 cm away. Participant's head was fixed to ensure the distance between eye and monitor. A second experiment was designed based on the hue unified facial images that was shown in Fig. 2. Hue unified facial image's color distribution in  $a^*b^*$  flat was shown in Fig. 3, the distribution was on one line, it can only change the hue angle value to control the original image color. The original image and its color distribution in  $a^*b^*$  flat was shown in Fig. 4. In the experimental 2, the original image (left) and the hue unified facial image (right) were placed side by side. The hue angle value was adjusted to make the color of two images looked the same.

## 3 Results and Discussion

### 3.1 Frame by Frame Analysis

In order to get the sight sequence and observation time on each part of the image, at first face images have to divide into several areas.

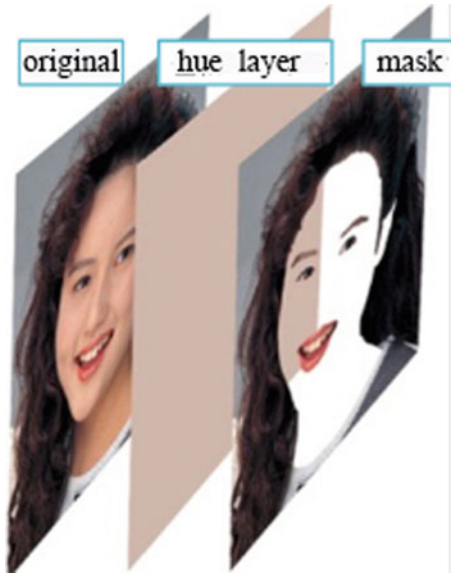


Fig. 2 The sample of the hue unified facial image

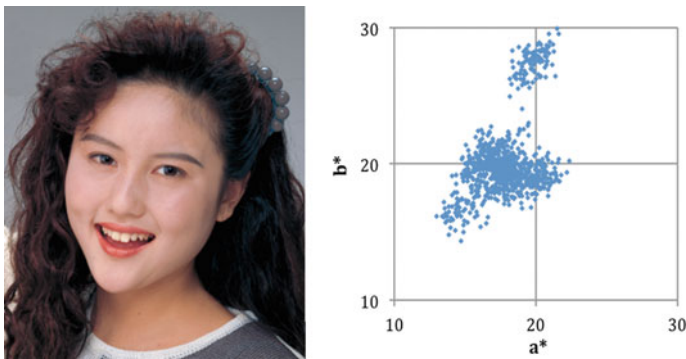
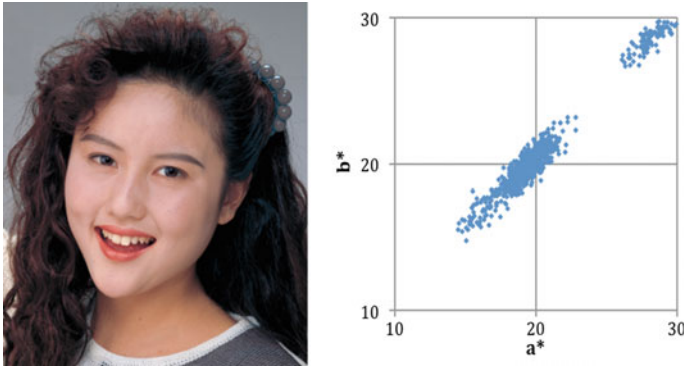


Fig. 3 Original image and its color distribution in a\*b\* flat

Yoshikawa [8] calculated 108 feature points. He then used the characteristics of these feature points to divide the facial areas into 93 areas and then used the average RGB value to fill each area. Facial shapes were linearized by averaging women's facial structure. It removed personal facial characteristics and darkened all outer facial parameter and left with 57 effective color regions. By using the principal component analysis, facial color region was divided into 9 areas as shown in the Fig. 5. They were 2 upper parts of the cheek (UC), 2 lower parts of the cheek (LC), nose and the surrounding (NS), eyes and surrounding (PE), mouth and the surrounding (PM), forehead (FH).

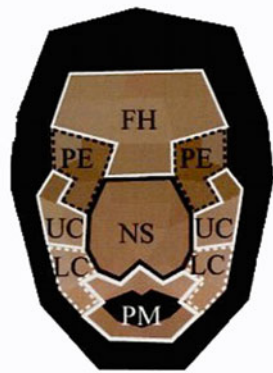
In this study, glabella, neck and outline were the important areas on the face, so a total of eight separate parts were segmented.





**Fig. 4** Unified facial images and its color distribution in a\*b\* flat

**Fig. 5** Divided facial color region into 9 areas



This study took the eye tracking moving results that participants were observed facial images as videos, to take observe time as a variable to investigate the order of observation and stops over time in the each area [9].

Figure 6 shows the 3 participants’ results of stops over time in the each area and the order of observation. The results show that participants’ behavior has a great influence on the order of observation and the gender of the images almost no influence on the results. But 3 participants’ results had common view. The start of the observe point was the center line of the facial images (forehead, nose and the surrounding and glabella). The possible reason was that could grasp the overall impression of the image when observed center line. So center line of the facial images was important parts on the perceptual understanding of the images.

### 3.2 Result of Color Matching

This study recorded eye moving focal points to understands its eye movement track further between the areas where the participants’ interested areas and other focus

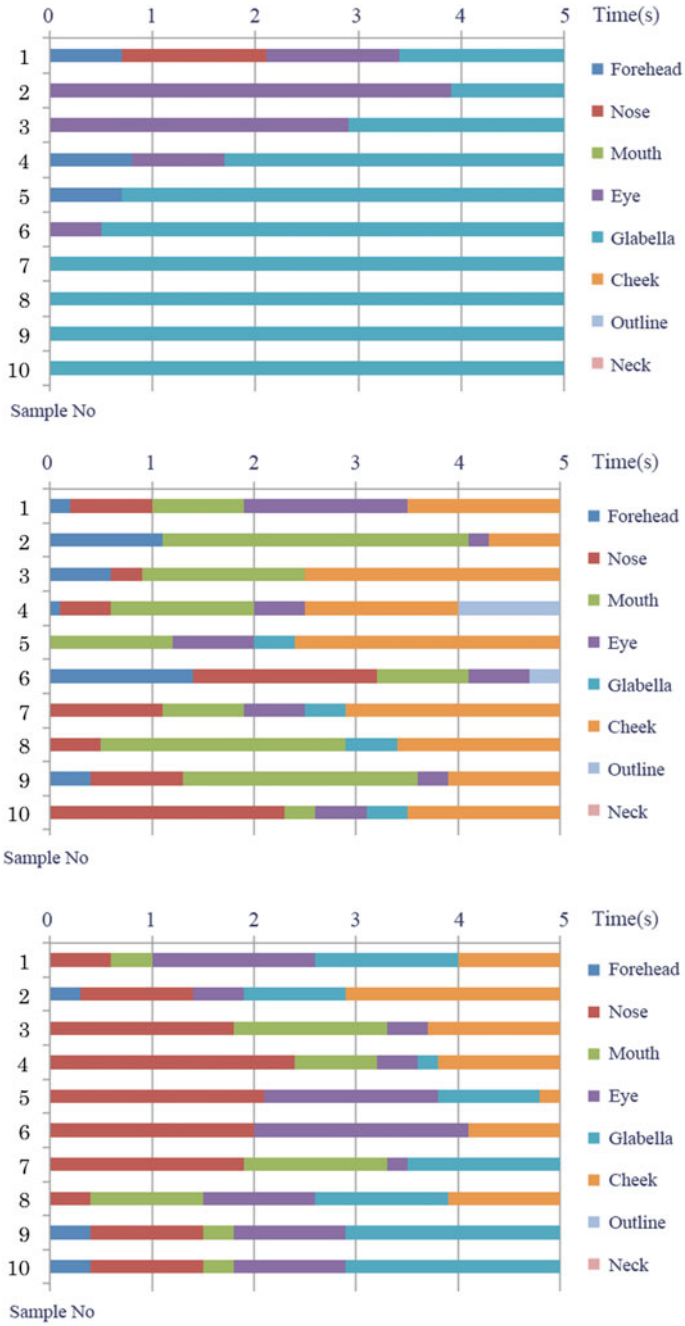


Fig. 6 3 participants' results of eye tracking when observed facial images

points around the images to analyze how each participant used a set of benchmark to complete the color matching experiments [10]. Finally, the eye tracking data on the image was recorded in the form of two-dimensional coordinates, which was then converted into Excel data format.

Through the observation of these 3 participants' eye tracking experiments, the results were obtained and shown in Fig. 7. The researchers found out that it has a minimal relation to the image and the gender of the person in the image, however it has a strong relation with each participants' observing behavior. The results
















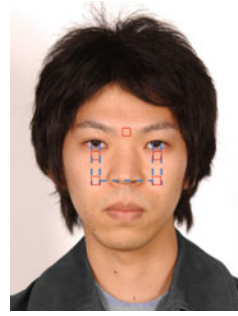
No	Participant A	Participant B	Participant C
1			
2			
3			
4			
5			

Fig. 7 Part of eye-tracking result of color matching experiments

**Fig. 8** Determined representative color location areas



were different in Experiment 1, right half of the original photo (left) and left half of the hue unified image (right) were each observed differently. The focus was mostly on the eyes and cheeks, and in order to determine the final value of the representative color, participants took a long time viewing on the adjusted images. It was observed that the participants spent more time on the large color areas such as cheeks and forehead, to determine the subtle changes in the facial color. These parts are also the focus for future facial image color measurement considerations.

According to the results of the facial image observation experiment (Experiment 1), and facial color matching experiment (Experiment 2) and also considering the perception of each participant when observing facial images, representative color location areas are determined. These locations were: two locations under the pupil, between eyelids, two locations on the cheeks (where the extended nostril lines and eyes cross each other), total of five locations on facial images and then measure its colors and take an average value between them to determine the representative color. As shown in Fig. 8.

## 4 Conclusions

This research analyzed participant's observation behavior by tracking their eye movements on student photos as well as color matching experiments. This further improves the approach to determine the representative color by having a correlation on participant's observation behavior. According to these experimental results, the final proposal was implemented by using the average value of 5 areas (two locations under the pupil, between eyelids, two locations on the cheeks) on facial images.

Future improvements to this study can be done by having larger group of sample participants and enlarge the participants' major study to all industries. These could have had a negative impact on the accuracy of data. The proposal from this study needs to be verified with effective methods and this is an important add-on procedure in all future experiments.

**Acknowledgements** This study is funded by Natural Science Foundation of Tianjin (13JCYBJC41800).

## References

1. Technical information institute CO.LTD, The manuals for the measurement and evaluation of the skin (2003).
2. Noiret, N., Carvalho, N., Laurent, E., Vulliez, L., Bennabi, D., & Chopard, G., et al. (2015). Visual scanning behavior during processing of emotional faces in older adults with depression. *Aging & Mental Health*, in press (3), 264–73.
3. M. Yamamoto, Y.-H. Lim, X. Wei, M. Inui, H. Kobayashi: On the preferred flesh colour in Japan, China and South Korea, *Imaging Sci. J.*, 51,163–174 (2003).
4. Naokazu AOKI, Kentaro ISHIT, Taku YAMAWAKI, Mari YAMAMOTO, Hiroyuki KOBAYASHI, Measurement Method of Facial Flesh Color Based on Impression, *Journal of The Society of Photographic Science and Technology of Japan* Vol. 71 (2008) No. 3 P 203–208.
5. García-Blanco, A., Salmerón, L., Perea, M., & Livianos, L. (2014). Attentional biases toward emotional images in the different episodes of bipolar disorder: an eye-tracking study. *Psychiatry Research*, 215(3), 628–633.
6. Perez, C. A., Palma, A., Holzmann, C. A., & Pena, C. (2001). Face and eye tracking algorithm based on digital image processing., 2, 1178–1183 vol. 2.
7. Liu, H., & Heynderickx, I. (2011). Visual attention in objective image quality assessment: based on eye-tracking data. *IEEE Transactions on Circuits & Systems for Video Technology*, 21(7), 971–982.
8. Yoshikawa, H., Kikuchi, K., Takata, S., & Yaguchi, H. (1951). A1-6 study on the evaluation method of skin color distribution using the face region division based on the feature points (special issue 39th annual meeting). *Andrologia*, 7(3), 241–53.
9. Winkler, S., & Subramanian, R. (2013). Overview of Eye tracking Datasets. Fifth International Workshop on Quality of Multimedia Experience (pp. 212–217).
10. Babcock, J. S., Pelz, J. B., & Fairchild, M. D. (2003). Eye tracking observers during color image evaluation tasks. *Proceedings of SPIE—The International Society for Optical Engineering*, 5007, 218–230.

# Study on Color Model on Green Gamut Part for High Fidelity Printing

Xiaoyan She, Shisheng Zhou and Guanjun Zhu

**Abstract** High-fidelity printing technology appears to make up the main flow of four color printing. The more numbers of the primary color becomes one of the important means to improve the quality of printing. Combined with the lookup table method, this paper builds the high-fidelity printing color model in green color area on the basis of the nonlinear and self-learning characteristics in the BP Neural Network algorithm, introducing in the LM\_BP algorithm to improve the traditional BP algorithm. At the same time, we train the model with MATLAB software, testing the model precision and analyzing the error. Based on the analysis of training results, we conclude that although the BP algorithm can meet the expected requirements, the LM\_BP algorithm has higher precision and better approximation effect.

**Keywords** High-fidelity printing · BP neural network · LM-BP algorithm · Color model

## 1 Introduction

Traditional four-color printing has limited color reproduction gamut, the color and saturation are not high enough, and the performance of color gamut between blue and green is poor. However, spot color can reproduce some colors out of printing color gamut of traditional four colors [1]. Multi-color printing [2] is on the basis of high-fidelity technology and means higher saturation color, richer tone image and more attractive effect [3]. In current several main algorithms, polynomial regression algorithm cannot guarantee the consistency of conversion accuracy of the entire gamut. Neugebauer correction algorithm [4] may appear the situation of color union after separation. Look-up table method is greatly affected by distribution uniformity

---

X. She (✉) · S. Zhou · G. Zhu

Faculty of Printing, Packaging Engineering and Digital Media Technology, Xi'an University of Technology, Xi'an, Shaanxi, China

e-mail: 1107397816@qq.com

of sampling space in the conversion process and modeling accuracy will be not stable due to the variation of the sample. The appearance and development of color matching model [5] based on neural network make up the deficiency of the above methods [6]. According to actual situation of high fidelity color printing and combing look-up table method with BP artificial neural network algorithm to establish gravure color printing model, and on this basis to optimize BP algorithm combing LM (Levenberg-Marquard) with BP algorithm its advantages.

## 2 Experiments

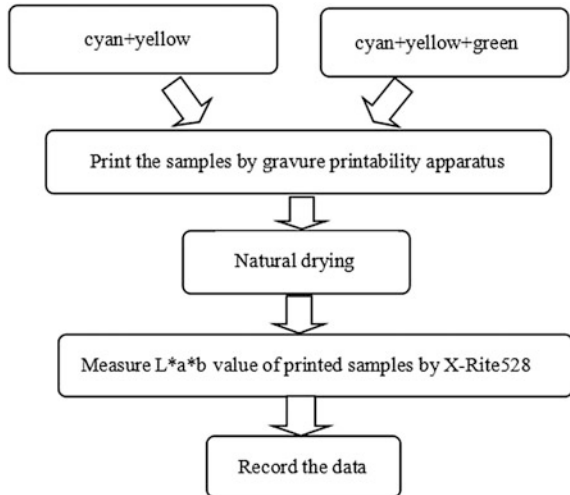
### 2.1 Experimental Process

The experiment includes two parts: one is to blend by cyan and yellow ink of original ink according to different proportion, the other is to blend by blue, yellow ink and special green ink of original ink according to different proportion (need to note that total ink of each group is 10–15 g) (Fig. 1; Table 1).

### 2.2 Experimental Results

In order to make the experimental results more clear, the experimental data should be dealt with. This paper uses Matlab tool software to deal with the data (Fig. 2).

**Fig. 1** Experimental process

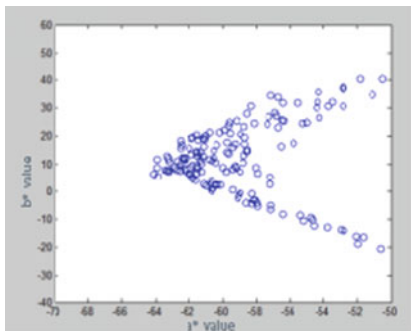


**Table 1** Part of the data of two experiments

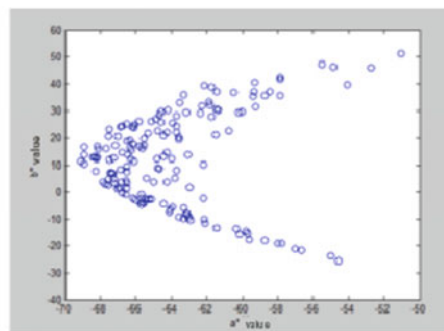
Experiment I:						
Sample S. N.	Blending ratio of printing ink		Measurement data of color			
	C	Y	L*	a*	b*	
1	1/(1 + 2)	2/(1 + 2)	65.51	-40.6	46.11	
2	3/(3 + 10)	10/(3 + 10)	63.4	-40.24	63.52	
3	4/(4 + 9)	9/(4 + 9)	53.38	-57.76	40.73	
4	1/(1 + 1)	1/(1 + 1)	65.51	-40.6	46.11	

Experiment II:						
Sample S. N.	Blending ratio of printing ink			Measurement data of color		
	C	Y	G	L*	a*	b*
1	1/(1 + 3 + 6)	3/(1 + 3 + 6)	6/(1 + 3 + 6)	49.53	-64.57	25.98
2	1/(1 + 4 + 5)	4/(1 + 4 + 6)	4/(1 + 4 + 5)	51.93	-61.47	30.73
3	2/(2 + 1 + 10)	1/(2 + 1 + 10)	1/(2 + 1 + 10)	47.54	-62.18	10.2
4	1/(1 + 1 + 4)	1/(1 + 1 + 4)	1/(1 + 1 + 4)	48.55	-63.06	13.67



Experiment I



Experiment II

**Fig. 2** a\*-b\* plan scatter plot

We can see that the two pictures basically reflect the situation of green color gamut (scattered points concentration part), including the yellow-green and blue-green, however, compared with scattered point concentration range of picture of experiment I (a(-65, -50)b(-20, 40)), the scattered point cover range of picture of experiment II (a(-70, -50)b(-30, 50)) is wider. The green information range of sample obtained in experiment II is wider, what shows that after adding green ink, the green color gamut obtained by three-color printing is wider than what of traditional original color printing.



### 3 MATLAB Simulation and Analysis of Color Model Algorithm

BP neural network model has three-layer network structure: input layer, hidden layer and output layer. This paper studies the relationship between  $L^*a^*b^*$  value of gravure printing sample and CYG monochrome ink dot area ratio. So, gravure sample  $L^*a^*b^*$  value as network input and the number of nodes of input layer is 3; when carrying out sample printing, the basis is CYG monochrome ink quantity, CYG monochrome ink quantity as desired output, and the number of nodes of network output is 3, the initial reference value of hidden layer nodes is about 5. In the network training process, constantly change the number of hidden layer nodes and ultimately determine the optimal number of hidden layer nodes.

#### 3.1 Color Model Simulation and Analysis of BP Algorithm

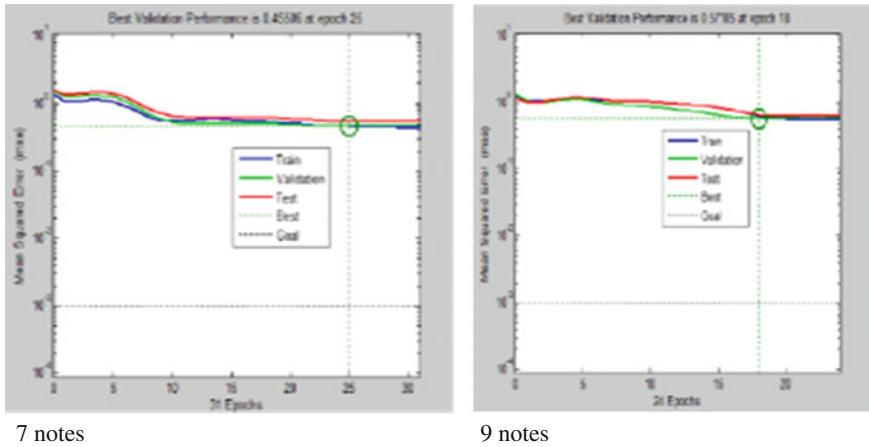
The training is shown in Table 2 (Fig. 3).

They are variation curves of network error in BP algorithm training process when the neurons number of hidden layer is 7 and 9 respectively. Based on observation we can know that, the parameter curve with node number of 7 earlier coincides with target curve, and the mean square error of optimal parameter is small; in the beginning, the parameter curve with node number of 9 does not well coincide, later, gradually approaches the target curve, though the number of iteration is small, but mean square error is large.

Carry out linear regression analysis to the data of training sample set, validation sample set and all sample sets of BP algorithm when the neurons number of hidden layer is 7 and 9 respectively, and obtain correlation coefficient R value between network simulation results and target output, the size of R can be used as judgment basis of network training results. Based on analysis we can know that, in general, R value of neuron number of 7 is larger than what of neuron number of 9; in the pictures with neuron number of 7, the scattered points are concentrated away from

**Table 2** The related parameters of simulation with BP algorithm

Nodes number of hidden layer	Training time (s)	Training number	Mean square error of training data	Error gradient
4	2.1264	63	0.462	0.1862
5	2.1257	22	1.01	0.131
7	2.1239	31	0.455	0.0914
9	2.1199	24	0.572	0.2998
11	2.1225	18	1.31	0.307



**Fig. 3** The training performance of BP neural network algorithm with 7 and 9 notes in the hidden layer

the fitting line, in the pictures with neuron number of 9, the scattered points are decentralized away from the fitting line.

In summary, when the neurons number of hidden layer is 7, the network training is more excellent in training error, training stability and simulation effect. Therefore, when using BP neural network algorithm to train sample set, choose single hidden layer structure with neuron number of 7 to establish color model.

### 3.2 Color Model Simulation and Analysis of LM-BP Algorithm

Through analysis to Table 3 to know that, when the neuron number of hidden layer is 9, though the error gradient of training data is small and training number is less, but the training time and error gradient parameter are higher; however, when the neuron number of hidden layer is 7, the training number and mean square error are minimum, the mean square error of training data is not very large, the change of mean square error is related to network weight and threshold value change.

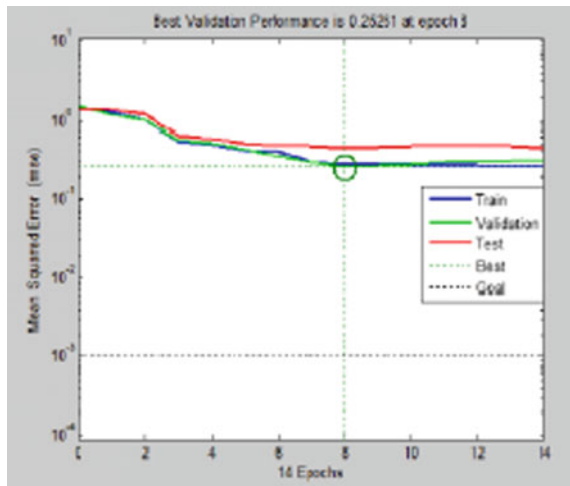
Initially, the choice of MATLAB training network’s weight and threshold value is random, so the training time and characterization of error gradient are the main characteristics parameters. The following chooses neural network training sample set with neuron number of hidden layer of 7 to compare with BP neural network (Fig. 4).

Based on the comparison between training error performance curve of LM-BP algorithm under the nodes number of hidden layer is 7 and what of BP algorithm under the nodes number of hidden layer is 7, we can know that, the iteration number

**Table 3** The related parameters of simulation with LM-BP algorithm

Number of hidden layer nodes	Training time (s)	Training number	Mean square error of training data	Error gradient
4	1.6365	56	0.942	0.0986
5	1.5473	43	1.15	0.131
7	1.4298	14	0.253	0.0755
9	1.4332	11	0.239	0.0836
11	1.4485	18	1.176	0.214

**Fig. 4** The training performance of LM-BP neural network algorithm with 7 notes in the hidden layer

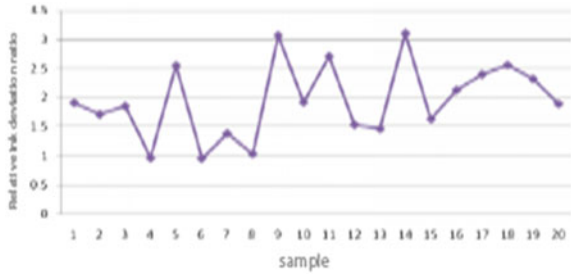


of training sample set of LM-BP algorithm is less and the error performance curve earlier coincides with target curve, in addition, the mean square error of optimal parameter is smaller and has certain improvement compared to BP algorithm.

Carry out linear regression analysis to the data of training sample set, validation sample set and all sample sets of LM-BP algorithm when the neurons number of hidden layer is 7, and obtain correlation coefficient R value between network simulation results and target output, compared with BP algorithm with nodes number of hidden layer is 7, in general, R value of LM-BP algorithm is larger than what of BP algorithm, the correlation coefficient of linear regression is larger, the scattered points of LM-BP algorithm are more concentrated away from the fitting line, and the included angle between fitting line and target curve is smaller, what also shows that network training results are better.

In summary, LM-BP algorithm model with neuron number of hidden layer of 7 can further improve BP algorithm, the training time is shorter, iteration number is less and training simulation effect is also more excellent, so it is an ideal network model.

**Fig. 5** The ink quantity deviation percentage distribution curve of sample



## 4 Discussions

By LM-BP algorithm with neuron number of hidden layer of 7 to establish color model, by relative ink deviation percentage method and color difference method to test the accuracy of the model (Fig. 5).

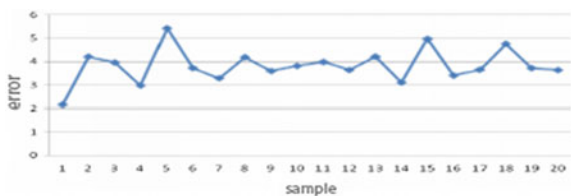
### 4.1 By Relative Percentage of Ink Deviation Method to Test the Accuracy of the Model

The deviation percentage is within 5% shows that the two data is very close. Through analysis we can know that, the deviation percentage of ink quantity of various original inks is almost within 5%, the average ink quantity deviation percentage is basically distributed 1–3%.

### 4.2 By Color Difference Method to Test the Accuracy of the Model

In order to test the accuracy of model, this paper selects 20 groups of samples, by model to calculate C, Y and G ink quantity correspondingly required by  $L^*a^*b^*$  of various samples; then print and use spectrophotometer to measure  $L^*a^*b^*$  value of printing samples, by color difference formula to calculate the difference between sample target color and printing color.

**Fig. 6** The color difference distribution curve of sample



We can see from Fig. 6 that, when calculating the color difference  $\Delta E$  between by model to calculate ink quantity simulating printing color sample and target sample, it is almost within the allowable range of error ( $\Delta E \leq 5 \sim 6$ ), therefore, we can say that it meets the requirements by color difference method to test the accuracy of model.

In order to ensure the accuracy of green area high fidelity printing color model, the paper combines look-up table method with neural network algorithm to solve the problem.

For a target color, if look-up table method can find that the color difference between its  $L^*a^*b^*$  value and the  $L^*a^*b^*$  value of a certain color piece in base database is within  $\Delta E \leq 0.5$ , the ink quantity of the target color should be consistent with color piece of base database.

If look-up table method cannot find sample color piece within color difference range, should use LM-BP neural network algorithm to establish mathematical model, to calculate the ink quantity of C, Y and G three original colors correspondingly by  $L^*a^*b^*$  value of target color.

## 5 Conclusions

Aiming at the limitations of current four-color printing, this paper achieves the expansion of printing gamut through increasing the quantity of original ink, so as to achieve high fidelity color reproduction effect, and ultimately determine that LM-BP algorithm is more suitable for the establishment of mathematical model. Accuracy test and analysis to model prove that the model has higher accuracy and practicability. The color system can also use fuzzy comprehensive evaluation or other genetic algorithm to do further optimization for color matching model, then can further improve the accuracy of the model.

**Acknowledgments** This study is supported by Scientific Research Program of Key Laboratory Funded by Shaanxi Provincial Education Department (14JS067).

## References

1. J A StePhen Viggiano, William J Hoagland. (2000) Colorant selection for six-color lithographic Printing [R]. Rochester NY: PIT Research Corporation.
2. Qi Yongqing, Zhou Shisheng. (2003) Blending of Spot Color and Spot Color Ink [J]. Print World, (6): 22–24.
3. Sun Yanqiong. (2011) The research progress of High fidelity printing technology [J]. Guangdong Printing, (3): 19–21
4. YanLiu. (1992) Spectral Reflectance Modification of Neugebauer Equation [J]. TAGA.
5. A Johustom. Color and Color Matching [J]. The Printing Ink Manual, Van Nostrand. Reinhold. (UK). Page5
6. Zhou Shoulin. (2010) The optimization algorithm and application of BP neural network [D]. Suzhou: Soochow University, 35: 7–9, 27–34

# Polynomial Fitting Approach for Colorimetric Values Transform Based on Large Scale Spectral Dataset

Yijing Xun, Qiang Liu, Xiaoxia Wan, Zheng Huang, Guo Cao  
and Haiwen Wang

**Abstract** Due to the variety of the illuminant-observer devices and different color media, people need to transform the color recorded in a source media into correlated color in another target media. In order to keep the color consistency in different media and achieve high color transform accuracy for digital color reproduction, a polynomial fitting approach based on large scale spectral dataset was proposed. The large scale spectral dataset includes most areas of color gamut and it was partitioned into 12 subsets according to dominant wavelength and excitation purity. The source colorimetric values of each subset were regarded as variate and it was made the variable dimension expansion following some principles. The coefficient matrix could be calculated by the source colorimetric values and the target colorimetric values. The experimental results of the proposed approach showed good transform precision for colorimetric values. So the approach based on polynomial fitting could realize the transformation between different colorimetric values with good performance.

**Keywords** Colorimetric values transform · Chromatic adaptation · Spectral dataset · Polynomial fitting · Color equivalency

---

Y. Xun · Q. Liu · X. Wan · Z. Huang  
School of Printing and Packaging, Wuhan University, Wuhan 430079, China

Q. Liu  
Shen Zhen Institute, Wuhan University, Shenzhen 518000, China

Q. Liu (✉)  
State Key Laboratory of Pulp and Paper Engineering, Guangzhou 510640, China  
e-mail: liuqiang@whu.edu.cn

G. Cao  
Shen Zhen Fu Tian N1 Digital Building Studio, Shenzhen 518000, China

H. Wang  
School of Biological and Chemical Engineering/School of Light Industry, Zhejiang  
University of Science and Technology, Hangzhou 310023, China

## 1 Introduction

Colorimetric values transformations are becoming more and more popular in recent researches. People need to transform the source color values in one condition into target color values in another condition, such as reproduction of painting, sensor excitations transforms and so on. There are many methods that play a bridge role between different color media. According to the existing researches, we sum up two ways to get the transform values.

Chromatic Adaptation Transform (CATs) [1] is the first way that focuses on the color constancy under digital imaging workflow. This method made the full use of the chromatic adaptation ability of human vision system (HVS) in order to decrease the color differences under various illuminants [2]. There are six CAT methods as Von Kris, Bradford, XYZ scaling, CMCCAT97, CMCCAT2000 and CAT02 that are typical CAT models and commonly used in many cases.

The second way pay more attention on colorimetric reproduction accuracy for digital color imaging. The method aims at predicting the colorimetric values of one spectral color under target illuminant-observer condition according to the corresponding values under source condition [3–5]. This kind of approach was classified as Material Adjustment Transform (MAT) [6, 7] in recently literature because it focuses on the color material. In 2014, Kreslin et al. [4] developed a linear delaunay triangulation method for image illuminant adaptation. According to this method, we can use Eq. 1 to get the predicted CIEX, Y, Z values, where  $C_{source}$  and  $C_{target}$  denote the CIEX, Y, Z values under source and target illuminant-observer condition,  $A_{source}$  and  $A_{target}$  indicate the Waypoint normalization matrix relative to source and target condition.

$$C_{target} = (A_{target})^{-1}(A_{source}) \cdot C_{source} \quad (1)$$

Derhak and Berns [8] summarized the research progress of CATs and MATs and defined those approaches as *color equivalency representation* in 2014. They proposed a Waypoint method for material adjustment transform [8]. Because we discuss the chromatic values in this study, we refer the proposed method to the colorimetric values transform which is one of the MAT methods.

Because the colorimetric location of these methods' training color samples cannot cover whole gamut of real world colors, the colorimetric transform precision is not always in a high level. These methods seem to suffer from poor transform performance in high saturation regions and don't have the prominent precision in real world color gamut. What's more, it may also bring transform errors if simulating the nonlinear process of colorimetric values transform with linear model.

According to previous works, a polynomial fitting approach based on large scale spectral dataset was proposed in order to enhance the transform precision. Meanwhile a typical Japan pigments color dataset together with a spectral image was used as testing samples to verify the proposed approach. And comparisons with all above methods about the colorimetric transform performance were adopted. The

verified tests were finished under several source and target conditions and the statistics of experimental results proves the effectiveness of the proposal.

## 2 Experimental

At the beginning of the study, the experimental data samples were gathered. Then a polynomial fitting approach was trained constantly to make an appropriate conversion factor to implement the color adaptation conversion and make reasonable explanations of the proposed method in the end.

The large scale dataset that used in this study was built up by two steps. First, we selected several existing spectral color datasets and grouped them together under the principle of gamut maximization. The spectral color datasets included the munsell glossy and matt color chips [9], the Dunhuang mineral pigment color chips painted by the thesis adviser [10], the Macbeth Colorchecker DC and IT8.7/2 color charts [11] as well as the ink-jet printed color samples of the former research [12]. A spectrophotometer was used to gain the spectral information for self-made color samples, from 400 to 700 nm in 10 nm intervals. Second, we picked up the final 8650 colors from the 13,035 color chips that collected in the first step, basing on their CIE 1931 chromaticity. Then divided the CIE 1931 chromaticity diagram under D50/2 condition by a grid and the length of each unit side equals to 0.002 diagram unit. We randomly chose one of the candidate colors locating in each grid unit finally.

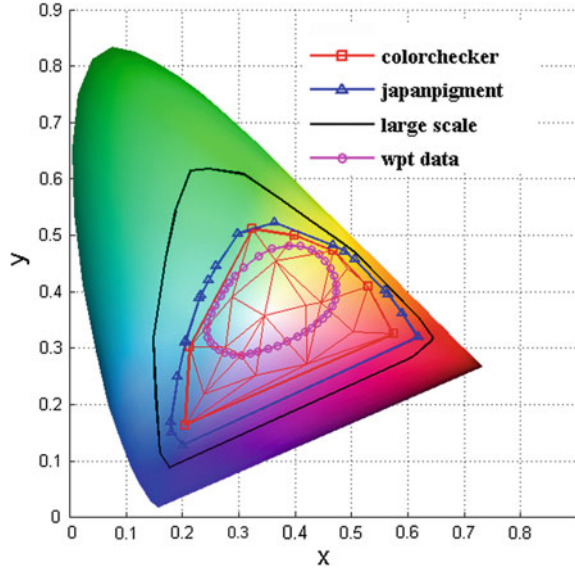
As for the following Fig. 1, it's a comparison among the 8560 color chips of the proposed large scale spectral dataset, the ColorChecker, Japan pigment, wpt data and large scale respectively represent the 24 Colorchecker color chips, the 1687 Japan pigment color chips and the 42 color samples used in Derhak's work. It's obvious that the proposed dataset was covered most of the real world color gamut.

Base on the large scale spectral dataset, a polynomial coefficient matrix was developed. Polynomial fitting is a straight way to get corresponding response values between the source spectrum space and target spectrum space through the modeling samples. And using the polynomial equation could approximate the real conversion mapping for real color space. Once the coefficient of polynomial equation determines, we can predict the target spectrum values by the multinomial coefficient for an arbitrary source illuminant-observer color value [13, 14].

The first step of this study, we analyzed the close relationship between the transform accuracy and the hue and chroma of the experimental colors. So the dominant wavelength and excitation purity were adopted to group the large scale spectral dataset for the reason that they respectively express hue and chroma in Colorimetry. Firstly, the dominant wavelength of colors was calculated with a source illuminant-observer combination. Then selected the colors with negative dominant wavelength to form a group, and other colors were uniformly divided into 5 groups based on the same metric. Afterwards, each group was further uniformly divided into 2 subsets according to the excitation purity of each spectral color. Finally we got 12 subsets and each subset is constituted by 700 spectrum on average.



**Fig. 1** Gamut comparison between different color datasets in CIE 1931 chromaticity diagram under D50/2 illuminant-observer condition



In this study, we use vector  $V_s$  represents the source illuminant-observer color values while  $P_t$  represents the target illuminant-observer color responding values. The correlation model can be described by Eq. 2, where  $A$  is the correlation coefficient.

$$P_t = A \cdot V_s \quad (2)$$

When  $V_s$  only have three terms, this is a linear conversion. If we increased the cross terms or high-degree terms to expand  $V_s$ , the conversion between  $V_s$  and  $P_t$  is nonlinear. Then we assume  $n$  as the terms of vector  $V_s$ , there are variety of forms about  $V_s$  with different  $n$ .

$$n = 3, V_s = [X Y Z]$$

$$n = 5, V_s = [1 X Y Z XY Z]$$

$$n = 7, V_s = [1 X Y Z XY YZ XZ XYZ]$$

$$n = 9, V_s = [X Y Z XY YZ XZ X^2 Y^2 Z^2]$$

$$n = 10, V_s = [1 X Y Z XY YZ XZ X^2 Y^2 Z^2]$$

$$n = 11, V_s = [1 X Y Z XY YZ XZ X^2 Y^2 Z^2 XYZ]$$

After calculating the coefficient matrix  $A$ , it's easy to get the predictive colorimetric values from the polynomial. When transferred certain CIEX, Y, Z values

from source to target condition, the dominant wavelength and excitation purity under source illuminant-observer condition were calculated. Then by comparing the dominant wavelength and excitation purity to the group threshold of 12 subsets under source condition, the appropriate subset and the corresponding coefficient matrix  $A$  would be chosen.

### 3 Experimental Verification

We have test the model in order to fulfill the precision requirement. The comparative experiments to verify the proposed polynomial fitting approach was adopted. The Japan pigment dataset was divided into 2 subsets as 1450 in-gamut colors and 237 out-gamut colors according to the positional relationship between each dataset color and the gamut of Colorchecker. The color difference between target values and predictive values were calculated when chose different  $n$  with in-gamut test samples at the same time. The results obviously have shown that we can get a high fitting precision when  $n$  equals to 9, which  $V_s = [X Y Z XY YZ XZ X^2 Y^2 Z^2]$ .

As the coefficient terms increasing that the accuracy gradually increasing but the accuracy begin to fall down after  $n$  equals to 9. High order regression model has led to the decrease of the generalization ability and it cannot ensure accuracy of optimization. That is to say, the model has a morbid equation when the polynomial order increase and decline occurs to the model generalization ability [13].

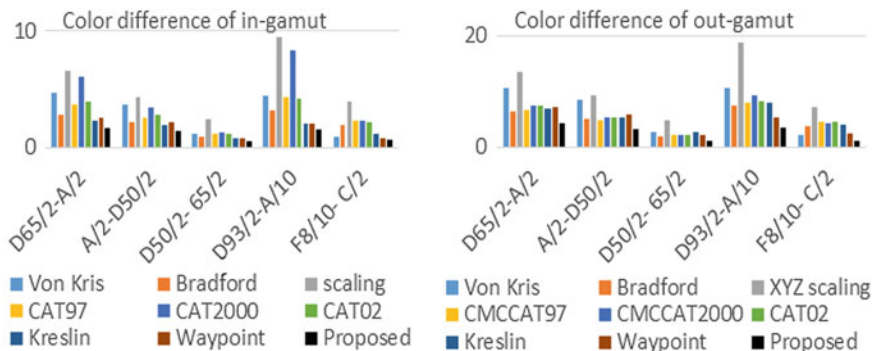
In colorimetric values transform study, eight existing methods as mentioned before: 6 typical CAT models as Von Kris, Bradford, XYZ scaling, CMCCAT97, CMCCAT2000 and CAT02, Kreslin method and Waypoint method were used. This study has already calculated the color difference for all above methods through the adoption of the Japan pigment dataset.

### 4 Results and Discussion

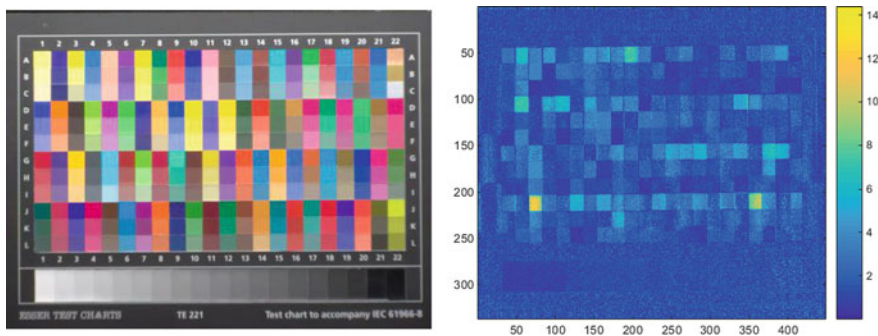
After calculating the color difference among different methods as Fig. 2, where show the average color difference about 1450 in-gamut and 237 out-gamut Japan pigment colors under 5 different source-target condition pairs with different methods. The colorimetric performance of those experimental transforms is represented in form of CIELAB color difference between the actual and predictive CIEXYZ values under target condition. In order to prove the effectiveness straightly and visualize the performance of the method, the spectral image of Esser TE221 colorchart [11] was adopted in the experiment as shown in Fig. 3.

We have got the following conclusions from these figures.

As can be seen from Fig. 2, the Waypoint method shows similar performance with Kreslin's approach. And the presented nonlinear polynomial fitting approach is



**Fig. 2** Color difference about the Japan pigment colors which locate inside gamut (*left*) and outside gamut (*right*) under 5 different source-target condition pairs with different methods



**Fig. 3** The image of Esser TE221 color chart rendered in sRGB space under D65/2 condition (*left*) and colorimetric values transform accuracy of proposed method from F2/2 to D65/2 (*right*)

better than the Kreslin’s linear matrix approach. Meanwhile, the CAT methods show the obvious defects in colorimetric values transform when compared with the regression of Kreslin, Waypoint and presented method generally. The problem straightly points to their maximum transform values. It’s mainly because of the fact that the original idea for the derivation of CATs was not for proceeding colorimetric values transforms but for predicting corresponding colors. What’s more, for the comparison among each CATs, the Bradford method has the best transform results regardless of the examined source-target condition pairs. For our proposed method, it plays a good performance that all average color differences are less than 2.

There are large transform errors in high saturated regions for all the other methods while the proposed method has a better accuracy. This is mainly because of the gamut incompleteness of the corresponding color datasets for the colorimetric transform issue. As for Kreslin’s method, since all of the 237 out-gamut color samples exceed the Colorchecker gamut, its transform accuracy turns out to be worse than that of Bradford. Similarly, because the 237 out-gamut colors are much

more saturated than training samples, the Waypoint method also suffers from poor performance. For our study, the average color differences only get a little better accuracy. Such phenomenon proves the necessity of the large scale spectral dataset. The disadvantage may be because of the polynomial fitting defects that the terms of coefficient matrix will influence the accuracy. The accuracy will increase when the degrees increased, but it will be hard to calculate if the model is too complex then the errors will come up in that regions where not involved the training samples.

The results of Fig. 3 indicate much more intuitive. This figure indicates the comprehensive evaluation for the performance of the method at whole-gamut level. It's straightforward to see that the method will always lead to remarkable transform accuracy. Although there have some big errors exceed 10 in some of the high-saturated colors. We can get a high transform precision when we used the polynomial fitting approach.

## 5 Conclusions

Most of the color information in digital color media is represented and transformed in colorimetric forms in current stage. Because of the diversity in colorimetric specification among different color media, certain approach must be developed to transform the colorimetric values among various illuminant-observer conditions. The best method is that gives the smallest color differences between computed XYZ values from spectral data and target XYZ values. In this research, a polynomial fitting approach based on a newly built large scale spectral dataset was proposed. The performance of the proposed approach was testified straightly in comparison with several existing methods under multiple source-target conditions. The experimental results indicate that this method is accurate for colorimetric values conversion.

In conclusion to this, the polynomial fitting method would be one of the competitive candidates for the applications in colorimetric imaging field.

**Acknowledgements** The authors acknowledge the support of the Open Fund of the State Key Laboratory of Pulp and Paper Engineering (grant No. 201528), the Nature Science Foundation of Hubei Province in China (grant No. 2015CFB204), Shenzhen basic research project (grant No. JCYJ20150422150029093) and National Natural Science Foundation of China (grant No. 61505149).

## References

1. Y. Nayatani (2006). Development of Chromatic Adaptation Transforms and Concept for Their Classification. *Col Res Appl*, 31(3), 205–217.
2. N. Bourbakis, P. Kakumanu, S. Makrogiannis, R. Bryll, and S. Panchanathan (2007). Neural network approach for image chromatic adaptation for skin color detection. *Int. J. Neural. Syst*, 17(1), 1–12.

3. S. Zuffi (2005). Colorimetric and spectral-based printing: a simple comparison. SPIE(M) Conference on Photonics in the Automobile, 178–185.
4. R. Kreslin, P. M. Calvo, L. G. Corzo, and P. Peer (2014). Linear Chromatic Adaptation Transform Based on Delaunay Triangulation. *Math. Probl. Eng.* 760123.
5. D. Dordevic, A. Javorek, and A. Hladnik (2010). Comparison of chromatic adaptation transforms used in textile printing sample preparation. *Color. Technol.* 126(5), 275–281.
6. A. D. Logvinenko and R. Tokunaga (2011). Color Constancy as Measured by Least Dissimilar Matching. *Seeing Perceiving*, 24(5), 407–452.
7. A. D. Logvinenko (2013). Object-Color Manifold. *International journal of Computer Vision*, 101(1), 143–160.
8. M. W. Derhak and R. S. Berns (2014). Introducing Wpt (Waypoint): A Color Equivalency Representation for Defining a Material Adjustment Transform. *Color Res Appl*, 40(6), 535–549.
9. O. Kohonen, J. Parkkinen, and T. Jääskeläinen (2006). Databases for spectral color science. *Col. Res. Appl*, 31(5), 381–390.
10. Q. Liu, X. Wan, Z. Liu, C. Li, and J. Liang (2013). Research on Developing the Spectral Dataset for Dunhuang Typical Colors Based on Color Constancy. *Spectrosc Spect Anal*, 33(11), 3077–3080.
11. G. Finlayson, S. Hordley and P. Morovic (2004). Using the spectra cube to build a multispectral image database. Proc. Conference on Color in Graphics, Imaging, and Vision, Aachen, Germany, 268–274.
12. Q. Liu, X. Wan and H. P. Xu (2013). Study on Ink Restriction of Ink-Jet Printing Based on spectral Gamut Maximization. *Spectrosc Spect Anal*, 33(6), 1636–1641.
13. Yong Wang, Haisong Xu (2007). Colorimetric Characterization for Scanner Based on Polynomial Regression Models [J]. *Acta Optica Sinica*, 27(6), 1135–1138.
14. Liang Hong, Xinzhong Jiang (2013). Research on the display color space conversion model based on polynomial regression method [J]. *Journal of Henan Institute of Engineering (Natural Science Edition)*, 25(3), 61–64.

# Study on Color Matching Technology of Flexographic Printing Ink

Ben Liu, Maohai Lin, Guichun Hu and Meiqi Lin

**Abstract** The environmental pollution problems cause for people's concern in recent years. Due to using environmental aqueous spot-color ink, flexographic printing shows a great potential, and the problem of high-precision flexographic printing color matching also becomes a hot topic. In this paper, the problem of computer color matching of flexographic printing aqueous spot-color ink was studied. Using flexographic IGT printability tester and yellow, magenta, cyan primary colors of ink to carry out color matching experiments and obtain the color samples by changing the concentration ratio of base ink. After utilizing the spectrophotometer to measure the chromatic, we take Kubelka-Munk theory as the guide theory, which studied the color model based on the theory of the new double constant Kubelka-Munk and the model of spectral matching based on weighting factor, and carried on the evaluation. The experimental results show that the spectral color model based on the weighting factor has higher precision of color matching in terms of color model of the new double constant Kubelka-Munk theory.

**Keywords** Flexographic printing · Kubelka-Munk theory · Color matching model

## 1 Introduction

At present, color matching by hand is the most used method for spot-color ink, this method requires engineers experienced with color matching and it is time consuming as well as leads to materials waste easily which can't meet the needs of printing industry [1]. The development of computer and instrument measuring color can solve the problems to some extent. Color matching by computer is usually

---

B. Liu · M. Lin · G. Hu · M. Lin

School of Printing and Packing Engineering, Qilu University of Technology, Jinan, China

M. Lin (✉) · G. Hu

State Key Laboratory of Pulp and Paper Engineering, South China University of Technology, Guangzhou, China

e-mail: imhlin@163.com

© Springer Nature Singapore Pte Ltd. 2017

P. Zhao et al. (eds.), *Advanced Graphic Communications*

and *Media Technologies*, Lecture Notes in Electrical Engineering 417,

DOI 10.1007/978-981-10-3530-2\_12

based on the double constant Kubelka-Munk theory which thus needs to get the  $k$  value and  $s$  value of each primary color of ink [2]. The computation of  $k$  value and  $s$  value is complex. He et al. [3] proposed a new double constant Kubelka-Munk theory to simplify the computation process. Yu et al. [4] also do the related research.

In this paper, taking Kubelka-Munk theory as the guide theory, which studied the color model based on the theory of the new double constant Kubelka-Munk and the model of spectral matching based on weighting factor, and carried on the evaluation [5]. The experimental results show that the spectral color model based on the weighting factor has higher precision of color matching in terms of color model of the new double constant Kubelka-Munk theory.

## 2 The New Double-Constant Tristimulus Value Color Matching

In this paper, yellow, magenta, cyan primary colors of ink carried out color matching experiments. Spectrophotometric data of each wavelength are available. Normally, this was done from 360 to 740 nm in 20-nm increments, yielding 20 points. Based on the new double constant Kubelka-Munk theory, the reflectivity  $R$  is a function of the absorption coefficient  $K$  and the reflection coefficient  $S$ , and the partial differential theory can be used,

$$\Delta R = \left[ \frac{\partial R}{\partial \left(\frac{K}{S_t}\right)} \Delta \left(\frac{K}{S_t}\right) + \frac{\partial R}{\partial \left(\frac{S}{S_t}\right)} \Delta \left(\frac{S}{S_t}\right) \right] \quad (2.1)$$

That is,

$$R_j^a - R_j^m = \frac{\partial R_j^a}{\partial (K^a/S_t)_j} \left[ \left(\frac{K^a}{S_t}\right)_j - \left(\frac{K^m}{S_t}\right)_j \right] + \frac{\partial R_j^a}{\partial (S^a/S_t)_j} * \left[ \left(\frac{S^a}{S_t}\right)_j - \left(\frac{S^m}{S_t}\right)_j \right]$$

where:  $a$  represents standard color sample;  $m$  represents matching color sample;  $i$  represents the type of base ink;  $j$  represents the specific wavelength,  $j = 360, 380, \dots, 740$  nm.

According to the new double constant Kubelka-Munk theory,

$$\frac{K^m}{S_t} = \left(\frac{K}{S}\right)^t + \sum C_i \left(\frac{K}{S_t}\right)^j \quad (2.2)$$

$$\frac{S^m}{S_t} = 1 + \sum C_i (S/S_t)^i \quad (2.3)$$

By formula (2.1)–(2.3) the difference between the standard color and the color matching spectral reflectance,

$$\begin{aligned}
 R_j^a - R_j^m &= \frac{\partial R_j^a}{\partial (K^a/S_t)_j} \left[ \left( \frac{K^a}{S_t} \right)_j - \left( \frac{K^m}{S_t} \right)_j \right] + \frac{\partial R_j^a}{\partial (S^a/S_t)_j} * \left[ \left( \frac{S^a}{S_t} \right)_j - \left( \frac{S^m}{S_t} \right)_j \right] \\
 &= \frac{\partial R_j^a}{\partial (K^a/S_t)_j} \left[ \left( \frac{K^a}{S_t} \right)_j - \left( \frac{K}{S} \right)_j^t - \sum_{i=1}^3 C_i \left( \frac{K}{S_t} \right)_j^i \right] \\
 &\quad + \frac{\partial R_j^a}{\partial (S^a/S_t)_j} * \left[ \left( \frac{S^a}{S_t} \right)_j - 1 - \sum_{i=1}^3 C_i \left( \frac{S}{S_t} \right)_j^i \right]
 \end{aligned} \tag{2.4}$$

Formula (2.4) is rewritten as a matrix form,

$$\Delta R = R^a - R^m = D_k (f_k^a - f^t - \Phi_k C) + D_s (f_s^a - n - \Phi_s C) \tag{2.5}$$

Formula matrix of CMY base ink combination  $C = [C^C C^M C^Y]^T$ ,  $n$  is the matrix of  $20 \times 1$ .

According to the new double constant Kubelka-Munk theory,

$$C = [T * E * (D_k * \Phi_k + D_s * \Phi_s)]^{-1} * T * E * [D_k (f_k^a - f^t) + D_s (f_s^a - n)]. \tag{2.6}$$

### 3 Spectrophotometric Color Matching

Color matching is performed by using the reflection spectrum of the object, even if the difference is the smallest between the spectral reflectance of the raw material formula and the spectral reflectance of the standard sample at each wavelength. That is  $\sum [\Delta R^2(\lambda)] \rightarrow 0$ . This kind of color matching method, regardless of the lighting source, who is the observer the color of the samples are consistent with the standard samples, is an ideal color scheme.

Wang Xichang et al. proposed panchromatic spectral color matching method of the uniform color space weighting factor, and panchromatic spectral color matching method of the uniform color space weighting factor minimize the color difference by direct spectral fitting curve [6]. The basic idea of this method is,

$$\sum_j \omega^2(\lambda_j) [\Delta R(\lambda_j)]^2 \rightarrow \min \tag{3.1}$$

where:  $\omega(\lambda_j)$  weighting factor;  $\Delta R(\lambda_j)$  spectral reflectance difference between the target color and matching color at the wavelength  $\lambda_j$ .

In this paper, considering the panchromatic spectral color matching method of the uniform color space weighting factor of the impact of changes in different



wavelengths of the chromatic aberration from the theory of colorimetry. The weight factor minimize the color difference caused by the spectral reflectance of a wave of changes, so the weight factor real anti the difference perception of color caused by the spectral reflectance of different wavelength changes, which can be considered a good weight factor. Its mathematical expression is,

$$\omega(\lambda_j) = S(\lambda_j) \left\{ [L'(Y)\bar{y}(\lambda_j)]^2 + [A'_X(X, Y)\bar{x}(\lambda_j) + A'_Y(X, Y)\bar{y}(\lambda_j)]^2 + [B'_Y(Y, Z)\bar{y}(\lambda_j) + B'_Z(Y, Z)\bar{z}(\lambda_j)]^2 \right\}^{\frac{1}{2}} \quad (3.2)$$

where:  $S(\lambda_j)$ -CIE Relative spectral power distribution of standard lighting body;  $\bar{x}(\lambda_j)\bar{y}(\lambda_j)\bar{z}(\lambda_j)$ -CIE three stimulus of standard colorimetric observer;  $L'(Y)A'_X(X, Y)A'_Y(X, Y)B'_Y(Y, Z)B'_Z(Y, Z)$ -parameters associated with the standard color three stimulus.

In addition, there is a mathematical expression of weight factor,

$$\omega(\lambda_j) = [(\bar{x}(\lambda_j) + \bar{y}(\lambda_j) + \bar{z}(\lambda_j))S(\lambda_j)]^{1/4} \quad (3.3)$$

and

$$\omega(\lambda_j) = \left[ (\bar{x}(\lambda_j) + \bar{y}(\lambda_j) + \bar{z}(\lambda_j))S(\lambda_j) \right]^{1/4} [R_{\text{std}}(\lambda_j)]^{-2/3} \quad (3.4)$$

To make the formula (3.1) set up, that is,

$$\omega\Delta R = 0 \quad (3.5)$$

The formula (2.5) into the formula (3.5), we can know,

$$[\omega(D_k\Phi_k + D_s\Phi_s)]C = \omega[D_k(f_k^a - f^t) + D_s(f_s^a - n)] \quad (3.6)$$

That is,

$$C = \left\{ [\omega(D_k\Phi_k + D_s\Phi_s)]^T [\omega(D_k\Phi_k + D_s\Phi_s)] \right\}^{-1} [\omega(D_k\Phi_k + D_s\Phi_s)]^T \times \omega[D_k(f_k^a - f^t) + D_s(f_s^a - n)]. \quad (3.7)$$

## 4 Evaluation of Color Matching Model

### 4.1 Experiment

1. Measure the reflectance of the paper and the ink with X-Rite i5 points spectrophotometric meter (10° field of view, D65). Spectrophotometric data of each wavelength are available. Normally, this is done from 360 to 740 nm in 20-nm

- increments, yielding 20 points and the color values of the primary ink. The data need to measure three times.
2. Selected the color lump as the target color, and then measuring their reflectance and chromatic values, measured in 3 averages. The data need to measure three times.
  3. Use the printability tester proofing after calculating the patch density formula, and then measuring the chromatic value of spline.

### 4.2 Experiment Procedure

First, obtain each ink’s new double-constant values, as shown in Table 1. Second, choose 8 color piece as the standard sample, denoted as 1, 2, ..., 8, and calculate their ratio by the models of the new double-constant Kubelka-Munk theory and the spectral matching based on weighting factor. Then printed it by using the flexographic printing printability tester, Finally measure their chromatic value with spectrophotometric meter and calculation color difference, as shown in Table 2 of using the new double-constant Kubelka-Munk theory and Table 3 of using the spectral matching based on weighting factor. Color difference use  $L^*a^*b^*$  CIE1976 in uniform color space [7].

### 4.3 Results and Analysis

From the Table 2, we can see that the color difference are within 9, in which the maximum value is 8.78, the minimum value is 2.76, and the color difference within 6 in the Table 3, in which the maximum value is 5.86, the minimum value is 1.35. Therefore, it can be concluded that the color difference calculated by the new double constant Kubelka-Munk theory model is generally higher than that calculated by the spectral color matching model. So the spectral color matching model is better than the new double constant Kubelka-Munk theory model.

**Table 1** Each ink new double-constant values

Wavelength(nm)	$k/S_i(c)$	$s/S_i(c)$	$k/S_i(m)$	$s/S_i(m)$	$k/S_i(y)$	$s/S_i(y)$
360	3.1829	-0.5769	1.0822	-0.2912	2.0430	-0.1262
380	1.1949	-0.9090	1.1225	-0.4202	2.3460	-0.4315
400	0.2416	-0.9551	1.1362	-0.5052	3.0510	-0.5317
...	...	...	...	...	...	...
740	0.3430	-0.9129	0.0007	-0.2869	-0.0015	-1.0493

**Table 2** Color difference between standard samples and target samples by the new double constant Kubelka-Munk theory model

Number	L1	a1	b1	L2	a2	b2	$\Delta E$
1	37.39	-23.28	8.16	43.70	-23.05	13.21	6.43
2	36.79	-16.69	-6.26	38.91	-20.47	1.74	6.80
3	45.71	-23.24	20.41	48.44	-23.70	25.42	3.65
4	41.66	-22.89	14.93	46.85	-23.05	19.25	5.42
5	58.52	43.75	43.73	56.12	47.95	36.41	5.51
6	35.42	-20.4	-0.36	40.22	-22.23	6.84	6.49
7	52.71	53.55	33.14	54.85	50.11	32.45	2.76
8	33.43	-12.94	-14.39	35.65	-18.26	-4.55	8.78

**Table 3** Color difference between standard samples and target samples by the spectral color matching model

Number	L1	a1	b1	L2	a2	b2	$\Delta E$
1	37.39	-23.28	8.16	42.02	-23.17	11.47	4.56
2	36.79	-16.69	-6.26	37.68	-19.92	-1.01	4.68
3	45.71	-23.24	20.41	48.21	-23.43	23.19	2.81
4	41.66	-22.89	14.93	45.32	-23.79	19.80	4.26
5	58.52	43.75	43.73	56.87	46.62	34.22	5.86
6	35.42	-20.4	-0.36	39.71	-21.07	3.52	4.58
7	52.71	53.55	33.14	53.92	52.03	31.53	1.35
8	33.43	-12.94	-14.39	36.57	-16.29	-9.43	5.28

## 5 Conclusions

In this paper, the new double constant Kubelka-Munk theory model and the spectral color matching model were studied, and then made a detailed introduction to the new double constant Kubelka-Munk theory model and the spectral color matching model, and the experiment has been done to evaluate it. The experimental results showed that the spectral color matching model has a high accuracy than the new double constant Kubelka-Munk theory model. However, the spectral color matching model still cannot meet the requirements of the printing industry. Therefore, it still needs to be further improved.

**Acknowledgements** This work was supported by State Key Laboratory of Pulp and Paper Engineering (201606 and 201609).

## References

1. TANG Yixiang, ZHOU Shisheng. Theory of Flexographic Spot-color Ink Matching[J]. PACKAGING ENGINEERING.2005,26(5):55-57.1001-3563.2005.05.019.
2. LUO Guanglin, GAO Hu, WANG Haimei. Method of Ink Color Matching Used in Gravure Printing Based on Kubelka-Munk Theory and Two Constants [J]. PACKAGING ENGINEERING. 2006. 12.
3. HE Guoxing. The Method of Determining New Two-constant of Colorant [C]. Proceedings of China Optical Society. 2004.
4. YU Mengmeng, TANG Zheng-ning, Research on Color Matching Algorithm for Spot Color Ink Based on New Two-constant Kubelka-Munk Theory [J]. PACKAGING ENGINEERING. Vol.31, No, 13. 2010. 07.
5. WANG Xichang.The Method of Full Spectrum Color Matching Space Weighting Factor. OPTICS AND PRECISION ENGINEERING.1998,10(30):1-4.
6. LI Yanni. Spectrophotometric Color Matching Based on Weight Factor [J]. PACKAGING ENGINEERING. 1001-3563 (2016) 07-0147-04.
7. XU Haisong, YE Guanrong. A Study of Computer Color Matching Predication Algorithms [J]. Acta Optica Sinica. 1996, 16(11): 1657-1661.

# Study on Gamut Mapping Algorithm Based on GRNN

Pukang Yuan, Qiang Wang, Lingjun Kong and Quanhui Tian

**Abstract** The paper proposed a new gamut mapping algorithm based on General Regression Neural Network (GRNN) for the problem that the color of pictures can't be reproduced perfectly in the cross media transmission. The two groups color samples were created by Matlab. One color group is Adobe RGB as the original gamut, and the other is sRGB as the aim gamut. Then they were converted into a Profile Connection Space (PCS), such as CIE LAB or IPT. The GRNN gamut mapping module, the mapping relationship of the original gamut and reproduction gamut, were calculated with color samples. The color differences of mapping and original pictures are small in general and the saturation of mapping picture is higher than that of original picture. The different PCS has effect on the mapping result of specific type picture. The gamut mapping result of GRNNGM (General Regression Neural Network Gamut Mapping) algorithm is better than the HPMINDE (Hue Perceived Minimum Color Difference Error) algorithm. Lab space is more fit with the face picture mapping and there are no significant differences to the other types of pictures.

**Keywords** Gamut mapping algorithm · CIE LAB · IPT · Generalized regression neural network

## 1 Introduction

Color management of devices or images is a foundation to make the color images as same as possible when they were converted to different color space or devices. The gamut mapping is the core process in ICC color management [1]. The gamut

---

P. Yuan (✉)

College of Communication and Art Design, University of Shanghai for Science and Technology, Shanghai, China  
e-mail: yuanpukang@hotmail.com

Q. Wang

School of Media and Design, Hangzhou Dianzi University, Hangzhou, Zhejiang, China

L. Kong · Q. Tian

Shanghai Publishing and Printing College, Shanghai, China

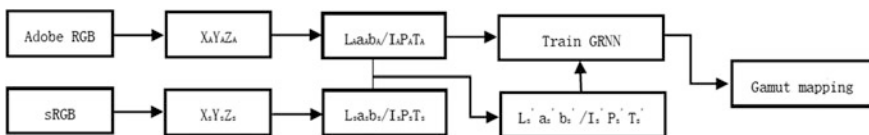
mapping algorithms can be divided into device-to-device algorithms and image-to-device algorithms. The suitable gamut algorithm should be chosen to minimize the difference of the original image and reproduced image.

In 2005, Lee and Han [2] proposed the gamut mapping based on the ANN, Zhao and Tang [3] presented the algorithm based on BP Neural Network, Wu et al. [4] raised an unsupervised algorithm based on Self-Organizing Maps Neural Network. The paper proposed a supervised gamut mapping algorithm based Generalized Regression Neural Network (GRNN), which was a kind of Radial Basis Function (RBF) Neural Network [5], two different steps and amounts color samples are used to train the GRNN in Matlab, which achieve the gamut mapping from Adobe RGB to sRGB and the mapping result and efficiency of the algorithm is better and higher than classical algorithm's.

## 2 Method

The implement flow of the experiment is shown in the Fig. 1. The source space is Adobe RGB and destination space is sRGB for the experiment verification. Two groups of Color blocks were created in the Matlab, which every channel value of pixels is from 0 to 255 and the step is 5 in one group and created 140,608 ( $52^3$ ) color blocks as the colors belong to sRGB, and the other group's step is 15 and the number of colors blocks is 5832 ( $18^3$ ) which belong to Adobe RGB. The color blocks of two groups were converted from RGB space to XYZ space through analytical equations. Finally color samples were transformed into Profile Connect Space (PCS). There are two kinds of PCS, CIELAB and IPT [6], were chosen in the algorithm. According to the literature [6], the linear relationship of hue angle of colors in IPT is better than in CIE LAB. In Lab space, 5832 color points was selected out from sRGB, which had closest Euclidean distance with the color points from Adobe RGB. Color points from the Adobe RGB are as the input samples and color points from sRGB are as output samples to create the GRNN as the gamut mapping model. Finally, input the data from Adobe RGB gamut and then get the result to sRGB gamut in the PCS. After a series inverse transformation, we get the sRGB three channels values. The algorithm was named GRNN Gamut Mapping (GRNNGM) and that GRNN trained in CIE LAB or IPT was named GRNNGM-Lab or GRNNGM-IPT.

1000 color blocks from Adobe RGB were converted into PCS and used GRNN-Lab or GRNN-IPT to change the gamut to sRGB and compared the color



**Fig. 1** Flow chart of the algorithm

difference with the 1000 color samples from sRGB which had same channel values and converted to the same PCS with the 1000 color blocks from Adobe RGB. The reference images from TID2008 were used to gamut mapping by GRNNGM and HPMINDE algorithm to compare the mapping results and efficiency.

### 3 Results and Discussion

The test result of the 1000 color blocks is shown in the Fig. 2a, b were the results from GRNNGM-Lab and (c), (d) were the results from GRNNGM-IPT. Vertical axes of (a), (c) were the color difference of the results values and object values, and horizontal axes were the index numbers of 1000 test colors. The distribution of the color difference is shown in the Table 1; (b), (d) were the result gamut and objective

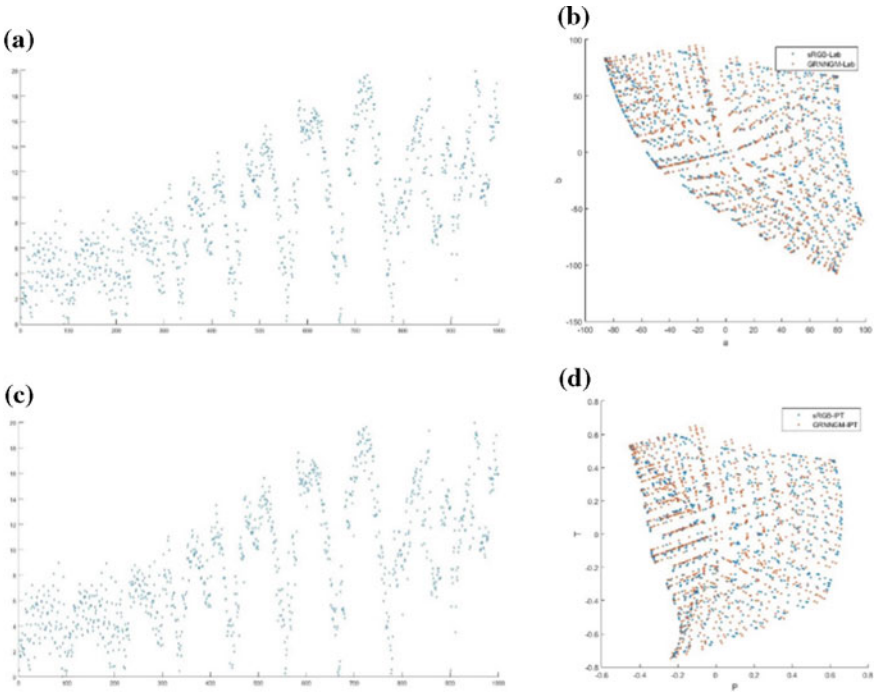


Fig. 2 The results of 1000 test color blocks

Table 1 The color difference of the mapped color with the reproduced color

	$D < 5$	$5 \leq D < 10$	$10 \leq D < 15$	$15 \leq D < 20$	$20 \leq D < 25$	Max.	Min.	Avg.
GRNNGM-Lab	199	342	329	97	33	24.82	0.00	9.62
GRNNGM-IPT	238	359	264	139	0	19.96	0.01	8.89



Fig. 3 Original images and result images of the experiment



gamut comparison on the a–b plane of Lab color space and on the P–T plane of the IPT color space

From Fig. 2 and Table 1, GRNNGM controls the color difference in a limited range and the range of GRNNGM-Lab is the 0–24.82 and the GRMMGM-IPT is the 0.01–19.96. But most of color differences are 5–15. Because GRNNGM is a clipping algorithm essentially which minimized the average color difference.

Two kinds of GRNN, net-Lab and net-IPT, which correspond to two types PCS, CIE LAB and IPT were built and compared in the experiment. And Hue Perceived Minimum Color Difference Error (HPMINDE) was also used in the experiment to compare with GRNNGM. HPMINDE is standard clipping algorithm proposed by CIETC8-03 to evaluate gamut clipping algorithm [7].

In the experiment, some reference images were chosen from database TID2008. The results of gamut mapping are shown in Fig. 3a, e; b, f; c, g; d, h corresponded to the original image, result images of GRNNGM-Lab, result images of GRNNGM-IPT and result images of HPMINDE.

All of the result images have color difference which compare with the original image (a) in general. The saturation of result images with GRNNMG is more saturated especially in the area of high saturation red.

In the first group images, the green leaves of (c) changes more smoothly than (b). The yellow feather on the neck of the parrot became obvious yellow blocks. In the second groups, the face area of (g) lost its tone.

The size of reference images is 512 by 384. The average time-consuming of GRNNGM is 39.7 s, the GRNNGM-IPT is 38.8 s, the GRNNGM-Lab is 40.6 s and the HPMINDE is 524.79 s. Because the calculation process of GRNNGM is simpler than HPMINDE which just need the input color point and get the mapping color point by GRNN.

## 4 Conclusions

The paper proposed a new gamut mapping algorithm based on GRNN to create a gamut mapping model. In the experiment on 1000 color samples, the average color difference of GRNNGM-IPT is less than GRNNGM-Lab's. In experiment on some different reference images, the GRNNGM-IPT is good at high saturation color gamut mapping and GRNNGM-Lab is good at low saturation color. And compared to HPMINDE, the GRNNGM is better on some high saturation color gamut mapping and higher efficiency.

Because the GRNNGM is an essentially gamut clipping algorithm, a method would be worked to solve tone merging problem. The experiment is the gamut conversion from Adobe RGB to sRGB, and more research on more different gamuts with GRNNGM should be done later.

## References

1. Hu, W.J, Tang, S.Q, & Zhu, Z. F. (2007). *Modern Color Science and Application*, 1st edn. Institute of Technology Press, Beijing.
2. Lee, H.S, & Han, D. (2005). Implementation of Real Time Color Gamut Mapping Using Neural Network. 2005 IEEE Mid-Summer Workshop on Soft Computing in Industrial Applications, 138–141.
3. Zhao, L, & Tang, B.L. (2010). A Simple Gamut Mapping Method Based on BP Neural Network. The 31st International Congress on Imaging Science. 658–661.
4. Wu, M. G., Zheng, P.B, & Cui, L. L. (2015). Gamut Mapping of Electronic Map Based on SOM Neural Network. *Acta Electronica Sinica*, 43(6), 1108–1112.
5. Specht, D. F. (1991). A General Regression Neural Network. *IEEE Transactions on Neural Networks*, 2(6), 568–576.
6. Huang, X. Q, & Shi, J. S. (2010). Study on the Uniformity of IPT Color Space [J]. *ActaOpticaSinica*, 30(7), 2170–2174.
7. Yang, L. (2014). Research on the Gamut Mapping Model for Map Color Reproduction. MD thesis, Nanjing Forestry University, Nanjing, China.

# Performance Test of Liquid Crystal Display Parameters

Hongyan Chen, Li Cheng and Xiao Jin

**Abstract** The effects of different set up parameters of liquid crystal display on the color gamut range and the accuracy of the display are studied. **Methods** we analyze some basic parameters of liquid crystal display settings, test the effects of different parameters on the display, and find the influence of common performance parameters such as color temperature, brightness, contrast ratio, gamma value and resolution value on LCD display color gamut and accuracy. **Results** Through multiple sets of experimental comparison, we get different LCD display effects under different parameter settings. **Conclusion** For general liquid crystal display, there is little influence of the changes of color temperature, brightness, gamma value and resolution value on color gamut, and the influence of contrast ratio is larger. For the LCD color, the influence of the changes of brightness and resolution parameter is not great, while the color temperature and the gamma value, contrast ratio is greater.

**Keywords** Liquid crystal display · Performance parameter · Color gamut · Display color accuracy

Liquid crystal display has become the mainstream of today's display device, and the performance of the liquid crystal display is directly related to our visual perception. Therefore, how to reasonably adjust the liquid crystal display performance parameters to make it work efficiently is more important. With the rapid development of the new display technology, display has changed from the traditional CRT displays to liquid crystal display. Liquid crystal display has become the mainstream of today's society displays and the performance requirement is also higher. Along with the display develops to the direction of light, thin, energy-saving and flexible-folding, people pay more attention to the display quality [1–3]. With the low carbon environmental protection concept deeply rooted in the printing industry, it is an inevitable trend for screen soft proofing to replace the digital proofing so as to control the printing process and printing products quality inspection. And to

---

H. Chen (✉) · L. Cheng · X. Jin  
Jingchu University of Technology, Hubei, China  
e-mail: 369861062@qq.com

complete the screen soft proofing, the first step is to choose a professional display of superior performance [4, 5].

## 1 Experimental Condition and Instruments

Experimental instruments: Host computer, Dell LCD, X-Rite Eye-one Pro.

Software: Measure 5.0, i1Profiler, Profile Maker, Profile Editor, ORIS Certified Monitor Excel, etc.

Test environment: In the monitor test, the test condition chooses D65 light; computer desktop background is set to grey. A hood should be put on the display. The distance of Eyes and display should be kept in 50–65 cm.

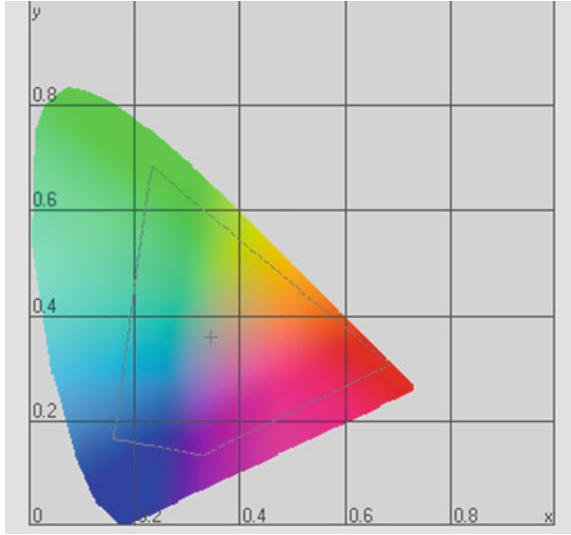
## 2 Experiment Process and Result Analysis

### 2.1 *Influence of Color Temperature on the LCD Color Gamut*

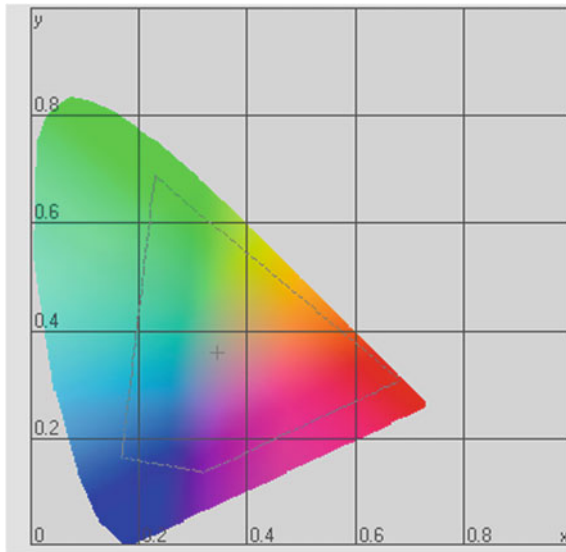
We set color temperature to 6500 K, and keep the brightness, contrast ratio and gamma value remain in 25, 100% and 2.2, and the resolution value is set to the maximum value. First we make use of i1-Profile and Profile Maker Software to build an ICC properties file for display. We open the software, click the display color management and then click calibration instrument. Then we get an ICC property file and color gamut according to the steps and name it “6500 K”. If we open the file, it is shown as Fig. 1. Using the same method, we adjust the color temperature to 7000 K and set an ICC property file named “7000 K” as Fig. 2 shows. We open Profile Editor, click “source and Destination Profiles”, and compare the two ICC files in the same coordinate system like Fig. 3. The method can be widely used in the comparison of 5500 and 6000 K, 6000 and 6500 K, 7000 and 7500 K.

From Fig. 3 we can find that in the 2D view, the difference of the size of color gamut when the color temperature is 6500 and 7000 K is not obvious. However, in 3D view, just as Fig. 4 suggests, when the color temperature is 6500 K, the display color gamut is the yellow area, and blue area while color temperature is 7000 K, most blue area is surrounded by the yellow area. Therefore when the color temperature is 6500 K, the size of color gamut is larger than that of 7000 K. In the comparison of 6000 and 5500 K, the color gamut size is similar while it is larger when the color temperature is 6000 K. And the size of color gamut when the color temperature is 6500 K is larger than that of 6000 K while the color gamut size is similar when the color temperature is 7000 and 7500 K.

**Fig. 1** The color gamut in 6500 K color temperature, 25% brightness, 100% contrast, 2.2 gamma value



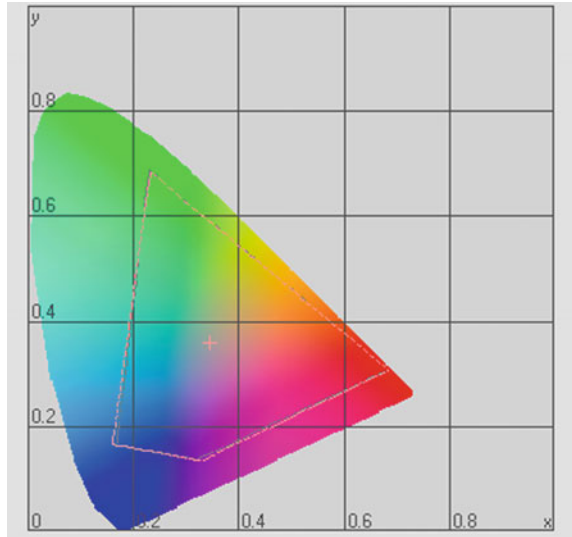
**Fig. 2** The color gamut in 7000 K color temperature, 25% brightness, 100% contrast, 2.2 gamma value



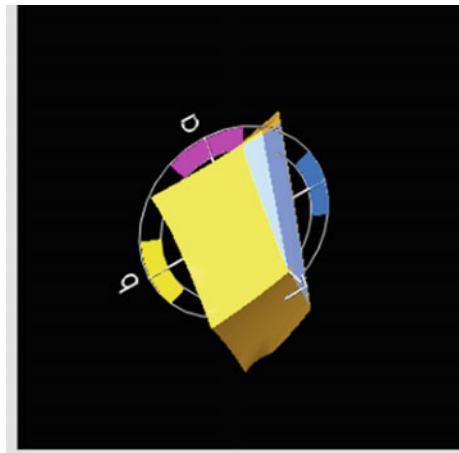
### ***2.2 Influence of Gamma Value on the LCD Color Gamut***

Form above we know that the color gamut size is the largest when the color temperature is 6500 K so we set the temperature to 6500 K, the brightness to 25% and the contrast ratio to 100% while the gamma value changes among 1.8, 2.0, 2.2, 2.4 and 2.6. Using the above method to test the color gamut Fig under different

**Fig. 3** The comparison of color gamut in 6500 and 7000 K color temperature, 25% brightness, 100% contrast, 2.2 gamma value



**Fig. 4** The 3D view comparison of color gamut in 6500 and 7000 K color temperature, 25% brightness, 100% contrast, 2.2 gamma value



gamma value and make comparisons. Just as the results suggest, with the changes of gamma value, the changes of LCD color gamut size changes little however in 3D view, the size is largest when the gamma value is 2.2.

### 2.3 Influence of Brightness on the LCD Color Gamut

The default brightness is 25% and we test the difference of color gamut by adding 25% to the brightness value every time. Since the 0% brightness make no sense for

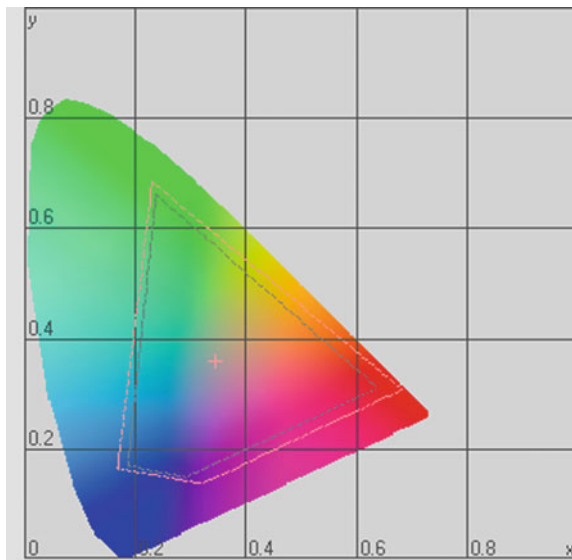
LCD, we set gamma value to 2.2, color temperature to 6500 K, contrast ratio to 100% and brightness to 15, 25, 50, 75, 100% and compare the size of color gamut. The results suggest that the change of brightness influences little on the color gamut however in 3D view, when the brightness is 100% the size of color gamut is the largest but the difference is quite little.

### 2.4 Influence of Contrast Ratio on the LCD Color Gamut

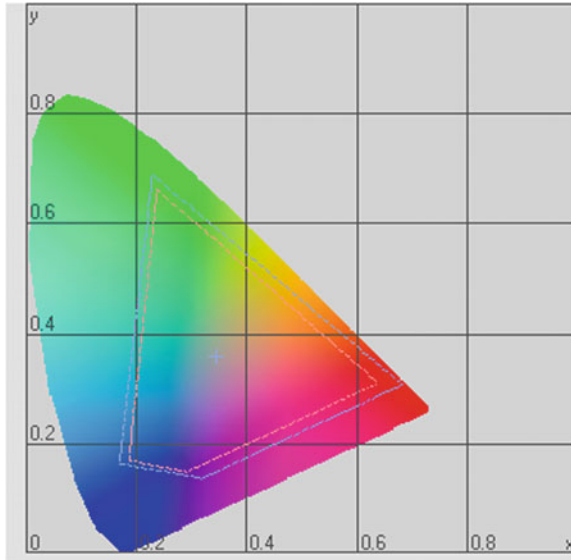
The default contrast ratio is 100% and we test the difference of color gamut by adding 25% to the contrast ratio every time. We set gamma value to 2.2, color temperature to 6500 K, brightness to 25% while contrast ratio to 100, 75, 50, 25 and compare the size of color gamut. The result is shown in Figs. 5, 6, 7 and 8.

Analysis: From Fig. 5, it is easy to find that when contrast ratio is 100%, the color gamut size is obviously larger than that of 75% if other parameters keep constant. From Fig. 6 we can find that when contrast ratio is 50%, the color gamut size is obviously larger than that of 75%. And Fig. 7 shows that although the difference of the color gamut size is not so obvious when contrast ratios are 100 and 25%, in 3D view, the color size gamut is a little larger when contrast ratio is 50%. Therefore we need to compare the color gamut size when the contrast ratios are 50 and 100%. From Fig. 8 we can find that they are similar no matter in 2D or 3D view, which means that there is little difference between the two color gamut sizes. In reality we can choose contrast ratio according to the fact [6, 7].

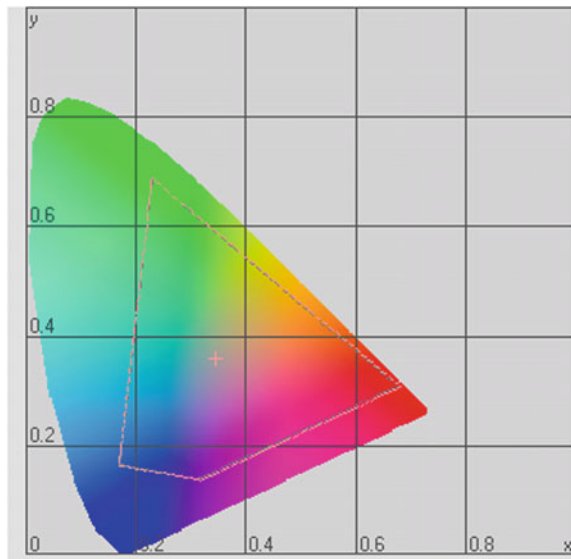
**Fig. 5** The comparison of color gamut in 75 and 100% contrast, 6500 K color temperature, 25% brightness, 2.2 gamma value



**Fig. 6** The comparison of color gamut in 50 and 75% contrast, 6500 K color temperature, 25% brightness, 2.2 gamma value



**Fig. 7** The comparison of color gamut in 25 and 50% contrast, 6500 K color temperature, 25% brightness, 2.2 gamma value

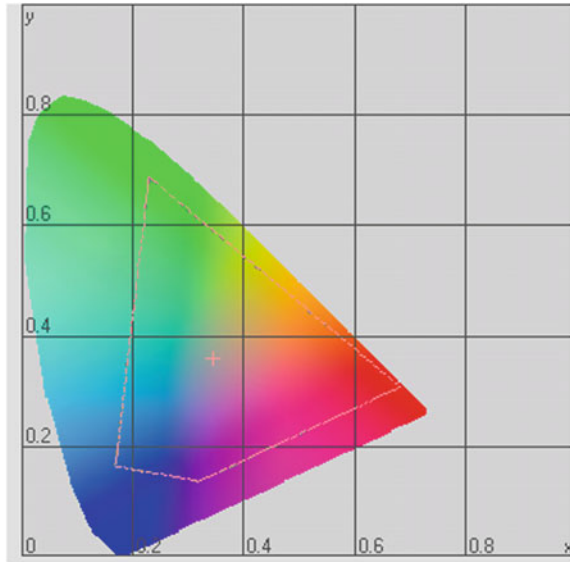


### ***2.5 Influence of Resolution Value on the LCD Color Gamut***

Keep color temperature, brightness, contrast ratio and gamma value remain to 6500 K, 25, 100%, 2.2 and change resolution value to test the color gamut size. Since the highest resolution value for experimental LCD is 1920 \* 1200 and in general the highest resolution ratio can leads to the best display effect, so we



**Fig. 8** The comparison of color gamut in 50 and 100% contrast, 6500 K color temperature, 25% brightness, 2.2 gamma value



compare the highest resolution value with the other two lower resolution values, 1680 \* 1050 and 280 \* 800. The results suggest that the difference is not obvious both in 2D view and 3D view. Therefore, the influence of resolution value on the size of LCD color gamut is little.

### ***2.6 Influence of Color Temperature and Gamma Value on the LCD Display Color***

We use the Auto button of LCD to adjust parameters including color temperature, brightness, contrast ratio, gamma value and resolution value. And we make use of ORIS Certified Monitor Software to choose a standard color car. The light used in the test is 3DAP V3, D65 Light, and the test object is LCD. By using Eye-one pro to test 99 color lumps which includes various typical colors and displaying through monitor, the calculation function of software can automatically calculates the difference between the reference color and the actual color.

First we study on the color temperature and set the temperature to 5500, 6000, 6500, 7000, 7500, 8000 and 8500 K, keep brightness, contrast ratio and gamma value remain to 5, 100%, 2.2, and then compare and analyze the average value of the color difference. We find that the influence of color temperature on the LCD display color is quite great. The higher color temperature, the better LCD displayed. However, color temperature is not the bigger the better. It is best for the temperature to remain in about 7500 K.

When we study the influence of gamma value on the LCD display color, we set the color temperature to 7500 K, brightness to 25%, contrast ratio to 100% and revolution value to the largest while set gamma value to 2.0, 2.2 and 2.4. The results are shown in Table 1 and Fig. 9.

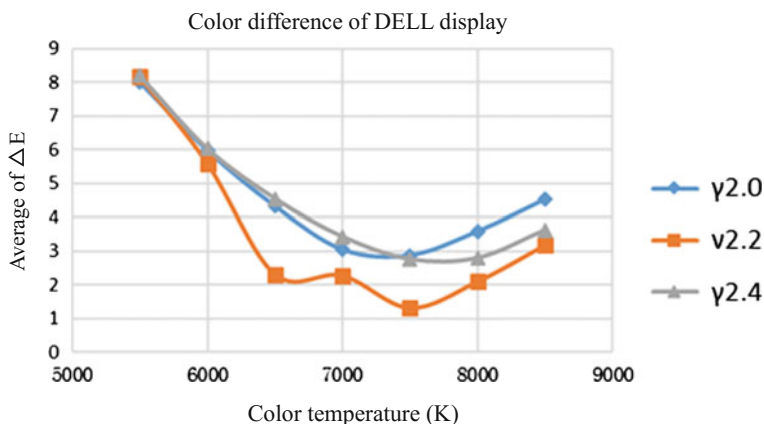
From Table 1 and Fig. 9, we can find that color temperature and gamma value have great influence on the LCD display color. With the increase of color temperature, the color differences first reduce then increase. When the color temperature is 7500 K and gamma value is 2.2, the color difference is minimum, which means the LCD display color is great.

### 2.7 Influence of Brightness and Contrast Ratio on the LCD Display Color

We set the color temperature to 7500 K, Gamma value to 2.2 while brightness changes from 10 to 100%, contrast ratio changes from 25 to 100% and test the color difference. The results are shown in Table 2 and Fig. 10.

**Table 1** Test data of color temperature ( $\Delta E$ ), gamma value ( $\gamma$ ) and color difference ( $T_C$ )

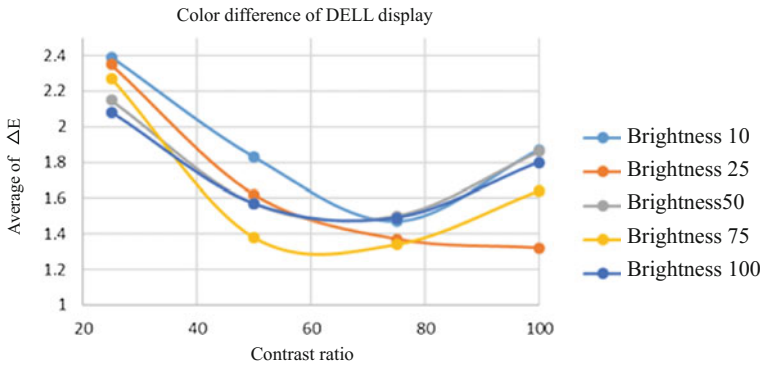
$\Delta E$	$T_C$						
$\gamma$	5500	6000	6500	7000	7500	8000	8500
2.0	8.01	5.98	4.33	3.05	2.88	3.59	4.53
2.2	8.17	5.59	2.32	2.28	1.32	2.10	3.18
2.4	8.20	6.03	4.55	3.43	2.76	2.80	3.63



**Fig. 9** Display color difference changing with color temperature and gamma value curve

**Table 2** Test data of brightness (B), contrast ratio (C) and color difference ( $\Delta E$ )

$\Delta E$	C			
	B	25	50	75
10	2.39	1.83	1.47	1.87
25	2.35	1.62	1.37	1.32
50	2.15	1.57	1.50	1.86
75	2.27	1.38	1.34	1.64
100	2.08	1.57	1.49	1.80



**Fig. 10** Display color difference changing with brightness and contrast ratio curve

**Table 3** Test data of resolution value and color difference

Resolution value	1920 * 1200	1680 * 1050	1280 * 800	800 * 600
Color difference	1.32	1.40	1.32	1.34

From Table 2 and Fig. 10, we can find that the influence of contrast ratio on the LCD display color is great while brightness is not. With the increase of contrast ratio, the color differences first reduce then increase. When we set the brightness in 25–50%, contrast ratio in 50–75%, the color difference is the least.

### 2.8 Influence of Resolution Value on the LCD Display Color

We set the color temperature to 7500 K, brightness to 25%, contrast ratio to 100%, gamma value to 2.2, while resolution changes from 1920 \* 1200, 1680 \* 1050, and 1280 \* 800 to 800 \* 600 and do the test. The result is shown in Table 3.

From Table 3 we can know that the effect of contrast ration on the LCD display color is little.

### 3 Conclusions

For general liquid crystal display, there is little influence of the changes of color temperature, brightness, gamma value and resolution value on color gamut, and the influence of contrast ratio is larger. For the LCD color, the influence of the changes of brightness and resolution parameter is not great, while the color temperature and the gamma value, contrast ratio change is greater. From above test data, due to the little influence of color temperature on display color gamut and great influence on color difference, the color temperature use in the experimental LCD should be set to 7500 K. When the gamma value is set to 2.2, there will be the largest color gamut as well as the least color difference. The influence of brightness on color gamut is not so great; however when the brightness is in the range of 25–50%, the color difference is the least. When the contrast ratio is 100%, the color gamut size is the largest while the color difference is the least. The revolution value has little difference on the color gamut and color difference, but the performance is the best when the revolution value is set to the largest one, 1920 \* 1200.

For practical application, the setting of brightness of the LCD display is not the higher the better. Considering energy-saving and health factors, it is generally to set the brightness to the range of 25–50%. If the brightness is too high, users will feel exhausted and the use life of LCD will be reduced. As for contrast ratio, we usually set it to the highest one and users can get the best display effect it is generally known that color temperature is the color characteristics of numerical value to indicate the color of the light source. Low color temperature leads to the display showing a bit yellower while high color temperature leads to the display showing a bit bluer. For common displays, we usually set the color temperature to the range of 6500–7500 K; of course you can adjust according to the reality [8, 9]. The generally setting of gamma value always uses the default one, and different brand or size displays have different values. In the tests, contrast ratio has little influence on the color gamut and color difference, but for users, the change of contrast ratio can lead to different display effects. Higher contrast ratio brings in the clearer display effects, so we usually choose the highest contrast ratio. We should adjust according to the practical application, work environment and personal interest. If we have strict requirement on the color performance of displays, we are supposed to increase contrast ratio and brightness, as well as adjust color temperature according to reality.

The study of the effects of different performance parameters such as color temperature, brightness, contrast ratio, gamma value and revolution value has certain guiding significance in reducing the labor intensity of operators and operating errors, improving test efficiency and the accuracy of measurements. In the increasingly competitive printing market, in order to achieve successful printing, it

is a necessary precondition to choose a professional display of superior performance, reasonably adjust and parameters to help print workers better design and soft proofing.

## References

1. Xiao Yunhong, LAN Hui, Zhou Fei, Hu Xiaobo, Chang di, editor in chief (2011). Display technology. Xi'an Electronic and Science University Press, 2011. 10, 90–96.
2. Wang Tao (2010). Research on electronic control optical devices based on liquid crystal display. Tianjin University, 2010. 06.
3. Wu Youlan, Zhu Gongsheng, Tang Feng (2013). The application of the electrical resistance tester in the intelligent electronic products course. Computer and Telecom, 2013. 03, 59–61.
4. Zeng Jiancheng (2012). The purchase of color displays. Computer Application Technology, 2004 (1), 59–60.
5. Hong Liang, Jiang Xinzong (2012). Research of liquid crystal display color management standardization. Printing Quality and Standardization, 2012. 08, 29–34.
6. Guo Zhunjia (2012). The theory of digital engineering drawing. Modern Trade Industry, 2012. 09, 152–153.
7. Tian Huirong, Wang Qiang, Liu Haoxue (2011). Printing color management. Beijing: Printing Industry Press, 2011. 08, 93–98.
8. Si Zhanjun, Hu Yuan, Zhang Xiandou (2012). Research on the testing method of display performance of professional packaging engineering, 2012. 03, 102–106.
9. Xu Baohui (2010). Display color characteristics and color space conversion technology. Xi'an University of Technology, 2010 thesisd.

# Simulation and Rejuvenation for Chinese Fading Paint Under Ultraviolet

Zhen Liu, Fang Cai, ShuangShuang Chen and Chong Sun

**Abstract** It is known that the Chinese painting has changed with the passage of time—some pigment has been darker and blacker, such as minimum and vermilion. So simulating the effects of aging and rejuvenating of paintings has great significance. This paper proposes a knowledge-based approach to simulate the fading states by physical experiment, by the aging phenomena of pigment and substrate caused by ultraviolet light. The exponent fading model was established by the spectral reflectance of color pigment ink and rice paper at different aging process, then the color was simulated by color mapping algorithm. The experiment shows that the work was effective and reflected the color fading rules, and it is of great significance for the precious heritage of the original color reproduction.

**Keywords** Fading model · Color rejuvenation · Ultraviolet · Chinese paint

## 1 Introduction

As time passes, traditional Chinese paintings often fall victim to physical and chemical changes, such as the traditional painting appears faded, yellowing and other diseases by the UV, temperature and humidity. So the aging problem becomes further complicated and difficult to simulate.

Previous literatures have focused on the variation of pigments or image processing technology. Such as Wu and Li [1–3] analyzed the pigment samples collected from the Mogao Grottoes, probed the stability and fading mechanism of the pigments under the environment facts. They pointed out that ultraviolet are the main reasons for color fading. Berns performing spectral reflectance measurements in situ on darkened and on paint-outs of comparable unaltered colors [4], more luminous appearance of La Grande Jatte was simulated using Kubelka–Munkand

---

Z. Liu (✉) · F. Cai · S. Chen · C. Sun  
College of Engineering, Qufu Normal University, Rizhao, China  
e-mail: zhen@whu.edu.cn

color-managed digital photography. Jiang [5–7] creates a color recovery system for traditional Chinese painting using computer digital image manipulation technology.

While most of approaches can alter an image of a painting to appear new, they cannot effectively simulate the aging process. To achieve this goal, firstly, we proposed the fading model characterized by two-constant K-M model; secondly, by the accelerating experiment of the rice paper and pigment, we established the exponent model for pigments concentration, and different aging appearance was simulated.

## 2 Color Fading Model

The traditional Chinese painting is usually used mineral and plant pigments, dissolved in oil or glue when paintings. However, the UV would lead to the color appearance changing caused by the chemical composition changing. Such as cinnabar' structure ( $HgS$ ) would be changed from six crystal (red) to vertical structure (black), the ocher would oxide from brown ( $Fe_2O_3$ ) to black ( $Fe_3O_4$ ), minimum would oxide form red ( $Pb_3O_4$ ) to black ( $PbO_2$ ).

Assumed that the thickness of the pigment layer has sufficient hiding power and can ignore the influence of the substrate, the concentration of the flash pigment is  $c_p$ , the gelatin is  $c_g$ , the fading pigment is  $(1 - c_p - c_g)$ , according to the two-constant K-M theory, the absorption coefficient and scattering coefficient at wavelength  $i$  as follows:

$$\begin{aligned} K_i^m &= c_p K_i^p + c_g K_i^g + (1 - c_p - c_g) K_i^f = c_p (K_i^p - K_i^f) + c_g (K_i^g - K_i^f) + K_i^f \\ S_i^m &= c_p S_i^p + c_g S_i^g + (1 - c_p - c_g) S_i^f = c_p (S_i^p - S_i^f) + c_g (S_i^g - S_i^f) + S_i^f \end{aligned} \quad (1)$$

where the  $K_i^p, K_i^g, K_i^f$  are absorption coefficient of the solid concentration for flash pigment, gelatin, and faded pigment at the wavelength  $I$ , and the  $S_i^p, S_i^g, S_i^f$  are the scattering coefficients. Equation (1) is simplified as

$$K^m = [\Phi_k - K^f u] C + K^f; \quad S^m = [\Phi_s - S^f u] C + S^f \quad (2)$$

where  $C = [c_p, c_g]^T$ ,  $u = [I, I]$ ,  $K^f, S^f$  is  $n$ -by-1 vector,  $K^f = [K_{400}^f, \dots, K_{700}^f]^T$ ,  $S^f = [S_{400}^f, \dots, S_{700}^f]^T$ ,  $\Phi_k, \Phi_s$  is  $n$ -by-2 matrix,  $n$  is the wavelength band of measured spectral.

Assumed the spectral reflectance measured in situ on samples is  $\rho_i^s$  at wavelength  $i$ , and the calculated reflectance by the K-M model is  $\rho_i^m$ . The pigment concentration was derived based on Allen's color matching model [8]

$$C = (TE\{D_k[\Phi_k - K^f u] + D_s[\Phi_s - S^f u]\})^{-1}TE\{D_k[K^s - K^f] + D_s[S^s - S^f]\} \quad (3)$$

where the  $D_k$ ,  $D_s$  is  $n$ -by- $n$  Diagonal matrix,  $K_m$ ,  $K_s$ ,  $S^m$ ,  $S^s$  is  $n$ -by-1 vector,  $T$  is 3-by- $n$  matrix for CIE1931 standard observer function and  $E$  is  $n$ -by- $n$  diagonal matrix for the light source spectral power distribution. The exponentially fading model of pigment concentration changing at time  $t$  can be derived easily using differential equation

$$C(t) = C_0 e^{-k(t-t_0)} + a \quad (4)$$

where  $C(t)$  is the painting composition concentration at time  $t$ ,  $C_0$  is initial concentration,  $t_0$  is initial time,  $k$  is aging rate,  $a$  is constants. For example, some studies have demonstrated that the ninety percent of minimum turned to black in less than one century, so the aging rate  $k$  for minimum equal to 0.023 by Eq. (4). It can be further learned that  $K^m$ ,  $S^m$  also changing exponentially. The spectral reflectance indicated by  $\rho$  can be simply calculated from absorption and scattering coefficients, as shown in Eq. (5).

$$\rho = 1 + \frac{K}{S} - \sqrt{\left(\frac{K}{S}\right)^2 + 2\frac{K}{S}} \quad (5)$$

### 3 Experiment

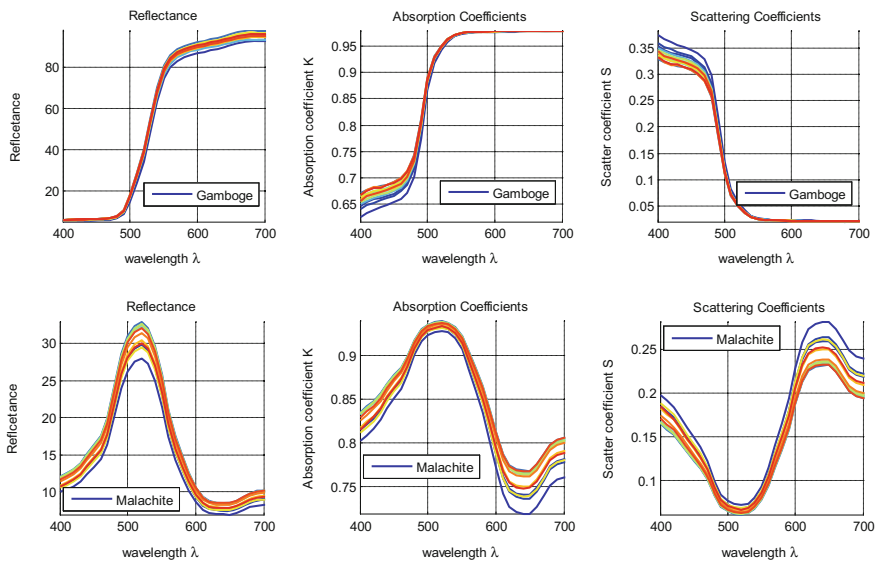
Samples of traditional Chinese pigment and papers were carefully prepared by our group members. There are in total of 53 colorants plus white paint, which contains 16 masstone samples and 37 mixing samples, then placed under the UV lamp for aging (365–400 nm, 300 W, OSRAM) 76 h, while measured the spectral every 2 h (X-Rite Spectroeye Spectrophotometer, D50,45/0,400–700 nm). Firstly, the database of  $K$ ,  $S$  coefficient is built, then concentration of the pigment components can be calculated according to the measured spectral, then the exponential fading parameters are obtained as shown in Table 1. It shows that the exponential models can representation of fading regular accurately. For the 16 kinds of pigments, the max color difference  $\Delta E_{76}$  between the measured and model calculated is 1.59, the mean difference is 0.30, the max Adj coefficient is 0.89 with the max value 0.98 and the mean of R-squared Adj is 0.86 with the max value 0.98. The results show that the color fading regular can be characterized by the exponential model.

For the pigment such as gamboge and malachite, the change of spectral, absorption coefficients and scattering coefficients were plotted in Fig. 1. For gamboges pigment, with the fading stages the obviously changing mainly located in

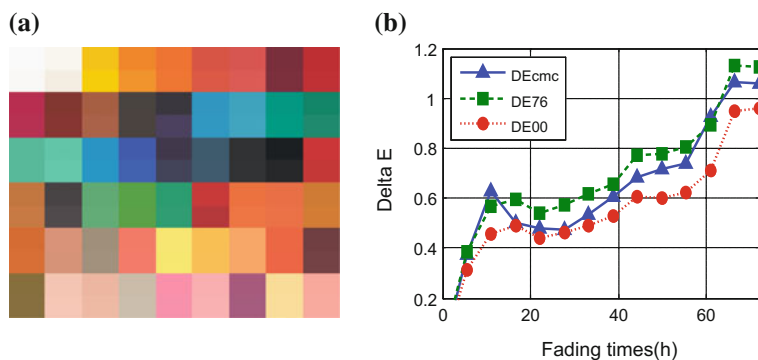


**Table 1** The accuracy of the fading model

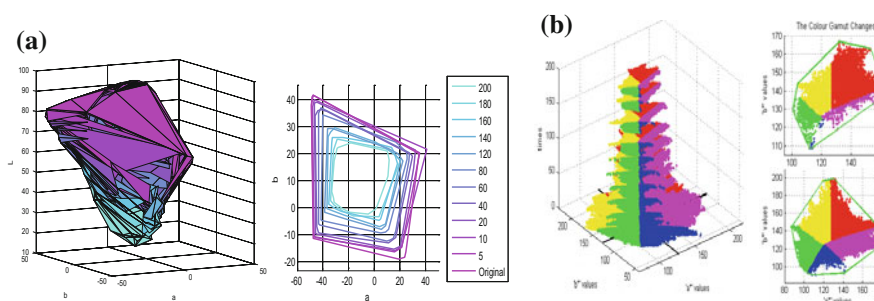
	$\Delta E$ 1976			Model accuracy		
	Min	Max	Avg	Adj	R_Adj	Rmse
Paper	0.11	1.04	0.38	0.46	0.30	1.21
Titanium white	0.02	0.56	0.23	0.94	0.92	0.41
Gamboge	0.03	0.57	0.32	0.95	0.93	0.24
Light yellow	0.00	1.59	0.63	0.88	0.84	0.34
Orange	0.00	0.76	0.38	0.83	0.78	0.23
Vermeil	0.02	0.38	0.19	0.95	0.94	0.09
Cinnabar	0.07	0.73	0.32	0.82	0.77	0.16
Ocher	0.18	1.20	0.67	0.86	0.82	0.37
Auburn umber	0.01	0.34	0.13	0.93	0.91	0.04
Purple	0.12	1.16	0.56	0.96	0.95	0.19
Azurite	0.00	0.28	0.13	0.93	0.90	0.15
Malachite	0.11	0.57	0.32	0.95	0.93	0.26
Acid blue	0.00	0.25	0.11	0.90	0.87	0.14
Ultramarine	0.00	1.39	0.44	0.95	0.94	0.41
Indigo blue	0.00	0.36	0.24	0.93	0.92	0.08
Flower blue	0.01	0.11	0.07	0.98	0.98	0.04
Black	0.00	0.09	0.05	0.97	0.96	0.01
Stastic (avg)	0.04	0.67	0.30	0.89	0.86	0.26



**Fig. 1** The changes of spectral, absorption and scattering coefficients for gamboge and malachite



**Fig. 2** a Variations appearance of color; b the color difference in different stages of gamboge



**Fig. 3** The variation of lab color gamut and a-b gamut at different fading stage. **a** 3D color gamut **b** a-b gamut

400–500 nm, also, for malachite the obviously changing mainly located at two ends of wavelength. The absorption and scattering coefficients increased or decreased alternately.

Figure 2 shows the variation of color appearance in different fading stages caused by the ultraviolet, the color appearance of most pigments changes obviously. We can obviously feel the color changing.

Figure 3 shows the simulation changes of 3D color gamut under different aging conditions according to the fading model. The color depth in the figure represents faded time. It shows that the Lab color gamut volume getting smaller and smaller, the image tone and range become smaller obviously, especially for saturation and brightness of image, e.g. the brightness and saturation decreased obviously; the color gamut of a-b reduced about 25% at initial aging 10 h, and the color gamut reduced about 52%.

## 4 Conclusions

In this paper, the spectral information at different stages was obtained by accelerated aging experiment, and the exponential fading model was established to represent the color fading regular. The result shows that the model can be used to realize the simulation of color appearance, also rejuvenated the fading paint. Our paper mainly focused on the fading phenomenon under ultraviolet without considering other factors such as high temperature and humidity. So there would be some difference for the actual fading phenomenon. Due to the commonality of interconnected basic theory and fading principle consistency, the proposed color faded variable model has strong practicality and reference for gouache, acrylic, oil paint and other paintings, which can provide a reference for the color restoration of other types of painting.

**Acknowledgements** This study is supported by the National Science Foundation of China (61405104) and Laboratory Open Fund of Qufu Normal University (SK201515).

## References

1. Wu, R. J. (2003). Chromatic applying of Dunhuang murals and the Cause of color changes. *Dunhuang Research*, 81(5), 44–50.
2. Li, Z. X. (2002). Pigment Analysis On Tang Dynasty Murals at The Mogao Grottes. *Dunhuang research*, 74(4), 11–18.
3. Shi, X., Lu, D. M. (2005). Colorimetric and Chemical Modeling Based Aging Simulation of Dunhuang Murals. 5th International Conference on Computer and Information Technology, doi: [10.1109/CIT.2005.85](https://doi.org/10.1109/CIT.2005.85), 11–15.
4. Berns, R. S (2006). Rejuvenating the color palette of Georges Seurat's A Sunday on La Grande Jatte—1884: A simulation. *Color Research & Application*, 31(4), 278–293.
5. Lei, J., Qian, Q. (2007). Computer color recovery system for traditional Chinese painting. *Journal of YunNan University*, 29(2), 290–294.
6. Zhang, S. P. (2010). Based on the Multispectral Imaging of Research on Method of the Color Rejuvenation of Chinese Paintings. Master thesis, Tianjin University, China.
7. Pan, Y. H., Lu, D. M. (2003). Digital Protection and Restoration of Dunhuang Mural. *Journal of system simulation*, 15(03), 310–314.
8. Allen, E. (1966). Basic equations used in computer color matching. *Journal of the Optical Society of America*, 56(9), 1256–1257.

# Study on Observers' Categories Based on Color Matching Experiments

Chunjie Shi, Min Huang, Yu Liu, Zeyang Li and Haoxue Liu

**Abstract** In order to study the observers' categories based on different color matching functions, 28 observers were organized to match the 50 color stimuli on LED monitor. The spectral power distribution of the target and the matched colors were measured and 10 sets CMFs were used to calculate the corresponding chromatic values. The mean CIEDE2000 color difference for each of all the tested observers was calculated and the observers were assigned to different observer categories. The results indicated that most of the observers belonging to the S6, S2, CIE1964 color matching functions.

**Keywords** Color matching experiment · Observer variability · Observer categories · Color matching functions

## 1 Introduction

In industry application, CIE1931 and CIE1964 Color Matching Functions (CMFs) were widely used to represent human color vision characteristics. And they were appropriate representation of the average color normal human observer. Later, some research [1, 2] suggested color perception of an observer is correlation with age (age-dependent) and visual field. Based on age and visual field parameter, the Technical Committee TC 1-36 of CIE proposed CIE2006 physiological observer model (CIEPO06 CMFs). However, observers would have different perception even within the same age-group [3]. And 8 colorimetric observer categories (S1–S8) were proposed by Sarkar et al. according to cluster analysis on 10° Stiles and Burch's 47 individual observers. Later, 4 cross-media color matching

---

C. Shi · M. Huang (✉) · Y. Liu · Z. Li · H. Liu  
School of Printing and Packing Engineering, Beijing Institute of Graphic  
Communication, Beijing, China  
e-mail: huangmin@bigc.edu.cn

C. Shi  
e-mail: 842980902@qq.com

experiments were conducted and the performances of 11 CMFs (CIE1931, CIE1964, CIE2006, S1-S8 CMFs) were tested by Huang et al. [4]. For the 4 experiments, CIE2006 and S6 performed the best and no observer was assigned to S7 and S8 CMFs.

The authors carried out a psychophysical experiment. 28 observers with normal color vision were organized to match the 50 test stimuli on the same monitor. The CIEDE2000 color difference between target color and matched color was calculated by 10 different observer categories (CIE1931, CIE1964, S1–S8 CMFs) and participants were assigned to different categories according to the calculated minimum CIEDE2000 value.

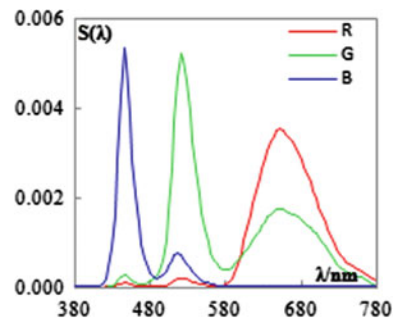
## 2 Experimental

### 2.1 Color Stimuli

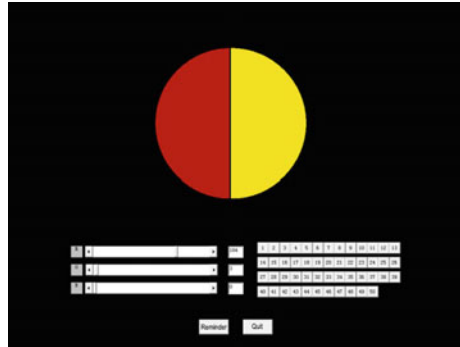
The NEC CG242W LCD display with LED backlight was chosen for the color matching experiment. The luminance of the full white was set close to  $168 \text{ cd/m}^2$ , the chromaticity value ( $x, y$ ) was (0.33, 0.34), and the correlated color temperature was 5944 K. The primary spectral power distribution is shown in Fig. 1 and the monitor stability was evaluated by measuring the primary colors over a period of 7 h, the color differences were below 0.6 CIELAB units 2 h later. Regarding the uniformity of the screen, measurements were taken at 9 different locations uniformly sampled across color area, the color differences were below 0.2 CIELAB units.

The 50 samples were uniformly distributed in CIELAB color space. The experimental interface is shown in Fig. 2. The test and reference stimuli were divided by a black thin line, and the diameter of the circle is 8 cm. The distribution of measured 50 color centers on CIELAB  $a^*b^*$  and  $L^*C^*$  plane is shown in Fig. 3.

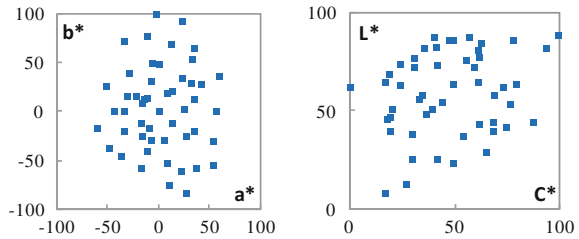
**Fig. 1** The spectral radiation curves of the monitor primary colors



**Fig. 2** Interface of the experiment



**Fig. 3** The distribution of 50 color centers in CIELAB  $a^*b^*$  and  $L^*C^*$  plane



## 2.2 Visual Experiment

A panel of 28 observers (18 female and 10 male) aging from 20 to 35 were organized to participate in the experiment. Their average age was 23 years old. In the experiment, each participant was presented with 50 test colors. Besides, for each participant, in order to examine the intra-observer variability, 6 of 50 colors were randomly selected.

The color matching experiments were conducted in a dark room. The reference stimulus was randomly displayed on the left or right of the monitor and all of them were presented in a random sequence by pressing 50 buttons on the bottom right of the interface (see the right button of Fig. 2). The observers were asked to adjust RGB channels to accomplish the color matching experiments with a distance of approximately 50 cm (field size approximately equals to  $10^\circ$ ). For each observer, the experiment was carried out 4 times, and there were 14 color matches every time (50 reference colors and 6 repeated colors). The corresponding spectral data was measured by PR655 spectroradiometer.

### 3 Data Analysis

#### 3.1 Observer Variations

Observer variations are usually divided into the intra- and inter-observer variability. Observer's intra-variation is used to determine the variation of the visual assessments, or repeatability, of a particular observer. It was calculated between each observer's individual session and the mean of the repetitions for the 6 randomly selected colors. Observer inter-variation represents the average deviation between individuals and the mean visual results for all observers. The mean CIEDE2000 values of the 50 colors were used to determine the values for each observer. See Table 1.

All observers performed the repetitions. It can be seen from Table 1 that the mean intra-observer variability (with 0.57 CIEDE2000 units) is almost one half smaller than the mean inter-observer variability (with 1.00 CIEDE2000 units). In comparison with other previous similar experiments [5], observer variations are very similar. So observer variations were acceptable in the experiment and the observers' data were valid.

#### 3.2 Characteristic of Different CMFs

The concept of colorimetric observer categories has been introduced in Sarkar's concluded doctoral thesis research [3]. Each such category represents a distinct colorimetric observer model, and they are applicable for the  $10^\circ$  visual field.

Figure 4 shows the comparisons of the CIE1931, CIE1964 and 8 Sarkar's CMFs. Except for CIE1931 CMF, the  $\bar{y}(\lambda)$  channels share the same responses in the medium wavelength (see Fig. 4b). The  $\bar{x}(\lambda)$ ,  $\bar{z}(\lambda)$  channels have the obvious differences and S1 has the deviation towards long wavelength (see Fig. 4c). The red color was taken for example, and the corresponding color perception of different observer categories on the monitor was shown in Fig. 4d. It can be seen that the performance of some categories seems to be similar (just a slight difference), and higher chroma will be perceived by observers belonging to CIE1931, S7 and S8 CMFs, especially for S7 and S8 CMFs.

For a given color stimulus, different observers will have different color perception. For the 5 color centers (such as gray, red, yellow, green and blue), the CMFs have different performance, as shown in Fig. 5. In general, the variability in  $b^*$  values is always smaller compared with  $a^*$  values, and it is particularly apparent

**Table 1** Observer variations

Observer variations	Mean	Max	Min
Intra-observer variability	0.57	1.08	0.32
Inter-observer variability	1.00	1.44	0.68

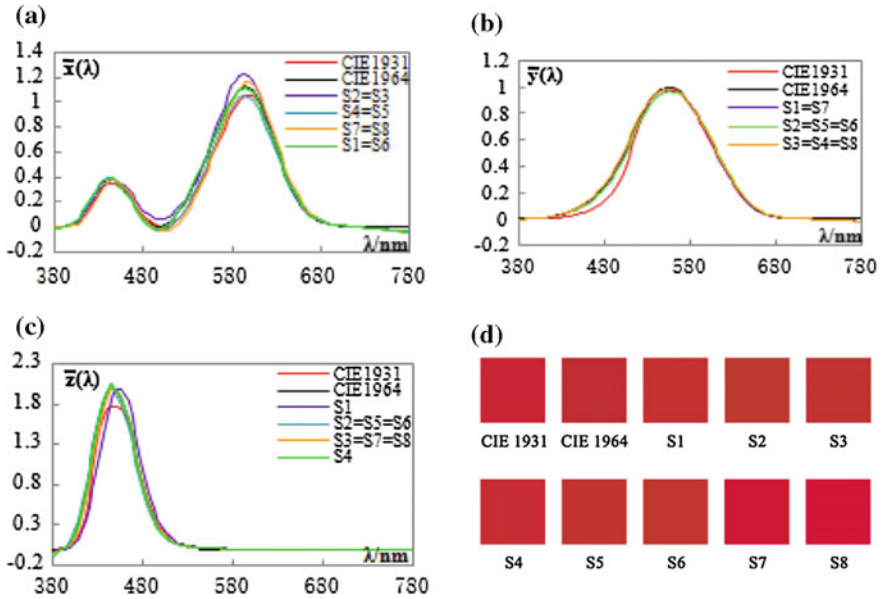


Fig. 4 Comparisons of the ten CMFs

at red, green colors and unapparent at gray color. S7 and S8 CMFs share the similar responses in the three channels (see Fig. 4), and the color perceptions described by them are similar (see Fig. 5). For a give color stimulus, the color sense aroused by S7 and S8 CMFs was more saturated.

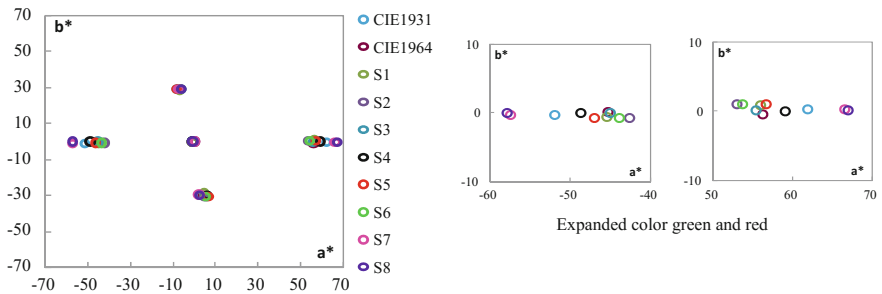


Fig. 5 Performance of the ten CMFs



**Table 2** The performances of the ten CMFs in terms of P%

CMFs	CIE1931	CIE1964	S1	S2	S3	S4	S5	S6	S7	S8
MIN $\Delta E_{00}$		21.43	10.71	25.00	10.71	3.57	3.57	25.00		
MAX $\Delta E_{00}$	7.14								46.43	46.43

### 3.3 Observer Categories

The spectral data  $S(\lambda)$  of the target and matched colors were measured by the spectroradiometer and used to calculate the corresponding XYZ tristimulus values [6], the corresponding CIEDE2000 color difference was calculated for each observer based on the ten CMFs. In order to investigate the performances of the ten CMFs, the percentage of the minimum/maximum CIEDE2000 values (P%) were calculated for the experiment. For example, the frequencies of the minimum/maximum CIE2000 values for the CMFs divided by the total numbers and plus 100, as Table 2 shown.

In Table 2, the observers would be assigned to 7 different observer categories even if they are of the same age (Most participant observers belong to young students). It can also be seen that no observer was assigned to CIE1931, S7 and S8 CMFs, which is accorded with the previous study using the printed samples [4]. And the results showed that most observers' CMFs are away from S7 and S8 CMFs. It indicated that color perception for most participant observers was less saturated. Meanwhile, no observer was assigned to CIE1931 CMF, because the experiment was conducted in large visual field which was close to the CIE1964.

## 4 Conclusions

In the study, 28 observers were organized to match the color stimuli on the LED monitor. They were assigned to different observer categories according to CIEDE2000 color difference of the target and matched colors based on ten CMFs. The minimum CIEDE2000 values between target color and matched color mainly belonging to S6, S2 and CIE1964 CMFs, which indicated that observers would have different perception even within the same age group and same visual field.

**Acknowledgements** This research was supported by national Natural Science Foundation of China (grant 61675029, 61308081), Beijing Nova Program NO. Z151100000315076, the Top Young Talents (CIT&TCD201404127), Beiyin Talents of Beijing Institute of Graphic Communication (Byyc201316-005).

## References

1. P. K. Kaiser, H. Hemmendinger (1980). The color rule: A device for color-vision testing. *Color Research & Application*, 5(2), 65–71.
2. A. Stockman, L. Sharpe (2000). The spectral sensitivities of the middle and long wavelength sensitive cones derived from measurements in observers of known genotype. *Vision Research*, 40(13), 1711–1737.
3. Sarkar A (2011) Identification and assignment of colorimetric observer categories and their applications in color and vision sciences. PhD thesis, Thomson Corporate Research, Rennes, France.
4. Huang Min, Cui Gui-hua, LIU Yu, LIU Hao-xue (2015). Analysis of observers metamerism differences for different retinal cone visual responses. *Spectroscopy and Spectral Analysis*, 35 (10), 2802–2809.
5. Chunjie Shi, Min Huang, Haoxue Liu (2016). Evaluation of color perception among different aged observers based on color matching experiments. *Lecture Notes in Electrical Engineering*, v369, 139–145.
6. Liu Haoxue et al: *Color Science and Technology* (China Light Industry Press, Beijing 2008).

# Measurement and Analysis of Colorimetric Values for Holographic Paper with Light Pillars

Zeyang Li, Min Huang, Yu Liu, Chunjie Shi, Haoxue Liu  
and Guihua Cui

**Abstract** The holographic paper has the light rainbow visual effect but it will arouse the color measurement inaccuracy. In order to measure the colorimetric values of holographic paper accurately and stably, an automatic measuring platform was used to collect the colorimetric values of the standard and test samples. Three 'moved methods' were used to align the two groups, and then the CIELAB color difference values of each corresponding sampling point were compared one by one. The minimum averaged value was chosen as the real-value of the tested paper which can show the color difference of them accurately.

**Keywords** Color measurement · Holographic paper · Holographic pattern · Period of light pillars

## 1 Introduction

The holographic paper with light pillars has been widely used in packing and printing industries for its visual rainbow characteristic and anti-fake function. But the color quality of holographic paper with light pillars is difficult to measure accurately and stably. In recent years, Wan et al. [1, 2], Huang et al. [3] proposed that the colorimetric values of holographic paper can be measured by the spectrophotometer with the integrating sphere at different positions or different directions of the same position. Wan et al. [4] and Feng et al. [5] designed a diffused light measurement system to measure the colorimetric values of the paper, but the instrument is not portable and the cost is too high. Xu et al. [6] indicated that color

---

Z. Li · M. Huang (✉) · Y. Liu  
School of Printing and Packing Engineering, Beijing Institute of Graphic  
Communication, Beijing, China  
e-mail: huangmin@bigc.edu.cn

C. Shi · H. Liu · G. Cui  
College of Physics and Electronic Information Engineering, Wenzhou  
University, Wenzhou, China

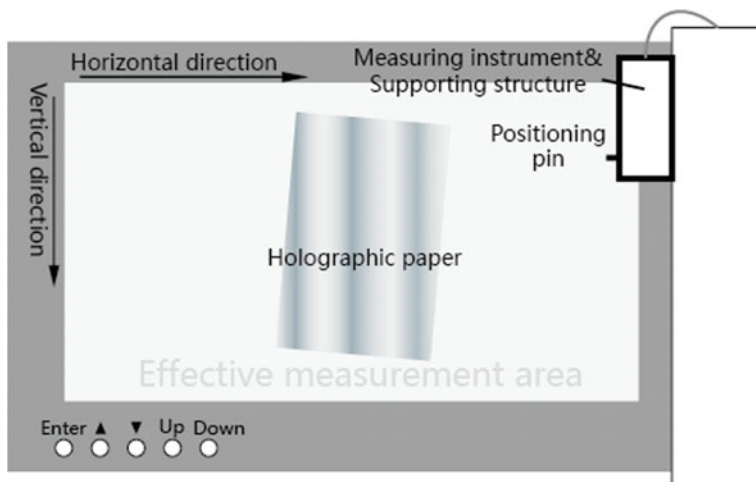
measurement of holographic paper can be conducted by line source scanning method, but the results will be affected by the errors of color conversion in different color spaces.

Considering the periodic distribution of light pillars and periodic variation of colorimetric values on holographic paper, an automatic measure platform was designed to collect the colorimetric values of the standard and test samples [7]. The CIELAB color differences of each corresponding sampling point were compared one by one and these color differences were averaged under 3 ‘moved method’ respectively, the minimum mean color difference was chosen as the real color-difference of the standard and tested holographic paper.

## 2 Color Measurements

3 holographic papers from different production batch were chosen, in which paper 1 was defined as the standard sample, Paper 2 and 3 were defined as the tested samples. Paper 4 and 5 from another manufacturer were chosen as the tested papers to test our methods.

The measuring conditions of the integrating sphere spectrophotometer were set as: D65 light illuminant, CIE 1964 10° observer, specular component included (SCI), 4 mm aperture and  $d/8^\circ$  [4]. Papers were automatically measured by the platform (as Fig. 1 shown) at the direction of perpendicular to the light pillars (including 60 sampling points with 2.5 mm spacing).



**Fig. 1** The sketch map of measure platform

### 3 Results and Discussions

#### 3.1 Calculation of Color Difference

Because of the different initial positions of the standard and tested holographic papers (as Fig. 2 shown) will arouse different colorimetric values. The sampling points with the same number on the standard and tested holographic papers should be rearranged and aligned to the same period to calculate the color difference one by one.

In other words, color differences calculated point by point (e.g. Point 1 of Paper 1 compared with Point 1 of Paper 2, Point 2 of Paper 1 compared with Point 2 of Paper 2...) couldn't represent the right difference of the papers. The colorimetric values of each sample should be 'moved' based on the maximum  $L^*$  value of the sampling point which was among the first period, and then  $a^*$  and  $b^*$  values moved accordingly. The  $L^*$ ,  $a^*$ ,  $b^*$  values of the standard (paper 1) and the compared (paper 2 and 3) moved before (Fig. 3) and after (Fig. 4) were shown.

The CIELAB color differences were compared one by one (shown in Fig. 5). P1&P2 represents the color differences of Paper 1 and Paper 2, and the mean CIELAB color difference was 1.37; P1&P3 represents the mean CIELAB color differences of Paper 1 and Paper 3, and the mean color difference was 2.62.

It can be concluded from Fig. 5 that the mean CIELAB color difference of Paper 1 and Paper 3 is larger than Paper 1 and Paper 2, which accorded with the visual results. Paper 3 is darker than Paper 1, Paper 2 is judged as a qualified product which had small mean color difference compared with Paper 1.

#### 3.2 Special Case

If the colorimetric values of each sample were 'moved' based on maximum  $L^*$  value of the sampling point which situate in the first period,  $a^*$  and  $b^*$  values of each sample should also be adjusted to the same position of the light pillars. It means colorimetric variation curves of sampling points in a line were 'aligned'

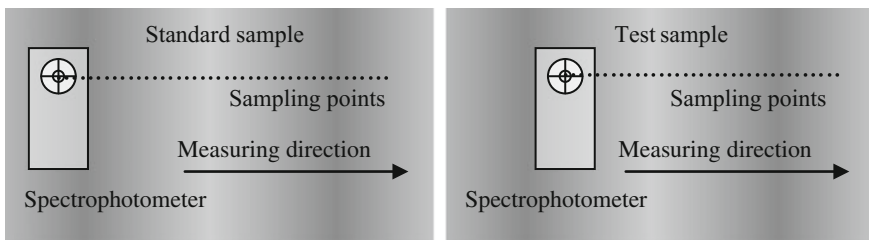
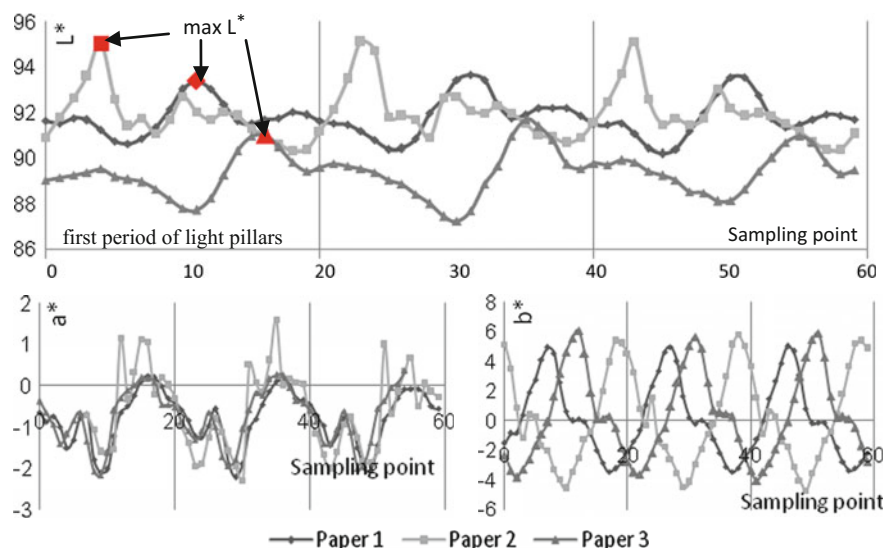


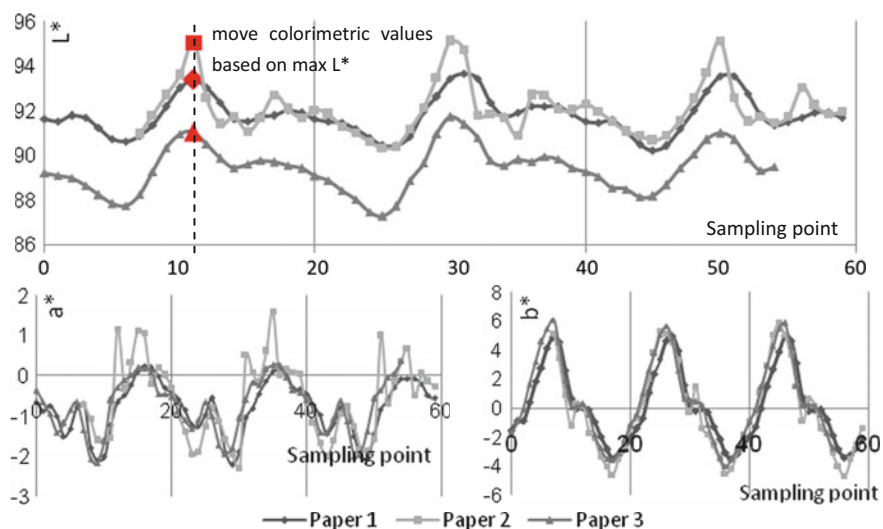
Fig. 2 The sketch map of measuring interface

(as Fig. 4 shown). But in consideration of the different microscopic structures of the holographic paper, sometimes exceptions persist.

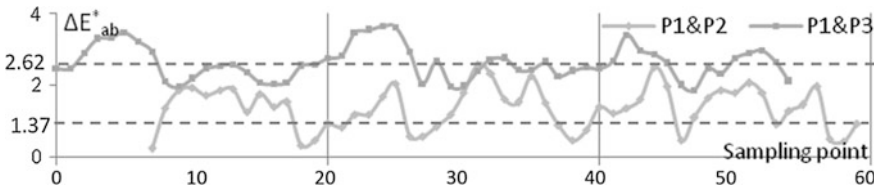
The colorimetric values of Paper 4 and 5 were ‘moved’ based on above-mentioned method, but colorimetric variation curves of  $a^*$  and  $b^*$  were not ‘aligned’ correctly (as Fig. 6 shown).



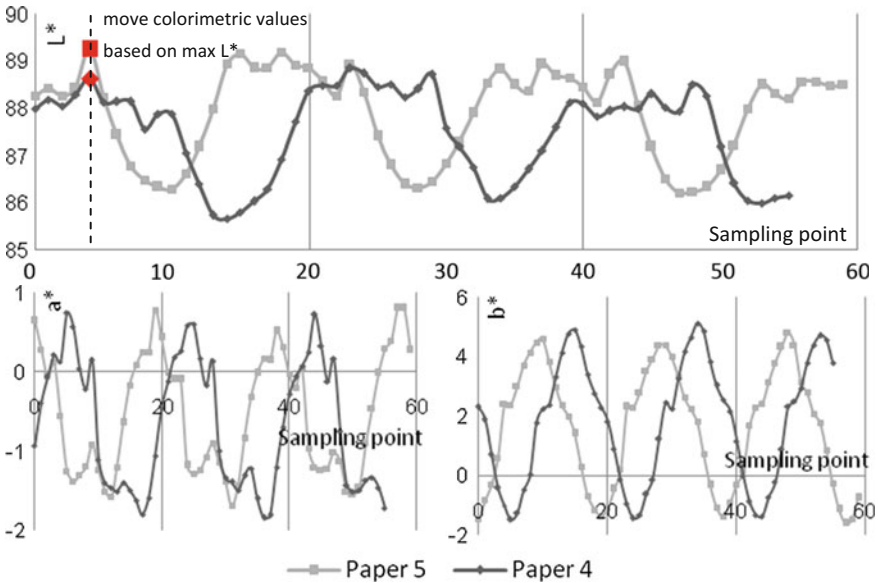
**Fig. 3** The distribution of original  $L^*$ ,  $a^*$ ,  $b^*$  values of different paper



**Fig. 4** The distribution of  $L^*$ ,  $a^*$ ,  $b^*$  values of different paper after adjusting



**Fig. 5** The CIELAB color difference of the corresponding position for different papers



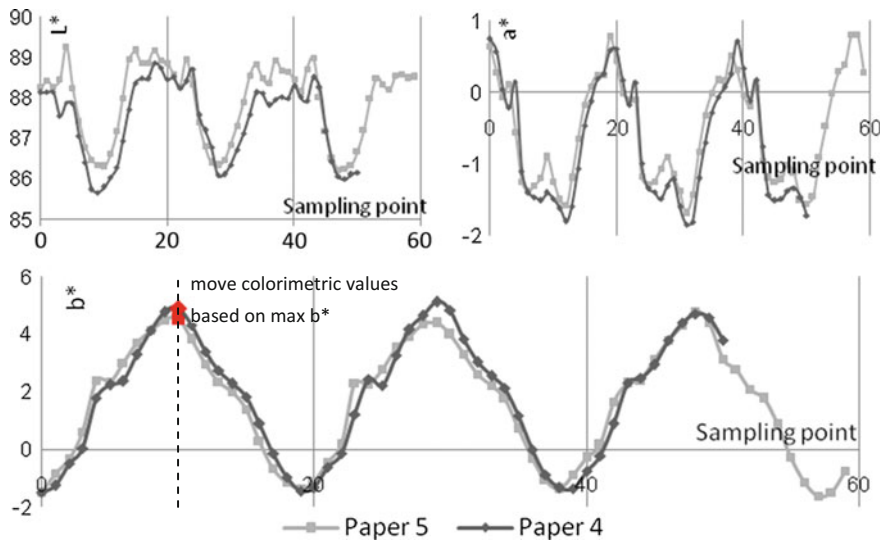
**Fig. 6** The distribution of  $L^*$ ,  $a^*$ ,  $b^*$  values of different paper after moving based on max  $L^*$  value

The CIELAB color differences of each corresponding sampling point were compared one by one, and the mean color difference of Paper 4 and 5 was 3.36.

But if the colorimetric values were ‘moved’ based on maximum  $b^*$ , all colorimetric variation curves were ‘aligned’ correctly (as Fig. 7 shown).

The CIELAB color differences of each corresponding sampling point were also compared one by one, and the mean CIELAB color difference of Paper 4 and 5 was 0.69. Compared with the visual results, the value is reasonable and credible.

In order to eliminate the interference of measurement errors and improve the accuracy, the colorimetric values of the standard and test samples should be ‘moved’ 3 times based on the maximum  $L^*$ ,  $a^*$ ,  $b^*$  values of the sampling point which situate in the first period, and the minimum mean CIELAB color difference was chosen as final result.



**Fig. 7** The distribution of  $L^*$ ,  $a^*$ ,  $b^*$  values of different paper after moving based on max  $b^*$  value

## 4 Conclusions

The colorimetric values of the standard and test samples were collected by an automatic platform, and they were ‘moved’ 3 times to adjusted to the same position of the light pillars based on the maximum  $L^*$ ,  $a^*$ ,  $b^*$  values of the sampling point which was among the first period. The CIELAB color differences of each corresponding sampling point were compared one by one and these color differences were averaged respectively under such 3 ‘moved method’, the minimum mean CIELAB color difference was selected as the real value of the tested papers.

**Acknowledgements** This research was supported by Beijing Nova Program (NO. Z15110000315076), National Natural Science Foundation of China (grant 61675029, 61308081) and Beiyin Talents of Beijing Institute of Graphic Communication (Byyc201316-005).

## References

1. Xinguo Huang, Xiaoxia Wan et al (2003). Optimization of the method for color measurement of printing on holographic paper. *Color Research & Application*, 38(2), 130–138.
2. Xiaoxia Wan, Xinguo Huang, Zhen Liu (2011). Color measurement for holographic photo paper (2010 Asian symposium: Next-generation printing science and technology). *Japanese Society of Printing Science and Technology*, 48(1), 21–26.
3. HUANG M, WANG L F et al (2014). Measurement and analysis of spectral and chromaticity values of pillars of light pattern holographic paper. *Acta Optica Sinica*, 34(6), s0633002.



4. Peng Sun, Chao Xiao, Xiaoxia Wan et al. The spectrophotometer for color measurement of holographic paper: China, ZL201010578507.7 [P], 2014-02-26.
5. FENG ZH X, ZHANG CH E, WANG Y S (2014). A new method of color measurement for laser rainbow holographic printed matter. *Acta Optica Sinica*, 34(9), 0933001.
6. Yanfang Xu, Yuehong Song, Yu Liu et al. Colorimetric characterization and measurement method of light pillars holographic paper: China, ZL201310118581.4 [P], 2014-11-26.
7. Min Huang, Chunjie Shi, Haoxue Liu et al. The automatic color measurement and quality evaluation system for light pillars holographic paper: China, ZL201520082729.8 [P], 2015-06-03.

# A Brief Review of Colour Quality Assessments of LED Lightings for Museums

Qiyan Zhai and Ming Ronnier Luo

**Abstract** Recent years the subject of colour quality of LED lighting in museum was extensively studied. It was found that different experimental results can be effectively described as *Comfort Zone* in terms of illuminance and colour temperature of the museum illuminations. Work of updating colour rendering index for LED lighting can also be used for museum lighting applications. Recent studies on museum lighting and some related work are reviewed in this paper. Important recommendations about how to achieve high colour quality museum lighting are also given.

**Keywords** Museum lighting · LED lighting · Colour quality

## 1 Introduction

With the development of LED lighting, the industry of museum lighting has come to an age of upgrading since the early 2010s. The conventional illuminance limitation in museum application suggested by CIE (The International Commission on illumination) is 50 lx for sensitive objects [1]. In consideration of some features of LED lightings such as the flexible spectrum and the easy cut-off of UV and IR which cause most of the radiation damages to fine arts, the illuminance may be not as low as 50 lx, and a recommendation of the chromaticity of museum illuminations should be made. To meet the needs of the special application in museum such as low radiation damage, high visibility and high colour fidelity [2–4], many researches have been done in global range to assess the colour quality of museum LED lightings. In terms of illuminance, CCT (Correlated Colour Temperature),

---

Q. Zhai · M.R. Luo (✉)  
State Key Laboratory of Modern Optical Instrumentation, Zhejiang University,  
Hangzhou, China  
e-mail: M.R.Luo@leeds.ac.uk

M.R. Luo  
School of Design, University of Leeds, Leeds, UK

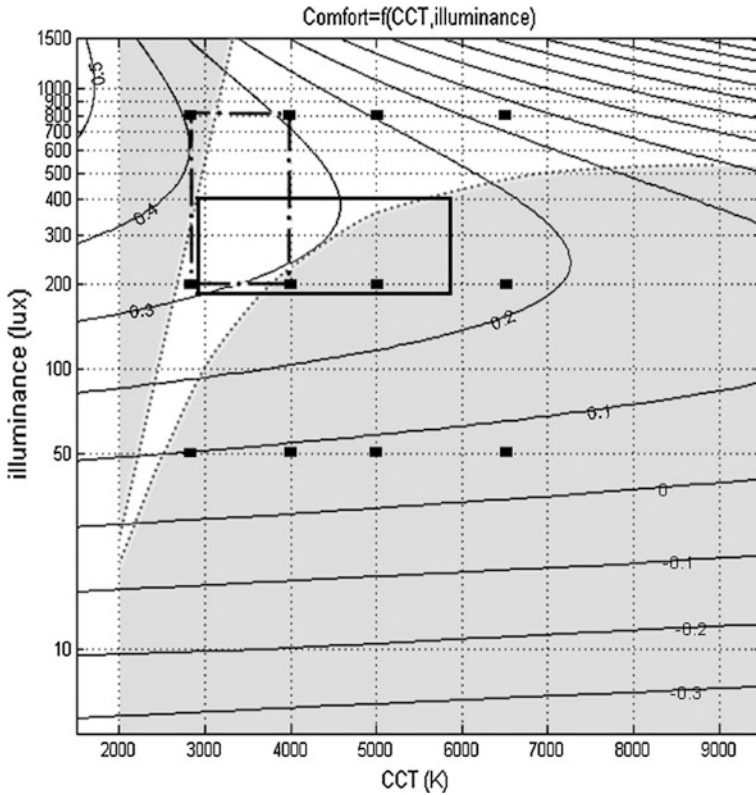
Duv (chromatic distance departing from the Blackbody locus in CIE1960 uv space), and CRI (colour rendering index), psychophysics experiments have been performed to investigate the impact of these parameters on viewing museum paintings. The different conclusions on optimization colour quality in museum LED lighting are compared as *Comfort Zone* in this paper, and followed by some discussions on recent updates of colour rendering index for LED lighting.

## 2 Studies for Defining *Comfort Zone*

The earliest illuminance-CCT investigation for visual comfort was carried by Kruithof in 1941 [5]. The Kruithof pleasing area was marked as low illuminance with low CCT and high illuminance with high CCT, which had been highly debated during years [6]. The Kruithof pleasing area is showed in Fig. 1. Even so, his methodology of finding visual *Comfort Zone* in terms of illuminance and colour temperature of lighting became a typical method in now-day studies.

Yoshizawa et al. [7] in Japan and Luo et al. [8, 9] in Taiwan performed experiments on the visual evaluation of fine art paintings under LED lighting, both finding two factors from the factor analysis, visibility and texture (warmth) governing visual perception for viewing museum paintings. Yoshizawa et al. studied LED illumination with changes of CCT (from 2700 to 5000 K), CRI (from 55 to 100) and illuminances (up to 400 lx) in two separate experiments, which were carried out in a mock-up room and in an exhibition room at Morohashi Museum of Modern Art in Japan. Each painting was assessed using eleven pairs of words, such as warm/cool and preferable/not-preferable. The factor ‘texture’ was associated with the moistness and warmth of the texture of a painting. Luo et al. performed a similar experiment in a viewing cabinet under a multichannel LED light source with illuminances up to 300 lx and CCTs ranging from 2700 to 6500 K and CRIs from 82 to 93 using eleven scales.

Zhai et al. [10, 11] in Zhejiang University, China, conducted two psychophysics experiments from 2012 to 2014. With three levels of illuminance, five levels of CCT, three levels of colour rendering index and two levels of Duv, a multi-channel LED source were used as illumination for fine art paintings. Twenty-four observers scored the lightings with over ten word pairs. The result showed that the increase of illuminance improves both the visibility and visual comfort of the fine art significantly in a range of 200 lx to 800 lx. The observers prefer LED lighting with lower CCT. We concluded that 3500 K would be the most comfortable CCT for museum lighting. The *Comfort Zone* was defined based on these results as showed in Fig. 1. Observers’ in the experiment preferred lighting with higher CRI and colour fidelity based CRIs have higher correlation coefficients than preference-based CRIs. A negative Duv value helps the appearance to be clearer and brighter. Similar to Yoshizawa, Luo and other studies in Europe (see later), two factors, *Visibility* and *Warm*, were identified to describe museum lighting appearance and atmosphere.



**Fig. 1** The Kruith of pleasing area (unshaded area within two dashed line); the comfort zone (within dotted-line rectangle) for museum lighting in terms of CCT and illuminance [10] from the experimental results at Zhejiang University and the contours of comfort scores; the comfort zone (within solid-line rectangle) based on the results from European studies

Szabo et al. [12, 13] in Hungary studied of colour quality (spectrum quality) in an EU (The European Union) joint project for upgrading the lighting in Sistine Chapel, Vatican with LED. Chromatic Adaptation Transform (CAT) was used to optimize the LED lighting spectrum to keep the colour appearance of frescos from daylighting into lower CCT. *Comfort Zone* was investigated and 5500 K of CCT was found to be the most pleasant while 4500 K to be the most preferred, which is significantly different from the results in Asian. The most preferred illuminance level was found to be 200 lx instead of higher than 200 lx. These differences could be caused by different experimental settings such as contents of paintings or cultural differences between Asian and European observers. Another similar visual experiment using both real paintings and monitors was conducted in Portugal by Nascimento et al. The best lighting appreciation of artistic paintings was found to be with a CCT of 5700 K, even higher than the result in Hungary. The *Comfort Zone* based on these results is showed in Fig. 1. The *Comfort Zone* is an effective tool for

quick positioning of the illuminance and colour temperature in a specific lighting application, but one of the disadvantages of using the *Comfort Zone* is that other parameters such as Duv and CRIs could be ignored.

A joint project between the National Gallery, London, UK, and Zhejiang University is being carried out to optimize LED lighting spectrum [15]. Note that the National Gallery is one of the earliest members in European museums or galleries taking apart into the upgrading of LED lighting. Conservators, Curators, Conservation scientists, and art, design and psychology students were invited as observers in this project. Further experiments and results are expected to verify the previous work to define the *Comfort Zone*.

### 3 Standards of Colour Fidelity and Appearance

The current standard of colour rendering index recommended by CIE is  $R_a$  [16] has been tested over the years and may not be suitable and stable for LED lightings. A new metric developed by IES (Illuminating Engineering Society of North America), TM-30-2015 [17], with two indices  $R_f$  for colour fidelity and  $R_g$  for colour gamut (preference based) stand out from numbers of CRIs leading the competition of new standard. To evaluate colour fidelity of LED lightings in museum,  $R_f$  of IES TM-30-2015 is recommended while  $R_g$  can be used to fine-tune the colour preference of illuminations in different applications. Some museums and galleries have already possessed knowledge to upgrading lighting to LED. One of the problems may be the colour quality control for different types of fine art or cultural relic. The traditional way of inviting the artist to adjust the lighting visually before exhibitions is still the main method in some museums. Further work of modeling  $R_f$  and  $R_g$  in IES TM-30-2015 would probably solve this problem.

When displayer printing reproductions for the fine art or the cultural relic in museum are carried out, colour appearances reproduction under different illuminations should be considered. CIECAM02 was proved to be reliable in the colour appearance reproduction in a simple and inexpensive way [18] while spectral imaging and printing technology would provide more accurate results to avoid the metamerism effect with a higher cost [19].

### 4 Conclusions

It is no doubt that the future museum lighting will apply tuneable LED light. The lighting parameters such as illuminance, CCT, CRI, Duv can be adjusted according to its spectra to achieve the desired atmosphere for a particular exhibition. Visibility and Warmth are the two perceptions for observing paintings could be used to characterize the desired atmosphere. *Comfort Zone* concept has proven to be useful in spectrum optimization of LED museum lighting. The preferred illuminance level

was found to be 200 lx while the preferred CCT varies according to contents and cultures. CRI and Duv also have impact on visibility. IES TM-30-2015 colour rendering index is recommended to use in museum LED lighting quality evaluation.

**Acknowledgements** The authors like to thank Prof. Jianming Song in the China Academy of Art and Ms. Jing Ai at in the National Museum of China for providing samples and opportunities of field survey.

## References

1. Commission Internationale de l'Éclairage. (2004) Control of Damage to Museum Objects by Optical Radiation. *Commission Internationale de l'Éclairage*. CIE Publication 157, Vienna: CIE, 2004.
2. Cuttle, C. (1996) Damage to museum objects due to light exposure. *Lighting Research and Technology*. 28: 1–9.
3. Berns, R. Designing white light LED lighting for the display of art: A feasibility study. *Color Research and Application* 2011; 36: 324–334.
4. Mou, X., Berns, R. (2013) Design of LED for Museum Lighting Application. *CIE Publication 038, Vienna: CIE2013*, pp. 758–766.
5. Kruithof, AA. (1941) Tubular luminescence lamps for general illumination. *Philips Technical Review* 1941; 6: 65–96.
6. Vienot, F., Durand, M., Mahler, E. Kruithof's rule revisited using LED illumination. *Journal of Modern Optics* 2009; 56: 1433–1446.
7. Yoshizawa, N., Fujiwara, T., Miyashita, T. (2012) A Study on the Appearance of Paintings in the Museum Under Violet and Blue LED. *CIE Publication x038, Vienna: CIE2012*, pp. 374–381.
8. Luo, H., Chou, C., Chen, H., Luo, M. R. (2012) Using LED technology to build up museum lighting environment: *Proceedings of AIC Colour, Volume 4, Newcastle upon Tyne, UK, July 8–12: 2013:1757–1760*.
9. Chen, H. S., Chou, C. J., Luo, H. W., & MR Luo. (2015). Museum lighting environment: designing a perception zone map and emotional response models. *Lighting Research & Technology*. doi:10.1177/1477153515596456
10. Zhai, Q., Luo, M. R., Liu, X. (2015) The impact of illuminance and colour temperature on viewing fine art paintings under LED lighting. *Lighting Research & Technology*. 2015; Vol. 47(7): 795–809
11. Zhai, Q., Luo, M. R., Liu, X. (2015) The impact of LED lighting parameters on viewing fine art paintings. *Lighting Research & Technology*. doi:1477153515578468
12. Szabo, F., Csuti, P., Schanda, J. (2012) Light Emitting Diodes in Museum Lighting—Colour Quality Requirements for Visitors' Acceptance. *CIE Publication x038, Vienna: CIE2012*, pp. 767–771.
13. Szabo, F., Csuti, P., Schanda, J. (2014) Colour fidelity for picture gallery illumination, Part 1: Determining the optimum light-emitting diode spectrum. *Lighting Research and Technology*. doi:1477153514538643.
14. Nascimento, S. M. C., Masuda, O. (2014) Best lighting for visual appreciation of artistic paintings—experiments with real paintings and real illumination. *Journal of the Optical Society of America A* 2014; 31: 214–219.
15. Padfield, J., Pearce, B. M., Luo, M. R., Hurlbert, A. C. (2016) Optimisation of Artwork Illumination Spectra by Museum Professionals. *Proceedings of the CIE Conference, Melbourne, 3–5 March 2016*. CIEx042: 7–11.

16. Commission Internationale de l'Eclairage. (1995) Methods of Measuring and Specifying Colour Rendering Properties of Light Sources. *CIE Publication 13.3*, Vienna: CIE, 1995.
17. David, A., Fini, P.T., House, K. W., Ohno, Y., Royer, M. P., Smet, K. A. G., Wei, M., Whitehead, L. (2015) Development of the IES method for evaluating the color rendition of light sources. *Optics Express* 2015; 23(12): 15888–15906.
18. Zhai, Q., Luo, M. R., Liu, X. (2015) Monitor reproduction of oil paintings under museum LED lighting using CIECAM02. *CIE2015, Jun–Jul. 2015, Manchester*. pp 941–947
19. Liu, Q., Wan, X., Liu, Z., Chan, L., Liang, J. (2013). Research on developing the spectral dataset for Dunhuang typical colors based on color constancy. *Spectroscopy & Spectral Analysis*, 33(33), 3071–4.

# Testing the Performance of Color Difference Formulae Using Two Distinct Glossiness of Color Printing Atlas

Jing Liang, Buyun Yao, Siyu Ning and Liang Sun

**Abstract** In modern color science field, the color difference is the important technology. The aim of this study is to evaluate the color difference of printing atlas. The experiments were assessed under two D65 and A light sources with color printing atlas. In addition, test the performance of color difference formulae on the color printing atlas which different distinct glossiness. The correlation of colorfulness visual experiment data and predicted results was the worst, hue was the best under the same light source. Research shows colorfulness was not almost affected in D65 light source. The common formula such as CIELAB, CIELUV, CAM02-UCS and CIEDE2000 were used to evaluate color-difference. The analysis has shown that CIEDE2000 perform better than other color difference formula.

**Keywords** Psychophysics experiment · Magnitude estimation technique · Color difference model · Printing atlas

## 1 Introduction

Under the different media and environment of observation, which color spaces models were used to resolve color high-fidelity reproduction and predict color properties. The CIE Technical Committee 1–28 on Parameters Affecting Color-difference Evaluation was formed to coordinate researchers conducting research in this area [1]. More recently, new color-difference equations and uniform color spaces have been developed such as CIEDE2000 and CAM02-UCS,

---

J. Liang (✉) · B. Yao · S. Ning · L. Sun  
School of Light Industry and Chemical Engineering, Dalian Polytechnic University,  
Dalian, China  
e-mail: ljlove426@163.com

J. Liang  
State Key Laboratory of Modern Optical Instrumentation, Zhejiang University,  
Hangzhou, China



respectively. Gloss effect [2] how to influence color appearance were researched by Zhejiang University from 2008 to 2015. Color difference evaluation for white light sources was researched by M.R. Luo.

This paper is to evaluate the color appearance and test the performance of color difference formulae. Meanwhile, the analysis has shown the influence of gloss levels. The hue, value and colorfulness were discussed, and so on.

## 2 Experiments

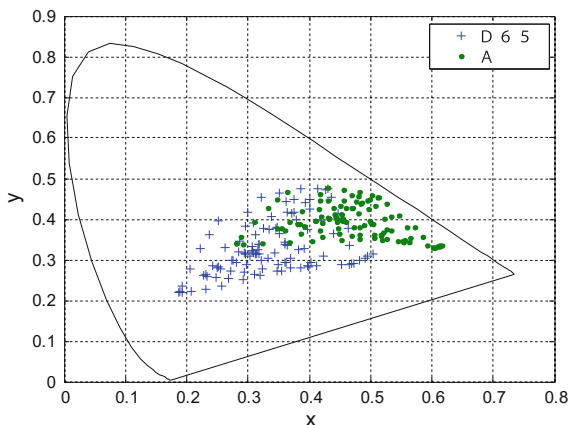
### 2.1 Magnitude Estimation Technique

Magnitude estimation technique usually has been used to psychophysical experiments. This technique derived from Stevens' ratio scaling method [3].

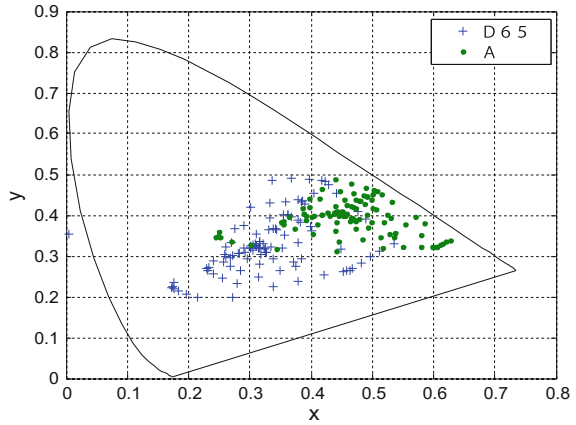
### 2.2 Test Atlas Samples

In terms of two-tone color which test atlas samples were overprinted in three pages (Y-C, Y-M, M-C) of printing atlas of different two distinct glossiness [4]. 216 ( $36 * 3 * 2 = 216$ ) test atlas samples were chose from high-gloss and low-gloss color printing atlas. Double-sided coated high-gloss printing atlas which is 4.1 of  $60^\circ$  average and 4.9 of  $85^\circ$  average respectively. Meanwhile, low-gloss printing atlas is 56.3 of  $60^\circ$  average and 84.0 of  $85^\circ$  average, respectively. The x, y plot of test colors were shown in Figs. 1, 2, 3 and 4.

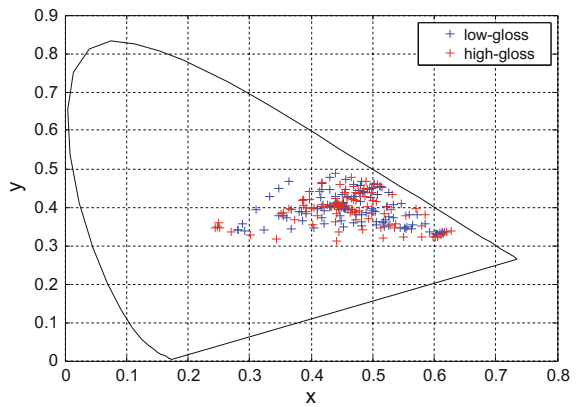
**Fig. 1** CIE x, y plot of test colors in low-gloss color printing atlas under D65 and A



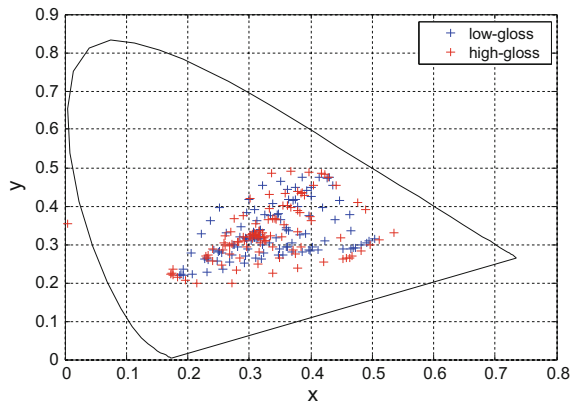
**Fig. 2** CIE x, y plot of test colors in high-gloss color printing atlas under D65 and A



**Fig. 3** CIE x, y plot of test colors in low-gloss and high-gloss color printing atlas under D65



**Fig. 4** CIE x, y plot of test colors in low-gloss and high-gloss color printing atlas under A



### 2.3 Light Sources

D65 and A light sources were selected in CIE illuminants. The 1931CIE x, y chroma numerical value and color temperatures are shown in Table 1. Their numerical values are very similar each other. The experimental values were measured in a standard CIE viewing cabinet and the measuring device was PR715.

### 2.4 Psychophysics Experiment Phase About Different Gloss Printing Atlas

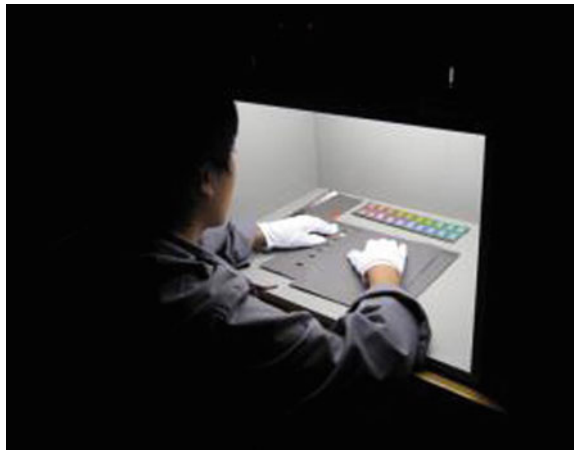
Experimental phase in this visual experiment is illustrated in Fig. 5. There were 10 observers who took part in the visual prediction experiment. They need normal color vision. The 5 males and 5 females were aged between 22 and 43.

Reference samples were viewed with  $0^\circ/45^\circ$  (illuminating/viewing). Six colors were selected from Munsell Book of Color Glossy Finish Collection. All color samples were  $12.5 \times 16.5$  mm size.

**Table 1** The chroma numerical value and color temperatures of the CIE illuminants and experimental light sources

Light source	Experimental measured		CIE standard		Color temperature (similar)
	x	y	x	y	
D65	0.3218	0.3310	0.3127	0.3290	5949
A	0.4550	0.4110	0.4476	0.4074	2765

**Fig. 5** Psychophysics experiment



The references for hue and colorfulness assessment corresponded to 5R, 5G, 5Y, 5B 6/8 from Munsell system. The references for lightness assessment corresponded to from 5R 0/1 and 9/1 from Munsell system.

For scaling lightness, observers were asked to assign a reasonable number (0–9) to describe the lightness of the test color. Describe test color by assigning a number (2, 4, 6, 8, 10, 12, 14). For scaling hue, there are 4 psychological primaries (R-G, Y-B). These colors were arranged a circle.

If the observer cannot perceive any hue at all, please reply neutral.

Finally, 8640 estimations were made. There were 2 viewing conditions \* 10 observers \* 2 times \* 216 samples [108 low-gloss samples + 108 high-gloss samples].

### 3 Results and Analysis

#### 3.1 The Intra-observer and Inter-observer Results

For great deal of the statistical analysis of this study, the STRESS (Standardized Residual Sum of Squares) measure was used. STRESS is a multidimensional scaling technique that was adapted by Garcia et al. In order to investigate the relationship between measured and perceived color difference [5]. Equation 1 shows the adapted version of the formula for testing color difference formulae. The multiplication by the factor 100 is added to produce results in percentage. Respectively, any dataset can be used as the factors  $\Delta V$  and  $\Delta E$  shown in Eq. (1).

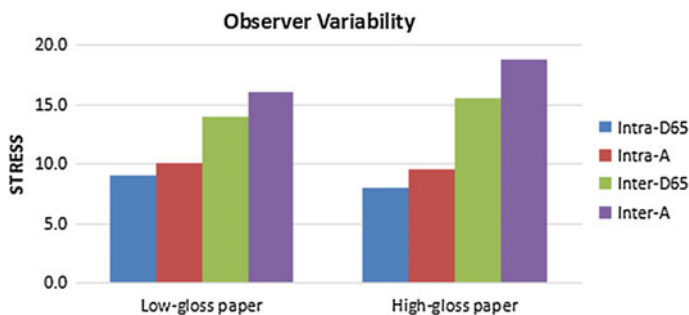
$$STRESS = 100 \sqrt{\frac{\sum (\Delta V_i - f \Delta E_i)^2}{\sum \Delta V_i^2}} \quad (1)$$

where  $f = \frac{\sum \Delta E_i \Delta V_i}{\sum \Delta E_i^2}$  is a scaling factor.

The STRESS measure was applied for the investigation of inter- and intra-observer variability in earlier similar studies. The results of this analysis are presented in Fig. 6. Furthermore, the values are within the same range with results of other studies such as by Luo et al. [6]. Finally, it can be seen that the repeatability of each individual's assessment for the test samples and test colors is significantly accurate.

#### 3.2 Comparing Predicted Results with Mean Visual Results

In statistics science, the R2 and CV are correlation coefficients which are generally used to investigate the relationship about two sets of data with each other in color



**Fig. 6** STRESS values for observer inter- and intra-observer

science [7]. We can get conclusions from Table 2 that the attributes (hue, lightness, colorfulness) of the linear relationships were better.

As shown in Table 2, the hue was very small variation under two light sources. The hue was the best in low-gloss printing atlas under A light sources. The colorfulness was the worst in low-gloss printing atlas under D65 light sources.

### 3.3 Testing Color Models' Performance

The mean visual results for each color samples were used to test uniform color spaces (CIELAB, CIELUV, CAM02-UCS) together with CIEDE2000 color difference formula. For the calculation of color difference from the three uniform color spaces together with CIEDE2000 color difference equation. The results are given in Table 3, again, in STRESS units.

**Table 2** CV and  $R^2$  results for printing atlas under light sources

Light source	Gloss	V		C		H	
		CV	$R^2$	CV	$R^2$	CV	$R^2$
D65	Low-gloss	17.91	0.95	42.33	0.73	7.57	0.97
	High-gloss	11.67	0.90	31.00	0.82	7.56	0.94
A	Low-gloss	20.03	0.62	36.60	0.98	6.81	0.99
	High-gloss	19.85	0.94	34.70	0.86	13.66	0.92

**Table 3** The performance of color difference metrics in STRESS unit

Light source	Gloss	CIELAB	CIELUV	CIEDE2000	CAM02-UCS
D65	Low-gloss	23	35	22	26
	High-gloss	25	38	24	26
A	Low-gloss	26	37	25	28
	High-gloss	28	37	26	29

It can be seen that CIEDE2000 space markedly outperformed the others. Furthermore, the results for the D65 data gave more accurate predictions than the ones for the A.

## 4 Conclusions

In conclusion, an experiment was carried out to investigate the color-difference discrimination for D65 and A light sources using different distinct glossiness printing atlas. The detailed analysis shows the predicted colorfulness was the worst, and hue was the best under the same light source. Meanwhile, the results showed that the CIEDE2000 based metrics outperformed those developed based on the surface colors such as CIELAB, CIELUV, CIEDE2000 and CAM02-UCS. CIEDE2000 should be recommended to define the color tolerance of surface colors samples. However, the magnitude of tolerance is highly dependent on different applications.

**Acknowledgements** This work is supported by Research and testing Foundation of Young teachers of Dalian polytechnic University in 2016.

## References

1. CIE. Technical report: parametric effects in color-difference evaluation. CIE Publ. No. 101. Vienna: Central Bureau of the CIE, 1993.
2. Fu L.J, Xu H.S, M.R. Luo. (2009). Estimating color appearance of pearlescent bottles using digital camera, *CHINESE OPTICS LETTERS*. 8, 744–747.
3. Liao N F, Shi J H, Wu W M. (2009). The Conspectus of Color Information Management for Digital Images, Beijing Institute of Technology Press, Beijing.
4. Liang J. Liao N.F. Song L. (2012). Establishment and Evaluation of Color Appearance Datasets about Low-Gloss Color Printing Atlas, *Acta Optica Sinica*. 5, 0533001-1–0533001-9.
5. Garcia, P.A., et al. (2007). Measurement of the relationship between perceived and computed color differences. *Journal of the Optical Society of America a-Optics Image Science and Vision*, 24(7): 1823–1829.
6. Cui, G.H., et al. (2001), Color-difference evaluation using CRT colors. Part II: Parametric effects. *Color Research and Application*, 26(5), 403–412.
7. M. R. Luo, A. A. Clarke, P. A. Rhodes. (1991). Quantifying color appearance. Part I. LUTCHI color appearance data, *Color Research and Application*, 166–180.

# Color Restoration Method of Underwater Multispectral Images

Ping Yang, Yilu Guo, Hong Song, Jingnan Sun, Yong Wang,  
Xiandou Zhang and Qiang Wang

**Abstract** Capturing accurate spectral data in water is challenging due to the heavily non-uniform attenuation of light in water across the visible spectrum. We build a spectrum, restoration method of underwater multispectral images in clear water. Firstly, a model for underwater imaging is established that takes attenuation and interface transmission of water into consideration. An algorithm of underwater spectral images restoration is deduced from the model, which estimates the influence of water in real time and then diminishes their impacts. Experiments are conducted with an area light source in a water tank. The results show that the relative residual of the method is less than 10%.

**Keywords** Underwater multispectral imaging · Image enhancement · Absorption

## 1 Introduction

Spectral imaging technique, combining spectral information with images, is a significant detecting method that has been used for underwater tasks such as coral recognition [1, 2], health checkout [1, 3, 4], species classification [5–7] and seafloor detection [8]. However, it is still a challenge to get accurate underwater spectral data because of the wavelength-dependent light attenuation caused by water. Different water types have different attenuation level, so that in-suit and in-time attenuation estimation and compensation are essential.

Most previous work decreases the influence of water by restricting the underwater imaging distances, e.g., in [3] the water depth is only 5 cm. Other literatures devote to solving water's effects on images. For example, Dierssen [8] described

---

P. Yang (✉) · H. Song · J. Sun · Y. Wang · X. Zhang · Q. Wang  
School of Digital Media and Design, Hangzhou Dianzi University,  
Hangzhou, Zhejiang, China  
e-mail: yangping@hdu.edu.cn

Y. Guo  
Ocean College, Zhejiang University, Zhoushan, Zhejiang, China

two spectral correction methods. The first one is using a known reflectance target that placed at a fixed distance and can be observed within the image to count the influence of water column, and then restores the image by Beer-Lambert's law. The other is using an AUV with spectral equipment to measure water optical properties. Both the methods are not easy to conduct.

In this paper, we propose a spectral restoration method of underwater multispectral images in clean water. First, we built a model of multispectral imaging with all components that light travel through being considered. Second, spectral attenuation coefficient of water was calibrated using spectral images of aim objects at different underwater distance, and then underwater images were restored by setting the estimated coefficients into the model. Finally, comparison between restored underwater images and images taken in the air is made to show the accuracy of the method.

## 2 Underwater Multispectral Imaging Model

The underwater staring spectral imaging system for underwater imaging uses wavelength-scan methods, whose structure is shown in Fig. 1. It consists of a set of color filters, a camera with an achromatic lens and a CCD panel detector. Wavelength scan is achieved by changing filters. According to underwater imaging theory in [9] and Jaffe-Mc Glamery approach [10], the relationship between the brightness of air and underwater image can be expressed as

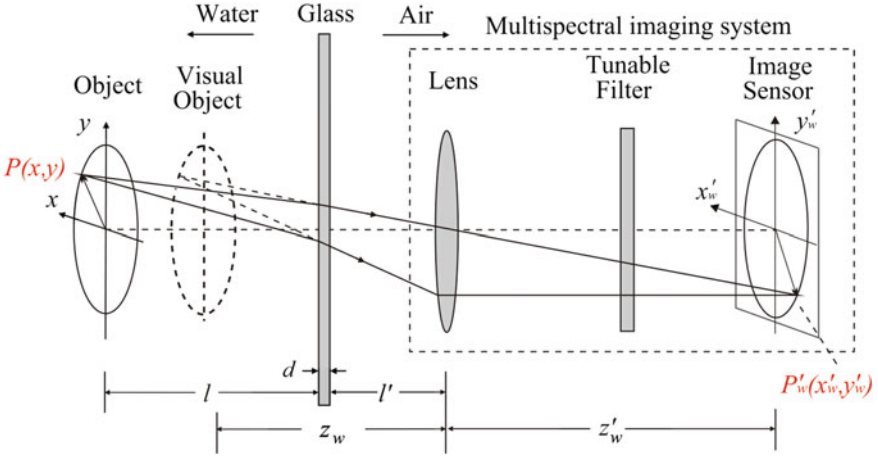
$$I_w(x'_w, y'_w, \lambda_c, z) = \frac{G(z_w)}{G(z)} \underbrace{\beta(\lambda_c) e^{-\alpha(\lambda_c)L}}_{k(\lambda_c, L)} I(x, y, \lambda_c, z) + b(\lambda_c) \quad (2.1)$$

where  $I_w(x'_w, y'_w, \lambda_c, z)$  and  $I(x, y, \lambda_c, z)$  are the brightness of underwater and air brightness, respectively;  $(x'_w, y'_w)$  and  $(x, y)$  are the position of imaging point in water and air, respectively;  $\lambda_c$  is the center wavelength of filters;  $z$  is imaging distance;  $\beta(\lambda_c)$  is the transmission coefficient on glass surface;  $\alpha(\lambda_c)$  is the attenuation of water;  $L$  is underwater distance;  $b(\lambda_c)$  is the contribution of stray light.  $G(z_w)/G(z)$  is the influence of lens' proprieties, which in most cases is more than 0.99 and can be neglected.

## 3 Spectral Image Restoration Methods

Considering images of a certain wavelength  $\lambda_0$ , for an underwater object with  $n$ -different brightness areas, Eq. (3.1) can be expressed as





**Fig. 1** Underwater multispectral imaging

$$\underbrace{\begin{bmatrix} I(i_1, j_1, \lambda_0, z) \\ I(i_1, j_2, \lambda_0, z) \\ \vdots \\ I(i_p, j_q, \lambda_0, z) \end{bmatrix}}_A \underbrace{\begin{bmatrix} k(\lambda_1, l_1) \\ b(\lambda_1, l_1) \end{bmatrix}}_X = \underbrace{\begin{bmatrix} I_w(i_{w,1}, j_{w,1}, \lambda_0, z_{w,1}) \\ I_w(i_{w,1}, j_{w,2}, \lambda_0, z_{w,1}) \\ \vdots \\ I_w(i_{w,p}, j_{w,q}, \lambda_0, z_{w,1}) \end{bmatrix}}_B \quad (3.1)$$

where  $p \in (1, \max\{i\})$ ,  $q \in (1, \max\{j\})$  and  $n$  is the number of  $(p, q)$  points. We can estimate the optimum  $k(\lambda_0, L_0)$  and  $b(\lambda_0, L_0)$  by least square linear fitting

$$X = (A^T A)^{-1} A^T B \quad (3.2)$$

By applying Eq. (3.2) to all calibration images,  $k(\lambda_0, L_0)$  and  $b(\lambda_0, L_0)$  of all wavelengths and calibration distances can be obtain.

Next step we estimate the optimal coefficients  $\hat{\alpha}(\lambda_0)$  and  $\hat{b}(\lambda_0)$  by exponential fitting  $k(\lambda_0, L_0)$  with distance  $L$ . That is, using Newton iteration method to make a minimum  $J$  that is defined as

$$J = \sum_{i=1}^m (\hat{k}(\lambda_0, L_i) - k(\lambda_0, L_i))^2 \quad (3.3)$$

where  $m$  is the number of underwater distances,  $k(\lambda_0, L_i)$  was achieved in Eq. (3.2) and  $\hat{k}(\lambda_0, L_i)$  is calculated by

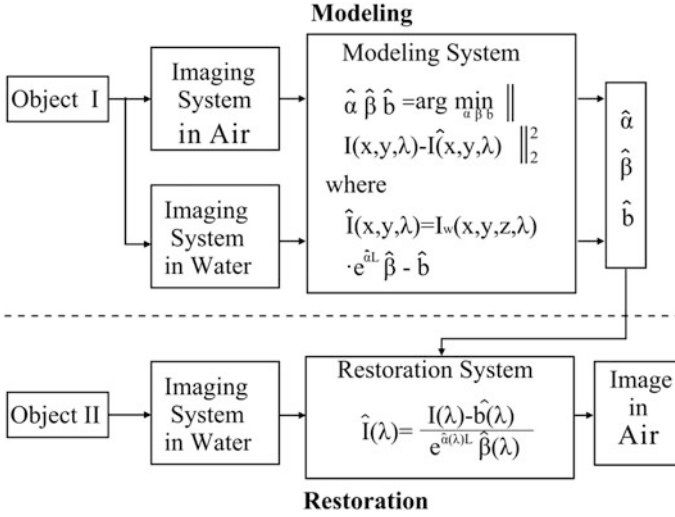


Fig. 2 Flow chart for image correction

$$\hat{k}(\lambda_0, L_i) = e^{-\hat{\alpha}(\lambda_0)L_i} \hat{\beta}(\lambda_0) \tag{3.4}$$

At last,  $\hat{b}(\lambda_0)$  is calculated by

$$\hat{b}(\lambda_0) = \frac{\sum_{i=1}^m b(\lambda_0, L_i)}{m} \tag{3.5}$$

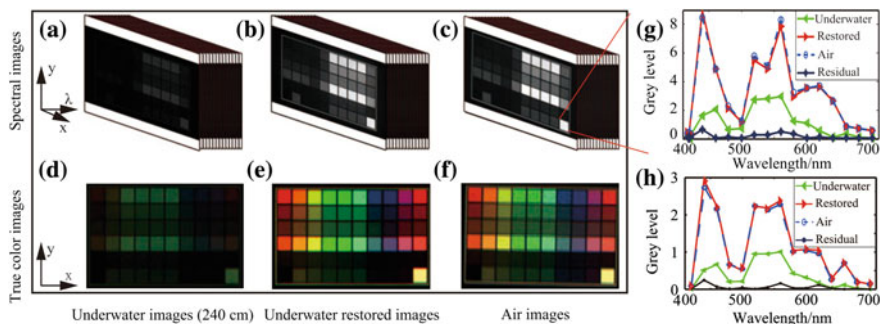
With all the coefficients being calibrated, according to Eq. (3.1), image restoration can be achieved by

$$I_c(x'_w, y'_w, \lambda_c, z) = \frac{I(x', y', \lambda_c, z) - b(\lambda_0)}{e^{-\hat{\alpha}(\lambda_0)L_0} \hat{\beta}(\lambda_0)} \tag{3.6}$$

The flow chart for image restoration is shown in Fig. 2.

### 4 Experiments and Results

A multispectral imaging system is built and shown in Fig. 3. It consists of a monochrome camera (F-032B, Pike, USA), an imaging lens (M5018MP, Computar, Japan) and a set of filters (FB serious, Thorlabs, USA). The FWHM of the filters are 10 nm and center wavelength (CWL) change from 420 to 700 nm at an interval of 20 nm. A smart phone with 60 different color pieces on it is used as



**Fig. 3** a–c Spectral images of underwater data, underwater restored results and air data. The wavelength of surface image is 440 nm. d–f True color images created using spectral images. g Spectral curve and residual of color piece (6,10). h Mean spectral curve and residual of images

**Table 1** Estimated coefficients  $\hat{\alpha}$ ,  $\hat{\beta}$ , and  $\hat{b}$

$\lambda$ (nm)	$\alpha$ ( $\times 10^{-3} \text{ cm}^{-1}$ )	$\beta$ (1)	$b$ ( $\times 10^{-2}$ )	$\lambda$ (nm)	$a$ ( $\times 10^{-3} \text{ cm}^{-1}$ )	$\beta$ (1)	$b$ ( $\times 10^{-2}$ )
420	10.5	0.87	0	580	2.8	0.83	-1.5
440	6.2	0.77	7.0	600	3.9	0.76	0.6
460	4.5	0.81	4.4	620	4.2	0.75	3.2
480	3.7	0.74	-0.2	640	6.2	0.64	0.7
500	3.4	0.85	0.9	660	6.3	0.74	1.0
520	3.1	0.86	5.6	680	7.5	0.70	0.5
540	3.0	0.86	4.4	700	8.3	0.68	0.2
560	2.8	0.85	4.8				

the object for imaging. We collected air multispectral images with an imaging distance of 240 cm, and underwater images with distances range from 10 to 260 cm with an interval of 10 cm.

Data with underwater distance  $L < 150$  cm are used to calibrate coefficients, and the rest are used for checking the accuracy. The calibrated coefficients are shown in Table 1.

According to the coefficients in Table 1 and Eq. (3.4), underwater multispectral images are restored. Figure 3a–c shows the restored results. True color images are also created to show the accuracy of the method, with the encoding principle being shown in Eq. (4.1).

$$I_f(x,y) = \frac{\sum_{\lambda=420}^{700} \frac{I(x,y,\lambda)S_f(\lambda\lambda)}{t(\lambda)\lambda_m(\lambda\lambda)}}{\max\left\{\sum_{\lambda=420}^{700} \frac{I(x,y,\lambda)S_f(\lambda\lambda)}{t(\lambda)\lambda_m(\lambda\lambda)}\right\}}, \quad f \in (r, g, b) \quad (4.1)$$

where  $M$  is the brightness that is used as the standard 1;  $S_f(\lambda)$  is quantum efficiency of a color camera (MER-030-120UC-L, Daheng, China);  $t(\lambda)$  is filters' peak transmittance,  $S_m(\lambda)$  is quantum efficiency of Pike F-032B;  $I_f(x, y)$  is true color

synthesis results. The results are shown in Fig. 3d–f. We can see that the color of the underwater image is shaded, while the air image is colorful, and that the color of restored image is similar to air image.

Figure 3g, h are the spectral curve of piece (6, 10) and mean spectrum of all color pieces, respectively, in which the Residual is defined as

$$\text{Residual} = |I_c - I| \quad (4.2)$$

It can be seen that the restored spectrum and air spectrum is quiet close. The Relative Residual, defined in Eq. (4.2), is about 7.5% on average, thus the accuracy of the method is proven.

$$\text{Relative Residual} = \frac{\text{Residual}}{I} \quad (4.3)$$

## 5 Conclusions and Future Works

In this paper, a model is built for underwater multispectral imaging, considering the attenuation of water, narrowband filters, lens and the camera. Calibration and the restoration methods are then proposed based on the model. An experimental setup is built in lab to verify the proposed method. The restored images are compared with images captured in air and results show that the relative restoration error is 7.5% in average for the test image group. Thus the accuracy of the restoration method is proved.

**Acknowledgements** The work is financially supported by the National High-tech R&D Program of China (863 Program) (No. 2014AA093400), National Natural Science Foundation of China (No. 61605038), Open Fund of State Key Laboratory of Satellite Ocean Environment Dynamics (No. SOED1606) and National Key Technology Research and Development Program of the Ministry of Science and Technology of China (2012BAH91F03).

## References

1. H. Holden and E. LeDrew. (1999). Hyperspectral identification of coral reef features [J]. *International Journal of Remote Sensing*, 20: 2545–2563.
2. E. Hochberg and M. Atkinson. (2000). Spectral discrimination of coral reef benthic communities [J]. *Coral reefs*, 19: 164–171.
3. H. Holden and E. LeDrew. (1998). Spectral discrimination of healthy and nonhealthy corals based on cluster analysis, principal components analysis, and derivative spectroscopy [J]. *Remote sensing of environment*, 65:217–224.
4. M. Mehrubeoglu, D. K. Smith et al. (2013). Investigating coral hyperspectral properties across coral species and coral state using hyperspectral imaging [J]. *SPIE Optical Engineering + Applications (International Society for Optics and Photonics, pp. 88700M–88700M.*

5. N. Stambler and N. Shashar. (2007). Variation in spectral reflectance of the hermatypic corals, *stylophorapistillata* and *pocilloporadamicornis* [J]. *Journal of Experimental Marine Biology and Ecology*, 351: 143–149.
6. K. Barott, J. Smith, E. Dinsdale, M. Hatay, S. Sandin, and F. Rohwer. (2009). Hyperspectral and physiological analyses of coral-algal interactions.
7. A. Gleason, R. Reid, and K. Voss. (2007). Automated classification of underwater multispectral imagery for coral reef monitoring [J]. *OCEANS 2007*, pp. 1–8.
8. H. Dierssen, P. Fearn, M. Ludvigsen, and M. Moline. (2013). Underwater hyperspectral imagery to create biogeochemical maps of seafloor properties [J].
9. Y. Guo, H Song, H Liu, H Wei, P Yang. (2016). Model-based restoration of underwater spectral images captured with narrowband filters [J]. *Optics Express*, 24(12): 13101–13120.
10. J. S. Jaffe. (1990). Computer modeling and the design of optimal underwater imaging systems [J]. *Oceanic Engineering, IEEE Journal of* 15, pp. 101–111.

# Research on the Conversion Algorithms of Monitor Color Management Based on WCS

Rui Zhang, Congjun Cao, Nana Liu and Jingshang Fan

**Abstract** This paper explores the color space conversion algorithms of display which is based on WCS color management and mainly studies of the conversion algorithms of RGB to XYZ color space. Compared the tetrahedral interpolation algorithm with the conversion algorithm of display in WCS to find the optimal algorithm and provide identifiable ground for the WCS color management technology research. The experimental results show that the tetrahedral interpolation algorithm is more accurate than the color space conversion algorithm of display in WCS.

**Keywords** WCS · Display color management · Color space conversion algorithm

## 1 Introduction

Microsoft and Canon jointly developed the Windows Color System (WCS). WCS has made a lot of innovations and improvements to the color management technology compared with ICC-based system. WCS color management can provide users with a greater color gamut and more accurate color reproduction results and fully reflect the device's ability to reproduce different colors [1].

The color space conversion algorithm is usually divided into the model method and the empirical method. The model method uses mathematical method to establish the approximate model of the device color by studying of the devices' color characteristics. The empirical method establishes mathematical formula which is only associated with the input and output data to describe the relationship of colors between different devices by sampling the input and output data without considering the devices' color rule. The empirical method can be divided into polynomial fitting, lookup table with interpolation and artificial neural network

---

R. Zhang · C. Cao (✉) · N. Liu · J. Fan  
Faculty of Printing, Packaging Engineering and Digital Media Technology,  
Xi'an University of Technology, Xi'an, Shaanxi, China  
e-mail: caocongjun@xaut.edu.cn

method [2]. In WCS, the color space conversion algorithm of RGB to XYZ for the monitor is model method. Through the research, the conversion algorithms based model method are built upon the principle that the RGB tristimulus values can be additive together. But in fact, there is a mutual interference and mutual inhibition between the three channels of RGB, which makes the color synthesis result of RGB in a certain degree of deviation from the ideal superposition principle [3]. Therefore, the WCS conversion algorithm may also diverge on the monitor, and in the current conversion algorithm, the lookup table and interpolation algorithm are widely used. So the paper compares the tetrahedral interpolation algorithm with the conversion algorithm of display in WCS to find the optimal algorithm and provide the reference for the WCS color management technology research.

## 2 Introduction of the Color Space Conversion Algorithm

### 2.1 *The Conversion Algorithm of Display in WCS*

In WCS color management technology, the establishment of the LCD monitor's conversion algorithm is composed of three parts.

First of all, a series of spot color chips display on the screen. Then measure these color samples to get the input and output data. According to the WCS document recommendation, the color data of the chips are monochrome as follows.

Red, green, and blue respectively take 15, 30, 45, 60, 75, 90, 105, 120, 135, 150, 165, 180, 195, 210, 225, 240, 255 and the other two channels are selected 0. And the neutral block with equal red, green and blue values were respectively taken 0, 15, 30, 45, 60, 75, 90, 105, 120, 135, 150, 165, 180, 195, 210, 225, 240, 255. Users can also design their own sampling, and increments can be uneven, that is, the samples' color values do not have to be spaced evenly apart, but to ensure that each red, green, blue and neutral gray channel must contain at least three samples.

Secondly, determine the tristimulus matrix. The tristimulus matrix of WCS based color management of display is divided into two steps:

1. Estimate the black point XYZ value. This step uses slightly modified nonlinear optimization objective function.
2. Calculate tristimulus matrix based on the step one and also from an averaging calculation on each channel measurements, rather than a maximum number of count results. Calculated as follows:
  1. Solve the nonlinear optimization problem to find the "best fit" black point  $(X_k, Y_k, Z_k)$  that will reduce the drift error in chromaticity as the display through the R, G and B channels. Based on the research of Berns to seek a set  $(X_k, Y_k, Z_k)$  which minimizes the following objective function.

$$\Phi(X_k, Y_k, Z_k) = \Psi(X_k, Y_k, Z_k; S_r) + \Psi(X_k, Y_k, Z_k; S_g) + \Psi(X_k, Y_k, Z_k; S_b) \tag{2.1}$$

where,  $S_r, S_g$  and  $S_b$  are the set of data points corresponding to the points on the R, G and B channels. For any set  $S$ , the formulas are defined as followed.

$$\Psi(X_k, Y_k, Z_k; S) = \sum_{i=1}^{i=S} \|f(X_i, Y_i, Z_i; X_k, Y_k, Z_k) - g(X_k, Y_k, Z_k; S)\|^2 \tag{2.2}$$

$$f(X, Y, Z; X_k, Y_k, Z_k) = \left( \frac{X - X_k}{X - X_k + Y - Y_k + Z - Z_k}, \frac{Y - Y_k}{X - X_k + Y - Y_k + Z - Z_k} \right) \tag{2.3}$$

$$g(X_k, Y_k, Z_k; S) = \frac{1}{|S|} \sum_{i=1}^{i=S} f(X_i, Y_i, Z_i; X_k, Y_k, Z_k) \tag{2.4}$$

As it can be seen from the above formula, the objective function is made up of many differentiable function squared and relative complex. So the optimization is often carried out by using the least square method. WCS conversion algorithm of display uses the Levenberg-Marquardt algorithm to optimize of the objective function [4].

2. After estimating black point  $(X_k, Y_k, Z_k)$ , determine the tristimulus matrix by calculating the average chromatic values in every three channels. The sample points used in calculating the average of chromaticity coordinates must be the same as the first step in optimizing.  $(\bar{x}_r, \bar{y}_r)$ ,  $(\bar{x}_g, \bar{y}_g)$  and  $(\bar{x}_b, \bar{y}_b)$  are the averaged chromaticity coordinates of the red, green, and blue channels. And the tristimulus matrix should be obtained using the following steps.

$$\begin{pmatrix} \bar{x}_r & \bar{x}_g & \bar{x}_b \\ \bar{y}_r & \bar{y}_g & \bar{y}_b \\ 1 - \bar{x}_r - \bar{y}_r & 1 - \bar{x}_g - \bar{y}_g & 1 - \bar{x}_b - \bar{y}_b \end{pmatrix} \begin{pmatrix} t_r \\ t_g \\ t_b \end{pmatrix} = \begin{pmatrix} X_w \\ Y_w \\ Z_w \end{pmatrix} \tag{2.5}$$

where,  $X_w, Y_w$  and  $Z_w$  are the measured white point tristimulus values, while  $t_r, t_g$  and  $t_b$  is the relational factors of three channels. After calculation, tristimulus matrix can be obtained as follows.

$$\begin{pmatrix} \bar{x}_r * t_r & \bar{x}_g * t_g & \bar{x}_b * t_b \\ \bar{y}_r * t_r & \bar{y}_g * t_g & \bar{y}_b * t_b \\ (1 - \bar{x}_r - \bar{y}_r) * t_r & (1 - \bar{x}_g - \bar{y}_g) * t_g & (1 - \bar{x}_b - \bar{y}_b) * t_b \end{pmatrix} \tag{2.6}$$

Finally, in order to determine the tone curve of display, each channel in the WCS is assumed to follow the model of ‘‘GOG’’:



$$f(x) = ((1 - k_g) + k_g * x)^\gamma \tag{2.7}$$

where,  $\gamma$  is the “gamma”,  $k_g$  is the “gain value” of red, green, and blue channels, and  $1 - k_g$  is the “offset” of red, green, and blue channels.

## 2.2 Lookup Table with Tetrahedral Interpolation Algorithm

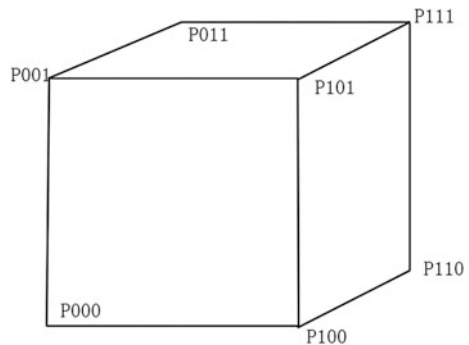
The first step of implement lookup table with interpolation algorithm is to build a color values’ lookup table in partition color space. Color partition is a process that using sampling grid points to divide the domain of the source color space into many small cubes.

In application users often want to build a three-dimensional lookup table, in which the input data points are uniform distributed, so that any input color can be quickly found in which color unit of lookup table. While researching on tetrahedral interpolation, this issue firstly uses five-level segmentation of the lookup table. That is selected R, G, B sampling data are separately as 0, 64, 128, 192, 255, which generates a total of 125 color patches. If the accuracy of the calculation is not up to the requirements, we will re-replacement the method.

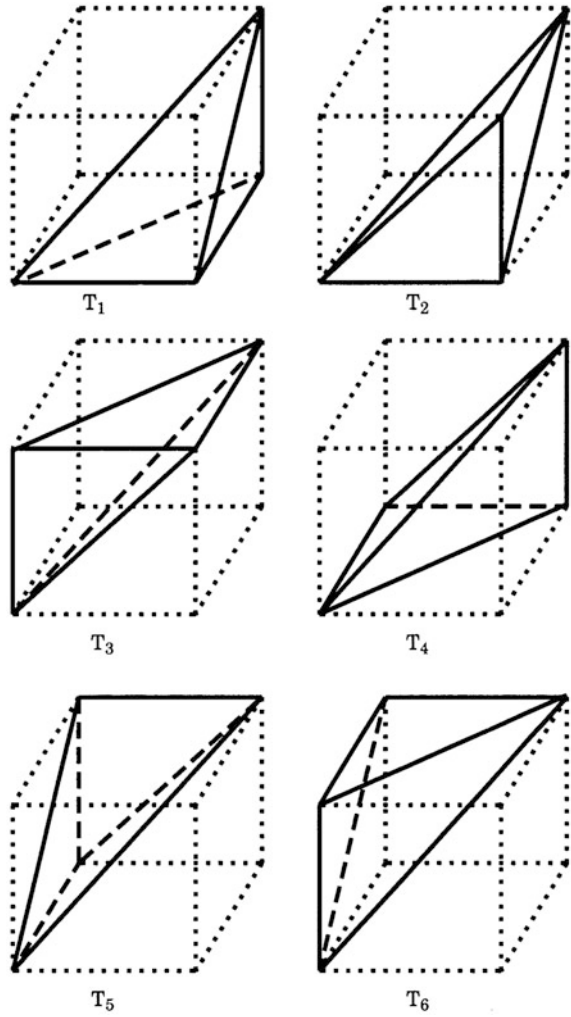
The second step, extraction the corresponding 8 vertexes of the small cube which containing object points. Enter the color values of a color device and then judge whether it is a grid point. If it is, output the corresponding chrominance values, if not, find the maximum and minimum value of interpolation grid which has nearest distance from the target point. Then Interpolation calculation should be made according to the rules of combination to determine the 8 vertexes in the target cube (Fig. 1).

The third step, establish tetrahedral interpolation algorithm. The small cube is divided into six tetrahedrons shown in Fig. 2, complete tetrahedron interpolation algorithm according to the rules in Table 1 [5].

**Fig. 1** The eight vertexes of the cube (0 represents the nearest minimum grid value from the point, and 1 represents the nearest maximum grid value from the point in the figure)



**Fig. 2** The way to divide the tetrahedral



**Table 1** Tetrahedral interpolation algorithm

Tetrahedral	Analyzing conditions	C <sub>1</sub>	C <sub>2</sub>	C <sub>3</sub>
T1	$\Delta R > \Delta G > \Delta B$	P <sub>100</sub> -P <sub>000</sub>	P <sub>110</sub> -P <sub>100</sub>	P <sub>111</sub> -P <sub>110</sub>
T2	$\Delta R > \Delta B > \Delta G$	P <sub>100</sub> -P <sub>000</sub>	P <sub>111</sub> -P <sub>101</sub>	P <sub>101</sub> -P <sub>100</sub>
T3	$\Delta B > \Delta R > \Delta G$	P <sub>101</sub> -P <sub>001</sub>	P <sub>111</sub> -P <sub>101</sub>	P <sub>001</sub> -P <sub>000</sub>
T4	$\Delta G > \Delta R > \Delta B$	P <sub>110</sub> -P <sub>010</sub>	P <sub>010</sub> -P <sub>000</sub>	P <sub>111</sub> -P <sub>110</sub>
T5	$\Delta G > \Delta B > \Delta R$	P <sub>111</sub> -P <sub>011</sub>	P <sub>010</sub> -P <sub>000</sub>	P <sub>011</sub> -P <sub>010</sub>
T6	$\Delta G > \Delta B > \Delta R$	P <sub>111</sub> -P <sub>011</sub>	P <sub>011</sub> -P <sub>001</sub>	P <sub>001</sub> -P <sub>000</sub>

For any set of input R, G and B values,  $R = R - R_0$ ,  $G = G - G_0$ ,  $B = B - B_0$ , it can be obtained the corresponding L, u, v values according to the following formula.

$$P(L, u, v) = P000 + C1\Delta R/(R1 - R0) + C2\Delta G/(G1 - G0) + C3\Delta B/(B1 - B0) \quad (2.8)$$

### 3 Comparison Study of Conversion Algorithms

#### 3.1 Methods and Procedures of the Experiment

Turn on the monitor to warm up for 30 min until the performance of monitor is stable. Then calibrate the monitor for the experiment.

1. Generate 254 color patches (69 color patches described in Sect. 2.1, 125 color patches from 5-level divided R, G, and B values uniformly and 60 more test color patches) and save them as profilemaker software available color target file format. Then store them in the appropriate location. Import the file to profilemaker. After calibration the measured data could be obtained shown in the form of spectral reflectance. And then use measure tool software to convert spectral reflectance to the form of LAB values.
2. Due to limitations of the experimental conditions, the XYZ or LUV values cannot be obtained directly. The XYZ or LUV values can only be calculated by the obtained LAB values.
3. Utilize MATLAB program to implement tetrahedron interpolation algorithm. The flowchart of tetrahedral interpolation algorithm is shown in Fig. 3. Due to WCS technical documentation recommendation, it is recommended to build a lookup table from RGB color space to LUV color space at first and then convert LUV values to XYZ values in establishing the lookup table algorithm of RGB to XYZ. This is because LUV color space is perceived more linear than XYZ color space. In order to compare the accuracy of the two lookup tables in the monitor, establish an RGB to LUV lookup table and a RGB to XYZ lookup table to compare with the conversion algorithm used in WCS monitor color management.
4. According to the calculation of the sample data, the conversion algorithm between RGB and XYZ color space based on the WCS display profile is obtained.
5. Compare the accuracy of tetrahedron interpolation algorithm and the algorithm used for describing the light-emitting principles of WCS monitors to find the optimal algorithm.

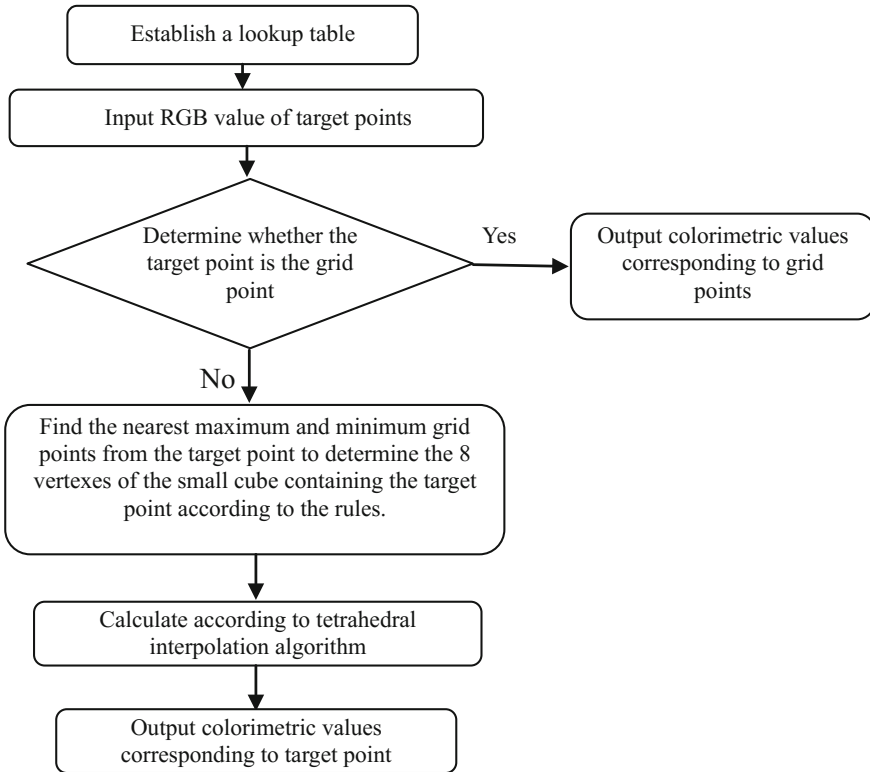


Fig. 3 Flowchart of Tetrahedron interpolation algorithm

### 3.2 Color Difference Formula Based on Color Appearance Model CIECAM02

Since the color gamut of WCS is determined by device profile and color appearance model profile together, so when you compare the accuracy of different algorithms, you use the color difference formula of CIECAM02. The specific algorithm is as follows.

$$\Delta E = \sqrt{(\Delta j/K1)^2 + \Delta a'^2 + \Delta b'^2} \tag{3.1}$$

$$M' = (1/c2) \ln(1 + c2M) \tag{3.2}$$

$$a' = M' \cos h \tag{3.3}$$

**Table 2** Comparison of conversion algorithms accuracy

Color difference	Conversion algorithm		
	RGB to LUV lookup table	RGB to XYZ lookup table	Model method used in WCS
0-1	40	30	25
1-2	6	15	5
2-3	5	4	15
3-4	3	5	5
4-5	3	3	4
More than 5	4	3	6

$$b' = M' \sin h \quad (3.4)$$

where,  $K1 = 1.24$ ,  $c1 = 0.007$ ,  $c2 = 0.0363$ ,  $j$  and  $M$  are lightness and visual chroma calculated by color difference formula of color appearance model respectively [6].

### 3.3 Data Analysis and Comparison

Establish programs of the three conversion algorithms, and then compare the measured value of 60 test patches with output values calculated by programs. The results are shown in Table 2.

According to the experiment, the precision of the tetrahedral interpolation algorithm is higher than the algorithm based on WCS monitors. And compared with the lookup table of RGB to the LUV, lookup table of RGB to XYZ has a higher accuracy.

## 4 Conclusions

By the comparison of RGB to LUV lookup table and RGB to XYZ lookup table with tetrahedral interpolation algorithm with the conversion algorithm used for WCS monitor, RGB to LUV lookup table with interpolation algorithm has higher precision. The results of the experiment have certain accuracy and certain reference value for the study of color space conversion algorithms for monitors in WCS color management system.

**Acknowledgements** This study is funded by key laboratory project of Shaanxi provincial department of education (No.16JS082).

## References

1. Mitchell Rosen, New Windows Color Management System [J], China Academic Journal Electronic Publishing House, 1994–2013.
2. Yanfang Xu, Principles and Applications of Color Management [M], Printing Industry Press, 2011.2, 54–55.
3. Jingya Xu, Haoxue Liu, Min Huang, Discussion on Calculation Methods of Liquid Crystal Display Color [J], China Printing and Packaging Study, 2010(11), 93–97.
4. Microsoft. Windows Color System: The Next Generation Color Management System [EB/OL]. (2005-09-13).<http://www.microsoft.com/whdc/device/display/color/WCS.msp>.
5. Ruijuan Li, Qian Deng, Research on Color Space Conversion from RGB to XYZ Based on Three Dimensional Lookup Table [J], Packaging Engineering, 2012(07), 16–118.
6. Bo Zhao, Research on Color Difference Formula Based on Color Appearance Model [D], Xi'an University of Technology, 2012.

# Presumption Evaluation of Color Reproduction Based on Multi-feature Model in Digital Printing

Yang Zhao, Xiaozhou Li, Xuelin Li, Qian Cao and Jingqiang Jia

**Abstract** Color difference formula is the main objective method to evaluate color reproduction quality in digital printing. It is singular to evaluate the color appearance consistency for color reproduction. A presumption of comprehensive evaluation method was developed. And a combinative feature model of color moments, gray level co-occurrence matrix and color appearance moments is established to evaluate the reproduction quality in digital printing process in order to guarantee the scientificity and comprehensivity of evaluation method. Konica Minolta digital printer was used to output the digital scale and color characteristics were measured by spectrophotometer. Color appearance characteristics were calculated using iCAM. And gray level co-occurrence matrixes of original and reproduction were obtained using gray scale spatial correlation. It showed the feasibility and effectiveness of the model used to evaluate the color reproduction quality. And the influence on prepress was analyzed comparatively which could improve the color reproduction quality.

**Keywords** Print image quality · Gray level co-occurrence matrix · Digital printing

## 1 Introduction

Printing image quality measurement and control plays an important role in the digitalization, standardization and normalization process. Printing image quality evaluation can be classified into three types, objective evaluation, subjective evaluation and comprehensive evaluation [1]. The physical properties of printing image and product are evaluated and described using test chart, scale and spectrophotometer according to printing quality and standardization in the objective evaluation. Printing quality is evaluated based on original according to printing

---

Y. Zhao · X. Li (✉) · X. Li · Q. Cao · J. Jia  
School of Printing and Packing Engineering, Qilu University of Technology,  
Jinan 250353, China  
e-mail: lixiaozhou2000@163.com

quality and standardization for subjective evaluation. For comprehensive evaluation, subjective evaluation and objective evaluation were used together to get the same evaluation standard and to make the method and standard more reasonable, which makes the subjective evaluation better agreement with objective data. Mathematical model for evaluating printing image quality using the parameters was developed to make the evaluation quantitatively in this paper. Mean square error (MSE), peak signal to noise ratio (PSNR) are often used in the evaluation process which are simple and intuitive [2]. However, the two methods produce more deviation to subjective evaluation. The method based structure similarity (SSIM) was performed according to the properties of single-scale or multi-scale SSIM [3]. A hypothesis of color evaluation method of combinative evaluation according to machine vision technique was developed based on the existing methods. The new model was composed of color moments, gray level co-occurrence matrix and color appearance moments.

## 2 Gray Level Co-occurrence Matrix

Gray level co-occurrence matrix is a tabulation of how often different combinations of pixel brightness values or gray levels occur in an image. Gray level co-occurrence matrix is to analyze the statistics of two pixels with value of  $V_i$  and  $V_j$  in specific space distance. Take an image  $I_{N \times N}$  as the example. Set the gray level co-occurrence matrix as  $W$ . The gray value set of pixel  $I_{i(x,y)}$  and  $I_{j(x+a,y+b)}$  is  $(V_i, V_j)$ . Then we can get all of the value sets through moving the pixel in the image. Where,  $x$  and  $y$  are the pixel position in the image. Set the gray level has  $K$  scales. As a result, the number of gray value set is  $K^2$ . Count the number of occurrences of every gray level set and arranged the set in a square formation. Then probability of the gray level set can be performed as  $P(V_i, V_j)$ . The  $W$  is as follows:

$$W = P(V_i, V_j) = \frac{R(V_i, V_j)}{R}, \quad R = \begin{cases} N(N-1), \theta = 0 \text{ or } 90 \\ (N-1)^2, \theta = 45 \text{ or } 135 \end{cases} \quad (1)$$

where,  $\theta = \arctan \frac{b}{a}$ ,  $(a, b)$  is distance difference which can be computed from vertical, horizontal and diagonal direction.

## 3 Characteristics of Gray Level Co-occurrence Matrix

The elements in diagonal direction of gray level co-occurrence matrix would be larger if there were more values of similarity in the image. And the elements which are not in the diagonal direction would be larger if the values change more in the image. Several characteristics including angular second moment (ASM), contrast,



inverse different moment (IDM), entropy and correlation are used to evaluate the gray level co-occurrence matrix [4, 5].

ASM is the sum of squared elements in the matrix which demonstrates uniform distribution of gray level and texture roughness. It can be computed as follows:

$$W_{ASM} = \sum_{i=0}^{K-1} \sum_{j=0}^{K-1} P(V_i, V_j)^2 \quad (2)$$

$W_{ASM}$  would be small if the elements were same in the matrix. It means the texture is fine. However,  $W_{ASM}$  would be large if the elements varied greatly. And the texture is rough.

Contrast returns a measure of the intensity contrast between a pixel and its neighbor over the whole image. It can be calculated as follows:

$$W_{CON} = \sum_{n=0}^{K-1} n^2 \left\{ \sum_{|V_i - V_j| = n} P(V_i, V_j) \right\} \quad (3)$$

Homogeneity returns a value that measures the closeness of the distribution of elements in the matrix to the matrix diagonal and can be calculated as follows:

$$W_{IDM} = \sum_{i=1}^k \sum_{j=1}^k \frac{P(V_i, V_j)}{1 + (V_i - V_j)^2} \quad (4)$$

Entropy returns the information included in the image and is a random metric for the image information.  $W_{ENT}$  is large when the image is random or the noised included in the image is large. It can be calculated as follows:

$$W_{ENT} = - \sum_{i=1}^k \sum_{j=1}^k P(V_i, V_j) \log P(V_i, V_j) \quad (5)$$

Correlation returns a measure of how correlated pixel is to its neighbor over the whole image.  $W_{COR}$  is large when the elements in the matrix are same and  $W_{COR}$  is small when the elements in the matrix vary greatly. It can be calculated as follows:

$$W_{COR} = - \sum_{i=1}^k \sum_{j=1}^k \frac{(V_i V_j) P(V_i, V_j) - U_i U_j}{S_i S_j} \quad (6)$$

where,  $U_i = \sum_{i=1}^k \sum_{j=1}^k V_i \cdot P(V_i, V_j)$ ,  $U_j = \sum_{i=1}^k \sum_{j=1}^k V_j \cdot P(V_i, V_j)$ ,  $S_i^2 = \sum_{i=1}^k \sum_{j=1}^k P(V_i, V_j) (V_i - U_i)^2$ ,  $S_j^2 = \sum_{i=1}^k \sum_{j=1}^k P(V_i, V_j) (V_j - U_j)^2$ .

## 4 Color Moments and Color Appearance Moments

In color moments, there would be three elements including *lightness*, *red-blue chromatic contrast sensitivity function (CSF)* and *yellow-blue chromatic contrast sensitivity function*. And the total color difference formula is often used in color evaluation for printing image. CIE1976L\*a\*b\* is one of the most important spaces for printing image quality evaluation. It can be calculated as follows:

$$\Delta E = \sqrt{\Delta L^2 + \Delta a^2 + \Delta b^2} \quad (7)$$

where,  $\Delta E$  is color difference between original color and destination color.  $\Delta L$  is the lightness difference.  $\Delta a$  is red-green chromatic difference and  $\Delta b$  is yellow-blue chromatic difference.

Color appearance model was used as objective evaluation method in this paper. Furthermore, the viewing conditions were included according to appearance models and iCAM was used as the connection space. Then it was used combined with the two above topics, color moments and gray level co-occurrence matrix, to give the evaluation comprehensively.

## 5 Conclusions

A presumption of comprehensive evaluation method according to machine vision technique was analyzed and developed based on the existing methods. The model would be composed of color moments, gray level co-occurrence matrix and color appearance moments. The characteristics of the gray level co-occurrence matrix were given in the paper and should be adapted in the model. Furthermore, the color moments including lightness and chromatic moments, color appearance moments should also combined together to give more scientific and reasonable objective evaluation. The further research will be performed in the future.

**Acknowledgements** This work was financially supported by Shandong Province Science and Technology Development Project (Grant No. 2012YD07016), Shandong Province Outstanding Young Scientists Research Award Fund (BS2014DX020), Jinan City Colleges and Universities Independent Innovation Project (Grant No. 201311032), and the International Cooperation Program for Key Professors of 2014 by Shandong Provincial Education Department, P.R. China.

## References

1. Xiaohui He (2011). Print quality measurement and control. Chinese Light Industry Press, Beijing.
2. Taiying Zeng, Xue Shao, Zuhui Wang (2016). A method for evaluating the quality of printed image based on feature similarity. Packaging Engineering, 37(11): 153–157.

3. Yubing Tong, Qishan Zhang, Yunping Qi (2006). Image quality assessing by combining PSNR with SSIM. *Journal of Image and Graphics*, 11(12): 1758–1763.
4. Xuebing Bai, Keqi Wang, Hui Wang (2005). Research on the classification of wood texture based on gray level co-occurrence matrix. *Journal of Harbin Institute of Technology*, 37(12): 1667–1670.
5. Baraldia Parmiggian F (1995). An investigation of texture characteristics associated with level co-occurrence matrix statistical parameters, *IEEE Tran. On Geo-science and Remote Sensing*, 33(2): 293–303.

**Part II**  
**Image Processing Technology**

# A New Parallel Hierarchical K-Means Clustering Algorithm for Video Retrieval

Kaiyang Liao, Ziwei Tang, Congjun Cao, Fan Zhao  
and Yuanlin Zheng

**Abstract** The K-means clustering algorithm has been widely adopted to build vocabulary in image retrieval. But, the speed and accuracy of K-means still need to be improved. In the manuscript, we propose a New Parallel Hierarchical K-means Clustering (PHKM) Algorithm for Video Retrieval. The PHKM algorithm improves on the K-means as the following ways. First, the Hellinger kernel is used to replace the Euclidean kernel, which improves the accuracy. Second, the multi-core processors based parallel clustering algorithm is proposed. The experiment results show that the proposed PHKM algorithm is very faster and effective than K-means.

**Keywords** Video retrieval · Clustering algorithm · Data mining · Parallel algorithm

## 1 Introduction

Clustering analysis plays a very important role in exploring the dataset's internal construction, and it has being widely used for video retrieval systems to analysis large datasets. There are many good reviews of the clustering methods that can be found in literatures [1, 2]. Most of clustering algorithms can only work on the middle and small sized database, which requires storing the entire data of the database in the memory. Nevertheless, for many special applications the entire database can not be loaded to memory because of the limitation of the size. Given a very large and high dimension database, how could we cluster the data? For large datasets that even don't fit on one hard disk, parallelism and hierarchy are maybe the good options.

---

K. Liao (✉) · Z. Tang · C. Cao · F. Zhao · Y. Zheng  
Faculty of Printing, Packaging Engineering and Digital Media Technology,  
Xi'an University of Technology, Xi'an, China  
e-mail: liaokaiyang@xaut.edu.cn

Stewénius and Nistér [3] presented a “vocabulary tree” which uses a HKM (Hierarchical K-Means) clustering method. The HKM method is widely used to build vocabulary in image retrieval system. Nevertheless, the speed and accuracy of the clustering algorithm still need to be improved. Parallel programs could efficiently execute clustering algorithms in large scale datasets [4]. Larus and Sutter pointed out that the multi-core computers can take advantage from the concurrent applications, because there are only few communication required between the running cores [5]. However, as far as we know, it is no Hierarchical K-Means clustering method could benefit from the massive cores.

We present a new parallel hierarchical k-means clustering method for video retrieval. In this paper, we make two main contributions. (1) The Hellinger distance is used to improve K-means. (2) A multi-core processors based parallel clustering algorithm is proposed to improve the clustering efficiency.

## 2 Improving K-Means with Hellinger Distance

In HKM algorithm [1], the K-means is used to cluster the data-items into a proper number of subsets. The Euclidean distance was designed to be used in the original K-means algorithm [2], but since image features are multidimensional vectors the question naturally arises as to whether it would also benefit from using other distance measures. We find that using the Hellinger [3] distance does indeed bring a great benefit.

Suppose  $n$  dimension vectors  $x$  and  $y$  are unit Euclidean norm ( $\|x\|_2=1$ ,  $\|y\|_2=1$ ), then their Euclidean distance  $d_E(x, y)$  is related to the kernel  $S_E(x, y)$  between them as

$$d_E(x, y)^2 = \|x - y\|_2^2 = \|x\|_2^2 + \|y\|_2^2 - 2x^T y = 2 - 2S_E(x, y) \quad (1)$$

where

$$S_E(x, y) = x^T y \quad (2)$$

and

$$\|x\|_2^2 = \|y\|_2^2 = 1 \quad (3)$$

In this paper, we want to use the Hellinger kernel to replace with the Euclidean kernel. The Hellinger kernel is also called the Bhattacharyya’s coefficient, for the given two  $L1$  normalized multidimensional vectors  $x$  and  $y$  (i.e.  $\sum_i^n x_i = 1$  and  $x_i \geq 0$ ), the Hellinger kernel is defined as:

$$H(x, y) = \sum_{i=1}^n \sqrt{x_i y_i} \quad (4)$$

Multidimensional vectors can also be compared with the Hellinger kernel, which uses some simple algebraic manipulation in the following two steps: Firstly,  $L1$  normalize the multidimensional vectors; Secondly, square root each element. Then as follows

$$S_E(\sqrt{x}, \sqrt{y}) = \sqrt{x}^T \sqrt{y} = H(x, y) \quad (5)$$

where the resulting vectors are  $L2$  normalized, for the reason

$$S_E(\sqrt{x}, \sqrt{y}) = \sum_i^n x_i = 1 \quad (6)$$

So, a new distance measure is defined, and it is a square root of the  $L1$  normalized distance. The most important is that comparing multidimensional descriptors using the Hellinger kernel is equivalent to using the Euclidean distance to compare the vectors:

$$d_E(\sqrt{x}, \sqrt{y})^2 = 2 - 2H(x, y) \quad (7)$$

K-means can use the new distance measure to cluster the multidimensional descriptors.

### 3 Parallel HKM Clustering Algorithm

**Parallel Data Classification:** The parallel Data Classification method partitions the task through Task spawn module and implements the clustering in each processor. The final merging step is performed serially in Results combining module. Since it only processes the descriptions in one clusters, which just need a tiny amount of processing and data. Figure 1 illustrates the process. The parallel data classification method firstly divides  $k$  group clusters into  $p$  parts, and every part with a equal size  $k/p$  of the original dataset. Secondly, every core process some computation. In the end, all the sub-clusters on different cores have to be got together and made to compute the global clusters.

**Parallel Data Partition:** In parallel version of Hierarchical K-Means, the data partition algorithm is processed in a parallel way on all cores. The parallel data partition divides the subdataset into some parts, and each part with a equal size computation. When the parallel threads need write to a shared buffer, it requires

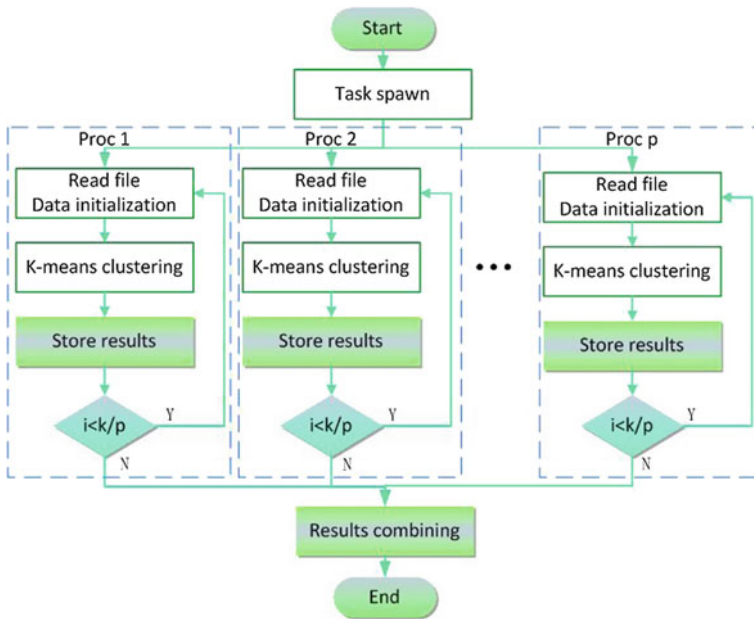


Fig. 1 Scheme of the parallel data clustering

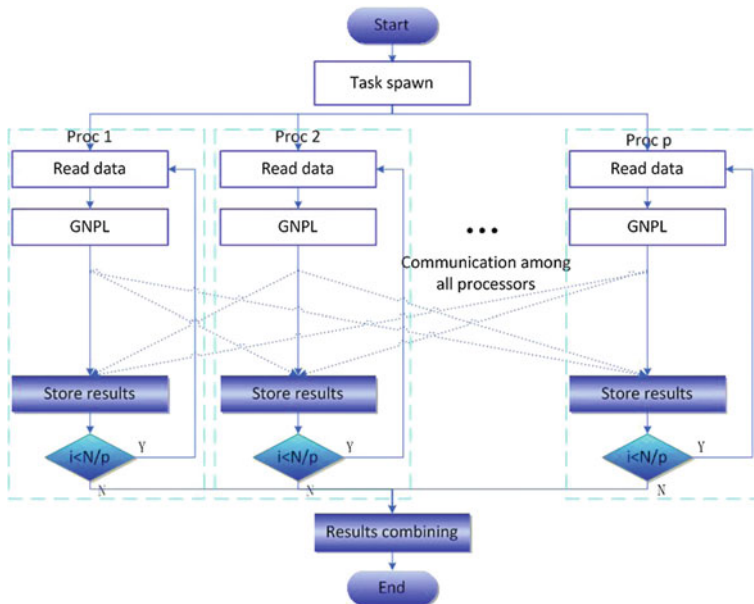


Fig. 2 Scheme of the parallel data partition



some communication between the cores, so it is necessary for the process to be mutually exclusive. Figure 2 shows the procedure for parallel data partition.

### 4 Experimental Setup and Results

The program of PHKM is implemented in C program. We runs all the programs on a Dell server with 16 CPUs of Intel Xeon E5-2600v3 Processor 2.4 GHz and 64G of RAM.

In order to evaluate the program of PHKM in the large databases, two databases of features with 128 dimensions are used in experiments, which the sizes of the features sets are about 268M and 58M with the databases tv.2010 and tv.2009 in TRECVID respectively. Table 1 shows the features sizes of the databases. To compare the quality of clusters, there are three clustering evaluation metrics Entropy [4], Purity [5] and FScore measure [6] are used in the paper.

**Quality of results:** Here, the following four clustering methods: IDHC [4], hierarchical K-means (HKM) [1], parallel version of HKM (PHKM) and SHAKM [7] are compared on the tv.2009 and tv.2010 datasets respectively. The results are showed in Tables 2 and 3. A lower entropy values means a better clustering result, while a higher values of the FScore and Purity means a better result.

From the figures in Table 2 it shows that the performances of IDHC and SHAKM are better than HKM. We can see that the PHKM is superior to those of the other methods too. The reason is that the clusters quality is improved by using the Hellinger kernel. The clustering time of the four approaches have also compared

**Table 1** The features sizes of the databases

Dataset	# Keyframes	# Features	Size
tv.2009	145,530	58,212,342	18.8G
tv.2010	672,114	268,845,792	89.4G

**Table 2** The result of the clustering quality on different datasets

	tv.2009		
	FScore	Purity	Entropy
IDHC	0.6793	0.6016	0.2321
SHAKM	0.6842	0.6227	0.2304
HKM	0.6247	0.5483	0.2826
PHKM	0.7691	0.6923	0.2252
	tv.2010		
	FScore	Purity	Entropy
IDHC	0.6687	0.5935	0.2569
SHAKM	0.6786	0.6077	0.2508
HKM	0.6136	0.5365	0.3044
PHKM	0.7518	0.6829	0.2431

**Table 3** The result of the time performance on different datasets

Database (# descriptors)	Clustering time (h)			
	IDHC	SHAKM	HKM	PHKM
tv.2009 (64M)	191.5	173.4	127.2	11.3
tv.2010 (256M)	312.6	282.5	210.8	20.4

**Table 4** PHKM's processing time with different core numbers

# Processors	Processing time (h)	
	tv.2009	tv.2010
1	162	428
4	41	107
8	21	54
32	8.4	21.4

shown in Table 3. From the figures in the table, it can be observed that the result of PHKM is better than HKM in clustering time.

**Speed-up results:** How does our method speed-up? This is an important question, and this section intends to answer it. For a fixed problem with size  $n$ , when we increase the number of processors, the running time will be significantly reduced. Now, the running time is compared to address the parallel computation cost. Though Table 4, we can see that the computing time decreased linearly when the cores number increasing.

From Tables 2 and 3, it can be observed that the result of PHKM is better than IDHC, SHAKM and HKM in all metrics. HKM and PHKM have employed the same tree structure, but the PHKM is still better than HKM in all results. This is owing to PHKM adopted the Hellinger kernel. And PHKM is faster than IDHC, SHAKM and HKM, which is owing to PHKM adopted multi-core parallel method.

The ratio of acceleration is often used to evaluate the performance of parallel computing. It can be defined as follows:

$$S_p = T_s/T_p \quad (8)$$

where  $p$  is the processors number,  $T_p$  is the time required for parallel program with  $p$  cores,  $T_s$  is the time required for one processor program. Figure 3 presents the relationship of the processors number and the acceleration ratio on the tv.2010 dataset.

**Scale-up results:** How does the proposed method scale-up? This section wants to answer this question. Scale-up is used to capture how well the multi-core parallel method deals with large datasets when more cores are available. The ratio of acceleration with different data sizes are in Fig. 4. The running time shown is the average time of 5 distinct runs. As shown in Fig. 4, the proposed method has desired scaling-up, and scalability linearly with the dataset size.

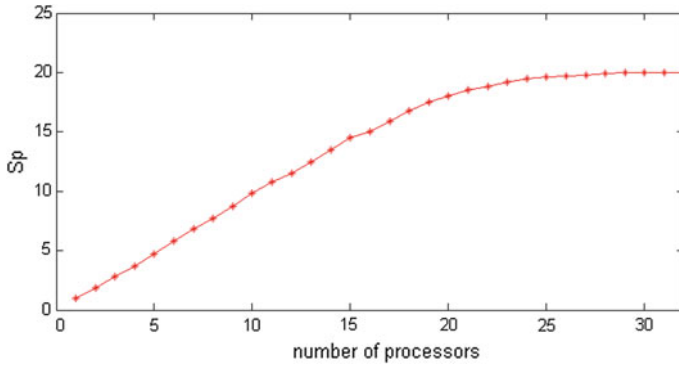
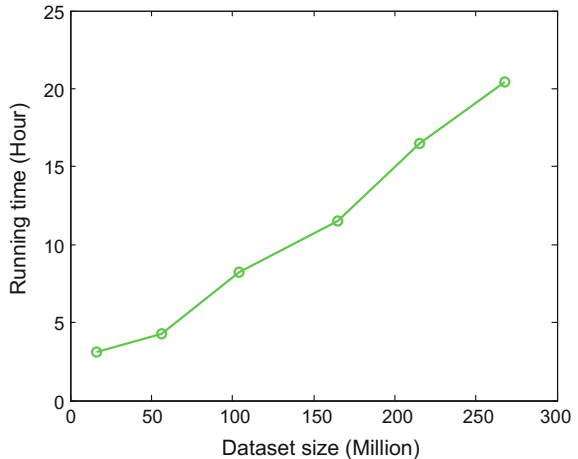


Fig. 3 Relationship of processors number and acceleration ratio on the tv.2010 datasets

Fig. 4 Running time versus dataset size, linear scale-up on database size



## 5 Conclusions

In this paper, we proposed a new PHKM clustering method, which uses Hellinger kernel to compute distance that improve the clustering results. The PHKM employs a parallel strategy to handle large databases. The major contribution of the proposed PHKM algorithm are: (1) the Euclidean kernel is used to replace the Hellinger kernel, which improves the accuracy; (2) the multi-core processors based parallel clustering algorithm is proposed. We conducted extensive experiments on large video tv.2009 and tv.2010 datasets. The experiment results show that the proposed PHKM algorithm is very efficient and effective.

**Acknowledgements** This work is supported by the National Natural Science Foundation of China Project No. 61671376, 11272253 and Natural Science Foundation of Shaanxi Province No. 2016JM6022.

## References

1. Nister, D. and H. Stewenius. Scalable recognition with a vocabulary tree. in IEEE Computer Society Conference on Computer Vision and Pattern Recognition 2006. IEEE.
2. MacQueen, J. Some methods for classification and analysis of multivariate observations. in 5th Berkeley Symp. 1967. California, USA.
3. Arandjelovic, R. and A. Zisserman. Three things everyone should know to improve object retrieval. in Computer Vision and Pattern Recognition (CVPR), 2012 IEEE Conference on. 2012. IEEE.
4. Malik, H.H., et al., Hierarchical document clustering using local patterns. *Data Mining and Knowledge Discovery*, 2010. 21(1): p. 153–185.
5. Hu, X., et al. Exploiting Wikipedia as external knowledge for document clustering. in Proceedings of the 15th ACM SIGKDD international conference on Knowledge discovery and data mining. 2009. ACM.
6. Zhao, Y. and G. Karypis, Hierarchical clustering algorithms for document datasets. *Data Mining and Knowledge Discovery*, 2005. 10(2): p. 141–168.
7. Liao, K., et al., A sample-based hierarchical adaptive K-means clustering method for large-scale video retrieval. *Knowledge-Based Systems*, 2013.

# Comprehensive Imaging Quality Assessment Method for Laser Printer Based on SVM

Yaohua Yi, Luolan Zhou, Yuan Yuan and Rui Li

**Abstract** Researches on the laser printer imaging quality assessment mainly focus on the independent quality assessment of the lines, dots, characters, images, etc. In this paper, a comprehensive method of imaging quality assessment for laser printers is presented based on support vector machine (SVM). Firstly, test samples are designed. The images of line and character, area and dot acquired from the laser printer are taken as samples. Then, different quality indexes are adopted to evaluate the different aspects of laser printer imaging quality, and the index values of those samples are calculated. The quality indexes are selected according to international standard ISO 13660, including line width error, roughness, ambiguity, darkness of the line and character, gray standard deviation, graininess, mottle of the field area and roundness error of the dot. Finally, the samples are evaluated by subjective assessment method of grade classification, and then the relation model between quality indexes and subjective assessment results are established using SVM. It is proved by experiments that the developed relation model is effective and feasible to predict comprehensive imaging quality results for laser printers, which has good consistency with human vision perception.

**Keywords** Laser printer imaging · Quality index · SVM · Comprehensive assessment

## 1 Introduction

With the rapid development of economy and information technology, the printers have broken the traditional commercial application, began to enter the family. As a high and new technology product, the laser printers has the advantages of high speed, low noise, high quality and high cost performance, which is favored by

---

Y. Yi (✉) · L. Zhou · Y. Yuan · R. Li  
School of Printing and Packaging, Wuhan University, Hubei, China  
e-mail: yyh@whu.edu.cn

users, and has an important position in the printer market [1]. The imaging quality of laser printers has become a matter of growing concern.

The imaging quality of laser printers is mainly reflected by the quality of printed images. In the image outputting process of printers, there are many kinds of distortions in the images, and their quality cannot be evaluated by the single index. More and more researchers commit to using the method of multi-index and multi-feature extraction to evaluate the image quality. By extracting a number of indicators of the images, training and classifying the images based on machine learning methods, we output the objective assessment results for the images. The most commonly-used machine learning methods are neural network and support vector machine [2], in which the SVM has better classification results in the situations of less samples and linearly inseparable data. In this paper, a comprehensive imaging quality evaluation method for laser printer based on SVM is presented. Through extracting three kinds of objective evaluation indexes of the printed images, training and learning by SVM method, we set up the comprehensive assessment model to evaluate the imaging quality of laser printers.

## 2 Imaging Quality Evaluation Index of Laser Printer

There is still a certain gap between laser printers and traditional printing modes, which will have a certain influence in the sharpness of lines and characters in the outputted images. In addition, certain randomness existing in the imaging process of toner transfer can also lead to the inhomogeneity of the field area and dot [3]. Therefore, the images of line and character, field area and dot acquired from the laser printers are taken as test samples in this paper.

### 2.1 Selection of Imaging Quality Evaluation Index

#### 2.1.1 Line and Character Index

Lines and characters are common contents in applications of the printers. Since characters can be seen as a combination of different lines, the quality evaluation of the lines can also be used to measure the quality of the characters. Reference to the international standard ISO13660 [4, 5], we select the line width error, darkness, roughness and ambiguity to measure the quality of both lines and characters.

Linewidth is the average width of lines or characters. Darkness represents blackness of the inside of lines and characters. The ambiguity is the average distance between the outer boundary and the inner boundary, while roughness is used to describe the degree of deviation from the ideal edge to the actual edge.

In the ISO13660 standard [6, 7], the reflection coefficient of the substrate is defined as  $R_{max}$ , while the reflectivity of the character and line area is defined as  $R_{min}$ . The formulas for the boundary points are as follows:

$$\text{The line edge : } R_{60} = R_{max} - 0.6 \times (R_{max} - R_{min}) \quad (2.1)$$

$$\text{The dark edge: } R_{75} = R_{max} - 0.75 \times (R_{max} - R_{min}) \quad (2.2)$$

$$\text{The inner edge: } R_{90} = R_{max} - 0.9 \times (R_{max} - R_{min}) \quad (2.3)$$

$$\text{The outer edge: } R_{10} = R_{max} - 0.1 \times (R_{max} - R_{min}) \quad (2.4)$$

### 2.1.2 Field Area Index

When grains, mottles and other defects are present in the field area, the ink in the region reflects uneven. Human vision is very sensitive to the uniformity of the field area, and the perception of the field area is considered to be a serious defect in the quality of the printed matter. We select the gray standard deviation, graininess and mottle to evaluate the field area according to ISO 13660.

The calculation of Gray standard deviation needs to get the average gray value of all the pixels, and the formula is as follows:

$$StdDev = \sqrt{\frac{1}{N-1} \sum_{i=1}^N (\sigma_i - \bar{\sigma}_i)^2} \quad (2.5)$$

The calculation models of graininess and mottle need to divide the field area into at least non-overlapping 100 squares of the same size, and then a density measurement operation with uniform and non-overlapping intervals is performed. The calculation formulas for the graininess and mottle are:

$$Graininess = \sqrt{\sum_{i=1}^n \frac{\sigma_i^2}{n}} \quad (2.6)$$

$$Mottle = \sqrt{\frac{1}{n-1} \sum_{i=1}^n \left[ m_i - \left( \frac{1}{n} \sum_{i=1}^n m_i \right) \right]^2} \quad (2.7)$$

### 2.1.3 Dot Index

Laser printer dots consist of the charging toner particles adsorbed to the discharge region on the surface of photoconductive material composition. Their ideal shape is

very important to keep the uniformity and definition of the image. Roundness error of the dots can effectively reflect the distribution of the direction of the dots.

The edge of the dot is determined by the edge of the  $R_{60}$ . We use the least square method to fit all the edge points obtained least square circle, calculate the maximum distance and minimum distance to the least square circle, and then denote as roundness error.

### 3 Comprehensive Evaluation Model Based on SVM

SVM provides 4 commonly-used kernel functions, the choice of kernel function and its parameters can affect the performance of quality evaluation model [8]. In this paper, we use the LibSVM [9] toolbox of Lin Chih-Jen to train and study. The comprehensive evaluation method based on SVM is shown in Fig. 1.

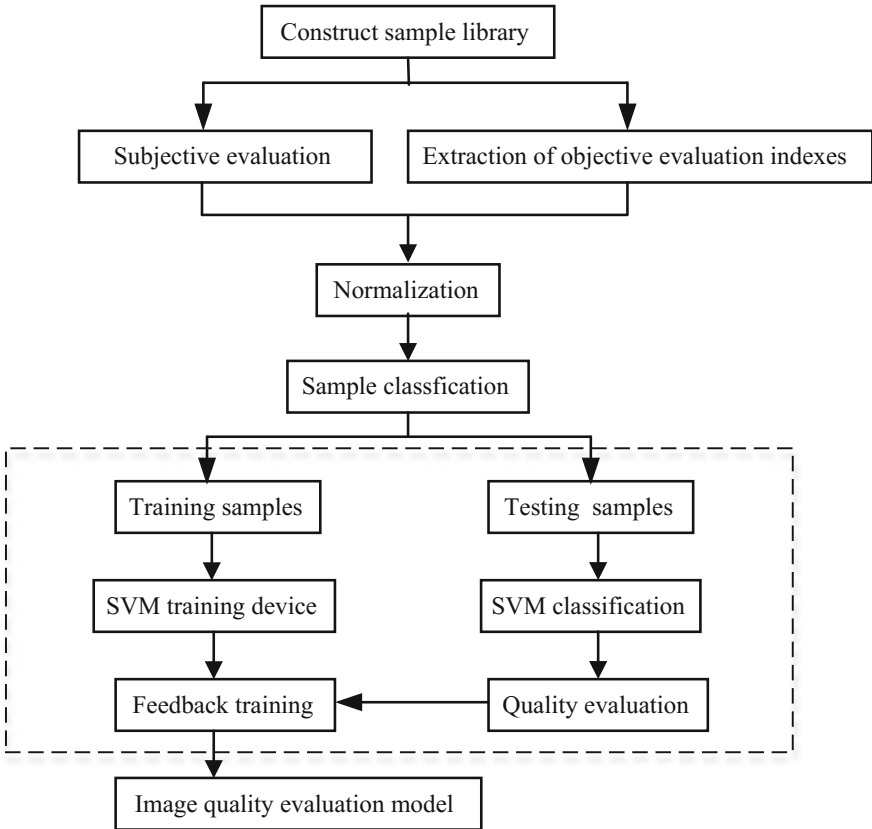


Fig. 1 Workflow of the evaluate method based on SVM



## 4 Experiment and Analysis

### 4.1 Preparation of the Test Sample

This paper chose the ordinary printing paper and coated paper as substrates, the test samples are outputted in four sets of laser printers. The printers include Canon MF4010B, FUJI Xerox CM2156, PANTUM P3205DN and PANTUM P2000. Test samples are designed with a resolution of 600 dpi, shown in Fig. 2.

Seven different qualities of samples are selected as a representative to have objective indexes calculation and subjective test. In the experiment, 7 lines, 3 field areas and 5 dots are selected in each print sample to calculate the indexes. The line widths include 1 mm, 3pt, 5pt, 7pt, 9pt, 13pt and 17pt [10], and the dot size is 24pt. For each sample, we calculate the average value of the indexes of the field area and the dot, and then combine with the test data of 7 lines to form 7 sets of data.

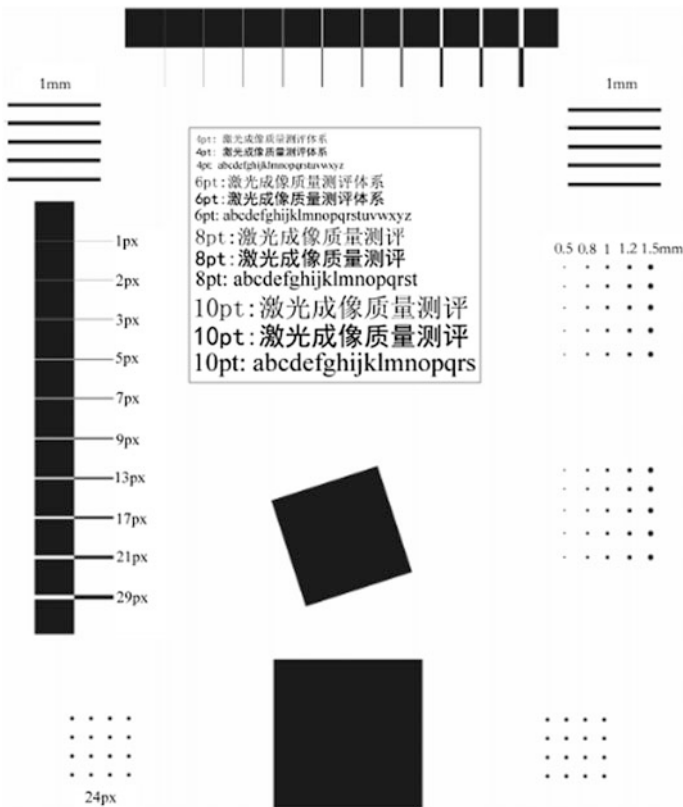


Fig. 2 Test sample

## 4.2 Subjective Evaluation of Test Samples

This study adopts five grade scores of quality and obstruction scale to evaluate samples subjectively, which is provided by the International Radio Consultative Committee (CCIR) [11]. The scoring method is shown in Table 1.

Twelve observers were selected to evaluate each line, including graphics professionals and non-professionals. Professionals use the scale of obstruction, while non-professionals select the quality scale. The test environment is under the  $D_{65}$  light source, and the illumination is 1500lux or so.

The subjective evaluation result is used to train the SVM. To satisfy the requirements of SVM, we regarded the sample with average score  $>3$  as the quality standard sample and made its label as 1; while the sample with average score  $<3$  are treated as unqualified and labeled as  $-1$ .

## 4.3 SVM Classification

Test 1: Four groups of data are selected in each samples to form 28 sets of data as the training samples, the remaining 21 sets of data are the test samples.

It was found that the parameter optimization results of RBF kernel function is slightly worse than the previous, so this model chooses the default parameters [12]. The classification results of 4 kernel functions are shown in Table 2.

Test 2: Four samples are select to form 28 sets of data as the training samples, the remaining 21 sets of data are the test samples.

It was found that the parameter optimization results of RBF kernel function is slightly better than that of the previous, so this model chooses the optimized

**Table 1** The scoring method

Grade	Obstruction scale	Quality scale
5	No changes in sample quality	Very good
4	Slight changes but without obstruction	Good
3	Little effects for viewing	General
2	Apparent deterioration for viewing	Bad
1	Very serious d for viewing	Very bad

**Table 2** Result of kernel function of test 1

Kernel functions	Correct samples	Error samples	Correct rate (%)
Linear	17	4	80.95
Polynomial	16	5	76.19
RBF	18	3	<b>85.71</b>
Sigmoid	17	4	80.95

**Table 3** Result of kernel function of test 2

Kernel functions	Correct samples	Error samples	Correct rate (%)
Linear	16	5	<b>76.19</b>
Polynomial	15	6	71.43
RBF	16	5	<b>76.19</b>
Sigmoid	16	5	<b>76.19</b>

parameters, while  $c$  takes 8, and  $\sigma$  takes 0.0078125. The classification results of 4 kinds of kernel functions are shown in Table 3.

#### 4.4 Experimental Result Analysis

As seen in Tables 2 and 3, in the case of relatively small number of samples, the use of RBF kernel function classification effect is generally better.

This experiment is validated from two aspects. (1) For multiple laser printers, whether the quality of the print output images obtained by different test lines is consistent with the human visual perception; (2) For laser printer or printer as to be evaluated which is not within the range of training samples, judge whether the print quality of the output image is consistent with human subjective evaluation results.

Experimental results show that the classification accuracy of the evaluation model is 85.71 and 76.19%, which can demonstrate the above two aspects in a certain extent and indicate the rationality of objective evaluation indexes selected in this paper.

## 5 Conclusions

In this paper, the comprehensive evaluation method based on SVM is proposed based on the analysis of the 3 imaging quality evaluation indexes of the laser printer. The prediction results show that the model can achieve a certain prediction accuracy and evaluate the imaging quality of the laser printer comprehensively.

## References

1. Sun Wenhui. Working principle and design of Hummingbird series laser printer [D]. Shandong University, 2005.
2. Zhu Jiajia. Research and implementation of image quality evaluation method based on HVS and SVM [D]. Nanjing University of Posts and Telecommunications, 2012.
3. Kong Lingjun, Liu Zhen, Jiang Kang. Digital printing quality detection and analysis technology based on CCD packaging engineering [J], 2010 (3): 92–95.

4. ISO/TEC13660, 2001 Information Technology-office Equipment-measurement of Image Quality Attributes for Hardcopy Output-binary Monochrome Text and Graphic Images [S].
5. Buczynski Ludwik, Bieniewski Adam. Analyze of image quality parameters on laser printouts as proposal to extension standard ISO 13660[C]. NIP & Digital Fabrication Conference. Society for Imaging Science and Technology, 2004: 98–101.
6. Briggs John C, Klein Alice H, Tse Ming-Kai. Applications of ISO-13660, a new international standard for objective print quality evaluation[J]. Japan Hardcopy, 2006, 99: 21–23.
7. Briggs John C, Forrest David J, Klein Alice H. Living with ISO-13660: Pleasures and perils [C]. NIP & Digital Fabrication Conference. Society for Imaging Science and Technology, 1999: 421–425.
8. Chi-Jen Lin. LibSVM: A library for support vector machines. 2010.3. <http://www.sie.ntu.edu.tw/~cjlin/>.
9. Wang Wenjian. Modeling and application of support vector machine [M]. Science Press, 2014.
10. Kong Lingjun, Liu Zhen, Sun Xiaopeng, et al. Evaluation of the perceptual quality of printed lines based on fuzzy neural network [J]. Journal of instrumental and instrument, 2013, 34 (12): 2675–2683.
11. Qian Xiaojun. Algorithm research and engineering application of image quality evaluation [D]. Xi'an Electronic and Science University, 2009.
12. Ding Wenrui, Wang Lei, Jin Wu, et al. Image quality evaluation method based on SVM and GA [J]. Computer Engineering, 2011, 37 (10): 195–197.

# An Efficient Approach of Color Image Matching by Combining Color Invariant and ORB Feature

Shenghui Li, Ruizhi Shi and Hui Ye

**Abstract** Through combine traditional prints with portable electronic devices by image matching algorithms, the traditional printing information can be expressed in a diverse way. During the process of image matching, color is an important component for distinction between images. Nevertheless, most of the existing approaches only use gray geometric-based feature extractors to realize image matching, such as ORB, SIFT, SURF, etc. For these approaches, neglecting color information may lead to poor illumination robustness and mismatching. In this paper, we present a new approach based on color invariant and ORB feature, called C-ORB. By combining color invariant and ORB feature, C-ORB could be more accurate, at the same time; C-ORB also retains the ORB's efficiency and performance. To validate C-ORB, we perform experiments that test the properties of C-ORB relative to ORB. Experimental results show that C-ORB is more accurate and stable with respect to variations in the photometrical imaging conditions. Therefore, the research of this paper can improve the accuracy and reduce the error during the process of image matching in mobile electronic equipment.

**Keywords** C-ORB · Color invariant · Image matching · ORB · Luminance

## 1 Introduction

By combining with mobile electronic equipment, the printed information, which printed on the traditional printed materials, can be presented in a more abundant and diversified mechanism. In order to combine traditional print and mobile electronic equipment, the relationship between the mobile phone equipment and the printing image should be established firstly. The relationship can be established in many

---

S. Li (✉) · R. Shi (✉) · H. Ye  
Zhengzhou Institute of Surveying and Mapping, Zhengzhou, China  
e-mail: lishenghui2006@126.com

R. Shi  
e-mail: ruizhishi@sina.com

ways, such as two-dimensional code identification, bar code identification or image matching. But compared with image matching, two-dimensional code and bar code identification technology need print special marks on the prints, which will impact the overall effect of prints. Therefore, the image matching technology is a better choice in some cases.

During the process of image matching, color is an important component for distinction between images. Although color image is more robust than the gray scale image with respect to color and photometrical variations, however, most of the existing approaches discard the color information and only use gray geometric-based feature extractors for image matching, which may increase the false matching rate during the process of image matching [1].

Compared with personal computer, the configuration of mobile electronic equipment is lower. Thus, the algorithm's complexity and efficiency should be taken into account. In this paper, we present an approach by combining color invariant and ORB (Oriented FAST and Rotated BRIEF) feature, called Colored ORB (C-ORB). Color invariant can preserve the color information from the image. Because of its better performance and efficiency, ORB is capable of being used for real-time performance in the mobile electronic equipment. Hence, by combining color invariant and ORB feature, C-ORB not only preserves the color information in the descriptors, but also retains the ORB's efficiency and performance. Figure 1 illustrates the process of image matching based on C-ORB.

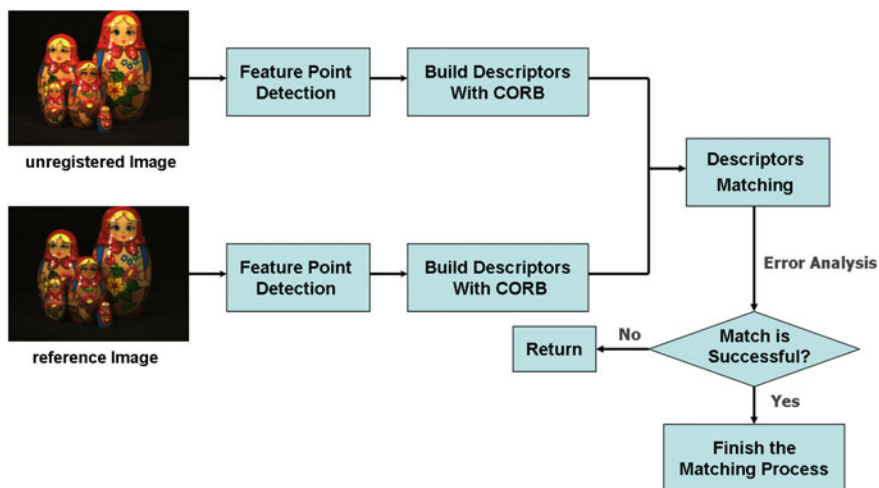


Fig. 1 Process of image matching based on C-ORB

## 2 C-ORB

### 2.1 Color Invariance Model

We use the color invariance model, which was developed by Geusebroek et al. [2] to build our C-ORB descriptors in this paper. The color invariants model depends on the Kubelka-Munk theory which models the reflected spectrum of colored bodies [3]. The Kubelka-Munk theory models the photometric reflectance by Eq. (2.1).

$$E(\lambda, \vec{x}) = e(\lambda, \vec{x})(1 - \rho_f(\vec{x}))^2 R_\infty(\lambda, \vec{x}) + e(\lambda, \vec{x})\rho_f(\vec{x}) \quad (2.1)$$

where  $\lambda$  is the wavelength,  $\vec{x}$  is a 2D vector which denotes the image position.  $e(\lambda, \vec{x})$  denotes the illumination spectrum and  $\rho_f(\vec{x})$  is the Fresnel reflectance at  $\vec{x}$ .  $R_\infty(\lambda, \vec{x})$  denotes the material reflectivity and  $E(\lambda, \vec{x})$  represents the reflected spectrum in the viewing direction.

For most of the practical cases, the spectral components of the source are variable over the position and constant over the wave length. Then,  $e(\lambda, \vec{x})$  can be denoted as  $i(\vec{x})$ .

$$E(\lambda, \vec{x}) = i(\vec{x}) \left[ \rho_f(\vec{x}) + (1 - \rho_f(\vec{x}))^2 R_\infty(\lambda, \vec{x}) \right] \quad (2.2)$$

By differentiating Eq. (2.2) with respect to  $\lambda$ , we can get Eqs. (2.3) and (2.4).

$$E_\lambda = i(\vec{x})(1 - \rho_f(\vec{x}))^2 \frac{\partial R_\infty(\lambda, \vec{x})}{\partial \lambda} \quad (2.3)$$

And

$$E_{\lambda\lambda} = i(\vec{x})(1 - \rho_f(\vec{x}))^2 \frac{\partial^2 R_\infty(\lambda, \vec{x})}{\partial \lambda^2} \quad (2.4)$$

By dividing Eq. (2.3) by Eq. (2.4), we can get Eq. (2.5).

$$H = \left( \frac{E_\lambda}{E_{\lambda\lambda}} \right) = \frac{\partial R_\infty(\lambda, \vec{x})}{\partial \lambda} / \frac{\partial^2 R_\infty(\lambda, \vec{x})}{\partial \lambda^2} = f(R_\infty(\lambda, \vec{x})) \quad (2.5)$$

H is the color invariant which is independent of Fresnel reflectance coefficient, viewpoint, illumination intensity, direction, and surface orientation. Under the standard condition of the human visual system and CIE-1964-XYZ, the relationship between RGB component and  $(E, E_\lambda, E_{\lambda\lambda})$  can be expressed as Eq. (2.6).

$$\begin{pmatrix} E \\ E_\lambda \\ E_{\lambda\lambda} \end{pmatrix} = \begin{pmatrix} 0.06 & 0.63 & 0.27 \\ 0.3 & 0.04 & -0.35 \\ 0.34 & -0.6 & 0.17 \end{pmatrix} \begin{pmatrix} R \\ G \\ B \end{pmatrix} \quad (2.6)$$

Thus, with Eqs. (2.5) and (2.6), we can get the color invariant of color image.

## 2.2 ORB Geometrical Invariance

Geometrical invariance means the extracted feature are invariant to rotation, scaling, or affine transformations. Therefore, for an image, a feature  $F(\vec{x})$  at a location  $\vec{x} = (x, y)$  should satisfy the Eq. (2.7).

$$F(\vec{x}) = F(T\vec{x}) \quad (2.7)$$

where,  $T$  denotes a transformation which includes rotation, scaling or affine transformations.

For geometrical invariance, ORB (Oriented FAST and Rotated BRIEF) features builds on the FAST key point detector and BRIEF descriptor. FAST is widely used because of its efficiency. However, FAST do not have an orientation component. To solve this problem, ORB uses a simple but effective measure of corner orientation, the intensity centroid. Hence, ORB has an orientation component and can be invariance to rotation. FAST does not produce multi-scale feature, Ethan Rublee et al. employed a scale pyramid of the image, and produce FAST features at each level in the pyramid [4].

## 3 Feature Point Detection and Matching

The image matching involves three main stages [5]:

1. Feature point detection. Select the highly informative points as feature point.
2. Descriptor building. For each of feature points, a feature descriptor is built to describe the local region around the feature point.
3. Descriptor matching. With the given threshold, match the descriptors to decide if this point belongs to the image of feature or not.

### 3.1 Feature Point Detection

Each of feature points should include highly feature information, and it also needs the extracted feature are invariant to rotation, scaling and luminance. For



unregistered image  $I1(x, y)$  and reference image  $I2(x,y)$ , the color invariants  $H1(x, y)$  and  $H2(x, y)$  can be obtained by Eqs. (2.5) and (2.6). Then,  $I1(x, y)$  and  $I2(x, y)$  are replaced by  $H1(x, y)$  and  $H2(x, y)$  for feature point detection. The feature point detection of CORB involves three main steps:

1. Get the location of each key point by FAST.
2. On the basis of detecting result of FAST, pick the top N points as feature points according to the Harris measure.
3. For each of feature points, use the intensity centroid to get the orientation information.

### 3.2 Descriptor Building

After getting the image feature points, we need build descriptors to characterize them. ORB combines the orientation information, which can get by the method described above, and BRIEF to describe these feature points. In order to solve the problem of sensitive to noise, for each of the feature points, ORB use  $5 * 5$  sub-windows of a  $31 * 31$  pixel patch to calculate. Because of more pixels are taken into account, the problem of noise sensitive can be solved. Then ORB use greedy search to find 256 points, which are little correlated, from all the possible results to get the final feature points.

The approach of C-ORB descriptors building is same as ORB, except for the difference that instead of using  $I1(x, y)$  and  $I2(x, y)$  in building the descriptors, we use the  $H1(x, y)$  and  $H2(x, y)$  color invariants, which are represented in the previous section.

### 3.3 Descriptor Matching

After building the feature descriptors, we can characterize the reference image and unregistered image by the feature descriptor database, D1 and D2. As Eq. (3.1), the matching process is performed by finding the nearest neighbor of each feature key from D2 in D1, then reject outliers. If the number of matching feature points is more than a certain amount, it can be regarded as the process of image matching is completed.

$$\Delta d = \sqrt{(x_1 - x'_1)^2 + (x_2 - x'_2)^2 + \dots + (x_{256} - x'_{256})^2} \quad (3.1)$$

### 4 Experimental Evaluations

Since the geometrical-feature structure of C-ORB and ORB are very close to each other, we focus on the comparison results between them with respect to photometric variations, including the comparison of the number of feature points and the mismatch ratio. In order to simulate the photometric variations in the nature, all the images used in the experiment come from ALOI (Amsterdam Library of Object Images) [6]. There are a lot of RGB images under different illumination conditions in ALOI, as shown in Fig. 2. The computer used in the experiment is 2.00 GHz Pentium Dual-Core CPU T4200 running Windows 7 Professional, Microsoft Visual Studio 2010 and OpenCV 2.4.10 are used to test the algorithm’s performance.

Figures 3 and 4 show the detected features result using the C-ORB which presented in this paper and ORB respectively. It is clear that the number of detected features using C-ORB is much larger than those using ORB. In other words, C-ORB, which is combined with color invariants, can extract more information from the image. It is known that as the number of detected features increases, the performance of the matching process is enhanced. Table 1 shows the contrast of features point number which extracted by C-ORB and ORB.

To further evaluate the proposed approach, the matching speed and mismatch ratio also need to be compared. Figure 5a shows the contrast of calculating time



Fig. 2 Sample image from ALOI

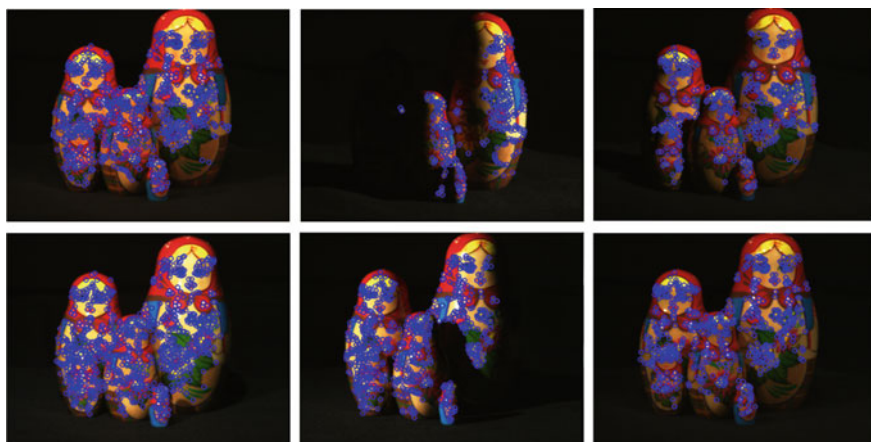


Fig. 3 Detected features based on C-ORB

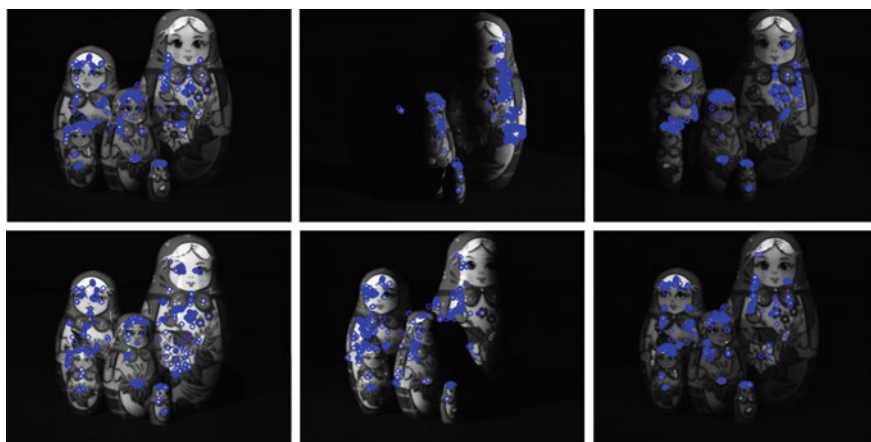


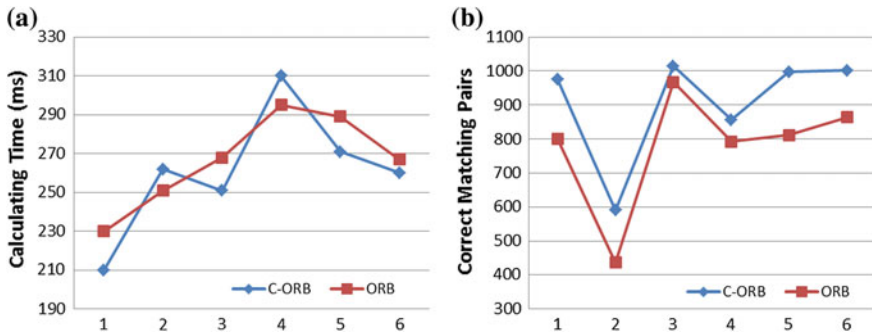
Fig. 4 Detected features based on ORB

Table 1 Contrast of features point number

	1	2	3	4	5	6
C-ORB	716	214	451	637	420	411
ORB	320	176	313	318	307	209

under different illumination direction and intensities, and Fig. 5b shows the contrast of correct matching pairs.

Although the number of feature points depends on the thresholding constraints of Hamming distance, but with the same threshold, C-ORB can get more feature points, and have more matching points. This means that compared with ORB,



**Fig. 5** **a** Illustrate the contrast of calculating time. **b** Illustrate the contrast of correct matching pairs

C-ORB, which is combined with color invariants, can get more image details, and the matching process have proven to be more accurate.

## 5 Conclusions

The SIFT algorithm have proven to be remarkably successful in image matching. However, it imposes a large of computational burden, especially for low-power devices such as cell phones. ORB is a computationally-efficient replacement to SIFT that has similar matching performance, and is capable of being used in the mobile electronic equipment [7]. Nevertheless, most of the existing approaches, including ORB, neglect color information, only use gray geometric-based feature extractors to realize image matching. For these approaches, neglecting color information may lead to mismatching.

We present an approach by combining color invariant and ORB feature in this paper, called Colored ORB (C-ORB). The proposed approach is more robust than conventional ORB with respect to photometrical and color variations. The experimental results also support the potential of C-ORB. However, one of the issues that have not been adequately addressed is that we only extract color information from RGB color mode. And how to enhance the image matching performance for low-power devices by extracting color information from other color mode is still need further experimental analysis and research.

## References

1. Li, D., Shi, R., Li, S., & Zhou, X. (2016). An Improved SIFT Algorithm Based on Invariant Gradient. *Advanced Graphic Communications, Packaging Technology and Materials*. doi:10.1007/978-981-10-0072-0\_29. 369:221–230.
2. J. M. Geusebroek, R. van den Boomgaard, A. W. M. Smeulders. (2001). Color invariance. *IEEE Transactions on Pattern Analysis and Machine Intelligence*. 23 (12):1338–1350.

3. Alaa E. Abdel-Hakim, Aly A. Farag. (2006). CSIFT: A SIFT descriptor with color invariant characteristics[C]. IEEE Computer Society Conference on Computer Vision and Pattern Recognition. 2: 1978–1983.
4. Ethan Rublee, Vincent Rabaud, Kurt Konolige, Gary Bradski. (2011). ORB: an efficient alternative to SIFT or SURF [J]. Computer Vision. Nov.:2564–2571.
5. Li, S., & Shi, R. (2016). The Comparison of Two Image Matching Algorithms Based on Real-Time Image Acquisition. Advanced Graphic Communications, Packaging Technology and Materials. doi:[10.1007/978-981-10-0072-0\\_31](https://doi.org/10.1007/978-981-10-0072-0_31). 369:241–248.
6. J.M. Geusebroek, G.J. Burghouts, A. W. M. Smeulders. (2005). The Amsterdam library of object images. International Journal of Computer Vision. 61(1):103–112.
7. Zhang Ruijuan, Zhang Jianqi, et al. (2008). Study on Color Image Registration Technique Based on CSIFT[J]. ACTA OPTICA SINICA. November, 28(11):2097–2103.

# Color Printing Image Quality Evaluation Method Based on Full Quaternion Matrix

Yunfei Zhong, Ruoqing Wang, Lujing Fu, Yaojian Hu and Lu Chen

**Abstract** This paper proposed a color printing image quality evaluation method on the basis of the full quaternion matrix. First of all, according to the properties of the quaternion matrix and the characteristics of the color image, color image luminance component of local variance are used as a real part of quaternion and built color printing images of the quaternion representation model. Then to singular value decomposition of quaternion, calculate the quaternion matrix corresponding to the block of singular value feature vector, take the maximum value as the main parameter of measuring structural similarity images. Color printing image quality evaluation is realized by comparing a maximum of two images' singular value feature vector. The experimental results show that the full quaternion method is used to express the structure of the color image information which highlight the human eye visual structure of sensitive information in the image quality assessment as well as realizes the RGB color image information in three-channel parallel processing, enhances and improves the efficiency and accuracy of color printing image quality assessment. At the same time the evaluation results conform to the human eye subjective visual perception.

**Keywords** Full quaternion · Image structure information · Local variance · Printing image quality evaluation

## 1 Introduction

At present, the researches of image quality evaluation method mainly focus on the image structure analysis and the reference evaluation method aspect of the human eye's sensitive information. Structure similarity [1] is a kind of image quality evaluation method based on image analysis. According to the image structure

---

Y. Zhong (✉) · R. Wang · L. Fu · Y. Hu · L. Chen  
School of Packaging and Materials Engineering,  
Hunan University of Technology, Zhuzhou, China  
e-mail: maczone@163.com

information which can be extracted by visual perception in the human eye vision system, the change of visual perception can be measured on the basis of the image structure information. At the same time, all kinds of image quality evaluation method were put forward based on SSIM to improve the structure of the similarity, such as wavelet transform [2], image gradient [3], etc. These methods overcame the deficiency of the traditional method of MSE and PSNR. Both the evaluation results and HVS consistency were improved. However, the improved methods still cannot evaluate the color image quality directly. In addition, the researchers through the study [4] found that compared with traditional color image structure information description method, quaternion has some advantages in color image structure information description, such as clear data structure, easy to describe and calculate. Thus it gradually has been used in color image quality evaluation. The quaternion singular value decomposition is applied to the video image quality evaluation in Literature [5]. To singular value decomposition of the image, calculate singular value standard deviation for the image structure distortion mapping. Through the analysis of distortion mapping distribution, image quality evaluation results are obtained. Wang et al. [6] used quaternion's to characterize the structure information of color image and calculate the characteristic vector angle to realize image quality evaluation through the quaternion matrix singular value decomposition (SVD).

Quaternion method is used to evaluate image quality which sensitively highlights the image HVS structure information, making the evaluation results more suitable for human visual characteristics. But through further study of the method, singular value decomposition of singular value feature vector matrix reflects the energy information, which is not sensitive to the human eye image structure information [7]. Literature [8] is proposed for color image quality evaluation of the quaternion method. Transforming the SSIM method of gray image structure to the quaternion field, so as to realize the structure comparison of two images, this method is superior to the traditional gray image in real number field structure similarity method, but the method of SSIM only be transformed to the pure quaternion field. Traditional framework of SSIM algorithm still cannot be directly applied to quaternion field, the evaluation results biased if directly applied to. Therefore, we need to find a suitable image quality evaluation algorithm of quaternion field.

To solve above problems, this paper use quaternions to represent color image structure information, with color image brightness component of local variance as real quaternion, color image RGB color components as quaternions imaginary part, the quaternion matrix structure are used to represent the structure information of color image, building the full quaternion of color printing image representation model by calculating the quaternion matrix singular value feature vector corresponding to the block. We take the maximum value as the characterization of partitioned image information and compare with the maximum of two image singular value feature vectors, so as to realize the quality evaluation of color printing image.

## 2 Quaternion Color Image Representation Model

Quaternion was put forward by Hamilton at the first time in 1843. It is composed of one real and three imaginary part of four components:  $q = q_r + q_i i + q_j j + q_k k$ . Between each quaternion can be regarded as a 1,  $i, j, k$  linear combination. Among them,  $q_r, q_i, q_j, q_k$  as the real and  $i, j, k$  is primitive.

Quaternion theory and method gradually applied in color image processing until 1996, such as color image decomposition [9], color image enhancement and denoising [10], color image information hiding [11] and color image compression [12], etc.

And according to the composition of quaternion, it can be known if the real component of quaternion  $q_r = 0$ , the remaining three imaginary part respectively red, green, and blue color components of color image. Then color image can use a pure quaternion matrix, namely:

$$f(x, y) = r(x, y)i + g(x, y)j + b(x, y)k \quad (1)$$

$r(x, y), g(x, y), b(x, y)$  respectively in the point of the color of red, green, and blue color values in color images. As a result, after the color image represented as a quaternion matrix, it can be handled by the entire color image as a whole on color image processing rather than dividing image into red, green, blue three color channels for processing respectively. Realizing the color chromaticity, brightness of the image as well as details of processing at the same time, improve the efficiency of color image quality evaluation.

In addition, we found that the quaternion matrix singular value feature vector with the human eye is sensitive to the image structure information [12] has certain relevance, but its associated degree is not high enough. In order to highlight color images in the quaternion matrix HVS sensitive structure information. Real quaternion can be set as the image luminance component of local variance [13], namely color image quaternion matrix can be further described as:

$$q(x, y) = Var(x, y) + r(x, y)i + g(x, y)j + b(x, y)k \quad (2)$$

$Var(x, y)$  for point of  $(x, y)$  luminance component of local variance, including:

$$Var(I_{i,j}) = \frac{1}{L} \sum_{p=1}^L (\eta_p - \bar{I}_{i,j})^2 \quad (3)$$

$$\bar{I}_{i,j} = \frac{1}{L} \sum_{p=1}^L \eta_p \quad (4)$$

Main structure information that the human eye sensitive in image is usually composed of image details, after we used local variance brightness component image as a real quaternion matrix, its description became more perfect. Not only it



highlights the HVS sensitive image structure information, but also it realizes the parallel processing of the image detail, brightness and color information.

### 3 Based on the Quaternion Largest Singular Value of Image Quality Evaluation Method

For an arbitrary rank  $r$  of quaternion matrix  $X_q$ , there must be two quaternion unitary matrix  $U_{(q)}$  and  $V_{(q)}$  make  $X_q = U_{(q)}\Lambda V_{(q)}^H$  [14]. The quaternion matrix  $X_q$  can take a singular value decomposition. There can be as follows:

$$X_q = U_{(q)} \begin{bmatrix} \Lambda & 0 \\ 0 & 0 \end{bmatrix} V_{(q)}^H \quad (5)$$

Among them,  $\Lambda = \text{diag}\{\lambda_1, \lambda_2, \dots, \lambda_r\}$ ,  $\lambda_1 \geq \lambda_2 \geq \dots \geq \lambda_r$ ,  $\lambda_r$  for the singular values of  $X_q$ .

Color image after SVD, quaternion for representation can be represented by the general form further as follows:

$$f_q(x, y) = U_{(q)}\Lambda V_{(q)}^H = \sum_{i=1}^r \lambda_i u_{i(q)} v_{i(q)} \quad (6)$$

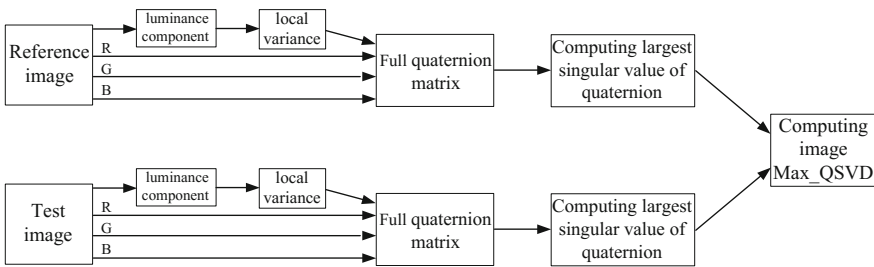
Type of product for each of the singular value corresponds to the characteristics of the image. According to the type 6 choose Lena image as experiment image quaternion which can take singular value decomposition and reconstruction. We get the singular value decomposition characteristics and reconstruction images. The results are shown in Fig. 1.

From image singular value decomposition experiment image, the image of the color and structural information mainly concentrated in the first few characters in the image, then the characteristics of image mainly contains details of image and edge and other high frequency information, and learn from the image reconstruction experiments can be further. By the top ten characteristics of the image can be basic to restore the main information of original image, the human eye can't tell the difference, therefore, image information includes mainly in singular value features in the image.

In this paper, based on human visual characteristics, quaternion and the singular value decomposition of the color image represented as a quaternion matrix form. Through the quaternion matrix singular value decomposition to get singular value vector, we realize printing image quality evaluation according to the two largest singular values in image singular value vector. Quaternion largest singular value-based method for image quality evaluation can be expressed as seen in Fig. 2.



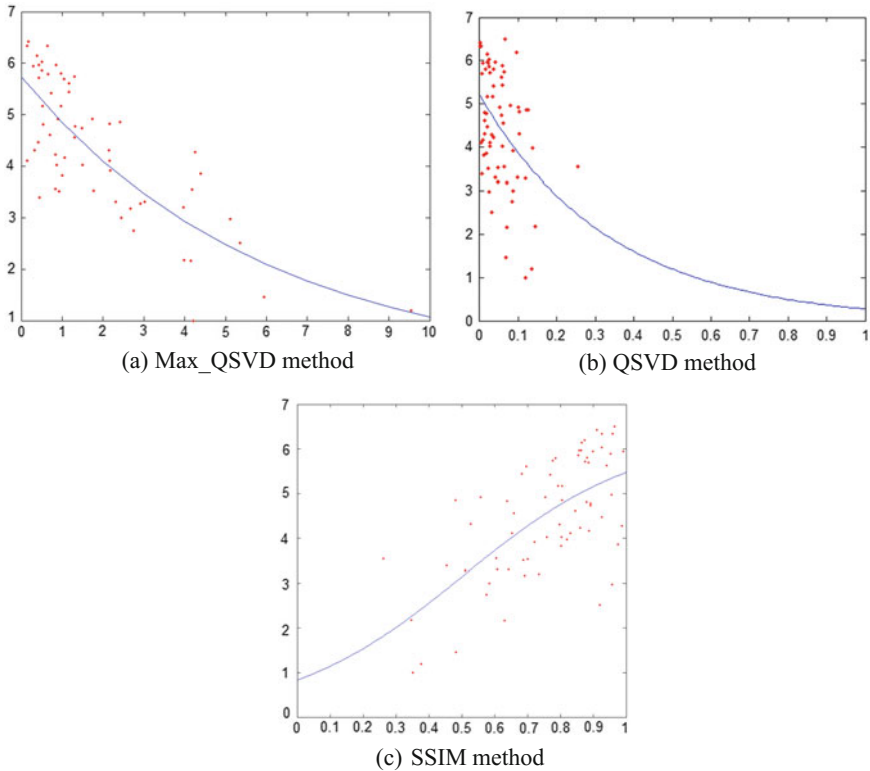
**Fig. 1** Singular value decomposition and reconstruction images



**Fig. 2** Quaternion largest singular value in image quality evaluation method

### 4 Based on the Quaternion Largest Singular Value of Image Quality Evaluation Method

This article selected TID2008 image database to verify the performance of image quality evaluation method. Through the TID2008 image subjective evaluation and objective evaluation of the results nonlinear fitting by using logistic function. Experiment result was shown in Fig. 3.



**Fig. 3** Logistic nonlinear fitting the experimental images

It can be seen from the Logistic nonlinear fitting results, Max QSVD method and QSVD method scatter distribution are more concentrated. The nonlinear fitting better than SSIM method, In order to obtain the more accurate analysis algorithm, this paper select printing image at the same time as the experimental images to validate the performance of image quality assessment. Printing image aberration range between 1 and 8. We also choose MSSIM method and QSVD as contrast experiment, the experimental results as shown in Table 1.

It can be seen from the results above, the three methods can better evaluate the quality of color printing image. The evaluation results are largely in line with subjective visual perception. But there are part of the evaluation results on deviation in the SSIM, mainly in the sub-channel printing image quality evaluation, especially when there is color deviation in printing image, the color difference is only exist in the image of one or two color channels and printing image quality evaluation results is by taking average value of each channel, leading to deviation or errors. Taking the entire printing image as a whole to proceed printing quality detection is a good way to avoid the problem. The loss of color image details,

**Table 1** Image quality evaluation method and performance comparison

	SSIM	QSVD	Max_QSVD
Aberration $\leq 1$	0.9807	0.0096	0.0266
	0.9839	0.0026	0.2082
	0.9795	0.0011	0.1041
1 < aberration $\leq 3$	0.9736	0.0068	0.3636
	0.9706	0.0267	0.7463
	0.9787	0.0095	0.8189
	0.9723	0.0031	0.6111
3 < aberration $\leq 6$	0.9691	0.0122	0.7903
	0.9576	0.0449	1.1471
	0.9749	0.0081	1.1494
	0.9655	0.0038	0.6735
Aberration $> 6$	0.9449	0.0589	1.4052
	0.9658	0.0208	1.4275
	0.9601	0.0044	2.3430

brightness and colors will be contained in the quaternion matrices, fits the human eye visual perception effect of image quality evaluation.

## 5 Conclusions

In this paper, we proposed an evaluation method based on the quaternion largest singular value of color printing image quality, using the quaternion matrix as a carrier of the structure information of color image. We took the image brightness local variance as a real quaternion which has enriched the quaternion matrix of HVS sensitive information structure. The image quality evaluation was realized by measuring the largest singular value feature vector energy information. The method is adopted to improve the image quality evaluation for color image details, brightness and the parallel processing of color information, further improved the representation of the image structure information in the meanwhile.

**Acknowledgements** Project is supported by Natural Science Foundation of Hunan Province (Grant No. 2016JJ6034 and 14JJ4057), Training Project of Hunan Industrial Application of Higher Education Institutions (Grant No. 15CY003), Hunan Province Higher Education Institutions Demonstration Base of Production, Education and Research (Grant No. 2014-117).

## References

1. Zhou, W., Bovik, A.C., Sheikh, H.R., et al (2004). Image quality assessment: from error visibility to structural similarity. *Image Processing, IEEE Transactions on*, 13(4):600–612.
2. Yang, C.I., Gao, W.R (2009). Research on Image Quality Assessment in Wavelet Domain Based on Structural Similarity. *Acta Electronica Sinica*, 04:845–849.

3. Sang, Q.B., Su, Y.Y., Li, C.F., et al (2013). No-reference blur image quality assessment based on gradient similarity, *Journal of Optoelectronics Laser*, 03:573–577.
4. Wang, Z., Li, Q. (2011). Information Content Weighting for Perceptual Image Quality Assessment. *IEEE Transactions on Image Processing A Publication of the IEEE Signal Processing Society*, 20(5):1185–98.
5. Zhang, F.Q., Li, J.L., Li, G., et al (2011). Video Quality Assessment Based on Quaternion Singular Value Decomposition, *Acta Electronica Sinica*, 01:219–223.
6. Wang, Y.Q., Liu, W.Y., Wang, Y. (2010). Assessment Method for Color Image Quality Based on Quaternion. *Journal of North University of China (Natural Science Edition)*, 31 (1):59–67.
7. Narwaria, M., Lin, W. (2010). Objective image quality assessment based on support vector regression. *IEEE Transactions on Neural Networks*, 21(3):515–519.
8. Kolaman, A., Yadid-Pecht, O. (2012). Quaternion structural similarity: a new quality index for color images. *IEEE Transactions on Image Processing A Publication of the IEEE Signal Processing Society*, 21(4):1526–1536.
9. Xing, Y., Tan J.Q. (2011). Color Image Decomposition Based on the SVD of Quaternion Matrix. *Journal of Engineering Graphics*, 2:93–101.
10. Lei, Y.J., Yu, Y.M., Zhou, J.L., et al (2007). Quaternion singular value decomposition approach to color image de-noising. *Journal of Sichuan University (Natural Science Edition)*, 44(6):1268–1274.
11. G.Q., Wang, M.W., Li, Z.L., et al (2008). Doubled random-phase encryption based on discrete quaternion fourier-transforms, *Acta Physica Sinica*, 57(11):6955–6961.
12. Luo, L.C., Hao, H.F., Ding, L.J. (2008). Color Image Compression Based on Quaternion Neural Network Principal Component Analysis. *International Conference on Multimedia Technology*. Ningbo: IEEE Press: 1–4, 29–31.
13. Wang, Y.Q., Zhu, M. (2013). Maximum Singular Value Method of Quaternion Matrix for Evaluating Color Image Quality. *Optica and Precision Engineering*, 21(2):469–478.
14. Zhang, F. (1997). Quaternions and Matrices of Quaternions. *Linear Algebra and Its Applications*, 251:21–57.

# An Output of Oil Painting Stylized Digital Image from Photographs with Optimum Tone Reproduction

Jing Geng, Congjun Cao, Jingshang Fan, Hirokatsu Shimizu,  
Naokazu Aoki and Hiroyuki Kobayashi

**Abstract** As one of the most important properties for transfer of gradation information, the quality of tone reproduction is the key index of an image system. In this paper, using non-photorealistic rendering method, oil painting stylized images are generated from photographs. The chroma of digital images of the style of portrait and landscape is adjusted. At the same time, the brush stroke of impressionist oil painting image is scanned, the characteristics of oil painting's brush stroke are extracted, the direction of brush stroke is analyzed, the amplitude intensity and the frequency of brush stroke is adjusted, in order to achieve an oil painting stylized image close to the original oil painting. On this basis, the tone reproduction curve of oil painting stylized image is adjusted. Then, through psychological evaluation, oil painting stylized image's optimum tone reproduction curve is obtained.

**Keywords** Optimum tone reproduction · Oil painting · Non-photorealistic rendering · Brush stroke

## 1 Introduction

Tone reproduction is the key index of image quality evaluation system. T.H. James's researches have summed up the optimum tone reproduction curves of digital photographs [1]. The solid S shaped line represents the optimum tone reproduction curve of portraits shot in studio, and the broken line shows optimum curve of

---

J. Geng (✉) · C. Cao · J. Fan

Faculty of Printing, Packaging Engineering and Digital Media Technology,  
Xi'an University of Technology, Xi'an, China  
e-mail: gengjing\_qianye@163.com

H. Shimizu · N. Aoki · H. Kobayashi

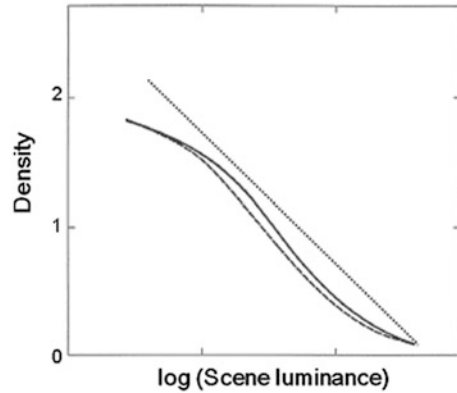
The Graduate School of Advanced Integration Science Chiba University,  
Chiba 263-8522, Japan

© Springer Nature Singapore Pte Ltd. 2017

P. Zhao et al. (eds.), *Advanced Graphic Communications  
and Media Technologies*, Lecture Notes in Electrical Engineering 417,  
DOI 10.1007/978-981-10-3530-2\_27

213

**Fig. 1** Optimum tone reproduction curves of digital photographs



outdoor landscapes, respectively in Fig. 1. The two lines are not simple straight line of slope 1 but an S shaped curve with slope 1.1–1.2 in the middle tone and lower slope in the shadow and highlight region.

This paper proposes that oil painting stylized image has the optimum tone reproduction as well.

The technique of continuous-tone [2], concentration of pigment expressing tone, has a long history. It can be seen in Paleolithic cave paintings in Lascaux and Altamira, in tens of thousands of years. The tone expressed by the density of dots and lines is introduced into drawing technique in Pre-Renaissance for the first time [3].

On the preceding paper [4], the optimum tone reproduction of line-drawings is investigated. These line-drawings are made of digital photographs, using non-photorealistic rendering. The optimum tone reproduction of line-drawing depends on the style of original digital photo image.

In this paper, using non-photorealistic rendering method, oil painting stylized images are generated from photographs, then we adjusted the tone curve of these images, and through psychological evaluation of these images subjectively. Finally the optimum tone curves are obtained. The results of this paper can be applied in the field of printing reproduction and cultural creativity industry.

## 2 Experiment

### 2.1 Photographs Are Used in the Paper

Four different types of photographs are used in this paper, two portraits and two outdoor landscapes. As shown in Fig. 2. Landscape1 is a low-key image and landscape2 is an image that the contrast of light and dark is small as a whole.



Fig. 2 Original photographs are used for making oil painting stylized images

Portrait1 is a high-key image. The contrast of light and dark in portrait2 is stronger, because the lightness of the person’s face is very high while the clothes are darker.

Brush stroke patch, Fig. 3b is cut from Fig. 3a which is Claude Monet’s oil painting “Bend in the Epte River near Giverny” [5]. The image with strong characteristics of stroke is the representative of the Impressionist.

## 2.2 Production Method of Oil Painting Stylized Image

### 2.2.1 Use of Brush Stroke

The algorithm of making oil painting stylized image is as follows [3]: ① The original photograph (Fig. 2) is converted to a frequency domain using fast Fourier transformation. ② Brush strokes texture patch (Fig. 3) is converted to a frequency



Fig. 3 Brush stroke image cut from an oil painting “Bend in the Epte River near Giverny” by Claude Monet



domain using fast Fourier transformation. ③ The original photograph is blurred and pasteurized to generate stepwise gradient. ④ The pasteurized image of ③ is edge-enhanced. ⑤ The information about gradient direction is acquired from density distribution of image ④. ⑥ Based on the information of gradient direction in ⑤, and the maintaining phase of the image of ①, frequency domain spectrum of filter in ②, is applied in the original photograph. ⑦ Then the image ⑥ is converted to spatial domain. ⑧ Finally, the  $a^*$  and  $b^*$  values of the original photograph is added (Fig. 4).

### 2.2.2 Adjustment of Brush Stroke's Strength and Original Photographs' Chroma

Through adjusting the contrast between light and dark of brush stroke patch, the spectrum strength of brush strokes is transformed. Table 1 shows the data from the adjustment of brush stroke's strength and original photographs' chroma. Figure 5 shows the print result of images after adjustment of brush stroke's strength and original photograph's chroma.

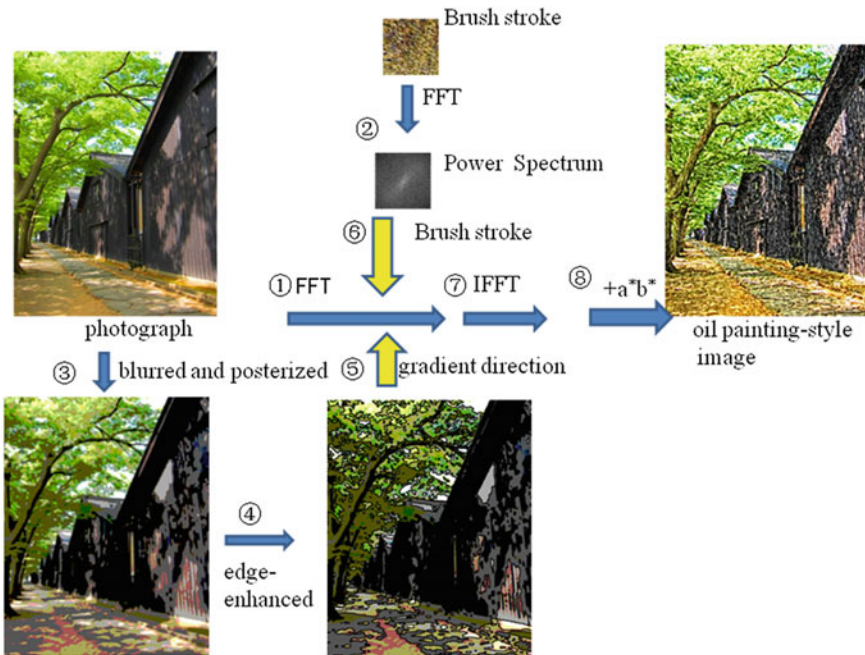


Fig. 4 Process of producing oil painting-style images made by non-photorealistic rendering

**Table 1** Adjustment of brush stroke’s strength and original photograph’s chroma

Sample		a	b	c	d	e	f	g	h	i
Landscape1	Chroma	60	75	90	60	75	90	60	75	90
	Contrast		40			60			80	
Landscape2	Chroma	60	75	90	60	75	90	60	75	90
	Contrast		40			60			80	
Porrtait1	Chroma	0	15	30	0	15	30	0	15	30
	Contrast		0			20			40	
Porrtait2	Chroma	40	50	60	40	50	60	40	50	60
	Contrast		0			20			40	

### 2.3 Control of Tone Reproduction

Line1 represent the optimum tone reproduction curve of digital photographs (Fig. 6). Then, in order to form the darker lines (line 2, 3, 4, 5, 6, 7, 8, 9) and the lighter line 10, line1 is adjusted. The lines with high contrast in the middle tone (line 11, 12) are also be made, and line with lower maximum density (line 13). Through the different lines, different images are made for experiments.

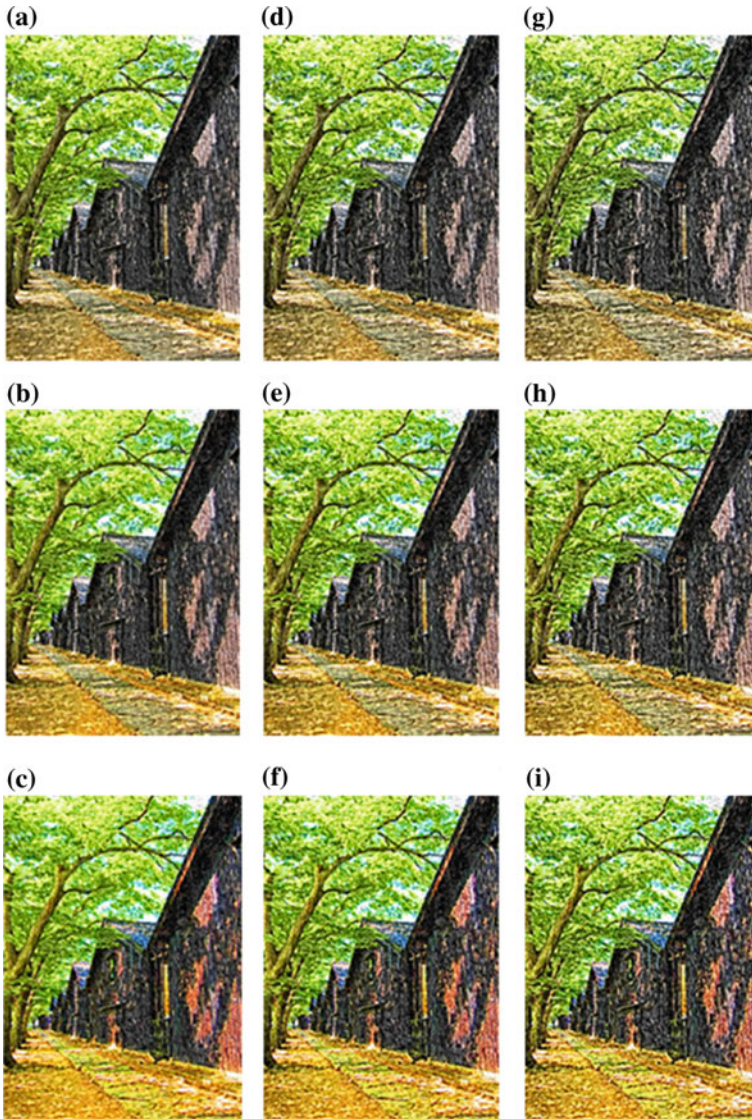
### 2.4 Evaluation of Experiments

#### 2.4.1 Environment of Evaluation

Images are evaluated under fluorescent lamp D50 with high color rendering properties up to 700 lxes. 35 students aged from 20 to 30 are chosen as testees. For the purpose of reducing error, 30 testees are the lowest level of experiments. The testees observe the sample images by naked eyes, and rank these images according to their personal preferences. The distance between testee and images is not limited.

#### 2.4.2 Similarity Degree Between Oil Painting Stylized Images and Original Oil Painting

The images acquired from the adjustment of brush stroke’s strength and original photographs’ chroma. Every testee rank these images according to the similarity degree between oil painting stylized images and original oil painting, choose the most similar ones. The most selected one is the sample of next step.



**Fig. 5** Print result of images after adjustment of brush stroke’s strength and original photographs’ chroma

### 2.4.3 Evaluation Method: A Method of Psychometric Scaling for a Ranking Scale [6]

The evaluation method was used for measuring the degree of psychological preference in mind. In particular, the evaluation method is based on the order for scale. In order to evaluate images’ quality, testees (J persons) were recruited for ranking

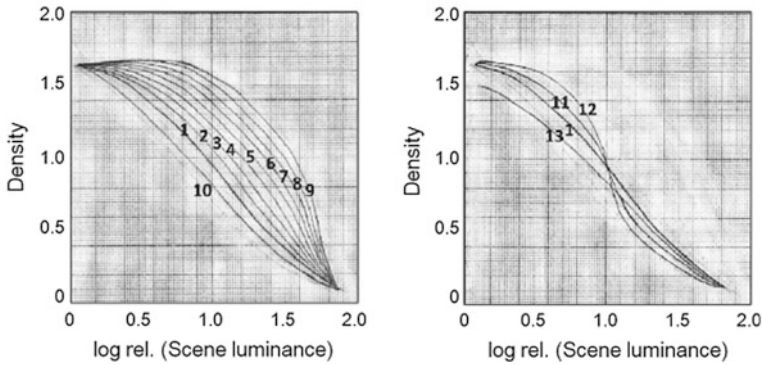


Fig. 6 Tone reproduction curves of the samples

the image samples (n) with the order of the individual favorite. The tessees (J) was row, and samples (n) was column, which achieved the rank of R (J × n).

$$\text{Average grade} = (1/J) [1111 \dots 111]R$$

Among them, [1111...111] represents 1 × J determinant

The average grade became the scale value. Moreover, in order to make the data more clearly, the average level of the scale value is set to zero. The positive value was higher than the average level, and the negative value was below the average level. The zero point here is not a real number.

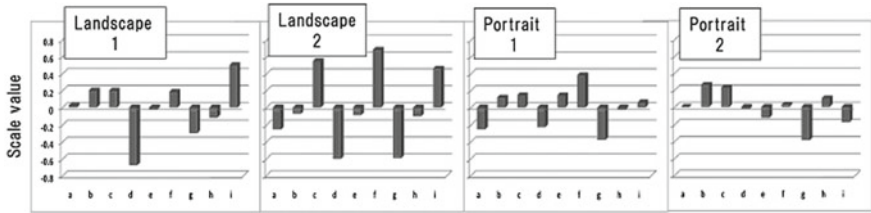
### 2.4.4 Optimum Tone Reproduction of Oil Painting Stylized Digital Image

The best sample of each theme chosen by the tessees, are adjusted into images with different tone reproduction. Then the images were arranged by the 35 tessees according to their preference.

## 3 Conclusion and Analysis

### 3.1 Similarity Degree Between Oil Painting Stylized Images and Original Oil Painting

Through the data of Table 1, 4 kinds of images are produced. According to psychological evaluation method, the images close to original oil painting are obtained. The image scale can be seen in Fig. 7. Sample i in landscape1, sample f in



Each image's number each image's number each image's number each image's number

Fig. 7 Scale values obtained from subjective evaluation

landscape2, sample f in portrait1 and sample b in portrait2 win the best evaluation. Compare with landscape images, portrait images rely more on spectrum energy intensity of stroke texture, basing on analysis, the testees pay more attention on portraits' face, the stroke texture with great spectrum energy intensity will destroy the beauty of the face. On the other hand, the chroma value set for the original photo has great influence on the oil painting stylized image. High chromatic value is not fit for portraits.

### 3.2 Optimum Tone Reproduction Curve of the Oil Painting Stylized Images

According to image's chroma, brush stroke's contrast between light and dark, and the tone reproduction curves in Fig. 6, the samples corresponding to oil painting stylized image of each theme are made. In order to reduce the experimental error, some images that appear to be not good are deleted. The other samples are used for experiment (show in Fig. 8). Using the method of psychometric scaling for a ranking scale, scale value is formed in Fig. 9.

In the samples with different tone reproduction of landscape1, sample 5 gets the most votes (scale value). In landscape2, sample 11 gets the most votes. In portrait1, sample 10 gets the most votes. In portrait2, sample 11 gets the most votes.

In each group, sample1 is the image made from digital photo's optimum tone reproduction. Sample 5's whole density was higher than sample 1. Sample 11's contrast between light and dark in the middle tone is higher than sample 1. Sample 10's curve is a bright soft tone curve.

The oil painting stylized image's optimum tone curve have great difference with digital photos' and line-drawings', landscape1's optimum tone curve moves rightward to the dark tone area, while portrait1's curve moves leftward to the light tone area (Fig. 10).

In Fig. 11, demonstrate the result of the optimum tone reproduction of digital photographs and line drawings [1, 4]. For digital photos, there's little difference in



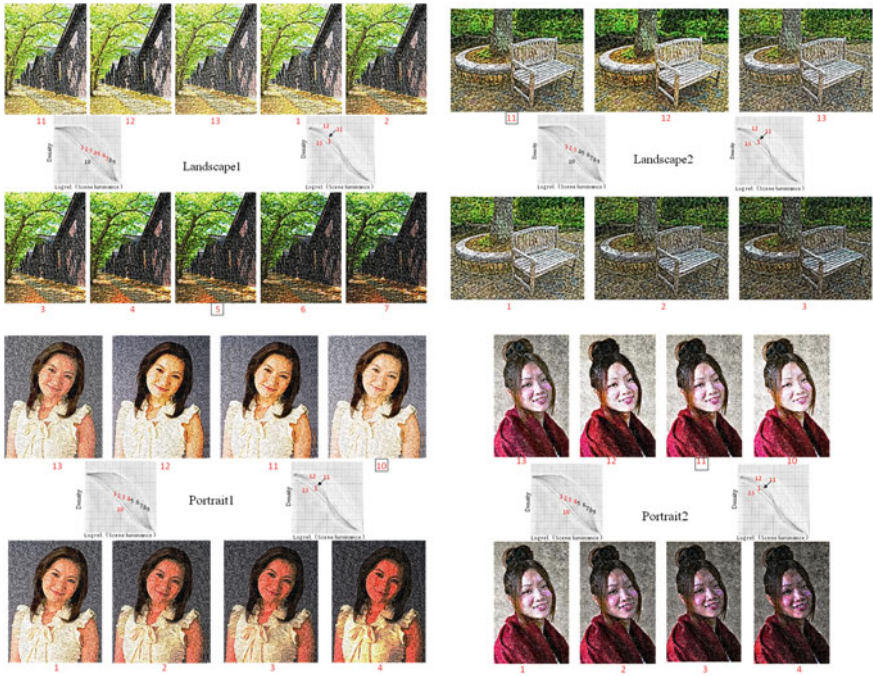


Fig. 8 Samples corresponding to oil painting stylized images of each theme

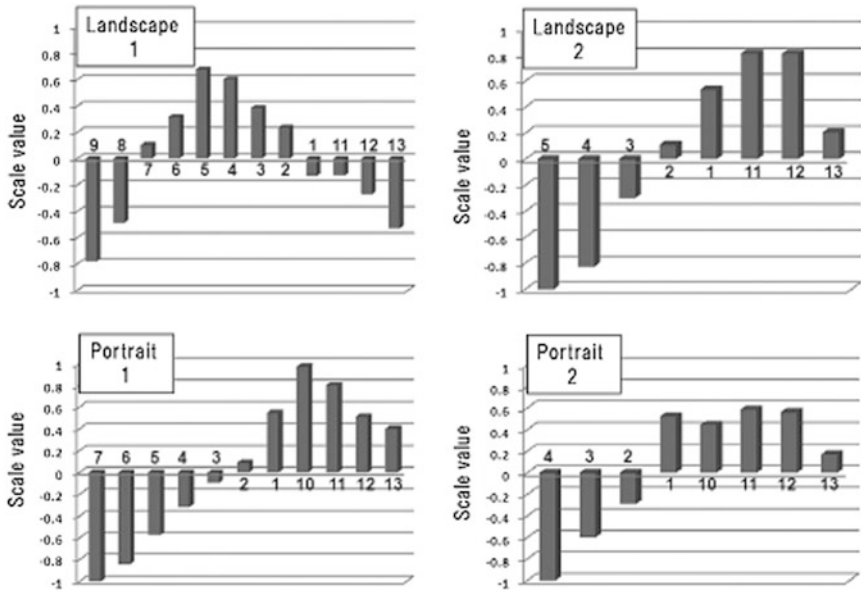
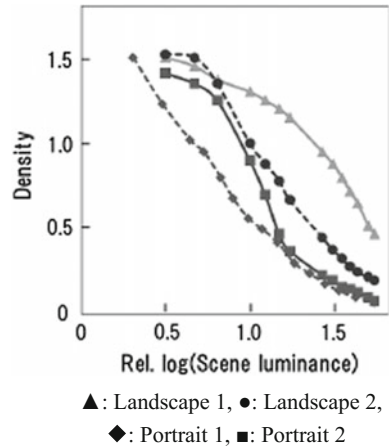


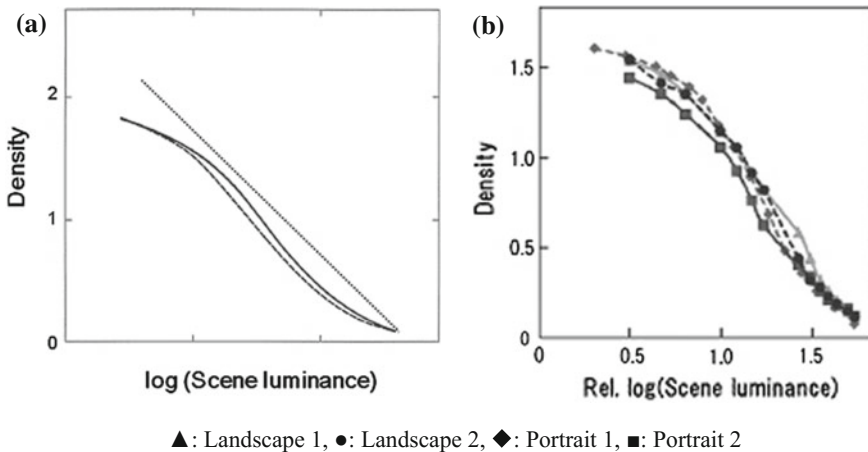
Fig. 9 Scale values obtained from subjective evaluation

**Fig. 10** Each oil painting stylized image's optimum tone reproduction curve



the middle tone between landscapes' and portraits'. The four curves of line-drawing basically are overlapping. From above, it can be seen that optimum tone reproduction of digital photos and line-drawings has less dependence on theme, dark tone or bright tone of original digital photos.

In Fig. 12, it reflects that each theme corresponding to digital photos, line drawings, oil painting stylized images. For landscape1 of dark tone, the oil painting stylized image's tone curve moves toward darker direction than the line-drawing's and the digital photos. The tendency of portrait1 with bright tone is opposite to landscape1, the oil painting stylized image's tone curve moving toward brighter direction than the line-drawing's and the digital photos. Portrait2 has higher



**Fig. 11** Tone reproduction curves evaluated as optimum for the photographs (a) and the line-drawings (b)

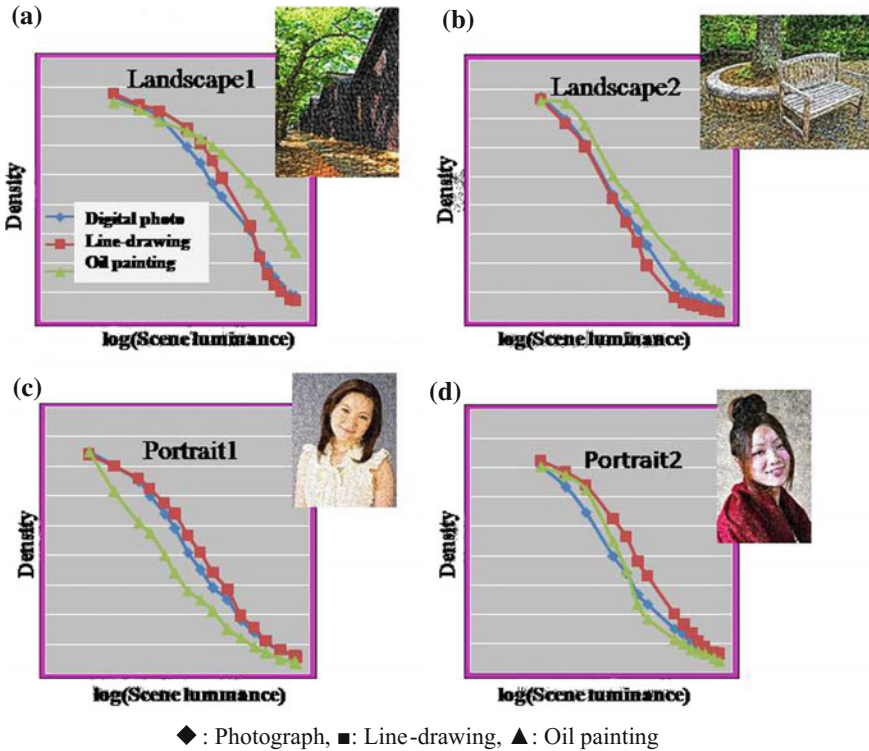


Fig. 12 Tone reproduction curves as optimum for Landscape 1 (a), Landscape 2 (b), Portrait 1 (c), and Portrait 2 (d)

contrast between light and dark. The oil painting stylized image corresponding to portrait2 has a hard tone curve.

## 4 Conclusions

The oil painting stylized images are produced by the original digital photos with dark tone, has darker optimum tone reproduction. The oil painting stylized images are produced by the original digital photos with bright tone, has brighter optimum tone reproduction. The oil painting stylized image of portrait 2, the hard tone is considered the best.

In digital photos, it can be considered that the optimum tone reproduction of portrait (Fig. 1) is harder than the landscape's. The brightness of original photo has a big influence on optimum tone curve of oil painting stylized image.

The chroma and the contrast between light and dark of original digital photo have great influence on the optimum tone reproduction of oil painting stylized



image. The chroma of optimum oil painting stylized image is greater than the digital photo with optimum tone curve.

Only the value of original landscape's chroma is about 20(In munsell color system), or the value of original portrait's chroma is about 10, the generated images can be recognized as oil painting stylized image.

Different artist has different stroke texture which has different spectrum energy intensity. Monet's Stroke textures are used in this paper. In future research, more kinds of stroke textures will be added for new discovery.

**Acknowledgements** This study is funded by a Startup Foundation for Doctors of Xi'an University of Technology awarded to the first author in 2015. This work is also supported by the Key Laboratory for printing and packaging engineering scientific effort plan of Education Department of Shaanxi Provincial Government (16JS082).

## References

1. T.H. James, *The Theory of the Photographic Process* [M] 4th edition., Macmillan Pub Co, New York, 1977, p. 557–558.
2. ADAMS J M, DOLIN P A. *Printing Technology* [M]. 5th edition, Published by Delmar Thomson Learning, 2001.
3. IVINS J W M. *Prints and Visual Communication* [M]. Cambridge: Harvard University Press, 1953.
4. GENG Jing, SHIMIZU Hirokatsu, AOKI Naokazu, et al. Automatic Making of Line-drawing with Optimum Tone Reproduction [J]. *Journal of Asia Digital Art and Design*, 2012, 15(3): 109–114.
5. NKAYAMA KIMIO “Art Gallery 「The art of modern world」 1 Monet” [M], SOBISHA Inc, Japan, 2000, p. 35–36.
6. Peter G. Engeldrum, *Psychometric Scaling: A Toolkit for Imaging Systems Development* [M], Imcotek Press, Winchester, 2000, Chap. 6.

# Contrastive Analysis on Emotional Cognition of Skeuomorphic and Flat Icon

Xiaoming Zhang, Qiang Wang and Yan Shi

**Abstract** In the field of designs of interface and icons, as the skeuomorphism style fades out in use while the flat design tends to be popular, research on which visual form accords to user's emotional cognition and future direction of design development has been the hot spot. In this paper, general mobile devices are taken as sample, data statistics and comparative evaluation are conducted via questionnaire survey and discriminant analysis. The identification process of users to use skeuomorphism and flat design and their emotional cognition are analyzed. In this experiment, the identification accuracy of the icon, cognition validity, and degree of emotion arousal as well as the emotion validity are compared. The impact factor that reaches the best user experience is summarized. Finally, based on the guidance of acquired conclusion, an available icon is designed.

**Keywords** Flattening · Skeuomorphism · Emotion · Cognition · User experience

## 1 Introduction

With the prevalence of smart phones in recent years, icons have become an important component of the smart phones' user interface, and also play a significant role as the virtual media which delivers user awareness and perception, using symbolic expressions [1]. Under the background that it becomes more complicated for people to handle the user interface of smart phones, icons represent both the functions of the application and an element in interactions. Good icon design provides an efficient, smooth experience for users, that's why the study of humanize and interactivity of icon design has a great significance.

The user experience of icons on mobile device is affected by aesthetic preferences, distinguishing degree, and many other factors. Currently scholars study impacts of icons mainly from their appearance, color choice and the changes of style.

---

X. Zhang (✉) · Q. Wang · Y. Shi  
School of Media and Design, Hangzhou Dianzi University, Zhejiang, China  
e-mail: 447416866@qq.com

For instance, Shi-Jian Luo et al. analyze the effects of icon background shapes and figure/background area ratios on visual search performance and user preference [2]. Mei-Ying Fan obtained the icon colors that users are more willing to accept by studying the basic principles of photochromic and human perception of color [3]. But they take the aesthetic principles of design merely into account, without paying attention to the influence of the user’s emotional experience and psychological needs. From the evolution of the calculator icon shown in Fig. 1, the icon design is evolved from skeuomorphism to flat design based on the impacts of these factors. Skeuomorphism reproduces the physical body through various design effects such as highlight, texture, material, shadow, etc. On the contrary, flattening pursuits to create a more abstract, simplified and symbolic design [4]. This paper takes application icons on mobile devices as a case, focusing on people’s needs, to study the impacts of application icons on user experience and to summarize the key factors that influence user experience from four aspects, including the identification accuracy of the icon, cognition validity, and degree of emotion arousal as well as the emotion validity.

## 2 Analysis of Factors Affecting the Icon Designs

In the development process where icon designs change from the real and friendly skeuomorphism to flat design, we analyze user needs and experience objectively, along with studying the effects of user experience on application icons from four dimensions including the identification accuracy of the icon, cognition validity, and degree of emotion arousal as well as the emotion validity is critical.

### 2.1 Identification Accuracy and Cognitive Validity

Visual search is a type of perceptual task requiring attention that typically involves an active scan of the visual environment for a particular object or feature among other objects or features [5]. Users are always facing an icon when communicating with an application. Identification and the cognitive process of the icon is particularly important, which makes identification and cognition validity an effective

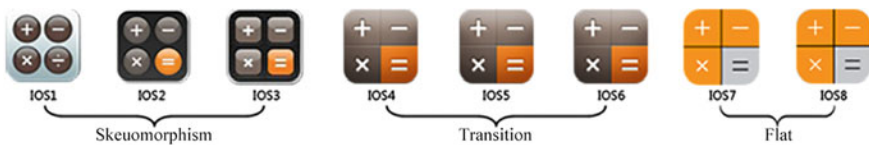


Fig. 1 Evolution of the calculator icon from ios1 to ios8

standard to measure the efficiency of visual search. Chun et al. proved the user preference can be increased along with search speed and accuracy [2]. Visual search efficiency could strongly influence user experience. Consumers' sense of pleasure would decrease while search time increases. So while the identification accuracy and cognition validity is not high, user experience satisfaction drops.

Thus, a higher degree of identification accuracy and cognition validity can increase user satisfaction when using mobile applications.

## **2.2 *Emotional Arousal***

Process of emotion arousal, is actually a transformation and sublimation the objects felt from natural level to aesthetic one [6]. User ratings of aesthetic preferences for interface designs are important because the aesthetic quality influences consumer attitudes and is a major determinant of a product's success [7]. Aesthetically pleasing icon designs can be more influential in affecting user preferences than conventional operational usability in interactive systems [8].

Therefore, this experiment will measure the user satisfaction on an icon based on the degree of user aesthetic preferences.

## **2.3 *Emotional Validity***

Validity refers to the degree of the particular psychological traits that a test measures. Emotion validity is the degree of emotional impacts on the user experience. Yan Ding et al. pointed out that brain will generate a wide range of neural responses rapidly while stimulated by emotional information, which will influence cognitive processes from awareness, perception, memory and other aspects [9]. Almost everything we do is affected by emotions. And emotions can change the way we think, and play a crucial role in our daily decisions [10].

Therefore, this study will design experiments through the impacts of icons indicating different emotions on people's emotional preferences.

## **3 Experiment Design**

In order to verify the effects of four factors previously proposed on user experience, this study did an experimental method design and a questionnaire design by comparing the role four factors played in icons.

### 3.1 Method

This study focuses on testing the impact of icons on user experience, including four aspects: the identification accuracy of the icon, cognition validity, the degree of emotion arousal and emotion validity. The questionnaire survey is used to test the general public in china. Meanwhile, the differences of user experience among different groups in age, gender, education and professional level are studied.

### 3.2 Questionnaire Design

In this study, a college in Zhejiang Province is taken as a gathering place to collect test data. 81.3% subjects are college students or teachers, with the remaining being off school staff. A total number of 160 questionnaires were recovered, excluding 5 invalid questionnaires; this study obtained 155 effective questionnaires finally.

Research sets a 5-point scale to test the identification accuracy of the icon type, a multiple-choice scale to measure cognition validity, a 5-point scale to test the degree of emotion arousal and 5-point scale to test emotion validity. The emotion validity scale is used to test the degree of individual emotion preference on icons with four basic human emotions. Ekman’s research findings led him to classify five emotions as basic: joy, sadness, anger, fear and disgust [11]. Taking into consideration the extreme rarity of icons that make people angry, the test is based on icons indicating the other four emotions.

### 3.3 Data Analysis and Results

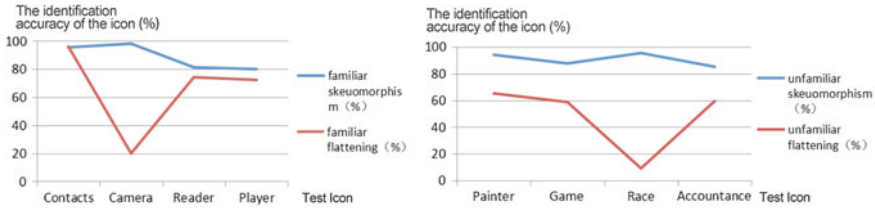
This study does a frequency analysis, a descriptive statistics and variance analysis.

As the factor for identification accuracy, the experiment sets two groups of icons; one is familiar to public while the other is not. Results are shown in Fig. 2.

There are eight pairs of icons in Fig. 2, two icons as a pair including one familiar to the public while the other is not. As can be seen from Fig. 3, whether application



Fig. 2 Test icons



**Fig. 3** Identification accuracy of the icon



**Fig. 4** Example of Icons from skeuomorphism to flat design

**Table 1** Descriptive statistics of emotional preference from skeuomorphism to flat design

Aesthetic preferences	N	Min	Max	Mean	Std. deviation
Instagram	155	1	5	1.80	1.224
Calendar	155	1	5	2.32	1.329
Calculator	155	1	5	2.79	1.262
Mail	155	1	5	2.43	1.591
Baidu map	155	1	5	2.57	1.254
Preference mean	155	1.00	4.40	2.382	0.70743

Note 5-point scale, 1 means fully skeuomorphic icon, and 5 totally flattened

icons are familiar to users or not, the identification accuracy of the skeuomorphic icons is higher than flat icons (Fig. 4). Familiar icons have higher accuracy than strange ones in flat design.

As can be seen from Table 1, the overall mean value of user preference is 2.38, from which a preference for skeuomorphism is seen. The results of preferences for skeuomorphism and flat design of different ages were as follows.

Table 2 shows that the elderly and children prefer skeuomorphic icons rather than the youth, who believe skeuomorphism, is better to identify an application (Table 3).

In order to understand how icons indicating emotions influence people’s likes (Fig. 5), the test sets the option “Just so-so” as the standard and make a one-sample T test on the data. The results were shown in Table 4.

As can be seen from Table 4, the four basic emotions have certain emotional impacts on the user preference: sadness has the least impact on user’s emotional preference ( $t = 6.004$ ); disgust has the strongest impact ( $t = 24.108$ ). And users prefer icons indicating a happy mood ( $t = -13.414$ ).

**Table 2** Different ages of emotion icon preference description

Aesthetic preferences	N	Mean	Std. deviation	Min	Max
Under the age of 15	6	1.17	0.408	1	2
15–20 years old	12	1.42	0.515	1	2
21–25 years old	105	1.41	0.494	1	2
26–30 years old	26	1.35	0.485	1	2
Above 30 years old	6	1.00	0.000	1	1
Total	155	1.37	0.485	1	2

**Table 3** Different ages of emotion icon preference ANOVA analysis

	Sum of square	df	Mean square	F	Significance
Between groups	1.272	4	0.318	1.362	0.250
The group	35.025	150	0.234		
Total	36.297	154			



**Fig. 5** Test icons with four basic emotions

**Table 4** One-sample T test

	N	Mean	Std. deviation	t	df	P
Joy	155	2.1355	0.80241	-13.414	154	0.000
Sadness	155	3.3677	0.76251	6.004	154	0.000
Fear	155	3.8161	0.95008	10.695	154	0.000
Disgust	155	4.4194	0.733	24.108	154	0.000

Note The test value = 3, the degree of user preference is general

Different users’ cognition validity of skeuomorphism and flat design are measured, with results shown in Fig. 6, it shows that the cognition validity of flat is lower than skeuomorphic one. It’s easier for users to cognize type and meaning of icons by skeuomorphism.

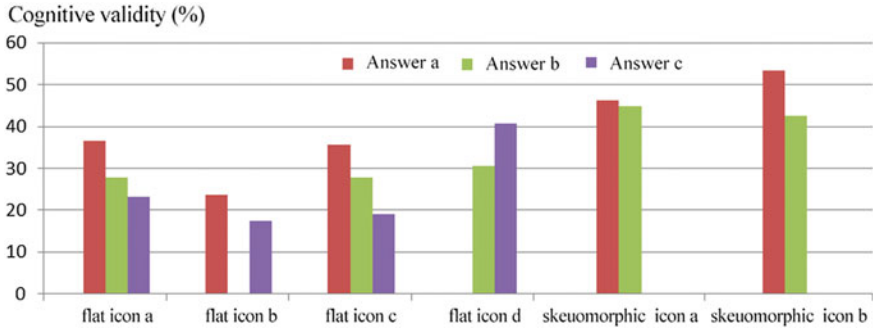


Fig. 6 Recognition of the validity of different icons

Fig. 7 Icon example



### 3.4 Example of Verification

Experimental data analysis of the results shows that skeuomorphic icons have higher identification accuracy and faster efficiency than flat icons. The cognition validity of flat icons is lower than skeuomorphic ones. Users like both forms of icons, but skeuomorphic icon seem to be in advantage. Human emotions have great impacts on user preferences. Meanwhile, according to the data obtained in this experiment, we design an icon on tourism (Fig. 7).

This study verified the icon also using questionnaires aspects of identification accuracy, cognition validity, the degree of emotion arousal and the emotion validity. 89.5% of users identify the type of icon correctly; the average user cognition validity of this icon has reached 56.6%. Two-thirds of users believe that this icon is intimacy, real and layering, belonging to skeuomorphic icon. Compared to a similar flat icon, 77.2% of users prefer this icon more. 91.2% of users think that this icon brought him a pleasant feeling. Only 7% of users illustrated they dislike it. Thus, the four factors affecting the user experience this study discusses make it to let the icon satisfy the majority.



## 4 Conclusions

This study explores the icon's identification accuracy, cognition validity, the degree of emotion arousal and emotion validity of icon design mainly based on human needs, it takes universal mobile devices for instance, with statistics and comparative evaluation conducted via questionnaires and variance analysis, whose results of the analysis are applied to the mobile App for schools and teachers. Data analysis showed that a good icon design must have a high degree of identification accuracy and cognition validity at first, for these two elements help to produce a better search performance. Secondly, icons with some skeuomorphism elements are preferred. Compared to typical flattening, those icons load off the trouble users may have in understanding how to use the products, while they also combine some advantages of fattening. Finally, based on the fact that emotions have strong impacts on user preferences, icons indicating a happy mood usually bring with higher satisfaction.

These results will help designers in the development of smartphone's icon designs, and improve the user experience while lifting brand image as well.

**Acknowledgements** This work is funded by National Key Technology Research and Development Program of the Ministry of Science and Technology of China (2012BAH91F03).

## References

1. Yu, T (2011). Humanized interaction design on icons of smartphone user interface. *Packaging Engineering*, 24, 73–83.
2. Luo, S.J, Zhou, Y.X (2015). Effects of smartphone icon background shapes and figure/background area ratios on visual search performance and user preferences. *Frontiers of Computer Science*, 5, 751–764.
3. Fan, M.Y (2014). Analysis of using color in mobile application UI design. *China Science & Technology Panorama Magazine*, 8, 44–45.
4. Gao, P, Yang, Z (2014). On the flattening and skeuomorphism of UI design. *The fine arts education research*, 10, 60.
5. Aeron Charline (2013). *Visual Search*. Onym Press, 1–2.
6. Zhang, J (2008). Emotional arousal and aesthetic expression. *Theoretical studies in literature and art*, 2, 99–105.
7. P.H. Bloch (1995). Seeking the ideal form: product design and consumer response. *Journal of Marketing*, 3, 16–29.
8. D.A. Norman (2014). Introduction to this special section on beauty, goodness, and usability. *Human-Computer Interaction*, 4, 311–318.
9. Ding, Y, Wang, Y.P (2005). Emotional Information stimulation on visual cognitive processes. *Chinese Journal of Clinical Rehabilitation*, 28, 152–155.
10. Donald Norman (2010). *Emotional Design*. China CTTIC Press, 5.
11. Paul Ekman (1999). *Basic Emotions*. 45–57.

# Reproduction of HDR Image Based on Multiple Bilateral Filtering

Yang Zhao, Xiaozhou Li, Jingqiang Jia and Qian Cao

**Abstract** Displays are often used to display HDR images. It is unable to solve the problem of gradient reversal artifacts or halo appearing on salient edges through the single bilateral filtering. In order to gain better visual perception, multiple bilateral filtering was put forward to optimize and adjust HDR image. Firstly, HDR image was processed by multiple bilateral filtering to reserve the edge and filter impulse noise. Then the basic layer of the image was conducted on contrast while detail layer is enhanced on the edge, and more details were reserved. The processed images were outputted using paper medium. The results showed that the method proposed in this paper could eliminate more noises and preserve more detail features.

**Keywords** High dynamic range image · Bilateral filtering · Gradient reversal · Print reproduction

## 1 Introduction

Natural scene has higher dynamic range [1]. The image with higher dynamic range is called HDR image. HDR image can't be displayed directly on common display devices with low dynamic range. Tone mapping technique is a useful strategy to represent the HDR image. The bilateral filtering is a nonlinear filtering technique which can reduce more noises and preserve more details [2]. In recent years, some typical dynamic range compression methods are developed to help to display HDR image for better perception. HDR images are processed to fit into a low dynamic range image by tone mapping operator.

HDR image contains a wide range of lightness. The scene information is recorded in HDR image format. The bilateral filter is always used to process HDR

---

Y. Zhao · X. Li (✉) · J. Jia · Q. Cao  
School of Printing and Packing Engineering, Qilu University of Technology,  
Jinan 250353, China  
e-mail: lixiaozhou2000@163.com

**Fig. 1** Sketch map of tone mapping

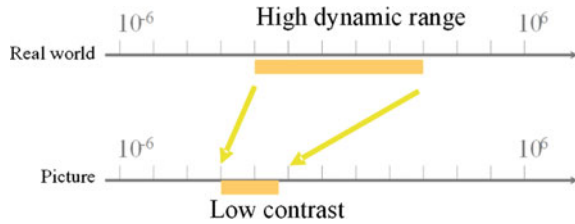


image to get two layers, basic layer and detail layer. However, the problems of gradient reversal artifacts or halo appearing on salient edges can't be solved well. In order to gain better visual perception and output effect, multiple bilateral filtering was developed to optimize and adjust HDR image. The tone mapped image could be better perceived with less halo phenomenon and more detail features. HDR image records the lightness values of the actual scene far beyond 256 levels. It can't be displayed directly using linear decoding technique which leads to some areas too bright or dim. The tone difference between HDR and LDR is shown in Fig. 1.

## 2 Bilateral Filtering

The bilateral filter is a kind of smoothing filter which is nonlinear and non iterative with preserving edge [3]. It contains two Gauss kernel functions. One is the weighted average of similar pixels in the neighborhood space. The other is the weighted average of the pixels close to the pixel value.

The original image model with Gaussian noise can be described as follows:

$$h(i, j) = f(i, j) + n(i, j) \tag{2.1}$$

where  $f(i, j)$  denotes the free noise image,  $n(i, j)$  is subject to Gauss distribution.  $h(i, j)$  is the image with noise. The noise  $n(i, j)$  of the image  $h(i, j)$  needs to be filtered and degraded.

HDR image can be decomposed into two layers, base layer and detail layer, using special technique, e.g., bilateral filter, Gaussian filter [4, 5]. Bilateral filter was used to process the original image. The image was processed as follows:

$$F(i, j) = \frac{\sum_{(i, j) \in s(x, y)} w(i, j) h(i, j)}{\sum_{(i, j) \in s(x, y)} w(i, j)} \tag{2.2}$$

where,  $s(x, y)$  represents the mask of the center point  $(i, j)$  whose size is  $N \times N$ .  $(i, j)$  is involved in filtering the pixel point,  $h(i, j)$  is the value of  $(i, j)$ . Each pixel in the field of  $(x, y)$  is made up of two parts as follows:

$$w_s(i, j) = e^{-\frac{|i-x|^2 + |j-y|^2}{2\delta_s^2}}, \quad w_r(i, j) = e^{-\frac{|h(i, j) - h(x, y)|^2}{2\delta_r^2}} \quad (2.3)$$

where,  $w_s(i, j)$  and  $w_r(i, j)$  represent the Gaussian function of pixel value correlation and the Euclidean distance correlation between the pixel at position  $(i, j)$  and the center pixel at position  $(x, y)$ , respectively.  $\delta_s^2$  is the standard deviation from the center pixel in spatial, and  $\delta_r^2$  indicates color difference between the pixels positioned with mask and the center pixel [6]. If the distance between the  $(i, j)$  point and the center pixel is increased, the spatial proximity factor  $w_s(i, j)$  will decrease. If the color difference between the  $(i, j)$  and the center pixel intensity is increased, the similarity factor  $w_r(i, j)$  will decrease [7]. When the  $\delta_s^2$  becomes larger, the number of pixels participating in the weighted number will make the image more blurry, while the edge will be protected due to  $\delta_r^2$  [8]. Multiple bilateral filtering to HDR image was developed and the work flow to reproduce HDR image was designed as shown in Fig. 2.

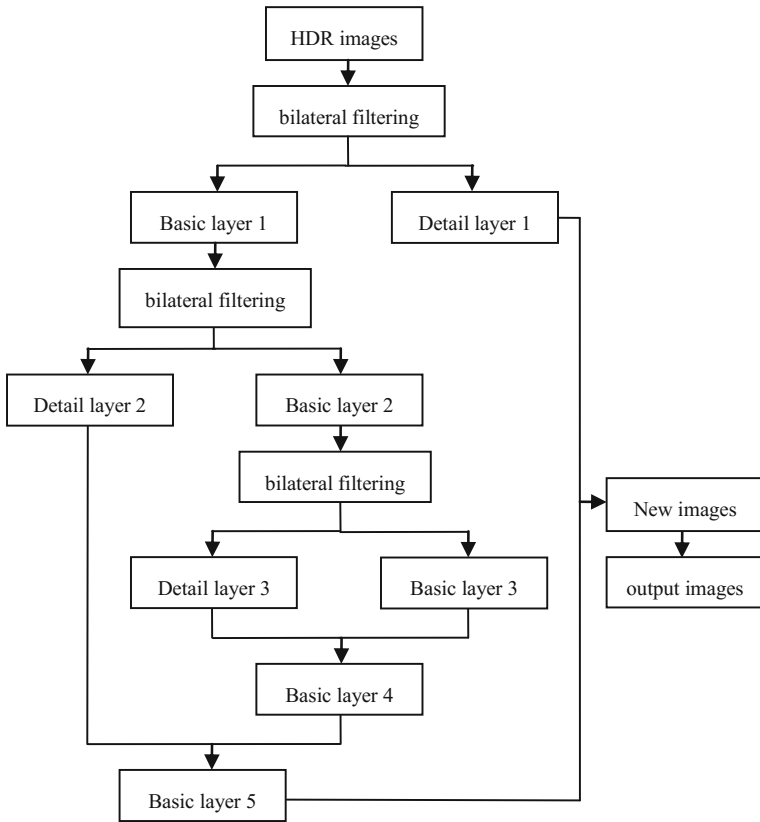
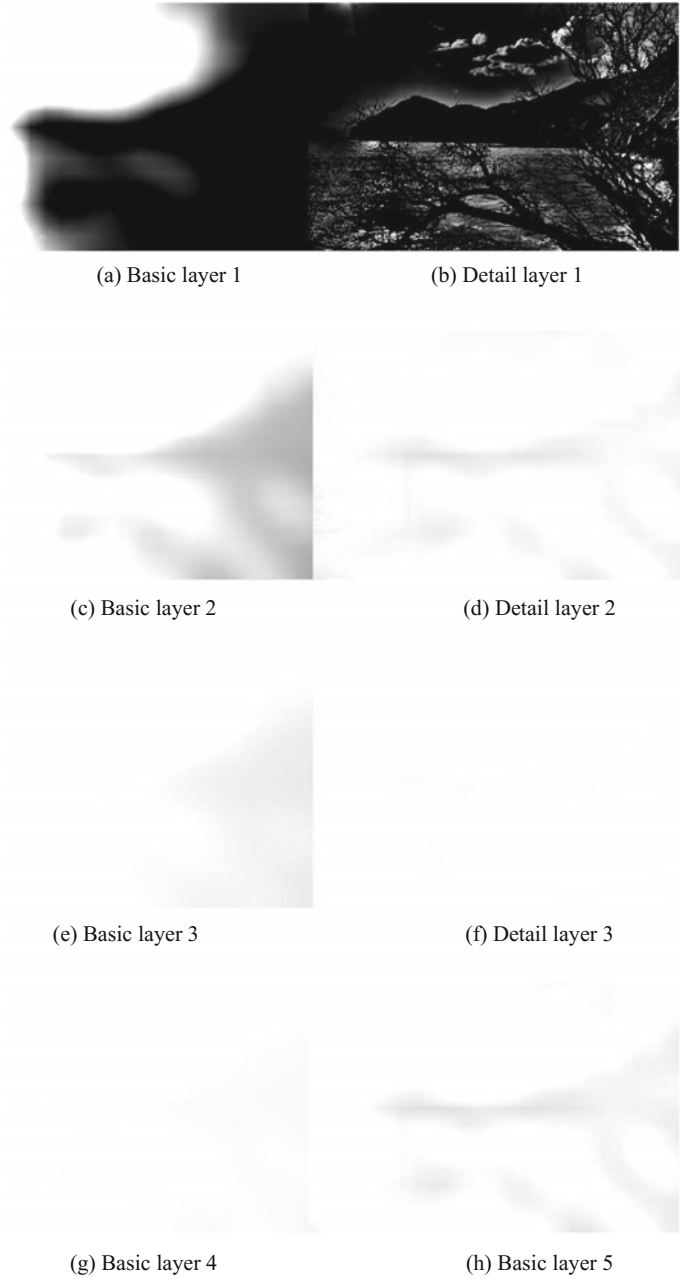


Fig. 2 Flowchart of the proposed tone mapping algorithm



**Fig. 3** Images processed by bilateral filter

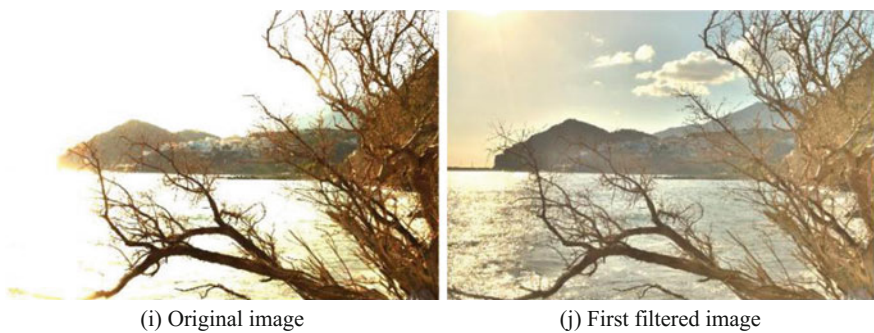
### 3 Experimental Results and Analysis

Firstly, the image was decomposed into basic and detail layer. The brightness compression was carried out on the basic layer. The edge of detail layer was remained. Then the basic layer was continued to divide into two layers by adjusting parameters, and repeated the above steps for the third time filter. The images of basic layer and detail layer were shown in Fig. 3. The brightness of the base layer was more and more small, the basic layer 4 and detail layer 3 were closed to the full white images.

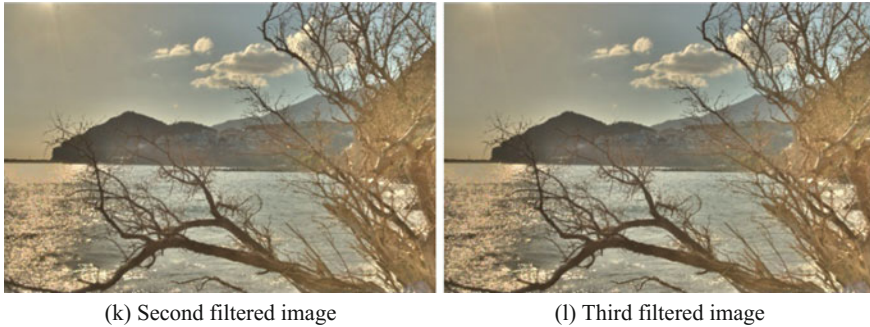
The dynamic range was compressed, and more detail was shown in LDR images, the result of first filtered image was shown in Fig. 4. The HDR image was reproduced by using the workflow developed by KONICAMINOLTA C6000 printer, the whole lightness of the image processed by bilateral filtering was compressed according to the tone relations of HDR image and LDR medium obviously in the first step. The mapped image is softer. The sun and clouds could be displayed with more detail.

The transition part from light area to shadow area was blurred and the detail was not clear. The image was performed for a second time, it showed that the sense of hierarchy was more obvious and the detail information was preserved more. The whole lightness was compressed excessively in the third time, and it achieved the best visual effect. The experimental results were shown in Fig. 5.

Consequently, bilateral filter was used three times in the process for HDR reproduction. And better perception and reproduction on paper medium could be implemented by digital printing. In the third time filtering process obviously and the detail of the sun and cloud area was improved. For the three time filtering process, the detail of the tree was more preserved and the whole perception was better.



**Fig. 4** Images processed by bilateral filter



**Fig. 5** Images processed for different frequencies

## 4 Conclusions

HDR Image was represented on paper medium using digital printing in this work. Multiple bilateral filtering was used to process the original HDR images. And the filter was used three time to get better perception and more detail preservation. It showed that HDR image processed based on multiple bilateral filtering could be represented on paper medium with better perception and preserve more detail information.

**Acknowledgements** This work was financially supported by Shandong Province Science and Technology Development Project (Grant No. 2012YD07016), Shandong Province Outstanding Young Scientists Research Award Fund (BS2014DX020), Ji'nan City Colleges and Universities Independent Innovation Project (Grant No. 201311032), and the International Cooperation Program for Key Professors of 2014 by Shandong Provincial Education Department, P.R. China.

## References

1. Kede Ma, Hojatollah Yeganeh, Kai Zeng, Zhou Wang. (2015). High Dynamic Range Image Compression by Optimizing Tone Mapped Image Quality Index. *IEEE TRANSACTIONSON IMAGE PROCESSING*, 24(10), 3086–3096.
2. JunFeng LI. (2013). Rapid implementation of bilateral filtering algorithm and its application in image processing. *Southern Medical University*.
3. CTomasi, R. Manduchi. (1998). Bilateral filtering for gray and color images. *Proceeding of IEEE International Conference on Computer Vision*, 836–846.
4. Jinsheng Xiao, Wenhao Li, Guoxiong Liu, Shih-Lung. (2014). Shaw; Yongqin Zhang. Hierarchical tone mapping based on image colour appearance model. *Computer Vision*, 8 (4),358–364.
5. Yongqin ZHANG, Ding YU, Jiaying LIU, Zongming GUO. (2013). Guided image filtering using signal subspace projection. *IET Image Processing*, 7(3), 270–279.

6. Jinsheng XIAO, Wenhao LI, Guoxiong LIU, Shih-LungShaw, Yongqin ZHANG. (2014). Hierarchical tone mapping based on image colour appearance model. *Computer Vision IET*, 8 (4), 358–364.
7. Ming JIN, Jianzhong SOGN. (2004). An adaptive bilateral filtering method for image. *Optoelectronic Component*, 31(7), 65–68.
8. HongXiao CHEN. (2012). Bilateral filtering algorithm based on similarity judgment. *Computer Engineering*, 38(22), 183–185.



# BOF Image/Video Retrieval Model with Global Feature

Mingzhu Zhang, Kaiyang Liao, Congjun Cao, Fan Zhao and Yuanlin Zheng

**Abstract** Local interest points serve as an elementary building block in many video retrieval algorithms, and most of them exploit the local volume features using a Bag of Features (BOF) representation. Such representation, however, ignores potentially valuable information about the global distribution of interest points. In this paper, we first present an R feature to capture the detailed global geometrical distribution of interest points. Then, we propose a fusion strategy to combine the BOF representation with the global R feature for further improving recognition accuracy. Convincing experimental results on several publicly available datasets demonstrate that the proposed approach outperforms the state-of-the-art approaches in video retrieval.

**Keywords** Video retrieval · BOF indexing method · Similarity search

## 1 Introduction

With the rapid development of the communication techniques, video editing softwares and video capture devices, the number of online videos is growing exponentially. It has been shown that there are a large number of near duplicate videos (NDVs) on internet [1]. The appearance of substantial NDVs imposes strong demand for effective near duplicate video retrieval on many new applications such as video result re-ranking, copyright enforcement.

In recent years, many research efforts have been made on NDVR. Most of the existing methods usually make use of the local features for NDVR [2]. Typically,

---

K. Liao (✉) · C. Cao · F. Zhao · Y. Zheng  
Faculty of Printing, Packaging Engineering and Digital Media Technology,  
Xi'an University of Technology, Xi'an, China  
e-mail: liaokaiyang@xaut.edu.cn

M. Zhang  
Department of Public Courses, Xi'an Fanyi University, Xi'an, China  
e-mail: mingzhusee@163.com

both temporal and spatial information are used to evaluate the similarity between two videos [1]. There are also some existing methods summarizing the whole video clip with a single and global feature to achieve real-time retrieval, but they are generally not effective in representing long time videos. A recent survey on near duplicate video retrieval can be found in paper [3].

Intuitively, the multiple features can complementary to each other, for each of the multiple features of video clips reflects the specific information of video data. At the same time, utilizing the multiple features is useful for disambiguation. So, it is particularly important to make use of multiple features for NDVR.

How to build efficient indexing structures to promote fast search over large scale video datasets is very important for online NDVR, which demands a real-time response. In order to deal with large video datasets, most of the recent video search systems are built upon the Bag of Features representation, which is introduced in the context of video search in paper [4]. Note that this approach would somewhat decrease the performance, because it is an approximation to the direct matching of individual descriptors. Moreover, most BOFs based representations ignore the global information of the interest points.

In this paper, we firstly propose a novel method to extract global features from the location information of interest points. We then make the distance between visual word frequency vectors more significant by using a more informative representation. We add IR features to the BOF model, which are compared with the Euclidean distance, resulting of an IR feature Embedding (IRE) of the SIFT descriptors. The IR feature captures the global location information, while the BOF representation encodes the discrimination ability of local features. So, these two features naturally complement to each other. To summarize, the proposed method combines two different characteristics and captures the underlying related information from videos.

## 2 IR Transform on Local Interest Points

The definition of image's Radon transform is determined by a set of image projections along lines taken from different angles. In this way, each nonzero pixel point on a discrete binary image is projected into a Radon matrix.

Let  $f(x, y)$  be an image, the Radon transform is:

$$T_{Rf}(\rho, \theta) = \int_{-\infty}^{\infty} \int_{-\infty}^{\infty} f(x, y) \delta(x \cos \theta + y \sin \theta - \rho) dx dy \quad (1)$$

where  $\delta(\cdot)$  is the Dirac delta function (if  $x = 0$ ,  $\delta(x) = 1$ , else  $\delta(x) = 0$ ),  $\theta \in [0, \pi)$  and  $\rho \in (-\infty, \infty)$ . That is to say,  $T_{Rf}$  is the integral of  $f(x, y)$  over the line  $L(\rho, \theta)$  defined by  $\rho = x \cos \theta + y \sin \theta$ .

If a given image is scaled, translated, and rotated, it is difficult to recover all the parameters of the transformations from the Radon matrices. In this paper, we propose an adaptation of the Radon transform to overcome the above problem.

Let the Improved Radon Transform, called IR-transform, be:

$$IR_f(\theta) = \int_{-\infty}^{\infty} T_{R'}^2(\rho, \theta) d\rho \quad (2)$$

where  $T_{R'}$  is the Radon transform of  $f(x, y)$ .

To summarize, the IR-transform is invariant under scaling and translation if the transform is normalized by a scaling factor (in this paper, we set the area of the IR-transform). A rotation of the image results in a translation of the transform modulo  $\theta$ . We can see that only the rotation transform modify the function. Let a single point image with the coordinate  $(x_0, y_0)$  be:  $I(x, y) = \delta(x - x_0)\delta(y - y_0)$ . According to the definition, the Radon transform is:  $T_{R'}(\rho, \theta) = \delta(\rho - x_0 \cos \theta - y_0 \sin \theta)$ .

### 3 IR Feature Embedded BOF for Video Retrieval

We use two types of features to represent each video sequence: the BOF representation of the local features and the global IR feature. We first employ the Harris affine detector to detect the local interest point for a given video. Afterward, we use the SIFT descriptor to describe the detected interest points. So, a video  $V$  can be denoted as  $(x_i, \alpha_i)$ ,  $1 \leq i \leq N$ , where  $N$  is the total number of interest points detected in the video,  $\alpha_i$  is the SIFT descriptor feature of the  $i$ th detected interest point, and  $x_i$  is the position vector.

Subsequently, two different types of features are extracted to characterize each video. The first is the BOF based representation, which uses the SIFT descriptor feature  $\alpha_i$  of each interest point. The second is the global IR feature, which only uses the position feature  $x_i$ . The minimal window that contains all the interest points extracted from a video frame can be regarded as a 2D model. On this 2D model, the binary function  $f(X)$  is defined as following:

$$f(X) = \begin{cases} 1 & \text{if interest point } X \subset D \\ 0 & \text{otherwise} \end{cases} \quad (3)$$

where  $X = (x, y)$  is the position of each interest point in the 2D model. The positions of interest points detected in a frame are denoted as  $\{(x_j, y_j)\}_{j=1}^J$ , where  $J$  is the total number of interest points in the frame. By Eqs. (1) and (2), IR-transform of the frame is given by:

$$\begin{aligned}
IR_f(\theta) &= \int_{\rho} T_f^2(\rho, \theta) d\rho \\
&= \int_{\rho} \left[ \sum_{j=1}^J f(x_j, y_j) \delta(x_j \cos \theta + y_j \sin \theta - \rho) \right]^2 d\rho
\end{aligned} \tag{4}$$

Afterwards, to achieve the robustness of rotation, we normalize the IR transform to get the rotation invariance by:

$$IR'_f(\theta) = \frac{IR_f(\theta)}{\max_{\theta} \{IR_f(\theta)\}} \tag{5}$$

For convenience, henceforward we use  $IR_f(\theta)$  to represent the normalized IR-transform. In the following, we present an approach that combines the advantages of a fine quantizer with those of a coarse quantizer. The main idea is refining the quantized index  $q(x_i)$  with a db-dimensional global spatial feature which encodes the location of the local interest point within the Voronoi cell.

It is designed that the distance between two features  $x$  and  $y$  lying in the same cell reflects the Euclidean distance  $d(x, y)$  is small. So that the distance of IR feature's between a descriptor and its NNs in the Euclidean space is also small. At this point, a descriptor is represented by  $q(x)$  and  $b(x)$ ,  $q$  is a quantizer and  $b$  is the IR feature. We can now define the IRE matching function as

$$f_{IRE}(x, y) = \begin{cases} (tf - idf(q(x)))^2 & \text{if } q(x) = q(y) \\ & \text{and } d(b(x), b(y)) \leq h_t \\ 0 & \text{otherwise} \end{cases} \tag{6}$$

where  $d$  is the Euclidean distance and  $h_t$  is a fixed threshold. Quantizer can be set sufficiently high to ensure that  $x$  and its NNs match, and  $h_t$  can be set sufficiently low to filter many improper points that lie in a same Voronoi cell.

## 4 Experiments

The proposed method is evaluated through comprehensive experiments on two datasets, including CC\_WEB\_VIDEO and MUSCLE VCD 2007. Our experiments are conducted on a Dell desktop computer under Windows 10 64 bits OS with I7 3.4 GHz CPU and 16 GB RAM.

To evaluate NDVR accuracy and efficiency, we present an extensive comparison of the proposed method G-BOF with a set of existing NDVR methods, BOF [5], BOF + HE [6], MFH [7], G-MFH [8], FF [9] and TBOW [10].

### 4.1 Parameter Evaluation of the IR Feature

Parameters  $\theta$  is sampled in the range of  $[0, 180]$ . Figure 1 shows the experimental results of seven different numbers of samples for  $\theta$ . It demonstrates that IR-transform feature has a good description ability and the  $(2D)^2$ PCA further improves the discriminating ability of the IR-transform feature. We set  $(\theta) = [1:10:180]$  in all other experiments on both datasets, and utilize  $(2D)^2$ PCA on IR-transform as the final IR feature. The final IR feature is an  $8 \times 8$  matrix.

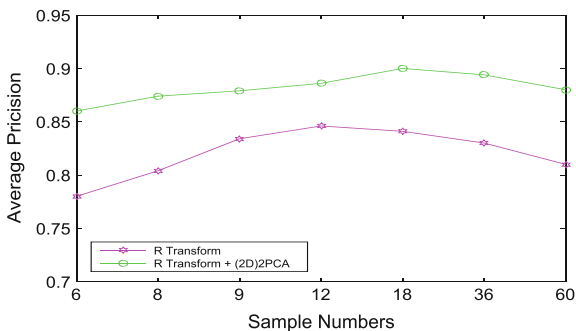
### 4.2 Parameter Evaluation of the Feature Fusion

We evaluate the fusion method on the MUSCLE VCD 2007 dataset. The IR feature can be used for building codebook and the local feature for embedding to BOF, referred to as ‘RBOF + LE’. Alternatively, the local feature can be used for building codebook and the IR feature for embedding to BOF, which is the proposed method referred to as ‘G-BOF’. Besides, we test single feature based methods. Namely, we employ the single feature (local feature or IR feature) for building codebook, referred to as ‘BOF’ or ‘RBOF’ respectively. The above four experiments are shown in Fig. 2. Moreover, Fig. 2 shows that the IR feature boosts the retrieval performance by 5.79% with respect to the ‘BOF’ averagely.

### 4.3 Experimental Results on Different Datasets

MUSCLE VCD 2007: As illustrated in Fig. 3a, the precision-recall curves of TBOF, BOF + HE, and the proposed G-BOF dominate the curves of BOF, FF, MFH, and G-MFH. As elaborated in Table 1, the proposed G-BOF is efficient than FF, G-MFH and TBOF with the same outstanding MAP. MFH and G-MFH

**Fig. 1** Retrieval average precision obtained with respect to seven different samplings of the parameter  $\theta$



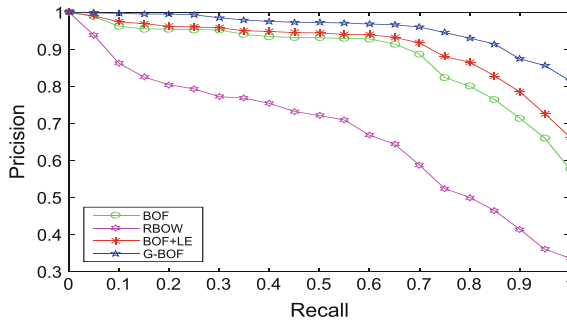


Fig. 2 Evaluate the fusion method on the MUSCLE VCD 2007 dataset

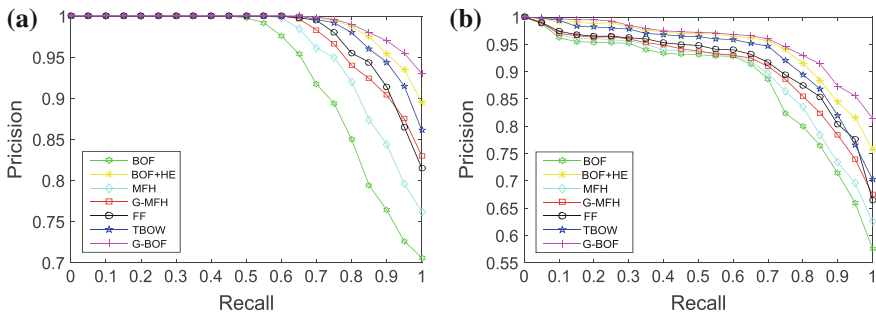


Fig. 3 Precision-recall curves among the proposed G-BOF and the other methods compared on **a** MUSCLE VCD 2007, **b** CC\_WEB\_VIDEO

can also retrieve all the near-duplicate videos efficiently; they are very efficient but not as effective as the proposed G-BOF, since they encode all information of a long video into one hash code. In the evaluation of efficiency, our proposed G-BOF is more efficient than other compared approaches and just next to MFH and BOF.

CC\_WEB\_VIDEO: As shown in Table 1, the MPTs of BOF, MFH and the proposed G-MFH are very closing on CC\_WEB\_VIDEO, showing little performance difference. Figure 3b shows the precision-recall curves of the seven methods on CC\_WEB\_VIDEO, wherein our proposed G-BOF is still the best one. Comparing with the state-of-the-art approaches BOF, FF, BOF + HE, TBOW, MFH, and G-MFH, the proposed G-BOF still achieves the highest MAP, as illustrated in Table 1. G-MFH slightly outperforms MFH in terms of MAP. As shown in Table 1, the MPT of G-BOF takes 62% of that of BOF + HE.

**Table 1** Performance comparison in terms of MAP and MPT among all the methods compared on MUSCLE VCD 2007 and CC\_WEB\_VIDEO

Method	MUSCLE VCD 2007		CC_WEB_VIDEO	
	MAP	MPT	MAP	MPT
BOF [4]	0.891	0.61	0.867	0.89
BOF + HE [6]	1.000	1.24	0.955	1.67
MFH [7]	0.948	0.64	0.933	0.95
G-MFH [8]	0.956	0.82	0.942	1.18
FF [9]	0.978	1.75	0.953	1.97
TBOW [10]	0.986	1.86	0.954	2.15
G-BOF	1.000	0.73	0.968	1.04

## 5 Conclusions

In this paper we propose a new NDVR framework based on IR features embedded BOF. In order to capture the global geometrical distribution information, we first presented a new holistic video representation, the 2D IR-transform on local interest points. We then proposed a new fusion strategy (IR features embedded BOF) to combine the global IR feature and the local feature for NDVR. Convincing experimental results on several publicly available datasets demonstrate that the proposed approach outperforms the state-of-the-art approaches in near duplicate video retrieval.

**Acknowledgements** This work is supported by the National Natural Science Foundation of China Project No. 61671376, 11272253 and Natural Science Foundation of Shaanxi Province No. 2016JM6022.

## References

1. Chou, C.-L., H.-T. Chen, and S.-Y. Lee, *Pattern-Based Near-Duplicate Video Retrieval and Localization on Web-Scale Videos*. Ieee Transactions on Multimedia, 2015. **17**(3): p. 382–395.
2. Fernandez-Beltran, R. and F. Pla, *Latent topics-based relevance feedback for video retrieval*. Pattern Recognition, 2016. **51**: p. 72–84.
3. Liu, J., et al., *Near-Duplicate Video Retrieval: Current Research and Future Trends*. Acm Computing Surveys, 2013. **45**(4).
4. Sivic, J. and A. Zisserman, *Efficient Visual Search of Videos Cast as Text Retrieval*. Ieee Transactions on Pattern Analysis and Machine Intelligence, 2009. **31**(4): p. 591–606.
5. Sivic, J. and A. Zisserman, *Video Google: a text retrieval approach to object matching in videos*. Proceedings Ninth IEEE International Conference on Computer Vision, 2003: p. 1470–7 vol. 2.
6. Douze, M., H. Jegou, and C. Schmid, *An Image-Based Approach to Video Copy Detection With Spatio-Temporal Post-Filtering*. Ieee Transactions on Multimedia, 2010. **12**(4): p. 257–266.

7. Song, J., et al. *Multiple feature hashing for real-time large scale near-duplicate video retrieval*. in *MM'11 - Proceedings of the 2011 ACM Multimedia Conference and Co-Located Workshops*. 2011.
8. Song, J., et al., *Effective Multiple Feature Hashing for Large-Scale Near-Duplicate Video Retrieval*. *Ieee Transactions on Multimedia*, 2013. **15**(8): p. 1997–2008.
9. Wei, S., et al., *Frame fusion for video copy detection*. *Circuits and Systems for Video Technology*, *IEEE Transactions on*, 2011. **21**(1): p. 15–28.
10. Min, H., et al. *Video Copy Detection Using Inclined Video Tomography and Bag-of-Visual-Words*. in *Multimedia and Expo (ICME), 2012 IEEE International Conference on*. 2012. IEEE.



# Applications of Personalized QR Code on Packaging Design

Xianjing Bao, Yunfei Zhong, Pengcheng Su and Ruoqing Wang

**Abstract** As the aesthetic value of man is rising, how to use QR code in an effective and attractive way has become an important issue in the process of packaging design. This paper is to satisfy QR code information storage, as well as to carry the QR code principle on thorough research under the premise of normal reading so as to find the QR code design constraint. And then, this paper is divided to recognition level and layer information level, combine QR code with packaging design to form new QR code. In the analysis and comparison of the existing design method of QR code, the target graphics of this method can be organically combined with data graphics. It will create more harmonious and more personalized visual effect of QR code, making the packaging design unique and promoting corporate image.

**Keywords** QR code · Personalized design · Vision communication · Packaging design

## 1 Introduction

QR code as a convenient way of graphical information has been widely used in various fields. However, most of the QR code is alike black and white, square modeling; single style, lack of personality. It is difficult to appeal the audience on vision [1, 2].

Gong [3] proposed a designer oriented QR code innovation personalized design method, namely, ‘Eight ninth’ reengineering design method, create a more harmonious, more individual barcodes and visual effect. Garateguy [4] take into consideration the improvement of visual appearance and the maximization of decoding robustness, presented allows to automatically embedding QR codes into

---

X. Bao · Y. Zhong (✉) · P. Su · R. Wang  
School of Packaging and Materials Engineering, Hunan University of Technology,  
Zhuzhou, China  
e-mail: maczone@163.com

color, grayscale or binary images with bounded probability of detection error and minimal intervention of the user. Chu [5] presented an automatic algorithm to create a new type of visual QR code, which combines halftone images with QR codes in order to improve QR code’s visual effect. Chen [6] designed a generation and recognition method of color QR code base on Zxing, which used 2k kinds of binary combination to encode date information, corresponding to k types of encoding colors which could be arbitrarily selected. Xie [7] put forward applied cryptographic QR code to the packaging of goods from counterfeit perspective, QR code paste or spray based on digital printing way to the correspondence product packaging as ‘one product one code’, enhanced QR code’s functionality.

This paper proposed a product’s visual design oriented QR code personalized design method, separated from recognition level and layer information level. Also, the methodology of emotional design is used in the research of individual design, so that the target graphics can be organically combined with data graphics; create a more harmonious, more individual visual effect of QR code.

## 2 QR Code Structure

QR codes are composed of a series of small square module; use the depth of the module’s color to represent data (Fig. 1). Dark module represent 1, light module represent 0. The function of the QR code graphics area, including finder patterns, separator, positioning graphics and correction is not used for data coding; Coding region includes data code word, error correction code word, version information and format information [8, 9].

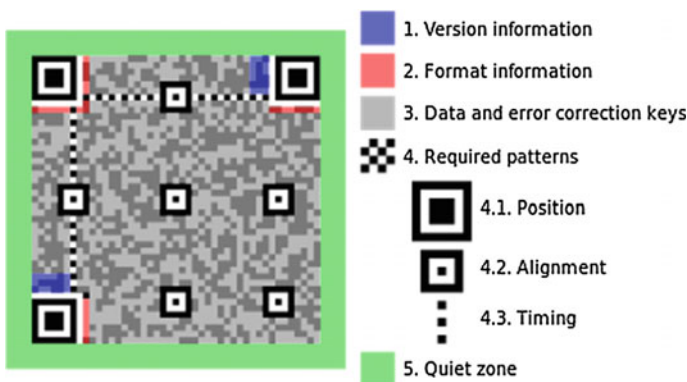


Fig. 1 QR code regions with the location, of each functional pattern highlighted in color

### 3 Personalized QR Code Design and Application in Packaging

QR codes have found great applicability since an effective way was provided to measure the impact and reach publicity campaigns. Each scan of code can be used to trace back the location, date and time in which a particular user expressed interest in the products. Therefore, it allows an accurate mapping and an impact of the evaluation campaign.

#### 3.1 Recognition Level

##### 3.1.1 Finder Graphic Design

- (1) Choose maximum and minimum values of the image reflectance to take the median, then the threshold is determined. The threshold value is used to convert the image into a series of dark and light color pixels.
- (2) Finder patterns. Finder graphic in QR code is composed of the three corners of the symbols, of which is the three detection graphics in the same position. Each position's detection graphics module consists of a dark-light-dark order, and the ratio of the relative width of each element is 1:1:3:1:1, as shown in Fig. 2. For this decoding algorithm, the allowable deviation of each element width is 0.5 (namely that the size of a single module block allows the range of 0.5–1.5, the width of the square in the three modules allows the size range of 2.5–3.5).

It is assumed that detection position pattern as ‘cross’, namely that only keep the X axis and Y axis of the pixel which through the center of the position detection graphics (left of Fig. 3). Test results show that with this ‘cross’ position detection graphic, QR code can be identified by the absence of rotation Angle. Therefore,

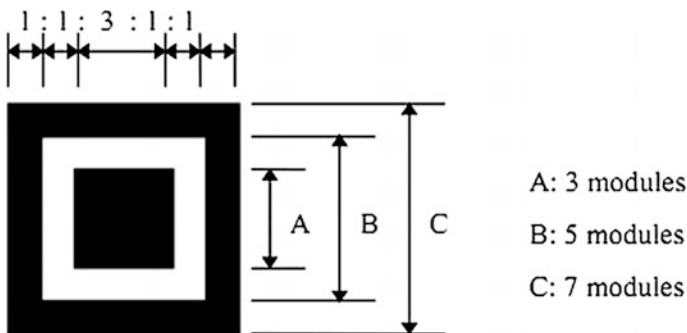
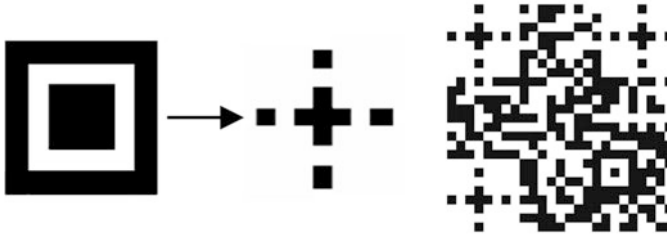
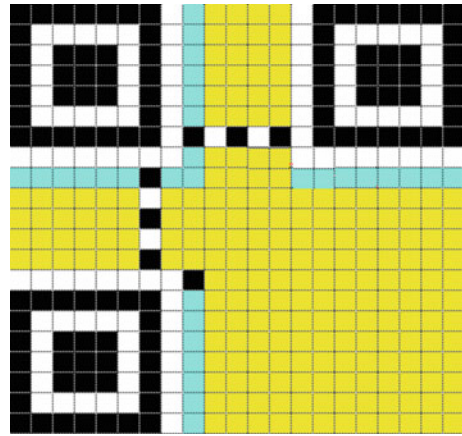



Fig. 2 Position detection graphics module



**Fig. 3** Position detection image assumption (*left*); QR codes in expectation (*right*)

**Fig. 4** *Yellow* area is used to store the encoded data content and correct the error information code; *blue* area is used to identify the level of error correction (Color figure online)



when the detecting graphics only under the premise of keeping the cross, the designer can do ‘additive’ design on the minimized position detection graphics according to package characteristics, rather than the traditional QR code which is limited to the “” pattern, as shown in right of Fig. 3.

### 3.1.2 Data Graphic Design

As the result of QR code powerful error correction ability (Fig. 4), under the condition of the maximum fault-tolerant coding mechanism, embedded some design elements related to products, consistent with company VI or some have adornment effect. These graphic design as long as within the scope of the fault-tolerant control, will not affect the normal recognition of QR code.

Figure 5 is based on the principle of decoding the QR code, using fault tolerance rate, do personalized design for a QR code generated by 30% fault-tolerant. First, ensure that the area of the cover design is within 30% of the QR code coding regions. Second, on the position, put away from the function graphic and version information area of the QR code.



Fig. 5 QR code using fault-tolerant rate

### 3.2 Information Level

QR code on the product packaging as a important entrance connecting users and merchants, once it has the property of the visual communication. Therefore, QR code of visual design and content communication should have a close correlation of the theme, personalized design according to different subjects, different activities and different environment.

The points in the design of topic relevance expression level can be summarized as the following aspects:

- (1) Take the commodity's own image as the main image.
- (2) Take the brand logo, trademark, or corporate mark as the main image. It is often happening to those who have had greater awareness in the market, as long as further strengthening which can be easily accepted by consumers.
- (3) Emphasize the characteristics of the commodity itself as the main image. Such as milk can be emphasize about its pure and fresh.
- (4) Take the products or raw material as the main image. Such as "Mengniu" milk brand to Mongolia grassland.
- (5) Take the using object as the main image. Such as children's milk powder packaging can use children as the main image.
- (6) Take common animals, plants, flowers, etc. in daily life as the main image.
- (7) Take the unique color of the products as the main image. Such as tea green, chocolate brown, etc.

### 3.3 Application in Packaging

Because of the addition of color information, Personalized QR code ensures that the color information of bar-code printing can produce detecting process as well as promote feeling of reading, show Fig. 6.



**Fig. 6** Guinness personalized QR cup

## 4 Conclusions

Based on the personalized features of packing product itself, QR code has more breakthroughs. The packaging orientation, product packaging should be used reasonably to combine with the QR code ‘fusion’ to create new ideas. Data graphics and design graphics should be united for a harmonious visual effect. However, some work has not been done, such as dynamic, emotional interactive personalized QR codes, variable data personalized QR code, personalized QR code with anti-fake function, etc. For the QR code display and the application in packaging design, it will be a great degree of improvement.

Along with the development of the mobile Internet and intelligent terminal, QR codes will have great development prospects. Therefore, the personalized design of QR codes will be improved by the changing demand of packaging.

**Acknowledgements** Project is supported by College Students Research Learning and Innovative Experiment Plan Project of Hunan University of Technology (Grant No. [2015]), Natural Science Foundation of Hunan Province (Grant No. 2016JJ6034 and 14JJ4057), Training Project of Hunan Industrial Application of Higher Education Institutions (Grant No. 15CY003), Hunan Province Higher Education Institutions Demonstration Base of Production, Education and Research (Grant No. 2014-117).

## References

1. Dai Jia. (2007). Individual Design of Product Base on Customer’s Affection Need. A Dissertation Submitted to Shanghai Jiao Tong University for Master Degree, 17–29.
2. Lo Hui Yi. (2014). Quick Respond Codes around us: Personality Traits, Attitudes toward Innovation, and Acceptance. *Journal of Electronic Commerce Research*. VOL 15, NO 1:225–38.

3. Gong Xue. (2014). Research on Individualized Design and Application of QR Codes. A Dissertation Submitted to Beijing University of Technology for Master Degree, 30–41.
4. Gonzalo J. Garateguy. (2014). Optimal Embedding of QR Codes into Color, Grayscale and Binary Images. ProQuest LLC. UMI Number: 3617881, 22–40.
5. Chu Hungkuo, Chang Chiasheng, Lee Ruenrone, Niloy J. Mitra. (2013). Halftone QR Codes. Transactions on Graphics(TOG). ACM Transactions on Graphics, Vol. 32, No. 6, Article 217.
6. Chen Yuanzhi, Deng Yan, Shi Shaoliang, Jiang Wenying. (2016). Generation and Recognition Method of QR Codes Base on ZXing. Journal of Guilin University of Electronic Technology. VOL 36, NO 4:333–337.
7. XIE Long, DU Yanping, CHENG Mingzhi, YANG Yixian, LI Jing. (2013). Packaging of Goods Anti-counterfeiting Technology Research Based on Encrypted QR Code. Journal of Beijing Institute of Graphic Communication. Vol. 21 No. 4:16–20.
8. Liu Ningzhong, Yang Jingyu. (2007). The three dimensional bar code coding theory and design. Journal of computers, 30 (4), 686–692.
9. Niu Wanghong, Yan Huiqin, Ge Yongbing. (2015). A Colored QR Code Design Principle and Encoding-Decoding Implementation. Transactions of Beijing Institute of Technology. Vol. 35 No. 10:1067–1073.

# Research on Augmented Reality of Printed Matter Based on Random Ferns and Orientation Gradient with Integral Graph

Da Li, Ruizhi Shi, Xuhui Zhao and Hui Ye

**Abstract** Though random ferns is a fast and robust method among the current feature matching algorithms, its way to build local binary feature through comparing single pixel's gray value is not stable with respect to noise, rotation, view variety or illumination changes. Orientation gradient descriptor is more robust than gray level, but the traditional histogram of orientation gradient descriptor is a little complicated and time consuming. This article used an orientation gradient descriptor combined with integral graph to improve the process in random ferns. The experimental results showed that the orientation gradient descriptor with integral graph effectively improved random ferns' matching accuracy while retain the efficiency advantage.

**Keywords** Random ferns · Orientation gradient · Integral graph · Augmented reality

## 1 Introduction

In recent years, with the popularity of smart phones and tablet PCs, people have more ways to get information quickly. New digital media, such as audio, video and animation, have become more and more popular because of their dynamic and realistic expressive effect; however, the traditional prints have single expression way through static text or pictures, which can't meet the needs of people to obtain diversified information [1]. Therefore, how to combine the traditional printed materials with the new electronic media so that the printed information can be represented by new digital media has gradually become a new research direction.

To establish the links between traditional prints and the new digital media, image recognition, which play a vital role in this process, can affect the final realization effect directly. The traditional recognition technology, such as two-dimensional

---

D. Li (✉) · R. Shi · X. Zhao · H. Ye  
Zhengzhou Institute of Surveying and Mapping, Zhengzhou, China  
e-mail: lld2013@sina.com



code and the special mark, needs to attach the special mark on the prints, having obvious influence to the prints' appearance. However, the feature matching algorithms based on natural feature points don't need any marker so it's more concise and flexible. SIFT [2] and SURF [3] algorithm have high feature matching accuracy, but the calculation process is complex so they cannot meet the real-time requirements. Comparing with other algorithms, BRIEF [4], ORB and FREAK have better efficiency, but their matching accuracy is not very well [5]. In 2010, Ozuysal proposed the random ferns algorithm [6] using naive Bays model and constructing non-hierarchical structure of random ferns to transform the feature matching problem for classification problems. Therefore, the time-consuming process can be finished in the offline training process, which greatly accelerates the speed of the random ferns algorithm. Random ferns have better performance in terms of robustness and accuracy, but under the condition of complex background, it still has many false matches. The way through comparing single pixel's gray value to constructed feature descriptor of local image is not well-stable for noise and deformation, so it has big influence on random ferns' matching performance. In view of the excellent robustness and fast computing speed of orientation gradient with integral graph, this paper applied it to random ferns algorithm to improve its matching accuracy, so it can better meet the accuracy demand in the augmented reality application for printed matter.

## 2 Random Ferns

Random ferns train the classifier matching features based on Naive Bayesian model, including two stages of offline training and online matching. The off-line training phase mainly consists of generating training samples, selecting class set, describing the features and calculating the conditional probability of features in each fern. And the online matching stage includes detecting and describing the feature points as well as voting for the matching results. Random ferns' working flow chart is shown in Fig. 1.

### 2.1 *Generating Training Samples*

In order to make the classifier robust to scale change, illumination change and image torsion, random ferns need a lot of sample data to train the classifier. In fact, it's difficult to collect enough sample data, so the algorithm adopts a flexible method generating a large number of images with affine transformation about object to simulate the changes for rotation, scale, illumination and so on. The affine transformation method is shown as Formula 1.

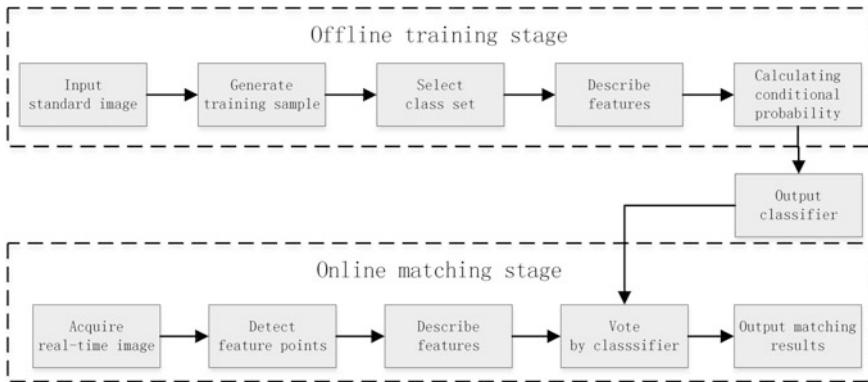


Fig. 1 Random ferns work-flow

$$R = R_{\theta}R_{\phi}diag(\lambda_1, \lambda_2)R_{\phi} \tag{1}$$

$R_{\theta}$  and  $R_{\phi}$  represent rotation matrix,  $\theta$  and  $\phi$  are rotation angle,  $\theta$  values range from 0 to  $\pi$ , and  $\phi$  values range from  $-\pi$  to  $\pi$ ,  $diag[\lambda_1, \lambda_2]$  represents scale variation diagonal matrix,  $\lambda_1$  and  $\lambda_2$  are the parameters for scale change, the range of values about  $\lambda_1$  and  $\lambda_2$  need to be determined according to specific application. Then change the brightness and image noise to make the classifier robust for noise and illumination change.

### 2.2 Build Feature Descriptor

Random ferns build feature descriptor through comparing N pairs of pixels' gray value in the neighborhood of feature points. The descriptor is constructed based on Formula 2.

$$f_i = \begin{cases} 1, & L(d_{j,1}) < L(d_{j,2}) \\ 0, & other \end{cases} \tag{2}$$

$L(d_{(j,1)})$  and  $L(d_{(j,2)})$  represent the gray value of randomly selected pairs of pixels.

### 2.3 Classify Feature Points

Random ferns converted feature matching problem to feature point's classification problem based on Bayesian model. Firstly, the algorithm treats each feature point

on the standard image as a class recorded  $C_i (i = 1, 2, \dots, H)$ ,  $H$  represents the number of chosen feature points on the standard image. The way to determine the category of the feature points is shown as Formula 3.

$$\hat{c}_i = \arg \max_{c_i} P(C = C_i | f_1, f_2, \dots, f_N) \quad (3)$$

We can obtain Formula 4 based on Bayesian formula.

$$P(C = C_i | f_1, f_2, \dots, f_N) = \frac{P(f_1, f_2, \dots, f_N | C = C_i) P(C = C_i)}{P(f_1, f_2, \dots, f_N)} \quad (4)$$

Suppose the priori probability  $P(C = C_i)$  as uniform distribution, the denominator part in Formula 4,  $P(f_1, f_2, \dots, f_N)$  has nothing with the category of feature points, then we can get Formula 5.

$$\hat{c}_i = \arg \max_{c_i} P(f_1, f_2, \dots, f_N | C = C_i) \quad (5)$$

If we classify the feature points according to Formula 5, then each feature point needs to occupy the storage space of  $2^N$  bytes for features with  $N$  dimension. Obviously, the larger parameter  $N$ , the more memory resources waste. Random ferns divided  $N$  dimension features into  $M$  groups, each group containing  $S$  dimension attributes means a fern. Suppose the attributes in the same group are related and each attribute is independent with the other attribute in different group, then we can obtain Formula 6 based on Formula 5.

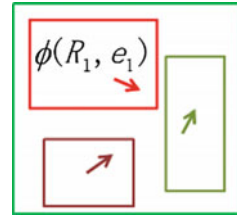
$$\hat{c}_i = \arg \max_{c_i} \prod_{m=1}^M P(F_m | C = C_i) \quad (6)$$

$F_m = \{f_{\sigma(m,1)}, f_{\sigma(m,2)}, \dots, f_{\sigma(m,S)}\}$  ( $m = 1, 2, \dots, M$ ) represents the Fern  $m$ ,  $\sigma(m, j)$  is random function values from 1 to  $N$ . If we classify feature points according to Formula 6, then each feature point will only occupy the storage space of  $M * 2^S$  bytes.

### 3 Orientation Gradients with Integral Graph

Random ferns describe image features through comparing pairs of pixels' gray value that is simple and effective, but not well-stable for image distortion and noise. SIFT algorithm adopted histogram of orientation gradient to describe image features that is highly robust. However, the computing process is complicated and time-consuming. This article uses a way to build descriptor through computing orientation gradient with integral graph [7] which can improve the matching accuracy of random ferns with little influence on the computing speed.

**Fig. 2** Orientation gradient with integral graph



As is shown as Fig. 2, the block area represents the neighborhood of detected feature points, the way to compute each feature attribute can be described as Formula 1.

$$h(R, e, T) = \begin{cases} 1 & \phi_{R,e} \leq T \\ -1 & \text{else} \end{cases} \tag{1}$$

R represents rectangular regions in the neighborhood of detected feature points, and e represents orientation parameter, and T is a threshold parameter.  $\phi_{R,e}$  can be computed by Formulas 2 and 3.

$$\phi_{R,e} = \sum_{m \in R} \xi_e(m) / \sum_{e' \in \phi, m \in R} \xi_{e'}(m) \tag{2}$$

$$\xi_e(m) = \max(0, \cos(e - O(m))) \tag{3}$$

O(m) represents the orientation gradient of pixel m, e represents an orientation parameter valued in a set of  $\phi$ ,  $\phi = \left\{0, \frac{\pi}{q}, \frac{2\pi}{q}, \dots, \frac{(q-1)\pi}{q}\right\}$ , this article set q as 8.

## 4 Experimental Verification

### 4.1 Matching Performance Test

To verify the feasibility of using orientation gradient with integral graph for random ferns, this paper did a comparative experiment choosing Lena as the standard image. In order to have a better expression, we recorded this article’s algorithm and the original random ferns as iferns and ferns separately (Fig. 3).

Be corrected by PROSAC algorithm, the number of retained internal points and running time are shown in Tables 1 and 2 separately.

As is shown in Table 1, the number of retained internal points based on iferns is 25% more than ferns, which proves that iferns has higher matching accuracy so it can better meet the demand of augmented reality application for printed matters. Besides, as is shown from Table 2, the orientation gradient with integral graph has little influence on the computing speed of random ferns so iferns still has good real-time performance.



**Fig. 3** **a** Matching image for scale change (*left* is ferns, *right* is iferns), **b** matching image for illumination change (*left* is ferns, *right* is iferns), **c** matching image for image rotation (*left* is ferns, *right* is iferns), **d** matching image for image distortion (*left* is ferns, *right* is iferns)

**Table 1** The number of internal points

	Scale	Illumination	Rotation	Distortion
Ferns	54	43	35	43
Iferns	67	56	43	53

**Table 2** Running time (ms)

	Scale	Illumination	Rotation	Distortion
Ferns	27.1	24.3	23.2	23.8
Iferns	28.1	24.7	23.5	24.5

**Fig. 4** Augmented reality instance



### 4.2 *Augmented Reality Instance for a Printed Matter*

This paper designed an augmented reality application. The application firstly recognize object image according to iferns algorithm, when the matching points exceeds parameter n, some new media information such as video, audio or animation will be displayed. As shown in Fig. 4, if the matching process is completed successful, a video, which about the print content, will appear on the screen.

## 5 Conclusions

In this paper, we adopted a way to compute orientation gradient with integral graph descriptor to improve random ferns' matching accuracy. Experimental results show that the adopted method can well meet the demand of augmented reality applications for printed matters. The augmented reality application for printed matters can effectively enrich the prints' expressions that is a promising research field, and how to improve the image recognition speed and accuracy will be the further research direction of this paper.

## References

1. Ding, F., Jiang, Z.M. (2014). Human Computer Interaction Design in Mobile Devices [J]. *Packaging Engineering*, 35(16):46–49.
2. Li, D., Shi, R., Li, S., & Zhou, X. (2016). An Improved SIFT Algorithm Based on Invariant Gradient. *Advanced Graphic Communications, Packaging Technology and Materials*. doi:[10.1007/978-981-10-0072-0\\_29](https://doi.org/10.1007/978-981-10-0072-0_29). 369:221–230.
3. Bay, H., Tuytelaars, T., Van, G.L. (2006). Surf: Speeded up robust features [A]. In: *Computer vision—ECCV 2006* [C], 2006:404–417.
4. Calonder, M., Lepetit, V., Ozuysal, M., et al. (2012). BRIEF: computing a local binary descriptor very fast [J]. *Pattern Analysis and Machine Intelligence, IEEE Transactions on*, 34(7):1281–1298.
5. Li, S., & Shi, R. (2016). The Comparison of Two Image Matching Algorithms Based on Real-Time Image Acquisition. *Advanced Graphic Communications, Packaging Technology and Materials*. doi:[10.1007/978-981-10-0072-0\\_31](https://doi.org/10.1007/978-981-10-0072-0_31). 369:241–248.
6. Ozuysal, M., Calonder, M., Lepetit, V., et al. (2010). Fast keypoint recognition using random ferns [J]. *Pattern Analysis and Machine Intelligence, IEEE Transactions on*, 32(3):448–461.
7. Trzcinski, T., Christoudias, M., Lepetit, V. (2015). Learning image descriptors with Boosting [J]. *Pattern Analysis and Machine Intelligence, IEEE Transactions on*, 37(3):597–610.

# BM3D Image Denoising Algorithm Based on K-Means Clustering

Jinru Gao and Qiang Wang

**Abstract** Block-matching and 3D filtering (BM3D) denoising algorithm has a problem of computational burden. In order to minimize the impact of the problem, an improved version of BM3D algorithm which combines BM3D with K-means clustering is proposed. K-means clustering is done to search similar blocks fast and accurate. According to certain similarity measure, image blocks within the same cluster are similar and image blocks from different clusters are dissimilar. The experimental results showed that the proposed modification greatly reduced the computational complexity, improved the execution speed and shortened the time consumption of the algorithm.

**Keywords** Block matching · Denoising · K-means clustering · BM3D

## 1 Introduction

Image denoising is a fundamental task in many applications. Traditional denoising algorithm mainly include two typical methods: Space domain filtering method, Frequency domain filtering method which utilizes the compactness property of signal energy on transform domain. Most successful approaches are based on: Gaussian scale mixtures (GSM) modeling in over-complete multi-scale transform domain; non-local filtering; the transform-based BM3D filter developed by Dabov et al. [1].

While BM3D producing state-of-the-art denoising results, the BM3D filter may introduce certain artifacts and the denoising is not very effective. Many scholars use some methods to improve BM3D, such as shape-adaptive discrete cosine transform (SA-DCT), Shape-Adaptive Principal Component Analysis [2, 3]. However, the complexity of the algorithm is linear with respect to the number of pixels in the input image and the computation time of these methods takes more than the

---

J. Gao (✉) · Q. Wang  
School of Media and Design, Hangzhou Dianzi University, Hangzhou, Zhejiang, China  
e-mail: 283307193@qq.com



original. In order to resolve this problem, an improved version of BM3D algorithm which use k-means clustering effectively reduces the computation time is proposed.

## 2 Block-Matching and 3-D Filtering

Combining the non-local means method with the transform domain filtering method, BM3D is the most recognized method that can achieve rather good results in terms of both objective evaluation and subjective visual. The algorithm consists of three processes: Grouping, Collaborative filtering and Aggregation.

### 2.1 Grouping

The BM3D processes an image in a sliding window manner. First, dividing the image into  $N \times N$ -sized image blocks after moving with a certain step scale from top to bottom, left to right. Then for each block, search for similar blocks within the input image according to certain similarity measure. Last, stacking similar image blocks over each other to form 3-D array.

Two patches are assumed similar if the normalized quadratic distance between blocks less than the distance threshold. The set of similar blocks is simply defined by:

$$K_r = \left\{ j : \|X_j - X_r\|^2 \leq \Delta \right\} \quad (1)$$

where  $K_r$ , the serial number is set of similar patches;  $\Delta > 0$  is the distance threshold for  $d$  under which two patches are assumed similar.

### 2.2 Collaborative Filtering

First, 3-D transform is applied to 3-D array and obtain 3-D coefficients, followed by shrinkage of the transform domain coefficient using thresholding/Wiener filtering. Finally the inverse linear transform is applied to reconstruct corresponding noise-reduced blocks.

The process of collaborative filtering is denoted by:

$$K_{3D} = T_{3D}^{-1}(\gamma(T_{3D}(S_{3D})), \mu_{thr}\sigma\sqrt{2\log_{10}(N^2)}) \quad (2)$$

where  $T_{3D}$  denote 3-D transform  $\sigma$  is the variance of the zero-mean Gaussian noise.  $\mu$  is the threshold coefficient of thresholding/Wiener filtering.  $T_{3D}^{-1}$  denote inverse

3-D linear transform.  $S_{3D}$  denote 3-D array.  $\gamma$  is a thresholding/Wiener filtering operator with threshold  $\mu_{thr}$ . For  $\mu \leq \mu_{thr}$ , one has  $\gamma = 0$ , other coefficients are unchanged.

### 2.3 Aggregation

The denoised image can be constructed by aggregation that all filtered image blocks in the 3-D arrays are scattered back to their original positions in the image with an appropriate weighting of the overlapping blocks [4].

$$K_{3D}(x) = \frac{v(x)}{\delta(x)} = \frac{\sum w_p f_p^{K_{3D}}(x)}{\sum w_p}, \quad (\forall x \in p) \quad (3)$$

where  $v(x)$  designates the numerator part of the estimates of the image.  $f_p^{K_{3D}}(x)$  is the estimate of the value of the pixel  $x$  belonging to the patch  $p$  obtained during collaborative filtering of the reference patch.

$$w_p = \begin{cases} \frac{1}{M_p} & \text{if } M_p \geq 1 \\ 1 & \text{otherwise} \end{cases} \quad (4)$$

$M_p$  is the number of non-zero coefficients in the 3D block after thresholding.

## 3 Optimization of BM3D Using K-Means Clustering

Despite an enormous success in image enhancement and noise removal applications, approaches like the BM3D remain spatially local. There is a common disadvantage with non-local algorithms of high time complexity [5].

### 3.1 Characteristics of BM3D

BM3D algorithm contains two major steps: Basic estimate and final estimate, both two steps are includes: Grouping, Collaborative filtering, Aggregation [6].

This algorithm is based on the assumption that there are exist mutually similar patches within a natural image [7]. Despite the method of searching similar block in the entire image have the benefits of avoiding aliasing, there are problem of time-consuming and low efficiency. Most of time is spent on searching similar blocking, image is bigger, and time is more.

BM3D takes advantage of the similarity inside the image of interest [8]. Enforcing the “energy compaction property” in the 3D arrays enables a sparse representation where most of the energy spectrum could be described by only few high coefficients. Since the remaining small transform coefficients mainly correspond to noise, discarding them by thresholding can effectively denoise corresponding blocks.

### ***3.2 Optimization of BM3D Using K-Means Clustering***

K-means clustering algorithm is a popular partitioning clustering algorithm and its success stems from simplicity and computational efficiency [9]. We can separate data into clustering after giving the initial cluster center and clustering convergence criteria, objects within the same cluster are similar and objects from different clusters are dissimilar according to certain similarity measure.

While producing state-of-the-art denoising results, BM3D is computationally impractical in blocking matching. We must use every block as reference block to finding similar blocks. This yields a computational complexity of  $O(RR s N)$  [10], where  $R$  is the number of blocks in the image horizontally or vertically, and  $N$  is the patch size.  $S(S)$  is the number of similar blocks. For larger images, this complexity is quite a burden. In order to accelerate the algorithm, we introduce K-means clustering algorithm instead of blocking matching to searching for similar blocks in the grouping. First, some image blocks are chosen randomly as initial cluster centers, then assign each image block in the image to the nearest center. Last, centers are recomputed and image blocks are reassigned to the nearest centers until meet the clustering convergence criteria or the number of iterations. After this step, all image blocks are divided into several 3-D arrays directly, which avoid the tedious process that finding similar blocks of the reference block. While other steps are maintained unchanged, this method reduces the computational complexity to  $O(KSN)$ , where  $K$  is the number of clusters. The K-means clustering algorithm allows for a fast and accurate selection of similar image blocks, thereby improve the overall efficiency.

In this paper, all blocks are divided into several clusters by K-means clustering algorithm, image blocks in the same cluster are then stacked together to form a 3-D array. Then the noise is attenuated by shrinkage in a 3D-transform domain with the fact that image blocks within the same 3D array having structural similarity and the redundancy of image. This results in a 3D array of filtered blocks. A denoised image is produced by aggregating the filtered blocks to their original locations using weighted averaging.

### ***3.3 Experimentation and Discussion***

In this section, we compare the K-means clustering algorithm and the BM3D algorithm under time criteria by MATLAB simulation experiment. Comparing the

time spent on the proposed algorithm and BM3D with changed image size and image block size. In all the experimentation we restrict the search of similar windows of size  $40 \times 40$  pixels for computational purposes of the BM3D algorithm.

We performed experiments with three standard image of size  $256 \times 256$  in a sliding-window with size of  $4 \times 4$ ,  $8 \times 8$  and  $16 \times 16$ . Tables 1, 2 and 3 shows that time spent by the proposed algorithm with  $4 \times 4$ ,  $8 \times 8$ ,  $16 \times 16$  sliding-windows are 18.3, 2.4, 4 s separately. The BM3D algorithm with  $4 \times 4$ ,

**Table 1** Computation times of the proposed algorithm and the BM3D algorithm

Picture name ( $256 \times 256$ )	The proposed algorithm	The BM3D algorithm
	Time (s)	Time (s)
House	18.47	58.26
Cameraman	18.32	58.56
Peppers	18.36	56.14
Average time (s)	18.38	57.65

The method were run with  $256 \times 256$  standard test images with  $4 \times 4$  sliding-window

**Table 2** Computation times of the proposed algorithm and the BM3D algorithm

Picture name ( $256 \times 256$ )	The proposed algorithm	BM3D	Picture name ( $512 \times 512$ )	The proposed algorithm	BM3D
	Time (s)	Time (s)		Time (s)	Time (s)
House	2.43	21.39	Lena	21.47	86.18
Cameraman	2.44	21.28	Barbara	21.32	85.76
Peppers	2.46	20.28	Boat	21.34	86.85
Average time	2.44	20.98	Average time	21.38	86.26

The method were run with  $256 \times 256$  and  $512 \times 512$  standard test images with  $8 \times 8$  fixed sliding-window

**Table 3** Computation times of two algorithms

Picture name ( $256 \times 256$ )	The proposed	BM3D	Picture name ( $512 \times 512$ )	The proposed	BM3D
	Time (s)	Time (s)		Time (s)	Time (s)
House	4.05	56.75	Lena	29.84	234.25
Cameraman	4.06	58.56	Barbara	29.70	234.94
Peppers	4.02	56.44	Boat	29.62	236.73
Average time	4.05	57.25	Average time	29.72	235.31

The method were run with  $256 \times 256$  and  $512 \times 512$  standard test images with  $16 \times 16$  fixed sliding-window

$8 \times 8$ ,  $16 \times 16$  sliding-windows are 57.6, 20.9, 57.2 s separately. It can be seen that the proposed algorithm with  $4 \times 4$  sliding-window is 3.1 times faster than the BM3D algorithm, with  $8 \times 8$  sliding-window is 8.6 times faster and with  $16 \times 16$  sliding-window is 14.1 times faster.

Meanwhile, we performed experiments with three standard image of size  $256 \times 256$  and three standard image of size  $512 \times 512$ . Table 2 shows that the average time spent by the proposed algorithm with size of  $256 \times 256$  and  $512 \times 512$  are 2.4, 21.3 s separately. The BM3D algorithm with size of  $256 \times 256$  and  $512 \times 512$  are 20.9, 86.2 s separately. It can be seen that the larger the image, the longer time required. The proposed algorithm with image size of  $256 \times 256$  is 8.6 times faster than the BM3D algorithm, with image size of  $512 \times 512$  is 4.0 times faster. Table 3 shows that the proposed algorithm with image size of  $256 \times 256$  is 14.1 times faster than the BM3D algorithm, with image size of  $512 \times 512$  is 7.92 times faster.

In the simulation experiment, we found that the improvement of the algorithm is limited when the image is become bigger. To verify the impact of image size, three standard image of size  $1024 \times 1024$  is used. With  $8 \times 8$  fixed sliding-window, the proposed algorithm with image size of  $1024 \times 1024$  is 2.25 times faster than the BM3D algorithm. We conclude that the advantage of the proposed algorithm is more obvious for image with size of  $1024 \times 1024$  or less.

In Figs. 1 and 2, we compare the original BM3D algorithm with our proposed modifications and their denoised version is presented. We found that the external appearance of denoising image got from the proposed algorithm and the BM3D algorithm are both well, but the proposed algorithm faster than the BM3D algorithm with changed image size and image block size.

**Fig. 1** Denoised image by the BM3D



**Fig. 2** Denoised image by our algorithm



## 4 Conclusions

In this paper, a new technique to speed up the original BM3D algorithm is proposed. K-means clustering allows for the efficient and sound selection of similar image blocks by means of the same distance measure as used by the filter itself. A direct comparison to the BM3D algorithm with changed image size and image block size has shown that this proposed algorithm is rewarded by favorable results regarding the quality and speedup. As shown by the experimental evaluation, the proposed algorithm is faster than the BM3D algorithm as the size of image block increasing. The proposed algorithm is faster than the BM3D algorithm while time spent by both two algorithms is increase as the size of image increase.

**Acknowledgements** This work is funded by National Key Technology Research and Development Program of the Ministry of Science and Technology of China (2012BAH91F03).

## References

1. Dabov K, et al. (2007). Image Denoising by Sparse 3-D Transform-Domain Collaborative Filtering. *IEEE Transactions on Image Processing*, 16(8): 2080–2095.
2. Urfalioglu IHO. (2015). Improving BM3D on Non-Stationary Gaussian Models for Real Image Noise. *Image Processing Theory, Tools and Applications*.
3. K Dabov. (2008). A nonlocal and shape-adaptive transform-domain collaborative filtering. In *SPIE electronic imaging*.
4. M Lebrun. (2012). An Analysis and Implementation of the BM3D Image Denoising method. *American Society of Mechanical Engineers*, 2(25): 175–213.
5. Xu zhongwei. (2011). Study on non-local means of the BM3D algorithm.
6. Antoni Buades B C J M. (2005). A non-local algorithm for image denoising.
7. Mahmoudi M, Sapiro G. (2005). Fast image and video denoising via non-local means of similar neighbourhoods. *IEEE Signal Processing Letters*. 12(12): 839–842.

8. Liu xiangle. (2010). Image Denoising by the BM3D algorithm in Wavelet Domain.
9. Mac Queen J. (1967). Some Methods for Classification and Analysis of Multivariate Observations. Proceedings of the 5th Berkeley Symposium on Mathematical Statistics and Probability, Berkeley, University of California Press, 281–297.
10. Thomas Brox OKAD. (2008). Efficient non-local means for denoising of textural patterns. IEEE Transactions on Image Processing, 17(7): 1083–92.

# Person Re-identification Based on Fusing Appearance Features in Perceptual Color Space

Caixia Fan, Yajun Chen and Lei Cao

**Abstract** Person re-identification is to match pedestrian targets observed from different camera views of multi-camera surveillance systems. Aiming at the issues that the color similarity pedestrian affect the recognition result, a person re-identification method based on multi-feature fusion in perceptual uniform color space is proposed, which is according to the characteristics of human vision system. Firstly, the color space which is suitable for similar pedestrian recognition is selected from five color spaces CIELAB, S-CIELAB, IPT, LAB2000<sub>HL</sub> and CAM02-SCD. Secondly, three kinds of pedestrian appearance features are extracted including spatial weighted histogram, local color and shape feature and global texture feature. Different distance measure methods are used to calculate the similarity of three different features. Finally, the linear fusion is performed by the adaptive weights. The experimental results based on VIPeR database and ETHZ database show that the proposed method is effective and can be used for the recognition of pedestrians with visual similarity.

**Keywords** Perceptual color space · Person re-identification · Multi-feature fusion

## 1 Introduction

Person re-identification is to determine whether an interest object in a camera view is in the other camera. But due to the low resolution, perspective changes, illumination changes, pedestrian posture changes and similar pedestrian's existence, result in a person in view of different monitoring looks very different. All of these

---

C. Fan (✉) · Y. Chen

School of Printing, Packaging Engineering and Digital Media Technology,  
Xi'an University of Technology, Shaanxi, China  
e-mail: fcx1981@xaut.edu.cn

L. Cao

College of Computer Science and Technology,  
Xi'an University of Science and Technology, Shaanxi, China

© Springer Nature Singapore Pte Ltd. 2017

P. Zhao et al. (eds.), *Advanced Graphic Communications and Media Technologies*, Lecture Notes in Electrical Engineering 417,  
DOI 10.1007/978-981-10-3530-2\_34

273



make it a great challenge for person re-identification. At present, there are two main research ideas: (1) the method based on the appearance characteristic description; (2) the method based on metric learning [1].

The method based on the appearance characteristic description generally assumes that pedestrians don't change their appearance in a short time. The weighted HSV histogram and maximally stable color regions are extracted using as the color features, combined with the high frequency and complex structure blocks to identify pedestrians [2]. In the literature [3], the spatial color information and the structural information are fused. In order to establish the integrated model, the paper combines the different color features of pedestrians in the decision-making stage by using the method of measuring [4]. But at present, the person appearance characteristic description methods don't take into account for the perceptual process of human vision. This leads to recognition results, in particular, the recognition results of similar pedestrian targets are not consistent with human perception, and thus produce false recognition.

The distance measure of feature is concerned with how to make the characteristics of the same target have a higher degree of similarity when the appearance model is set up [5–7]. This kind of method needs to carry on the study of the choice of the sample and the distance measure, when the scene changes, the general need to retraining.

This paper proposes a person re-identification method based on multi-feature fusion in perceptual uniform color space. Firstly, the pedestrian images are transformed into the perceptual uniform color space, which is consistent with the human visual system, and the appearance characteristics of the target are extracted. Then the pedestrian recognition is performed by the method of adaptive weights. Experimental results based on VIPeR database and ETHZ database show that the proposed algorithm has a greater distinction.

## 2 Selection of Perceptual Color Space

In video monitoring system, the efficiency of person re-identification with color as the main feature can be severely affected by the pedestrians with similar clothing (i.e. small color difference images). The human visual system is able to identify the color of the pedestrians. Therefore, converting image to the perceptual color space which is consistent with human vision to extract the feature can be more effective distinguish between similar goals. So, the study of the performance of the different perceptual color spaces can provide the basis for the identification of similar pedestrians. At present, the color spaces and their corresponding color difference formulas for small color difference image are: CIEDE2000 color difference formula based on CIELAB color space [8], CAM02-SCD based on CIECAM02 color appearance model [9], S-CIELAB [10], color difference based on IPT color space [11] and color space based on LAB2000<sub>HL</sub> [12]. In this paper, we choose the color

space which is suitable for person re-identification by visual experiments and pedestrian recognition results.

According to the characteristics of video surveillance scene, six standard images are selected as test images of visual experiments. These images cover still life, animals, figures and landscapes, contain the highlights and shadows, complicated texture changes, memory color and typical color. Detailed visual experimental procedure is seen in the literature [13]. By the comparison of the calculated color differences and the corresponding visual evaluation values and the STRESS values of statistical significance of color difference formulas, we can draw the following conclusions: for the small color difference image data, IPT color space is relatively stable. For all the attributes of the image transform its performance is better. The color difference formulas based on IPT color space is more close to the human eye’s visual evaluation results.

For person re-identification, the characteristics of different uniform color spaces are illustrated by experiments based on CAMPUS-Human database. There is a small change of illumination condition between the pedestrians in the database and there are many similar small color difference images [14]. Firstly, pedestrian images are transformed into different perceptual color spaces, then the recognition results are obtained by calculating Bhattacharyya distance of color histograms. The experimental results are evaluated by the ratio of finding the correct match in the top n matches. The experimental results in five different color spaces are shown in Table 1. The table includes the rank 1, 5, 10, 15, 20, 25 matching rates. It can be seen from the table, the poor performance of the CIEDE2000 color difference formula and S-CIELAB model when the rank is small, CAM02-SCD and LAB2000<sub>HL</sub> have high recognition rates, the recognition rates of IPT color space of second. But with the increase of the rank, the pedestrian recognition rates based on IPT color space are rising fast, which show that the IPT color space is more stable and less affected by the environment.

Therefore, this paper will extract the person appearance characteristics to establish the person appearance model in the IPT color space.

**Table 1** Rates of the target recognition in different color space

Color space	Top ranked matching rates%					
	r = 1	r = 5	r = 10	r = 15	r = 20	r = 25
CIEDE2000	9.37	15.23	17.78	27.18	36.23	40.88
S-CIELAB	9.37	15.42	18.96	25.55	35.40	39.51
CAM02-SCD	12.11	20.33	28.13	34.03	42.25	53.58
IPT	11.36	17.95	28.18	36.77	42.38	53.63
LAB2000 <sub>HL</sub>	13.48	18.62	24.44	29.92	39.51	47.73

### 3 Person Appearance Model

#### 3.1 Global Feature Based on Spatial Histogram

In order to describe the image spatial structure information, the second-order spatial histogram in IPT color space is used to represent the whole color characteristics of the target. Second-order spatial histogram of the image can be express as Eq. (1):

$$\mathbf{S}_I^{(2)}(b) = \langle \mathbf{n}_b, \boldsymbol{\mu}_b, \boldsymbol{\varepsilon}_b \rangle, \quad b = 1, \dots, B \quad (1)$$

In the formula,  $B$  is quantification series,  $\mathbf{n}_b$  is image quantification histogram,  $\mu_b$  is the mean value of all pixels with the same color value,  $\varepsilon_b$  is the coordinate covariance matrix for all pixels with the same color value [3].

The similarity of the spatial histograms ( $\mathbf{S}, \mathbf{S}'$ ) can be calculated by the similarity weighted sum of the two histograms and the pixel positions.

$$\rho(\mathbf{S}, \mathbf{S}') = \sum_{b=1}^B \psi_b \rho_n(\mathbf{n}_b, \mathbf{n}'_b) \quad (2)$$

$\rho_n(\mathbf{n}_b, \mathbf{n}'_b)$  is the similarity between the histograms, which used Bhattacharyya distance to calculate,  $\psi_b$  is spatial similarity. It can be express as Eq. (3):

$$\psi_b = \eta \exp \left\{ -\frac{1}{2} (\boldsymbol{\mu}_b - \boldsymbol{\mu}'_b)^T \hat{\boldsymbol{\varepsilon}}_b^{-1} (\boldsymbol{\mu}_b - \boldsymbol{\mu}'_b) \right\} \quad (3)$$

$\eta$  is Gaussian normalization constant,  $\hat{\boldsymbol{\varepsilon}}_b^{-1} = (\boldsymbol{\varepsilon}_b^{-1} + (\boldsymbol{\varepsilon}'_b)^{-1})$ .

#### 3.2 Local Feature

In order to eliminate the influence of small areas, the person is divided into a number of regions with similar color by mean shift image segmentation algorithm; retain more than 30 of the total number of pixels as main color areas. The local features are described by the color and shape information [3].

$$F = (\hat{C}, \lambda \hat{H}) \quad (4)$$

$F$  is the description of the combination of color and shape,  $\hat{C}$  is the normalized IPT color histogram,  $\hat{H}$  is 128 dimension normalized SIFT features,  $\lambda$  is the weight parameter,  $\lambda = 0.6$ . Principal component analysis (PCA) in feature space is performed in this paper, and the feature vectors  $V$  corresponding to the first 30 eigenvalues are obtained to describe the different regions, combined with the central

location information  $Cent$  and regional size information  $Re\ size$  of each region to describe the local characteristics of the image.

This paper adopts the improved EMD (Earth Mover’s short Distance) to calculate the similarity between the two local image characteristics [15]. Set  $A = \{(a_1, w_{a1}), (a_2, w_{a2}), \dots, (a_m, w_{am})\}$  is the representation of image A with m cluster and  $a_i$  is the description of the cluster,  $w_{ai}$  is the weights of clustering. As well as  $B = \{(b_1, w_{b1}), (b_2, w_{b2}), \dots, (b_n, w_{bn})\}$ .  $D = [d_{ij}]$  is distance matrix,  $d_{ij}$  is distance function between clustering  $a_i$  and  $b_j$ . The improved EMD in image A and image B can be defined as:

$$EMD_{\alpha}(A, B) = \left( \min_{f_{ij}} \sum_{i=1}^m \sum_{j=1}^n d_{ij} f_{ij} \right) + \left| \sum_{i=1}^m a_i - \sum_{j=1}^n b_j \right| \times \alpha \max_{i,j} \{d_{ij}\} \quad (5)$$

The solution method of the Formula (5) can be found in the literature [15].

In this paper, the representation method for the local characteristics of person is  $O = \{(o_1, w_{o1}), (o_2, w_{o2}), \dots, (o_m, w_{om})\}$ ,  $o_i$  is the local characteristics of image regions,  $w_{oi}$  is the coordinates of the feature points,  $d_{ij}$  is the Euclidean distance between different areas. By experiment, this paper takes  $\alpha = 0.3$ .

### 3.3 Texture Feature Description

In this paper, we extract the LBP texture information to make up the deficiency of the overall color feature and the local feature [3]. The similarity of the texture features is obtained by Bhattacharyya distance.

## 4 Multi-feature Fusion

Person re-identification has two sets of image data, the candidate target  $P$  and the identify target  $Q$ . The similarity of the two targets is obtained by the linear fusion of feature similarities.

$$S(P, Q) = \alpha \cdot S_S + \beta \cdot S_L + \gamma \cdot S_{LBP} \quad (6)$$

$S_S$  is the spatial histogram similarity,  $S_L$  is the similarity of local characteristics,  $S_{LBP}$  is the similarity of the texture features,  $\alpha, \beta, \gamma$  are the weights.

An adaptive weight selection method is presented by comparing the color features and texture features of the target with the global features of all pedestrians. Firstly, The Bhattacharyya distances between the hue histogram of each candidate and global hue histograms are calculated, the greatest distance for  $DC_{max}$ . Then, the distance between the hue histogram of the person to be identified and global hue

histogram is obtained, referred to  $DC_p$ . Finally, the importance and distinguish ability of color characteristics are calculated through  $DC_p$  divided by  $DC_{\max}$ , recorded as  $S_{color}$ . If  $S_{color}$  is high, according to the color information can achieve higher recognition rate. Similarly the importance  $S_{texture}$  of texture feature can be calculated. Based on the importance and the ability of distinguishing of different visual information, the weights of multi-feature fusion are obtained according to the Formula (7). Spatial histogram features and the local features are color based features, and select the same weight. The weight of the texture feature is selected according to its importance.

$$\begin{aligned}\alpha &= \frac{S_{color}}{2S_{color} + S_{texture}} \\ \beta &= \frac{S_{color}}{2S_{color} + S_{texture}} \\ \gamma &= \frac{S_{texture}}{2S_{color} + S_{texture}}\end{aligned}\quad (7)$$

$\alpha$ ,  $\beta$ ,  $\gamma$  are range between 0 and 1, and  $\alpha + \beta + \gamma = 1$ .

## 5 Experimental Results and Analysis

In this paper, the algorithm effectiveness is tested in VIPeR database and ETHZ databases. They include different issues that need to be addressed for person re-identification. The experimental results are evaluated by the cumulative matching characteristic cumulative (CMC) curve [16, 17].

### 5.1 VIPeR Database

There are 632 sets of 28 human targets in the VIPeR database. Images in the database are obtained from two different cameras, different views, pose, and illumination conditions [16]. The comparison of the algorithm and the literature [3] is shown in Fig. 1. It can be seen from the figure, in the first column based on the perceptual color space, person re-identification rate of 40.1%, compared with the literature [3] result 31.3% increased by 8.8%. Fifth column in the literature [3] the target recognition rate is 56%, and the result of this paper is 65.3%. In the first 15 columns, the recognition rates in the perceptual color space are growing fast. It shows that the extracted features in uniform color space are more distinguished, and they can distinguish visually similar pedestrian targets effectively.

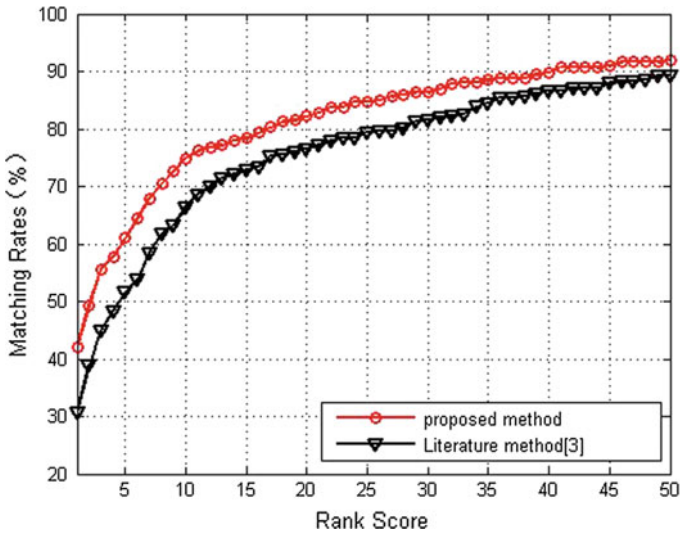


Fig. 1 Comparison of experimental results in VIPeR database

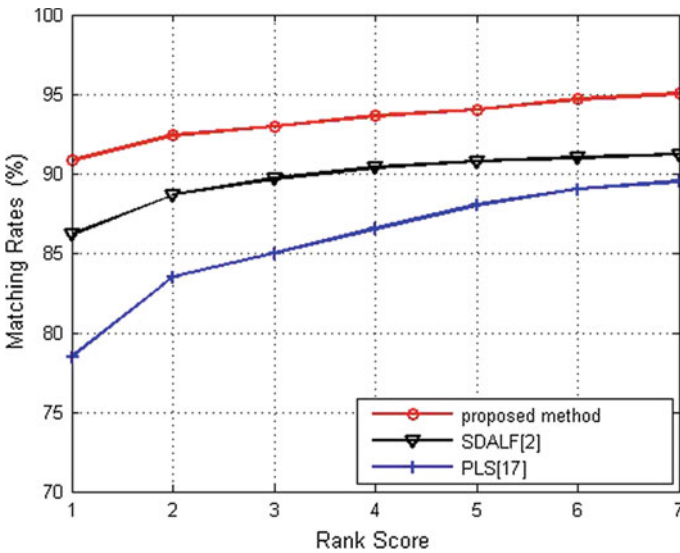


Fig. 2 Results in ETHZ1 database

### 5.2 ETHZ Database

The ETHZ database consists of three sequences: ETHZ1, ETHZ2 and ETHZ3 [17]. There are small change of attitude and light condition. The results of three data sets in the ETHZ database are shown in Figs. 2, 3 and 4. The appearance model of the candidate target is established by 5 frame key frames, and the target is matched with

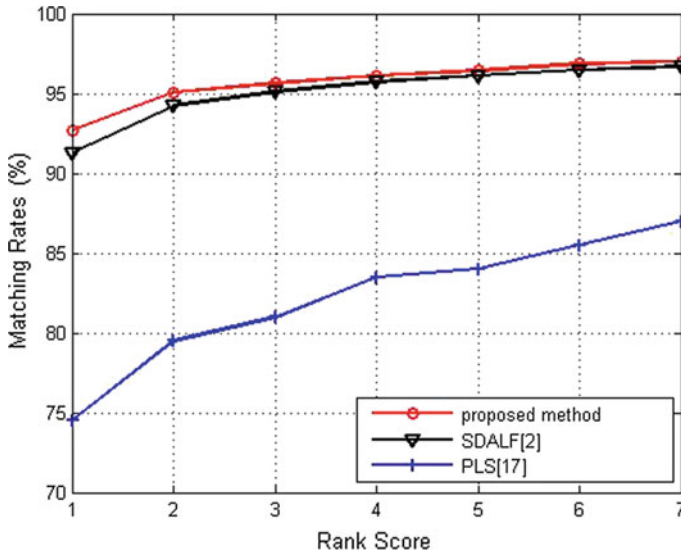


Fig. 3 Results in ETHZ2 database

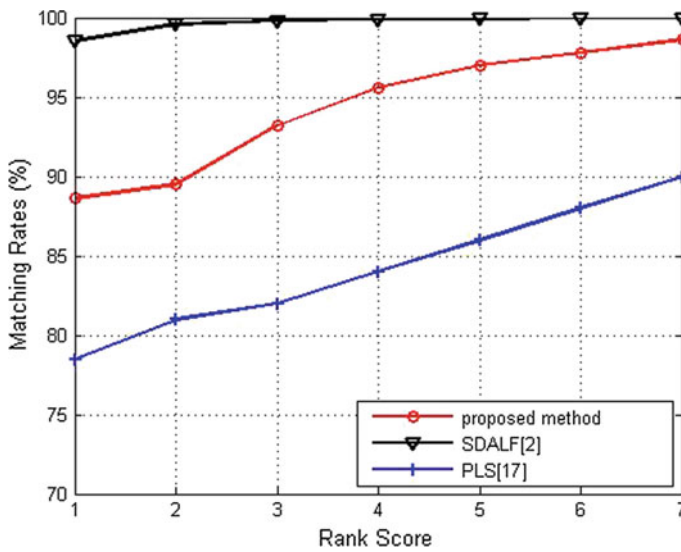


Fig. 4 Results in ETHZ3 database

1 frame. In order to get the stable experimental results, this paper selects 10 sets of targets for person re-identification, and the experimental results are the average of the results of several experiments. As can be seen from the figures, the algorithm can improve the recognition rate of the target in the top 5. In ETHZ1 image

sequences the algorithm is better than the SDALF algorithm and PLS algorithm. In the ETHZ2 data set, the algorithm and SDALF algorithm to identify the difference is not much, better than the PLS algorithm. In the ETHZ3 data set, this algorithm is better than PLS algorithm, but less than SDALF.

## 6 Conclusions

This paper proposes a new method of person re-identification based on multi-feature fusion in perceptual uniform color space. The method is based on the characteristics of human vision system, which mainly solves the problem of the influence of similar targets. The experimental results based on VIPeR database and ETHZ database show that the features extracted from the uniform color space have a stronger ability to distinguish the pedestrian recognition problem. The validity of the algorithm is illustrated. How to establish a more effective similarity evaluation criterion is the focus of follow-up study.

**Acknowledgements** This study is funded by the Doctoral scientific research start-up fund (108-451115001) and School science research program (2015CX021).

## References

1. Bedagkar-Gala A, Shah S K (2014). A survey of approaches and trends in person re-identification. *Image and Vision Computing*, 32(4): 270–286.
2. Farenzena M, Bazzani L, Perina A (2010). Person re-identification by symmetry-driven accumulation of local features. *CVPR*: 2360–2367.
3. Fan Caixia, Zhu Hong (2013). Person re-identification based on multi-features. *Journal of Image and Graphics*, 18(6):711–717.
4. Liu X, Wang H, Wu Y (2015). An ensemble color model for human re-identification. *WACV*: 868–875.
5. Ahmed E, Jones M, Marks T K (2015). An improved deep learning architecture for person re-identification. *CVPR*.
6. Du Yu-Ning, Ai Hai-Zhou (2014). A statistical inference approach for person re-identification. *Journal of Electronics and Information Technology*, 36(7): 1612–1618.
7. Qi Meibin, Tan Shengshun (2016). Multi-feature subspace and kernel learning for person re-identification. *ACTA AUTOMATICA SINICA*, 42(2):299–308.
8. LUO M R, CUI G, RIGG B (2001). The development of the CIE 2000 colour-difference formula: CIEDE2000. *Color Research & Application*, 26(5): 340–350.
9. LUO M R, CUI G, LI C (2006). Uniform colour spaces based on CIECAM02 colour appearance model. *Color Research & Application*, 31(4): 320–330.
10. ZHANG X, WANDELL B A (1997). A spatial extension of CIELAB for digital color-image reproduction. *Journal of the Society for Information Display*, 5(1): 61–63.
11. EBNER F, FAIRCHILD M D(1998). Development and testing of a color space (IPT) with improved hue uniformity. In *proceedings of the 6th Color Imaging Conference*, 11. 17–20.
12. LISSNER I, URBAN P (2012). Toward a unified color space for perception-based image processing. *IEEE Transactions on Image Processing*, 21(3): 1153–1168.



13. Fan Caixia, Chen Yajun (2016). Evaluation of perceptual uniform color spaces and application in image processing. *Journal of Xi'an university of technology*, 32(2):191–198.
14. Xu Y, Lin L, Zheng W S, et al (2013). Human re-identification by matching compositional template with cluster sampling. In *proceedings of the IEEE International Conference on Computer Vision*: 3152–3159.
15. Pele O, Werman M(2008). A linear time histogram metric for improved sift matching. *ECCV*: 495–508.
16. Gray D, Tao H (2008). Viewpoint invariant pedestrian recognition with an ensemble of localized features. *ECCV*:262–275.
17. Schwartz W R, Davis L S(2009). Learning discriminative appearance-based models using partial least squares. In *Proceeding of Tutorials of the XXII Brazilian Symposium on Computer Graphics and Image Processing*: 322–329.

# A Night Image Enhancement Algorithm Based on Guided Filtering

Xuxin Tang, Zhijiang Li and Yuhang Chen

**Abstract** Colored night images lead to various problems in real life, such as low dynamic range, detail blurring and so on, which are waiting to be solved. For this reason, it proposes an algorithm for night image enhancement based on guided filtering in the paper. This image process includes three main steps. Firstly, by transforming to HVS color space, the targeted image is separated coarsely into two images—base layer image and detail layer image in the result of guided filtering. In the second step, the base layer and detail layer are processed by different strategies selectively and respectively to lighten the whole, but remain details as much as possible. Eventually, the base layer, which has been previously increased contrast, is added detail layer to keep the details and margins. The result image can be retained after reverting to the original color space. Our result illustrates the comparison among result images and images enhanced by other methods, which obviously proves that the algorithm in our paper can obtain relatively better results in the ways of detail enhancement and color fidelity.

**Keywords** Image enhancement · Guided filter · Night image

## 1 Introduction

Due to low illumination at night caused by poor light conditions and device itself, the quality of night image gets lower, presented on the overall image grey value and low contrast so hard to identify. In addition, blended background in important parts formed by insufficient light makes local information hard to be recognized. Therefore, enhancing night image in civilian life and military usage, such as transportation system, security systems, video surveillance, plays a significant role.

---

X. Tang · Z. Li (✉)

School of Printing and Packaging, Wuhan University, Wuhan, China  
e-mail: lizhijiang@whu.edu.cn

Y. Chen

Hangzhou Hikvision Digital Technology Co., Ltd., Hangzhou, China

© Springer Nature Singapore Pte Ltd. 2017

P. Zhao et al. (eds.), *Advanced Graphic Communications*

and *Media Technologies*, Lecture Notes in Electrical Engineering 417,

DOI 10.1007/978-981-10-3530-2\_35

At present, various methods are created to solve the problems resulted from low illumination image enhancement, including histogram equalization, Retinex [1], MSRCR [2], homomorphic filtering [3], the HDR method and so on.

Based on guided filtering, this paper focuses on the enhancement of night image. The image will be separated into two layers by being coarsely decomposed by guided filter, with the layers are processed by different strategies selectively.

This paper is divided into four parts. The second part will introduce the basic concepts and main characteristics of guided filtering. Then, the third part will elaborate the new method in this paper in the form of graph with detail analysis and how the two layers improve respectively. The fourth part will show the result of our method, which will be compared with MSRCR. The conclusion and prospect can be found in section five.

## 2 Guided Filter

The guided filter [4], a local linear model, consists of the guidance image  $I$  and the filter output  $q$ . In a window  $\omega_k$  where center point is  $k$ , it is assumed that the  $q$  can be obtained by being transformed linearly by  $I$ , so Eq. (2.1) can be obtained:

$$q_i = a_k I_i + b_k, \quad \forall i \in \omega_k \quad (2.1)$$

where the guidance must be set in advance, or directly use the input image  $I$ .

It can be deduced that the edge-preserving properties of the method for the local linear relation  $\nabla q = a \nabla I$ . Therefore, the input image can be smoothed with edge preserved.

Compared with traditional kernel function, the guided filtering achieves higher performance in edge-preserving and detail enhancement with non-approximate linear-time algorithm, which due to the independent computational complexity from the linear-time algorithm. It can use in various computer vision and computer graphics applications including detail enhanced for a night image in the paper.

## 3 Night Image Enhancement

Inspired by the better performance of original detail remaining of guided filtering, this paper creates a new way to adjust the low-illuminated image to high contrast so that enough to be recognized. In the beginning, the RGB color space of the targeted image will be transformed to HVS color space for higher efficiency and better effect in practice. Then the main process of the method will be stated in four steps as followed.

### 3.1 Layer Decomposition

The first step is to separate the original image into two layers according to practical need.

Set  $I$  as the input image and firstly gain the base layer  $b$ , we get the base layer by Eq. (3.1).

$$b = \sum_i W_i(I)I_i \quad (3.1)$$

where  $i$  and  $j$  are the pixel and  $W_i$  are the kernel function of guided filtering, it can be computed by Eq. (3.2).

$$W_i(I) = \frac{1}{|\omega|^2} \sum_{i \in \omega_k} \left( 1 + \frac{(I_i - \mu_k)^2}{\sigma_k^2 + \varepsilon} \right) \quad (3.2)$$

where  $\omega_k$  are the  $k$ -th windows of kernel function and  $|\omega|$  are the number of pixels in the window.  $\mu_k$  and  $\sigma_k$  are the mean value and variance in window.  $\varepsilon$  is the smoothing factor.

The detail layer  $d$ , extracted from the difference value of original image and the base image, can be presented as follow.

$$d = I - \sum_i W_i(I)I_i \quad (3.3)$$

### 3.2 Detail Layer

The detail layer remains the margins and noise of the image. The aim of this step is to selectively strengthen the margins and reduce the noises. Consequently, it is denoised by guided filter and the result is  $d$ . Then details are enhanced by Arctan curve figure. The Arctan transformation is showed by Eq. (3.4).

$$d'' = \sum_i G_r * \tan(c * d'_i) \quad (3.4)$$

where  $G_r$  is the gray dynamic range of the HVS image and  $c$  is the coefficient.

### 3.3 Base Layer

The theory of base layer processing bases on a simple point-wise operation [5], which gains the output  $O$  after mapping input  $I$  with the coefficient  $\gamma$  as follow.

$$O = 255 * \left( \sum_i \frac{I_i}{255} \right)^\gamma \tag{3.5}$$

It is assumed that the input image is a gray image or single-channel image in which grey values ranging from 0 to 255. In our algorithm,  $\gamma$  is calculated according to the nearby pixels through an exponential function as follow.

$$\gamma = 2^{\frac{128 - I_i - imv}{128}} \tag{3.6}$$

where the new coefficient is the inverted low-pass filtered input image.

Equation (3.6) shows that only the pixels whose values are close to 128 will not be changed too much among all pixels. This method could stretch the contrast of the dark and bright regions. If the image is processed in the RGB color space, it will get grayer output than in the HVS color space. In this case, in HVS, the enhanced image can avoid the washed-out effect. With the help of gamma correction, the low-illuminated condition can be improved and the black corner of the image is lighter enough to recognize. The separation and disposition of the base and detail layers can enhance night image while strengthening the important details.

### 3.4 Image Confusion

The fusion image is achieved by image confusion of base layer and detail layer in the form of simple addition in the single channel in the HVS color space. After returning to RGB color space, the result image can be obtained.

Figure 1 concludes the whole process of our procedure to enhance the night image. It can be found that the dynamic range enhanced base layer is stretched and

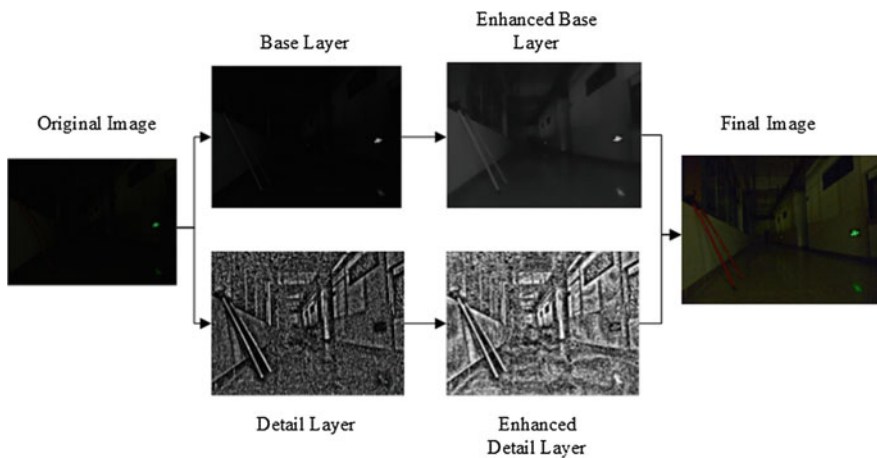


Fig. 1 The process of the image enhancement

the margins in enhanced detail layer get sharp-edged. The final image becomes not only lighter but also clearer.

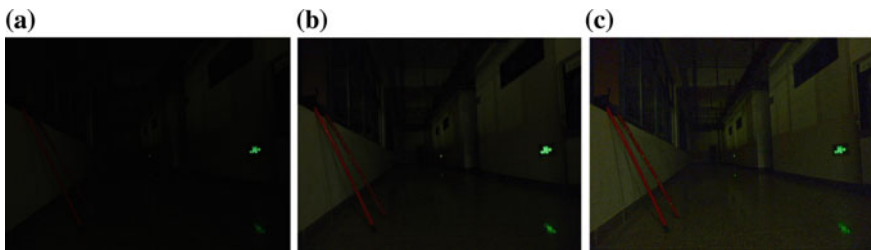
The parameters that are set for this test will be shown in the next section.

## 4 Experimental Results and Analysis

The targeted image is firstly separated by guided filtering into base layer and detail layer, in which local window radius is 2 and regularization parameter is 10. Then base layer is processed by gamma of 1/2, while detail layer is processed by Arctan of 8.

Figure 2a is a targeted night image, which shows the corridor building at night that too dark to recognize except a green emergency exit light. Figure 2b is the result image processed by MSRCR, being stretched the dynamic range compared to original image. However, the corner of the room still remains unclearness. Figure 2c shows the result of the algorithm proposed in this paper, which is obviously the lightest and clearest one among three results, especially the edge of the trees, windows and red ladder, gaining best visual effect. The door in the distant place where is not able to identify before also starts to show up after the enhancement.

Otherwise, the quality assessment in Table 1 shows that the algorithm proposed in this paper is better for the higher MSE and Gray mean value than MSRCR, proving that the proposed algorithm can achieve higher range of contrast stretching. In the meantime, the details are kept better as the comparison between the proposed algorithm and reference original image.



**Fig. 2** Comparison of gamma correction, MSRCR and our method. **a** Target picture. **b** Result of MSRCR. **c** Result of proposed algorithm

**Table 1** The effectiveness of the experiment

	Targeted image	MSRCR	Proposed algorithm
MSE	–	22.1202	48.8849
Gray mean value	31.3661	13.4980	24.9658

## 5 Conclusions

This paper proposes a new method for night image enhancement, dramatically improving the edge-preserving compared to other methods. The experiment indicates that the test image is clearer, lighter and closer to the original image. It has higher performance to solve the problems for low contrast image as conclusion. The algorithm may be used in the image recognition and color image artistic rendition.

## References

1. Jobson, D. J., Rahman, Z., & Woodell, G. A. (1997). Properties and performance of a center/surround retinex. *IEEE Transactions on Image Processing*, 6(3), 451–462.
2. Jobson, D. J., Rahman, Z. U., & Woodell, G. A. (1997). A multiscale retinex for bridging the gap between color images and the human observation of scenes. *IEEE Transactions on Image Processing*, 6(7), 965–976.
3. Myagmarsuren, G., Tkach, V. S., Suslov, D. S., & Schmidt, F. K. (2006). Sub-Image Homomorphic Filtering Technique for Improving Facial Identification under Difficult Illumination Conditions. *International Conference on Systems, Signals & Image Processing*, IwSSIP (71), 439–473.
4. He, K., Sun, J., & Tang, X. (2010). Guided image filtering. *IEEE Transactions on Pattern Analysis & Machine Intelligence*, 35(6), 1397–1409.
5. Zhang, D., Park, W. J., Lee, S. J., & Choi, K. A. (2012). Histogram partition based gamma correction for image contrast enhancement. *2012 IEEE 16th International Symposium on*, 12880500, doi:[10.1109/ISCE.2012.6241687](https://doi.org/10.1109/ISCE.2012.6241687).

# Three-Dimensional Color Gamut Visualization and Interaction for Digital Images

Zhijin Li, Maohai Lin, Guangyuan Wu, Yehong Chen and Meiqi Lin

**Abstract** In recent years, digital image technology continue to make new progress, but high-fidelity reproduction of images has become a hot issue with the image in different digital imaging equipment showing significant differences. Based on three-dimensional imaging and data mapping technology, interactive technology between three-dimensional color gamut and digital image is studying in this paper. By real time position acquisition technique and digital image color gamut conversion technology, source image gamut was constructed in three dimensions. At the same time, by establishing a real-time mapping between the color space and source image data, an interactive operation was implemented. This will further reveal the mechanism of color mapping information transfer and conversion process. Also reach the fidelity color reproduction of digital image.

**Keywords** Digital · Color gamut · Interactive technology

## 1 Introduction

In the process of color reproduction, color transfer is a process which is mainly from the original color gamut mapping to the target media color gamut. On the one hand, if the target color gamut completely contains the source color gamut, image will be transferred directly without loss of image color information; on the other hand, if manuscript gamut is greater than target color gamut or gamut do not overlap, you need to target color gamut color gamut mapping [1]. In terms of color reproduction based on display technology, the color gamut of the grasp occupies a crucial low [2].

---

Z. Li · M. Lin (✉) · G. Wu · Y. Chen · M. Lin  
School of Printing and Packing Engineering, Qilu University of Technology,  
Jinan, China  
e-mail: imhlin@163.com

M. Lin · G. Wu  
State Key Laboratory of Pulp and Paper Engineering, South China University of Technology,  
Guangzhou, China



On the basis of 3D modeling and data mapping technology, this paper maps the color data of the target image, and realizes the 3D construction of the color gamut.

### ***1.1 Color Gamut of Digital Image***

The transfer process of digital images in different devices is the important basis of digital printing. The construction of three-dimensional color gamut digital images can help users understand the color range of one digital picture better. Gamut mapping algorithms can be divided into two categories: device to device (device based) and image to device (image based) [3]. In recent years, there are a lot of color gamut mapping algorithm based on image, which can be classified into four categories: point by point compression, point to point expansion, space color gamut mapping, spectral color gamut mapping, and so on. Space color gamut mapping is the direction of development because of its remarkable detail protection ability [4]. In the space color gamut mapping algorithm, it is necessary to obtain a precise color gamut.

### ***1.2 Scatter Point Color Gamut Mapping***

Method for determining the color gamut of the image can be directly obtained, and some common methods can be used, such as convex hull, alpha shape, partition maximization algorithm, or other special methods. But, when we have to describe and view the location of each pixel in the color gamut coordinates, the algorithm is often the best solution. Using scatter on the color gamut performance is a very, very simple and original description method for color gamut, but for the image, this method represents the color gamut by rendering each pixel color in 3D color space, this part is always the most accurate method for image gamut description [5].

Scatter point description algorithm achieves the specified point in the image of the color gamut mapping by mapping the pixels in the digital image from the RGB color space to XYZ color space according to the specific conversion algorithm, and then converted from the XYZ color space to the  $L^*a^*b^*$  CIE color space. Through the scattered point description algorithm, it can be clearly observed in the image of the point and the target color gamut mapping, clear and accurate.

### ***1.3 CIE $L^*a^*b^*$ Color Space***

Lab color space was developed by the international lighting Committee (CIE) in 1976, respectively, Lab color space of the three-dimensional model of three-dimensional space model and plan [6]. Any color hue and characteristics can be with  $a^*$ ,  $b^*$  value,  $L^*$ ,  $a^*$ ,  $b^*$  value can describe the nature of any color [7].

1976 CIE recommendation and released in 1987, our country's GB7921-1987 provisions: CIELAB and CIEluv two uniform color space are used to represent the color of light source and object color and color difference, the two system in visual uniformity of very close to the practical selection in CIELAB or CIEluv to represent the color or color difference is in line with international standards and national standards [8]. However, in recent 20 years, the color printing has matched and evaluated of most of the CIELAB system.

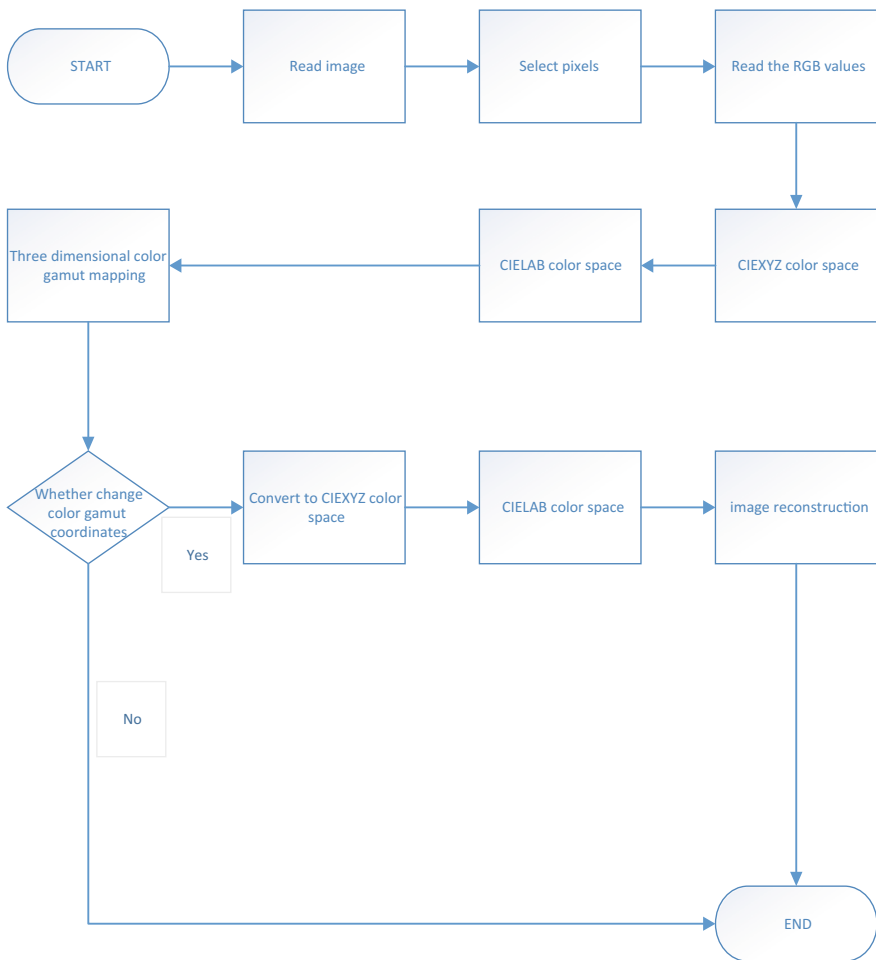


Fig. 1 Flow diagram of experiment

## 2 Image Color Gamut Visualization and Interaction

This paper achieves the interactive construction of 3D color gamut and digital image by Matlab. The flow chart is shown in Fig. 1.

### 2.1 Visualization of the Color Gamut of the Image and Its Midpoint

#### 2.1.1 Selected Pixel

After the image reading success, the first step is to choose the pixel to view, press the Enter key to end the selection process, as shown in Fig. 2.

#### 2.1.2 Three Dimensional Color Gamut Display of Selected Points

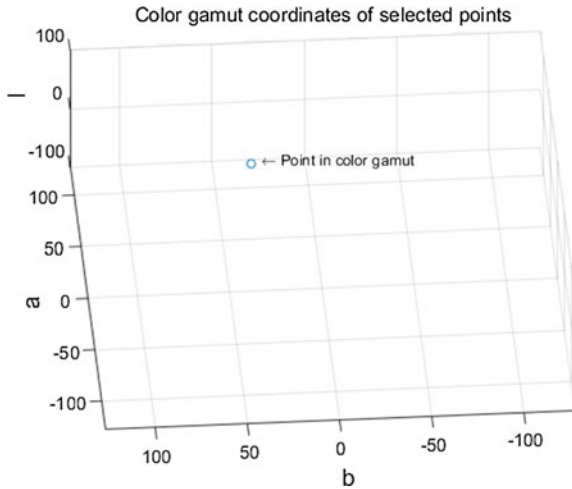
The pixel value of the selected point is converted to tristimulus values under the observation condition of the CIE standard illumination body D65 illumination and the 2° field of view. Then transformed into CIE color space by a nonlinear transformation, finally construct the three-dimensional color gamut. Figure 3 shows the complete three-dimensional color gamut.

In 3D coordinates, users can observe the value of the current pixel point and its position by rotation angle.



**Fig. 2** Image reading (*left*) and select pixels in the image (*right*)

**Fig. 3** Three dimensional color gamut coordinates corresponding to the selected pixels



**Fig. 4** New color gamut coordinate input interface

Please enter a new "L" value (between -128 and 127) :

Please enter a new "a" value (between -128 and 127) :

Please enter a new "b" value (between -128 and 127) :

## 2.2 Interactive 3D Color Gamut and Image Coordinate

### 2.2.1 Resetting of Three-Dimensional Color Gamut Coordinates

If the color coordinate of the point changes, program will show the changes of image. You can choose to enter the new coordinate color gamut as shown in Fig. 4.

When the new color gamut coordinate value is specified, the program will achieve the same pixel properties as the pixel information by the color gamut conversion technology.

### 2.2.2 Original Image Reconstruction

When a new color gamut mapping is set up, the new input color gamut coordinates will be transformed into CIE color space by inverse transform. Then the coordinates

**Fig. 5** Reconstructed image



are output for the RGB value from the CIEXYZ color space by the Minimum chromatic aberration method. In the process of the final image output, the program will replace these pixels all the new RGB value, the RGB value of these pixel points are the same as the RGB value of the initial selected pixels. Figure 5 shows an enlarged image after the reconstruction.

From the above, we can clearly see the changes after the modification of the color gamut coordinates.

### 3 Conclusions

In this paper, a new simple and efficient method is proposed to solve the three-dimensional color gamut mapping of digital images. The original color data will be processed by real time position acquisition technique and digital image color gamut conversion technology, after mapping, the target 3D color space and image color data established real-time contact, and ultimately realize the real-time interaction of image and color gamut. We use this method to implement and test the performance of the method with a series of images. The experimental results show that the new method can realize the real-time interaction of different images in the range of accuracy.

**Acknowledgements** This work was supported by State Key Laboratory of Pulp and Paper Engineering (201606 and 201609).

## References

1. Yun Hui Luo, Mao Hai Lin. Three-Dimensional Color Gamut Visualization of Digital Output Device Based on ICC Profile [J]. *Applied Mechanics and Materials*. 2012:36–39. 28(1): 20–23.
2. Mao Hai Lin, Yun Hui Luo, Shi Sheng Zhou. Perceived Image Gamut Based on Human Visual System and Wavelet Transform [J]. *Advanced Materials Research*. 2010:16–19.
3. Ling Lu, Mao Hai Lin, Yong Wen Jiang. A Novel Determination Algorithm for Gamut Boundary of Digital Media Image [J]. *Computer Knowledge and Technology*. 2015:141–143.
4. Katoh, Naoya; Ito, Masahiko; Ohno, Shin. Three-dimensional gamut mapping using various color difference formulae and color spaces [J]. *Journal of Electronic Imaging*. 1999, Vol. 8 (No. 4):365–379.
5. Gijsenij A, Gevers T, Van DeWeijer J. Generalized Gamut Mapping using Image Derivative Structures for Color Constancy. *International Journal Of Computer Vision* [serial online]. January 15, 2010;86(2/3):127–139.
6. Lin Maohai, Zhou Shishen, Luo Yunhui. Image Gamut Visualization Based Oil Ball-Pivoting Algorithm [C]. *China Printing And Packaging Study*, 2010.
7. Wei Jie Hu, Shun Qing Tang, Zheng Fang Zhu. *The Principle and Application of Modern Color Technology* [M]. Beijing: Beijing Institute of Technology press, 2007:237–245.
8. Na Li. *Research on the Data Processing of Three Dimensional Color Gamut and Its Theoretical Construction* [D]. Tianjin Normal University, 2014.

# Application of Multi-spectral Technology in Presswork Forgery Prevention

Yan Li and Dongsheng Jiang

**Abstract** No matter how similar the genuine printed matter is to counterfeit printed matter, the spectral information will be different owing to their difference in paper and ink composition. Therefore, multi spectral technology can be applied to the research on forgery detection of printed matter. In this paper, the difference of the spectral information is mainly due to the different ink used. Firstly, the feature points of the printed product which has different ink and same graphic messages are collected by using ASD portable spectrometer. Then, the spectral curves of two feature points were analyzed by using the method of continuum removal and spectral angle. The result of analysis proves that these methods that study the printed matter's spectral information is feasible to detection printed matter authenticity. This also opens up a new field for anti fake printing.

**Keywords** Multi-spectral technology · Printed matter · Forgery prevention

## 1 Introduction

With the rapid development of the market economy, all walks of life begin to flourish. How to make anti fake products is particularly important for a manufacturer. However, how to identify genuine and fake goods and eliminate the use of three non-products is a problem that related to the life for consumers. Any product needs packaging and labels, therefore, the research of anti fake technology of printed matter is of great significance.

In this paper, we study the anti fake technology based on the spectral information of several printing dots. It includes the dots' reflection under a series of bands. The reflectivity data reflects the composition of the material. Therefore, some enterprises in order to protect their products, they adding some kinds of

---

Y. Li (✉) · D. Jiang  
School of Printing and Packaging Engineering,  
Beijing Institute of Graphic Communication, Beijing, China  
e-mail: 1261795948@qq.com

materials or increasing component's content to their ink. According to the spectral data analysis of the production, that has identifiable characteristics under a wavelength, then determining whether the printed product is the company's products based on this feature.

## **2 Experimental Principles and Processing Algorithm of High Spectral Data**

### **2.1 Principle of Detecting Printed Matter Based on the Ink's Spectral Information**

Ink is an important constituent for printing. The different multi-spectral data is reflected in the difference of the ink's composition. In addition to fluorescent ink and other security inks, multi-spectral printing detection is mainly due to the different ink in the minerals.

ENVI has its own spectrum library, which is divided into 5 standard libraries, they are USGS mineral spectrum, vegetation spectrum, JPL "pure" mineral spectrum, IGCP264 spectrum library and JHU spectrum library. When finding a band absorption peak or trough, through matching the spectral library's spectral curve to get the main material which affecting this bands. It is also possible to add a substance to the ink, which changes the spectral curve of the printed material in particular [1].

### **2.2 Enhancement and Comparison of Spectral Features**

#### **2.2.1 Continuum Removal**

Continuum Removal Method which can effectively highlight the absorption and reflection characteristics of the spectral curve is an effective method to enhance the absorption characteristics of the spectrum, and it normalized the reflectance to 0–1.0. Spectral absorption features are normalized to consistent spectral background, which is beneficial to compare the characteristic values with other spectral curves, so as to get characteristic bands for classification and recognition. Continuum removal is usually defined as connecting the prominent peak point on spectral curve straightly. The ratio of the value of the original spectrum curve to the corresponding value of the continuum line is called spectral removing enveloping line. The algorithm is shown as Formula (1).

$$R_c = \frac{R_j}{R_{cj}} \quad (1)$$



$R_c$  and  $R_{cj}$  represent spectral reflectance that removed and spectral reflectance of band  $J$  at the continuum. However,  $R$  and  $j$  represent the value of the original spectral reflectance and wavelength. After wiping off the enveloping line for the original spectral reflectance, the characteristic absorption bands and their spectral reflectance data can be seen clear [2].

### 2.2.2 Spectral Absorption Index

Spectral absorption index is a parameter that can characterize the absorption characteristics of the spectrum, and it can be used as a single feature to recognize the printed matter.

### 2.2.3 Spectral Angle Analysis

Spectral angle mapping technology defines the similarity of two vectors using angle of  $n$ -dimensional vector space. The smaller angle between the two vectors is the more similar between them.

$$\theta = \arccos \frac{(\vec{a}, \vec{b})}{|\vec{a}| |\vec{b}|} \quad (2)$$

For a pixel of two printed matters, we can define a multidimensional vector, and then calculate the angle between the two vectors. If the angle is less than the tolerance, it is possible to think that the two spectra are matched even if one spectrum is much larger than the other. Spectral angle classification is considered the direction of the spectral vector rather than the size of the spectral vector. Spectral angle mapping can only identify the spectral angle differences which are due to different material and chemical composition [3].

## 3 Experiments

### 3.1 Data Acquisition System

This experiment uses the ASD Field Spec Pro portable spectrometer to collect high spectral data of two printed matters which have different inks and same graphic messages. Selecting three points which exhibit a wide range of colors and collecting their reflectivity information. Getting the information of tricolor ink and black ink is our final purpose. So, whether the points' graphic message is same is inessential.

The band is 350–2500 nm. Each sample was collected three characteristic points of hyper spectral data, and each feature point was collected three times.

### 3.2 Data Processing and Result Analysis

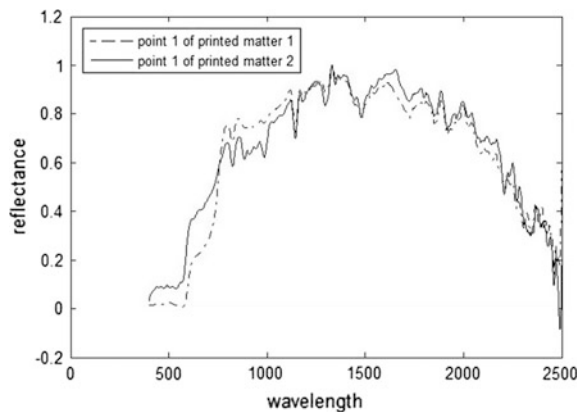
Due to the difference in the energy response between the spectral bands, the spectral curves always have some noises. So 35 points moving average smooth method is used to remove the noise from spectral data [4]. The resulting new spectral curve is the general trend line of the old spectrum, partly eliminate the high frequency components and bring convenience and good results for further analysis of absorption bands and spectral characteristics of the printed matter.

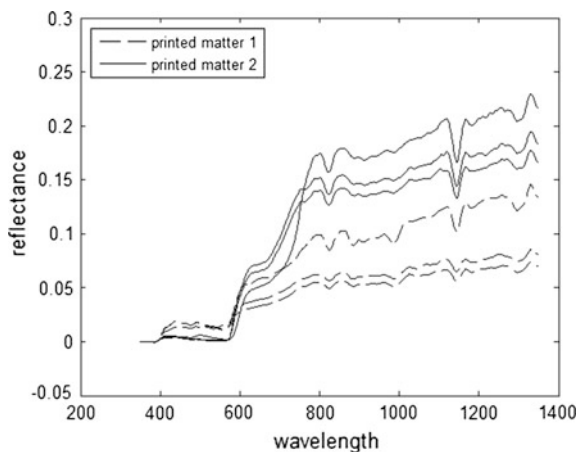
#### 3.2.1 Continuum Removal and Spectral Absorption Index

Continuum Removal method is a commonly used spectral analysis method and it can effectively highlight the spectral curves of characteristics of absorption and reflection, and then normalized to a consistent spectral background. It is so beneficial to have a comparison with other spectral curve that extracts the characteristic bands for classification and recognition [5]. 350–2500 nm bands are divided into 43 sections, select maximum points of the spectral reflectance on each section, using a straight line to connect all points to make the continuum, as shown in Fig. 1.

Figure 2 shows that the spectral line of two printed matters have obvious difference from 350 to 1350 nm. Printed matter 2 has bigger spectral slope than printed matter 1 from 580 to 620 nm. Near the 1000 nm, printed matter 1 has a small absorption peak, in turn, printed matter 2 has small reflection peak. Furthermore, their spectral absorption index at bands 827 and 1144 nm are different, too. It is shown in Table 1.

**Fig. 1** Spectral difference at point 1 of two printed matters through continuum removed





**Fig. 2** Spectral difference between two printed matters from 350 to 1350 nm

**Table 1** Two printed matters' SAI

	Print matter	SAI
827	Printed matter 1	0.77
	Printed matter 2	1.01
1144	Printed matter 1	0.89
	Printed matter 2	1.20

**Table 2** Data of spectral angle of printed matter

		Point 1	Point 2	Point 3
Same print and same point	Print 1	0.112 (6.4°)	0.112(6.4°)	0.093(5.3°)
	Print 2	0.079 (4.5°)	0.071(4.1°)	0.112(6.4°)
Different print and same point	Print 1 and print 2	0.133 (7.6°)	0.176 (10.1°)	0.195 (11.2°)

It is obvious that the spectral absorption index of the two printed matters at 827 and 1144 nm are obviously different. This difference can be used as the basis for distinguishing between the two types of printed matter. Iron ion has absorption at 600–900 and 1000–1100 nm, and copper ion's absorption peak at about 800 nm [6]. So, the difference that absorption index may be related to the two kinds of metal ions. This is just a conjecture that needs to be further verified.

### 3.2.2 Spectral Angle Mapping

Table 2 shows the size of the spectral angle between the same sample points in the same printed matter or different printed matter.

Whether it is printing 1 or 2, the average of spectral angle between the same sample points is less than  $7^\circ$ , but the average of spectral angle between the 1 and the 2 is greater than  $7^\circ$ . Those  $7^\circ$  can be used as a judge tolerance of these two kinds of printed matter, if it is greater than  $7^\circ$  for different printing, less than  $7^\circ$  for the same kind of printed matter.

## 4 Conclusions

This paper analysis two kinds of printed matters that have different inks and same graphic and text information using continuum removal method and spectral angle method. By using remove continuum removal method, the spectral information of different bands was found. At the same time, it is found that the spectral absorption indexes of the two printed matters at the two bands are obviously different. If we know the degree of tolerance, we can determine whether the printed matter is same using the index. By spectral angle mapping method, the spectral angle range of two kinds of printed matter is obtained.

Application of multi spectral analysis technology to detect the authenticity of printed matter, as well as the printing of counterfeit proof is completely feasible. The spectral data completely reflect the composition of the material. If there is a different material composition of the two kinds of printed matter, then the difference can react on the spectral data. It is possibly to find the difference by analyzing the spectral data. If the difference is greater than the tolerance, that is fake, if less than the tolerance, that is the real thing, and the tolerance degree can be through a number of tests.

This paper just proves that spectral information is different between two printed matters when their inks are different. If the quantity of the experimental objects is more, we can get the quantitative identification of printed products by the method of this paper.

## References

1. Shubin Deng. ENVI Remote sensing image processing method, The Science Publishing company, 2010, chapter 1–2.
2. Lixia Ding, Zhihui Wang, Hongli Ge. (2010). Continuum removal based hyperspectral characteristic analysis of leaves of different tree species. In: Journal of Zhejiang Forestry College, 27(6):809–814.
3. Quanxiang Liu, Leilei Tang. (2009). Study of Printing Identification Based on Multi-spectrum Imaging Technology. In: China Printing and Packaging Study. 1(6):30–33.

4. Yingying Liu (2014) Study on the hyper-spectrum data processing and extraction of hyper-spectrum mineralization information. MA thesis, AnHui University of Science and Technology, Aahui, China.
5. Jiwei Bai, Qingxi Tong, Lanfen Zheng (2002) The Study on the Spectral Mapping Technique based on the Hyperspectral database. MA thesis, Graduate University of Chinese Academy of Sciences, Beijing, China.
6. Fan Ye, Maozi Wang (2013) Hyperspectral identification technology research based on spectral matching. MA thesis, Chengdu University of Technology, Chengdu, China.

# Scene Text Segmentation Method Based on MSER and MLBP

Miaomiao Guo, Yaohua Yi, Juhua Liu and Ying Li

**Abstract** An effective algorithm for segmentation of scene text based on maximally stable extremal regions (MSER) and MLBP (Multiple Local Binary Patterns) is proposed to overcome the interference of uneven illumination and clutter background to scene text segmentation. Firstly, MSER algorithm is used to extract character candidates. Secondly, in the process of character classification, character candidates represented by the effective texture feature MLBP are verified using an AdaBoost trained classifier. Then, we use some heuristic rules to carry on character refinement. The final text segmentation output is obtained by combining the results from the R, G, B color channels in two polarities (bright text on dark background and dark text on bright background). The proposed method is evaluated on the ICDAR\_2013 datasets and experiments show that it performs well and can achieve good segmentation results especially in case of uneven light and complex background.

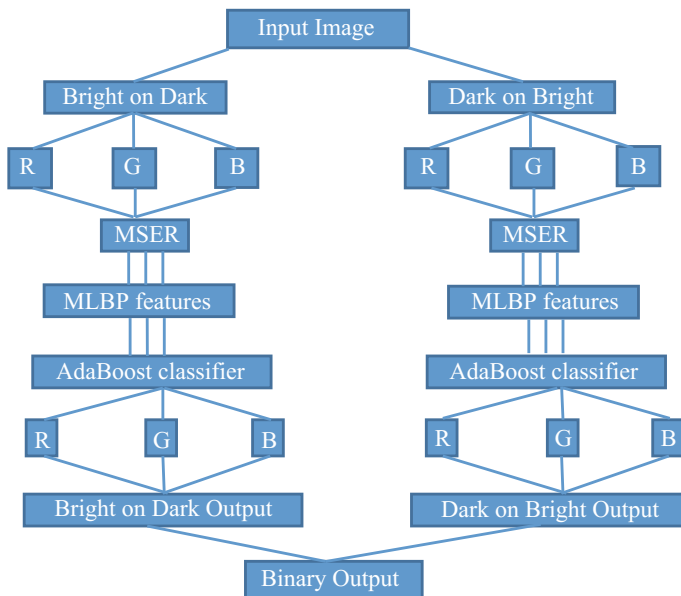
**Keywords** Text segmentation · Maximally stable extremal regions (MSER) · Adaboost · MLBP feature

## 1 Introduction

In recent years, the automatically extraction of text information in scene images is a very challenging problem in the field of computer vision. The text information in the scene images provides the key clues for the understanding of the scene, so it has been widely concerned by researchers [1, 2]. Scene text segmentation is a key technology in the process of text information extracted, it's main purpose is from the text region localization as accurately as possible to extract character pixels. Scene images are complicated in terms of color, font, layout etc. Such disturbing

---

M. Guo · Y. Yi (✉) · J. Liu · Y. Li  
School of Printing and Packaging, Wuhan University, Wuhan, China  
e-mail: yyh@whu.edu.cn



**Fig. 1** The overall process of the proposed text segmentation method

factors impose great challenges for scene text segmentation which is critical to improve the text recognition accuracy [3].

Existing methods for scene text segmentation can be largely categorized into three groups: methods using threshold, methods using clustering and methods using statistical model. These methods are still some problems that have not been solved well for the light condition and the complex and changeable background of scene text images.

MSER [4] has been proposed to establish correspondence points between images and it has been increasingly popular in many fields like object recognition [5], stereo matching [6], object tracking [7]. After character candidates are extracted, we use an AdaBoost-trained classifier that uses mean local binary patterns (MLBP) [8] to classify each character candidate into either character or non-character. Finally, we use simple heuristic rules to filter out misclassified characters. Figure 1 shows the overall process of the proposed text segmentation method.

## 2 Related Work

The algorithm proposed in this paper can be divided into three parts: sub-channels of images and MSER candidate character extracting, MLBP feature extraction and AdaBoost classification, eliminating non-characters and merging channels.

### 2.1 Image Preprocessing

The text area images after text localization from natural scene images are as the input images, which are divided into R, G, B color channels in two polarities (bright text on dark background and dark text on bright background). Comparing to a color channel, this can be extracted more image information.

### 2.2 Character Candidate Extraction

MSER proposed by Matas et al. is mainly based on the robust wide baseline stereo reconstruction and the use of the concept of the terrain in the watershed to solve the stability of local areas. Experiments [9] show that the method has the advantages of radiation invariance, good stability, simple and efficient calculation, and can be detected in different fine degree of the region. Its mathematical formula is defined as

$$q(i) = \frac{|Q_{i+\Delta} - Q_{i-\Delta}|}{|Q_i|} \tag{1}$$

where  $Q_i$  represents a connected area when the threshold is  $i$ ,  $\Delta$  is tiny variation of gray threshold,  $q(i)$  is the rate of change of  $Q_i$  area when the threshold is  $i$ . When  $q(i)$  is a local minimum value, the  $Q_i$  is the maximally stable extremal region.

Form the Formula (1), we determine whether extremal regions are maximally stable, in the case of the given  $i$  and  $\Delta$ , just judging the number of pixels to change between  $i - \Delta$  and  $i + \Delta$  gray values is a local minimum. We take a great value of  $\Delta$  will get less stable extremal regions, and smaller  $\Delta$  can be made a lot less stable regions. We should determine the value of  $\Delta$  before using MSER algorithm. As  $\Delta$  is equal to 4, the results on the R, G, B color channels in two polarities as shown in Fig. 2.

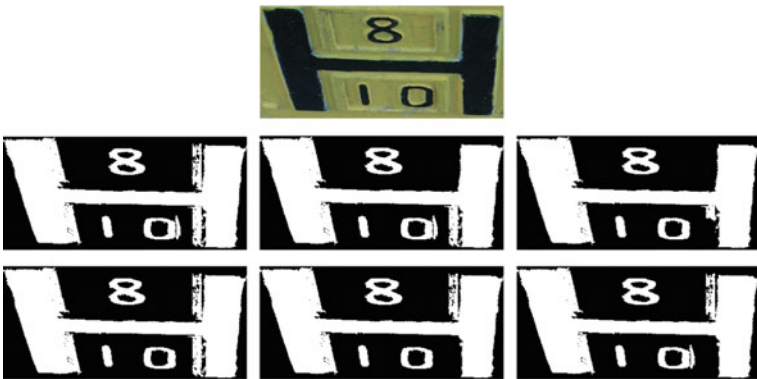


Fig. 2 MSER illustration. The first row is original image. Second row of images from left to right are dark on bright stable regions detected in the R, G, B channel. Third row of images from left to right are bright on dark stable regions detected in the R, G, B channel



### 2.3 Character Classification

MLBP is to set the number of layers of the scanning window, and set the cell size in the order from large to small. Then we extract features of the overall information using a larger scale of LBP in the upper layer of the scanning window, the features of describing the detail information are extracted from the final layer of the scanning window. Finally, all the extracted feature vectors are concatenated together to form the final features.

MLBP combines the global and local information, and makes the feature vector from 256 dimensions down to 59 dimensions to achieve the role of dimensionality reduction. Not only can in case of a reduction in the amount of data well represent the image texture information, but also it can reduce the effects of high frequency noises caused.

In this process, we prepared 23,612 positive samples and 70,419 negative samples from ICDAR2013 training data set, and transformed them to the R, G, B color channels in two polarities with a size of  $32 \times 32$ . The AdaBoost algorithm is implemented using GML AdaBoost Matlab Toolbox, constructing a depth of 2 CART decision tree as a weak classifier, and using Gentle AdaBoost, Modest AdaBoost and Real AdaBoost to train AdaBoost classifier with 200 times of iterations and 500 times of cross validations.

## 3 Results and Discussion

The evaluation of the proposed method is performed on ICDAR2013 [10] dataset, which consists of 233 images. The segmentation performance is evaluated in both pixel level and atom level as presented in ICDAR2013 Robust Reading Competition.

Performance of the algorithms based on the pixel level evaluation and atom level evaluation by the accuracy rate of  $P$ , the recall rate of  $R$  and the overall performance of  $F$  three measures, respectively defined as

$$P = \frac{TP}{TP + FP} \quad (2)$$

$$R = \frac{TP}{TP + FN} \quad (3)$$

$$F = \frac{2 \times R \times P}{R + P} \quad (4)$$

where  $TP$  represents the number of correctly labeled word pixels;  $FP$  represents the number of labeled word pixels from background pixels;  $FN$  represents the number of labeled word pixels from word pixels.

**Table 1** Evaluation on ICDAR2013 datasets (%)

Method	Pixel level			Atom level		
	R	P	F	R	P	F
Proposed	84.29	41.51	55.63	38.60	27.05	31.81
OTCYMIST	46.11	58.53	51.58	41.79	31.60	35.99
NSTsegmentator	68.41	63.95	66.10	68.00	54.35	60.41

### 3.1 Pixel Level and Atom Level Evaluation

Pixel level evaluation is widely used in document image processing and adopted in the robust reading competitions [11]. It can give a very direct measure of the text segmentation performance. Atom level evaluation is more accurate for text segmentation since it is designed to measure how well the text structure has been preserved instead of just comparing pixel by pixel with the ground truth. Detailed results are given in Table 1. From Table 1 we can see our proposed method can also deal with these challenging problems and need further improvement.

### 3.2 Sample Results

Several sample segmentation results are shown in Fig. 3 to give a direct illustration. Our method takes into MLBP feature extraction and a huge number of positive and



**Fig. 3** Illustration of our proposed method. Each row on the *left* is the original image, and the *right* is the result of text segmentation

negative samples training classifiers, in dealing with text area uneven illumination and complex background issues have been good results.

## 4 Conclusions

We proposed an overall process of the proposed text segmentation method. An MSER algorithm is used to extract character candidates. And in the process of character classification, character candidates represented by the effective texture feature MLBP are verified using an AdaBoost trained classifier. Also we obtained the final text segmentation output combining the results from the R, G, B color channels in two polarities, which more image information can be obtained.

As the texts in scene images have a little constraint, we should find more features about scene text to be used into classifier, which can pick out the best-quality candidates. We will investigate this in our future work.

## References

1. Sharma N, Pal U, Blumenstein M. Recent advances in video based document processing: A review [C]. Proc of the 10th IAPR Int Workshop on Document Analysis Systems. Queensland: IEEE Press, 2012: 63–68.
2. Zhang H G, Zhao K L, Song Y Z, et al. Text extraction from natural scene image: A survey [J]. *Neurocomputing*, 2013, 122: 310–323.
3. D. Kumar, M. Prasad, and A. Ramakrishnan, “ Benchmarking recognition results on camera captured word image data sets,” in *Proceeding of the workshop on Document Analysis and Recognition*, 2012, pp. 100–107.
4. J. Matas, O. Chum, M. Urban, and T. Pajdla, “Robust wide-baselin stereo from maximally stable extremal regions,” *Image and Vision Computing*, vol. 22, no. 10, pp. 761–767, 2004.
5. Nist’er, D., Stew’ enius, H. Scalable recognition with a vocabulary tree [C]// *IEEE Conference on Computer Vision and Pattern Recognition (CVPR)*, 2006, 2: 2161–2168.
6. Obdrzalek, S., Matas, J. Object recognition using local affine frames on distinguished regions [C] // *British Machine Vision Conference*, 2002, 1:113–122.
7. Donoser, M., Bischof, H. Efficient maximally stable extremal region (mser) tracking [C] // *IEEE Conference on Computer Vision and Pattern Recogniton (CVPR)*, 2006: 553–560.
8. G. Bai, Y. Zhu, and Z. Ding, “A hierarchical face recognition method based on local binary pattern,” *Proc. Congr. Image Signal Process*, pp. 610–614, 2008.
9. Mikolajczyk K, Tuytelaars T, Schmid C, et al. A comparison of affine region detectors [J]. *International Journal of Computer Vision*, 2005, 65 (1–2): 43–72.
10. D. Karatzas, L. Gomez-Bigorda, A. Nicolaou, S. Ghosh, A. Bagdanov, M. Iwamura, J. Matas, L. Neumann, V. R. Chandrasekhar, S. Lu, et al. In *Document Analysis and Recognition (ICDAR)*, 2015 13th International Conference on, pages 1156–1160. IEEE, 2015.
11. S. M. Lucas, A. Panaretos, L. Sosa, A. Tang, S. Wong, and R. Yong, “Icdar 2003 robust reading competitions,” in *Document Analysis and Recognition*, 2003 International Conference on, 2003, pp. 682–687.

# Research on Stereo Image Rendering Based on Micro Lens Array

Wei Liu, Guangxue Chen and Mengyu Li

**Abstract** Micro lens array is a quick way to display stereoscopic vision which has 360° view multi-dimensional effect. It is also an inevitable trend used in anti-fake technology, but the research of the basic principle of micro lens array imaging technology is limited. This paper analyzed micro lens array's stereo imaging printing principle based on the principle of moire fringe and lens imaging technology, designed arrays of three-dimensional image original manuscripts under different technical parameters, and then analyzed the stereoscopic present effect. Experimental data showed that for square lens, when space between micro graphics array unit is between 174 and 186  $\mu\text{m}$ , it displays good stereo effect.

**Keywords** Micro lens array · Micro graphics array · Moire fringe

Stereoscopic image reproduction technology which provides multi-dimensional effect has very wide application prospect. Stereoscopic image reproduction combined with printing technology can be observed by naked eyes today. It is an inevitable trend which can quantity produce by factories and easily observed mainly including cylindrical lens and micro lens array. Micro lens array has both horizontal parallax and vertical parallax thus it displays multi-dimensional effect with 360° view compared with only vertical parallax of cylindrical lens [1]. Micro lens array can also avoid the vertiginous sensation which caused by cylindrical lens [2]. But the research on the basic principle of micro lens array imaging technology and its technical parameter is limited.

This paper analyzed micro lens array's stereo imaging printing principle based on the principle of moire fringe and lens imaging technology designed arrays of

---

W. Liu · G. Chen (✉)

State Key Laboratory of Pulp and Paper Engineering, South China University of Technology, Guangzhou, China  
e-mail: chengx@scut.edu.cn

M. Li

South China University of Technology, Guangzhou, China

© Springer Nature Singapore Pte Ltd. 2017

P. Zhao et al. (eds.), *Advanced Graphic Communications and Media Technologies*, Lecture Notes in Electrical Engineering 417, DOI 10.1007/978-981-10-3530-2\_39

311

three-dimensional image original manuscripts under different technical parameters and then analyzed the three-dimensional effect [3, 4].

## 1 Introduction

Moire fringe is a visual result caused by interference fringe between two lines or two objects with constant angle and frequency positioned. When human eyes cannot distinguish these two lines or two objects but can only see interference fringe, this optical phenomenon is the moire fringe.

Moire fringe is extremely sensitive to slight displacement, rotation and deformation, which is the most common harmful defect in planographic printing. It should be avoided as possible as we can. But in the micro lens array three-dimensional printing technology, those play a very important role, using moire fringe amplification theory of micro lens array to micro graphic array. It can produce a variety of three-dimensional effects: stereoscopic, dynamic and transformational products with parallax effect, including the float, sinking, parallel movement, orthogonal moving and dual-channel, etc. [5]. Moire fringe formation mechanism of the micro lens has a vital guiding significant to micro lens array stereoscopic image reproduction.

The theoretical formula of moire fringe is

$$P = \frac{P_1 \cdot P_2}{\sqrt{P_1^2 + P_2^2 - 2P_1P_2 \cos \theta}} \quad (1)$$

Direction angle of moire fringe is:

$$\partial = 90^\circ \pm \arccos\left(\frac{P \sin \theta}{P_2}\right) \quad (2)$$

Among (2), counting positively when  $P_1 \cos \theta < P_2$ , negatively otherwise.

## 2 Experiments and Discussion

Line number of micro lens array is lens numbers in per unit length. Measured space between adjacent micro lens units of micro lens array optical grating (unit is  $\mu\text{m}$ ), we can calculate optical grating line number of micro lens array [6]. If line number of micro lens array is  $L$ , space between adjacent micro lens units is  $D$ , there is:

$$L = 2.54 \times 10^4 / D \quad (3)$$

Line number of micro lens array is a critical reference data to original manuscripts. It has two kinds optical grating line number, transverse and longitudinal. Longitudinal optical grating line number is expressed by multiple of transverse. In this paper, we use square lens of which longitudinal optical grating line number is one times and space between micro graphic array units is 180  $\mu\text{m}$ . Changed diameter of micro graphics array unit, we can get stereoscopic effect.

## 2.1 *Experimental Materials and Equipment*

Experimental materials and equipment: square lens from GRAPAC Japan company; metaloscope of Axio Imager A2m brand from German; Canon camera of IXUS 115 HS.

## 2.2 *Experimental Procedure and Discussion*

1. The files of different spaces of micro graphics array unit have been made by Illustrator CS5. Roundness was chosen as micro graphic. Its color is solid black, and the diameter of micro graphics array unit is 80  $\mu\text{m}$ . The size of each file is 5 cm  $\times$  5 cm. We chose 174, 176, 177, 178, 179, 180, 181, 182, 183, 184, 186  $\mu\text{m}$  as  $s$  which refers to space between micro graphics array units. Recorded micro graphics array units of one line, donated by  $n_1$ .
2. Put files made in procedure (1) in pre-pressed publication system and type setting, screening output CTP. Screen line is 200 lines, screen angle is 45° and the output resolution is 2540 dpi.
3. The CTP plate and optical grating of micro lens array was glued with intersection angle of 43°. Observed each micro graphics array unit, it can easily observed depth of field. Recorded present micro graphics array units of one line, donated by  $n_2$ . The present effect took by cameras are as follows.

For depth of field effect, we can found that from pictures, when space between micro graphics array units is between 174 and 180  $\mu\text{m}$ , pictures display long shot, its depth of field is deeper when space is bigger; when space between micro graphic array units is between 180 and 182  $\mu\text{m}$ , depth of field has the most deep effect; when space between micro graphics array unit is between 182 and 186  $\mu\text{m}$ , pictures show close shot, its depth of field is shallower when space is bigger.

As for amplification effect, the magnification times formula is:

$$M = n_1/n_2 \quad (4)$$

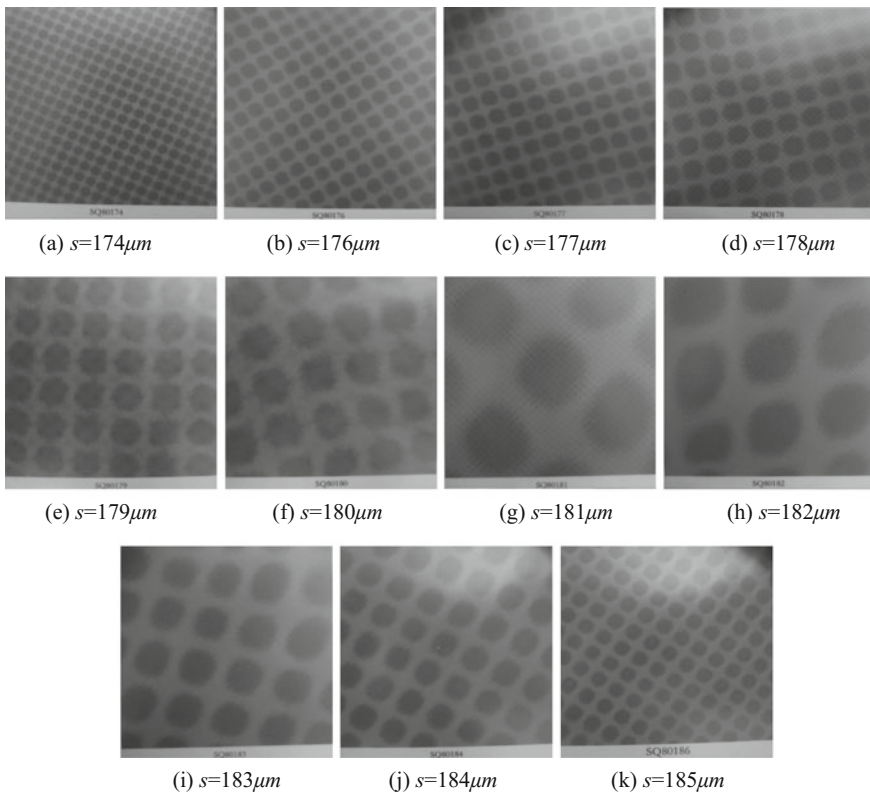
$n_1$  Micro graphics array units of one line made by Illustrator CS5

$n_2$  Present micro graphics array units of one line.

Then the relationship between the magnification times and space between micro graphics array units is as follows:

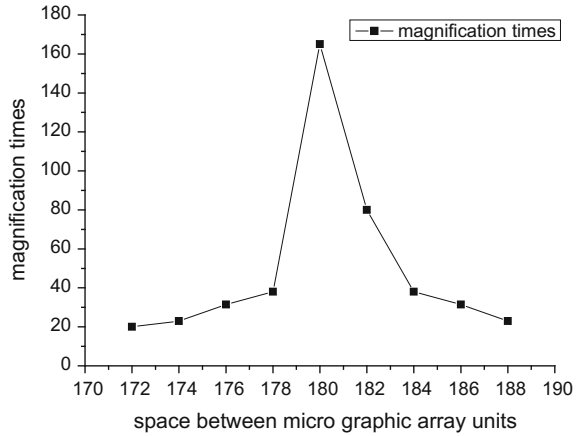
From Figs. 1 and 2, when space between micro graphics array unit is between 174 and 180  $\mu\text{m}$ , magnification times of picture gradually increases when space becomes bigger; when space between micro graphics array units is between 180 and 182  $\mu\text{m}$ , magnification times of picture becomes the biggest; when space between micro graphics array unit is between 182 and 186  $\mu\text{m}$ , magnification times of picture gradually decreases. Also it displays symmetrical trend.

As for present picture quality, when space between micro graphic array units is between 174 and 186  $\mu\text{m}$ , the picture quality is good. Those space parameters can all put in stereoscopic printing technology.



**Fig. 1** The present effect of different spaces between micro graphics array units

**Fig. 2** Relationship between the magnification times and space between micro graphics array units



### 3 Conclusions

Space between micro graphics array units affects depth of field and amplification effect of picture. When space is less than 180  $\mu\text{m}$  and vicinal 180  $\mu\text{m}$ , it shows long shot, magnification times of picture gradually increases when space becomes bigger; when space is greater than 182  $\mu\text{m}$  and vicinal 182  $\mu\text{m}$ , it shows close shot, magnification times of picture gradually decreases when space becomes bigger; when space is between 174 to 186  $\mu\text{m}$ , the picture quality is good. Those space parameters can all put in stereoscopic printing technology.

**Acknowledgements** This research was financially supported by the Guangdong Provincial Science and Technology Project (2013B090600060).

### References

1. Xie, H., Zhao, X., Yang, Y., et al. Cross-lenticular lens array for full parallax 3D display with crosstalk reduction [J]. *Science China Technological Sciences*, 2012, 55(3): 735–742.
2. Zhao, Y., Yao, R., Ouyang, L., et al. Three-dimensional printing of HeLa cells for cervical tumor model in vitro [J]. *Biofabrication*, 2014, 6(3): 035001–035001.
3. Lee, J. Y., Choi, B., Wu, B., et al. Customized biomimetic scaffolds created by indirect three-dimensional printing for tissue engineering [J]. *Biofabrication*, 2013, 5(4): 380–387.
4. Lim, Y. J., Yu, J. H., Song, K. H., et al. Film patterned retarder for stereoscopic three-dimensional display using ink-jet printing method [J]. *Optics Express*, 2014, 22(19): 22661–6.
5. Dai, H. T., Liu, Y. J., Sun, X. W., et al. A negative-positive tunable liquid-crystal micro lens array by printing [J]. *Optics Express*, 2009, 17(17):4317–23.
6. Xie, D., Chang X., Shu X., et al. Rapid fabrication of thermoplastic polymer refractive micro lens array using contactless hot embossing technology [J]. *Optics Express*, 2015, 23(4):5154–66.



# Research on Reading Recognition Technology of Gas Meter Based on Key Feature Matching

Wenfa Qi, Bowen Xue and Yuxin Liu

**Abstract** In this article, we proposed a reading recognition technology for gas meters that can greatly substitute for artificial reading. The proposed technology includes three phases of work, which are image preprocessing, character location and segmentation, and character recognition respectively. The location method of color background and the vertical projection feature are employed to locate and segment characters, while the closed curve detection method, the template matching method and the pass line detection method are utilized and incorporated in character recognition phase. Finally, an experiment is conducted containing reading images of 100 samples with different angles and illumination, and experimental results verify the effectiveness of the proposed method.

**Keywords** Image processing · Number recognition · Feature extraction · Image template matching

## 1 Introduction

With the rapid development of computer science and technology, it is very common that machines and computers have replaced many artificial works. Among them, the most typical one is computer vision technique, which makes the computer replace human brain to understand and recognize images. However, in most scenarios, the gas meters reading and recording are still manual operations and that could not only consume tremendous manpower, but also may cause unavoidable errors. In this light, an automatic gas meter recognition system is greatly expected, by which the reading of meter can be accurately recognized and accessed by users.

Many researches have been done recently focusing on similar recognition demands, such as license recognition system [1–4]. Most image recognition systems are composed of three parts: image preprocessing, feature extraction and

---

W. Qi (✉) · B. Xue · Y. Liu

Institute of Computer Science and Technology, Peking University, Beijing, China  
e-mail: qiwenfa@pku.edu.cn

© Springer Nature Singapore Pte Ltd. 2017

P. Zhao et al. (eds.), *Advanced Graphic Communications*

and *Media Technologies*, Lecture Notes in Electrical Engineering 417,

DOI 10.1007/978-981-10-3530-2\_40

image classification [5]. The proposed gas meter recognition system is composed of three parts which are image localization, character segmentation, and character recognition. In image localization phase [6, 7], the reading number area of a gas meter is extracted from background, after that, the image is binarized and normalized into required forms. Then, characters in reading area are separated into individual digitals in segmentation phase. Finally, a series of individual characters are feed into character recognition phase and the final reading results are composed by the output of character recognition phase. Though, many complex and efficient character recognition algorithms are available [8], we decide to choose three conventional methods to integrate the proposed recognition system considering the gas meter recognition scenario. Specifically, short response time and high efficiency are key measures to classifier selection [9], since the proposed system is expected to extend to mobile terminals.

## 2 Image Location and Character Segmentation

### 2.1 Image Location

Based on the feature that the background of reading area is all red compared with neighboring region, we firstly detect all closed regions with red as background colors. Then, it records each closed region as a rectangle using four vertexes coordinates. In terms of prior knowledge, some unrelated regions are discarded, while the final location of reading area is determined considering inclusion relationships and relative position of all the remaining regions. Finally, the detected reading area is cut out, normalized to fixed size and binarized. Due to the dramatic gray change between the foreground and background partition around the digits area and nearby, the meters can be effectively captured in the binarized pictures. In Fig. 1, the images of gas meter before and after location are displayed, which shows the effectiveness of the proposed location method.



**Fig. 1** a Gas meter images before location process and b gas meter images after location process

## 2.2 Character Segmentation

With the normalized reading area, we dedicated to segment the reading number into individual character in this subsection so as to facilitate the character recognition process in next section. Observing the located normalized images, each character is distributed uniformly with equal interval. Thus, the vertical projection feature can be utilized to effectively separate each character. The distribution of histogram will have obvious wave crests with similar intervals, by which we can estimate the boundary of each character and finally separate them efficiently, just as shown in Fig. 2.

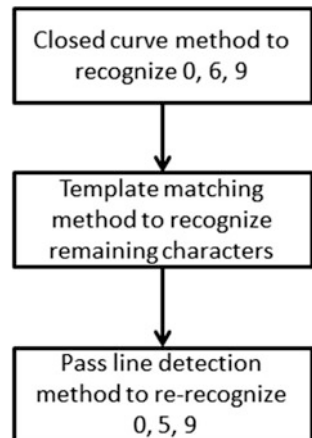
## 3 Character Recognition Process

In this section, we propose to incorporate three simple but effective recognition methods to recognize each separated character. Specifically, the closed curve detection algorithm [10] is utilized to detect characters 0, 6 and 8. Then, the template matching method is employed to detect the remaining seven characters. However, based on plenty of testing experiments, we find that the characters 0, 5, 6 and 9 are easily confused. Thus, the pass line detection method is added to re-recognize the preceding four characters before outputting the final recognition results. The flowchart of the proposed recognition process is shown in Fig 3.

Fig. 2 Characters after segmentation process



Fig. 3 Flowchart of proposed recognition process



### 3.1 Closed Curve Detection Method

The closed curve is important structure information for digital character images, e.g., the circles in characters. In this subsection, the Freeman chain code tracking method is employed to detect circles in digital characters and the characters of 0, 4, 6, 8 and 9 will be detected for having circles. Digit 8 is distinct for it has two circles and thus can be directly recognized, digits 0 and 6 can be recognized as well for each of them has only one circle which located in center or lower part of individual character respectively. However, digit 4 and 9 are hard to distinguish since they all have only one circle located in higher part of the character image. Thus, by the closed curve detection method, 0, 6 and 8 are firstly recognized.

### 3.2 Template Matching Method

Template matching is one of the most basic methods in character recognition fields. The aim of template matching method is to compare the input character with the pre-defined templates and calculate the similarity between them; the recognition results are obtained by the similarity values.

Let the known image template as  $T$ , with the size  $M*N$ . Then let the image to be recognized as  $I$ , with the size  $L*W$  ( $L > M$ ,  $W > N$ ). The matching process is to try to overlay the image  $T$  into image  $I$ , and compare the difference between  $T$  and  $I$ . If the difference is less than the predetermined threshold, the  $T$  is considered to have a better match with the sub-image of  $I$ , that is, to find the target object. The mathematical description of the matching process can be described as:

$$D(i,j) = \sum_{m=1}^M \sum_{n=1}^N I_{ij}^2(m,n) - 2 \sum_{m=1}^M \sum_{n=1}^N I_{ij}(m,n) * T(m,n) + \sum_{m=1}^M \sum_{n=1}^N T^2(m,n) \quad (1)$$

while the first and third term indicate the autocorrelation between the subset of image  $I$  and template  $T$ , and the second term indicates the cross-correlation between them, so the larger of this term, the smaller of  $D(i,j)$ , which means that the input sub-image has a better match with the template image. If  $D(i,j)$  equals to zero, we say that there is a perfect matching.

Based on the traditional template matching method described above, our method makes some improvements to reduce the complexity of program which includes:

- (1) Compute the number of black pixels in image  $I$  as  $N$ ;
- (2) For each black pixel position at  $(i,j)$  in template image, find the pixel position at  $(i,j)$  in image  $I$  and its eight neighbor, those nine points are consisting of a window.

- (3) Consider all the pixels in the window, if there exists a black pixel, then input image and template image is matched in this position, and let the number of matching pixels  $pixel\ match + 1$ ;
- (4) Repeat step 2 and 3 until all the black pixels in the template image are processed.
- (5) Compute the matching rate of template image result as  $pixel\ match/N$ ;
- (6) Repeat step (1)–(5), compute the matching rate of all template images;
- (7) Set the highest matching rate as the recognition result.

### 3.3 Pass Line Detection Method

Based on the above two recognition methods, some experiments are conducted to test the character recognition performance. The results show that misrecognition concentrates on characters 0, 5 and 9. Thus, we integrate the pass line detection method to re-recognize the afore-mentioned three characters.

The pass line detection method is indeed a variation of conventional template matching method, which only extracts certain useful features to compare with template images. Based on the structure invariance feature of printed figures, we extract six features for the pass line detection: the pixel-jump numbers along six pass lines in horizontal and vertical directions. Specifically, the pixel-jump numbers in horizontal direction is explained below in detail.

Firstly, divide the character image into upper, middle and lower parts, and for each part, a horizontal line is utilized to scan and count the pixel-jump. Suppose the character image is of size  $M*N$ , then the three horizontal lines are located as:  $y_1 = \frac{M}{6}$ ,  $y_2 = \frac{M}{2}$  and  $y_3 = \frac{5M}{6}$ .

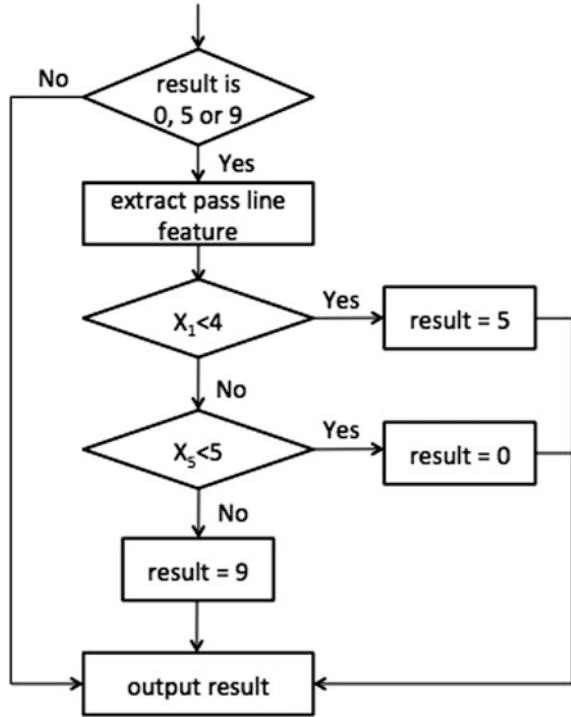
Then, along each pass line, the pixel jump numbers are counted. As for the pixel-jump, we count the times of pixel values jumping from 0 to 255 and vice versa. Considering the existence of noise, between each pair of jump, we set a threshold  $k$  such that only jumps between at least  $k$  continuous pixels are counted.

The process of the other three pass lines on vertical directions is just the same as the horizontals, where the three lines are located as  $x_1 = \frac{N}{6}$ ,  $x_2 = \frac{N}{2}$  and  $x_3 = \frac{5N}{6}$ . The pixel jump numbers along pass lines make up a feature vector  $X = (x_1, x_2, \dots, x_6)$  of size 6. We extract the pass line feature for all the templates of the ten characters and the average results are shown in Table 1, from which it can be noted that the confusing characters 0, 5 and 9 can be easily identify. The classification process is drawn in Fig. 4.

**Table 1** Average pass line features for template character images

Character	Pass line feature vector					
	$x_1$	$x_2$	$x_3$	$x_4$	$x_5$	$x_6$
0	<b>4.00</b>	4.00	4.00	3.61	<b>3.97</b>	3.67
5	<b>2.26</b>	2.26	2.00	4.90	<b>5.67</b>	5.87
9	<b>4.03</b>	2.20	2.07	5.33	<b>5.87</b>	4.67

**Fig. 4** Classification process for pass line process



## 4 Experimental Results

The performance of our gas meter image recognition system is evaluated by our own database. The images in our database are photographed by smart mobile phones with high resolutions. In order to evaluate the robustness of the algorithm under different environmental conditions, the images are obtained under different visual angles and illumination conditions. The database consists of 50 images and each of them has similar ratio of gas meters.

The recognition process is divided into three parts. The first part is the initial stage, and we choose 100 samples of 0–9 ten printed digits as initial samples which are consciously covers the left, right, up and down deviation of positions and different illumination cases. Each sample are manually specified the output, and extract the features into feature database. The second part is the stage of growth. In this part we choose 100 samples use the same method with the recognition method, compare the extracted feature with the feature in database to rectify the error output, and save these feature data into the database to improve the database. The third part is the verification stage. In this stage we use 30 samples for each digit to recognize and record the classification rates. The recognition results are shown in Table 2.

Carefully observe the recognition results, and the interval with highest error rates, we can find out that 5 can be easily identified as 6, while 9 easy to be identified as 4. The detail results are shown in Table 3.

**Table 2** Recognition result of verification stage

Sample	Number of samples	Recognition correctness	Recognition rates (%)
0	30	25	83.33
1	30	30	100
2	30	29	96.67
3	30	28	93.33
4	30	28	93.33
5	30	26	86.67
6	30	28	93.33
7	30	29	96.67
8	30	27	90.00
9	30	27	90.00

**Table 3** Detail recognition results

Characters	The recognition results									
	0	1	2	3	4	5	6	7	8	9
0	25	0	0	0	2	0	1	0	0	2
1	0	30	0	0	0	0	0	0	0	0
2	0	0	29	0	0	0	0	1	0	0
3	0	0	1	28	0	1	0	0	0	0
4	0	0	0	0	28	0	0	0	0	2
5	0	0	0	1	0	26	3	0	0	0
6	0	0	0	0	0	2	28	0	0	0
7	0	0	0	0	0	0	0	29	0	1
8	0	0	0	0	0	0	2	0	27	1
9	0	0	0	0	3	0	0	0	0	27



**Fig. 5** Gas meter images and recognition results

It can be seen that the above two kinds of circumstances is a common mistake due to the image shifting and losing half of the image. Because of the limited time, our database cannot cover all the conditions, and the correctness of the above errors is not performed. One of the potential methods is to consider it as special case and do some further researches.

Finally, some recognition results of the proposed technique are shown in Fig. 5, with the original gas meter images.

## 5 Conclusions

In this paper, we proposed a recognition technique for gas meter images, which can reduce the manpower and artificial mistakes. The image location and character segmentation phase is essential to increase the recognition accuracy. By locating the red background of reading area and using vertical projection method to separate character, the gas meter image is transformed into a series of normalized binary character images. Then, in recognition part, three methods are corporately utilized to accurately recognize each individual character, which finally make up the output reading.

However, there are still some improvements to be researched in the future. In actual use, if the gas meter image is too red or greenish, or overexposed, the recognition rate will decrease greatly. Therefore, to enrich the template database and improve the recognition algorithm is very important work in the future.

## References

1. WU Chuan-sun, ZOU Yang-de, ZHOU Ding-kang. The Application of Binaryzation Algorithms in License Plate Recognition. *Computer and Modernization*. Beijing. 2003.94(6): 13–16.
2. CHEN Jian-kun, Fan Chun-nian. Neural network based vehicle license plate location. *Journal of Liaoning Technical University(Natural Science Edition)*. Liaoning. 2005.24(1): 97–100.
3. YANG Jun, QI Fei-hu. A License Plate Location Approach Based on Shape and Texture Characteristics. *Computer Engineering*. Beijing. 2006.32(2):170–171.
4. HUANG Hao-jie, LI Rong, CHANG Hong-sen. A Novel Method for License Plate Location Based on Edge Color Distribution. *Laser Journal*. Beijing. 2007.28(3): 57–59.
5. SHEN Ting-zhi, WANG Wei-hong, YAN Xue-mei. *Digital Image Processing and Pattern Recognition*. Beijing Institute of Technology Press. Beijing. 2007:54.
6. Xie Hong, LIU Ling, LIU Yan-yan. Research on Complicated Sea-sky-line Area Detection Algorithm. *Applied Science and Technology*. 2006.33(6). Beijing: 96–98.
7. LI Kai-mo. Analysis of Application of Edge Operators in Positioning License Plate. *Journal of Zhengzhou Polytechnic Institute*. Zhengzhou. 2004.20(3):1–2.
8. WANG Ya-kun, ZENG De-liang, Li Xiang-ju. *New Algorithm for Digital Recognition*. Power Science and Engineering. Beijing. 2009.25(1): 76–78.
9. S.R. Dubois, F.H. Glanz. An Autoregressive Model Approach to two-dimensional Shape Classification. *IEEE Trans.PAMI*.1986. Page 56–65.
10. R.L. Kashyap, R. Chellappa. Stochastic Models for Closed Boundary Analysis. *IEEE Trans. Inform. Theory* IT-27.1981. Page 627–637.



# Image Quality Assessment Scheme Based on Structural Contrast Index and Gradient Similarity

Li Liu, Yuanlin Zheng and Wei Wang

**Abstract** Image quality assessment (Anmin et al. in Image Proc, IEEE Trans 21 (4):1500–1512, 2012 [1]) is very important for image processing. A good image evaluation algorithm is consistent with subjective evaluations and has low computational complexity. A lot of image quality assessment methods have been proposed in recent years. Structural Contrast Index (SCI) has been proved can effectively reflect the complexity of image texture and model the masking effect of human visual system (HVS), so SCI is used as an important feature. HVS is very sensitive to edge region, however, SCI can't correctly model the edge region structure. So the gradient similarity was incorporated into our method. An image quality assessment scheme based on structural contrast index and gradient similarity was proposed in our paper. Extensive experiments conducted on TID2013 image database demonstrate the performance this scheme is slightly better than the state-of-art methods not only on prediction accuracy but computational complexity.

**Keywords** Image quality assessment · Masking effect · Structural contrast index · Gradient similarity

## 1 Introduction

With the development of computer vision and image processing, a lot of image quality assessment methods are proposed. According to the availability of reference image, the presented metrics can be classified into full-reference ones, reduced-reference ones and no-reference ones. In this paper, the discussion focuses on FR methods.

---

L. Liu · Y. Zheng (✉) · W. Wang  
Faculty of Printing, Packing Engineering and Digital Media Technology,  
Xi'an University of Technology, Xi'an, China  
e-mail: zhengyuanlin@xaut.edu.cn

Y. Zheng  
Shaanxi Provincial Key Laboratory of Printing and Packaging Engineering, Xi'an, China

IQAs like peak-to-noise ratio (PSNR) and root-mean-square error (RMSE), which are based on the mean square error (MSE) correlate poorly with HVS [1]. As we know more about the HVS, some HVS based methods are operated on image contrast rather than pixel value are presented. The Mean Structure Similarity Index (SSIM) proposed in paper [2] is quite a big breakthrough in image quality assessment modeling. Structure based methods like SSIM is based on the hypothesis that HVS is very sensitive to some structure information in the visual scene. So the result is more consistent with perceptual quality. The upgraded versions MS-SSIM [3], measure the structure loss of image. It is well known that edges are very important image structures and crucial for visual perception. Recently, gradient/edge based or gradient combined methods were proposed in succession. Multiscale visual gradient similarity (VGS) [4] is a very reliable one to some extent. Cheng et al. presented a GSD [5] method based on gradient magnitude and orientation. It has a good performance on LIVE image database and a low computational complexity. Xue et al. modified the GSD algorithm, proposed the gradient magnitude similarity deviation (GSMD) method [6]. Gradient similarity was also incorporated into methods feature similarity index (FSIM) [7] and visual saliency-induced index (VSI) [8].

Inpaper [9], Structural Contrast Index (SCI) has been proved that it can effectively reflect the complexity of image texture and model the masking effect of human visual system (HVS). Inpaper [10], SCI is used as one of the six important features to get a good result. Inspired by these methods above, we proposed a structural contrast index and gradient similarity based method. Color distortion is also considered in our work. It is very simple and can be operated with low complexity. The method conducted on image database outperforms most of the other ones.

## 2 Proposed Method

### 2.1 SCI (*Structural Contrast Index*)

Masking effect is one of the important characteristics of the human visual system. It means that when a masking stimulus appearing in the background of an image will reduce or increase the visibility of the image signal. Texture region is more complex than homogeneous region. To an observer, there is less priori knowledge. As a result, masking effect in texture area is more serious than it in homogeneous region. Since masking effect is closely related to background texture,  $SCI(\tau)$  [10] is devised to consider the structure complexity and contrast intensity of a pattern. The details of SCI is described in [10]. HVS sensibility is inversely proportional to structure complexity. So inverse  $SCI(\tau^*)$  is used as an feature to assess the image quality. The calculation of  $\tau^*$  is simplified to

$$\tau^* = \frac{\sum_{(\mu,v) \in B} \{(\mu^2 + v^2)^2 \cdot (\varepsilon + |c(\mu, v)|)\}}{\sum_{(\mu,v) \in B} \{(\mu^2 + v^2) \cdot (\varepsilon + |c(\mu, v)|)\}^2} \quad (1)$$

where  $c(u, v)$  is the  $(u, v)$ -th DCT coefficient value. Parameters in the formulas are empirically set. The  $\tau^*$  similarity calculation between  $f_1$  (reference image) and  $f_2$  (distorted image) is defined as:

$$S_{\tau^*} = \frac{2\tau_1^* \cdot \tau_2^* + C_1}{\tau_1^{*2} + \tau_2^{*2} + C_1} \quad (2)$$

## 2.2 Gradient Similarity

HVS is very sensitive to edge region, however edge regions often have high structure complexity. Masking effect is wrongly modeled by SCI in edge regions. To solve the problem above, edge regions should be considered in our method. There are three commonly used operators to compute the image gradient. Here we use Scharr operator. The partial derivatives of image  $f_1$  along horizontal and vertical directions are  $G_{1x}$  and  $G_{1y}$ . They are calculated as:

$$G_{1x} = \frac{1}{16} \begin{bmatrix} 3 & 0 & -3 \\ 10 & 0 & -10 \\ 3 & 0 & -3 \end{bmatrix} * f_1$$

$$G_{1y} = \frac{1}{16} \begin{bmatrix} 3 & 10 & 3 \\ 0 & 0 & 0 \\ -3 & -10 & -3 \end{bmatrix} * f_1 \quad (3)$$

the gradient modulus (GM) is defined as  $G = \sqrt{G_x^2 + G_y^2}$ . The gradient similarity calculation between  $f_1$  (reference image) and  $f_2$  (distorted image) is calculated as:

$$S_G = \frac{2G_1 \cdot G_2 + C_2}{G_1^2 + G_2^2 + C_2} \quad (4)$$

## 2.3 Color Space Transformation

To measure the color distortions, chrominance information of the image is incorporated in our method. The original images in RGB space are transformed to LMN space, in which the luminance factor  $L$  can be eliminated. The conversion from RGB space to LMN space is achieved by:

$$\begin{bmatrix} L \\ M \\ N \end{bmatrix} = \begin{bmatrix} 0.06 & 0.63 & 0.27 \\ 0.30 & 0.04 & -0.35 \\ 0.34 & -0.6 & 0.17 \end{bmatrix} \begin{bmatrix} R \\ G \\ B \end{bmatrix} \tag{5}$$

Let  $M_1$  ( $M_2$ ) and  $Q_1$  ( $Q_2$ ) be the  $M$  and  $N$  chromatic channels of image  $f_1$  ( $f_2$ ). Similar to the definitions of  $S_{\tau^*}$  and  $S_G$ , the similarity between chromatic features is defined as:

$$S_G = \frac{2M_1 \cdot M_2 + C_3}{M_1^2 + M_2^2 + C_3} \cdot \frac{2N_1 \cdot N_2 + C_3}{N_1^2 + N_2^2 + C_3} \tag{6}$$

Parameters  $C1$ ,  $C2$  and  $C3$  are positive constants to avoid the denominator being zero.

### 2.4 Proposed SCGM Method

Similarity between  $f_1$  and  $f_2$  is calculated as:

$$S = \frac{\sum_{\Omega} S_{\tau^*}^{\alpha} \cdot S_G^{\beta} \cdot S_C^{\gamma} \cdot \omega_{f_1, f_2}}{\sum_{\Omega} \omega_{f_1, f_2}} \tag{7}$$

$\alpha, \beta, \gamma$  in (7) are parameters to measure the importance of corresponding feature.  $\omega_{f_1, f_2}$  is the local weight, we use inverse SCI ( $\tau^*$ ) as the local weight in pooling

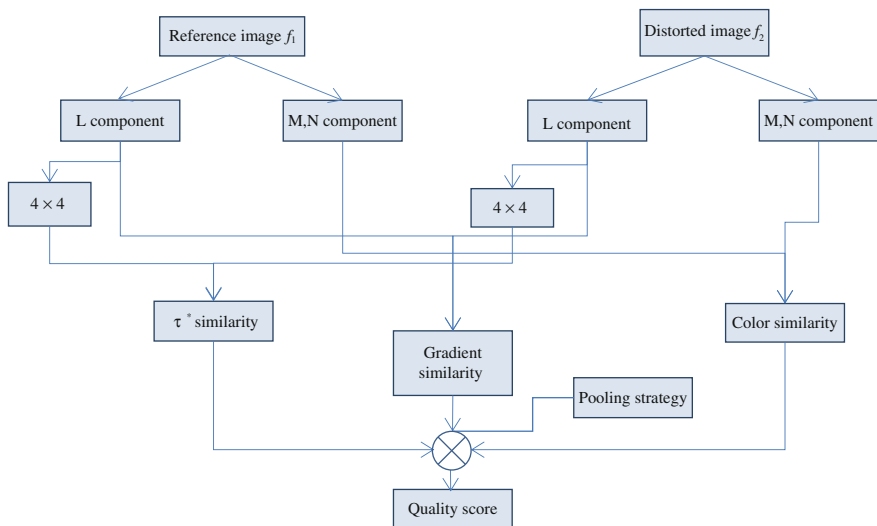


Fig. 1 Flowchart of proposed method

**Table 1** SROCC values of IQA indices for each type of distortions on TID2013

Distortion type	SSIM	MSSIM	VIF	MAD	IW-SSIM	GSM	SR-SIM	FSIM	GSM-D	Proposed
1	0.8671	0.8671	0.8994	0.8443	0.8438	0.9064	0.9256	0.9101	0.9462	0.9499
2	0.7736	0.7730	0.8299	0.8019	0.7515	0.8175	0.8594	0.8573	0.8693	0.8892
3	0.8505	0.8544	0.8835	0.8911	0.8167	0.9158	0.9224	0.8900	0.9350	0.9494
4	0.7985	0.8073	0.8450	0.7380	0.8020	0.7293	0.7864	0.8094	0.7080	0.7275
5	0.8688	0.8604	0.8972	0.8876	0.8553	0.8869	0.9130	0.9040	0.9166	0.9232
6	0.7896	0.7629	0.8537	0.2769	0.7281	0.7965	0.8286	0.8251	0.7637	0.8733
7	0.8411	0.8706	0.7854	0.8514	0.8468	0.8841	0.8505	0.8807	0.9051	0.8629
8	0.9724	0.9673	0.9650	0.9319	0.9701	0.9689	0.9619	0.9551	0.9114	0.9671
9	0.9296	0.9268	0.8911	0.9252	0.9152	0.9432	0.9401	0.9330	0.9524	0.9557
10	0.9227	0.9265	0.9192	0.9217	0.9187	0.9248	0.9377	0.9339	0.9508	0.9516
11	0.9575	0.9504	0.9516	0.9511	0.9506	0.9602	0.9675	0.9589	0.9657	0.9446
12	0.8581	0.8475	0.8409	0.8283	0.8388	0.8512	0.8545	0.8610	0.8401	0.8897
13	0.8856	0.8889	0.8761	0.8788	0.8656	0.9182	0.9166	0.8919	0.9135	0.9231
14	0.7885	0.7968	0.7720	0.8315	0.8011	0.8130	0.7975	0.7937	0.8140	0.7278
15	0.4563	0.4801	0.5306	0.2812	0.3717	0.6418	0.4736	0.5532	0.6625	0.6989
16	0.7845	0.7906	0.6276	0.6450	0.7833	0.7875	0.6635	0.7487	0.7366	0.7713
17	0.3800	0.4634	0.8386	0.1972	0.4593	0.4857	0.4704	0.4679	0.3328	0.4634
18	0.4208	0.4099	0.3099	0.0575	0.4196	0.3578	0.1393	0.8359	0.2657	0.8229
19	0.8092	0.7786	0.8468	0.8409	0.7728	0.8348	0.8773	0.8569	0.8889	0.9005
20	0.8711	0.8528	0.8946	0.9064	0.8762	0.9124	0.9256	0.9135	0.9297	0.9177
21	0.9173	0.9068	0.9204	0.9443	0.9037	0.9563	0.9609	0.9485	0.9629	0.9394
22	0.8351	0.8555	0.8414	0.8745	0.8401	0.8973	0.8810	0.8815	0.9102	0.9280
23	0.8771	0.8784	0.8848	0.8310	0.8682	0.8823	0.8745	0.8925	0.8533	0.8824
24	0.9488	0.9483	0.9353	0.9567	0.9474	0.9668	0.9613	0.9576	0.9683	0.9602

stage. This method is denoted as SCGM. The local weight for  $f_1$  is expressed as  $w_{f_1} = 0.2 + \tau_1^{*3}$ ,  $\omega_{f_1, f_2}$  is defined as:

$$w_{f_1, f_2} = (A + B)^{-1} (A \cdot \omega_{f_1} + B \cdot \omega_{f_2}) \quad (8)$$

in which  $A = \exp(\chi \cdot \omega_{f_1})$  and  $B = \exp(\chi \cdot \omega_{f_2})$  and  $\chi$  is a scale factor. The proposed method flowchart is depicted as: (Fig. 1)

### 3 Experiment Results

We operate this method on image databases TID2013 [11]. The performance is evaluated by the consistency between objective score and the subjective mean opinion scores (MOSs). We use Spearman rank as the performance measure. The mean SROCC value on TID2013 is 0.8741 which indicate a high consistency between the two. The SROCC values of ten IQA metrics for each distortion type on TID2013 are listed in Table 1 and the best result is highlighted in italic. As we can see from Table 1, the performance of our method for each distortion type outperforms the other nine methods.

### 4 Conclusions

In the proposed SCGM method, structure contrast index, gradient and color similarity were combined to better assess the image quality. Comparisons done on the TID2013 database in this work prove this method is quite competitive with other methods in terms of prediction accuracy and computational complexity.

**Acknowledgements** This study is funded by Shaanxi Provincial Key Laboratory of project-Printing image quality assessment based on human visual features (13JS082).

### References

1. Anmin, L., Weisi, L., & Narwaria, M. (2012). Image Quality Assessment Based on Gradient Similarity. *Image Processing, IEEE Transactions on*. [10.1109/TIP.2011.2175935/21\(4\)](#), 1500–1512.
2. Zhou, W., Bovik, A. C., Sheikh, H. R., & Simoncelli, E. P. (2004). Image quality assessment: from error visibility to structural similarity. *Image Processing, IEEE Transactions on*. [10.1109/TIP.2003.819861/13\(4\)](#), 600–612.
3. Wang, Z., Simoncelli, E. P., & Bovik, A. C. (2003). Multiscale structural similarity for image quality assessment. *Journal*. [10.1109/ACSSC.2003.1292216/2](#), 1398–1402 Vol. 1392.
4. Jieying, Z., & Nengchao, W. (2012). Image Quality Assessment by Visual Gradient Similarity. *Image Processing, IEEE Transactions on*. [10.1109/TIP.2011.2169971/21\(3\)](#), 919–933.

5. Guangquan, C., JinCai, H., Cheng, Z., Zhong, L., & Lizhi, C. (2010). Perceptual image quality assessment using a geometric structural distortion model. *Journal*. [10.1109/ICIP.2010.5649265/325–328](#).
6. Wufeng, X., Lei, Z., Xuanqin, M., & Bovik, A. C. (2014). Gradient Magnitude Similarity Deviation: A Highly Efficient Perceptual Image Quality Index. *Image Processing, IEEE Transactions on*. [10.1109/TIP.2013.2293423/23\(2\)](#), 684–695.
7. Lin, Z., Zhang, D., Xuanqin, M., & Zhang, D. (2011). FSIM: A Feature Similarity Index for Image Quality Assessment. *Image Processing, IEEE Transactions on*. [10.1109/TIP.2011.2109730/20\(8\)](#), 2378–2386.
8. Zhang, L., Shen, Y., & Li, H. (2014). VSI: A Visual Saliency-Induced Index for Perceptual Image Quality Assessment. *IEEE Transactions on Image Processing*. [10.1109/TIP.2014.2346028/23\(10\)](#), 4270–4281.
9. Bae, S. H., & Kim, M. (2014). A Novel Generalized DCT-Based JND Profile Based on an Elaborate CM-JND Model for Variable Block-Sized Transforms in Monochrome Images. *IEEE Transactions on Image Processing*. [10.1109/TIP.2014.2327808/23\(8\)](#), 3227–3240.
10. Bae, S. H., & Kim, M. (2016). A Novel Image Quality Assessment With Globally and Locally Consistent Visual Quality Perception. *IEEE Transactions on Image Processing*. [10.1109/TIP.2016.2545863/25\(5\)](#), 2392–2406.
11. Ponomarenko, N., Ieremeiev, O., Lukin, V., Egiazarian, K., Jin, L., Astola, J., ... Kuo, C. C. J. (2013). Color image database TID2013: Peculiarities and preliminary results. *Journal*. 106–111.

# Study on Memory Color Extraction Method of Image Processing

Jingnan Sun, Ping Yang and Qiang Wang

**Abstract** A new technique for extract memory colors is proposed. Firstly, color shift caused by different illuminant is corrected. Based on the color characteristics of the image, memory colors could be separated using K-means algorithm while the rest of non-memory colors were filtered off. Finally, to improve the accuracy of memory color extraction, grey world color correction combined with color clustering algorithm were used. Experimental results showed this method can improve the accuracy of memory colors extraction, thus reducing the impact of external light environment when images were captured. It can be implemented as memory colors detection method for many applications.

**Keywords** Memory color · K-means algorithm · Grey world color correction

## 1 Introduction

Memory color is an important indicator of evaluating whether the image color is reproduced correctly [1], and finding memory color regions of image is crucial to achieve satisfactory results in subsequent image processing. In recent years, there are numerous studies on memory colors extraction. In 2007, Tunde Tarczali's doctoral thesis "Investigation of color memory" mentioned the study of memory color extraction by ripe bananas, grass, sky, etc [2]. In 2009, Mustafa Jaber, Eli Saber used Bayesian network to extract memory colors [3]. In 2011, Byong used genetic algorithm to optimize the geometric boundary of the memory color region, which further improved the accuracy of the algorithm [4]. In 2014, Kevin et al. studied the effects of different cultures on memory color. The study involved the memory color of ripe bananas, skin color, lemon and other 20 kinds of familiar objects [5]. Although these algorithms provide better results in memory color

---

J. Sun (✉) · P. Yang · Q. Wang  
School of Digital Media and Art Design, Hangzhou Dianzi University,  
Hangzhou, Zhejiang, China  
e-mail: 649498091@qq.com



extraction, but they did not consider the impact of lighting conditions. In practical applications, image capture will be affected by the illuminant. If the same natural scene was captured in different illuminant, the color will appear differently, which could lead to memory color extraction inaccurate or even fetch error. Therefore, we proposed a method that the grey world color correction combined with K-means algorithm, which could reduce influence of illuminants. Simulation experiments verify the accuracy of memory color extraction and achieved a good result in memory color extraction.

## 2 Methodology

Currently, there are two memory color extraction method. One uses boundary of geometric figure, which is defined based on training samples, as a criterion to extract the boundary of memory color. But ignores the image brightness information, and furthermore does not consider the impact of illuminant. The other sets classification principle from training sample, by which memory colors are extracted if they meet the principle. But the result proves poor with a relatively less number. In order to solve the shortage of above methods, improve the accuracy and efficiency of the memory colors extraction, this study uses the grey world method to correct color and K-means clustering algorithm to fusion memory color region extraction, to achieve good calculation speed and accuracy of memory colors extraction.

### 2.1 Grey World Color Correction Method

Based on the hypothesis that “A picture with a great variety of colors, three components of RGB average values tend to be the same grey level [6]”, Grey world color correction method reduce or eliminate the effect of illuminant, eliminates the color shift, and improve the accuracy of memory color extraction by illuminant pre-processing.

### 2.2 K-Means Algorithm

K-means clustering algorithm is widely used in image processing, which is simple and easy to implement, with low time complexity. The main steps of the K-means algorithm are as follows:

First, from a given dataset  $A = (a_1, a_2, a_3 \dots a_n)$  is determined to satisfy the condition  $k \leq n$  the number of cluster centers.

Secondly, according to the formula (2.1), respectively, the distance between data of A and K cluster center is calculate, the minimum value

$$\operatorname{argmin}_Q \sum_{i=1}^K \sum_{a_j < q_i} \|a_j - \mu_i\|^2 \tag{2.1}$$

where  $Q = \{Q_1, Q_2 \dots Q_k\}$ , the data is divided into k classes,  $a_i$  is an m-dimensional vector,  $\mu_i$  is the average of  $Q_i$ .

Finally, according to the principle of minimum distance, the data is assigned to the nearest class, calculate a new clustering center, if convergence is output, otherwise repeat the above process, iterate until the clustering center convergence [7]. Each cluster is finally obtained.

### 3 Experiment Design and Implementation

In this study, in order to reduce the impact when the memory color extraction caused by other light sources, the grey world color correction method is used to improve the accuracy of memory color extraction, by utilizing clustering algorithm of computing faster to extract. The algorithm flow is shown in Fig. 1.

#### 3.1 Construction of the Image Dataset

In this research, we use the image dataset for a total of 20 samples, including ripe bananas and apples. The images were captured in standard darkroom, under uniform illumination. A Canon PC 1587 digital camera was used with automatic mode set. There are in all four kinds of illuminants used in the experiment, named F, D65, TL84 and UV. A total of 10 kinds light condition were achieved by the

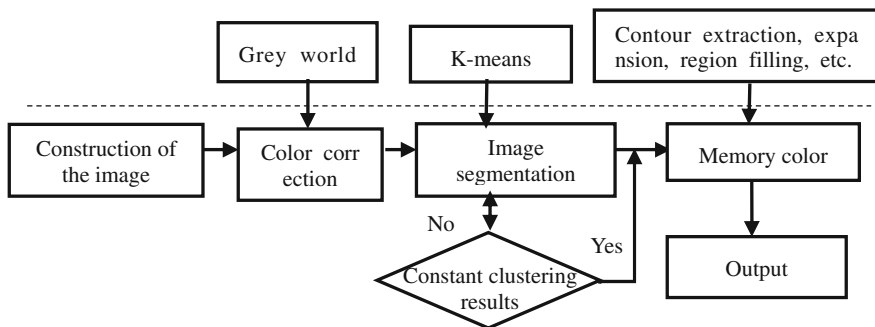
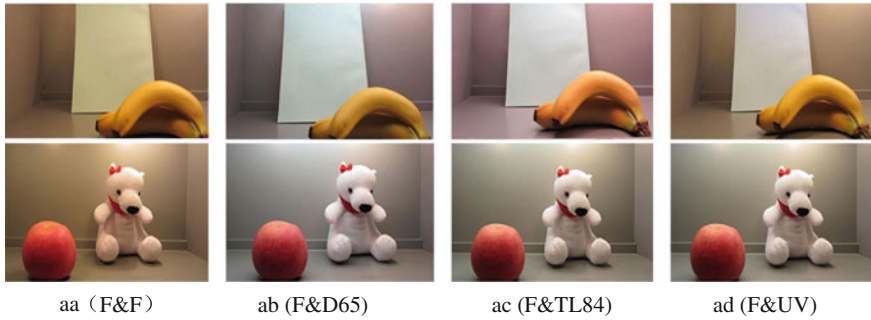


Fig. 1 Work flow of the proposed method



**Fig. 2** Image dataset

mixture of any two of them. Figure 2 shows some images, a, b, c, d represent four kinds of light sources respectively, F, D65, TL84 and UV.

Among them, ab represents the image achieves under the mixture of two kinds illuminant of F and D65, ac represents the image achieves under the mixture of two kinds illuminant of F and TL84, ad represents the image achieves under the mixture of two kinds illuminant of F and UV.

### 3.2 Grey World Color Correction Based on Image Entropy Constraint

In this study, we use the grey world color correction method based on the image entropy. The algorithm is based on the amount of information contained in the aggregation features of gray level distribution, which is based on whether the color information of the image is rich or not to correct the constraint gain coefficient. The specific process is listed as follows:

Firstly, according to the formula (3.1), we calculate the relative entropy of the RGB three channels of the collected image

$$H_{\text{KLD}}^k = \frac{-\sum_{i=0}^{255} P_{k,i} \log_2 P_{k,i}}{8} \quad (3.1)$$

where  $H_{\text{KLD}}^k$  is one-dimensional discrete relative entropy,  $k = R, G, B$ ;  $P_{k,i}$  shows the proportion of pixels which represents  $k$  component's grey scale in the image [8].

According to the formula (3.2), the RGB three channel constraint gain coefficient is calculated.

$$\begin{cases} k_r^{rc} = (k_r - 1) \cdot H_{KLD}^R + 1 \\ k_g^{rc} = (k_g - 1) \cdot H_{KLD}^G + 1 \\ k_b^{rc} = (k_b - 1) \cdot H_{KLD}^B + 1 \end{cases} \quad (3.2)$$

where  $k_r, k_g, k_b$  are the gain coefficients of three channels in the traditional grey world algorithm.

Finally, the constraint gain coefficient is corrected. The richer the color image information, the  $H_{KLD}^k$  closer to 1, whereas fewer color images, the  $H_{KLD}^k$  closer to 0, thereby preventing excessive correction [9].

### 3.3 Memory Color Extraction Based on Clustering Algorithm

In this study, considering the results of traditional clustering algorithm have a great relationship with the sample position. In order to achieve better clustering results, first, the image is divided into a  $4 * 3$  macro block, then, each a small block is clustered. Specific process is as follows:

The first step, RGB color space is first converted into Lab color space [10]. Next, the image is divided into  $4 * 3$  macro block; each small block based on the distribution of colors is clustered.

The second step, assuming the image has  $m * n$  pixels, either take the cluster center  $C_i$  ( $i = 1, 2, 3$ ), the image of each pixel  $X_i$  ( $j < m * n$ ), where assigned according to the minimum distance criteria a cluster centers and meet:

$$D_{ij} = \min\{[X_j - C_i]\} \quad (3.3)$$

According to the expression:

$$C_i = \frac{\sum_{X \in D_i} [X_j]}{q} \quad (3.4)$$

The value of the cluster center is corrected, all pixels based on the new cluster centers to re-clustering, iteration, until no change in the clustering results.

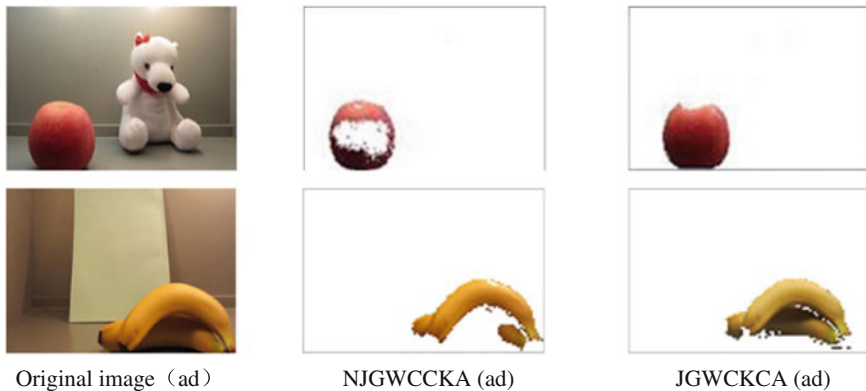
Third step, using different color mark pixels, generated color clustering index graph and selected memory color area. Non-memory colors regions are set to 0. Find the maximum degree contains salient points of the segmentation map, contour extraction, dilation, erosion and region filling etc. Extract memory color area.

## 4 Results and Analysis

The extraction accuracy is evaluated to reflect the effectiveness and advantages of the method used in this research. By the average subjective opinion (MOS) method, and selecting 10 standard observers, where professional staff 4, non-professional staff 6. Score is divided into excellent, good, general, poor and very bad, denote by 5, 4, 3, 2, 1. The evaluation process was conducted by 10 standard observers and each observer was asked to give scores for memory color area extracted by two methods subjectively, which are NJGWCCKA and JGWCCKA respectively. According to scores, two methods were compared and calculated the extraction accuracy. Results are shown in Fig. 3 and Table 1, where 1–10 represents 10 standard observers, aa, ab, ac, ad, bb, bc, bd, cc, cd and dd represents the images captured under 10 different illuminants irradiation separately.

First Column: original. Second Column: capture of not joint grey world color correction and K-means algorithm (NJGWCCKA). Third Column: capture of joint grey world color correction and K-means algorithm (JGWCCKA).

As is shown in Fig. 3, the method in the study is obviously superior to previous method in memory color area integrity and edge sharpness. Table 1 shows the method in the memory color extraction accuracy is greatly improved, from the original 50 to 90%. In addition, the algorithm used in this study has a total consumption of time 86.95 s, which has a good efficiency.



**Fig. 3** Renderings of two extraction methods

**Table 1** Comparison of precision of two extraction methods

Method	NIGWCKCA										JGWCKCA									
	aa	ab	ac	ad	bb	bc	bd	cc	cd	dd	aa	ab	ac	ad	bb	bc	bd	cc	cd	dd
Observer	3	4	4	3	3	4	4	3	4	1	4	5	4	5	5	5	5	4	5	2
1	3	4	4	3	3	4	4	3	4	1	4	5	4	5	5	5	5	4	5	2
2	3	4	4	3	3	4	4	3	4	1	4	5	4	5	5	5	5	4	5	2
3	3	4	4	3	3	4	4	3	4	1	4	5	4	5	5	5	5	4	5	2
4	3	4	4	3	3	4	4	3	4	1	4	5	4	5	5	5	5	4	5	2
5	3	4	4	3	3	4	4	3	4	1	4	5	4	5	5	5	5	4	5	2
6	3	4	3	3	3	4	4	3	4	1	4	5	4	5	5	5	5	4	5	2
7	3	4	4	3	3	4	4	3	4	1	4	5	4	5	5	5	5	4	5	2
8	3	4	4	4	3	4	4	3	4	1	4	5	4	5	5	5	5	4	5	2
9	2	4	4	3	4	4	4	3	4	1	4	5	4	5	5	5	5	4	5	2
10	3	4	4	3	3	4	4	3	4	1	4	5	4	5	5	5	5	4	5	2
Accuracy	50%										90%									

*Note* Score greater or equal to 3 is considered that memory colors can be extracted completely, otherwise, considering it cannot be extracted completely

## 5 Conclusions

On the basis of having depth theoretical research and technical analysis on memory region extraction principle and implementation process, a new approach for joint grey world color correction and color clustering (JGWCCKA) was proposed that could reduce the influence of external illuminant. The method aims at improving the accuracy of memory color extraction. The experiment shows that the memory color extraction method used in this study can effectively solve the problem of the extraction accuracy of ambient light environment. At the same time, the method used has the advantages of simple calculation and easy realization. It provides a good solution for the memory color region extraction, and has good application value in the field of image detection, color reproduction and so on.

**Acknowledgements** This work is funded by National Key Technology Research and Development Program of the Ministry of Science and Technology of China (2012BAH91F03).

## References

1. Jin Hongyong, Zhao Xiuping. (2007). Application of memory color in print quality inspection and control [J]. *Print Today*, (4):35–37.
2. Tunde Tarczali. (2007). Investigation of color memory [J]. Doctoral school of Information Sciences University of Pannonia.
3. Mustafa Jaber, Eli Saber, Ferat Sahin (2009). Extraction of Memory Colors Using Bayesian Networks [J]. IEEE Conference.
4. Byong Tae yu, Choon-woo Kim. (2011). Optimum Memory Color Extraction for Digital TVs Based on Genetic Algorithm [J]. IEEE Conference on Computer Vision and Pattern Recognition, 57(2):638–645.
5. Kevin A.G. Smet, Yandan Lin, et al. (2014). Cross-cultural variation of memory colors of familiar objects [J]. *OSA publishing*.
6. Li Zhiyong. (2011). Application of Gray World color balance method in skin color detection [J]. *Modern Electronics Technique*, 34(5):198–200.
7. Wu Suhui, Cheng Ying, et al. (2011). Review of K-means algorithms research [J]. *New Technology of Library and Information Service*.
8. Gu Yuanbao, Fu Yuzhuo. (2005). A method of automatic white balance based on grey world model [J]. *Computer Simulation*, 22(9):185–187.
9. Xu xiaoZhao, Cai Yiheng, et al. (2010). Improve Grey World color correction algorithm [J]. *ACTA PHOTONICA SINICA*, 39 (3): 559–564.
10. Hu Weijie, Tang Shunqing, Zhu Zhengfang. (2007). Theory and application of modern color technology [M]. Beijing Institute of Technology Press.

**Part III**  
**Digital Media Technology**



# Semantic Based Text Similarity Computation

Yaqi Liu and Zhijiang Li

**Abstract** Text similarity algorithm is widely used in plurality fields, such as copy detection, text classification, machine translation, intelligent question answering system and natural language processing. At present, vector space model algorithm, which is more commonly used, does not consider the information of semantic features adequately, and the accuracy of the semantic similarity computation results can be further improved. This paper proposes a text similarity computation method which combines the HowNet with vector space model. Similarity computation is divided into two levels. In the level of words, words-similarity calculation based on HowNet prevents the loss of semantic information. In the level of texts, text-similarity calculation by vector space model ensures the integrity of the information expressed in the texts. This paper designs an experiment of news text classification based on KNN algorithm, in which data obtained from a part of the Chinese news in Sogou data corpora. Experimental results show that the method proposed in this paper is more accurate than the traditional vector space model algorithm.

**Keywords** Semantic · Text similarity · HowNet · Vector space model

## 1 Introduction

In daily life, people use text to express and transmit the information, so the information retrieval technology and data mining depends on the processing and operation of text information [1]. Text similarity computation is an effective and direct method to solve the problem of resource acquisition and analysis. Generally, we use text similarity to measure the degree of association between the two different texts. When the similarity value is larger, the correlation degree of the two texts is

---

Y. Liu · Z. Li (✉)

School of Printing and Packaging, Wuhan University, Wuhan, China  
e-mail: lizhijiang@whu.edu.cn

© Springer Nature Singapore Pte Ltd. 2017

P. Zhao et al. (eds.), *Advanced Graphic Communications and Media Technologies*, Lecture Notes in Electrical Engineering 417,  
DOI 10.1007/978-981-10-3530-2\_43

343

higher, and vice versa. Salton et al. proposed vector space model (VSM) which maps the text into a high dimension space vector [2]. In this way, the mathematical computation can be easily carried out, and the computation process is simplified. However, semantic information is often lost in the process of mapping, due to the linear independent hypothesis of the space vector model, which affects the accuracy of the final results.

This paper will introduce the text preprocessing and vector space model, and proposes a computation method of text similarity, which is based on HowNet and vector space model, aiming at the problem of absence of semantic information.

## 2 Vector Space Model

### 2.1 Chinese Text Preprocessing

Compared with English text, Chinese text has no space to separate the words. Chinese word segmentation is a technology to segment Chinese text into a series of individual words. There are some words which have a very small contribution to the meaning of the text and appear many times, known as the stop word [3]. These words do not provide any value to the meaning of the text, but also increase the dimension of the text representation. It would increase the computational complexity and time overhead, so it needs to be removed.

### 2.2 Vector Space Model

Vector space model is simple. It will map a text into a space vector, and use a vector to represent the text information. By using the knowledge of space mathematics, we can directly compute the similarity between two text vectors, which is measured by the cosine value of the angle of the vectors.

The vector space model has a basic assumption, which feature item that can represent text content is only related to the number of times it appears, but has nothing to do with its position and sequence [4]. Vector space model is composed of features and their weights. Features usually refer to non-redundant words after text preprocessing, and each feature corresponds to a weight, which describe the important degree of the feature in the text. When computing the similarity of text, the cosine theorem is generally used, the formula is as follows:

$$\text{Sim}(D_1, D_2) = \frac{\sum_{k=1}^n W_{1k} * W_{2k}}{\sqrt{\sum_{k=1}^n W_{1k}^2} * \sqrt{\sum_{k=1}^n W_{2k}^2}} \quad (1)$$

$D_1$  and  $D_2$  represent two texts,  $W_{ik}$  represents the weight of the  $k$ -th feature in the  $i$ -th text.

We use the TF-IDF method to calculate the weight. The formula is as follows:

$$W_k = TF_{(i,k)} * IDF_{(i,k)} = q * \log\left(\frac{N}{n} + \alpha\right) \tag{2}$$

In Eq. (2),  $q$  stands for the number of times that feature  $T_k$  appears in the text  $D_i$ .  $N$  is the total amount of texts,  $n$  is the number of texts containing the feature  $T_k$ , and  $\alpha$  is called empirical constant whose general value is 0.01.

### 3 Text Similarity Computation

#### 3.1 HowNet

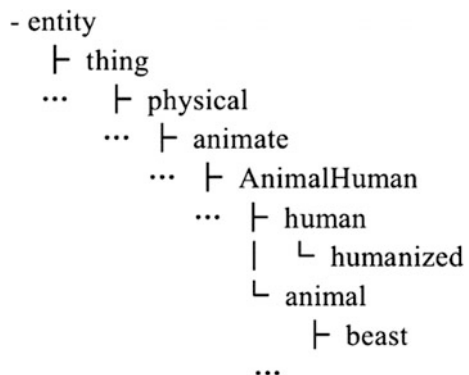
Concepts and sememes are the foundation of HowNet [5]. Concept is the description of the words, and each word can have a number of concepts which are generally described by knowledge description language that is made up of sememes. HowNet uses one or more of the sememes to describe the concept, and a forest model is used to describe the relationship between sememes [6].

There are ten trees in sememe forest. The relationship between sememes is complicated, which is usually gotten from upper and lower relations. This relationship is called sememe hierarchy tree, showed in Fig. 1 [7]. The description of the concept, in addition to the use of sememes, is also applied to a variety of semantic symbols for assist.

#### 3.2 The Similarity of Words

According to the distance between the two sememes on sememe hierarchy tree, the sememe similarity is calculated by Eq. (3).

Fig. 1 Sememe hierarchy tree



$$\text{Sim}(p_1, p_2) = \frac{\alpha}{d + \alpha} \quad (3)$$

Two sememes is  $p_1$  and  $p_2$ .  $d$  is the distance between the two sememes on referenceeeme hierarchy tree. If they are on different tree, the value of  $d$  towards infinity.  $\alpha$  is adjustable parameter which value is 1.6.

Because Eq. (3) only considers the upper and lower relations, but not the depth of the sememe, the public father node and the antisense of sememes. It needs to be improved.

$$\text{Sim}(p_1, p_2) = [e^{dis(p_1, p_2)^{-1}}]^{a(p_1, p_2)} \frac{\alpha \cdot c(p_1, p_2)}{\alpha \cdot c(p_1, p_2) + (1 - \frac{dep(p_1, p_2)}{dep(t)} + 0.01) \cdot dis(p_1, p_2)} \quad (4)$$

$$dep(p_1, p_2) = dep(p_1) + dep(p_2) \quad (5)$$

$dep(p_1)$  means the depth of sememe  $p_1$  on the tree.  $dep(t)$  is amount of the depth of tree.  $dis(p_1, p_2)$  is the distance between the two sememes.  $c(p_1, p_2)$  is the amount of the public father nodes of  $p_1$  and  $p_2$ .  $a(p_1, p_2)$  means whether there is antisense on the path of  $p_1$  and  $p_2$ . If there is, the value is 1, otherwise, the value is 0.  $\alpha$  is adjustable parameter which value is 1.6.

Knowledge description language is made up of independent sememe description, relation sememe description and symbol sememe description (Table 1).

In general, if two specific words are same, the similarity is 1, otherwise, the similarity is 0.

For independent sememe description, make pairs of sememes or specific words alternately, select the maximum similarity, and record the value. Then select the most similar pairs in the remainder of the match repeatedly until one of them is complete, and discard the remaining sememes and specific words. Finally, carry out an arithmetic average value of maximum similarity values, and record the value as  $sim_1$ .

For relation sememe description, if relation is same, make pairs of sememes or specific words alternately, select the maximum similarity, and record the value repeatedly. Get the arithmetic average eventually, and record the value as  $sim_2$ .

**Table 1** Sememe descriptions

Descriptions	Description method
Independent sememe description	“Sememe”, or “(specific word)”
Relation sememe description	“Relation = sememe”, or “relation = (specific word)”, or “(relation = specific word)”
Symbol sememe description	“Symbol sememe”, or “symbol (specific word)”

For symbol sememe description, the processing likes relation sememe description. Here to judge symbol rather than relation, record the arithmetic average value as  $sim_3$ .

Formula for calculating the similarity between concept  $C_1$  and  $C_2$  is as follows:

$$\text{Sim}(C_1, C_2) = \sum_{i=1}^3 \beta_i \prod_{j=1}^i sim_j \quad (6)$$

$\beta_i$  ( $1 \leq i \leq 3$ ) is adjustable parameter, and meets the conditions:  $\beta_1 + \beta_2 + \beta_3 = 1$ ,  $\beta_1 \geq \beta_2 \geq \beta_3$  General experience is:  $\beta_1 = 0.7, \beta_2 = 0.17, \beta_3 = 0.13$ .

Assume that the word  $W_1$  has  $m$  concepts:  $C_{11}, C_{12}, \dots, C_{1m}$ . And the word  $W_2$  has  $n$  concepts:  $C_{21}, C_{22}, \dots, C_{2n}$ . The similarity between the words  $W_1$  and  $W_2$  is expressed as  $\text{Sim}(W_1, W_2)$ .

$$\text{Sim}(W_1, W_2) = \max_{i=1\dots m, j=1\dots n} \text{SIM}(C_{1i}, C_{2j}) \quad (7)$$

### 3.3 The Similarity of Texts

Chinese text preprocessing of semantic based text similarity computation is same as text similarity computation based on VSM. Assume two Chinese texts after preprocess and expressed as:  $D_1 = (T_{11}, W_{11}, T_{12}, W_{12}, \dots, T_{1m}, W_{1m})$ ,  $D_2 = (T_{21}, W_{21}, T_{22}, W_{22}, \dots, T_{2n}, W_{2n})$ .  $T_{11}, T_{12}, \dots, T_{1m}$  are feature terms of text  $D_1$ ,  $W_{11}, W_{12}, \dots, W_{1m}$  are weights of the feature terms.

Use Eq. (7) to calculate the similarity of each feature item between two texts. Then construct feature items similarity matrix  $A$  ( $a_{ij} = \text{Sim}(T_{1i}, T_{2j})$ ). In the matrix  $A$ , find the largest element, and compare it with adjustable threshold, the value of the threshold in this paper is 0.7. If the element value is larger than the threshold value, delete the row and column of the element from the matrix  $A$  while keeping elements index in matrix  $A$  unchanged, and record the row and column of the element. Keep this step repeatedly until all the elements in matrix  $A$  are not larger than the threshold value or there is no element in matrix  $A$ .

Treat the feature items which the similarity is larger than threshold as the same dimension, and use Eq. (1) to calculate the text similarity.

## 4 Experimental Results and Analysis

According to the part of the data of Chinese news corpus of Sogou, design an experiment of news text classification based on KNN algorithm which  $K$  value is set to 7. The data contains five fields of electronics, sports, tourism, education and

**Table 2** The classification accuracy of the experiment

Field	VSM	Equation (3)	Equation (4)
Electronics	0.42	0.52	0.60
Sports	0.72	0.68	0.80
Tourism	0.46	0.54	0.62
Education	0.44	0.60	0.72
Military	0.42	0.62	0.68

military. The total number of text data is 1000 and 200 text data in each field. The training set for each field is 150 text data, and the test set is 50 text data (Table 2).

The classification experimental results show that the two semantic algorithms are much better than the traditional algorithm based on VSM. Besides, the algorithm proposed in this paper is more efficient than the other semantic based algorithm.

## 5 Conclusions

This paper mainly discusses the text similarity computation based on VSM and the semantic based text similarity computation, and improves the method of computing the similarity between words. Finally, a text classification experiment based on KNN is designed to analyze the advantages and disadvantages of the two different methods of text similarity computation. In the course of the study, we find a problem which is worth studying and solving: considering the order of sequence of words to prevent losing a part of useful text information.

## References

1. Jin Xiqian. (2009). Research on Semantic Based Chinese Text Similarity Algorithm. (Doctoral dissertation, Zhejiang University of Technology).
2. G. Salton, A. Wong, and C.S. Yang, A Vector Space Model for Information Retrieval, *Journal of the ASIS*, 18:11, 613–620, November 1975.
3. Liu Xiaojun, Zhao Dong, & Yao Weidong. (2007). A Two Factor Similarity Algorithm for Chinese Text Search. *Computer Simulation*, 24(12), 312–314.
4. Chen Feihong. (2011). Research on Chinese Text Similarity Algorithm Based on Vector Space Model. (Doctoral dissertation, University of Electronic Science and Technology).
5. Kuai Yuanyuan. (2014). Research on Semantic Based Text Similarity Algorithm. *Computer CD software and Applications* (9), 302–303.
6. Liu Qun & Li Sujian. (2002). Based on the HowNet Lexical Semantic Similarity Computation. *Chinese of computational linguistics*.
7. Fan Hongyi, & Zhang Yangsen (2014). A method for semantic similarity of words based on HowNet. *Journal of Beijing Information Science and Technology University: Natural Science Edition* (4), 42–45.

# Design and Manufacture of 3D Printers of Virtual Assembly Display Platform

Haiyue Zhang and Zhanjun Si

**Abstract** With the rapid development of Internet technology, as a product of manufacturing technology and simulation technology, virtual assembly technology provides a good condition for the product assembly display. Although 3D printing has become more and more popular as a new printing technology, the assembly display of 3D printer is very scarce. In this study, the way to achieve the production of virtual assembly display platform for 3D printers is introduced to meet the needs of new product development, maintenance and operation training. Makerbot Replicator2 3D printer is used and the structure of 3D printer is modeled through the 3D modeling software Solidworks. Afterward, the processes of mapping and animation are conducted in 3ds Max. Finally, the fabrication of the interactive display platform is completed in the import VRP. What is obtained is the virtual assembly platform which can realize the function of model display and assembly demonstration of 3D printer. The application of virtual reality technology to 3D printer can present the overall structure and function of 3D printer in a digital interactive mode so that it will no longer be restricted by environment and location conditions. Besides, it also provides a new way for the design, improvement, maintenance and management of industrial products, which is convenient to users to understand the internal and external structure and related functions of the 3D printer as quickly as possible.

**Keywords** Virtual assembly · 3D printers · Interaction

## 1 Introduction

According to the relevant statistics, the cost of assembly process accounts for 30–50% or even higher of the total manufacturing cost. The traditional assembly is complex and cumbersome, which can neither improve the efficiency, nor save the

---

H. Zhang · Z. Si (✉)  
College of Packaging & Printing Engineering, Tianjin University of Science & Technology, Tianjin, China  
e-mail: szj@tust.edu.cn

resources [1]. The emergence of virtual assembly has changed the present situation, which provides the conditions for assembly, maintenance and evaluation of the products in digital environment. In this way, the cost of assembly is largely reduced and the efficiency of production and training is improved. According to statistics, the application of virtual assembly technology to manufacturing can save 25% of the development funds. The design paper of Boeing 777 aircraft is a typical application of virtual technology to the assembly of three million parts [2].

Virtual assembly combines many technologies such as visualization, simulation, decision theory, assembly and manufacturing process. These techniques promote the virtual assembly technology to move gradually towards maturity in China's industrial sector [3]. In the virtual reality system, users no longer accept information passively, but use interactive input devices to manipulate virtual objects. However, the application of virtual assembly technology in the industrial field depends on its simulation degree of the real world. Such kind of industry needs to improve its comprehensive ability of model construction technology, virtual reality technology and human-computer interaction technology. Moreover, application effect and true extent of virtual assembly should also be improved [4].

## **2 Analysis of Design**

### **2.1 Concept of Design**

The model chose in this article is the Makerbot Replicator2 3D printer. The overall appearance is rectangular and the internal details are difficult to view. To ensure the navigation in three-dimensional environment, related information should be read and the internal and external structure of the 3D printers should be learnt. Through the three-dimensional modeling software Solidworks, the establishment of the structure model of the 3D printer is realized, and then texture mapping and animation in 3ds Max are conducted. Finally it is imported to VRP for post-processing to test whether it met the requirements or not. If not, go back to the three-dimensional modeling software or VRP scene to conduct adjustment according to the specific problem. If no problem is texted, export to the display device to interact with the user. The functional modules of virtual assembly platform of 3D printer can be divided into four parts, which are the overall browsing, assembly animations, assembly steps and the physical display respectively [5].

### **2.2 Production Software and Development Environment**

Modeling environment: Windows 7 system, Intel (R) Core (TM) CPU i5, 4G memory, 64 bit operating system.



Post processing environment: Windows 7 system, Intel (R) Core (TM) CPU i5, 4G memory, 32 bit operating system.

Production software: 3ds Max2010, SolidWorks2014, VRP2010, Photoshop CS6.

### 3 Production of Virtual Assembly Display Platform

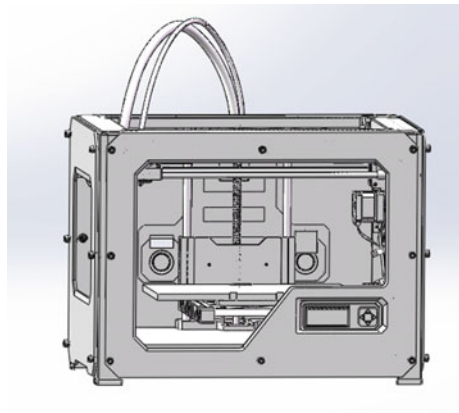
#### 3.1 Construction of the Model

Through collecting the measured parameters of the overall structure and the internal components of the 3D printer, the precise modeling is conducted with the help of SolidWorks. The main reason for choosing SolidWorks software is that it is not only a professional machinery three-dimensional design tool including a large number of standard components library, but also can be used for the design, parametric modeling and assembly modeling of parameterized feature modeling [6]. By measuring data modeling, the part model is assembled and molded together with special tools. After completion, mechanical parts are assembled specifically to generate the corresponding assembly (Fig. 1).

#### 3.2 Optimization of the Model

Completed model files are imported into 3ds Max. In order to facilitate export, the size of the memory model should be reduced and the operation speed of system should be improved (Fig. 2). In the way of redundant face removal, external references and collapse method the 3DSmax file is optimized. In addition, the size of baking texture will have a significant impact on the final results, and the complexity

Fig. 1 The 3D printer model



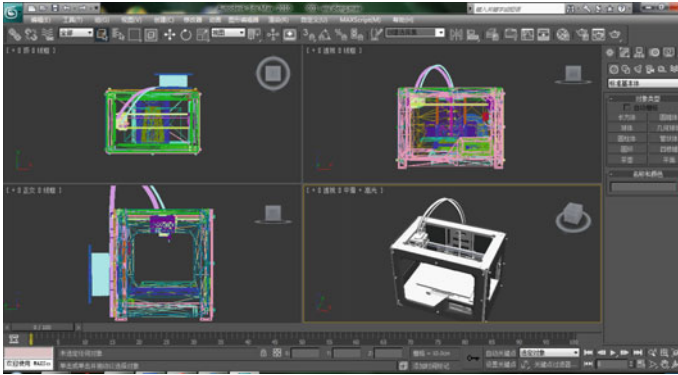
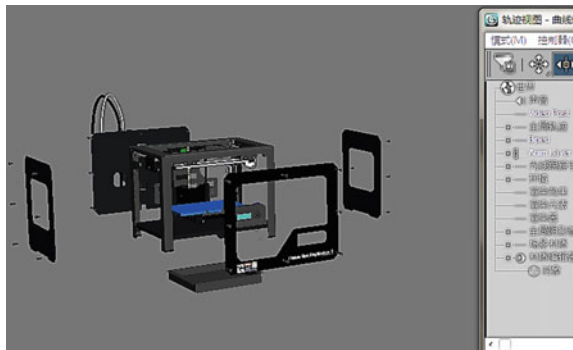


Fig. 2 The 3D printer model in 3ds max

Fig. 3 The animation of the 3D printer



of the texture will affect the speed of rendering. The larger the texture is, the larger the computer's resources consumption is, and the longer the rendering time is [7].

### 3.3 Assembly Animation

First of all, the overall animation display process is planned. According to the initial scene of the plan, each part is separated. Meanwhile, the edited group command is also conducted upon multiple items.

According to the key points and the position of the model on the time configurator, the selected component is moved to the position required with the help of move tool. Then the button of "Setting Key Point" will be pressed again to make the model animate. After the completion of the overall animation, animation is played to observe its effects and the corresponding changes are made (Fig. 3).

### ***3.4 Interaction Function***

The editor VR-Platform is used to import the model from 3ds Max to VRP. Different cameras are created for the model so that it can be easily observed from a variety of angles. Fixed point observation camera and rotation camera are included. Here, the timer shaft panel is opened first, then the button of “Setting time shaft” is pressed and the duration of that animation is entered in the resulting dialogue box. Afterward, advanced panel is switched to set the corresponding size. The button of “Recording keyframe” on the panel is clicked at the time of 0.00 s to record the current status as the first frame. After that, image element is established as a button in advanced screen and window interface in order to design and beautify the basic interface, as well as establish the platform interface [8].

### ***3.5 VRP Scene Test and Release***

After the interaction design is completed, the file is tested. The integrity of the design is checked, and then the.exe file is published and compiled. In addition, it is necessary to use the VRP resource file manager to automatically collect all the resources such maps, models, animations and other multimedia resources files in the scene to save the work. Both the correct operation of the program and the correct operation of the project functions should be ensured, so that the realization of the virtual assembly display platform of the 3D printer is accomplished.

## **4 Results and Discussion**

### ***4.1 Compatibility Between Software***

VRP2010 is compatible with 3ds Max2010 while VRP2011 is incompatible with 3ds Max2011. Besides, VRP2010 can only support 32-bit operating system while 64 bit cannot be supported. These problems should be focused in the initial design to avoid the unnecessary troubles [9]. What should also be focused is the problem of different file format. It is important to note that the quality of the original drawing in Solidworks model has direct effect on the graphic quality of 3ds Max. Similarly, the rendering effect of 3ds Max can directly affect the effect of the import to the VRP software. Full preparation should be made in advance in each of the software to avoid the errors.

## 4.2 *How to Real Map*

For instance, if Multi/Sub-Object of multidimensional material is used to bake lightingmap in 3ds Max and import to VRP, the map will be lost. Thus, it is necessary to solve the problem by using manual exhibition UV. However, using proper texture mapping method in 3ds Max environment and importing to VRP after rendering and baking may also lead to wrong display. Therefore, in order to make sure that the texture can get real visual effect, the establishment of some details should be reduced as much as possible. Besides, there should not be too many kinds of maps, which should be unified to the greatest extent [10].

## 4.3 *Simplified Model*

For some display effects which cannot be seen or have no function, they can be simplified such as internal circuit structure of the power box, thread of each bolt and the consumable coil. Since it will occupy a lot of memory, as long as it can reflect the effect of the model, it is not necessary to draw so much turns. To some extent, this can improve the read speed and the generating speed of the file, and reduce the pressure of the system and the software.

## 5 **Conclusions**

The design and implementation process of the entire assembly system can mainly reflect aspects like the equipment operation, assembly process, equipment appearance, component identification, etc. The modeling of each component is the foundation of the whole virtual assembly system. Through the seamless integration of SolidWorks, 3ds Max and VRP, the expected effect can be achieved, which can lay a foundation for the future 3D printer virtual assembly display.

## References

1. Ning Ruxin, Zheng Yi. (2005). Research status and development trend of virtual assembly technology of [J]. In: Chinese mechanical engineering, 15:1398–1404.
2. Zheng Yi, Ning Ruxin, Liu Jianhua, Du long. (2006). Key technology of virtual assembly and its development [J]. In: System simulation 03:649–654.
3. Li Bin. (2011). Research on the automatic generation of process plans based on SolidWorks machining process [D]. Zhengzhou University.
4. Jiang Ling. (2009). The conquest of Max 3DS 2009 complete combat manual [M]. In: Science Press. 06:106–150.

5. Li Yu, our Zhanjun. (2013). Based on Virtual Assembly System Based on VR platform of digital printing machine design and implementation[J]. In: Computer knowledge and technology. 9 (33): 7599–7603.
6. Fan Ji, Ji Song Wei. (2013). VR platform in the development of virtual machine tool fixture assembly show system [J]. In: Tool technology, 03:40–42.
7. Wang Hongjiang. (2014). Design and implementation of virtual roaming system for game scenes based on 3ds max and VRP platform [J]. In: Journal of Jilin College of Education (late), 30 (2): 148–149.
8. Xie Jiabin. (2010). Realization process of virtual disassembly and assembly of hydraulic turbine [J]. In: Enterprises technology of virtual assembly of hydraulic turbine, 15:170–171.
9. Zhu Wanxia. (2011). Design and development of network virtual experiment platform for photography technology[D]. In: Huazhong Normal University.
10. Wang Yu. (2013). The virtual reality technology application of landscape design in the exit of rail transit [D]. Xi'an University of Technology.

# Research on the Application Process of Mobile Augmented Reality in Printed Product

Hui Ye, Ruizhi Shi, Shenghui Li and Da Li

**Abstract** Compare with mobile phone, traditional printed products can only display information limited to the content printed on the paper, which has not been able to meet the diverse needs of people. And augmented reality technology (AR) can solve these problems very well. With the rapid development of the hardware for mobile terminals, the application of AR technology based on mobile terminals is more and more popular. By combining traditional prints with mobile phone to express more information which contained in the printed matter has become a new choice for traditional printing. With the help of mobile-phone camera, we can combine traditional prints with mobile phone by image recognition technology. Through the analysis of mobile augmented reality (MAR) application, the process of image recognition based on MAR is established in this paper. Based on the process of image recognition proposed in this paper, a 3D model of the interactive system for 3D map is developed. The interactive system shows that the research of this paper can not only enrich the information of print content, but also make the expression of traditional print information become more diverse.

**Keywords** Mobile terminal · Augmented reality · Image recognition

## 1 Introduction

Augmented reality (AR) is an innovative human–computer interaction technology that can not only overlay the virtual 3D model animation, video, text, images and other digital information to the real scene in real-time but also interact with real objects or users [1], which can be used as a bridge of the real world and virtual world to extend the real world [2]. AR enhances a user’s perception of and

---

H. Ye · R. Shi (✉) · S. Li · D. Li  
Zhengzhou Institute of Surveying and Mapping, Zhengzhou, China  
e-mail: ruizhishi@sina.com

H. Ye  
e-mail: 260094480@qq.com

interaction with the real world [3], which has most often been used in advertising and commercial, entertainment and education, medical, and mobile application for iPhones. Moreover, the application of AR technology in traditional printed product is comparatively mature in advertising and product publicity, which can not only improve the reading experience of the audience and the transmissibility of the printed product, but also bring a good economic benefit [4]. In order to further expand the AR application in printed product, this paper establish a technology process of image recognition based on MAR, which can enrich the forms and connotation of traditional prints.

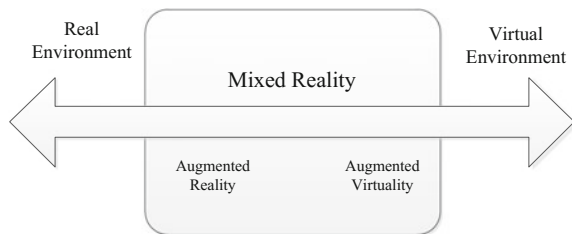
## 2 Augmented Reality Technology and Its Application in Printing

### 2.1 Augmented Reality and Mobile Augmented Reality

The domestic and foreign researchers have defined AR diversely. Paul Milgram and Fumio Kishino proposed a concept of “Reality-Virtuality Continuum”, as indicated in the Fig. 1, where real environments, are shown at one end of the continuum, and virtual environments, at the opposite extremum. The Mixed Reality is between real environments and virtual environments, besides, AR is close to the real environments [5]. Azuma defined AR as a system that fulfills three basic features: a combination of real and virtual worlds, real-time interaction, and accurate 3D registration of virtual and real objects [3]. Klopfer and Squire indicated that AR could be broadly defined as “a real world context that is dynamically overlaid with coherent location or context sensitive virtual information” [6].

In recent years, mobile augmented reality (MAR) has been a realizable thing because of the rapid development of computer technology, image processing technology, photoelectric display technology, sensor technology, multimedia technology, etc. and mobile terminals’ powerful functions. Besides, compared with the traditional AR, MAR is easy to carry and flexible to use, and the application field of AR also have been broadened.

**Fig. 1** Milgram’s reality-virtuality continuum



## 2.2 *Interactive Application of AR Technology and Printed Product*

### 2.2.1 AR and Advertising

The advertising based on AR is not only simple to experience but also of strong interactive experience and interest. As shown in Fig. 2, it is the advertising fragment of Japanese Glico. A 3D game character can be produced to interact with users by using the camera of phones or other mobile devices to aim the picture on the printed product. This form of advertising can bring users an excellent visual effect and user experience. What's more, the brand awareness can be increased by this novel form of advertising.

### 2.2.2 AR and Product Publicity

AR technology can make the form of traditional product publicity to be further expanded. Many international well-known brands such as BMW, ikea furniture, general electric and lego toys have repeatedly used AR technology in product publicity. As shown in Fig. 3, it is the most common product brochure. The equipment will show 3D model, animation, video or other more abundant information when users aim the camera of mobile device at the picture on printed

Fig. 2 Advertisement

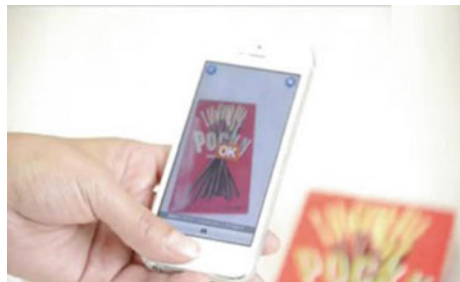
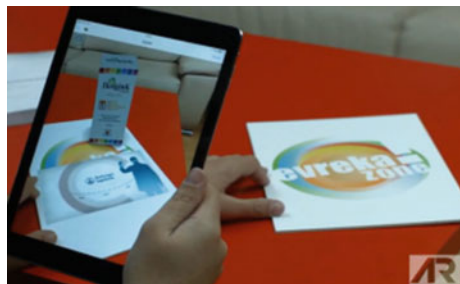
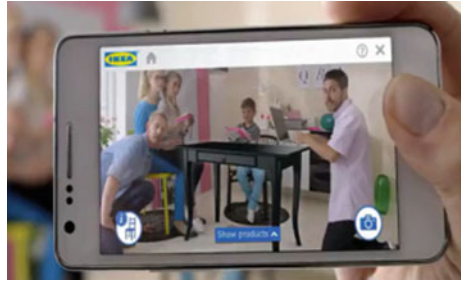


Fig. 3 Product brochure





**Fig. 4** Product publicity

product. Figure 4 is the product publicity for Ikea. On the screen of mobile device, users can see the effects that different furniture is overlaid to different places in a room. And therefore, users can make the most reasonable choice for their furniture matching.

### 2.2.3 AR and Auxiliary Teaching

Studies have shown that AR technology can greatly enhance educational outcomes [7]. For instance, AR can support students in visualizing abstract science concepts or unobservable phenomena, such as airflow or magnetic fields [8]. AR could also help students to visualize different learning objects, interact with theories and deal with the information in a totally new, effective, and interactive way by presenting lessons in a 3D format [9].

The traditional teaching materials are paper printing products that are limited to text and two-dimensional images, making it difficult to show some principles, models and phenomenon of mathematics, physics or chemistry to students intuitively. The enthusiasm and interest of students can be improved for the reason that AR can not only visualize many abstract concepts but also allow learners to interact with the virtual object.

## 3 Establishment and Application of Image Recognition Process Based on MAR

### 3.1 Image Recognition Process Analysis

The general process of AR based on mobile terminal is as follows, first of all, identifying the target objects in real scene by the video stream from the camera, and then using 3D registration technology to analyze the position and pose of camera in real scene, finally, overlapping and displaying the processed virtual information with real scene in accurate position.

In the process of the realization for AR, the image recognition method is mainly divided into two kinds, one is based on mark and another one is based on natural features. A specific mark is needed in advance for image recognition method based on mark. Moreover, the mark will be recognized according to grayscale characteristics of pixel after threshold segmentation for image in the process of recognition. The image recognition method based on natural features is to recognize the geometric features of the image, which does not need to set up the specific artificial marks. The recognition method used in this paper is the image recognition method based on natural features, and the recognition of the paper map is realized on the basis of image calculation and detection for the geometric features after image analysis.

Figure 5 illustrates the process of image recognition [10], the image is preprocessed simply after captured and collected by the camera of mobile terminal, and then feature extraction and recognition matching is carried out in the mobile terminal. If matching successfully, the local database or cloud database will be accessed and the following steps, tracking and registration for image, rendering fusion for virtual 3D model and the real scene, will be continued. If the recognition fails, the mobile-phone camera continues to collect and identify the image.

### 3.2 The Establishment of Image Recognition Process Based on MAR

The image recognition technology can establish the link between traditional paper map and digital media in the interactive printing, and realize the seamless combination of paper map and the corresponding digital media. Through the analysis of the

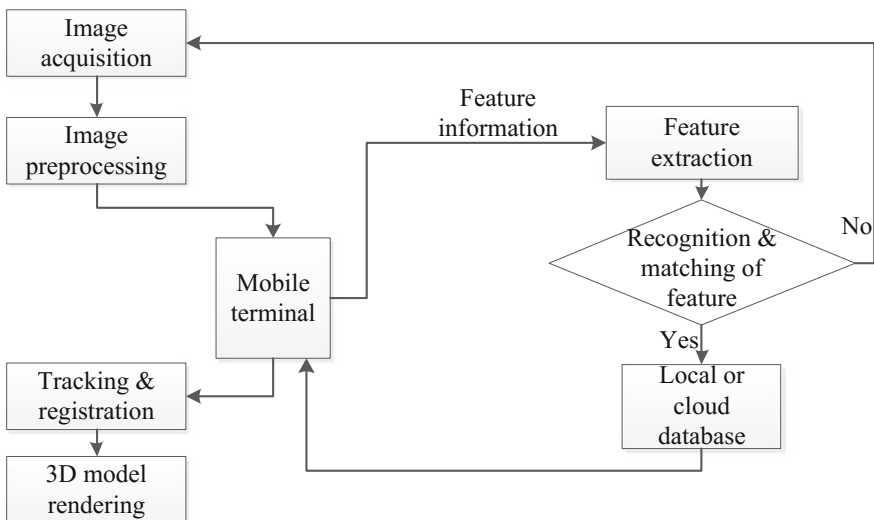
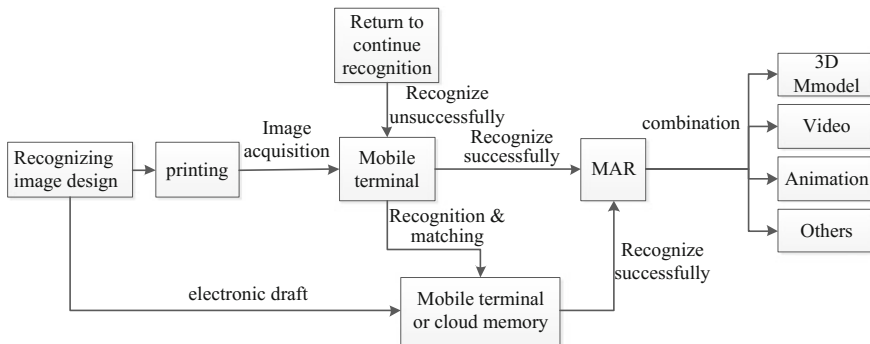


Fig. 5 Image recognition process



**Fig. 6** Interactive application technology process of MAR technology and printed products

image recognition process we sum up the interactive application technology process of MAR technology and printed the product, which is shown in Fig. 6.

The process of image recognition based MAR includes the following three steps:

### 1. Recognizing image design

Current recognition algorithms mostly recognize the image by the geometrical features, namely the feature points of image. Thus, the number of feature points should be increased as far as possible. Then print the designed image, and the electronic draft is stored in the mobile terminal or in the cloud as the target image for recognition and matching.

### 2. Image recognition and matching

The mobile terminal can extract the image feature information after capture and acquisition of image. Then the feature information can be recognized and matched by the recognition algorithm. The digital media information for the printed product will be shown on the screen of the mobile terminal when matching successfully. If the recognition fails, return to the recognition.

### 3. Combination of virtuality and reality

The digital media information (3D models, videos, animation, etc.) that is related to the printed product should be designed in advance. AR can combine digital media with real scene in the form of overlapping the digital media information to printed product. At the same time, users can also use mobile terminal to control and interact with these media information, such as rotation, scaling and editing of the 3D model.

## 3.3 The Application of Image Recognition Process Based on MAR

Based on the process of image recognition proposed in this paper, we develop a 3D model of the interactive system for 3D map. The traditional paper maps, used to be

the most important carrier for people to express spatial information, have such advantages as easy to carry, convenient to read, strong sense of essence and high collection value. At the same time, they are more complex than general printed product, and only by printing the content to express spatial information, has become increasingly unable to meet the needs of people for information. As a result, the traditional paper maps have been increasingly unable to meet the demands of map users. Traditional paper maps need to create a new form of expression to increase their competitiveness, and the combination of AR and paper maps can greatly expand the content of the map and increase the interactive function. For example, the three-dimensional terrain and landform, roads, buildings, land cover, hydrogeology, traffic signals, municipal facilities, etc. can be described vividly through the AR system. What's more, the detailed information of some specific objectives can be design and stored in a relational database that is associated with those targets in 3D model so that users can query conveniently.

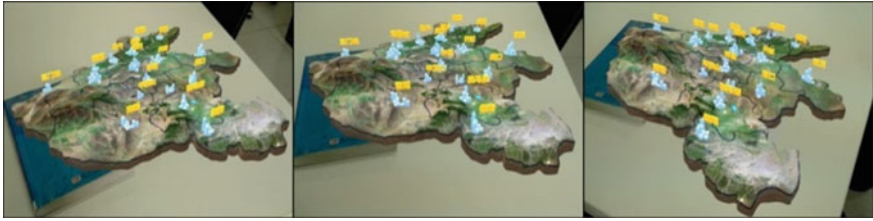
Qualcomm vuforia is an open-source SDK, which has stable image recognition and image tracking technology. Based on the process of image recognition proposed in this paper, we developed a mobile augmented reality map using Qualcomm vuforia and the Android SDK for Henan province. The mobile phone used in this experiment has 13-megapixel camera and 3G memory running Android 4.4.4. The application is implemented as follows:

Opening the software on the phone, and then feature points will be extracted and matched after real-time image captured by the camera. As shown in Fig. 7, it is the scanning process of feature points. If matching successfully, the designed 3D model will be overlapped after 3-D registration and model rendering. The combination of virtual 3D models and real scene contribute to users observing the three-dimensional effect that traditional paper maps can't express more intuitively [11] (Fig. 8).

The mobile terminal has become the connection bridge between traditional printed product and digital media in the process of realization for system's function. The system in this paper is only an example for the application image recognition and MAR in the printing field, which has a certain reference value for the new development of the paper map.

**Fig. 7** Scanning of feature points





**Fig. 8** Display effects from different perspectives

## 4 Conclusions

On the basis of the research and analysis for image recognition technology, MAR and interactive printing theory, an interactive application technology process of MAR technology and printed product is proposed and applied. And the developed system achieves the combination between digital media and traditional printed product. This combination can not only enrich the content of traditional printed product but also implement the diversification of the paper maps expressing [12].

The research of this paper can provide some theoretical reference value for the application of MAR in printing, and it can provide a series of technical support for the research and development of the related system platform. However, there are still many problems need further research for MAR, for example, improving the recognition ability of the image recognition algorithm, improving the position and pose accuracy for 3D model, enriching and beautifying the digital media information etc. [13]. With the development of related technology and mobile terminal hardware, we believe that the application of MAR in printed matter will become more and more widely.

## References

1. Wu, F. Zhang, L. (2012). A Survey on Development and Application of Augmented Reality. *Computer Engineering and Applications*. *Computer Knowledge and Technology*(34), 8319–8325.
2. Li, WX. Si, ZI. Gu, C. (2013). Discuss Augmented Reality. *Computer Knowledge and Technology*(28), 6411–6414.
3. Azuma, R. T. (1992). A survey of augmented reality. *Presence Teleoperators & Virtual Environments*, 6(4), 355–385.
4. Wang, N. (2015). Study on the application of Augmented reality in the field of Communication: The application of Augmented reality in the print. (Doctoral dissertation, Beijing Institute of Graphic Communication).
5. Milgram, P., & Kishino, F. (1994). A taxonomy of mixed reality visual displays (special issue on networked reality). *IEEE Transactions on Information & Systems*, 77(12), 1321–1329.
6. Klopfer, E., & Squire, K. (2008). Environmental detectives—the development of an augmented reality platform for environmental simulations. *Educational Technology Research & Development*, 56(2), 203–228.

7. Chiu, J. L., De Jaegher, C. J., & Chao, J. (2015). The effects of augmented virtual science laboratories on middle school students' understanding of gas properties. *Computers & Education*, 85, 59e73.
8. Wu, H. K., Lee, W. Y., Chang, H. Y., & Liang, J. C. (2013). Current status, opportunities and challenges of augmented reality in education. *Computers & Education*, 62(2), 41–49.
9. El Sayed, N. A. M., Zayed, H. H., & Sharawy, M. I. (2011). ARSC: augmented reality student card – an augmented reality solution for the education field. *Computers & Education*, 56(4), 1045–1061.
10. Li, S., & Shi, R. (2016). The Comparison of Two Image Matching Algorithms Based on Real-Time Image Acquisition. *Advanced Graphic Communications, Packaging Technology and Materials*. doi:[10.1007/978-981-10-0072-0\\_31](https://doi.org/10.1007/978-981-10-0072-0_31). 369:241–248.
11. Chen, ZG. Li, SG. (2010). Research on the 3D User Interface in the Virtual Environment. *Packaging Engineering*(2), 37–40.
12. Fang, XJ. Wu, QY. (2014). Paper map expression and its application based on mobile augmented reality. *Microcomputer & Its Applications*(7), 41–43.
13. Shatte, A., Holdsworth, J., & Lee, I. (2014). Mobile augmented reality based context-aware library management system. *Expert Systems with Applications*, 41(5), 2174–2185.

# Research and Application of Online Image Processing Technology Based on HTML5

Chunxia Dong and Zhanjun Si

**Abstract** This study aimed to develop a web image processing application in order to process the pictures online. First, the front-page was designed and layout by HTML, CSS and Bootstrap, then using File API to read the pictures or invoke the local camera to take pictures, and draw them into Canvas. Next the basic image processing algorithm were studied, and through the JavaScript scripting language to achieve pixels processing. The result is that a web image processing application was developed. Users can get the basic adjustment function to the acquired images such as brightness, contrast and basic filter such as mosaic. This study used Canvas technology that provided by HTML5 to develop a high quality native applications without relying on plug-ins. Users do not need to download the client, just a web site that can get the basic adjustment function to the images. It was worth researching.

**Keywords** Image processing · Web · HTML5 · Canvas

## 1 Introduction

Due to the continuous improvement of the browsers' performance and the growing popularity of wireless networks, whether a mobile phone or a computer, it is more and more dependent on the browser. In the application of many web pages, the field of image processing has attracted the attention of developers [1, 2].

Currently the most commonly used image post-processing software is client. Their processing platform is traditional C/S architecture. It is difficult to maintain, sharing and occupies large memory as well as suits the users with certain technical basis [3, 4]. In this paper, an image processing application was developed based on

---

C. Dong · Z. Si (✉)

College of Packaging & Printing Engineering, Tianjin University of Science & Technology, Tianjin, China  
e-mail: szj@tust.edu.cn

© Springer Nature Singapore Pte Ltd. 2017

P. Zhao et al. (eds.), *Advanced Graphic Communications and Media Technologies*, Lecture Notes in Electrical Engineering 417,  
DOI 10.1007/978-981-10-3530-2\_46

367

HTML5 Canvas. It has the advantages of easy maintenance and sharing, users can process the pictures without installing the client. It will solve the problems that C/S architecture applications brought well.

## 2 HTML5 Canvas

HTML5 is the choice of many mobile application and website now. It offers many new features such as local storage, geographic location, web multimedia, web works and so on [5, 6]. At present, the major browsers have a better support for Canvas. The support as follows (Table 1):

Canvas is a new element of HTML5. It contains two attributes: height and width. The former defines the height and the latter defines the width of the Canvas. The element hasn't the capabilities of rendering, only as a container of carrying pictures. It gets the drawing environment by calling the getContext() method of Canvas's. Then use the build-in API combined with JavaScript language to draw graphics and handle pixels on the webpage. Canvas API provides two important functions: getImageData() and putImageData(), so that the browser has a capacity of pixel processing [7]. Another important function is ClearRect (x, y, width, height). It is equivalent to an eraser, used to empty specified pixels within a given rectangle.

Canvas makes the browser directly display graphics or animation images without Flash or Silver light and other plug-ins [8]. Compare to the traditional server, which draw pictures first and then send them to the browser, it combines closely with the browser rendering engine. What's more, it can save resources and greatly simplifies the interactive process of the graphics with other elements [9].

## 3 Designing and Implementation

The application collects information through opening pictures, taking pictures then creates a new canvas, and then processes image's color. At last, the canvas is converted to a picture and saved in the local. The flow chart of the system is as follows (Fig. 1):

**Table 1** The support of the browsers for Canvas

Platform	MAC				WIN								
Brower	Chrome	FireFox	Opera	Safari	Chrome	FireFox	Opera	Safari	IE				
Ion	5	3.6	10.1	4	4	3.6	3	10	10.5	4	6	7	8
Canvas	✓	✓	✓	✓	✓	✓	✓	✓	×	×			



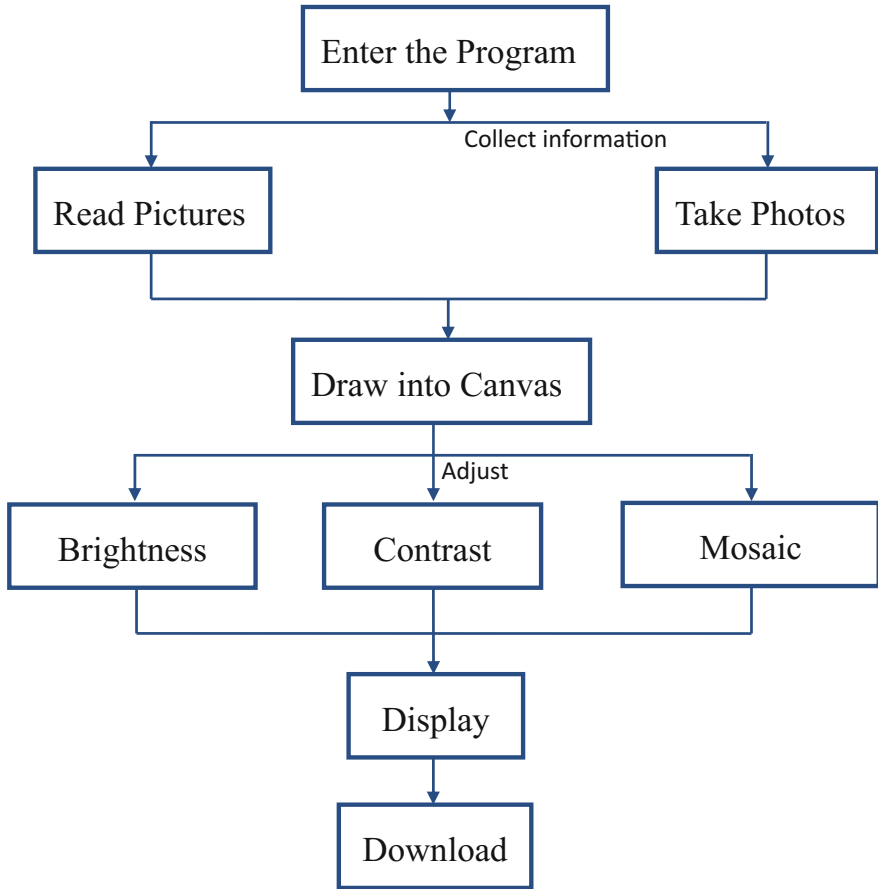


Fig. 1 Application process flowchart

### 3.1 Page Layout

This study use Canvas technology to develop the program. First the draft of the program interface was designed. Then according to the draft, the page was layout using HTML, CSS, Bootstrap. The final result is as follows (Fig. 2):

### 3.2 Capture Information

#### 3.2.1 Upload Images

There are three ways to upload a file: form submission, flash upload, and plug-in. The appearance of File API in HTML5 has brought us another way to upload files.



Fig. 2 The final program interface

It defines a new set of API, by calling its objects, methods and interfaces in the file API, we can easily implement the browser to access the local file.

### 3.2.2 Taking Pictures

The Media Capture API of HTML5 provides a programmable access to the camera, the developer can directly use the method of getUserMedia() to get camera’s video stream. Add an <video> tag in the HTML5, and the video stream from the camera is used as the input source for this tag.

## 3.3 Research and Implementation of Algorithm

### 3.3.1 Brightness and Contrast

The brightness and contrast adjustment of an image belongs to the gray linear transformation. Their integrated algorithm is as follows:

$$y = [x - 127.5 * (1 - B) * k + 127.5 * (1 + B)] \tag{3.1}$$

x is the pixel values before adjustment; y is the pixel values after adjustment. The value range of B is [-1, 1], which is used to adjust the brightness; k adjust contrast,  $k = \tan((45 + 44 * c)/180 * \pi)$ . The value range of c is [-1, 1], it was used to set contrast.

When B = 0,  $y = (x - 127.5) * k + 127.5$ , only contrast was adjusted;

When c = 0,  $k = 1$ ,  $y = x + 255 * B$ , only brightness was adjusted.

So the algorithm formula of brightness and contrast were obtained, and the code of brightness and contrast as follows:

```

function drawBrightness(obj,num){
    var oImg=cxt.getImageData(0,0,obj.width,obj.height);
    var data = oImg.data;
    var brightness = num / 50;
    for(var i = 0,n = data.length;i < n;i += 4){
        for(var j = 0;j < 3;j ++){
            data[i + j] = data[i + j]+255*brightness;
            if (data[i+j]>255) {
                data[i+j]=255;}
        }
    }
}
function drawContrast(obj,num){
    var oImg=cxt.getImageData(0,0,obj.width,obj.height);
    var data = oImg.data;
    var arg2 = num || 0;
    var c = arg2 / 50;// -1,1
    var k = Math.tan((45 + 44 * c) * Math.PI / 180);
    for(var i = 0,n = data.length;i < n;i += 4){
        for(var j = 0;j < 3;j ++){
            data[i + j] = (data[i + j] - 127.5) * k + 127.5;
        }
    }
}

```

### 3.3.2 Mosaic

To achieve the effect of mosaic, first the pictures should be divided into blocks and the size of them are the same. Each image block is a square, and in the square, all pixel values are the same and equal to the square where is in the upper left corner's first pixel. After processed by this method the mosaic effect will be appeared. The size of the square determines the size of the mosaic block, that is, the degree of mosaic. The code is as follows:

```

Function drawMosaic(obj,num) {
    var oImg = cxt.getImageData(0,0,obj.width,obj.height);
    var w = obj.width; var h = obj.height;
    var newImage = cxt.createImageData(obj.width,obj.height);
    var stepW = w/num; var stepH = h/num;
    for(var i=0;i<stepH;i++) {
        for(var j=0;j<stepW;j++) {
            var color =
getXY(oImg,j*num+Math.floor(Math.random()*num),i*num+Math.floor(Math.ra
ndom()*num));
            for(var k=0;k<num;k++) {
                for (var l=0;l<num;l++) {
                    setXY(newImage,j*num+k,i*num+l,color);}
                }
            }
        }
    }
    cxt.putImageData(newImage,0,0);}

```

The parameter “num” is used to control the size of the square, and it is given when the function was called.

### 3.4 Download

Canvas API provides a interface of `toDataURL()`, using this function the canvas can be easily converted into Base64 coding image. Then use the function of `replace ()` to change the image’s mime Type into “steam” type, such as ‘image/octet-stream’ and save the image in the local.

## 4 Conclusions and Prospects

HTML5 provides good cross-platform software application architecture, making the users experience richer web applications, especially Canvas. It has brought good news to the development of image processing applications based on web browser. The field of image processing involves all aspects of human lives and works. People can use images to keep, spread and exchange information. With the continuous

expansion of people's range of activity and the development of thought, image processing is also applied to face recognition, measurement face similarity and so on.

## References

1. Yu Fei. A Research and Implementation of Graph and mage Collaborative Processing Technology Based on HTML5 [D]. Yangtze University, 2015.
2. Zhu Wen. The Research of Online Image Processing Method Based on HTML5 Canvas Technology[D]. GuangZhou:South China University of Technology, 2013.
3. HOU Shu-ying. Comparison to Advantage of B/S Pattern and C/S Pattern [J]. Journal of Shenyang College of Education, 2007, 02:98-100.
4. Liu Qian. The Research of Graphics and Image Processing Technology in HTML5 [J]. Soft Development, 2014, 08:93.
5. Zhang Yuqing, Huang Jinping. Research and Implementation of Key Technology of Cross Platform Mobile Application Based on HTML5[J]. Industrial Control Computer, 2013, 03: 56- 58.
6. Shen Ke, Si ZhanJun. Study on the Effect of 360 Degree Display of Goods Based on HTML5 [J]. Software Giude, 2015, 09:169-171.
7. Boulos Maged N Kamel, Warren Jeffrey, ect. HTML5 and the canvas element for interactive online mapping [J]. International Journal of Health Geographics, 2010, 9:30-32
8. Zheng Meirong. Research and Implement of HTML5-based Web Application[J], 2014, 27 (12):120-122.
9. Yu Fei. Research on the Processing Technology of HTML5 Graphics [J]. Computer CD Software and Applications, 2013, 12:261-263.

# Information Publishing System Based on the Framework of Django

Shenliang Li and Zhanjun Si

**Abstract** The development of Internet has broken time and space limits of information dissemination. That a large amount of information filled in the network makes it more convenient to people to obtain information. To attract more users, the provider has to provide more rich and high quality contents. But the content is not the same as the time that the content is made by the words and pictures. Now, it needs to deal with the sounds and movies. So the content has to be made by the one who has the special skills. In order to reduce the cost of human resources, many digital publishing content providers often outsource their production to other companies. And much of the work can be completed by the students selecting the relevant classes. Therefore in order to make the digital publishing enterprises, schools and individuals can communicate with each other, this paper set up a B/S platform based on the Django framework. It can provide resources processing and display the service demand for digital publishing companies. The development of platform can improve the working efficiency of the enterprise, which has a certain practical application value.

**Keywords** Django · Website · Information publish system · Digital publishing

## 1 Introduction

In 2015, China's digital publishing industry has exceeded 330 billion. It is the most import focus of China's press and publication industry. That prompts digital publication provider to provide more rich and high quality content for the users. But in order to reduce the cost of human resources, many digital publishing content providers always outsource their production to other companies. Actually, many

---

S. Li · Z. Si (✉)

College of Packing and Printing Engineering, Tianjin University of Science & Technology, Tianjin, China

e-mail: szj@tust.edu.cn

© Springer Nature Singapore Pte Ltd. 2017

P. Zhao et al. (eds.), *Advanced Graphic Communications*

and *Media Technologies*, Lecture Notes in Electrical Engineering 417,

DOI 10.1007/978-981-10-3530-2\_47

students in the university can produce good contents. Because of the lack of communication, the companies always outsource to other companies.

However, building a vertical platform can let enterprises and students contact directly, thus helping students to understand the corporation or company needs and find their favorite direction to develop at the same time. It will also be easy for companies to find suitable employees and reduce the training costs of enterprises.

Therefore, in this paper, the main work is to set up an information processing platform for enterprises, schools and students to communicate with each other. Compared with other platforms, the platform is a specialized for enterprises and universities. The aim of the platform is to promote the communication between enterprises and universities.

## 2 System Design

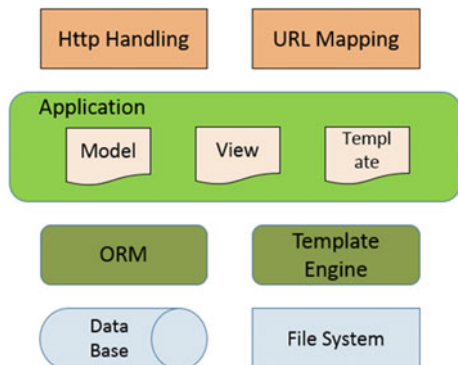
### 2.1 *The Framework of the Platform*

The platform is based on the framework of Django. The Django is an open source framework written by python [1]. It was designed to make common Web-development tasks fast and easy [2]. It has many advantages such as easy learning, high efficiency, and portability and so on. It uses the MVC software design mode, so the web application has created with low coupling, reusability and extensibility (Fig. 1).

### 2.2 *System Function*

The system based on the MVC mode of the Django framework [3]. There are 3 main functions in the system.

**Fig. 1** The architecture of the Django framework



1. User registration

The system has realized the registration function. The user registered can enter the user management page. They can modify the basic information and manage their work to present themselves in the page. They also can get the contract information by viewing the released articles (Fig. 2).

2. Role division

In order to better manage the system, the registered user has different roles. Different roles have different permissions. The system divides the user into three roles: visitors, registered users, system administrators. Set different permissions for users according to different roles (Fig. 3).

Fig. 2 Visitors and registered users use case diagram

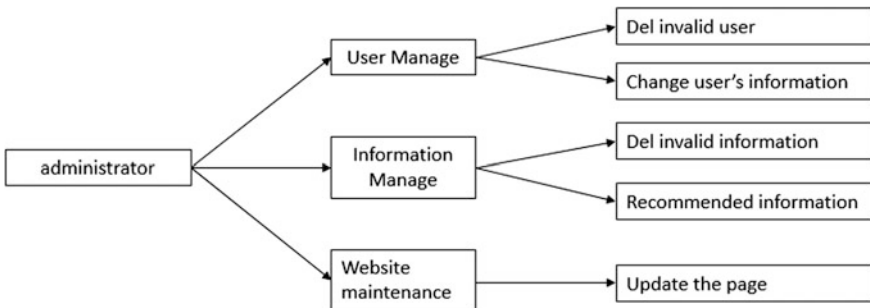
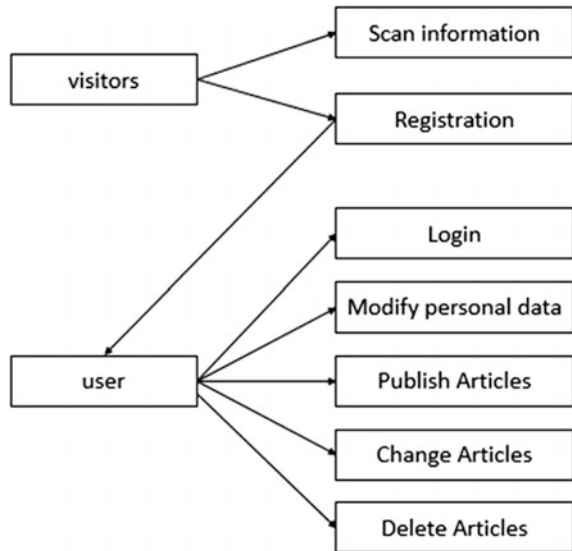


Fig. 3 Role division



### 3. Information manage

Only the user registered can release the information on the website. The information is divided into 3 categories. The work for the individuals is to present themselves, the demanding information for the enterprises is to out-source and the special courses for the university is to advertise. The released information in the page is sorted by the time in default. So when the user views the page, the information is always up to date. There are six demanding information can be recommended in the home page.

## 3 System Implementation and Deployment

### 3.1 Model Design

The models are the base of the system and the model in Django are corresponding to the tables in the database. Each model has a table in the database, and the properties of each model are also corresponding to the fields in the table. In this paper, there are six models: Exuser, Servers, Lesson, Service Model, Class Model and Article.

Exuser model is the extension of the user model in the Django. It is one of the core models in the system. The user model in Django does not have enough property to satisfy the needs of the system. So, to do the extension, the paper uses the property of One To One Field to link with the user model in Django. Using extension can add more property to a user, such as the nickname which is shown in the browser, and the company name which company the user belong to etc.

The model of Article is the news that register user published. It is another core model in the system. Each article must be published by a user, so there is a property of user in the model. An article must belong to a user, but a user may publish many articles, so the user property is models ForeignKey. In order to facilitate the management of the article, the trial also carried out a classification of articles.

In the system, there also are some professional teams which are called Servers. The Servers provide more professional and authoritative services. Each server must be good at some fields. The model of Lesson is to store the information of the fields.

### 3.2 URL Design

In the file of urls.py, configure the path location for the user to access the system page [4]. The configuration is the link between the browser and the background program. It can show what the user wants to do. In the system, to deal with the logical relationship better, the file of urls.py is separated into two: one used in the front, the other one used in the background. The following is the configuration navigating to the front web page.

navigating to the front web page.

```
# view the servers
url(r'^servers/$',ServersView.as_view(),name="serversView"),
# view the server detail by the server id
url(r'^server/(?P<pk>[0-9]+)/$',server)
url(r'^contactus',ContactUsView.as_view(),name="contactUsView")
url(r'^classmodel/(?P<modelId>[0-9]+)/$',classModel),
url(r'^check/(?P<username>\w{3,30})/$',checkUserName),
url(r'^servicemodel/(?P<serviceModelId>[0-9]+)/$',serviceModelArticles),
url(r'^servicemodel/(?P<serviceModelId>[0-9]+)/classmodel/(?P<classModelId>[0-9]+)/$',classModelArticles),
url(r'^articles/(?P<serviceModelId>[0-9]+)/(?P<pageId>[0-9]+)/$',serviceArticle),
url(r'^articles/(?P<serviceModelId>[0-9]+)/(?P<classModelId>[0-9]+)/(?P<pageId>[0-9]+)/$',classArticle),
```

### 3.3 View Creating

View is the center of processing data. Whether the data is from the front or background, all are processed by the view. Then each stores the data into the database or sends it to the browser. View at the same time also has the authority to control, to detect whether the user login and so on.

In the article, there are many functions or classes need to do the permissions control. In order to make the code simple and follow the rules of DRY, in this paper create a class named `LoginProtectedView` inherits from the `TemplateView`, and define a function name `dispatch` which annotated by `method_decorator` (`login_required` (`redirect_field_name = 'next', login_url = '/manage/user/login/'`)). The class that needs to do the permissions control can inherits it.

```
classLoginProtectedView (TemplateView):
```

```
@method_decorator(login_required (redirect_field_name = 'next', login_url = '/manage/user/login'))
```

```
def dispatch(self, *args, **kwargs):
```

```
return super (LoginProtectedView, self).dispatch(*args, **kwargs)
```

### 3.4 Deployment and Release

Development can use the WSGI server to carry out test and development. But in the real production environment, the WSGI cannot meet the actual demand. Apache2

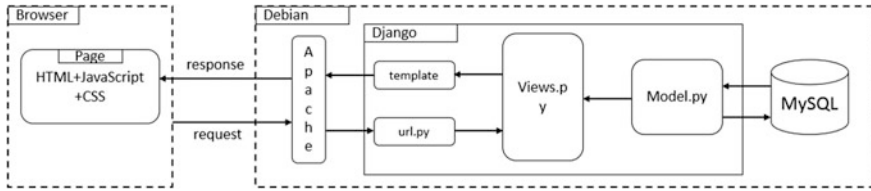


Fig. 4 The system architecture



Fig. 5 The home page

web server supports a variety of development languages, and Apache2 also has the characteristics of open source and stability. In this paper, Apache2 as the server to deploy the website by changing the Apache2's configuration file `apache2.conf`, adding the code as follows: `WSGIPython/web/web.` and modifying the `000-default.conf` file in the sites available directory. Finally configure the directory for static files. Change the `DEBUG` option to `False`, and fill in the `ALLO_HOSTS` property in the domain name or IP (Figs. 4 and 5).

## 4 Summarize and Prospect

As the result of the usage of the Django framework, there are less codes in the system [5]. The system achieves the release of information, registration and login. Building up a platform for the company and individuals, it can not only make the students know more about the company, give them more chances to practice themselves, but also can help the company find more suitable employees and reduce their cost.

This paper uses relatively sophisticated technology in the Django, such as classes based view, named URL, static resource configuration and basically satisfy

to build a small system. But the function of the system is simple. There is no message function in it. Later the system can be combined with social networking, so that users can be more convenient to use.

## References

1. Zhou Yao (2013) Django-Based Campus Print Reservation Website Design and Implementation[D] JiLin University.
2. DjangoDocumentation <https://docs.djangoproject.com/en/1.9/intro/overview/>. Accessed 25 Mar 2016.
3. XiaZhifu, Wang Hanlu, Li Yuping, Cao Lei, Xia Bin (2016) The design of intelligent business monitoring system based on the Django framework. Software and Algorithms, [10.19358/j.issn.1674-7720.2016.12.008](#), 21–27.
4. Zhao Yanbin (2015) A Analysis on The Establishment of Webpage Data Model Based on Django Technology[A] Times Agricultural Machinery.
5. Yan Qinghai, Zhao Zili, Wang Ruiqing(2015) Development of a Business Management System for Planning Design & Survey Units Based on Django[A] Urban Geotechnical Investigation & Surveying.

# Trends of Digital Publishing: A Case Study of Taiwan's Tourist Press

Yungcheng Hsieh, Mingchw Wei and Yungchao Ting

**Abstract** When Steve Jobs introduced Apple's iPad in 2010, it opened the door to new opportunities in the digital publishing industry. However, five years have passed, and only a small amount of publishers have made the move to digital publishing. In addition to lack of funds, most publishers have limited knowledge of digital publishing and mistakenly think that digital publishing will have a negative impact on traditional paper book publishing business. This paper identifies new opportunities for digital publishing by analyzing data from the 2012 Survey of Taiwan Book Publishing Industry. Statistics shows that tourism-related books are in great demand, with a reading rate of 60.3 and 23% of new writers mainly focus on writing tourism-related books when they first start their careers. Studies from Europe and America show that digital publishing has much potential, but has yet to deliver substantial sales growth. Nonetheless, digital publishing has begun to impact publishers' business strategies. In Taiwan, the majority of publishers think that the traditional publishing industry is in decline. Yet, more than half of traditional publishers are concerned about having the resources, including adequate funds, to make the transition to digital publishing. This paper focuses on a well-known tourism publisher, T Publisher, a company with more than 20 years of experience in the publishing industry. This paper used a case study approach and expert interview, fully evaluating T Publisher's digital publishing strategies from 2014 to 2015 and interviewing two experienced experts in the publishing industry. Finally, this paper presents a number of recommendations, which can hopefully serve as a reference for publishers who would like to enter the digital publishing industry.

---

Y. Hsieh (✉) · Y. Ting

Department of Graphic Communications Arts, National Taiwan University of Arts,  
New Taipei, Taiwan  
e-mail: ych@ntua.edu.tw

Y. Ting

e-mail: leont.kathy@gmail.com

M. Wei (✉)

Graduate School of Creative Industry Design, National Taiwan University of Arts,  
New Taipei, Taiwan  
e-mail: ntua10070801@gmail.com

**Keywords** Publishing · E-book · Digital publishing · Tourism e-book · Taiwan

## 1 Introduction

Taiwan's digital publishing can be traced back to the year of 2000, when the Internet started to emerge. At that time, some companies in the technology industry had already explored the idea of digital publishing, people reading on computer screens. However, due to the negative perceptions of screen readers, digital publishing failed to catch on. In the United States, the e-book sector started to grow exponentially when Amazon first introduced its Kindle in 2007. Smart phones, spearheaded by the first generation of iPhone, swiftly took over the world in the same year. In 2010, Steve Jobs from Apple Company introduced the iPad to the public, which allowed digital publishing to be combined with mobile devices. This technology launched a new trend in digital reading. Starting in 2015 Taiwan's publishing industry faced a battle for survival. According to literature, the total revenue for Taiwan's publishing industry was six billion and seven million NT dollars from January to April in 2015. Compared to the same time period in 2014, 2015 revenue declined by 37%. If the revenue continued at this rate through the end of 2015, total revenue for the year would be below NT\$20 billion. Compared to 2010 revenue of NT\$36.7 billion, it would be a decline of nearly 50%. The Association of American Publishers released a statistical report, which indicated that the sales of e-book during the first nine months of 2015 declined by 11.1% compared to 2014 sales. The Association of American Publishers has membership of 1200 publishers, accounting for a significant portion of the publishing industry. International publisher, the Lagardère Group released a financial report that verifying the drop in e-book sales. General and Managing Director of the Lagardère Group, Arnaud Lagardère stated in the report that the company's revenue of e-book sales in the United States reached its peak in 2013, which was 30%, but, revenues declined to 22% in 2015. Nowadays, Taiwan is facing a similar challenge in declining paper book sales. There is very little research using case studies to evaluate sales' revenue in the digital publishing industry. This paper, therefore, seeks to close this research gap, through an evaluative case study of T Publisher's e-book revenues with the aim of exploring turning points for digital publishing in 2016.

## 2 Literature Review

Chen [1] suggested that in the digital era, many industries are experiencing the dramatic disruption that changes in information technology have brought. The publishing industry is no exception. Upstream, midstream, and downstream information flows have created massive amounts of digital content requiring the publishing industry to have fundamental changes. During 2010–2015, e-book sales

showed a significant increase. There are two main reasons driving the increase: First, reading devices, such as iPhone, iPad and Kindle, became very popular. This presents an opportunity for publishers to change their image. Second, digital publishing becomes focusing on “social sharing,” “interactive reading,” and “reading scenario building.” Electronic books and electronic book readers are different from traditional reading. They are light, convenient, easy to store, eco-friendly, efficient, easily accessible and have a user-friendly interface.

As far as electronic content is concerned, ePub is the most popular open book format. The latest version is ePub3.0, which was released by IDPF in 2011, to replace ePub2.0’s Open Electronic Book Standard. The main difference between the two versions is that ePub3.0 supports HTML5, CSS3, audio and video, as well as Chinese vertical layouts and text on the side of a character (e.g., phonetics). In addition, one can synchronize file content and pre-recorded audio or use software to synthesize text to audio. ePub3.0 supports right-to-left and top-to-bottom text directions, which is the format for Chinese, Japanese, and other traditional Asian languages. As a result, ePub3.0 caters to both Chinese and Japanese readers’ reading habits [2].

### **3 Research Methodology**

Our study adopted a case study approach and expert interview. [3] suggested that a case study is a bounded system which means with a well-defined subjects. We evaluated T Publisher’s actual sales revenue, and conducted in-depth interviews with two experts. One of the experts is the managing director from T Publisher, who has more than 25 years of experience in the paper book publishing industry. He proposed a marketing strategy for the digital publishing industry in 2016 after reviewing the data. The other is managing director Mr. Fu from Perse Press, LLC, who has more than 20 years of experience in publishing. Fu is also the manager of Puomo Digital Publishing and has published more than 300 electronic books in Google Play Books and Apple iBook Store. Currently, Puomo Digital Publishing produces a digital magazine with interactive applications; whereby paper books and electronic books are published simultaneously. Fu addressed topics related to digital publishing from an outside expert’s point of view.

## **4 Research Analysis**

### ***4.1 Annual Sales Revenue Growth Increased by 15.6% Compared to 2014***

T Publisher currently collaborates with 15 digital publishing channels, similar to most publishers do in Taiwan. Table 1 indicates that the total sales revenue of digital publishing increased by 15.6% annually (see Table 1).

**Table 1** Annual sales revenue growth rate currency: new Taiwanese dollar (NT)

Year	Annual total marketing
2014	1,169,000
2015	1,385,000
Growth rate	15.6%

**Table 2** Digital sales ranking for worldwide Chinese population

Sales ranking	Region/Country	Number of purchase
1	HK	1347
2	TW	1326
3	MY	189
4	US	166
5	SG	115

This paper only evaluated one single tourism publisher, any data that indicates a decline may not be projected onto the entire publishing industry. There are no comprehensive reports available in this regard in Taiwan. If we had the complete data to estimate the decline, it should not be too different from the data in the literature. Therefore, if one looks beneath the surface of the sales growth numbers it should raise great concern. As it reveals that most digital channels are experiencing a decline. B2L (Business to library) and Google Play Books accounted for more than 50% of the sales revenue in 2015. If we look at the numbers more closely, we will find that the growth of the library digital publishing channels is slowing down. T Publisher has close to 250 digital publications in Google Play Books. On average, four new digital publications are published monthly. Among the 15 digital publishing channels, every channel accepts PDF except for Apple. Since 2016, some digital channels would like publishers to provide digital publications in ePub3 format. The result might not be successful. The reason is that ePub3 is not a standard format for electronic books, but only a reference. Therefore, one ePub3 file that meets one company's requirements may not meet another's. It requires a significant amount of time and money to produce various ePub3 files. At present, digital publishing channels are still responsible for ePub3 conversion.

#### ***4.2 International Digital Platforms: Promoting Digital Publications to International Markets***

Google Play's sales ranks (see Table 2) high in Taiwan and Southeast Asian countries. One can also retrieve data on the number of downloads from Chinese consumers worldwide. This is not possible for paper book publishing. There is no data for China because Google Play is banned in China. The Google Play Books' platform was launched in Taiwan in mid-October 2013. Apple iBookstore and Amazon have not expanded their markets into Taiwan. As a result, Google Play



Books is the only international ebookplatform in Taiwan. Compared to iBookstore, Google Play Books has three advantages:

1. In Taiwan, people with a Google account outnumber those with an Apple account.
2. E-books from Google Play Books can be read on any type of computer browser; either Mac or Windows operating systems. It also provides applications for iOS and Android operating systems. On the other hand, e-books from iBookstore can only work with Mac OS X 10.9, iPhone, and iPad. (The iOS operating system has an iBook interactive publication format, which cannot be found in Google Play Books or Android operating systems.)
3. Google Play Books takes both PDF and ePub file formats. Readers can choose based on their preferences.

Generally Speaking, Google Play Books is convenient for both publishers and readers. Publishers can provide several free books in Google Play Books as a marketing strategy to attract readers. From a sales' point of view, in 2014, sales in Hong Kong, Macau, Singapore, and Malaysia equaled those in Taiwan. Hong Kong surpassed Taiwan in 2015. Growth can also be seen in other countries. Google Play Books perfectly illustrates digital publishing's boundary less characteristics.

### ***4.3 Price Does not Necessarily Affect Readers' Willingness to Purchase***

After reviewing the data retrieved from Google Play Books and analyzing the sales numbers from 2014 and 2015, we can conclude that price does not play a crucial role. This is different from the impression that digital readers care more about free publications. Indeed, free publications attract a certain amount of readers, but content is what really matters for most of the readers. Providing content that suits readers' needs will make it easier to achieve sales goals. The 2016 Digital Book World Keynote Presentation further pointed out that if we only look at traditional publishers' sales, we would think that e-books have a higher price range—between US\$9 and US\$14. In fact, if we take self-publishers, single-author publisher, and Amazon imprints into consideration, the price range actually falls between US\$2 and US\$5, which is also the price range that generates the most sales. Half of the readers still choose e-books over paper books even if paper books are cheaper by US\$3 to US\$7. In principle, most Publishers still price paper books higher than e-books (2016, [authorearnings.com](#)). In January, 2016, Amazon China released Kindle 2015 E-book Reading Behavior Report. Chief Marketing Office, Hong Yu, reported that paid e-book sales have grown remarkably during the past three years. Readers are learning to “pay for the better content.” In the 100 Chinese cities that have the top completion rates for reading e-books, completion rates for reading paid e-book is three times more than that for reading free e-books. Foreign e-books have an even more distinct ratio.

## **4.4 Interview Findings**

### **4.4.1 Does Digital Publishing Cost Less Than Paper Book Publishing?**

Compared to paper book publishing, the main appeal of digital publishing is to save the printing cost. There are always extra mailing and book release costs in addition to printing costs. These are tangible costs that can be seen easily. The cost of one e-book is the same as the cost of one paper book except for the printing costs. Hidden costs such as editing costs, on the other hand, are less appreciated. This is the type of challenge paper book editors will face in the digital era. Editing costs are just one of the implicit costs that challenge the digital publishing industry. Digital editing is different from paper book editing in terms of the mode of thinking. For instances, digital editors sometimes need to delete certain content and use multimedia in its place to express the same ideas. To accomplish such tasks, whether publishers are going to re-train their editors or recruit new ones? However, to pinpoint that digital publishing may save tangible costs; yet implicit costs need also to be taken into account when publishers convert from paper book publishing to digital publishing. The electronic version not only has to fulfill both iOS and Android operating systems' requirements, but also has to be adapted to both tablets and cell phone screens. The turnaround time for an electronic magazine is therefore extremely tight. In addition, interactive magazines sometimes require audio or video effects, which then require the publisher to edit the various videos or convert audio files. There are also times when the publisher needs to animate some illustrations in the electronic version. All these requirements need to be discussed in publishing meetings in order to plan and design the electronic version. If it is an e-book sold through digital channels; then connection costs, system costs, and lifetime services model will be involved. Such requirements present the questions of whether e-books are really cheaper than paper books, or are e-books even free? How do publishers fill these gaps? This is a problem that needs to be solved by the publishing industry.

### **4.4.2 Course from Paper Book Publishing to Digital Publishing**

There are several challenges when publishers transition from paper book publishing to digital publishing. First, publishers are often unfamiliar with smart devices. Second, publishers do not have enough information regarding the markets for iOS and Android operating systems. Third, publishers do not fully understand how digital publishing operates, and digital publishing is not as real as the paper book publishing. Fourth, the publishers wonder how to start. It is very important to understand the concept of digital publishing. Digital publishing utilizes interactive UI and multimedia to improve paper book versions. In the meantime, publishers must continue to meet the demand of their existing paper book consumers. After publishers overcome all the abovementioned challenges, their next move is to select

the tools for digitization. As far as technology, content, and graphic design needs are concerned, every tool has its own strength. Some companies spend a significant amount of money on developing their own reading software; others have slide-shows with JPEG files; still others use the ePub format that is mostly pure text. Moreover, there are companies that use PDF with zoom-in functions or publishing software such as Adobe Digital Publishing Solution tools to meet their needs [4]. Each of these tools are equally good; what to use depends purely on a publisher's goals.

## **5 Conclusion and Suggestions**

### **5.1 Conclusion**

Nowadays, the media industry is facing various challenges, especially the traditional ones. A successful transition from paper book publishing to digital publishing cannot be based solely on intuition. Data must play a role. The most difficult part when looking at sales numbers after transformation is to conquer the fear inside one's mind. Transforming to digital publishing requires a change in business discipline, whereby success is most likely to be judged on sales numbers to determine success. There are no absolute rules in the digital era. Everything is possible. This is also the most challenging part in the digital era. In 2007, iPhone brought us to the mobile era. Applications and content were much-yalked-about topics. Nonetheless, Big Data is the next spotlight. Applications are out of the game, and are merely viewed as tools. The future battle field for publishing industry is in the websites.

Digital publishing does have significant benefits over paper book publishing in terms of marketing promotion. For paper book publishers, there are lessons to learn when digitizing their content: digital publications' storage and transmission, digital editors' responsibilities, accessibility of interactive digital publication materials, and so on. These lessons can also serve as good references for publishers who would like to enter digital publishing business. Digital publishing has various forms, and interactive digital publication is just one example. Different paper book contents should be presented with different digital publication forms when converting the content. Every publisher should focus on meeting digital readers' needs and expectations.

### **5.2 Suggestions**

After conducting the interview with T Publisher's managing director and analyzing the sales revenue during 2014–2015, Suggestions for digital publishing are:

1. Strengthen the cooperation with library channels, and expand actively into China's digital publishing market, including establishing partnerships with publishers in Hong Kong by attending major book festivals in Taiwan and China, such as Taipei International Book Exhibition, Beijing Book Fair, Cross-Strait Book Fair, and Beijing International Book Fair (BIBF). Taiwan's two major library digital channels have been expanding their markets into China since 2015. The two channels were attested by the libraries of general and vocational high schools in China. Introducing Taiwan's quality content to the libraries in China will generate new revenue. One concern is that China's digital publications cost less than that of Taiwan. However, if the sales remain at a certain level, the revenues should not be affected. In addition, Taiwan's Publishers can work with Amazon China. Taiwan's e-book channels can convert the content from Taiwan that is approved by the Chinese government to Amazon's unique e-book format. The content can then be sold in China. In the vast digital reading market, China has many other digital publishing channels in addition to libraries and Amazon China. They all need Taiwan's e-book channels to help bring Taiwan's quality content to China's market.
2. International digital publishing channels should consider entering the Taiwanese market to improve annual sales revenue. Google Play Books was launched in Taiwan at the end of 2013. However, since the launch of Google Play Books, there have not been any other international digital publishing channels launched in Taiwan. It is said that Apple will launch its eBooks in Taiwan, but so far this is just a rumor. In September 30, 2015, Apple announced in Beijing, China that the company would introduce Apple Music™, iTunes® movies, and eBooks® in China. However, the Chinese central government (the State Administration of Press, Publication, Radio, Film and Television of the People's Republic of China) shut down Apple's online e-books and movie services. There are many different stories regarding the reason for the shutdown, and this does demonstrate that publishing remains a very sensitive industry in China. Introduce Simplified Chinese books for a bigger digital content selection to increase sales revenues. It shows that it is easy to connect with Chinese reading markets around the world through international digital publishing channels. Taiwan's publishers face fewer restrictions; China, on the other hand, is subject to more. However, China has some quality content as well. In this way, both Traditional Chinese and Simplified Chinese readers can enjoy the books. It can be a new way for Taiwan's publishing industry to grow sales.
3. Digital content reaches Chinese readers worldwide is a must. Digital publishing, is an ongoing service because every magazine is in the cloud storage and readers can download any of them through their applications. Compared to paper book publishing, it is undeniable that sales of digital publishing are high among Chinese readers around the world. The amount of published paper books is fixed, whereas digital content is usually stored in the cloud and can be downloaded by readers at any time. It does not matter whether the magazine is the current issue, as long as readers are interested in the content, they will download it. As a result, the number of downloads will increase as time goes by, which leads to a long tail effect.

## References

1. CHEN, ZHAO-ZHEN (2004), The Developing State and Trend of Digital Publishing. Special Topic: For J LIS 30th Anniversary. p 107–115.
2. WU, PEI-YUN, PENG, YE-QI (2013). Research on the current situation and profession training in digital publishing industry in Taiwan. *Journal of Cultural Enterprise and Management* No. 11:p 12–23.
3. Stake, Robert E (1995), *The Art of Case Study Research*. Sage.
4. Jame, Fred (2012), *A Digital Publishing History of My Own*.
5. Chang, Yi-Cheng (2014), *Business Model of Digital Publishing Industry of Taiwan*, Master thesis, Nan Hua University.
6. Lin Cheng-Jung (2004), *The viewpoints of Digital Publishers on the Content and Style of Digital Publishing*, Master thesis, National Taiwan University of Arts.
7. Li, Wei-Shou (2011), *Research on the Entry Strategies of Taiwan Digital Publishing Industry Landing in China*, Master thesis, National Taiwan University.
8. Lin, Li-Hun (2011), *Digital-publishing strategies and development patterns of major publishers in Taiwan*, Master thesis, National Chengchi University.
9. Apple.com. (2015). *Apple Brings Apple Music, iTunes Movies & iBooks to Customers in China Starting Today*. Apple Music, iTunes Movie and iBooks. Retrieved 20 June, 2016, from <http://www.apple.com/pr/library/2015/09/30Apple-Brings-Apple-Music-iTunes-Movies-iBooks-to-Customers-in-China-Starting-Today.html>.
10. Oaks. Xinhuanetcom. (2016). 2015 Kindle e-book reads report. Retrieved 20 June, 2016, from [http://news.xinhuanet.com/book/2016-01/25/c\\_128665803\\_2.html](http://news.xinhuanet.com/book/2016-01/25/c_128665803_2.html).
11. Xinhuanetcom. (2016). 2015 Kindle e-book reads report. Retrieved 20 June, 2016, from [http://news.xinhuanet.com/book/2016-01/25/c\\_128665803\\_2.html](http://news.xinhuanet.com/book/2016-01/25/c_128665803_2.html).
12. Yang, jia-rong. (2013). *Relationship between UX and UI*, Computer& Information Networking Center. Retrieved 08 January, 2016, from [http://www.cc.ntu.edu.tw/chinese/epaper/0027/20131220\\_2704.html](http://www.cc.ntu.edu.tw/chinese/epaper/0027/20131220_2704.html).
13. Zhou, yi-ling. (2016). *Current situation of digital publishing industry in Taiwan: Reading through social networks*. Retrieved 03 October, 2014, from <http://mymkc.com/articles/contents.aspx?ArticleID=21994>.

# Design and Implementation of Interactive Courseware Based on Mobile Terminal

Ying Wang, Zhanjun Si and Lu Zhang

**Abstract** Electronic courseware is an important tool for teachers to impart knowledge to students, and an innovative education mode in the environment of multimedia, but the courseware in the modern class only stays in the visual display stage of knowledge points, audio-video, animation and other elements, and is lack of interaction of multimedia courseware. The design is based on the interaction between teachers and students, students and students, and the popularity of mobile electronic devices, combined with image-processing and typesetting tools to designed a course which will meet the teaching demands, applying the FounderFX 6.0 digital version to realize the static effects of pages, and then according to the user experience, to realize the interactive effects, finally release it to the mobile terminal to assist the classroom teaching. The design makes full use of multimedia technology to transfer the interactive courseware to the mobile terminal, and students are really participate in the curriculum, which has provided a more flexible teaching environment for the modern classroom.

**Keywords** Multimedia courseware · Interaction · Mobile terminal

## 1 Introduction

With the development of science and technology, the full use of information technology in the education field has subverted the prime teaching patterns, and gradually bring us some new teaching ideas, all kinds of innovative teaching methods constitute innovative teaching mode in the circumstance of multimedia [1]. The most typical is the appearance of multimedia interactive courseware and its applications in modern classrooms.

---

Y. Wang · Z. Si (✉) · L. Zhang  
College of Packaging & Printing Engineering,  
Tianjin University of Science & Technology, Tianjin, China  
e-mail: szj@tust.edu.cn

Interaction can be interpreted as a two-way interactive characteristic [2, 3]. From the perspective of the basic mode of teaching, teaching is a two-way process, is a teacher to student, student to student, two-way interactive process. Whether between teachers and students, or between students and students, interaction is essential link in the information education, not only can make learners promote the understanding and application of knowledge by communicating with others (teachers and students), but also can help realize the perfection of emotion and personality [4].

## **2 Preparation**

### ***2.1 Development Environment***

Windows 7 Ultimate, Intel(R) Core(TM) i5-2410M CPU, 4 GB SD card, 64 bit operating system.

### ***2.2 Introduction of Softwares***

Multimedia courseware contain texts, pictures, audio, video and all kinds of elements [5]. Therefore the word typesetting software Adobe Illustrator CS6 is required during the producing process, Adobe Illustrator CS6, graphics image processing software, Adobe Photoshop CS6, professional video processing software, Adobe Premiere Pro, audio processing Gold Wave software, micro curriculum recording software Camtasia Studio 8, format conversion tool factory and with multimedia courseware static page layout and dynamic design effect, the software founder fly digital textbook version 6.0 are also required.

## **3 Design Subject and Framework**

### ***3.1 Subject***

This paper takes the course of Digital Publishing Technology as an example, designing and producing courses with all kinds of manifestations, then released at the mobile terminal. The position of this interactive multimedia courseware is enhancing the students to take use of extracurricular time to review the keypoints, knowledge points and expand contends which imparted by teachers in classroom, through reading this interactive courseware by the mobile terminal, rather than just carry the content of the textbooks to the multimedia courseware.

This course covers many orientations like website design, auto-video, animation, games and visual reality, digital publishing protection, which has a high demand of interactivity between teachers and students. Thus, this course is based on content, it has a significant meaning in designing and producing electronic courseware to satisfy the interactive demands to support teaching in off-line classes.

### 3.2 Framework

After making a clear of the subject contents of this multimedia interactive courseware, according to the course system, we divided the knowledge points, through the learning of the software, we mastered the courseware making method and interactive function, then designed and made the process framework as shown in Fig. 1 shows that:

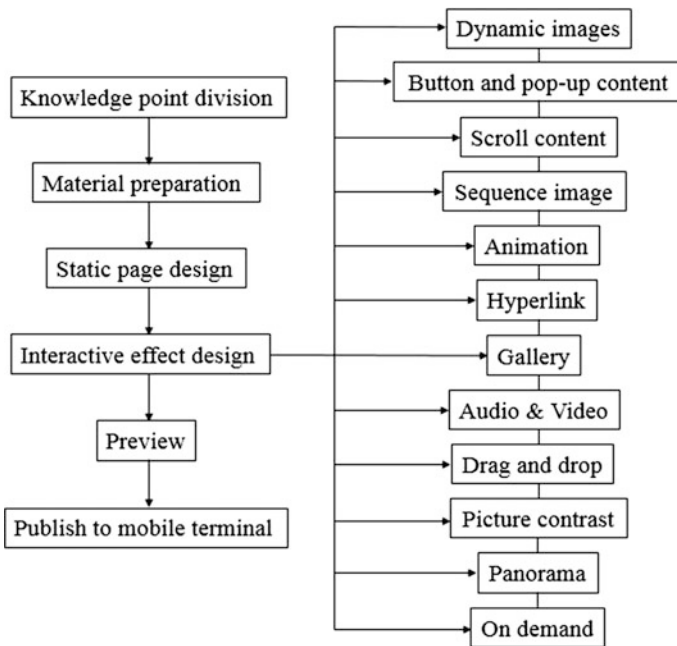


Fig. 1 Process framework



## 4 The Making Process of Interactive Courseware

### 4.1 *Editing and Processing of Material*

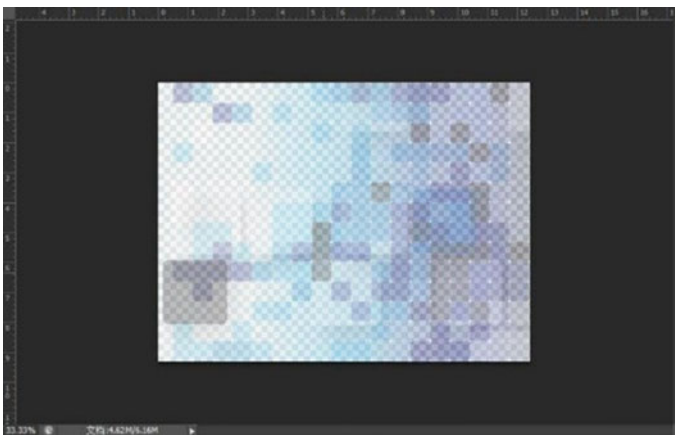
#### 4.1.1 Picture Processing

The requiring pictures of this course ware are processed by PS and AI. Here, take the making of background of the home page for example, first open the prepared pictures by PS, then click on the cutting tools on the left toolbar, then input the size of the iPad's screen ( $1024 \times 768$ ) in the toolbar above the cutting tools, after that, adjust the cutting areas to cut the background pictures, then adjust the opaqueness, brightness, contrast ratio, hue, saturation and so on, the result is shown in Fig. 2.

#### 4.1.2 Animation

Taking a designed image sequential animation (a little man is pushing something) for example. In order to achieve the effect that the little man walk with two legs change by turn, so the image sequence derived from the simple image sequence in the Flash is not applicable. Therefore, preparing the original sequence picture is necessary, including different action in each frame, as Fig. 3 shows.

Click on [file] → [new object], a sketchpad can edit ever frame of image, just by dragging the image to the new sketchpad, then click on [file] → [export]export a vector image in the form of “png”, during this process must assure the size and position of person in every frame is same. The saving name must follow 1-n order, and ensure all the images are saved alone in a file.



**Fig. 2** Finished figure of background of the home page



Fig. 3 Image sequence

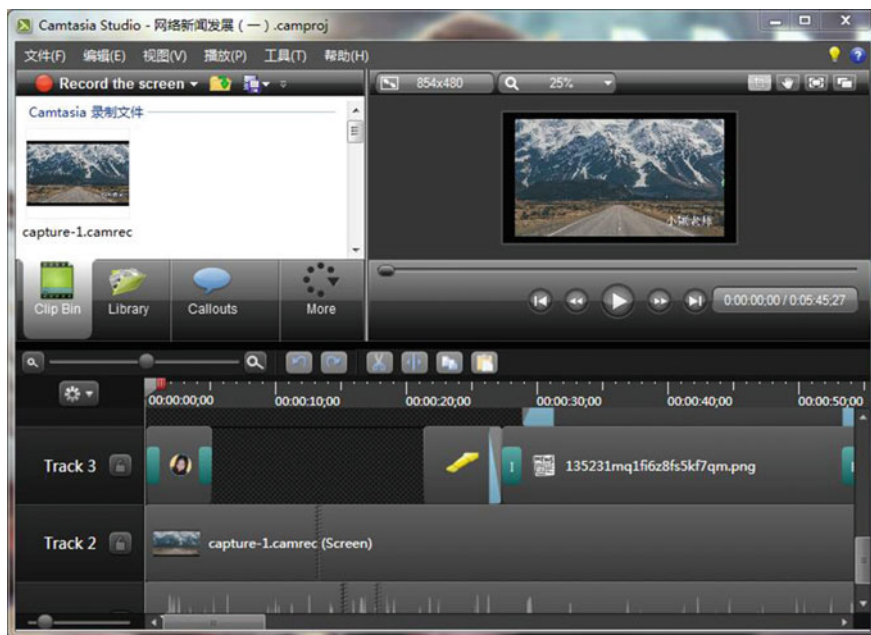
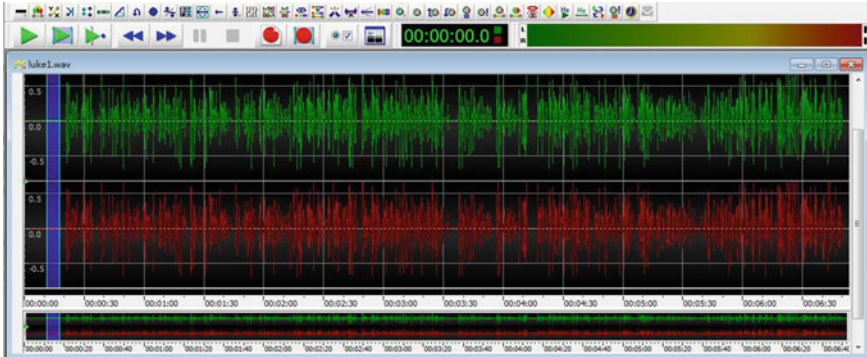


Fig. 4 The making of micro-course

### 4.1.3 Micro-course

Adding the micro-course to the interactive courseware, using Camtasia Studio 8 to record the video of knowledge points and carry out the editing matters in the later stage, as the Fig. 4 manifested.



**Fig. 5** Noise reduction

#### **4.1.4 Handle of Audio**

It is found that the audio file has evident noise which need de-noising process after record micro-course. Click on [file] → [professional produce] → [audio export] in Camtasia Studio can extract audio file from the video. Then open the audio file by GoldWave, as picture 5 manifested, then choose the band without crest, then right click on [copy] to copy to the clipboard, right click on [choose all], through [effect] [filter] → [de-noise] can get the de-noise panel, then check [use click-pad] and click [confirm] finished (Fig. 5).

## **4.2 Making of Static Layout**

According to course plan, insert images, create textbox or directly insert files in the form of txt, draw vector, insert vector, formulation, other material and so on. The according to the format design theories layout out the graphics and texts information in each pages, the design process of static layout contains the design of text information, the insert an setup of the images, pick on, displacement, rotational tilt, double, marshalling of all elements, wrap-around aspects and so on.

## **4.3 Design of Interactive Effects**

In interactive digital courseware, image, vectorgraph, audio and video, animation, free drag, button, on-demand, frame all belongs to interactive effect. This effect can reach a pretty experience effect in the electronic device and iPad terminals, it can't realized by traditional paper publications.

Based on the static layout, according to the features of each layout and the demand of each knowledge points to design the interactive effect. This courseware has designed and implemented 12 interactive effects in total as picture 1 shows.

**Dynamic images:** users can click on export device screen or dynamic images to interact, the gathering or diffuse effect can increase some special effects to the page.

**Buttons and Pop-up content:** they are general function of interactive courseware, generally there are bound with each other. The button is applying to trigger the pop-up effects and other skip, including skip to the previous screen or next screen, to homepage or appointed page, to URL and so on.

**Scroll content:** this effect can convert unfinished text to scroll content. Employing this import device you can look over the finished text with gestures.

**Image sequences:** a series of a subject's pictures that are taking by chronological order in different time can display animation effect.

**Animation:** to make the page more living, and it can make the page clearer.

**Hyperlink:** users can click these hyperlinks to skip to the website (finished set-up), which can promote the users' comfort sense of users experience.

**Gallery:** to display several pictures, put many pictures in the gallery, the user can control them by gestures in the export device to realize the compact displaying effect.

**Audio and video:** in a interactive courseware, the users can get the most direct user experience, and the courseware can work better by displaying contents that are connect to corresponding audio and video.

**Free drag:** can guide several pictures to the layout, readers can make gestures to control the pictures' position at random.

**Picture's contrast:** insert two same sized images to the layout and scroll the line of correlation to contrast the two pictures in a same orientation.

**Panorama:** interactive function can make users to get a whole display of the image from all the orientations at the export terminal. You can appoint a panorama of a plane or a sphere in the dialogue box, and appoint 6 pictures (have been split) to constitute a panorama subject.

**On-demand function:** can play music in the form of MP3, meanwhile display corresponding lyrics, what's more it can set the placeholder as lyrics compose, manifest the rate of the lyrics during the playing process.

#### **4.4 Preview and Release**

After finishing the dynamic layout and interactive effect's design, check the whole courseware to exclude some potential faults, and modify the fault in the PC terminal, the import it in the form of dPub data package, during the import process preprocessing of all the elements is required, finally we can download the reading software (can be opened) in the form of dPub data package in the mobile terminal, namely the release of the mobile terminal is over.

## 5 Conclusions

The interactive courseware that was designed and implemented in this study is based on the mobile terminal, which will provide the online study supporting interactive courseware through the mobile terminal in the class, and to achieve the effect of the review about the knowledge attained in the class, and to raise the interests of student effectively, thus to stimulate students to better absorb knowledge, and reach the objective of excellent teaching.

## References

1. He Hongmei, The Design and Implementation of the Interactive Multimedia Teaching Courseware, *Sci-Tech Information Development &Economy*, 2007(5).
2. Zhou Mingchao, Deep Research on the design and Development of the Interactive Multimedia Teaching courseware, Guanxi Teachers Education University, 2014.
3. Liu Jingxian, The Research on Innovative Extended Development Based on Interactive Gene of Android Platform, Hunan University, 2012.
4. Wang Chunsheng, Brief Analysis of the Interactive Multimedia Teaching courseware's Design, *Journal of Chongqing University of Science and Technology (Social Science Edition)*, 2011.
5. Marshall D. Developing Interactive Courseware on the World Wide Web[J]. 1999.

# Generating Customized PDF Document Based XML Source Data

Rubai Luo, Meng Wang and Shisheng Zhou

**Abstract** To study the generation method of customized PDF document in Publishing on demand (POD) system with one source data. First, based on the study of the requirements of source data description in POD system, the publishing data description with XML is proposed; then, the customized content and layout are described using XSL-FO; Finally, the XML source data is converted to customized PDF document using XSL-FO in FOP transformation engine, which is open source. The automatic generation method of customized PDF document based XML source data is proposed. The customized PDF documents are successfully generated using FOP in a experimental. The experimental result shows that the generation method of customized PDF document based XSL-FO is available.

**Keywords** Publishing on demand · XML · PDF · Layout

## 1 Introduction

With the continuous integration of the Internet and publishing and printing, the on-demand publish based in Internet has become an important form of publication. Among them “on demand and output of the same data source” is more and more widely applied, so if we want to achieve efficient execution for the on-demand output in the same data source, the whole process of the layout design should be digitized and automatized. Therefore, in this paper, an on-demand output technology based on XML data source is proposed by analyzing the on-demand publishing printing workflow in the same data source. First, the published content data are described by XML. Then, using XML node traversal function of XSLT gets the required publishing contents.

---

R. Luo (✉) · M. Wang · S. Zhou  
The Faculty of Printing and Packing Engineering, and Digital Media Technology,  
Xi'an University of Technology, Xi'an, China  
e-mail: 421848719@qq.com

Finally using FO to control the location of pictures and texts content on the page orientation and generate PDF files for printing output.

## 2 On-demand Publishing Based on XML

### 2.1 *On-demand Publishing Process Analysis of the Same Data Source*

From the viewpoint of personalized data processing and analysis, the same data source of print-on-demand printing [1] process can be divided into two parts: the “personalized publishing data preparation stage” and “personalized printing stage”. Among them, “the individual needs of content” contains the content and format of personalized requirements for publication; “Create personalized needs” contains personalized requirements for publications printing processing, such as printing, paper gram, binding mode, delivery time requirements.

In preparation for the personalized publishing data [2], it needs extract the corresponding graphic data from the data source according to the requirement from “the individual needs of content”. Then, according to the requirement from the format proceeds graphic layout and generate personalized publishing data for printing, such as PDF data. When personalized publishing data comes into the personalized printing stage, printing system choose the right printing and post-press processing process for printing according to “create personalized needs” in the printing process control parameters in the mode of delivery period. Finally get the customer’s expectations personalized publications.

Obviously, the automatic generation of personalized publishing data preparation process is the foundation to realize the digitization and automation of on-demand printing process. Because at present most of the prepress process is based on the PDF of the prepress process, so this article discusses the automatic generation technology of the personalized published data based on PDF [3] format data.

From the Angle of the theory analysis, data can be defined as a limited data set  $DS$ ,  $DS = (W_1, \dots, W_i, f_1, \dots, f_j)$ . The element  $w$  is composed of data sources of each paragraphs, the element  $f$  is composed of data sources of each images. Personalized published data is a function  $PD = L(W, F)$ .  $PD$  is personalized data.  $W$  is a collection of paragraphs elements.  $F$  is a collection of images elements.  $L$  is the format for the position of each element of  $w$  and  $f$ .

Therefore, in order to realize the automatic generation of personalized data published, the first thing needs to describe the text and graphics as the distinguish object of each elements in data sources, but also needs to conveniently found the element object in the collection data.

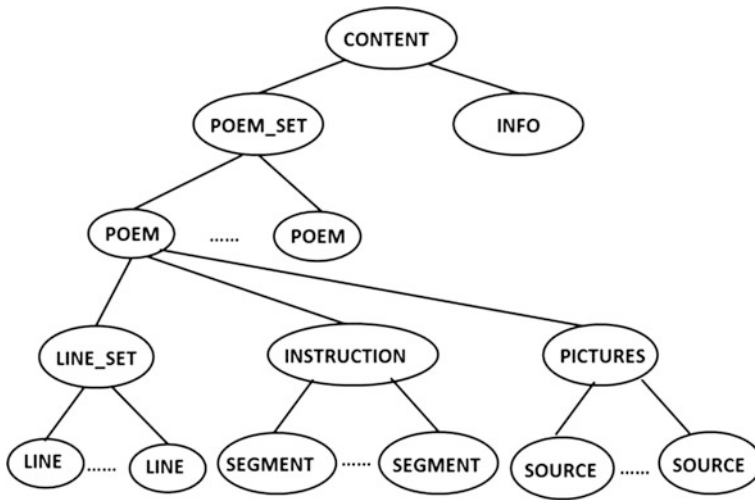


Fig. 1 The XML node tree of collection of poems

## 2.2 A Structured Description of the Published Data Based on XML

In the process of publishing, the paragraphs and the picture with consisting of several sentences are the basic object of format processing [4].

Since XML is a structured extensible markup language [5], this article uses the XML data format to describe the publishing data in construction. In the process of description, we can use the “XML element” to describe the text and graphics image element object, use “XML element names” to identify the element object, use the “element attributes” to describe the element object, use “XML element construction” to describe the logical structure of elements between objects, which uses the “tree diagram” to describe its construction.

In the process of this study, the author uses a poetry as the content of the published data sources for researching. Figure 1 describes the published data of tree structure of XML documents.

Every node element can describe element by element attribute. Such as “POEM” element “the POEM ID =” 1 “Name =” maple leaf and seven stars “Poet =” north “>”, through the “Name” attribute to describe the Name of the POEM, “the Poet” attribute description the author of the POEM.



### 3 Principle of Multiple Format PDF Output Based on the XSL-FO

#### 3.1 Extensible Stylesheet Language-Formatting Objects

Extensible Stylesheet Language-Formatting Objects abbreviated to XSL-FO [6], can gather the needed data in XML data and convert itself into FO standard description format file.

XSL-FO files use “XSL: stylesheet” as the root element to indicate the file for an XSL file to transform the XML documents. Its child elements “XSL: template” indicates the style goal template for transformation. From “fo: root” element defines a printed page format description for FO template, such as the L in the  $PD = L(W, F)$ . In XSL-FO, in order to achieve the goal of targeting content W and F, Using XPath path navigation elements and attributes in the source XML document. Its basic principle is to traverse the node in XML node tree to position the needed information.

Such as, A Xpath path “CONTENT/POEM\_SET/POEM[@ID=1]/LINE\_SET” path described in Fig. 1 as follows: start from node “CONTENT” when traversing the node “POEM SET” child node, choose to contain the ID attribute value of “1” “POEM” node to traverse down to his sub-node “LINE\_SET”. So, when making print-on-demand data gather, only need the information of XPath path given, XSL-FO documents can accurately find the needed data.

After find the needed data through XPath path, XSL-FO through FO XSL-FO describes how to display the data content. XSL-FO markup by defining the size of the printed page, the page margins, header, footer and other information to describe the printed page.

#### 3.2 Auto On-demand Publish Based on XSL-FO

The formatted printing output of XML data source is on the basis of XSL-FO. The following is the fundamental procedure. First of all, In XSL conversion engine, XML data are transferred into FO files through utilizing XSL-FO files. Afterwards, in the FO conversion engine, FO files are transferred to PDF files which are applied in output in printing system. Eventually, PDF files are used in production according to the requirement of printing.

In the procedure of on-demand publish, the individual requirement includes the on-demand customization of contents and layouts. Apparently, on the basis of sharing the same XML data source, it is possible to realize the customization by revising XSL-FO files. If same layouts are used while contents are different, the corresponding XPath paths in XSL-FO files are changed. If same contents are used while layouts are different, the FO codes of fo: root elements in the XSL-FO files which include layout description are supposed to be revised. If both of the layouts and the contents are different, both of the XPath paths and the FO codes are

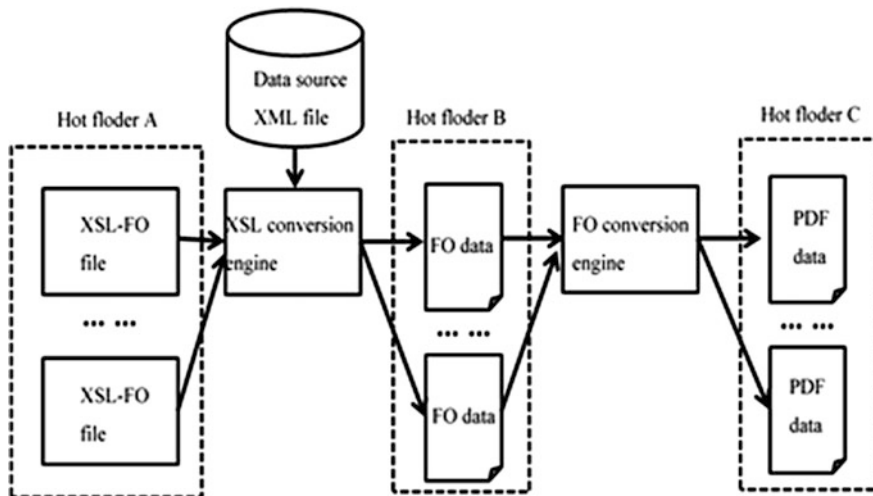


Fig. 2 PDF data preparation based XSL-FO and hot folder

supposed to be revised. Therefore, in the data preparation of on-demand publishing based on XSL-FO, the conversion procedure is displayed in Fig. 2.

Hot folder technology is applied to realize the automated data preparation in on-demand publishing system. Hot folder belongs to a certain program. This program scans the folder periodically. When some new file is found in the folder, the program boots automatically to deal with the new file. The folder mentioned above is called as the hot folder of the program.

As is shown in Fig. 2, hot folder A, hot folder B and hot folder C belong to XSL conversion engine, FO conversion engine and prepress workflow respectively. When a new XSL-FO file is saved in hot folder A, XSL conversion engine will find this file in the periodic scan. Then the conversion program boots automatically to convert the file into FO file and save it in hot folder B. In the same way, FO conversion engine will find the new FO file and then convert it into PDF file which is about to be saved into hot folder C in the meanwhile. The new PDF file in hot folder C will trigger the prepress program. In this way, an automatic on-demand publish workflow is realized.

## 4 FOP Conversion Engine and Preparation for the Data of On-demand Publish

### 4.1 FOP and Support of Chinese Character

FOP (Formatting Objects Processor) is an open source project realized in JAVA. In FOP, plentiful classes is supplied for realize the conversion between FO and PDF

data. FOP conversion engine is able to convert FO data into PDF files directly and convert XML data into PDF files by using XSL-FO data as well. Therefore, FOP conversion engine has the functions of XSL conversion engine and FO conversion engine which are displayed in Fig. 2.

Since there are simply a few of western fonts preset in FOP, it is necessary to configure the required Chinese fonts in FOP before the conversion for Chinese. Firstly, `org.apache.fop.fonts.apps.TTFReader` class is called to convert TTF or TTC font data into a font matrix file suffixed in.xml. Then the font is registered in `fop.xconf` document. In this way, the font name can be used directly for the attribute value of `font-family` in XSL-FO document,

## 4.2 PDF Data Generation Operation Based on FOP

In this paper we use a poetry publishing process to expound print-on-demand PDF data generation technique based on FOP. First, data of publish of 10 poems are described in XML. The text contents are directly described in XML document, and the picture contents are indexed by its absolute URL. Then, XSL-FO is used to respectively define the printing page of the cover page and the content pages. Meanwhile, data of 2 poems are picked from XML data by Xpath [7] and FO labels are used to define their page layouts for the cover page and the content pages. Finally, the FOP, which has been configured with Chinese fonts, is utilized to generate PDF files by the customized publish contents [8].

## 5 Conclusions

To the print-on-demand customized PDF data generation problems, the author proposed the print-on-demand data generation method based on XML and XSL-FO data format proved to be effective by experiments. It has realized the separation of content and format In the solution mention, which greatly improve the efficiency of print-on-demand. In a follow-up study, the emphasis things is how to use a XML data sources which has graphic information and audio and video information, to realize the cross-media publishing technology for computer terminals, intelligent terminals, paper books and e-books.

**Acknowledgements** This work was supported in part by NSF of the Science and Technology Department of Shaanxi Province under Grant Nos. 2016JM5068 and NSF of the Key Laboratory of Shaanxi Provincial Department of Education under Grant Nos. 15JS075.

## References

1. Ouyi, Yan Jin Wei. On-demand printing and on-demand publishing to the impact on the book industry, *Library Theory and Practice*, 2011, Doi:1005-8214-0036-04.
2. Liu Guo, Tie Jun. Personalized Expression of the Theory of Digital Publishing. Editorial Friend, Doi:10.13786/j.cnki.cn14-1066/g2.2014.03.020.
3. Joan Hope. Take advantage of data portability options enabled by PDF/XML standard. *The Successful Registrar*, 2015, Vol. 15 (4).
4. Richard Nash. Publishing 2020. *Publishing Research Quarterly*, 2010, Vol. 26 (2), pp. 114–118. Doi:10.1007/s12109-010-9155-6.
5. FengJin, DingBo, ShiDian-xi, ZhangZhu-xi, XUKai. The XML Parsing Technology Research, *Computer Engineering & Science*, Doi:1007-130x(2009)02-0120-05.
6. Simonaitis Linas, Belsito Anne, Warvel Jeff, Hui Siu, McDonald Clement J. Extensible Stylesheet Language Formatting Objects (XSL-FO): a tool to transform patient data into attractive clinical reports. *AMIA Annual Symposium proceedings AMIA Symposium. AMIA Symposium*, 2007, pp. 719–23.
7. GAO Jun, YANG Dong-Qing, TANG Shi-Wei, WANG Teng-Jiao. Tree Automata Based Efficient XPath Evaluation over XML Data Stream. *Journal of Software*, 2005, Doi:1000-9825/2005/16(02)0223.
8. Zhang, Wende. Converting PDF files to XML files *Informatica Economica. The Electronic Library*, 2008, Vol. 26 (1), pp. 68–74.

# Research on Presswork to eBook Conversion Method

Ying Hu and Huiqiang Lu

**Abstract** The paper provides a method and computer system for providing digital content of a presswork. A request is received from a sending computer by a recording device for the recording device to generate a digital copy of the presswork, wherein the digital copy is substantially similar to the presswork. The request includes a unique identification of the presswork and verification that both ownership of the presswork by the presswork's owner and disablement of the presswork have been recorded. In response to having received the request, the recording entity generates the digital copy and a unique identifier of the digital copy which associates the digital copy with the unique identification of the presswork, the digital copy and the unique identifier of the digital copy is transmitted to the sending computer.

**Keywords** e-Book · Presswork · Digital copy · Conversion method

## 1 Introduction

E-books are made available in both Android and iOS platforms as increasingly, technology savvy readers choose to read digital e-books. E-book apps have transformed reading habits [1]. The paper provides a method for processing a presswork, recording by computer storage units, a first entity's ownership of a presswork that is lawfully owned by the first entity, said presswork being a physical copy of an original copyrighted work in a literary work category for which copyright protection is provided to a second entity under copyright law, subject to a

---

Y. Hu

School of Digital Media and Design, Hangzhou Dianzi University, Hangzhou, China  
e-mail: hdhy@hdu.edu.cn

H. Lu (✉)

Computer Science Technology College, Zhejiang University of Technology, Hangzhou, China  
e-mail: lhq@zjut.edu.cn

© Springer Nature Singapore Pte Ltd. 2017

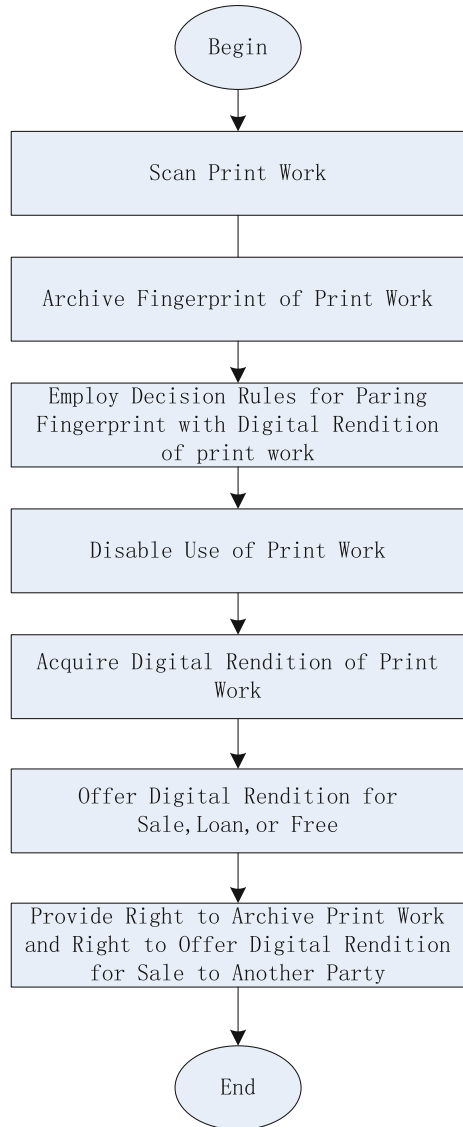
P. Zhao et al. (eds.), *Advanced Graphic Communications*

and *Media Technologies*, Lecture Notes in Electrical Engineering 417,

DOI 10.1007/978-981-10-3530-2\_51

limitation that the physical copy is fixed in a physically tangible form that is a non-electronic form and a non-digital form, said print copy being under copyright protection for the second entity that owns a copyright for an original work from which the presswork was generated, said first and second entities being different entities [2]. Conversion presswork process is shown in Fig. 1.

**Fig. 1** Process for conversion presswork to e-book [2]



## **2 Process for Conversion Presswork to e-Book**

### ***2.1 Scan Presswork***

A digital rendering of a presswork comprises an act of generating a digital copy of the presswork. Thus, a digital rendition of a presswork is a digital copy of the presswork. A presswork is defined herein as a discrete physical copy of an original copyrighted work in a literary work category for which copyright protection is provided under United States or foreign copyright law, subject to a limitation that the physical copy is fixed in a physically tangible form that is a non-electronic form and a non-digital form. Some e-books are produced simultaneously with the production of a printed format, as described in electronic publishing, though in many instances they may not be put on sale until later.

Often, e-books are produced from existing hard-copy books, generally by document scanning, sometimes with the use of robotic book scanners, having the technology to quickly scan books without damaging the original print edition. Scanning a book produces a set of image files, which may additionally be converted into text format by an Optical Character Recognition (OCR) program. Occasionally, as in some e-text projects, a book may be produced by reentering the text from a keyboard.

### ***2.2 Archive Fingerprint of Presswork***

The archived fingerprinting of the presswork and a record of disablement of the presswork is written to a database in one or more hardware storage devices which may be a public database. A digital rendition may be subsequently acquired, which may be a copy unique identifier (ID) which identifies an association of the digital rendition with the fingerprint of the presswork. The ID of the digital rendition and/or of the association may be linked to the digital record of the fingerprinting of the presswork and written to the database. All further transactions involving the digital rendition such as transfers of ownership may be written and tracked in a database or embedded in the digital rendition so that the history of the rendered digital item is traceable.

### ***2.3 Decision Rules for Paring Fingerprint with Digital Rendition of Presswork***

The archived fingerprinting of the presswork and a record of disablement of the presswork is written to a database in one or more hardware storage devices which may be a public database. A digital rendition may be subsequently acquired

(i.e., generated by the party who scanned the presswork or obtained from another party), which may be a copy from a digital master and may include DRM (digital rights management protection) and a unique identifier (ID) which identifies an association of the digital rendition with the fingerprint of the presswork. The ID of the digital rendition and/or of the association may be linked to the digital record of the fingerprinting of the presswork and written to the database. All further transactions involving the digital rendition such as transfers of ownership may be written and tracked in a database or embedded in the digital rendition so that the history of the rendered digital item is traceable.

## ***2.4 Digital Rendition of Presswork***

The digital rendition should be noted that the steps in the steps in the preceding may be performed in any sequence, and not necessarily in the sequence described supra. That allow transactions between content rights holders and buyers as well as for a centralized store of rights and content. Authorized access to digital content, otherwise known as digital rights, may be transferred from one user to another.

A further provision may be made for a public database repository of said one to one associations of a presswork and its digital rendition wherein a historic transaction record is maintained and is publically accessible for verification that the original presswork existed, who the owner was, that is disabled from further use, and the specific identification of a single associated digital rendition which may be further prevent copying. A further record of future resales or other transfers of ownership right of the digital rendition may be maintained in said repository.

Disabled presswork may be maintained either physically or in the form of digital documentation of ownership and destruction which back an up to exact number of digital renditions of said pool of specific presswork; wherein the digital renditions may be offered for sale in a quantity up to and equal to the said pool of disabled presswork.

## ***2.5 Digital Rendition for Applications***

An automated means is not provided to document instances of print ownership, association with a digital rendition of said presswork, or a database repository, which may be public, of all transaction history associated with a disabled presswork serving as the basis for transactions involving its digital rendition [2]. Figure 2 is a flow chart describing a method for processing a presswork.



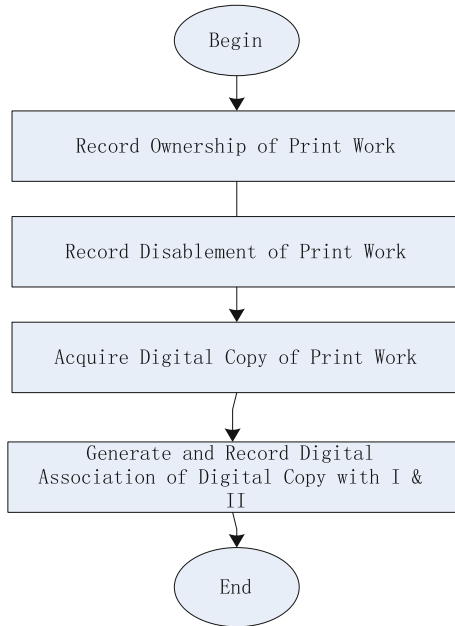


Fig. 2 A flow chart describing a method for processing a presswork [2]

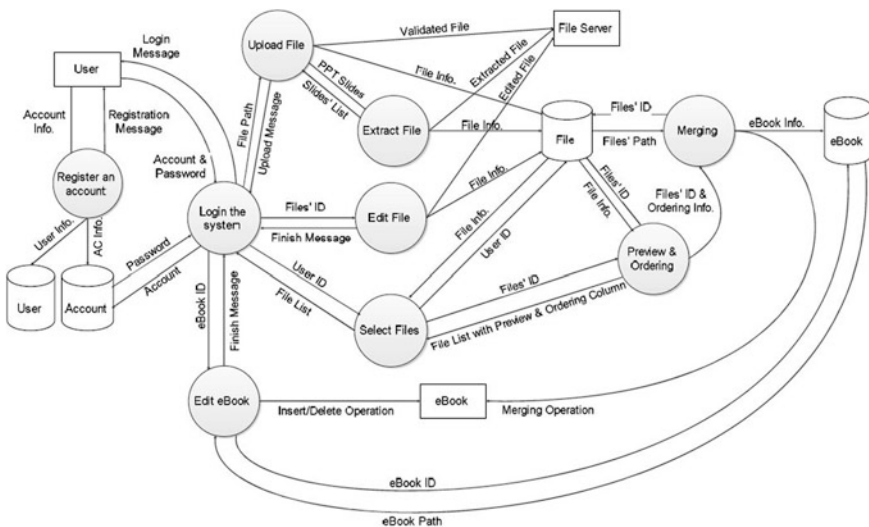


Fig. 3 Data flow diagram of the editable, multi-media, authoring eBook system [3]

## 2.6 *Right to Archive Presswork*

The digital copy and the presswork are may be substantially similar copies of the original work aside from the digital copy being in a digital format. The digital copy is not generated from the disabled presswork. The acquiring of the digital copy is initiated in using eBook system can generates a digital association linking the digital copy with both the recorded ownership and the recorded disablement; and records the digital association in the digital copy and/or in the one or more hardware storage units [3]. The digital association is generated before completion of generating the digital copy. An eBook Data flow diagram of the editable, multimedia, authoring eBook System are shown in Fig. 3.

## 3 Conclusions

The paper provides a method and computer system for providing digital content of a presswork. A request is received from a sending computer by a recording device for the recording device to generate a digital copy of the presswork, wherein the digital copy is substantially similar to the presswork. Using an editable, multimedia, authoring eBook system can solve the digital association.

## References

1. Hu, Ying (2016). Research and development on e-book apps based on iOS development platform. Lecture Notes in Electrical Engineering, v 369, p 395–400, 2016, Advanced Graphic Communications, Packaging Technology and Materials.
2. Pfister; Anthony R (2015). Print to eBook Conversion, United States Patent Application, 20150186622. July 2, 2015.
3. Joseph Fong, Vincent Chung, Kenneth Wong(2014). Hybrid Learning. Theory and Practice. Volume 8595 of the series Lecture Notes in Computer Science pp 184–195 2014.

# Interactive Design of Mobile Game Interfaces Based on UCD

Jing Zhao, Lei Guo and Chunhong Zhang

**Abstract** The objective of this essay is to provide a solution to interface design of recreational games on mobile phone and to finalize it based on the analysis of design requirement and strategy of mobile game interfaces. The author attempts to design a game interface under the guidance of UCD (user-centered design) and from the prospective of user experience through a combination of the features and limiting factors of run-time environment of mobile games according to game types, playing methods, art style and color scheme. The final interactive design of the mobile game surface should be equipped with a reasonable and effective combination of elements and layout with user-friendly detailed design to construct a satisfying user experience. In conclusion, it achieves the information interaction between mobile games interfaces and users, and improves the easiness and playability of mobile game products through combining the UCD design theory, prioritizing the operational habit of users, considering the full expression of interface functions based on the gaming logic and merging with the limitation and features of mobile game platform.

**Keywords** Interface design · User-oriented · Design requirements and strategy · User experience · Mobile game

## 1 Introduction

Mobility is the future trend of everything. The mobile technology has changed our life styles, including the way we play games. With the advent and popularization of mobile network platforms like smart phones and tablet pcs, the most important recreational games gaining great popularity among mobile users. As an interactive entertaining application, mobile game, has rapidly developed with light product, the

---

J. Zhao (✉) · L. Guo · C. Zhang

Department of Art and Design, Zhongshan Institute, University of Electronic Science and Technology of China, Zhongshan, Guangdong, China  
e-mail: 13531897885@163.com

© Springer Nature Singapore Pte Ltd. 2017

P. Zhao et al. (eds.), *Advanced Graphic Communications and Media Technologies*, Lecture Notes in Electrical Engineering 417,  
DOI 10.1007/978-981-10-3530-2\_52

415

quality of a mobile game is usually judged by its game-play and user experience [1]. Game-play refers to the game's playability, which means the amusement level with the focus on creativity and plot designs; player experience is completely decided by the game's interface [2].

To design interface based on UCD (user-centered design) is a completely new way of thinking and method of working, whose essence is to lay emphasis on both products and players [3]. It can better combine the features of the platform and the operational habits of players to design an enjoyable interactive mode, which means a successful design of game interface is more achievable with the help of UCD [4].

## 2 Limitation of Mobile Game Platform

User survey is the first step to apply UCD approach. Mobile terminal, as the carrier of mobile game products, has certain dissimilarities compared to other platforms like personal computer or game consoles in terms of product features, which will limit and restrain the design and use of mobile game interfaces to some extent.

First of all, in comparison with game platforms like personal computer or game consoles, mobile terminal is relatively lower in capability including RAM, VRAM, etc. Therefore, it requires us to consider all the detailed problems with a capability-prioritized thinking approach during the process of designing the mobile games.

Secondly, mobile terminal is featured with smaller viewing and operational screen, which is decided by its portability.

Thirdly, currently, touch screen prevails among mobile terminals, which means there is no hardware keyboard or button, nor mechanical touch feedback or reminder within them. That means, it would be hard to provide in-game experience like PC or game console, especially in terms of some complicated games.

Last but not the least, there are mobile phones and pc tablets of various sizes. At the same time, when playing games, players always need to hold the device. Then, design of the interface layout requires consideration of physical size of mobile devices and the way users hold their phones.

## 3 Design Requirement of Mobile Game Interfaces

Game interaction based on the feature of mobile devices is bound to follow the trend as easy-to-operate and console-game-alike interactive with a low entry threshold [5]. This is because only if the players are provided with a relaxing game experience will a better performance achieved on the basis of delivering them game content [6]. According to such a game trend of being interactive, when designing the interface of mobile games, it requires serious consideration of user habits and reachable screen area to be the focus of operational area. It was designed to the

interface layout in accordance with handheld operational habit. It also emphasizes that the most important information and content should be placed in the most noticeable position [7], redundant elements should be eliminated, and to enlarge operational area and expressive space through approaches like planning the layout and optimizing the navigation structure and the interface elements to maintain a perfect-arranged interface with noticeable key points for ease of operation. In terms of technology, design of repetitive elements should be based on resources-sharing strategy to ensure the fluency of the game.

## **4 Design and Development of Trans-Dozer, A Mobile Casual Game**

### ***4.1 Process of Applying UCD in Game Industry***

It requires designers to understand the demands of user at all time before introducing UCD into game design, which will not only produce creative elements for game products design but also solve the endless debate amid the design team, effectively lowering the percentage of inferior user experience. In general, the process of UCD in game industry can be divided into three major stages: 1. Understand the demand; 2. Design and develop; 3. Launch. In other words, the first step is to analyze the demand of target users of the game, dig into their thinking habit, preference, psychological demand and physiological limitation, etc., which also serves as the first point of the guidance in game design and development. Repetitive test and verify of the scheme are needed along with improvement before launching.

The following passage is to elaborate on the concept and technique of UCD based on test and improvement of the UI design scheme of a mobile casual game.

### ***4.2 Game Design***

Operated on IOS or Android, Trans-Dozer is a causal game that the author participated into design and development. Multiple versions are designed to fulfill the demands of mobile phones or PC tablets with different sizes, aiming at solving the screen-adapting problem of the game.

The game is properly featured with social elements based on console game experience to make it as easy, simple and fluent as possible.

This mobile game is originated with the inspiration of arcade games. But the playing method of this game is simplified compared to the traditional coin dozer games. Players just need to touch the area of coin factory in the screen, then the coins will be produced endlessly. The arcade game style is also embodied in the artistic style and color theme. The models and texture are classic and fashion,

demonstrated by the heavy and mottled effect of metal with functions like mechanical arm and fan.

The key problem of designing this game is how to make full advantages of mobile platform while reduce the unease induced by small screen or inconvenient control. To commit subtraction in the operation is to take away burden from players while to add various playing methods is to generate pleasure for players. For example, players can select a fan and blow away the coin from the desk and earn double points if the coins drop exactly into the target box. They can also choose mechanic arm to pick up diamonds and other items on the desk.

### ***4.3 Design of the Interface Layout***

Design of the interface layout requires consideration of physical size of mobile devices and the way users hold their phones.

Written in *Designing Mobile Interfaces* in 2011 by Steven Hooper, Thumb Zone is defined as the most comfortable and touchable area on the screen operated with a single hand. The theory is produced through analysis and observation of 1333 cases of mobile phone using. According to the analysis, 49% users would use their thumb to operate the device with a single hand; 36% users hold their phones with a thumb or another finger on the screen; 15% users hold their phones with both hands, among them 90% would hold vertically and 10% horizontally [8].

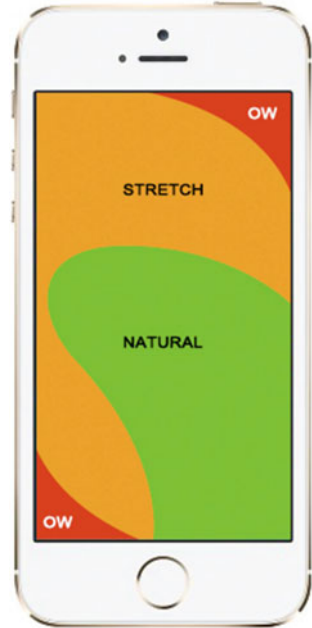
Take iPhone5 and iPhone5s for example. The following photos of thumb zone illustrate the different situations of screen touching (Figs. 1, 2 and 3).

In line with the operational habit of most people and the hot zone of two hands (Fig. 3), the first step is to set the game into paralleled vertical view without support of horizontal view. Then, place the most important button as Click to Play, in the middle part where is also the natural and the comfortable-to-reach area. At same time, the most functional or interactive buttons are placed in difficult area, also known as the area that you need to stretch to reach. All interactive buttons are set away from the painful area where is hard to reach (Fig. 4). In this way, players can easily control the game with only one hand or hold the device with one hand and use the other hand to operate [10].

### ***4.4 As Many Hidden Designs as Possible***

The game mentioned above is equipped with hidden menu with the button Click to Produce as the major function in the game interface. Specifically, massive production workshop, order management functions and game level display are placed in the hidden and simple menu. Besides mechanical arm, fan and barrier, everything is foldable with hidden design and can only be activated when the related buttons are touched.

**Fig. 1** Hot zone of right hand



**Fig. 2** Hot zone of left hand [9]



**Fig. 3** Hot zone of two hands



**Fig. 4** Divided areas of different difficulty degree for finger touching (e.g. iPhone5s)





### 4.5 Fingers Control Design

To touch the screen is the major operation on mobile device, so that feedback interaction of game buttons need to agree with the finger-touch experience. Size of icons need to be designed corresponding to the physical size of the screen for better user experience. Usually, icons or buttons for PC games (webpage game) are designed with 30 pixels. Considering the difference between touch-screen games and mouse-operated games on PC, buttons and icons within mobile games are usually larger. Take iPhone5s for example, icons and buttons for games on this platform are designed with more than 80 pixels due to its  $1136 \times 640$  resolution ratio [11] (Fig. 5).

**Fig. 5** Design drawing of game interface size. The resolution ratio is  $1136 \times 640$  pixels. Buttons and icons for the game interface are set with more than 80 pixels



## 5 Conclusions

The product characteristics of mobile devices have determined that game products on mobile terminal platform are restricted and restrained to a certain extent, which drives the designers to apply some specific design approaches and strategies with the aim of meeting the design requirements of mobile game interface, improving the game play performance and interaction, fulfilling the demand of users for game experience. More than an attitude and a value, UCD is also a scientific and feasible theory. UCD is not complicated so that it could be flexibly exerted through breakdown and simplification to get in line with the characteristics of mobile terminal and operational habits of target users. To apply UCD theory in the early stage of game design is to focus on improving user experience and practically intensifying game play effects.

**Acknowledgements** This study is supported by Guangdong Province University key platform and major scientific research projects (Education and Scientific Research Projects) “Research on the Mode of Interdisciplinary Cooperative Teaching Based on the Application Innovation Talents Training—Taking Game Art and Technology Courses for Example”. This work is also supported by Youth Fund Project of UESTC, Zhongshan Institute “Research on the Location and Design of Small Mobile Games in Internet Plus Background” and Quality Engineering Project of UESTC, Zhongshan Institute (No. JY201626).

## References

1. Tim Marsh. Slow serious games, interactions and play: Designing for positive and serious experience and reflection. *Entertainment Computing* 14 (2016) 45–53.
2. Pippin Barra, James Noble, Robert Biddle. Video game values: Human–computer interaction and games, *Interacting with Computers* 19 (2007) 180–195.
3. Hans-Jörg Bullinger, Wilhelm Bauer, Günter Wenzel, Roland Blach. Towards user centred design (UCD) in architecture based on immersive virtual environments. *Computers in Industry* 61 (2010) 372–379.
4. Loïc Caroux, Ludovic Le Bigot, and Nicolas Vibert. Maximizing Players’ Anticipation by Applying the Proximity-Compatibility Principle to the Design of Video Games. *Human Factors* Vol. 53, No. 2, April 2011, pp. 103–117.
5. Stefan L. Pauwels, Christian Hübscher, Javier A. Bargas-Avila, Klaus Opwis. Building an interaction design pattern language: A case study. *Computers in Human Behavior* 26 (2010) 452–463.
6. M.L. Wong, C.W. Khong, H. Thwaites. Applied UX and UCD Design Process in Interface Design. *Procedia—Social and Behavioral Sciences* 51 (2012) 703–708.
7. Wang Bo (2015). On the Usability Design Strategy in Mobile Game Product Interface Design. *Packaging Engineering*, 36(12),49–53.
8. Steven Hoober, Eric Berkman (2011). *Designing Mobile Interfaces*. O’Reilly Media.
9. How Phablets Are Changing Mobile UX(2015). Armen Ghazarian. <http://designmodo.com/phablets-ux/>. Accessed 15 June 2016.
10. Ahreum Lee, Kiburm Song, Hokyoung Blake Ryu, Jieun Kim, Gyuhyun Kwon. Fingerstroke time estimates for touch screen-based mobile gaming interaction. *Human Movement Science* 44 (2015) 211–224
11. The difference of interaction design of mobile phone game (2014). [http://www.gameres.com/msg\\_247918.html](http://www.gameres.com/msg_247918.html). Accessed 15 June 2016.

# Research and Implement of HTML5 Game Based on WebSocket

Ke Shen, Zhanjun Si and Lu Zhang

**Abstract** With the rapid development of mobile Internet, people's requirements of the efficient real-time communication are also increasing. WebSocket and HTML5 has brought a new impetus to the mobile Internet. WebSocket is a network technology of full duplex communication between client and server, which is provided by HTML5. It is different from the previous real-time communication scheme which based on polling technique. WebSocket has no frequent server requests and saves a lot of bandwidth and server resources. This paper analyzes the shortcomings of the traditional technology and concentrates on HTML5 and WebSocket. Finally, we design and complicated a game based on HTML5 and WebSocket.

**Keywords** WebSocket · HTML5 · Game · Mobile development

## 1 Introduction

With the rapid development of the mobile Internet, multi-platform mobile client is becoming increasingly popular. With the continuous improvement of the network environment, people have a higher demand for the amount of information and the efficiency of the application. So efficient real-time communication technologies will become more and more important. Past the traditional sites are mostly based on HTTP polling mode to request the latest data and resources from the server, or use Ajax to request asynchronously from server. But these technologies do not allow the client and server for real-time communications.

WebSocket is a new protocol in the HTML5 specification, it enables full duplex communication between the browser and the server. The long connection between client and server can be achieved by this technology. The server can always take the

---

K. Shen · Z. Si (✉) · L. Zhang  
College of Packaging and Printing Engineering, Tianjin University of Science  
and Technology, Tianjin, China  
e-mail: szj@tust.edu.cn

initiative to send the update data, and does not require the client to make frequent requests.

## 2 Traditional Poll Versus WebSocket

### 2.1 Traditional Poll

Traditional polling [1] based on HTTP acts like this, the browser sends a HTTP request to the server at a particular time interval (e.g. every second), then the server responds to the latest data returned to the client browser. It can simulate real-time communication, but it is not true real-time communication. And this method has a lot of disadvantages, namely the browser needs to constantly sends requests to the server. The request header must be sent whenever the data is requested from the server. This will add a lot of data traffic, wasting a lot of broadband resources and time, but also a burden to the server.

### 2.2 WebSocket

WebSocket [2] will create a WebSocket object, it will send a HTTP request to the server from the client. After the responding of server, the HTTP protocol will be upgraded to WebSocket. The head of the urlals changed to ws://or wss://. After carrying out a complete legal handshake agreement, it will establish a connection between browser and server. Both sides can receive and send messages, unless the client or server side of a party initiative to close the connection, otherwise the connection will continue to go down. This is the full duplex two-way communication (Fig. 1).

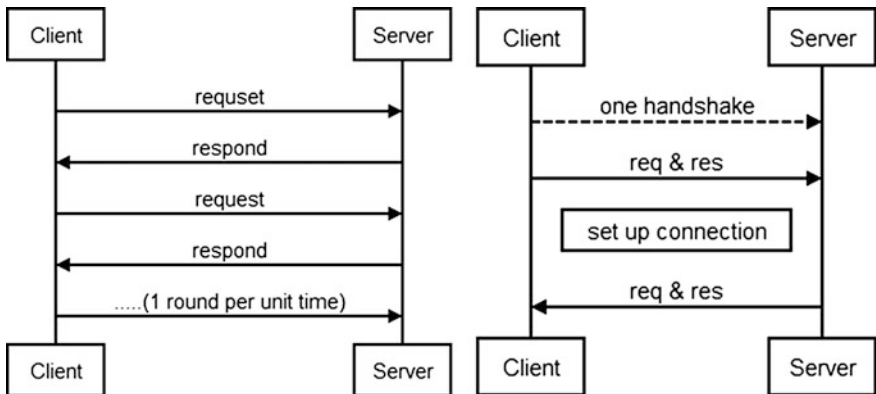


Fig. 1 Pollingmode versus WebSocket mode

As can be seen from the above analysis, WebSocket has the following advantages compared with the traditional HTTP.

- (1) WebSocket just need to establish a TCP [3] protocol simply without disconnecting and reconnecting frequently like HTTP. It also saving network resources.
- (2) Flexible and efficient, the server can send data directly to the client.

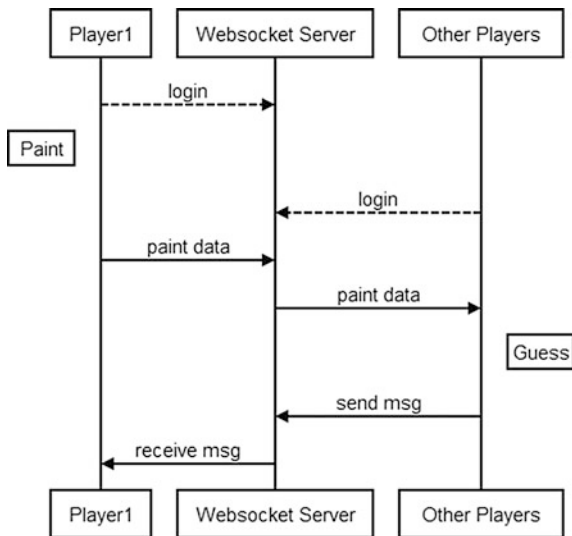
### 3 Development Technology and Theory

#### 3.1 Integrated Architecture

Before developing a project, it is important to design a good logical architecture. The system establishes a WebSocket connection between the client and the server. After all players landing, Player1 paints on the canvas according the given topic, then the client send the painting data to the server. The server will process the data in real time and transmit to other Players. Other players have to guess the answer and send message data to the server. Using the WebSocket technology, client and server can maintain a lasting full duplex TCP link channel. The client and server data can do bidirectional transmission in the channel.

It ensure the real-time of the data. The main architecture is shown in Fig. 2.

Fig. 2 Main architecture and game logic



### 3.2 *Client*

The client is divided into front-end UI, game logic, as well as the painting modules. In order to build the entire client and implement the game logic, the HTML + CSS + Javascript + JQuery will be used in the development.

#### (1) Front-end UI

According to the functional analysis [4], the front-end UI part is divided into three modules: login module, drawing module and chat module. These can be created by HTML, JavaScript and CSS.

First, the player enters the login interface and enter the nickname, click the login button, the connect to the local WebSocket server, then enters the main game interface. Switch interface can be achieved by JavaScript.

#### (2) Game logic

The entire game logic is mainly for the following process.

After the user logs in successfully, system assigns one player drawing. This player paints on the canvas according to the given answer. The remaining players can't see the answer and guess it. If someone guess the answer correctly, this player and the player who paints score at the same time, the end of the current round to the next round. If no one guessed the answer, all the players can not get the score, and at the end of the round time to the next round.

#### (3) Paint

The function of painting is one of the most important functions of the game, we can use Canvas which HTML5 provides to achieve this function. Canvas itself has no action, but it defines an API that support JavaScript to operate drawing action. We add events of 'mousedown', 'mousemove', 'mouseup' to canvas. When the mouse is pressed, we can get the coordinate of the pressed point, then set the point as initial point. When the event of 'mousemove' fires, canvas strokes the path that mouse moved. Finally, after the mouse lifted, the event of 'mousemove' was canceled.

### 3.3 *Server*

This project uses Node.js as the development platform of game server. The client uses socket.io.js framework. The server and client communicate with each other through WebSocket. Through programming, we create a Server Object, import the http module and the client module. The Server Object provides some common methods. The method of listen() is used to listen the port. Then we bind the event of connection to the port of io. In the event of connection, once a new connection arrives, the server will create a client instance. Server Object has a property named clients, this property stores all clients that properly connect to the server. In

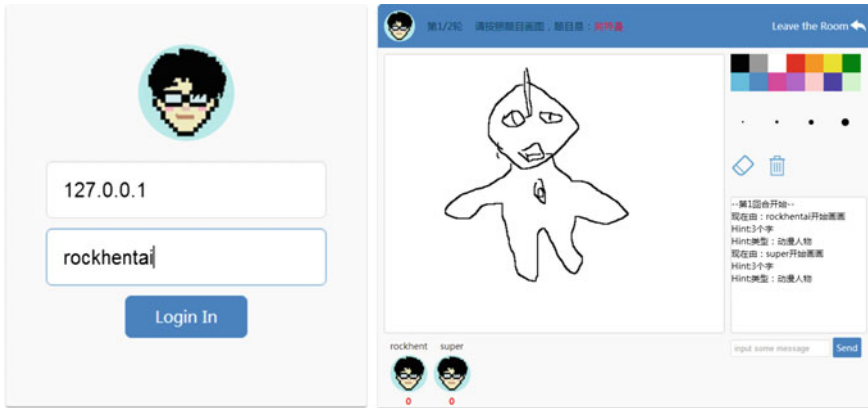


Fig. 3 Game screen

addition, in order to ensure that the server broadcast message and event to all clients, Server Object provides the method broadcastMsg() and broadcastEvent().

When the player is painting on the canvas, client transfers the current player’s drawing data to the server, then the server broadcasts the data to other players. At last, the data will be presented on the drawing board. In order to achieve this function, you can use the “socket.broadcast.emit” method. We can package the pushing method in client.js firstly. Then call this method in the event of drawing in paint.js. So the server can get the drawing data and then broadcast to other players.

### 3.4 Test and Display

Throughout the development process, the test is easily overlooked, but it is an essential step in the development. Rigorous test can identify the problems hidden in the project. Firstly, run the local web services, then open multiple clients for testing.

Test environment: Node.js System: windows8 Browser: Chrome

After testing, the game development is generally completed, but there are also some places that can be optimized, such as how to solve the problem of server balance load, network delay between different users and the problem of safety (Fig. 3).

## 4 Conclusions and Prospects

WebSocket has brought great convenience to the real-time communication and solved the problem of serious server load and insufficient performance in the traditional HTTP [5] scheme. But before the appearance of WebSocket, the mode of

HTTP request between front and back has been used for many years. This pattern has formed many solution in the development for years. When the WebSocket is applied to the actual project, the costs are unknown. These costs include two aspects of cost and the code maintenance. In the future, I believe WebSocket will get very good development. The solutions that deal with the problems will be more and more mature.

## References

1. C.N. Yu Development of chat room application based on HTML5 WebSocket installed in smartphone[D]. BUPT.2014.
2. C. Lu, X.Y. Feng, H.Q. Su Study and implementation of HTML5 WebSocket handshake protocol [J]. Computer Applications and Software. 2015, 01:128–131+178.
3. C. Lin Intelligent Mobile Phone and Web Game Interactive System based on WebSocket [J]. Computer CD Software and Application. 2015, 03:100–101
4. H.B. Bai The research and application of WebSocket on sports and games websites[D]. DHU. 2014.
5. G. Liu, J.Y. Li, Y. Zhang. Application of WebSocket on Real-time information in EMS system [J]. Power information and communication technology, 2013, 10:30–33.



**Part IV**  
**Printing Engineering Technology**

# Research on a New Reflectance Model for Printing Based on Dot Shape

Qi Wang, Xi Yang and Honghao Liu

**Abstract** The relation between dot shape and printing reflectance is researched. Considering the structural characteristics of halftone prints, a new reflectance model of amplitude modulation screening dot is provided. Based on Monte Carlo thinking method, the whole route of photons propagation including incidence, diffusion and termination is simulated in mathematical language according to the particle properties of light. The simulation process not only reflects influencing factors of ink, substrate and dot structure, but also can illustrate two dimensions morphology of screening dots. The results showed that Monte Carlo model indeed can reflect the influence of dot shape. Besides, the simulated value of reflectance model closely approached to the measured data of different dot shape. This new model can visualize various dot structures, which provide a new idea to evaluate printing quality.

**Keywords** Reflectance model · Monte carlo method · Dot shape

## 1 Introduction

As an information carrier, prints are important resources for people to obtain information. Presswork is a complex layered structure material, the form of light propagation in prints is diverse, containing mirror reflection, specular transmittance, internal reflection interface, the interface outer reflector and light scattering [1]. Existing studies have focused on different aspects, the minority care about combination effects of ink and paper, and more researchers pay attention to the description of light propagation phenomena. Murray-Davies model was the first

---

Q. Wang · X. Yang · H. Liu (✉)  
College of Light Industry Science and Engineering, University of Nanjing Forestry,  
Nanjing, China  
e-mail: mobeikehan@126.com

Q. Wang  
e-mail: wangqi\_3639@163.com

reflectance models [2, 3]. Yule-Nielsen model incorporated edge effects by introducing correction parameter  $n$  [4, 5], based on the Murray-Davies modified model. Clapper-Yule model paid a new attention to the interface reflection and scattering phenomena between the ink and the paper [6].

After the Saunderson correction, Kubelka-Munk theory [7, 8] focusing on the influence of multiple reflections in the medium was produced. Due to the complexity and indescribability of light propagation, the results of these studies were established on a certain kind of simplification and assumption, which could not be able to take various factors into account.

Early S.A. Prahl and M. Keijzer, who described Monte Carlo simulation of light propagation in different mediums [9, 10], and then, Lihong Wang and S.L. Jacques proposed a method to improve the simulation of light propagation in multi-media [11, 12]. Based on that, we propose another Monte Carlo simulation model, which shows a new idea to study the light propagation in halftone prints.

## 2 Simulation of Light Propagation

When light shines on halftone printing, it will interact with ink, paper and other media and eventually decompose to electromagnetic waves carrying different energy. So the whole process of simulation can be divided into three parts, photon generation, communication in media and photons termination [8, 13].

Photon initialization is to simulate the illuminant that emits photons, including the initialization of photon energy, position and direction. During the simulation, the photon incident direction is supposed to be perpendicular to printed materials. Initialized photon energy artificially defined as  $w$ , each photon moves will be accompanied by energy absorption and scattering. Suffering from ones move, part of the photon energy is absorbed; another will scatter out into the next process which can be written as  $w'$ .

$$w' = \frac{\sigma_s}{\sigma_a + \sigma_s} w \quad (1)$$

where  $\sigma_s$  and  $\sigma_a$  are the absorption and the scattering coefficients. In three-dimensional media, photon scatter direction can be defined with azimuthal angle  $\alpha \in [0, 2\pi]$  and deflection angle  $\beta \in [0, \pi]$  shown in Fig. 1.

Judging from whether paper was covered with ink, printing surface can be divided into blank area and inked area. If the position of incident photons locates in inked area, it has to undergo absorption process. When transmittance of the ink is  $t_i$ , the photon energy becomes  $w * t_i$ .

Random sampling of the step-length and direction is the first thing. The step-size can be described by probability density function [8].

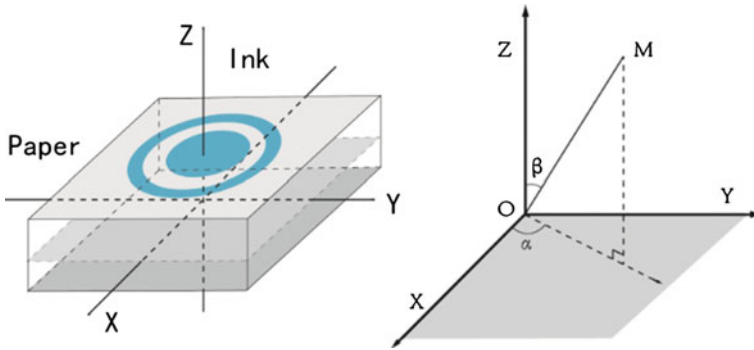


Fig. 1 Illustration of coordinates and angle  $\alpha, \beta$

$$p(s) = \sigma_t e^{-\sigma_t s} \tag{2}$$

The parameters  $\sigma_t, \sigma_a, \sigma_s$  are the attenuation, the absorption, and the scattering coefficients respectively. So, step-size  $s$  is

$$s = \frac{-\ln \varepsilon}{\sigma_a + \sigma_s} \tag{3}$$

Sampling of scattering direction is to define the value of azimuthal angle  $\alpha$  and declination angle  $\beta$ . Azimuth  $\alpha$  is a uniform distribution in the interval  $[0, 2\pi]$ , and could be determined by random variable  $\varepsilon'$

$$\alpha = 2\pi\varepsilon' \tag{4}$$

Deflection angle  $\beta$  follows the probability distribution function of Henyey-Greenstein [5].

$$p(\cos \beta, g) = \frac{1 - g^2}{2(1 + g^2 - 2g \cos \beta)^{3/2}} \tag{5}$$

The parameter  $g \in [-1, 1]$  is anisotropy coefficient Deflection angle  $\beta$  can then be determined by using another random value  $\varepsilon \in [0, 1]$ .

$$\cos \beta = \begin{cases} \frac{1}{2g} \left\{ 1 + g^2 - \left[ \frac{1-g^2}{1-g+2g\varepsilon} \right] \right\} & g \neq 0 \\ 2\varepsilon - 1 & g = 0 \end{cases} \tag{6}$$

Scattering direction  $(u'_x, u'_y, u'_z)$  satisfies the following formula:

If  $|u_z| > 0.99999$

$$\begin{cases} u'_x = \cos \alpha \sin \beta \\ u'_y = \sin \alpha \sin \beta \\ u'_z = \frac{u_z}{|u_z|} \cos \beta \end{cases} \tag{7}$$

If  $|u_z| \leq 0.99999$

$$\begin{cases} u'_x = \frac{\sin \beta}{\sqrt{1-u_z^2}} (u_x u_z \cos \alpha - u_y \sin \alpha) + u_x \cos \beta \\ u'_y = \frac{\sin \beta}{\sqrt{1-u_z^2}} (u_y u_z \cos \alpha - u_x \sin \alpha) + u_y \cos \beta \\ u'_z = \frac{-\cos \alpha \sin \beta}{\sqrt{1-u_z^2}} + u_z \cos \beta \end{cases}$$

Photon energy loss occurs in propagation. When the photon energy is extremely small, either the final photon is reflected or transmitted from the medium; its effect is quite limited. To avoid endless calculation and improve simulation efficiency, roulette filtering rule is proposed [7]. That means when the photon energy is less than a certain threshold  $w''$ , photons have the chance of  $1/m$  to survive and then their energy becomes  $m * w''$ , otherwise photon can be completely regard as absorbed photon. Surviving photons will continue to move until they leave the printing or be absorbed. Roulette filtering rule come true with the help of presetting value  $m$  and generating a random number between  $\varepsilon \in [0, 1]$

$$w'' = \begin{cases} mw'' & \varepsilon \leq \frac{1}{m} \\ 0 & \varepsilon > \frac{1}{m} \end{cases} \tag{8}$$

When each photon moves as step-size  $s$ , it is likely to strike the interface between the air and the media and then leave the media, or be internally reflected. Whether the internal reflection will occur depends on the moving step and the angle between moving direction and interface. The refractive index of the media and the air are  $n_i, n_t$ . Total reflection occurs when photons moving angle  $\alpha_i$  is greater than the total reflection angle  $\alpha_c$ .

$$\alpha_i = \cos^{-1}(|u_z|) \tag{9}$$

$$\alpha_c = \sin^{-1}(n_t/n_i) \tag{10}$$

In other cases, total reflection is determined by Fresnel reflection coefficient  $R(\alpha_i)$

$$R(\alpha_i) = \frac{1}{2} \left[ \frac{\sin^2(\alpha_i - \alpha_t)}{\sin^2(\alpha_i + \alpha_t)} + \frac{\tan^2(\alpha_i - \alpha_t)}{\tan^2(\alpha_i + \alpha_t)} \right] \tag{11}$$

According to Snell’s law, the relationship between angle of incidence on the boundary  $\alpha_i$  and the angle of transmission  $\alpha_t$  is

$$n_i \sin \alpha_i = n_t \sin \alpha_t \tag{12}$$

The random number  $\varepsilon$  can be used to decide whether photon will emit or internally reflect. When  $\varepsilon \leq R(\alpha_i)$ , the photon is internally reflected, otherwise the photons emit from media. By calculating the point  $(x, y, z)$  and the direction cosine  $(u_x, u_y, u_z)$ , the location where photon will emit can be deduced. If the photon is internally reflected, the direction of movement will correspondingly change to  $(u_x, u_y, -u_z)$ . If the photon emits from the top surface, it is recorded as reflected light. When photon emits from the bottom, then it is deemed as transmitted light.

### 3 Simulation of Dot Structure

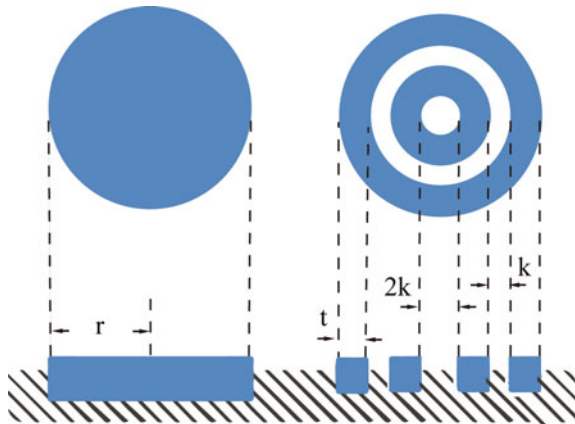
The concentric dot is a double ring structure which is similar to the AM round dot, and the inked area is called strip, the blank area is called empty shown in Fig. 2.

When the screening lines and dot area are defined as  $L, a$ , the radius of the round dot is obtained by the equation

$$r = \frac{2.54}{L} \sqrt{\frac{a}{\pi}} \tag{13}$$

The particular feature of concentric dot is a fixed ratio of empty arguments. Its image area is called strip and the blank part is called empty. The empty ratio refers to the ratio between the empty and the stripe. The stripe width is  $t$ . The width of the empty is described as  $k$  and the ratio  $m/n$ . Figure 2 [14] shows the details. The

**Fig. 2** Geometry of round and concentric dot



formula 14 shows the calculation of  $t$  through certain screening value  $L$  and dot area ratio  $a$

$$\begin{cases} t = \frac{2.54}{L} \sqrt{\frac{am}{\pi(4m+6n)}} \\ k = \frac{m}{m} \end{cases} \quad (14)$$

In order to easily distinguish the inked area and blank part, when building a coordinate system, the center of the screening grid can be regarded as the origin of  $XY$  coordinate system [15]. By comparing the radius size with the distance between the origin and the location of photon, whether photon is in the inked area can be judged. The distance between the location of photon and the origin is written as  $d$  and the round radius is  $r$ . If  $d \leq r$ , photons will appear in the inking dot area, the ink layer will absorb the photon energy. If  $d > r$ , photons will appear in the blank area, the photons energy will not decay.

In the same way, round, diamond, oval and square dot can be simulated separately.

## 4 Result and Discussion

According to the Monte Carlo simulation flow, algorithms for different dot structures can be obtained. The algorithm has strong applicability and scalability. The printing parameter including line screens, dot shape, dot area, paper properties, or ink attributes can be set accordingly.

### 4.1 Printing Dot Shape Simulation

Various dot structures can be simulated according to different dot area. Figure 3 shows the simulation results of concentric dot.

Figure 3 shows that in the simulation diagram, concentric dot is illustrated perfectly. Dot shape varies according to dot area. Overall, the simulation algorithm can intuitively reflect microstructure. In addition, different dot structures also can be simulated. The results are shown in Fig. 4.

In order to verify the new model rationality, the comparison result has to be made. Figure 5 shows the compared result. Only from the point of dot shape, printed dots are much close to the simulated dots. There are only two differences. The real printed dots have a blurred edge and the variation of grey scale is more obvious than the simulated results. These could be caused by the low resolution of

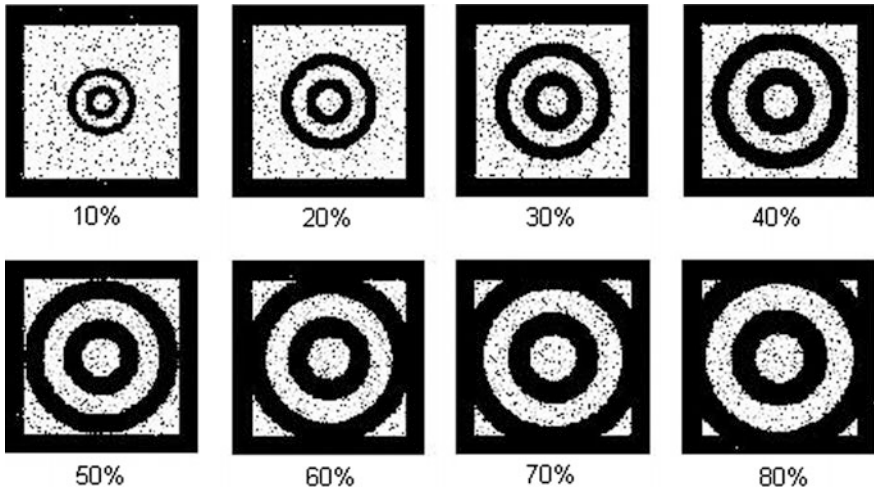


Fig. 3 Simulation of concentric dot. Concentric dot *screen line* is 175 lpi, and empty strip ratio is 1.8/1.3. *Dot area* ranges from 10 to 80%

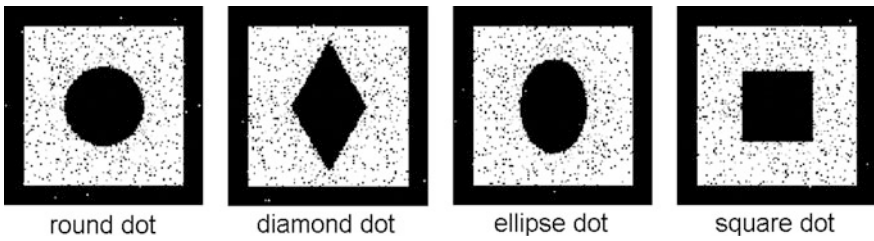


Fig. 4 Simulation of different dot structures including *round*, *diamond*, *ellipse* and *square dot*. *Screen lines* are all 175 lpi and *dot area* is 20%

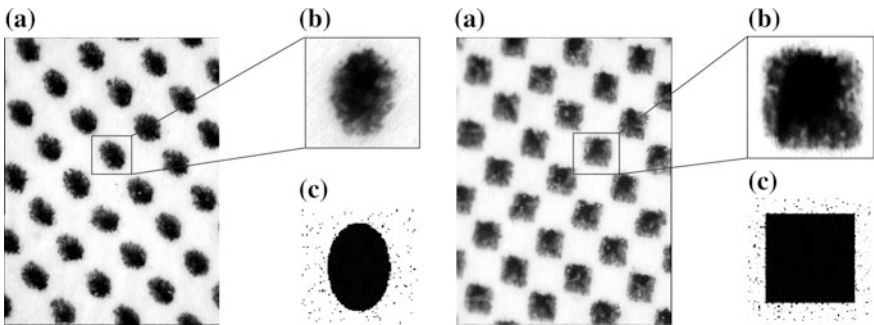


Fig. 5 Comparison result between printed dots and simulated dots. **a** The real printed sheet of *ellipse* and *square dot* which were obtained by DT2000 microscope.in 10 times magnification. **b** The selected *single dot* of printed sheet. **c** The simulation result of reflective model



display. The simulated results have to make a compromise between good display and high efficiency. Besides, the printed sheet has been made for a long time before microscope research. The property of printing ink is changed, which could also cause that difference [16]. Figure 5 proves that the new reflectance model can rationally give simulated dot shape.

## 4.2 Reflective Verification of the Simulation

After deciding the optimal parameters and showing the stability of simulation results, this paper verifies the accuracy of models for ellipse and concentric dot structure. Figure 6 shows the result which obtained by the spectroeye.

In the range of whole tonal, the measured reflectance of ellipse dot is much consistent with simulated reflectance, which indicates that the Monte Carlo model of ellipse dot is accurate.

Figure 6 shows that: in tonal range of 10–60%, the simulation results of concentric dot are reasonable, but when dot area is more than 60%, big deviation occurs. The interaction between dots and dots cause that deviation. Interactive effects appear for 175 lpi concentric dots when dot area is above 60%. The higher dot area rate is, the more seriously overlap phenomenon occurs [17], resulting in data deviation increases.

The new model has a fresh feature that it also can show photons distribution of various dots, which provide a new way to research printing quality. As what was shown in Fig. 7a, three different kinds of photons were illustrated. The top layer was reflected photons which show a clear ellipse dot shape. The absorbed photon was distributed in the middle and the transmission photon was in the bottom layer. How many photons were absorbed or reflected were illustrated in Fig. 7b. Different parts of photons varied with dot area. With this information, farther study can be made to improve printing quality.

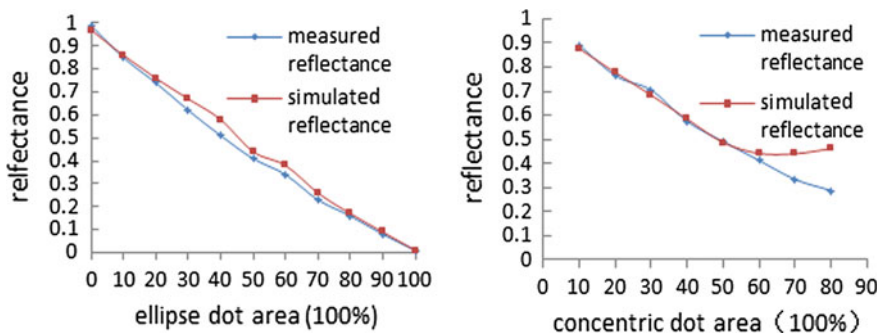
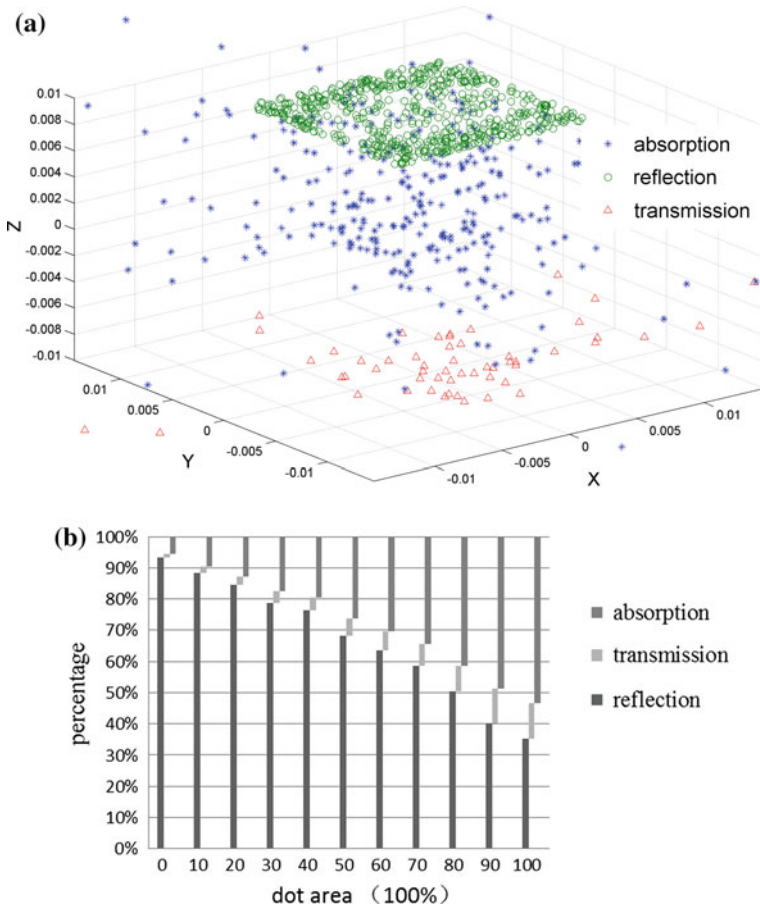


Fig. 6 Verification of concentric and ellipse dot



**Fig. 7** Distribution of simulated photons. **a** The photon state when photons escapes prints. Parameters include photons numbers = 1000, dot area = 70% and 157 g/m<sup>2</sup> coated paper. **b** The proportion of three different kinds of photons for ellipse dot shape

## 5 Conclusions

This paper provides a new way to study the behavior of light propagation in halftone printing within Monte Carlo method. The method can reasonably reflect the interplay between light and printed materials, which is useful for microscopic quality control for printed products. The simulation process contains several kinds of interactive forms between substrate and ink. Based on Monte Carlo method and combined with dot shape and dot area, light propagation behavior is completely simulated. Besides, the results of reflectance prove the method is practicable. Although this paper only roughly shows the reflective results of 175 lpi ellipse and concentric dots, at least it provides new ideas for microscopic research and quality control of printed materials. The method can continue to be improved from different

aspects in the future, such as transmission, absorption and distribution of the position of the energy. In addition, it is also a good idea to study how different dot structures and paper parameters affect the quality of prints

**Acknowledgements** This work was supported by the project of Open Fund of Jiangsu Provincial Key Lab of Pulp and Paper Science and Technology with grant number of 201513.

## References

1. Clapper, F., & Yule, J. (1953). The effect of multiple internal reflections on the densities of half-tone prints on paper. *JOSA*, 43(7), 600–603.
2. Arney, J., Engeldrum, P., & Zeng, H. (1995). An expanded Murray-Davies model of tone reproduction in halftone imaging. *The Journal of imaging science and technology*, 39(6), 502–508.
3. Arney, J., Engeldrum, P., & Zeng, H. (1995). An expanded Murray-Davies model of tone reproduction in halftone imaging. *The Journal of imaging science and technology*, 39(6), 502–508.
4. Arney, J., Arney, C. D., & Engeldrum, P. G. (1996). Modeling the Yule–Nielsen halftone effect. *Journal of Imaging Science and Technology*, 40(3), 233–238.
5. Hébert, M., & Hersch, R. D. (2010). Analyzing halftone dot blurring by extended spectral prediction models. *JOSA A*, 27(1), 6–12.
6. Ke, N., He, X., Wang, Y., & Zhang, Y. (2014). Improving Clapper–Yule model of the reflectance prediction by the path branching factor depending on the screen frequency of color halftone imaging. *Optik-International Journal for Light and Electron Optics*, 125(20), 6242–6244.
7. Murphy, A. (2006). Modified Kubelka–Munk model for calculation of the reflectance of coatings with optically-rough surfaces. *Journal of Physics D: Applied Physics*, 39(16), 3571.
8. Džimbeg-Malčić, V., Barbarić-Mikočević, Ž., & Itrić, K. (2012). Kubelka-Munk theory in describing optical properties of paper (II). *Tehnički vjesnik*, 19(1), 191–196.
9. Prahl, S. A., Keijzer, M., Jacques, S. L., & Welch, A. J. (1989). A Monte Carlo model of light propagation in tissue. *Dosimetry of laser radiation in medicine and biology*, 5, 102–111.
10. Modrić, D., Bolanča, S., & Beuc, R. (2009). Monte Carlo modeling of light scattering in paper. *Journal of Imaging Science and Technology*, 53(2), 20201–20208.
11. Modric, D., Maretic, K. P., & Milkovic, M. (2012). Modeling Light Dispersion in the Printing Substrate within the Monte Carlo Method. *Tehnicky Vjesnik-Technical Gazette*, 19(1), 77–81. Light Scattering in Paper. *J. Imag Sci Tech*, 53, 2(2009), pp. 020201–020201-8.
12. Maeda, T., Arakawa, N., Takahashi, M., & Aizu, Y. (2010). Monte Carlo simulation of spectral reflectance using a multilayered skin tissue model. *Optical Review*, 17(3), 223–229.
13. Hajdek, K., Miljković, P., & Modrić, D. (2014). Some aspects of modelling of line screen element reflectance profile within the Monte Carlo method. *Tehnički vjesnik*, 21(4), 779–788.
14. Nemedanian, M., Nystrom, D., Elias, P. Z., & Gooran, S. (2014). Physical and optical dot gain: characterization and relation to dot shape and paper properties. *Color Imaging Xix: Displaying, Processing, Hardcopy, and Applications*, 901509–90110
15. Zoia, A., Brun, E., Damian, F., & Malvagi, F. (2015). Monte Carlo methods for reactor period calculations. *Annals of Nuclear Energy*, 75, 627–634.
16. Debeljak, M., & Gregor-Svetec, D. (2010). Optical and Color Stability of Aged Specialty Papers and Ultraviolet Cured Ink Jet Prints. *Journal of Imaging Science and Technology*, 54(6), 60402-1–60402-9
17. Rogers, G. L. (1997). Optical dot gain in a halftone print. *Journal of Imaging Science and Technology*, 41(6), 643–656.

# Impact of Screening Parameters for Electrostatic Imaging Quality

Kaili Zhang and Guangxue Chen

**Abstract** With the development of information technology, the digital age of printing also obtain a rapid development. Furthermore, exploring the output characteristics of AM screening under different screening parameters and the printing quality as well as its possible directions. Learned through the experiments, for different output resolutions and screen frequency, imaging machine has its own laws. But the impact of screening parameters should also be considered. In short, the factors of electrostatic image printing quality are multifaceted.

**Keywords** Xerographic · Screen frequency · Printing quality · Device resolution

## 1 Introduction

In recent years, with the development of cross-media and the improvement of e-publishing technology, there is a huge impact on the market of the traditional printing under the age of digital information. In addition, the on-demand printing has achieved a great growth in the face of the different needs of different customers [1]. As is known to all, electrostatic imaging digital printing is widely used in the printing industry, so that the research on the quality of digital printing has become more and more necessary, facing the higher and higher requirements of customers [2].

## 2 Experiments

As is known to all, the device resolution has a lot of influence on the quality of printing matter [3, 4], the traditional offset printing technology has been able to meet the requirement of the human eye. Nowadays, we use experiments to explore

---

K. Zhang · G. Chen (✉)  
State Key Laboratory of Pulp and Paper Engineering,  
South China University of Technology, Guangzhou, China  
e-mail: chengx@scut.edu.cn

the output characteristics of digital printing press and the quality of the printing. Last but not least, it will be a powerful measure to analysis the image from micro and macro aspects.

## ***2.1 Purpose and Contents of Experiments***

There are some parts in the experiment, just as follows:

- (1) As known to all, use the standard image testing standards.
- (2) With the same type of the paper as the substrate of the digital printing, it is necessary to set a fixed value of the device resolution, use the same in the angle and dot shape, we can get the different number of screening line digital printing. And changing the device resolution but using the same method to get the printing products, after that, choosing the better printing for measurement of the physical parameters.
- (3) It is necessary to analysis the objective data preliminarily which obtained from the experiment to establish the mathematical relationship between the measured data and the different screen ruling.

## ***2.2 Section of Experiment***

### **2.2.1 Experimental Equipment**

- Canon C9065 PRO The digital printing machine,
- EFI Fiery Command Workstation The workflow control software,
- Dino-lite Digital Microscope,
- X-rite 528 Densitometer,
- A computer, the operating system is Windows XP.

### **2.2.2 Materials of the Experiment**

Printing materials used in this study are 125 grams of coated paper.

### **2.2.3 Procedural Details of the Experiment**

According to the experimental conditions, use the same machine and paper, but the different output resolution and screen ruling, we choose the experimental scheme of Table 1.

**Table 1** Five groups of control experiment

Sequence number	Screen ruling (lpi)	Output resolution (dpi)
1	75	600
2	100	600
3	125	600
4	150	600
5	175	600

Preprinting preparation: adapting machine, these printing are not taken during proof printing because the working state of the digital printing machine is not stable and the chromatic aberration is obvious. After adapting, start print.

Under standard illumination, use the Dino-lite Digital Microscope amplification equipment, choose the better cyan icon, apply 25% halftone and choose the image, calculate the number of the area for 16 cm<sup>2</sup> size of the step wedge which is used for color formation, and then, count the number of formatting color in the way of different output resolution and different screen ruling.

Choose the better imaging of cyan step wedge; use the X-rite 528 density meter to measure the dot gain and density of 25, 50, 75 and 100% in the case of different screen ruling, after that, analysis the measurement data.

## 2.3 Analysis of Experiment Results

### 2.3.1 Micro Quality Analysis

Count the number of formatting color in the way of different output resolution and different screen ruling, just as Table 2.

Therefore, it has little influence on the quality of printing, which has no significant effect on improve the quality of printing products.

With the same screen ruling, there is difference in the certain area when the digital printing machine's output resolution respectively is 600 and 1200 dpi.

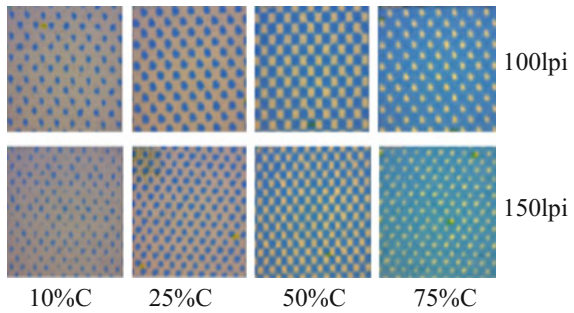
The output image of cyan dots is as shown in Fig. 1.

From the above analysis, the number of dots is too few in the certain area when the output resolution is 1200 dpi. This phenomenon proves that the output of the digital printing machine is not stable at the stage of higher resolution, and the shape of the dot is approximately chain, the rough selvage of dot starts to appear, which is not good as the traditional printing, just like Fig. 2. So it is necessary that electrostatic imaging digital machine at the stage of high resolution need to improve the stability of the machine.

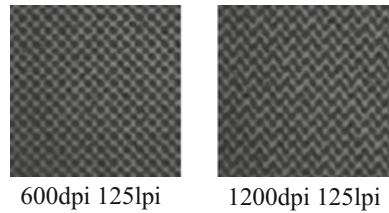
**Table 2** Dot number under the condition of different screen ruling

	600dpi	1200dpi
75lpi	162	140
100lpi	288	265
125lpi	371	366
150lpi	512	493
175lpi	721	691

**Fig. 1** Dot of cyan wedge under different screen ruling



**Fig. 2** Shape of dots under the condition of different resolution and same screen ruling



**2.3.2 Measurement and Analysis of Dot Gain and Density**

Use X-rite528 Densitometer to measure the dot gain and density under the condition of different resolution and different screen ruling, then analyze the measured data, get Table 3.

As is shown in Table 3, the partial light tone part of the image, the dot gains little and it can better reproduce the original halftone of the image when the resolution of machine is higher. And the in the darkened area of the image, while the output resolution is higher, the dot gain is bigger, the quality is not better than lower resolution.

Use the X-rite528 to measure the density under the condition of different resolution and different screen ruling, and then, analyze the measured data, as is shown in Table 4.

From Table 4, with the same resolution, the screen line is higher, the solid density and mesh density is bigger, but the solid density is not large enough, it can not compare with the traditional offset printing quality, and the imaging quality is related to many factors. So in the further research, we should think it as a whole.

**Table 3** Dot gain under the condition of different parameters

	600dpi				1200dpi			
	25%	50%	75%	90%	25%	50%	75%	90%
75lpi	12%	15%	13%	19%	9%	12%	17%	20%
100lpi	12%	20%	15%	25%	11%	15%	15%	25%
125lpi	14%	22%	12%	22%	14%	19%	17%	22%
150lpi	13%	24%	17%	23%	12%	21%	19%	23%
175lpi	16%	28%	16%	24%	11%	22%	16%	24%

**Table 4** Density of the dot under the condition of different parameters

	600dpi				1200dpi			
	25%	50%	75%	100%	25%	50%	75%	100%
75lpi	0.29	0.54	0.80	1.27	0.27	0.49	0.75	1.15
100lpi	0.29	0.59	1.00	1.39	0.28	0.53	0.80	1.26
125lpi	0.30	0.57	1.05	1.53	0.28	0.58	0.92	1.36
150lpi	0.29	0.62	1.10	1.55	0.29	0.61	1.10	1.45
175lpi	0.31	0.65	1.15	1.63	0.30	0.62	1.16	1.53

### 3 Conclusions

This paper gets these conclusions, just as follows:

- (1) With different screen ruling, the number of dots in a certain area is different, in actual output, it is better not to use the number of the screen line below 100 lpi but better to use the number above 100 lpi.
- (2) When the resolution of the machine of digital printing is high, it can reproduce the original image well. So it is better consider the other factors, just like materials, the screening and the image-forming part.

**Acknowledgements** This research was financially supported by the Guangdong Provincial Science and Technology Project (2013B090600060).

### References

1. Cancai Wang. (2011). The development of electrophoto graphic. *Screen Printing*, 9: 44–47.
2. Jialing Pu. (2000). The present situation and development trend of digital printing technology. *The technology of printing*, 9:69–74.
3. Zhiwen Liao. (2006). Analysis of digital printing. *Screen Printing*, (8): 40–42.
4. Sizhen Wang. (2005). Research on the methods of color management of digital printing based on electrophotography, Wuhan University: 15–20.



# Effect of Paper Optical Properties on the Color Reproduction in Ink Jet Printing

Guichun Hu, Haoran Fang, Maohai Lin and Fuqiang Chu

**Abstract** Paper properties, especially paper optical properties, are important factors for ink-jet print color reproduction. The objective of this work was to explore the influences of paper optical properties on print color reproduction. Herein, papers were sized with different dyes which affect paper optical properties but had little effect on the other properties. CIE whiteness is better than ISO brightness to express the paper color, because CIE whiteness not only shows the paper lightness but also exhibits the color of paper. CIE whiteness of paper is an effective way to express the color reproduction. The color reproduction is mainly influenced by  $a^*$  and  $b^*$  values of paper.  $L^*$  value above 94 did not have a significant impact in lightness of printed sample. The effect of paper CIE whiteness on color reproduction could be decreased by improving ink cover properties.

**Keywords** Paper · Optical properties · Color reproduction · Ink-jet printing

## 1 Introduction

Ink-jet printing is one of the most important printing technologies and now commonly used in the home and office [1–3]. The print quality should be put on an important place. Paper is an important factor on determining the final print quality. The effect of paper properties on the final printed colors has been widely studied [4]. Optical properties do have a significant impact on the quality of print. The perceived whiteness of paper unprinted areas significantly affects on neighbouring colors [5]. Fernandez-Reche et al. [6] studied the relationship between the colorimetric characteristics of 29 different commercial papers and color reproduction

---

G. Hu (✉) · H. Fang · M. Lin · F. Chu  
School of Printing & Packaging, Qilu University of Technology, Jinan, Shandong, China  
e-mail: hu2004326431@163.com

G. Hu · M. Lin  
State Key Laboratory of Pulp and Paper Engineering, South China University of Technology, Guangzhou, China

capabilities on inkjet printers. The results show no systematic correlation between color reproduction and specific colorimetric properties of the type of paper, which is similar to Perales's study [7]. Norberg and Andersson [8] studied the influence of paper whiteness on perceived color reproduction and found an improved color rendering with increasing whiteness up to a certain level after which the paper whiteness did not have a significant impact in rendering.

In these studies, papers are treated with different manufacture or finishing methods which not only change paper optical properties but also other properties (such as surface roughness, ink absorption) [5–8]. These properties also highly influence on color reproduction. In the present work, we propose new method to treated paper with changing optical properties instead of the other properties. The treated paper was printed with ink-jet printing to better understand the relationship between paper optical properties and color reproduction.

## **2 Experimental**

### **2.1 Materials**

Commercial ink-jet paper was provided by Chenming Paper Mill (Weifang, China). Three kinds of pen ink (blank, blue and red) were provided by Shanghai Ink Factory (Shanghai, China) and were filtered with 0.22  $\mu\text{m}$  filter membrane and the filtrate was used to size the paper.

### **2.2 Treatment of Paper and Testing**

Ink-jet paper was sized with different concentration ink. The treated paper was measured with X-rite 530 spectrodensitometer (X-Rite Color Management, USA) to obtain the CIE whiteness [4]. Paper properties (PPS roughness, Cobb value and ISO brightness) were measured at  $23 \pm 1$  °C and  $50 \pm 2\%$  relative humidity following the corresponding ISO standard methods.

### **2.3 Ink-Jet Printing Procedure and Testing**

The standard test sample was made by provide by GATF Company and treated with Photoshop CS5, as shown in Fig. 1. A desktop ink-jet printer (Epson Stylus C88+) was used to apply inks to the treated paper. The  $L^*$ ,  $a^*$  and  $b^*$  values of different dot area were measured with X-rite 530 spectrodensitometer (X-Rite Color Management, USA), according to SCAN-P 36:02.

**Fig. 1** Standard testing sample for ink-jet printing



**Table 1** Paper properties of treated paper

Sample	CIE whiteness			ISO brightness (100%)	Cobb (g/m <sup>2</sup> )	PPS roughness
	L*	a*	b*			
1#a	73.11	0.41	4.42	58.53	20.7	5.27
1#b	85.53	0.41	3.31	73.46	21.0	4.95
1#c	94.67	0.22	1.29	91.42	20.5	5.12
2#a	97.43	0.34	-2.32	94.35	19.8	4.96
2#b	97.90	0.30	-1.83	96.76	21.4	4.98
2#c	98.08	0.27	-1.71	96.97	20.0	5.21
2#d	98.14	0.13	-1.35	97.34	21.8	5.15
3#a	95.19	8.46	-2.41	80.36	19.5	5.11
3#b	94.99	1.98	-0.36	91.54	21.2	5.21
3#c	97.42	3.80	-1.56	91.36	20.6	5.05
4#	98.13	0.01	-0.04	97.00	21.0	5.00

### 3 Results and Discussion

#### 3.1 Paper Properties After Sizing

Paper properties such as CIE whiteness, ISO brightness, surface roughness, Cobb value, play an important role in color reproduction. Surface roughness is an important property for paper printability and color reproduction. Ink permeability affects the print color reproduction. For home or office ink-jet printer, water is the main component in ink fluid and accounts for 65% [1]. Cobb value is tested water permeability on paper and is used to characterize ink permeability. Table 1 shows paper properties of treated paper. The samples 2#b, 2#c, 2#d, and 4# show similar ISO brightness and different CIE whiteness. The samples 1#c, 3#b and 3#c also have similar ISO brightness but obviously different in CIE whiteness. The surface roughness and Cobb value were not affected by the size treatment.

### 3.2 Effect of Paper Optical Properties on the $L^* a^* b^*$ Color Space

The different papers printed with cyan and yellow inks at various dot area percentages (from 0 to 100%). Figure 2 shows the  $L^*$ ,  $a^*$  and  $b^*$  values of papers printed with cyan ink. The  $L^*$ ,  $a^*$  and  $b^*$  values of printed samples 4#, 2#a, 2#b, 2#c, and 2#d are similar. These samples have the very similar ISO brightness and the  $L$ ,  $a^*$  and  $b^*$  values (Table 1). Samples 1#c, 3#b and 3#c also show very similar ISO brightness. However, the  $a^*$  and  $b^*$  values of printed sample 1#c is significantly difference with printed samples 3#b and 3#c and samples 3#b and 3#c have almost the same  $a^*$  and  $b^*$  value ranges. The  $a^*$  values of samples 3#b and 3#c are greater than 0 and the  $b^*$  values are less than 0 (shown in Table 1). Both  $a^*$  and  $b^*$  values of sample 1#c are greater than 0. So we conclude that the color reproduction is mainly influenced by  $a^*$  and  $b^*$  values of paper. This is also borne out by the fact that the color reproduction of the sample 1#a is very similar to sample 1#b. But the  $L$  value of sample 1#a is obvious different to sample 1#b. The lightness of printed paper decreases with the  $L$  value of paper below 94 above which the  $L$  value did not have a significant impact in lightness of printed sample.

Figure 3 shows the  $L^*$ ,  $a^*$  and  $b^*$  values of different papers printed with yellow ink. The  $L^*$ ,  $a^*$  and  $b^*$  values of samples 4#, 2#a, 2#b, 2#c and 2#d printed with cyan and yellow ink show similar change tendency. The printed sample 3#a contains more red compared to samples 3#b and 3#c. Samples 3#b and 3#c shows the similar  $a^*$  and  $b^*$  value. The possible reason is that the sample 3#a contains more red than samples 3#b and 3#c and the yellow ink cover is lower than cyan. The  $L$  values of these printed samples proved once again that  $L$  value above 94 did not have a significant impact in lightness of printed sample.

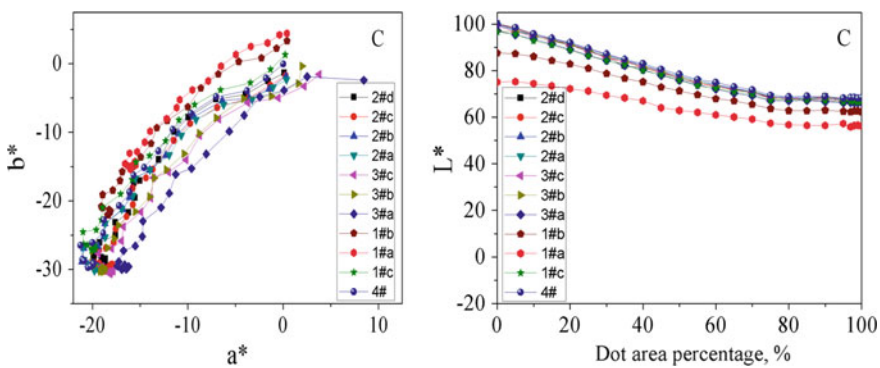


Fig. 2  $L^* a^* b^*$  value of papers printed with cyan ink

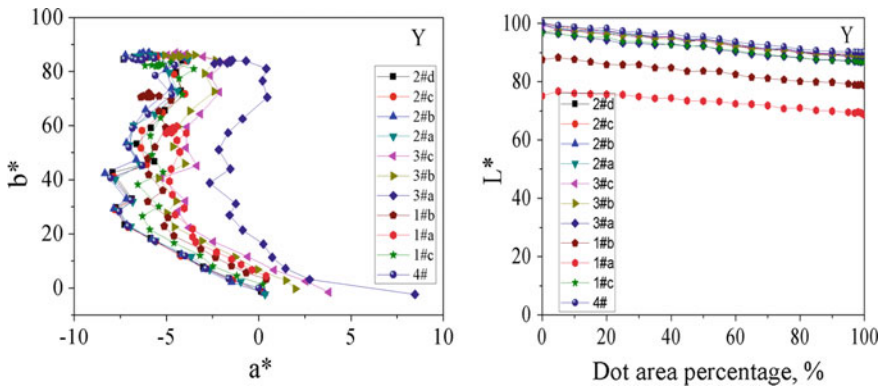


Fig. 3  $L^*a^*b^*$  value of paper printed with yellow ink

## 4 Conclusions

This study presented an attempt to explain the influence of paper optical properties on the print color reproduction. CIE whiteness is better than ISO brightness to express the paper color. Unlikely ISO brightness, CIE whiteness is used three parameters to expose the color change of paper. The color reproduction could be influenced by  $a^*$  and  $b^*$  values of paper.  $L^*$  value above 94 did not have a significant impact on lightness of printed sample. The effect of paper CIE whiteness on color reproduction could be decreased by improving ink cover properties.

**Acknowledgements** This work was supported by State Key Laboratory of Pulp and Paper Engineering (201606 and 201609).

## References

1. Lee, H. K., Joyce, M. K., Fleming P. D. et al. (2005). Influence of silica and alumina oxide on coating structure and print quality of ink-jet papers. *Tappi Journal*, 4(2), 11–16.
2. Johansson, L., Kruse, B. (2005). The influence of paper properties on color reproduction with dynamic inks. *2005 Beijing International Conference on Imaging*, Beijing, China.
3. Juric, I., Karlovic, I., et al. (2013). Optical paper properties and their influence on colour reproduction and perceived print quality. *Nordic Pulp & Paper Research Journal*, 28: 264–273.
4. Yang, L. (2003). Ink-paper interaction. PhD thesis, Linköping University, Linköping, Sweden.
5. Coppel, L.G., Norberg, O., Lindberg, S. (2010). Paper whiteness and its effect on perceived image quality. <https://www.researchgate.net/publication/25855395>.
6. Fernandez-Reche, J., Uroz, J., Espanola, H. et al. (2004). Color reproduction on inkjet printers and paper colorimetric properties. *Color Imaging IX: Processing, Hardcopy, and Applications*. doi:10.1117/12.526511.

7. Perales, E., Martinez-Verdu, F.M., Viqueira, V. et al. (2009). Comparison of color gamuts among several types of paper with the same printing technology. *Color Research & Application*, 34: 330–336.
8. Coppel, L., Norberg, O., Lindberg, S. (2010). Paper whiteness and its effect on the reproduction of colors. *Human Vision and Electronic Imaging XII*. 64920V. doi:[10.1117/12.703013](https://doi.org/10.1117/12.703013).

# Study on Fidelity of Inkjet Dots Based on Multiple Linear Regression Analysis

Fangfang Lu, Zhitao Zhang, Yang Zou and Yanfen Zhang

**Abstract** The paper is intended to study the relationship between ink dot fidelity, color gamut, solid density and dot gain. The method of multiple linear regression is adopted to analyze the above relationship, and then determine the evaluation parameters of the effect of printing color reproduction. Finally, it obtains the nonlinear relationship between ink dot fidelity and color gamut, also the linear relationship between ink dot fidelity and dot gain, solid density, and establish corresponding mathematical models through inkjet printing experiment. The correlation coefficient method verifies that the fidelity of ink dots can be replaced by the solid density and dot gain as the quality control parameters of ink jet printing.

**Keywords** Ink dot fidelity · Dot gain · Regression analysis

## 1 Introduction

With the rapid development of science and technology today, inkjet printing technology makes unceasing progress. Faster production, higher quality and lower cost are always the goal that we pursue. However, in China, there is no unified standard. The lack of standard makes the inkjet printing enterprises produce randomly [1].

---

F. Lu

Packaging and Printing Department, Henan University of Animal Husbandry, Longzilake, Zhengzhou, China

Z. Zhang

R&D Department, Hunan Education Publishing House, Yuhua District Changsha, China

Y. Zou (✉)

Technical Department, BST International (Shanghai) Co. Ltd.,

Songjiang District Shanghai, China

e-mail: 396239464@qq.com

Y. Zhang

Media Communication System, Dongguan Polytechnic, Songshanlake, Dongguan, China

© Springer Nature Singapore Pte Ltd. 2017

P. Zhao et al. (eds.), *Advanced Graphic Communications*

and *Media Technologies*, Lecture Notes in Electrical Engineering 417,

DOI 10.1007/978-981-10-3530-2\_57

Since the ink-jet printing graphic is formed by dots, therefore dot-fidelity should be studied as control parameter.

## **2 Experiment**

### ***2.1 Experimental Instruments and Materials***

- Stylus Pro Epson 7910 digital ink jet printing machine;
- Color proof EFI 4.0 digital proofing system;
- Mabeth Profilemaker 5.5 color management software;
- X-Rite 530 densitometer;
- Gretag spectroscan spectrometer;
- Five kinds of paper with different performance parameters.

### ***2.2 Printer Characterization***

Print IT8 standard color specification file in the five kinds of paper respectively, measure the color, and then the printing overview document will be generated [2].

### ***2.3 Experimental Procedures and Measurements***

#### **2.3.1 Color Gamut**

Print IT8.7/3 standard color specification file in the five kinds of experimental paper respectively. Using Gretag spectroscan photometer and profilemaker to measure, the measured color gamut is shown in Fig. 1.

#### **2.3.2 Solid Density, Dot Gain and Ink Dot Fidelity**

Print color scale on five kinds of paper was measured using X-Rite 530 densitometer.

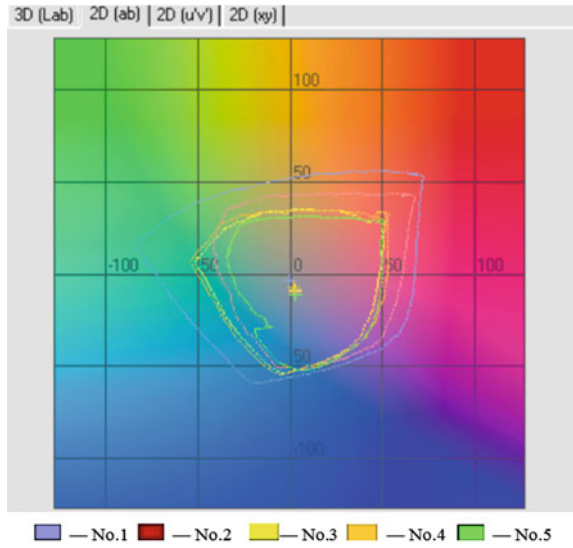
Using densitometer to measure five kinds of paper's C, M, Y, K solid density.

Using densitometer to measure five kinds of paper's dot gain (Tables 1 and 2).

For the measurement of ink dot fidelity, the Photoshop software is used to create one sheet with a  $180 \times 180$  pixel, in which  $36 \times 36$  square dot is arranged (Fig. 2).



**Fig. 1** Color gamut of experimental proofs



**Table 1** Solid density of experimental samples

No.	C	M	Y	K	Average value
1	1.81	1.67	0.79	2.18	1.61
2	1.75	1.58	0.76	1.92	1.50
3	1.62	1.43	0.79	1.80	1.41
4	1.57	1.44	0.81	1.79	1.40
5	1.53	1.42	0.75	1.72	1.35

This size of the image, the actual size of the ink point spread, which will not be the overlap of the ink point, is conducive to the ink point image of the camera and measurement. Measure color ink dot area and ink dot perimeter by image processing software (Tables 3 and 4).

The evaluation of the quality of ink jet is measured by calculating the value of the ink dot fidelity. Correlative algorithm, such as formulas (1)–(4) [3].

$$\text{Diffusion area ratio} = \frac{\text{Actual area}}{\text{Theoretical area}} \tag{1}$$

$$\text{Edge Roughness} = \frac{\text{Actual perimeter}}{\text{Theoretical perimeter}} \tag{2}$$

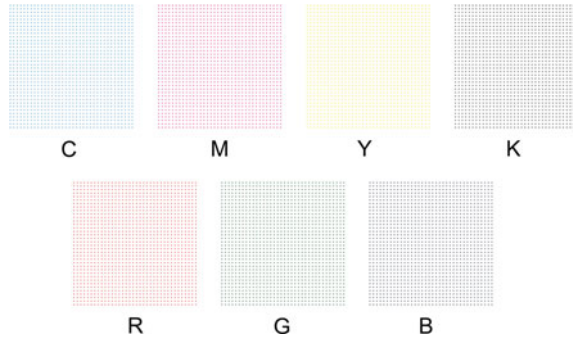
$$\text{Roundness} = \frac{4\pi \times \text{Ink dot area}}{\text{Dots perimeter}^2} \tag{3}$$

$$\text{Ink dot fidelity} = \frac{\text{Diffusion area ratio} + \text{Edge Roughness} + \text{Roundness}}{3} \tag{4}$$

**Table 2** Paper CMYK color dot gain value (%)

Input value	No. 1			No. 2			No. 3			No. 4			No. 5								
	C <sub>1</sub>	M <sub>1</sub>	Y <sub>1</sub>	K <sub>1</sub>	C <sub>2</sub>	M <sub>2</sub>	Y <sub>2</sub>	K <sub>2</sub>	C <sub>3</sub>	M <sub>3</sub>	Y <sub>3</sub>	K <sub>3</sub>	C <sub>4</sub>	M <sub>4</sub>	Y <sub>4</sub>	K <sub>4</sub>	C <sub>5</sub>	M <sub>5</sub>	Y <sub>5</sub>	K <sub>5</sub>	
100	0	0	0	0	0	0	0	0	0	0	0	0	0	0	0	0	0	0	0	0	0
80	9	10	10	12	11	11	9	13	12	12	9	15	11	12	10	14	13	13	13	11	15
60	18	17	15	18	17	19	15	21	21	22	16	24	19	22	15	23	22	22	22	19	23
40	14	16	15	19	17	19	15	22	20	22	17	24	19	23	15	23	23	22	23	20	24
20	8	9	11	12	11	12	10	13	12	13	12	15	12	13	10	13	14	14	14	13	16
10	7	6	7	9	7	8	6	9	9	9	7	10	9	9	7	9	10	10	10	9	11
5	4	4	3	5	5	5	4	6	6	6	5	7	5	4	3	4	5	4	4	3	4

**Fig. 2** Test chart of ink dot fidelity



**Table 3** Actual measurement value of CMYK color ink dot area

No.	C ( $\mu\text{m}^2$ )	M ( $\mu\text{m}^2$ )	Y ( $\mu\text{m}^2$ )	K ( $\mu\text{m}^2$ )
1	2600.15	2561.05	2267.80	3694.95
2	3343.05	3245.30	2502.40	3616.75
3	2365.55	3323.50	2893.40	3734.05
4	2912.95	3206.20	3479.90	3910.00
5	3714.50	3362.60	3167.10	4222.80

**Table 4** Actual measurement value of CMYK color ink dot perimeter

No.	C ( $\mu\text{m}$ )	M ( $\mu\text{m}$ )	Y ( $\mu\text{m}$ )	K ( $\mu\text{m}$ )
1	266.90	240.21	226.08	243.35
2	309.29	249.63	235.50	244.92
3	274.75	270.04	262.19	249.63
4	268.47	262.19	260.62	244.92
5	295.16	240.21	262.19	244.92

According to Formulas (1)–(4), the experimental sample dot fidelity data can be calculated.

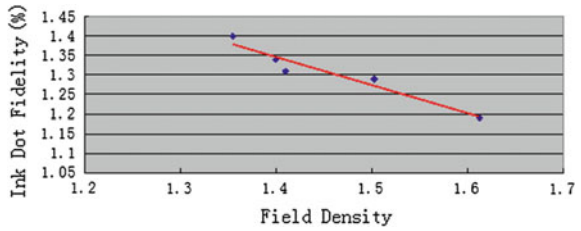
### 3 Experimental Data Analysis

#### 3.1 Relationship Between Color Gamut and Ink Dot Fidelity

We can see from Fig. 3, in all samples, No. 1’s color gamut is maximum, so we set No. 1 as standard sample to calculate the color difference between No. 1 and others by Profile Maker. The difference of dot fidelity can also be calculated according to Table 5. The result is shown in Table 6.

By means of linear regression of the above data,  $\frac{\Delta DF}{\Delta E} \neq K$ , there is no linear relationship between ink dot fidelity and color gamut [4, 5].

**Fig. 3** Relationship between ink dot fidelity and solid density



**Table 5** Actual measurement value of CMYK color ink dot fidelity (%)

No.	C	M	Y	K	Average value
1	1.15	1.14	1.06	1.41	1.19
2	1.37	1.30	1.12	1.39	1.29
3	1.18	1.33	1.23	1.50	1.31
4	1.24	1.30	1.36	0.82	1.34
5	1.44	1.33	1.29	1.54	1.40

**Table 6** Color difference value, ink dot fidelity between sample and others

Sample	No. 2	No. 3	No. 4	No. 5
$\Delta E$ (color difference)	11.8	14.42	17.75	15.34
$\Delta DF$ (difference of dot fidelity)	0.1	0.12	0.15	0.21

### 3.2 Relationship Between Solid Density and Ink Dot Fidelity

The data of Tables 1 and 5 are analyzed by means of linear regression analysis, the results are as follows.

From Fig. 3, the linear relationship between the dot fidelity and the density of the field is  $Y = -0.7239X + 2.3599$ . At the same time, we can get the correlation coefficient  $R^2 = 0.9302$  of the two, which shows that the linear regression of the two is significant.

### 3.3 Relationship Between Dot Gain and Ink Dot Fidelity

The experimental proofs in the calibration area ratio are 25%, 50% and 75%, the dot gain value is shown in Table 7.

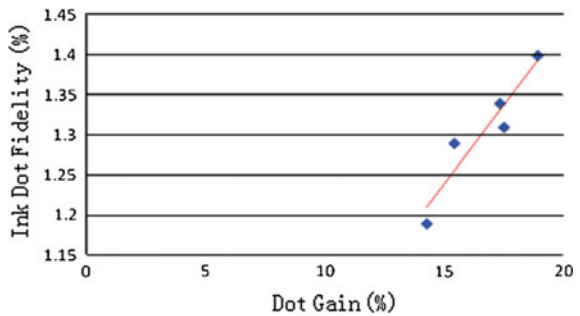
The relationship between ink dot fidelity and dot gain can be gained by means of a linear regression analysis.

The linear regression expression of dot fidelity and dot gain is  $Y = 0.039X + 0.647$ . At the same time, the correlation coefficient of the expression  $R^2 = 0.895$  can be obtained. It shows that the regression expression is linear and significant, and the two can establish the linear model.

**Table 7** Dot gain value at 25, 50, 75% of five samples (%)

No.	25%	50%	75%	Average value
1	12.25	18.25	12.25	14.25
2	13.5	20	13.5	15.41
3	15.5	22.5	14.5	17.5
4	15.25	22	14.75	17.33
5	16.75	24.25	15.75	18.92

**Fig. 4** Relationship between ink dot fidelity and dot gain



From Fig. 4 we can see, there is an obvious linear relationship between the ink dot fidelity and dot gain.

## 4 Conclusions

In the experiment, the relationship of ink dot fidelity and color gamut, solid density and dot gain are studied. The method of multiple linear regression to analyze the relationship between ink dot fidelity and paper printing parameters is employed. Finally, through research, the relationship between dot fidelity and color gamut, solid density, dot gain is established.

- (1) There is no linear relationship between dot fidelity and color gamut.
- (2) There is a linear relationship between the dot gain and Ink dot fidelity, solid density, and establish corresponding mathematical models. The correlation coefficient method verifies that the fidelity of ink dots can be replaced by the solid density and dot gain as the quality control parameters of ink jet printing.

## References

1. GX Bao, WY Jiang. (2012). The influence of paper’s whiteness and smoothness on colorimetric effects. *Applied Mechanics & Materials*: 361–364.

2. Yandong Zhao. (2014). Color measurement and analysis based on the konica minolta bizhub pro c6501 digital press, *Applied Mechanics and Materials*: 62–67.
3. Juan Lin. (2009). Study on the evaluation parameters of ink jet printing paper printing performance. Nanjing Forestry University.
4. Paul D Fleming, James E. Cawthorne. (2003). Interpretation of Dot Fidelity of Ink Jet Dots Based on Image Analyse. *The Journal of Imaging Science and Technology*.
5. Yan Zhao. (2011). Research on fuzzy comprehensive evaluation of printed matter quality. Xi'an University of Technology.

# Study on the Mode of the Printing Industry in Cloud Computing

Yunzhi Chen, Yongkai Wang and Chong Gu

**Abstract** In recent years, with the emergence and development of cloud computing, the printing industry has also begun to step into the so-called “cloud”, giving rise to the appearance of the cloud printing which becomes a hot topic of discussion among the global printing enterprises. Cloud printing makes it possible to achieve a new printing model of B2C instead of the traditional B2B model through the “cloud”, which helps to combine the traditional printing with the new media and realize the flexible one-to-many mass communication. In addition, cloud printing, with the merits of all-weather, good experience, easy in management and popularization, etc, not only is preferred by the printing enterprises both at home and abroad, but also helps the cloud printing service providers to attract active consumers with the aid of personalized print.

**Keywords** Cloud computing · Cloud printing · Active consumption

## 1 Cloud Computing and Cloud Printing

The so-called cloud exists in many places of people’s daily life, such as browsing websites, sending and receiving e-mails, watching videos, listening online music and any other things which stored in the cloud instead of our hard disk devices. Then what on earth is “cloud”? In fact, the so-called cloud is a metaphor for the Internet, which refers to a huge virtual server cluster with high availability, timely delivery, dynamic development and other characteristics.

In 2006, the concept of cloud computing was first proposed by Google’s former CEO Eric Schmidt. Through constantly improving its cloud processing ability, the core of cloud computing is to reduce the processing burden of the end-users and simplify the user terminal into a simple input or output device, enabling the

---

Y. Chen · Y. Wang · C. Gu (✉)

College of Packaging and Printing Engineering, Tianjin University of Science and Technology, Tianjin, China  
e-mail: guchong217@126.com

© Springer Nature Singapore Pte Ltd. 2017

P. Zhao et al. (eds.), *Advanced Graphic Communications and Media Technologies*, Lecture Notes in Electrical Engineering 417, DOI 10.1007/978-981-10-3530-2\_58

461

end-users to enjoy the powerful computing capabilities of the cloud according to their demand [1]. The importance of cloud computing is that it is not only a technological innovation, but also a new business and service model. The experts generally believe that compared with other modes, the mode which is entirely based on the browser to offer service, is the most recommended one.

Then, what is cloud printing? The cloud printing, actually, can handle every single print orders' confirmation, payment, storage and delivery procedure by digital network technology [2]. It not only can be used as a tool to promote production operation business and enterprise marketing process, also can upgrade the traditional type of printing enterprises to marketing printing business process through new business model changes.

More than establishing network platform, the core competitiveness of cloud printing is the great breakthrough in the aspects of design assistance, efficient processing, automatic edition, customization and others, which provides a new solution for small batch, individuation and so many needs. At present, cloud printing is no longer limited to printing, but provides the public with multi-channel network services. Cloud printing is changing the printing industry even a wider range of industrial ecology.

## 2 Characteristics of Cloud Printing

The traditional off-line printing enterprise, regardless of the large batch of printing factories based on the traditional printing process, or the quick printing shops with small batch reproduction based on the digital printing, can only rely on the customers in its surrounding areas, which led to a relatively fixed scope of their services, business with geographical restrictions and poor cross regional marketing. However, in the aid of the network, cloud printing can receive customers' orders anywhere in the world including the potential customers theoretically. Consequently, there are almost no geographical restrictions.

Although, cloud printing is good at personalized printing and widely use the digital printing method to finish the production process, it does not abandon the traditional way of printing. Usually the enterprises of could printing select a method to handle the orders of the customers operated on the cloud service platform according to product categories, customers' requirement, printing volumes and other conditions. The large printing amount orders are usually completed through the traditional printing. As for the small and personalized ones, the combined printing and digital printing will be adopted. Hence, cloud printing not only integrates the merits of traditional printing in long run, also allows full play to the advantages of digital printing in short run and individualization.

In addition, the customers of traditional printing enterprises are essentially the one with whom long-term partnership has already established, so the business are handled just by the corresponding sales. Unlike traditional printing enterprise, cloud printing's customers aren't relatively concentrated. Therefore, it is necessary to set



**Table 1** Comparison of traditional printing and cloud printing

Project	Traditional printing	Cloud printing
Quotation method	Factory sales quotation	Online quote
Order form	Agreed with the factory sales	Online order
Whether personalized	No	Absolutely
Editorial freedom	Low	High
Supply-demand conditions	Mainly in large quantities	Can be large or small
Production site	Fixed-point factory	Online service, instant distribution
Business hours	Only business hours	24 h

up specialized customer service department to deal with the problems in the printing design, order payment, order tracking, after-sales services and so on, which highlights the properties of their own online printing business (Table 1).

In 2015, the total production value of printing industry in China has reached RMB 1124.62 billion, increasing 3.6% compared with last year, while the number of digital printing achieved RMB 17.62 billion, with the year-on-year growth of 73% [3]. Printing with Internet +, represented by cloud printing, is prevailing throughout the world. Over 300 different e-commerce platforms are constantly promoting the business model and the product service innovation.

### 3 Printing to Active Consumption

As the main consumer groups in contemporary China, the generation after 80s and 90s consumers' consumption concepts, habits and characteristics show considerable difference from their parents. They are willing to try new things, be with open-minded and curiosity, and prefer personalized and unique style of things. They not only have their own opinions on brands and products, but also desire to participate in designing and producing process. They hope to customize products with exclusive label as masters. Consequently, products such as individual customization and DIY experience enjoy great favor and admiration of the generation. We can assert that the contemporary consumer is active.

By the boom of e-commerce, cloud printing service providers supply a short-run of personalized printing products such as photo books, cards, self-adhesive label and personality T-shirt and so on to meet the consumers' personalized printing demand based on a design interactive online platform. It has become a good choice in the current fashion of life. The growth process of personalized printing process in China, however, is not so smooth as expected. The homogeneity phenomenon regarding to the product ranges offered by the varieties of cloud printing enterprise is serious. Not only the products are of varying quality, the multifarious editing

process also makes poor user experience, which makes it difficult to attract consumers to hold the second order, so there can be a handful websites of popular approval.

So, how to attract active consumption by printing industry? We can start from the following aspects [4–6]:

First of all, the simplest method can avoid homogeneity phenomenon, but also the most difficult one is the product innovation. The smart bracelet, for example, which swept the world, is an innovation which we have never seen before. People, no matter when and where, can view their own movement, sleep, diet and other real-time data with the matching APP and guide a healthy life intuitively according to the summary data chart. However, the innovation of the product is not only limited to starting from scratch, also can be a better progress of existing products. In recent years, the appearance of some pokers with fire safety knowledge makes cards turn into a fire safety publicity ambassador. This kind of combination of the practice of interesting pokers with the boring fire control knowledge has won people's great praise.

Secondly, the personalized printing is often realized by the way of digital printing. The single order is usually with less printing amount and carried mainly by non-professional customer groups. What's more, it rarely can confirm every process before finalized printing. When it comes to be produced, the factory will not set up dedicated merchandiser to be responsible for. As a result, the print quality problems will not easy to be found. The establishment of the printing quality standardization, however, not only can solve the problem of production allocation of resources which arouse in fragmentation orders, also guarantee better quality of the finished products. Meantime, the crises of confidence caused by poor quality of printing product can be avoided.

Thirdly, the cloud print service providers are using the online template to assist with the DIY editing process and provides the editor instruction combined with artificial service to help consumers to design manuscript. Although with good functionality, the platform of maturity is not enough from the point of view of usability. Even consumers adopt the approach of import material automatically, they still need to deal with the problems such as resolution, bleed, typesetting, retouch processing and spend a lot of time in the tedious editing process. Most consumers tend to lack patience, so some of them is likely to deterred by the multifarious editing process. How to further the humanized product template design, improve the editor's usability to save the user's time cost or provide moderate price and professional aided design services are the contents what should be considered by the printing enterprise.

Finally, the domestic personalized printing should not take the road to grab a single route at a lower price, but focus on relatively broad market with prospects to subdivide, such as catering, pictorial, office supplies, etc. They should rely on the line boutique stores and other entities to carry out regional promotion, making use of the advantages of the Internet + to enter into the national market to constantly enhance the brand awareness and customer recognition. However, many customers do not have a good knowledge of personalized printing at present, which requires

the cloud printing companies to help potential customers to understand the personalized printing and tap their consuming hot spots to nurture and develop their market.

## 4 Conclusions

Cloud printing makes a combination of the traditional printing industry and the mobile Internet, which reduce the enterprise cost, improve the production efficiency and expand the business scope of print factory to a certain extent, bringing new profit and development space. Colorful electricity printing not only enhance the ability of external marketing, also provide a new direction of innovation for the traditional printing enterprises, which help the traditional printing enterprises transit from the manufactures to the service enterprises and finally transform into market oriented corporations. Today, faced with a cold winter of sharply drop in orders and increasing cost, the cloud printing enterprise should stand on the consumers' point of view and make further research on their demand to eliminate the adverse conditions that hinder the consumer to order individual printed products and achieve the goal of attracting active consumer through a reasonable use of the short-run of personalized printing. Each of the printing enterprises which is seeking revolution should highlight this problem.

We believe that with the common efforts of the practitioners, printing companies and general consumers, the cloud printing is bound to be full of power, turning the potential of the market into reality and becoming a strong support for the printing industry!

## References

1. Information on: [https://en.wikipedia.org/wiki/Cloud\\_computing](https://en.wikipedia.org/wiki/Cloud_computing).
2. Information on: [https://en.wikipedia.org/wiki/Cloud\\_printing](https://en.wikipedia.org/wiki/Cloud_printing).
3. Information on: <http://www.keyin.cn/news/sczc/201609/01-1097988.shtml>.
4. Yong-kai Wang. (2016). The printing industry in the climate of cloud technology. *Printing Field*. (6): 37–40.
5. Jian Wang. (2011). Standing in the clouds of printing, *Printing field*. (12): 12–15.
6. Li-xia Wang, Ning Ding. (2014). Development strategy of cloud printing enterprises. *Packaging Journal*. (3): 44–49.

# A Pre-actuation Method for Initial Droplets Accurateness of Inkjet Printing with Volatile Materials

Zhiqiang Gao, Cheng Sun, Liqiang Huang and Xing Yin

**Abstract** A pre-actuation method for initial droplets accurateness of inkjet printing with volatile materials is proposed. Inkjet printing has been used as the low-cost and efficient manufacturing technology indifferent fields. Some fields such as the electronics industry require precise drop-on-demand. The initial droplets, as reported by some research, are different in morphology, trajectory, velocity, and volume from subsequent drops within a burst. In this study, firstly drops dissimilarity caused by evaporation on meniscus surface was investigated. In order to improve the accuracy of initial droplets, the pre-actuating waveform was used to condition the meniscus. Experimental results showed that the input pre-actuation waveform is optimized such that the difference between the initial drops and subsequent drops behavior is minimized.

**Keywords** Inkjet · Refill · Initial droplets · Pre-actuation · Volatile ink

## 1 Introduction

The ink-jet technology is used as an efficient production tool for advanced manufacturing technology [1]. The ability of accurate and repeated delivering nanogram quantities of a given substance to a precise target location is critical to the development of new technologies.

For inkjet applications broaden, the ink droplets must be accurately deposited at the target location. To control the total amount of material delivered to the target,

---

Z. Gao · C. Sun (✉) · L. Huang  
Packaging and Printing Engineering College, Tianjin University of Science and Technology,  
Tianjin, China  
e-mail: chengsun55@sina.com

Z. Gao  
e-mail: gaofantuan@qq.com

C. Sun · X. Yin  
Tianjin Vocational Institute, Tianjin, China

drop-on-demand operation allows adjustment of drop size as well as the number of drops delivered per trigger. However, there has been very limited work conducted to characterize how changes to the number of drops delivered per burst might affect ejection behavior. Using drop number as a control for the quantity of material delivered to locations along a target assumes that each drop is equal in mass, implying a linear relationship between quantity of drops and total ejected mass.

Previous works, particularly by Verkouteren and colleagues, have challenged this assumption indicating that the initial drops in a given sequence may differ significantly from those that follow [2]. The work by Amin further elucidates this effect and shows how, specifically, the initial ejected drops can be different in both quality and quantity from those that come after it, resulting in a nonlinear response between number of drops in a burst and ejected mass [3].

The commonly referenced [4, 5] initial drops problem refers to clogging or misfiring of an inkjet due to solvent evaporation at the orifice. Depending on the solvent of ink, this effect would take on the order of seconds or minutes to present itself at a level significant enough to have this kind of impact.

This work shows the ink refill process in the nozzle, specifically, refill principle during inkjet process and further elucidates the evaporation effects. The pre-actuating waveform method used for conditioning the meniscus is presented. By using the proposed method for filling nozzles and the proposed interval time before eject, we need to determine repeat times of pre-actuation to improve the similarity of droplets.

## 2 Oretical Model

The inkjet printhead consists of many nozzles. Each nozzle ejects ink droplets through the orifice, and refill ink from the reservoir through the chamber.

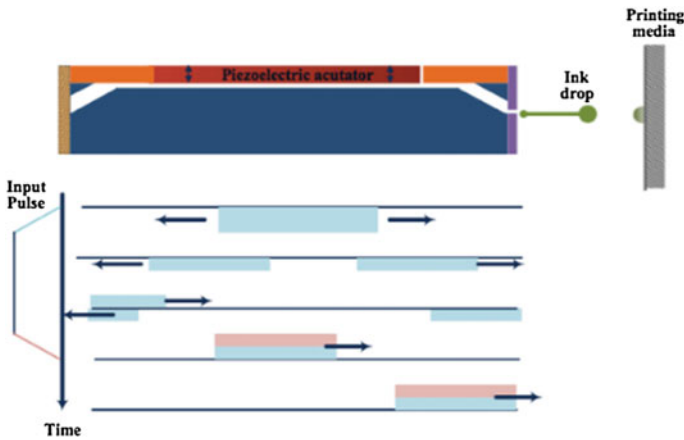
The position of the meniscus position depends on two refill processing, orifice wetting effects and acoustic pressure waves residual vibrations.

Before printing, evaporation effect does not be taken into account, orifice wetting effects is the important role for refilling [6]. Equations are derived for a circular tube and the force balance can be expressed by:

$$f = Fc + Fg - Fv \quad (1)$$

In the formula  $f$  is net force,  $Fc$  is capillary force,  $Fg$  is gravity force,  $Fv$  is viscous force. Because the gravitational force it is much less than the capillary force, it can be negligible. Therefore, when the printhead is not working, the viscous force is very weak, nozzles can be passive refilled driven by the capillary force. If the evaporation rate is too fast, capillary force cannot fill the volatile mass, then the meniscus surface drew back which leads droplets missing or deviation.

Inkjet printing is the process of ink injection and filling inside the nozzle. When the ink is ejected, new ink must be filled before the next ejection. At short time



**Fig. 1** Drop jetting mechanism

scale this refilling process is affected by the residual vibration inside the nozzle. After one droplets fly out, the residual vibration recover from the nozzle end and reverberates. The outward pushing force by residual vibration can not break through the capillary force cause the ink to fill [7] as shown in Fig. 1.

The principle of pre-actuation is to simulate pressure wave process in the nozzle, but without jetting any droplets. Unlike the jetting waveform, a low magnitude of input voltage should be used as pre-actuation waveform that can't lead jetting. Such that the small mass of ink can't get enough acceleration to break surface tension force, and still fill nozzles. Repeat this process, it can compensate for the lack of evaporation then restore meniscus locations.

### 3 Experiments

An inkjet printhead (KJ4A) from Kyocera Corporation was used as the jetting device which has 2656 nozzles with orifice diameter of 28  $\mu\text{m}$ . Jetting material is the water-based ink with 15 wt% phenolic aldehyde resin, 15 wt% ethanol and 1 wt % dye, and viscosity 45 mPa s, surface tension 39 mN/m. Phenolic aldehyde was used as jettable functional material. Ethanol was used to amplify evaporation affect in nozzle, and dye was for easy watching. The test waveform is a typical single-pulse trapezoidal waveform. Neighboring nozzles were blocked to prevent cross-talk effects in this study.

In this paper, adrop-watch system was used for watching meniscus motion and droplets are proposed for the experiment. The proposed system includes a strobe LED and a high-speed CCD camera. The CCD camera is triggered synchronized with the jetting signal or pre-actuation signal.

In order to investigate the impact on the real printing process, a scanning-stepping print system was used in this study. The Precision Print System (NT-116C, Nano-think Print Technology) consists of granite frame, linear motors with precision grating to ensure the motion accuracy with displacement error  $\pm 3 \mu\text{m}$ .

Printing media is aluminum plate coating with nano-ZnO. It is a hydrophobic coating, which could prevent droplet spreading on the aluminum plate. The mechanism is through the organic coating and reduces the polarity of nanometer zinc oxide. Another measure for prevent spreading is heating system plate to  $40 \text{ }^\circ\text{C}$ . Heat can be transferred to media plate. This can speed up the volatilization of droplets on media. These methods were used to accurately reproduce printing results.

## 4 Results and Discussion

In this section, the meniscus motion was researched with drop-watch system to get the proposed voltage. With printing sequential dot on plate, the effect of pre-actuation times was investigated.

### 4.1 Voltage of Pre-actuation

In order to observe the effect of voltage on the droplet morphology, a droplet-watching system was used in the experiment. The system consists of a high-speed CCD camera and LED. Camera and the printhead can be triggered simultaneously or separately. By adjusting the trigger time of the camera and the printhead, we got the ink droplet image sat different times.

The test waveform is a typical single-pulse trapezoidal waveform which rising time, falling time and dwell time were set to  $2.1 \mu\text{s}$ . Nozzle firing frequency was set at 300 Hz, and tested with driving voltage 8–20 V. Figure as shown in Fig. 2 is pre-actuation waveform formed small droplets. This process is similar to inkjet drop formation, but drop wouldn't break off from meniscus surface in pre-actuation.

The influence on surface motion of driving voltage was shown in Fig. 2. It must be pointed out that symmetrical image is caused by the mirror effect of the smooth nozzle plate. The drop top position was higher with the increase of voltage. When driving voltage under 10 V, hardly the meniscus was pulled out the orifice. And the little ink would overflow after droplet retract when driving voltage was 15 V. Once voltage was higher than 16 V, there will be a large number of droplets jet out, but droplets' mass much smaller than normal inkjet droplets, just like fog under the printhead.

In this observation, the overflow occurred at 15 V reduced in few microseconds. The reducing time was difference, depending on the mass of the overflow.

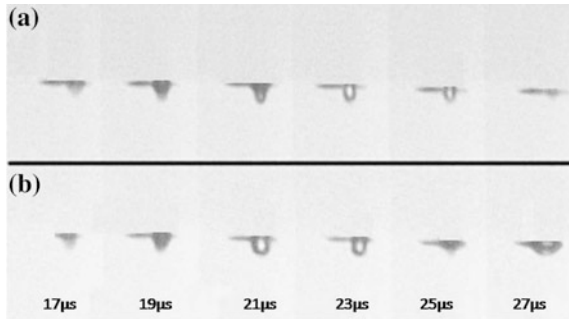
This phenomenon may be caused by evaporation and capillary force. It will not be discussed in this study. However, overflow of the ink can influence formation process of the droplet. Therefore, the available driving voltage for pre-actuation range is from 10 to 14 V.

### 4.2 Pre-actuation Times

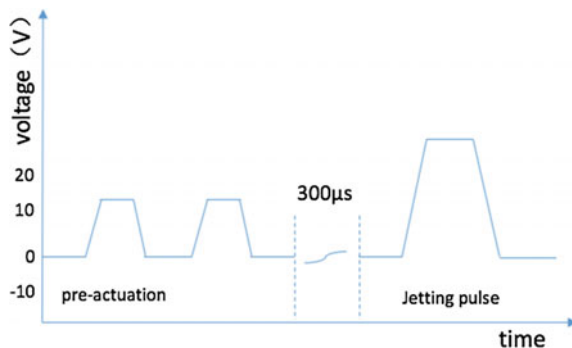
As described above, meniscus depression caused by evaporation. Pre-actuation fills little mass each time, lots repeats are needed for fullfill. Unfortunately, this narrowly defined model cannot be used to solve real-world engineering problems. Multiple aspects must be considered, such as evaporation, capillary force, ink properties, environmental factors. In the study, the fill level was either inadequate or too much.

How to make the nozzle internal just fullfill is a very important issue to make this work have the engineering significance. Inspired by the previous work of overflow reduce in microseconds. A time slot 300  $\mu$ s interval without driving voltage was set between pre-actuation and ejection, as shown in Fig. 3. During the interval meniscus, it adjusted itself by evaporation and capillary force. It was

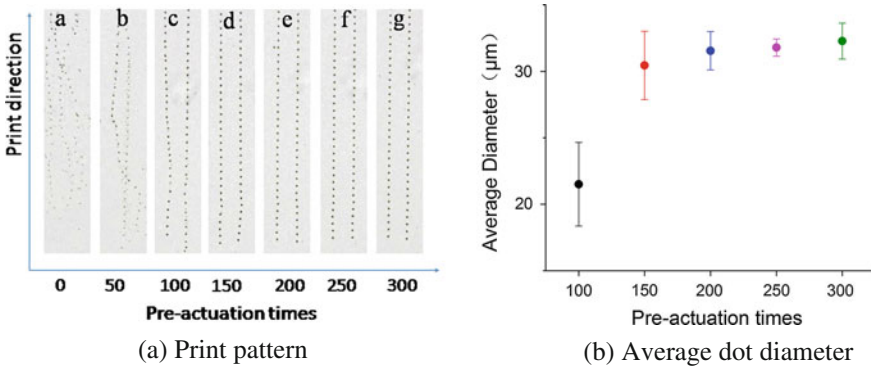
**Fig. 2** Surface motion that stimulated by pre-actuation changes with time. At different voltage: **a** 11 V, **b** 15 V



**Fig. 3** Pre-actuation and ejection waveform







**Fig. 4** Comparing the printed images and dot diameter

difficult to distinguish which part made more contribution in this process, but it worked between pre-actuation and ejection.

In order to eliminate the impact of printhead movement, the printing speed was controlled to 400 mm/s. The nozzle firing frequency was set at 300 Hz, voltage of pre-actuation 14 V. It was difficult to observe inside the nozzle. But the nozzle was considered full refill after a jetting action. The print quality was studied after different lengths of time after last jetting. After a certain time, 3 min here, print the test pattern with different pre-actuation times. The number of pre-actuation times was from 0 to 300 times. Then the printed images and dot diameters were separately compared in Fig. 4.

The results showed that if there is no pre-actuation, a large number of dots are loss and distort. At 100 times of the dot placement accuracy improved significantly, more than 200 times there is no difference in visual.

From 100 to 250 times, the dot diameter and uniform is increasing with the number of pre-actuation. However, the dot diameter becomes larger in 300 times. We observed that the earliest several dots diameter are too large, and the subsequent dots are similar. This phenomenon is due to too many pre-actuation times, leading to overfill.

## 5 Conclusions

In this article, a pre-actuation method for initial droplets accurateness cause by evaporation was proposed. This method imitated the ink filling process by pressure wave oscillation after jetting. Conventional trapezoidal waveform drives lower voltage preventing ejection, while promoting ink filling. In the actual printing process, by adding an interval between pre-actuation and ejection solves the problem of overfilling. The results showed that there is no ink droplet lost after the pre-actuations. When the pre-actuations set at 200–250 times the initial droplets

consistency increased significantly, the average dot diameter is about 32  $\mu\text{m}$ . This method is simple and has great significance in improving production.

## References

1. D. Albertalli, (2005). Gen 7 FPD inkjet equipment—Development status. SID Symp. Dig. Tech. Pap., vol. 36, no. 1, pp. 1200–1203.
2. R. M. Verkouteren, J. R. Verkouteren. (2009). Inkjet metrology: Highaccuracy mass measurements of microdroplets produced by a drop-on-demand dispenser. *Anal. Chem.* 81, 8577.
3. Famili A, Palkar S A, Baldy Jr W J. (2011). First drop dissimilarity in drop-on-demand inkjet devices. *Physics of Fluids*, 23(1): 012109.
4. P. Calvert. (2001). Inkjet printing for materials and devices. *Chem. Mater.* 13, 3299.
5. H. Dong. (2006). Drop-on-demand inkjet drop formation and deposition. Ph.D. thesis, Georgia Institute of Technology.
6. Moon K S, Choi J H, Choi D J, et al. (2008). A new method for analyzing the refill process and fabrication of a piezoelectric inkjet printing head for LCD color filter manufacturing. *Journal of Micromechanics and Microengineering*, 18(12): 125011.
7. Wijshoff H. (2010). The dynamics of the piezo inkjet printhead operation. *Physics reports*, 491 (4): 77–177.

# Analysis of Print Quality of UV Flatbed Inkjet Printer

Ying Wu and Ang Xu

**Abstract** UV flatbed inkjet printer is suitable for all kinds of materials of paper packing. In order to discuss the differences of print quality of the UV flatbed inkjet printer on various types of paper, in the experiment, Coated paper, White board and Kraft paper were chosen. After that, we adjusted the distance between nozzle and paper and printed the test charts, measured the color values and analyze the data. The print quality was analyzed in terms of resolution, color gamut, solid density and tones reproduction curve. Finally we get the difference of printing quality among different paper. The result showed that the printing quality of both Coated paper and White board are better than the printing quality of Kraft paper. There are differences of printing quality when the distance between nozzle and paper was changed. When the range of nozzle's height is 0–1 mm, color reproduction, tone reproduction and sharpness are very well. When nozzle's height is 1.5 mm, in this range, printing quality is general. When it is greater than 1.5 mm, it is not suitable for the requirements of the printing quality.

**Keywords** UV flatbed inkjet print · Color reproduction · Tones reproduction · Sharpness

## 1 Introduction

UV flatbed printer was used to print hard material, which thickness was a few centimeters. The application areas of UV flatbed inkjet printer are many, including the packaging industry [1, 2]. Because the paper of packaging has a lot of type, and the surface of packaging is uneven, this paper studied two problems. Firstly, the effects of printing quality among different paper were analyzed. Secondly, the effects of printing quality among different nozzle's height were analyzed.

---

Y. Wu (✉) · A. Xu

School of Packaging and Printing Engineering, Beijing Institute of Graphic Communication, Beijing, China

e-mail: jinmomo@126.com

© Springer Nature Singapore Pte Ltd. 2017

P. Zhao et al. (eds.), *Advanced Graphic Communications*

and *Media Technologies*, Lecture Notes in Electrical Engineering 417,

DOI 10.1007/978-981-10-3530-2\_60

## 2 Research Method

### 2.1 Experiment Design

In the experiment, a print test target was designed to evaluate printing quality of color reproduction, tone reproduction and sharpness. The test target was composed of IT8 7/3 test chart, ISO CMYK images, CMYK patches with different gray levels, lines with different widths, text with different scales and typeface. The print test target is shown in Fig. 1 [3–5].

### 2.2 Experimental Apparatus

- Roland Dbe DF-712U LED-UV flatbed printer;
- X-Rite Eye-One Spectrophotometer;
- X-Rite SpectroEye Spectrophotometer;
- Roland VersaWorks professional software;
- X-Rite Profile Maker color management software;
- Materials: Coated paper, White board; Kraft paper.

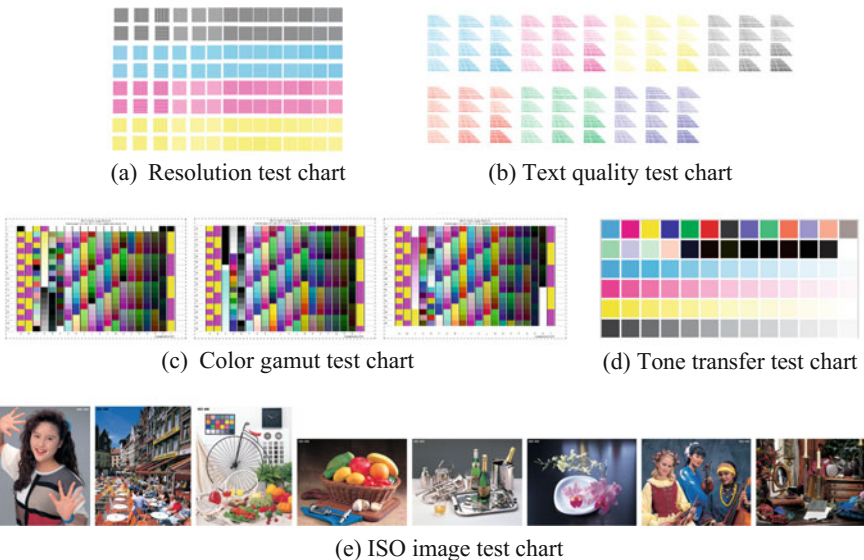


Fig. 1 Test target

### 3 Result and Analysis

#### 3.1 Resolution and Sharpness Analysis

##### 3.1.1 Resolution and Sharpness Analysis with Line

The resolution and sharpness test chart was set to 1440 dpi  $\times$  1440 dpi, UV Flatbed Printer was set to 720 dpi  $\times$  1440 dpi. Firstly, the nozzle's height was set to 0 mm, Next, the nozzle's height increased 0.2 mm ever time and it repeated five times to obtain 6 test charts [4].

When the nozzle's height is between 0 and 1 mm, 6 px lines can be discernible, and resolution is 240 dpi. In this range, lines are clear when it is between 0 and 0.6 mm, lines are blurring when it is between 0.8 and 1 mm.

Then, the nozzle's height is set to 1.5, 2 and 3 mm. When it is 1.5 mm, 10 px lines can be discernible, and resolution is 144 dpi.

When it is 2 mm, 16 px lines can be discernible, but the lines are blurring. Although the resolution reached 90 dpi, there also have some problems with poor visual effects and image quality.

When it is 3 mm, 30 px lines can not be discernible. It does not suitable for the requirements of printing.

According to the test, the range of the nozzle's height for analysis is determined between 0 and 1.5 mm, as shown in Table 1 and 2.

##### 3.1.2 Sharpness Analysis with Text and ISO Image Test Chart

When nozzle's height is 0 to 1 mm, 6p text is clear, ISO image test chart is clear too.

When it is 1.5 mm, there are some problems with the text sharpness and the image quality. They take on a downward trend.

When it is 2 mm, the text and images are blurred. It is not suitable for the requirements of printing (Table 2).

The result showed that the height of the nozzle has an effect on the resolution and sharpness. But when the experiment chose Coated paper, White board and Kraft paper, the difference of the paper has no effect on the resolution and sharpness.

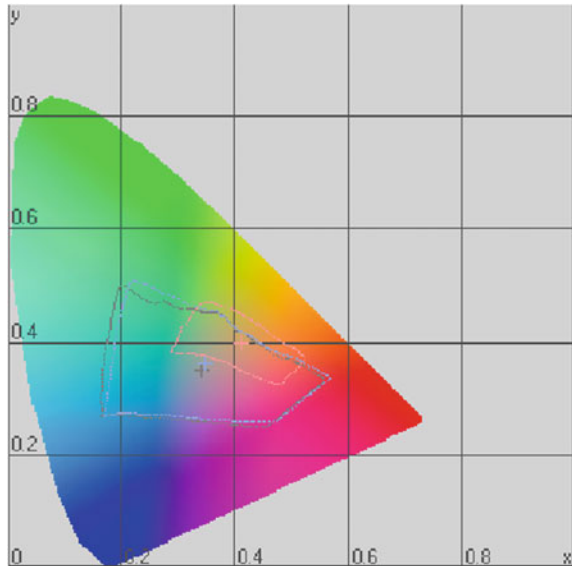
**Table 1** Line resolution and sharpness of different heights

Nozzle's height (mm)	Line width (px)	Sample status	Resolution
0–0.6	6	Clear	240 dpi
0.8–1	6	Slightly blurred	240 dpi
1.5	10	Blurry	144 dpi
2	16	Very blurred	90 dpi
3	30	Unrecognizable	Uncertain

**Table 2** Text and image sharpness of different heights

Nozzle's height (mm)	Text size (px)	Sample status of text	Sample status of image
0-1	6	Clear	Clear
1.5	10	Blurry	Slightly blurred
2	16	Very blurred	Blurry
3	30	Unrecognizable	Very blurred

**Fig. 2** Color gamut of three kinds of paper

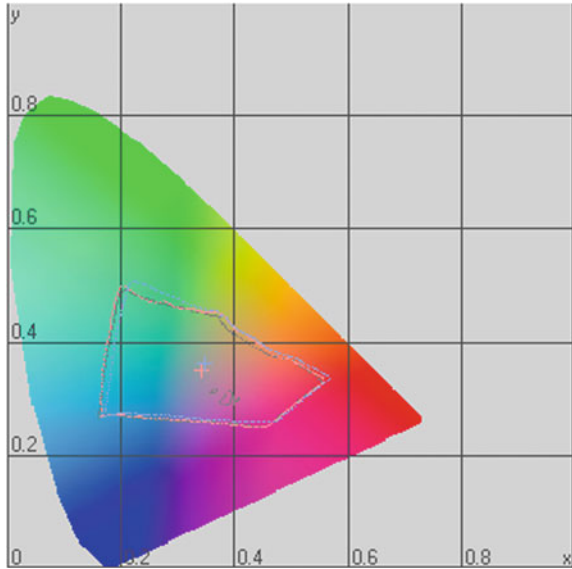


### 3.2 Color Reproduction Analysis

Figure 2 showed color gamut of three kinds of paper. The experiment showed the color gamut of Coated paper is wide. The color gamut of White board is narrower than the color gamut of Coated paper. The color gamut of Kraft paper is the narrowest.

Figure 3 showed comparison of color gamut for three kinds of nozzle's height. The experiment selected Coated paper as the printing material. Then, the nozzle's height was set to 0, 1 and 1.5 mm to print IT8. 7-3 CMYK test chart. The result showed there is such a tiny difference between three kinds of nozzle's height [5, 6].

**Fig. 3** Color gamut of three kinds of nozzle's height



**Table 3** Solid density of coated paper

Nozzle's height ink color	0 mm	1 mm	1.5 mm
Y	0.99	0.97	0.99
M	1.49	1.48	1.47
C	1.96	1.92	1.90
K	1.47	1.51	1.46

**Table 4** Solid density of white board paper

Nozzle's height ink color	0 mm	1 mm	1.5 mm
Y	0.96	0.92	0.89
M	1.33	1.30	1.27
C	1.34	1.28	0.25
K	1.29	1.29	1.28

### 3.3 Tone Reproduction Analysis

#### 3.3.1 Solid Density

The data of measuring solid density was shown in Tables 3, 4 and 5. The result showed that the nozzle's height is between 0 and 1.5 mm, the solid density does not change [7].

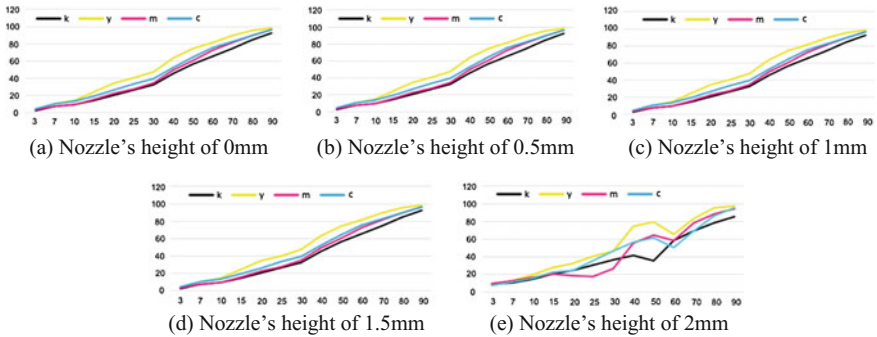
Comparing three kinds of paper, among them, solid density of Coated paper is higher than solid density of White board. Solid density of Kraft paper is the lowest, as shown in Table 6.

**Table 5** Solid density of kraft paper

Nozzle's height ink color	0 mm	1 mm	1.5 mm
Y	0.43	0.44	0.44
M	0.76	0.73	0.72
C	0.68	0.68	0.66
K	0.92	0.86	0.85

**Table 6** Solid density of different paper

Nozzle's height ink color	Coated paper (0 mm)	White board paper (0 mm)	Kraft paper (0 mm)
Y	0.99	0.96	0.43
M	1.49	1.33	0.76
C	1.96	1.34	0.68
K	1.47	1.29	0.92



**Fig. 4** Comparing the tone transfer curve in different nozzle's height

**3.3.2 Tone Transfer Curve**

The experiment set nozzle's height to 0, 0.5, 1, 1.5 and 2 mm. Next, printed halftone scale, and measured dot value [7].

In Fig. 4, the result showed it is not different when nozzle's height is 0–1.5 mm, and the tone transfer curve is smooth. When it is 2 mm, the tone transfer curves appear more serious fluctuations. It is not suitable for the requirements of printing quality.

In Fig. 5, we compared tone transfer curve in different paper. The result showed that the tone transfer curve is smooth and it is suitable to print. The tone transfer curve of Coated paper and White board are better than the curve of Kraft paper.



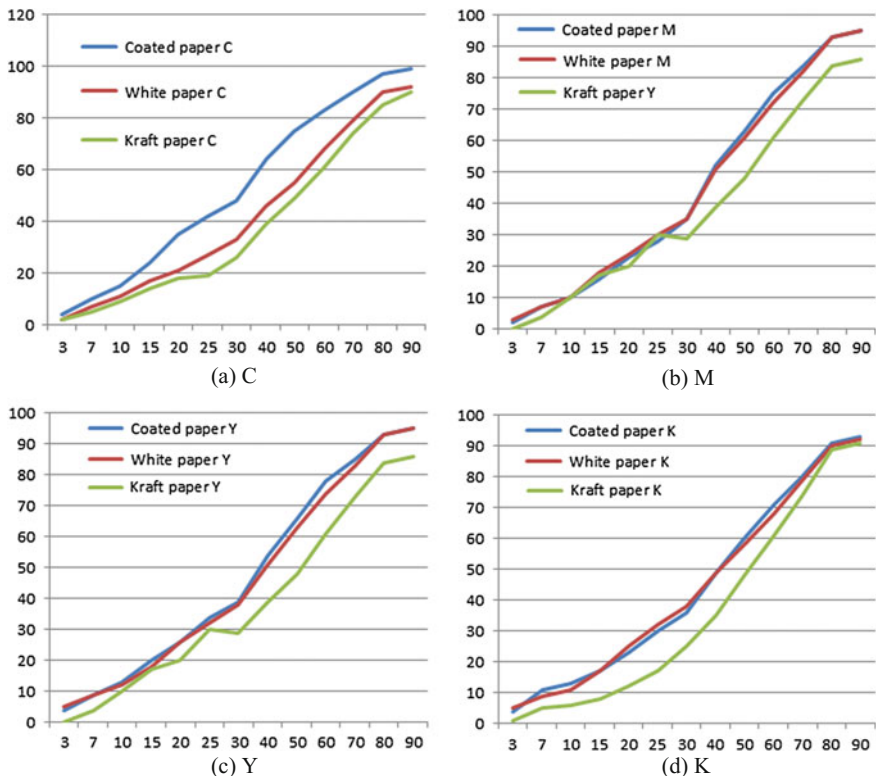


Fig. 5 Comparing the tone transfer curve of different paper (Nozzle’s height of 0 mm)

### 4 Conclusions

This paper chose Coated paper, White board and Kraft paper. After that, it adjusted the distance between nozzle and paper, printed the test charts, measured the color values and analyzed the data. The print quality was analyzed in terms of resolution, color gamut, solid density and tones reproduction curve. Finally we get the difference of printing quality among different paper. The result showed that the printing quality of both Coated paper and White board are better than the printing quality of Kraft paper. There are differences of printing quality when the distance between nozzle and paper is different. When the range of nozzle’s height is 0–1 mm, color reproduction, tone reproduction and sharpness are very well. When nozzle’s height is 1.5 mm, in this range, printing quality is general. When it is greater than 1.5 mm, it is not suitable for the requirements of the printing quality.

## References

1. Zhao Ling. (2015). The market prospect and future development of UV flatbed printer. <http://www.bisenet.com/article/201508/151928.htm>.
2. Development and market prospect of UV flatbed plate ink jet printer (2016). <http://www.keyin.cn/news/sczc/201602/14-1091953.shtml>.
3. S. Liao, M.T. Tai, S.C. Lin and C.K. Lin. (2013). A Study of Print Quality of UV Ink-Jet Printing on Glass. *Advances in Printing and Packaging Technologies, Applied Mechanics and Materials*, Vol. 262, 287–290.
4. W. Zhang, X.F. Wei, B.Q. Huang and L. Zhao. (2013). The Effect of UV Inkjet Ink's Performance on the Line Printing Quality. *Advances in Printing and Packaging Technologies, Applied Mechanics and Materials*, Vol. 262, 273–277.
5. Y.C. Hsieh, H.T. Lee and S.Y. Cheng. (2013). Color Gamut of UV Wide-Format Inkjet Printing on Special Substrates. *Advances in Printing and Packaging Technologies, Applied Mechanics and Materials*, Vol. 262: 345–348.
6. H.M. Wang, G.X. Chen. (2013). Gamut of UV Ink-jet Printer. *Software Guide Packaging Engineering*, Vol. 34, No. 21, 110–113.
7. W.M. Jin, D.X. Ning and D.Q. Liu. (2014). Study on the Influencing Factors of the Quality Reduction Characteristics of UV Color Inkjet Printer. *Publishing & Printing*, No. 1, 30–33.

# Process Analysis of Seamless Adhesion for Cutting Model Printed by Color Paper-Based 3D Printing

Jiangping Yuan, Yimin Liu, Guangxue Chen and Liuxi He

**Abstract** Cutting-Bonding Frame is an effective visualization strategy for solving the large-size color 3D models in cultural creativity field using the color paper-based 3D printing. Under this strategy, the printing quality of current paper-based 3D printing technology is urged to explore and optimize. Given two evaluation indicators including adhesive strength and smoothness of junctions, the effects of cutting angles, adhesive brands and bonding temperatures on printing quality of current color paper-based 3D printed models were analyzed specifically by using the printed banana scaling models. According to the results, the negative impact was shown for the bonding strength on cutting angle variables, and the selected four kinds of non-genuine adhesives indicated the practical bonding strength ability. At last, the plant starch glue, as an low-cost alternative to replace the original adhesive, was sensitive to bonding temperature and also was found a negative correlation among short range.

**Keywords** 3D printing · Cut model · Seamless adhesion · Paper-based printing · Printing optimization

## 1 Introduction

3D printing was praised as a technology which would lead a new manufacturing era, and applied extensively in traditional field and new cultural creativity field [1]. From the view of industrialization, Color 3D printing technology would be more popular among the manufacturing managers. Then, this huge promising market will be took up by the color powder-based 3D printing and paper-based 3D printing.

---

J. Yuan · Y. Liu · G. Chen (✉) · L. He  
State Key Laboratory of Pulp and Paper Engineering,  
South China University of Technology, Guangzhou, China  
e-mail: chengx@scut.edu.cn

J. Yuan  
e-mail: yuanjiangping2009@126.com

Given the unique color reproduction, low-cost and eco-friendly functions, the paper-based 3D printing is the best choice. The color paper-based 3D printer, which provided thousands of color by Mcor technology company, was distributed at Germany exhibition since 2012 [2]. This paper-based 3D printing technology is based on the paper-based Selective Deposition Lamination (SDL) process, which can be divided into two main procedures: colorization and model cutting. In other words, both sides of A4 office paper were printed firstly by the Epson color ink-jet printer, and later delivered to forming base to cut contour and bond layer by layer until finishing a completed model.

However, the maximum printing size of latest paper-based 3D printer is limited to 256 mm × 169 mm × 150 mm (for A4 paper) and 9.39 inch × 6.89 inch 5.9 inch (for Letter paper). The print size is not enough for its applications and industrialization in cultural creativity field. Moreover, the large-size and super-size models will take up a bigger proportion of 3D printing market. Then the Cutting-Bonding Frame (CBF) was proposed as a feasible solution to print an oversize color model by dividing whole one into two or more sub-parts. To match the balance between sub-parts and whole printing time, this case is focused on half-cutting method.

Currently, color 3D printing researches had changed from shape printing to color reproduction using powder-based and paper-based 3D printers [3]. Stanic et al. [4] presented clearly the colorimetric probability and stability of 3D prints using the Z510 3D printer. Vaezi et al. [5] mainly analyzed the effects of layer thickness and blinder saturation level parameters on 3D printing process. Yuan et al. [6, 7] firstly put forward a speedup method for paper-based 3D color printing used STL file, and later evaluated the effects of key parameters of large-size model visualization on the printing time based on the CBF. Under the CBF, the printing quality of color 3D model had to discuss and evaluate to enrich their applications in cultural creativity field.

## 2 Experiments and Methodology

Based on the CBF, just as mentioned previously, the large-size model implementation is regarded as cutting step and bonding step. In the cutting step, the cutting angles and sections were the key parameters influenced the printing quality. Then three kinds of cutting methods were used to contrast and analysis from the basis of given symmetric center. In the bonding step, the adhesives and bonding temperatures were also the key parameters produced the printing quality optimization. In this case, four kinds of adhesives and five temperatures were used for color banana model focused on the horizontal cutting method. The bonding strength and smoothness of junctions were both used for two evaluation indications of 3D printing quality. The bonding strength is expressed by the force to divide the bonding completed model into two sub-parts. The smoothness of junctions is the degree which surface of junction look like a completed part given by five observers.

In this paper, two group experiments were conducted including cutting methods based on adhesives contrast test, and bonding temperatures based on plant starch glue contrast test. All the color 3D models used in this paper were designed by open-source Blender software and printed by Mcor IRIS HD 3D printer, given the ripe banana scaling model with  $140 \times 50 \times 50$  mm shape size. All experiment materials were including A4 office paper (Epson), original adhesive (Mcor-Tech), 3dHi-Tech brand adhesive (3dHi-Tech Ltd.), Plant starch glue (Garefu Ltd.), HORI Glue (HORI Ltd.), SHLI Glue (SHLI Ltd.), Heat collecting thermostat (YuHua Instrument), Beaker, thermometer and Spring dynamometer (TestSmart Ltd.).

Cutting methods based on adhesives contrast test was that three cutting angles which included the  $0^\circ$  (horizontal),  $45^\circ$ ,  $90^\circ$  (vertical) based on symmetric center, their bonding strengths using the above five adhesives were measured. The outputs of above cutting methods were shown in Fig. 1 respectively. Bonding temperatures based on plant starch glue contrast test was that five bonding temperatures including 28, 35, 40, 45 and  $50^\circ\text{C}$  were compared for the plant starch glue by measuring their bonding strength. Considering some abilities of certain adhesive, bonding temperatures were not selected smaller than  $28^\circ\text{C}$ . To be statistical simply, the weightiness of adhesive usage for each model to acquire the statistic average is assumed as consistent.

### 3 Results and Analysis

For the implementation of large-size color model, based on the CBF, three key parameters including cutting angle, adhesive brands and bonding temperature, which were compared and evaluated by bonding strength and smoothness of junctions of 3D printed species, respectively.

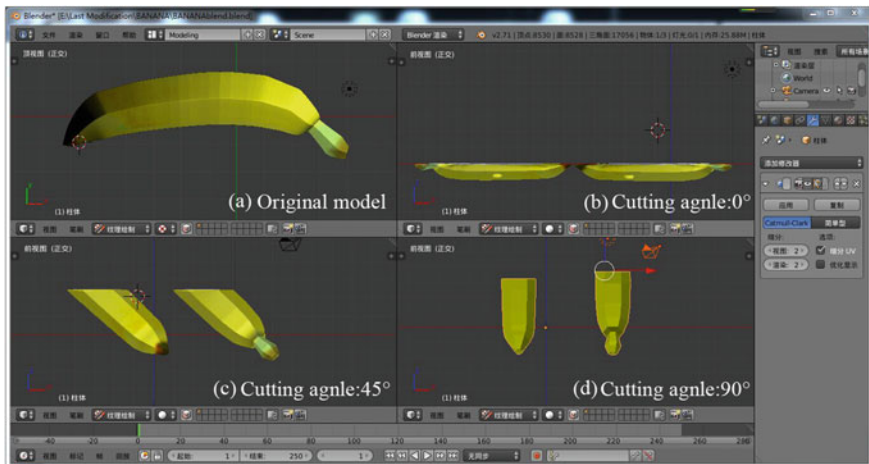


Fig. 1 Three cutting angles

### 3.1 Cutting Methods Contrast Test

Before printing, the original digital model was divided into two sub-parts with cutting surface both turn up layout. After slicing, all species were sent to printing system, and bonded by hands, respectively. The bonding time is set as 10 min, the laboratory humidity is measured as 79%, and the bonding temperature is measured as 28 °C in laboratory. The results of bonding strengths based on five adhesive brands were shown in Fig. 2. The results of smoothness of junctions were shown in Table 1, and bonding species of Garefu Glue case were shown in Fig. 3, respectively. From the Fig. 2, it is obvious that bonding strengths were almost negative correlation with cutting angles, which may be caused by the different bonding surface size. According to adhesive usage, this trend was easy understandable even if the usage of each adhesive brand is not all the same. In the other sidles, given the same cutting angle, five adhesive brands showed the same trend with different decline rate. Moreover, the statistic bonding strengths were usually bigger than 150 N which can provide enough physical strength for practical 3D printed applications.

Given in Table 1, the smoothness of five adhesive brands was statistically evaluated as good degree and excellent degree even for some species by observers. That is to say, the surface of junctions based on the CBF can be met the most industrialization requirements from appearance sense by using the non-genuine

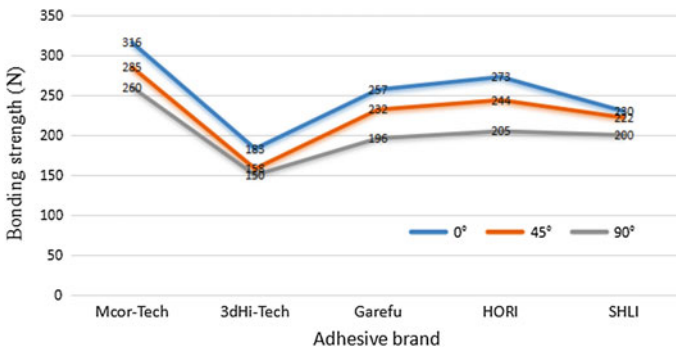


Fig. 2 Bonding strengths based on three cutting angles

Table 1 Smoothness of five adhesives with three cutting angles

Cutting angle	Adhesive brand				
	Mcor-Tech	3DHi-Tech	Garefu	HORI	SHLI
0°	E	G	E	G	E
45°	E	G	G	G	G
90°	E	E	E	E	G

The E is short for excellent and G is for good

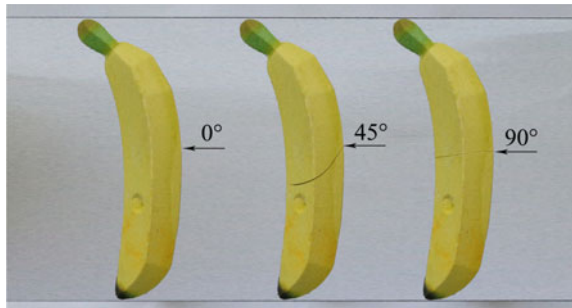
adhesives which is usually dear for customized persons. Combined with bonding strengths, the mentioned four adhesives may be a good choice, especially for Garefu glue.

### 3.2 Bonding Temperatures Contrast Test

Actually, adhesives, which consisted of different special compositions were developed and used in the low or normal temperature. But sometimes high temperature would be need in other substrate 3D printing not paper-based 3D printing. At the same time, the eco-friendly adhesive will be the main adhesive in 3D printing, which can be recycled and dissolved easily. So the plant starch glue is a good promising product which is not expensive. The bonding temperature test of plant starch glue was conducted in the following conditions including 79% humidity, 28 °C constant laboratory and 10 min bonding time. The Garefu glue was water-bath heating from 35 to 50 °C with the 5 °C interval. The cutting angle is selected 90 °C which mentioned in Fig. 1. To be simpler, assuming that the speed of connecting two sub-part is fast and leave it bond to 10 min.

From the Table 2, it was easily found that bonding strength is negative correlated with the increasing bonding temperature. In this case, when the bonding is higher than 45 °C, its statistic bonding strength is decreased sharply and lowly. For the Garefu glue, if the bonding strength can be extended than 200 N with the bonding temperature near 28 °C, the super-size color model ... should be implemented

**Fig. 3** Bonding cases of Garefu Glue with three cutting angles



**Table 2** Bonding temperatures for Garefu glue case

Garefu glue	Bonding temperature (°C)				
	28 °C	35 °C	40 °C	45 °C	50 °C
Bonding strength	195 N	180 N	162 N	145 N	78 N
Smoothness	E	E	G	G	G

N is the magnitude of force, E is short for excellent, and G is for good

widely by paper-based 3D printer based on the CBF. About the smoothness, it can be acquired a good appearance of junctions among working temperature range. When the bonding temperature is rising, the smoothness degree declined slightly.

## 4 Conclusions

In this paper, the Cutting-Bonding Frame (CBF) is certified and evaluated to be a feasible solution using banana scaling model. In color 3D printing procedure, three key parameters of cutting step and bonding step including cutting angle, adhesive brand and bonding temperature, were discussed and correlated with bonding strength and smoothness of junctions. According to the statistic results, cutting angle had affected the bonding strength with negative correlation among five adhesive brands. Given certain 90° cutting angle, for the Garefu glue, it was influenced by the bonding temperature and determined a stable range. In summary, original adhesive would be replaced soon by the plant starch glue with cheap price and environmental protection, even if the bonding strength is needed to enhance further.

**Acknowledgements** This work was financially supported by the Guangdong Provincial Science and Technology Project (2013B010401007), the Guangzhou Science and Technology Project (201607020045), National Students' Innovation and Entrepreneurship Training Program funded by South China University of Technology (Grant No. 201410561089).

## References

1. Dimitrov, D., Wijck, W. V., Schreve, K., & Beer, N. D. (2013). Investigating the achievable accuracy of three dimensional printing. *Rapid Prototyping Journal*, 12(12): 42–52.
2. Mcor Technologies (2015). (Accessed in March. 2016) Mcor IRIS HD, True color 3D printer. <http://mcor technologies.com/3d-printers/iris/>.
3. Wang H.M., Chen G.X. (2014). 3D Printing of Topographic Map Based on UV inks. *Packaging Journal*, Vol. 6: 48–52.
4. Maja S., Lozo, B., & Gregor Svetec, D. (2012). Colorimetric properties and stability of 3D prints. *Rapid Prototyping Journal*, Vol. 18 No. 2, pp. 120–128.
5. Vaezi M., Seitz H., Yang S. (2013). A review on 3D micro-additive manufacturing technologies. *The International Journal of Advanced Manufacturing Technology*, 67(5–8): 1721–1754.
6. Yuan J.P., & Guangxue, C. (2015). Speedup method for paper-based 3d color printing based on STL file. *Applied Mechanics and Materials*, Vol. 731: 269–272.
7. Yuan, J., Chen, G., Liao, J., & Yu, Z. (2016). Visualization of large-size model based on paper-based 3D printing. *Advanced Graphic Communications, Packaging Technology and Materials*.



# Study of Printing Process of Creative Prints Based on TFEL Technology

Rubai Luo, Ming Lu and Shisheng Zhou

**Abstract** Electroluminescent (EL) is an illumination phenomenon due to the solid luminescent materials excited in the electric field. With the development of material science, some EL material has been able to be made into paste and be transferred efficiently and uniformly to certain submit in certain shape through printing process. In this study, we discuss the availability of utilization of TEFL (flexible thin-film electroluminescent) creative printing products. Firstly, the principle of TEFL is introduced in this paper. Secondly, the printing process and the relative attentions are simply explained. Finally, an example is to be given to prove the availability of the printing process mentioned in the paper.

**Keywords** Flexible thin-film electroluminescent · Creative printing · Printing process

## 1 Introduction

Electroluminescent (EL) is an illumination phenomenon due to the solid luminescent materials excited in the electric field. With the development of material science, some EL material has been able to be made into paste and be transferred efficiently and uniformly to certain submit in certain shape through printing process [1]. There is, however, few documents focus on EL technology applied in creative printing production. Therefore, on the basis of the fundamental principles of EL, this paper will expound the structure of inorganic EL film based on printing process and expose the printing process based on EL technology. In the final, an example is to be given to prove the availability of the printing process mentioned in the paper [2, 3].

---

R. Luo (✉) · M. Lu · S. Zhou  
Faculty of Printing Package and Digital Media,  
Xi'an University of Technology, Xi'an, China  
e-mail: luorubai@xaut.edu.cn

## 2 Principle of Inorganic Thin Film Electroluminescence

### 2.1 Principle of Electroluminescence

Electroluminescence is a kind of photoelectric phenomenon which is able to convert electric energy into light energy directly. Under the strong electric field, electrons are excited by the field and their energy is increased correspondingly. When the energy exceeds the energy of electron in thermal equilibrium state, hot electrons are formed. Then electrons become electron hole pairs through the impact ionization during their motion. These electron hole pairs will radiate light when they recombine or the excited luminescence center return to the ground state.

### 2.2 Structure of Thin Film Electroluminescent

In display field, EL substance is made into a thin layer in Sandwich structure and placed into the capacitance which is constructed of several solid planes to produce the thin-film Electroluminescent (TFEL) device. Using inorganic EL substance as the fluorescent substance, TFEL generally has 2 structure as is shown in the Fig. 1. In Fig. 1a, layer 1 is transparent film, layer 2 is transparent electrode layer, layer 3 is inorganic EL substance, layer 4 is dielectric layer, layer 5 is transparent electrode layer and layer 6 is transparent seal protect layer. In Fig. 1b, layer 1 is based material, layer 2 is back electrode layer, layer 3 is dielectric layer, layer 4 is inorganic EL substance, layer 5 is transparent electrode layer and layer 6 is transparent seal protect layer. Apparently, the light radiate through layer 2 and layer 1 in Fig. 1a and b, the light radiate through layer 5 and layer 6 [4].

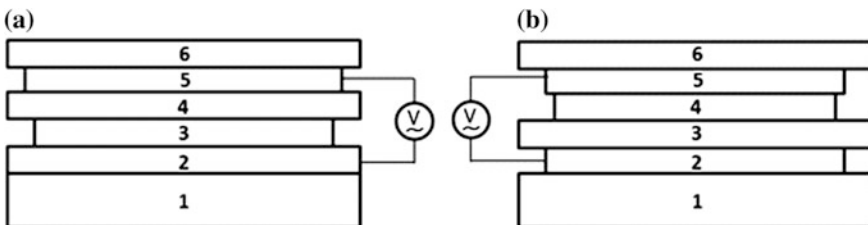


Fig. 1 Sandwich structure of TFEL

### 3 Flexible Thin Film Electroluminescent Light Source Printing

#### 3.1 Selection of Flexible Transparent Based Material

With the development of material science, it is possible for TEFL light source to be transfer layer by layer on the substrate through printing process.

In creative printing products, substrate of TEFL light source has the feature of flexibility which contributes to the fusion of TEFL light source and other part of press. It's necessary for each layer to be dried under about 130°C hot wind during the printing production of TEFL light source and thus, fine thermal stability is required for the substrate of TEFL light source. It's obvious for the substrate itself to have good electrical insulation since TFEL structures the capacitance over the substrate. For certain, as the substrate during the printing production of TEFL light source, the substrate needs to have good printing adaptability with the substance of the layer upper itself.

Besides the requirements mentioned above, the substrate shown in Fig. 1a requires having transparency as well. Therefore, this paper focuses on discussion about the selection of transparent substrate during the printing production of TEFL light source [5].

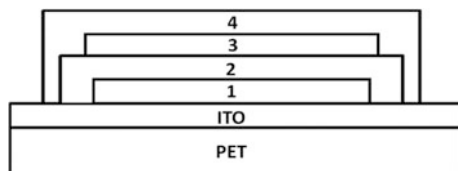
#### 3.2 Flexible TFEL Light Source Printing Process

The whole printing process of the flexible TEFL light source is divided into 3 stages which are prepress, printing and post-press.

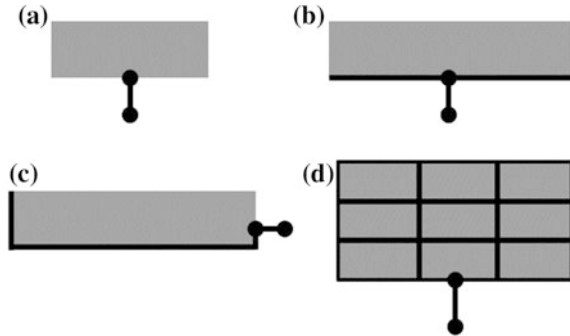
##### 3.2.1 Pre-press

In the stage of prepress, it is first to design the shape of the light source. Afterwards, the shape of each structural layer is supposed to be designed according to the shape of the light source. Take the TEFL light source in the sandwich structure shown in Fig. 1a for example, PET film coated with ITO is to be set as the substrate; its longitudinal sectional view is displayed in Fig. 2 which represents the size relation of the outer boundary between each structural layer.

**Fig. 2** Longitudinal sectional view of TEFL light source



**Fig. 3** Method of reducing the obvious voltage drop in electrode layer



As displayed in Fig. 2, layer 1 is inorganic substance, layer 2 is dielectric layer, layer 3 is back electrode layer and layer 4 is seal protection layer. The shape of inorganic substance layer is the same as the shape of TEFL light source. The next layer should expand for 3 mm on the basis of the last one.

In order to reduce the appearance of the obvious voltage drop in electrode layer, it is possible to design the position of power contact point and create a certain shaped circuit which printed by low-resistivity conductive ink. As shown in Fig. 3, the gray layer in Fig. 3 is electrode layer, the black point is power contact point, and the black line circles the low-resistivity circuit.

If the electrode area is small, as is shown in Fig. 3a, the contact point should be set at the middle of the long side in the electrode layer. If the electrode area is larger, it is possible to design a low resistivity bus circuit shown in Fig. 3b at the edge of the long side of electrode layer. When the power contact point is unable to be placed in the middle, the designation of the circuit should refer to Fig. 3c. In Fig. 3d, the grid shaped low resistivity circuit is suitable for large area electrode layer.

### 3.2.2 Printing

During printing, it is essential to pay attention to the following point:

Each layer is supposed to be dried under the recommended degree before over-printing upon the next structural layer.

The pasty inorganic EL substance is supposed to be mixed fully before printing. During the printing, each structural layer should be thickness uniformed and without leak points.

In order to reach the thickness recommended by the manufacturers, electrode layer is able to be printed repeatedly.

### **3.2.3 Post-press Finishing**

Electrode contact should be set up when flexible TFEL source has been printed. The substrates besides TEFL light source are supposed to be die cut according to the demand for designation.

## **4 Printing for Creative Printing Products Based on Flexible TFEL Light Source**

### ***4.1 Designation of Creative Printing Products Based on Flexible TFEL Light Source***

Overall, EL creative printing products are divided into two parts, EL light source and non EL light source. It is called assembly type designation of EL creative printing products whose two parts are printed on different substrates. Otherwise, it is called integrated designation of EL creative printing products whose two parts are printed on the substrate of the flexible TEFL light source.

The manufacturability should be focused on while designing integrate EL creative printing products. The following are the problem caused by manufacturability.

- (1) The ink should prove to have well printability with the substrates while printing non EL parts.
- (2) The dry method of later printed substances should not affect with the substances which have been printed.
- (3) The printing process of non EL part is strictly restrained.

For assembly type of EL creative printing products are assembled with the EL and non EL part which are printed individually. Therefore, the trouble caused by manufacturability of the integrate EL creative printing product mentioned above will not take place. In addition, the assembly type is more cost-effective than the integrate since the price of TEFL light source substrates is higher than the price of papers.

Above all, the designation of EL creative printing should take the features of printing into account, and structure of products is supposed to be selected under consideration of manufacturability and cost control.

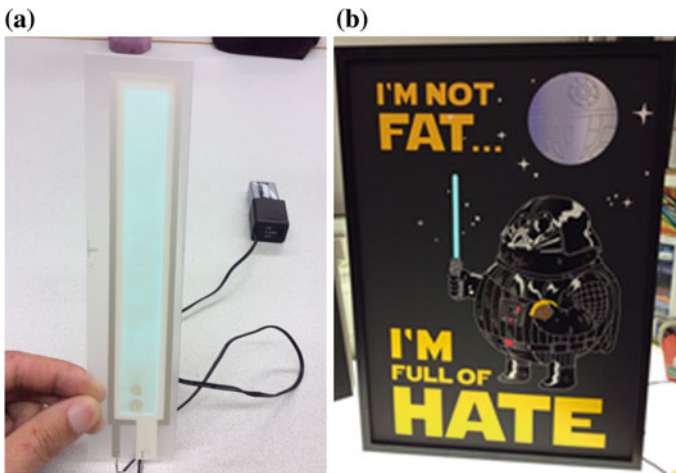
### ***4.2 Example***

There is an EL creative printing product which EL light source accounts for small part and non EL parts account for the large. As a result, the assembly structure is

selected. The whole process is divided into flexible TEFL light source printing and non-light source printing. The EL creative printing product is displayed in Fig. 4a.

#### 4.2.1 Flexible TEFL Light Source Printing

Flexible TEFL light source takes PET film coated with ITO as the substrates. It is printed in the structure shown in Fig. 1a. The materials and relative parameters of each layer are displayed in the following Table 1, and in Fig. 4b, the printed EL light source is displayed.



**Fig. 4** EL creative printing product

**Table 1** Printing materials and parameters of TEFL light source

Ink	Ink type	Screening frequency (threads/inch)	Printing times	Average thickness ( $\mu\text{m}$ )
EL fluorescent ink (yellow-green)	Dupont7154 J	156	1	39.32
Dielectric ink	Dupont120817	156	2	21.54
Conductive ink		195	1	8.03
Seal protection layer		195	1	8.96

### 4.2.2 Printing of Non EL Parts

The non EL parts are printed through the process of screening printing. Afterwards the district of light source is dying cut out. Finally, it is assembled with the printed flexible TEFL light source, as displayed in Fig. 4a.

**Acknowledgements** This work was supported in part by NSF of the Science and Technology Department of Shaanxi Province under Grant Nos. 2016JM5068 and NSF of the Key Laboratory of Shaanxi Provincial Department of Education under Grant Nos. 15JS075.

## References

1. Minami, T., Miyata, T., & Sakagami, Y. (1998). TFEL devices using oxide thin films without vacuum process. *Surface & Coatings Technology*, 108(98): 594–598.
2. Tiku, S. K., & Smith, G. C. (1984). Choice of dielectrics for TFEL displays. *IEEE Transactions on Electron Devices*, 31(1): 105–108.
3. Sun, S. S. (1990). TFEL device having multiple layer insulators. US, US 4897319 A.
4. Ono, Y. A., Kawakami, H., Fuyama, M., & Onisawa, K. (1987). Transferred charge in the active layer and el device characteristics of TFEL cells. *Japanese Journal of Applied Physics*, 26(9): 1482–1492.
5. Sun, S. S., & Tuenge, R. T. (1997). AC TFEL device having a white light emitting multilayer phosphor. US, US 5598059 A.

# Study on the Influence of Paper Surface Efficiency on Ink Color Effect

Li Cheng, Xuejun Tian and Xi Xiong

**Abstract** The paper surface efficiency is the physical measurement of the paper gloss and ink absorption ability, it is also the paper printing eligibility index related to the optical properties and the quality of printing products. We chose the different types of paper, print paper with three kinds of primary color ink and test the color strength, color deviation, gray level and color efficiency. We also analyzed the relationship between paper surface efficiency and ink color effect to provide data reference for practical production. The experimental results showed that the surface efficiency of the paper has great influence on the ink color effect. The paper with good surface efficiency has great ink reproduction performance, while the paper with poor surface efficiency has poor ink reproduction performance. Therefore, the actual printing should be based on the need and choice of suitable paper. High gloss paper should compensate with high absorbency and low gloss paper need to compensate with low absorption in order to improve paper surface efficiency and get printing products of high quality.

**Keywords** Paper surface efficiency · Ink · Color effect

## 1 Introduction

With the change and development of times, the development of printing industry has become one of the symbols of modernization and industrialization to measure of a country. For general printing, the performance of paper and ink has important influence on printing color effect [1–4]. In recent years, in order to adapt to people's requirements on appearance and quality when choose printing product, the printing technology develops steadily and quickly [5–7]. Printing paper manufacturer also improve in the choice of materials and production process to adapt to the printing needs. As a method of evaluating printing quality, the test of paper surface effi-

---

L. Cheng (✉) · X. Tian · X. Xiong  
Jingchu University of Technology, Hubei Province, China  
e-mail: 284881546@qq.com



ciency considers the gloss, ink absorption and their comprehensive effect, which is an important part to achieve the standardization of process and have great significance in correcting color deviation, stabilizing grey level and improving color efficiency [8, 9]. Through theory and experiments, the paper analyzed the influence of paper surface efficiency on ink color effect and provides reference for the choice of printing paper as well as improving printing quality.

## 2 Experiment

### 2.1 Materials

70, 80 and 100 g/m<sup>2</sup> offset paper from Jindong; 128 and 200 g/m<sup>2</sup> coated paper from Hangzhou Taigu; 200 g/m<sup>2</sup> single-sided photographic paper from Shenzhen Liwu; 170 g/m<sup>2</sup> UH170 easicolor from Fantaike; 48 g/m<sup>2</sup> newsprint from Anhui Shanying.

Absorbefacient paper printing ink from Tianjin Tianshi (K&N value); ink from Tianjin Dongyan.

### 2.2 Instruments

YT-GM Gloss Tester; YT-48A Whiteness Tester; IGT C1-5 Printability Tester; X-Rite SpectroEye.

### 2.3 Methods

#### 2.3.1 Test on Paper Surface Efficiency

- (1) Test specular glossiness of paper (75° measurement angel) through GB8941-2007 method.
- (2) Test ink absorption of paper through ink stain test method(TAPPI Standard RC-9) [10]. Use XT-48A to test whiteness of paper. The calculation formula for ink absorption of paper (K&N value):

$$K\&N = \frac{R_F}{R_\infty} \times 100\% \quad (1)$$

In the Formula (1),  $R_F$  is Reflectivity of ink stain area;  $R_\infty$  is Reflectivity of thick blank paper.

(3) Calculation of paper surface efficiency

The paper surface efficiency is the physical measurement of the paper gloss and ink absorption ability, it is also the paper printing eligibility index related to the optical properties and the quality of printing products [11, 12]. The calculation formula of paper surface efficiency is as followed:

$$PSE = \frac{100 - A(\%) + G(\%)}{2} \tag{2}$$

In the Formula (2), A is Ink absorption of paper (K&N value); G is Paper gloss (specular gloss in 75° angel).

**2.3.2 Test of the Ink Color Effect on Paper**

We used 700 N printing press, 2 ml ink, IGT C1-5 Printability Tester to do the tests when the ink color is yellow, magenta and cyan. We also used X-Rite SpectroEye to measure the solid ink density of the inking paper under RGB color filter and calculated color strength, color deviation, grey level and color efficiency [13].

**3 Experiment Results and Discussion**

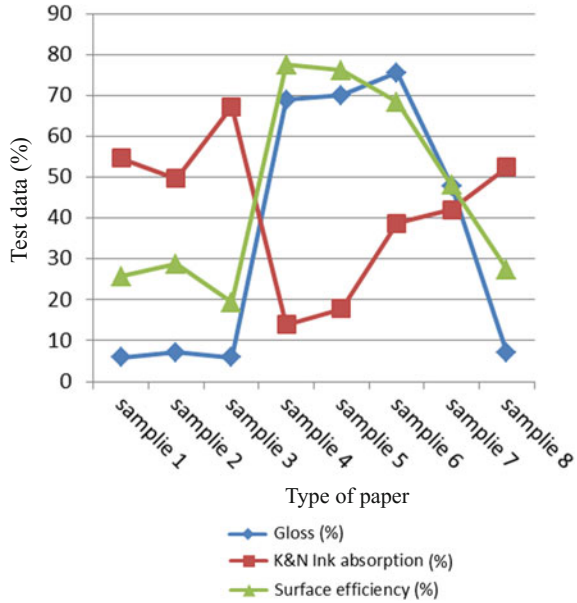
**3.1 Paper Surface Efficiency**

The test results of paper gloss, ink absorption and surface efficiency are shown in Table 1 and Fig. 1.

**Table 1** Test results of paper surface efficiency

Type of paper	Gloss (%)	K&N ink absorption (%)	Surface efficiency( %)	
Sample 1	70 g/m <sup>2</sup> offset paper	5.9	54.6	25.7
Sample 2	80 g/m <sup>2</sup> offset paper	7.1	49.7	28.7
Sample 3	100 g/m <sup>2</sup> offset paper	5.9	67.3	19.3
Sample 4	128 g/m <sup>2</sup> coated paper	68.9	13.9	77.5
Sample 5	200 g/m <sup>2</sup> coated paper	70.0	17.8	76.1
Sample 6	200 g/m <sup>2</sup> single-sided photographic paper	75.5	38.7	68.4
Sample 7	170 g/m <sup>2</sup> UH170 easicolor	47.9	42.0	48.0
Sample 8	48 g/m <sup>2</sup> newsprint	7.0	52.4	27.3

**Fig. 1** Relationship between paper surface efficiency and gloss as well as ink absorption



From Fig. 1 we can know that, the gloss of photographic paper is 75.5%, the highest, and the next are coated paper and UH170 easicolor, the gloss of newsprint and offset paper are quite low since they are not coated paper and the paper structure is rough which leads to the low gloss.

The ink absorption of offset paper and newsprint is relatively great around 50% and the ink absorption of two coated paper is the lowest. Their absorption value is lower than 20%. The reason is that after coating pressure process, the surface structure of coated paper is much tighter, which leads to the peer absorption, while offset paper and newsprint hasn't been processed through coating pressure process and the interspaces of fiber are larger, which leads to great absorption.

From Fig. 1 we can find that the surface efficiency of coated paper and photographic paper is much higher, whose value are both more than 60%, while the value of offset paper and newsprint are less than 30%. Through the analysis of Fig. 1, we conclude that when the gloss of paper is high, its ink absorption is poor and its surface efficiency is great. When the gloss of paper is poor, its ink absorption is high and the surface efficiency is poor. The surface efficiency is determined by the paper gloss and ink absorption. If the paper gloss is high and ink absorption is poor, its surface efficiency is great. From the value of UH170 easicolor, we can find that when the gloss and ink absorption are both great, the surface efficiency is great, too. Therefore in order to get great surface efficiency, high gloss paper should compensate with high absorbency and low gloss paper need to compensate with low absorption.

### 3.2 Influence of Paper Surface Efficiency on Ink Color Effect

The test results of ink color strength, color deviation, grey level and color efficiency are shown in Table 2.

From Table 2 we can find that since the color deviation and grey level of yellow is much lower than the other two in the three primary colors, it is generally known that the color deviation of magnet and the grey level of cyan are used to measure the color change as well as the quality of ink. For color efficiency, we choose the cyan ink as the representative and for color strength, we prefer the largest value among three primary color. In this way we find the Relationship between paper surface efficiency and color ink effect, which is shown in Table 3.

**Table 2** Test results of the influence of paper on ink color effect

Type of paper		Color	Color Filter			Color Strength	Color Deviation	Grey Level (%)	Color Efficiency (%)
			R	G	B				
1	70 g/m <sup>2</sup> offset paper	C	1.67	0.77	0.38	1.59	30.2	22.8	65.6
		M	0.33	1.30	0.87	1.30	55.3	25.3	53.8
		Y	0.01	0.13	1.01	1.0	12.0	1.0	93.1
2	80 g/m <sup>2</sup> offset paper	C	1.59	0.74	0.37	1.67	30.3	23.3	65.9
		M	0.29	1.25	0.82	1.25	55.2	23.2	55.6
		Y	0.01	0.13	1.38	1.4	8.5	0.7	95.1
3	100 g/m <sup>2</sup> offset paper	C	1.67	0.76	0.38	1.59	27.3	22.8	65.1
		M	0.31	1.25	0.83	1.25	55.7	24.8	54.4
		Y	0.01	0.12	1.42	1.3	8.6	0.8	95.0
4	128 g/m <sup>2</sup> coated paper	C	1.96	0.53	0.23	2.25	17.3	11.7	80.6
		M	0.29	1.77	0.96	1.77	45.6	16.4	64.7
		Y	0.02	0.14	1.29	1.6	7.7	1.3	92.5
5	200 g/m <sup>2</sup> coated paper	C	2.23	0.61	0.27	2.23	17.3	12.1	80.3
		M	0.29	1.87	1.01	1.87	45.3	15.5	65.2
		Y	0.02	0.14	1.57	1.6	7.7	1.3	92.4
6	200 g/m <sup>2</sup> single-sided photographic paper	C	2.16	0.66	0.31	2.16	18.9	14.4	80.7
		M	0.35	2.02	1.10	2.02	44.9	17.3	64.1
		Y	0.01	0.12	1.50	1.5	7.4	0.7	95.7
7	170 g/m <sup>2</sup> UH170 easicolor	C	2.25	0.60	0.27	1.96	16.7	12.0	77.5
		M	0.32	2.06	1.06	2.06	42.5	15.5	66.5
		Y	0.02	0.11	1.41	1.4	6.5	1.4	95.4
8	48 g/m <sup>2</sup> newsprint	C	1.75	0.87	0.56	1.75	26.1	32.0	59.1
		M	0.48	1.57	1.11	1.57	57.8	30.6	49.4
		Y	0.03	0.13	1.30	1.3	7.9	2.3	93.8

From Table 3 we can conclude the relationship of paper surface efficiency and color strength, color deviation, grey level, as well as color efficiency, which are shown from Figs. 2, 3, 4, 5, 6, 7, 8 and 9.

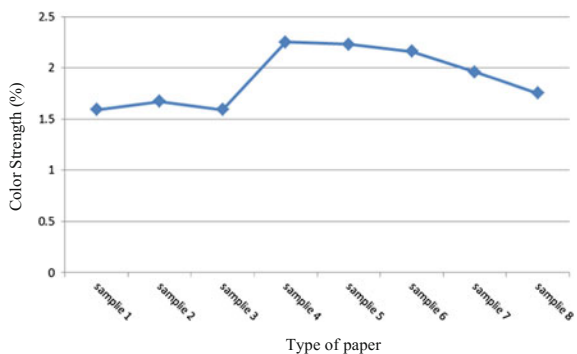
### 3.2.1 Relationship Between Paper Surface Efficiency and Color Strength

Form Fig. 2 we can find that the color strength of coated paper can photographic paper is quite higher while offset paper and newsprint are poorer. In the three types of offset paper, the color strength of 80 g/m<sup>2</sup> is the highest and the strength of 70 g/m<sup>2</sup> as well as 100 g/m<sup>2</sup> is poorer. For coated paper, the strength of 128 g/m<sup>2</sup> is higher than that of 200 g/m<sup>2</sup>. Figure 3 suggests that the gap of the values of color strength and paper surface efficiency is quite significant so their relationship is not clear. However through comparison with Fig. 2, when the paper surface efficiency is higher, the color strength is greater.

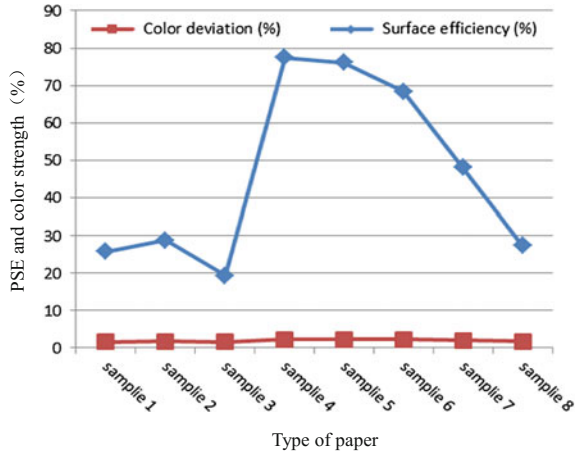
**Table 3** Relationship of paper surface efficiency and color strength, color deviation, grey level, as well as color efficiency

Type of paper		Surface efficiency (%)	Color strength	Color deviation (%)	Grey level (%)	Color efficiency (%)
1	70 g/m <sup>2</sup> offset paper	25.7	1.59	55.3	22.8	65.6
2	80 g/m <sup>2</sup> offset paper	28.7	1.67	55.2	23.3	65.9
3	100 g/m <sup>2</sup> offset paper	19.3	1.59	55.7	22.8	65.1
4	128 g/m <sup>2</sup> coated paper	77.5	2.25	45.6	11.7	80.6
5	200 g/m <sup>2</sup> coated paper	76.1	2.23	45.3	12.1	80.3
6	200 g/m <sup>2</sup> single-sided photographic paper	68.4	2.16	44.9	14.4	80.7
7	170 g/m <sup>2</sup> UH170 easicolor	48.0	1.96	42.5	12.0	77.5
8	48 g/m <sup>2</sup> newsprint	27.3	1.75	57.8	32.0	59.1

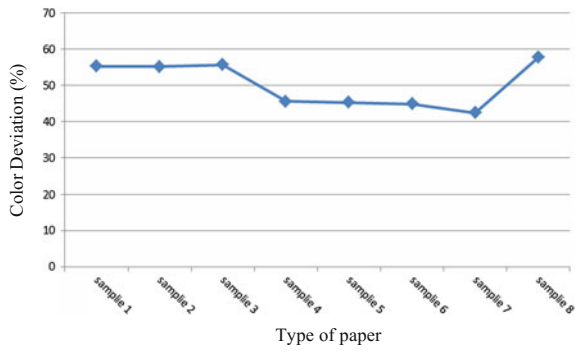
**Fig. 2** Contrast figure of color strength



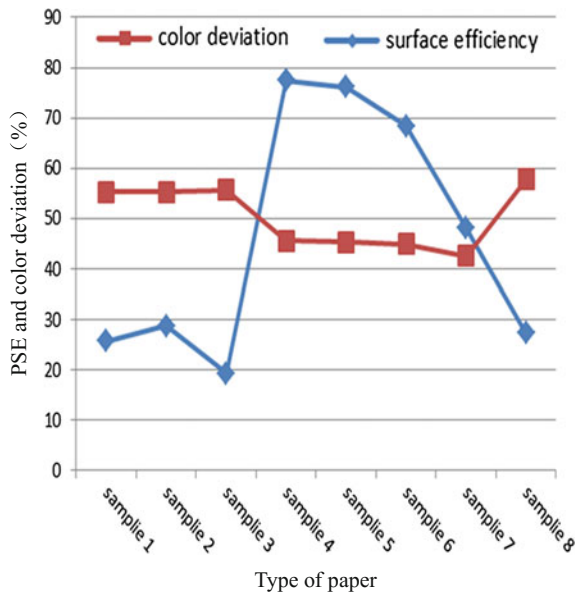
**Fig. 3** Relationship between paper surface efficiency and color strength



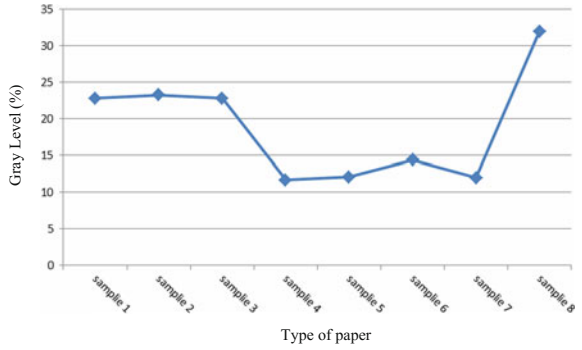
**Fig. 4** Contrast figure of color deviation



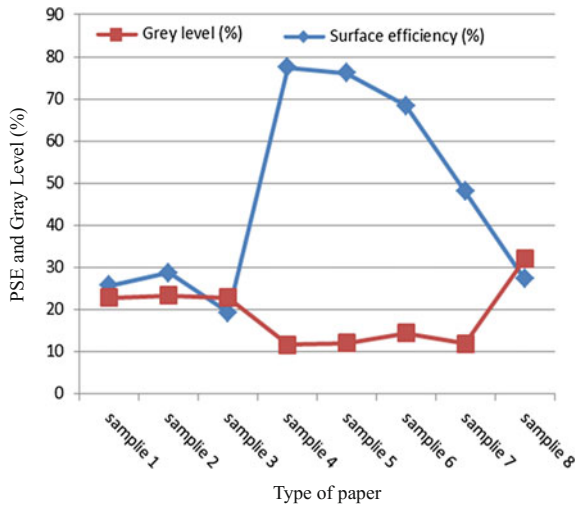
**Fig. 5** Relationship between paper surface efficiency and color deviation



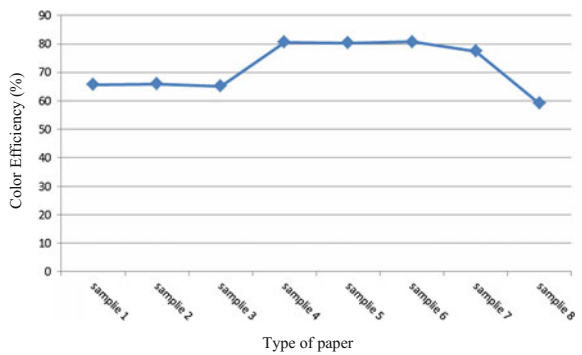
**Fig. 6** Contrast figure of grey level



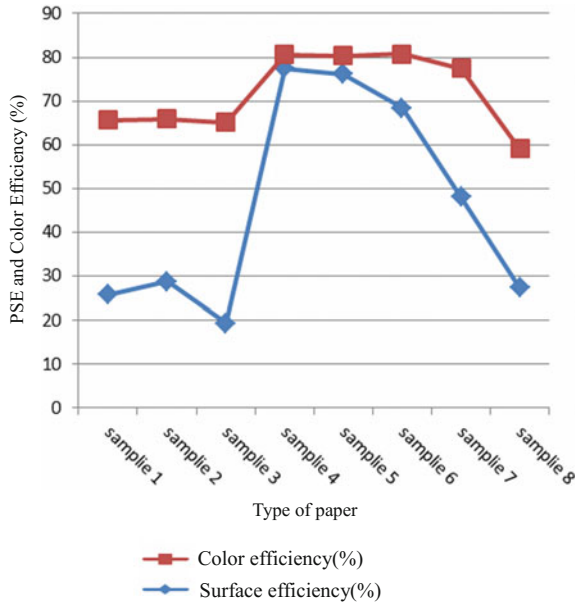
**Fig. 7** Relationship between paper surface efficiency and grey level



**Fig. 8** Contrast figure of color efficiency



**Fig. 9** Relationship between paper surface efficiency and color efficiency



### 3.2.2 Relationship Between Paper Surface Efficiency and Color Deviation

Form Fig. 4 we can see that the color deviation of three primary colors in UH170 is the lowest while offset paper and newsprint are the largest. In the two types of coated paper, the color deviation of 128 g/m<sup>2</sup> is lower than 200 g/m<sup>2</sup>. And as for offset paper, the color deviation of 80 g/m<sup>2</sup> is the lowest while 70 g/m<sup>2</sup> is the second lowest and 100 g/m<sup>2</sup> is the largest. The relationship between color deviation and surface efficiency can be found in Fig. 5. When the surface efficiency is greater, the color deviation is lower, which suggests that paper surface efficiency has great influence on the color deviation of ink color effect.

### 3.2.3 Relationship Between Paper Surface Efficiency and Grey Level

Figure 6 shows that the grey levels of offset paper and newsprint are higher while coated paper, UH170 easicolor and photographic paper are lower. For offset paper, the grey level of 80 g/m<sup>2</sup> is the lowest, and the grey levels of 70 and 100 g/m<sup>2</sup> are higher. And for coated paper, the grey level of 128 g/m<sup>2</sup> is lower than that of 200 g/m<sup>2</sup>. Form Fig. 7 we can see that the influence of surface efficiency on grey level is similar to that on color deviation. When the surface efficiency of paper is higher, the grey level is lower.



### 3.2.4 Relationship Between Paper Surface Efficiency and Color Efficiency

From Fig. 8 we can find that the color efficiency of coated paper and photographic paper is higher, while offset paper and newsprint is much lower. The color efficiency of 128 g/m<sup>2</sup> coated paper is higher than that of 200 g/m<sup>2</sup> coated paper. However for offset paper, the color efficiency of 80 g/m<sup>2</sup> is the highest, 70 g/m<sup>2</sup> is the second highest while 100 g/m<sup>2</sup> is the lowest. From Fig. 9 we can see that the paper of larger size will have greater surface efficiency while the color efficiency of smaller paper is lower.

## 4 Conclusions

There are three types of paper with high surface efficiency. One is the paper with high gloss and poor ink absorption, one is the paper of both high gloss and ink absorption, the other one is the paper with low gloss and poor ink absorption. When the paper gloss is low and ink absorption is high, the surface efficiency is generally great. Therefore if we would like to get paper with great surface efficiency, high gloss paper should compensate with high absorbency and low gloss paper need to compensate with low absorption. Otherwise we can choose paper of high gloss and poor ink absorption.

When the paper surface efficiency is high, under the same printing condition, the ink color strength and color efficiency are both great while the color deviation and grey level is low. On the contrast, when the paper surface efficiency is poor, the ink color strength and color efficiency are both poor while the color deviation and grey level is high. Therefore when considering the ink color effect through paper surface efficiency, it is common that great ink color effect can be seen on the paper with great surface efficiency while awful ink color effect can be seen on the paper with poor surface efficiency.

## References

1. Yang Quan. (2006). Research on the complex and arduous paper printing eligibility - An brief data analysis and introduction of the PPT. *China Printing Supplies Business*. 09: 35–38.
2. Chen Qingtao. (2011). Research on the paper surface properties. *Tianjin Paper Making*. 02: 15–33.
3. Huang Xuelin, Jiang Wenyan. (2014). The influence of paper surface properties on digital printing color reproduction. *China Paper Making*, (12): 29–32.
4. He Zifen (2005). Relationship between printing paper properties and print quality. *Guangdong Printing*, (01): 49–50.
5. Yu Ju Wu. (2008). The effect of substrate properties on print attributes for gravure printing - from proof to press. Western Michigan University, 2008.

6. B. Havlinova, L. Hornakova, V Brezova, et al. (2006). Ink receptivity on paper-characterization of paper materials. *Colloids and Surfaces*, (168): 251–259.
7. O. Norberg, M. Anderson. (2007). The Influence of Paper Properties on Color Reproduction and Color Management. *NIP 19*: 836–840.
8. Yang Song, Zhai Ruyun. (2006). The influence of paper surface efficiency on printing quality. *Printing Quality and Standardization*. (07): 26–27
9. Qi Xiaokun, Zhou Wenhua, Ynag Yonggang. (2014). *Printing material and eligibility*. Second Edition. Beijing: Prinying Industry Press, 68–82.
10. Chen Yongchang. (2004). Performance of printing, ink and printing eligibility. Beijing: Chemistry Industry Press, 115–121.
11. Wang jinling, Gao Yujie. (2009). The effect of paper surface efficiency on print color reproduction. *Packaging Engineering*, (04): 76–77.
12. Tu Jifang (2011). The effect of absorption speed of paper surface on print quality. *Shanghai Packaging*, (10): 54.
13. Tian Huiquan, WangQiang, Liu Haoxue. (2011). *Printing Color Managemnet*. Third Edition. Beijing: Printing Industry Press, 18–23.

# Effect of Different Basic Weight of Paper on Microfluidic Devices Fabricated by UV Inkjet Printing

Yingzhe He, Guangxue Chen and Junfei Tian

**Abstract** The paper studied effect of different basic weight of paper and width of hydrophilic channel on microfluidic devices fabricated by UV inkjet printing. Then, we made 4 different basic weight of paper and tested free diffusion length of liquid on paper that we initially made. Next, we designed a pattern which contains 4 different width of hydrophilic channels, the pattern was printed on paper through Mimaki UV inkjet printer. Through the test results and comparison we could find an optimal condition. The final results were as follows: printing time of ink layer in hydrophobic area is in proportion to the basic weight of paper in a certain range except that printing over 4 layers, the optimal channel width is 2 mm in the condition of ensuring that liquid is normally spreading.

**Keywords** Paper-based microfluidic device · UV inkjet printing · Basic weight

## 1 Introduction

Paper-based microfluidic devices or Microfluidic paper-based analytical devices ( $\mu$ PADs), chip-on-lab for short had been a hot point in recent years of micro analytical field [1]. The traditional materials of fabrication were quartz, glass, silicon, polymers such as PDMS, etc. [2, 3]. Application of paper could be a breakthrough due to the significant advantages: rich resources of paper could greatly reduce production cost, paper mainly composed of cellulose, had a good hydrophilic ability allowing the liquid spreading by capillary force without external

---

Y. He · G. Chen · J. Tian (✉)

State Key Laboratory of Pulp and Paper Engineering,  
South China University of Technology, Guangzhou, China  
e-mail: jftian\_scut@163.com

Y. He  
e-mail: 234237285@qq.com

G. Chen  
e-mail: chengx@scut.edu.cn

power, paper was a highly biocompatible material [4] and could be easily modified to meet the production requirements.

Paper-based microfluidic chips could be traced back to the earliest 17 century and Muller invented chromatography eluting pigment on a thin paper, Whitesides [5] research group first claimed photolithography applied to fabrication of chip in 1988. Martinze connected mobile phone and chip to make a devices realizing long distance monitoring in 2007 and he also the first made a 3D chip by overlapping method [6], Lin research group came up a way of wax printing in 2008 which received a wide range of concentration.

With the development of application of paper chips, the fabrication methods had continuously been innovating, such as photolithography, UV printing, wax printing, and other ways [7, 8]. But not many papers talked about how different basic weight of paper effect on microfluidics. So, this paper aimed to find the effect of different weight of paper and width of hydrophilic channel printed by UV printer.

## 2 Experiment

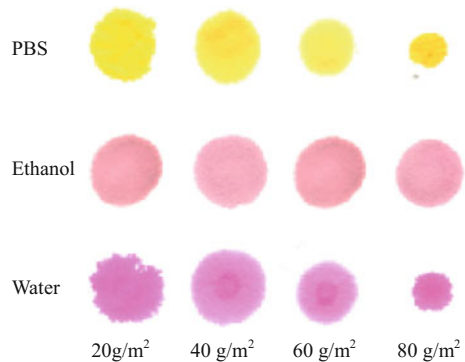
### 2.1 Preparation of Different Weight of Paper

We chose eucalyptus pulp to make 4 kinds of paper with basic weight of 20, 40, 60 and 80  $\text{g/m}^2$ , according to TAPPI hand sheet making standard.

### 2.2 Liquid Penetration Test on Untreated Paper

In order to make diffusion result more apparent, we colored 3 different liquid (PBS, water, ethanol), and dropped 10 $\mu\text{L}$  liquid into the paper, and observed the free diffusion length of different paper. We selected a sample from 5 test points (Fig. 1).

**Fig. 1** Free diffusion of different liquid on different basic weight of paper



### 2.3 Relationship Between Printed Ink Layers and the Hydrophobicity of the Barriers

By printing the hydrophobic pattern on different paper with the condition of increasing printing times, we observed the diffusion results in hydrophobic area after dropping the liquid and found the optimal ink layer (Figs. 2 and 3).

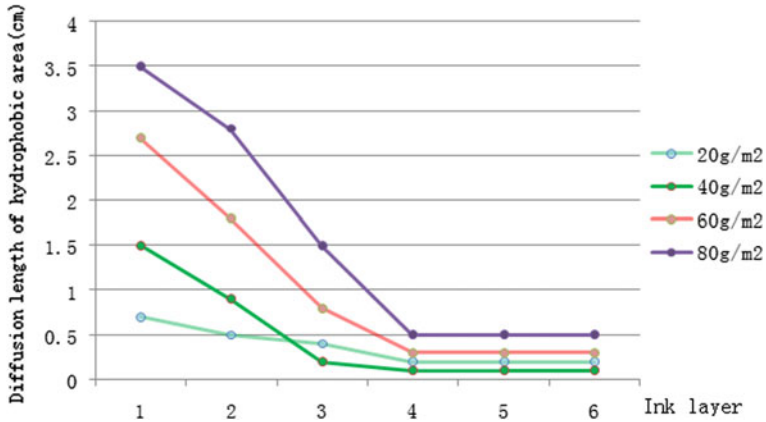


Fig. 2 Diffusion length of liquid spreading to hydrophobic area with different ink layers and basic weight of paper

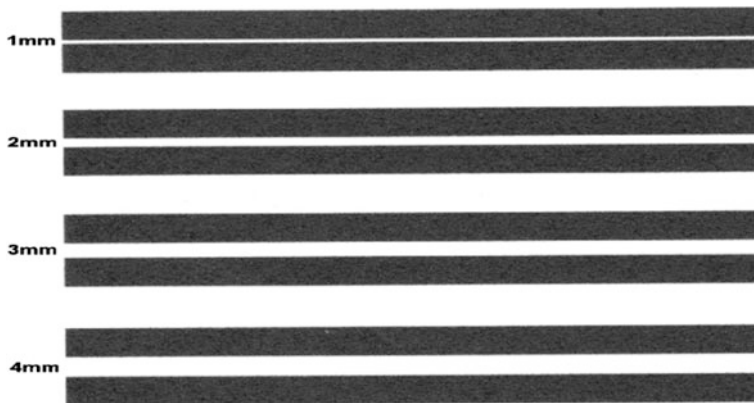
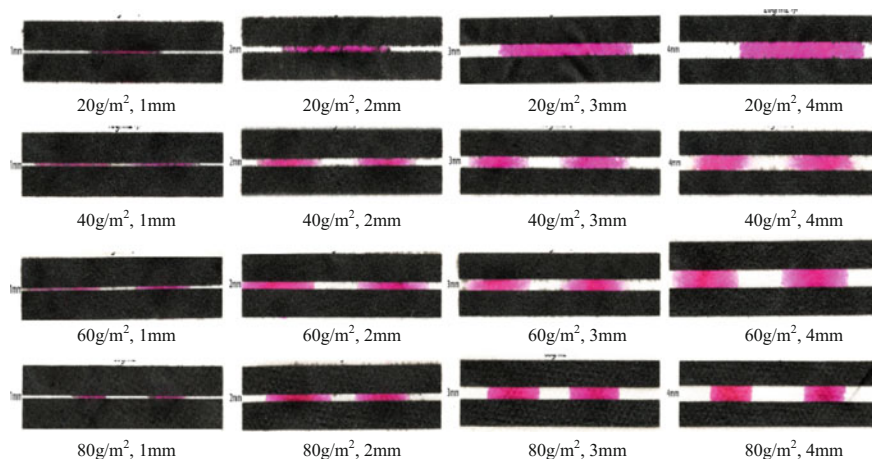


Fig. 3 Printed pattern with different width



**Fig. 4** Water diffusion length of different channels and basic weight of paper

#### ***2.4 Liquid Penetration Test Within Channels on Paper Sheets with Different Weight Basis***

We designed pattern containing a group of different width of hydrophilic channels (1, 2, 3 and 4 mm) through Adobe Illustrator, and printed them on one side of paper and back side was a cover pattern and tested diffusion length (Fig. 4).

#### ***2.5 Fabrication of Paper-Based Microfluidics and the Glucose Test and Protein Test***

Through the experimental results, we selected paper with 20 g/m<sup>2</sup>, 2 mm width of hydrophilic channel and 4 times of printing to fabricate the microfluidics using UV printer. We used enzyme system (GOD, HRP, potassium iodide) to test glucose, (Tbpb, PBS) to test protein [5–8]. We could observe the change of the color.

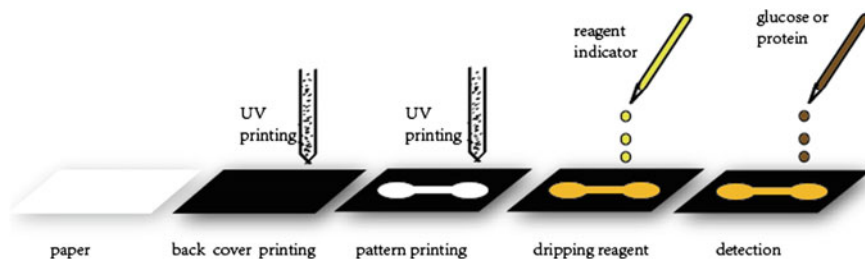
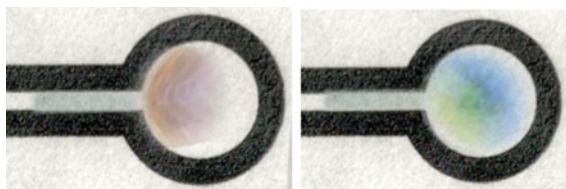
### **3 Results and Discussion**

According to the test results, we recorded the data shown in Table 1.

We found that the free diffusion length of the liquid decreased with the increasing of basic weight of paper, this is probably a consequence of high basic weight of paper contained much more cellulose which could absorb water (Figs. 5 and 6).

**Table 1** Penetration length of different paper

	20 (g/m <sup>2</sup> )	40 (g/m <sup>2</sup> )	60 (g/m <sup>2</sup> )	80 (g/m <sup>2</sup> )
Untreated paper	1.9	2.0	1.7	1.0
1 mm width	3.2	3.0	2.6	1.3
2 mm width	5.0	2.7	3.0	2.8
3 mm width	4.9	2.5	2.6	2.1
4 mm width	4.3	2.6	2.7	1.9

**Fig. 5** Process of fabricating of microfluidics by UV printing**Fig. 6** Test results of glucose and protein

It's apparently that the printing times of the hydrophobic pattern should be increased to ensure a good hydrophobic effect with the increasing of basic weight of paper, when printing over 4 times, the diffusion length of liquid remained stable.

Not only the basic weight of paper but also the width of hydrophilic channel would affect the diffusion length of liquid. According from the experimental results, the most effective width of channel would be 2 mm with 20 g/m<sup>2</sup> of paper that could appear the longest diffusion length.

## 4 Conclusions

We believed that basic weight of paper was really an important factor for fabricating paper-based microfluidic devices. In addition, printing times of hydrophobic pattern and width of hydrophilic channel would also have an impact when using UV inkjet printing to finish the fabrication. Finally, we got that 2 mm width of

channel along with 20 g/m<sup>2</sup> of paper, printing 4 times of hydrophobic pattern to fabricate the paper-based microfluidic devices would reach the most optimal results.

**Acknowledgements** This research was financially supported by State Key Laboratory of Pulp and Paper Engineering (2015TS01), National Natural Science Foundation of China (81671780), and the Guangdong Provincial Science and Technology Project (2013B010401007).

## References

1. Martinez A W, Phillips S T, Butte M J, Whitesides G M. (2007). Patterned paper as a platform for inexpensive, low-volume, portable bioassays. *Angewandte Chemie International Edition*, 46: 1318–1320.
2. Martinez A W, Phillips S T, Wiley B J, Gupta M, Whitesides G M. (2008). FLASH: a rapid method for prototyping paper-based microfluidic devices. *Lab on a Chip*, 8: 2146–2150.
3. Kentaro Yamada, Terence G. Henares, Koji Suzuki, and Daniel Citterio. (2015). Paper-based inkjet-printed microfluidic analytical devices. *Angewandte Chemie International Edition*, 54: 5294–5310.
4. Wang, J. (2008). Electrochemical glucose biosensors. *Chemical Reviews*, 108: 814–825.
5. Bruzewicz D A, Reches M, Whitesides G M. (2008). Low-Cost printing of poly (dimethylsiloxane) barriers to define microchannels in paper. *Analytical Chemistry*, 80: 3387–3392.
6. Al-Tamimi M, Shen W, Zeineddine R, Tran H, Garnier G. (2012). Validation of paper-based assay for rapid blood typing. *Analytical Chemistry*, 84(3): 1661–1668.
7. Schilling K M, Lepore A L, Kurian J A, Martinez A W. (2012). Fully enclosed microfluidic paper-based analytical devices. *Analytical Chemistry*, 84: 1579–1585.
8. Zhu W J, Feng D Q, Chen M, Chen Z D, Zhu R, Fang H L, Wang W. (2014). Bienzyme colorimetric detection of glucose with self-calibration based on tree-shaped paper strip. *Sensors and Actuators B*, 190: 414–418.



# Performance Study of Flexible Capacitive Pressure Sensor Based on Dielectric Structures

Qichao Hou, Mengmeng Liang, Ruping Liu and Wei Wang

**Abstract** In recent years, with the emergence of the flexible electronic devices for artificial skin, wearable electronics, robotics, etc., more and more attention has been paid to the flexible force sensor. In this study, we designed and fabricated a flexible capacitive pressure sensor with unique washer structure and dielectric layer microstructure. The sensor consists of the flexible substrate, main dielectric and the electrode materials, using polyethylene terephthalate (PET) film, the air and the silver nanoparticles (AgNPs), respectively. Then, we systematically investigated the effect of the thickness of the washer and dielectric layer microstructure on the performance of the flexible capacitive pressure sensor. It shows that the thinner the thickness of the washer, the better the sensitivity of the sensor. However, it might lead to the degraded performance in terms of the repeatability and the stability. Besides, the dielectric layer microstructure has also a significant effect on the performance of the sensor. Furthermore, the sensitivity of the single-layer microstructure sensor is superior to those of the double-layer microstructure and no-microstructures. In respect of the stability and the repeatability of the sensor, double-layer microstructure sensor is best, followed by the single-layer microstructure and the no-microstructure. In summary, the highest sensitivity of the sensor we fabricated is  $0.17 \text{ kPa}^{-1}$ , and the minimum detectable pressure is several pF. It has a large dynamic range and stable performance. Thus, our sensor can be widely used in many applications in the emerging fields of medical testing equipment and robotics.

**Keywords** Flexible pressure sensor · Capacitive · Thin-film · Microstructure

---

Q. Hou · M. Liang · R. Liu · W. Wang (✉)  
Beijing Engineering Research Center of Printed Electronics,  
Beijing Institute of Graphic Communication, Beijing, China  
e-mail: 18900616029@189.cn

© Springer Nature Singapore Pte Ltd. 2017  
P. Zhao et al. (eds.), *Advanced Graphic Communications  
and Media Technologies*, Lecture Notes in Electrical Engineering 417,  
DOI 10.1007/978-981-10-3530-2\_65

515

## 1 Introduction

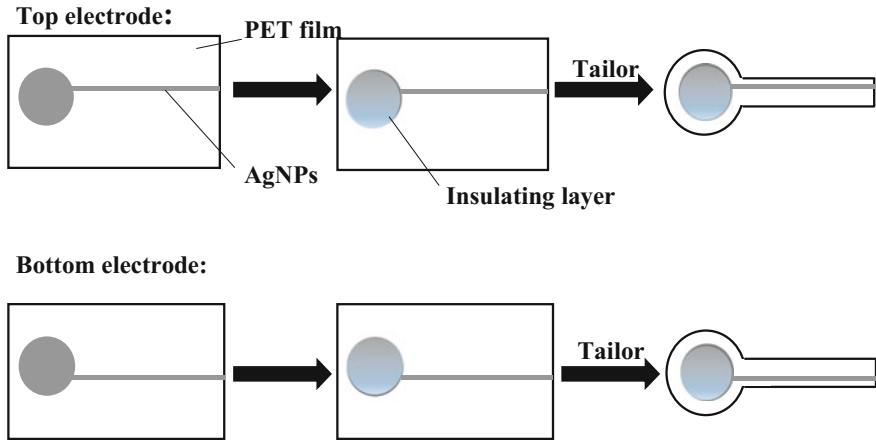
With the emergence of the wearable devices for robotics [1], artificial skin [2], health monitoring devices [3] and flexible displays [4], there is an increasing demand for flexible thin film sensors [5]. Flexible capacitive pressure sensor is one of the most useful flexible sensors and there are many studies on its design, material, fabrication, and performance analysis. Ting Zhang [6] et al., in Suzhou Nano Institute, Chinese Academy of Sciences, fabricated a highly-sensitive sensor, with 0.6 Pa of the minimum detection limit, by transferring silk microstructures to the sensor electrode. Zhenan Bao et al., in Stanford University [7] designed the microstructure cilia on the sensor surface, greatly improving the sensitivity and resolution of the device. Lee et al., in University of Michigan [8] fabricated the sensor with the sensitivity up to  $0.03 \text{ mN}^{-1}$ , the response time less than 160 ms, and the detection range in 0–20 mN, by evaporating copper electrode on the surface of polydimethylsiloxane (PDMS), and adopting hollow structure as a dielectric layer. These results have shown that flexible capacitive pressure sensor exhibits the outstanding sensitivity and response speed performance. However, due to the complexity and high cost of the fabrication of the device, the large volume production of such sensor is still limited.

In our work, we designed a flexible capacitive pressure sensor with unique washer structure and dielectric layer microstructure. The sensor consists of the flexible substrate, main dielectric and the electrode materials, using polyethylene terephthalate (PET) film, the air and the silver nanoparticles (AgNPs), respectively. The dynamic range of the sensor is large from several grams to 100 kg. In this study, we carry out the performance study for this sensor. We mainly studied the effect of the thickness of the washer and dielectric layer microstructure on the performance of the flexible capacitive pressure sensor. We also did a preliminary exploration of its application performance and prospects.

## 2 Experimental Parts

### 2.1 *Electrode Preparation*

We use screen printing to prepare an electrode of the sensor. Firstly, taking a certain mass fraction of the AgNPs (laboratory-made [9]), using polyethylene terephthalate (PET) film as printing substrate, with the help of semi-automatic screen printing machine (OLAT, OS300FV, Hong Kong), silver electrodes were printed on the PET film (including the top and bottom electrodes, each possessing a circular electrode plate and an electrode lead). Then the electrodes were being sintered, by heating 2 h at 80 °C. Next, we print a layer of insulating material on the printed circular electrode plate, so as to isolate the two silver electrodes of the sensor, and prevent contact shorting. After printing, the PET film which printed on silver



**Fig. 1** Fabrication process of the electrode

electrode and insulating layer was cut into a certain shape. Specific production process was shown in Fig. 1.

## 2.2 Sensor Packaging

The sensor package includes an annular washer and bonding the upper and lower electrodes, and the production of lead terminals of the sensor. The specific production process is as follows: After cutting the printing electrode into the shape, shows in Fig. 1, the edges of PET was coated with adhesive. Then, the annular washer is placed in the middle of the upper and lower electrodes. It can be fitted tightly under certain pressure. Followed by heating 1 h at 65 °C, the adhesive is being to dry. After the upper and lower electrode with the annular washer fit, we use automatic double-headed terminal machines (BESTON, BST06A, China) to make the terminal at the end of the electrode lead terminals. The packaging process was shown in Fig. 2.

## 2.3 Performance Testing

During the test, we used a capacitance measuring instrument (Tonghui, TH2617, China) to clamp the two two-pin end of the sensor and use digital force gauge (Fort Eide, HP-50) to make a pressure on the surface of the sensor. As the pressure change, the distance between the two plates of the capacitive sensor will change, so that the capacitance of the sensor was changed. Finally, we test and record the changes of the capacitance at different pressure sensors.

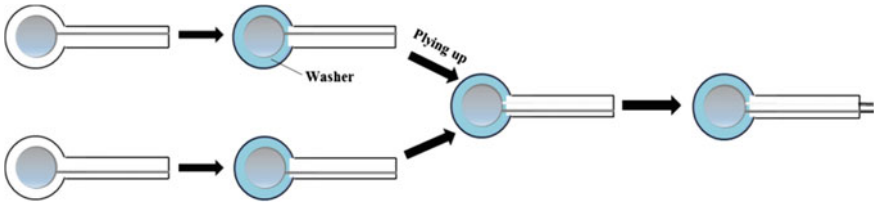


Fig. 2 Package process of the sensor

### 3 Results and Discussion

#### 3.1 Effect of Washer Thickness on the Sensor Performance

Repeatability and sensitivity are two important factors of the measure of the sensor. The sensitivity of the capacitive sensor can be defined as:

$$S = \frac{\delta(\Delta C/C_0)}{\delta P} \quad (1)$$

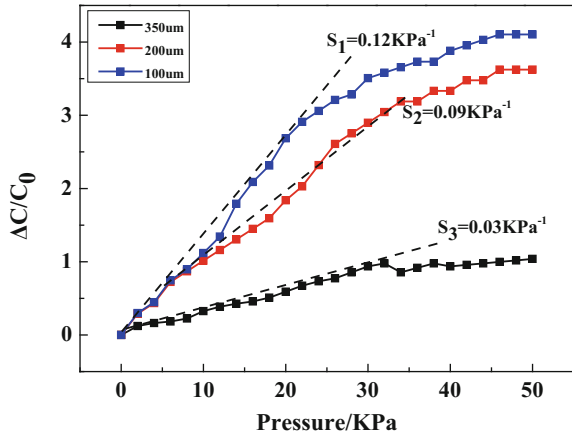
$$\Delta C = C - C_0 \quad (2)$$

where  $C$  is the capacitance of the sensor, and  $C_0$  is the capacitance value of the sensor corresponding to the zero pressure.  $P$  is the applied pressure. The repeatability of the capacitive sensor is the changeable of the value of capacitance sensor, in the condition of the repeated measurement in the same sensor at the same pressure range. The small change of the capacitance value indicates the good repeatability of the sensor, and vice versa.

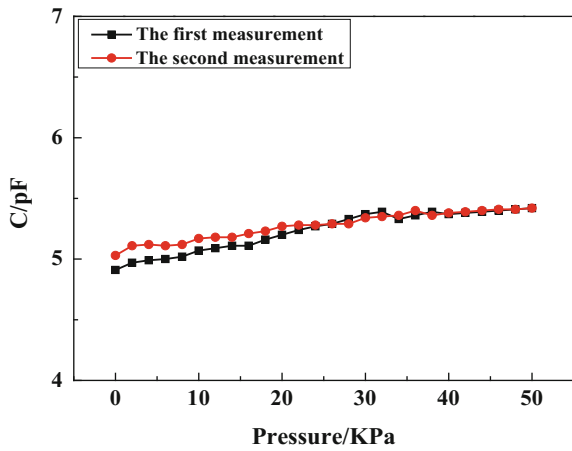
In this work, we used three different sensors with 100, 200 and 350  $\mu\text{m}$  thickness washer in experiment. The sensitivity characteristic curve was shown in Fig. 3. It showed that, in certain pressure range, the thinner the thickness of the washer, the better the sensitivity of the sensor. It can be explained that the sensor's sensitivity is inversely proportional to the initial distance between the two parallel plates. The thinner the thickness of the washer, the smaller the initial distance.

Figures 4, 5 and 6 represent three different washer thicknesses repeating characteristic curve of the sensor. It showed that significant difference exists in the repeatability of three kinds of sensor. The thicker the thickness of the washer, the better the repeatability of the sensor. It may be understood that the thicker the thickness of the washer, the more the air (possessing good spring) that can be encapsulate, the faster the sensor capacitive returning to the original value, in the condition of the certain pressure.

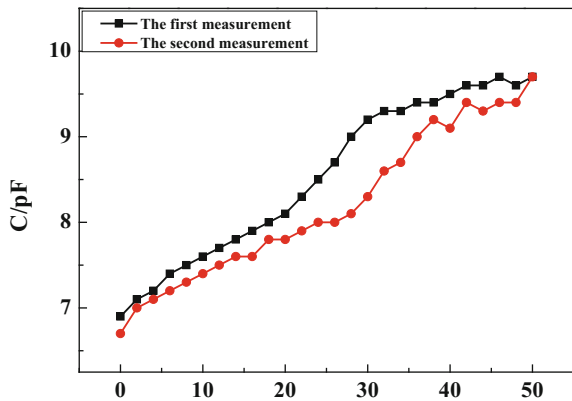
**Fig. 3** Capacitive change of the flexible pressure sensors with different washer thickness



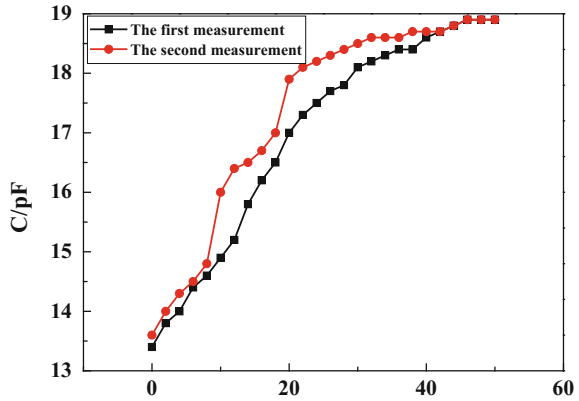
**Fig. 4** Repeatability of the flexible pressure sensor with 350  $\mu\text{m}$  washer thickness



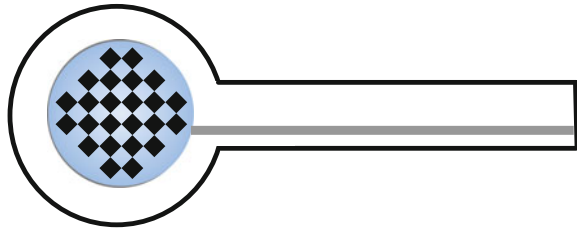
**Fig. 5** Repeatability of the flexible pressure sensor with 200  $\mu\text{m}$  washer thickness



**Fig. 6** Repeatability of the flexible pressure sensor with 100  $\mu\text{m}$  washer thickness



**Fig. 7** Sensor electrode printed with microstructure



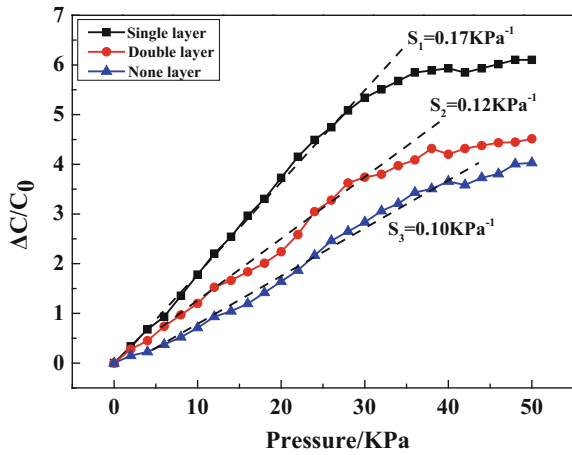
### 3.2 Effect of Dielectric Layer Structure on the Sensor Performance

In the study of the impact of the dielectric layer structure on the sensor performance, we will print the microstructure on the insulating layer of the sensor electrode, as shown in Fig. 7. Each microstructure unit possess diamond-shaped, with about 1 mm side length and about 25  $\mu\text{m}$  thickness. In our study, we mainly studied and analyzed the performance and features of three different sensors with no microstructure, a single-layer and double-layer microstructure.

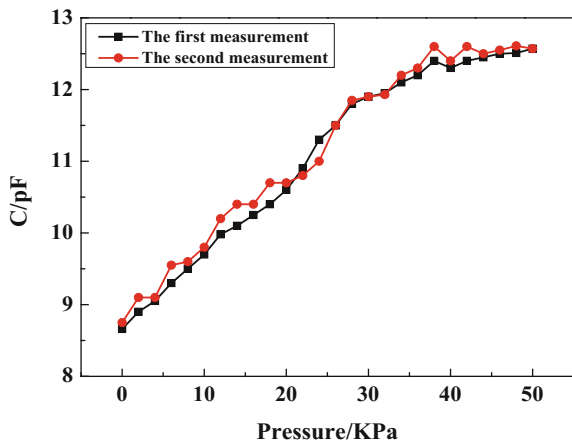
Sensitivity characteristics curves of different layers microstructure sensor were shown in Fig. 8. It showed that the sensitivity of the single-layer microstructure sensor is the best. Microstructure can improve the performance of the sensor in a certain degree. However, the big thickness of the microstructure also affects the performance of the sensors. The existence of microstructure, make the dielectric constant of the sensor changeable within a certain range. At the same time, microstructure has certain elasticity, makes a better sensitivity of the sensor. The combined actions of the two factors result in the improvement of the performance of the sensor.

Figures 9, 10 and 11 represent the repeatability curve of three sensors with different layers of microstructure. As we can see from the figure, with respect to the repetitive of the sensor, double microstructure sensor is the best. Relatively

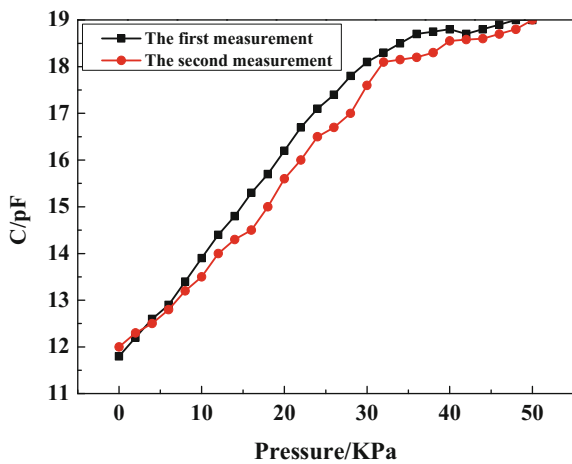
**Fig. 8** Capacitive change of the flexible pressure sensors with different dielectric layer



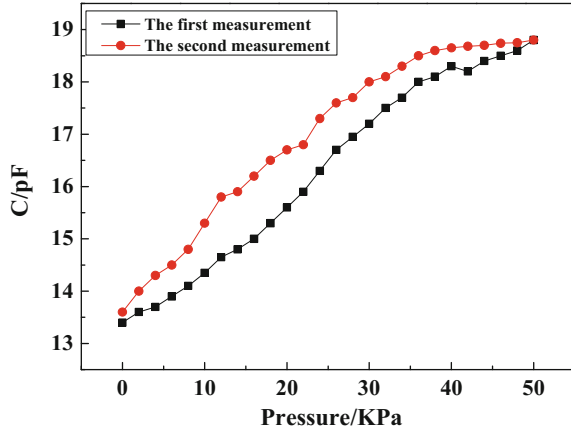
**Fig. 9** Repeatability of the flexible pressure sensor with double microstructure layer



**Fig. 10** Repeatability of the flexible pressure sensor with single microstructure layer



**Fig. 11** Repeatability of the flexible pressure sensor with no microstructure layer



speaking, the resilience of the double microstructure is better. Therefore, when the pressure is applied to the sensors within a certain range, the repeatability of the sensor with double microstructure is better than the two others.

## 4 Summary

In this study, we designed a new type of flexible capacitive pressure sensor, with unique washer structure and dielectric layer microstructure. The sensor is suitable for large volume manufacture and has a large dynamic range. We systematically investigated the effect of the thickness of the washer and dielectric layer microstructure on the performance of the sensor. The results have been shown that the thinner the thickness of the washer, the better the sensitivity of the sensor. However, the repeatability and the stability of the sensor will be degraded. Besides, the dielectric layer microstructure has also a significant effect on the performance of the sensor. The sensitivity of the single-layer microstructure sensor is the best. With respect to the repeatability of the sensor, double microstructure sensor is the greatest. Thus, it is important to choose the appropriate washer thickness and microstructure to obtain good performance. Due to its many advantages, the proposed sensor can be widely used in applications of medical testing equipment, robotics and artificial skin.

**Acknowledgements** This study is supported by the National Natural Science Foundation of China (61501039), the Beijing Research Grant (No. Z15110000915071), the Beijing Natural Science Foundation (2162017), the Initial funding for the Doctoral Program of BIGC (27170116005/039), and the Elite Program of BIGC (27170116004/019).



## References

1. S. Yao and Y. Zhu. (2014). Wearable multifunction sensors using printed stretchable conductors made of silver nanowires, *Nanoscale*: 62345–2352.
2. T. Yamada, Y. Hayamizu, Y. Yamamoto, Y. Yomogida, A. Izadi-Najafabadi, D.N. Futaba and K. Hata. (2011). A stretchable carbon nanotube strain sensor for human-motion detection, *Nat. Nanotechnol.* 6: 296–301.
3. S. Gong, W. Schwalb, Y. Wang, Y. Chen, Y. Tang, J. Si, B. Shirinzadeh and W. Cheng. (2014). A wearable and highly sensitive pressure sensor with ultrathin gold nanowires. *Nat. Commun.* 5: 3132–3139.
4. J. Liu, C. Yang, H. Wu, Z. Lin, Z. Zhang, R. Wang, B. Li, F. Kang, L. Shi and C. P. Wong. (2014). Future paper based printed circuit boards for green electronics: fabrication and life cycle assessment. *Energy Environ. Sci.* 7: 3674–3682.
5. S. Yao. (2009). Research status and prospects of remote sensing technology. *Science and Technology Information.* 1931–1935.
6. X. Wang, Y. Gu, Z. Xiong, Z. Cui and T. Zhang. (2014). Silk-molded flexible, ultrasensitive, and highly stable electronic skin for monitoring human physiological signals. *Adv. Mater.* 26: 1336–1342.
7. D9. J. Lipomi, M. Vosgueritchian, B.C-K. Tee, S.L. Hellstrom, J.A. Lee, C.H. Fox and Z. Bao. (2011). Silk-like pressure and strain sensors based on transparent elastic films of carbon nanotubes, *Nat. Nanotechnol.* 6: 788–792.
8. H.-K. Lee, S.-I. Chang and E. Yoon. (2006). A flexible polymer tactile sensor: fabrication and modular expandability for large area deployment. *J. Microelectromech. Sys.* 15: 1681–1686.
9. W.W. Li, L.H. Li, X.W. Hu, H. Fang, X. Leng, W.B. Li and S.K. Li. (2011). Influence of concentration modes on morphology of nano-silver. *Mat. Sci. Forum.* 694: 284–287.

# Paper Suitable Analysis Based on Printed Electronics

Zhongmin Jiang and Yingmei Zhou

**Abstract** With the development of printed electronic, the material cost needs change from film or glass to paper which is very convenient and lower cost for users. The papers suitable for printed electronics was studied based on one layer circuit. An exploratory experiment was designed to evaluate the relationship between designed line width and visual lines. According to the surface uniform and luminescent data, the rules should be gotten with different type papers. Coated paper, paperboard and offset paper have different characters in printed electronics. Coated paper is more variable than paperboard. The luminance and surface uniform data show the result that art paper and paperboard are more suitable than the other two kinds of paper in printed electronics with substrate.

**Keywords** Printed electronics · One-layer circuit · Subtract · Coated paper · Uniform · Luminescent

## 1 Introduction

Printing technology is one of service fields, specially get the added values [1] from 3D printing, printed electronics. Printed electronics circuits devices are applied with fabricated on flexible plastic, thin metal substrates [2]. The application includes solar photo-voltaic [3], flexible display, lighting, electronic devices and circuits, integrated intelligent systems and other cutting-edge areas [4].

---

Z. Jiang

Publishing and Printing College, University of Shanghai for Science and Technology, Shanghai, China

Y. Zhou (✉)

Printing and Packaging Department, Shanghai Publishing and Printing College, Shanghai, China

e-mail: wintersweet0605@163.com

© Springer Nature Singapore Pte Ltd. 2017

P. Zhao et al. (eds.), *Advanced Graphic Communications and Media Technologies*, Lecture Notes in Electrical Engineering 417, DOI 10.1007/978-981-10-3530-2\_66

525

Traditional electronic manufacturing technology in the high temperature process on the substrate material has certain requirements, flexible substrate materials, such as plastic film, paper, fiber and so on it is difficult to realize the electronic manufacturing [5]. The choice of substrate is usually considered as follows: physical mechanical strength, thermal stability, weather resistance, chemical stability, optical properties, surface roughness and permeability [6]. Paper as the most common economic benefits of the media, is the future of intelligent packaging industry [7] must be considered factors. This experiment is aimed at the low cost of different types of paper printed circuit application to expand the experimental research, the low cost and practical application of the material to provide data.

## 2 Experimental

This experimental was designed in Adobe Illustrator with different width lines, which included 1, 2, 3, 4, 6, 7, 8, 9 and 10 pt lines with same distance between every two lines. The designed lines are all black color lines to find the rules among width, uniform and luminance. Then the accurate line width for future circle design was got. Figures 1 and 2 were both printed by traditional printing technologies. The line width and uniform were measured with QEA (Quality Equipment Analysis device), The luminance was measured by Illumino Meter.

The lines in Figs. 1 and 2 were printed by screen printing technology. Figure 1 was output on paperboard, coated paper, art paper and offset paper. The lines on different type papers will get different variable resistance and suitable line width for next step. Figure 2 will design the circle lines width proper result from Fig. 1. According to uniform and luminance from measurement data of different papers, the suitable paper for silver circle will be chosen correctly.

The paper is very common in commercial application with low cost and portability. This experimental process silver ink was supplied by Du-pond 5025 type. The products were heated under 120 °C temperature for 15 min after printing.

**Fig. 1** Different width lines



Fig. 2 Designed circuit

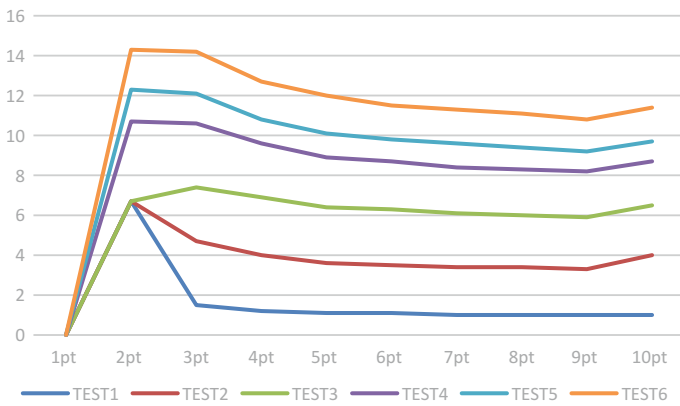
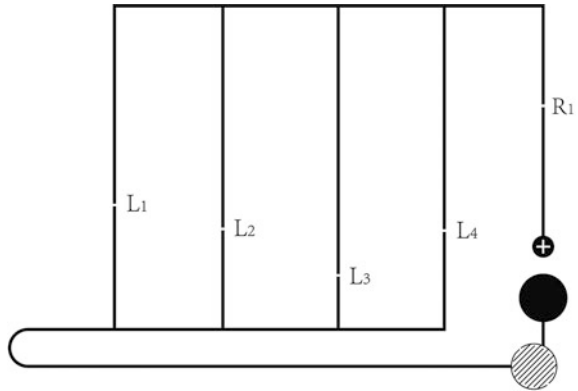


Fig. 3 Different samples width and resistance

### 3 Data Comparison and Discussion

According to the data and chart in Fig. 3, the resistance before 2 pt width is steep and the resistance after 2 pt is steady. The definition of resistance formula is  $R = \rho l/S$ . As we can see, the area and resistance value is inverse ratio. To keep the low cost and steady R value, the suitable line width between 2 pt and 3 pt is recommended. The designed circle line in Fig. 2 will choose 2 pt and 3 pt width, round 1 mm.

The design line width on paperboard, coated paper, art paper and offset paper is about 1 mm. The electronic line width and printed line width have gap difference. That's why the higher reflection on the coated paper will get the less absorbing silver ink on the paperboard [8]. According to the paper suitable and the definition of ISO 13660 [9], the line quality parameter properties was analyzed [10]. The disposed art paper was rough with high roughness, and the silver ink permeate into

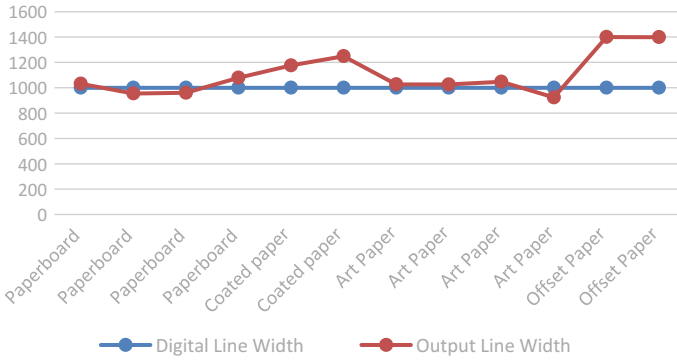


Fig. 4 Designed line width and printed line width

Table 1 Different paper with uniform and average luminance value

Paper type	Roughness	Blurriness	Uniform	Luminance
Paperboard	6.42	274.06	1.28	149.77
Paperboard	9.65	244.02	2.08	271.67
Paperboard	14.48	268.21	1.84	314.67
Paperboard	19.76	242.48	8.29	292.00
Coated paper	8.08	506.45	5.26	253.33
Coated paper	12.26	456.42	10.33	260.00
Art paper	8.93	245.92	1.22	140.13
Art paper	5.87	282.9	2.75	436.67
Art paper	12.63	224.21	1.92	352.00
Offset paper	27.24	308.95	8.13	48.40
Offset paper	35.6	301.21	11.39	67.37
Offset paper	6.2	288.85	2.04	58.93

paper surface which cause line width thicker [11]. The paperboard and art paper have same digital file line width and output line width. The coated paper and offset paper have not same line width between digital file and printed line (Fig. 4).

The luminance data [12] of LED was gotten by many times measurement in this study. The roughness, blurring and uniform on all kinds of papers influence the luminance. The data is shown in Table 1.

The uniform value change on paperboard and art paper is small. The reason should think about the relationship between printed suitable [13] and roughness. The coated paper and offset paper did the reverse side. The luminance data of LED on art paper is higher than other three. The result showed the art paper is the most suitable paper for printed electronics in Fig. 5.

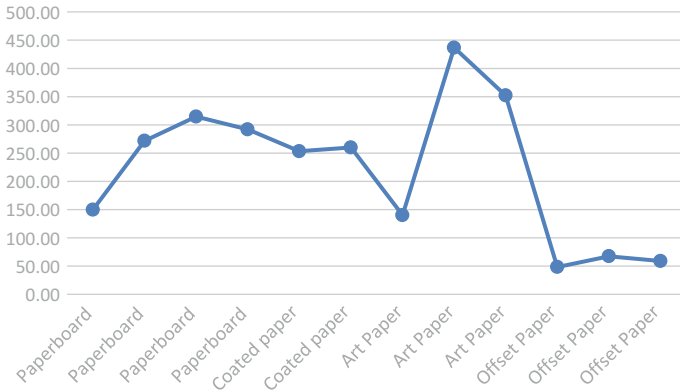


Fig. 5 Different luminance value

### 4 Results and Conclusions

By the assistant of Image Capture device and luminance theory [14], the experimental data is useful for reducing cost of business products on printed electronics [15] promotion. The result was included below:

- (1) Printed electronics circle line width influenced the products conductivity. It is very important to get the suitable resistance and line width from measurement.
- (2) Recently, film, paper and other low cost substrate are all options for printed electronics products. The digital file and printed file of line width have fluctuation range caused by paper surface roughness and smoothness property among different kinds of papers. The ink permeating on offset paper and coated paper is more than paperboard and art paper.
- (3) The data of uniform, blurriness and luminance showed the higher uniform value the lighter of luminance value. The measured luminance value and luminance value of art paper and paperboard have the same result with visual inspection.

This experimental studied the printed electronics line width and suitable paper type. The result will guide the future packaging and personalized printing development which promote the low cost printed electronic products application.

**Acknowledgements** This study was Supported by Innovation Program of Shanghai Municipal Education Commission (Grant No.: 14YZ172).

## References

1. Xiong xingfu. (2014). Solar photovoltaic application products. *Packaging Engineering*, 35 (24): 35–38.
2. Cui Zheng. (2013). Status and prospects of the printed electronics industry in China. *Printed Electronics*, 12: 4–7.
3. Hübler Arved. Trnovec Bystrík, Zillger Tino. (2011). Printed paper photovoltaic cells. *Advanced Energy Materials*, 1(6): 1018–1022.
4. Zou jing. (2014). Review of progress in printed electronics industry. *Imging Science and Photochemistry*, 32(4): 342–381.
5. Sunjiazhen. etc. (2014). Overview printed electronics technology. *Screen Printing Industry*, 8: 27–29.
6. Wu wei. (2014). Educational reform of printing engineering program under the background of developing printed electronics. *Packaging Journal*, 6(4): 88–92.
7. Fan Meijuan. (2012). Concept and classification of intelligent packaging. *Printing Quality and Standardization*, 2: 10–14.
8. Wang Lei. Liu Jing. (2014). Research progress of liquid metal printing ink. *Imging Science and Photochemistry*, 32(4): 382–390.
9. International Standard ISO 13660. (2001). Information technology — Office equipment — Measurement of image quality attributes for hardcopy output — Binary monochrome text and graphic images.
10. YAO Hai-gen. (2011). Proposed Test Regulation to Edge Quality of Lines. *China Printing and Packaging Study*, 3(5): 28–33.
11. ZHOU Ying-mei, JIANG Zhong-min. (2012). Effect of Paper Types on the Digital Printing Noise. *China Printing and Packaging Study*, (2): 83–89.
12. Veronica Kopp. (2011). Design and Production Aspects of an Electroluminescent Segment Display.
13. Roger Bollström. (2014). Impact of humidity on functionality of on-paper printed electronics. *Nanotechnology*, 25.
14. Xiaoying Rong. (2010). Characterize Screen Printing Parameters for Electroluminescent Inks. California Polytechnic State University.
15. Vivek Subramanian. (2009). Printed electronics for low-cost electronic systems: technology status and application development. *China Printing And Packing Study*, Vol.01 No.03

# Water Washing Improving the Conductivity of Flexography Printed ITO-Free Transparent Electrode for Polymer Solar Cells

Yi Fang, Lu Fu, Yuanyuan Li, Yafang Feng, Shiqi Zhu, Yanfang Xu, Li Yang and Luhai Li

**Abstract** This work demonstrated a simple method to obtain polymer solar cells used high conductivity transparent electrode by flexography printing and water washing treatment. The silver grid of square and hexagon shapes was fabricated by flexography printing on poly(ethylene terephthalate) (PET) substrate. The silver pattern was firstly dried in an oven under 120 °C, then was placed into the deionized water. The sheet resistance of two shape grid is reduced nearly two orders of magnitude to those without water washing. The ITO-free polymer solar cells based on poly(3-hexylthiophene) (P3HT) and [6, 6]-Phenyl C<sub>61</sub> butyric acid methyl ester (PCBM) was fabricated. The poly(3, 4-ethylenedioxythiophene) poly(styrene sulfonate) (PEDOT:PSS) was coated on the transparent electrode as the anode modification layer. The confocal laser scanning microscope (CLSM) showed the morphological changes of the two silver patterns after water washing and the PEDOT: PSS coating. We completed two devices by spin coating the active layer and vacuum thermal evaporating cathode. The device with hexagon shape silver grid achieved a power conversion efficiency of 0.37%.

**Keywords** Water washing · Flexography · Transparentelectrode · Polymer solar cells

---

L. Fu · Y. Li · Y. Feng · S. Zhu · Y. Xu · L. Yang  
School of Printing and Packaging Engineering,  
Beijing Institute of Graphic Communication, Beijing 102600, China

Y. Fang (✉) · L. Li  
Beijing Engineering Research Center of Printed Electronics,  
Beijing Institute of Graphic Communication, Beijing 102600, China  
e-mail: fangyi@bigc.edu.cn



## 1 Introduction

Polymer solar cells (PSCs) have attracted broad interests as a viable technology for low-cost power production today, due to their unique advantages, such as light weight, low-temperature fabrication and compatibility with flexible substrates [1, 2]. The power conversion efficiency (PCE) of PSCs based on tandem structure has reached 10.6% and the single junction architecture has also already reached efficiency of 8.6% [3, 4]. Indium tin oxide (ITO) is the most commonly used transparent electrode for PSCs. It has good transparency in the visible range of the solar spectrum as well as high conductivity for electronic devices. However, some problems still exist for utilizing ITO such as poor mechanical property of ITO-coated flexible substrates, low conductivity for fabricating large-area devices, limited availability of indium and complex vacuum sputtering process [5]. These deficiencies of ITO limit the commercialization of low-cost PSCs. To solve this problem, there has been some works on exploring conductive polymer, graphene, carbon nanotube and metal nanoparticles as potential candidates to replace ITO. However, higher sheet resistance compared to ITO can hardly meet the requirements of the PSCs. Metal grids have also been investigated as a promising approach to transparent electrode [6–8]. Utilizing printing process, metal grids coated substrates can achieve high transparency and low sheet resistance for PSCs [9, 10]. Currently, metal grids transparent electrodes are usually fabricated with silver nanoparticles based inks to form conductive structures on poly(ethylene terephthalate) (PET) or Poly(ethylene naphthalate) (PEN) substrates [11]. The nano-silver inks can be printed by different printing methods, such as flexography, gravure, screen and inkjet [12–15]. However, the nano-silver inks (especially flexography inks and gravure inks with high silver content) usually contain soluble protective agent (e.g. poly(vinyl pyrrolidone), PVP), leading to result a thin nonconductive film upon the printed silver pattern [16–18]. Such a thin film of protective agent increases the sheet resistance of the printed silver pattern.

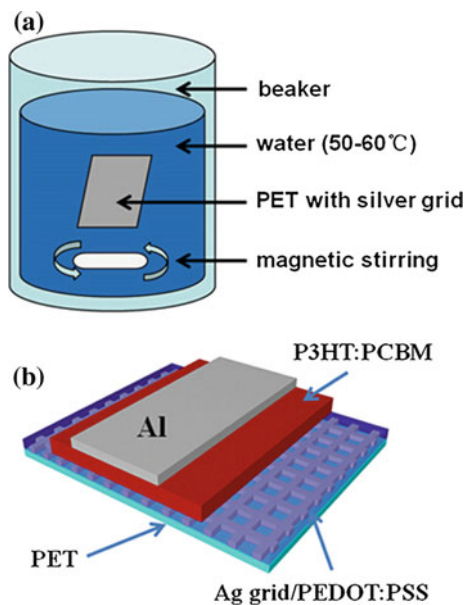
Here, we reported a simple method to obtain high conductivity transparent electrode by flexography printing and water washing, and then fabricated ITO-free polymer solar cells based on poly(3-hexylthiophene) (P3HT) and [6]-Phenyl C61 butyric acid methyl ester (PC<sub>60</sub>BM). The silver grid of square and hexagon shapes was designed to optimize the transparency and conductivity of the silver grid. The printed silver patterns of square and hexagon shapes show considerable sheet resistance decrease by water washing. The poly(3, 4-ethylenedioxythiophene) poly(styrenesulfonate) (PEDOT:PSS) was coated on the transparent electrode as the anode modification layer. The confocal laser scanning microscope (CLSM) shows the morphological changes of the two silver pattern after water washing and the PEDOT:PSS coating. We completed two devices by spin coating the active layer and vacuum thermal evaporating cathode. The method realizes high conductive printed silver layers on PET substrates and can be utilized in mass production.

## 2 Experiments

The silver nanoparticles based ink (shown in the inset of Fig. 1b) was purchased from Beijing Beiyin Zhongyuan which is specific for flexographic printing. The silver content of the ink is 60 wt% and the solvent is isopropanol and ethylene glycol. The ink uses poly-vinylpyrrolidone (PVP) as the dispersant for stabilization. The PET film was purchased from China Lucky Group Corporation. PEDOT:PSS (Baytron P, 4083) was purchased from HC Stark. The P3HT and PC<sub>60</sub>BM were purchased from Rieke Metals Inc and Nichem Fine Technology Co. Ltd, respectively.

Before printing, the PET films were cleaned with acetone and blown dry with nitrogen. Silver patterns on PET substrates were printed using an IGT-F1 printability tester with flexo-plates. The flexo-plates were designed by Matlab and Photoshop and were made by a plate manufacturing company. The flexo-plates of square and hexagon shapes have the line length of 200, 300  $\mu\text{m}$  and the line width of 20  $\mu\text{m}$ . The plates were stuck onto the IGT-F1 printability tester. The silver ink was added on the surface of the anilox of the tester. The printing pressure is 150 N. The printing speed is 0.3 m/s. The silver ink would be transfer from the anilox onto the plates, when the tester started. The flexography printed silver pattern on the PET film was firstly dried in an oven under 120  $^{\circ}\text{C}$ , then was placed into the deionized water for washing treatment. The diagram of water washing treatment is illustrated in Fig. 1a. After several hours, the washed silver grid on the PET films was blown dry with nitrogen. The PEDOT:PSS was coated onto the washed substrates by using the doctor blade technique. Then the PET substrates with the washed silver

**Fig. 1** Schematic illustration of the water washing treatment (a) and the device's structure (b)

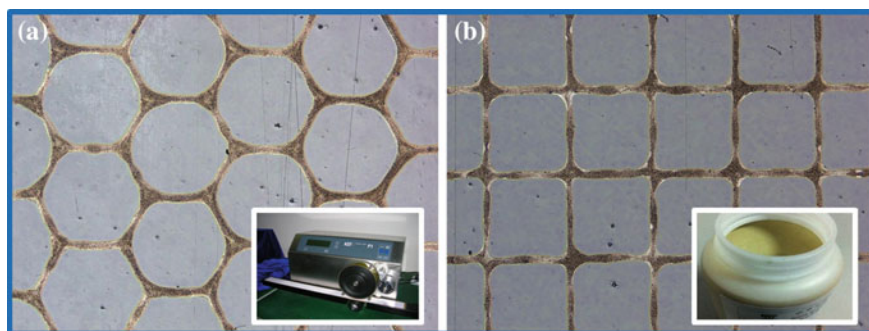


grids and the PEDOT:PSS layer were annealed at 120 °C for 15 min. The dichlorobenzene solution consisting of P3HT and PC<sub>60</sub>BM was spin cast. The concentration of P3HT is 20 mg/mL and the weight ratio of P3HT and PCBM is 1:1. Lastly, to complete the devices, a 100 nm thick Al film was deposited by thermal evaporation under a vacuum of  $5 \times 10^{-6}$  Torr. The structure of the devices is PET/Ag grid/PEDOT:PSS/P3HT:PC<sub>60</sub>BM/Al and the schematic is shown in Fig. 1b. The active area of the devices is 9 mm<sup>2</sup>.

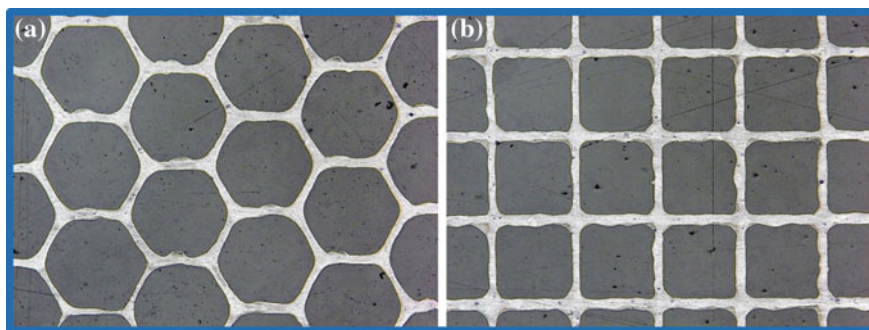
### 3 Results and Discussion

The printing quality of the hexagon silver pattern with the side length of 200 μm and the square silver pattern with the side length of 300 μm are well, as shown in Fig. 2a, b. The silver ink would gather at the intersection of the printed silver lines if the grid was designed closer, especially for square structure. That is why we choose different side length for the two shapes. The conductivity of the initially obtained silver patterns, which reaches to the level of KΩ, is not good for polymer solar cells. After water washing, the silver patterns exhibit the apparent metallic luster rather than the pattern before water washing. Figure 3 shows the morphology of water washed silver patterns of hexagon and square by CLSM capturing. The silver pattern washed in water is evidently brightened due to the removing and dissolving of PVP which deposits above the silver patterns. Meanwhile, the resistance of hexagon silver pattern washed in water reaches to 22 Ω/Υ and that of the square silver pattern reaches to 37 Ω/Υ, as shown in Table 1. It implies the PVP is thoroughly removed from the surface of silver pattern by water washing.

The total resistance of metal grid is determined by the large-area grid network with complex series-parallel structure. Herein, the hexagon grid exhibit lower resistance than the square grid, which is probably owing to the shorter side length. Moreover, the hexagon grid has better and more uniform conductivity than the



**Fig. 2** CLSM pictures of the flexography printed silver grid of hexagon (a) and square (b), the inset of a is the IGT-F1 printability tester, the inset of b is the flexographic nano-silver ink



**Fig. 3** CLSM pictures of the flexography printed silver grid with water washing

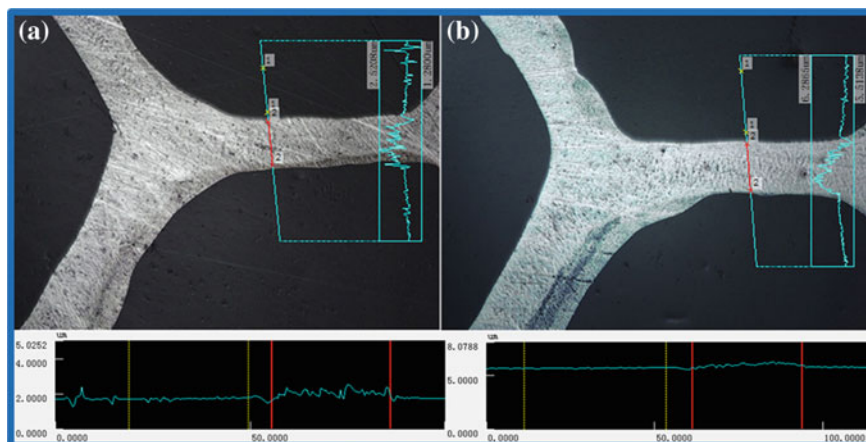
**Table 1** Sheet resistance of silver patterns

Silver pattern	Before washing ( $\Omega/\square$ )	After washing ( $\Omega/\square$ )
Square	1320	37
Hexagon	760	22

square grid. The hexagon has six symmetrical axis on the plane, while the square just has four symmetrical axis. The theoretical analysis was reported in our previous work [19].

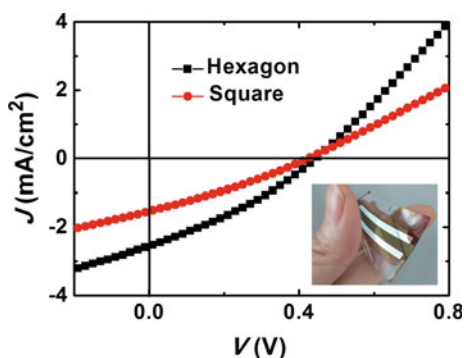
To modify the silver grid based transparent electrode, the PEDOT: PSS was coated by using the doctor blade technique. The morphological change of silver pattern with or without the PEDOT: PSS layer is shown in Fig. 4. The hue of the silver pattern in Fig. 4b changes into a little blue because of the PEDOT: PSS coated, compared to Fig. 4a. The height of the silver pattern in both silver grid with coating is about 100 nm, which is flattened out by the PEDOT: PSS on top. While the height of the lines in printed silver grid without PEDOT: PSS coating is about 500 nm.

P3HT: PC<sub>60</sub>BM based solar cells were prepared on the top of PET/Ag grid/PEDOT:PSS. The completed device is shown in the inset of Fig. 5. The J-V characteristics of both devices under AM1.5G 100 mW/cm<sup>2</sup> illumination are also shown in Fig. 5. The device with hexagon grid exhibits a PCE of 0.37% and a fill factor (FF) of 0.32. The open-circuit voltage (Voc) and the short circuit current density (Jsc) are 0.45 V and 2.56 mA/cm<sup>2</sup>. The device with square grid shows a PCE of 0.21% and an FF of 0.30. The Voc and Jsc are 0.43 V and 1.44 mA/cm<sup>2</sup>. Table 2 shows the summary of the devices' parameter. The device with hexagon grid shows a better performance owing to the better conductivity and better transparency of electrode (analyzed in our previous work). Although the power conversion efficiency of both devices is quite low, the metallic grid by water washing can be utilized as a low-cost, ITO-free transparent electrode.



**Fig. 4** Surface analysis of the silver grid with (b) or without (a) PEDOT: PSS layer by CLSM capturing

**Fig. 5**  $J$ - $V$  curves of the devices (the *inset* is a picture of the fabricated device)



**Table 2** Summary of the device's performance

Device	$V$ (V)	$J$ (mA/cm <sup>2</sup> )	FF	$\eta$ (%)
Square grid	0.43	1.44	0.30	0.21
Hexagon grid	0.45	2.56	0.32	0.37

## 4 Conclusions

The square and hexagon silver grid were fabricated by flexography printing. The conductivity of both silver grid was apparently improved by water washing, owing to the removing and dissolving of PVP which deposits above the silver patterns. The silver grid after water washing shows the metallic luster by the confocal laser scanning microscope capturing. The resistance of the hexagon silver grid by water washing reduces to 22  $\Omega/\gamma$ . The polymer solar cells based on P3HT: PCBM are

fabricated on the metallic grid substrates as the anode. The device with hexagon grid exhibits a power conversion efficiency of 0.37%. This simple method provides a low cost, easy handle process of fabricating ITO-free transparent electrode for polymer solar cells.

**Acknowledgements** This work was financially supported by the Key Project of Beijing Institute of Graphic Communication (Ea201501), Initial Funding for the Doctoral Program of BIGC (09000114/125, 27170115005/051, 27170116005/050), Course Construction Project of BIGC (22150116008/026), 2015 Materials and Technology of Printed Electronics Research Ability Improving Program (Eb201530), Beijing Municipal Undergraduate Science Research Project (08150115/047), Beijing Municipal Commission of Education Foundation for School Innovation Ability Promotion Plan (TJSHG201310015016).

## References

1. B. Kippelen, J.L. Bredas, (2009). Organic photovoltaics, *Energy & Environmental Science*, 2: 251–261.
2. M. Helgesen, R. Sondergaard, F.C. Krebs, (2010). Advanced materials and processes for polymer solar cell devices, *Journal of Materials Chemistry*, 20: 36–60.
3. Jingbi You, Letian Dou, Ken Yoshimura, Takehito Kato, Kenichiro Ohya, Tom Moriarty, Keith Emery, Chun-Chao Chen, Jing Gao, Gang Li & Yang Yang, (2013). A polymer tandem solar cell with 10.6% power conversion efficiency, *Nature Communications*, 4: 1446.
4. Z.C. He, C.M. Zhong, X. Huang, W.Y. Wong, H.B. Wu, L.W. Chen, S.J. Su, Y. Cao. (2011). Simultaneous enhancement of open-circuit voltage, short-circuit current density, and fill factor in polymer solar cells, *Advanced Materials*, 23: 4636–4643.
5. Jingyu Zou, Hin-Lap Yip, Steven K. Hau and Alex K.-Y. Jen. (2010). Metal grid/conducting polymer hybrid transparent electrode for inverted polymer solar cells, *Applied Physics Letters*, 96: 203301–203303.
6. D. Deganello, J.A. Cherry, D.T. Gethin, T.C. Claypole. (2010). Patterning of micro-scale conductive networks using reel-to-reel flexographic printing, *Thin Solid Films*, 518: 6113–6116.
7. Sukanta De, Thomas M. Higgins, Philip E. Lyons, Evelyn M. Doherty, Peter N. Nirmalraj, Werner J. Blau, John J. Boland and Jonathan N. Coleman. (2009). Silver nanowire networks as flexible, transparent, conducting films: extremely high dc to optical conductivity ratios. *ACS Nano.*, 3: 1767–1774.
8. Bin Su, Cong Zhang, Shuoran Chen, Xingye Zhang, Linfeng Chen, Yuchen Wu, Yiwen Nie, Xiaonan Kan, Yanlin Song and Lei Jiang. (2014). A General Strategy for Assembling Nanoparticles in One Dimension. *Adv. Mater.*, 26: 2501–2507.
9. Burhan Muhsin, Roland Roesch, Gerhard Gobsch, Harald Hoppe. (2014). Flexible ITO-free polymer solar cells based on highly conductive PEDOT:PSS and a printed silver grid. *Solar Energy Materials & Solar Cells*, 130: 551–554.
10. Jong-Su Yu, GwanHo Jung, Jeongdai Jo, JungSu Kim, JunWoo Kim, Sun-Woo Kwak, Jong-Lam Lee, Inyoung Kim, Dojin Kim. (2013). Transparent conductive film with printable embedded patterns for organic solar cells, *Solar Energy Materials & Solar Cells*, 109: 142–147.
11. M. Allen, J. Leppaniemi, M. Vilkmann, A. Alastalo and T. Mattila. (2010). Substrate-facilitated nanoparticle sintering and component interconnection procedure, *Nanotechnology*, 21:475204.
12. M. Allen, C. Lee, B. Ahn, T. Kololuoma, K. Shin and S. Ko. (2011). R2R gravure and inkjet printed RF resonant tag, *Microelectron. Eng.*, 88: 3293–3299.
13. M. Allen, M. Aronniemi, T. Mattila, P. Helisto, H. Sipola, A. Rautiainen, et al. (2011). Contactless read-out of printed memory, *Microelectron. Eng.*, 88: 2941–2945.

14. M. Hosel and F. C. Krebs. (2012). Large-scale roll-to-roll photonic sintering of exo printed silver nanoparticle electrodes, *J. Mater. Chem.*, 22: 15683.
15. Y. Galagan, J.-E. J. M. Rubingh, R. Andriessen, C.-C. Fan, P. W. M. Blom, S. C. Veenstra, et al. (2011). ITO-free flexible organic solar cells with printed current collecting grids, *Sol. Energy Mater. Sol. Cells*, 95: 1339–1343.
16. Juuso Olkkonen, Jaakko Leppaniemi, Tomi Mattila and Kim Eiroma. (2014). Sintering of inkjet printed silver tracks with boiling salt water, *J. Mater. Chem. C*, 2: 3577–3582.
17. Michael Layani and Shlomo Magdassi. (2011). Flexible transparent conductive coatings by combining self-assembly with sintering of silver nanoparticles performed at room temperature. *Mater. Chem.* 21: 15378–15382.
18. Jolke Perelaer, Antonius W. M. de Laat, Chris E. Hendriks and Ulrich S. Schubert, Inkjet-printed silver tracks: low temperature curing and thermal stability investigation, *J. Mater. Chem.*, 18: 3209–3215.
19. Liu Wei, Fang Yi, Xu Yanfang, Li Xiu, Li Luhai. (2014). The effect of grid shape on the properties of transparent conductive films based on flexographic printing, *Sci China Tech Sci*, 57, 12: 2536–2541.

# Study of the Screen Printing Technology on RFID Tag Antenna

Wei Liu, Guangxue Chen and Yusi Zhang

**Abstract** In order to stabilize the RFID tag antenna's printing quality and improve the production efficiency, it is fundamental to test RFID tag antenna's properties under different printing conditions, but the research about the real recognizable distance under different printing conditions is limited. In this paper, we have mainly studied the effect of scraper blade speed, curing time and curing temperature on RFID tag antenna's properties. The experimental data showed that when scraper blade speed is between 50 and 70 m/min, the antenna have the longest recognizable distance with stable impedance; antenna's impedance declines as the curing time becoming longer or curing temperature rising, recognizable distance showed adverse trend compared with impedance. It also guides that longer recognizable distance combined with smaller resistance comparatively. The recognizable distance tested by right above and down the reader is lower than the recognizable distance right ahead the reader.

**Keywords** RFID tag antenna · Impedance · Recognizable distance

## 1 Introduction

Nowadays, conductive ink has been used for printing RFID tag antenna by screen printing technology which is the most effective way to reduce antenna fabricating cost. Silk-screen printing technology could better control the accuracy and the printing thickness which is the key parameter to RFID tag's radiance.

---

W. Liu · G. Chen (✉)

State Key Laboratory of Pulp and Paper Engineering,  
South China University of Technology, Guangzhou, China  
e-mail: chengx@scut.edu.cn

Y. Zhang

School of Light Industry and Engineering,  
South China University of Technology, Guangzhou, China

© Springer Nature Singapore Pte Ltd. 2017

P. Zhao et al. (eds.), *Advanced Graphic Communications and Media Technologies*, Lecture Notes in Electrical Engineering 417,  
DOI 10.1007/978-981-10-3530-2\_68

539



It is fundamental to test RFID tag antenna's properties under different printing conditions to get good printing quality. There are some researches based by theories now [1, 2], but the experiment to test the real recognizable distance with chip is limited. In this paper, the NT-SR102 silver paste had been used, the RFID tag antenna's properties and recognizable distance under different scraper speeds and curing conditions had been tested.

## 2 Background and Preparation

### 2.1 Radiant Efficiency of Antenna

For passive RFID tag, the tag chip energy comes from tag antenna's electromagnetic radiation, which directly affects the RFID tag's recognizable distance. The practical electromagnetic power of radiation is lower than transmitted power because of conduction losses which dues to finite conductivity of the antenna and dielectric loss which dues to the conductive dielectric substance in the working process. Radiation frequency of antenna can be defined as:

$$\eta = \frac{R_r}{R_r + R_l} \quad (1)$$

$R_l$  refers to antenna's impedance loss;  $R_r$  refers to antenna's radiant resistance.

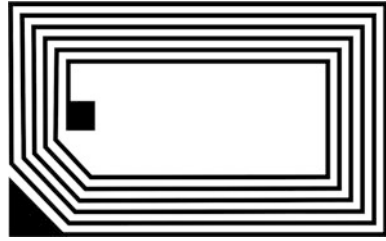
As can be seen from Formula (1), to improve the antenna's radiation efficiency, it is necessary to maximize the radiation resistance and reduce the impedance loss which is also significance to get better impedance matching [3]. Tag antenna's impedance is influenced greatly by printing technology and curing condition, when tag antenna's impedance is big, resonant frequency and  $QF$  will decline, therefore it is significant to control low but stable impedance as possible.

### 2.2 Design of RFID Tag Antenna

The RFID tag antenna of *HF* frequency band is based on the theory of magnetic dipole, the antenna is coil structure usually. The number of coils  $N$  can be estimated based on coil's induced voltage requirements [4].

For the RFID system of *HF* band, when the system is accorded with *ISO 15693* standard and carrier wave is 423 kHz. RFID tag chip's input capacitance is generally between 20 and 100 pF, in order to satisfy the tag's high working frequency 13.56 MHz, the inductance of the tag antenna is usually located in the 2–6  $\mu\text{H}$ . RFID antenna structure used in experiment is shown in Fig. 1, its dimension parameters are shown in Table 1. Coupling capacitance of the coil is about 3 pF, inductance value is about 2.5  $\mu\text{H}$ .

**Fig. 1** RFID antenna structure used in experiment



**Table 1** RFID antenna's dimension parameters

Number of coils	Lengths of outermost side (mm)	Line width (mm)	Line space (mm)	Thickness of coils (mm)
7	65 × 40	0.8	1.0	0.012

### 3 Experiment

Experimental equipment and materials: Ke Zhiyi SCIEN-ART screen printing machine (the screen lines is 350 mesh/inch), Zhongke Natong conductive silver paste (the sheet resistant is 15 mΩ/Y/mil, the content of Ag particles is 60%, the fitness is below 15 μm, the viscosity is between 10,000 and 14,000 cp), multimeter, drying oven. USA ST Microelectronics SR176 Wafer chip(the working frequency is 13.56 MHz with 847 kHz subcarrier frequency, memory capacity is 176 b, recognizable distance is between 2 and 15 cm), computer was installed DEMO system.

#### 3.1 Effect of Scraper Blade Speed to RFID Tag Antenna's Impedance and Recognizable Distance

Experimental procedures are as follows:

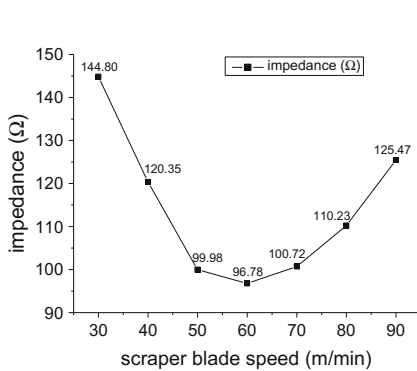
- (1) The Scraper blade pressure was 100 N/m and scraper blade angle was 75°;
- (2) The scraper blade speed were set at 30, 40, 50, 60, 70, 80 and 90 m/min, under each condition there were 5 tag antennas have been printed;
- (3) All printed tag antennas were put on drying oven (70 °C) for 30 min, measured the resistance of the antenna with multimeter, then calculated the average values of the antenna resistances;
- (4) The chips had been installed into printed antennas;
- (5) The reader was connected with computer via USB, opened DEMO system;

Test environment: there were no other interferential field strength and signal during the experiment; there were no other barrier and electromagnetic signal emission source; while electromagnetic signals reflected from surrounding objects around RFID antenna were also should be avoided as possible as we can.

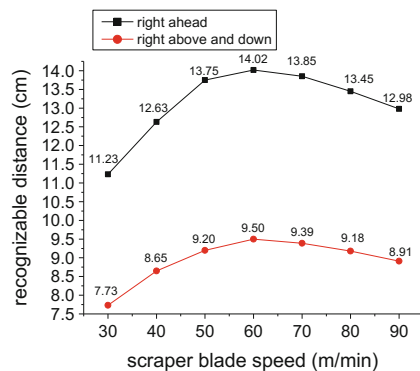
- (6) Those labels had placed right ahead of reader, then tested the maximum recognizable distance, recorded them and calculated the averages;
- (7) Placed the label right above and down the reader, tested the maximum recognizable distance, recorded them and calculated the averages.

The relationships between scraper blade speed and tag antenna’s impedance and recognizable distance are as follows:

From Fig. 2a, the RFID tag antenna’s resistance exhibits a U-shaped variation trend as the increasing of scraper blade speed. It can be found that when the scraper blade speed is low, the impedance decreases with the increasing of scraper blade speed; the antenna’s impedance becomes stable when scraper blade speed is between 50 and 70 m/min; when exceeds 70 m/min, the resistance increases with faster scraper blade speed. This is because when scraper blade speed is small, the Ag particles of conductive ink easily clog the screen’s mesh, thus ink passing rate is poor, caused conductive Ag particles density of antenna decreasing and lower conductivity; when scraper blade speed is moderate, conductive ink have good ink passing rate, conductive Ag particles can transferred to the substrates effectively, reducing the impedance and the conductive performance is improved; when scraper blade speed is too large, residence time of ink is too short when they transferred from screen to the substrate, ink supply amount of printing process is low, therefore the antenna’s conductivity reduces, in addition, it is easy to appear bubble above ink marks with fast scraper blade speed, those all affect print quality [5, 6]. Therefore, scraper blade speed is better controlled in the range of 50–70 m/min in order to ensure the filler content of ink and Ag particles, get small impedance of RFID tag antenna.



(a) Relationships between scraper blade speed and tag antenna’s impedance



(b) Relationships between scraper blade speed and recognizable distance

**Fig. 2** Relationships between scraper blade speed and tag antenna’s impedance and recognizable distance

From Fig. 2b, the recognizable distance tested by right above and down the reader is lower than the recognizable distance right ahead the reader. This is because radiant directivity of electronic tag antenna determined that it is higher in horizontal direction, but smaller in vertical direction [7]. We can found that recognizable distance increases at first but decreases lately with the increasing scraper blade speed. This rule is contrary to the rule of impedance variation (Fig. 2a). It follows the rule that the smaller impedance is, the longer recognizable distance is, and this also conforms to Formula (1).

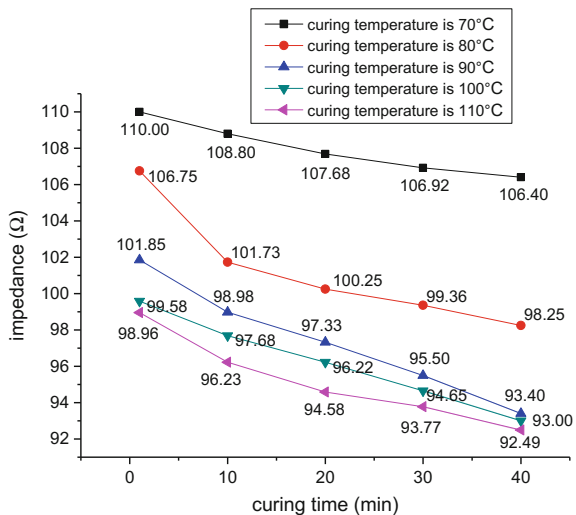
### 3.2 Effect of Curing Condition to RFID Tag Antenna's Impedance and Recognizable Distance

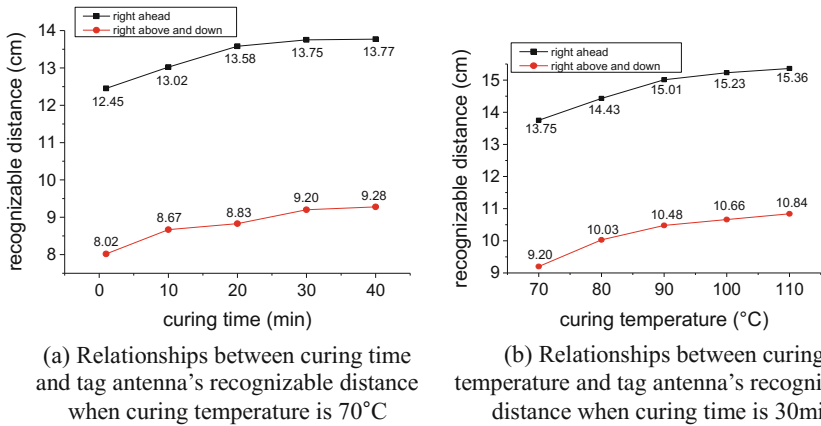
Experimental procedures are as follows:

- (1) Scraper blade speed was 50 m/min, scraper blade pressure was 100 N/m.
- (2) There were five groups of tag antennas have been printed and each group have five tag antennas been printed. The curing temperature is 70 °C, curing time of five groups were set at 1, 10, 20, 30 and 40 min. The resistance of the antennas measured by multimeter, then calculated the average values of antenna resistance.
- (3) Curing temperature were set at 80, 90, 100 and 110 °C, repeated step (2).
- (4) The test of recognizable distance referred to Sect. 2.1.

The relationships between curing time, curing temperature and tag antenna's impedance are as follows (Fig. 3).

**Fig. 3** Relationships between curing time, curing temperature and tag antenna's impedance





**Fig. 4** Relationships between curing time, curing temperature and tag antenna's recognizable distance

From Fig. 4, with the increasing of curing time, the RFID tag antenna's resistance reduces, decreasing rate declines and tends to be stable later, recognizable distance becomes longer; with the increasing of curing temperature, RFID tag antenna's resistance reduces, reduction rate declines and tends to become stable later also, recognizable distance becomes longer.

When curing time is fixedly, the higher curing temperature improves the rate of membranous oxidation process, following higher organic solvent volatilize rate which is more efficient for curing ink of antenna; the particles inside ink have higher density, the space between silver particles decreases which promotes a better contact, it forms penetrating effect, therefore improving antenna's electric conductivity and resistance decreases, in addition, recognizable distance is longer.

When curing temperature is fixedly, the longer curing time ensures enough time for membranous oxidation and volatilization of organic solvent process which is efficient for curing ink of antenna; the particles inside ink have higher density, space between silver particles decreases which promotes a better contact, it forms penetrating effect, therefore improving antenna's electric conductivity and resistance decreases. But a long time have gone by, the reaction will gradually stabilized; therefore decreasing rate declines and tends to be stable later. Variation trend of recognizable distance is contrary to resistance, it also explains longer recognizable distance combined with smaller resistance comparatively. The recognizable distance tested by right above and down the reader is lower than the recognizable distance right ahead the reader, those vide supra.

## 4 Conclusions

In this paper, we have mainly studied the effect of scraper blade speed, curing time, and curing temperature to RFID tag antenna's properties. The experimental data showed that when scraper blade speed at the range of 50–70 m/min, antenna has the longest recognizable distance with stable impedance; antenna's impedance declines as the curing time becoming longer or curing temperature rising, recognizable distance becomes longer which shows adverse trend with impedance. It also guides that longer recognizable distance combined with smaller resistance comparatively. The recognizable distance tested by right above and down the reader is lower than the recognizable distance right ahead the reader.

**Acknowledgements** This research was financially supported by the Guangdong Provincial Science and Technology Project (2013B010401007) and Guangzhou City Science and Technology Project (201607020045).

## References

1. Wang, S., Qian J. H. (2011). Study on influencing factors of ink thickness by RFID screen printing. *Packaging Engineering*, 32: 97–100.
2. Ma, C. S. (2014). RFID Technology Application. Beijing Institute of Technology Press. Beijing.
3. Tan, B. (2006). An improved method for the measurement of antenna radiation efficiency. *Journal of Huaihai Institute of Technology (Natural Sciences Edition)* 15: 37–39.
4. Xia, H., Wu J. W. (2012). Design and implementation of ultra high frequency RFID reader system. *Journal of Computer Application*. 32: 2369–2373.
5. Jiang, J. J., Liu, W. T., Huang, L. G. (2015) State-of-the-art of the studies on conductive ink for radio frequency identification antenna. *Materials Review*. 29: 121–126.
6. Xu, Y., Chen, J. (2013). The theory and application of RFID. Tsinghua University Press. Beijing.
7. Li, X. M., Lu X. M. (2004). The property and application of telecommunication antenna. *Jiangsu Water Resources*. 04: 31–32.

# Research on the Covering Property of White Ink Applied on Transfer Paperboard

Xinting Wang, Guorong Cao, Ling Cheng and Xu Wang

**Abstract** In order to study covering property of different white ink applied on transfer paperboard, dispersity and covering property of white ink is analyzed. At the same time, covering power of white ink applied on transfer paperboard at different printing speed and dot area coverage is tested. Experimental results show that the narrower the range of distribution of white ink, the higher dispersity. The covering property of white ink is much better. If printing speed or dot area coverage change, the covering property of white ink also changes. The covering power of low dispersity of white ink is affected by transfer paperboard. However, transfer paperboard has a little influence on high dispersity of white ink. The covering property of white ink on high-quality laser paper is much better than two other types of transfer paperboard.

**Keywords** White ink · Transfer paperboard · Dispersity · Covering property

## 1 Introduction

White ink applied on transfer paperboard is an important step in cigarette packaging printing. White ink in printing ink generally uses as render ink which plays an important role for graphic reproduction, and the covering power of white ink is required as high as possible [1–3]. So the study of covering property of white ink is very important. In actual production, covering power of white ink is not particularly good due to its composition. And the performance of transfer paperboard has little effect on covering property of white ink.

---

X. Wang · G. Cao (✉) · L. Cheng · X. Wang  
School of Printing and Packaging Engineering,  
Beijing Institute of Graphic Communication, Beijing, China  
e-mail: caogorong@bigc.edu.cn

© Springer Nature Singapore Pte Ltd. 2017  
P. Zhao et al. (eds.), *Advanced Graphic Communications  
and Media Technologies*, Lecture Notes in Electrical Engineering 417,  
DOI 10.1007/978-981-10-3530-2\_69

547

Dispersity and covering property of white ink were tested. The paper analyze covering property of white ink applied on different transfer paperboard at different speed and dot area coverage, so that it can study factors about covering property of white ink applied on transfer paperboard.

## 2 Experiment

### 2.1 Experimental Materials

The type of experimental materials is shown in Table 1.

### 2.2 Experimental Facilities and Specimen Parameters

- (1) Cut-off knife. It cuts transfer paperboard into a sample of 150 × 100 mm proofs. Each transfer paperboard is cut 90 pieces.
- (2) K printing proofer. Proofs are printed at the speed of 20, 30 and 40 m/min respectively.
- (3) Glossmeter TC-108DPA. According to GB/T 8941-2013 Paper and board-Measurement of specular gloss, experiment tests gloss of prints [4].
- (4) Microtrac S3500 laser particle size analyzer (Region:America). It tests dispersity of white ink.
- (5) Ref. 310 covering power tester. It tests covering power of white ink. There are three types of white ink. Each type of ink is tested five times and takes the arithmetic average.

### 2.3 Performance Test

- (1) Dispersity performance test. YF-18 and GC860 white ink are diluted with ethanol. Water-based white ink is diluted with deionized water. White ink

**Table 1** Experimental materials

Materials	Type
Transfer paperboard	Silver luster
	Dumb silver
	High-quality laser
White ink	YF-W18
	GC860
	Water-based



particle size is tested by Microtrac S3500. As white ink particle size distribution shows, the particle size distribution is narrower and the value of 95% of particle size is smaller. The dispersity of white ink is much better; conversely, the dispersity of white ink is worse.

- (2) Covering property test. White ink is coated onto the surface of covering property test paper. Ref. 310 covering power tester tests ink area of black grid in covering property test paper. Write down the numerical  $R_B$ . And tester tests area of white grid. Write down the numerical  $R_W$ . The ratio of  $R_B/R_W$  represents the white ink covering power. If the ratio is much larger, the covering property is much better [5].
- (3) Measurement of gloss. Gloss of printed samples is tested by Glossmeter TC-108DPA which is chose the angle of 20 because of the high gloss of transfer paperboard. Generally, the smaller particle size of pigment and the higher dispersity of white ink, which are beneficial to form smooth ink film, so the gloss of printed samples is much higher [6–8].

### 3 Results and Discussion

#### 3.1 Dispersity and Covering Property of White Ink

Dispersity of white ink is tested by Microtrac S3500, as shown in Fig. 1. Gray segment represents distribution of white ink particle size of pigment. The distribution is narrower and the value of 95% of white ink particle size is smaller, so the dispersity is much higher. As shown in Fig. 1, YF-W18 white ink has a maximum range of distribution of white ink and the value of 95% of particle size of pigment is 76.21  $\mu\text{m}$ , so the dispersity of YF-W18 white ink is the lowest; The range of distribution of GC860 white ink is narrower than YF-W18 white ink and the value of 95% of pigment particle size of GC860 white ink is 74.78  $\mu\text{m}$ , so the dispersity of GC860 white ink is higher than YF-W18. Water-based white ink has the narrowest range of distribution and the value of 95% of pigment particle size is 2.069  $\mu\text{m}$ , so the dispersity is the highest.

As shown in Fig. 2, covering power of white ink is different with the change of dispersity. The covering property generally becomes better with the dispersity of white ink becoming higher. The covering power of YF-W18 white ink is 0.8524, so it's covering property is the worst. The covering power of GC860 white ink is 0.8703, so its covering property is better. The covering power of water-based white ink is 0.9, so its covering property is the best.

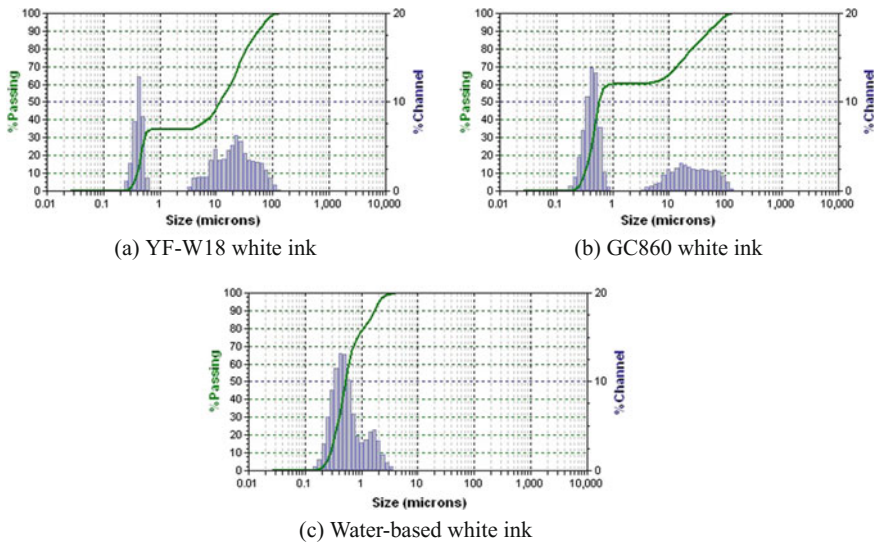
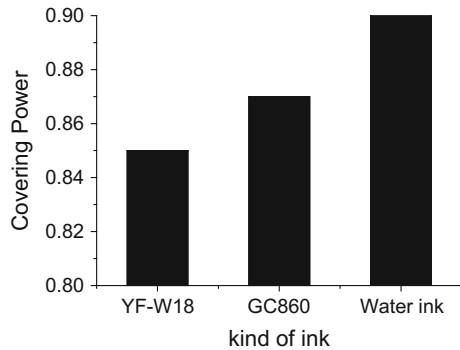


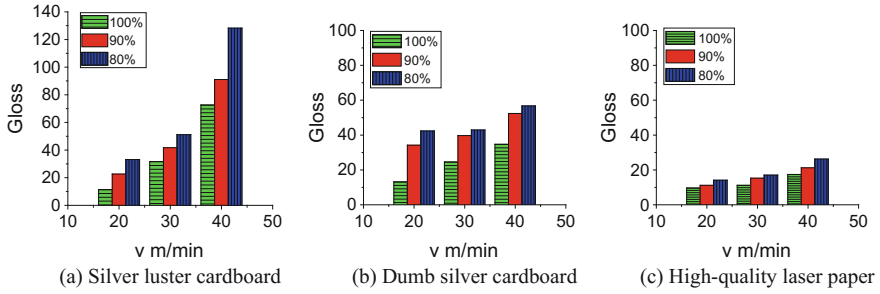
Fig. 1 Dispersity of three types of white ink

Fig. 2 Covering power of three types of white ink

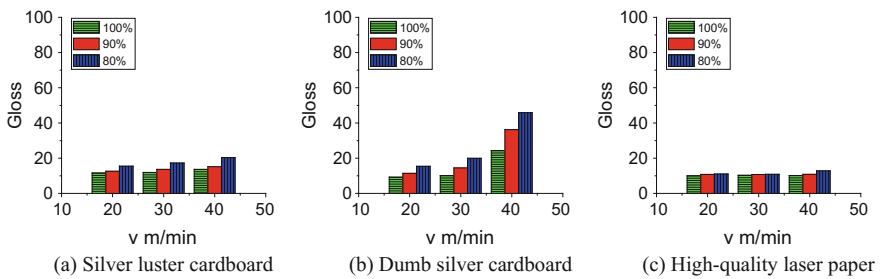


### 3.2 Printing Parameters and Covering Property of White Ink

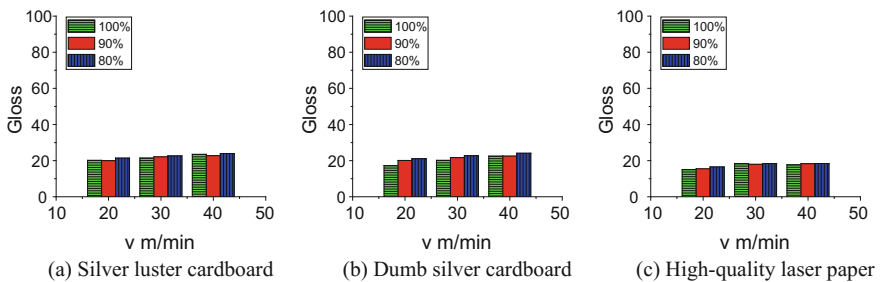
Known from Figs. 3, 4 and 5, gloss of transfer paperboard which is printed with YF-W18 white ink is the highest, when YF-W18, GC860 and water-based white ink print on the same type of transfer paperboard respectively. Because covering property of YF-W18 white ink is bad, it cannot cover the gloss of transfer paperboard. Especially, the gloss of printed samples is much higher with the increase of printing speed and decrease of dot area rate, so covering property of YF-W18 white ink is the worst. Known from Figs. 4 and 5, gloss of transfer paperboard which is



**Fig. 3** Gloss of three types of transfer paperboard which is printed with YF-W18 white ink at the different printing speed and dot area coverage



**Fig. 4** Gloss of three types of transfer paperboard which is printed with GC860 white ink at the different printing speed and dot area coverage



**Fig. 5** Gloss of three types of transfer paperboard which is printed with water-based white ink at the different printing speed and dot area coverage

printed with GC860 white ink is much lower than gloss of transfer paperboard which is printed with water-based white ink. Pigment particle size of GC860 white ink is larger, so its dispersity is worse. Covering property of GC860 white ink is worse than water-based white ink. At the same time, gloss of printed samples which

have the same transfer paperboard generally rises with the increase of printing speed and decrease of dot area rate, because white ink cannot cover the gloss of transfer paperboard. In conclusion, when the printing speed is 20 m/min and dot area coverage is 100%, the covering property of white ink is much better.

### 3.3 *Transfer Paperboard and Covering Property of White Ink*

As you can see from Fig. 3, when YF-W18 white ink prints on three types of transfer paperboard, gloss of printed samples is different. However, as shown in Fig. 5, water-based white ink prints on three types of transfer paperboard, gloss of printed samples has almost no change. Transfer paperboard has little impact on covering property of water-based white ink. So transfer paperboard affects covering property of white ink which its dispersity is bad and has little effect on covering property of white ink which its dispersity is good. Known from Figs. 3, 4 and 5, when three types of white ink prints on high-quality laser paper, its covering property is much better.

## 4 Conclusions

In this study, the higher dispersity of white ink, the smaller particle size of the pigment. The covering property of white ink is much better. When the printing speed is 20 m/min and dot area coverage is 100%, the covering property of white ink is much better. Transfer paperboard affects covering property of white ink which its dispersity is bad. And transfer paperboard has little effect on covering property of white ink which its dispersity is good. When white ink prints on high-quality laser paper, its covering property is much better.

**Acknowledgements** This study is funded by packaging engineering teaching team (construction) of Beijing institute of graphic communication (22150116006/017).

## References

1. Ying Gong, Xinfu Wei, Changlong Guo, Beiqing Huang. (2014). Studies on the relations between dispersivity and covering property of white water-based ink. *Journal of Beijing Institute of Graphic Communication*, 22(06): 10.
2. Hailong Ai. (2014). *Printing Material*. Beijing: China Light Industry Press, 130–131.
3. Jiangzhong Wang, Xudong Xu. (2006). Test and evaluation of gravure ink. *China Printing Materials Business*, (03):49.

4. Standardization Administration of China. Paper and board-measurement of specular gloss. Beijing: China Standard Press, 2014.
5. Ying Gong, Beiqing Huang, Xianfu Wei. (2014). Research on the Preparation and Performance of White Water-based Flexo Covering Ink Applied in Lottery Printing. Beijing Institute of Graphic Communication: 19–28.
6. Chenghong Qin, Yuanyuan Ning, Chunyan Bai. (2008). Analysis of the printed ink gloss effects. *Print Magazine*, (11): 69.
7. Xiaofeng Wu. (2006). The development of the hose white ink. *Anhui Chemical Industry*, 140 (02): 49.
8. Jiazheng Sun, Xianfu Wei, Beiqing Huang, Xiaoshun Zong. (2012). Influence of pigment dispersion on the performance of water-based plastic gravure ink. *China Printing and Packaging Study*, 4(03): 49–50.

# Research on Theory and Application of Computer Ink Color Matching

Guhong Liu, Qifeng Chen and Guangxue Chen

**Abstract** Spot color ink has been essential in security printing. Convenient computer ink color matching become more and more popular. The color matching model is the core part of computer color matching. It is very important to understand and master the theory of color matching. In this paper, the principle of computer color matching based on Kubellka-Munk theory was also described. Finally, four color spots (356C, 717C, 7431C, 643C of PANTONE) were measured. Color differences of formulations respectively were 1.4, 0.3, 0.5 and 0.5, which all meet the requirement of printing standard. Therefore, the accuracy of the computer color matching was demonstrated.

**Keywords** Computer ink color matching · Color matching model · Kubellka-Munk theory · Color difference

## 1 Introduction

In traditional, spot color ink was made artificially. However, it has been identified that artificial matching ink color was unstable. With the development of electronic information technology, computer can copy and transit huge amounts of data. Computer is recommended in the color matching system.

The idea of computer color matching is very simple. It is required to store color data in the computer firstly. Then use matching model to calculate the mixing proportion of basic ink. Finally, the corresponding formulation was generated. In order to solve the problem of spot ink color matching, many theories have been proposed, such as Neugebauer equation, masking equation and Kubellka-Munk (K-M) theory. K-M theory is one of the most commonly used in the theory of color

---

G. Liu · Q. Chen · G. Chen (✉)  
State Key Laboratory of Pulp and Paper Engineering,  
South China University of Technology, Guangzhou, China  
e-mail: chengx@scut.edu.cn

matching. The core idea of K-M theory is that the feature of ink is determined by the absorption coefficient (K) and the scattering coefficient (S) [1].

That means if the value of K and S was known, the reflectivity (R) will be gained. The formulas are shown in Formula (1)–(3) [2].

$$R = \frac{1 - R_g(a - b \coth bS_x)}{a - R_g + b \coth bS_x} \quad (1)$$

$$\frac{K}{S} = \frac{(1 - R_\infty)^2}{2R_\infty} \quad (2)$$

$$R_\infty = 1 + \frac{K}{S} - \sqrt{\left(\frac{K}{S}\right)^2 + 2\frac{K}{S}} \quad (3)$$

In above formulas,  $R_\infty$  represents the wavelength reflectivity of the ink layer thickness at infinity, X represents ink layer thickness and R represents substrate reflectivity.

According to the formulas, the values of K and S will be known by calculated R based on two different reflection backgrounds. According to additive principle, the K and S of blending ink are equal with the combination of K and S of basic ink [3]. Therefore, the principle of computer color matching is to seek an optimal combination of basic ink to represent target color.

The accuracy of computer color matching is leak with color matching models, the way to generate formulations and the capacity of basic database. According to tri-stimulus values, Dong, J.J. has created a color matching model of spot color ink. She also used the Kubelka-Munk theory to set up the corresponding parameters in this model [4]. The results are highly consistent with existing methods. Liu, J.J. used iterative method to improve the accuracy of color matching model. And the accuracy of the model is verified through application [5]. Guo, Q.Q. has demonstrated the rationality of computer ink color matching [6]. Zhao, C.F. found that using three-dimensional look-up table to obtain ink formulation can save a lot of time and improve the color matching efficiency [7].

## 2 Experiments

### 2.1 Experimental Instruments and Materials

X-Rite spectrodensitometer-SpectroEye was used to measure the values of  $L^*$ ,  $a^*$ ,  $b^*$ . Color samples was printed by the printability tester at fixed printing pressure (300 N/cm) and printing speed (0.8 cm/s). PANTONE color spots were selected as the target colors. According to PANTONE Process colors, China Hangzhou four kinds of basic ink, yellow, red, blue and black were selected. Coated papers

(128 kg/m<sup>2</sup>) were cut as printing patches (10 cm × 5 cm). InkFormulation 6.0 (X-Rite, Shanghai, China) whose color matching model is based on three stimulus values.

## 2.2 *Methods*

Firstly, the blending ink (5 g) was been mixed by basic ink according to the proportion of 2, 4, 8, 16, 32, 64, 90, 100% (precision is 0.01 g).

Secondly, color patches of basic ink were printed by the printability tester at the stage of fixed pressure (300 N), ink volume (0.3 g) and blending time (100 s).

Thirdly, the spectral reflecting of all samples was measured by spectrophotometer. Each color sample measured two different points.

Fourthly, all measurement results were record into the computer. The color matching system automatically calculated the average value and stored them. Then, it is need to input the basic information of Hangzhou ink, such as price, the total amount of ink and so on. Then the basic ink database has been built up.

Fifthly, the quality of basic database needed to be evaluated. If unqualified, repeat above steps till establish a qualified one.

Finally, four PANTONE color cards were selected to be measured.

## 3 *Results and Discussion*

### 3.1 *Testing of Basic Database*

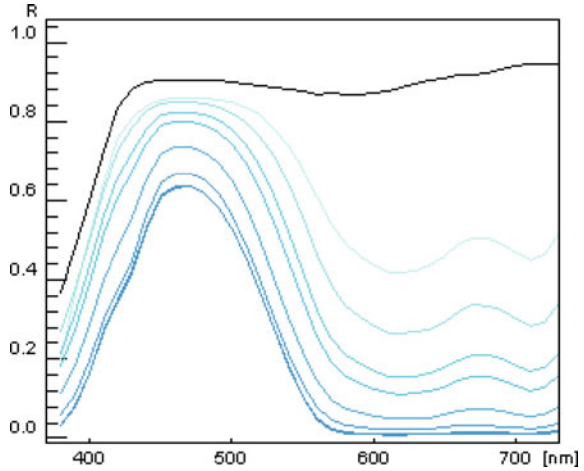
There are many relative errors in proofing process. Therefore, the established basic database may not be qualified. The smaller concentration is, the higher the reflection value is. The reflectance curve of qualified basic database should be parallel distribution [8]. If the curve is irregular or cross, correction is need to be done. The spectral reflectance curves of cyan ink are shown in Fig. 1 as an example. The curves show parallel distribution and no cross phenomenon. Therefore, the established basic database is qualified.

### 3.2 *Measurement Results*

Generally speaking, if the color difference is not more than 2 CIELab, the human eyes cannot distinguish difference colors. Therefore, a formulation which is small color difference will be optimal choose. The color differences of all samples are



**Fig. 1** Spectral reflectance curves of different concentrations cyan ink



**Table 1** Color differences of all color samples

Color difference	356C-1	356C-2	717C	7431C	643C
d L	1.0	-1.2	0.0	0.0	-0.2
d a	5.1	-0.1	0.2	-0.5	-0.2
d b	-2.4	0.8	-0.2	-0.1	0.2
d E	5.7	1.4	0.3	0.5	0.3

**Table 2** Ink formulations of all samples

Formulation	356C	717C	7431C	643C
C	2.0257 g	0.0007 g	0.0092 g	0.0427 g
Y	3.646 g	3.4372 g	0.1259 g	-
W	1.5059 g	1.2379 g	6.1204 g	5.229 g
M	0.0443 g	0.3242 g	0.4174 g	0.2337 g
Bk	-	-	0.0313 g	-

shown in Table 1. The blending color of 356C-1 is brighter, redder and bluer than the target color. However, after correction, the result is satisfied with a small color difference of 1.4.

Compared with the first sample, the next experiments are more successful. Though the color of 717C is redder and bluer than the PANTONE color, the color difference is only 0.3. The reasons are predicted that the apparatus and the printability tester are cleaned carefully. The color of 7431C is greener and bluer than the target color and the color difference is only 0.5. The color of 643C is darker, greener and more yellow than the target color, the color difference is only 0.5. In this table, 356C-1 represents the first ink formulation of 356C and 356C-2 is the revised. The statistics of ink formulations for all samples are shown in Table 2.

## 4 Conclusions

According to the theory of color matching, it is convinced that basic database is very important to the precision of ink formulation. There are many methods to improve the quality of basic database. Increase data capacity of basic ink is a simple way.

This paper has measured four spot colors (356C, 717C, 7431C and 643C). It was found that the largest color difference of the ink formulation is 1.4, which is absolutely met the requirements of generic fine products. The precision of the formulation could achieve 0.001 g, which is higher than other methods of ink color matching. Therefore, computer ink color matching is much more precise, faster and more efficient than manual operation.

**Acknowledgements** This paper is funded by “the key Laboratory of pulp and paper science and technology, ministry of education” (NO. KF201502). This paper is supported by “the Fundamental Research Funds for the Central Universities” (NO. D2154620). This research was financially supported by the Guangdong Provincial Science and Technology Project (NO. 2013B010401007). This research was supported by the Guangzhou Science and Technology Project (NO. 201607020045).

## References

1. KUBELKA P, MUNK F. (1931). Ein Beitrag Zur Optik Der Farbanstriche. *Zeitschrift Fur Technische Physik*, 12: 593–601.
2. Yuchang Wei, Wenmin Zhou, Zhilang Chen. (2010). Performance of computerized spectrum color matching based on Kubelka-Munk theory and its color rendering on offset ink sets. *China Printing and Packaging Study*, 2(21): 98–101.
3. Hu Gao, Mei Yan, Ju Li. (2005). Computer color matching for spot color ink. *Printing World*, (11):18–20.
4. Dong, J. J., (2007). Computer match color theories and practice of hectograph special color printing ink. Xi'an, China.
5. Liu, J. J., (2005). Computer match color method of hectograph special color printing ink. Xi'an, China.
6. Guo, Q. Q., (2006). Study on theory and experiment of color matching. Xi'an, China.
7. Pi, Y. X., & Gong, H. S., (2014). The example of matching special color printing ink by ink formulation software. *Printing Journal*. 05: 34–36.
8. Lin. C. R., (2009). A study on computer ink matching color base on spot-color ink printing in packaging printing. Wuxi, China.

# PTC Effect of Conductive Composites Based on Resin Mixed with Carbon Nanoparticle

Mengmeng Liang, Qichao Hou, Ruping Liu,  
Xudong Wu, Wei Wang and Luhai Li

**Abstract** In this article, the temperature response of the composite materials based on resin mixed with carbon nanoparticle was studied under the temperature of 30–70 °C. Through the experiment we found that the conductive composites have a positive temperature coefficient (PTC) characteristic in this temperature range, meaning the resistance value increases when the temperature increases. We also studied the effect of the conductive particles content on the temperature-sensitive property of the composites. In a certain temperature range, the conductive network of the internal material would be more stable when the carbon nanoparticle content is higher, showing lower sensitivity to temperature. Furthermore, we used the same samples carrying on heat treatment experiment at different temperatures. The results showed that the higher the heat treatment temperature is, the lower is the resistivity, as well as the resistance change rate when carrying temperature loading test on the samples. Furthermore, when decreasing the temperature to room temperature, this sample also kept a part of morphology in high temperature.

**Keywords** Carbon nanoparticle · Resin · Conductive composites · Heat treatment · Thermal-sensitive characteristic

## 1 Introduction

With the progress of information technology, the research of flexible robot tactile skin has become an important direction of the robot technology development. Robot bionic skin is moving toward the direction of flexible, super sensitive, easy to maintain and massive tactile perception to develop [1]. The matrix of the PTC

---

M. Liang · Q. Hou · R. Liu · X. Wu · W. Wang (✉) · L. Li (✉)  
Beijing Engineering Research Center of Printed Electronics,  
Beijing Institute of Graphic Communication, Beijing 102600, China  
e-mail: 18900616029@189.cn

L. Li  
e-mail: liluhai@bigc.edu.cn

material is organic polymer. Then it is added with some inorganic conductive filler and formed a kind of composite materials. Those materials combine the flexibility of the polymer and the conductivity of inorganic fillers well, which have very good comprehensive performance. Conductive composite based on resin filled by carbon nanoparticles is a new type of conductive polymer composite material like this, which has become a usual sensitive material to make flexible robot tactile skin. Because of the good flexibility, simple process and low cost etc., many scholars have begun to use the conductive carbon nanoparticle/resin to make the flexible tactile sensor, and measured the temperature sensitive characteristics. If the geometry size of carbon nanoparticle/resin composite materials are not fettered by the environment, the volume will change with temperature, the material will have the PTCR effect, otherwise there was no PTCR effect [2].

We have used carbon nanoparticles filling resin as conductive composites to get 4 kinds of formula sample depending on different content of carbon nanoparticles. And analyze the temperature sensitive feature of these samples according to the temperature loading test at 30–70 °C. We use three same samples carrying on heat treatment experiments at different temperatures, and then analyze the mechanism of heat treatment on resistance characteristics.

## 2 Experiments

### 2.1 Raw Materials and Preparation

The base material is sensor resin; Solvent is ethylene glycol butyl ether acetate; Conductive material is conductive carbon nanoparticle; Electrode material is conductive silver paste. Resin is added to the solvent with stirring until completely dissolved, then adding carbon nanoparticles and other additives. Continue to stir until the carbon nanoparticles dispersed evenly, then grinding in three roller grinder. The carbon paste is printed to the PET film with interdigital electrode using screen printing press, then drying the samples. The printed sample is shown in Fig. 1, left one for the inter digital electrode and the sectional configuration of the sample while the right one for the front view of the sample. We made a total of 4 kinds of formula sample in which carbon black relative with the resin mass fraction are 10.4, 13.9, 17.4 and 20.4% respectively.

### 2.2 Testing Instruments

Conductive composites based on resin mixed with carbon nanoparticles were scattered by Hot type constant temperature heating magnetic stirrer (DF-101S); The temperature-resistance was measured by Gas sensitive analyzer. In order to ensure the accuracy of the temperature test and the consistency of time, we should wait

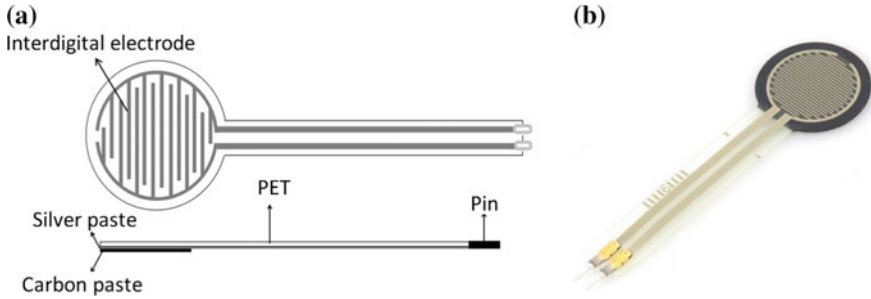
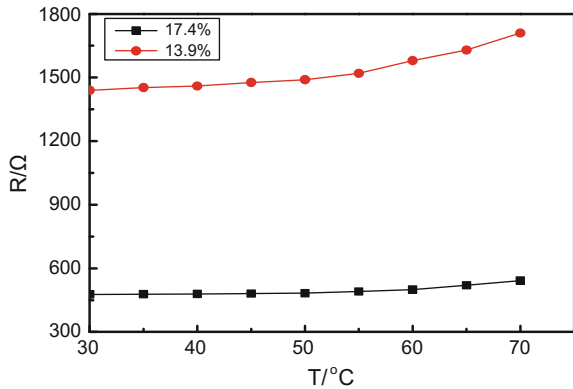


Fig. 1 Sample photos

Fig. 2 Sample resistance curve when temperature increasing



approximately 10 min from the temperature setting and record numbers until the temperature settled and resistance stabilized.

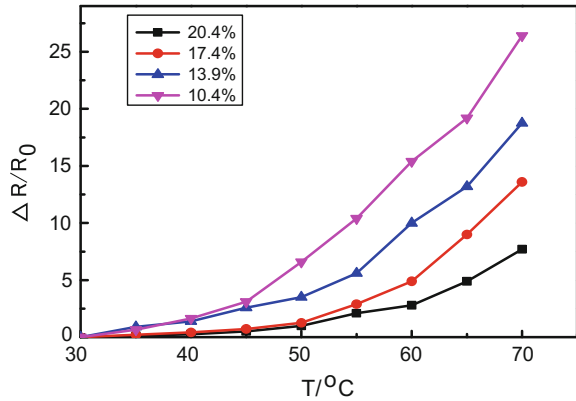
### 3 Results and Discussions

#### 3.1 Effect of Conductive Particle Content on the Resistance Temperature Characteristic

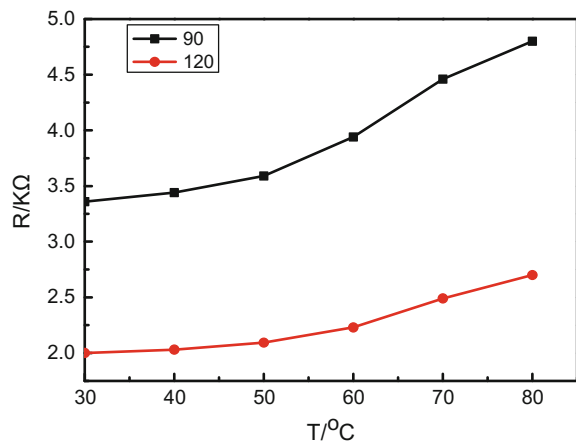
We conduct the temperature loading test to the samples at 30–70 °C and test the resistance response of the samples. Figure 2 shows the curves of resistance and temperature of samples with carbon nanoparticles content 13.9 and 17.4% respectively. As we can see in this figure, when the temperature is increased (increasing from 30 to 70 °C), the sample resistance is increased too. What’s more, the resistance value of the high carbon content sample is higher than the resistance value of the low carbon content sample at any temperature.

Assume the resistance change rate is  $\Delta = \Delta R/R_0$ , in which  $R_0$  is the initial value, meaning resistance value at 30 °C. The  $\Delta R$  is resistance change value. The four

**Fig. 3** Curve of change rate of resistance relative to temperature for different formulation samples



**Fig. 4** Sample resistance curve when temperature increase



$\Delta R/R_0$  curves were shown in Fig. 3. Ordinate is resistance change rate while abscissa is temperature. We can see that the resistance rate of conductive composites increasing with the temperature increasing. The greater the carbon nanoparticle content is, the smaller the curve slope is, so the smaller the change rate of the resistance value is, so that means the thermal stability of resistance is better. So we can know the thermal stability of the 10.4% sample is best in this experience.

### 3.2 Effect of Heat Treatment on the Resistance Temperature Characteristic

The three same samples with carbon content 13.9% are heat-treated for 30 min at respectively 60, 90 and 120 °C, then measuring the resistance value at a temperature range from 30 to 80 °C and observing the resistance value of the change rate.

**Fig. 5** Curves of change rate of resistance relative to temperature for samples heat-treated at different temperatures

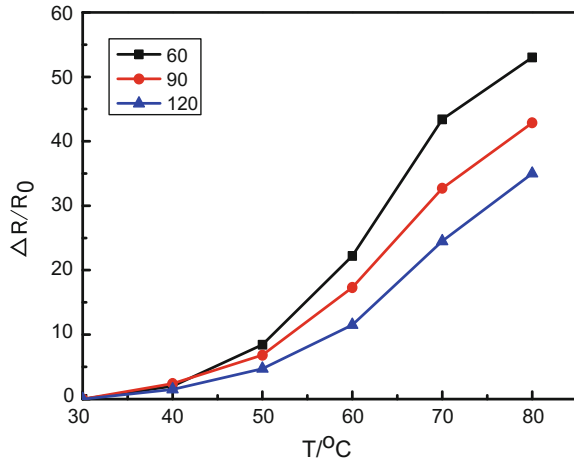


Figure 4 shows the resistance value of the two samples which were heat-treated at 90 and 120 °C respectively under the temperature of 30–80 °C. In Fig. 4, we can find that the higher the heat treatment temperature is, the lower the resistance is. In Fig. 5, the relationship between the temperature and the resistance change rate of the samples which are heat-treated with different temperatures is different. The higher the heat treatment temperature is, the smaller the slope of the curve is. In this set of experiment, the resistance change rate of the sample under 60 °C heat-treat is largest with the change of temperature.

## 4 Discussions

In Fig. 2, due to the interaction between resin-carbon nanoparticle and carbon black particles, even if the initial carbon nanoparticle filler dispersed well in resin matrix, carbon nanoparticle filler will also form filler network due to the agglomeration formation [3]. As the carbon nanoparticle filler volume fraction is increasing gradually, filler network increase and the resistance of conductive composites will be transferred from high to low. In Fig. 3, effect of temperature on the resistance has two main aspects. On the one hand, because the resin is heated to produce expansion to lead to the conductive particles gap widened so that the conductivity will be affected. On the other hand, because the temperature increased and thermal disturbance produced, then changing the electric field  $E$ . Electronic thermal activation also effect the conductivity.

Sheng et al. [4–6] established relationship of composites conductivity  $\sigma$  and temperature  $T$  and tunneling distance  $\omega$  according to the theory of electron tunnel. As follows:

$$\sigma = \sigma_0 \exp[-M\omega/(T + K)] \quad (1)$$

Under the improvement of the Xie et al. [7], obtained the theoretical model as follows:

$$\rho = \rho_0 \exp[M\omega/(T + K)] \quad (2)$$

In this model, M and K are constants, so the resistivity  $\rho$  is just about a function of particle clearance  $\omega$  and temperature T. So according to the formula (2), with temperature increasing, the resin volume expand, leading to an increase of particle clearance  $\omega$  so that the resistivity  $\rho$  increase; Electronic energy increase with the temperature increasing, improving the probability of electron transition (thermal disturbance) so that the resistivity decreases, thus, resistivity of conductive composites is affected by the thermal expansion and thermal disturbance. And both of the effects on the resistivity are opposite. In this experiment, when the temperature rise, the thermal expansion of the material's volume will lead to particle clearance  $\omega$  increasing and the resistivity increasing; Although the temperature increase will improve the ability of electron transition, but the impact is relatively weak. So the comprehensive result of the two aspects for resistivity is increasing, namely the sample resistance value increasing with the temperature increasing. The curve is shown in Fig. 2. And the more the carbon nanoparticle content is, the more stable the inner conductive network of composite is. So the impact of thermal expansion on the resistance will be lower as well as the change rate of resistance value, as shown in Fig. 3.

Because the energy level of conduction band and forbidden band of semiconductor materials are relatively close. With the temperature increasing, carrier concentration increased and a large number of electron transition made the sample resistivity decrease when the sample is heat-treated. Return to room temperature after heat treatment, because the samples also keep a part of morphology in high temperature, so resistance is lower than that of the untreated. And the higher the heat treatment temperature is, the lower the resistance value of the sample is, like in Fig. 4. Continue to carry on the temperature loading test, as shown in Fig. 5, at a certain temperature range, the higher the heat treatment temperature is, the smaller the resistance change rate is.

## 5 Conclusions

1. Conductive composites based on resin mixed with carbon nanoparticles show a positive temperature coefficient (PTC) characteristics in a certain temperature range, namely the resistance increases with the temperature increases.
2. The higher the content of conductive carbon nanoparticle is, the better the thermal stability of the composite is, and that is, the lower the temperature sensitivity is.



3. After the sample was carried out heat treatment, the resistivity dropped. The higher the heat treatment temperature is, the lower the resistivity is, the smaller the resistance change rate is as the temperature increasing.

**Acknowledgements** This work is supported by the National Natural Science Foundation of China (61501039), the Beijing Research Grant (No. Z15110000915071), the Beijing Natural Science Foundation (2162017), the Initial funding for the Doctoral Program of BIGC (27170116005/039), and the Elite Program of BIGC (27170116004/019).

## References

1. Wang X W, Gu Y, Xiong Z P, et al. (2014). Silk-molded flexible, ultrasensitive, and highly stable electronic skin for monitoring human physiological signals. *Advanced Materials*, 26(9): 1336–1342.
2. AneliDN. (1986). Composites based on rubber filled by carbon black. *International Polymer Science and Technology*, 13(10): 91–99.
3. Tian H, Liu P. (2015). Working principle of temperature sensor based on conductive rubber filled by carbon black. *Journal of Hefei University of Technology*, 38(9): 1230–1233.
4. Sheng P, Sichel E K, Gittleman J I. (1978). Fluctuation-Induced Tunneling Conduction in Carbon-Polyvinylchloride Composites. *Phys Rev Lett.*, 40: 1197–1200.
5. Sheng P. (1980). Fluctuation-Induced Tunneling Conduction in Disordered Materials. *Phys Rev.* B21: 2180–2195.
6. Sichel E K, Gittleman J I, Sheng P. (1978). Transport Properties of the Composite Materials Carbon-Poly (vinyl chloride). *Phys Rev*, B18: 5712–5716.
7. Xie Q, Liu R S, Xu Z Y, et al. (1998). Influence of the content of the white carbon black and carbon black on the pulling sensitive characteristic of the conductive silicon rubber. *Polym. Mater. Sci. & Eng.* 14(1): 94–97.

**Part V**  
**Packaging Engineering Technology**

# Preservation Effect of Thymol Active Packaging Films on Sugar Oranges

Xiaowen Liu, Yabo Fu, Dongli Li and Wencai Xu

**Abstract** Sugar orange is a popular but perishable fruit. In order to improve the preservation period of sugar oranges during storage and transportation, a kind of active packaging materials contains thymol preservative were developed in this work. The films were made by melt blending and film blowing method. The experiment was carried out on the sugar orange by using the films at  $20 \pm 2$  °C and 65% RH. In the experiments, unpacked groups were set as control, the LDPE thin film with thymol natural essential oils were experimental groups. Weight loss rate, sugar content, acid content, vitamin C content, rotten fruit rate, as well as sensory and taste evaluation were tested in the experiments. The results showed that the control group of the samples lost its value in 4 days, while the LDPE film containing preservative agent thymol could maintain the quality and prolong the shelf life of the sugar orange up to 13 days.

**Keywords** Thymol · Active packaging · Sugar orange · Preservation

## 1 Introduction

Physiological processes of post-harvest fruit are mainly respiration and transpiration, which play a significant role in the modified atmosphere packaging. Respiration is an energy metabolism that provided biochemical reactions of plants. An important method to manage suitable temperature and humidity is controlled atmosphere (CA) and modified atmosphere (MA) packaging [1]. Modified atmosphere packaging (MAP) can change the composition of gases in package. It depends on the respiration rate of the product, and the gases transfer through the interaction between the packaging material [2]. Respiration and permeation take place simultaneously in MAP [3, 4].

---

X. Liu · Y. Fu (✉) · D. Li · W. Xu  
Beijing Key Laboratory of Printing & Packaging Materials and Technology,  
Beijing Institute of Graphic Communication, Beijing, China  
e-mail: fuyabo@126.com

The incorporation of antimicrobial into film has been increasing in recent years. The antimicrobial agent is incorporated by blending with packaging material, immobilization or coating on surface [5]. Guarda et al. [6] studied that antibacterial agent (containing thymol or carvacrol) loading microcapsules, coated on the biaxially oriented polypropylene film to inhibit the growth of microorganisms. Solano et al. [7] studied the incorporation of thyme into LDPE by ionizing treatment or extrusion. Thymol (or thyme alias brain, thymol, lamellae), is easily soluble in alcohol, ether, acetic acid, chloroform and benzene. It naturally presents in the Labiatae genus thymus, thyme genera spicy aroma and grassy plants [8]. Thymol has antibacterial antiseptic properties so it can be used in fruit preservation [9].

Various methods were found to involve in the preservation of sugar orange fruit. Li et al. [10] treated sugar orange with 1-MCP on leaf to inhibit abscission, and did not influence fruit quality. Xia et al. [11] argued that the treatment of 4.0% calcium chloride would protect cellular tissue thus delayed senescence of sugar orange. Jiang et al. [12] chose chitosan as film substrate to make chitosan-nano ZnO film which could effectively reduce the respiration intensity of sugar orange. But other research hasn't found that using thymol modified film on preservation of sugar orange. In this experiment, thymol modified film was studied to extend the shelf life of sugar orange.

## 2 Materials and Method

### 2.1 Preparation of Thymol Modified Film

Initially, 3% Thymol, 15% EVA, 25% SBS, 57% LDPE and 5% thymol, 15% EVA, 25% SBS, 55% LDPE were mechanically blended by high-speed mixer respectively, and then co-rotating twin screw extruder was used for re-extrusion granulation. After this, films were made by using single screw plastic extrusion film machine. Finally, Thymol-EVA-SBS-LDPE films of content of 5 and 3% were obtained. They are kept at room temperature.

### 2.2 Sensory Evaluation

Sensory evaluation is divided into following categories: (1) taste is normal and skin is hydrated; (2) slight loss of water; (3) water loss is serious and taste is slightly abnormal; (4) skin is completely dry and taste is serious or strange. According to the sensory and taste evaluation, sugar oranges will be divided into 1 to 8 grades; 8 means excellent and 1 is terrible [13].

### ***2.3 Weight Loss Rate***

Relative weight loss was weight loss of treated fruit as a percentage of weight loss of the control.

### ***2.4 Headspace Gas Analysis***

The internal gas composition is determined by a headspace gas analyzer and a conductivity detector.

### ***2.5 Sugar Content***

The plant can produce a certain amount of sugar during anaerobic respiration, and the loss of water will change sugar content.

### ***2.6 Titration Acid Content***

Standard: Determination of total acid in foods of GB/T12456-2008.

### ***2.7 Vitamin C Content***

Standard: Determination of vitamin C content of fruit and vegetables of GB/T 6195-86 (2,6-chlorophenol indophenol sodium titration method).

### ***2.8 Rotten Fruit Rate***

The rotten amount of each sugar orange was divided into 0, 1/4, 1/2, 3/4 and 1 grades. The percentage of rotten fruit rate of each bag samples was the ratio of the rotten fruit grades and the total number.

### 3 Results and Discussion

#### 3.1 Sensory Evaluation

The changes in overall appearance of fruit are shown in Fig. 1. Control group is in air. The deterioration rate of control group is significantly fast at room temperature. It has been completely degenerated or rotten in eighth days. Overall, 3% Thymol modified film can extend preservation time of sugar orange until 13 days; 5% Thymol modified film can extend preservation time until 8 days. Control group only can preserve fruit within 3–4 days.

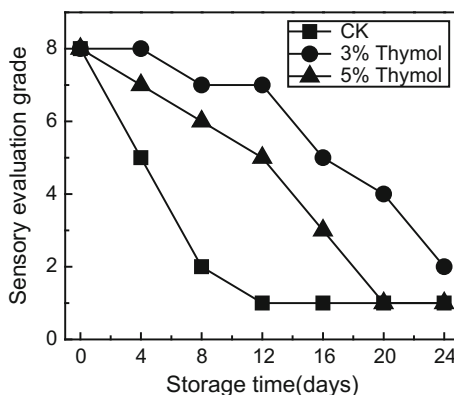
#### 3.2 Weight Loss Rate

The changes in weight loss of fruit are shown in Fig. 2. All the test samples were in weightlessness during storage time, and the weight loss rate was in accordance with the sensory and taste evaluation. 3% Thymol modified film has the best effect comparing to other groups. 5% Thymol modified film was superior to the control group.

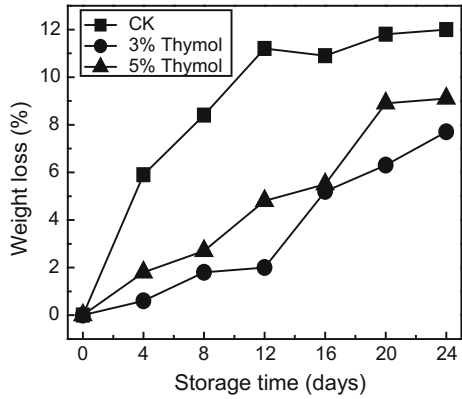
#### 3.3 Headspace Gas Analysis

The films selectively allow free diffusion of gases, which maintains an equilibrium between the external gas and that inside the package due to tissue respiration. The carbon dioxide content of each packaging bag is showing a downward trend after the first rise, the control group did not change. After harvest, sugar orange remains alive. The changes in CO<sub>2</sub> concentration in fruit packages sealed with thymol film are shown in Fig. 3.

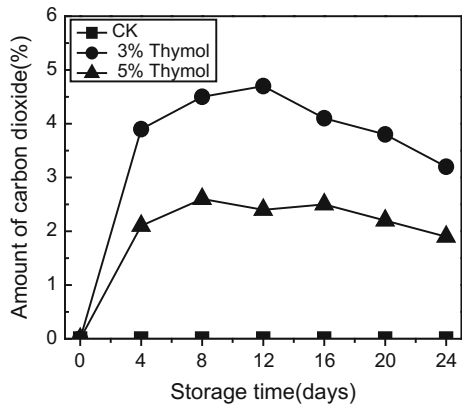
Fig. 1 Sensory grade



**Fig. 2** Weight loss rate



**Fig. 3** Amount of carbon dioxide



In this experiment, the highest point of carbon dioxide content in 3% Thymol modified film is about 12 days. The content of the sugar orange carbon dioxide using 5% Thymol modified film is about 8 days.

The changes in O<sub>2</sub> concentration in fruit packages are shown in Fig. 4. Oxygen content in packaging bags have dropped after the first rise, because of respiration of orange sugar. Analyzing of carbon dioxide and oxygen content in the bag, plastic film package formed inside the low oxygen content and high carbon dioxide content atmosphere by controlling the amount of oxygen and carbon dioxide through the film. It can inhibit cell respiration, and gradually reach a state of equilibrium. Oxygen content of 3 and 5% thymol film began to rise about 12 days. But the performance of 3% thymol packaging film is better.

Fig. 4 Amount of oxygen

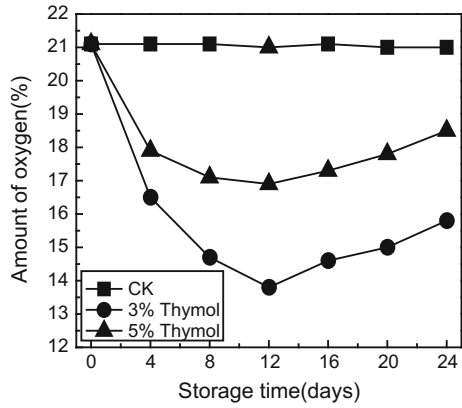
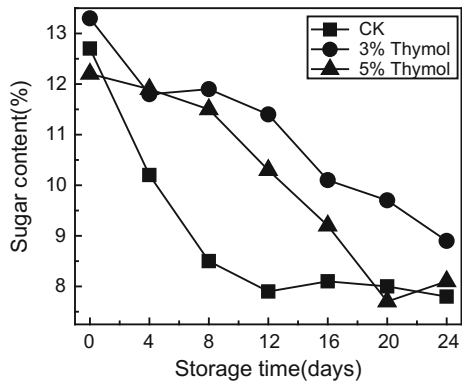


Fig. 5 Sugar content



### 3.4 Sugar Content

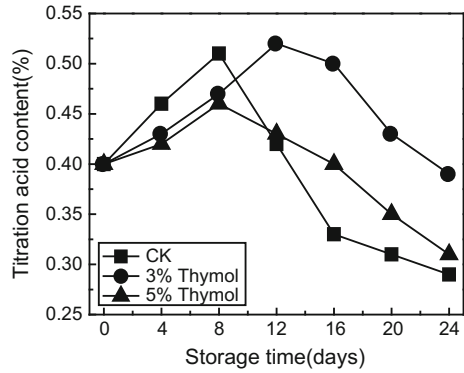
Sugar content of fruit in the storage bag shows a downward trend in Fig. 5. This figure reflects a downward trend in line with the results of Brix taste tests. Since each fruit own initiation sugar content have some differences, as reflected in the trend line chart there will be some fluctuations, but the overall trend is relatively stable. Sugar content rate of decline of orange sugar with film containing thymol is slower than control group, Brix of 3% thymol film showed the slowest rate of decline. In 24 days, the total amount of sugar (3% thymol film) is still higher than the other two groups.

### 3.5 Titration Acid Content

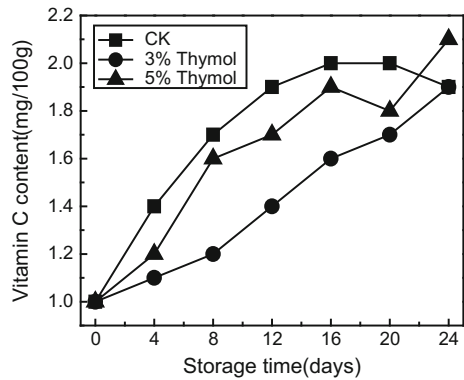
The content of the titration acid content of the sugar orange in each package in Fig. 6 showed the trend of first increasing and then decreasing. The increase of



**Fig. 6** Titration acid content



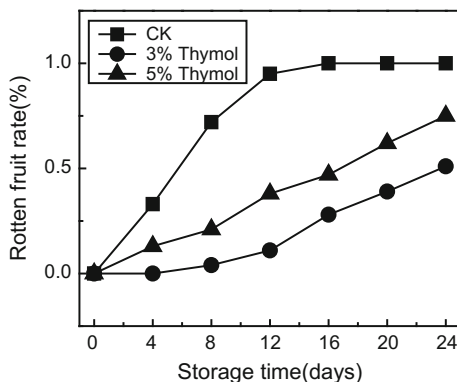
**Fig. 7** Vitamin C content



titration acid content is due to the respiration of the sugar, which causes the loss of nutrients in the plant. The content of titration acid can be decreased after the decomposition of sugar orange. Therefore, 3% thymol film has better preservation effect compared to other materials.

### 3.6 Vitamin C Content

The vitamin C content of all the samples showed an upward trend in Fig. 7, but the rising speed of VC content in the samples with using thymol is lower than the control group. The increase of VC content in the films containing 3% thymol is the slowest, which indicated this film played a better role in prolonging the shelf life of the sugar orange.

**Fig. 8** Rotten fruit rate

### 3.7 Rotten Fruit Rate

The changes in rotten fruit in packages are shown in Fig. 8. Rotten fruit rate index reflects the change of the degree of decay of sugar orange, which is consistent with sensory evaluation. In the first 8 days, thymol films showed a good effect of keeping fresh. The rotten fruit rate of the film containing 3% thymol is lowest.

## 4 Conclusions

During 24 days preservation experiments, the preservation ability of active MAP film was assessed. The experimental results showed that oranges in control group were significantly rotted in 4 days at room temperature. On the contrary, thymol active film group showed excellent performance in preservation, and its shelf life could be extended to 13 days. 3% thymol active films showed the optimal preservation effect, it is capable to prohibit the orange respiration significantly. This active MAP system, which used packaging materials incorporated with natural essential oil as preservation agent, provides a feasible way to prolong the shelf life of fresh fruits and vegetables at ambient environment.

**Acknowledgements** This work was financially supported by the Science and Technology Project of Collaborative Innovation Center of Beijing Municipal Commission Education (04190116008), Institute Level Youth Talent Program (27170116004/002) and Scientific Research Project (E-b-201503) of Beijing Institute of Graphic Communication.

## References

1. Irtwange, S. V. (2006). Application of modified atmosphere packaging and related technology in postharvest handling of fresh fruits and vegetables. *Agricultural Engineering International: CIGR Journal*, 5(6), 22–28.
2. Siracusa, V. (2012). Food packaging permeability behaviour: a report. *International Journal of Polymer Science*, 1(6), 222–230.
3. Mangaraj, S., Goswami, T. K. (2009). Modified atmosphere packaging of fruits and vegetables for extending shelf-life-A review. *Fresh produce*, 3(1), 1–31.
4. Mangaraj, S., Goswami, T. K., Mahajan, P. V. (2015). Development and validation of a comprehensive model for map of fruits based on enzyme kinetics theory and arrhenius relation. *Journal of food science and technology*, 52(7), 4286–4295.
5. Duncan, T.V. (2011). Applications of nanotechnology in food packaging and food safety: barrier materials, antimicrobials and sensors. *Journal of colloid and interface science*, 363(1), 1–24.
6. Guarda, A., Rubilar, J. F., Miltz, J., Galotto, M. J. (2011). The antimicrobial activity of microencapsulated thymol and carvacrol. *International journal of food microbiology*, 146(2), 144–150.
7. Solano, A. C. V., de Rojas Gante, C. (2012). Two different processes to obtain antimicrobial packaging containing natural oils. *Food and Bioprocess Technology*, 5(6), 2522–2528.
8. Solomakos, N., Govaris, A., Koidis, P., Botsoglou, N. (2008). The antimicrobial effect of thyme essential oil, nisin, and their combination against *Listeria monocytogenes* in minced beef during refrigerated storage. *Food microbiology*, 25(1), 120–127.
9. Solórzano-Santos, F., Miranda-Novales, M. G. (2012). Essential oils from aromatic herbs as antimicrobial agents. *Current opinion in biotechnology*, 23(2), 136–141.
10. Li, Q., Wu, F., Li, T., Su, X., Jiang, G., Qu, H., Duan, X. (2012). 1-Methylcyclopropene extends the shelf-life of ‘Shatangju’ mandarin (*Citrus reticulata* Blanco) fruit with attached leaves. *Postharvest biology and technology*, 67, 92–95.
11. Xia, X. Z., Wu, X. B., Zhang, Z. Q., Dong, Q. B., Liang, Z. Q. (2009). Study on Effect of Calcium Treatment on Fruit Quality in Storage of Postharvest Hongjiang Orange [J]. *Storage Process*, 5, 006.
12. Jiang, M., Ye, X.L., Qiu, Q. H. (2012). Study on the preservation effect of chitosan and nano-ZnO compound coating on Shatang mandarin. *Sci Tech Food Industry*, 33, 348–351.
13. Lawless, H.T., Heymann, H. (2010). Sensory evaluation of food: principles and practices. *Springer Science Business Media*, 11, 48–51.

# Experimental Investigation of Influence Factors for Compression Strength of Thin Honeycomb Paperboard Box

Shibao Wen, Xiaoke Chu and Jujie Sun

**Abstract** The main purpose of the paper is to investigate the influencing factors of box compression test (BCT) strength that made by the thin honeycomb paperboard (THP). Box type of thin honeycomb paperboard box (THPB) is FEFCO-code 0201. Boxes are tested respectively which have different direction of paperboard, different structure size and opening hole. The results showed that: BCT strength is consistent with the strength of longitudinal and transverse of THP; Structure size of THPB—length breadth ratio, perimeter and height—has great impact on BCT strength; Opening hole of side panel has a great influence on BCT strength of THPB. The direction of paperboard, structure size and opening hole on BCT strength are needed to be focused when THPB is manufactured by carton processing, and the results have important significance for the application of THPB.

**Keywords** Thin honeycomb paperboard · Carton · Box compression test · Edgewise compression strength

## 1 Introduction

The corrugated paperboard box is the most commonly used transport packaging, its production has more than one hundred years of history, its large-scale application has sixty years at least [1]. Performance investigation and processing of corrugated paperboard box (CPB) have been very complete and mature. Due to a better flat compression, bending and edgewise compression performance, honeycomb paperboard is also widely used as packaging material, mainly used as a cushioning structure and the material of heavy-duty paper pallet and box. Limitation of

---

S. Wen (✉) · X. Chu · J. Sun  
School of Polymer Science and Engineering,  
Qingdao University of Science & Technology,  
Qingdao, Shandong, People's Republic of China  
e-mail: wenshibao@126.com

© Springer Nature Singapore Pte Ltd. 2017  
P. Zhao et al. (eds.), *Advanced Graphic Communications  
and Media Technologies*, Lecture Notes in Electrical Engineering 417,  
DOI 10.1007/978-981-10-3530-2\_73

581

honeycomb core production process, the thickness of the honeycomb paperboard are normally 10 mm or more, but relative to corrugated paperboard, the honeycomb paperboard has a good flat compression [2] and bending strength. Honeycomb paperboard creasing is difficult due to high flat compression strength, and paperboard fold is also difficult due to high bending strength. Unlike the production of CPB, honeycomb paperboard box (HPB) cannot be made automatically applying to box production line. The HPB is usually made by bonding of single piece paperboard directly or by bonding between paperboard and paper corner indirectly [3, 4]. Thus production of HPB is inefficient and expensive, the large-scale application of HPB is inconvenient.

Taking into account the above problems of HPB, Ningbo Chengming Honeycomb Paper Co., Ltd successfully developed the *5–8 mm thin honeycomb paperboard (THP) production process* [5] technology in 2009. THP can be manufactured into box mechanically with the corrugated box production line by little improvements, thus productivity of THPB is greatly improved. Compared with CPB, THPB has higher BCT strength. There are a large number of literatures [1] for the investigation of box compressive strength and its factors. Among of them, empirical Kellcutt formula [6] and McKee formula [7] about box compressive strength are well-known. However, currently there is not any research on applications and influence factors for THPB strength, the further guidance on its application cannot be given. To find the influence factor pattern on the BCT strength of THPB, five factors—length breadth ratio, perimeter, height, core strip direction and side panel opening hole of THPB box—are chosen to investigate the impact on the box compression strength according to factors of CPB compression strength. The results will provide a preliminary experimental data for THPB application.

## 2 Experiment

### 2.1 Test Apparatus and Material

Computer universal testing machine, GT-TCS-2000, Gotech testing equipment Co., Ltd.; Electronic balance(scale 0.001 g), Sartorius Mechatronics Beijing Ltd.; Electronic compressive strength tester, ZSD-3, Changchun paper sheet testing equipment Co., Ltd.; Box Compression Tester, DRK123, Shandong Drick Instruments., Ltd.

THPB is manufactured by Ningbo Chengming Honeycomb Paper Co., Ltd, which has 4 mm honeycomb side length, 5.5 mm thickness and  $960 \text{ g m}^{-2}$  grammage. Core paper of THPB is 0.274 mm thickness,  $120 \text{ g m}^{-2}$  grammage and grade A corrugated paper; Internal and external liner are grade A test liner board, which thickness are 0.460 and 0.490 mm, and grammage are 300 and  $320 \text{ g m}^{-2}$  respectively. Honeycomb paperboard is anisotropic, specimen boxes are divided into transverse and longitudinal direction in the box compression strength test

according to the core strip of the side of box [8, 9], transverse THPB is a honeycomb core strip of box side perpendicular to the box compression direction and vice versa.

## ***2.2 Box Preparation, Test Method and Preconditions***

Die cutting and creasing of THPB is by ProDigi high speed plotter made by the German LASERCOMB company. Sampling head of the plotter is designed specially for CPB, the creasing depth and width are not enough, so plotting sample does not meet the requirements of THP fold. On the basis of the creasing by ProDigi plotter, we press the creasing using a metal rod manually, it can be avoided paperboard folding fracture at the creasing location. Box type produced by THP is FEFCO-code 0201 in the paper, and the slotting width is 6 mm, other dimensions are set as required.

Box compression test (BCT) refers to ASTM-D642 and TAPPI/ANSI T 804 standards. All experiments are carried out in 23 °C and 50% relative humidity, and precondition time of the box is not less than 24 h before the experiment. Loading speed of BCT is set to  $10 \pm 3$  mm/min, initial compression of box is 220 N.

## **3 Results and Discussions**

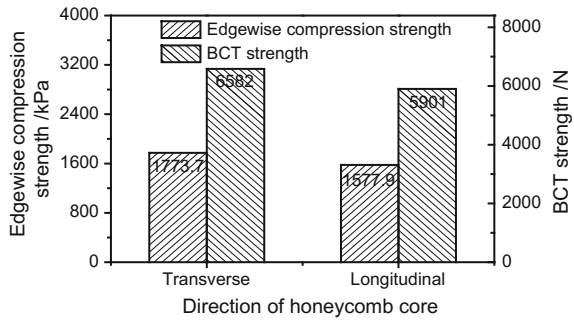
Edgewise compression strength of transverse honeycomb structure is generally greater than that of longitudinal sample [8], in theory the core of THPB side panel should be transverse. However, because of the manufacturing process restrictions, the width of honeycomb paperboard (Cross Direction, CD) in the production line has limitations, box is usually manufactured in MD (Machine Direction), in which of the situations the core of THPB side panel is longitudinal. In the paper if it is not explained, the core of THPB side panel is longitudinal.

### ***3.1 Core Strip Direction Influence on BCT Strength***

Test edgewise compression strength of transverse and longitudinal THPB referring to ASTM standard [9] firstly, sample size 120 mm × 60 mm, loading speed 1 mm/min. The transverse and longitudinal THPB of side panel are produced respectively, THPB size is 350 mm × 200 mm × 200 mm, then BCT strength of transverse and longitudinal THPB are investigated respectively.

Histogram of edgewise compression strength of THP and BCT strength of THPB draws as shown in Fig. 1, edgewise compression strength of longitudinal THP is 11% smaller than that of transverse THP, BCT strength of longitudinal

**Fig. 1** Core strip direction influence on the edgewise compression strength of paperboard and BCT strength



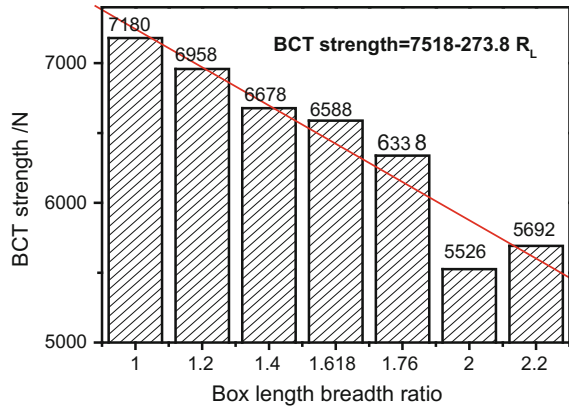
THPB is 10.3% less than that of transverse THPB at the same time. That is, core strip direction influence on the edgewise compression strength of paperboard and BCT strength is exactly the same, it also shows that there is a close relationship between the edgewise compression strength of paperboard and the BCT strength of THPB. BCT strength of THPB is showing a very clear directionality, core strip direction of side panel for THPB should be a rational choice according to need.

### 3.2 Length Breadth Ratio Influence on BCT Strength

Under the same height 350 mm and perimeter 1440 mm, seven groups with different length breadth ratio are set. Length breadth ratio is 1.0:1, 1.2:1, 1.4:1, 1.618:1, 1.76:1, 2.0:1 and 2.2:1, and  $360 \times 360$ ,  $392 \times 328$ ,  $420 \times 300$ ,  $445 \times 275$ ,  $460 \times 260$ ,  $480 \times 240$  and  $495 \times 225$  are corresponding to length  $\times$  breadth.

As shown in Fig. 2, it can be found that BCT strength decreases with the length breadth ratio increment on the whole. That is, BCT strength has the largest compression strength when the length breadth ratio is 1:1, it is obviously different from CPB that the maximum BCT strength is between 1.2 and 1.4 length breadth ratio [10, 11]. BCT strength depends on the edgewise compression strength of paperboard, and the edgewise compression strength of paperboard relates to width in a range when the width is greater than a specific value, the edgewise compression strength reduces with the width increase, and vice versa. In the constant perimeter, a pair of side panel width is greater, another pair is smaller definitely, BCT strength should be unchanged logical. However, in Fig. 2 BCT strength decreases with the length breadth ratio increase all along, that is, the reduction of edgewise compression strength in long side panel is greater than the increase of that in the short side panel during the changing of the length breadth ratio. The center breakout in the long side panel is more serious than that of in the short side panel with the length breadth ratio increase before failure in the testing, it can verify the above speculation.

**Fig. 2** Length breadth ratio of THPB influence on BCT strength



In the range of 1.0–2.2 length breadth ratio ( $R_L$ ), 5692 N BCT strength when  $R_L$  is 2.2 is 20% lower than that of  $R_L = 1$ . BCT strength is fit to  $R_L$  linearly, formula (1) is got.

$$\text{BCT strength} = 7518 - 273.8 R_L \tag{1}$$

where:  $R_L$  is length breadth ratio of THPB.

According to the formula (1) BCT strength can be calculated within the range of 1.0–2.2 the length breadth ratio.

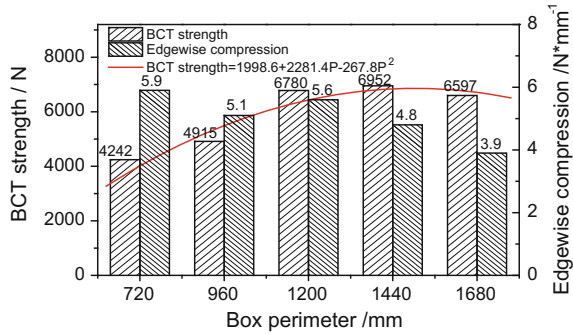
### 3.3 Perimeter Influence on BCT Strength

BCT strength of corrugated paperboard box increases first, then reduces with the perimeter increase. Distribution of the BCT strength along the perimeter is different, BCT strength near to corner is larger than near to the middle on the side [12]. There is no literature in this area for THPB, we have designed different perimeter to examine its influence on BCT strength. Length breadth ratio (1.4:1) and height (300 mm) is unchanged, then BCT strength with different perimeter is tested. The experimental perimeter is 720, 960, 1200, 1440, and 1680 mm, 210 × 150, 280 × 200, 350 × 250, 420 × 300 and 490 × 350 are corresponding to length × breadth.

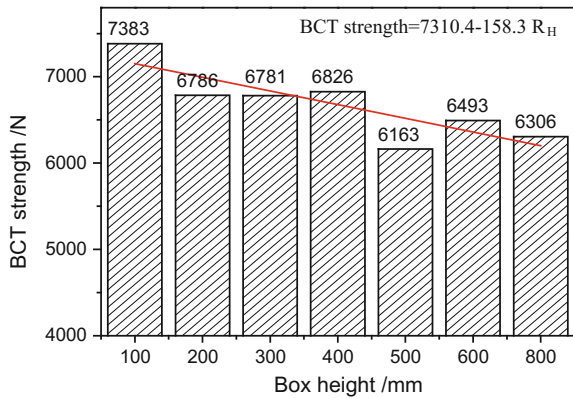
As shown in Fig. 3, it can be found that BCT strength is a convex curve with the perimeter between 720 mm and 1680 mm. The rule of THPB curve of BCT strength is the same with CPB with the change of perimeter. The max BCT strength of THPB appears in 1440 mm perimeter. At the same time, edgewise compression strength of side panel from BCT strength divided by perimeter is decreasing gradually, it can verify that the edgewise compression strength of side panel decreases with the width increase when the width is greater than a specific value (Fig. 3).



**Fig. 3** Perimeter of THPB influence on BCT strength



**Fig. 4** Height of THPB influence on BCT strength



The perimeter influence on BCT strength can be described by the quadratic polynomial formula (2).

$$\text{BCT strength} = 1998.6 + 2281.4P - 267.8P^2 \tag{2}$$

where: P is perimeter of THPB.

### 3.4 Height Influence on BCT Strength

Under the same length breadth ratio (1.4:1) and perimeter (1200 mm), height of THPB influence on BCT strength is investigated. The height of THPB is 100, 200, 300, 400, 500, 600 and 800 mm. As shown in Fig. 4, BCT strength of THPB decreases gradually with the height increase. The relationship between BCT strength of THPB and height can be described by linear formula (3) roughly.

$$\text{BCT strength} = 7310.4 - 158.3R_H \quad (3)$$

where:  $R_H$  is height of THPB.

In Fig. 4, it can be found that BCT strength of height 800 mm only reduces 15% than that of height 100 mm within the height range of the experiment, that is, height of THPB influence on BCT strength is not obvious.

### 3.5 Side Panel Opening Influence on BCT Strength

Vent and hand hole in the side panel is often necessary for CPB, opening of side panel has a great influence on BCT strength [13], literature about opening in the side panel has not been found for THPB. A scheme is designed to examine the opening hole influence on BCT strength. THPB size is 350 mm × 200 mm × 200 mm, the symmetrical opening hole is a 100 mm × 30 mm rectangle in the middle center of the long side panel.

BCT strength without opening and with a pair opening are 6582N and 4984N respectively. Relative to THPB without opening, BCT strength of THPB with symmetrical opening decreases by 24%, in fact the length of the opening position in the perimeter direction is only covered 18% ( $200 \times 100\%/1100$ ) that of the total perimeter. It shows that stress concentration caused by openings in the side panel will greatly reduce BCT strength of THPB, opening influence of the side panel on BCT strength should be considered when design THPB.

## 4 Conclusions

All other things being equal, it can be concluded: Core strip direction influence on the edgewise compression strength of paperboard and BCT strength is exactly the same, core strip direction of side panel for THPB should be rational choice; BCT strength has the largest compression strength when the length breadth ratio is 1:1; BCT strength is convex curve with the perimeter change, the perimeter influence on BCT strength can be described by quadratic polynomial formula; BCT strength decreases linear gradually with the height increase; Stress concentration caused by openings in the side panel will greatly reduce BCT strength of THPB. The results have important implications for the application of THPB, then a wider range of data test will be considered. Based on that an empirical formula about the BCT strength of THPB, will be integrated including length breadth ratio, perimeter, height, core strip direction and side panel opening.

## References

1. Benjamin Frank (2013). Corrugated Box Compression—A Literature Survey. *Packaging Technology and Science*, doi:10.1002/pts.2019.
2. Youmei Ping, Benlong Yu, Wenquan Shao (2005). Investigation on the Flat Crush Test of Honeycomb Paperboard. *Packaging Engineering*, 26(5): 115–117.
3. Lirong Yan, Yong Xie (2010). Discussion on the Creasing and Folding Method for the Honeycomb Cardboard [J]. *Packaging Journal*, 2(4): 14–18.
4. Xinchang Zhang, Yongguang Wang, Jinzhi Yang, et al (2004). Research on Folding-Forming Process for the Honeycomb Cardboard Boxes. *Journal of Southern Yangtze University (Natural Science Edition)*, 3 (2): 164–167.
5. Guobao Liang. (2009), A manufacturing method of honeycomb paperboard, Chinese Patent, CN101554788.
6. Kellicutt, K. Q. (1959), Compressive strength of boxes-Part I. *Package Engineering*, 4(12): 88–89.
7. McKee, R C; Gander, Wachuta (1963). Compression strength formula for corrugated boxes. *Paperboard Packaging*, 48 (8): 149–159.
8. Shibao Wen (2012). Compressive Performance Investigation between Thin Honeycomb Paperboard and Corrugated Paperboard of Flute A. *Advanced Materials Research*, 487: 198–202.
9. ASTM C364-99, Standard Test Method for Edgewise Compressive Strength of Sandwich Constructions, ASTM International, West Conshohocken, PA, 1999, DOI:10.1520/C0364-99.
10. Cheng Sun (2010). *Packaging Structure Design*. China Light Industry Press, Beijing.
11. M. E. Biancolini, C. Brutti (2003). Numerical and Experimental Investigation of the Strength of Corrugated Board Packages. *Packaging Technology and Science*, 16(2), 47–60.
12. Maltenfort, G. G. (1980). Compression Load Distribution on Corrugated Boxes. *Paperboard Packaging*, 65(9), 71–72.
13. Jongkoo Han, Jong Min Park (2007). Finite Element Analysis of Vent Hand Hole Designs for Corrugated Fiberboard Boxes. *Packaging technology and science*, DOI:10.1002/pts.741.

# Research on Application of WSN in Cold Chain Logistics' Warehousing and Transportation

Hanyue Zhang and Shijuan Yang

**Abstract** Cold Chain Logistics has been closely surrounding the people in their own life, which nearly contains all the perishable food. In Cold Chain Logistics, warehousing and transportation are the parts that are most liable to accidents. Regarding the cold-chain food's safety as the starting point and combining with the requirements of warehousing and transportation, the paper adopts Wireless Sensor Networks (WSN) technology, Zigbee network technology to build the intelligent monitoring system of three-tier framework containing perception control-network transmission-application service. That is to say, the various types of sensors are placed in warehouses, carriages and packaging of goods to monitor environment information such as temperature humidity, illumination, behaviors of goods in real time. And based on maximum similarity's multiple characteristic recognition (MSMCR), the decision method of fuzzy control, the monitoring terminal analyses the information and makes the judgment in time to adjust the environmental factors automatically, which realize real-time intelligent monitoring and visible management in warehousing and transportation.

**Keywords** WSN · Cold chain logistics · Warehousing · Transportation · Food safety

## 1 Introduction

There is a popular proverb which goes that bread is stall of life and security is stall of bread. With material and cultural life being increasingly rich, cold-chain food has been on the table, such as vegetables, fruit, dairy products, meat. Hence Cold Chain Logistics has been on the way to meet the food demand.

---

H. Zhang · S. Yang (✉)  
Tianjin University of Science & Technology, Tianjin, China  
e-mail: 862702407@qq.com

© Springer Nature Singapore Pte Ltd. 2017  
P. Zhao et al. (eds.), *Advanced Graphic Communications and Media Technologies*, Lecture Notes in Electrical Engineering 417,  
DOI 10.1007/978-981-10-3530-2\_74

According to investigation, the value of the product descended as high as 35% because of unreasonable control of temperature [1]. Moreover, the overturn and the collision of goods always give rise to a severe effect on the quality of food in transit. To ensure the food safety, the paper utilizes Wireless Sensor Network (WSN) to the warehousing and transportation in Cold Chain Logistics to monitor environment parameters in real time and to implement corresponding measures. It's constructing an intelligent monitoring system of environment in warehousing and transportation that brings in higher economic benefits to cold chain logistics.

## **2 Overall Design of the Environment Monitoring System**

### ***2.1 Demand Analyses on Environment Parameters of System***

Aiming at the characteristics of cold-chain food and problems of food safety, following environment parameters need to be strictly monitored.

1. Temperature: Most of the cold-chain food requests to be refrigerated, which has severe rules on temperature range. Otherwise, physical or chemical changes will appear to reduce edibility of cold-chain food.
2. Humidity: If humidity is too high, it's apt to breed microorganisms. To the contrary, it's extremely likely to cause food dehydration. And air humidity is much affected by the environmental temperature.
3. Illumination: As every coin has two sides, so does influence on illumination. At the same time, the staff also needs proper lighting to work.
4. Behaviors of goods: Due to non-standard operation in transportation, the overturn and other behaviors have happened frequently, threatening food safety.

### ***2.2 Structure of the Overall System***

WSN is composed of a large number of sensor nodes scattered in the area of the overlay network. It owns unique properties, such as small size, large scale, low cost, dynamic and flexible structure [2]. In Fig. 1, the technology of WSN is occupied to set up a three-tier system framework.

As is the bottom of system, perception control layer is used for information collection on fundamental environment parameters by different kinds of sensors. Zigbee, a type of ad hoc network technology, can realize communication between sensor nodes and the monitoring terminal. The monitoring terminal, on basis of the standard environmental parameters set in advance and the certain algorithm, analyzes information in time and commands the actuator to control the related equipment so as to achieve a safe and stable environmental atmosphere.

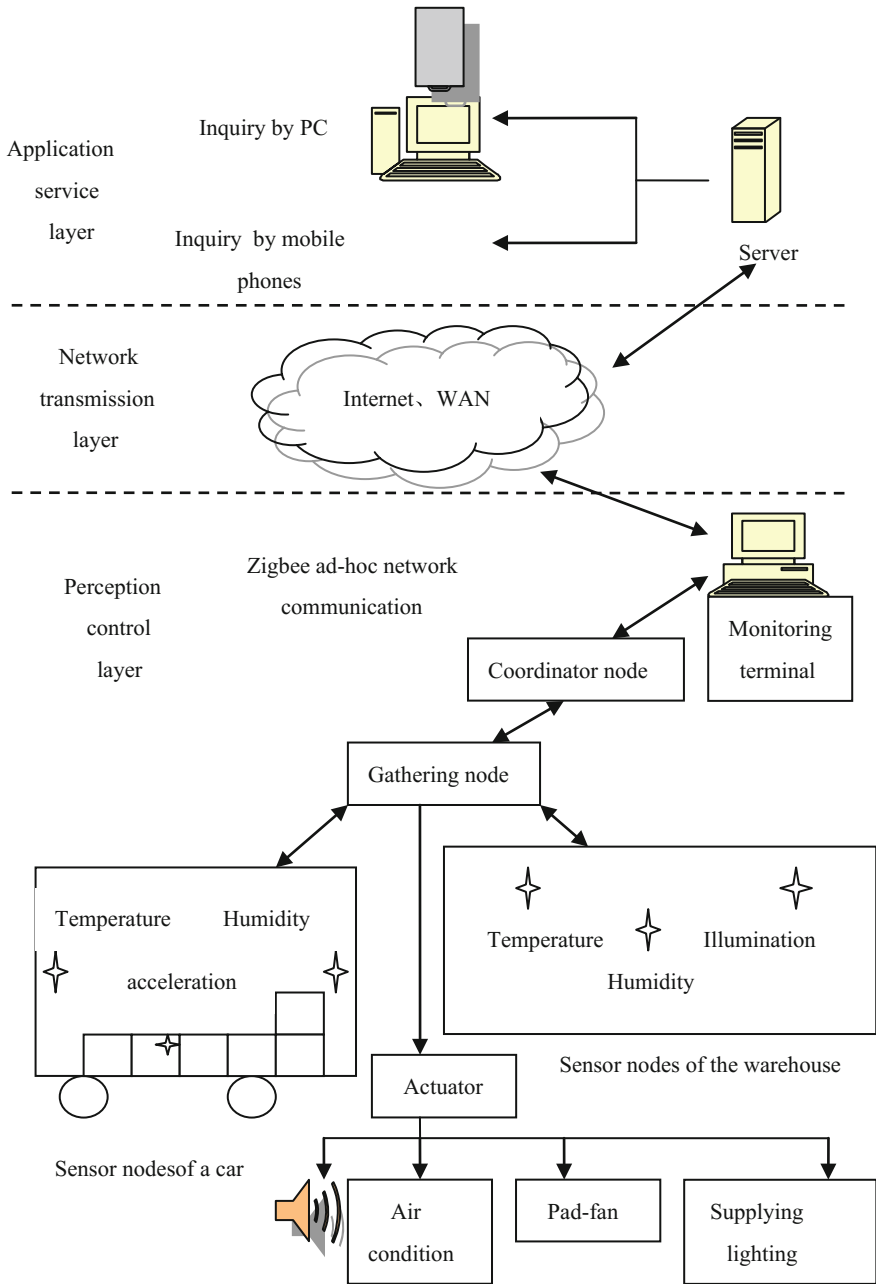


Fig. 1 The system's overall structure

Network transmission layer is the bridge between perception control layer and application service layer. It is mainly responsible for delivering information processed and analyzed to the server through the Internet and WAN, so that the data successfully have access to the application service layer.

In the application service layer, the staff can always check the real-time information of environment parameters by the client interface where relevant parameters can be set directly to control equipment. Meanwhile, using the remote phone, people browse the real-time data whenever and wherever they are to fulfill remote monitoring and management.

### ***2.3 Layout of Sensor Nodes***

Based on the actual situation, temperature sensors, humidity sensors and illumination sensors are put in warehouses and cars. Acceleration sensors are often attached to the packaging of goods. The following is a setting optimization scheme of sensor nodes in fair shape of the warehouse.

Taking advantage of the way of grid subdivision, the warehouse is divided into multiple small cubes, each of which is the perceptual areas to be monitored. It's assumed that sensor nodes are regarded as spheres' centers of areas where sensor nodes are able to monitor parameters. Namely, it's the circumscribed spheres of these small cubes. Hypothetically, the side length of a small cube is  $a$ , and each of sphere's radius is  $r$ . When the side length of the small cube meets the condition of  $a \leq 2\sqrt{3}r/3$ , the single coverage could come true. In this case, the center of the sphere is the location of the sensor node.

To solve the problem of sensor nodes' energy and to prolong the service life, sensor nodes introduce the wakeup model to work. It's the meaning that the sensor nodes abide by the collection command and the sleep command to work circularly.

### ***2.4 Choice of Zigbee's Topological Structure***

In order to overcome the limitation of network protocol of previous wireless sensors, the intelligent monitoring system adopts Zigbee technology to meet the lower costs, lower energy consumption and higher fault tolerance of wireless sensors [3]. Zigbee is made up of 65535 wireless communication nodes at most [4]. The Zigbee network is divided into coordinators, routers and terminal devices.

There are three kinds of Zigbee's topological structure. The star network topology is simplest in the structure, so it is applicable to situations with smaller network coverage and less nodes. The cluster structure has certain scalability and stability, used for larger occasions. By contrast, the net topology structure is the most complex with strong dynamic capabilities, while it relies on the network's connection quality excessively.

Taking the actual warehousing and transportation’s environment of Cold Chain Logistics into consideration, this part takes advantage of the cluster topology to form the network of the monitoring system.

### 2.5 Operation Analyses on Controlling Equipment

In the light of cold-chain food requires, the monitoring terminal controls related equipment based on the decision method of fuzzy control including fuzzy set theory, fuzzy language and fuzzy logic [5]. There is the model of fuzzy control about operating the air condition to adjust temperature in the following.

1. The definition of input, output, fuzzy sets and the domain of discourse

The  $e$  is taken as the environmental temperature deviation and  $ec$  is taken as the change rate of temperature deviation, both of which are the input. The  $u$  represents the control output. As is seen, Fig. 2 shows the structure on a fuzzy controller of double input and single output.

In effect,  $e$  is for acquisition of actual temperature minus cold-chain food’s appropriate storage temperature, and  $ec$  is the quotient that acquisition of the temperature deviation minus the last temperature deviation divided by the cycle time is. The corresponding fuzzy language sets of  $e$ ,  $ec$ ,  $u$  are deviation  $E$ , the change rate of temperature deviation  $EC$ , output  $U$ . According to the temperature demand of cold-chain food,  $E$  is divided into the fuzzy language’s variables including negative big (NBe), negative median (NMe), negative small(NSe), zero (Ze), positive small (PSe), positive median (PMe), positive big (PBe), whose the domain of discourse is  $\{-6, -5, -4, -3, -2, -1, 0, 1, 2, 3, 4, 5, 6\}$ .  $EC$  of the fuzzy language set is  $\{NBec, NMec, NSec, Zec, PSec, PMec, PBec\}$ , of which the domain of discourse is  $\{-6, -5, -4, -3, -2, -1, 0, 1, 2, 3, 4, 5, 6\}$ . And then,  $U$  of the fuzzy language’s set is  $\{NBu, NMu, NSu, Zu, PSu, PMu, PBu\}$ , of which the domain of discourse is  $\{-6, -5, -4, -3, -2, -1, 0, 1, 2, 3, 4, 5, 6\}$ .

2. Fuzzification of input and output

According to the temperature requirements, the range of  $e$  is  $[-30, +30]$ , the range of  $ec$  is  $[-24, +24]$  and the range of  $u$  is  $[-36, +36]$ . Then,  $k_e$ ,  $k_{ec}$ , on behalf

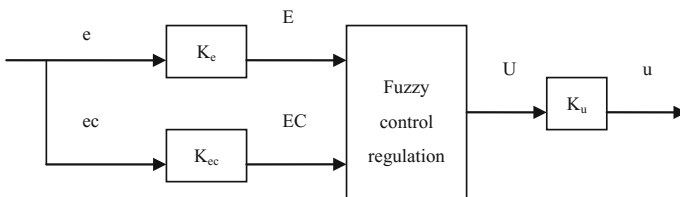


Fig. 2 The fuzzy controller’s structure



of the quantitative factors, and  $k_u$ , on behalf of the scale factor, are introduced in the fuzzy controller.  $k_e, k_{ec}, k_u$  can be gotten by formulas (1), (2) and (3).

$$k_e = \frac{2m}{e_H - e_L} \tag{1}$$

$$k_{ec} = \frac{2m}{ec_H - ec_L} \tag{2}$$

$$k_u = \frac{u_H - u_L}{2m} \tag{3}$$

$e_H, ec_H$  and  $u_H$  represent the highest values.  $e_L, ec_L, u_L$  represent the lowest values. That's to say,  $k_e = 1/4, k_{ec} = 1/3, k_u = 5$ .

The values of  $e$  and  $ec$  are transformed into input  $E$  and  $EC$  by formula (4), (5). In formula (4), (5),  $\langle \rangle$  represents rounding operation.

$$E = \left\langle k_e \cdot \left( e - \frac{e_H + e_L}{2} \right) \right\rangle \tag{4}$$

$$EC = \left\langle k_{ec} \cdot \left( ec - \frac{ec_H + ec_L}{2} \right) \right\rangle \tag{5}$$

The actual input value of  $u$  is able to be acquired by formula (6).

$$u = k_u \cdot U + \frac{u_H + u_L}{2} \tag{6}$$

### 3. Formation of the fuzzy control regulation table

In the fuzzy controller of double input and single output, fuzzy control regulation is in the form of “if  $E = E_i$ , and  $EC = EC_i$ , then  $U_{ij}$  ( $i, j = 1, 2, \dots, 5, 6$ )”. Table 1 shows the statement of fuzzy control regulation.

**Table 1** The statement of fuzzy control regulation

U	E						
EC	NBe	NMe	NSe	Ze	PSe	PMe	PBe
NBec	PBu	PBu	PBu	PMu	PMu	NMu	NBu
NMec	PBu	PBu	PSu	PSu	PMu	NMu	NBu
NSec	PBu	PMu	PSu	PSu	PSu	NMu	NBu
Zec	PBu	PMu	PSu	Zu	NSu	NMu	NBu
PSec	PBu	PMu	NSu	NSu	NSu	NMu	NBu
PMec	PBu	PMu	NMu	NMu	NSu	NSu	NBu
PBec	PBu	PMu	NMu	NMu	NBu	NBu	NBu

4. Quantization of fuzzy control regulation

Introducing triangle-shape grade of membership function with formula (7), quantization of E, U and EC can be going on. b is the abscissa value of the vertices in the triangle, and a, c are abscissa values of other two points in the triangle.

$$f(x, a, b, c) = \begin{cases} 0 & x \leq a \\ \frac{x-a}{b-a} & a \leq x \leq b \\ \frac{c-x}{c-b} & b \leq x \leq c \\ 0 & x \leq c \end{cases} \tag{7}$$

With the weighted average method as formula (8), the more accurate output values can be obtained. There are the final values of U in Table 2.

$$C = \frac{\sum_{i=1}^n k_i w_i}{\sum_{i=1}^n k_i} \tag{8}$$

C is the accurate value of the output; ki is the weight coefficient; wi is the corresponding output values of each rule.

After calculation at U, the value of U is transformed into the value of u which is the final execution value of an air condition with formula (6). And the final execution value is transferred to control operation of an air conditioning through Zigbee Network.

**Table 2** The inquiry about fuzzy control

U	E												
EC	-6	-5	-4	-3	-2	-1	0	1	2	3	4	5	6
-6	6	6	6	6	6	5	4	4	4	0	-4	-5	-6
-5	6	6	6	5	4	4	3	4	4	0	-4	-5	-6
-4	6	6	6	4	2	2	2	3	4	0	-4	-5	-6
-3	6	6	5	4	2	2	2	3	3	-1	-4	-5	-6
-2	6	5	4	3	2	2	2	2	2	-1	-4	-5	-6
-1	6	5	4	3	2	2	1	1	0	-2	-4	-5	-6
0	6	5	4	3	2	1	1	-1	-2	-3	-4	-5	-6
1	6	5	4	3	0	-1	-1	-2	-2	-3	-4	-5	-6
2	6	5	4	1	-2	-2	-2	-2	-2	-3	-4	-5	-6
3	6	5	4	1	-3	-3	-3	-3	-2	-5	-3	-5	-6
4	6	5	4	0	-4	-4	-4	-3	-2	-2	-2	-4	-6
5	6	5	4	0	-4	-4	-4	-4	-4	-4	-4	-5	-6
6	6	5	4	0	-4	-4	-4	-5	-6	-6	-6	-6	-6

## 2.6 Algorithmic Design of Cold-Chain Goods' Behaviors

To avoid the cold-chain goods' abnormal behaviors, the system collects goods' acceleration data in three-dimension directions at certain time by acceleration sensors, judging the current behavior of the cold-chain goods. As the goods show abnormal behaviors, the actuators command warning bells ringing.

The general classification of goods' behaviors is indispensable for identifying goods' behaviors, including the balance, the shake, the move, the overturn, the collision. Cold-chain goods behaviors could be judged by the accelerations' changes of goods in three dimension directions. As a result, relying on the behavior characteristics of goods, maximum similarity's multiple characteristic recognition (MSMCR) is applied to accurately identify the behaviors.

MSMCR refers to a type of the decision tree that is constituted by many data of the characteristic arranged according to the characteristic priority sequence, which represents all the behaviors of goods [6]. Each branch shows a kind of path to discriminate the goods' behavior, and the shorter the path is, the more obvious characteristics of the good's behavior are.

There is a decision tree on MSMCR in Fig. 3.

Looking over the picture, five of goods' behaviors could be identified by following conditions.

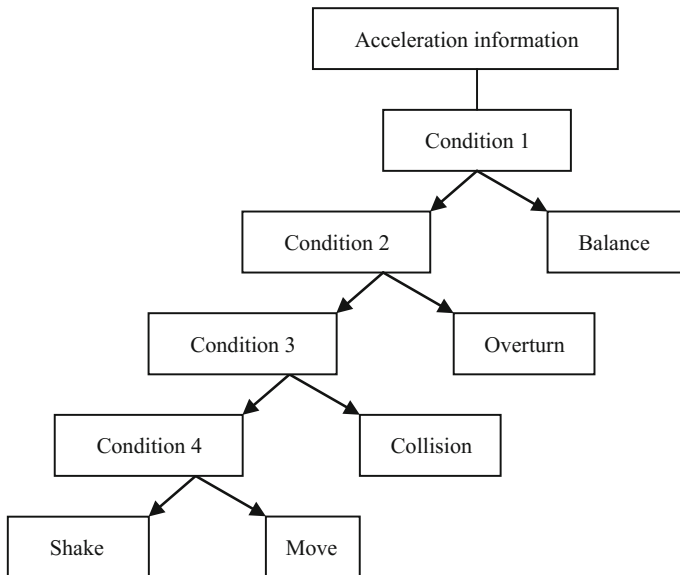


Fig. 3 The decision tree on MSMCR

Condition 1:  $a_{\max} - a_{\min} < a_b$  (The  $a_{\max}$  represents the goods' maximum acceleration in each direction.  $a_{\min}$  represents the minimum acceleration, and  $a_b$  represents a critical acceleration. When  $a_{\max}$  minus  $a_{\min}$  is smaller than  $a_b$  in certain time, the goods are in the state of balance)

Condition 2:  $|g_1 - g_0| > g_r$  ( $g_1$  means the acceleration on the Z axis, as goods are overturned.  $g_0$  is behalf of the acceleration on the Z axis before goods are overturned. When the absolute value of the difference is greater than the critical acceleration, namely  $g_r$ , it can be identified as the overturn)

Condition 3:  $S_{n-m} > S_h$  ( $S_{n-m}$  represents goods' acceleration variance on the Z axis in the time from n to m. Then when the variance is greater than the critical value, namely  $S_h$ , it can be identified as the collision)

Condition 4:  $S_{\max}(x, y, z) < S_m$  (When the maximum variance of goods' accelerations in three dimensions is smaller than the critical value of  $S_m$ , the goods can be judged to be the move)

After the conditions to identify goods' behaviors are set, acceleration data can be judged from the decision tree's root to each branch based on MSMCR, which matches with the corresponding goods' behavior.

### 3 Conclusions

The application of wireless sensor network technology makes the monitoring and management of Cold Chain Logistics enter a new time. Especially, for monitoring the various environment parameters, not only has it achieved the purpose of real-time monitoring, but also the collected data have been also more accurate, to meet the demand of Cold Chain Logistics. Therefore, on basis of wireless sensor network, this paper uses Zigbee ad hoc network model to build the system's framework of perception control—network transmission—application service. Moreover, the fuzzy control decision is applied to regulate the equipment operation so as to keep the environment parameters in a suitable and stable range. Finally, with MSMCR adopted, acceleration sensors are placed in transportation to test the goods' behaviors at any time, ensuring the safety of cold-chain food.

### References

1. S. Zöllner, M. Wachtel, F. Knapp, R. Steinmetz. (2013). Going All the Way - Detecting and Transmitting Events with Wireless Sensor Networks in Logistics, Eight IEEE Workshop on Practical Issues in Building Sensor Network Applications.
2. Qian Rongbo. (2011). Research on the storage's monitoring system based on WSN. Guangzhou Maritime College Journal.
3. Luo Kexue. (2012). Design and implementation on the wireless temperature and humidity monitoring system based on the Zigbee protocol. Jilin University.

4. Yi Cuipng. (2012). Research on the temperature and humidity real-time monitoring system in grain depots based on WSN, Changchun University of Science and Technology.
5. Lv Hong, Huang Dingjin. (2012). Wireless temperature data acquisition and transmission based on the technology of low power. *Foreign Electronic Measurement Technology*. 31 (2):58–60.
6. Sun Yuyan, Yang Hong, Liu Zhuohua, Huang Fuwei. (2011). Deign of the intelligent tracking system in Logistics based on WSN. *Computer Research and Development*.

# Effect of Pressure Sensitive Adhesive Polypropylene Tape on Performance of Corrugated Box

Bingjie Shi and Xiaohui He

**Abstract** The aim of this work was to study the effect of polypropylene pressure sensitive adhesive tape on the compression strength of corrugated box. The 180° peel strength, tensile strength and static shear adhesion of 3 different adhesive tapes were tested. Corrugated box divided 2 states: outer flaps were weighted and side panels were weighted. Each state included 4 groups. Three of them were sealed by 3 different adhesive tapes and the rest wasn't sealed. Then, the compression strength of these 4 groups corrugated boxes were tested. The result showed that the effect of adhesive tapes with different characters on compression strength wasn't obvious. When the outer flaps were weighted, there wasn't obvious difference on the compression strength between sealing and not sealing. When the side panels were weighted, the compression strength of sealing corrugated box had a great increase.

**Keywords** Corrugated box · Compression strength · Adhesive tapes · Pressure on outer flaps · Pressure on side panels

## 1 Introduction

In 2015, China express delivery industry has complete 20.67 billions express deliveries. With preliminary estimates, it has consumed 9.9 billions packing boxes and 169.5 billions meters of adhesive tape. Most of used boxes and adhesive tapes become garbage and bring high pressure to the environment [1]. And some sellers use lots of adhesive tapes to protect goods from damaging in transport. So the tape's function on the corrugated box needs to test. It is important to find that the tape's function on corrugated box for protecting environment. And it also can help using tapes rational.

---

B. Shi (✉) · X. He  
School of Printing & Packaging Engineering,  
Beijing Institute of Graphic Communication, Beijing, China  
e-mail: 460660708@qq.com

180° peel strength, tensile strength and static shear adhesion are the main ways to evaluate adhesive tape [2]. Compression strength is the main way to evaluate corrugated box. Our country scholars made many researches on compression strength. Liu Yang studied the influence of hot charging contents on compression strength of corrugated box [3]. Xie Yong studied the effect of handing hole's shape on compression strength of corrugated box [4]. Liu Xin studied the effect of punch position on compression strength of corrugated box [5].

## 2 Experiment

### 2.1 Experiment Preparation

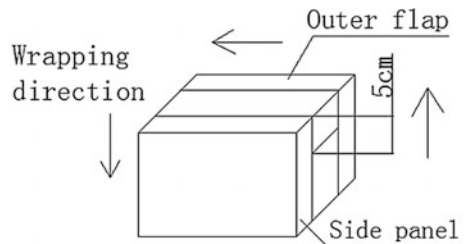
The type of the corrugated box is 0201 with UV shape and B cord. The size of the corrugated box is 210 mm × 110 mm × 140 mm. The three different pressure sensitive adhesive polypropylene tapes have the same width of 48 mm. No. 1 adhesive tape is 30203 adhesive tapes of Deli group. No. 2 tape is AJD97338 adhesive tape of M&G. No. 3 tape is 30313 adhesive tape of Deli group. The experiment instruments include SANA electronic universal testing machine, Labthink XLW intelligent electronic tensile testing machine, Labthink CZY-6S static shear adhesion tester. The experiment temperature is  $(23 \pm 1)^\circ\text{C}$ , and the humidity is  $(50 \pm 5)^\circ\text{C}$ .

The corrugated boxes of each state are divided into two groups. One of the groups is sealed by 3 different adhesive tapes. The other group isn't sealed, but the flaps are also fold. The method of sealing is that tape is pasted on the side panel and it is 5 cm away from outer flaps. It wraps 2 circles along the side panel and outer flap, as shown in Fig. 1.

### 2.2 Experiment Procedure

Measuring the static shear of adhesive tape according to GB/T 4851-2014 *Measurement of Static Shear Adhesion for Adhesive Types* [6, 7]. The size of the sample is 15 mm × 70 mm. Measuring the 180° peel strength of the adhesive tape

**Fig. 1** Schematic diagram of sealing method



according to GB/T 2792-2014 *Measurement of Peel Adhesion Properties for Adhesive Tapes* [7, 8]. The test size is 15 mm × 45 mm, the distance between clamps is 100 mm. Measuring the tensile strength of adhesive tape according to GB/T 30776-2014 *Measurement of Break Strength and Elongate at Break for Adhesive Tapes* [7, 9]. The size of the sample is 30 mm × 100 mm. Measuring the compression strength of the corrugated boxes according to GB/T 4857.4-2008 *Packaging-Basic Test for Transport Packages-Part 4: Compression and Stacking Tests Using a Compression Tester* [10]. The placement status includes that outer flaps close/closes to press boards and side panels close to press boards. The speed of the press board is 10 mm/min. When outer flaps are weighted, the movement distance of the press board is 20 mm. When side panels are weighted, the movement distance of the press board is 40 mm.

### 3 Results and Discussion

#### 3.1 Pressure Sensitive Adhesive Polypropylene Tape Performance Experiment

##### 3.1.1 180° Peel Strength

According to Table 1, 180° peel strength of number 2 adhesive tape is the best. Number 3 is the worst.

##### 3.1.2 Tensile Strength

According to Table 2, tensile strength of number 3 is the best, number 1 is the worst.

##### 3.1.3 Static Shear Adhesion

According to Table 3, the static shear adhesion of number 3 is the best, number 2 is the worst.

**Table 1** Average of 180° peel strength

Number	1	2	3
Average of 180° peel strength (N/cm)	1.6	2.2	1.2

**Table 2** Average of tensile strength

Number	1	2	3
Average of tensile strength (N/cm)	7.84	8.09	8.17



**Table 3** Average of static shear adhesion

Number	1	2	3
Time (h)	13	10	18

### 3.2 Compression Strength Experiment

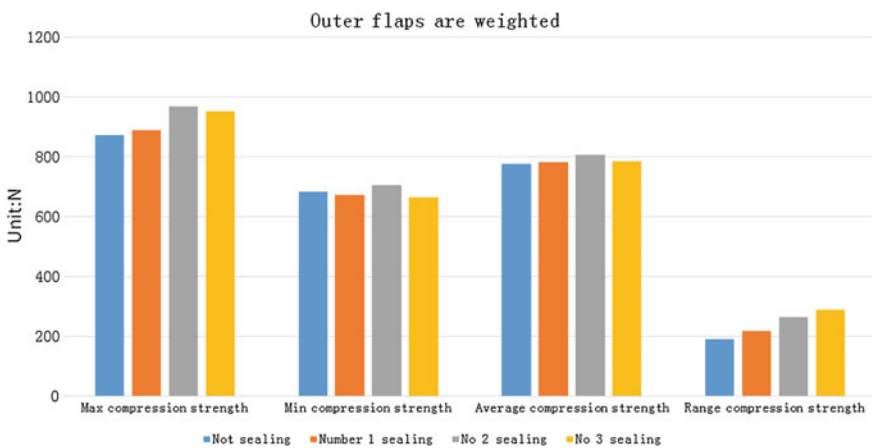
#### 3.2.1 Outer Flaps Are Weighted

As shown in Fig. 2, the compression strength of corrugated boxes with sealing or not are all in the range of 600N–1000N. Specially, compression strength of corrugated boxes with not sealing and the number 1 adhesive tape sealing are the closest.

When outer flaps are weighted, the force of it is shown in Fig. 3 [11]. The force acceptance place is the same whatever seal or not. Side panels and end panels appear different degrees of protrusion and depression. The compression strength of corrugated boxes with the same adhesive tape seals changes in the range of 300N. But number 1 seal and not sealing in the same range. So, when outer flaps are weighted, the effect of adhesive tape on the compression strength of corrugated box isn't obvious.

#### 3.2.2 Side Panels Are Weighted

As shown in Fig. 4, the compression strength has improved obviously after sealing. The compression strengths of corrugated box with different adhesive tapes are in the same range.



**Fig. 2** Compression strength of corrugated box with outer flaps are weighted

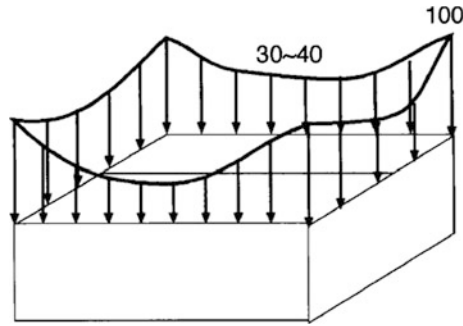


Fig. 3 Stress sketch map of corrugated box

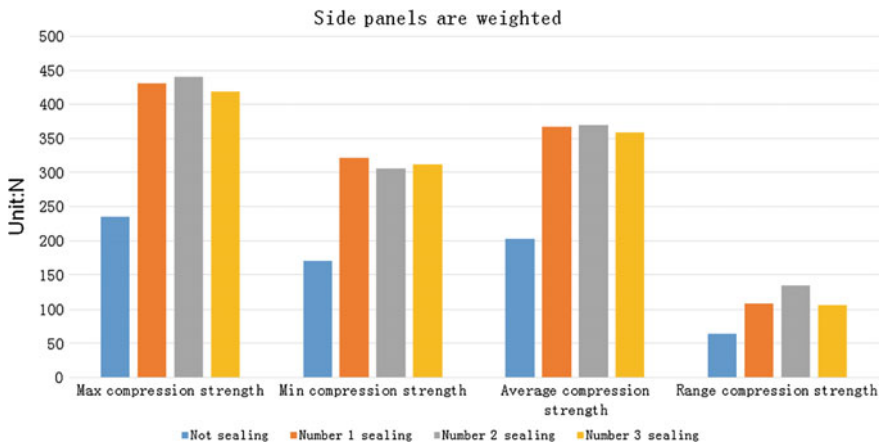
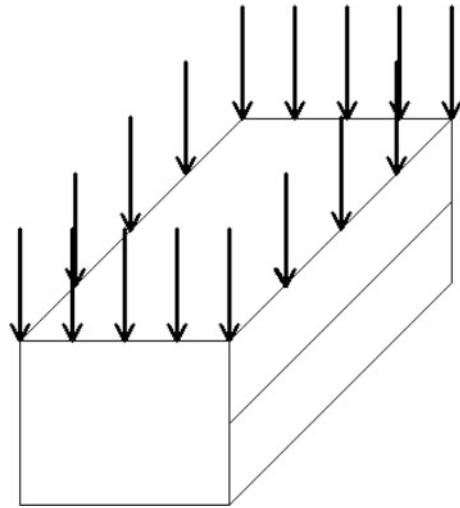


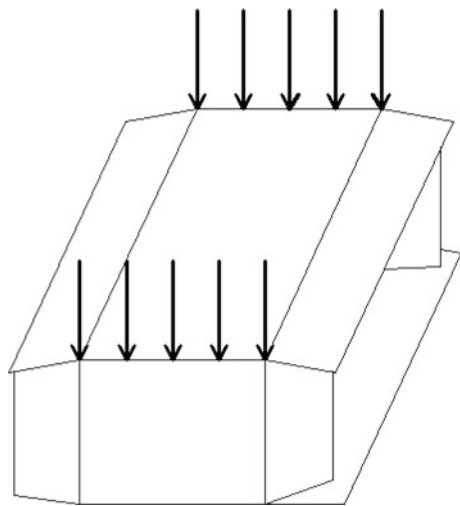
Fig. 4 Compression strength of corrugated box with side panels are weighted

When the forces go from top to down, the other panels and edges accept the forces. When the side panels are weighted with not sealing, only the end panels and associated edges accept the forces, as shown in Figs. 5 and 6. The openings of sealing box are limited by adhesive tape. So, sealing with adhesive tape increases the number of acceptance range. When side panels are weighted, the compression strength of corrugated box with sealing is better than the corrugated box is not sealed.

**Fig. 5** Schematic diagram of force with sealing



**Fig. 6** Schematic diagram of force with not sealing



## 4 Conclusions

The compression strength of corrugated box in same statue with different adhesive tapes sealing were tested in this paper. The result showed that the adhesive tape wasn't obvious to compression strength of corrugated box. When the outer flaps are weighted, the compression strengths in different tapes almost are the same. So, it is no way to enhance the compression strength by using lots of adhesive tapes. If the packaging can prevent the goods from the box, the adhesive tape is enough. This can save resources and protect environment. The compression strength is enhanced a lot by sealing. In practical use, the sealing is important.

## References

1. Ningyu Yang. (2016). China express garbage amazing: Consumption of tape are 16.95 billion meters and packaging box are 9.9 billion in one year. Reference News. [http://news.xinhuanet.com/herald/2016-04/28/c\\_135320581.htm](http://news.xinhuanet.com/herald/2016-04/28/c_135320581.htm). Cited 28 Apr 2016.
2. Liuhui Gu. (2008). Study on test methods of BOPP PSAT and affect from the change of the PSA thickness. MA thesis, Jiangnan University, China.
3. Yang Liu, Huizhong Zhang. (2015). Influence of hot charging contents on compression strength of corrugated box. *Packaging Engineering*, 37(3), 111–115.
4. Yong Xie, Yaping Hu. (2013). Effect of handing hole's shape on compressive strength of corrugated box. *Packaging Engineering*, 34(21), 31–34.
5. Xin Liu, Yi Ding, Linping Jia. (2013). Experiment research for the effect of punch position on compressive strength of corrugated carton. *Packaging and Food Machinery*. Doi: [10.3969/j.issn.1005-1295.2013.05.005](https://doi.org/10.3969/j.issn.1005-1295.2013.05.005).
6. GB/T 4851-2014. Measurement of static shear adhesion for adhesive types.
7. Liuhui Gu. (2008). Study on test methods of BOPP PAST and affect from the change. MA thesis, Jiangnan University, China.
8. GB/T 2792-2014 Measurement of peel adhesion properties for adhesive tapes.
9. GB/T 30776-2014 Measurement of break strength and elongate at break for adhesive tapes.
10. GB/T 4857.4-2008 Packaging-Basic test for transport packages Part 4: Compression and Stacking Tests Using a Compression Tester.
11. Yutian Li. (2011). Influence factors of compression strength of corrugated box. *China Packaging*, 40–45.

# Finite Element Analysis of Moisture Diffusion in Damp-Proof Packing

Hongtao Miao

**Abstract** In this paper, the feasibility of using the finite element analysis method to predict the shelf life of the tea moisture proof package is studied. The finite element software was used to construct the diffusion model, with the aid of the finite element software heat conduction module, and the suitable conductivity coefficient was input into the heat conduction module to simulate the moisture diffusion. And by using Henry's second diffusion law, the guarantee period of the moisture proof package is calculated. It is found that the heat conduction module with the help of the finite element software can be used to predict the moisture proof package's guarantee period and match with the result of the calculation. A convenient, fast and accurate forecasting method is put forward, which has important significance in the actual production.

**Keywords** Finite element analysis · Thermal conductivity · Moisture diffusion · Shelf life prediction · Damp-proof packaging

## 1 Introduction

In the purchase of tea, we often pay attention to the storage period of the tea's packaging. The storage period of the product packaging is the shelf life of the product, also known as the shelf life, is the date of the goods from the factory, through the circulation link to reach the consumer hand, it can maintain the quality of the same time length. A product from the production to the circulation of sales, in the provision of environmental conditions, to maintain the quality of qualified and consumer safety time commitment. Obviously, with the national health standards and enterprise management standard and accurately estimate the storage period of

---

H. Miao (✉)  
Packaging and Printing Department, Henan University  
of Animal Husbandry and Economy, Zhengzhou, China  
e-mail: 774609787@qq.com

the packaging of tea, can improve the safety and reliability of tea in the use of consumers, so as to improve the manufacturers in the public mind of corporate image and reputation. Therefore, it is very important to accurately calculate the storage time of tea.

There are many factors that affect the quality of the storage period of the tea's packaging, which is one of the causes of food deterioration, but it is not equal to the moisture content of the food. If there is little water in food, no more than the content of food spoilage, food will not cause deterioration, so dry food is not easy to. Only when the water content in food is suitable for the growth and reproduction of biological, it is possible to grow and reproduce in food. For the tea, the main factor causing the deterioration of the water content is the moisture content. Tea has a strong moisture absorption, its moisture absorption is not reached before saturation, with the relative humidity in the air increased and increased. Tea production through the drying of its water content is about 3% (mass fraction, after the same), in the relative humidity of 20%, to achieve a balance. If the relative humidity is 8.0%, and the content of water is about 13%, but in relative humidity is 5.0% balance of tea moisture content was 5.5%. Meanwhile, the tea to mildew, quality has dropped sharply, so the tea of moisture-proof packaging, it is necessary to guarantee in the storage period of tea packaging content of not more than 5.5%.

## **2 Traditional Calculation of the Storage Period of the Tea's Packaging**

### ***2.1 Overall Train of Thought to Get the Packaging of Tea Storage Period Calculation Formula***

Using tea moisture absorption curve can that contained with water packed inside relative humidity relationship, so if we know relative of humidity and time, you can deduce the relative of water content and time, understanding every moment in the storage period Changes of water content in tea. According to the above, the water content of the tea must be guaranteed within 5.5%, so if know the time of the water content to reach 5.5%, you can know the packaging of tea storage period.

### ***2.2 Deduction and Conclusion of the Calculation Formula of the Tea Packing Storage Period***

Based on the above analysis, this paper is divided into 4 steps to the calculation formula of the storage period of tea packaging is derived, the process is as follows.

### 2.2.1 Relationship Between the Moisture Content of Tea and the Relative Humidity Inside the Package

According to the results of the study by Xie [1], the relationship between the moisture content and the relative humidity of the package:

$$S_t = 0.0935C_0 + 0.9250 \quad (1)$$

$S_t$ —tea water content (%);  $C_0$ —the relative humidity within the package (%).

### 2.2.2 Relationship Between Relative Humidity and Storage Time in Packaging

Relative humidity within the package is refers to the packaging in the actual water vapor density and isothermal saturation water vapor density percent ratio. The formula is:

$$f = \frac{\rho_0}{\rho_1} \times 100\% \quad (2)$$

In the formula:  $f$ —relative humidity;  $\rho_0$ —water vapor density ( $\text{kg m}^3$ );  $\rho_1$ —the density of saturated steam in the same temperature ( $\text{kg m}^3$ ).

In formula (7) the numerator and denominator multiplied by the packaging volume  $V$ , as a unit  $\text{m}^3$ , the formula (7) becomes:

$$f = \frac{m_0}{\rho_1 V} \times 100\% \quad (3)$$

$m_0$  Water vapor quality (kg)

$$m_0 = Q_\theta A t \quad (4)$$

$Q_\theta$  moisture permeability of packaging materials ( $\text{g}/(\text{m}^2 \cdot 24 \text{ h})$ );

$A$  packaging areas ( $\text{m}^2$ );

$t$  storage time (d).

According to the calculation formula of vapor transmission rate of packaging materials:

$$Q_\theta = K Q_{40} (C - C_0) \quad (5)$$

$K$  coefficient;

$Q_{40}$  moisture permeability of packaging materials when temperature is  $40^\circ \text{C}$  ( $\text{g}/(\text{m}^2 \cdot 24 \text{ h})$ );

$C_0, C$  relative humidity of inside and outside the packaging (%).

Let (4), (5) into Eq. (3) can be obtained:

$$f = \frac{KQ_{40}(C - C_0)At}{\rho_1 V} \times 100\% \quad (6)$$

Due to the storage environment temperature is generally 20–30 °C, according to the saturation water vapor density and temperature of the regression equation:

$$y = 0.01(0.00315x^2 - 0.027x + 1.0091) \quad (7)$$

$y$ —Temperature of the saturated water vapor density ( $\text{kg}/\text{m}^3$ );  $x$ —the temperature of the storage environment.

The formula (7) into Eq. (6) and the unity of the numerator and denominator unit of available:

$$f = \frac{0.001KQ_{40}(C - C_0)At}{[0.01 \times (0.00315T^2 - 0.027T + 1.0091)]V} \times 100\% \quad (8)$$

$T$  Temperature in a storage environment.

The formula (8) is multiplied by 100 on both sides of the equation, which  $C_0$  is used as the dependent variable,  $t$  as the independent variable, and the rest of the parameters are known as the amount of the solution:

$$C_0 = \frac{0.1KQ_{40}CA_t}{[0.01 \times (0.00315T^2 - 0.027T + 1.0091)]V + 0.1KQ_{40}At} \quad (9)$$

The formula (9) is the relationship between the relative humidity and storage time in the packaging.

### 2.2.3 Derivation of the Relationship Between Water Content and Storage Time

Therefore, according to the above, can be deduced:

$$S_1 = 0.0935 \times \frac{0.1KQ_{40}CA_t}{[0.01 \times (0.00315T^2 - 0.027T + 1.0091)]V + 0.1KQ_{40}At} \quad (10)$$

Formula (10) is the relationship between moisture content and storage time of tea.

Tea after production, packaging, and then shipped to the store to sell. When determining the quality of tea and packaging materials, in formula (10) the packaging volume, area,  $K$  value, moisture permeability is known. At the same time, tea in the store of storage time is relatively long, so the temperature of the external environment of tea packaging, relative humidity is certain, so (10) only containing



content and storage time of two variables, which will help us to know the tea water content changes with storage time can be calculated at any time of tea water, and thus be able to monitor tea quality changes.

### 2.2.4 Calculation Formula of the Storage Period of Tea Packaging

Through the analysis above, we can know that when the water content of the tea is more than the maximum allowable water content, the tea is going to be bad, so you can roll out the calculation formula of the storage period:

$$t = \frac{[0.045795 \times (0.00315T^2 - 0.027T + 1.0091)]V}{0.1 \times (0.0935C - 4.5795)KQ_{40}A} \tag{11}$$

K—the packaging material coefficient;  $Q_{40}$ —moisture permeability of packaging materials when temperature is 40 °C; C—relative humidity.

Assuming an existing tea 100 g, storage conditions for 20 DEG C, relative humidity was 65%, the materials used low density polyethylene,  $Q_{40}$  and the K value is known by looking the table and packaging with a total area of 200 cm<sup>2</sup>. Film thickness 0.003 cm, total volume of packaging for 200 cm<sup>3</sup>, obtained t = 531.

## 3 Finite Element Analysis Mathematical Model

For wet diffusion, it is widely believed that it is in accordance with the second law of Fick diffusion:

$$\frac{\partial C}{\partial t} = Q \left[ \frac{\partial^2 C}{\partial z^2} + \frac{1}{A} \frac{\partial A}{\partial z} \frac{\partial C}{\partial z} \right] \tag{12}$$

In the formula, C is the humidity; t is the time; Q is decided by the constant of the material nature; A is the area; Z is the Descartes coordinate [2].

For temperature, humidity and other diffusion can be described by Fick’s law [3]. If A is a constant, then the formula (12) is the basic equation of the one-dimensional diffusion equation. Therefore, the non steady diffusion equation can be written as

$$\frac{\partial C}{\partial t} = Q \left( \frac{\partial^2 C}{\partial x^2} + \frac{\partial^2 C}{\partial y^2} + \frac{\partial^2 C}{\partial z^2} \right) \tag{13}$$

In the formula, Q is the wet diffusion rate; X, y and Z are the Descartes coordinates.

Under certain temperature conditions, the maximum moisture absorption capacity of the material is described by the saturated humidity C<sub>sat</sub>. It represents the

moisture absorption capacity of the material at this temperature. For different materials, the moisture absorption capacity is not the same, so  $C_{sat}$  is not the same. At the junction of a variety of materials, humidity  $C$  will no longer be a continuous quantity. In order to facilitate the research, the concept of relative humidity was introduced into  $W = C/C_{sat}$ . It can be proved that  $w$  is a continuous quantity in the multi material interface, and it also follows the Fick diffusion law.

$$\frac{\partial W}{\partial t} = Q \left( \frac{\partial^2 W}{\partial x^2} + \frac{\partial^2 W}{\partial y^2} + \frac{\partial^2 W}{\partial z^2} \right) \quad (14)$$

The initial conditions and boundary conditions for the moisture absorption process are given by the following formula:

$$C(x, y, z, 0) = C_{sat} \quad (15)$$

$$\begin{aligned} C(0, y, z, t) = C(h_x, y, z, t) &= 0 \\ C(x, 0, z, t) = C(x, h_y, z, t) &= 0 \\ C(x, y, 0, t) = C(x, y, h_z, t) &= 0 \end{aligned} \quad (16)$$

In the formula,  $h_x, h_y, h_z$  is the largest size in  $x, y, z$  direction, that is the size of the boundary.

To get the analytical solution, we can get the following equations.

$$C(x, y, z, t) = C_x(x, t)C_y(y, t)C_z(z, t) \quad (17)$$

The formula (17) can be transformed into, three-dimensional diffusion equation for solving 3 one-dimensional 3 direction independent diffusion equation. After the transformation, the equation is

$$\begin{aligned} C(x, y, z, t) &= \frac{4^3 C_{sat}}{\pi^3} \\ &\left\{ \sum_{n=0}^{\infty} \frac{1}{(2n+1)} \sin \frac{(2n+1)\pi x}{h_x} \exp \left[ -\frac{Qt}{h_x^2} (2n+1)^2 \pi^2 \right] \right\} \\ &\left\{ \sum_{n=0}^{\infty} \frac{1}{(2n+1)} \sin \frac{(2n+1)\pi y}{h_y} \exp \left[ -\frac{Qt}{h_y^2} (2n+1)^2 \pi^2 \right] \right\} \\ &\left\{ \sum_{n=0}^{\infty} \frac{1}{(2n+1)} \sin \frac{(2n+1)\pi z}{h_z} \exp \left[ -\frac{Qt}{h_z^2} (2n+1)^2 \pi^2 \right] \right\} \end{aligned} \quad (18)$$

The above equation is the basis of the study of diffusion behavior. According to the similarity of the moisture diffusion and heat conduction equation, the material coefficient of heat conduction is transformed into the material coefficient in the wet diffusion, and then the behavior of the wet diffusion is simulated by the heat

**Table 1** Finite element calculation of heat conduction and moisture conductivity parameters of the corresponding table

Conduction of heat parameter	Conduction of wet parameter
$T$	$W$
$\rho$	$\rho$
$K$	$Q \cdot C_{sat}$
$c$	$C_{sat}$

**Table 2** Moisture absorption properties of PE materials at 20 °C/65%RH

Materials density (g/cm <sup>3</sup> )	Diffusion rate (cm <sup>2</sup> d <sup>-1</sup> )	Saturated humidity (g/cm <sup>3</sup> )
PE	0.91	$4.6052 \times 10^{-5} < 0.001$

conduction module [4]. The corresponding relations between the two materials are shown in Table 1.

For the specific heat capacity, density is 1, and conductivity K relative corresponding the product Q (moisture diffusion rate) and  $C_{sat}$ . This can be used to simulate the distribution of moisture diffusion module [5].

For Q and  $C_{sat}$ , another Arrhenius formula described like this.

$$\begin{aligned}
 Q &= Q_0 \exp(Z_D/RT) \\
 C_{sat} &= C_0 \exp(Z_C/RT)
 \end{aligned}
 \tag{19}$$

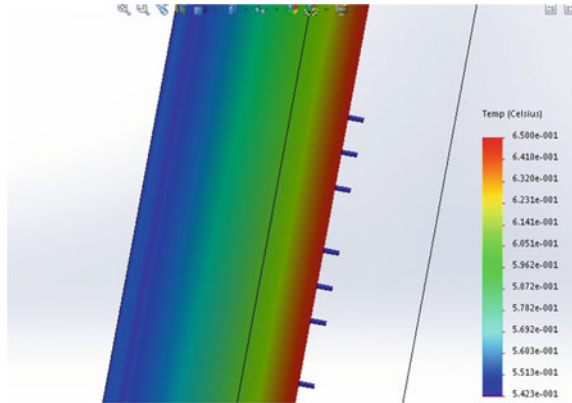
$Z_Q, Z_C$  is the active energy constant;  $R$  is the Boltzmann constant;  $T$  is the thermodynamic temperature;  $C_0$  is constant coefficient.

## 4 Finite Element Model Analysis

In this paper, the simulation of the moisture diffusion behavior of tea package was carried out using the large-scale finite element Software Solidworks. The software comes with the quality of the diffusion module. Wet diffusion behavior is a very complex process, many factors, it is difficult to directly simulate. For this purpose, the model is simplified as follows: All the materials in the structure are isotropic, and the material parameters are not changed due to time and relative humidity changes. Material is considered as homogeneous material. It is assumed that the test piece is in zero deformation and zero stress at the beginning of moisture absorption and is completely dry. The assumption that the moisture absorption process, similar moisture expansion and thermal expansion, volume expansion volume and relative humidity is proportional to [6]. The materials for the moisture diffusion rate (WVTR) and saturated humidity using the following measured data, specific data are shown in Table 2 [7].

Loading: moisture diffusion analysis, the established model of the outer surface of the surface humidity load, load size is 0.65, namely surface relative humidity of

**Fig. 1** Simulation results of the relative humidity of materials at the time of the after 500 days



65%, the whole model of the initial humidity load is 0, i.e., the relative humidity was 0%.

## 5 Simulation Results

Application of Solidworks software package to simulate the moisture diffusion behavior of tea package. The absorption process of moisture absorption at room temperature was simulated with different moisture absorption time, and the relative absorption capacity was expressed by the unit conversion analysis process for 1 days, as shown in Fig. 1.

## 6 Conclusions

The results showed that the tea quality guarantee period of the new formula for calculating the expiration days 532 days, the results of the finite element simulation of about 500 days, both error within the allowable range and the results of the finite element simulation safer. So the mathematical model and finite element analysis model proposed in this paper can be used to simulate the moisture diffusion behavior of tea package with Solidworks software package. Although this process is relatively slow, but for the storage and use of tea or should be a high degree of attention.

## References

1. XIE LI. (2009). Shelf Life Calculation of Tea Based on Moisture Absorption Curve. *Packaging Engineering*, 30(1): 46–49.

2. Zheng Yu qing, Bie Jun. (2014). Based on the Lsdyna97 explicit algorithm of the beverage packaging design evaluation method. *Packaging Engineering*, 05: 37–43.
3. Pan Liao, Lu LiXin. (2014). Study on Time Prediction Model of Temperature Controlled Packaging. *Packaging Engineering*, 2(05): 56–59.
4. XU Jianxin, XU Hang, et al. (2015). Simulation and Analysis of Composite Milling Process Based on ABAQUS. *Machine Tool & Hydraulics*, 125: 78–83.
5. Cheng Xiuhua. (2011). CFD model construction and prediction analysis of the temporal and spatial distribution of greenhouse environmental factors. *Jiangsu University*, 4(6): 71–75.
6. kura J H. (2002). Hygro-Mechancial Durability of Under filled Flip\_Chip on-Board (F(X)B) Interconnects. *J Electro Pack*, 124(9): 184–187.
7. Ee Hua wong, Kai Chong Chan, Tong Yan Tee (2002). Comprehensive Treatment of Moisture Induced Failure in IC Packaging. *Electronics Packaging Manufacturing, IEEE Transaction*, 25(3): 223–230.

# Analysis of the Dynamic Performance of the Cushion Material Composed of EPE and EPS Based on Finite Element Method

Xiaoli Song, Gaimei Zhang, Jiandong Lu and Fanjun Meng

**Abstract** This paper analyzes the dynamic compression performance of the cushion material which is composed of EPE and EPS. The mechanical properties, the maximum acceleration and buffering coefficient of the cushion material are studied on FEM. The performance of the cushion material is analyzed quantitatively and qualitatively, the results show that: (1) The stress distribution of the cushion material and the stress are different if the arrangement mode of EPE and EPS is different. (2) When the stress area of the cushion material is added, the stress is mainly concentrated in EPS and at the contact point between EPE and the heavy hammer. And the stress area gradually becomes larger. (3) When the area percentage of EPS (D) is different, the stress distribution of the cushion material is not same. When D is greater than 81%, the stress is mainly concentrated in EPE. And EPE produces a deformation in the impact process. (4) With the increasing of static stress, the maximum acceleration and buffering coefficient first decreases, reaches its minimum, and then increases monotonously. When the static stress is equal to  $0.00800 \text{ kg/cm}^2$ , the maximum acceleration and buffering coefficient reach the minimum.

**Keywords** Finite element method · Cushioning material · Dynamic properties

## 1 Introduction

In the process of transportation, goods will inevitably be affected by mechanical shock, vibration and other functions. If the packaging is not good enough, it is easy to cause damage to the product and cause huge economic losses to businesses. The cushion materials can absorb the energy generated by the impact, so it can effectively protect goods to avoid the damage [1–3]. Therefore, cushion materials are

---

X. Song (✉) · G. Zhang · J. Lu · F. Meng  
School of Printing & Packaging Engineering,  
Beijing Institute of Graphic Communication, Beijing, China  
e-mail: songxiao109@163.com

applied. At present, EPE (Expandable Polyethylene) and EPS (Expanded Polystyrene) are mainly used for product's protection in our country. The cushioning properties of the two kinds of cushion materials are slightly different. The resilience of EPE is better, but the price is higher. Generally speaking, the price of EPE is more than 2 times higher than EPS which has the same density with EPE. EPS can withstand greater stress, but its resilience is poor [4, 5]. However, shock and vibration are often unpredictable in the process of transportation. The cushioning properties of a certain material are very limited. If two or more than two kinds of cushion materials are used together, they can play each other strengths to enhance the performance and reduce the cost. The static performance and the dynamic performance were widely tested to study the cushioning properties of materials. However, it is found that the "dynamic" data is more realistic than the "static" data in the course of the study [6, 7]. The acceleration is one of the basic parameters of cushioning performance. The maximum acceleration is one of important indexes to reflect the cushioning performance of cushion materials [8]. At present, the maximum acceleration is tested by impact experiment. We only get some experimental data after spending a lot of time and money. However, we can obtain a lot of experimental data and the structural deformation mechanism based on finite element method (FEM) [9–11]. So this method is more effective.

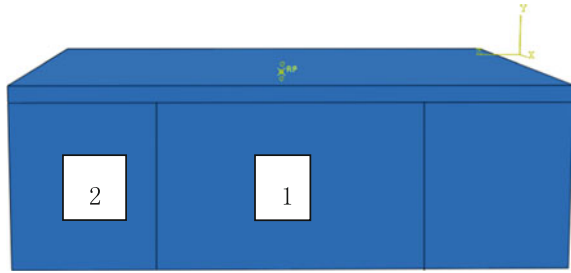
In order to constantly perfect design of the cushioning packaging and reduce the economic losses caused by vibration and shock, this paper analyzes the dynamic compression performance of the cushioning material which is composed of EPE and EPS. The mechanical properties, the maximum acceleration and buffering coefficient of the cushion material are investigated in different drop height, under different stress area and different area percentage of EPS (D) on FEM.

## 2 Modeling and Analysis Process

We builds three-dimensional models of EPE, EPS and a heavy hammer, which is shown in Fig. 1. And the number 1 is EPS in Fig. 1. The number 2 is EPE in Fig. 1. The shape parameters of them are shown in Table 1. The material parameters of EPE and EPS are shown in Table 2. The stress-strain data of EPE and EPS is respectively shown in Tables 3 and 4 [12].

It is very difficult to simulate free fall through ABAQUS/Explicit. So in order to simplify the process, we specify the speed on heavy hammer to simulate the initial speed from H (m) high. The calculation can refer to Eq. (1) [13, 14].

**Fig. 1** A three-dimensional model of dynamic compression for the cushion material



**Table 1** The shape parameters of EPE, EPS and the heavy hammer (mm)

Model	Length	Width	Thickness
EPE	100	100	30
EPS	50	50	30
The heavy hammer	100	100	6

**Table 2** The material parameters of EPE and EPS

Model	Density/(g/cm <sup>3</sup> )	Elastic modulus/(MPa)	Poisson's ratio
EPE	0.029	3	0.01
EPS	0.020	1	0.01

**Table 3** The stress-strain data of EPE

$\sigma$ /kPa	0.000	9.934	20.203	30.301	40.041	190.050	260.055	296.741
$\varepsilon$	0.000	0.100	0.200	0.300	0.400	0.700	0.800	0.840

**Table 4** The stress-strain data of EPS

$\sigma$ /kPa	95.000	106.360	120.630	139.090	163.920	199.080	252.730	344.640	538.460	1214.400
$\varepsilon$	0.000	0.100	0.200	0.300	0.400	0.500	0.900	0.700	0.800	0.900

$$V = \sqrt{2gh} \tag{1}$$

Here, g is 9.810 (m/s<sup>2</sup>).

In order to investigate the dynamic performance of the cushion material, we set the different drop heights, the different stress area and the different area percentage of EPS. After solution, the largest acceleration-static stress curve and buffering coefficient-static stress curve can be drawn. The analyses of the cushion material is given.



### 3 Results and Analysis

#### 3.1 Stress Distribution of the Cushioning Material in the Impact Process

When the mass of the heavy hammer is 0.500 kg, the drop height is set as 0.400 m. The stress distribution of the cushion material at different time is shown in Fig. 2. We found that the stress of the cushion material is not uniformly distributed from the results. And it is mainly concentrated in EPS at different time. There is a certain change in the stress on EPE in the impact process, but the change is not very big.

#### 3.2 Effect of Different Arrangement Mode on the Stress Distribution of the Cushion Material

When the mass of the heavy hammer is 0.500 kg, the drop height is set as 0.400 m. We just change the arrangement mode of EPE and EPS. Therefore, the number 1 is EPE in Fig. 1. The number 2 is EPS in Fig. 1. The stress distribution of the cushion material is shown in Fig. 3. From the results, the stress of the cushion material is not uniformly distributed. And it can be found that the stress concentration area appears alternately between EPS and EPE. At a certain moment, the stress distribution of EPE and EPS is not quite different.

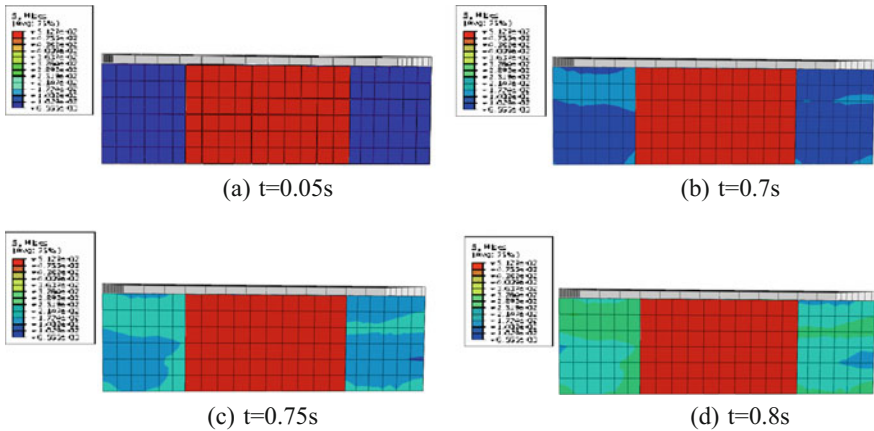


Fig. 2 The stress distribution of the cushion material at different time

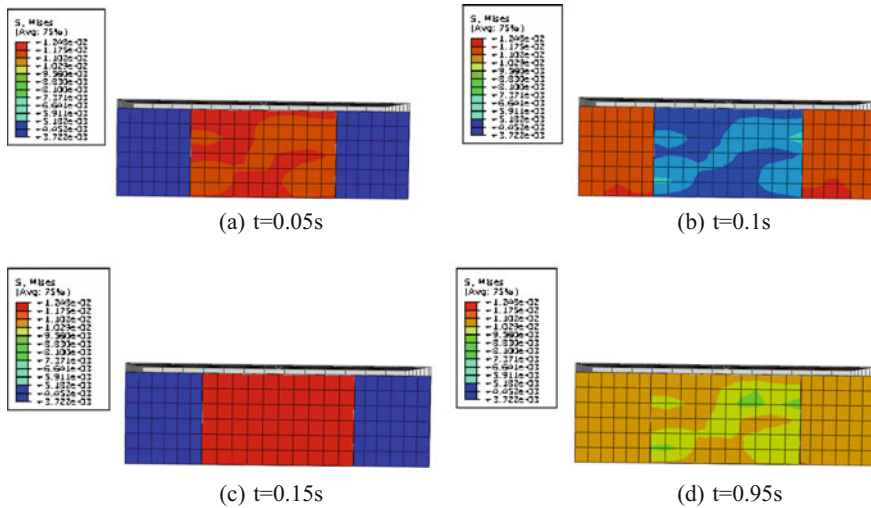


Fig. 3 The stress distribution of the cushion material in other arrangement mode at different time

### 3.3 Effect of Different Stress Area on the Stress Distribution of the Cushion Material

When the mass of the heavy hammer is 0.500 kg and the drop height is 0.400 m, the model of EPE with size of 150 mm × 150 mm × 30 mm is set. The stress distribution of the cushion material at different time is shown in Fig. 4. We found that the stress of the cushion material is not uniformly distributed. And it is mainly concentrated in EPS and at the contact point between EPE and the heavy hammer at different time. The stress area gradually becomes larger.

### 3.4 Effect of Different Area Percentage of EPS on the Stress Distribution of the Cushion Material

When the size of EPE is 100 mm × 100 mm × 30 mm, the size of EPS is set as 50 mm × 50 mm × 30 mm, 80 mm × 80 mm × 30 mm, 90 mm × 90 mm × 30 mm. The stress distribution of the cushion material at different time is shown in Fig. 5. From the results, it can be found that when the area percentage of EPS (D) is different, the stress distribution of the cushion material is not same. When D is less than 25%, the stress is mainly concentrated in EPS. When D is greater than 25% and less than 81%, the stress concentration area appears alternately between EPS and EPE. When D is greater than 81%, the stress is mainly concentrated in EPE. And EPE produces a deformation in the impact process. We found that the

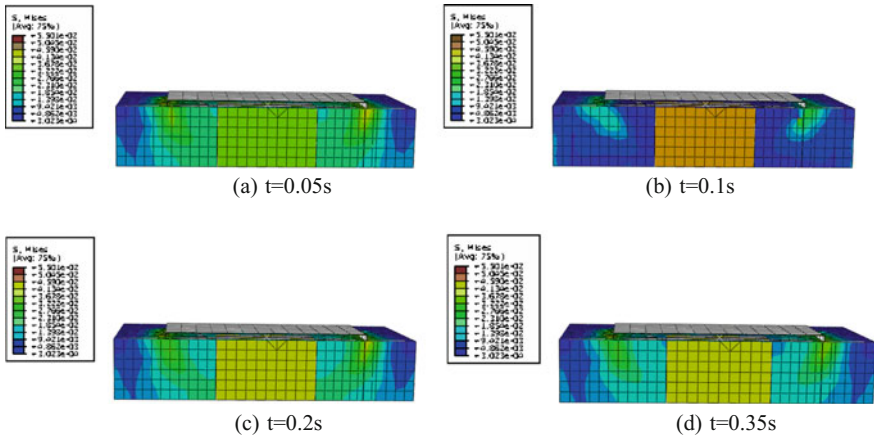


Fig. 4 The stress distribution of the cushion material with different size

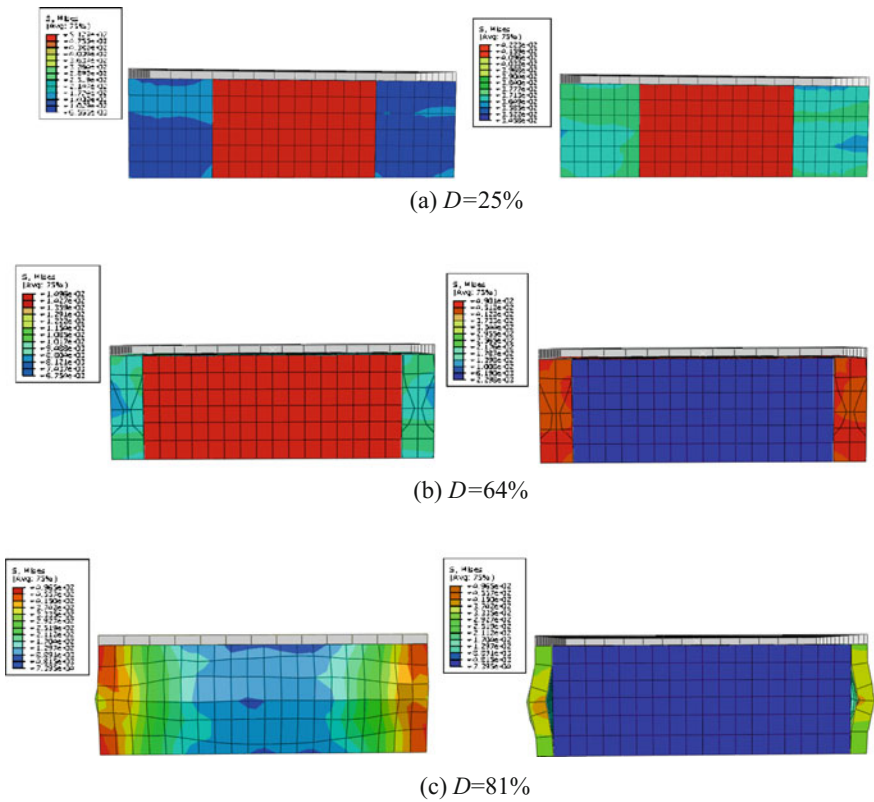


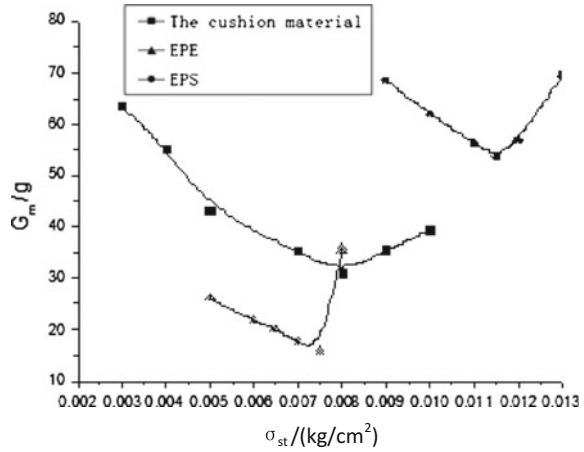
Fig. 5 The stress distribution of the cushion material with the different area percentage of EPS

maximum stress of EPS is 48.100 kPa when D is equal to 25% by querying the data. The maximum stress of EPE is 21.949 kPa and the maximum stress of EPS is 47.854 kPa when D is equal to 64%. The maximum stress of EPS is 54.712 kPa when D is equal to 81%.

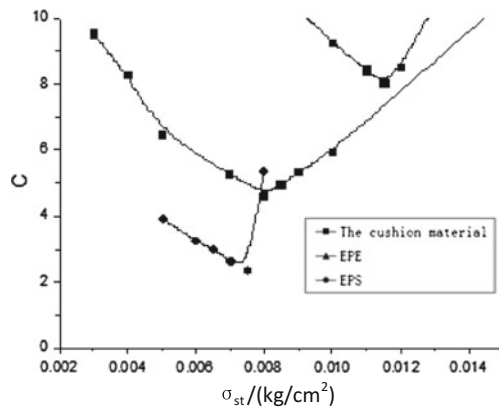
### ***3.5 Effect of Different Mass of the Heavy Hammer on the Stress Distribution of the Cushion Material***

When the drop height is 0.400 m, the mass of the heavy hammer is set as 0.500, 0.300, 0.400, 0.700, 0.900, 1.10, 1.15 kg. After solution, the maximum acceleration can be obtained. Then the curve with static stress as abscissa and the maximum acceleration as vertical coordinate is made, which is shown in Fig. 6a. Make the curve with static stress as abscissa and cushion coefficient as vertical coordinate, which is shown in Fig. 6b. From the results, it can be found when the static stress is less than  $0.00800 \text{ kg/cm}^2$ , the maximum acceleration and buffering coefficient decreases with the increase of static stress. When the static stress is equal to  $0.00800 \text{ kg/cm}^2$ , the maximum acceleration and buffering coefficient reach the minimum. That is, the acceleration is the smallest and the absorbed energy is the most. The thickness of the cushion material reaches the minimum, and the cost is saved at this time. When the static stress is greater than  $0.00800 \text{ kg/cm}^2$ , the maximum acceleration and buffering coefficient will increase monotonously with the increasing of the static stress. The curve shows that the minimum buffer coefficient of the cushion material is 4.635. And the value is greater than the minimum buffer coefficient of EPE and the one of EPS.

**Fig. 6** The curve of the maximum acceleration with static stress and the curve of the coefficient with the static stress



(a) The curve of the maximum acceleration with the static stress



(b) The curve of the coefficient with the static stress

### 4 Conclusions

Comparing the results, the conclusion can be obtained:

- The stress distribution of the cushion material and the stress are different if the arrangement mode of EPE and EPS is different.
- When the stress area of the buffer material is added, the stress is mainly concentrated in EPS and at the contact point between EPE and the impact material. And the stress area gradually becomes larger.

- When the area percentage of EPS (D) is different, the stress distribution of the cushion material is not same. When D is less than 25%, the stress is mainly concentrated in EPS. When D is greater than 25% and less than 81%, the stress concentration area appears alternately between EPS and EPE. When D is greater than 81%, the stress is mainly concentrated in EPE. And EPE produces a deformation in the impact process.
- With the increasing of static stress, the maximum acceleration and buffering coefficient first decreases, reaches its minimum, and then increases monotonously. When the static stress is equal to  $0.00800 \text{ kg/cm}^2$ , the maximum acceleration and buffering coefficient reach the minimum. That is, the acceleration is the smallest and the absorbed energy is the most. The thickness of the cushion material reaches the minimum, and the cost is saved at this time. The curve shows that the minimum buffer coefficient of the cushion material is 4.635. And the value is greater than the minimum buffer coefficient of EPE and the one of EPS.

**Acknowledgements** The project is supported by the National Natural Science Foundation of China (51305038) and Bei Yin talent selection and development project of Beijing Institute of Graphics Communication (Byyc201316-016).

## References

1. Yonghui Liu, Yin Zhang. Dropping Simulation and Design Improvement of a Washing Machine based on FE Analysis [J]. *Journal of Vibration and Shock*, 2011, 30(2):164–166.
2. Tingxin Song, Yaohe Liu, Ruoyan Zhu. Structure Optimization Design of Cushion Packaging Based on Dynamic Property Test and Orthogonal Design [J]. *Packaging Engineering*, 2006, 27(5):56–63.
3. Gaimei Zhang Ji-hong Wu, Fubin Guo. Drop Analysis of Pop Can Based on ANSYS/LS-DYNA [J]. *Packaging Engineering*, 2011, 32(5):4–5.
4. Xiaoyan Liu, Huaming Zheng, Guorong Cao. Study of the Mechanical Performance of EPS and EPE Combination [J]. *Packaging Engineering*, 2006, 27(6):17–18.
5. Huiguo Du, Weiwei Wang, Yingchun Liu. Experimental Study on Buffer Performance of EPS and EPE combination System [J]. *Modern Science*, 2009(6), 39.
6. De Gao, Dechang Xi. Dynamic Modeling of the Corrugated Board and Parameter Identification[C]//11th IAPRI World Conference on Packaging. Singapore: PSB, 1999;7:423–430.
7. De Gao, Zhenlin Wang, Naili Chen. The Dynamic modeling of flat compression cushioning made up of B-flute Double-wall Corrugated Fiberboard [J]. *Journal of Vibration Engineering*, 2001, 14(2):172–177.
8. Dechang Xi, Zhenlin Wang, De Gao. Several problems in packaging dynamics [J]. *Packaging Engineering*, 1990, 20(3):1–5.
9. HICKS Ben James, MULLINEUX Glen, SIRKETT Daniel. A Finite Element-Based Approach for Whole-System Simulation of Packaging Systems for Their Improved Design and Operation [J]. *Packaging Technology and Science*, 2009, 10(12):84–87.
10. Tao He, Jing Yang, Xin Jin. The Example Tutorial of Nonlinear Finite Element Based on ANSYS/LS-DYNA [M]. BEIJING: China Machine Press, 2007.

11. Wenfeng Zhang Anning Zhang. Research on Static Properties of Honeycomb Paperboard based on ANSYS8.0 [J]. *Packaging Engineering*, 2006, 27(2):57–58.
12. Xue Liu. Finite Element Analysis of Dynamic Properties of Expanded Polyethylene Cushion Packaging System [J]. *Packaging Engineering*, 2011, 32(13):11–13.
13. Shaoyun Zhang Huo Chu, Fude Lu. Finite element analysis for dynamic response of cushioning system made out of honeycomb paperboard and foam [J]. *Journal of Vibration and Shock*, 2014, 33(2):52–54.
14. De Gao, Jing Dong, Jun Li. Research on Simulation of Dynamic Response of Corrugated Board with Nonlinear Finite Element [J]. *Packaging Engineering*, 2006, 27(5):1–3.

# Modal Analysis on Laptop and Its Packaging System Based on Finite Element Method

Gaimei Zhang, Xiaoli Song, Xiongbin Zhao,  
Jingting Zhang, Yue Shi and Fan Su

**Abstract** Vibration is a common risk factor during its circulation process for product. To avoid the happening of the damage, vibration test of product and its packaging system must be done. However, this test is always destructives for products and it needs high cost. In this paper, the models of laptop and its packaging system are built; the vibration modes for the laptop are analyzed based on the finite element method. The vibration process of transport circulation environment is simulated and the resonance frequency and vibration mode are obtained. Comparing two different types without and with cushion, it can found that the vibration frequencies are different for two types. The results show that the laptop without the packaging cushion, the impact force is bigger than another, the resonant frequencies are different for them also.

**Keywords** Finite element method · Vibration mode · Resonance frequency · Cushion

## 1 Introduction

Packaging is influenced by various environmental factors such as dropping impact and vibration, so the damage occurs unavoidably during transport [1]. During a variety of environmental factors, vibration is one of the main factors causing the package and products damage, especially for high-tech products and precision instruments [2]. For studying the process of damage of the package it is generally for physical test, but the test of the product is usually destructive and the high test cost is also needed, and this test is not easy to control [3]. Effective way to solve this problem is the simulating based on finite element method. The drop properties of laptop were studied based on the ANSYS by some scholars [4–6].

---

G. Zhang (✉) · X. Song · X. Zhao · J. Zhang · Y. Shi · F. Su  
Beijing Institute of Graphic Communication, Beijing, China  
e-mail: zhang\_gaimei@163.com

© Springer Nature Singapore Pte Ltd. 2017  
P. Zhao et al. (eds.), *Advanced Graphic Communications  
and Media Technologies*, Lecture Notes in Electrical Engineering 417,  
DOI 10.1007/978-981-10-3530-2\_78

627



In this paper, the packaging cushion of laptop was designed, and the models of laptop with and without cushion were built, and the vibration modes are analyzed using the finite element software ABAQUS [7–9]. The first 15 orders resonance frequencies and vibration types are output. The results show that for the laptop without the packaging cushion the impact force and deformation is bigger than another; the resonant frequencies are different for them.

## 2 Model of Laptops With and Without Cushion

Using Hypermesh software, the parameters are set and the models are built for the laptop with 345 mm length, 239 mm width and 32.8 mm thickness, such Fig. 1. It is simplified as two parts including the LCD display and base shell, which parameters are listed in Table 1 [1] (Fig. 2).

The element length is respectively 3 and 5 mm for the LCD and shell, the junction between the LCD and shell is with rbe2. The meshed models of laptop with and without cushion can be seen in Fig. 3.

## 3 Mode Analysis of Laptop Without/With Cushion

### 3.1 Vibration Mode Analysis With and Without Cushion

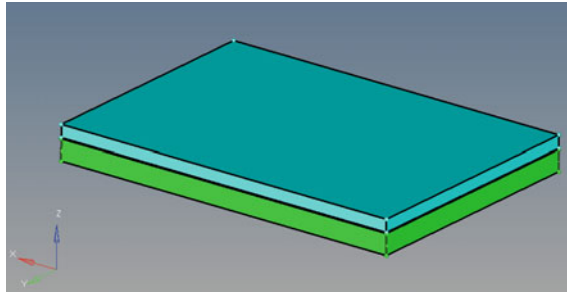
The vibration modes are analyzed, and vibration modes of the first 15 orders are output. The vibration mode of three orders for laptop without and with cushion can be seen in Figs. 4 and 5. The resonance frequencies of first ten orders are obtained in Table 2.

**Fig. 1** The picture of the laptop

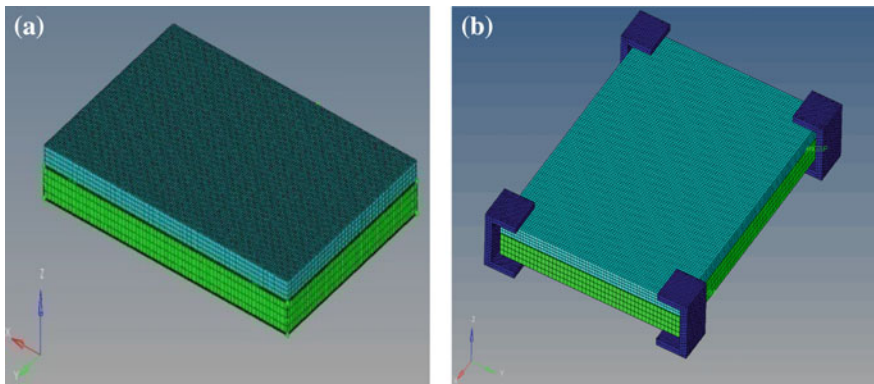


**Table 1** Material parameters

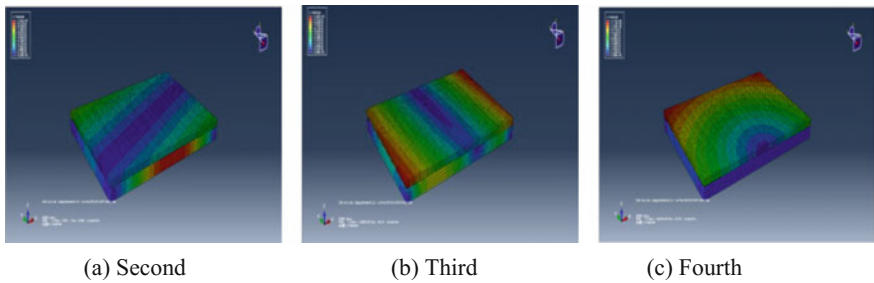
Part	Elastic modulus (GPa)	Poission's ratio	Density (kg/m <sup>3</sup> )	Yield strength
Shell	0.2	0.394	1.260	57.5
LCD	720.0	0.130	2.500	1960.0
EPE	0.0000314	0.3	23.9	



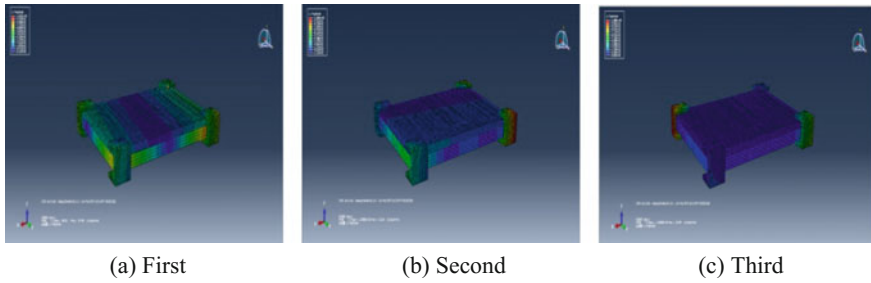
**Fig. 2** The simplified model of laptop



**Fig. 3** The model of laptop after mesh without (a) and with (b) cushion



**Fig. 4** Three orders of vibration mode of laptop without cushion



**Fig. 5** Three orders of vibration mode of laptop with cushion

**Table 2** First ten orders resonance frequencies of laptop with and without cushion (Hz)

Mode	1	2	3	4	5	6	7	8	9	10
Without (Hz)	21.7	49.7	56.7	65.4	76.8	86.2	94.4	118.9	146.4	168.9
With (Hz)	39.8	51.8	52.9	53.9	55.0	58.8	78.4	89.9	101.4	104.4

From Figs. 4 and 5, it can be found that the vibration forms are different for different orders. The directions of wave travel of the LCD display are from the bottom right to the top left, from the left to right, from the center to outside respectively for second, third and fourth orders if the cushion is not used. Using the cushions the waves are importantly spread through the cushions. From Figs. 4 and 5, we can find that the vibration forms are different for different orders and there are also different resonance frequencies for with and without cushion. There are also different resonance frequencies for with and without cushion, which can be seen in Table 2.

### 3.2 Deformation Analysis of Laptop

From Fig. 6 the deformation can be found at the base shell of laptop for first order and from ninth to fifth orders. The deformation for the LCD display is small for tenth to fifteenth orders.

From Fig. 7 the deformation can be found at the cushions for all orders. For later twelve orders the cushions are separate from the laptop.

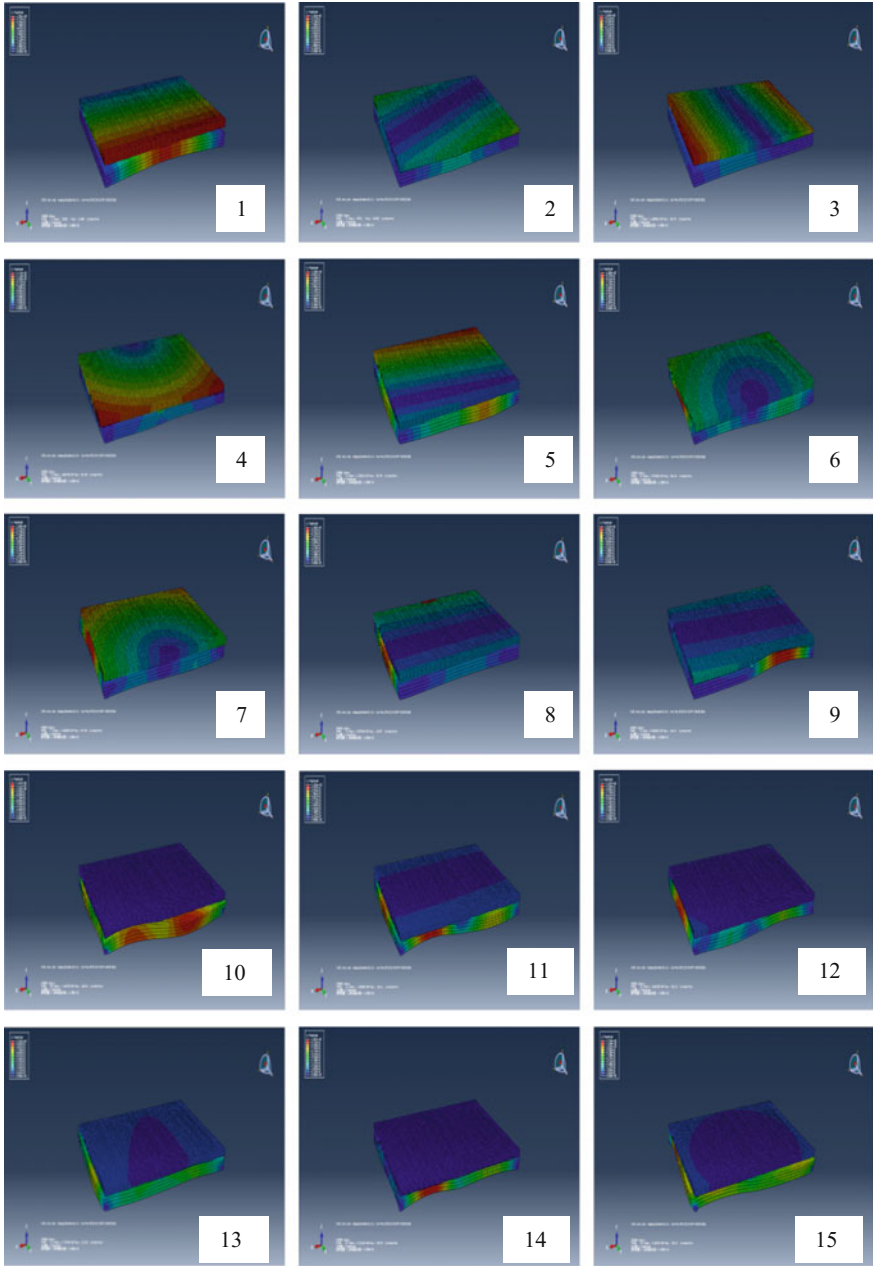


Fig. 6 The first three orders of vibration mode of notebook without cushion

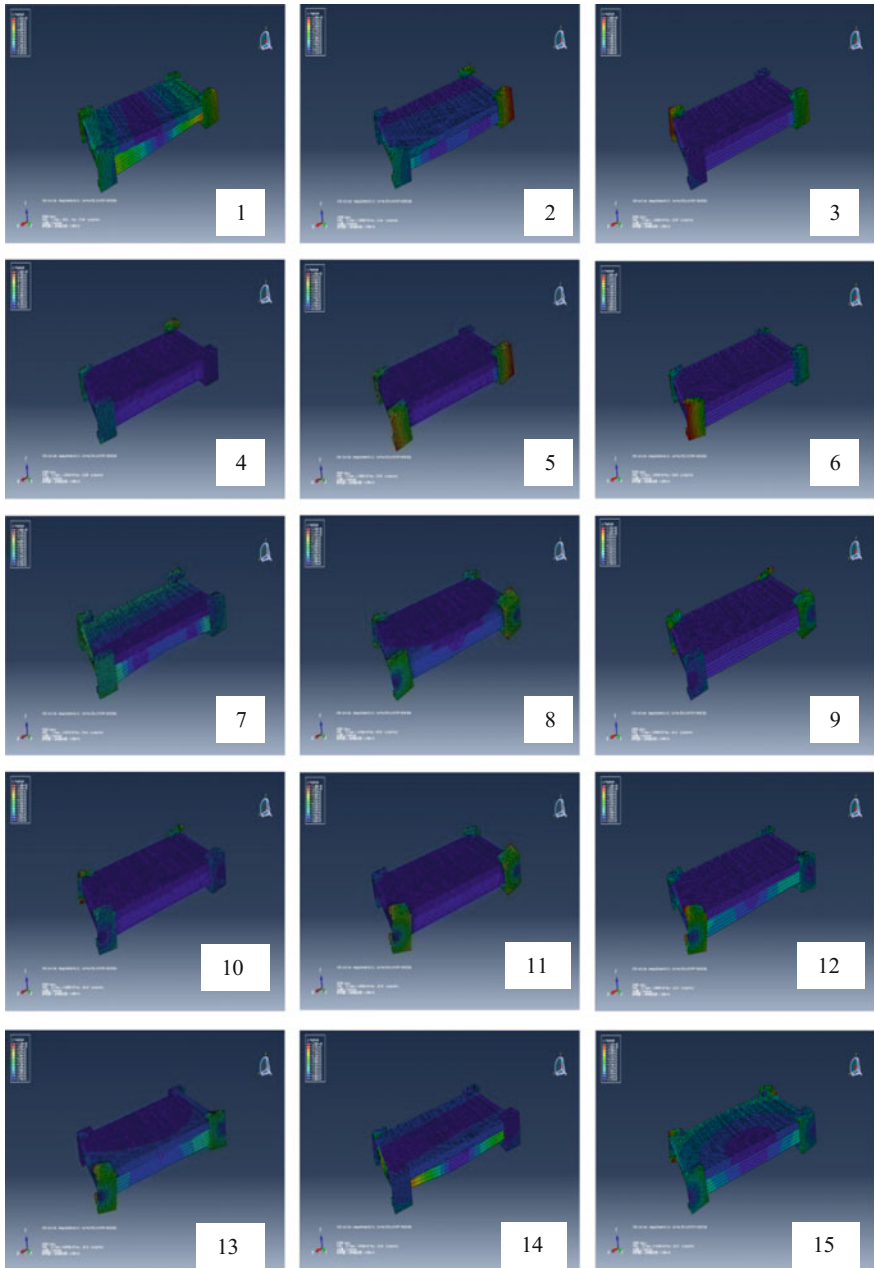


Fig. 7 The first three orders of vibration mode of laptop without cushion

## 4 Conclusions

It can be seen from the simulation results of the vibration frequency, using the EPE cushion pad the vibration frequency of the laptop are different from other type. Using the cushion, the vibration and impact happen to the cushion, so the laptop can be protected by the packaging cushion.

**Acknowledgements** This work was supported by the National Natural Science Foundation of China (No. 51305038).

## References

1. Peng Guoxun. Logistics and transport packaging design [M]. Beijing: Printing Industry Press, 2006.
2. Li Xiaogang. Random vibration frequency domain analysis of transport packaging system [J]. Packaging engineering. 2012, 33(15):50–54.
3. Dian Huming, Shi Feng, Xie fei, et al. A survey of road roughness study [J]. Journal of vibration and shock, 2009, 28(9):95–101.
4. Zhang Bin. Free Fall Test Simulation Analysis and Research Based on Laptop [D]. Suzhou, Suzhou University, 2014.
5. Song Riheng, Zhang Zhiguo. Simulation on laptop package dropping by using ANSYS software [J]. Journal of Zhejiang University of Science and Technology, 2009, 21(4):332–335.
6. Che Xianxiang. Computer simulation on drop tests of packaging and optimization of cushion foams structure [D]. Jinan, Shandong University, 2013.
7. Shi Yiping, Zhou Yurong. Detailed Examples of the Finite Element Analysis Based on ABAQUS [M]. Beijing: China Machine Press, 2006.
8. Zhuang Zhuo, You Xiao-chuan, Liao Jianhui, et al. Finite Element Analysis and Application Based on ABAQUS [M]. Beijing: Tsinghua University Press, 2009.
9. Zhang Jianwei et al. ABAQUS Finite element analysis from entry to master. Beijing [M]: Chinese machine Press, 2014.

# Analysis of Mechanical Properties of Glass Packaging

Jiang Chang, Xue Gong and Zhihui Sun

**Abstract** To study the mechanical properties of the glass packaging. A goblet cushion package model was led into ANSYS/LS-DYNA, the material parameters and boundary conditions were determined, drop simulation, analysis of simulation results. According to the simulation results of the stress drop, analysis the stress change and packaging of the contents in the fall and rebound process, based on the maximum acceleration analysis showed that the buffer packaging structure design could make the maximum acceleration goblet below 80g, met product fragility, reached the effect of cushioning packaging.

**Keywords** Goblet · Cushion packaging · Fragility · Mechanical properties

## 1 Introduction

With the progress of society, people's life and social way is becoming more and more diversified, western culture has gradually entered our daily life, in some social occasions and activities, often with Western-style food to entertain guests [1]. The environment of Western restaurants were commonly spacious, elegant, in the public relations banquets, was a popular and convenient desirable form of hosting. Along with the western culture gradually entered Chinese, goblet has become the new darling of China social occasions [2], it was called goblet because of the cup's a slender feet stand on the cup, liked a graceful swan, proudly independent form its style. In order to facilitate the appreciation of the color of wine, to judge the level of wine [3], goblets were mostly made into glass or crystal products to achieve higher light and transparent [4], such products are beautiful, good chemical stability,

---

J. Chang · X. Gong  
School of Light Industry, Harbin University of Commerce, Heilongjiang, China  
e-mail: kahn82@163.com

Z. Sun (✉)  
Academic Affairs Office, Harbin University of Commerce, Heilongjiang, China  
e-mail: sunzhihui1962@163.com

not easy to be corroded, the production process is mature and so on, but when subjected to shock vibration is very prone to damage to the phenomenon and it is imperative for cushioning package design system.

## 2 Goblet Cushion Packaging Design

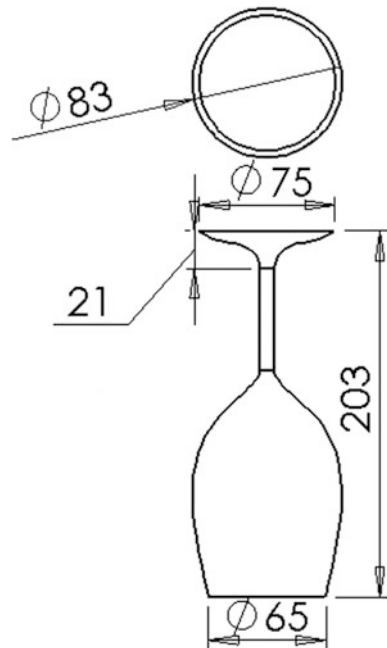
### 2.1 Tall Specification

The object selected packaging design is the glass products in the mid-range, the blow molding glass, suitable for most social occasions and household, belongs to the general glass, its structure is shown in Fig. 1.

### 2.2 Goblet Cushion Packaging Design

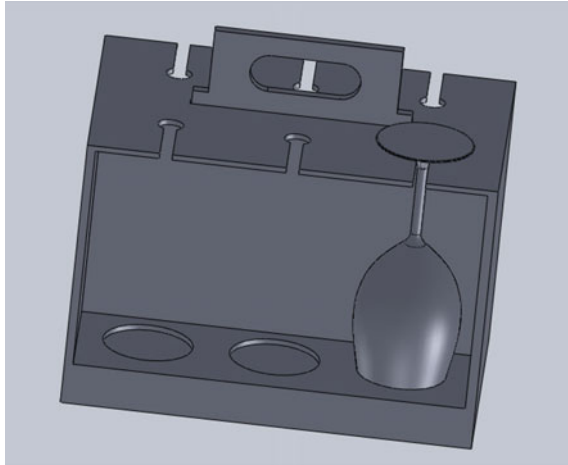
Design of 3 layer C type corrugated board as cushioning material [5]. Combined with the structural features of goblet, cushion combined with local buffer packaging and suspension cushioning packaging design of the Goblet [6]. A pad of paper forming, clever use of a hanging buckle fixed stem cup bottom and the cup opening,

Fig. 1 Structure of goblet





**Fig. 2** Structure diagram of buffer gasket



**Fig. 3** Impression drawing of buffer gasket



the goblet in the pad will not collide with each other and shake [7]. According to the ordinary family purchase requirements, with 6 goblets for the 1 set buffer unit sales package. Buffer pad structure and effect diagram showed as Figs. 2 and 3.

### 3 Goblet Cushion Packaging Mechanics Performance Analysis

#### 3.1 Packing a Finite Element Model Was Established

In the analysis of the ANSYS/LS-DYNA, generally do not consider the entity model, it is usually set by the boundary conditions and constraints applied to the

finite element model for finite element analysis, so before, must be transformed into the entity model, the finite element analysis model ANSYS/LS-DYNA [8].

### 3.1.1 Import Entity Model into ANSYS/LS-DYNA

Through the interface of the finite element software and SOLIDWORKS modeling software, the solid model established in SOLIDWORKS is introduced into PARA in ANSYS/LS-DYNA format, and the model is divided into grid, and then the finite element model is generated.

### 3.1.2 Generating Finite Element Model

Corrugated cardboard cushion packaging material selection glass, it is a kind of anisotropic material, in order to simplify the calculation process, select the bilinear isotropic model designed in this paper, the density is  $300 \text{ kg/m}^2$ , the elastic modulus is 0.19 GPa, the Poisson ratio is 0.15, the ultimate stress is 0.000784 GPa [9]. Glass material is glass, is a brittle material, in theory, is not suitable for elastic analysis, but the main simulation of protective packaging, to determine the stem damage with fragility [10]. Using the bilinear follow-up model, its density is  $2530 \text{ kg/m}^2$ , the modulus of elasticity is 90.3 GPa, Poisson's ratio is 0.243, the limit stress is 3 GPa [11].

### 3.1.3 Grid Division

Grid division is an important step in the finite element analysis, and the size and shape of the mesh will directly affect the accuracy of the results. A buffer packaging unit type shell163, using the surface mesh, goblet unit type solid164, using the body mesh. A cushion package grid is shown in Fig. 4.

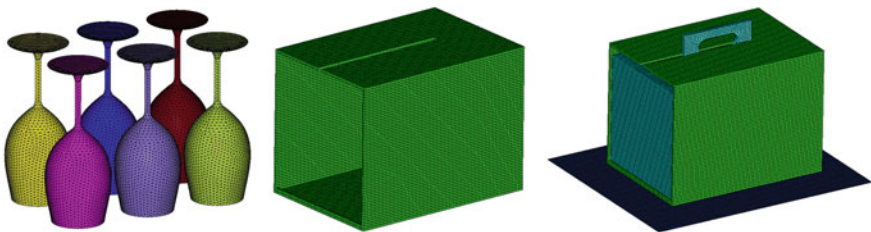


Fig. 4 Meshing of cushioning packaging of goblet

### 3.2 Drop Simulation Analysis

#### 3.2.1 Simulation Environment Settings

The simulation analysis, the type of contact between the various parts (the outer box and the inner liner, inner liner and goblet and goblet cushion package and the drop target surface) are used in automatic single surface contact ASSC. The static friction coefficient is 0.2, the dynamic friction coefficient is 0.1, and the damping value of the product liner system is 0.25 [12, 13]. In this paper, the drop simulation is that the packing piece is in the case of ignoring the surface friction, and it falls down to the target surface at a height of the gravity field [14]. DTM will be separated by gravity acceleration, drop height, initial velocity, time and other steps to simplify the 1 modules, DTM dialog box see Fig. 5, the dialog box contains 4 tags.

#### 3.2.2 Simulation Analysis Results

In ANSYS/LS-DYNA, the stress distribution of the whole package is usually expressed in the stress distribution, so as to determine the risk area during the fall [15]. Goblet and cushion package in the fall, the moment of contact and rebound at different time instant change of equivalent stress is shown in Fig. 6, we can clearly see that the stress distribution model changes with time, reaching a maximum of 2.42 GPa at the moment of contact, does not exceed the limit stress of the goblet.

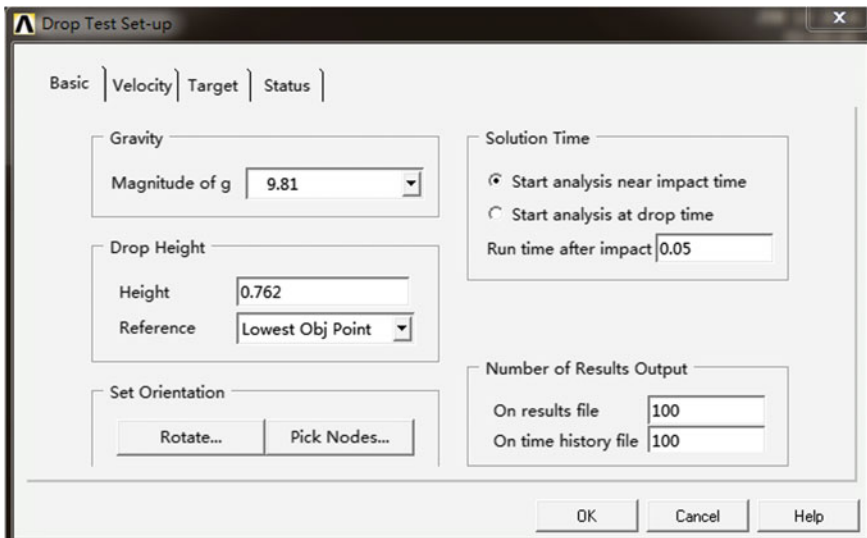


Fig. 5 The dialog box of Drop Test

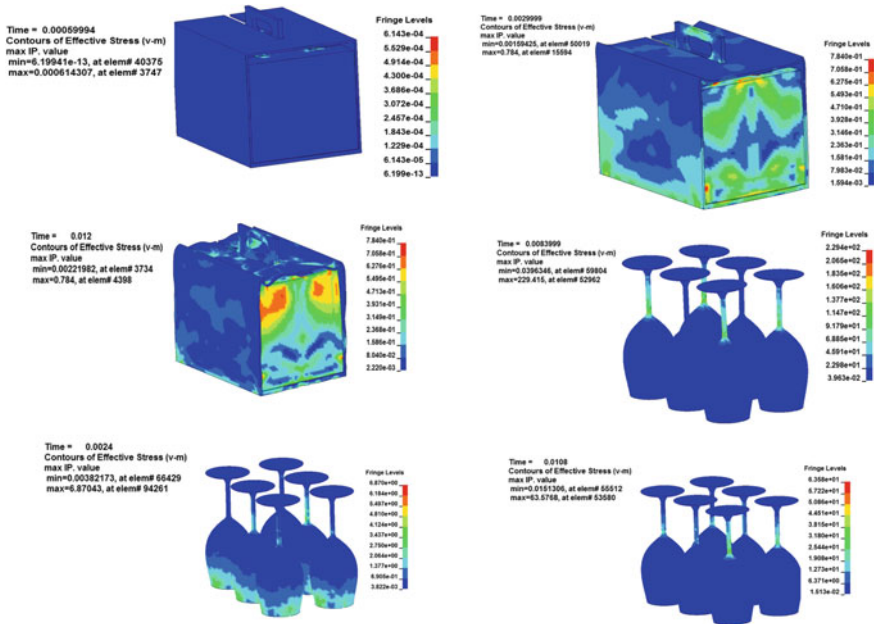


Fig. 6 The variation of stresses of cushioning packaging and goblet

### 4 Conclusions

Using SOLIDWORKS and ANSYS/LS-DYNA to establish the finite element model of drop simulation goblet cushion package, to determine the maximum drop height goblet cushion package, and set the simulation analysis of the boundary conditions, the diagonal drop process of the simulation analysis, the whole package, packing box and goblet, coat the inner liner, stress strain response, the response simulation results are analyzed. The analysis results show that the glass cushioning packaging design in drop, the maximal acceleration is 48g, the result is less than the crisp value of 80g glass products, to cushion the effect.

**Acknowledgement** Funds: Project of Education Department of Heilongjiang Province: (12541207).

Harbin University of Commerce research team support program: (2016TD005).

### References

1. Guo dong li, Wang yi wen (2009). Make Chinese people end up the goblet. Chinese wine, 2009, (8): 45–47.
2. Liu yan (2006). Goblet in complex and worship obsequious tendency. Journal of Chengde national teachers college journal, 26 (4): 69–70.

3. Ni xiao wei (2010). Encounter in red wine goblet - logistics center adventure. *Journal of modern Suzhou*, (30): 100–103.
4. Tao yang, Zhu hua (2013). The innovation design and manufacture of glass. *Industrial technology*, (2): 76.
5. Peng guo xun, Wu zhou ping, etc. (2007). *Corrugated packaging design*. Beijing: the printing industry press.
6. Sun cheng, Jin guo bin (2012). *Packaging structural design*. Beijing: China light industry press.
7. Hu ming xi, Gao wan yu, Du zhen jie, etc. (2005). Hanging cushion packaging structure design based on ANSYS study. *Journal of packaging engineering*, 26 (5): 138–139, 144.
8. Jin Zong zhe, Bao yi wang (1996). *Brittle material mechanics performance evaluation and design*. Beijing: China railway publishing house.
9. Li Zhaoyuan (2008). Typical buffer performance and computer simulation of corrugated paper harden components. Wuxi, Jiangnan University.
10. Chen qiong (2009). Drop impact analysis of the honeycomb cardboard packaging system. *Journal of packaging engineering*, (7): 10–12.
11. Gao de, Dong jing, Li jun (2006). Based on the nonlinear finite element dynamic simulation of shock response of corrugated board research. *Journal of packaging engineering*, 27 (4): 10–11.
12. Dong hai dong, Ge zheng hao (2010). Based on ANSYS/ls-dyna products drop simulation. *Journal of Luoyang institute of technology (natural science edition)*, 20 (3): 36–39.
13. Fu-de Lu, Wei-ming Tao, De Gao (2013). Virtual Mass Method for Solution of Dynamic Response of Composite Cushion Packaging System. *Packaging Technology and Science. Packag. Technol. Sci.* 26(Suppl. 1): 32–42.
14. Chen zhen qiang, Chen zhi qiang, Du min (2012). Parse the small free transport packaging drop test standard. *Journal of printing technology*, (10): 41–43.
15. Hu ming xi, Chen ye, Du zhen jie, etc. (2007). Based on ANSYS/ls-dyna drop simulation analysis of packaging. *Journal of packaging engineering*, 28 (11): 53–54.

# Investigation of Active MAP Film with Menthol on Sugar Orange Preservation

Hui Liu, Yabo Fu, Dongli Li and Wencai Xu

**Abstract** In order to develop film which can extend shelf life of sugar oranges at room temperature to solve the problem of preservation, this experiment used three kinds of polymer materials (LDPE, EVA and SBS) and menthol fresh-keeping agent to made four kinds of fresh-keeping films. Raw material mixed in different proportions and in turn through the granulation and extrusion process. Under room temperature ( $T = 20\text{ }^{\circ}\text{C}$ ,  $\text{RH} = 70\%$ ), experiment was carried out on the preservation of sugar orange. The test and analysis of experiment samples were carried out with the headspace gas, weight loss rate, hardness, color, soluble solids, titratable acid, Vc, sense and taste. Results showed that preservation effects of LDPE films containing menthol were best, the shelf life of sugar orange could be extended to more than 20 days. Preservation effects of SBS-EVA modified LDPE films were also better in the films without preservatives.

**Keywords** MAP · Active packaging · Sugar orange · Preservation

## 1 Introduction

Orange is rich in nutrients and popular as people's favorite fruit. It is very susceptible to mechanical injury and microbial infection with short storage period than other citrus fruit which was peel and crisp, juicy and with high sugar content [1]. Under the normal temperature, it is perishable with a great loss in the storage and transportation process. At present, chemical preservatives are commonly used in the storage of citrus, but they are more toxic residues and also has a certain adverse effects on human health [2]. Therefore, storage and preservation of sugar orange after picking is an important link and also the focus of our study. Active modified atmosphere packaging with natural essential oils mainly includes mechanical air conditioning

---

H. Liu · Y. Fu (✉) · D. Li · W. Xu  
Beijing Key Lab. of Printing and Packaging Materials and Technology,  
Beijing Institute of Graphic Communication, Beijing, China  
e-mail: fuyabo@126.com

and spontaneous air conditioning. Spontaneous modified atmosphere packaging control proportion of gas content in packaging, which mainly through the unique oxygen permeability, carbon dioxide permeability and water vapor permeability of different films. The gas inside packing bag can be formed to inhibit the autonomic respiration, slow down the metabolism and prolong the storage time of the packing bag [3–5]. This method with low cost has good effects and technical feasibility.

In this study, the packaging films which developed in laboratory were carried out on the preservation of sugar orange. Through modification of materials and the combination of two methods of chemical preservative and MAP, the preservation effects of sugar orange was great.

## 2 Experiments

### 2.1 *Experiment Materials*

Fresh sugar oranges (Purchased from Beijing Xinfade Market); SBS/LDPE film; EVA-SBS/LDPE film; menthol (Nanjing Zelang Biotechnology Co. Ltd.); oxalic acid (Xilong Chemical Limited by Share Co. Ltd.); 2,6-dichlorophenol indophenol sodium (Tianjin Recovery Fine Chemical Industry Research Institute); sodium hydroxide (Beijing Chemical Factory); phenolphthalein indicator (Tianjin Recovery Fine Chemical Industry Research Institute); cotton network (Jiaozuo Union Medical Material Limited by Share Ltd.).

### 2.2 *Experimental Instrument*

DZ-280/2SD vacuum envelope machine (Shanghai Star Field Packaging Machinery Co. Ltd.); PAC CHECK Model 65 headspace analyzer (MOCON American company); DT-200B electronic balance (Changshu Goldengoat Counter Balance Instrument Factory); GY-1 fruit hardness meter (Mudanjiang Machinery Research Institute); PR-101 alpha digital sugar instrument (Japan Altago Corporation); WSC-S spectrophotometer.

### 2.3 *Packing Method*

Three kinds of films which laboratory independent research and development were used to make fresh keeping bags ( $25 \times 25 \text{ cm}^2$ ). Group A was unpacked oranges; experimental packaging material of group B was SBS/LDPE film; group C was EVA-SBS/LDPE film; group D was menthol-EVA-SBS/LDPE film. Under the condition of  $T = 20 \text{ }^\circ\text{C}$  and  $\text{RH} = 70\%$ , select fresh sugar oranges which had

uniform size and no mechanical injury into bags. Each set had six parallel samples with a bag had 6 samples.

## 2.4 Experiment Tests and Methods

- (a) Headspace gas composition testing: test the gas composition (oxygen and carbon dioxide) inside the packaging bag by headspace gas meter and test the average value of three times in each group.
- (b) Weight loss rate testing: use electronic balance to test weight of samples before the experiment at 4, 8, 12, 16, 24, 20 days. Record data and calculate according to the formula (1).

$$\text{Weight loss rate} = \frac{\text{Initial weight} - \text{Post storage weight}}{\text{Initial weight}} \times 100\% \quad (1)$$

- (c) Hardness testing: use hardness tester to test samples, each sample test five times to get the average value [6].
- (d) Brightness testing: use spectrophotometer to measure the brightness of samples [7], the brightness of sample can be displayed visually.
- (e) TSS testing: the appropriate amount of sugar orange juice was measured and recorded by using digital PR-101 alpha digital sugar meter, and the average value of each sample was measured three times.
- (f) Titration acid content testing: according to GB/T12456-2008, each group was measured three times and taken the average as test result, the difference between two measurements of the same sample was not more than 2% [8].
- (g) Vc content testing: according to 6195-86 GB/T, each group of sample was measured three times and taken the average as the test results which the parallel test allows the error was 0.2 mg/100 g [9].
- (h) Sensory and taste evaluation: (1) skin bright and smooth, without rotting moldy signs, taste normal; (2) skin slightly dim, but without rotting moldy signs, slight dehydration flesh; (3) skin dull, slightly moldy and rotten, pulp dehydration serious, abnormal taste; (4) surface serious discoloration or moldy and rotten, unusual taste. The score of sugar orange was divided into 1–8 and 8 ranks the best [10].

## 3 Experimental Results and Analysis

### 3.1 Headspace Gas Composition Analysis

Sugar orange was still breathing after picking. As the storage time increased, the nutrient content in the sample was consumed, the plant cell vitality was gradually



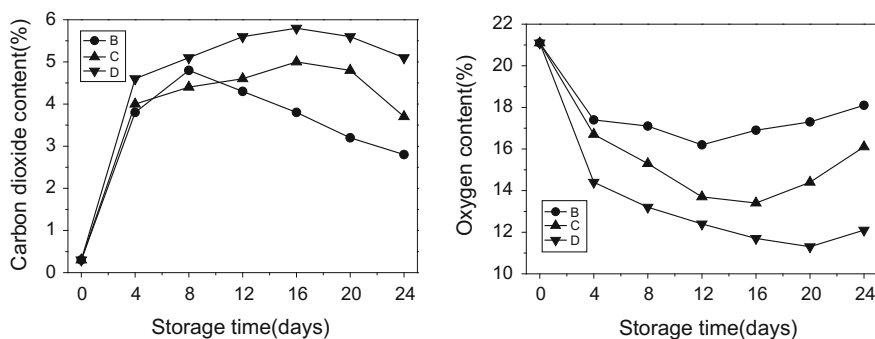


Fig. 1 CO<sub>2</sub> and O<sub>2</sub> contents in packaging versus storage time

decreased and the respiration intensity decreased. So oxygen content was decreased and the carbon dioxide content was increased in packing bag. Gas content in package was determined by the gas permeability of the film. Packaging bag formed a low oxygen and high carbon dioxide ambient atmosphere by controlling the amount of gas through the film which could inhibit cell respiration and gradually reach the balance of the state [11]. In Fig. 1, group D had the highest carbon dioxide content and lowest oxygen content, so that the decline rate of freshness in sugar orange was slower than the other groups. The results showed that the package bag of group D provided a suitable atmosphere environment for sugar orange which was suitable for the respiration of the sample.

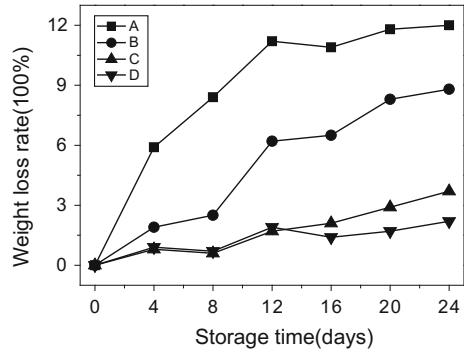
### 3.2 Weight Loss Rate and Hardness Analysis

The main reasons for loss of weight were respiration and water evaporation (Fig. 2). On day 20, the weight loss rate of group D was not more than 2% and that of group C was 2.9%. The other samples were significantly increased after 8 days. Hardness was the embodiment of sugar orange flesh fresh degree which as a part of taste evaluation and direct response to weight loss rate. Hardness decreased with the increase of weight loss rate. In Fig. 3, change of hardness was consistent with the conclusion of weight loss rate and taste evaluation.

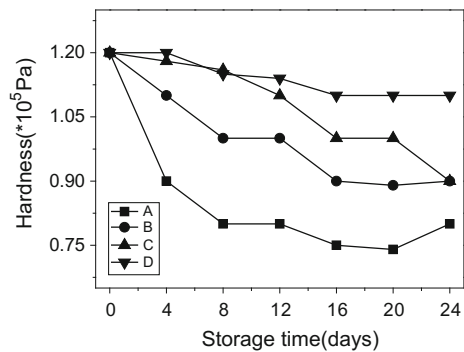
### 3.3 Brightness Analysis

In Fig. 4, the value of surface brightness gradually decreased according to weight loss with the increase of storage time. Because of the difference between sugar orange, the change of brightness of each group was not obvious. However, the skin

**Fig. 2** Weight loss rate versus storage



**Fig. 3** Hardness versus storage time



of samples was dry or even black, so that they had not measurement value in the late stage of storage. For the observation of surface color, it needed to combine with the sample rotten fruit rate.

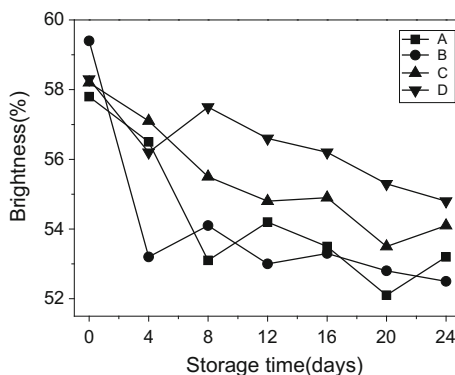
### 3.4 Analysis of Physical and Chemical Indexes of Sugar Orange

The respiration of sugar orange resulted in the increase of titratable acid content with nutrient loss during pre experimental period [12]. The slower rising rate showed that preservation film could inhibit the respiration of cells and the longer preservation time. The content of titration acid decreased with the experiment and meanwhile the quality of samples were also decreased.

In Table 1, Vc content of sugar orange was on the rising when D group increased significantly slower than the other groups which showed the best preservation effect for sugar orange.

Decreasing speed of TSS could reflect the preservation effect of film and less sugar loss expressed good preservation effect. Each sugar orange had a certain

**Fig. 4** Brightness versus storage time



**Table 1** Changes of physical and chemical indexes of sugar orange with storage time

Physical and chemical index	Experience group	Storage time (day)						
		0	4	8	12	16	20	24
Titration acid	A	0.4	0.46	0.51	0.42	0.33	0.31	0.29
	B	0.4	0.43	0.51	0.49	0.46	0.43	0.38
	C	0.4	0.42	0.45	0.48	0.53	0.50	0.46
	D	0.4	0.42	0.44	0.45	0.47	0.48	0.45
VC (%)	A	1.0	1.4	1.7	1.9	2.0	2.0	1.9
	B	1.0	1.2	1.4	1.5	1.7	1.9	2.0
	C	1.0	1.0	1.2	1.1	1.2	1.4	1.6
	D	1.0	1.1	1.0	1.1	1.2	1.2	1.3
TSS (°Brix)	A	12.7	10.2	8.5	7.9	8.1	8.0	7.8
	B	12.6	11.2	11.6	10.3	9.6	7.8	8.2
	C	13.1	12.1	12.3	12.0	11.2	10.9	10.5
	D	12.5	12.4	12.7	12.4	12.1	12.3	11.5

degree of initial sugar content, so that there were some fluctuations in the experimental data, but the overall trend was relatively stable. Decreasing rate of TSS in D group was slowest and stayed above 12° Brix within 20 days. The effect of C group was better within 12 days and other groups were significantly decreased in 8 days or so.

### 3.5 Sensory and Taste Evaluation

As shown in Table 2, the degenerative samples of group A had increased to more than 70% at 8th day. Samples of group B began to appear in varying degrees of

**Table 2** Changes of sensory evaluation with storage time

Sensory items	Experience group	Storage time (days)						
		0	4	8	12	16	20	24
Rotten fruit rate	A	0	0.33	0.72	0.95	1.00	1.00	1.00
	B	0	0.19	0.34	0.46	0.58	0.71	0.83
	C	0	0	0	0.15	0.22	0.31	0.38
	D	<b>0</b>	<b>0</b>	<b>0</b>	<b>0.03</b>	<b>0.08</b>	<b>0.1</b>	<b>0.13</b>
Sensory scores	A	8	5	2	1	1	1	1
	B	8	7	7	5	4	2	1
	C	8	8	8	7	6	5	5
	D	<b>8</b>	<b>8</b>	<b>8</b>	<b>7</b>	<b>7</b>	<b>7</b>	<b>6</b>

decay at 12th day, fresh effects of group C and D were good at the same time. A small amount of samples in group C became bad in the 16th day. The samples of group D had the best effect of preservation because it can still be normal consumption in 20th day.

## 4 Conclusions

In this paper, we study the preservative effect of modified atmosphere packaging on sugar orange at normal 20 °C temperature. SBS/LDPE film made preservation time up to 7 days, EVA-SBS/LDPE film made the preservation time to reach 16 days and the amount of sugar in accordance with the standard of consumption was about 70% when the storage time more than 20 days. Menthol-EVA-SBS/LDPE film extended the shelf life of sugar orange to more than 20 days, the indicators and taste still acceptable. The active MAP films played an important role in prolonging the shelf life of sugar orange at room temperature and provide a possible way for fruit and vegetable preservation.

**Acknowledgements** This work was financially supported by the Science and Technology Project of Collaborative Innovation Center of Beijing Municipal Commission Education (04190116008), Institute Level Youth Talent Program (27170116004/002) and Scientific Research Project (E-b-201503) of Beijing Institute of Graphic Communication.

## References

1. Ye Zixing, Zeng Tai, Xu Jiankai et al (2006). Breeding of Seedless citrus Shatangju (October orange). *Journal of fruit science*, 23(1), 149–150.
2. Droby S, Chae, Wilson CI (1991). Antagonisms biological control agents of postharvest diseases of fruits and vegetables. *Postharvest News and Information*, 2, 169–173.

3. Yang Yanfen, Wang Zejin (2003). Research progress of controlled atmosphere storage and fresh keeping technology of fruits and vegetables in China. *Fujian agricultural machinery*, 2, 18–19.
4. Wei Shunchang, Wei Baodong, Xiong Zhenghua, Ji Shunjuan (2014). Research progress of Postharvest broccoli preservation technologies. *Food science*, 04, 270–275.
5. Maria Serrano (2008). The Addition of Essential Oils to MAP as a Tool to Maintain the Overall Quality of Fruits. *Trends in Food Science & Technology*, 19(9), 464–471.
6. Valverde J. M., Valero D, Nez-Romero D. M (2005). Novel Edible Coating Based on Aloe Vera Gel to Maintain Table Grape Quality and Safety. *Agric Food Chem*, 53:7807–7813.
7. Glesias I, Echeverria G, Soria Y (2008). Differences in fruit colour development, anthocyanin content, fruit quality and consumer acceptability of eight ‘Gala’ apple strains. *Scientia Horticulturae*, 119(1), 32–40.
8. Shou jiang Chena, Min Zhanga, Shaojin Wang (2011). Effect of Initial Hermetic Sealing on Quality of ‘Kyoho’ Grapes During Storage. *Postharvest Biology and Technology*, 59, 194–199.
9. GB/T6195–1986. Determination of Vitamin C in Vegetables and Fruits (2,6-Indophenol Titration Method). Beijing: Standard Press of China, 1986.
10. Zhao Lei, Liu Wen, Wang Houyin (2008). General principles and methods for establishing the index system of food sensory evaluation. *Chinese Journal of food science*, 8, 121–124.
11. Huang Huirong (2014). Preparation of bentonite/PVA and its application in mango preservation. Guangxi, Guangxi University.
12. Li Chen, Liu Ying, Weng Zheng, et al (2013). Effect of storage environment on the quality of grape. *Modern food science and technology*, 29 (2), 230–235.

# Effect of Oxygen Permeability and Water Vapor Permeability of Fresh-Keeping Bags on the Preservation Effect of Nectarine

Juanping Li and Dongli Li

**Abstract** The combination of membrane with high water vapor permeability and another membrane with high oxygen permeability in different proportions, conducted preservation experiments on nectarine at room temperature. By determination and analysis of the fresh-keeping bag of head-space gas composition, nectarine fruit weight, hardness, appearance quality, total soluble solid (TSS) content, total acid content and vitamin C content, to study effect of different proportion of high water vapor permeable membrane on nectarine fresh-keeping effect. The results showed that the naked put group and 50% of high water vapor permeable membrane group of nectarine in the six days have begun to severe dehydration, and the hardness, VC content also dropped larger, but the shelf life of 10 and 20% of high water vapor permeable membrane preservation of nectarine was significantly prolonged, and it can ensure the good fruit quality.

**Keywords** Nectarine · High water vapor permeable membrane · Preservation · Shelf life

Nectarine is variant of common peach (peel covered with hairs) native to the northwest region of China. It has some features such as bright color and its fruit surface is bright and clean; crisp; sweet and delicious; rich nutrition and it has comprehensive flavor of peach, plum, apricot and other fruits [1]. Some varieties of nectarine fruit are crisp and hard after maturity, extremely resistant to long-distance transport, and its storage performance greatly exceeds the common peach. But nectarine due to the fruit surface is smooth and glabrous and the toughness of peel is poor, thus most varieties are easily lead to mechanical damage or decay in storage and transportation process. In order to effectively alleviate the nectarine centralized

---

J. Li · D. Li (✉)

Printing and Packaging Engineering Institute,  
Beijing Institute of Graphic Communication, Beijing, China  
e-mail: lidongli@bigc.edu.cn

sales difficulties caused by the listed, reducing decay, promote circulation, the storage technology of nectarine research has important theoretical and practical significance.

Gao Wei et al. had treatments before storage such as precooling, chemical treatment on nectarine. These treatments delayed the change of fruit color and reduced the water loss of fruit during storage, effectively improved the shelf life of nectarine. She also proposed main storage technologies of nectarine have refrigeration, temperature changes and controlled atmosphere storage, and researched the most appropriate storage temperature of nectarine is 0–1 °C, relative humidity is 90–95% [1]. But because of the low temperature storage is easy to cause unnecessary cooling injury [2], and the temperature changes and gas atmosphere storage is not easy to control. So, this paper studies a kind of double function integrated preservation packaging which was seldom reported in international. And this packaging using different proportions of membrane with high water vapor permeability combined with high oxygen permeable membrane, through slowed water loss and inhibited nectarine respiration to prolong the shelf life of nectarine.

## 1 Experiment

### 1.1 *Treatment of the Nectarine*

Fresh nectarine was brought from the fruit wholesale center with bright color, smooth fruit surface without mechanical damage, then selected uniform size and similar hardness of nectarine and divided to four groups. The control group is naked put group, and the experimental group is high water vapor permeable membrane respectively with 10, 20 and 50%, and each group containing three, placed in the room temperature. From the naked put group and the function fresh-keeping bag group took a sample respectively on the 0, 3, 6, 9 days. To test head-space gas of O<sub>2</sub> and CO<sub>2</sub> content, weight, hardness, soluble solid content, total acid content, vitamin C content in every bags, and to observe the appearance quality of each nectarine.

### 1.2 *Treatment of the Fresh Bags*

To accurately measure the 10, 20 and 50% positions on the fresh-keeping boxes, then strictly accordance with these positions covered with the high water vapor permeable membrane, and the rest is covered with another membrane.

### **1.3 Experimental Test**

#### **1.3.1 Weight Loss Rate Test**

Using electronic balance to weigh and record the weight of each group of nectarine before bagging. In the experimental observation days (3, 6 and 9 days) to weigh and record the weight of each group respectively before the test, then according to the formula (1) for computing weight loss rate.

$$\text{weight loss rate} = \frac{\text{initial weight}}{\text{weight of observation days}} \times 100\% \quad (1)$$

#### **1.3.2 Head-Space Gas of CO<sub>2</sub> and O<sub>2</sub> Content Test**

The mixed gas in the head-space of the packing bag is determined by using the head-space gas analyzer to measure the content of CO<sub>2</sub> and O<sub>2</sub> in the packaging bag before opening the package on each sampling day. And the results expressed as a percentage.

#### **1.3.3 Hardness Test**

Each fruit peeled 1 cm<sup>2</sup>, using GY-1 fruit hardness meter (Mudanjiang Machinery Research Institute) uniform wear 10 mm in fruit, measuring and recording the under pressure. Finally, the average value of the hardness of fruit in each test group samples was measured [3].

#### **1.3.4 Determination of Total Soluble Solids (TSS) Content in Nectarine**

Take the nectarine into juice, and take the right amount of nectarine juice measured by hand-held refraction instrument. The results were the average value of three times [4].

#### **1.3.5 Determination of Total Acid Content of Nectarine**

To filter the above preparation of juice with cotton, following took 2 g supernatant to 50 ml volumetric flask and diluted with deionized water to scale and shake it up. Then drawn 10 ml sample solution into 50 ml Erlenmeyer flask, dripping 3–4 phenolphthalein indicator, and titration with 0.1 mol/L sodium hydroxide standard solution until the solution was appeared to reddish continuing 30 s which was not



fade as the endpoint. Finally write down the consumption of sodium hydroxide volume. The content of acid can be get by calculating [5]. Or using the PH tester directly to measure the pH of nectarine juice. It can proof the change trend of the total acid content indirectly.

### 1.3.6 Determination of VC Content of Nectarine

Weigh 10 g prepared juice to 50 ml volumetric flask, diluted with oxalic acid (mass fraction is 2%) to the scale and shake it up. Drawn 10 ml sample solution into the 50 ml Erlenmeyer flask, with 2,6-dichloroindophenol sodium solution for titration till the solution was pink continuing 15 s which was not fade. And to write down the consumption 2,6-dichloroindophenol sodium solution volume. The VC content can be get by calculating, and the unit is mg/100 g [6].

## 2 Results and Discussion

### 2.1 Head-Space Gas Test and Analysis

The results showed that, similar to the previous fruit preservation experiment, the concentration of O<sub>2</sub> in the packaging decreased during storage, while the CO<sub>2</sub> concentration increased during storage.

### 2.2 Weight Loss Rate and Hardness of Nectarine

Loss of substrate caused by loss of water and respiration is the main reason for the loss of quality in the storage of fruits and vegetables [7]. It can be seen from Table 1, weight loss rate of naked put group in test days was significantly higher than that in those groups using high water vapor permeable membrane. While in comparison of three groups with using high water vapor permeable membrane, weight loss rate in 10 and 20% of high water vapor permeable membrane was significantly lower than 50% of the high water vapor permeable membrane.

Hardness to a certain extent, on behalf of the maturity of the fruit and the degree of loss of water, but also a major indicator of consumers judge the freshness of the

**Table 1** The weight loss rate of nectarine

	Day 3 (%)	Day 6 (%)	Day 9 (%)
Naked put group	4.32	9.56	13.48
10% W membrane	1.60	3.76	6.44
20% W membrane	1.69	4.04	6.87
50% W membrane	2.66	6.29	11.32

**Table 2** The hardness of nectarine

	Day 0	Day 3	Day 6	Day 9
Naked put group	4.9	1.3	0.5	0.2
10% W membrane	4.9	1.4	0.7	0.5
20% W membrane	4.9	1.8	0.9	0.6
50% W membrane	4.9	1.7	0.8	0.3

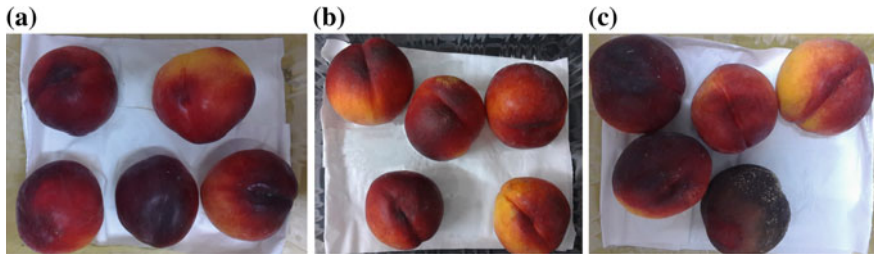
**Table 3** Effects of different packaging conditions on soluble solids, total acid and nectarine VC content

Physical and chemical index	Experience group	Storage time (day)			
		Day 0	Day 3	Day 6	Day 9
TSS content The mass fraction of (%)	Naked put group	8.2 ± 0.1	8.5 ± 0.1	7.8 ± 0.3	6.6 ± 0.1
	10% W membrane	8.2 ± 0.1	7.9 ± 0.1	7.3 ± 0.2	7.5 ± 0.1
	20% W membrane	8.2 ± 0.1	7.5 ± 0.1	7 ± 0.1	7.2 ± 0.1
	50% W membrane	8.2 ± 0.1	9.3 ± 0.2	8.1 ± 0.1	6.4 ± 0.1
pH value	Naked put group	2.25	2.33	3.52	3.51
	10% W membrane	2.25	2.31	3.45	3.58
	20% W membrane	2.25	2.3	3.59	3.55
	50% W membrane	2.25	2.25	3.35	3.47
VC content (mg·(100 g) <sup>-1</sup> )	Naked put group	0.38	1.05	0.38	0.08
	10% W membrane	0.38	0.9	0.38	0.3
	20% W membrane	0.38	0.45	0.23	0.18
	50% W membrane	0.38	0.75	0.38	0.23

fruit. Crisp flesh nectarine is a favorite of consumers, but with the extension of storage time, the fruit hardness decreased. From Table 2, it can be seen that the measured hardness of nectarine is 4.9 at the begin of the storage. Both naked put group or high water vapor permeable membrane group, its hardness has relatively larger decline during the storage. On the ninth day, the hardness of the naked put group was almost the lowest.

### 2.3 Soluble Solids (TSS), Total Acid Content and VC Content Analysis

At beginning of storage, the physiological activity of nectarine fruit is larger. In this period, the starch in fruit is less, polysaccharide constantly transforming into soluble carbohydrate; And sugar, acid and VC of fruit continue to be decomposed consumed as respiratory substrates [8]. As shown in Table 3, at the begin, the TSS content is increased and in later stage is decreased. It is due to in early storage, starch, pectin, crude cellulose hydrolysis product was increased, monosaccharide increasing resulting in TSS content increased, and decreased of the TSS in the late



**Fig. 1** **a** 6th days using 20% of high water vapor permeable membrane group; **b** 6th days naked put group; **c** 9th days using 50% of high water vapor permeable membrane group

stage due to the respiration consumption. With the increase of storage days, the pH value increased gradually, that is, the total acid content is gradually reduced, and the taste of the flavor has become pale. VC content also increased at first with the increase of storage days and then decreased, but the VC content was significantly lower in the naked put group compared to the use of the high water vapor permeable membrane group.

## 2.4 Appearance of Nectarine

After 6 days of the experiment, using 10 and 20% of high water vapor permeable membrane group of nectarine fruit surface is bright and clean, colorful, plump fruit, moderate sweet and sour taste. While the naked put group and 50% of high water vapor permeable membrane group of nectarine surface due to severe dehydration showed obvious shrinkage and tasted no crispness. On the ninth day, the naked put group and the use of 50% of the high water vapor permeable membrane group have begun to appear rotten phenomenon, and has no commodity and edible value. It can be seen from Fig. 1.

## 3 Conclusions

The experiment with naked put group as control group, studies the influence of using different percentages of high water vapor permeable membrane on preservation effect of nectarine. The results show that using 10 and 20% of high water vapor permeable membrane can reduce nectarine weight loss percentage and reduce the hardness decreased. Compared to naked put group and the group using 50% of the high water vapor permeable membrane, it can effectively prolong the shelf life of nectarine, and maintain the good texture and taste.

**Acknowledgements** This work was financially supported by the National Natural Science Foundation of China (contract grant number 31471653) and the Science and Technology Project of Collaborative Innovation Center of Beijing Municipal Commission Education (04190116008).

## References

1. Gao Hui & Rao Jingping (2003). Postharvest physiology and storage technology of Nectarine. *Shanxi Agricultural Sciences*, (4), 55–58.
2. Gao Hui, Rao Jingping & Zhang Shaoying (2007). Under different storage temperature of nectarine fruit chilling injury physiology research. *Journal of Northwest Agriculture and Forestry University*, 35 (10), 61–65.
3. Liu Qing, Li Dongli, Liu Guanyi, Chen Xuerou, Li Kexin, Feng Yafang & Fan Qipeng (2015). Quality Loss of Pitaya as Affected by Active Packaging Film at Room Temperature. *Packaging engineering*, 36 (9), 12–15.
4. Liu Qing, Li Dongli, Xu Wencai, Liao Ruijuan & Ishi Kako (2015). Preservation Effect of Different Films on the Cherry at Low Temperature (2 °C). *Processing of Agricultural Products*, (7), 5–7.
5. Chen Shoujiang, Zhang Min & Wang Shaojin (2011). Effect of Initial Hermetic Sealing on Quality of Kyoho Grapes During Storage. *Post-harvest Biology and Technology*, 59, 194–199.
6. GB/T 6195—1986, Determination of Vitamin C in Vegetables and Fruits (2,6-Indophenol Titration Method).
7. Zhang Jingyong, Li Dongli & Xu Wencai et al (2013). Effect of SO<sub>2</sub> Controlled Release Packaging on Preservation Performance of Cherry. *Packaging Engineering*, 34 (15), 49–52.
8. He Yue, Xu Qiuyun & Wang Mingli et al (2015). Postharvest Physiology Research of peach. *Agriculture Forum*, 32 (4), 11–13.

# Identification Method of Egg Freshness by Principal Component and Discriminant Analysis

Yinghao Xing, Qigen Tong, Xiujuan Zhi and Bin Du

**Abstract** Eggs with relatively low cost contain all essential amino acids which human body needs. The freshness of the eggs reduces gradually with the extension of time. Albumen pH, yolk color, haugh units, density, weight loss and increasing rate of gas chamber diameter are often considered as the evaluation indexes under egg preservation. In this paper, the study about the freshness was undertaken on the screening of measurement indicators by principal component and discriminant analysis. The results showed that water loss and protein degeneration were two principal components of its freshness. Typical discriminant functions were built based on different days of diversified index. 30 unknown samples were analysed by discriminant functions, with accuracy of nearly 63%.

**Keywords** Egg · Freshness · Principal component analysis · Discriminant analysis

## 1 Introduction

Eggs are rich in protein, fat, vitamins, minerals and essential amino acids, etc., and can provide high quality animal protein for human body [1]. Meanwhile, Eggs are organisms and easily influenced by internal and external environmental factors attributed to its quality deterioration. Generally, the evaluation indexes of egg

---

Y. Xing  
Beijing Wonder Technology Co., Ltd., Beijing, China

Q. Tong · X. Zhi (✉) · B. Du (✉)  
Beijing Laboratory of Food Quality and Safety, Beijing Key Laboratory of Agricultural Product Detection and Control of Spoilage Organisms and Pesticide Residue, Beijing University of Agriculture, Beijing, China  
e-mail: 38534891@qq.com

B. Du  
e-mail: bindu80@bua.edu.cn

freshness include the pH of egg white, yolk color, haugh units, density, weight loss [2], increasing rate of gas chamber diameter, and sensory evaluation, etc. However, these indicators are not always consistent [3], and the correlation of the indexes are questionable [4]. In this article, the correlation and principal components of freshness indexes were compared during storage; Effective informations had been extracted from mixed and disordered data, and discriminant functions were built to estimate the shelf life of eggs, thus providing the basis for quality assessment of eggs.

## 2 Experiment and Method

### 2.1 Material and Instrument

Eggs; egg analyzer, ORKA Food Technology Ltd.; electronic balance, Germany Sartorius Co., Ltd.; XPT-D high-speed disperser, The HI-2225 pH meter, egg candler, compasses.

### 2.2 Method

Fresh eggs, laid less than 24 h, storage temperature  $25 \pm 3$  °C and humidity  $60 \pm 5\%$ . Measurements were carried out every three days till 36 days.

### 2.3 Measurement Indicators

Weight loss: the rate of weight loss after a storage period, it was calculated as:

$$w_i = (m_0 - m_i) \times 100\% / m_0$$

$m_0$ : initial weight;  $m_i$ : weight in the  $i$  day;  $w_i$ : weight loss in the  $i$  day.

Haugh units: an indicator of egg quality, it is the determination result of egg analyzer.

Yolk color: measured by egg analyzer.

pH value (Whole egg): eggs were homogenized by homogenizer and then measured with pH acidity meter.

Increased rate of gas chamber diameter: in a dark room, the gas chamber using egg candler was found and outlined by the pencil, and then width was measured by with the compass and vernier caliper at the interval of  $120^\circ$  for three times to make average; finally, the percentage of increase was determined in the gas chamber.

Determination of egg volume: filling water in a 500 ml measuring cylinder and make a record  $V_0$ ; sliding an egg into it and make a new record  $V_1$ ; the volume equals the value ( $V_1$  minus  $V_0$ ).

Egg density: calculated by the weight and volume.

$$\rho_i = m_i \div v$$

$m_i$ : weight in the  $i$  day;  $v$ : volume;  $\rho_i$ : density in the  $i$  day.

## 2.4 Data Processing

In each day, 20–30 parallel samples were measured [5], with discrete values eliminated, and the results were treated as the original data. In SPSS19.0 software, the data were detected by correlation, principal component and discriminant analysis [6].

## 3 Results and Discussion

### 3.1 Correlation

According to the related research, the egg freshness indicators included the albumen pH, yolk color, haugh units, density, weight loss and the increasing rate of gas chamber diameter et al. These indexes directly reflect the moisture loss and egg protein degeneration. Therefore, the storage time and various indicators were treated as independent variables to make multiple correlation and significant analysis. The data arised from our measurement in the experiment on the egg preservation were shown in Table 1. By analyzing every index's contribution to the egg freshness, some non-significant indicators were weeded out. Finally, haugh units, density, weight loss and the increasing rate of gas chamber diameter were used for the principal composition and discriminant analysis.

### 3.2 Principal Component Analysis

Principal component analysis could reduce data dimension, and the main compositions are linear combination of the original variables. At the same time, the principal component need represent as much as possible the original variables without loss of characteristics of data. It is better to make main components unrelated, or orthogonal, meaning the informations non-overlapped. The number of

**Table 1** Duncan's multiple comparison

Day	Haugh unit	Weight loss (%)	Increased rate of gas chamber diameter (%)	Density	pH	Yolk color
0	78.3 ± 6.86 <sup>a</sup>	0.07 ± 0.01 <sup>a</sup>	3.99 ± 2.22 <sup>a</sup>	1.08 ± 1.01 <sup>a, b</sup>	8.68 ± 0.22 <sup>a</sup>	7.59 ± 0.73 <sup>a, b</sup>
2	75.42 ± 4.81 <sup>a</sup>	0.28 ± 0.06 <sup>a</sup>	3.98 ± 1.92 <sup>a</sup>	1.07 ± 0.05 <sup>a, b, c</sup>	9.34 ± 0.08 <sup>b</sup>	7.6 ± 0.87 <sup>a, b</sup>
5	67.79 ± 5.66 <sup>b</sup>	0.49 ± 0.08 <sup>a</sup>	14.74 ± 7.96 <sup>b</sup>	1.08 ± 0.02 <sup>a</sup>	9.59 ± 0.05 <sup>c, d</sup>	7.46 ± 0.51 <sup>a</sup>
9	61.29 ± 5.88 <sup>c</sup>	1.3 ± 0.28 <sup>b</sup>	30.35 ± 10 <sup>c</sup>	1.06 ± 0.04 <sup>b, c</sup>	9.63 ± 0.06 <sup>c, f</sup>	7.78 ± 0.75 <sup>a, b</sup>
13	57.58 ± 9.57 <sup>c, d</sup>	2.36 ± 0.33 <sup>c</sup>	41.7 ± 15.07 <sup>d</sup>	1.07 ± 0.05 <sup>a, b, c</sup>	9.72 ± 0.03 <sup>g</sup>	7.93 ± 0.73 <sup>b</sup>
17	55.66 ± 4.17 <sup>d, e</sup>	4.07 ± 0.42 <sup>d</sup>	65.79 ± 10.29 <sup>e</sup>	1.05 ± 0.04 <sup>e</sup>	9.66 ± 0.03 <sup>f</sup>	8.44 ± 0.7 <sup>c</sup>
20	53.19 ± 6.81 <sup>e</sup>	4.54 ± 0.71 <sup>d</sup>	78.02 ± 13.69 <sup>f</sup>	1.03 ± 0.02 <sup>d</sup>	9.67 ± 0.02 <sup>f</sup>	8.56 ± 0.89 <sup>c, d</sup>
24	45.38 ± 4.8 <sup>f, g</sup>	6.01 ± 0.99 <sup>e</sup>	76.3 ± 18.84 <sup>f</sup>	1 ± 0.02 <sup>e</sup>	9.58 ± 0.02 <sup>c</sup>	8.78 ± 0.58 <sup>c, d</sup>
27	48.66 ± 8.29 <sup>f</sup>	6.23 ± 0.75 <sup>e</sup>	91.15 ± 17.18 <sup>g</sup>	0.99 ± 0.07 <sup>e, f</sup>	9.64 ± 0.01 <sup>e, f</sup>	8.86 ± 0.59 <sup>d</sup>
31	46.11 ± 8.93 <sup>f, g</sup>	7.78 ± 0.94 <sup>f</sup>	96.04 ± 21.66 <sup>g</sup>	0.98 ± 0.01 <sup>f</sup>	9.62 ± 0.02 <sup>c, d, e</sup>	9.43 ± 0.57 <sup>e</sup>
34	43.6 ± 6.76 <sup>g</sup>	8.47 ± 1.19 <sup>g</sup>	98.64 ± 18.25 <sup>g</sup>	0.98 ± 0.02 <sup>f</sup>	9.63 ± 0.03 <sup>d, e, f</sup>	9.3 ± 0.61 <sup>e</sup>
36	42.44 ± 8.75 <sup>g</sup>	10.25 ± 2.07 <sup>h</sup>	109.97 ± 24.09 <sup>h</sup>	0.95 ± 0.03 <sup>g</sup>	9.6 ± 0.03 <sup>c, d, e</sup>	9.33 ± 0.68 <sup>e</sup>

<sup>a-h</sup> stand for significant difference between each other



**Table 2** Eigenvalues of correlation matrix

Component	Initial eigenvalues		
	Total	Variance (%)	Accumulation (%)
1	2.107	52.678	52.678
2	1.062	26.552	79.230
3	0.561	14.013	93.243
4	0.270	6.757	100.000

principal components determined by the cumulative contribution rate, usually are 80–90%, and then these principal components can be used for further analysis.

Through comparative analysis, 20 days, more or less, is a critical time of freshness under current storage time, and the analysis results are representative. In the principal component analysis, correlation matrix eigenvalues are shown in Table 2. The first two principal components of information accounted for 79.23% of the total information, and basically retained the original variable information. Therefore, it is feasible and reliable to take the first two compositions as main components to distinguish freshness.

$X_1, X_2, X_3, X_4$  represent haugh units, weight loss, density and percentage of increased gas chamber diameter, respectively. Two no-correlation comprehensive index models are obtained by principal component analysis:

$PC_1 = 0.014X_1 + 0.904X_2 + 0.751X_3 - 0.853X_4$ . The results obviously showed that 52.678% of the original data could be described by PC1 based on the Table 1. It could be summed as the indicator mainly related to moisture loss.

$PC_2 = 0.968X_1 - 0.005X_2 - 0.270X_3 - 0.228X_4$  showed that 26.565% of the original datas could be represented, and be redefined as protein denaturation.

### 3.3 Discriminant Analysis

There are some limitations on the application of different storage recognition of eggs by using principal component analysis. In addition, the shelf life of the egg samples with unknown storage intervals could not be predicted. Therefore, discriminant analysis need be used in this paper. Four canonical discriminant functions were developed, with characteristic values 21.744, 0.459, 0.107, and 0.066, respectively. The characteristic values could explain the variation of model variance of 97.2, 2.1, 0.5, 0.3%, respectively. The former two canonical discriminant function could explain 99.3% change of the variation, and contained the main information. The differences and relations between days and freshness could be described. Scatter plot of the first two canonical discriminant functions were shown in Fig. 1.

In 0, 2, 5, 9, 13, 17, 20, 24, 27, 31, 34, 36 days, correct discrimination rates are 68.18, 52, 76.92, 85.19, 85.19, 85.19, 85.19, 55.56, 50, 28.57, 33.33 and 74%, respectively. Overall discriminant rate is 62.6%. With the increase of time, the discriminant accuracy increased firstly and then decreased. From 5 to 20 days,

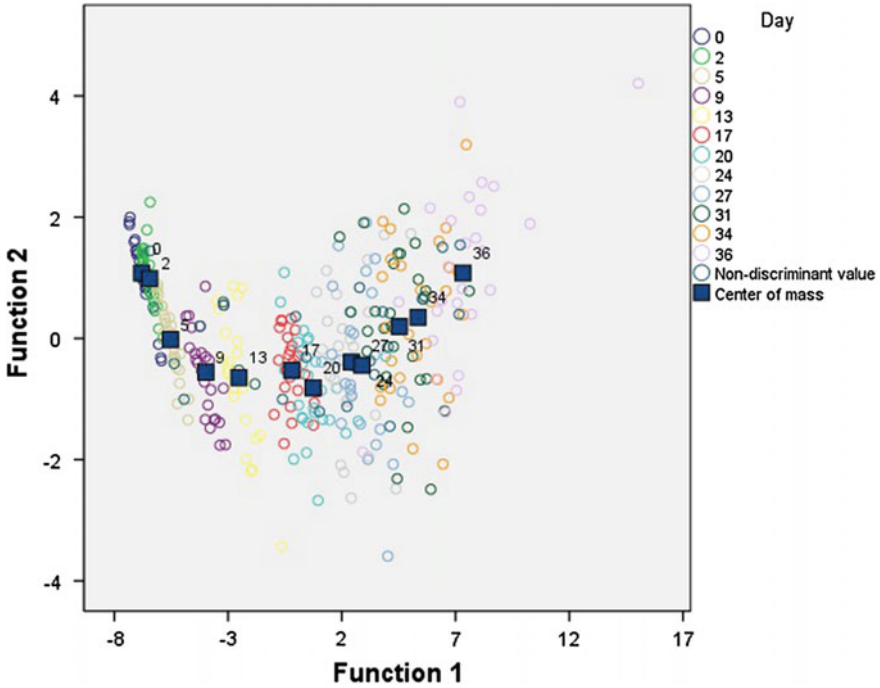


Fig. 1 Scatter plot of canonical discriminant functions

discriminant accuracy is relatively high, probably because the barrier functions of the natural membrane of external eggshell can make the egg quality changed unobviously within 5 days after oviposition. In the later days, more and more samples could not be measured owing to the deterioration, thus leading to the lower accuracy of model distinguish.

### 4 Conclusions

Shelf life of eggs is important, but there are a lot of freshness indexes which sometimes are inconsistent. The albumen pH, yolk color, haugh units, density, weight loss and the increasing ratio of gas chamber diameter were determined every 3 days till 36 days in this article. Principal component analysis and discriminant analysis were used to developed the comprehensive model under the current storage condition. Water loss and protein degeneration are summarized as two principal components of freshness change; Based on diversified typical discriminant function, the average accuracy of is nearly 63% with 85.19% of highest accuracy. Principal components and discriminant analysis provide a new basis and considerations for egg freshness evaluation.

**Acknowledgements** This study is funded by Beijing Municipal Commission of Education Project (KM2015100220013), Scientific Research Project of Beijing Educational Committee (KM201410020011), and The Comprehensive Reforming Project to promote talents training of BUA.

## References

1. Zhang L., GUO W., MA Y. (2008). Changes of hen eggs' fresh quality and dielectric properties during the storage. *Journal of agricultural mechanization research*, 4:146–148.
2. Li J., Yan K., Wu J. (2012). Effects of different storage methods on egg quality. *Acta Ecologiae Animalis Domastici*, 01:47–49+102.
3. DU Dan-meng; WANG Feng-nuo; WANG Shi-ping. The laws of the egg freshness change with storage conditions. *Food science and technology* 05:26–29+33.
4. LIU Yan-de, QIAO Zhen-xian (2002). A correlative analysis on the freshness of chicken eggs and storing conditions. *Acta Agriculturae Universitatis Jiangxiensis*, 2002, 01:48–51.
5. WANG Lingjin, WANG Guihua. (2002). *Chemical Industry Press: Basis of analytical chemistry*, 2nd edn. Beijing, China.
6. Huo Danqun, Zhang Miaomiao, HouChangjun, et al. (2011). Recognition method of liquor brands based on principal component and linear discriminant analysis. *Trans actions of the CSAE*, 27(Supp. 2): 297–301.

# Application of Ultra-High Pressure Technology in the Processing of Shellfish Shell

Xue Gong, Jiang Chang and Zhihui Sun

**Abstract** Shellfish was modern popular seafood, because of its rich nutrition and by consumers, the key problem of shellfish shelling process. Ultra high pressure shell was a kind of food processing technology emerging, it could complete the shelling process and could reduce the harmful microorganisms, shellfish meat, modern popular and commonly used shelling technology. Through the investigation and analysis of the present application of shelling technology to provide a theoretical basis and technical support for further studies and industrial production for shellfish hulling technology.

**Keywords** Shellfish · Shelling · Ultra high pressure · Quality

## 1 Introduction

China was the world's largest shellfish farming country, its yield was about half of the world total yield of shellfish 60% [1], bivalve with its delicious meat, low fat, high protein, was rich in various mineral elements and vitamins, nutritional value higher, more and more loved by consumers [2]; as a nutrient rich marine treasures, shellfish was produced in addition to selling fresh products, most of which were made of the ready to eat food or dry products, to prolong the shelf life, improved sales flexibility. At this stage, developed countries bivalve shell was usually used heating shell method, microwave shelling method, laser hulling method and super high pressure shell method [3]. Under the action of pressure rise of not only China

---

X. Gong · J. Chang  
School of Light Industry, Harbin University of Commerce,  
Harbin, Heilongjiang, China  
e-mail: kahnannie@163.com

Z. Sun (✉)  
Academic Affairs Office, Harbin University of Commerce,  
Harbin, Heilongjiang, China  
e-mail: sunzhihui1962@163.com

shellfish processing method and equipment also there was a big gap, shellfish hulling mainly was the artificial stripping, the processing efficiency was low, the health was difficult to be guaranteed. At the same time, the complete shellfish meat was obtained that it was not easy, shellfish products processing Limited. With the ultra high pressure technology on ultra high pressure shelling technology researched had gradually increased [4], using ultra high pressure technology of shelling rate than the manual shelling compared, high 17.26% [5].

## **2 Study on the Status of the Shelling Technology**

### **2.1 *Ultra High Pressure Treatment on the Texture Effect of Adductor Muscle Protein***

Lv [6] of mussels hot pressing opened shell mechanism study found in the shelling process, adductor muscle actomyosin in hot pressing produce gel, protein degeneration, contraction effect was reduced, increased the brittleness of the adductor muscle, achieved the shelling; Cui [7] and so on of freezing mode of bay scallop adductor muscle protein degeneration mechanism and structure determination of physical and chemical properties. The experimental were resulted show that, in the process of frozen storage, pH value decreased, at the same time, the oxidation of sulfhydryl groups were formed disulfide bonds; Yang [8] shrimped of ultra high pressure treatment on ultra high pressure, shrimp and shrimp between adhesion tissue protein degeneration, making shrimp and shrimp separation and shelling progenitor of iron oxide red of the frozen storage of bay scallop adductor texture properties. The results showed that the  $(-35 \pm 1)$  C, adductor muscle elasticity and hardness of small. Li [9] of the ultra high pressure, protein molecular structure, The results showed that the protein molecular size in ultra high pressure Study found that the equal pressure occurred under the action of the compression force was smaller in 800 MPa ultra high pressure, protein, three and four level structure were changed, among them, the four protein secondary structure of the most sensitive, three primary structure, secondary structure had changed a little, and a structure did not change; Hu [10] of ultra high pressure on protein secondary structure, the study found that with the pressure increasing, the myofibrillar protein alpha helix and beta sheet content decreased. Liu [11], when deal with the pressure of 300 MPa. Trypsin activity, structure of alpha helice and beta angle of peak area ratio reached maximum; hat under the action of 8 GPa pressure were found by Chen [12]. The primary structure of the protein amino acid residued sequence would be changed, the activity decreased.

## 2.2 *Effects of Ultra High Pressure Treatment on Product Quality and Shelling Rate*

Yi [13] of abaloned super high-pressure shelling process parameters for the determination. The experimental resulted show that, the abalone under 300 MPa ultra high pressure processing, could make the hulling rate reached 100%; Yi [14], on South American white prawn shelling industry and trade Art were studied. The results be showed vannamei applied 300 MPa ultra high pressure and maintains 1 min, could get the better effect of shelling; super high-pressure shelling effect of oyster were studied by Li [15], it was found that, for oyster of ultra high pressure treatment could get ideal effect of the shelling, especially under the 300 MPa pressure conditions be kept 1 min; Chen [16] studied of ultra high pressure on South American white prawn shell and processing properties of the influence. The results showed that the southern white shrimp in 200 MPa super high pressure treatment for 3 min, would increase of meat rate; Wang [17] studied of ultra high pressure on mussel Effect of shelling and quality. The results showed that the mussels in ultra-high pressure 300 MPa keeping 2 min, could have get the ideal effect of the shelling, had improved texture of mussel meat; Yuan [18] had studied the effects of ultra high pressure treatment on frozen abalone fresh-keeping effected and changed of quality. The experimental had resulted show that, abalone 400 MPa ultra high pressure after 10 min could had change abalone internal structure of muscle tissue; Bao [19] from the point of view of mechanics of hulling mechanism had been studied, results showed that, in the ultra-high pressure, the maximum had contacted stress in the adductor muscle and shell near the middle position when the contact stress reaches a certain value, it could have made the clam meat and shell separation diffusion model, Wang [20] based on neural network platform of oyster meat ultra high pressure sterilization process conditions had been optimized; the ultra high pressure had treated conditions of shrimp quality change dynamics were studied by Huang [21], the results showed that in different ultra high pressure Stress conditions, the establishment of the mass loss of shrimp, hardness, yellowness value  $b^*$  changed the zero order reaction kinetic model and the moisture content; layer structure characteristics of oyster adductor muscle scar muscle prism of research by Lee [22] found that muscle prismatic layer was connected structure of adductor muscle scar edge from the top of the shell, but a composed of mineral and organic matrix of multilayer; Martin [23] had been studied based on cold/heat treatment automatic oyster shell technology development and test. The results of the study had showed that this method could get better effect of shelling; Yi [24] studied the ultra—high pressure of bay scallop on shelling and adductor muscle physical quality effect, and the traditional manual shelling phase Ratio, ultra high pressure technology to have obtained a higher yield; Adams [25] had studied the oyster shell process parameters, through the experiment, it has been found, in 310 MPa ultra high pressure on oysters through instant processing, could get 100% of the hulling rate; Hsu [26] of oyster ultra high pressure shell of the process parameters, had studied shown that, 250 MPa holding pressure for 3 min or 300 MPa treatment could have get the instantaneous hulling rate of 100%.

### 3 Conclusions

At present, domestic and foreign has researched on EHV shelling technology research and application of concentrated in quality, protein degeneration and hulling rate and so on, and to study on ultra high pressure shell mechanism was less, for the research of shell mechanism could provide the technical support for the ultra high pressure shelling technology development and industrialization, it would also become mainstream and the key of the study in the future.

#### Acknowledgments

##### Funds:

National Science and technology support program: (2016YFD0400301)

Harbin University of Commerce research team support program: (2016TD005)

### References

1. Sun Yu, Mu Yongtong (2014). Scallop yield and output value in the world China's position. *Journal of fishery economy in China*, 32(4):100–106.
2. Liu Shucheng, Guo Minghui, Huang Wanyou (2015). Superhigh pressure technology in the application of shrimp freshness and processing. *Journal of food industry science and technology*, 36(9):376–383.
3. Lu Xinchun, Sun Xingzhao, Wang Wei. Bivalves hulling pretreatment technology present situation and development trend. *Modern agricultural machinery*, (9):74–76.
4. Zhu Songming, Su Guangming, Wang Chunfang (2014). Ultra-high pressure processing technology research and application of aquatic products. *Journal of agricultural machinery*, 45(1):168–177.
5. Junjie Yi, Qian Xu, Xiaosong Hu, ect. (2013). Shucking of bay scallop (*Argopecten irradians*) using high hydrostatic pressure and its effect on microbiological and physical of adductor muscle. *Innovative Food Science and Emerging Technologies*, (18):57–64.
6. Lv Fei, Sheng Junliang, Ding Yuting (2014). Hot-pressing impact on quality of mussels open shell and shell mechanism. *Journal of modern food science and technology*, 30(11):175–182.
7. Cui Ruiying, Jiao Xueqin, Reng Hui, etc. (2013). Frozen way effect the performance of the bay scallop shell texture, closed. *Journal of food industry science and technology*, 34(20):349–352.
8. Yang Hui. Based on the research on shrimp shell process and quality detection of ultra-high pressure technology. Hangzhou: zhejiang university, 2011.
9. Li Renjie, Liao Xiaojun, Hu Xiaosong, etc. (2014). Ultrahigh pressure effect on the protein. *Journal of high pressure physics*, 28(4):498–506.
10. Hu Feihua, Lu Haixia, Chen Qing, etc. (2010). Ultra-high pressure treatment on mei fish minced fish gel properties. The influence of *journal of fisheries*, 34(3):329–335.
11. Liu Ping, Hu Zhihe, Wu Zijian, etc. (2015). Ultrahigh pressure causes pancreatic protein conformation change and the relationship between enzyme activity. *Spectroscopy and spectral analysis*, (35):1335–1339.
12. Chen W, Heymann G, Kursula P, et al. (2012). Effects of gigapascal level pressure on protein structure and function. *J Phys Chem B*, 116(3):1100–1110.
13. Yi Junjie, Dong Peng, Hu Xiaosong, etc. (2014). Abalone ultra-high pressure shell process optimization and quality study. *Journal of high pressure physics*, 28(2):239–246.

14. Yi Junjie, Ding Guohui, Hu Xiaosong, etc. (2012). South America white shrimp shell technology comparison, its influence on the quality of shrimp. *Journal of agricultural engineering*, 28(17):287–292.
15. Li Xuepeng, Zhou Kai, Wang Qi, etc. (2014). Oyster effect of ultrahigh pressure shell. *Journal of food industry science and technology*, 35(15):210–214.
16. Chen Shaohua, Hu Zhihe, Wu Zijian (2014). Ultra-high pressure technology on South America white shrimp shells and the influence of processing performance. *Journal of food science*, (22):11–16.
17. Wang Min (2012). Ultrahigh pressure influence on mussel shells and quality research. Hangzhou: zhejiang university, 2012.
18. Yuan Shao, Zhou Feng, Zhou Deqing (2015). Ultra-high pressure treatment on frozen abalone preservation effect and the influence of the quality change. *Journal of food industry science and technology*, 36(17):312–316.
19. Bao Zhendong (2015). Based on the analysis of the mechanics mechanism of clam shell ultrahigh pressure shell[D]. Harbin: Harbin university of commerce.
20. Wang Xiaoqian, Zhong Saiyi, Qin Xiaoming, etc. (2015). Give neural network platform of oyster meat super-high pressure sterilization process conditions optimization. *Journal of food industry science and technology*, 36(6):257–261.
21. Huang Wanyou, Liu Shucheng, Ji Hongwu, etc. (2013). Under the condition of ultrahigh pressure processing shrimp quality change dynamics. *Journal of food industry science and technology*, (22):100–105.
22. Seung-Woo Lee, Young-Nam Jang, Jeong-Chan Kim. Characteristics of the Aragonitic Layer in Adult Oyster Shells, *Crassostrea gigas*: Structural Study of Myostracum including the Adductor Muscle Scar. *Evidence-Based Complementary and Alternative Medicine*, (5):1–10.
23. Daniel E. Martin, John Supan, Jeremy Theriot, etc. Development and testing of a heat-cool methodology to automate oyster shucking. *Aqua cultural Engineering*, (37):53–60.
24. Junjie Yi, Qiao Xu, Xiaosong Hu, ect. (2013). Shucking of bay scallop (*Argopecten irradians*) using high hydrostatic pressure and its effect on microbiological and physical quality of adductor muscle. *Innovative Food Science and Emerging Technologies*, (18):57–64.
25. He H, Adams R M, Farkase F, et al. (2002). Use of high pressure processing for oyster shucking and shelf life extensor. *Journal of Food Science*, 67:640–645.
26. Hsu K C, Hwang J S, Chi H Y, et al. (2010). Effect of different high pressure treatments on shucking, biochemical, physical and sensory characteristics of oysters to elaborate a traditional Taiwanese oyster omelette. *Journal of Science of Food and Agriculture*, (90)3:530–535.



# Research on Storage Location Technology Based on RFID

Hanyue Zhang, Xixi Feng and Jiao Wen

**Abstract** Along with the development of the logistics technology and the expansion of the warehouse scale, the difficulty of warehouse management has also greatly been increased. It puts forward the new requirements to the method and precision of storage location. This paper intends to study the positioning method and technology based on RFID. The RFID positioning technology is introduced into the information management of the warehouse, in order to realize the real-time positioning of goods, and improve the accuracy and efficiency of the warehouse operation management. At the same time, using the received signal strength method (RSSI), constructed the storage location algorithm and the model, which can provide important support for the realization of intelligent storage management, inventory positioning and identification.

**Keywords** RFID · Warehouse management · RSSI · Positioning

## 1 Introduction

With the rapid development of Internet and information technology, radio frequency identification technology (RFID) as a new automatic identification technology, has been used to the warehouse management. The RFID positioning technology makes it possible for real-time accurate locating of the warehouse storage, and is a new perspective for building a modernized, visualized and dynamic warehouse management system.

Among the RFID indoor positioning algorithms, the method based on RSSI is low cost and relatively easy to implement positioning technology. Therefore, this paper adopts the positioning algorithm based on RSSI to carry out three-dimensional analysis of cargo inventory positioning in warehouse logistics,

---

H. Zhang · X. Feng (✉) · J. Wen  
Tianjin University of Science and Technology, Tianjin, China  
e-mail: fxx19910304@163.com

and select the three side measurement method to calculate the unknown node coordinates [1].

## 2 Positioning Analysis of Three-Dimensional Warehouse Inventory Based on RSSI Positioning Algorithm

### 2.1 Principle of Distance Measurement

The principle of RSSI ranging technology is by measuring the intensity of the received radio signal, and then estimates the distance between the nodes and the unknown node based on propagation path loss of a radio signal. The present paper uses the long distance path loss model to calculate the distance between the unknown node and the known. The formula is as follows:

$$P_r(d) = P_0(d_0) - 10n \lg\left(\frac{d}{d_0}\right) + X_\sigma \quad (1)$$

Among them,  $d_0$  takes 1 m,  $X_\sigma$  is 0, and the model is simplified, and the distance between unknown node and known node is obtained:

$$d = 10^{(A_I - \overline{RSSI})/10n} \quad (2)$$

where  $A_I$  represents the reference distance  $d_0$  is 1 m, the node receives the radio signal strength.  $\overline{RSSI}$  is the mean of the wireless signal strength received by the node,  $n$  is for a radio signal propagation path loss coefficient [2, 3].

### 2.2 RSSI Ranging Based on Known Node Information as Reference

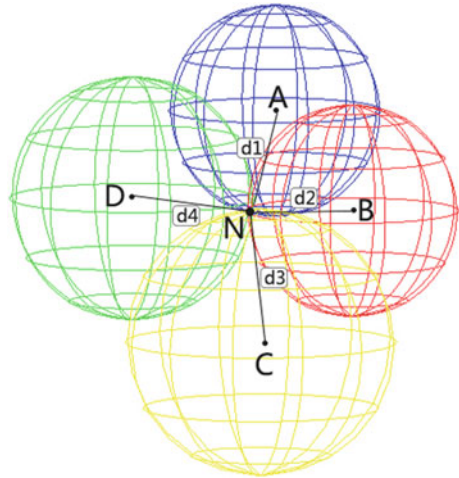
According to the previous surveys, the reference signal strength  $A_I$  generally take -45 dBm, path loss coefficient  $n$  generally takes 4.

In Fig. 1, the unknown node N receiving the radio signal from known nodes A, B, C, D, the  $A_I$ ,  $n$  are substituted into the formula to calculate the distance between the unknown node N and the known node A, B, C, D respectively,  $d_1$ ,  $d_2$ ,  $d_3$ ,  $d_4$ .

### 2.3 Position Calculation

The three dimensional diagram of trilateration is shown in Fig. 1 [4].

**Fig. 1** Trilateration method in three dimensional environment



The four known node A, B, C, and D are placed in the center of the ball A, B, C, D. the coordinates of the four centers are  $(x_A, y_A, z_A)$ ,  $(x_B, y_B, z_B)$ ,  $(x_C, y_C, z_C)$ ,  $(x_D, y_D, z_D)$ . The unknown node N  $(x_N, y_N, z_N)$  is the intersection of the four ball. The distance between the unknown nodes and four known nodes are  $d_1, d_2, d_3, d_4$ .

According to the principle of trilateration method, the formulae of three-dimensional space are shown below (3):

$$\begin{cases} \sqrt{(x_A - x_N)^2 + (y_A - y_N)^2 + (z_A - z_N)^2} = d_1 \\ \sqrt{(x_B - x_N)^2 + (y_B - y_N)^2 + (z_B - z_N)^2} = d_2 \\ \sqrt{(x_C - x_N)^2 + (y_C - y_N)^2 + (z_C - z_N)^2} = d_3 \\ \sqrt{(x_D - x_N)^2 + (y_D - y_N)^2 + (z_D - z_N)^2} = d_4 \end{cases} \quad (3)$$

In practical applications, due to the measurement error, the four balls are very likely have no intersection. In view of this problem, the least squares method can be put into data processing.

It is assumed that the known nodes  $l = (x_i, y_i, z_i)$  in the three dimensional space. Its measurement distance to unknown nodes  $N = (x, y, z)$  is  $d_i$ .  $0 < i < n$  represents the number of known nodes. The least squares of the 3D coordinates can be represented as:

$$\begin{aligned} (\hat{x}, \hat{y}, \hat{z}) = \arg \min_{x,y,z} & \left[ \frac{1}{n} \sum_{i=1}^n \left( d_i - \sqrt{(x_i - x)^2 + (y_i - y)^2 + (z_i - z)^2} \right)^2 \right] \\ & i = 1, 2, \dots, n \end{aligned} \quad (4)$$

The solution is obtained.

$$(x, y, z) = (A^T A)^{-1} A^T B \quad (5)$$

Corresponding with Fig. 1, there are:

$$A = 2 \begin{bmatrix} (x_A - x_D) & (y_A - y_D) & (z_A - z_D) \\ (x_B - x_D) & (y_B - y_D) & (z_B - z_D) \\ (x_C - x_D) & (y_C - y_D) & (z_C - z_D) \end{bmatrix} \quad (6)$$

$$B = \begin{bmatrix} x_A^2 - x_D^2 + y_A^2 - y_D^2 + z_A^2 - z_D^2 + d_4^2 - d_1^2 \\ x_B^2 - x_D^2 + y_B^2 - y_D^2 + z_B^2 - z_D^2 + d_4^2 - d_2^2 \\ x_C^2 - x_D^2 + y_C^2 - y_D^2 + z_C^2 - z_D^2 + d_4^2 - d_3^2 \end{bmatrix}$$

## 2.4 Error Sources

1. randomly assigned known nodes for unknown nodes
2. experience values directly given for environmental parameters the positioning calculation regardless of the environmental differences is bound to cause errors.

The accumulation of minor errors will directly affect the final positioning result. Therefore, it is necessary to optimize the RSSI positioning algorithm to improve the positioning accuracy to meet the requirements of the automatic positioning.

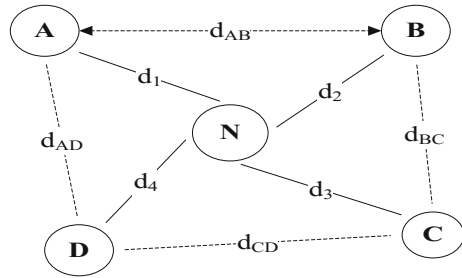
## 3 Optimization Method of RSSI Positioning Accuracy

### 3.1 Neighbor Node Selection

The essence of the neighbor node selection method is to select the known nodes which are close to the unknown nodes for relatively accurate positioning. The inductive signal strength will become smaller and weaker with the increase of the distance. Using this feature, we can choose the adjacent known nodes to achieve the precise localization by comparing the difference of the signal strength.

First, using a reader identifies the node within the readable range, then makes a difference comparison for the known node RSSI value and the unknown nodes RSSI value. The smaller the difference, the closer the distance between the node and the unknown node is. According to the principle of the least difference, four nearest known nodes are chosen for subsequent unknown position calculation. This optimized method can reduce the positioning error caused by the random allocation of known nodes, at the same time, improve the positioning accuracy of the system to a certain extent, and ensure the maximum reliability of the source data [5].

**Fig. 2** Known node communication method



### 3.2 Known Node Communication Method

The known node communication method is to real time get the  $A_1$  and  $n$  value from the location environment as shown in Fig. 2. **N** is unknown node, by the method described in Sect. 3.1, to get the nearest four known nodes **A**, **B**, **C**, **D** which can communicate with each other. The distance between each other are represented by  $d_{AB}$ ,  $d_{BC}$ ,  $d_{CD}$  and  $d_{AD}$ . The known nodes communicate with each other by using the signal strength information to estimate the environmental parameters  $A_1$  and  $n$ .

Assuming that  $RSSI_{AB}$  is the signal strength of the known node **A** received by the known node **B**, while  $RSSI_{AD}$  is the signal strength of the known node **A** received by the known node **D**. From the derived formula  $d = 10^{(A_1 - \overline{RSSI})/10n}$ , the signal strength can be represented by:

$$\begin{cases} RSSI_{AB} = A_{1A} - 10n_A \lg(d_{AB}) \\ RSSI_{AD} = A_{1A} - 10n_A \lg(d_{AD}) \end{cases} \quad (7)$$

The environmental parameters  $A_{1A}$  and  $n_A$  of the known node **A** in the quadrilateral **ABCD** region can be obtained from the above formula, as shown in Formula (8):

$$\begin{cases} A_{1A} = RSSI_{AB} + \frac{RSSI_{AB} - RSSI_{AD}}{\lg(d_{AD}/d_{AB})} \lg d_{AB} \\ n_A = \frac{RSSI_{AB} - RSSI_{AD}}{10 \lg(d_{AD}/d_{AB})} \end{cases} \quad (8)$$

Similarly to the environment parameters of other three known node **B**, **C**, **D**, respectively,  $A_{1B}$  and  $n_B$ ,  $A_{1C}$  and  $n_C$ ,  $A_{1D}$  and  $n_D$ . For simplicity, the environmental parameters in the quadrilateral **ABCD** region are as follows:

$$\begin{cases} A_1 = \frac{A_{1A} + A_{1B} + A_{1C} + A_{1D}}{4} \\ n = \frac{n_A + n_B + n_C + n_D}{4} \end{cases} \quad (9)$$

## 4 Simulation Experiment and Result

The experimental operation platform used in this paper is TAG ZK Smart intelligent storage system.

### 4.1 Simulated Shelf Layout

Two rows of shelves and a roadway makes a testing unit and a rectangular simulation structure is to establish.

$$L \times W \times H = 12000 \times 3900 \times 4500 \text{ (mm)}$$

Due to the space constraints of experiment environment, only two rows with eight columns four-layer shelves are arranged. Here is the grid size for each cargo:

$$1500 \times 1200 \times 1500 \text{ (mm)}$$

In this three-dimensional space, five known nodes A, B, C, D, E are set, the coordinate respectively is:

$$\begin{aligned} A(0, 0, 3); \quad B(3.9, 12, 3); \quad C(3.9, 0, 0); \quad D(0, 12, 0); \\ E(1.95, 6, 1.5) \end{aligned}$$

Known nodes in three-dimensional space area distribution shown in Fig. 3, five known nodes are represented by five colors, the coordinates have been marked out as in the Fig. 3.

Three unknown nodes are arranged in the simulation model, and five known nodes are used to locate the nodes.

### 4.2 Positioning Results Compared Before and After Optimization Algorithm

1. Assuming that the computational coordinates of the unknown node are  $(x_n, y_n, z_n)$ , while the true location of the coordinates is  $(x_{0n}, y_{0n}, z_{0n})$ , then the positioning error EE is:

$$EE = \sqrt{(x_n - x_{0n})^2 + (y_n - y_{0n})^2 + (z_n - z_{0n})^2} \quad (10)$$

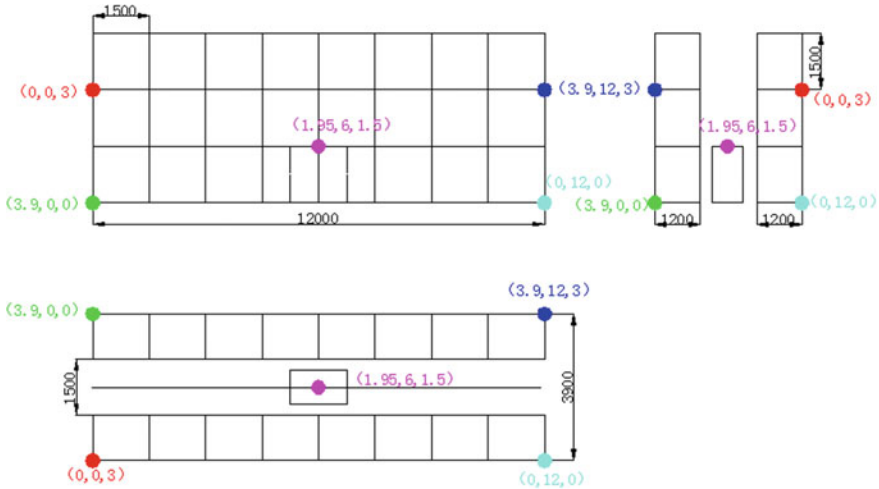


Fig. 3 Known node distribution in 3D space

According to the measured data we can get  $EE_{00} = (EE_1 + EE_2 + EE_3)/3 = 18.1024063$ .

This kind of basic location algorithm has a large positioning error, which cannot meet the requirements of three-dimensional warehouse inventory positioning.

2. “Neighbor node selection” optimization simulation

The unknown node coordinates and the distance between the unknown node and the known node can be obtained by calculating under the optimal localization algorithm:

$$EE_{01} = (EE_1 + EE_2 + EE_3)/3 = 7.8366305$$

$$(EE_{00} - EE_{01}) \div EE_{00} = 56.71\%$$

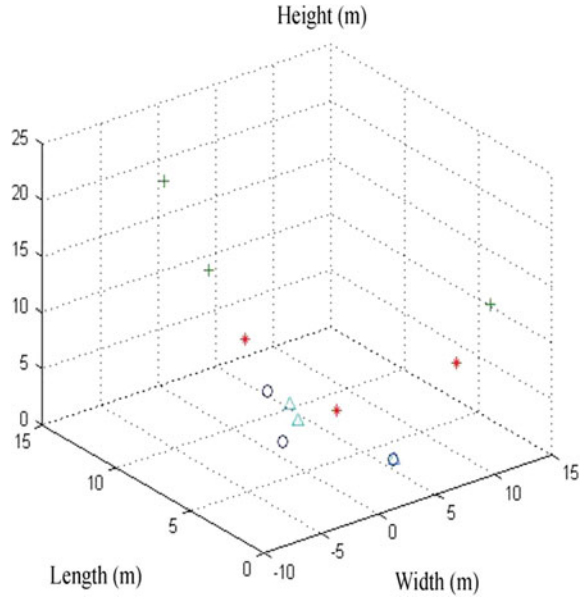
3. “Known node communication method” optimization simulation

The method is the optimized inter-node communication by calculating mutual induction of RSSI values to determine the  $A_1, n$  value from different unknown node locations. After selecting adjacent known nodes and determining the different location of the regional environmental parameters  $A_j, n$ , the unknown node coordinate and the distance between the unknown and the known node can be obtained by calculating under the double optimal localization algorithm.

$$EE_{02} = (EE_1 + EE_2 + EE_3)/3 = 2.83911326$$

$$(EE_{01} - EE_{02}) \div EE_{01} = 63.8\%$$

**Fig. 4** Location results contrast visual chart



After the double optimization, the positioning error is reduced by 63.8%. The positioning accuracy is improved a lot, the effect is obvious, and the optimization effect is improved.

Figure 4 shows the position difference before between the localization algorithms before and after the optimization. It's obvious from the figure that the difference between the unknown node position and the actual position is decreased after double optimization.

“O”: the actual node position

“+”: position calculated by the basic location algorithm

“\*”: position after the preliminary optimization calculation

“Δ”: position after double optimization calculation.

The innovation points of this paper are as follows: first, the technology of RFID is applied to the cargo localization of the three-dimensional warehouse; second, the precision of the RSSI positioning algorithm is optimized.

## 5 Conclusions

Due to various factors, although it has achieved some success, but it does not completely meet the requirements of the positioning. And the factors that affect the results of this paper, in addition to the selection of environmental parameters, there



are a number of known nodes and density, the hardware specifications of electronic tags, and so many factors. In the future, when the experimental conditions permit, these factors can be further analyzed.

## References

1. Wang Zhiliang (2011). Internet of Things Engineering [M]. Machinery Industry Press, 90–96.
2. Yin Qing (2014). Application of the Internet of things in the positioning of logistics pallet [D]. Tianjin: Tianjin University of Science and Technology, Vol. 11, 215–217.
3. Zhang Lingyu (2014). LANDMARC positioning system and its algorithm research [D]. Hunan: Central South University.
4. Chen Xiaoyu (2014). Research on key technology of 3D spatial localization based on [D]. RFID Jiangsu: Nanjing University of Posts and Telecommunications.
5. Zhou Yancong, Dong Yongfeng, Sun Lunan (2015). RFID based virtual reference label for 3D indoor localization algorithm [J]. computer engineering and design, 36 (6): 1535–1539.

# Simulation Research About the Influence of Particle Characteristics on Transition of Particles in the Horizontal Screw Conveyor

Jiandong Lu, Tianshu Zhao, Lizheng Zhang and Xiaoli Song

**Abstract** Particle products widely exist in the packaging field, such as capsules and nut foods etc. In the practical packaging process, particle products are often needed to be transmitted in the horizontal screw conveyor. Based on the discrete element method, the particle transportation state in horizontal screw conveyor is simulated with EDEM simulator which is extensively used to simulate the movement of particles. The simulation results show that the characteristics of particle itself, such as size, density and the surface rolling friction coefficient, can affect the transition of the particles in the horizontal screw conveyor. Firstly, the average velocity of the particles decreases greatly with the increasing of particle size. Secondly, the average velocity of the particles increases when the particle density increases. Thirdly, the average velocity of the particles decreases with increasing of the surface rolling friction coefficient.

**Keywords** Particle · Particle characteristics · Transition · Horizontal screw conveyor

## 1 Introduction

Granular particle is a mechanical mixture consisted of solid particles with different shapes and sizes [1]. Granular particle products widely exist in the packaging field, such as capsules, tablets and nut foods etc. Particles are often transmitted through the horizontal screw conveyor in the packaging process. The transition velocity of grain particles is one of the important indexes which are used to evaluate the transition efficiency of the particles in the screw conveyor. With regard to the influence factors of the transition velocity, the previous research always focused on the speed of the screw, the filling coefficient of particles, the separation distance

---

J. Lu (✉) · T. Zhao · L. Zhang · X. Song  
School of Printing and Packaging Engineering,  
Beijing Institute of Graphic Communication, Beijing, China  
e-mail: lululu0831@sina.com

between screw blades, and so on. The research about the influence of the characteristics of particle itself on the transition of the particles in the screw conveyor is little.

The obtained experimental and theoretical results have proved that the characteristics of particle itself can influence the flow of particles. MIDI GDR indicates that the surface friction of particle can be characterized by the angle of repose determined in the rotating drum [2]. The experimental results obtained by Pohlman show that the bigger friction coefficient of particle, the larger angle of repose, the worse mobility of particle [3]. Ouyang Hongwu studied the effect of particle surface friction on the flow of particles in the hopper [4]. These results show that the movement of particles can be affected by the characteristics of particle itself.

In our work, the influence of particle characteristics on movements of particles in the horizontal screw conveyor is analyzed. In terms of the simulation about particle, EDEM simulator is often applied to simulate the movement of particles. Based on EDEM simulator, the transition of particles in horizontal screw conveyor is simulated to determine the effect of particle characteristics.

## 2 Simulation

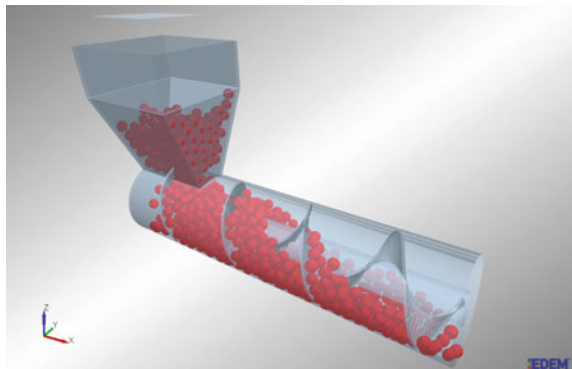
### 2.1 Construction of Model

As a 3D model software, Rhinoceros software is used to build the 3D model of horizontal screw conveyor, which is shown in Fig. 1.

The dimensions of this screw conveyor are shown in Fig. 2. Units of all the dimensions in Fig. 2 are millimeter. The screw rotates constantly. The angular velocity of the screw is 345 deg/s.

Some assumptions are made before the simulation. The material of this screw conveyor is steel. Poissons's ratio and shear modulus of the particles are respectively 0.3 and  $2.3e+07$  Pa. The total number of particles is 1000. The total simulation time is 10 s. The simulation time step is 0.05 s.

**Fig. 1** 3D model of horizontal screw conveyor



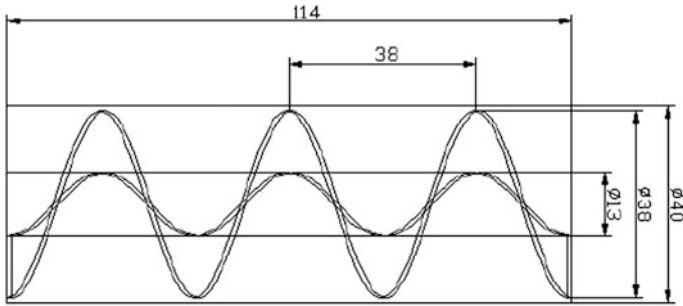


Fig. 2 The dimensions of horizontal screw conveyor

## 2.2 Variables of Model

In this work, we focus on three kinds of particle characteristics, including size, density and the surface rolling friction coefficient. The three kinds of particle characteristics, which may affect the transition of particle in the horizontal screw conveyor, are simulated respectively.

In the simulation, the value range of the three factors comes from the common data in the practical packaging process. The set variable values will be mentioned in the experimental results. Because the transition velocity of grain particles is critical to evaluate the transiting efficiency in the horizontal screw conveyor, the simulation results plan to show the relations between the transition velocity and the three kinds of particle characteristics.

## 2.3 Theoretical Basis of Model

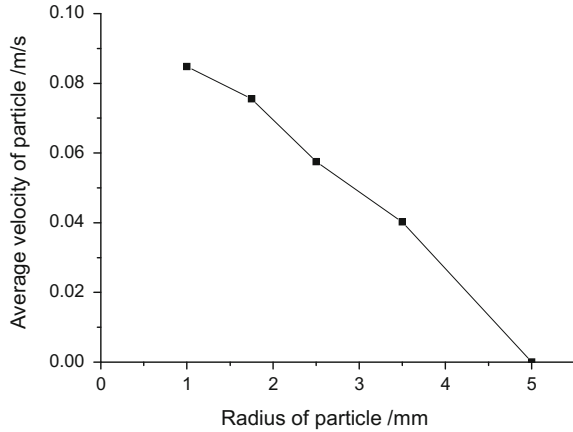
In this model, Hertz-Mindlin (no slip) model is applied to describe the mechanical properties not only between particles, but also between particle and screw conveyor. According to Hertz-Mindlin (no slip) model, the normal force is based on Hertzian contact theory [5], the tangential force is base on the research of Middlin-Deresiewicz. In addition, normal force and tangential force both have damping component [6]. The tangential friction force accords with the Coulomb friction law [7].

## 3 Results and Analysis

### 3.1 Effect of Particle Size

Five different particles size are simulated. The diameters of the particles are respectively 1, 1.75, 2.5, 3.5 and 5 mm. In this whole simulation process, the other

**Fig. 3** Relation between average velocity and particle size



parameters of the particle and the screw conveyor are unchanged except the particle size. According to the data acquired through the simulation, Fig. 3 is plotted.

As shown in Fig. 3, the average velocity of the particles decreases with the increasing of particle size. The reason for this is that when the larger particles pass through the channel with the same dimension, there are more contact among the particles or between the particle and the screw conveyor. The forces exerted on the particle are increased. Specially, with rising of the pressure between particles, the difficulty of particle movement is increased. Therefore, it is more difficult for the larger particles to pass the channel.

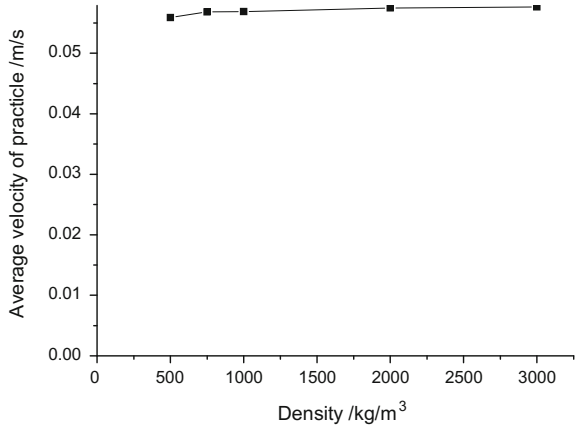
In addition, jamming happens in the transiting process of particles, when the diameter of particle is 5 mm. According to the related research [4], jamming will inevitably happen when the diameter of channel is smaller or equal to 4.5 times than the diameter of particle. It can be shown that the size of particle can influence the particle transition in the horizontal screw conveyor.

### 3.2 Effect of Particle Density

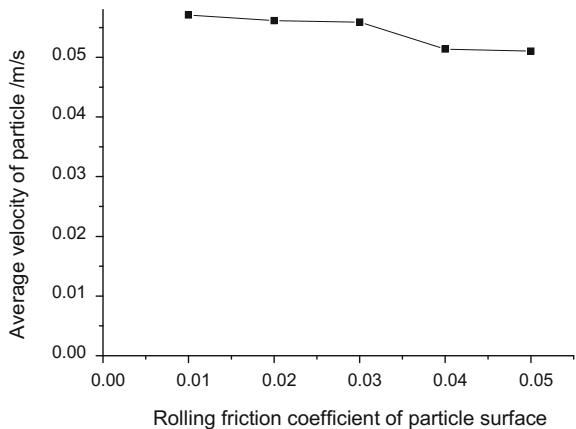
Similarly, five kinds of particle densities are simulated. The sizes of particles are respectively 500, 750, 1000, 2000 and 3000 kg/m<sup>3</sup>. When simulating, the other parameters of the particle and the screw conveyor are unchanged except the particle density. The simulation results are shown in Fig. 4.

In Fig. 4, the average velocity of the particles increases slightly when the particle density increases. The reason for this is that the angular velocity of the screw is still 345 deg/s, although the particle density is varied. The change of particle density can not affect the movement characteristics of particle. Therefore, when the particle density only changes, the particle density has the effect on the transition of particle, but a little.

**Fig. 4** Relation between average velocity and particle density



**Fig. 5** Relation between average velocity and particle rolling friction coefficient



### 3.3 Effect of Particle Surface Rolling Friction Coefficient

Five kinds of particle surface rolling friction coefficient are simulated respectively, including 0.01, 0.02, 0.03, 0.04 and 0.05. In the same way mentioned above, the other parameters of the particle and the screw conveyor are unchanged except the surface rolling friction coefficient of particle. According to the data acquired through the simulation, Fig. 5 is plotted.

As shown in Fig. 5, the average velocity of particle decreases with the increase of the surface rolling friction coefficient of particle. It is obvious that particle surface rolling friction can influence the movements of particles in the horizontal screw conveyor. Because the average tangential friction force between particles increases with the rising of particle surface rolling friction coefficient, the increasing of rolling friction coefficient of particle surface raises the flow difficulty of particles

in the screw conveyor. Only when larger friction resistance is overcome, particles can move. Therefore, the average velocity of particle decreases with the increase of rolling friction coefficient of particle surface.

## 4 Conclusions

Base on EDEM simulator, Hertz-Mindlin (no slip) contact model is applied to simulate the particle movement in the screw conveyor. The simulation results show that the characteristics of particle itself can influence the particle transition in the horizontal screw conveyor. The following results are obtained. At first, the average velocity of the particles decreases with the increasing of particle size. Next, the average velocity of the particles increases slightly when the particle density increases. At last, the average velocity of particle decreases with the increase of rolling friction coefficient of particle surface.

**Acknowledgements** This work is funded by Beiyin talent selection and development project of Beijing Institute of Graphic Communication (No. Byyc201316-016), The College Student Research Program of Beijing (2016, No. r1512000454).

## References

1. Detlef Lohse, Raymond Bergmann, René Mikkelsen et al (2004). Impact on Soft Sand: Void Collapse and Jet Formation. *Physical Review Letters*, 93 No. 19, 198003.
2. MIDI GDR (2004). On dense granular flows. *European Physical Journal E*, 14, 341–365.
3. Nicholas A. Pohlman et al (2006). Surface roughness effects in granular matter: Influence on angle of repose and the absence of segregation. *Physical Review E*, 73, 031304.
4. Ouyang Hongwu et al (2008). Jamming of granular matter. *Materials Science and Engineering of Powder Metallurgy*, 13(5), 260–268.
5. Hertz, H. (1882). On the contact of elastic solids. *J. Reine und angewandte Mathematik*, 92, 156–171.
6. Tsuji, Y., T. Tanaka, and T. Ishida (1992). Lagrangian numerical simulation of plug flow of cohesionless particles in a horizontal pipe. *Powder Technology*, 71, 239–250.
7. Cundall, P. A., and O. D. Strack (1979). A discrete numerical model for granular assemblies. *Geotechnique*, 29, 47–65.

# Design and Material Selection of Shopping Malls Point-of-Purchase Displays

Deqing Chen and Miaomiao Zhong

**Abstract** To occupy the domestic and international Point-of-purchase (POP) displays market, comparative research method has been used to analyze differences of between POP and traditional displays, and even the difference of POP displays at home and abroad. Market demands, design and material selection of POP displays were analyzed. Some enlightenment have been achieved for Chinese packaging enterprises. Results show that market demands of POP displays is huge and they are gradually replacing traditional displays. POP displays with easy assembling, technicolor and multiple-shapes have made them easily recognized and have attracted consumer's more attention, indicating that they are more suitable for shopping malls by being compared with traditional displays. Ecological-friendly and low-cost corrugated cardboard as substitute of metal, plastic and wood has been applied into POP displays. POP displays will be widely used in major shopping malls and will cover most of the cities in China. Packaging enterprises should pay attention to research and develop POP displays.

**Keywords** Easy assembling · Technicolored · Multiple-shapes · Corrugated cardboard · POP displays · Shopping malls

## 1 Introduction

With rapid development of economy, fast and efficient consumption pattern of “one-stop” has been praised [1, 2]. Shopping malls as the typical representation of “one-stop” have been rapidly spread across the world. Meanwhile, POP displays as a collection of “one-stop” have been rapidly increasing in consumer market and have become a mainstream of commodity display in shopping malls. Market demands of POP displays are huge, which gives the way for POP displays to replace traditional displays gradually. Therefore, it is imperative for us to know the

---

D. Chen · M. Zhong (✉)  
Shenzhen DNS Industries Co., Ltd., Shenzhen, Guangdong, China  
e-mail: zmm19900226@163.com



common POP display structures, choose ecological-friendly and low cost materials, and improve the existing display structures for fully displaying and protecting products [3–6]. In this paper, comparative research method has been used to analyze differences of POP displays between POP and traditional displays, and even the difference of POP displays at home and abroad. POP displays with easy assembling, technicolor and multiple-shapes have made them easily recognize and have attracted the attention of the customers, indicating that they are more suitable for shopping malls by being compared with traditional displays. Ecological-friendly and low-cost corrugated cardboard as substitute of metal, plastic and wood materials has been applied into POP displays. POP displays will be widely used in major shopping malls and will cover most of the cities in China. Packaging enterprises should pay attention to research and develop POP displays.

## 2 Market Demands of Shopping Malls POP Displays

Throughout US market, the traditional retail market has still been the mainstream of consumer market by competing with the online retail market [7–9]. According to the “2016 US Electricity Supplier Market Report”, the share of US online retail sales have increased from 6.03% in 2001 to 10.6% this year [10]. While maintaining an average growth rate of 15.35% per year, the total share of online retail is only about 10%. Furthermore, more and more online retail began to develop initiative shops, and online-offline double side development mode has become the mainstream of today’s online retail. Therefore, the traditional retail mode has still been the main retail mode. At same time, the shopping malls market share has increased from 42% in 1987 to 87% this year, which maintains a steady growth rate [11, 12]. Therefore, the shopping malls are the current mainstream in US market. Meanwhile, the POP displays as a collection of “integration” and “one-stop” consumer mode is the core of US markets.

POP displays is not only occupying the core of US market, but also affecting the global market. So POP displays began to appear in the China market and have been developing rapidly since 2000. Although POP displays maintain strong growth momentum, we cannot ignore the impact that the booming of online retail market brought to traditional retail market. Therefore, it is important for POP displays to improve continually the structures and materials in order to ensure POP displays enduring vitality.

## 3 Designs of Shopping Malls POP Displays

Technicolor and multiple-shapes are the typical features of POP displays, resulting in products freshness for consumers. As shown in Fig. 1, POP displays can be seen everywhere in foreign market. POP displays are featured with unique

appearance, vibrant color, oversize price tag card and head card, which make them easily recognized and attract consumers' attention. While same color and single appearance traditional displays make it lack characteristic and attractive, leading consumer to lose interest in the displays. Therefore, the traditional displays are gradually replaced by the POP displays in an inevitable trend. In addition, it is simple and easy to assemble for POP displays. Easy assembling is also a typical feature of POP displays. Foreign Wal-Mart POP displays are usually assembled by splicing, no need for nails or glue as shown in Fig. 2. So it is convenient, safety and ecological-friendly to assemble for POP displays. Moreover, the POP displays volume is small and its height is generally 1.2–1.5 m. So they can move freely between shelves to avoid free space wasting. POP displays have higher flexibility.

The traditional displays compared with POP displays as shown in Figs. 1 and 3. Traditional displays are only located in channel central after assembled, and cannot free to change its placement in shopping malls because of its own weight or hardly disassemble. So, traditional displays have not enough flexibility. In addition, the traditional display structures and colors have been modeled, such as metal gray, traditional red and black. So the basic appearance of traditional displays has also been fixed. What's worse, the current consumers market of "one-stop" can constantly updated products, and so it can keep consumers feeling of freshness. So, traditional displays cannot be unchanged for adapting to different shopping malls atmosphere such as different products, festival and climate. Due to the high cost of the material, the traditional displays changes its appearance only by pasting the posters corresponded with product, festival and climate to adapting to different shopping malls atmosphere. So it is lack of specifics, and would easily bring beauty fatigue and stationary thoughts to customers. But POP displays can timely adapt to new shopping malls atmosphere and keep lower cost than traditional displays. Hence, it is more suitable for POP displays than traditional displays to adopt for current Fast Moving Consumer Goods (FMCG) market [2].



**Fig. 1** Foreign shopping malls POP displays

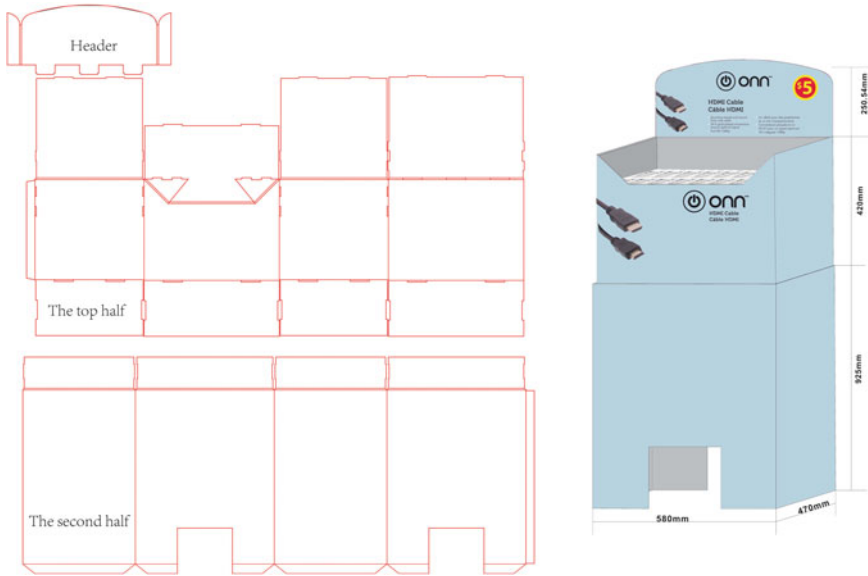


Fig. 2 Foreign Wal-Mart POP displays



Fig. 3 Traditional displays

#### 4 Material Sections of Shopping Malls POP Displays

Theme of current society development is Eco-friendly. No matter what a company is, it should not ignore environment issues especially for packaging companies. The metal, wood and plastic materials can also cause environmental problems during production or the using process and it also need higher costs. Currently, the renewable material has been widely used in POP displays in response to calling of the Eco-friendly. In particular, the corrugated cardboard POP displays have almost



**Fig. 4** Displays for shopping malls (the *left picture* is US shopping malls POP displays; the *right picture* is demotic shopping malls traditional displays)

started to occupy consumer markets, making it the most common materials for POP displays at abroad as shown in Fig. 1.

Compared with foreign shopping malls, most shopping malls in China are still using traditional metal, wood or plastic materials. The reason is that the China's shopping malls consumer mode started too late, and related business pattern and supply chain management are not mature, especially the promotion mode of shopping malls, which has still been staying in the traditional promotion mode as shown in Fig. 4. The promotion displays are made from metal or wood in China's market, which are different from the foreign shopping malls. At same time, it has been found that the metal, wood and plastic displays have some limitations for its characteristics and cost. Such as:

- (1) Metal POP displays. Although it has been used widely in consumer markets, it is not easy to be assembled and disassembled, and it is also hard for moving. Besides, it is only suitable for displaying electronic products and books due to its cold gray color;
- (2) Plastic POP displays (acrylic). It is generally suit for colorful and small bulk products;
- (3) The wood POP displays. It is generally used to display some goods with a long history and culture like tea and vessels.

What's more, with the development of technology, a variety of the composite papers with other material properties have been developed and applied to POP displays instead of traditional materials. Therefore, the recycle paper has become the mainstream in the packaging industry, especially the corrugated keyboard.

## 5 Enlightenment to Our Country's Packaging Enterprises

With the popularity of FMCG, the usage of foreign shopping malls POP displays has been increasing year after year. Meanwhile, China as the major supplier of the foreign consumers market should have knowledge of common display structures, choose ecological-friendly and low cost materials and improve the existing displays structure for fully displaying and protecting products as soon as possible. In addition, the popularity of foreign POP displays has also driven the reform of China's promotion mode. There is no doubt that POP displays will be widely used in major shopping malls and will cover most of the cities in China. Hence, there is enormous potential for POP displays in the future. However, there is only little company focusing on POP displays in China. Our design and techniques for POP displays are far behind the foreign. What's more, it is necessary for improvement of design ability and technique to strengthen the core competitiveness of traditional retailing when facing the challenge of new-born online retail. Otherwise, the demands of POP displays will shrink. Therefore, our packaging enterprises should start studying POP displays at the soonest possible in order to seize the domestic and international POP displays markets.

## 6 Conclusions

1. POP displays with easy assembling, technicolor and multiple-shapes have made them easily recognized and attract consumers more attention. While the same color and single appearance traditional displays make it lack characteristic and attractive. Ecological-friendly and low cost Corrugated keyboard as substitute of metal, plastic and wood materials has been applied into POP displays.
2. POP displays are more suitable for shopping malls by being compared with traditional displays. Market demand of POP displays is huge and they are gradually replacing the traditional displays. POP displays will be widely used in major shopping malls and will cover most of the cities in China. Packaging enterprises should pay more attention to research and develop POP displays.

## References

1. Goldman, A., Hino, H. (2005). Supermarkets vs. traditional retail stores: diagnosing the barriers to supermarkets' market share growth in an ethnic minority community. *Journal of Retailing and Consumer Services*, 12(4), 273–284.
2. Scholderer, J., Grunert, K. G. (2005). Consumers, food and convenience: The long way from resource constraints to actual consumption patterns. *Journal of Economic Psychology*, 26(1), 105–128.
3. Cheng, S. (2006). *Paper Packaging Design*. China Light Industry, Beijing.

4. Jinling, W., Binqing, S., Weiqi, Z et al (2015). The structure analysis of FMCG corrugated cardboard display. *Packaging World*, (6), 58–59.
5. Ling, W., Cheng, S., Yan, H et al (2008). Structure design of corrugated cardboard display frame. *Packaging Engineering*, 29(10), 180–182.
6. Yuping, E., Guang, Y. (2008). Design of display stand made in corrugated fiberboard. *Journal of Hunan University of Technology*, 22(4), 1–3.
7. MacGoldrick, P. J. (1990). *Retail marketing*. McGraw-Hill, London.
8. Baker, J., Levy, M., Grewal, D et al (1992). An experimental approach to making retail store environmental decisions. *Journal of retailing*, 68(4), 445.
9. Feng, W., Figliozzi, M. (2013). An economic and technological analysis of the key factors affecting the competitiveness of electric commercial vehicles: A case study from the USA market. *Transportation Research Part C: Emerging Technologies*, 26, 135–145.
10. Jian, D. (2016). 2016 US Electricity Supplier Market Report: sales expected to reach \$350billion. <http://www.iwshang.com/Post/Default/Index/pid/245668.html>. Cited 14 June 2016.
11. Xuefeng, L. (2013). From the United States to Retail electricity suppliers: the rise of Wal-Mart. *Pintu Business Review*. <http://www.pintu360.com/article/54d7015214ec53c11660e672.html>. Cited 9 June 2013.
12. Discount store (2016). Wikipedia. [https://en.wikipedia.org/wiki/Discount\\_store#cite\\_note-6](https://en.wikipedia.org/wiki/Discount_store#cite_note-6). Cited 15 June 2016.

# Present Situation and Ideas of Express Packaging Greenization

Ling Cheng and Guorong Cao

**Abstract** This paper took the greenization of express packaging as the visual angle, through questionnaires to consumers, express employees, express companies and express packaging material suppliers, market analysis, literature review and other means, we discovered the following questions: non greenization of express packaging materials; unsystematic of express packaging standard; difficult recycling of express packaging; excessive of express packaging. According to domestic and foreign advanced cases, accounting for above issues, a few ideas to greenization express packaging was raised from the point of view of consumer, e-commerce enterprises, express companies, express packaging suppliers and management.

**Keywords** Express · Packaging · Greenization

With the development of electronic commerce in our country, online shopping had become the main way of shopping. According to the State Post Bureau statistics, business volume of postal enterprises and the national express service enterprise totaled 20 billion 600 million in 2015, an increase of 48%. Express business volume would complete 27 billion 500 million in 2016 [1]. Express industry's rapid development brought not only economic effect, but also environmental problems, which couldn't be ignored. This made people more concerned about its greenization process and the implementation of green express packaging was imperative.

---

L. Cheng · G. Cao (✉)  
College of Printing and Packaging Engineering,  
Beijing Institute of Graphic Communication, Beijing, China  
e-mail: caogorong@bigc.edu.cn

© Springer Nature Singapore Pte Ltd. 2017  
P. Zhao et al. (eds.), *Advanced Graphic Communications  
and Media Technologies*, Lecture Notes in Electrical Engineering 417,  
DOI 10.1007/978-981-10-3530-2\_87

697

# 1 Express Packaging Problems

## 1.1 Non Greenization of Express Packaging Materials

Nowadays, express packaging was mainly composed of four parts: ① External packing: main part of the package, there were envelope, waterproof bag, cardboard box, woven bags, boxes, etc. Among them, waterproof bag, carton were the most common. ② Inner packing: played a role in delivery of goods, collection and basic protection, generally for items of the original packing, bubble film, air column bag, foam plastic etc. ③ Auxiliary packaging: strapping and identification of packages, such as tape, label, seal etc. ④ Waybill: function was indicated information of delivery goods, transportation contract and receipt of credentials [2]. Packaging material was the main cause of the express packaging waste. Moreover current express companies, e-commerce enterprises and packaging materials suppliers blindly pursue low prices, green material was rarely selected. For example, waterproof bag, tape, cushioning materials for express packaging were generally plastic materials. First of all, a lot of use would cause the waste of oil resources; secondly, due to low price, plastic products consisted of inferior recycled material contained a lot of plasticizer, flame retardant and so on. It was great harm to the users [3]. Finally, used plastic products were mostly discarded at random, buried in the soil, which couldn't be degraded for a long time, brought irreversible damage to the ecological environment.

## 1.2 Unsystematic of Express Packaging Standard

Today express standards were shown in Tables 1 and 2.

From the Tables 1 and 2, we could see 6 standards for express packaging, but they were limited to some kind standard of express external packaging. Standard for other external packaging, inner packaging and auxiliary packaging were in blank

**Table 1** Current express package standards

Number	Standard number	Standard name
1	GB/T 16606.1-2009	Packing for express service-part 1: envelopes
2	GB/T 16606.2-2009	Packing for express service-part 2: packaging boxes
3	GB/T 16606.3-2009	Packing for express service-part 3: packaging bags
4	YZ/T 0093.1-2003	Mail packaging boxes part 1: domestic
5	YZ/T 0094.1-2003	Mail packaging bags for postal parcels part 1: packaging bags for air spring film
6	YZ/T 0094.2-2003	Mail packaging bags for postal parcels part 2: packaging bags for plastic woven fabric



**Table 2** Current related express standards

Number	Standard number	Standard name
1	GB/T 28582-2012	Express waybill
2	YZ/T 0135-2014	Measurement method of greenhouse gas emission for express industry
3	YZ/T 0148-2015	Express electronic-waybill
4	YZ/T 0149-2015	Operation specification in safety production for express service

state. Secondly, there were no relevant standards for the specific requirements of the packaging. In order to protect the safety of express, courier, consumer and e-commerce enterprise believed that more layer of packaging, more protection for safety, resulted in unnecessary waste.

### ***1.3 Difficult Recycling of Express Packaging***

Currently, express packaging recycling was mainly concentrated in cartons and waybill. Carton's recovery rate was high, but it was difficult to directly use because the breakage of packing in the dismantling process [4]. That needed to be beating, which could only produce lower level of paper packaging products. Whether it was traditional or electronic waybill, we mainly recovered only one layer of paper. Furthermore, waybill paper was different from the general paper, they needed special treatment after recycling, so cost was relatively high. Other express packaging materials recovery rate was essentially zero because of a wide range of materials, difficult recycling, low recycling profit and so on.

### ***1.4 Excessive of Express Packaging***

People who online shopping would go through such a process, tearing layers of tape, opening the carton, and then cutting thick buffer material to see their own purchased items. A lot of people attributed excessive packaging to e-commerce enterprises and express companies, but packaging was also cost, why would they take it? There were two reasons: first, ensured that goods were not damaged in the course of transport; second, lack of industry norms. Due to uncivilized operation occurred frequently, couriers and consumers were assumed that the tighter of package, the more safety of express, so excessive packaging was difficult to avoid.

## **2 Greenization Ideas of Express Packaging**

### **2.1 Greenization Ideas of Consumers**

1. Changes in consumption concept. From consumer survey, the reason of 68.88% consumers choosing express companies was fast. This pursuit of rapid consumption concept would bring e-commerce enterprises and express companies a lot of pressure, so consumers could properly change this consumption concept.
2. Idea renovating. From the questionnaire, it could be found that many couriers raised that secondary express packaging was difficult to be used. Consumers couldn't accept, even if its performance met the needs. According to consumer survey, 93.36% of consumers could accept the recycling of cartons as express packaging box. But consumers didn't have high degree of recognition with other recycling express packaging, such as plastic bags, envelopes, etc. If consumers agreed the recovery of packaging with good performance, express companies and e-commerce enterprises would be happy to use. So, it not only could promote recovery, also provide the using way of recycling packaging, improve the using rate.
3. Strengthen the awareness of recycling. From the consumer survey, we could know that 55.6% of consumers threw the express packaging when getting them. This caused a lot of waste and pollution, consumers needed to strengthen the awareness of recycling, and recovered the express packaging through the channels for recycling.

### **2.2 Greenization Ideas of E-Commerce Enterprises**

According to survey and statistics, more than half of the express package was provided by e-commerce enterprises, especially in cardboard boxes, fillers and other materials, there was a huge amount of consumption. As major production of parcel, e-commerce enterprises must bear the burden of greenization of express packaging.

First, we needed source control for ensuring of material quality and safety, reducing the amount of package as far as possible and using environmentally friendly material. For example, FedEx envelope, waterproof bag, carton were environmentally friendly recyclable materials. In 2012, FedEx also launched a document express plan named carbon neutral, manufacturing by rate of 100% recyclable materials and recycling was 100% [5].

Secondly, recycle of packaging materials. For example, in 2014, store No. 1 launched a program named one environmental protection and carton recycling [4, 6]. Users received parcel from store No. 1, then gave empty boxes to courier, that was involved in a carton recycling activities. Each recycling of one carton, user could get 50 points from store No. 1. Points could be used for the purchase of goods, participating in lottery, deduction vouchers, etc. From January

to September in 2014, store No. 1 total recycled carton more than 2.46 million, 27 thousand average month.

### ***2.3 Greenization Ideas of Express Companies***

Express industry needed an overall green express process. On the one hand, express companies needed to set up a special recycling mechanism for packaging, using actual action to support recycling of packaging. For example, SF best, which was e-commerce supplier brand of SF Express's, had launched the project of recycling carton packaging. The courier would ask whether customer needed it in the distribution. If not, they recovered them directly. YTO had implemented an activity for handing over ten pieces of express packaging returned for free to send one express [6]. Although these initiatives faced a lot of difficulties, but this was still one of the effective ways to express packaging recycling.

On the other hand, express companies needed to improve the quality of employees and eliminate violence sorting, brutal handling and other phenomena. For example, in March of 2016, YTO express in Heilongjiang province organized a courier safety operation training. Clearly put forward the principles and general requirements of safety operation for employees. Training required that courier should adhere to the principle of civilized operation, avoided human damage to the express delivery in sections of collection, sorting, transport and delivery.

### ***2.4 Greenization Ideas of Express Packaging Suppliers***

As the source of courier packaging, suppliers should optimize the product. On the one hand, develop green products. For example, a British company had developed an alternative environmental protection foam roll, on which there were a lot of small gaps. It occupied less space. When the paper roll was opened, it would become a three-dimensional honeycomb. The area reached 10 times of the original. It could play the role of buffer cushion, suitable for filling and protection of packaging products. The paper roll made of recycled fiber, which was recyclable and reusable. Finally, it could be biodegradable [7].

On the other hand, optimize the design of product structure. For example, Yiside had designed 2 cm wide brace on the top of box, without using adhesive tape. The opening process didn't need any auxiliary tools, you could quickly open it. Not only that, compared with traditional package, Yiside package save time more than 50% on packaging. The double layer cover plate increased the strength of carton and protected the product. As shown in Fig. 1.



Fig. 1 Diagram of Yiside package

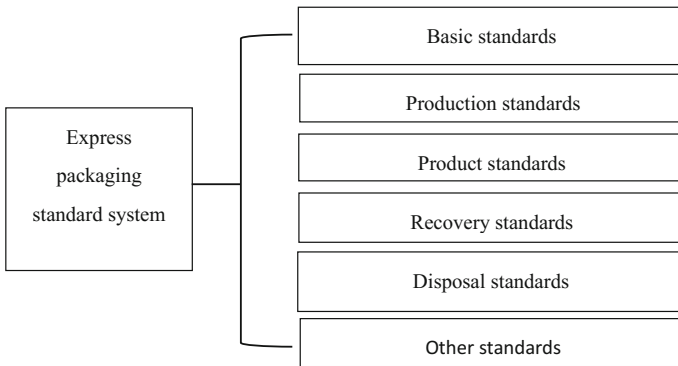


Fig. 2 Standard system of express packaging

### 2.5 Greenization Ideas of Management

Improve the express packaging standard system. The post industry already had a mature standard system, but it involved little about package of express. So express packaging needed to establish a standardized system of their own express packaging, covering all aspects of the express packaging, in order to facilitate the greenization of express packaging, which was shown in Fig. 2.

Strengthen the propaganda and supervision of the government. Social management needed public participation. To resolve the issue of express packaging, the awareness of the citizens should be enhanced. Relevant departments and express industry associations should be active, increase environmental protection propaganda, strengthen the supervision of the express company, dispel the concerns of consumers so that it was safe to recycle and reuse [8]. Standard was the premise, implementation was the main body, and supervision was the guarantee. Without a favorable regulatory system, the implementation of the standard was difficult to achieve. Relevant government departments needed to strengthen the supervision of all participants in the express package to ensure the implement of standards.

Implement of incentive system. Gave them tax incentives and financial support which had made contribution to the greenization of express package, such as recycling express packaging waste, development and use of green express packaging materials, specification of express package operation process and so on.

### 3 Conclusions

In summary, the greenization of express package was a complex and long-term project covering e-commerce companies, express companies, packaging materials suppliers, consumers and related management departments and other aspects, which needed common efforts. Consumers changed the concept of consumption and packaging and improved their awareness of recycling; e-commerce enterprises controlled the use and recycle of materials and package from the very beginning; express companies standardized the express process, promoted the formation of recycling mechanism; packaging suppliers should develop green product and optimize product structure; management established a green express standard system and play the role of publicity and supervision. Starting with the main body of express packaging, green express point the day and await for it.

**Acknowledgements** This study is funded by packaging engineering teaching team (construction) of Beijing institute of graphic communication (22150116006/017).

### References

1. Yingchuan Zhang (2016). China's development situation and trend of green express package in express industry. *Logistics & Material Handling*, 04, 105–108.
2. Jing Jin Gengui Zhou (2011). The development strategy of express logistics based on the new packaging of green whole express process. *Marketing Management Review*. 08, 171–173.
3. Aixia Xu (2015). Study on the problems and countermeasures of express packaging in online shopping. *Logistics engineering and management*. 37(06), 126–128.
4. Huo Jiang, Xiaohui Zhang (2015). Build express carton recycling mechanism for e-commerce enterprises. *Shanghai Packaging*. 10, 38–40.
5. Yi Su (2016). FedEx: a charity project will be decades. *Philanthropy Times*. 13, 1–2.
6. Nameless (2015). Where is the difficulties of Express packaging recycling? *China Packaging*. 03, 62–65.
7. Yonghua Lu (2016). Study on the present situation and influencing factors of express packaging. *Value Engineering*. 08, 215–217.
8. Zhiqiang Shan (2014). Everyone can't be absent for express packaging recycling. *Fujian daily*. 10, 1.

# Problems and Solutions for Express Logistic Packaging

Chenyang Liu and Lijiang Huo

**Abstract** The paper describes the state-of-the-art of express logistic packaging. Existing problems are analyzed from packaging structure design, packaging waste recycling, information security and user experience. The solutions of these problems are presented in aspects of express packaging low carbon, greening, humanization and so on. Finally, the related development of express logistic packaging was foresighted.

**Keywords** Express logistic · Logistics packaging · Green packaging · Packaging countermeasures

## 1 Introduction

With the increasing development of electronic commerce, the logistics industry has entered a heyday. By 2014, China's express delivery business volume has increased to 15 billion and the total output value is 200 billion yuan [1]. However, along with the rapid development of the logistics industry, the various problems of the logistics packaging are also more and more serious. Data shows that the social logistics costs in developed countries account for about 9% of GDP, while China reached 18% in 2014. In summary, some problems still remain [2, 3].

---

C. Liu · L. Huo (✉)

Light Industry and Chemical Engineering Institute,  
Dalian Polytechnic University, Dalian, Liaoning, China  
e-mail: lijianghuo@163.com

## **2 Main Problem of Express Logistics Packaging**

### ***2.1 Excessive Packaging***

Express will inevitably happen to bump in the transportation process. In order to ensure the safety of the contents, the general express package has reached four layers, with an average of 0.2 kg of corrugated cardboard packaging to calculate. 3 million tons of corrugated cardboard have been used only in the year of 2014, and 182 thousand tons of among them are due to excessive packaging waste; These excessive packaging not only increases the cost of logistics, but also waste a great number of resources.

### ***2.2 Low Recovery and Environmental Pollution***

According to statistics, China's annual packaging waste more than 2 tons, annual scrap value reached 400 billion yuan, but the recycling rate is less than 40%; Especially, it is difficult to recycle the express package, due to the difficulties of recycling and high cost recovery. The polyethylene plastic bag, deep gray nylon packing bag, and other plastic products used in the process of express logistics are difficult to degrade in the natural environment. These existing problems have made the contradiction between express logistics packaging and the natural environment more and more serious [4].

### ***2.3 Serious User Information Leakage***

From the Xinhua news reports, people spend only more than 1000 yuan to buy 1400 express information via the internet. The cases triggered by the leakage of express information are increasing year by year. A former courier entered a woman home to rob according to the information on the express orders in Haidian District, Beijing, May 2016. Some courier employees replace the valuables according to the insured information on the express orders and infringe the legitimate rights of consumers.

### ***2.4 Poor Customer Experience***

In order to prevent product damage during distribution, the tape is used to a special multi-layer package. It not only affects the overall appearance, but also causes great inconvenience to open the outer packaging. In many cases, it is difficult to open the

package without the use of scissors and other tools, sometimes the content will be damaged accidentally. These factors have caused the user experience in the receipt of the parcel is often not very good.

### **3 Solutions and Countermeasures**

#### ***3.1 Moderate Packaging***

It is necessary to accelerate the courier packaging automation process; the Robo-Pick researched and developed by the Promat, can pack 2400 packages an hour, and can greatly reduce the gap between express packaging and products. For enterprises, Robo-Pick not only can reduce labor costs, improve logistics efficiency, but also can reduce the occurrence of excessive packaging [5]. Beyond these, through the improvement of express package structure, it is very helpful to reduce the use of packaging materials.

#### ***3.2 Establish the Corresponding Recycling Mechanism***

With the rapid development of China's express delivery logistics industry, express waste recycling is becoming more and more important. In addition to the school and a small number of areas, express in most parts of China are using door-to-door way, which brings great convenience to the recovery of express package. Zhang and Liang [6] developed the courier packaging recycling APP, in the campus publicity and promotion. This not only enhances the students' awareness of recycling, but also makes the courier packaging recovery rate significantly improved and provided a great convenience for the recycling industry. The country should accelerate the development of express packaging recycling, promote the development of reverse logistics in China, the express delivery companies should also pay attention to reverse logistics.

#### ***3.3 Green Express Packaging***

To promote the delivery of green packaging, packaging products should meet the 3R1D principle. Lightweight (Reduce), that is the delivery process in the express package can ensure product safety under the premise, as far as possible to reduce the amount of material, reduce energy consumption. Recyclable (Return) and reusable (Reuse), refers the courier packaging can be reused or recycled after the production of recycled products. DAL Silva et al. [7] found that a local company in



Brazil to the British transport engine, with Recyclable packaging instead of disposable packaging, 18% reduction in logistics costs. Biodegradable (Degradable), refers the packaging waste will not form a permanent waste. Degradable packaging materials is one of the hot spots in the research of green packaging, such as starch based biodegradable packaging materials, poly lactic acid based biodegradable plastics. They have been used in the field of food, medicine and other fields. With the preparation process as well as the efficiency of the improvement in the future, degradable packaging materials are expected to replace petroleum based plastic packaging materials [8].

### ***3.4 Improve the Information Interaction Mode***

On the one hand, the encrypted two-dimensional code instead of existing express information is used. Two dimensional code verification technology has the advantages of high flexibility, high error correction, low cost, and it is an effective way to replace the existing methods [9]. On the other hand, using RFID instead of express order information can avoid irrelevant personnel to see the personal information on express delivery, even if the courier is missing. It is necessary to have a professional equipment to get the information on the courier. With the use of RFID labeling technology, the courier only need to install the card reader in the reader, the sender's identity information can be recorded and recognition, this way can not only protect the safety of users, but also can reduce the workload of express [10].

### ***3.5 Pay Attention to Express Packaging Brand and Structure Design***

Express package should highlight the electricity supplier or courier brand, and the higher "face value" in the design, in addition to protect the effectiveness of the product, which impresses users more deeply and improves their favorability [11]. The packing box designed by Yiside (Fig. 1), in the way of sealing, changes the traditional adhesive tape sealing, with special double-sided adhesive from the inside. It not only guarantees the corrugated box appearance, but also can save the sealing time of 15–70%; The middle part of the zipper design, without any tools out of the box, as long as a tear can be instantly out of the box, and the box cannot be recovered once opened. The design enhances its security in the convenience of users at the same time.

**Fig. 1** Yiside packing box

## 4 Conclusions

With the progress of science and technology, the improvement of living standards, people have higher requirements for the express logistics packaging. Conditioned on the exiting problems and present situations of current express logistics packaging, it is necessary to increase the express packaging in safety, environmental protection and other aspects of research, while developing new packaging materials actively, designing more carbon packaging structure to adapt the rapid economic development and people's needs.

## References

1. Zhou hao, Ke xianwen, Wang Lijie (2016). Problems and countermeasures of fresh products' e-commerce packaging. *Packaging Engineering*, 37(5):185–189.
2. Jin Guo-bin (2011). Research on existing problems and developing tactics for logistic packaging. *The journal of packaging*, (2): 1–6.
3. Liu Shiya, Feng Hong ju. et al (2015). Problems and solutions for e-commerce logistic packaging. *Packaging Engineering*, 36(5):144–148.
4. Ye Chong, Zhuang Wenjuan, Chen Ting (2012). Development status and problems of logistics packing in China. *Logistics Engineering and Management*, (5):3–5.
5. Bloss R (2011). Automation meets logistics at the Promat Show and demonstrates faster packing and order filling. *Assembly Automation*, volume 31(31):315–318.

6. Zhang Yi, Liang Zi-jing (2016). Application Study of express package recycling APP in college students online shopping. *Value Engineering*, 35(6):184–186.
7. Silva D A L, Renó G W S, Sevegnani G, et al (2013). Comparison of disposable and returnable packaging: a case study of reverse logistics in Brazil. *Journal of Cleaner Production*, 47(5):377–387.
8. Liu Lin, Wang Kaili, Tan Haihu, et al (2016). Research and application status of green packaging materials in China. *Packaging Engineering*, (5):24–30.
9. Ke Shenghai (2013). Exploration of e-commerce zero-waste packaging design base on two-dimensional bar code technology. *Packaging Engineering*, (8):120–123.
10. Li Shi (2016). The solution of express surface single information disclosure. *Internet of Things Technology*, 6(2):83–84.
11. Liu Bingbing (2016). “Face score” in packaging structure design. *Packaging Engineering*, (4):156–159.

# Research on Packaging Evaluation System of Fast Moving Consumer Goods Based on Analytical Hierarchy Process Method

Lizheng Zhang, Jiandong Lu, Guorong Cao and Hongtao Miao

**Abstract** The packaging evaluation system of fast moving consumer goods (FMCG) with four-layer structure, including target layer, first and second assessment impact factor layers, packaging solution layer, was established. The analytical hierarchy process (AHP) was employed to analyze and assess the system. The target layer was focused on optimal packaging solution according comprehensive evaluation. The assessment impact factors were defined from three aspects included display effect, production cost and environmental influence. The pair-comparison matrix was built. The maximum characteristic root and vector were computed by the root method. The weight value and the importance order of each impact factor were defined and gained. Three packaging solutions were analyzed in packaging solution layer, and comparison matrix between packaging solutions and assessment impact factors were built and the weight value was defined. Finally, the consistency of different layer comparison matrix was tested and the optimal packaging solution was selected. The packaging evaluation system combined with quantitative and qualitative analysis, can provide reference for commercialized packaging solution selection of fast moving consumer goods.

**Keywords** Analytical hierarchy process · Packaging evaluation · Fast moving consumer goods packaging

---

L. Zhang (✉) · J. Lu · G. Cao  
School of Printing and Packaging Engineering,  
Beijing Institute of Graphic Communication, Beijing, China  
e-mail: zhanglizheng@bigc.edu.cn

H. Miao  
Packaging and Printing Department, Henan University of Animal  
Husbandry and Economy, Zhengzhou, Henan, China

## 1 Introduction

Continuous progress of commodity economy and technology constantly extends the functions of product packaging: packaging performs protective function during the process of commodity circulation; it performs information transmission, social recognition, and value-added functions during the marketing process of commodity; packaging can have convenient function when user uses it [1]. According to these functions, we conduct a qualitative and quantitative integrated systematic evaluation of packaging schemes with multiple indexes.

Analytical hierarchy process (AHP) is an evaluation and decision-making method that combines qualitative analysis with quantitative analysis. It mathematizes and systemize evaluator's thinking process. Besides, it requires evaluator to have a clear understanding of objects' properties and logic relation between these properties. The system of total packaging cost comprehensive evaluation was analyzed and evaluated using fuzzy AHP model [2]. Qiuwang-jian analyzed frequently used Chinese reproduction combinations in digital publishing by questionnaires and AHP [3]. Xie Ming-hui compared reasonable evaluation of packaging in developed countries [4]. Wang Jen-hung employed AHP and life-cycle assessment approach to assess the environmental impacts from offset lithographic printing on color-box packaging [5].

As for packaging of fast moving consumer goods (FMCG), complex and diverse factors will influence customer's evaluation. This article employs AHP in the principles of representativeness, comprehensiveness, universality, feasibility, dynamic and systematization, and combines research results of existing evaluation systems to create an evaluation index system for FMCG.

## 2 Experiment and Methods

### 2.1 *Experiment Principle*

The most basic and the most important function of packaging is protective function, also known as physical function. Its primary purpose is to protect goods from external damages and influences of external factor during the process of circulation and to deliver products to the hands of customer, intact and safe. Packaging design should not only consider intrinsic features and environmental influences of content, but also consider proper packing material, packing container and packing method, adopting certain technical process to pack commodity properly to prevent adverse factors from happening.

Packaging's decoration design is embodied in numerous macroscopic aspects, including package's appearance and shape, visual communication, convenience in display, and satisfying consumption.

As for packaging’s convenience, according to various factors in commodity circulation and using process, designers should thoroughly consider whether material, shape and structure of packaging are easy for production, for handling and transportation, for warehousing and marketing, for consumption and use, and for recycling after discarded, in order to strive for convenience of the whole process from production to recycling in a scientific way.

Packaging’s economic efficiency means reducing packing cost in terms of consumption of materials and difficulty of forming process.

Packaging’s environmental protection property means it is reusable, recyclable and degradable, and is moderate package that will not cause any harm to human body or the environment during the whole life cycle of product. Normally, packaging’s environmental protection property has four dimensions: Degradability of materials; easy to reuse and recycle; waste combustion produces new energy instead of secondary pollution; minimum packing material and spontaneous decomposition without polluting the environment.

## 2.2 Evaluation Model for FMCG

We adopt Delphi method, asking for anonymous opinions of 40 packaging professionals in three rounds and summarizing with anonymous feedback. Finally, we get an evaluation model, as shown in Figs. 1 and 2. General objective of evaluation is listed in layer A, first-grade evaluation criteria is listed in layer B, and second-grade evaluation layer is listed in layer C.

Decoration design B<sub>2</sub> includes Style design C<sub>5</sub>, color matching C<sub>6</sub>, composition of picture C<sub>7</sub>; Convenience B<sub>3</sub> includes easy to open C<sub>8</sub>, portability C<sub>9</sub>, easy to use C<sub>10</sub>, reusable C<sub>11</sub>; economic benefit B<sub>4</sub> includes consumption of materials C<sub>12</sub>, difficulty level of forming process C<sub>13</sub>, storage and transport convenience C<sub>14</sub>; environmental protection B<sub>5</sub> includes biodegradability of materials C<sub>15</sub>, recycling and reusing C<sub>16</sub> emission of production process C<sub>17</sub>, volume fraction C<sub>18</sub>.

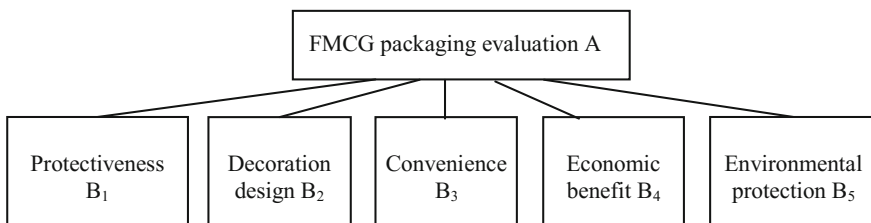
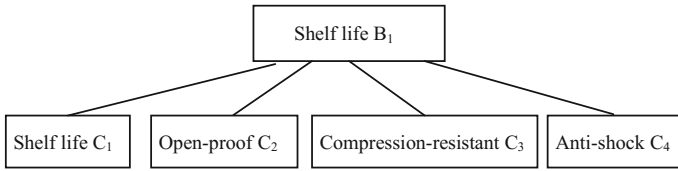


Fig. 1 Evaluation model A–B layer



**Fig. 2** Evaluation model  $B_1-C_{1-4}$  layer

**Table 1** Judgement matrix A–B

A	B <sub>1</sub>	B <sub>2</sub>	B <sub>3</sub>	B <sub>4</sub>	B <sub>5</sub>
B <sub>1</sub>	1	5	3	3	7
B <sub>2</sub>	1/5	1	1/3	1/3	3
B <sub>3</sub>	1/3	3	1	1	4
B <sub>4</sub>	1/3	3	1	1	3
B <sub>5</sub>	1/7	1/3	1/4	1/3	1

**Table 2** Judgement matrix  $B_1-C_{1-4}$  and  $B_2-C_{5-7}$

B <sub>1</sub>	C <sub>1</sub>	C <sub>2</sub>	C <sub>3</sub>	C <sub>4</sub>	B <sub>2</sub>	C <sub>5</sub>	C <sub>6</sub>	C <sub>7</sub>
C <sub>1</sub>	1	5	3	3	C <sub>5</sub>	1	3	5
C <sub>2</sub>	1/5	1	1/5	1/3	C <sub>6</sub>	1/3	1	3
C <sub>3</sub>	1/3	5	1	1	C <sub>7</sub>	1/5	1/3	1
C <sub>4</sub>	1/3	3	1	1				

### 2.3 Building a Judgement Matrix

In the same grade, grade them by their degree of importance. Normally, 5-grade quantitative method is adopted, that is, equivalent, weak, strong, very strong and extremely strong, their corresponding assignments can be 1, 3, 5, 7, and 9. When an element is subordinate to another element, then quantitative assignments can be reciprocal of the above-mentioned. If some problems' grading has higher precision and 5-grade quantitative method is considered as insufficient to describe clearly, use four numerical value (2, 4, 6, 8) for interpolation and extend to 9-grade quantitative method. For example, number 5 in the third column of the second line indicates that relative to objective A, B<sub>1</sub> criterion has a higher grade than B<sub>2</sub> criterion in degree of importance, as shown in Table 1. The values of judgement matrix B–C are shown in Tables 2, 3 and 4.

### 2.4 Conducting a Consistency Check

Solve the matrix's maximum eigenvalue  $\lambda_{max}$  and corresponding orthonormal eigenvector W, eigenvector' component is weight of each factor. Square-root method or sum product method may be used for calculation. This article uses

**Table 3** Judgement matrix  $B_3-C_{8-11}$  and  $B_4-C_{12-14}$

$B_3$	$C_8$	$C_9$	$C_{10}$	$C_{11}$	$B_4$	$B_{12}$	$B_{13}$	$B_{14}$
$C_8$	1	1/3	1/5	1	$B_{12}$	1	3	1/3
$C_9$	3	1	1/3	3	$B_{13}$	1/3	1	1/5
$C_{10}$	5	3	1	5	$B_{14}$	3	5	1
$C_{11}$	1	1/3	1/5	1				

**Table 4** Judgement matrix  $B_5-C_{15-18}$

$B_5$	$C_{15}$	$C_{16}$	$C_{17}$	$C_{18}$
$C_{15}$	1	3	5	5
$C_{16}$	1/3	1	3	5
$C_{17}$	1/5	1/3	1	3
$C_{18}$	1/5	1/5	1/3	1

**Table 5** Judgement matrix’s dimensionality corresponding RI value

n	1	2	3	4	5	6	7	8	9	10
RI	0	0	0.58	0.9	1.12	1.24	1.32	1.41	1.45	1.49

square-root method. The square-root method firstly multiplies factors of each line in n-rank judgement matrix, then nth power the product of every line. Last, normalize all vectors to identify the weight of middle and lower layers for upper layers in hierarchical structure.

$$CI = \frac{\lambda_{\max} - n}{n - 1} \tag{1.1}$$

Equation (1.1) is used to calculate CI value. The n is judgement matrix’s dimensionality.  $\lambda_{\max}$  is maximum eigenvalue. New single-layer judgement matrix’s average random consistency indexes RI change with the matrix’s dimensionality, see Table 5 for its value.

$$CR = \frac{CI}{RI} \tag{1.2}$$

Equation (1.2) is used to calculate CR value. When  $CR < 0.1$ , the consistency of the judgement matrix is considered as acceptable, otherwise, the matrix should be corrected properly. The result of consistency checking is shown in Table 6.

### 2.5 Determining Priority of All Factors in Criterion Layer

The weights and ranks of  $C_{1-18}$ -A are calculated and shown in Table 7 last two columns. The second line in Table 7, and the weights of  $B_{1-5}$ -A are listed. The



**Table 6** Consistency checking

	$\lambda_{max}$	CI	RI	CR
A–B <sub>1–5</sub>	5.15	0.03	1.12	0.027
B <sub>1</sub> –C <sub>1–4</sub>	4.049	0.016	0.9	0.018
B <sub>2</sub> –C <sub>5–7</sub>	3.037	0.019	0.58	0.033
B <sub>3</sub> –C <sub>8–11</sub>	4.041	0.014	0.9	0.015
B <sub>4</sub> –C <sub>12–14</sub>	3.037	0.019	0.58	0.033
B <sub>5</sub> –C <sub>15–18</sub>	4.19	0.063	0.9	0.07

**Table 7** Assessment impact factor layer C<sub>1–18</sub>’ weight corresponding evaluation object A

A	B <sub>1</sub>	B <sub>2</sub>	B <sub>3</sub>	B <sub>4</sub>	B <sub>5</sub>	Weight	Rank
	0.475	0.088	0.199	0.188	0.050		
C <sub>1</sub>	0.511					0.243	1
C <sub>2</sub>	0.067					0.032	9
C <sub>3</sub>	0.224					0.107	4
C <sub>4</sub>	0.197					0.094	5
C <sub>5</sub>		0.637				0.056	6
C <sub>6</sub>		0.258				0.023	11
C <sub>7</sub>		0.105				0.009	16
C <sub>8</sub>			0.096			0.019	13
C <sub>9</sub>			0.254			0.051	7
C <sub>10</sub>			0.558			0.111	3
C <sub>11</sub>			0.096			0.019	14
C <sub>12</sub>				0.258		0.049	8
C <sub>13</sub>				0.105		0.020	12
C <sub>14</sub>				0.637		0.120	2
C <sub>15</sub>					0.540	0.027	10
C <sub>16</sub>					0.275	0.014	15
C <sub>17</sub>					0.123	0.006	17
C <sub>18</sub>					0.062	0.003	18

weights of C<sub>1–4</sub>–B<sub>1</sub>, C<sub>5–7</sub>–B<sub>2</sub>, C<sub>8–11</sub>–B<sub>3</sub>, C<sub>12–14</sub>–B<sub>4</sub> and C<sub>15–18</sub>–B<sub>5</sub> are listed from the B<sub>1</sub> to B<sub>5</sub> columns and C<sub>1</sub>–C<sub>18</sub> lines.

### 3 Packaging Solution Layer Discuss

While evaluating multiple packaging schemes, 18 comparison matrixes of criterion layer versus scheme layer are built according to 18 criterions, and then orthonormal eigenvector is calculated and verify consistency is verified. At last, multiply scheme

**Table 8** Potato chips packaging solution evaluation result

	Paper box	Composite barrel package	Expandable plastic package
Combined weight	0.213	0.538	0.249

layer’s weight by criterion layer’s weight to get combined weights, then compare the combined weights to identify optimal packaging scheme. Three schemes for potato chips—paper box, composite barrel package and expandable plastic package, are evaluated. Results are shown in Table 8.

That is, for three different types of packages for the same type of products, composite barrel package gets the highest score in comparison and evaluation of 18 indexes of given structural model, thus, it is assumed that adopting this scheme is the best.

Fuzzy evaluation theory is also applicable to the evaluation of scheme layer [6]. Each packaging scheme is graded according to 18 evaluation criteria, e.g. excellent, good, average, and bad. Next is questionnaire and building a fuzzy evaluation matrix. Multiplying criterion layer’s comprehensive weight by fuzzy evaluation matrix to get scheme’s grade evaluation ratio. Choose the packaging scheme that enjoys the highest ratio of excellent and good in the grade evaluation.

## 4 Conclusions

The selection of packaging schemes for FMCG should proceed from five aspects essential to product packaging—protectiveness, decoration design, convenience, economic benefit and environmental protection property. By applying AHP to analyze and evaluate three types of packages for potato chips, it is easy to find that protective function is the most basic function of packaging and plays the most vital role in choosing way of packing. Through the calculation, it is founded that shelf life and convenient usability have quite strong conditionality.

**Acknowledgements** This work is funded by talent selection and development project of Beijing Institute of Graphics Communication (Byyc201316-016), course reform project of Beijing Institute of Graphic Communication (22150116008/028), packaging engineering teaching team (construction) of Beijing Institute of Graphic Communication (22150116006/017).

## References

1. Wu, Q. (2008). Production packaging system design. Printing Industry Press, Beijing.
2. Gong, G., Lan, M., & Yin, K. (2013). Research on comprehensive evaluation AHP model of total packaging. *Packaging engineering*, 35(3), 100–103.

3. Qiu, W., Wang, Q., & Shi, Y. (2016). Optimization of Chinese reproduction on mobile terminal based on reading experience. *Lecture notes in electrical engineering*, 369, 387–394.
4. Xie, M., Li, L., Zhu, X. (2009) Comparative study of packaging rationality evaluation system. *Packaging engineering*, 30(1), 194–198.
5. Wang, J., Hou, C., & Lin, P. (2013). Two-phase assessment for the environmental impacts from offset lithographic printing on color-box packaging. *Journal of cleaner production*, 53, 129–137.
6. Zhang, G., Ma, L. (2013). Decision science. Capital university of economics and business press, Beijing.

# Research on the Embedding of Brocade Pattern of Li Nationality in Tourism Product Packaging

Wenjia Liu, Junwei Hu and Jinmin Gao

**Abstract** Regional tourism products not only serve the tourism industry, but also represent the regional cultural connotation, which is an important window of Hainan's tourism economy. The tapestry pattern in the culture of Li Nationality forms a distinctive characteristic of strong sense of artistic expressive force and visual tension and regional culture connotation after a long history. This paper, by analyzing the artistic form of Li brocade patterns, in accordance with the premise of Li Culture and local product its own particularity, explores the application of Li brocade patterns in packaging design of tourism products in Hainan from four aspects including theme, graphics, color and material, focuses on regional characteristics of packaging, and promotes the construction of regional culture brand.

**Keywords** Brocade pattern of Li nationality · Regional · Packaging design

## 1 Introduction

Hainan's unique geographical location gives birth to the distinctive Hainan culture, and the culture of Li Nationality is the representative of Hainan local ethnic characteristics. Traditional brocade is popular for its delicate making, rich patterns, beautiful appearance and durability as the ancients admire it with the words "beaming" and "as brilliant as sun glow". Today, Li brocade has been on the world intangible cultural heritage protection list. Obviously, the culture of Li Nationality has become a new breakthrough in the further development of Hainan tourism economy. At the same time, under the impact of the policy, the majority of enterprises also pay increasing attention to the humanistic value that the local national culture brings to the products.

---

W. Liu (✉) · J. Gao  
Xi'an Academy of Fine Arts, Xi'an, Shaanxi, China  
e-mail: wendycook@163.com

W. Liu · J. Hu  
Hainan College of Software Technology, Qionghai, Hainan, China

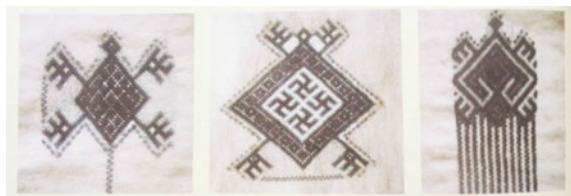
At present, almost all Hainan's tourism product packaging designs are imitations of domestic and foreign style, without obvious local characteristics and cultural atmosphere of Hainan elements so that the products related to the brocade of Li nationality is rare. At the same time, the local product packaging with the culture of Li Nationality is processed simply and crudely. The lack of the local product overall planning is caused by several reasons. The first is because enterprises do not pay enough attention on local culture. Affected by the rapid development of economy, most enterprises is crazy about foreign culture blindly, to a great extent, impacting the people's focus on the local folk customs. Secondly, Hainan's regional product resources are very rich, especially the representative natural resources. However, majority of small and medium-sized enterprises only pack the natural resources roughly, inferiorly and vulgarly and sell in the tourism market, directly resulting in the ordinary of the appearance and the low quality of Hainan existing regional natural resources, failing to reflect the value of the products.

## 2 The Artistic Features of Brocade Pattern of Li Nationality

### 2.1 Creative Thinking of Brocade Pattern of Li Nationality

The study on the brocade pattern should begin with the study on ethnic cultural background. "To convey the thought and truth by writings and graphs" is the common recognition since ancient times. Li women, through the observation of a long-term social life, learn how to create Li brocade patterns, which show Li people's love for natural environment, living environment and tribal group. Affected by the impact of the living environment, the Li people distributed around the Hainan Li nationality is divided into five group according to the dialects, each of which has independent characteristics of the clan [1]. People with different dialects weave brocade in different techniques and style patterns. Environmental impact is the main reason for the formation of patterns. Women in mountain areas like patterns of sambar deer, birds and beasts, flowers, butterflies, bees, small reptiles, kapok trees and flowers; Women in plain like animals such as fish, shrimp, frog and herons eagle as design material [2]. There is always a close relationship between art works and reality. As shown in Fig. 1, moire is a pattern regarded as auspicious pattern by the Li people, symbolizing immortality and longevity.

**Fig. 1** The brocade pattern of Crawling tortoise, longevity tortoise and swimming tortoise



Though they are composed of diamond and linear, the various designs in the quadruped of the turtle create the vivid shapes.

## 2.2 The Shaping Methods of the Brocade Pattern

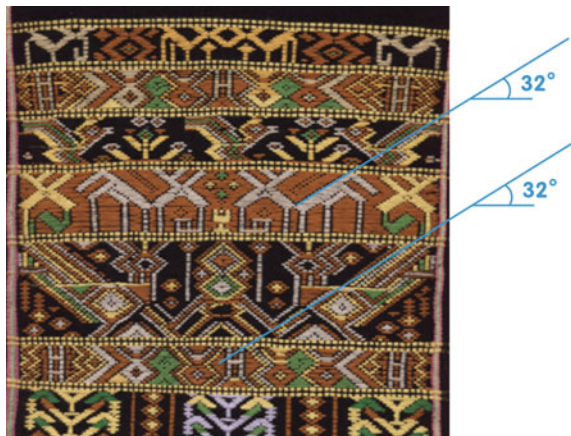
### 2.2.1 The Sublimation of Art—Abstract Geometry

The brocade is created mainly through the weaving of latitude and longitude lines including straight lines, parallel lines, broken lines etc. Li women acquire aesthetic consciousness from natural objects, focus on using concise form in decorative patterns, exaggerate and enhance images of the essential characteristics, and employ reasonable deformation technique to present the patterns in the weaving of latitude and longitude lines. From the point of view of the modern design, this is the basic form of the creative process, in accordance with the principle of artistic composition, with a very strong artistic beauty. Patterns should also have their important points to make the level clear and the prominence focused [3]. The combination technique of points and lines are rich enough to present the main characteristics of the visual process, as shown in Fig. 2.

### 2.2.2 Rules of the Form of Beauty—Frame Duplication

Because of the restriction of weaving process, the Li brocade patterns often employ the arrangement characteristics of Frame Duplication. According to the needs of cloth, repeatedly array the small basic shaped patterns in skeletal styles to dominate the changes of pattern elements. Although it is not like other graphic language to be flexible, it still can reach the same effect of graphic visual language through skeletal

**Fig. 2** The analysis of geometric shape and angle of the brocade pattern



**Fig. 3** Dictionaries of the tapestry pattern



arrangement of the basic shape. The skeletal elements of Li brocade patterns determine the size and distance of each basic shape.

In the Li clan, the inheritance techniques of the brocade pattern vary. As shown in Fig. 3, the patterns called by Li as “dictionary”, are created by the mother in order to leave the children a reference in the future, which is just as a material library waiting for another artistic processing. These patterns are often represented by the basic shape of sub patterns or repeated frame on brocade.

### 2.2.3 Features of the Brocade Pattern Colors

The colors of Li brocade mainly include black and red with other colors such as yellow, white, pink, orange, brown, green and so on, but with less neutral colors. On the whole, the color collocation pays attention to complementary color contrast including hue, purity and lightness contrast. Such a color matching, is mainly directly related with the difficulty of collecting a variety of colors. The dyes of Li brocade color are gathered from the plants or minerals in mountain areas. The basic colors of red, black and yellow can be easily acquired from these plants and minerals with a sufficient amount, while other neutral colors needed to deploy and are less in amount [4]. When Li apply the colors, they are most likely to use black bottoming as the weft and then according to patterns intersperse with other colors, to create a sharp contrast. The brocade of black bottom collocating with other colors, can meet the needs of their life and production that the cloth would not become dirty easily when they are farming and hunting.

## 3 The Research on the Embedding of Brocade Pattern of Li Nationality in Tourism Product Packaging

In the research on the embedding of Li brocade patterns in the tourism product packaging to let Li brocade patterns combine with tourism product packaging, we must have a clear identification ability, weighting the advantages and disadvantages

in the use of travel products packaging design with Li brocade patterns. Li brocade patterns is a member of many elements in the tourism product packaging language. We should use them both from the perspective of the protection of traditional culture and today's aesthetic taste and art expression to combine effectively to create some innovative products.

### ***3.1 Direct Citation***

Many modern graphic design works of simple geometry by abstract exaggerated graphics creation technique can employ directly the Li brocade pattern elements. Especially in the corporate culture of the national characteristics, we will interconnect it with the graphic design, widely apply it in visual works such as public recognition system and business publications, to make the corporate culture have modern fashion senses based on the tradition. For example, when Starwood group, which has many well-known brands such as Westin and Sheraton Hotel, stationed in Hainan tourism resort hotel market, it specially emphasize on the application of Li elements. Many travelers will find, Starwood Hotels will put the brocade in the hotel at every significant position. Even in some souvenirs, gifts and hotel service facilities, you will find the figure of Li brocade patterns. The area manager of Starwood Hainan, Boettcher believe that the Starwood ideas of the international hotel brand management are with an important point of view that making the details of hotel management combine with the local cultural characteristics to have the hotel culture deeply rooted in the local culture. This is Starwoods personalized choice in new form of competition.

### ***3.2 Element Simplification***

Simple summary of the complex patterns is to retain its essence, so that the main image could be clearer. Transformed graphics not only retain the traditional charm, but also have the aesthetic feeling of modern design. As shown in Fig. 4, the graphic elements of book cover design are extracted from two groups of Li brocade patterns, respectively by stamping technique and embossing technique to present the on the cover. The colors follow the features of brocades color matching, the black as bottom together with the red design of the book title to form a contrast, hot gold brocade pattern elements and the convex and concave chic paper-based texture to generate the overall sense of decoration of the book. In decoration, simplified pattern elements are simple with exquisite craft, demonstrating the charm of Li brocade, beautiful and with national style.



**Fig. 4** Application of brocade patterns in the book cover design



### ***3.3 Deconstruction and Reorganization***

Use graphic design techniques of deconstruction and reorganization to decompose and reconstruct the Li brocade patterns, and then design. According to the design theme and creative direction, in order to reconstruct the Li brocade patterns with the new visual effects, it is necessary to decompose the pattern elements first. And the process of the decomposition of the pattern is the process of analysis through the decomposition of the original understanding of the inherent characteristics of the main body. Reconstruction is the integration. Only through the analysis can it achieve the purpose of integration. When design the tourism product packaging, focus on its theme to conduct the decomposition of the elements, and select the most representative and unique form of expression as the object of re-integration.

### ***3.4 Color Application***

Color itself is an integral part of the design elements. Color matching, if appropriate, would be certainly the best creative point of the packaging design. In Li brocade, color collocation includes various forms, warmth, brightness and purity comparison. Its colors also bring unique artistic atmosphere to the brocade. The color feature extraction is applied to the product packaging to present a more visual stimulation of distinctive national characteristics and achieve more intensive artistic effect.

## 4 Conclusions

Li's people, with a long-term accumulation of experience, create a large number of patterns and forms of artistic expression of the brocade, fully reflecting the artistic features of exquisite layout, concise design, neat and extensive style. All of these characteristics are reflected by Hainan's tourism product packaging design, combining the respect for the traditional elements and the exploration of integration of Li brocade patterns and tourism products. It provides with a variety of forms of expression and graphic language, as an inexhaustible source of art.

Li brocade pattern is used in the packaging design of tourist products, not only in the aspect the traditional elements, but also in exploring the combination of Li brocade patterns and tourism products. The brocade of cultural heritage, from the perspective of improving packaging design strategy, should be based on Li's cultural tourism product packaging design principle. The innovation should be done on the basis of the protection of traditional culture. The implementation should combine effectively today's aesthetic taste and art expression way effectively to achieve effective convergence of the artistic connotation and pattern elements.

## References

1. Boera, E.C., "The Aborigines of Hainan", *Notes and Queries on China and Japan*, 1:7, pp 83-84, July 1867
2. Calder, *Notes on Hainan and its Aborigines*, *The China Review*, vol. XI, pp 42-50, 1822-1883
3. Gilman, F.P. *The language and dialect of northern and western Hainan*, *China, Review*, XX, 1892-1893
4. *The Isle of Palms, Sketches of Hainan*, Presbyterian Church in the U.S.A. Board of Foreign Mission, Hainan Station, Shanghai, Commercial Press, 1919

**Part VI**  
**Mechanical Engineering & Numerical**  
**Control Technology**

# Research on Warpage Deformation Mechanism & Control Method of Fused Deposition Parts

Linlin Liu, Chuliang Wan, Kaikai Li and Jimei Wu

**Abstract** This paper aims to establish the suppression scheme of warping deformation during the fused deposition modeling process. The warping deformation mechanism of FDM forming parts is expounded and the theoretical analysis model is established. The influence factors such as filling density, layer height, shell thickness and molding room temperature are analyzed. The orthogonal experiment analysis that explores the influence degree of each factor is designed. A way to prevent warping deformation control method is proposed. So as to achieve the aim of improve the quality of molding.

**Keywords** Warpage deformation · Control method · Process parameters

## 1 Introduction

Fused Deposition Modeling (FDM) is a manufacturing technique that the filamentous or granular hot melt plastic melts and it is squeezed out by a fine nozzle [1, 2]. The material of FDM is a hot-melting plastic like PLA, ABS and Nylon [3]. And hot-melting plastic goes through the process of melting and solidification. Shrinkage occurs from the molten material to solidify necessarily, and the shrinkage is uneven, which will lead to the part warpage [4–6]. The parts assembly will be difficult due to small deformations. More seriously, the deformations will lead to the parts scrap [7, 8]. Warpage problem occurs not only in the FDM process, but also commonly in SLA, SLS and LOM process [9–13].

In this paper, the distribution of inner layer and layer stress were analyzed, theoretical model of warpage was established, and the main factors influencing the deformation were determined.

---

L. Liu (✉) · C. Wan · K. Li · J. Wu

Faculty of Printing, Packaging Engineering and Digital Media Technology, Xi'an University of Technology, Xi'an, Shanxi, China  
e-mail: Liulinlin1978@gmail.com

© Springer Nature Singapore Pte Ltd. 2017

P. Zhao et al. (eds.), *Advanced Graphic Communications*

and *Media Technologies*, Lecture Notes in Electrical Engineering 417,

DOI 10.1007/978-981-10-3530-2\_91

## 2 Calculation of Warpage Deformation

For quantitative analysis of the deformation and the relationship between various factors, the forming process will be simplified. The assumptions are as following.

1. After high-temperature molten wire from the nozzle, the cooling rate is rapid. So the cooling time is negligible. The process can be simplified to that the wire changed into glassy state after molten from the nozzle and the temperature between molding room and molded part is the same.
2. Wire has not solidified from molten state to glassy state. Resistance to the role of the external force is small, and there is no gathering of internal stress. Internal stress produced mainly in the glassy state to chamber temperature.
3. Assume that the process of filling is instantaneous and each layer of the filling are closely integrated. So each molding layer will be simplified as tablet.

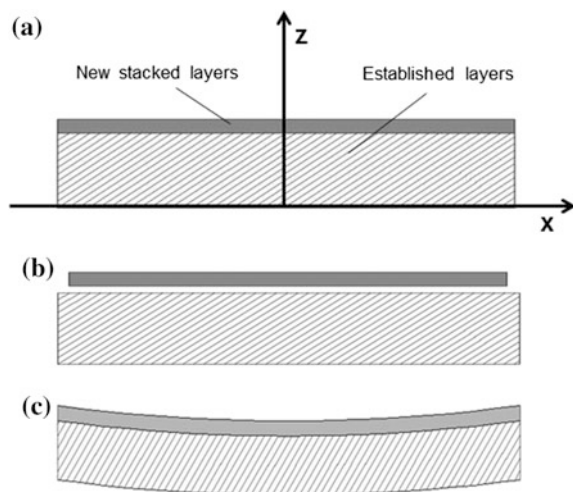
Stress deformation process is shown in Fig. 1. When the new stacked layers free shrinkage, and is not affected by external forces, there is no internal stress, as shown in Fig. 1b. And the shrinkage is

$$\varepsilon = \alpha\Delta\theta \quad (1)$$

When new stacked layers adhesion to established, it is equivalent to use tensile force to the original length, as shown in Fig. 1c. At this point, the shrinkage is zero and the internal stress is

$$\sigma_1 = -E\alpha\Delta\theta \quad (2)$$

Fig. 1 Principle diagram



The new stacked layers will produce internal stress on the formed part and make it occurred bending deformation. This stress is  $\sigma_0$ . The bending stress is

$$\sigma_2 = \frac{E(z - d)}{R} \tag{3}$$

Within the coupled the total stress is

$$\sigma = \sigma_0 + \sigma_1 + \sigma_2 \tag{4}$$

The strain is

$$\varepsilon = \frac{\sigma^*}{E} + \frac{z - d}{R} \tag{5}$$

- $\varepsilon$  thermal strain
- $\sigma$  internal stress
- $E$  elastic modulus
- $\alpha$  linear shrinkage coefficient
- $d$  the distance between bending neutral axis to the nozzle surface
- $R$  warping radius
- $\theta_g$  wire's glassy temperature
- $\theta_e$  the temperature of the molding room
- $\Delta\theta$  the difference between  $\theta_g$  and  $\theta_e$
- $\theta_0$  extrusion temperature

According to the assumption (1) and (2),  $\Delta\theta$  is a step function.

$$\Delta\theta = \begin{cases} \theta_g - \theta_e & L \leq z \leq H \\ 0 & 0 \leq z \leq L \end{cases} \tag{6}$$

After forming, the confluence of internal stress is zero. The confluence of internal torque is zero too. As shown in Fig. 1a, evaluate the integral.

$$\int_0^h \left[ -E\alpha\Delta\theta + \sigma_0 + \frac{E(z - d)}{R} \right] dz = 0 \tag{7}$$

$$\int_0^h \left[ -E\alpha\Delta\theta + \sigma_0 + \frac{E(z - d)}{R} \right] z dz = 0 \tag{8}$$

As two independent equation contains three unknowns ( $\sigma_0, d, R$ ), there needs to go through merging processing parameters. Assumption that

$$\sigma' = \sigma_0 - \frac{Ed}{R} \tag{9}$$

The equation is simplified to

$$\int_0^h \left[ -E\alpha\Delta\theta + \sigma' + \frac{Ez}{R} \right] dz = 0 \tag{10}$$

$$\int_0^h \left[ -E\alpha\Delta\theta + \sigma' + \frac{Ez}{R} \right] z dz = 0 \tag{11}$$

Simultaneous equations to obtain warp curvature.

$$k = \frac{1}{R} = \frac{6\alpha}{H} (\theta_g - \theta_e) \left( 1 - \frac{L}{H} \right) \frac{L}{H} \tag{12}$$

And H minus L equals h For the accumulation of the n-layer prototype,

$$\frac{L}{H} = \frac{(n - 1)}{n} \tag{13}$$

$$k = \frac{1}{R} = \frac{6\alpha}{H} (\theta_g - \theta_e) \left( 1 - \frac{n - 1}{n} \right) \frac{n - 1}{n} = \frac{6\alpha}{n \times h} (\theta_g - \theta_e) \frac{n - 1}{n^2} \tag{14}$$

According to the geometric relations of Fig. 2, there is

$$\cos \beta = \frac{R - \delta}{R} \tag{15}$$

$$\delta = R \left( 1 - \cos \frac{D}{2R} \right) \tag{16}$$

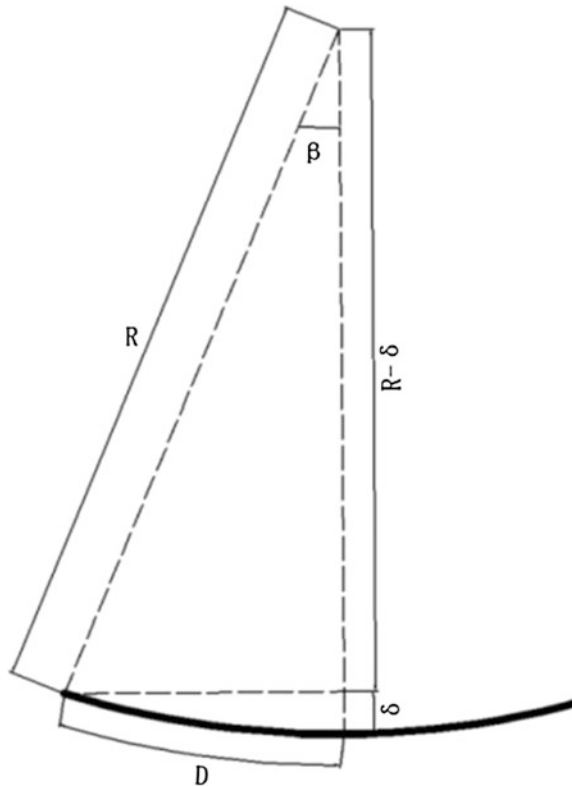
$$\cos \frac{D}{2R} = 1 - \frac{1}{2} \left( \frac{D}{2R} \right)^2 + \dots \tag{17}$$

While D is much less than 2R, the higher order terms can be ignored. Calculate the maximum warping deformation by Eqs. (14), (16) and (17).

$$\delta = \frac{D^2}{8R} = \frac{3D^2\alpha(\theta_g - \theta_e)(n - 1)}{4n^3h} \tag{18}$$

- L prototype sectional length
- δ the maximum amount of warpage
- R warping radius
- N amount of stacked layers
- Δh the thickness of the accumulation

**Fig. 2** Relationship of parameters



### 3 Experimental Analysis of Warpage

This paper took the part model which is  $240 \times 160 \times 10$  mm. STL file stores the model information. Import three-dimension parts by Cura software. According to the above parameters and the final shaped model as shown in Fig. 3, analyze the thermal deformation of FDM molding model.

#### 3.1 Influence of Fill Density on Warping Deformation

High fill density can ensure the strength of the model, but which consumes large amounts of molding material and time. And it is prone to warpage deformation. Set the fill density varying from 5% to 95% evenly. Measure the deformation of each corner of model, and then calculate the average. As shown in Fig. 4, the deformation of model increased as the fill density increases. While the fill density is 95%, the deformation is the largest. And the micro structure of model is shown in Fig. 5. Because in the process of filling in the same layer, the higher fill density, the higher



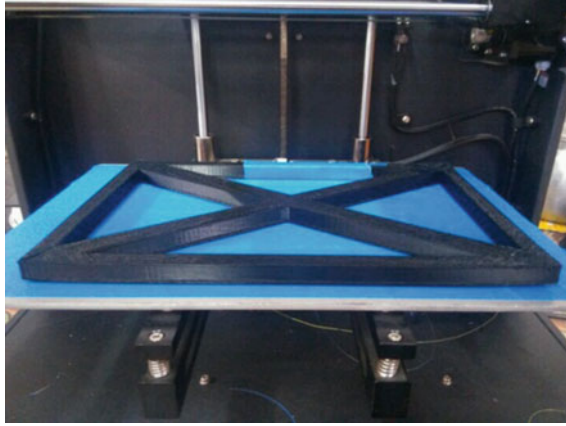


Fig. 3 The final shaped model

Fig. 4 Fill density curve

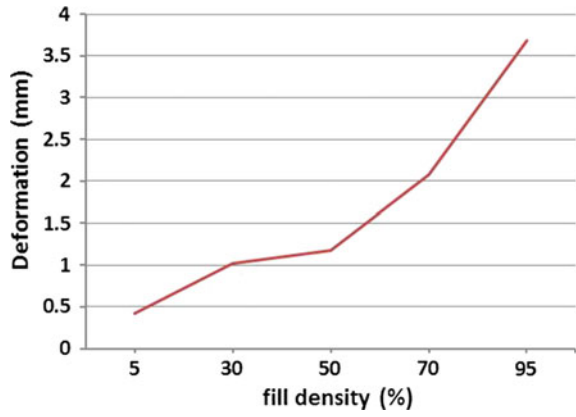
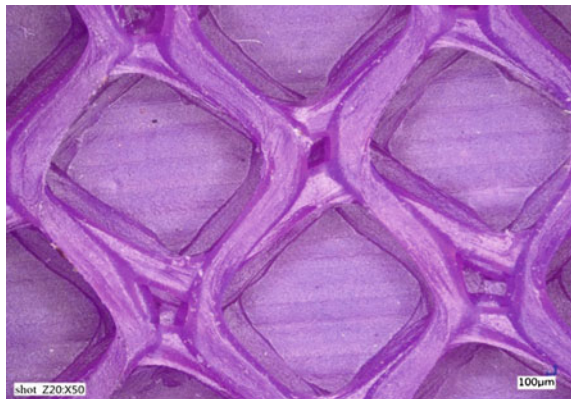
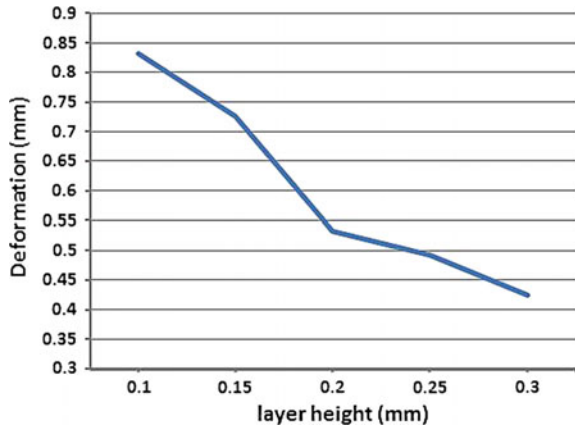


Fig. 5 The micro structure



**Fig. 6** Layer height curve



fill quantity. The more gathered the corresponding residual stress and deformation will be larger. Therefore, in order to reduce warpage, it may be appropriate to reduce the fill density.

### 3.2 Influence of Layer Height on Warping Deformation

Layer height has a great impact on the forming speed and forming quality. Set the layer height varying from 0.1 to 0.3 mm evenly. The curve of deformation is as shown in Fig. 6. The deformation of model increased as the layer height increases. Subjected to the conditions of nozzle aperture, the maximum of layer height is 0.3 mm. Therefore, choose the biggest layer height which can effective prevent warpage.

### 3.3 Influence of Shell Thickness on Warping Deformation

Set the shell thickness varying from 0.4 to 3.0 mm. Measure the deformation of each corner of model, then calculate the average. As it can be seen from Fig. 7, the deformation of model increased as the shell thickness increases.

The smaller the shell thickness, the warpage amount is reduced accordingly, but the surface quality of the part is deteriorated accordingly. Therefore, when setting the shell thickness to ensure surface quality and strength, at the same time, the shell thickness should be as small as possible.

Fig. 7 Shell thickness curve

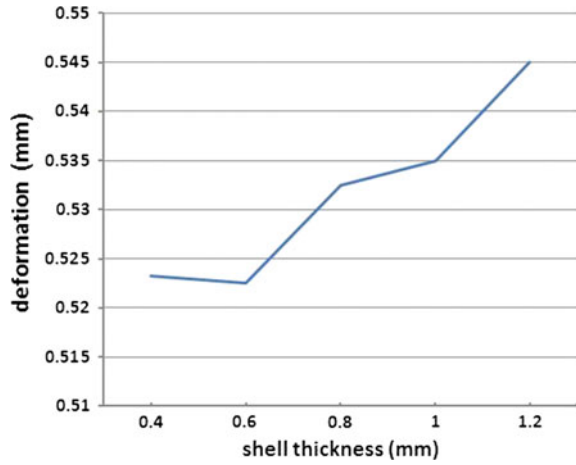
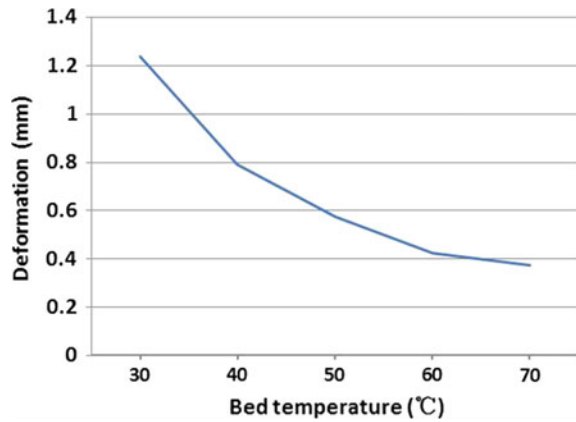


Fig. 8 Bed temperature curve



### 3.4 Influence of Bed Temperature on Warping Deformation

Set the bed temperature varying from 30 to 70 °C. Measure the deformation of each corner of model, and then calculate the average. As shown in Fig. 8, as the bed temperature increases, the amount of deformation is smaller and smaller within certain limits. Because the temperature rises of the entire molding chamber temperature, the temperature difference becomes smaller.

## 4 Conclusions

The paper established theoretical model of warpage in FDM process and analyzed the mechanism of warpage. And the conclusions are as follows:

1. Higher fill density lead to more amount of deformation. In order to reduce warpage, it may be appropriate to reduce the fill density.
2. The deformation of model increased as the layer height increases. Choose the biggest layer height which can effective prevent warpage.
3. Shell thickness has great influence on warping deformation. When setting the shell thickness to ensure surface quality and strength, at the same time, the shell thickness should be as small as possible to reduce deformation.
4. As the bed temperature increases, the amount of deformation is smaller and smaller within certain limits. To reduce the deformation, the bed temperature can be appropriately increased in the molding process.

**Acknowledgements** National Natural Science Foundation of China (Grant No. 11272253), Science Foundation of Shanxi Educational Department (Natural Science 16JS083), and Science Foundation of Beilin District (GX1620).

## References

1. Yunlong Zhao. (2006). Advanced manufacturing technology. XiDian university press.
2. Chong Ren. Yue Dai. Hong Pu. Shen Zhi-juan. (2015). Research on FDM process of the scanning speed design based on ANSYS software[J]. Journal of Inner Mongolia University of Science and Technology.
3. Pengfei Sang, Kai Liu, Yangwei Wang. A model research for prototype warp deformation in the FDM process[J]. Machine Design and Research, 2015(31).
4. LINLIN LIU, RONG MO, NENG WAN, YIBO HUANG, "Process knowledge of procedure machining cell modeling: On the basis of factor space theory", International Journal of Earth Sciences and Engineering, Vol. 7, 2015.
5. Fu DaNing, Cong Weilong, Jing JingQiu, JunHua Wei et. Additive manufacturing of carbon fiber reinforced thermoplastic composites using fused deposition modeling [J]. Composites Part B, 2015(80).
6. HaiboYu, Zhujun Qin. Precision analysis and counter measures of rapid prototyping machine by FDM [J]. Equipment Manufacturing Technology, 2014(5).
7. Guanghui Xu, Yongbo Huang, Jun Deng. (2011). Anti-Distortion Design of the warping distortion in Fused Deposition Modeling. Journal of Dongguan University of Technology. doi:10.3969/j.ssn.1009-0312.2011.03.022.
8. Tianming Wan, Juntong Xi, Ye Jin. (2006). Prototype warp deformation in the FDM process. Chinese journal of mechanical engineering. doi:10.3321/j.issn:0577-6686.2006.03.042.
9. Sood, A.K., R.K. Ohdar and S.S. Mahapatra. (2010). Parametric appraisal of mechanical property of fused deposition modelling processed parts. Materials & Design. 31(1): p. 287–295.
10. ZongpengWu. Research the effects of FDM process parameters on the surface roughness of molding products [J]. Mechanical Engineer, 2015(2).
11. LINLIN LIU, CHULIANG WAN, KAIKAI LI, "CFD Simulation and Structure Optimization on Hot-air Drying Oven of Gravure Printing Machine!", International Journal of Heat and Technology, Vol. 33, 197-202, 2015. doi:10.18280/ijht.330426.
12. Linlin Liu, Rong Mo, Neng Wan, "A MBD procedure model based on machining process knowledge", International Journal of Applied Mathematics and Statistics, Vol. 51, 2013.
13. Li SuLi. Wei ZhengYing. Lu BingHeng. Finite element analysis of Titanium alloy droplet deposition forming[J]. Journal of Zhengzhou University(Engineering Science), 2014(35).

# Incomplete 3D Model's Repair Based on AFPF Technology

Shun Pan, Jiong Liang, Kun Hu and Yonghao Xiao

**Abstract** A created 3D model based on the scanned point cloud data of an object is usually incomplete owing to low ambient lightness or insufficient reflectivity on the surface when scanning. The paper suggested an AFPF (Advancing Front Patch Feature) method for model's repair. In this method, the collected point cloud data are divided into orderly 3D volume element sets, called Octree nodes, which are deployed using Octree Data Structure. The nodes' total number changes with a threshold setting, which is helpful to create optimized curved surface. If some holes appear on the curved surface, characteristics of the holes' boundary are utilized to determine their position. With the calculation of angles between any two adjacent edges of a polygon hole and the average edge length, the holes could be repaired by inserting triangle vertices accurately. The method is proved not only to make the created model complete, but also to be more efficient than some other algorithms, which will be apt in the fields of cultural relic's repair, plastic surgery and construction of 3D geological model etc.

**Keywords** 3D model Octree · Interpolation method · Hole repair

## 1 Introduction

3D object's digitalization has always been one of the research focuses in computer graphics [1], and 3D modeling is one of the most main branches in it. When a 3D laser scanner is used to obtain the point cloud data from one object surface, the data would record 3 coordinate values on location of the points. Whereas the amount of the disordered points is generally very large, some factors might cause some points

---

S. Pan · J. Liang (✉) · K. Hu (✉) · Y. Xiao  
School of Printing & Packaging Engineering, Beijing Institute  
of Graphic Communication, Beijing, China  
e-mail: joanlian@bigc.edu.cn

K. Hu  
e-mail: hukun@bigc.edu.cn

missing, and directly lead to an incomplete created model. Many researches are on how to create a complete model as point cloud data are incomplete. Most of the methods focus on hole repair after curved surface reconstruction, but they ignore the aspect of data optimization before surface reconstruction, which might degrade the algorithm's efficiency.

The algorithm proposed by Zhang [2] is to fill polygon holes by iteratively constructing new triangular patches, the concept of characteristic surface of holes introduced in it. The algorithm can well avoid intersection between the new triangle patch and the original polygon holes, but it is not apt for large amount points and long and narrow polygon holes; In the algorithm proposed by Chen [3], polygon hole boundary is projected onto its characteristic plane, and mesh growth will happen on the planar projection polygon. Although with optimization before and after the grid growth, it is also not very apt to deal with some complex situation, such as large amount points and long and narrow mesh polygon holes; Zhao [4] utilizes Poisson equation to adjust the position of new vertices which created from hole boundary grid vectors. It can be used to repair the model with uniform normal vectors on the hole's boundary mesh, not on the contrary or with large amount data; Hanh T.-M. Ngo [5] regards recovering object's shape features as the primary objective. After detecting the crest line of hole boundary, some user intervention is required, which lowers the processing speed.

Practically, the pre-processing of point cloud data is helpful for rapid and accurate reconstruction of curved surface. The AFPF technology (Fig. 1) proposed here considers two steps for manipulation of point cloud data: preprocessing, then hole repair. Octree structure (Fig. 2) is used to optimize volume elements' structure of point cloud in the preprocessing step.

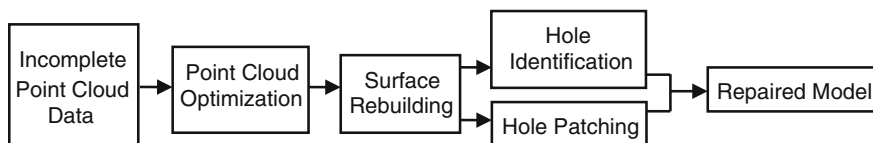


Fig. 1 Shows the framework of AFPF method. Firstly, incomplete point cloud is optimized based on the construct of volume elements. Then the surface model is recreated. Finally, the holes are detected and repaired

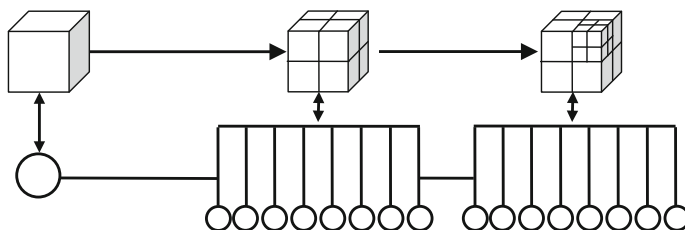


Fig. 2 Shows Octree node structure [7] and its next layers

## 2 AFPF Algorithms

### 2.1 Point Cloud Simplification

Octree is used to deploy the point cloud data's structure in order, proposed firstly by Dr. Hunter in 1978 [6]. Figure 2 shows the structure of Octree nodes [7]. The number of volume elements could be set on the nth power of 2 on each dimension. Each Octree node links to one volume element. Here, the cloud data is divided into 8 nodes firstly as the first layer. While the center of some volume element is regarded as the top of next volume elements layer, the volume element can be separated into eight child nodes again. The following is the details of the Octree organized:

1. To find the max and min coordinate values from the point cloud, which limit the coordinate value range of Octree's root nodes, noted here as (node\_x\_max, node\_x\_min), (node\_y\_max, node\_y\_min), (node\_z\_max, node\_z\_min). And any point's coordinate values are noted as point.x, point.y, point.z;
2. To form eight child nodes based on any parent node, following which to set the index of the eight nodes.

$$\begin{aligned}
 \text{index\_x} &= (\text{point.x} < (\text{node\_x\_max} + \text{node\_x\_min}) / 2) ? 0 : 1 \\
 \text{index\_y} &= (\text{point.y} < (\text{node\_y\_max} + \text{node\_y\_min}) / 2) ? 0 : 1 \\
 \text{index\_z} &= (\text{point.z} < (\text{node\_z\_max} + \text{node\_z\_min}) / 2) ? 0 : 1
 \end{aligned}
 \tag{1}$$

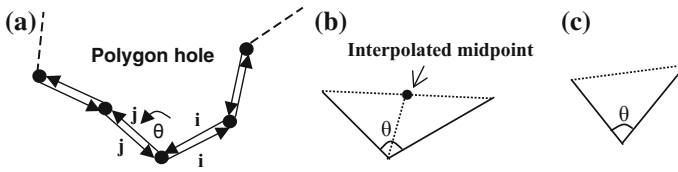
The eight nodes will be indexed as: 000, 001, 011, 010, 100, 101, 110, 111;

3. To judge which nodes need to be separated into the next layer on the limitation of a predetermined minimum amount of point data  $\mu$  in a volume element, set as 5 here. If the volume in an element is larger than the threshold, the next layer will be needed. Then the node is regarded as the parent node of next layer. The procedure from step 1 to step 3 will be iterative;
4. To optimize the volume element's data, Euclidean metric  $\rho$  between any point noted as point1 and the center point noted as point2 in the node is calculated with Formula 2. Finding minimum Euclidean metric, the corresponding point will be saved as a part for surface rebuilding.

$$\rho = \sqrt{(\text{point1.x} - \text{point2.x})^2 + (\text{point1.y} - \text{point2.y})^2 + (\text{point1.z} - \text{point2.z})^2}
 \tag{2}$$

### 2.2 Surface Rebuilding

3D surface reconstruction process has been widely used in the field of 3D scanning modeling. In this paper, the Poisson surface reconstruction algorithm by the point cloud data with normal vectors is used.



**Fig. 3** Shows polygon hole and its half-edge structure (a) also the third edge with (b) and without (c) midpoints inserted

### 2.3 Hole Identification

With simple and intuitive characteristics, the triangular mesh has become the main form of expression on geometric model. The ‘half the table’ structure of OpenMesh library [8] can store the geometric elements of triangular mesh model in detail, such as vertices, edges, faces, etc. In this paper, the functions of OpenMesh are used to identify the holes and to traverse and record these geometric elements, and these data will be used to repair holes.

### 2.4 Hole Patching

Half-edge data structure is utilized to organize the mesh components when a hole is ready to be patched. In this structure, every edge is split down the length, and the pair of edges has opposite directions as in Fig. 3a. There is a corner between any two adjacent edges of hole boundary in an incomplete mesh model, noted as  $\theta$ , the unit vectors of two adjacent edges are noted as  $\mathbf{i}$  and  $\mathbf{j}$ . The average length of a polygon hole edges is noted as  $L_a$ .

Calculating  $\theta$  by dot product between  $\mathbf{i}$  and  $\mathbf{j}$ , then selecting two adjacent edges with the smallest angle  $\theta$ , we can get  $L$ , the length of the third side of a triangle that the selected two adjacent edges close.

If the calculated  $L > L_a$ , the midpoint must be inserted for constructing two triangles as shown in Fig. 3b. Otherwise, one triangle is closed directly as shown in Fig. 3c.

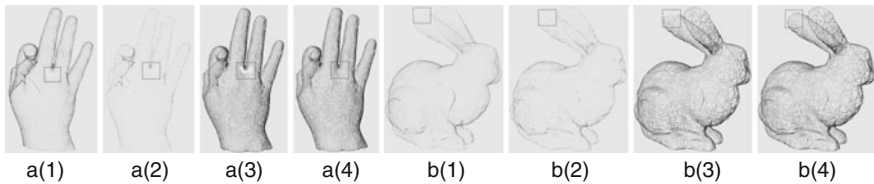
## 3 Application and Analysis

Two instances, a hand cloud and a rabbit cloud, are chosen to verify the AFPF method’s practicability. Data comparison between the original and the optimized points is listed in Table 1. The surface rebuilding time is apparently reduced after point cloud data optimization, but the patched result is still natural and complete Fig. 4.



**Table 1** Data comparison between the original and the optimized points

Instance		Points	Octree nodes	Triangle facets	Surface rebuilding time (s)
a_Hand	Original	150,084		99,999	6.7
	Optimized	134,224	39,302	67,072	5.2
b_Rabbit	Original	35,950		71,792	3.0
	Optimized	29,060	39,823	21,771	2.5



**Fig. 4** Instances: Hand and Rabbit. a(1) and b(1) are original points cloud; a(2) and b(2) are optimized points cloud; a(3) and b(3) are created mesh triangular mesh models from a(2) and b(2); a(4) and b(4) are patched models

From the above analysis, it is quite evident to the AFPF’s usability. The AFPF method is proved not only to be able to make the model complete, but also to improve the repair efficiency than some other algorithms without optimization point cloud data.

## 4 Conclusions

In AFPF method, to optimize point cloud data using Octree structure before hole patching process is very necessary, and the quality of point cloud data optimization will affect the process of surface rebuilding and hole patching. The proposed AFPF method is proved to be efficient and reliable. However, the threshold value  $\mu$  on point data’s volume is determined by many times training on various 3D model data, and the AFPF method cannot repair a model with multiple holes, which will be left to further research.

**Acknowledgements** This study is funded by “2016 The College Student Research Program” of Beijing Institute of Graphic Communication and a university scientific research project of BIGC—3D Printing mineralized collagen-based child mandible (Grant No. 20190116002/037).

## References

1. Qian. (2008). Research on mesh reconstruction and repair from scattered point cloud. Doctoral Dissertation of Zhejiang University. 1–2.

2. ZHANG, ZHOU. (2002). Research on the Algorithm of Hole Repairing in Mesh Surfaces. *JOURNAL OF APPLIED SCIENCES*, 20(3), 222–224. doi: [0255-8297\(2002\)03-0221-04](https://doi.org/10.1007/s00371-007-0167-y).
3. CHEN., GAO. (2011). Hole filling algorithm in triangular meshes. *Computer Integrated Manufacturing Systems*, 17(8), 1821–1826. doi: [10.13196/j.cims.2011.08.255.chenj.027](https://doi.org/10.13196/j.cims.2011.08.255.chenj.027).
4. ZHAO. (2007). A robust hole-filling algorithm for triangular mesh. *Visual Comput.* doi:[10.1007/s00371-007-0167-y](https://doi.org/10.1007/s00371-007-0167-y).
5. H.W. (2012). Feature-First Hole Filling Strategy for 3D Meshes. School of Information Technology and Engineering, University of Ottawa. 53–63.
6. Research and Application of Octree Algorithm. <http://www.docin.com/p-374354765.html>. Cited 17 July 2016. 2–3.
7. L., B. (2012). Integrated Point Cloud Storage Structure Based on Octree and KDTree. *Computer Systems & Applications*, 21(3), 88–89.
8. W., Z. (2008). Point by Point Insertion Into Delaunay Triangulation Algorithm Based on Half Edge Data Structure [J]. *Journal of Shenyang Construction University: Natural Science Edition*, 24 (6): 1103–1108.

# Object Tracking Algorithm Based on Adaptive Learning Parameter by Online Loss Detection

Yehong Chen, Pil Seong Park, Pingli Lv and Maohai Lin

**Abstract** The goal of this paper is to improve the robustness of the tracking by detection system. We gain the aim by dynamic tuning the learning parameters for an accumulative learned classifier according to online performance evaluation. Firstly, two kinds of tracking loss measures are distinguished: one is positive due to object appearance variation which does not result in drift; the other is negative which really causes drift. Then, according to these two situations, different parameter updating strategies are proposed to maintain adaptive model updating. Our proposed algorithm adopts the ability of identifying track loss and controls the tracking process to enhance the stability and robustness of the original algorithm (CT), and experimental results show better performance with negligibly small additional running time on some challenging video fragments which original CT failed on.

**Keywords** TIM performance evaluation of tracking · Dynamic adjustment of parameters · Model based tracking

## 1 Introduction

The main challenge of visual object tracking comes from the variation of the video over time, e.g., noise, illumination change, occlusion, the cluttered background, and so on. During the past decades, researchers gained a lot of progress in real-time object tracking system, and the result is the advent of many excellent algorithms like Particle filter [1], HOG plus SVM tracker [2], online AdaBoost tracker [3] etc. However, none of this tracking algorithm can perfectly work under all conditions.

---

Y. Chen (✉) · P. Lv · M. Lin  
School of Printing & Packaging, Qilu University of Technology, Jinan, China  
e-mail: chenyh@qlu.edu.cn

P.S. Park  
Department of Computer Science, University of Suwon, Suwon, Gyunggi-Do, Korea

Hence online determination functionality of track loss is necessary and a criterion to evaluate the performance of a tracking algorithm is crucial. A model based tracker usually is a recognition system based on adaptive model parameters and environment parameters [4]. As the situation in the video Changes, this kind of tracker is not guaranteed to work well all the while, and tracking sometimes ends up with a drift.

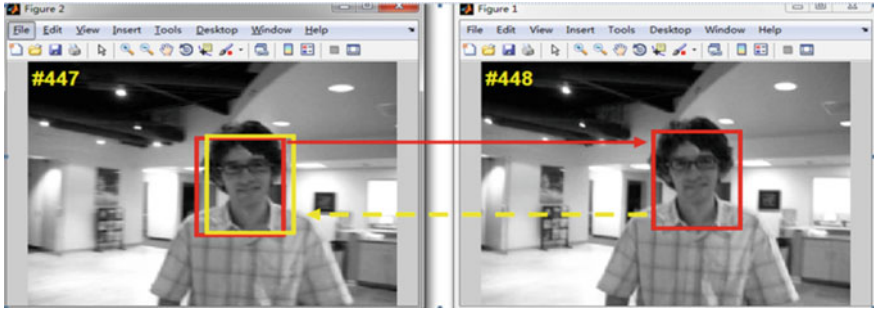
There are two main reasons for a drift: one is because of inaccuracy of the current tracking algorithm, i.e., the accumulated error in object model of every frame will finally results in a drift; the other is due to the fixed environment parameters used in the tracking algorithm. San Miguel et al. [5] presented a comparative evaluation method showing that the observation likelihood measure is appropriate for overall tracking performance evaluation, while the Template Inverse Matching (TIM) measure [5, 6] is appropriate to detect the start and end instants of tracking failures.

In this paper, the real time compression tracking (CT) algorithm is improved by the proposed algorithm which aimed at constructing a strategy that is able to control the tracking process, no matter before or after a drift trend was detected, and the chosen parameter is automatically adjusted according to track loss measure from TIM which can detect track loss without ground truth. In order to make things as simple as possible, so only one parameter: learning parameter  $\lambda$  is choose to be adjustable by the feedback of TIM. Experiments on two videos show better performance with negligibly small additional running time.

## 2 Related Works

### 2.1 *Template Inverse Match (TIM)*

Under template-based tracking context, Liu et al. [6] introduced a special performance evaluation method TIM. As an online performance evaluation method, TIM is an inverse process of tracking which position the target by finding the region in the frame that matches the current template as closely as possible. The result location of TIM is compared with the target position in the previous frame captured by tracker, and the distance  $d$  between these positions is thought as a tracking loss measurement. Figure 1 shows the match result of TIM, together with the actual positions in the previous and current frames. Red rectangles show the tracking results in the previous and current frames by tracker. The yellow rectangle is the result of TIM in the previous frame. The red arrow shows the common tracking direction, and the dashed yellow arrow denotes the loss detection direction of TIM.



**Fig. 1** An example showing the match result of TIM. The video is from Zhang et al. [7] and free for research purpose only

### 2.2 Real Time Compression Tracking (CT)

Zhang et al. [7] proposed a highly efficient state-of-the-art real-time compression tracking algorithm CT. The object representation used in CT is a compressed feature vector in a general Haar-like feature space. For each image sample  $I$ , its low-dimensional representation is  $v = (v_1, \dots, v_m)$ ,  $m = 50$ . CT assumes all elements in  $v$  are independently distributed and models them with a naive Bayes (NB) classifier  $F(v)$ . Thus  $F(v)$ 's conditional distribution is assumed to be Gaussian with four parameters  $p^t = (\mu_1, \sigma_1, \mu_0, \sigma_0)$ , where  $\mu_1, \sigma_1$  or  $\mu_0, \sigma_0$  respectively are the mean and standard deviation of the positive sample set  $X^1$  or the negative sample set  $X^0$ . At the current  $t$ -th frame the newly learned model parameters  $p^t$  are incrementally updated as a combination of these Gaussian parameters by the weighted average of the current and incremental values by:

$$\sigma_t^1 \leftarrow \sqrt{\lambda(\sigma_{t-1}^1)^2 + (1 - \lambda)(\sigma^1)^2 + \lambda(1 - \lambda)(\mu_{t-1}^1 - \mu^1)^2} \tag{1}$$

$$\mu_t^1 \leftarrow \lambda\mu_{t-1}^1 + (1 - \lambda)\mu^1 \tag{2}$$

Here,  $\mu^1, \sigma^1$  is the mean and standard deviation on current collected training samples, i.e.  $X^1$  and  $\lambda$  is a learning parameter. When  $\lambda$  equal to 0, none history information of the model remembered at all, the model always corresponds to the current captured target sample and clears up all previous learned knowledge; however when  $\lambda$  equal to 1, none variation information incremented into the object model at all, the model keeps fixed for ever. In CT,  $\lambda$  is fixed to 0.85.

### 3 Outline of the Proposed Approach

#### 3.1 The Proposed Method TIM-Aided CT

Figure 2 is the illustration of the proposed algorithm TIM-aided CT in this paper, which using the feedback of track loss to adjust the learn parameter  $\lambda$  so that the model adaptability on the next frame is improved. The basic procession in this proposed algorithm is the same as what inside the original CT algorithm; hence the main improvement is to embed a TIM procedure in the end of the original tracking by detection loop. In every frame, after capturing the current target, firstly the tracker updates the NBC classifier using current captured target as the predictive model. Then our proposed algorithm triggers the TIM procedure using the predictive model to match the target in the previous frame, the distance between the TIM result and target location in the previous frame is called the track loss distance noted as  $d$  in this paper.

Because the appearance change doesn't always indicate poor tracking performance, yet sometimes it does, a threshold of the tracking loss distance is defined as  $d_T$  to distinguish two kinds of track loss measurements: one is positive due to object appearance variation which does not result in tracking drift; the other is negative which really causes drift. At present, the threshold setting  $d_T$  comes from experimental tuning.  $d$  is the detected loss measurement, then If  $d < d_T$ , the tracking loss is considered as valid, otherwise if  $d > d_T$ , a drifting is detected. When a drifting is detected, then the predicted model should be discarded and the model parameters will roll back to the last valid model which has been stored in the memory before the drift trend. At that time, there is a system reinitialization, so the learning parameter  $\lambda_t$  is reset to a ceiling value  $\lambda_R$  to refrain from too low.

From the experiments, if  $\lambda_1$  (the initialization of the learning parameter  $\lambda$ ),  $d_T$  and  $\lambda_R$  is suitable, once dropping of the faired frame will guide whole system to recover from the drift trend. The initialization learning parameter  $\lambda_1$  and the ceiling value  $\lambda_R$  are all set depending on video data and comes from experimental tuning.

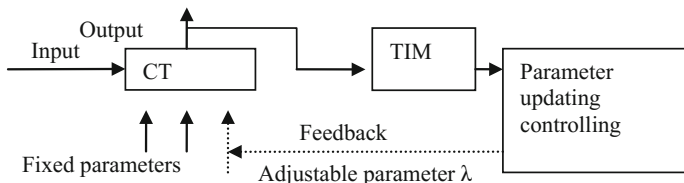


Fig. 2 Illustration of the proposed algorithm TIM-aided CT

### 3.2 Algorithm

Our proposed algorithm is described in pseudo code as following:

Algorithm (TIM-aided CT)

Input:  $z^1$ : the initial target position.

$d_T$ : threshold of track loss.

$\lambda_1$ : initialization of the learning parameter  $\lambda$ .

$\lambda_R$ : reset value of  $\lambda$ .

Output:  $z^i$  ( $i >= 1$  and  $i <= n$ )

#### 1. Initialization

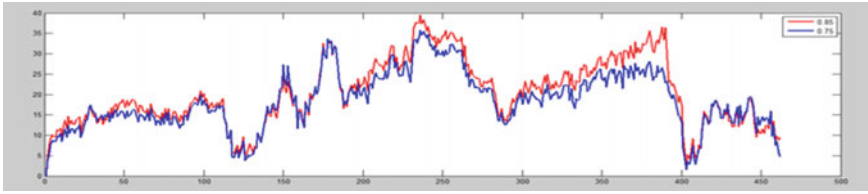
- 1) Collect positive and negative training sets around  $z^1$ .
- 2) Extract features in reduced dimensionality  $v_1$ .
- 3) Learn parameters of the NB classifier  $F^1()$ .
- 4)  $d_o = 0$ .

#### 2. For frame index from $t=2$ to $n$

- 1) Sample a set of image patches around  $z^{t-1}$ .
- 2) Extract features in reduced dimensionality  $v_{t-1}$ .
- 3) Apply  $F^{t-1}()$  to each sample vector to find the target candidate  $z^t$ .
- 4) Collect new training samples around  $z^t$ .
- 5) Save  $F^{t-1}()$  as back up;
- 6) Incrementally update the NB classifier to  $F^t()$  by  $\lambda_{t-1}$ .
- 7) Apply the TIM process using  $F^t()$  to find the target candidate  $z^{t-1}$ .
- 8) Compute track loss measure  $d_t$ .
- 9) If  $d_t >= d_T$ ,
  - Roll  $F^t()$  back to  $F^{t-1}()$ .
  - $\lambda_t = \lambda_R$ .
  - else
  - $\lambda_t = \lambda_{t-1} / (1 + d_t)$

## 4 Experiments

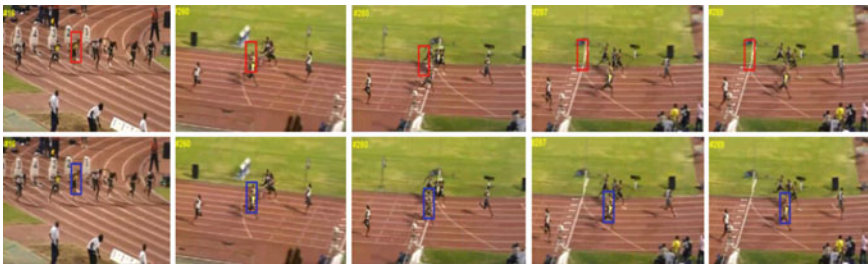
The source code of CT was obtained from [8]. Our experiments were performed on the PC equipped with Intel<sup>®</sup> Core<sup>™</sup> i3-3110 M CPU running at 2.40 GHz and having 4 GB of main memory. Original CT and our proposed MIM-aided CT tracker are both implemented using MATLAB running on 64-bit Windows 7 and around 30 frames per second. The ground truth was manually settled and averaged by three times for per video which usage was limited in comparisons.



**Fig. 3** These are the comparison of results by original CT (red,  $\lambda = 0.85$ ) with learning parameter setting to 0.75 (blue bottom)

The video “David in door” is obtained from [8]. In our first experiment, we ran CT a few times with different  $\lambda$  setting, e.g.  $\lambda = 0.75$ ,  $\lambda = 0.90$  or  $\lambda = 0.95$  to compare with the original setting of 0.85. We did not tune any other parameters except  $\lambda$  in the published code of CT. Under the learning parameter set of 0.75 nearly every frame with a little bit correction from original CT, it guarantees entirety improvement from the original one. From Fig. 3, we suggest setting the fix learning parameter  $\lambda$  to 0.75 rather than 0.85, and then the performance of CT will be improved when applied on “David in door”.

Then both the original CT and TIM-aided CT were run on the video “Bolt” [8] which is about a running race of 7 players. However using original CT (set learning parameter  $\lambda = 0.85$ ), tracking task of some runners ended by drifting. The experiments below show that TIM-aided CT can get better tracking results than what got from CT on this challenging video. In Fig. 4, every row is for one player’s tracking result, blue box is by TIM-aided CT, and red box is by original CT. In Fig. 4, CT begins to lose the runner 1 from frame #280 and follows a wrong object until the end, while TIM-aided CT with  $d_T = 0.02$  successfully follows the runner until the end. Here the TIM-aided CT has carefully tuned the initial parameter  $\lambda_1$  to 0.65, threshold  $d_T$  to 0.02, and ceil parameter  $\lambda_R$  to 0.95.



**Fig. 4** Tracking results for one runner in some frames



## 5 Conclusion and Future Works

This paper presents a model based tracking system with feedback of online performance evaluation measurements to guide the adjustment of the model learning parameter. Another contribution of this paper is to distinguish two kinds of tracking loss measurement by define a distance threshold  $d_t$ , and according to this distinguish different model adjustment strategies were proposed. Experiments proved that the proposed TIM-aided CT tended to prevent drift to some extent with negligibly small extra time. In the future, our proposed online parameter adjustable work frame intends to combine more widely used algorithms and involved more environment parameters.

**Acknowledgements** This work was supported by the GRRC program of Gyeonggi province, South Korea [GRRC SUWON 2015-B1, Cooperative Recognition and Response System Based on Tension Sensing, South Korea].

## References

1. Zhang, X., Hu, W., Maybank, S., Li, X. and Zhu, M.: Sequential particle swarm optimization for visual tracking. CVPR 2008. IEEE Conference on (pp. 1–8). June, 2008.
2. Pang, Y., Yuan, Y., Li, X., & Pan, J. (2011). Efficient HOG human detection. *Signal Processing*, 91(4), 773–781.
3. Grabber, H., Grabner, M. and Bischof, H.: Real-Time tracking via On-line boosting. In *BMVC* (Vol. 1, No. 5, p. 6). September, 2006.
4. Renno J, Lazarevic-McManus N, Makris D, et al. Evaluating motion detection algorithms: Issues and results[C]//IEEE International Workshop on Visual Surveillance. 2006: 97–104.
5. SanMiguel, J. C., Cavallaro, A., & Martinez, J. M. (2010, September). Evaluation of on-line quality estimators for object tracking. In *Image Processing (ICIP), 2010 17th IEEE International Conference on* (pp. 825–828). IEEE.
6. R. Liu, S. Z. Li, X. Yuan, and R. He. Online determination of track loss using template inverse matching. In *The Eighth International Workshop on Visual Surveillance-VS*, (2008).
7. K. Zhang, L. Zhang, and M. H. Yang. Real-time compressive tracking. In *Computer Vision–ECCV 2012* (pp. 864–877). (2012).
8. A Real-time Compressive tracker. <http://www4.comp.polyu.edu.hk/~cslzhang/CT/CT.htm>.

# Structure Design of Front-Edge Paper Feeder in the Production Line of Corrugated Carton

Jin Wang, Rongyu Ge and Jiatai Wang

**Abstract** The corrugated carton as a common packaging tool is usually produced in production line. It is crucial to design the structure of paper feeding unit in the line which has a large influence on the accuracy of subsequent printing and cutting position. Front-edge paper feeder is the standard way to transport corrugated boards in the current market. Firstly, working principle of front-edge paper feeder is introduced. And then the intermittent driving and lifting mechanism are analyzed in detail. The intermittent driving mechanism is a combined mechanism by the cam indexing and gear mechanism. The lifting mechanism can flexibly adjust the time and lifting height to rise the corrugated board. The structure of front-edge paper feeder is designed with high accuracy and speed in this paper.

**Keywords** Corrugated carton · Front-edge paper feeder · Cam indexing mechanism · Lifting mechanism

## 1 Introduction

At present, corrugated carton production line mainly includes paper feeding unit, printing unit, slotting unit, die-cutting unit and so on at home and abroad [1]. Each functional unit is arranged on the guiderail by the process sequence, and the transmission power is transferred through the gear meshing of the gear units, and the synchronous operation of the whole production line is realized. The paper feeding unit can combine with grooving unit or die-cutting unit named slotting machine or rotary die-cutting machine in the domestic market. Paper feeding unit has an essential importance in corrugated carton production line or single machine

---

J. Wang · R. Ge (✉)

School of Mechanical Engineering, University of Jinan, Jinan, Shandong, China  
e-mail: me\_gery@ujn.edu.cn

J. Wang

Zaozhuang Vocational College of Science & Technology, Zaozhuang, Shandong, China

© Springer Nature Singapore Pte Ltd. 2017

P. Zhao et al. (eds.), *Advanced Graphic Communications*

and *Media Technologies*, Lecture Notes in Electrical Engineering 417,

DOI 10.1007/978-981-10-3530-2\_94

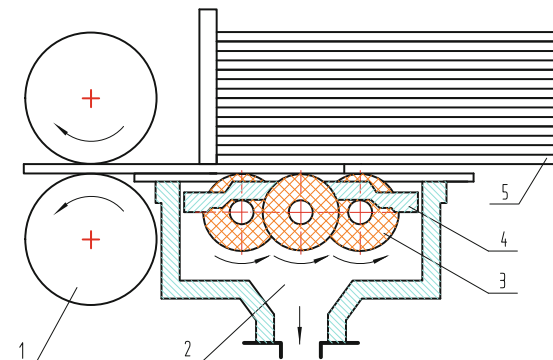
processing equipment, and the paper feeding precision directly determines the subsequent printing precision and the subsequent die-cutting precision.

Paper feeding unit will put a piece of corrugated cardboard accurately and smoothly into the carton processing equipment. There are three main types of paper feeder. Firstly, it is chain type which uses the chain wheel and chain to transport the corrugated board. It has many disadvantages such as low efficiency, high noise, low precision up to 3 through 5 mm, and can only satisfy the low requirement of the fruit box. Second, it is reciprocating with push slab, which uses the crank and connecting rod mechanism to drive the reciprocating movement of the pushing slab, but the moving speed of pushing slab cannot be too high and push the warpage corrugated board. In the third, it is the front-edge paper feeder with the advantages of high speed and high precision, generally in  $\pm 0.5$  mm, so it is the standard way to transport corrugated boards in the current market.

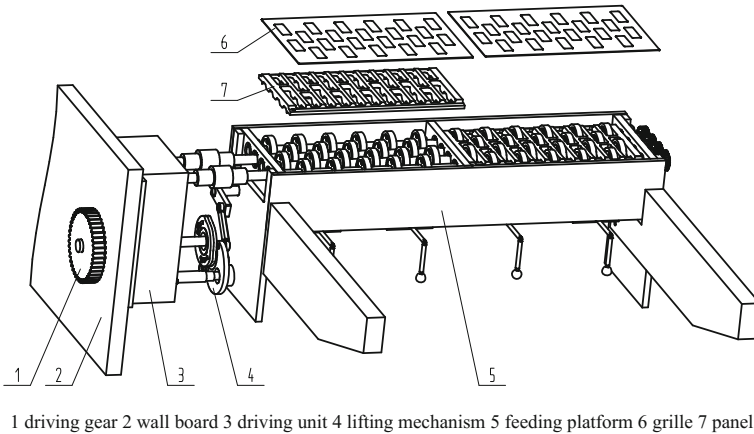
## 2 Working Principle of the Front-Edge Paper Feeder

Figure 1 is the structure schematic of the front-edge paper feeder [2]. A plurality of suction outlets connected with the fan pipeline, are arranged side by side at the bottom of the feeding platform and then the feeding platform is turned into a vacuum because of the role of fan. A lot of corrugated boards stacked on the feeding platform will be adsorbed on the feeding platform. When the corrugated boards are transported, the feeding rollers begin to rotate periodically. Then the bottom corrugated board begins to move forward by virtue of the friction between feeding rollers and the corrugated board, and then the corrugated board will be transported to the processing unit under the action of two drawing rollers. When corrugated boards are not transported, the grille will be raised up, feeding rollers and corrugated papers will be separated. In short, combining periodic rotation of the feeding roller with periodic fluctuation of the grille, the front-edge of paper feeder puts the

**Fig. 1** Paper feeding schematic in corrugated carton production line 1 drawing roller 2 vacuum 3 feeding roller 4 grille 5 corrugated board



1 drawing roller 2 vacuum 3 feeding roller 4 grille 5 corrugated board



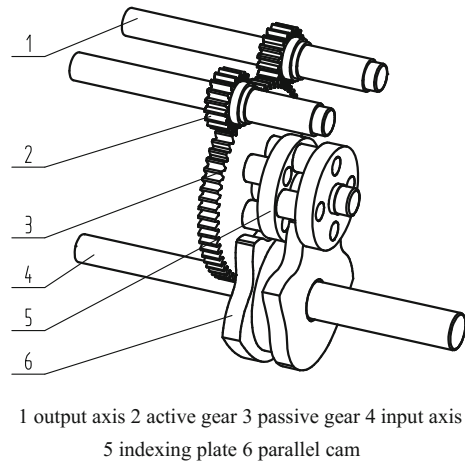
**Fig. 2** General structure diagram of front-edge paper feeder

stacked boards into the production line based on the front edge of the board. The driving mechanism of feeding rollers and the lifting mechanism of the grille are the key structures for the front-edge paper feeder. The function of driving mechanism is to drive a group of rollers and make an intermittent motion. The intermittent mechanisms include cam mechanism, ratchet mechanism, intermittent gear mechanism and so on, among that cam mechanisms can arrive the highest drive precision by the designed cam profile [3]. The lifting mechanism can lift feeding platform in order to reduce the wear of the feeding roller, however, most of the designed lifting mechanism cannot flexibly adjust the time and distance, so it is inconvenience for installation and use. Therefore, as shown in Fig. 2, a innovative front-edge paper feeder is designed in this paper, whose structure mainly includes a feeding platform, a driving unit and a lifting mechanism with the advantages of high precision, fast working speed, little damage to the boards and longer service life of feeding rollers.

### 3 Design of Intermittent Driving Unit

As shown in Fig. 2, the driving unit is fixed on the wall board of the production line. The input axis passing through the wall board is connected with driving gear, and the power of the main motor of the production line is transmitted to the drive gear through the gear transmission. The feeding platform is designed with four rows of feeding rollers and the two output axes of the driving unit are respectively connected with the two rows of feeding rollers, and then through the gear transmission, the four rows of feeding rollers can rotate synchronously. As shown in Fig. 3, driving unit consists of the parallel indexing cam mechanism and the gear transmission mechanism, both installed in the drive box. A parallel indexing cam is fixed through the input axis of the drive box and three indexing plates which are

**Fig. 3** Structure diagram of driving unit



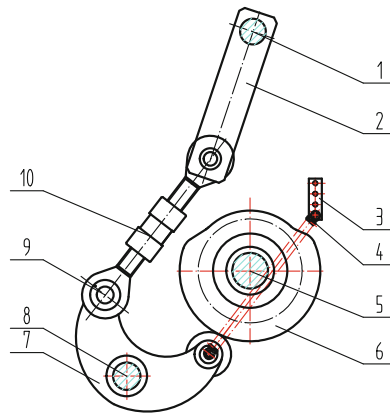
assembled together with two rows of cylindrical rollers are fixedly connected to the indexing axis in the middle of the drive box. In addition, the diameter of one indexing plate is larger than the others and the outer profile of that will be machined into a active gear. In this way, the indexing plate and the gear are integrated into one body. There is a same passive gear on each output axis, simultaneously meshing with the active gear on the indexing plate. We should select the appropriate tooth number of active gear and passive gear to mate paper feeding speed with that of subsequent units. Parallel indexing cam consists of two pieces of cam plates to achieve indexing motion, but both of them are machined as a whole to avoid the machining error and assembling error.

## 4 Design of Lifting Mechanism

The lifting mechanism is composed of an oscillating cam mechanism and some rods shown in Fig. 4. The oscillating cam is fixedly connected with the shaft end of the input axis of the intermittent driving box inside the wallboard. There is a support axis installed on the side of the drive box and a oscillating support with a hole in the middle fixed through the support axis. One end of the support is connected with a cam follower bearing and a spring which is held on the spring seat, so by spring force, the cam follower bearing and the outer contour of oscillating cam have been attached together. The other end of the support is connected with the joint bearing and the joint bearing is connected with a adjusting sleeve through the left-hand thread. In addition, the other end of the adjusting sleeve is connected with another joint bearing through the right-hand thread. As a result, the joint bearing and the adjusting sleeve form a connecting rod with adjustable length. In this way, when the input axis of driving unit rotates, the oscillating cam will rotate simultaneously.

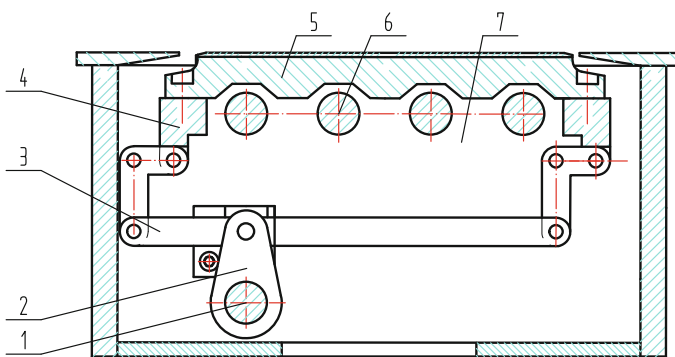
Finally the outside oscillating rod and oscillating axis will swing through oscillating support and adjusting sleeve.

As shown in Fig. 5, when the oscillating axis swings, the inside oscillating rod in the feeding platform will swing simultaneously. Then the lifting block is moving because of the help of parallelogram linkage mechanism, so that the grille is rose and dropped. When the grille is rose, the corrugated board on the feeding platform and feeding roller are detached. Then the process of paper feeding is stopped. On the contrary, when the grille is dropped, then the process of paper feeding is continued.



1 oscillating axis 2 outside oscillating rod 3 spring seat 4 spring 5 input axis of driving unit  
6 oscillating cam 7 oscillating support 8 support axis 9 joint bearing 10 adjusting sleeve

**Fig. 4** Structure diagram of lifting mechanism outside of feeding table



1 oscillating axis 2 inside oscillating rod 3 parallelogram linkage mechanism  
4 lifting block 5 grille 6 feeding roller axis 7 feeding platform

**Fig. 5** Structure diagram of lifting mechanism inside of feeding table

## 5 Conclusions

In recent years, with the rapid development of packaging industry, the request for front-edge paper feeder is much higher, and it has been paid much more attention by industry. The front-edge paper feeder above mentioned is designed with advantages such as compact structure, flexible adjustment and high feeding speed, which can meet the production requirement of corrugated carton.

**Acknowledgements** This study is funded by a Key Research Project of Shandong Province in 2015 (No. 2015GGX103005).

## References

1. Zhang, X. S. (2007). Process and equipment of post press. Printing industrial Press, Beijing.
2. Ge, R. Y. (2013). A novel front-edge paper feeder in corrugated carton production line. China Patent, CN103252919A:1–15.
3. Robert L Norton. (2009). Cam design and manufacturing handbook (2nd ed). Industrial Press, New York.

# Traction Characteristics of Guide Roller with the Air Entrainment

Mingyue Shao, Jimei Wu, Li'e Ma and Zhen Tian

**Abstract** The guide roller of Shaanxi Beiren FR-400 high-speed gravure printing unit type is taken as the research object, and the guide roller traction model is established with air entrainment by using the fluid lubrication theory and mechanics theory. The influence factors such as wrap angle, guide roller diameter, web tension, equivalent roughness are analyzed. The results show that the traction force decreases with the increase of the guide roller diameter, and traction force increases with the increase of the equivalent roughness, wrap angle and web tension. Therefore we should as far as possible to design small wrap angle and we can choose a small diameter and a big equivalent roughness of guide roller to improve traction characteristics. So the study lays the theoretical foundation for the selection of the guide roller and the stable transmission of the web.

**Keywords** Guide roller · Traction characteristics · Air entrainment

## 1 Introduction

The gravure printing machines are mainly used to print web products, and the guide rollers are important parts to ensure the web stable transmission. During the web transport process, the guide rollers are idle rollers driven by the friction between the web and the roller. However, web traction over rollers is known to deteriorate due to air entrainment at high web speed [1], which can cause web wrinkles, lateral drift

---

M. Shao · J. Wu (✉)  
Faculty of Mechanical and Precision Instrument Engineering,  
Xi'an University of Technology, Xi'an, China  
e-mail: wujimei@xaut.edu.cn

L. Ma (✉) · Z. Tian  
Faculty of Printing, Packaging and Digital Media Engineering,  
Xi'an University of Technology, Xi'an, China  
e-mail: malie@xaut.edu.cn



and fracture phenomena, which can directly affect the processing quality and the accuracy of the web in printing process [2].

Eshel [3] established the air film thickness formula in the package region of the guide roller and tape. Ducotey and Good [4, 5] found that circumferential grooves were very effective in reducing the effects of air entrainment. A modified capstan equation predicted air film thickness between roller and traction was applied by Rice et al. [6, 7]. Müftü and Jagodnik [1] proposed a model that predicted traction characteristics of the web over a smooth roller. Sasaki et al. [8] considered relationship between traction of the moving web and guide roller and the increase of air entrainment on the theory and experiment. Si et al. [9] studied the effect of air entrainment phenomenon between a web and spirally grooved roller. Research showed that the average traction coefficient of the circumferentially grooved roller was higher than that of the spirally grooved roller. Aoki et al. [10] showed that the air entrainment could reduce guide roller traction, and experiment results showed that the friction coefficient decreased with the increase of air film thickness. Hashimoto [11] studied friction coefficient between uncoated paper-web and steel roller by using the contact mechanics theory under air lubrication. A study in [12] described traction characteristics of a flexible web moving through a grooved, concave, and soft surface roller with air entrainment.

In this paper, the influence factors and change rules of the guide roller traction characteristics with the air entrainment are analyzed.

## 2 Guide Roller Traction Model with the Air Entrainment

In order to establish traction model so the following assumptions [13] are made.

We do not consider bending rigidity of the web. The entrained gas is incompressible, and gas viscosity and gas pressure are constant. Do not consider the effects of temperature and web's centripetal acceleration.

The traction model of the web and roller when the web is slipping over the roller ( $i - 1$ ) and force diagram of a micro web element in the contact area is shown in Fig. 1, guide roller radius denotes  $R$ ,  $\theta$  is wrap angle,  $v$  is the web transport speed,

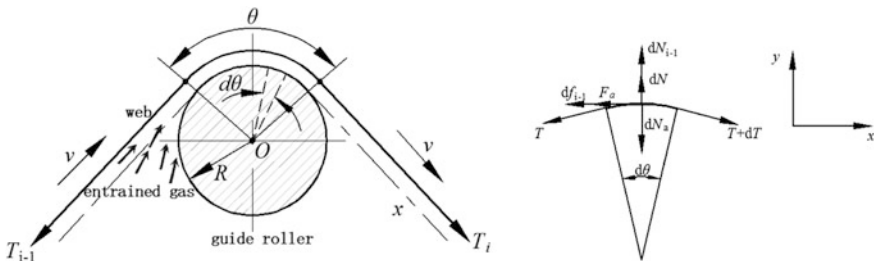


Fig. 1 Model of web and guide roller with the air entrainment

$T_{i-1}$  is web tension to enter the roller ( $i - 1$ ),  $T_i$  is web tension in guide roller ( $i - 1$ ) output side.  $F_a$  is air viscous force, we can ignore it because it is very small [7].  $f_{i-1}$  is the friction force, which also is the traction force by web at the roller  $i - 1$ .  $N_{i-1}$  is the normal force,  $dN_{i-1}$  is the web to the guide roller pressure,  $dN$  is entrained gas pressure for web,  $dN_a$  is the ambient air pressure for the web. Then the force balance along the  $x$  and  $y$  directions are analyzed.

$$df_{i-1} = -T \cos\left(\frac{d\theta}{2}\right) + (T + dT) \cos\left(\frac{d\theta}{2}\right) = dT \cos\left(\frac{d\theta}{2}\right) \quad (1)$$

$$dN_{i-1} + dN - dN_a = T \sin\left(\frac{d\theta}{2}\right) + (T + dT) \sin\left(\frac{d\theta}{2}\right) = (2T + dT) \sin\left(\frac{d\theta}{2}\right) \quad (2)$$

As  $d\theta \approx 0$ , we note that  $\sin\left(\frac{d\theta}{2}\right) \approx \frac{d\theta}{2}$  and  $\cos\left(\frac{d\theta}{2}\right) \approx 1$ , ignoring the product  $dt \cdot \frac{d\theta}{2}$ , we obtain

$$dN_{i-1} = [T - (P - P_a)R]d\theta \quad (3)$$

$$df_{i-1} = \mu dN_{i-1} = dT \quad (4)$$

where  $\mu$  is the friction coefficient.

Combining Eqs. (3) and (4), we obtain

$$\frac{dT}{T - (P - P_a)R} = \mu d\theta \quad (5)$$

Integrating over the entire wrap angle area in Eq. (5)

$$\int_{T_{i-1}}^{T_i} \frac{dT}{T - (P - P_a)R} = \mu \int_0^\theta d\theta \quad (6)$$

Traction force of the guide roller in the air entrainment can be defined as

$$f_{i-1} = T_i - T_{i-1} = [T_{i-1} - (P - P_a)R](e^{\mu\theta} - 1) \quad (7)$$

The entrained gas pressure  $P$  in the wrap angle area [5] can be expressed as

$$P = \frac{3.094\eta(v_r + v)}{R} \left( \frac{R}{\sqrt{\alpha_r^2 + \alpha_w^2}} \right)^{3/2} + P_a \quad (8)$$

where  $v_r$  denotes the roller surface speed,  $\eta$  denotes the dynamic viscosity of air,  $\alpha_r$  denotes guide roller surface roughness,  $\alpha_w$  denotes web surface roughness.

Substituting Eqs. (8) into (7), the traction force  $f_{i-1}$  is obtained.

$$f_{i-1} = \left[ T_{i-1} - 3.094\eta(v_r + v) \left( \frac{R}{\sqrt{\alpha_r^2 + \alpha_w^2}} \right)^{3/2} \right] (e^{\mu\theta} - 1) \quad (9)$$

### 3 The Factors and Laws of Traction Characteristics

The calculation and analysis of the guide roller traction model is based on the parameters of web and guide roller in Shaanxi Beiren FR-400 gravure printing unit. The basic parameters of the web and guide roller are shown in Table 1.

#### 3.1 Influence on Traction Force Due to Web Tension and Wrap Angle

When the web tension varies from 140 to 200 N/m, according to the Eq. (9) and the parameters in Table 1, we acquire variation laws of the traction force and the web tension, as shown in Fig. 2.

The Fig. 2 shows that traction force increases when the web tension bigger increases, and wrap angle is greater, the increase rate of the traction force is bigger.

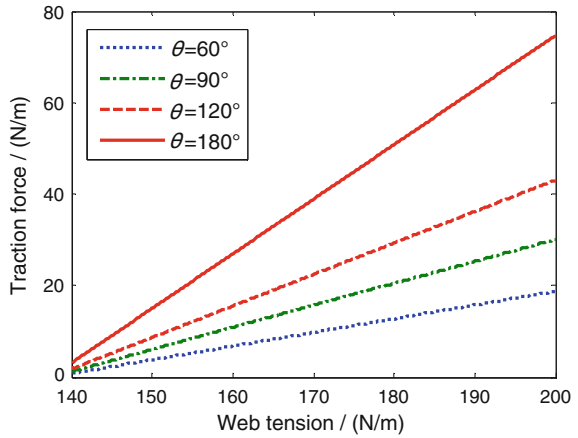
When the wrap angle varies from 60° to 180° and web tension is respectively 140, 160, 180 and 200 N/m, we acquire variation laws of the traction force and the wrap angle, as shown in Fig. 3.

The Fig. 3 shows that traction force increases with the increase of the wrap angle. Due to traction force increases when the web tension increases, and wrap

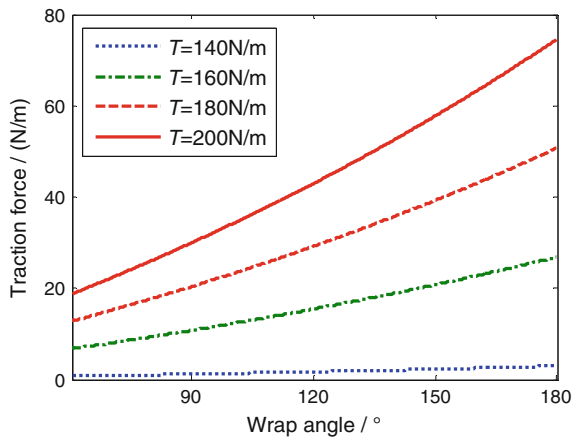
**Table 1** The guide rollers and web parameters

Parameters name	Parameters	
Web speed $v$ (m/min)	$v$	300
Guide roller surface speed (m/min)	$v_r$	300
Dynamic viscosity of air (N s/m <sup>2</sup> )	$\eta$	$1.81 \times 10^{-5}$
Ambient air pressure (Pa)	$P_a$	$1.01 \times 10^5$
The friction coefficient	$\mu$	0.25
Web surface roughness ( $\mu\text{m}$ )	$\alpha_w$	0.66
Guide roller surface roughness ( $\mu\text{m}$ )	$\alpha_r$	15.3
Guide roller radius (mm)	$R$	60
Wrap angle (°)	$\theta$	90
Web tension (N/m)	$T$	200

**Fig. 2** The traction force and web tension



**Fig. 3** The traction force and the wrap angle

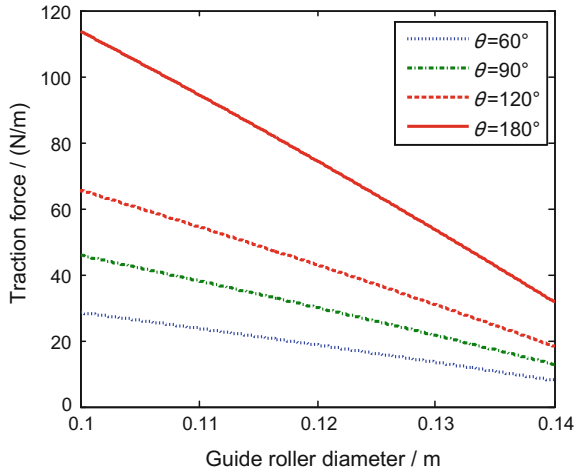


angle is greater, the increase amplitude of the traction force is bigger, and the greater the traction force, the greater the tension changes when the web through the guide roller. Therefore, we should as far as possible to design small wrap angle to improve traction characteristics in the actual production process.

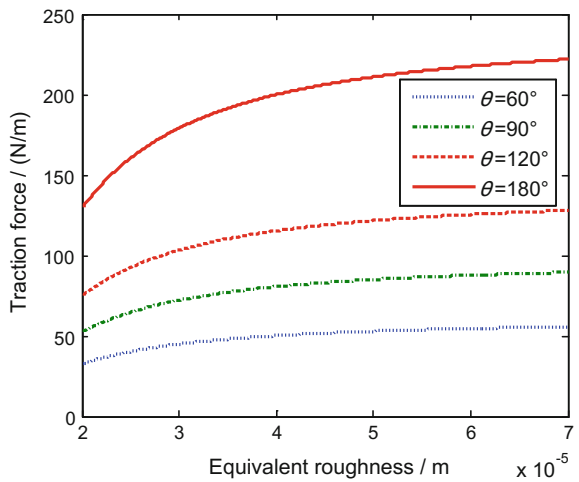
### 3.2 Influence on Traction Force Due to Guide Roller Diameter and Equivalent Roughness

Guide roller diameter increased from 100 mm to 140 mm, the guide roller parameters such as wall thickness is constant, when the wrap angle is respectively 60°, 90°, 120° and 180°, we acquire variation laws of the traction force and the guide roller diameter, as shown in Fig. 4.

**Fig. 4** Guide roller diameter and traction force



**Fig. 5** Equivalent roughness and traction force



The Fig. 4 shows that traction force decreases with the increase of the guide roller diameter. Therefore, we should design small guide roller diameter to improve traction characteristics in the actual production process, and that is based on the stable operation of the guide roller.

Equivalent roughness varies from 20 to 70  $\mu\text{m}$ , and the wrap angle is respectively  $60^\circ$ ,  $90^\circ$ ,  $120^\circ$  and  $180^\circ$ , we acquire variation laws of the traction force and the equivalent roughness, as shown in Fig. 5.

The Fig. 5 shows that traction force increases with the increase of the equivalent roughness when the wrap angle is constant. Therefore, we should improve traction characteristics by increasing equivalent roughness in the actual production process.

## 4 Conclusions

The traction characteristics with the air entrainment between the web and the guide roller are researched. The results show that:

1. Warp angle, web tension, guide roller diameter and equivalent roughness are the main factors affecting the guide rollers traction characteristics. The effects of tension and wrap angle are both analyzed, we should as far as possible to design small wrap angle to improve traction characteristics in the actual production process.
2. The traction force decreases with the increase of the guide roller diameter, and traction force increases with the increase of the equivalent roughness. Therefore, we should improve traction characteristics by increasing equivalent roughness or decreasing guide roller diameter in the actual production process, which is based on the stable operation of the guide roller.

**Acknowledgements** This study is funded by the National Natural Science Foundation of China (Grant No. 51305341, 11272253 and 51505376). This work is also supported by the Natural Science Foundation of Shaanxi (Grant No. 2016JM5023 and 2016JQ5038).

## References

1. Müftü, S., Jagodnik, J.J.(2004). Traction between a web and a smooth roller. *Journal of Tribology*, 126(1), 177–184.
2. Nguyen, Q.C., Hong, K.S. (2011). Stabilization of an axially moving web via regulation of axial velocity. *Journal of Sound and Vibration*, 330 (2), 4676–4688. doi: [10.1016/j.jsv.2011.04.029](https://doi.org/10.1016/j.jsv.2011.04.029).
3. Eshel, A., Elrod, H.G. (1964). The theory of the infinitely wide, perfectly flexible self-acting foil bearing. *Journal of Fluids Engineering*, 87 (4), 831–836.
4. Ducotey, K.S., Good, J.K. (1998). The effect of web permeability and side leakage on the air film height between a roller and web. *Journal of Tribology*, 120(3),559–565.
5. Ducotey, K.S., Good, J.K. (2000). A numerical algorithm for determining the traction between a web and a circumferentially grooved roller. *Journal of Tribology*, 122(3), 578–584.
6. Rice, B.S., Mutu, S., Cole, K.A. (2002). A model for determining the asperity engagement height in relation to web traction over non-vented rollers. *Journal of Tribology*, 124(3), 584–594.
7. Rice, B.S., Gans, R.F. (2005). Predictive models of web-to-roller traction. *Journal of Tribology*, 127(1),180–189.
8. Sasaki, M., Kohno, K., Tanimoto, K., et al. (2007). Traction force between rotating rolls and moving web considering the effect of air-entrainment. *Microsystem Technologies*, 13(8–10), 1161–1167.
9. Si, B.Q.T., Yong, H.Y., Jin, H.K, et al. (2009). Experimental and numerical study of air entrainment between web and spirally grooved roller. *Journal of Tribology*, 131(2), 021502–021509. doi: [10.1115/1.3070582](https://doi.org/10.1115/1.3070582).
10. Aoki, K., Hashimoto, H. (2010). Characteristics of air film thickness and flow visualization for transporting film. *Journal of Fluid Science and Technology*, 5(781), 503–514.

11. Hashimoto, H. (2012). Friction characteristics between paper and steel roller under mixed lubrication. Proceedings of the Institution of Mechanical Engineers. *Journal of Engineering Tribology*, 226 (12), 1127–1140. doi: [10.1177/1350650112461880](https://doi.org/10.1177/1350650112461880).
12. Mongkolwongrojn, M., Jeenkour, P. (2013). Analysis of a flexible web on a grooved concave surface under soft EHL. *Tribology International*, 61, 194–204. doi: [10.1016/j.triboint.2013.01.002](https://doi.org/10.1016/j.triboint.2013.01.002).
13. Zhang, G.Q., Wu, J.M. (2006). Fluid mechanics. Mechanical industry press, Beijing.

# Virtual Design of Web-Fed Typed Paper—Feeding Mechanism with Virtual Prototyping Technology

Hongqiang Wan, Minru Yao and You Li

**Abstract** This paper studies the Web-fed typed paper-feeding mechanism to improve the design quality and shorten the development cycle. The structure of the roll paper feed mechanism is innovative design, which can change paper on reel automatically, and cut off paper easily. Application of virtual prototype technology is used to finish design of the Web-fed typed paper—feeding mechanism through the kinematics analysis with the help from the theoretical design data. The new design method for printing press is given with virtual prototyping technology, the assembly model of this paper-feeding mechanism for virtual prototyping is given and the related motion of the mechanism is simulated through Pro/E software. This method can make design process simply and design cycle short, finally result to bringing much convenience to printing machinery.

**Keywords** Virtual prototyping · Three-dimensional model · Paper-feeding mechanism · Web-fed type · Motion simulation

## 1 Introduction

Printing press may have been invented as early as 13th century, and has been developing with new technologies, especially mechanical development. Recently increasing application of many new technology born over the past few decades, such as the network technology, direct plate-making technology, computer technology, optical fiber transmission and so on, leads to rapid development of intelligent automatic control. The physical prototype has been always used to verify the overall performances of product in the traditional design process, through there are the disadvantages of this process. Some of them are obvious, for example, long production cycle and high cost. Fortunately, virtual prototype technology comes

---

H. Wan (✉) · M. Yao · Y. Li  
Mechanical and Electrical Engineering Institute, Xi'an Technological University,  
Xi'an, China  
e-mail: 413162931@qq.com



into being under the help from development of computer technology, and finds its own way in many fields even taking the irreplaceable role in certain fields.

Virtual prototype has been used in product design and manufacturing as one of key supporting technologies, the most features from it is to make product design faster through the simulation analysis of assembly parts under various working conditions as well as the prediction for the overall performance of the product. The precondition of them is the help from high performance computer and modeling software, which are easily available to common customer at acceptable price, additionally it usually does not take quite a little time and energy to grasp this new technology, which is right for young users, especially undergraduates.

This paper designed a new type of reel used in the send paper machine, to work out replacement of the paper roll problem of rotary intaglio printing press using virtual prototype technology. This new machine is able to change paper automatically and without downtime.

## **2 Summary of Virtual Prototype**

Virtual prototype is the essence of physical prototype on the computer, which emphasizes the characteristics of being systematic and integrity compared with the traditional simulation model. By replacing the physical prototype in the terms of product innovation design, test and evaluation, Virtual prototype makes the development cycle short, production design quality better and cost less much [1, 2].

The development of Virtual Prototyping of printing products can be described as the followings: firstly, product virtual prototype in a virtual environment can be built according to the demand of the product development, secondly, modification scheme of product design can be done based on the results of simulation analysis above, finally the virtual prototype to meet the expected design goal can be gotten through several recycle of repeated modeling/simulation analysis as well as model improvement activities.

## **3 The Application of Virtual Prototype in the Web-Fed Type Paper-Feeding Machine Design**

Printing machinery is a kind of typical mechanical and electrical products with high level of automation. So some high stand requirements in many fields should be met, such as the dynamics and kinematics of mechanical structure and components, as well as the control performance of product. Unfortunately the traditional physical prototype method has been unable to meet the production requirements above; while a good way to solve the above problems is to use virtual prototyping. The design of printing machine using virtual prototype technology is feasible, with

the help from computer components of the three-dimensional modeling and the actual production situation. Additionally, this design can handle various fault quickly, make the design quality and efficiency better, improve the stability and performance of the product, save the production cost to do well to the enterprises [3, 4].

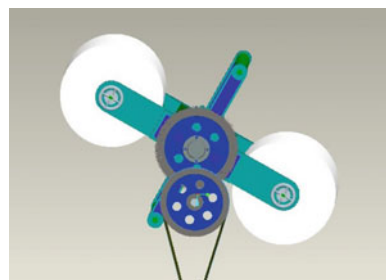
### ***3.1 Innovation Design and Modeling of the Web-Fed Type Paper-Feeding Machine***

To replace the paper roll of printing machinery in traditional way is to pick up paper manually. The printing machinery was shut down when the old paper roll out, the following activities should be done. Firstly unloading the old paper roll spindle, then, taking the new tape on the old paper tape. This way needs a long time to preparation when changing the speed of turning of the roll, so the efficiency is obviously low. What's more, when there are driving slowly down and up, the printing quality cannot be easily controlled and guaranteed, resulting to the low rate of good quality.

This new method to pick up paper automatically is used on the high-speed web press. The new paper roll of tape cement by paper receiving device automatically is printing paper tape, it does not need non-stop when cutting off the old paper immediately, while converting the working position among two paper rolls. So the auxiliary time in process can be reduced substantially and the utilization rate of machines can be improved and waste can be reduced. Paper requirement in terms of quality and tension and joint can be not high in this machine.

This paper gives the center of rotation in the way of paper double roll structure showed in Fig. 1. When the paper roll will be finished being under the status of non-stop, the back-up roll in place are rotated by the force from electric engineers, taking the place of finished paper roll. Then the automatic papers are connected, the circulation in turn begin to work, then the old paper roll was cut off from sending paper machine.

**Fig. 1** Three-dimensional model of structure center of rotary



### 1. Design of the paper roll installation device

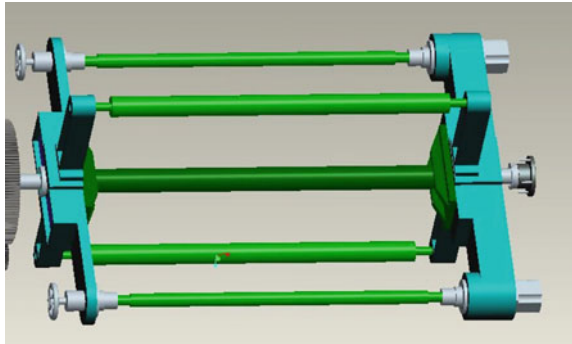
Figure 2 describes the paper scroll driving mechanism and the rotary support paper scroll. The device as feed function has been installed replacing the paper roll used traditionally.

### 2. Design of the transmission system

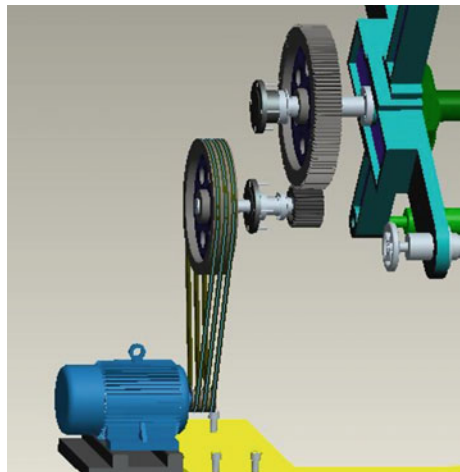
The motor with low speed and high torque of was selected; its full speed was 180 r/min, and the power 1 Kw. Double reduction being belt wheel and then gear were selected in view of rotary bracket driven design retarding mechanism. Gear reduction ratio was 4 and corresponding pulley was 5, so the total reduction ratio was 20, and the rotary speed of the bracket was 9 r/min. The drive system in design was shown in Fig. 3.

The material transmission problem was brought out, due to material in front of the sheet were accelerated to the corresponding speed, and the roll was expected

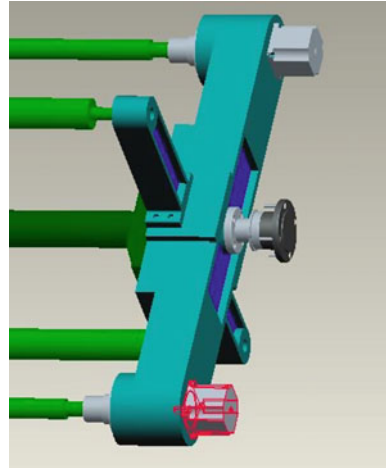
**Fig. 2** Three-dimensional model of scrolls and bracket of rotary paper scroll



**Fig. 3** Three-dimensional model of rotary bracket drive



**Fig. 4** Three-dimensional model of material drive structure



to rotate with the rotation of the rotary bracket. This article selected the stepper motor to drive directly material, and the stepper motor was directly connected to the material on one side of the scrolls, two blocks of material were driven respectively by two stepper motors. The designed structure to drive material was seen in Fig. 4.

### 3. Design of the paper tape guiding system

This system can guide and control the movement of the tape line, which includes the paper guide roller, steering rods and automatic equipment and so on. And this system meets the function of design.

### 4. Design of rack device

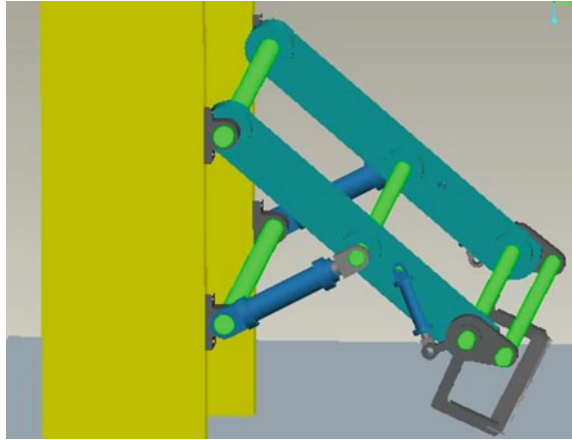
Frame was made up of left and right parts, such as frame and base frame play a role of reel to support the send paper machine bracket, its strength being the larger. This rack was made of casting and increased internal stiffeners to increase the intensity.

Feeder Rack also included the left and right rack and the base frame. The machine frame plays the supporting role of the rotary support of the roll paper feeder requiring a larger strength. The machine frame was processed by the casting, and the reinforcing ribs were added to increase the strength.

### 5. Design of the control device of paper tape cutter

The control device of paper tape cutter was adopted to realize movement like a link mechanism. The device is driven by a hydraulic cylinder, which is an auxiliary device of components collection of paper web presses, and whose role is to take the paper and breaks. The control device of paper tape cutter is shown in Fig. 5.

**Fig. 5** Tape paper control device



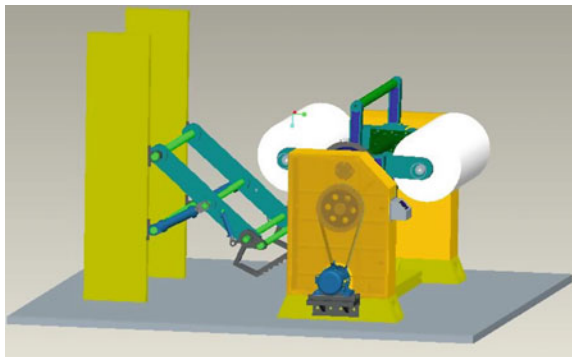
### 3.2 Virtual Prototype Design Based on Pro/E

In this paper, paper feed mechanism by virtual prototype was designed based on Pro/E software. Three-dimensional model of the whole machine was seen in Fig. 6.

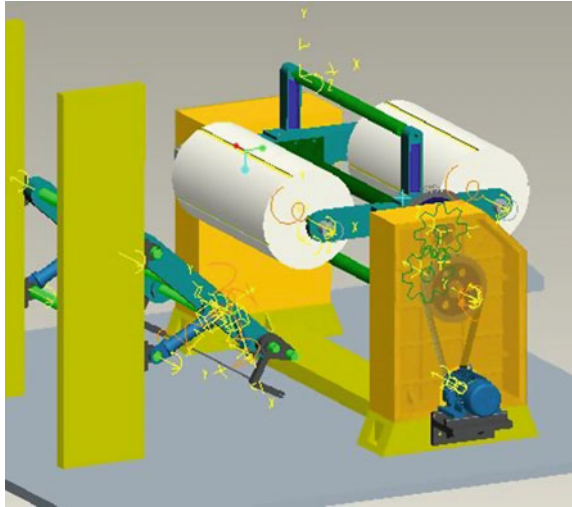
In addition to create the model based on the modeling primitives, a new “Analysis of the definition of” dialog box can be used, to define the analysis (Fig. 7).

Once defined, the analyses were saved. Buttons “Applications”, “Standard” in the environmental agency were clicked to return to the assembly environment. Then, mile such as “analysis”, “Motion Analysis” were clicked to open the “Motion Analysis” dialog box, button “Run” was clicked, the web press Feeder entire movement can be visually seen.

**Fig. 6** Three-dimensional model of the web-fed type paper-feeding whole machine



**Fig. 7** Results have modeled after elements



## 4 Conclusion

In this paper, the structure of the roll paper feed mechanism is innovative design, which can change paper on reel automatically, and cut off paper easily. Application of virtual prototype technology is used to finish design of the Web-fed typed paper—feeding mechanism through the kinematics analysis with the help from the theoretical design data, not like traditional way. This design can simplify the design process, shorten the design cycle, and bring convenience to printing machinery design.

**Acknowledgements** This study is funded by Science and Technology Research and Development Program of Shaanxi Province (2014K09-12).

## References

1. Qiu Haifei, Wang Yixuan. (2014). Research and Development of Digital Prototyping Technology and New Looms. *Cotton Textile Technology*. 42(11), 78–82.
2. CHEN Xiao-xi, WANG Yue-lin. (2008). Application of digital mock-up technology in mechanical system design. *Journal of Tianjin University of Technology and Education*, 18(2), 33–36+54.
3. DU Bao-jiang, LV Wei-bin, LIN Ling, YU Ya-jun. (2009). Simulation of printing system based on virtual prototype technology. *Information Technology*. 33(8), 98–99+101.
4. Xin zheng. (2009). Application of Virtual Prototyping Technology in Printing Mechanical design. *Guangxi Journal of Light Industry*, 25(8), 98–99+101.

# Transducer Torque Control System of the Web Wind-up Tension in Gravure Press

Qiumin Wu, Hanxiao Zhang and Jimei Wu

**Abstract** The correct math model is the basis and the guarantee for the design of the control system. In the paper, the tension control system with torque control is developed. It improves the defect of tension control system with speed control, and the math model of web wind-up control is established in each link. It includes the real-time model of moment of inertia and the rolling diameter, the dynamic model of web wind-up, tension model, the vibrating model for detecting and the frequency control model by vector. The PID controller of wind-up tension system has the good control efficiency, and the performance in torque mode is better than it in speed mode. The tension control system with torque control provides a theoretical basis for the more precise tension control of the gravure press.

**Keywords** Gravure printing machine · Winding tension · Frequency converter · Torque control

## 1 Introduction

Gravure press is the important equipment of printing and packaging industry and the printing material is feed through the roller [1]. After printing, the web is wound by the winding device for the further processing. In the winding process, the tension control system is the key device of gravure press. The factors such as variation of the web diameter, the coil out of round, the jitter of the web and the variation of the

---

Q. Wu · H. Zhang · J. Wu (✉)

Faculty of Printing, Packaging and Digital Media Technology,  
Xi'an University of Technology, Shaanxi, China  
e-mail: wujimei@xaut.edu.cn

Q. Wu

e-mail: wuqiumin@xaut.edu.cn

H. Zhang

e-mail: 1458228137@qq.com

© Springer Nature Singapore Pte Ltd. 2017

P. Zhao et al. (eds.), *Advanced Graphic Communications and Media Technologies*, Lecture Notes in Electrical Engineering 417, DOI 10.1007/978-981-10-3530-2\_97

printing speed have the important influence on the variation of the web tension. Furthermore, it causes the fault and quality defects as follows: the instability of web feeding, the ruffle of web, double image, even the broken and blocked occurred [2, 3]. Therefore, how to maintain a constant tension of the web wound is an important problem.

Today, the shaft of reeling and unreeling is driven by asynchronous motor for cost saving. The rotate speed is adjusted by the converter and then completes the tension adjustment of reeling and unreeling indirectly. In practice, the tension controlled by the speed adjustment has some disadvantage: the web wound is irregular: the web wound is thick in middle and thin in both sides. Meanwhile, the speed control is in low real-time and the precision is not high. So the torque control is adopted in the web winding system of the upscale printing press [4, 5]. But it's more expensive than the converter of speed control. It is urgent to design the device to complete the torque control. In literature [6, 7], the tension control system of printing press was analyzed, the scheme of tension control was present, but the control method was not mentioned. In this paper, the mathematic model of web winding in each stage is established by kinetic theory, and a mathematic model of a complete control system is built.

## 2 Fundamental of the Tension Control in Web Winding

In the whole web winding process, the tension or the taper tension must keep constant. When the coil is small, the tension should be not too large to break the web, and when the coil is big, the web should not be loosening while at the start moment. In acceleration, deceleration or the stop moment, the cases above should not be occurred.

The stress analysis of the web winding device is shown in Fig. 1.

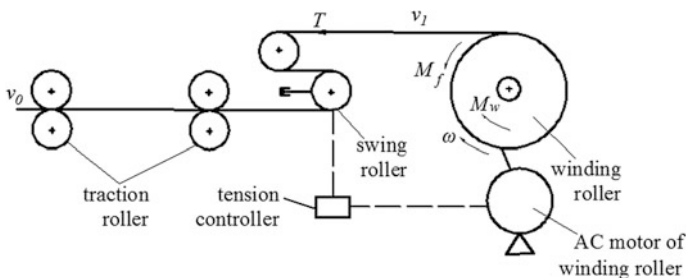


Fig. 1 The stress analysis of the web winding device



### 2.1 Tension Model

The web is driven by the carry-over pinch rolls; its linear speed is equal to working speed  $v_1$  of printing press. The linear speed of wind-up roller is  $v_2$ ,  $T$  is the web tension before winding,  $E$  is the elasticity modulus of web,  $A$  is the cross sectional area,  $L$  is the length from wind-up roller to vibrating roller nearest. On the basis of Hooke's law, Eq. (1) obtained [8].

$$T = \frac{EA}{L} \int_0^t (v_1 - v_0) dt \tag{1}$$

If the tension of web should be controlled, the speed difference  $v_1 - v_0$  must be controlled. So the tension control system is also a linear speed tracking system. The linear speed of the web can be kept in a relatively constant state by the control system which adjusted the rotational speed of each link in real time.

### 2.2 Winding Device Model

The winding device is composed of alternating current dynamo for web wind-up, wind-up roller, vibrating roller, pulling roller and tension controller. The vibrating roller is to detect load tension, and then it is magnified and sent to the controller with microprocessor as the core. The tension controller synthesizes and feeds back tension, output control signals [9]. The transducer controls the alternating current dynamo, then acts on shaft, the closed-loop tension control system is developed.

Based on the load relation, the torque equilibrium equation of tension system is obtained as Eq. (2).

$$\frac{d}{dt}(J\omega) = M_w - Fr - M_f \tag{2}$$

In Eq. (2),  $M_w$  is electromagnetic torque,  $M_f$  is moment of resistance,  $r$  is roller diameter winding in real time,  $\omega$  is angular velocity,  $J$  is uniaxial equivalent moment of inertia.

Suppose that the density of web is  $\rho$ , acceleration of gravity is  $g$ , mandrel radius of wind-up roller is  $r_0$ , and Eq. (3) can be developed:

$$J_r = \frac{1}{2} \pi \rho g b (r^4 - r_0^4) \tag{3}$$

For  $J = J_0 + J_L = J_0 + J_{l_0} + J_l$ , Then  $\frac{dJ}{dt} = 2\pi\rho g b r^3 \frac{dr}{dt}$  (4)

$$\frac{i\omega}{n_p} = \frac{2\pi n}{60} \tag{5}$$

Induce Eqs. (4) and (5) to Eqs. (2), (6) is obtained.

$$M_w - Fr - M_f = P_1 n r^3 \frac{dr}{dt} + P_2 [J_0 + J_l + \frac{1}{2} \pi \rho g b (r^4 - r_0^4)] \frac{dn}{dt} \tag{6}$$

Where  $P_1 = \frac{2\pi n_p}{60i} \frac{2\pi \rho g b}{r^2}$ ,  $P_2 = \frac{2\pi n_p}{60r}$ ,  $P_1$  and  $P_2$  are constant. Equation (6) is the torque equation of motor. The winding tension  $T$  is relation to winding radius  $r$  in real time and motor speed  $n$ .

Tension model input is the voltage signal in torque mode. The relationship between voltage signal and drive roller speed and the tension is obtained [10].

$$J(t) \frac{d\omega(t)}{dt} = (T_r - T(t))R(t) + C u(t) - f\omega(t) \tag{7}$$

Equations (6) and (7) together form a mathematical model of the winding-tension system of a gravure machine in torque mode, in which the voltage signal  $u(t)$  is the system input and  $T(t)$  is the system output.

### 3 Tension System Controller Design

#### 3.1 PID Controller

Tension control is a bottleneck to improve the performance of the gravure printing machine. In the tension system controller design, the factors such as the system parameters and the coupling of controlled quantity are all considered. Moreover, all kinds of interference factors have an important efficiency on the control system.

PID control is an easy and effective method for tension control. In the design of the close-loop controller for the tension system output feedback in gravure press, PID control is adopted. On the basis of the close-loop, the PID controller is designed as Fig. 2.

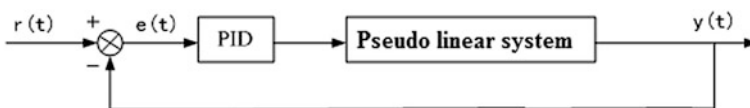


Fig. 2 PID control diagram of winding tension system

### 3.2 Simulation Study of PID Controller in Torque Mode

In order to test the control performance of PID controller in torque mode, the simulation study is developed. The fixed step mode is chosen and the step is 10 ms. The parameter of the PID controller is as shown in Table 1. All the parameters is obtained as  $R_1 = 0.05$  m and  $\omega_c = 200$  r/min.

While  $\omega_c = 200$  r/min and  $R$  is equal to 0.05, 0.1 and 0.2 m respectively, make the tension in each period from 0 up to 50 N, The simulation curve of robust performance controller PID torque mode is as shown in Fig. 3.

As is shown in Fig. 3, with the decrease of the  $R$ , the performance of controller PID in torque is varied in a certain degree. While  $R$  is equal to 0.2 and 0.05 m respectively, the overshoot of the tension is 5.4 and 16.2%. When  $T$  reaches to the steady state, the time is 0.5 and 0.7 s respectively and the time is shorter than the speed mode.

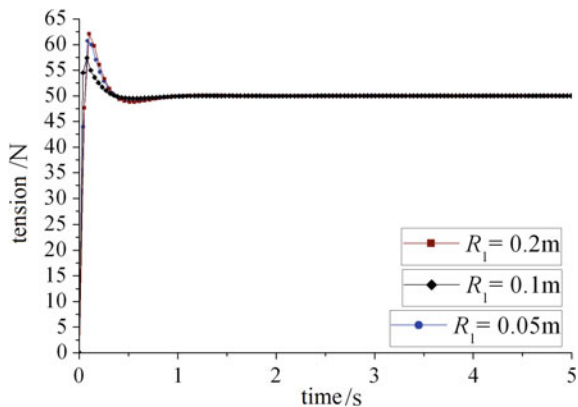
While  $\omega_c = 200$  r/min and  $R$  is equal to 0.2, 0.1 and 0.05 m respectively, and after tension  $T$  reaches to the steady value (50 N) 1, 2 and 3 s, the system has the step disturbance of 10, 2 and 2 N. The simulation curve of anti jamming performance of PID torque controller mode is shown in Fig. 4.

As is shown in Fig. 4, the wind-up tension fluctuated. While  $\omega_c = 200$  r/min and  $R_1 = 0.2$  m, the amplitude of fluctuation is 3.1% and it's smaller than the fluctuation in the speed mode. The tension error in PID controller decreased with the decrease of  $R$ . Compared with speed mode, the duration of the error of tension  $T$  is shorter and its performance is better. Meanwhile, it can be seen the PID controller has the better anti jamming capability.

**Table 1** Parameters of PID for tension control system in torque mode

PID controller	Parameter
PID	$K_{P1} = 18; K_{I1} = 70; K_{D1} = 1.8$

**Fig. 3** The simulation curve of robust performance of controller PID in torque mode



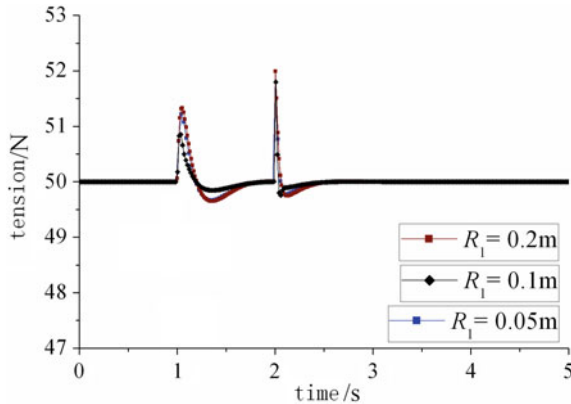


Fig. 4 The simulation curve of anti jamming performance of PID torque controller mode

## 4 Conclusions

Based on the dynamic principle, all links of winding device under stress and their motion process are analyzed, and then mathematic model of a complete N control system is built. The simulation results showed that the PID controller of wind-up tension system has the good control efficiency, and the performance in torque mode is better than it in speed mode. The results provide a theoretical basis for further study in tension control system in gravure press.

**Acknowledgements** This study is funded by national natural science foundation of China (11272253, 11302003) and natural science foundation of Shaanxi (2014JM7290).

## References

1. Hu Gengsheng. (2005). Gravure printing technology. Chemical Industry Press, Beijing.
2. Wang Shuhua, Zhu Songlin. (2005). Usage and regulation of modern gravure press. Beijing: Chemical Industry Press.
3. Zhang Chenghui, Cui Naxin, Li Ke. (2008). Ac motor frequency control of motor speed and its application. Mechanical Industry Press, Beijing.
4. Zhang Haiyan, Zheng Junjun, Yanglei. (2009). Tension control system of the web winding. Light Industry Machinery, 27(5), 52–55.
5. Liu Rong, Jiang Song. (2009). Nonlinear finite element modeling of the tension device in the skin pass mill for hot strip. *Mechanical & Electrical Engineering Magazine*, 26(8), 21–24.
6. SHENG Weifeng, ZHOU Yijie, JIANG Min. (2001). Controlling Tension on Printing Machines. *Packaging Engineering*, 22(2), 4–7.
7. Tang Guolan, Chen Linshan, Wu Yunzhong. (2003). Tension control and application based on AC convector. *Packing and Food Machinery*, 21(5), 34–36.

8. Liu Guoqing. (2002). The control system of printing machine. Kunming: Kunming University of Science and Technology.
9. Zhang Haiyan, Xu Jingling, et al. (2010). Research on modeling frequency conversion winding tension control system in gravure press, *Light Industry Machinery*, 28(4), 60–63.
10. Liu Shanhuai, Mei Xuesong. (2014). Decoupling controller design for unwinding tension system, *Journal of Xi'an Jiaotong University*, 23(12), 39–41.

# Study on the Flow Mixing Results of Revolving Static Mixer Used in Solventless Laminator

Hongwei Xu, Wei Li, Xusheng Wang, Hang Zhang and Donghong Liu

**Abstract** For solventless lamination, the mixing process of A/B materials adds a significant value to the performances of solventless lamination adhesives. Static mixers are always the main device of the solventless laminator to be used to mix A/B materials. Both design and operation of mixing unit itself has a strong effect on the quality of final product of lamination. In this paper, Fluent software is used to develop the two dimensional models of flow mixing process within the static mixer under different status. One static mixer is revolving during the mixing process, the other one is static during the mixing process. The simulation results show that the result of mixture process within the revolving static mixers is much better than the result of mixture process within the static mixer which did not revolve. Through this simulation and analysis, the revolving static mixer is recommended to be used in the situation where it is strict required for the mixing results, though the structure of revolving static mixer is complicated. This research will supply a good help for the design of solventless laminating machine.

**Keywords** Solventless laminator · Revolving static mixer · Simulation · Mixing quality

---

H. Xu (✉) · W. Li · X. Wang · H. Zhang  
Xi'an University of Technology, Xi'an, China  
e-mail: xuhongwei@xaut.edu.cn

W. Li  
e-mail: 846561809@qq.com

X. Wang  
e-mail: Xusheng.Wang@hotmail.com

H. Zhang  
e-mail: 361805337@qq.com

D. Liu  
Weinan Outai Printing Machinery Technology Co. Ltd., Weinan, Shaanxi, China  
e-mail: ldh200588@126.com

## 1 Introduction

Solventless laminating allows the A/B materials mixing processing without toxic, “non-friendly” solvents [1]. Therefore, the lamination materials don’t need drying and not volatile a harmful gas which pollute the environment. Now, solventless lamination technique is widely used in flexible packaging products [2]. Solventless lamination machine includes solventless lamination adhesive mixing machine which is used to mix the A/B lamination adhesives, and lamination machine which is used to make two kinds of materials into one lamination material [3].

Static mixer has the advantages of energy saving and structure simple. Therefore, static mixer is widely used in most lamination machine. There are two parts in static mixer. One is an inserts and the other is a tube. The inserts’ function is cut, fold twist and re-combine fluid elements to make the fluid elements mixing enough [4]. For laminating adhesives, the mixing of A/B materials is important. The mixing quality mostly depends on the static mixer. Because the obvious advantages of static mixer, In many industry, various type static mixers are used. But in practical, the information about flow and mixing in static mixers is few [5].

In order to improve the mixing quality, Brandao et al. [6] use a revolving static mixer to mix materials. There are several factors of structure or process which have an influence on the mixing quality. For the mixing process, there are a lot of researches. The mixing process of static mixer is often studied with some simulation software. Jovanovic et al. [7] use the discrete element method (DEM) to model granular flow in various multiple Komax and Ross mixing applications, and model the fluid flow through the Eulerian multiphase model with computational fluid dynamic (CFD) method. In this paper, the effect of revolving static mixer on the mixing result is investigated through simulation.

## 2 Mathematical Model Descriptions

The simulations are based on the solution of conservation equations of mass, momentum and energy. The fluid flow problems of continuity equation, momentum equation and energy equation can all be expressed by the follow general variable equation.

$$\frac{\partial(\rho u \phi)}{\partial t} + \text{div}(\rho u \phi) = \text{div}(\Gamma \text{grad} \phi) + S \quad (1)$$

where  $u$  is the velocity of fluid (m/s),  $\phi$  is general various parameters,  $\rho$  is the density of fluid ( $\text{kg/m}^3$ ),  $\Gamma$  is the generalized diffusion coefficient,  $\text{div}$  is the divergence function of vector function,  $S$  is the generalized source item,  $\text{grad}$  is the gradient function of vector function.

Mixture model is a simple multiphase model which is used to simulate the fluid flow under different speeds of double phase or multiphase. Through solve the Eq. (1), the mixture flow process can be studied.

Hobbs et al. [8] study the relation between the mixing results with velocity field. They gave the values for each component of the rate of strain tensor  $D$  as:

$$D = \frac{1}{2}(\nabla u + \nabla u^T) = \frac{1}{2} \begin{vmatrix} 2 \frac{\partial u_x}{\partial x} & (\frac{\partial u_x}{\partial y} + \frac{\partial u_y}{\partial x}) & (\frac{\partial u_x}{\partial z} + \frac{\partial u_z}{\partial x}) \\ \frac{\partial u_x}{\partial y} + \frac{\partial u_y}{\partial x} & 2 \frac{\partial u_y}{\partial y} & (\frac{\partial u_y}{\partial z} + \frac{\partial u_z}{\partial y}) \\ \frac{\partial u_x}{\partial z} + \frac{\partial u_z}{\partial x} & \frac{\partial u_y}{\partial z} + \frac{\partial u_z}{\partial y} & 2 \frac{\partial u_z}{\partial z} \end{vmatrix} \quad (2)$$

The whole value of the rate of strain tensor is expressed by  $\zeta$ :

$$\zeta = \frac{1}{2} |D : D|^{\frac{1}{2}} = \frac{1}{2} \left| \sum_i \sum_j D_{ij} D_{ji} \right|^{\frac{1}{2}} \quad (3)$$

For tetrahedral mesh,  $\zeta$  can be expressed as:

$$\zeta = [(\frac{\partial u_x}{\partial x})^2 + (\frac{\partial u_y}{\partial y})^2 + (\frac{\partial u_z}{\partial z})^2 + \frac{1}{2}(\frac{\partial u_x}{\partial y} + \frac{\partial u_y}{\partial x})^2 + \frac{1}{2}(\frac{\partial u_x}{\partial z} + \frac{\partial u_z}{\partial x})^2 + \frac{1}{2}(\frac{\partial u_y}{\partial z} + \frac{\partial u_z}{\partial y})^2]^{\frac{1}{2}} \quad (4)$$

Using mixing parameter  $\beta$  express the ratio of the phase boundary area of time  $t$  to the phase boundary area of initial time  $t_0$ .

$$\beta = \frac{a_t}{a_{t0}} \quad (5)$$

The relationship of  $\beta$  changing rate of time with the strain rate tensor can be express as:

$$\frac{d\beta}{dt} = \varphi(E:E)^{\frac{1}{2}} \quad (6)$$

This mixing efficiency is a measure of the rate of phase interface growth which can be called the upper bound of mixing efficiency.

### 3 Simulation Model and Computing

Generally, the flow field within the static mixer is difficult to be computed by analytical solution. The inserters of static mixer are often composed of a number of helical blades. And these blades are all twisted. These twisted blades can make the different material mixing. In this paper, two different static mixers model are



founded and the mixing processes are studied. One static mixer is static when the A/B material mixing. And the other static mixer is revolving during the A/B material mixing.

The 3D model of the these two static mixer is founded and meshed with Gambit. The model is imported to Fluent software and the computing regime is determined.

In this simulation, the standard  $k - \epsilon$  turbulence model equation is chosen. Two inlets are set as flow velocity inlets. And the wall function is chosen as enhanced wall treatment. The outlet is set as pressure outlet. The pipe wall is set as wall. The fluid is set as self-determine fluid. The material A's density and viscosity are 1.12 and 1.1 kg/ms, and the material B's density and viscosity are 0.98 and 0.7 kg/ms. The finite volume method is used to solve the governing equation.

### 4 Simulation Results and Discussions

Numerical simulations are performed for static mixers with different status of different static mixer structure. The mixing results are obtained via CFD calculations. Figure 1 is a simulation result of mixing process within a corrugated plate static mixer which is not revolving during mixing process.

Figure 1 shows the contour chart of the volume fractions of mixing of A/B materials. In order to make the mixing results clear, the mixing volume

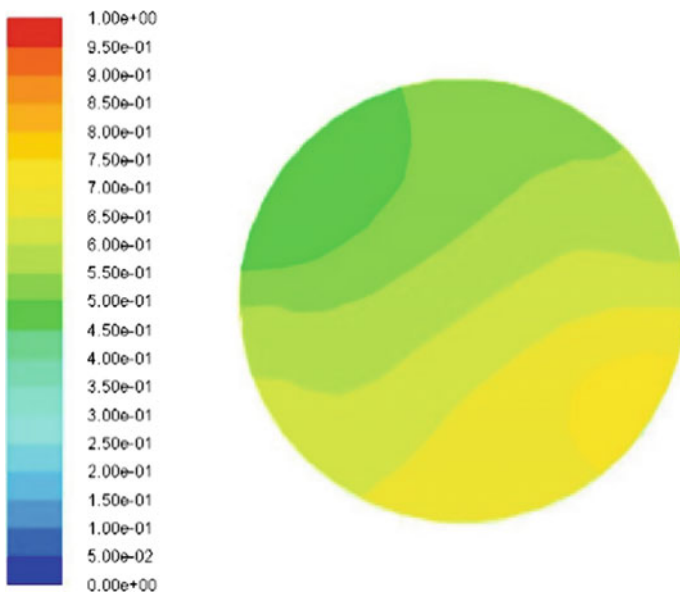
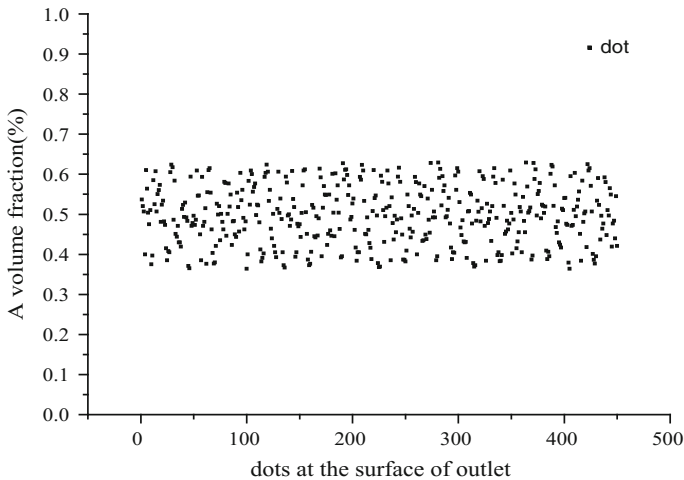


Fig. 1 Contour chart of mixing process in outlet of static mixer which is static



**Fig. 2** Scatter graph of volume fractions at the surface of outlet

fraction information of every dot is extracted and the scatter graph is plot as shown as Fig. 2.

Figure 2 shows that the mixing volume fractions of all dots at the surface of outlet are not all 50%. Some dots' volume fractions are higher than 60%, and some dots' volume fractions are less than 40%. Through computing, the mean value of the mixing volume fractions of all these dots is 0.49782, and the standard deviation is 0.06. This means it can make the mixing not very evenly that if mix the A/B material of solventless laminating adhesives by the static mixer which is not revolving. Therefore, the mixing simulation is done to mix the A/B material of solventless laminating adhesives by the static mixer which is revolving.

The Fluent software is used to simulate the mixing process. The parameters are set just as the first set. The speed of the revolving static mixer is set as 30 r/min. Figure 3 is the simulation result of mixing process within a corrugated plate static mixer which is revolving during mixing process.

Figure 3 shows the contour chart of the volume fractions of mixing of A/B materials. In order to make the mixing results clear, the mixing volume fraction information of every dot is extracted and the scatter graph is plot as shown as Fig. 4.

Figure 4 shows that the mixing volume fractions of all dots at the surface of outlet are basically distribute around the mean value of 0.5 which means the proportion of A/B materials is 1:1. Through computing, the mean value of the mixing volume fractions of all these dots is 0.5, and the standard deviation is 4.18E-8. This simulation results are compared with the simulation results which is shown in Fig. 2. The mixing result of the A/B materials of solventless laminating adhesives on the situation of the static mixer is revolving is much better than the mixing result of the A/B material of solventless laminating adhesives on the situation of the static mixer is revolving.

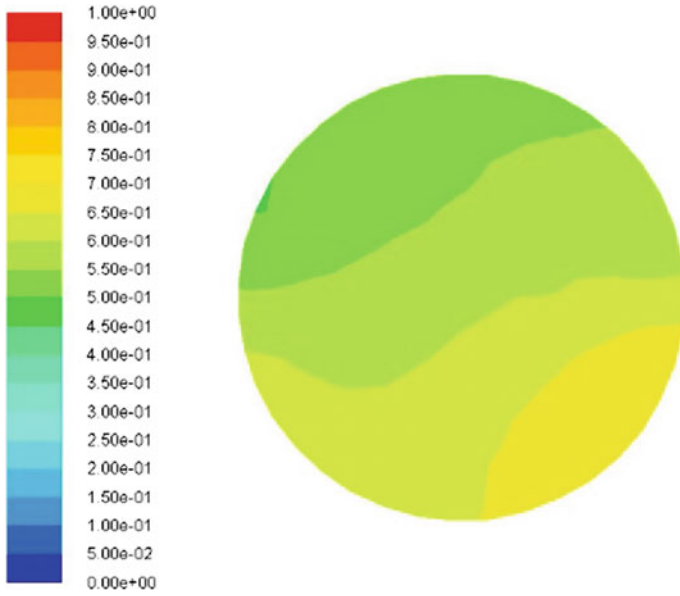


Fig. 3 Contour chart of mixing process in outlet of static mixer which is revolving

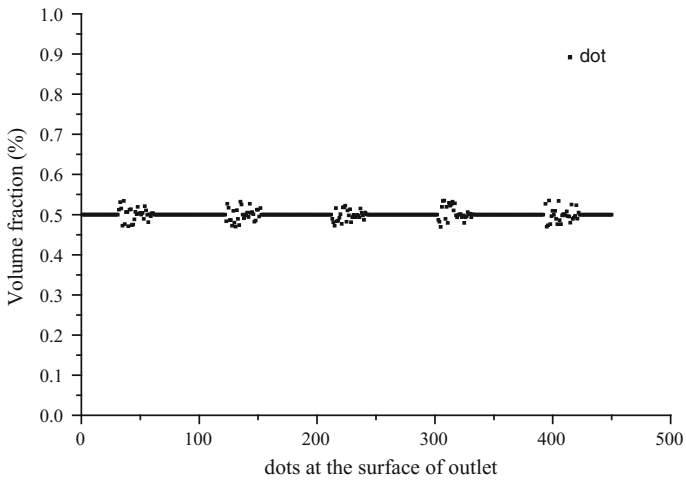


Fig. 4 Scatter graph of volume fractions at the surface of outlet

## 5 Conclusions

The mixing process of A/B materials of solventless laminating adhesives on the different situations are simulated by using the Fluent software. The results are analyzed and the conclusions are gotten. The results show that the mean value of the mixing volume fractions of all these dots of the outlet surface of static mixer which is not revolving is 0.49782, and the corresponding standard deviation is 0.06. In comparison, the mean value of the mixing volume fractions of all these dots of the outlet surface of static mixer which is revolving is 0.5, and the corresponding standard deviation is  $4.18E-8$ . This simulation is done in the condition that the proportion of A/B materials is 1:1. The value 0.5 of volume fractions means the mixing is complete. This study will remind the user of static mixer that using the static mixer to mix the A/B materials of solventless directly can make the mixing complete. There will be a big error in the mixing efficiency. Therefore, it is better to mixing the A/B materials of solventless under the situation of the static mixer is revolving.

**Acknowledgements** This work was financially supported by the Shaanxi Province Education Department Service Special Plan Project Foundation (14JF018).

## References

1. Lucia Brandao, David G. Bucknall, Gabriel Bernardo (2013). Solventless processing of conjugated polymers-A review. *Synthetic Metals*, 197, 23–33.
2. Lv ling, Xu Wencai, Zuo Guangshen (2010). Characteristics research about coating system of solventless laminator. *Proceedings of the 17<sup>th</sup> IAPRI World Conference on Packaging*.
3. Hongwei Xu, Hang Zhang, Donghong Liu. Characteristics research of static mixer used in solventless laminator (2015). *2015 4th China Academic Conference on Printing and Packaging*.
4. E. Saadjan, A.J.S. Rodrigo, J.P.B. Mota (2012). On chaotic advection in a static mixer. *Chemical Engineering Journal*, 187, 289–298.
5. Vimal Kumar, Vaibhav Shirke, K.D.P. Nigam (2008). Performance of Kenics static mixer over a wide range of Reynolds number. *Chemical Engineering Journal*, 139, 284–295.
6. Milada Pezo, Lato Pezo, Aca Jovanovic et al. (2016). DEM/CFD approach for modeling granular flow in the revolving static mixer. *Chemical Engineering Research and Design*, 109, 317–326.
7. Aca Jovanovic, Milada Pezo, Lato Pezo et al (2014). DEM/CFD analysis of granular flow in static mixers. *Powder technology*, 266, 240–248.
8. D.M. Hobbs, P.D. Swanson and F.J. Muzzio (1998). Numerical characterization of low Reynolds number flow in the Kenics static mixer. *Chemical Engineering Journal*, 97, 1565–1584.

# Effect of High Temperature on Morphology and Structure of a New Composite as Raw Material of Filament for Fused Deposition Modeling Processes

Yonghao Xiao, Jia Yan, Kun Hu, Lin Zhu, Shun Pan, Luhai Li and Yen Wei

**Abstract** Hydroxyapatite and collagen are mainly inorganic and organic components of human natural bone. Nanocrystal hydroxyapatite/collagen (nHAC) composite has good biological properties, and polylactide (PLA) is a biodegradable polymer material. Both can be well applied to organism and play a critical role in bone tissue engineering materials. In this paper, a new nano-hydroxyapatite/collagen/PLA composite with the thought of bionics as raw material of filament for fused deposition modeling (FDM) processes was developed in order to observe the thermal structure properties of the new filaments. The structure and components of the samples were investigated by energy dispersive spectrograph (EDS), X-ray powder diffraction (XRD), Scanning Electronic Microscopy (SEM) and Fourier transform infrared (FTIR). The results of FTIR and XRD showed that the nHAC/PLA changed greatly at 220 and 240 °C compared with the room temperature. And SEM and EDS showed that nHAC/PLA had a complete microstructure and components at 200 °C.

**Keywords** High temperature · nHAC/PLA · Filament · Morphology · Structure

## 1 Introduction

3D printing is a kind of rapid additive manufacturing technology [1, 2] which is usually divided into the following categories, SLA (Stereo Lithography Apparatus), SLS (Selective Laser Sintering), FDM (Fused Deposition Modeling), CLIP

---

Y. Xiao · J. Yan · K. Hu (✉) · L. Zhu · S. Pan · L. Li · Y. Wei  
Beijing Engineering Research Center of Printed Electronics,  
Beijing Institute of Graphic Communication, Beijing, China  
e-mail: hukun@bigc.edu.cn

L. Li  
e-mail: liluhai@bigc.edu.cn

Y. Wei  
Tsinghua University, Beijing, China

(Continuous Liquid Interface Production), etc. [3–5]. This kind of 3D printer, FDM, uses nozzle to create high temperature making the materials melted into liquid. After the materials are squeezed out from the nozzle and would cool down at room temperature within a few seconds. With this way, the complicated shapes would be manufactured. 3D machine of FDM is easy to operate and cheap, and the material it used is filament [6].

Bone defects and bone repair are important subjects of bone tissue engineering. Autograft can solve rejection phenomenon and immune response. However, the bone's quantity in autograft and secondary damage are two main problems [7–9]. Using bionics principle and based on conventional synthesis of collagen-tricalcium phosphate composite, the nano-hydroxyapatite/collagen (nHAC) we synthesized has good biocompatibility [10, 11] and will be widely used in biomaterials. Polylactic acid materials could provide porous spatial structure which are similar to natural bone and have good cell affinity [7–9, 11].

nHAC/PLA composites [7–9] have all the advantages of each raw materials and whether it could be printed by the FDM printer. Therefore, this article focuses on the high temperature performance of nHAC/PLA composite frame materials [7–9], especially the morphology and structure properties.

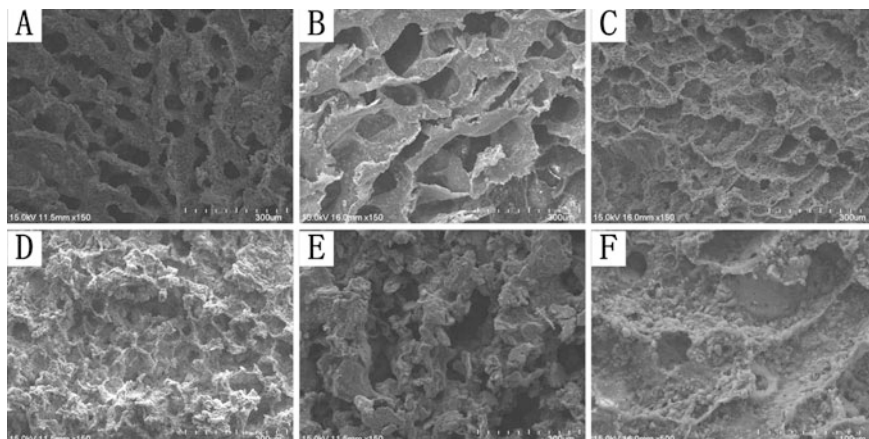
## 2 Materials and Methods

Nano-hydroxyapatite/collagen composite were prepared at room temperature via biomimetic self-assembly. nHAC/PLA with the proportion of 1:1 were mixed by ultrasonic dispersion for 30 min, the samples were obtained after cooling down in Teflon molds.

Under atmosphere, nHAC/PLA was conducted at room temperature, 180, 200, 220 and 240 °C for 10 min respectively. The morphology of nHAC/PLA was examined with scanning electron microscopy (SEM) and energy dispersive spectrograph (EDS). FTIR and XRD are also used to characterize the morphology and structure properties of products.

## 3 Results and Discussion

Years past, the property of nHAC/PLA composite frame material has been wildly studied. In this paper, SEM of nHAC/PLA at different temperatures was showed Fig. 1. From the SEM images, it was easy to see that the composite materials have porous structure. The macropore's diameter was about 100  $\mu\text{m}$ , and there were also many of porous between two macropores, whose diameter were about 4.5  $\mu\text{m}$ . The image of nHAC/PLA at 180 °C (B) was similar to (A), while images of the



**Fig. 1** SEM pictures of nHAC/PLA conducted at different temperatures for 10 min (a) image at room temperature, (b) image at 180 °C, (c) image at 200 °C, (d) image at 220 °C, (e) image at 240 °C, (f) image at 200 °C and at 500X (b) was similar to (a), but nHAC/PLA in (d) and (e) agglomerated

nHAC/PLA at 220 °C (D) and 240 °C (E) changed greatly compared with (A) and (B). Image (C) was a transitional stage, for it has the structure of porous and macroporous. Meanwhile, it had little agglomeration compared with image (E). The last image (F) is an enlarged picture of image (C). The temperature less than 200 °C is viable according to the SEM results. Consequently, a good morphology and structure could be obtained below 180 °C and a barely satisfactory below 220 °C.

Tables 1, 2 and 3 shows the result of nHAC/PLA varying at different temperatures measured by EDS. Weight ratio of oxygen and carbon were ranging from 29.05 to 38.35% and 29.18 to 47.16% at these four temperatures. It is believed that the composite materials have a relatively stable performance below the temperature of 220 °C from Tables 1 and 3, and 200 °C will be a proper temperature.

The structural development of the composites was further demonstrated by FTIR spectroscopy. The great difference of the composite materials processed at 240 °C for 10 min was shown in Fig. 2. Phosphate peaks appeared at 1030, 600, and 561  $\text{cm}^{-1}$  in those spectrums. The amide A peaks of nHAC/PLA at 180, 200, 220 and 240 °C were lower than the one at room temperature, indicating that N–H bonds in the amino groups were probably destroyed partly under high temperature. Also, the peak appeared at 1087  $\text{cm}^{-1}$  was C–O stretch. Generally speaking, the materials may be destroyed partly under high temperature, especially more than 240 °C.

The five calculated intensity curves are identical with each other except under 240 °C. The pattern and peak intensity proportion of curve were similar with pure hydroxyapatite (HA) which could be speculated the inorganic phases of the samples were hydroxyapatite (HA). The X-ray diffraction results (Fig. 3) shows that the

**Table 1** EDS results of nHAC/PLA at different temperatures for 10 min

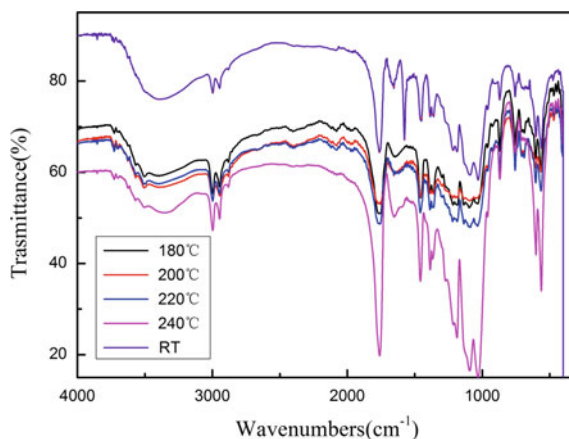
Element	Weight ratio (%)				
	Room temperature	180 °C	200 °C	220 °C	240 °C
Carbon	38.28	47.16	45.79	36.51	29.18
Oxygen	38.32	31.46	38.35	29.05	36.67
Calcium	17.78	15.72	11.14	24.48	25.03
Phosphorus	5.62	5.65	4.72	9.96	9.12

**Table 2** EDS results of nHAC/PLA at different temperatures for 10 min

Element	Atomic ratio (%)				
	Room temperature	180 °C	200 °C	220 °C	240 °C
Carbon	51.34	60.71	57.42	55.52	43.08
Oxygen	38.59	30.41	36.1	31.37	40.62
Calcium	7.15	6.06	4.18	10.55	11.07
Phosphorus	2.92	2.82	2.29	5.56	5.22

**Table 3** EDS results of nHAC/PLA at different temperatures for 10 min

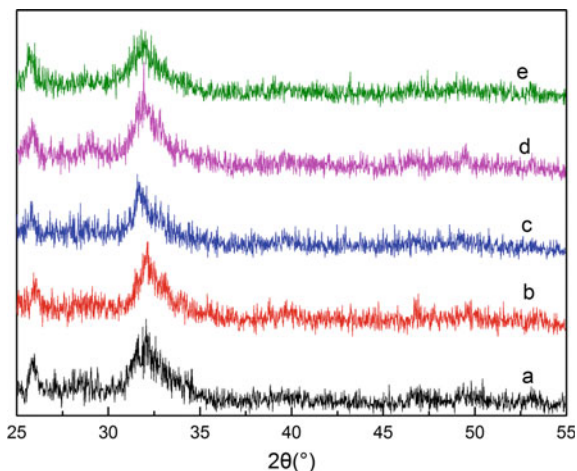
Specific value	Temperature				
	Room temperature	180 °C	200 °C	220 °C	240 °C
Ca/P	2.45	2.15	1.83	1.90	2.12

**Fig. 2** Infrared spectrum of nHAC/PLA processed at different temperatures for 10 min under atmosphere

broadening peaks of the nHAC composite processed at room temperature were consistent with those at 180, 200 and 220 °C, both similar to previous report. The results demonstrated that the crystal character of HA under 220 °C was identical with the one at room temperature. Above 240 °C was greatly changed compared with the other composite materials under 220 °C.



**Fig. 3** XRD patterns of nHAC/PLA processed at different temperatures for 10 min under atmosphere (a) room temperature, (b) 180 °C, (c) 200 °C, (d) 220 °C, (e) 240 °C



## 4 Conclusions

The research of morphology and structure of nHAC/PLA processed at high temperature is rare because of the existence of collagen. The results of FTIR and XRD for nHAC/PLA changed greatly from 220 to 240 °C in comparison with room temperature. SEM and EDS show that nHAC/PLA have a complete microstructure and components at 200 °C. It can be concluded that the morphology and structure of nHAC/PLA at 200 °C were similar to those at room temperature and nHAC/PLA has the possibility to be applied in heating process. Furthermore, we could use this composite to make filament for FDM 3D printing. Of course, the biological function and degrade and mechanical properties need to be further researched.

**Acknowledgements** This study is funded by Horizontal issues—cerebrovascular stent surface printing coating technology (Grant No. 11000300378), University scientific research project—3D Printing mineralized collagen-based child mandible (Grant No. 20190116002/037), The functionalization of graduation design—packing biodegradable polyester (Grant No. 22150116004/007), Students research—Medical X-ray imaging measurement tape prepared by screen printing (Grant No. 22150116005/074) and Initial Funding for the Doctoral Program of BIGC (Grant No. 27170116005/055).

## References

1. Zhai Y, Lados D A, Lagoy J L. Additive Manufacturing: Making Imagination the Major Limitation[J]. *Jom the Journal of the Minerals Metals & Materials Society*, 2014, 66(5):808–816.
2. Satyanarayana B, Prakash K J. Component Replication Using 3D Printing Technology [J]. *Procedia Materials Science*, 2015, 10:263–269.
3. Gross B C, Erkal J L, Lockwood S Y, et al. Evaluation of 3D printing and its potential impact on biotechnology and the chemical sciences[J]. *Analytical Chemistry*, 2014, 86(7):3240–53.

4. Tumbleston J R, Shirvanyants D, Ermoshkin N, et al. Additive manufacturing. Continuous liquid interface production of 3D objects[J]. *Science*, 2015, 347(6228):1349–1352.
5. Gibson I, Rosen D, Stucker B. Additive Manufacturing Technologies[M]. 2015.
6. Vijayaraghavan V, Garg A, Lam J S L, et al. Process characterisation of 3D-printed FDM components using improved evolutionary computational approach[J]. *International Journal of Advanced Manufacturing Technology*, 2014, 78(5–8):781–793.
7. Liu B, Chen P. The study on preparation and ectopic osteogenesis capacity of active nano hydroxyapatite/collagen/PLA[J]. *Chinese Journal of Prosthodontics*, 2009.
8. Liu X, Liu H Y, Lian X, et al. Osteogenesis of mineralized collagen bone graft modified by PLA and calcium sulfate hemihydrate: in vivo study[J]. *Journal of Biomaterials Applications*, 2013, 28(1):12–19.
9. Liao S S, Cui F Z, Zhang W, et al. Hierarchically Biomimetic Bone Scaffold Materials: Nano-HA/Collagen/PLA Composite J. *Journal of Biomedical Materials Research Part B Applied Biomaterials*, 2004, 69(2):158–65.
10. Song Q, Hu K, Cui F Z, et al. Effect of High Temperature on Morphology and Structure of Nano-Hydroxyapatite/Collagen Composite[C]// 2009:1360–1363.
11. Fu-zhai Cui, QingLing Feng: biomaterials science (second edition) (Tsinghua Universtiy Publication, China. 2004).
12. Armentano I, Bitinis N, Fortunati E, et al. Multifunctional nanostructured PLA materials for packaging and tissue engineering[J]. *Progress in Polymer Science*, 2013, 38(10–11):1720–1747.

# Mechanical Property and Structure Improvement of Sleeve Mandrel in Central Impression Flexographic Press

Li'e Ma, Jierui Li, Jimei Wu, Shuaichao Huang and Shanhui Liu

**Abstract** The sleeve mandrel is the core element of the plate cylinder in the central impression flexographic press. It is a cantilever beam structure during the installation of the sleeve. So a large deflection appears at the free end of the mandrel under the force of self weight because of the larger span of the mandrel. The stress and deflection analysis are carried on firstly. Based on the static analysis, the structure optimization is developed to satisfy the low deflection requirement. The carbon fiber material is used to replace the material of the mandrel body. Then the mass and maximum deflection of the mandrel is greatly reduced after the optimization. So the mandrel is easy to replace and the dynamic characteristics will be better.

**Keywords** Sleeve mandrel · Flexural deformation · Carbon fiber · Mechanical properties

## 1 Introduction

The sleeve mandrel is the core element of the plate cylinder in the modern central impression flexographic press. It is the most important part in the print unit. Its performance has direct influence on the quality of the print [1].

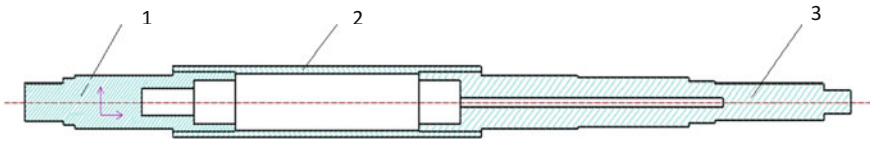
The sleeve mandrel of central impression flexographic press is shown as in Fig. 1. The length of the sleeve mandrel is 2400 mm, the length of the sleeve

---

L. Ma (✉) · J. Li · J. Wu (✉) · S. Liu  
Faculty of Printing, Packaging Engineering and Digital Media Technology,  
Xi'an University of Technology, Xi'an, China  
e-mail: malie@xaut.edu.cn

J. Wu  
e-mail: wujimei@xaut.edu.cn

S. Huang  
China Aviation Lithium Battery Co., Ltd., Luoyang, China



**Fig. 1** Simplified model section of the sleeve mandrel. 1, 3—spindle head, 2—roll barrel

mandrel is 1420 mm and the diameter of the sleeve mandrel is  $\Phi 105$  mm. The sleeve mandrel will be a cantilever beam structure during the installation of the sleeve. In this situation, because of the larger span of the mandrel, a large deflection appears on the free end of the mandrel under the force of self weight. This will result that it is very difficult for the mandrel head to match with the bearing and also the mandrel cannot work properly. On the other hand, the mandrel deflection due to self weight will lead directly to the printing accuracy decline [2–4].

To solve the large bending deformation problems, some manufacturers may commonly increase the drum wall thickness and the size of the cylinder to increase the rigidity of the mandrel and to reduce the roller deflection. But the long-term experience shows that this is not very ideal [1]. The mechanical analysis for the beam is very important [3–5]. The carbon fiber material used for the sleeve mandrel is a new technology.

In this paper, based on the static analysis, for reducing the deflection and mass, the optimization is developed using ANSYS module. After size optimization is completed, we select new material for the sleeve body to continue the optimization.

## 2 Mechanical Properties of Sleeve Mandrel

### 2.1 Simplified Model

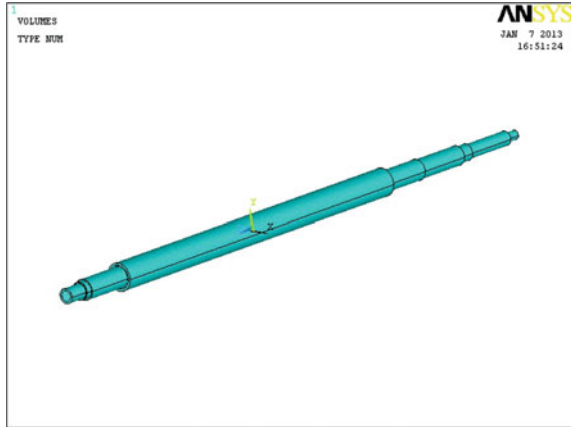
The complex structure of the sleeve mandrel is simplified as a cylindrical elastic cantilever beam [6, 7]. The simplified model without chamfer and cone angle is shown in Fig. 1. The simulation model of sleeve mandrel is shown in Fig. 2.

The parameterization model consists of 16 different parts. The beam starting rotating angle is  $0^\circ$  and the beam ending rotating angle is  $360^\circ$ .

The original material of the mandrel body and spindle head is 45 steel. The material properties of 45 steel are shown as Table 1.

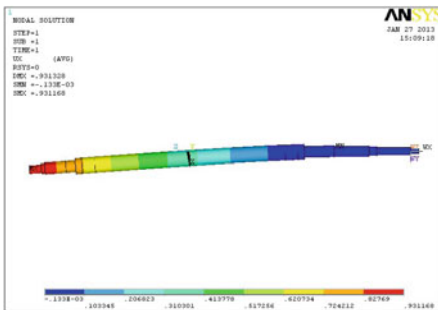
The element type of the finite element model is SOLID185. The element has 8 nodes and each node has 3 degrees of freedom. The element model has 67,523 units. The model is fully-constrained in cartesian coordinates. Only its gravity is given. In the cartesian coordinate the acceleration in X coordinate direction is  $9.8 \text{ m/s}^2$ .

**Fig. 2** The simulation model of sleeve mandrel

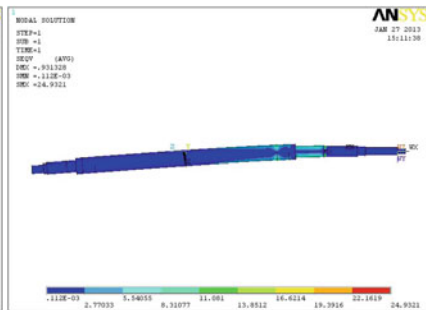


**Table 1** The material properties of 45 steel

Material	Properties		
	Modulus of elasticity (pa)	Poisson's ratio	Density (g/cm <sup>3</sup> )
45 steel	2.09E11	0.269	7.89
40 Cr	2.11E11	0.277	7.87
Carbon fiber	1.80E11	0.200	1.75



(a) The displacement nephograms



(b) The stress nephograms

**Fig. 3** The deflection deformation in X direction

## 2.2 Static Analysis

The deflection deformation in X coordinate direction is the biggest considering the inertia load in the X direction [8]. So the displacement and stress nephograms in X direction are extracted as the analysis object. They are shown in Fig. 3.

The maximum flexural deformation is at the free end of the sleeve mandrel in X direction in the Cartesian coordinate system. The size of the maximum flexural deformation is 0.93117 mm and the maximum stress is 24.229 MPa.

### 3 Structure Improvement of the Sleeve Mandrel

The principle of the optimization is not to change the maximum outer diameter and length of the mandrel, only to change the wall thickness and the volume of the interior cavity [9]. The thickness of the body will be changed to generate the different thickness and different volumes of the cavity model.

Geometry constraints and stress constraints will be set into state variables. There are two state variables for the roll mandrel optimization. One is the stress constraint ( $S_{\max}$ ) which must be smaller than the material allowable stress. The other is the deflection constraint ( $U_{x\max}$ ) which must be less than the limit deflection. The deflection limit of this mandrel is 0.5 mm provided by the enterprise experience value.

The volume is selected as the objective function providing that the strength and stiffness are sufficient.

#### 3.1 Size Optimization and Result Analysis

Two major optimization methods are used [10]. Zero order optimization method is selected to find out the optimization scope roughly. First order optimization method is selected to optimize accurately. The optimized structure sizes compared with the original sizes are shown in the Table 2.

The deflection is reduced to 0.62304 mm and the stress is reduced to 22.281 MPa after the optimization. According to the volume decrease, the mandrel mass is not reduced almost. But the deflection is still greater than the required value 0.5 mm. The result still does not satisfy the production needs. Only size optimization is impossible to reach the design requirements because the maximum outer diameter and length of the mandrel are constant. Some alternative materials must be selected.

#### 3.2 The Structure Optimization with Carbon Fiber Material

If the smaller density but more rigidity material are used to replace the 45 steel, the deflection will be smaller. So we select 40 Cr and carbon fiber to make further optimization. The material properties of 40 Cr and carbon fiber are shown in Table 1. First the 40 Cr material is used to replace the original 45 steel material of the whole mandrel completely. The results are close to the above. Then we select carbon fiber to replace the original 45 steel of the mandrel body.

**Table 2** The comparison between the original and the optimized

Variable types	Variable name	Range (mm)	Original value (mm)	Size optimized value (mm)	Material optimized value (mm)	
Design variables	<i>Th</i> 3	1-8	5.0000	7.9391	5.4094	
	<i>Th</i> 4	1-8	5.0000	1.2698	1.0157	
	<i>Th</i> 5	1-3	2.0000	1.9954	1.0082	
	<i>Th</i> 6	1-6	4.0000	1.0000	1.1395	
	<i>Th</i> 7	1-12	8.0000	1.7085	1.0221	
	<i>Th</i> 9	1-5	5.0000	1.0112	2.3547	
	<i>Th</i> 10	1-2.5	2.5000	1.9143	2.4969	
	<i>Th</i> 11	1-4.5	4.5000	1.0683	1.6687	
	<i>Th</i> 12	0.5-3	1.0000	1.6801	2.9949	
	<i>Th</i> 13	1-4	4.0000	1.4581	3.4607	
	<i>Th</i> 14	1-10	9.5000	9.9549	3.0468	
	<i>Th</i> 15	1-11	10.500	8.6660	11.000	
	<i>L</i> 3	98-226	226.00	99.096	98.261	
	Results	$S_{max}$ (MPa)	$S_{max} \leq [\sigma] = 197$ MPa	24.229	22.281	15.871
		$U_{x_{max}}$ (mm)	$U_{x_{max}} \leq 0.5$	0.931	0.623	0.461
Objective function	<i>Volume</i> (mm <sup>3</sup> )		0.8659E + 07	0.8452E + 07	0.8024E + 07	

The above optimization methods are still used. After 30 times iteration, the final optimization results are given in Table 2. According to the table, we know the deflection is reduced to 0.461 mm and the stress is reduced to 15.871 MPa after optimization. The maximum deflection of mandrel is under 0.5 mm. The results can satisfy the production needs.

The mandrel mass is also greatly reduced to 14.04 kg. It is easy to replace and the dynamic characteristics will be better.

## 4 Conclusions

After the carbon fiber material is used for the mandrel body, the deflection is reduced dramatically. The carbon fiber material can reduce the weight while keeping the stiffness requirements. The tensile strength of the resin composite material is much superior to steel and the tensile modulus of elasticity is higher than steel. The mechanical properties indicate that the carbon fiber has broad application prospects in engineering.

**Acknowledgements** This project is supported by National Natural Science Foundation of China (Grant No. 11272253, 51305341 and 51505376) and by the Natural Science Foundation of Shaanxi (Grant No. 2016JM5023 and 2016JQ5038).

## References

1. Bates, I., Zjakic, I., & Budimir, I. (2015). Assessment of the print quality parameters impact on the high-quality flexographic print visual experience. *Imaging Science Journal*, 63(2), 103–110. doi:10.1179/1743131X14Y.0000000094.
2. Zheng, Z.J., Chen, P., & Wang, D.J. (2012). Oscillation property of modes for FE models of bars and beams. *Journal of Vibration and Shock*, 31(20), 79–83.
3. Cheng, C.J., & Zhu, Y.Y. (2005). Elastic mechanics. Shanghai: Shanghai University Press.
4. Ashjari, M., & Khoshrovan, M.R. (2014). Mass optimization of functionally graded plate for mechanical loading in the presence of deflection and stress constraints. *Composite Structures*, 110, 118–132. doi:10.1016/j.compstruct.2013.11.025.
5. Hossain, J., Islam, Q., & Ali, M. (2013). Lift and drag on cylinder of octagonal cross-section in a turbulent stream. *Journal of Engineering Science and Technology Review*, 6(3), 105–110.
6. Shi, P.A., Hu, W.J., & Huang, P. (2008). Finite element analysis of micromechanic behavior on particle-filled materials. *Journal of Mechanical Strength*, 30(3), 411–416.
7. Vairis, M. P., Vidakis, N., Stefanoudakis, G., & Kandyla, B. (2013). Finite element modelling of a novel anterior cruciate ligament repairing device. *Journal of Engineering Science and Technology Review*, 6(1), 1–6.
8. Ali, N.J., & Garcia, J.M. (2010). Experimental studies on the dynamic characteristics of rolling element bearings. *Proceedings of the Institution of Mechanical Engineers Part J - Journal of Engineering Tribology*, 224(7), 659–666. doi:10.1243/13506501JET698.
9. Tian, H.L., Fang, Z.F., Zhu, D.L., & Qin, H.L. (2011). Investigation on tangential static elastic stiffness of fixed contact interface. *Chinese Journal of Applied Mechanics*, 28(5), 458–464.
10. Shang, Y.J. (2005). The finite element theory and ANSYS application guidelines. Beijing: Tsinghua University Press.



# Digital Stamping Control System Design Based on the STM32 SCM

Ming Mu and Yujie Ouyang

**Abstract** Different from the traditional stamping, digital stamping which is designed for individual needs and plate less stamping will have a good future. In this paper, a set of embedded control system based on STM32 SCM was designed for digital stamping equipment. This system combined DGUS graphic application technology, Non-shaft transmission technology, sensor technology and so on. The technical features and advantages of STM32 in high performance, high integration and low power consumption have been given full played and realized the automatic controlling of complex process flow.

**Keywords** Embedded · STM32 · Shaft less drive · Stamping without plate making

## 1 Introduction

As the development and improvement of people's living standard, traditional printing and packaging effect cannot meet the requirement. Instead, beautiful personalized packaging becomes popular. As the stamping business which is only one or small amount becoming more and more popular, using the traditional stamping will make a high cost, long production cycle and moreover, material wasting cannot be avoided. For these businesses, digital stamping which has a quick response has an advantage over traditional stamping [1], which can save production cycle and costs, avoid materials wasting and protect the environment.

It is very important for stamping equipment to have a good stability and rationality to meet the complex technological requirements. In this paper, a kind of embedded [2] stamping control system with core of STM32 SCM is designed. The STM32 SCM is high integration, economical, low power consumption and easy to

---

M. Mu (✉) · Y. Ouyang  
Beijing Key Laboratory of Packaging and Printing New Technology,  
China Academy of Printing Technology, Beijing, China  
e-mail: muming@keyin.cn

use as well as a fast processing speed and strong anti-interference, which can achieve stable and accurate control of stepper motor [3]. Combined with DGUS graphics technology, a friendly interface was established, which can provide a better using experience and a higher efficiency under the circumstances of guaranteeing running stability of the stamping equipment.

## 2 Design of Hardware System

### 2.1 Structure of Hardware System

The digital stamping platform is consisted of three main parts: moving platform, pressure roll unit and rolling unit, which are shown in Fig. 1. The driving mode of the platform is screw and it is driven by a stepper motor to achieve functions of acceleration, deceleration and fixed distance according to different process requirements. The rolling unit uses drive shaft and is driven by a DC generator. It can achieve rolling, peeling or other actions. Pressure roll unit provides pressure for stamping, which is driven by a stepper motor to make pressure and combined with pressure algorithm to control the pressure through the feedback signal of sensor [4]. It can get different proper stamping pressure on different stamping materials. This digital stamping system can complete wider kinds of stamping work of printing materials by its unique control methods and mechanical design makes. The system adopts embedded control systems which can pre-set the software programs. With the coordination of three parts, the system completes stamping process.

The hardware structure of digital stamping control system is shown in Fig. 2. The system adopts embedded control system whose main control chip of the system is STM32. Through the LCD display, the current parameter values and equipment operating status can be seen. As the input module of system, metal buttons is equipped and the user can set parameters and control the device. Finally, the system completes the entire process by driving three motors. The 485 communication interface of the main controller is left to dock with the PC to upload and download underlying program. The 485 communication circuit is shown in Fig. 3.

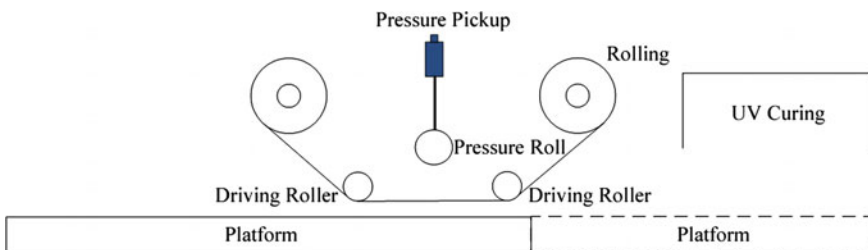


Fig. 1 Mechanical structure diagram

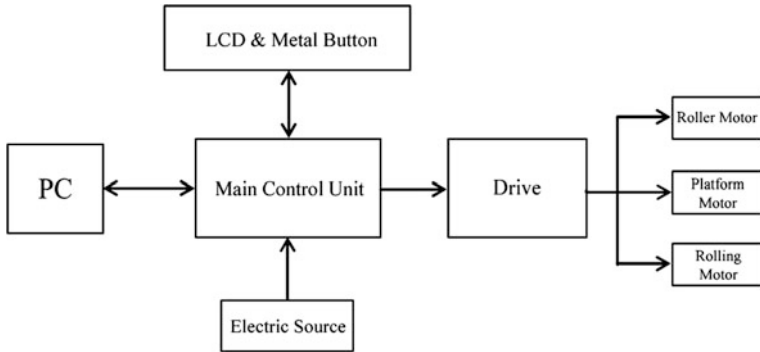


Fig. 2 Hardware structure diagram of the tension control system

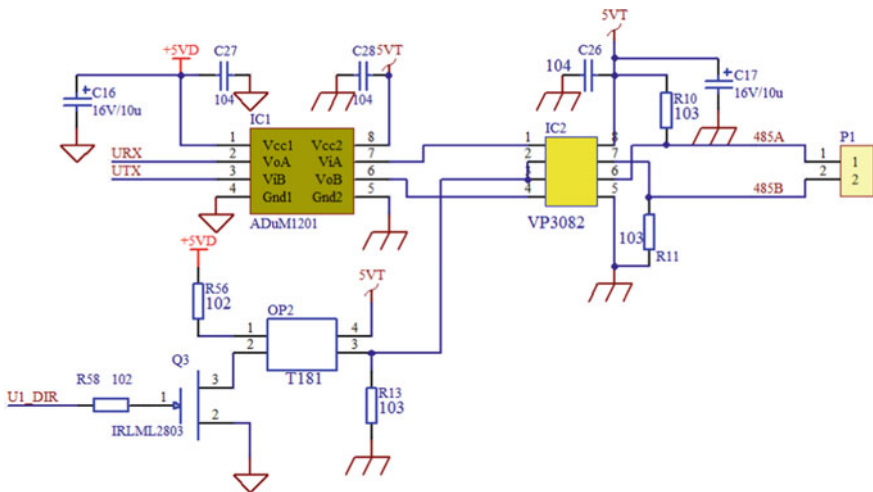


Fig. 3 485 Communication circuit

The human-computer interaction platform of this system consists of DWIN LCD and metal buttons. The LCD shows pressure, stamping speed, curing time, warm-up time and so on. Users can set parameters and operate the equipment through metal buttons. The key parameters are left setting interface to make sure the flexible of the system based on the embedded controlling.

### 2.2 Motion Module of the System

Based on the process requirements of the digital stamping systems, this design uses two stepper motors to drive the printing platform and the press roller separately.

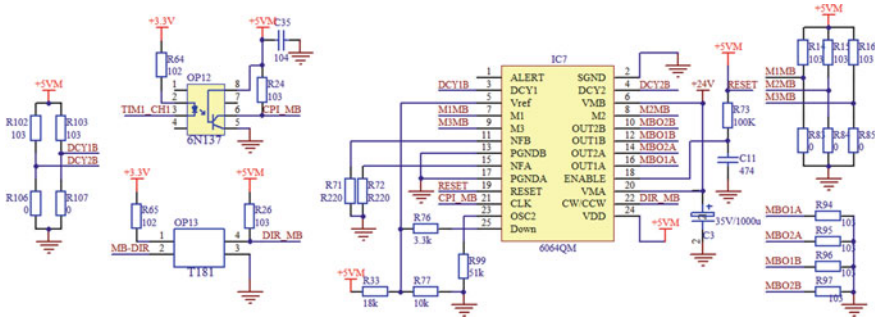


Fig. 4 Stepping motor driving circuit

The rolling part is driven by a DC generator and can achieve precise rolling by calculating the press size. Three power units cooperate with each other to achieve stable operation of the system without wasting the gold film.

Click the Start button, the machine starts to run. The LCD shows the current stamping pressure, running speed of the stamping platform and the current stamping size. When reach the preset size, the press roller starts to lift and at the same time the DC motor starts which begins to rolling. The rolling size equals to the stamping size. After the rolling, the DC motor stopped and the press roller continues to. The platform continues to run to the positive top to start curing. After curing, the platform resets. If the user press reset button during operation, the platform stopped, the press roller lifted and reset as well as the platform.

A variety of unforeseen circumstances is taken into account during the design of the control program. In order to avoid operational errors, each input means is prohibited during normal operation of the equipment. If the power is off during the operation, when powers up again, the system will initialize and the platform as well as the press roller will reset. Stable hardware configuration with a variety of interrupt subroutine provides a strong guarantee for the safe and stable operation of the equipment. Figure 4 is a drive circuit diagram of stepper motor which uses TB6559FG drive chip and is designed with 4 groups of pull-down resistor. It can avoid the resonance problems effectively during the process of motor start and acceleration, which provides a strong guarantee for the stability of the equipment operation.

### 3 Software Design of the System

The design of the software part of this research system consists of two parts: the main control unit and the host computer. The STM32 microprocessor of the main control unit is the core of the whole system. This software system is developed in the keil environment and support C language compilation. It can use communication interface 485 to achieve human-computer exchange of underlying control program with PC-side. The host computer of the system is made up of DWIN LCD

and metal buttons. Design and compile facilities under the DGUS Tool environment and the interface is designed by using Photoshop. Through the compilation and application of human-computer interface of the main program, the friendly interactive platform is established.

### ***3.1 Software Flow***

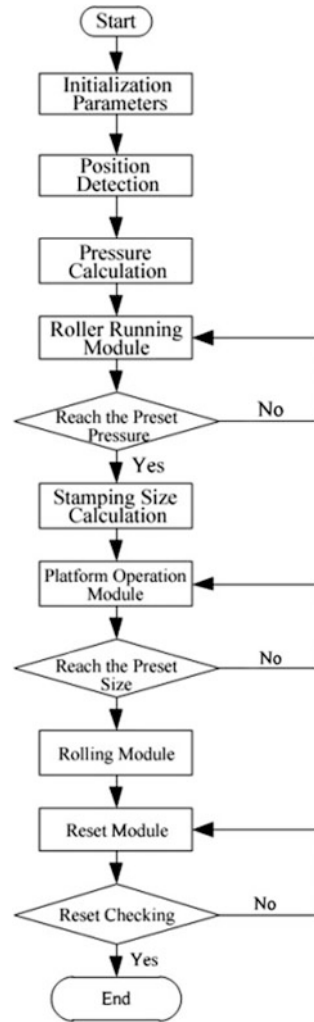
The software of this system includes many subroutine modules such as main program, parameter initialization module, sensor check module, platform operation module, press roller operation module, communication module and display module. The main control program is divided into two parts: the stamping pressure module and printing platform module. These two modules all consist of algorithm modules of position detection and motor control pulse calculation. The closed-loop control of these parts also makes the whole digital stamping system more precise and stable. The software flow chart of the digital stamping control system is shown in Fig. 5.

1. Initialization parameters: Power on. After starting the control program, the system will automatically reads the last parameter setting.
2. Position detection: System boot self-check. To make sure that all moving parts are in the initial position, otherwise, the moving parts device will automatically run back to the initial position.
3. Pressure calculation: Calculate the down size of press roll according to the setting pressure to ensure the precise pressure during the stamping process.
4. Stamping size calculation, platform and rolling operation: set pressing size according to the stamping size. The load platform, the pressure roller and the rolling can cooperate better after calculating. When stamping position is precise, the stamping film can be saved maximally as well as meeting the stamping requirement.
5. After stamping, all moving parts reset automatically.
6. End: There are stop and emergency stop buttons on the device. Once the variable is triggered the system will shut down or the program continues to run.

### ***3.2 Pressure Control***

The pressure of stamping system is provided by a stepper motor and three customized springs. System will calculate compression decrement of the spring according to the pressure. The way of pressure calculation is as formula 1 and formula 2:

**Fig. 5** Hardware structure diagram of the tension control system



$$F = \left[ d \cdot \left( \frac{1000}{c} \right)^3 \cdot N \right] \times \tag{1}$$

$$c = (D - d)/d \tag{2}$$

- F* Spring Pressure
- d* Spring Wire Diameter
- D* external diameter of Spring
- c* constant

## N Spring Working Cycle

### x Compression Decrement of Spring

The system will calculate the needed running angle of the stepper motor according to setting pressure value and get the output drive pulses of the control driver. Then the system controls the stepper motor precisely to drive the pressure roller to get down to the substance and completes the stamping process. The pressure control program is as follows:

```

unsigned char i;

PlateRun = 0xAA;
MotorB_Dir = 0;
Roll_Range = SettingS.Pressure_x10;
Roll_Range /= 10;
Roll_Range /= Base_KG; //the distance after getting the setting pressure
Roll_Range /= Roll_Screw; //helical pitch is 2 mm, then get the turns number of
motor
Roll_Range * = 360; //get the rotation angle of the moter
Roll_Range /= 0.05625;
Work.Roll_Zero = 0;
Roll_Total = Roll_Range;
i = 0;
while((Roll_Total/65535) >=1)
{
Roll_PLS_Sect[i] = 65535;
Roll_Total -= 65535;
i += 1;
}
if(Roll_Total > 0) //less than 65535
{
Roll_PLS_Sect[i] = Roll_Total;
}

```

## 4 Experiments and Analysis

Facing the growing demand of personalized stamping, the digital stamping system has met the requirements of high quality, highly active and cost-saving. By combining the hardware and software properly, the system not only improves the automation degree of stamping operations, but also ensures the consistency of multiple stamping by precise motion controlling.

**Table 1** Manual stamping

Group number	1	2	3	4	5	6	7	8
Stamping size (cm <sup>2</sup> )	5	5	5	5	10	10	10	10
Stamping precision (mm)	2	3	2	1	2.5	2	2	1.5
Sand holes number	3	4	1	5	6	5	4	3

**Table 2** Digital stamping

Group number	1	2	3	4	5	6	7	8
Stamping size (cm <sup>2</sup> )	5	5	5	5	10	10	10	10
Stamping precision (mm)	0.5	0.6	0.3	0.5	0.4	0.6	0.6	0.4
Sand holes number	1	0	0	0	0	1	0	1

In order to test the stability and accuracy of the digital stamping system, the authors made 16 groups of coated paper samples in two ways: manually stamping and digital stamping to make a comparison. Use the width of the stamping line to measure the precision of stamping and use the number of sand holes in same area to measure the degree of adhesion. The experiment data are shown in Tables 1 and 2.

Through the experiments we can see that in the same experimental conditions, the digital system is much better than manual stamping in precision and adhesion effect and it has a better stability. This experiment can prove that this control system can meet the requirements of stamping process and its stable and accurate operation achieve the expected target of the digital stamping system.

## 5 Conclusions

Digital stamping system is an automatic stamping system based on new process. The experiments show that the parameters are calculated accurately, the experimental platform can operate normally and the stamping results are precise, which reaches the expected targets. The digital stamping system has the advantages of environmentally friendly, lightweight, fast and wide adaptability of printing material. The embedded control systems of the digital stamping based on STM32 is simple, inexpensive and easy to install, [5] which makes the digital stamping system get rid of the complex operational processes in the traditional stamping process and integrate the intelligent and convenient operating concept into the field of stamping. In the future printing industry, intelligent control system of the digital stamping will have a very important leading effect.

Moreover, although the stamping results have been recognized by the insiders of the industry, the stability and accuracy of the equipment still can be improved. In the future, improving the system performance and the automation degree of system will be the main work.



## References

1. Dietrich H. Naunin & Hans-Christian Reuss (1990). Synchronous Servo-Drive: A Compact Solution of Control problems by Means of a Single-Chip Microcomputer. *IEEE Transactions on Industry Application*. VOL. 26. NO. 3, MAY / JUNE 1990, 408–414.
2. Zhang Lili, Li Liang, Shi Xiaohua study PIC chip embedded motor controller [J] *Based on modern electronic technology*, 2009 (09): 164–167.
3. Wang Yonghong, Xu Wei, Hao Liping. *STM32 series ARM Cortex-M3 Microcontrollers Principles and Practice* [M] Beijing: Beijing Aerospace University Press, 2008.
4. Wan Wen Bin, Shi Yong electrical automation application and design ZigBee intelligent switch control system [J]. 2010,32 (3): 57–59.
5. Xu Jianguo and motor control [M]. Wuhan: Wuhan University of Surveying and Mapping Science and Technology Press, 1998.

# Print-Defect Detection Method Based on the Modified Artificial Immune Algorithm

Guanjun Zhu, Shisheng Zhou and Xiaoyan She

**Abstract** This paper presents a rapid print-defect detection method with high accuracy. Gray level co-occurrence matrix (GLCM) is employed to obtain texture feature values of print images in the respective direction of  $0^\circ$ ,  $45^\circ$ ,  $90^\circ$  and  $135^\circ$ . “Vaccine” is introduced to modify the negative selection algorithm of artificial immune algorithm for the identification of print defects and defect types. The five texture feature values of print image, i.e., Energy, Entropy, Contrast, Correlation, Homogeneity, are calculated from the four directions, the averages of each feature value composes a feature vector. The identification of print defects is carried out following the modified negative selection algorithm. In this method, real values are used in coding, Euclidean distance in calculating affinity, feature vectors of defect-free print samples and defect-known print samples in composing distinctive detector sets. The experiment conducted proves that this method responds rapidly in the identification of print defects and defect types with high accuracy.

**Keywords** Print · Defect detection · Artificial immune system · Negative selection algorithm · GLCM

## 1 Introduction

In the printing industry, print-defect detection plays a major role in the assessment and control of print quality. Prints with defects are supposed to be eliminated in the actual production [1]. Based on the negative selection algorithm of artificial immune algorithm, this paper adopts the negative selection algorithm adjusted to print-defect detection [2] and modifies it with the introduction of “vaccine”. GLCM is used to calculate texture feature values of defect-free print images and print images with three common defects (overprint deviation, color splashes, and

---

G. Zhu (✉) · S. Zhou · X. She  
Faculty of Printing, Packaging Engineering and Digital Media Technology,  
Xi’an University of Technology, Shaanxi, China  
e-mail: 2933537087@qq.com

streaks). Then a comprehensive artificial immune model [3] is established to do print-defect detection. Finally an experiment is carried out to testify the validity of this method in print-defect detection.

## 2 Artificial Immune Algorithm

### 2.1 Human Immune Mechanism

Biological immune system has an interesting identification mechanism to tell “non-self” from the “self”. Immune identification refers to the case that an antigen is bound to the antigen receptor on lymphocyte. T-cell lymphocytes mature within the thymus where they undergo an examination; only those that are not activated by the self-cell will be released into the immune system. When the self-cell is infected by pathogen, those T-cells would identify non-self cells and make immune responses, preventing T-cells from attacking the self-cell by mistake. This process, namely negative selection, is the main way of immune identification [4].

### 2.2 Negative Selection Algorithm

Inspired by the negative selection of human immune mechanism, Forrest et al. [5] (1994) developed the negative selection algorithm to detect abnormally. According to the algorithm, the first step is to define the self-set. Then a set of candidate detectors are generated randomly. Those detectors activated by any self are eliminated while those activated by any non-self are maintained. After that, the trained detector set is ready to detect new cases.

1. Defining the self-set: There are defect-free prints and defect prints in quality. The set of feature vectors describing defect-free print images is given as the self-set, represented by  $S: S = \{S_i\}, i = 1, 2, \dots, n$ , where  $S_i$  indicates the feature vector of defect-free print image  $i$ . Similarly, the set of feature vector describing defect print image is given as defect set or non-self-set, represented by  $NS: NS = \{NS_i\}, i = 1, 2, \dots, n$ , where  $NS_i$  indicates the feature vector of defect print image  $i$ .
2. The Generation of Detectors: After a detector is generated randomly, its vector is used to match with each feature vector in the self-set. If there is any match, the detector will be eliminated and substituted by a new detector to undergo the same trial; otherwise the detector proves to be effective and joins the effective detector set  $R_0$ . This process keeps on unless the number of detectors reaches a certain quantity. The trained detective set  $R_0$  are ready for new case detection. Matching the feature vectors of print images to be examined with each element

of the set  $R_0$ , if there is any match, there is non-self element, i.e., the defect print is found.

3. **Matching Rule:** Matching rule is used to find whether a data item matches with or identified by detectors [6]. Matching possibility is decided by affinity between feature vectors. The most commonly used affinity is distance affinity. When the affinity achieved the matching threshold  $r$ , the vectors are regarded as matched. The formulation of affinity goes as follows:

Let  $X = (x_1, x_2, \dots, x_n)$  and  $Y = (y_1, y_2, \dots, y_n)$  be  $n$  dimension normalized vectors of the print quality space while  $n$  is a natural number, the affinity between  $X$  and  $Y$  is shown as:

$$d = \sqrt{\sum_{i=1}^n (x_i - y_i)^2}, \quad 1 \leq i \leq n \quad (1)$$

Detector generation is constraint by the inequality  $E(d, s) > r$ , where  $E(\cdot)$  denotes Euclidean distance,  $s$  denotes any feature vector in the self-set,  $r$  denotes the matching threshold. Detectors generated following the inequality procedures are distributed in non-self space.

While matching the feature vectors to be examined with detector in the set  $R_0$ , if any matching distance  $E(d, s) \leq r$ , the vector in question is considered as matched and defect print is found.

### 3 Modification of the Algorithm

The negative selection algorithm suggested by Forrest adopts binary coding to represent data and r-contiguous bits matching rule. However, binary coding is not readily to demonstrate the texture features of print images, and the r-contiguous bits matching rule does not work well in reflecting texture feature variations on print images [7, 8]. To deal with this problem, the real-valued vectors are utilized to explain texture features of print images and Euclidean distance is applied to obtain affinity in this paper.

In real cases of print-defect detection, what to be identified are not only prints with defects, but also defect types. Thus, a modified algorithm is required. The introduction of “vaccine” is adopted modifying the algorithm with the aim to identifying the type of defects. Procedures go as follows. First, the feature vectors of print images with each type of defect are extracted respectively as “vaccine”. Then each detector in the set  $R_0$  undergoes matching with the “vaccine” when the set  $R_0$  is classified by affinity. Detectors failing to match with “vaccine” are eliminated for the formation of a new detector set  $R$ . Each detector sub-set reflects the most prominent features of a certain print defect and was only sensitive to the specified defect, making defect types identifiable by checking the coding number of the detector that matches.

## 4 Texture Features Extracting from Print Images

The extraction of image features, which mainly embody gray level, shape and texture [9], has a direct influence on the accuracy of the final detection result. GLCM is applied in this paper to express feature values of print images, which functions well in describing image texture features.

### 4.1 GLCM

GLCM, proposed by Haralick et al. [10], is a conventional texture analysis method. According to this method, the appearance frequency of the gray gap between two pixels situating in given direction and distance is calculated to obtain the comprehensive information of image texture in terms of direction, adjacent interval, amplitude and speed of variation. GLCM is defined as the appearance probability of the gray level  $j$  in the distance of  $\delta$  from the spot of gray level  $i$ . It is shown as,  $P(i, j; \delta, \theta)$ , ( $i, j = 0, 1, \dots, L - 1$ ), where  $L$  denotes gray level,  $i, j$  respectively denote the gray level of pixel,  $\delta$  denotes the distance between two pixels,  $\theta$  denotes the direction of GLCM.

### 4.2 Texture Features

GLCM, in the usual case, is too large to be used directly as texture features; it should be regularized to extract statistics of the second-order characteristics. Haralick defined fourteen feature values to describe image textures according to GLCM. Five of them, namely Energy, Entropy, Contrast, Correlation, Homogeneity, are calculated as texture features of print images in this paper. Following equations define these features:

1. Energy or Angular Second Moment (ASM):

$$ASM(\delta, \theta) = \sum_{i=0}^{L-1} \sum_{j=0}^{L-1} [P(i, j; \delta, \theta)]^2 \quad (2)$$

2. Entropy (ENT):

$$ENT(\delta, \theta) = - \sum_{i=0}^{L-1} \sum_{j=0}^{L-1} P(i, j; \delta, \theta) \log P(i, j; \delta, \theta) \quad (3)$$

3. Contrast (CON):

$$CON(\delta, \theta) = \sum_{i=0}^{L-1} \sum_{j=0}^{L-1} (i-j)^2 P(i, j; \delta, \theta) \quad (4)$$

4. Correlation (COR):

$$COR(\delta, \theta) = \frac{\sum_{i=0}^{L-1} \sum_{j=0}^{L-1} (i-t)(j-t)P(i, j; \delta, \theta)}{\sum_{i=0}^{L-1} \sum_{j=0}^{L-1} (i-t)(j-t)m(i)} \quad (5)$$

$$t = \sum_{i=0}^{L-1} \sum_{j=0}^{L-1} i \times P(i, j; \delta, \theta), \quad m(i) = \sum_{j=0}^{L-1} P(i, j; \delta, \theta)$$

5. Homogeneity or Inverse Difference Moment (IDM):

$$IDM(\delta, \theta) = \sum_{i=0}^{L-1} \sum_{j=0}^{L-1} \frac{P(i, j; \delta, \theta)}{1 + (i-j)^2} \quad (6)$$

### 4.3 Extraction of Print Image Texture Features

To obtain print image feather values, the first step is to gray the acquired print pictures. It is necessary to pre-process them by de-noising and smoothing to guarantee the validity of image features [11]. Then the GLCM of the grayed images are to be normalized to meet the actual gray level requirement. Owing to the normalization process, the calculation burden is reduced. The final step is to get the five texture feature values from the regularized GLCM.

It is important to note that GLCM is directionally dependent. To avoid direction component and get texture features free of directions, the usual solution is to calculate the texture feature value of GLCM in the direction of  $0^\circ, 45^\circ, 90^\circ$  and  $135^\circ$  respectively and represent feature vector by the average of each feature value.

The five feature values of feature vector have various physical significance and data range. When big numbers are compared with small ones in terms of Euclidean distance, the latter are easily ignored. Therefore, there is a need to normalize each feature value in accord to its internal characteristics. The Gaussian normalization method is employed in this paper to equip each feature value with the same weight before calculating the matching distance.

Let the original feature vectors be  $[f_1, f_2, f_3, f_4, f_5]$ , and the feature vectors after normalization be  $[F_1, F_2, F_3, F_4, F_5]$ , the normalization goes as follows.

The premise of normalization is to work out the average value of the original feature vectors  $\mu$  and the standard deviation  $\sigma$ . Then it is ready to use the Eq. 7:

$$F_i = \frac{(f_i - \mu)}{\sigma} \quad i = 1, 2, 3, 4, 5 \quad (7)$$

After that, the final feature vectors are shown as:

$$F = [\overline{ASM}, \overline{ENT}, \overline{CON}, \overline{COR}, \overline{IDM}] \quad (8)$$

## 5 Experiment Design

### 5.1 Acquiring and Pre-processing Print Images

In order to acquire print images, we need photograph the prints with high-speed cameras as soon as the last color is painted [12]. Then defect-free and defect-known print images are picked out separately from plenty of the acquired print images for off-line training and experiments (Fig. 1).

The pre-processing of images begins with graying the acquired print images. To improve image quality, the next step is to de-noise the grayed images by median filtering. Then we need compress the gray level from level 256 to level 16 to narrow down the size of GLCM and improve processing speed.

### 5.2 GLCM and Feature Value Calculation

The information loss of image texture increases with the distance between pixel dots. To decrease information loss, This work give the distance between pixel dots  $\delta = 1$ . Due to the fact that image textures are directional dependent, GLCM from different  $\theta$  express different texture information. GLCM from the four directions of  $0^\circ$ ,  $45^\circ$ ,  $90^\circ$  and  $135^\circ$  are set up for the calculation of the feature values in terms of ASM, ENT, CON, COR and IDM from the precious four directions. The average of the feature values obtained are used to compose feature vectors, which are finally processed by Gaussian normalization to erase impacts among data.

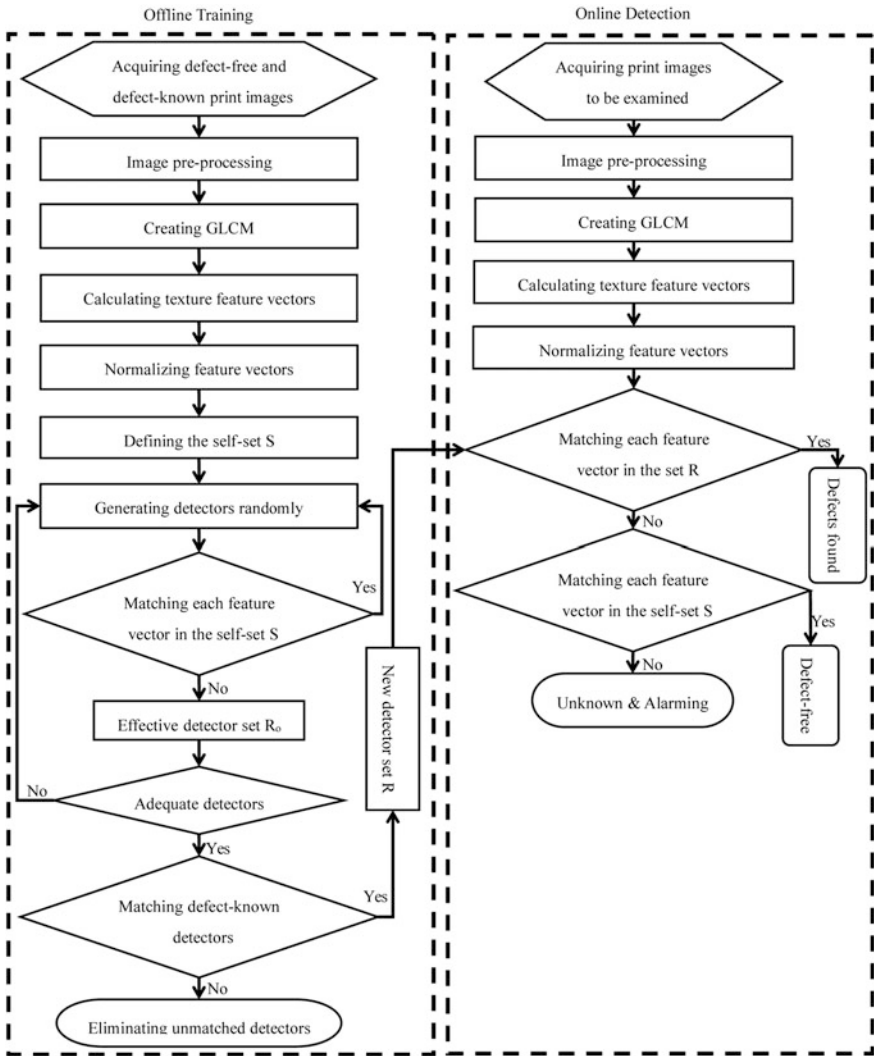


Fig. 1 Flow chart of print-defect detection based on artificial immune

### 5.3 Process of the Modified Negative Selection Algorithm

According to the modified negative selection algorithm, the experiment goes on as follows:

- Step 1 Define the self-set S, namely the texture feature vector set of defect-free print images.
- Step 2 Generate detectors randomly.



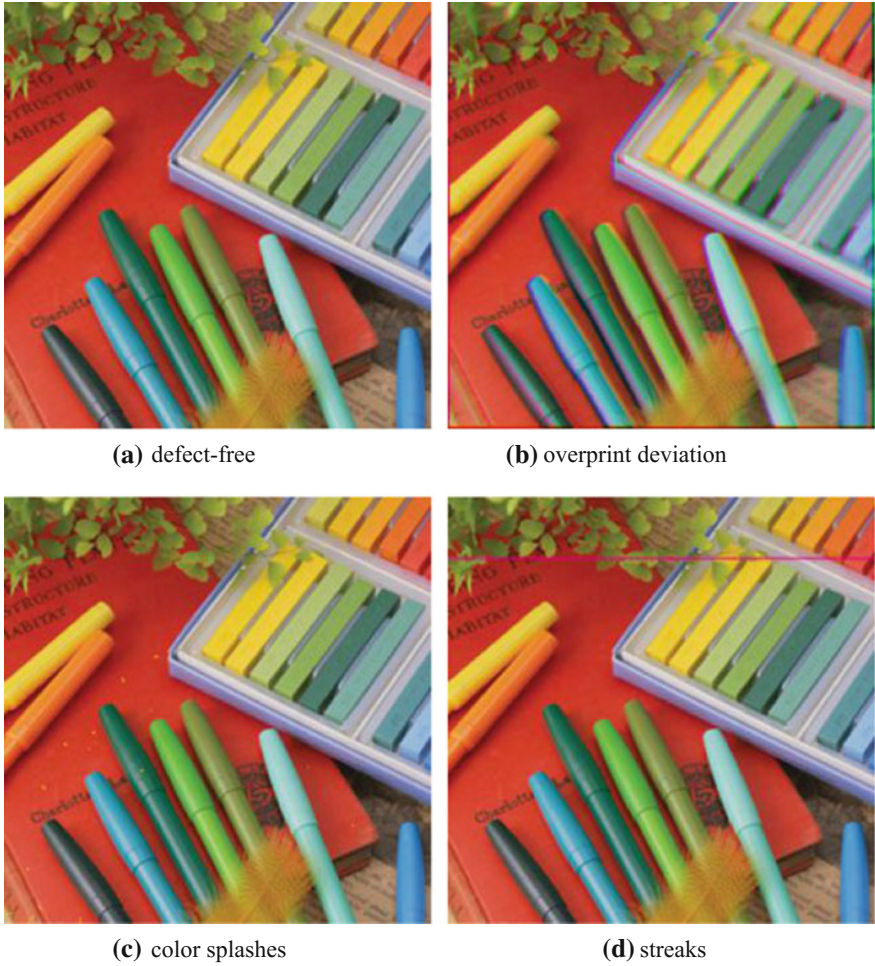
- Step 3 Match each candidate detector and feature vectors from the self-set  $S$ . If the detector does not match, it joins the effective detector set  $R_0$ ; otherwise eliminate it and jump to step 2.
- Step 4 Check whether the number of effective detectors reaches  $n$ . If so, carry on to step 5. Otherwise, jump to step 2 to continue the cycling.
- Step 5 Use feature vectors of the three defect-known print images as “vaccine” and match the “vaccine” with each detector in the set  $R_0$ . Eliminate those detectors that fail to match with “vaccine” while retain and classify the left to get a new detector set  $R$ .
- Step 6 Detect defects by comparing the trained detector set  $R$  with feature vectors of print images to be examined. If feature vectors to be examined matches with any detector in the set  $R$ , the detector in concern is activated and defect-print is recognized. By checking the coding number of the detector activated, the defect type can be identified.
- Step 7 Compare feature vectors to be examined with the self-set  $S$  respectively [13] if there is no match between feature vectors to be examined and the detector set  $R$ . If matching, the print image proved to be free of defects.
- Step 8 If there is no match between detectors from the self-set  $S$  and feature vectors to be examined, it is assumed that some new defect type was found. The algorithm will need mark and retain it, and alarm for human intervention.

## 6 Experiment and Results

To ensure the validity of the method in this paper, three common print defects are examined in the experiment. We classify print images in four types: defect-free, overprint deviation, color splashes and streaks. Then we select 80 images of each type, 320 images in total. The first 20 images of each type are used as training sample and the rest 60 as test sample. Figure 2 denotes the sample images with image size  $512 \times 512$  in the four types.

Having Grayed the color print images and suppressed their gray scale from 256 to 16, we make  $\delta = 1$ , and obtain GLCM from the directions of  $0^\circ$ ,  $45^\circ$ ,  $90^\circ$  and  $135^\circ$ . ASM, ENT, CON, COR and IDM are calculated according to the GLCM from the four directions. The average values of each feature value form the feature vectors of images. And those feature vectors are processed by Gaussian normalization.

With the feature vectors of print images in the four states obtained, the next step is to use those feature vectors in generating and training the real-valued vector detectors off-line. Each detector set for a certain defect type has 50 detectors and the given the matching threshold  $r = 0.1$  in this experiment. The trained detector sets are then used to examine test samples and get detection results.



**Fig. 2** Images of experiment samples

This method is realized by MATLAB [14] on a PC (2.2 GHz; 2 GB). The average calculating time for each print image is 0.21 s, when printing presses running at speeds up to 16,000 sheets per hour, meeting the basic requirement of print-defect on-line detection. The experiment results are represented by Table 1.

The Table 1 shows that there exist misjudgments, for which there are mainly two reasons to account. First, the print-defect is complex. Usually print-defects do not appear singly; one print-defect is probable to be followed by other similar defect characteristics. Second, the matching threshold would influence the detection result [15]. If the threshold value is too big or small, misjudgments will occur. Only when

**Table 1** Statistics of print-defect detection result

Image type	Size of test sample	Defect-free	Overprint deviation	Color splashes	Streaks	Unknown and Alarming	Correct (%)
Defect-free	60	60	0	0	0	0	100.00
Overprint deviation	60	0	56	3	1	0	93.33
Color splashes	60	1	0	58	1	0	96.67
Streaks	60	0	0	4	56	0	93.33
Average rates							95.83

the given threshold value is proper will the matching with the essential features of defects similar to trained defect samples be effective with a reasonable testing result.

## 7 Conclusions

With print images being the study object, this paper presented a print-defect detection method based on artificial immune algorithm. According to this algorithm, the acquired print images were pre-processed; image feature values were extracted directly from GLCM; print-defect detection was carried out by applying negative selection algorithm. This method, testified with the experiment, has a high detection rate and functions well in print-defect detection.

**Acknowledgements** The authors thank the Scientific Research Program of Key Laboratory Funded by Shaanxi Provincial Education Department (No.14JS067) for financial support.

## References

1. N.G. Shankar, N. Ravi, Z.W. Zhong. (2009). A real-time print-defect detection system for web offset printing. *Measurement*, Vol. 42: 645–652.
2. Gonzalez. F, Dasgupta D, Kozma R, (2002). Combining negative selection and classification techniques for anomaly detection. *Proceedings of the 2002 Congress on Evolutionary Computation*: 705–710.
3. Dasgupta D, Yu S, Nino F. (2011). Recent advances in artificial immune systems: models and applications. *Applied Soft Computing*, Vol. 11: 1574–1587.
4. Dong Li, Shulin Liu, Hongli Zhang. (2015). Negative selection algorithm with constant detectors for anomaly detection. *Applied Soft Computing*, Vol. 36: 618–632.
5. Forrest S, Perelson A S, et al. (1994). Self-nonsel self discrimination in a computer. *Proceedings of IEEE Computer Society Symposium on Research in Security and Privacy*: 202–212.

6. Hongwei Mo, Xingquan Zuo. (2009). Artificial immune system. Beijing: Science Press: 426–427.
7. Xu Aiqiang, Liu Yong, et al. (2011). Optimization and application of real-valued negative selection algorithm. 2011 International Conference on Power Electronics and Engineering Application. *Procedia Engineering*, Vol. 23 (2011): 241–246.
8. Zhou J, Dipankar D. (2006). Applicability issues of the real-valued negative selection algorithms. *Proceedings of the genetic and evolutionary computation conference*: 111–8.
9. A. Tinku, K.R. Ajou. (2005). *Image processing: principals and applications*. Wiley Interscience. New Jersey.
10. R.M. Haralick, K Shanmugam. (1973). Textural features for image classification. *IEEE Transactions on Systems, Man and Cybernetics*, 3(6): 610–621.
11. Mohammad H. Karimi, Davud Aseman. (2014). Surface defect detection in tiling Industries using digital image processing methods. Analysis and evaluation. *ISA Transactions*, Vol. 53: 834–844.
12. Yang ou, Guo baoping, Hu tao, Guo xuan. (2007). A real-time vision system for defect detection in printed matter and Its key technologies. 2007 Second IEEE Conference on Industrial Electronics and Applications: 2157–2161.
13. T. Stibor, J. Timmis, (2007). Comments on real-valued negative selection vs. real-valued positive selection and one-class SVM. *IEEE Congress on Evolutionary Computation*.
14. Gonzalez R C, Woods R E. (2004). *Digital image processing using MATLAB*. Beijing: Publishing House of Electronics Industry: 154–160.
15. J. Zhang, W.J. Luo, et al. (2014). An improved evolutionary algorithm for generating detectors in the real-valued Negative Selection Algorithms. *Applied Soft Computing*, Vol. 19 (2014): 18–30.

# Design of the Remote Fault Diagnosis System for the Printing Machines Based on the Internet of Things and Fuzzy Inference

Hongbo Liang, Shaozhong Cao, Xinpei Li and Hongfeng Xiang

**Abstract** In view of the maintenance difficulties of printing machines due to their wide distributions and high degree of automation, a remote diagnosis system based on Internet of things and fuzzy inference is designed. By deploying a variety of sensors in the main parts of printing machines, the remote diagnosis system can obtain, analyze and process the real operation data of printing machines, achieving the intelligent diagnosis to the printing machine faults. Besides, combined with the web application, it can be connected with remote fault diagnosis center to provide remote fault diagnosis service together. The system overcomes the shortages of traditional fault diagnosis technology, achieving the purpose of diagnosing the printing machine faults remotely.

**Keywords** Internet of things · Printing machine · Fuzzy inference · Remote fault diagnosis

## 1 Introduction

With the rapid development of the publishing and printing industry, printing machines have distributed in every corner of the world. Although the production equipment are basically the same, but due to the uneven level of the maintenance personnel, the grasp of maintenance content, arrangements of maintenance period and the disposals of emergency maintenance tasks are all just relied on personal experience, resulting in remarkable differences in equipment fault reasons, fault phenomenon and solutions to the faults etc. Therefore, the fault diagnosis often needs many technical personnel to work together to complete the diagnosis, which

---

H. Liang (✉) · S. Cao (✉) · X. Li · H. Xiang  
Beijing Key Laboratory of Signal and Information Processing for High-End Printing  
Equipment, Beijing Institute of Graphic Communication, Beijing, China  
e-mail: lianghongbobigc@163.com

S. Cao  
e-mail: caoshaozhong@bigc.edu.cn

takes a long time and causes a high misdiagnosis rate. So, it is of important practical significance to develop the remote fault diagnosis system of printing machine.

## 2 Theoretical Foundation

### 2.1 Internet of Things Technology

In order to achieve the real-time judgment and analysis to the printing machine, we adopt the Internet of things technology and deploy the sensors in the key parts of the printing machine to collect the data periodically or in real time. Data acquisition includes voltage, current, temperature, pressure and flow of testing equipment, as well as the information of power state, communication state, alarm status, input and output interface state, sensor working state for data collection center [1]. First, the data is aggregated by the wireless communication and the sink node sends the preliminary processed data to the remote service platform for fault diagnosis by Ethernet. Then the service platform will store the real-time operating information of equipment and maintenance information into the database, providing the data basis for the remote fault diagnosis expert and timely reminding the users of maintaining the equipment. In this way, the operating and management personnel can easily supervise the fault information and operation information through the web page in real time [2]. So, the overall operating structure of the system is shown in Fig. 1.

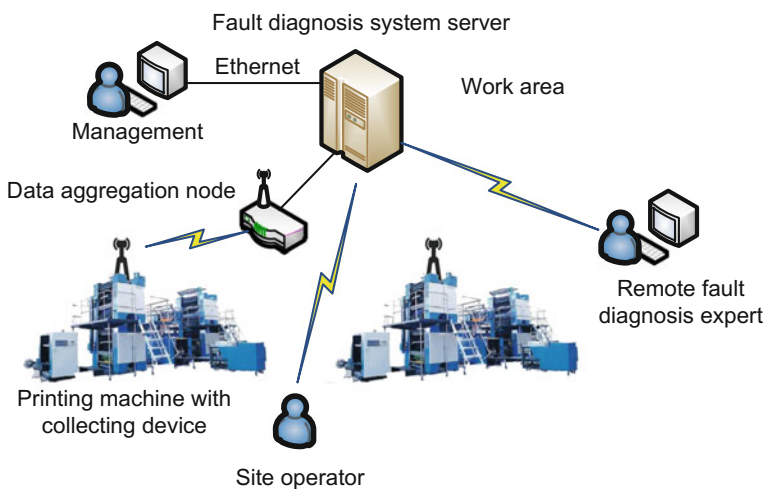


Fig. 1 Operating structure diagram of the system

## 2.2 Fuzzy Inference

Fuzzy diagnosis method is an automatic diagnosis method based on the knowledge. It employs the fuzzy logic to describe the fuzzy relation between fault causes and fault phenomena, as well as solves the fault causes and state identification problem through membership functions and fuzzy relation equations [3].

Suppose a set of possible causes of failure in the printing machine which is shown in Eq. (1).

$$Y = \{y_1, y_2, y_3, \dots, y_n\} \tag{1}$$

Where,  $n$  means the total number of types of fault causes, the collection of various symptoms caused by  $N$  fault causes is shown in Eq. (2).

$$X = \{x_1, x_2, x_3, \dots, x_m\} \tag{2}$$

$m$  means the total number of fault symptom types.

Assume that a symptom set is  $(x_1, x_2, x_3, \dots, x_m)$  and determine the membership degree  $\mu_{x_i}(x_i)$  of each component element  $x_i$  in the symptom set and symptoms  $X_i$ . So the fault symptom can be expressed as a fuzzy vector which is shown in Eq. (3).

$$X = (\mu_{X_1}(x_1), \mu_{X_2}(x_2), \dots, \mu_{X_m}(x_m)) \tag{3}$$

It is assumed that the symptom set is generated by the fault reason  $y$  and the membership of  $y$  to various fault causes is  $\mu_{y_i}(y_i)$ . Likewise, the fault reason is represented by a fuzzy vector which is shown in Eq. (4).

$$Y = (\mu_{Y_1}(y_1), \mu_{Y_2}(y_2), \dots, \mu_{Y_n}(y_n)) \tag{4}$$

Because there is a cause and effect relationship between the fault and the fault symptoms, the fuzzy relationship equation between  $X$  and  $Y$  is obtained according to the principle of fuzzy inference synthesis. The fuzzy relationship equation is shown in Eq. (5).

$$Y = X \circ R \tag{5}$$

Where  $R$  is the fuzzy relation matrix, which is expressed as Eq. (6).

$$R = \begin{bmatrix} r_{11} & r_{12} & \dots & r_{1n} \\ r_{21} & r_{22} & \dots & r_{2n} \\ \vdots & \vdots & & \vdots \\ r_{m1} & r_{m2} & \dots & r_{mn} \end{bmatrix} = (r_{ij})_{m \times n} \tag{6}$$

Fuzzy relation matrix  $R$  is the  $m \times n$  dimensional matrix, in which the row indicates the fault symptoms and the column shows the fault reasons. Matrix element  $r_{ij}$  indicates the degree of membership of the  $i$ th symptom on the  $j$ th fault cause, which can be described as  $r_{ij} = \mu_{y_j}(x_i)$ . The greater the possibility of the  $i$ th fault symptom is, caused by the  $j$ th fault cause, the higher the value of the degree of membership will be. Symbol  $\circ$  is a fuzzy operator, which can be used in the application for different algorithms [4]:

- Rule 1  $M(\wedge, \vee)$  is used in the main elements to decide the situations for review combinations;
- Rule 2  $M(\bullet, \vee)$  reflects the mind of weighting, but still highlights the situation of the main elements;
- Rule 3  $M(\wedge, \oplus)$  employs the summation to replace the maximization operator, weakening the role of the main elements.
- Rule 4  $M(\bullet, \oplus)$  reflects an integrated mind, in fact, which has been transformed into matrix multiplication operation.

*Rule 4* not only considers the influence of all factors, but retains all the information of the single factor evaluation. Thus, this paper chooses  $M(\bullet, \oplus)$  as the fuzzy operator.

### 2.2.1 The Determination of Fuzzy Relation Matrix $R$

The fuzzy diagnosis matrix  $R$  is directly related to the correctness of fuzzy reasoning. The conformance degree between value of each element and actual situation will directly affects the diagnosis effects. Therefore, the determination of membership degree is the key to the whole diagnostic reasoning [5]. At present, there are many methods in determining the degree of membership. Most of fault diagnosis system first take the degree of membership by expert experience as well as statistical data and then correct it in practice. This fault diagnosis system adopts the method of literature [6]. The specific process to determine the degree of fuzzy membership is shown as follows:

- Step 1 Determine the degree of membership by empirical data and the method is shown in Eq. (7).

$$v_{ij} = n/N \quad (7)$$

Where  $n$  means the number of the  $i$ th symptom belonging to the  $j$ th fault cause.  $N$  means the total number that  $i$ th symptom appeared.

- Step 2 The initial membership value  $s_{ij}$  is determined by the expert precedence method. Suppose that a fault has  $n$  possible causes, as for  $x_i$ , we compare any two causes among the  $n$  causes and write down the most possible



reason causing the fault symptoms as a priority order. So an expert has  $n(n - 1)/2$  priority comparisons. If you have  $M$  printer experts, there will be  $Mn(n - 1)/2$  kinds of priority order comparisons. Based on the  $Mn(n - 1)/2$  kinds of comparisons, we name the comparison number for priority order of  $y_j$  as  $t_j$  and  $t_k = \max\{t_j|j = 1, 2, \dots, n\}$ , so the initial membership degree of the fault symptom  $x_i$  to the cause  $y_i$  can be expressed in Eq. (8).

$$s_{ij} = t_j/t_k, \quad j = 1, 2, \dots, n \tag{8}$$

Step 3 Assuming the expert experience weight is  $w_1$ , the empirical data weight is  $w_2$ , where  $w_1, w_2 \geq 0$ . Then we can obtain comprehensive fuzzy membership degree by the empirical data and expert experience which is shown in Eq. (9).

$$r_{ij} = w_1s_{ij} + w_2v_{ij}, \quad i = 1, 2, \dots, m; \quad j = 1, 2, \dots, n \tag{9}$$

Thus we can determine the fuzzy diagnosis matrix  $R = (r_{ij})_{m \times n}$ .

### 2.2.2 Typical Fault Analysis

Roller mark is a common fault in the printed matter. This paper is introduced by taking the black roller mark as an example. The possible fault symptom set of black roller mark is shown in Eq. (10).

$$X = \{x_1, x_2, x_3, x_4, x_5\} \tag{10}$$

- $x_1$  The thick roller marks of equal gear interval;
- $x_2$  The wide roller marks appearing in gripper;
- $x_3$  Roller marks appearing in the fixed area;
- $x_4$  Roller marks appearing in different position;
- $x_5$  A lot of ink particles and ink stains appearing on roller marks.

The set for the reason causing the roller marks can be shown in Eq. (11).

$$Y = \{y_1, y_2, y_3, y_4, y_5, y_6\} \tag{11}$$

- $y_1$  severe wear of the cylinder gear
- $y_2$  severe wear of the cylinder bearing

- $y_3$  large pressure between the plate cylinder and the blanket cylinder
- $y_4$  large pressure the forme inking roller causing to typeface;
- $y_5$  large pressure between the forme inking roller and the distributing roller
- $y_6$  Floating roller marks

The fuzzy segmental scoring method is used to quantitatively analyze the fault symptoms by using the fuzzy understanding of the severity of the fault phenomena [7]. Quantization rule is shown in Table 1.

In this paper, the maximum membership principle is used to diagnose the fault. If there are 2 symptoms on the printed matter, the fuzzy segmental method is used to deal with the fault symptoms and the fault symptom set is determined as Eq. (12).

$$X = \{x_1, x_2, x_3, x_4, x_5\} = \{0.9, 0.2, 0, 0, 0\} \tag{12}$$

Matrix  $R$  is a fuzzy relation between fault and symptom set, which is determined by mechanism analysis of printing machine, expert experience and MBA Library [8]. The fuzzy relation between the fault symptoms and the fault causes of the roller marks in  $R$  is shown in Table 2.

According to the fuzzy reasoning rule, we can obtain the vector of the fault causes for the roller marks, which is shown in Eq. (13).

$$\begin{aligned}
 Y &= X \circ R \\
 &= (0.9, 0.2, 0, 0, 0) \circ \begin{bmatrix} 0.9 & 0.1 & 0 & 0 & 0 & 0 \\ 0.1 & 0.9 & 0.1 & 0 & 0 & 0 \\ 0 & 0 & 0.9 & 0 & 0 & 0 \\ 0 & 0 & 0 & 0.8 & 0.5 & 0 \\ 0 & 0 & 0 & 0 & 0 & 0.9 \end{bmatrix} \\
 &= (0.83, 0.27, 0.02, 0, 0, 0)
 \end{aligned} \tag{13}$$

According to the principle of maximum membership degree, the diagnosis is  $y_1$ .

The problem of severe wear of the cylinder gear leads to the appearance of aforementioned symptoms. However, when there are two maximum results, we can use the method of multiplication. Its main mind is to take a small value to replace

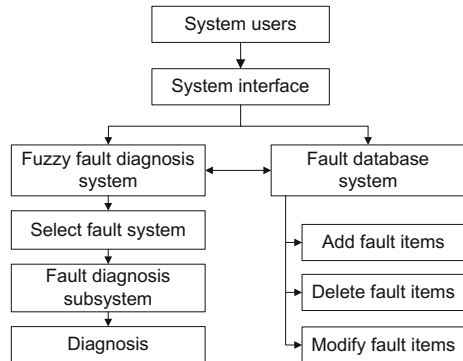
**Table 1** The quantitative analysis of fault symptom severity

The expression fault symptom	The value ranges of X
Normal	0
Slight	0–0.3
Slightly serious	0.3–0.6
Serious	0.6–0.8
More serious	0.8–1
The most serious	1

**Table 2** The fuzzy relation between causes and symptoms sets

Fault symptoms	Fault causes					
	$y_1$	$y_2$	$y_3$	$y_4$	$y_5$	$y_6$
$x_1$	0.9	0.1	0	0	0	0
$x_2$	0.1	0.9	0.1	0	0	0
$x_3$	0	0	0.9	0	0	0
$x_4$	0	0	0	0.8	0.5	0
$x_5$	0	0	0	0	0	0.9

**Fig. 2** The overall structure of diagnostic module



the 0 element in the fuzzy matrix, such as 0.1, and then multiply all the related elements by columns. Finally, comparing the relative value of the products,

We can use the greatest value as our diagnostic result.

### 3 Diagnosis Module Design

#### 3.1 Overall Structure Design

In order to establish the fault diagnosis system of printing machine, we need to design a friendly man-machine interface, an efficient reasoning strategy, a convenient method of knowledge acquisition and a perfect database. The overall structure of the design is shown in Fig. 2.

The database is the data source of the whole system, which plays an important role in the application software. The management of the database includes adding faults, updating faults and deleting faults. In this system, the fault phenomena, the failure causes and the fuzzy matrix are stored in three tables. According to the requirement of our algorithm, the three tables are stored in a certain number of tables [9] according to different fault types. Then, we conduct a joint query while writing programs.

Corresponding to the database module, the working interface also adopts the interactive and connected invocation methods. Each working interface corresponds

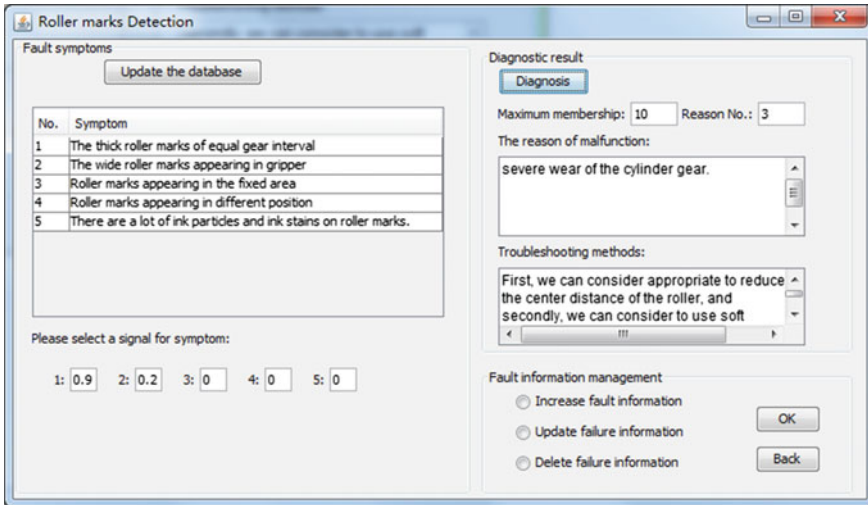


Fig. 3 Fault diagnosis design interface

to the corresponding database and can be called each other. The diagnostic design interface of roller marks is shown in Fig. 3.

### 3.2 Process Design of Fuzzy Reasoning Algorithm

This design uses the man-machine conversation way to reason the diagnosis, then step by step finds out the faulty parts as well as causes of the printer. Its algorithm flow diagram is shown in Fig. 4.

## 4 Function Model of Fault Diagnosis System

The system is divided into 4 main functions: information retrieval, intelligent diagnosis, network consultation and remote monitoring. The overall structure of the system is shown in Fig. 5.

The fault diagnosis system is divided into 3 stages [10].

- Stage 1 When the printing machine fails, the users can look up the corresponding technical or maintenance manual data from the information retrieval module provided by the system to judge the causes of the fault by themselves.
- Stage 2 It is the automatic diagnosis of the system. The users input the necessary parameters of fault phenomena and they are transmitted to corresponding

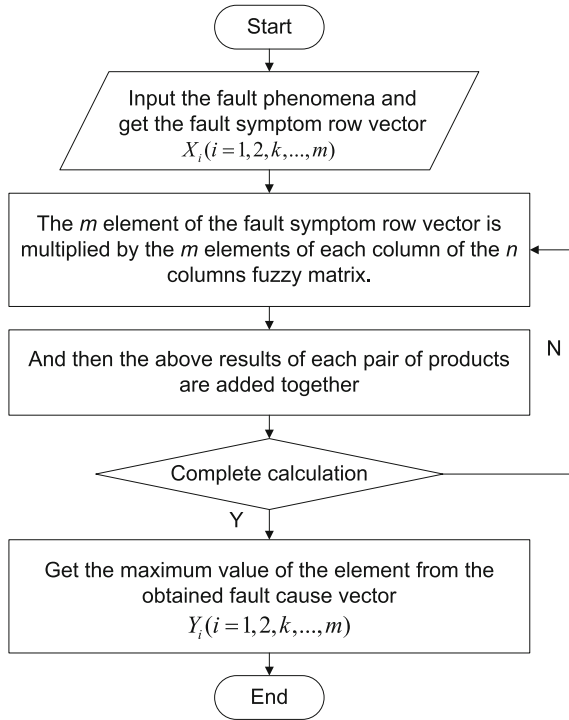


Fig. 4 Chart of algorithm flow

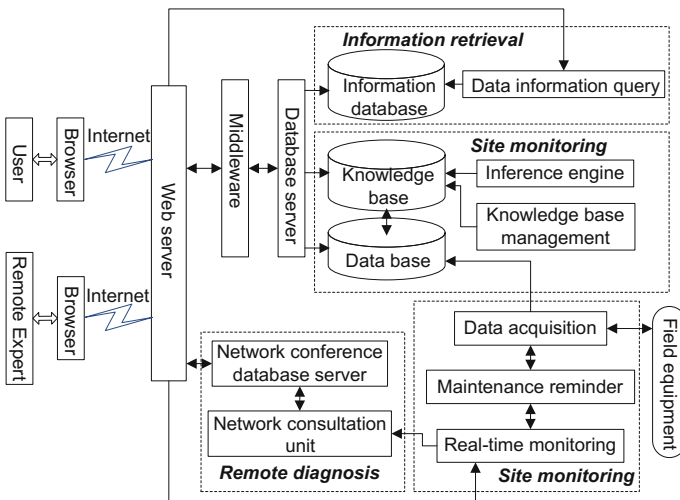


Fig. 5 System general structure

intelligent diagnosis module in diagnosis center through the network. When the diagnosis results are obtained, they will be sent back to the user terminal.

- Stage 3 It is the union consultation. If the stage 1 and stage 2 cannot meet the needs of maintenance, the diagnostic center of system will send requests to the relevant experts and then mobilizes all experts and technical resources on networks to accomplish the network consultation of system faults. After finding out the failure causes of the printer equipment, the system will generate the maintenance guidelines to direct the maintenance personnel on the spot and store the useful information in the diagnosis process to the knowledge base of the diagnosis center to improve the its knowledge level. In addition, the users can also release the fault diagnosis requests through the mature Web technologies such as e-mail, forums and chat to obtain technical assistance from other people on the Internet, as well as exchange the experience and implement the non-real-time diagnosis.

## 5 Conclusions

In the system, the Internet of things and fuzzy reasoning technique are applied to fault diagnosis of printing machine. It provides a convenient way for the remote, networking, multi-expert collaborative diagnosis and the sharing of diagnostic resources of printing machine, which greatly improves the work efficiency of fault diagnosis for equipment, overcomes the shortcomings of traditional fault diagnosis technology and realizes the purpose of remote fault diagnosis of printing machine.

**Acknowledgements** This paper was supported by National Natural Science Foundation “Analysis and Solution of Nonlinear Dynamic Process in High Speed Printing Equipment” (No. 61272030) and “Nonlinear Dynamics model and Analysis of Gear Systems for Offset Press” (No. 61472461).

## References

1. FU Renxuan, SHI Anwei. Design and Application of Remote Monitoring Fault Diagnosis System of Internet of Things [J]. *MOBILE COMMUNICATIONS*, 2014, (2): 0080–0085.
2. SU Xianli, ZHENG Yilin. Design and Implementation of Machine Things Net Work Based on RT-thread [J]. *Modular Machine Tool & Automatic Manufacturing Technique*, 2015. (6): 0061–0065.
3. WU Jiping, WU Yunxin, Long Zhili. Design and Realization of Fault Diagnosis Expert System Based on Fuzzy Mathematics [J]. *Packing Engineering*, 2003(02): 49–51.
4. YANG Gui, LI Renwang, YAN Zhongzi. Application of fuzzy mathematics to valve fault diagnosis [J]. *VALVE*, 2007, 05: 26–28.

5. Wang Xu, Zhang Lida. The Application of Fuzzy Set Theory to the Fault Diagnosis of Gate Operating Mechanism [J]. Water Power, 2008. (03): 62–64.
6. ZHOU Zhiying. Application of fuzzy technology in fault diagnosis of diesel engine [J]. Coal Mine Machinery, 2005. (12): 162–164.
7. Wang Ke, XIA Liqun. Actuator Fault Diagnosis Based on Fuzzy Logic [J]. MACHINE TOOL & HYDRAULICS, 2010, 38(15).
8. Wang Bingren, Jiang Xiaoli, Zhang Lei. Study on Automobile Fault Diagnosis Based on Fuzzy and Logical Reasoning [J]. Mechanical & Electrical Engineering Magazine, 2005, 22 (10): 46–50.
9. Zhao Nan, Cheng Ganghu, Liu Guodong. Design of fault diagnosis system for printing machine based on fuzzy inference [J]. Printing Field, 2007, (255): 67–69.
10. MAO Hongbao, XU Qing, Liang Wei. Research of remote fault diagnosis technique based on Web-model. Computer Engineering and Design, 2005, 26(3): 0686–0687, 749.

# A Method of Printing Press Fault Diagnosis Based on Image Texture Information

Xueqian Bai, Haiyan Zhang, Weibo Chun, Zhuofei Xu  
and Qianqian Xu

**Abstract** Fault diagnosis plays an increasingly important role in the safety of printing press, and how to judge the fault quickly and accurately has aroused people's attention. During the printing progress, substrate have contacted with many parts of printing press, which makes the printing pictures obtained many useful information, and these information can be used to diagnose printing machine faults. By analyzing these information, a new method for fault detection and diagnosis in printing press based on image texture information is presented. Firstly, the gray level co-occurrence matrix (GLCM) was used to extract the data. Secondly, the principal component analysis (PCA) method was used to process the data. Thirdly, the support vector machine (SVM) was used to analyze the data. Finally we realized the fault diagnosis with software. The availability of the diagnostic approach is verified by experiments, and we have realized the high accuracy and efficiency of fault diagnosis. It is practical in the field of printing machine fault diagnosis.

**Keywords** Fault diagnosis · Gray level co-occurrence matrix · Principal component analysis · Support vector machine

---

X. Bai · H. Zhang · Z. Xu (✉) · Q. Xu  
Faculty of Printing, Packaging Engineering and Digital Media Technology,  
Xi'an University of Technology, Xi'an, China  
e-mail: xzf\_34216606@163.com

X. Bai  
e-mail: xqbai187@163.com

W. Chun  
ZheJiang JingSheng Mechanical and Electrical Co. Ltd., Shangyu, China



## 1 Introduction

With the rapid progress of science and technology, printing machinery industry also expanded, and printing machinery will be a high degree of automation. The faulty condition will result in huge losses, so the printing press fault diagnosis is particularly important. Fault diagnosis method based on the different method have their disadvantages, such as vibration signal fault diagnosis, knowledge, artificial neural network and image [1–4]. The development of computer technology and artificial intelligence is a new research, so the development of a new fault diagnosis system is necessary. In this paper, the feature sets are extracted and reduced with PCA, and the support vector machine is used for fault diagnosis.

## 2 Researching on the Application of the Printing Picture Information

### 2.1 *Difference Images*

Images Difference is an algebraic operation of image pixels, and it subtracts the two pictures of the corresponding pixels. It commonly used to match between images with minor changes. The printing defects are the main differences between the standard proofs and printing proofs [5]. The standard proofs and printing proofs are dealt with Difference Images to get differential image after capturing the printing images. The images contain the fault information, so we can calculate the difference parameters of image texture features.  $A(x, y)$  is standard proofs,  $B(x, y)$  is printing proofs,  $C(x, y)$  is images difference. Difference images can be expressed as:

$$C(x, y) = A(x, y) - B(x, y) \quad (1)$$

### 2.2 *Characteristic Texture Parameters and Gray Level Co-occurrence Matrix*

Texture is an important feature of images. It is formed by the different gray values appearing in different position again and again, so there is a certain relationship between the two pixels in the image. GLCM can accurately describe the texture of the roughness and space complexity, and four parameters are extracted as (1)–(4). It has 4 directions, and 16 parameters are used to characterize the feature image. Where  $P(i, j/d, \theta)$  denotes the elements in the gray level co-occurrence matrix,  $\theta$  denotes the direction,  $d$  denotes the distance,  $i$  and  $j$  denotes the number of two pixels. Angular two moments (energy) is shown in (2), and contrast is shown in (3). Entropy is shown in (4). Linear correlation coefficient is shown in (5).

$$ASM = \sum_{i,j} \{P(i,j/d, \theta)\}^2 \tag{2}$$

$$CON = \sum (i - j)^2 P(i,j/d, \theta) \tag{3}$$

$$ENT = \sum_{i,j} \{P(i,j/d, \theta)\} - \log\{P(i,j/d, \theta)\} \tag{4}$$

$$COR = \sum_{i,j} (i - \mu_x)(j - \mu_y)P(i,j/d, \theta) / \sigma_x \sigma_y \tag{5}$$

### 3 Application of PCA Method in Fault Diagnosis of Printing Machine

Principal component analysis is a method that can reduce the dimension of image data and simplify the data structure. The essence of PCA is to map high dimensional spatial data to low dimensional space by orthogonal transformation, so that the main features of printed images can be extracted. In practical problems, the original data is represented by the principal components, and the dimension of the original data is realized [6].

Component Contribution: the ratio of the eigenvalues of the No.  $i$  to the sum of the eigenvalues. Formula for:

$$a_i = \lambda_i / \sum_{i=1}^p \lambda_i \tag{6}$$

Cumulative Contribution: the ratio of the eigenvalues of the first  $k$  principal components to the sum of the eigenvalues. Formula for:

$$M_k = \sum_{i=1}^k \lambda_i / \sum_{i=1}^p \lambda_i \tag{7}$$

The process of PCA is as follows. (1) Calculating sample mean vector. (2) Sample Data Center. (3) Constructing covariance matrix. (4) Calculating the characteristic value and characteristic vector in descending order of eigenvalues. (5) According to the contribution rate of the principal component, the first  $d$  eigenvalues is taken as the result of the subspace. (6) Reconstructing data.

## 4 Application of SVM in Fault Diagnosis of Printing Machine

The proposed method uses Support Vector Machines, and it performs a non-linear classification by projecting the data points into higher dimensional hyper plane through Kernel Function. Linear classifier is the simplest but the most effective form of classification. For a two-dimensional space, there are only two categories of samples:

$$T = \{(x_1, y_1), (x_2, y_2), (x_3, y_3), \dots, (x_n, y_n)\} \quad (8)$$

Among them:  $x \in R, y \in R$

Linear classifier can only deal with the linear separable sample data. If the sample data is nonlinear, the solution of the linear classifier will be infinite loop. In order to use it, we must make the non-separable data inseparably [7].

## 5 Systems and Experiments

The development language of the system is C#. The developed environment is VS2013. The database development software is Access Microsoft 2010. Operating environment is Win7.NET Framework Microsoft 4. Figure 1 is the basic process of fault diagnosis.

Samples contained 1 pieces of tag information and 16 pieces of feature information. Users added the standard image and the select image to detect, then clicked on the “identification”. System finally displayed fault types, characteristics and solution and so on (Fig. 2).

This paper analyzed three kinds of fault features. Equal distance ink bar is shown in Fig. 3a. An ink bar is shown in Fig. 3b. Dirty version is shown in Fig. 3c.

Experiment had 45 samples, they contains 30 training samples and 15 test samples. When the number of principal component was 3, the rate of cumulative contribution was more than 90%. The sample data after dimensionality reduction was obtained by multiplying the original data and the matrix, and the dimension of data was reduced from 16 to 3. The comparison of the fault parameters is shown in Fig. 4.

The sample data after dimensionality reduction was inserted into the SVM to train, then got a recognition model, and it contained the training parameters and support vector. The model was tested with 15 sets of test samples, and the rate of

correct was very high-100%. It was easy to distinguish, because the difference of the data was relatively large, but with the increase of the samples, the rate of correct will down. It can be explained that the recognition model has certain value.

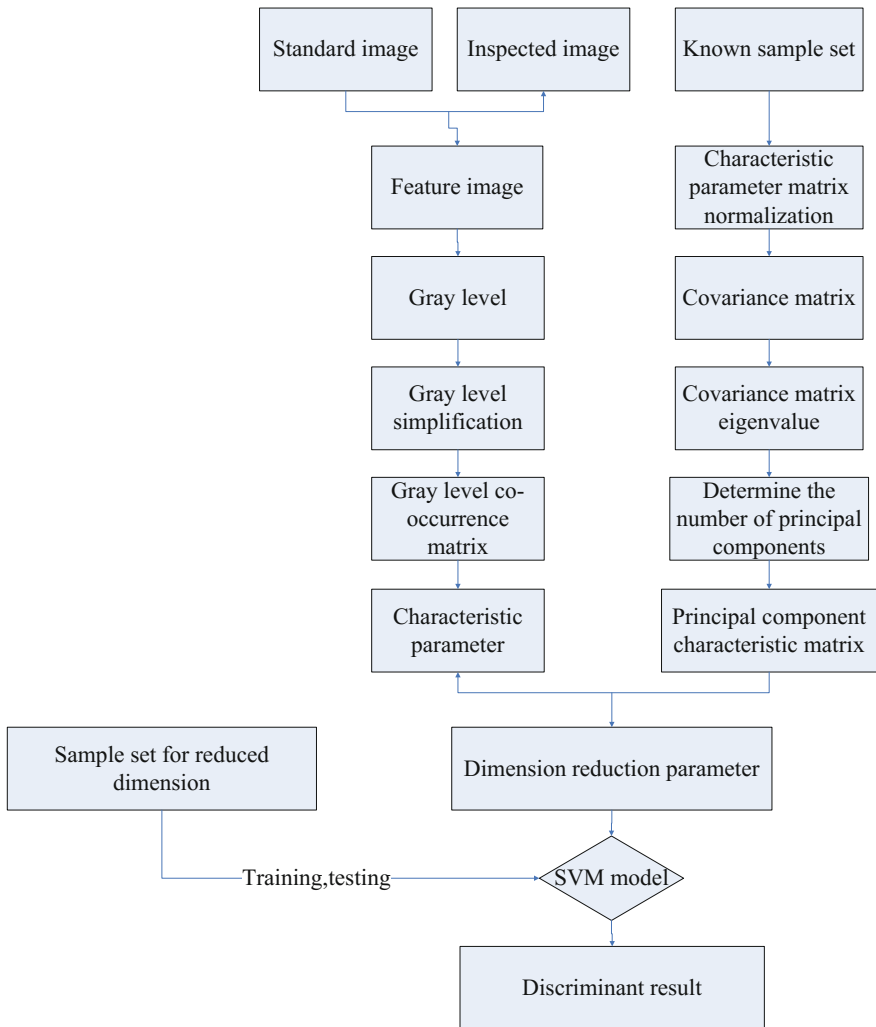


Fig. 1 The basic flow graph

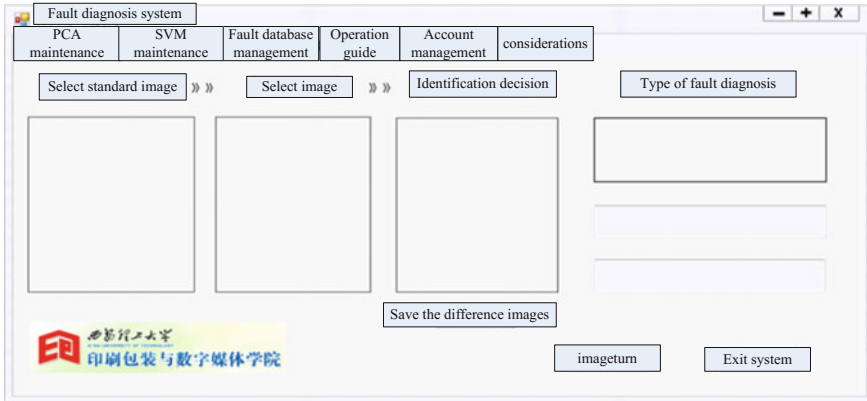


Fig. 2 The main screen

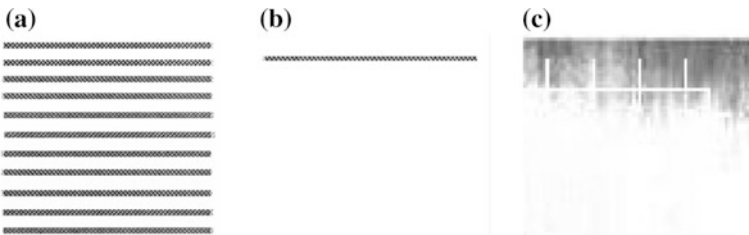


Fig. 3 Three kinds of fault characteristics

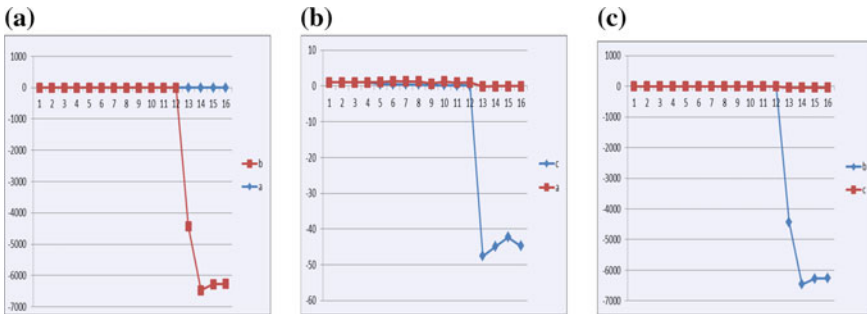


Fig. 4 Fault parameters comparison chart

## 6 Conclusions

Combining Principal Component Analysis and Support Vector Machine, printing pictures are analyzed reasonably, and a new printing press fault diagnosis method is proposed. The software is simple, and the rate of recognition is high. The method is mainly used in the production of the fault diagnosis, and it helps technicians to deal with faults efficiently and quickly, and it can solve the problem of low diagnosis rate and diagnosis difficult in traditional printing machine fault diagnosis. Experiment shows that this method is feasible and effective for the fault diagnosis of printing machine.

**Acknowledgements** This work was supported by National Natural Science Foundation of China (51305340) and The PhD Stand-up Fund of Xi'an University of Technology (108-451115002).

## References

1. Changwoo Lee, Hyunkyoo Kang, Keehyun Shin. Advanced Taper Tension Method for the Performance Improvement of a Roll-To-Roll Printing Production Line With a Winding Process [J]. *International Journal of Mechanical Sciences*, 2012, 59(1): 61–72.
2. Lei Zhang, Yiming Wang, Shuqin Wu. Vibration analysis and Research on the transmission system of printing machine based on case-based reasoning [J]. *packaging engineering*, 2012, 33(9): 85–89.
3. W.L. Tan, N.M. Nor, M.Z. Abu Bakar, et al. Optimum Parameters for Fault Detection and Diagnosis System of Batch Reaction Using Multiple Neural Networks [J]. *Journal of Loss Prevention in the Process Industries*, 2012, 25(1): 138–141.
4. N. G. Shankar, N. Ravi, Z. W. Zhong. A Real-time Print-defect Detection System for Web Offset Printing [J]. *Measurement*, 2009, 42: 645–652.
5. HONEYCUTT ChrisEbey, PLOTNICKRoy. Image, Analysis Techniques and Gray-Level Co-Occurrence Matrices (GLCM) for Calculating Bioturbation Indices and Characterizing Biogenic Sedimentary Structure [J]. *Computers & Geosciences*, 2008, 34(11): 1461–1472.
6. Kairui Yang, Fanrong Meng, Zhizhen Liang. An adaptive weight PCA algorithm [J]. *computer engineering and applications*, 2012, 48(3): 189–191.
7. Xuegong Zhang. Chinese Journal of statistical learning theory and support vector machines [J]. *Journal of automation*. 2000, 26(1): 32–42.

# A Method of Diagnosis for Printing Press Ink Roller Bearing Based on Acoustic Signal and Spectrum Analysis

Yanyan Li, Haiyan Zhang, Qianqian Xu and Zhuofei Xu

**Abstract** Bearings are printing roller subsystems. The fault signal is weak and high integration. It is important to propose diagnosis method of presses bearing based on acoustic signal and spectrum analysis. Firstly, a sound signal filter of non-uniform distribution for presses is designed. Secondly, a sound signal characteristic value of the printing press is constructed based on spectrum analysis; Lastly, the failure contribution rate is calculated of each band by Fisher and the fault frequency is determined. It is proved that the method in this paper is feasible and efficient.

**Keywords** Non-uniform filters · Cepstral coefficients · Fisher ratio method · Inking roller bearings · Fault diagnosis

## 1 Introduction

Printing equipment comprises multiple sets of roller system. Roller system is the core of printing machinery transmission parts. The condition monitoring and fault diagnosis of bearings is important, to guarantee the normal operation and improve the printing quality. However, the noise of printing press is high. The vibration test system construction is limit and the research is very difficult.

Sound signal detection is a non-contact measurement. It avoid create complex test line on the equipment. It can also eliminate the effects of the sensor weight to

---

Y. Li · H. Zhang · Z. Xu (✉)  
Faculty of Printing, Packaging and Digital Media Technology,  
Xi'an University of Technology, Xi'an, China  
e-mail: xzf\_34216606@163.com

Y. Li  
e-mail: liyan625627@163.com

Q. Xu  
Faculty of Mechanical and Precision Instrument Engineering,  
Xi'an University of Technology, Xi'an, China

working parts. The fault can be determined by the EEMD (Ensemble Empirical Mode Decomposition) on sound signals of bearing. This method can effectively extract fault feature of train bearing [1]. A diagnostic method of a motor fault analysis is proposed based on the type of noise. This method has a high accuracy [2].

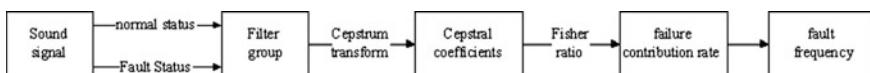
Cepstrum is a new technology in modern signal processing [3], and it can separate and extracted signal component period [4]. It is very effective to complex signal analysis [5]. Cepstrum transformation is a nonlinear signal processing technique in speech and image processing. It is used widely in the actual fault diagnosis. An improved local cepstrum analysis is raised for signal analysis and fault simulation test. The fault can be detected in a low noise signal [6]. The fault feature is extracted by using Fisher ratio method and non-uniform frequency bands Cepstral. It is verified out that this fault feature extraction algorithm has high recognition rate [7]. Wind turbine gear box gear crack diagnosis method is proposed based on wavelet packet and cepstrum analysis. The method can accurately diagnose gear fault [8].

A set of non-uniform filters is designed based on the cepstrum transform and the characteristics of sound signal. Then, the sound signal characteristic of the printing is constructed based on spectrum analysis. At last, the failure contribution rate is calculated of each band using Fisher to determine the fault frequency. It is shown that this method is a high accuracy-viable-efficient method for printer.

## 2 Selection and Distribution of the Band of Filters

The main contents are shown as follows. Firstly, the sound signal of press is collected on normal and fault state. Secondly, the sound signal is passed by a non-uniform distribution filters suitable printer, and the sound signal characteristic value is constructed based on spectrum analysis. Lastly, the failure contribution rate is calculated of each band by the Fisher ratio method [9]. Its technical route is shown in Fig. 1.

A voice filter group of press is designed. It is the main content of this paper. The center frequency of Mel scale is widely used in the extraction of speech recognition and voice feature value. Distribution of this filter center frequency is well simulated the human ear's perception of sound, but it is not suitable for the printer directly. So a filters group of nonuniform banks is designed in this paper according to the press sound signal characteristics and Fisher ratio method. The process is shown in Fig. 2.



**Fig. 1** The main technical route



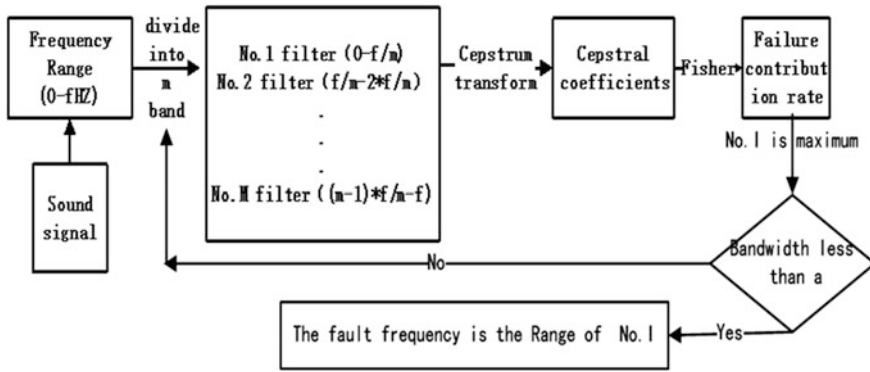


Fig. 2 Design roadmap of nonuniform filters for presses sound signals

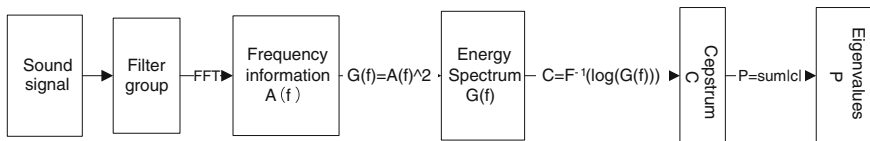


Fig. 3 The schematic diagram of extracting cepstrum characteristic value

### 3 Cepstral Coefficients and Extraction of Eigenvalues

Cepstrum transform as a nonlinear signal processing technique is widely used in speech and image processing. It is the basis of the theory of homomorphic systems.

Cepstrum conversion has its unique advantages in processing the combined signal. The cepstrum transformation method is the inverse Fourier transform of the power spectral density. Its calculation formula is:

$$C = F^{-1}(\log(G(f))) \tag{1}$$

$G(f)$  is the value of the energy spectrum,  $F^{-1}$  is the inverse Fourier transform. The process of Cepstral value extraction is shown in Fig. 3.

### 4 Experiments to Diagnosis for Press Inking Bearing Fault

The small offset ink roller bearing of BENREN is tested to verify the effectiveness of this method. LMS sound signal acquisition device is used. It is a high performance and precision 16-channel data acquisition system. The sampling frequency is

12,800 Hz, and rotational speed of the ink roller is 132 r/min. The 608 bearings are used in experiments. Parameters related are shown in Table 1, and experimental apparatus are shown in Fig. 4.

Bearing failure is artificially processed by wire cutting. The diameter is 1.0 mm and the depth is 0.8 mm. The bearing outer ring fault characteristic frequency formula is follows:

$$f_0 = \frac{1}{2} \left( 1 - \frac{d}{D_m} \cos \alpha \right) f_n Z \tag{2}$$

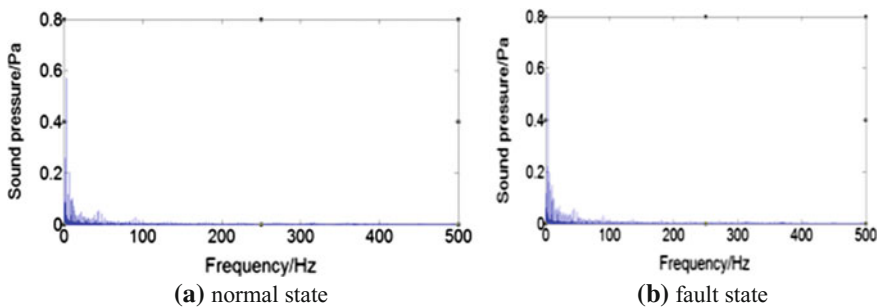
$Z$  represents the number of rollers.  $d$  indicates the diameter of rolling elements.  $\alpha$  denotes the bearing pressure angle.  $D_m$  represents the pitch diameter of the bearing raceway.  $f_n$  is the rotation frequency. The fault characteristic frequency of outer bearing is 5.7855 Hz.

**Table 1** The parameters of the bearing

Inside diameter	Outer diameter	Pitch diameter	Rolling diameter	Number of roller
8 mm	22 mm	15 mm	3.969 mm	7



**Fig. 4** The experimental platform of press sound signal acquisition



**Fig. 5** The frequency spectrum

The experimental procedure as follows:

1. The sound signal of press is measured in normal and failure status. The frequency-domain information is calculated by Fourier transformation as shown Fig. 5a, b.
2. The sound signal of press is passed through 1–5 filters. The bandwidth is 100, 0–100, 100–200, 200–300, 300–400, and 400–500 Hz. The spectrum information through the filter is shown as follows.

The characteristic value of the sound signal passed by 1–5 filters is calculated based on the Fig. 3. The value is shown in Table 2. As can be seen from the Table 2, the difference between normal and fault state is focused on the No. 1 (0–100 Hz) (Figs. 6, 7, 8, 9 and 10).

3. The failure contribution of each band is calculated according to the Fisher ratio method, as shown in Fig. 11.

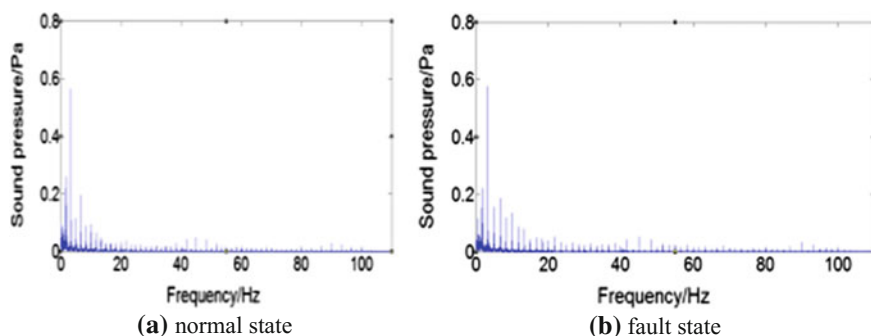
As shown in Fig. 11, the fault contribution of No. 1 filter is maximum.

4. The fault message is focused on the No. 1 filter (0–100 Hz). Then sound signals of normal and fault state press are passed by 6–10 filters. The frequency bandwidth is 20 Hz and passband frequencies are 0–20, 20–40, 40–60, 60–80, and 80–100 Hz. Lastly, the cepstrum coefficient of presses for each band is calculated, as shown in Table 3. The process is the experimental procedure in steps 2 and 3.

The contribution of failure of each band is calculated, according to the Fisher ratio method. The result is shown in Fig. 12.

**Table 2** The characteristic values of the count sound signal passed by 1–5 filter

Number	No. 1	No. 2	No. 3	No. 4	No. 5
Normal state	22.0947	28.5032	28.9600	34.2744	28.4846
Fault state	11.4328	26.1538	33.7544	35.7736	30.8377



**Fig. 6** The signal spectrum after filter No. 1

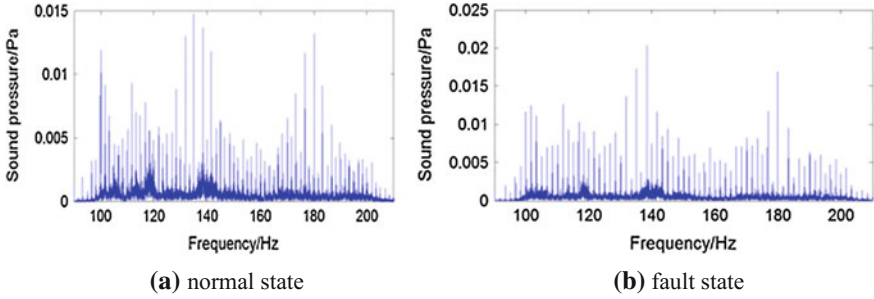


Fig. 7 The signal spectrum after filter No. 2

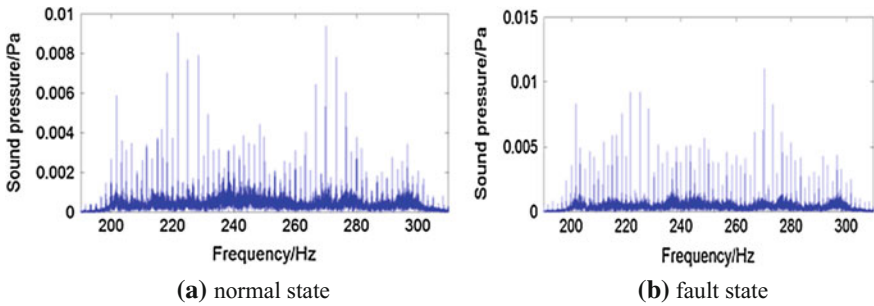


Fig. 8 The signal spectrum after filter No. 3

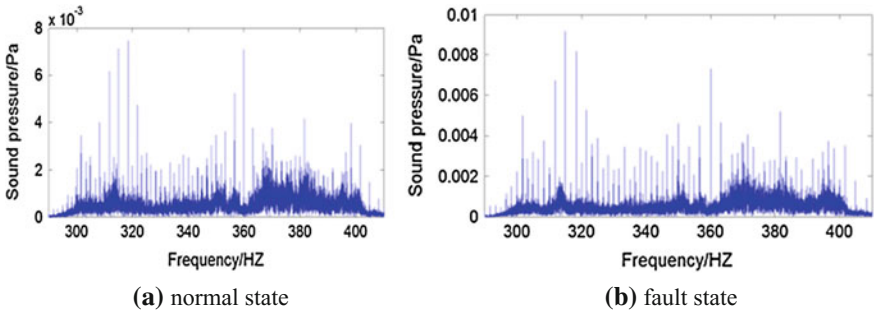


Fig. 9 The signal spectrum after filter No. 4

5. From the Fig. 12, the fault message is focused on the No. 6 filter (0–20 Hz). Then, the sound signal of normal and fault state press is passed through a set of digital resonators No. 11–20. The frequency band is 2 Hz. Bandpass frequencies are 1–3, 3–5, 5–7, 7–9, 9–11, 11–13, 13–15, 15–17, 17–19, and 19–21 Hz. Cepstrum coefficients are calculated, as shown in Table 4. Then, the

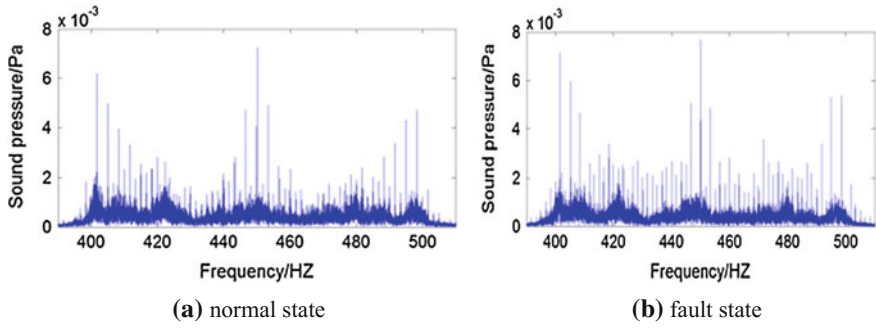


Fig. 10 The signal spectrum after filter No. 5

Fig. 11 The histogram of failure contribution for No. 1-5

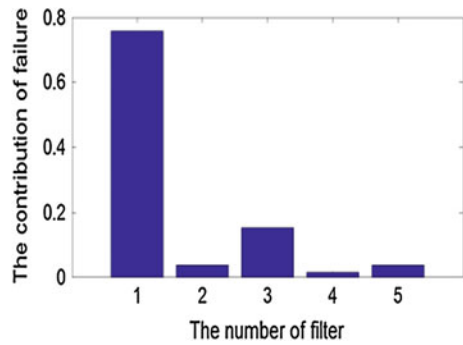
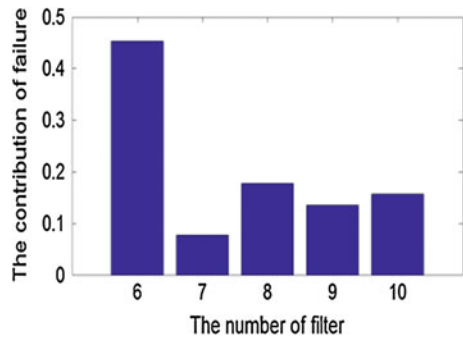


Table 3 The characteristic values of sound signal passed by 6-10 filter

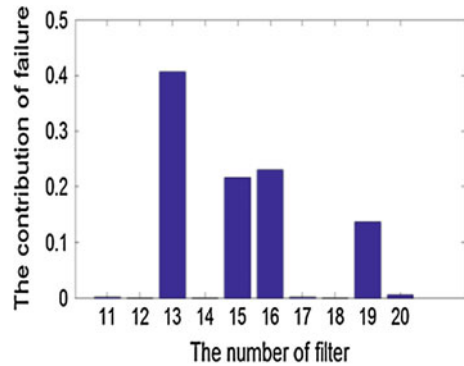
Number	No. 6	No. 7	No. 8	No. 9	No. 10
Normal state	19.8026	26.0638	26.2594	28.7853	30.9220
Fault state	12.2377	22.9492	21.5294	24.6489	26.4770

Fig. 12 The histogram of failure contribution for No. 6-10



**Table 4** The characteristic values of the count sound signal passed by 11–20 filter

Number	No. 11	No. 12	No. 13	No. 14	No. 15
Normal state	10.2006	12.4751	8.9230	17.1140	12.9474
Fault state	10.5528	12.3345	15.7399	17.3213	17.9178
Number	No. 16	No. 17	No. 18	No. 19	No. 20
Normal state	14.6738	17.3630	15.7930	16.3759	19.6451
Fault state	19.8055	17.7553	15.8973	20.3369	20.4997

**Fig. 13** The histogram of failure contribution for No. 11–20

contribution rate of each frequency band is calculated according to Fisher ratio method, as shown in Fig. 13.

As can be seen from Fig. 13, the sound signal fault information is focused on the No. 13 filter (5–7 Hz). The calculated frequency (5.7855 Hz) is consistent with the tested fault frequency (5–7 Hz). This method is proved correct.

## 5 Conclusions

A fault diagnosis method for bearing in printing machine is given in this paper. The following conclusions can be received. (1) Gradual filters of bank analysis can quickly identify the range of faulty frequency. (2) Sound signal characteristics of press can be well reflected by the cepstral coefficient for each band. (3) The contribution rate of failure can be calculated efficiently and quickly by Fisher ratio method. In summary, the fault diagnosis method based on the sound signal and cepstral coefficient is a feasible and efficient method for printer.

**Acknowledgements** This work is supported by National Natural Science Foundation of China Project (51305340). The PhD Start-up Fund of Xi'an University of technology (108-451115002).

## References

1. LIU Fang, SHEN Changqing, HE Qingbo, et al. Wayside acoustic fault diagnosis for locomotive bearing based on Doppler effect correction and EEMD method in time domain [J]. *Journal of Vibration and Shock*, 2013, 24(017): 104–109.
2. ZHANG Yuan, WANG Fei, WANG Wancheng. Research of Motor Fault Based on Noise Analysis [J]. *Micromotors*, 2012, 45(8): 83–88.
3. BORGHESANI P, PENNACCHI P, RANDALL R B, et al. Application of cepstrum pre-whitening for the diagnosis of bearing faults under variable speed conditions [J]. *Mechanical Systems and Signal Processing*, 2013, 36: 370–384.
4. BALSAMO L, BETTI L, HEIGI H. A structural health monitoring strategy using cepstral features [J]. *Journal of Sound and Vibration*, 2014, 333: 4526–4542.
5. BISPO B C, FREITAS D R S. The use of cepstral analysis in acoustic feedback cancellation [J]. *Digital Signal Processing*, 2015, 44(1): 88–101.
6. ZHANG Xining, LI Bing, LEI Wei. An Improved Local Cepstrum Analysis Method [J]. *Journal of XI'AN Jiaotong University*, 2016, 50(8), 1–5.
7. BAI Huining, MA Jiancang, LI Junjie, et al. Method for Bearing Vibration Signal Processing Imitating Auditory Frequency Decomposition Characteristics [J]. *Measurement and Instrument*, 2015, 4, 49–53.
8. LUO Yi, ZHEN Lijing. Diagnosis method of turbine gearbox gearcrack based on wavelet packet and cepstrum analysis [J]. *Journal of Vibration and Shock*, 2015, 34(3): 210–215.
9. GAO Lixin, REN Zhiqiang, ZHANG Jianyu. Diagnosis method of roller bearing based on Fisher ratio method and SVM [J]. *Journal of Beijing University of Technology*, 2011, 37(1): 13–18.

**Part VII**  
**Ink and Related Technology**



# Study of Factors on Ethanol Resistance Stability of Water-Based Acrylic Resin Emulsion

Changming Yin, Xiaoyu Li and Haiqiao Wang

**Abstract** Acrylic emulsion is the most widely used binder in water-based inks due to its low price, safety, resource and energy saving, and environmentally friendly. The stability of acrylic emulsion is one of the most basic and important performance. In the process of using water-based inks, a certain amount of ethanol is often added into inks to improve the drying rate, hence, excellent ethanol resistance stability is often needed for the emulsion. In this paper, acrylic resin emulsion with core-shell structure was prepared by means of semi-continuous seeded emulsion polymerization and pre-emulsification technology. Effects of emulsifier types, latex particle size, and chain transfer agent on stability of the emulsion, including polymerization stability and ethanol resistance stability, were investigated, which would provide an important guidance for the broad readships.

**Keywords** Acrylic resin · Core-shell structure · Ethanol resistance · Stability

## 1 Introduction

An increase in environmental awareness has led to the replacement of processes that use solvent-based by cleaner water-based systems, more and more researchers have attached importance to the water-based ink, which has a low or zero VOC. Polyacrylate emulsions have been applied widely in water-based inks in virtue of good performance, such as chemical resistance, film forming ability, affinity to the pigments and so on [1].

Compared with the single-component emulsion, the core-shell emulsion structure exhibits improved physical and chemical properties. Li et al. [2] prepared

---

C. Yin · X. Li (✉) · H. Wang  
Key Laboratory of Carbon Fiber and Functional Polymers, Ministry of Education,  
Beijing University of Chemical Technology, Beijing, China  
e-mail: lixy@mail.buct.edu.cn

H. Wang  
e-mail: wanghaiqiao@mail.buct.edu.cn

core-shell cross linkable latices with MMA and BA as the main comonomers, and DAAM and ADH as cross-linker. It was found that the core-shell cross linkable particles with a low  $T_g$  core and a high  $T_g$  shell have better film properties than these particles with a high  $T_g$  core and a low  $T_g$  shell.

The stability of the polyacrylate emulsions during the polymerization and preservation is as important as its performance. However, polyacrylate emulsions are a thermodynamic instability system, so how to improve the stability of the polyacrylate emulsions to meet the needs of the practical application has been a challenging topic.

The factors which effect on the stability of emulsion contain emulsifier types, latex particle size and so on, and emulsifiers play an important role in stability of the emulsions. Kahraman et al. [3] studied two types of emulsifiers to compare the colloidal and physicochemical properties of vinyl acetate (VAc)/(BuA) emulsions. The results demonstrated that the composition of mixed emulsifiers and emulsifier concentration was sensitive to parameters such as viscosity, particle size, and surface tension, which are related to the stability of the emulsion. However, to the best of knowledge, there is not report on the stability of the polyacrylate emulsions with core-shell structure so far.

In this paper, polyacrylate emulsion with core-shell structure was firstly prepared, and then effects of emulsifier types, latex particle size, chain transfer agent on polymerization stability and ethanol resistance stability of the emulsion were studied.

## 2 Experimental

### 2.1 Materials

Methacrylate or acrylate monomers used in this paper were technical grade. Acrylic acid was provided by Tianjin Fuchen Chemical Reagents Factory and was analytical reagent (AR). N-Dodecyl mercaptan was chemically pure (CP) and provided by Sinopharm Chemical Reagent Co., Ltd. Ammonium persulfate (APS) was purchased from Beijing Chemical Works and used as the initiator. Emulsifiers were used as received. De-ionized water was used throughout the work.

### 2.2 Emulsion Preparation

The core-shell emulsion polymerization was carried out in a 2-L four-neck round flask equipped with a stirrer, a reflux condenser, a nitrogen inlet and a thermometer. A certain amount of emulsifier, buffer agent, distilled water and a part of mixed monomers were added into the flask, and then heated to 82 °C for 15 min under

nitrogen atmosphere. One-third of the initiator was added into the flask to initiate the polymerization. After the reaction system turned into light blue, let the reaction run further for half an hour at 82 °C. Then, another one-third of the initiator and the core monomers were added to the flask in 1 h. After the addition was completed, the reaction was maintained for another 1 h at 82 °C, then the shell pre-emulsion and initiator solution were added in 1 h throughout the process and the reactor was maintained at 82 °C for 2 h after the addition was finished. Finally, it was cooled to room temperature, filtered through a 200 mesh filter cloth and neutralized to pH 9.0–9.3 by AMP-95.

### 2.3 Characteristic

1. Particle size: The particle size was determined by dynamic light scattering using a zetasizer Nano-ZS. The reported results are average of 3 runs.
2. Gel ratio: Aluminum foil (weight  $m_1$ ) containing gel was dried in an oven at 50 °C until constant weight, and the total weight was weighted as  $m_2$ . The gel ratio is defined as follows:

$$\text{gel ratio} = \frac{m_2 - m_1}{\text{the total weight of monomers}} \times 100\% \quad (1)$$

3. Ethanol resistance: 40 g emulsion was placed into a beaker under stirring using high mixing machine. Then, 15 g grinding resin was instilled into the emulsion, and kept stirring for half an hour. Next, 15 g ethanol was added, and stirred for another 15 min. Stability of the prepared emulsion was analysed by employing turbiscan lab. Turbiscan Stability Index (TSI), which characterizes the stability of the emulsion, can be obtained from this instrument. The higher the TSI is, the poorer the stability of the emulsion is.

## 3 Results and Discussion

### 3.1 Effect of Emulsifier Types on the Stability of the Emulsion

Several emulsifiers including anionic RE, SDS and nonionic surfactants Tu-80 and X-30 were selected to prepare the latex by semi-continuous emulsion copolymerization. Table 1 depicted the fundamental properties of the obtained emulsions.

**Table 1** The fundamental properties of the emulsions

	Emulsifier system	Outward appearance	Gel ratio (%)	Particle Size (nm)	Water absorption (%)
A	RE:X-30:SDS	Pale blue	0.3473	83.40	11.78
B	RE:Tu-80	Pale blue	3.458	149.2	13.52
C	RE:X-30	Pale blue	1.730	134.9	14.00
D	RE	Pale blue	0.2689	98.73	11.30

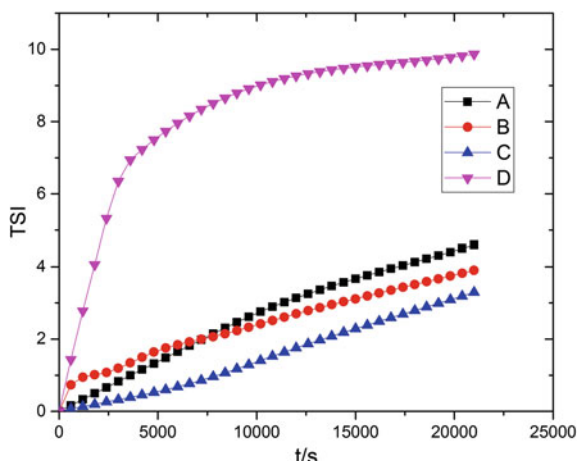
**Fig. 1** The stability of emulsions with different emulsifier types

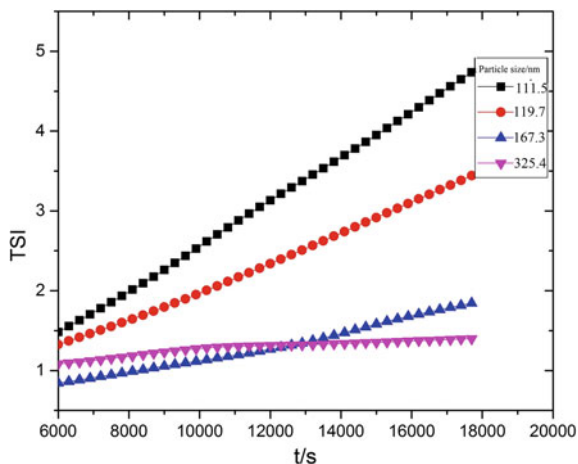
Figure 1 depicts the stability of latexes synthesized employing different emulsifier systems. The stability of latex prepared with a single reactive emulsifier is very poor. On the contrary, the latex with compound anionic and nonionic emulsifiers shows good stability. It is known that the mixed anionic and nonionic emulsifiers have the synergetic effects provided by both the electrostatic and steric stabilization mechanisms, which could greatly improve the colloidal stability of the polymerization system [3].

### 3.2 Effect of the Particle Size on the Stability of Emulsion

The particle size can be controlled by changing the ratio of emulsifier content in the seed emulsion to that in pre-emulsion.

Figure 2 illustrated the stability of latexes with different particle size. It is obviously that the smaller the particles are, the poorer the stability of latex is. There are two primary reasons for this behavior: on the one hand, smaller size of particles

**Fig. 2** The stability of emulsion with different particle size



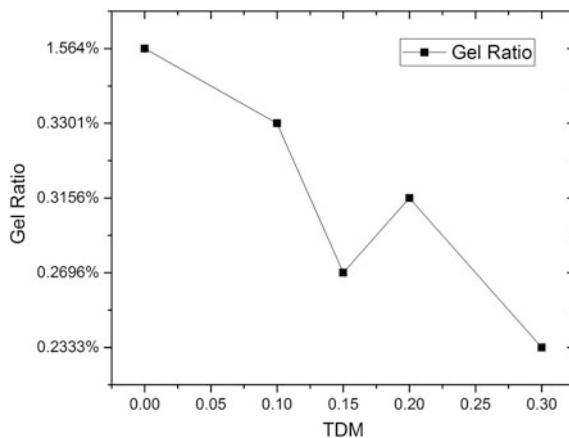
causes severe Brownian motion, which increases the rate of particles aggregation; on the other hand, smaller particles have bigger interface energy than the larger particles, leading to the coagulation of latexes.

### 3.3 Effect of the Chain-Transfer-Agent on the Stability of Emulsion

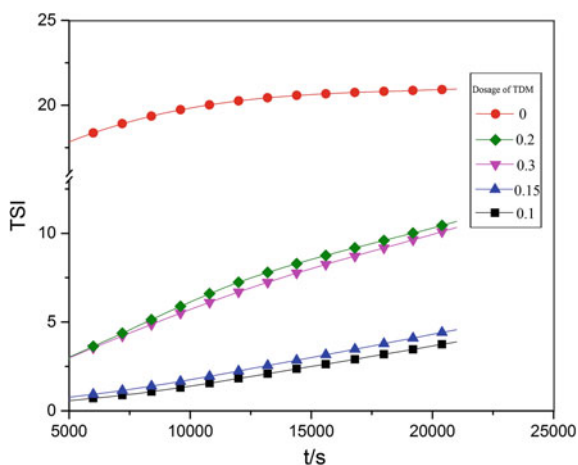
Figure 3 shows the gel fraction of emulsion polymerization at different CTA (N-Dodecyl Mercaptan) dosages. The gel of latex without N-Dodecyl Mercaptan (NDM) is the largest. This is because the polymer resin possesses the highest molecular weight in the absence of CTA, and high molecular weight species are more prone to hydrogen abstraction and chain transfer because of the higher number of tertiary carbon atoms per chain [4]. The gel arose from termination by the coupling of propagating long-chain branches formed by intermolecular chain transfer to polymer. The presence of modest amounts of NDM made the polymer chain transfer to NDM. Therefore, the gel fraction was significantly decreased. Obviously, when the dosage of NDM was 0.10%, the gel fraction was almost completely avoided.

Figure 4 illustrated the stability of latex with different contents of NDM. The results indicate that the addition of NDM will improve the stability of the latexes, but there is no significant principle in stability that was observed with increasing the content of NDM. However, NDM is considered volatile organic compound and has an offensive odor, the dosage of NDM is 0.1wt% would be recommended.

**Fig. 3** Variation of the gel content with the TDM content



**Fig. 4** The stability of emulsions with the TDM content



## 4 Conclusions

The core-shell structural polyacrylate emulsion was prepared to study the effect of the emulsifiers, particle size, and dosage of NDM on the stability of the emulsions in detail. The mixed anionic and nonionic surfactants have the synergetic effects provided by both the electrostatic and steric stabilization mechanisms, which can greatly improve the colloidal stability of the polymerization system. As for the particle size, the smaller the particles are, the poorer the stability of latex is. The addition of NDM will reduce the gel ratio in the polymerization and enhance the stability of the final latexes. However, there is no significant principle in stability was observed with increasing the content of NDM.

## References

1. Zhang, J., Li, X., Shi, X., et al (2012). Synthesis of core-shell acrylic-polyurethane hybrid latex as binder of aqueous pigment inks for digital inkjet printing. *Chinese Material Research Society*, 22(1), 71–78.
2. LI Mu, LIN Xiaosong, LI Xiaoyuand WANG Haiqiao (2013). Preparation and Property Study of Core-Shell Ambient-Temperature Crosslinkable Polyacrylate Binder. *Research on Food Packaging Technology*, 469, 3–6.
3. Ayc,a Kahramana, Ayfer Sarac (2009). Semibatch emulsion copolymerization in the presence of n-methylol acrylamide: effects of emulsifier type and concentration. *Polymers Advanced Technologies*, 303–306.
4. Hanzi Shen, Jiyang Zhang, Shuangjin Liu, Guodong Liu, Liqun Zhang, Xiongwei Qu (2007). Effect of the Chain-Transfer-Agent Content on the Emulsion Polymerization Process and Adhesive Properties of Poly (n-butyl acrylate-co-acrylic acid) Latexes. *Journal of Applied Polymer Science*, DOI 10.1002.

# Research of Water-Based Graphene Conductive Screen Printing Ink and Its Property

Minghui Zhang, Xianfu Wei, Beiqing Huang and Bin Long

**Abstract** Graphene has become a hot new material in various fields due to its excellent physical properties such as high conductivity and heat resistance. As conductive filler for preparing water-based conductive ink, graphene has a significant influence on the development and promotion of water-based conductive ink. Based on the previous studies, the dispersion stability of graphene was studied by changing the ways of dispersion; the conductive property and printing adaptability of graphene conductive ink was studied by changing the kinds and content of film-forming resin and finally the best formulation of graphene conductive ink obtained by formula experiments. The conductive property and printing adaptability of ink were also studied by changing the amount of thickener based on the formulation. It is concluded that the ink obtained by the formula experiment of which the average sheet resistance was  $156.43 (\Omega/\square)$  has a good printability which was able to meet the production requirements for screen printing.

**Keywords** Graphene · Water-based conductive ink · Conductive property · Printing adaptability

## 1 Introduction

With the rapid development of ink industry and printing technology, ink is no longer limited to the general printing industry and the application of printed electronic devices of which good conductive ink was needed has gradually become a trend [1]. Meanwhile water-based conductive ink came into being with the continuous improvement of people's awareness of environmental protection [2].

---

M. Zhang (✉) · X. Wei · B. Huang · B. Long  
School of Printing and Packaging Engineering, Beijing Institute of Graphic Communication,  
Beijing, China  
e-mail: 843451017@qq.com

X. Wei  
e-mail: weixianfu@bigc.edu.cn



There are many kinds of conductive fillers which mainly divided into metal-based conductive filler and carbon-based conductive filler. The high production cost and complex production process make the metal-based conductive ink a certain constraint on its application although it has excellent conductive properties [3]. The production of carbon-based conductive ink is relatively cheap and its production process is simple [4], but its conductivity is low.

Novoselov successfully prepared carbon material using micro-mechanical exfoliation in 2004 and this material was denoted as graphene [5] which has excellent physical properties such as heat resistance and high conductivity [6]. Applying the conductive ink which was prepared by graphene in printing preparation devices can not only make up for poor conductive properties of today's inorganic non-metal-based conductive ink but also reduce the cost of printing electronic components to a certain extent [7]. Therefore the study of water-based graphene conductive ink contributes to promoting the application of ink in microelectronic devices.

## **2 Experiments**

### ***2.1 Experimental Materials***

Conductive filler: graphene (Prodio International Inc); Grinding resin: HPD 96; film-forming resin: Joncryn<sup>®</sup> S2916, Joncryn<sup>®</sup> S2919, Joncryn<sup>®</sup> 813, Joncryn<sup>®</sup> 503; dispersion agent: 750; defoamer: 810; thickener: 803; deionized water.

### ***2.2 Experimental Instrument***

Temperature magnetic stirrer; JJ-I type mechanical stirrer; GJ-2S high-speed grinder; Four-probe tester; GLOSS METER TC-108DPA gloss meter; Cone viscometer; RK K303 MULTICOATER type coater; Screen printing machine.

### ***2.3 Proofing Method***

Use screen printer for proofing. Selection of 210 × 297 mm 160 mesh nylon screen version, printed net margin is 3 mm.

### **3 Preparation of Ink**

#### ***3.1 Preparation of Based Ink***

Firstly, get the graphene, grinding resin, defoamers and dispersion agent into a beaker, and placed on an electric stirrer pre-dispersed 30–60 min. Finally, the pre-dispersed ink poured over the high speed grinding machines, a high speed grinding 120–150 min, so that graphene ink system fully wetting and dispersion, based ink to be obtained after the filtration.

#### ***3.2 Preparation of Ink***

According to the ink formulation, a certain proportion of the film-forming resin and additives were added to the based ink, placed the ink stirred for 20–30 min on the electric mixer to obtain graphene conductive ink, and ink can be used for screen printing proofing.

### **4 Test Method of Ink Performance**

#### ***4.1 Test of Dispersion Stability***

Use the static method. To set aside the ink, see whether the ink appear layered or sinking, and recorded the time of stratification, so as to compare the stability of the ink.

#### ***4.2 Test of Square Resistance***

Use the four-probe instrument to test the sheet resistance of the sample, and assess the conductive property of the film.

#### ***4.3 Test of Gloss***

The 75° angle measurement samples using GLOSS METER TC-108DPA gloss meter.

### 4.4 Test of Adhesion

Experimental proofs use coated paper. Printing ink proofing, 3 M tape tightly attached on the surface of the film, and then quickly lift it, according to the amount of conductive ink stripped to evaluate the adhesion of ink. As shown in Table 1.

### 4.5 Test of Leveling

Observe the surface performance of samples, according to Table 2 leveling evaluation standard, to give the subjective rating by observing the apparent performance of the samples.

### 4.6 Test of Apparent Film-Forming

In this study, we have a comprehensive evaluation of the apparent film-forming, which is based on leveling, gloss and adhesion. The calculation rules are as follows:

$$\begin{aligned} \text{The score of apparent film - forming} &= \text{leveling} \times 0.7 \\ &+ \text{adhesion} \times 0.2 + \text{gloss} \times 0.1 \end{aligned}$$

## 5 Experimental Results and Analysis

### 5.1 Effect of Different Dispersion Methods on the Dispersion Stability of Graphene Conductive Ink

In the preparation of ink, the choice of the appropriate dispersion contributes to improving the quality and performance of ink. The effect of two kinds of dispersion methods on the dispersion stability of the conductive ink are discussed, and the experimental results are shown in Table 3.

**Table 1** Adhesion evaluation criteria

Peeling amount (%)	0-10	10-20	20-30	30-40	40-50	50-60	60-70	70-80	80-90	90-100
Adhesion ratings	10	9	8	7	6	5	4	3	2	1

Note The score of the adhesion is 1 to 10 points, of which 10 points on behalf of the best adhesion, 1 point represents the worst adhesion

**Table 2** Leveling evaluation standard

The apparent performance of film	Leveling level
Smooth, no air bubbles, uniformity	1
Smooth, with few bubbles	2
Slightly uneven, a little bubble	3
A very irregular surface, there are a lot of foam	4
Severely uneven, white grave	5

*Note* The level of the flow is divided into 1 to 5 levels, of which 1 represents the best level, and the 5 represents the lowest level

**Table 3** Different dispersion effect on the dispersion stability of graphene conductive ink

Dispersion	Dispersion effect	Settling time (min)
Stirring dispersion	Instability, easy layering	25
Grinding dispersion	More stable, longer for stratification	45

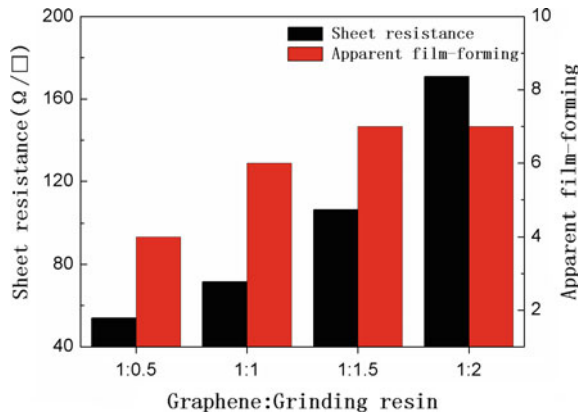
From Table 3, the different dispersion methods have obvious influence on the dispersion stability of ink. Grinding dispersion stability is much better than that of stirring dispersion. The reason is that the shear force of grinding dispersion is greater than the stirring dispersion. Under the action of high shear force, the dispersion of graphene in the grinding resin is more complete and stable. Therefore, it is beneficial to improve the dispersion stability of the ink by grinding dispersion.

## 5.2 *Effect of Solid Content Ratio of Graphene and Grinding Resin on the Film-Forming Properties and Conductivity of Graphene Conductive Ink*

As the dispersion medium and the protective agent, the grinding resin can reduce the aggregation of graphene in the dispersion process, which is favorable for the stability of graphene in the dispersed phase. Therefore, the suitable solid content ratio of the graphene and the ground resin can ensure the best performance of the ink to a certain extent. Changing the solid content ratio of the graphene and the grinding resin, the experimental results are shown in Fig. 1.

Figure 1 shows, different solid content ratio of graphene and grinding resin have significant influence on apparent film-forming properties and conductivity of based ink. For the electrical conductivity, with the increase of the grinding resin, the sheet resistance of ink increases, and the conductivity decreases. The reason is that the increase of grinding resin makes relative reduction in the content of graphene in ink, and therefore the contact opportunities between the graphene sheet layers reduced which makes the sheet resistance of the graphene ink increased, conductivity decreased. As for the film-forming properties, with the increase of the grinding resin, the film-forming properties improved and then basically unchanged. The

**Fig. 1** Effect of resin content on film forming properties and conductivity of the graphene conductive ink



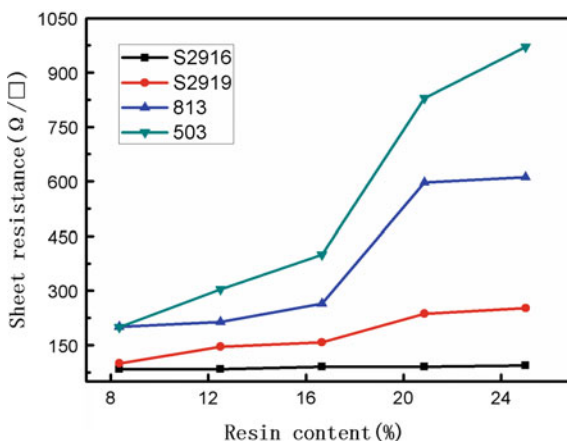
reason is that at the time of adding a small amount of grinding resin, grinding resin improves the graphene dispersion, so make film-forming properties of the graphene ink has some improved; But with the increase of grinding resin, extra grinding resin wrapped in the edge of the graphene sheet layer which does not improve the film-forming of graphene ink. Through the study of the relationship between the amount of the graphene and grinding resin, it was confirmed that the film-forming and conductive properties of graphene conductive ink was relatively good when the solid content ratio of graphene and grinding resin was 1:1.

### 5.3 Effect of Different Kinds of Film-Forming Resin on the Properties of Graphene Conductive Ink

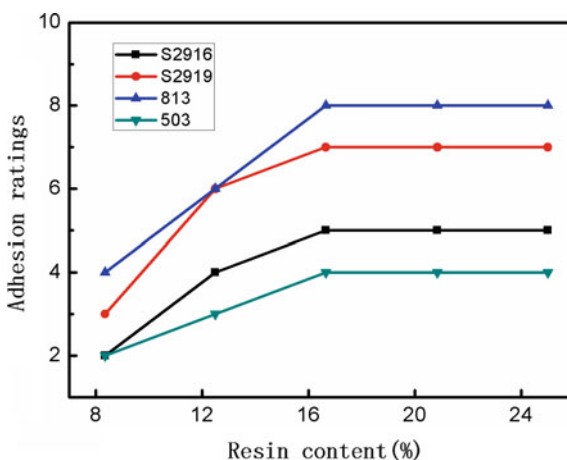
Different kinds and different content of the film-forming resin added to a certain amount of based ink to explore the effect of different water-based film-forming resin on conductivity and adhesion of graphene conductive ink. The experimental results are shown in Figs. 2 and 3.

Figure 2 shows that, with the increase of the film-forming resin, the sheet resistance of ink increases, and the conductivity decreases. The reason is that the increase of film-forming resin makes relative reduction in the content of graphene in ink, therefore the contact opportunities between graphene sheet layers reduced, which makes the sheet resistance of conductive ink increased, conductivity decreased; At the same time, the formation of conductive channel is blocked by the film-forming resin, which further affects the conductive properties of graphene conductive ink. It also can be seen that the influence of different kinds of film-forming resin on the conductive property of ink is different in the case of the same resin content. Addition of film-forming resin S2916 ink conductivity is the best, the conductivity of S2919 ink is better than that of resin 813, and the conductivity of film-forming resin 503 is the worst.

**Fig. 2** Effect of resin content on conductivity of the graphene conductive ink



**Fig. 3** Effect of resin content on adhesion of the graphene conductive ink



The Fig. 3 shows that, with the increase of the film-forming resin, the adhesion of ink is improved, and then tends to be stable. In the case of the same resin content, the influence of different kinds of film-forming resin on the adhesion of ink is different. Addition of film-forming resin 813 ink's adhesion is the best, the adhesion of S2919 ink is better than that of resin S2916, and the adhesion of film-forming resin 503 is the worst. This is due to the different kinds of film-forming resin and its molecular composition and molecular structure is different, the functional groups of the adhesion are also different, so the adhesion of conductive ink is not the same.

It is found that both conductivity and adhesion were the worst when joining the film-forming resin 503. Therefore, the selection of film-forming resin 503 was excluded in the later experiments and the conductivity and printability of graphene conductive ink of three film-forming resins (i.e. S2919, S2916 and 803) are discussed.

### 5.4 Film-Forming Resin Formulation Experiment

Based on all above experiments, it is found that different kinds of film-forming resin have different effect on the performance of the ink. According to a single effect of film-forming resin on the performance of ink, the effect of composite resin on the performance of ink was explored via the formulation experiment using S2916, S2919 and 813 film-forming resins in order to explore the effect of composite resin on the performance of ink. Film-forming resin S2916, S2919 and 813 respectively formula tests for X1, X2 and X3, the results as shown in Table 4.

The weights are set as follows: sheet resistance 0.5, adhesion 0.3, gloss 0.1, and leveling 0.1. By Simplex-barycenter design principle to calculate the regression equation of ink:

$$y = 0.69x_1 + 0.74x_2 + 0.35x_3 - 0.23x_1x_2 - 0.41x_1x_3 + 0.43x_2x_3 - 1.77x_1x_2x_3$$

It can be drawn via the Solver that regression equations can get maximum value for the 0.742511 when  $X_1 : X_2 : X_3 = 0:0.95:0.05$ . That means the overall performance of graphene conductive ink is ideal when S2919:813 = 19:1. According to the optimal formulations prepared inks, test ink performance, the results as shown in Table 5, ink comprehensive performance better.

### 5.5 Effect of Thickener Content on Conductive Properties of Ink

Adding the thickening agent to the ink can make the ink viscosity to meet the requirements of screen printing in order to adjust the ink viscosity. However, the

**Table 4** Film-forming resin formulation results

Number	X <sub>1</sub>	X <sub>2</sub>	X <sub>3</sub>	Sheet resistance (Ω/□)	Gloss	Leveling	Adhesion
1	1	0	0	89.878	18.9	3	5
2	0	1	0	157.898	19.7	3	7
3	0	0	1	364.1	15.5	3	8
4	1/2	1/2	0	82.7762	18.1	2	4
5	1/2	0	1/2	136.684	16.1	4	4
6	0	1/2	1/2	147.874	16.3	2	6
7	1/3	1/3	1/3	139.235	16.8	4	5

**Table 5** performance of the optimized formulation preparation of inks

Sheet resistance (Ω/□)	Gloss	Leveling	Adhesion
156.43	17.2	2	7

**Table 6** Effect of thickener content on conductivity and printability of graphene conductive ink

Thickener proportion (%)	Viscosity (mPa·S <sup>-1</sup> )	Sheet resistance ( $\Omega/\square$ )	Gloss	Adhesion	Leveling
1	4500	160.336	9.76	7	3
1.25	5250	183.55	9.63	7	3
1.5	6224	199.135	9.63	7	3
1.75	7350	224.822	10.2	7	3
2	9675	255.186	9.375	7	3

thickening agent at the same time not only change the ink viscosity but also affect the conductivity and printability of ink, and therefore the amount of thickener is very important. Experimental results are shown in Table 6.

As can be seen from Table 6, with the increase of thickener, the viscosity and sheet resistance of the graphene conductive ink has increased, but gloss, adhesion and leveling did not change much. For the conductivity, with the addition of thickener, the thickener between film-forming resin for forming hydrogen bridges or hydrogen bonding and gathered, so that the ink viscosity increases. However, the aggregation of the resin dispersed in the graphene sheet layer, so that the contact point between the graphene sheet is reduced, resulting in a decrease in the conductivity of graphene, the sheet resistance of ink increased; In terms of gloss, leveling and adhesion, the effect of thickener on these properties was not significantly changed. It can be seen that when the proportion of the thickener is 1%, the viscosity of ink has reached the minimum viscosity requirements of screen printing, so the proportion of thickener was determined to be 1%.

## 6 Conclusions

The following conclusions are obtained in this experimental condition by the study of water-based graphene conductive ink:

1. Grinding is helpful to improve the dispersion of grapheme and therefore the ink has better dispersion stability;
2. The content of the grinding resin has a significant influence on the conductivity and film-forming properties of the ink. With the increase of grinding resin, the conductive properties of the ink decreased, and the film-forming property improved first and then remained unchanged. The film-forming properties and electrical conductivity of graphene conductive ink was relatively good when the solid content ratio of graphene and grinding resin was 1:1.
3. The content of the film-forming resin has a significant effect on the conductivity and adhesion of the ink. With the increase of film-forming resin, the conductivity of the ink decreased, and adhesion improved first, and then stabilized.



When the content of film-forming resin was 16.65%, the conductivity and adhesion were relatively excellent;

4. The effect of different film-forming resin on the conductivity and printability of the ink was different. The conductivity of film-forming resin S2916 ink was the best, and the adhesion of film-forming resin 813 ink was the best. When the film-forming resin S2919:813 = 19:1, the comprehensive performance of the ink was ideal.
5. With the increase of the thickener, the conductivity of the ink drops rapidly, and the viscosity becomes larger. However, gloss, leveling and adhesion basically unchanged. When the adding amount of the thickener was 1%, the viscosity of the ink can meet the requirements of screen printing.

## References

1. Lei Chen, Jie Yu. (2008). Study on Preparation and properties of conductive ink. *Chemical and Biological Engineering*, (08): 1–3.
2. Guofeng Zhang, Junna Wang, Anna Wei. (2010). Study on the preparation and properties of novel water-based conductive ink. *Packaging Engineering*, (21): 92–94.
3. Cheng Qi (2007). The application of inorganic conductive ink in the screen printing of printed circuit board. *Printed circuit information*, (11): 2–3.
4. Kui Liu, Zicheng Li (2006). The relationship of carbon in conductive ink and the binders. *Hebei Chemical Engineering*, (03): 1–2.
5. K. S. Novoselov, A. K. Geim, S. V. Morozov, et al. (2004). Electric Field Effect in Atomically Thin Carbon Films. *Science*, 306: 666–669.
6. Wang Wang, Yanfeng Guo, Zhenxiu Sun (2015). Progress of research on carbon based conductive ink filler. *Chemical industry development*, 34 (12): 1–3.
7. Xiaomei Shi, Changyan Xu, An Ji, et al. (2015). Progress of research on graphene conductive ink. *Packaging Engineering*, (12): 1–5.

# Effect of the Polyols Content on the Properties of the Waterborne Polyurethane

Xin Wang and Fuqiang Chu

**Abstract** The anionic waterborne polyurethane emulsion was synthesized with the chemicals such as isophoronediiisocyanate (IPDI), polycarbonatediol (PCDL-1000), polyethylene-1, 4butylenea dipateglycol (PBA-2000), dimethylol propionic acid (DMPA) and 2-hydroxyethylacrylate (HEA). The effect of the mole ratio of (PBA/PCDL) on the mechanical properties of the waterborne polyurethane (WPU) dispersion was studied. The chemical structure of emulsion particle was determined by Fourier transform infrared spectroscopy (FT-IR). Some properties were measured such as the particle size of the emulsion, the elongation at break, tensile strength and thermal stability of the film. The results indicated that when increasing the mole ratio of (PBA/PCDL), the tensile strength and thermal stability of the film was improved, the elongation at break was the contrary, and the particle size of the emulsion was increased. The films showed improvement in the thermal stability and mechanical properties when increasing the molecular weight of the polyol due to the increase in the formation of strong interaction between the hard segment and soft segment. The vinyl group on the WPU provides a crosslink site when the polymerization between the WPU and the acrylate.

**Keywords** Waterborne polyurethane · Film · Mechanical properties

## 1 Introduction

Waterborne polyurethane dispersions are prepared with a wide range of applications including adhesives, coatings, paints and textile industries [1–3]. They exhibit excellent adhesive properties, low film-forming temperature and flexibility [4]. However the physical and mechanical properties of waterborne polyurethane were insufficient compared with solvent based polyurethane. Furthermore, the better

---

X. Wang · F. Chu (✉)

College of Printing and Packing Engineering, Qilu University of Technology, Jinan, Shandong, China

e-mail: fqchu@126.com

performance polyurethane dispersions were generally expensive due to the high cost of raw materials and other additives, which limited the application in some areas.

The physical and mechanical properties of the polyurethane film were significantly influenced by the particle size and the structure of the hard and soft segments [5]. The hard segments concluding urethane or urea domains which have strong hydrogen bonding exhibited a great influence on the hardness and resistance of the films. While the soft segments concluding polyols would influence the film flexibilities and resistance [6]. There were varieties of polyols which provided flexibility and cross-linking site during the reaction. Each polyol in the waterborne polyurethane dispersion has their unique nature and plays an important role on the properties of the waterborne polyurethane (WPU).

Yildirim and Yurtsevera [7] studied the extent of intermolecular interactions between urethane hard segments (U-U) and interactions of urethanes with the soft blocks quantitatively by calculating the needed Florye-Huggins interaction parameters. They founded that self-interactions between urethane hard segments were found to be much stronger than their interactions with the soft segments due to the strong hydrogen bonds between urethane groups. Lili et al. [8] reported the polyurethane acrylates (PUA) modified by different amounts of stearyl alcohol. The results showed that the greater amount of stearyl alcohol in synthesized PUAs, the lower the volume shrinkage and the better the adhesion to glass, PC, and PVC substrates.

In this paper, a series of WPU dispersions modified by different mole ratio of PCDL/PBA were synthesized. The physical and mechanical properties of the WPU were analyzed by the transform infrared spectroscopy (FTIR), Thermogravimetric Analysis (TGA) and grain size analyzer. The relationship between the physical and mechanical properties and the different contents of polyols were investigated. It was expected that the PU modified by different ratio of polyols would exhibit better performance as well as low cost. The vinyl group on the WPU provide a crosslink site when the polymerization between the WPU and the acrylate.

## 2 Experimental

### 2.1 Materials

Polycarbonate diol ( $M_n = 1000$ , PCDL) was supplied by Asahi Kasei Co., Japan. Poly-1,4-butylene adipate glycol ( $M_n = 1000$ , PBA) was supplied by Qingdao Yutian Chemical Co., Qingdao, China. Isophoronediiisocyanate (IPDI) was supplied by Shanghai First Reagent Co., Shanghai, China. Dimethylol propionic acid (DMPA) was purchased by Aladdin Chemical Co., Germany. 2-Hydroxyethyl acrylate (HEA) was purchased by Guangzhou Sanshu chemical Co., Guangdong, China. 1,1,1-Tris (hydroxyethyl) propane (TMP) was supplied by Shanghai

Macklin Biochemical Co., Shanghai, China. Dibutyltindilaurate (DBTDL) was supplied by Shanghai shangpu Chemical Co., Shanghai, China. Acetone was supplied by Laiyang Chemical Co., Shandong, China. All the above materials without purified.

## ***2.2 Preparation of the Waterborne Polyurethane Dispersion***

The calculated amount of PCDL-1000 and PBA-1000, DMPA, IPDI, TMP, DBTDL was charged into a 250-ml four-necked flask equipped with a mechanical stirrer, nitrogen inlet, condenser, and thermometer. The mixture was heated to 80 °C for 5 h. Then the system was cooled down below 50 °C, and the calculated HEA was added into the system reacted at 65 °C, until all terminal –NCO group was capped. Then the TEA were added into the flask subsequently and reacted at 45 °C for 30 min. After neutralization, the deionized water was added into the system with vigorous stirring. The steady WPU dispersion was prepared.

## ***2.3 Preparation of the Films***

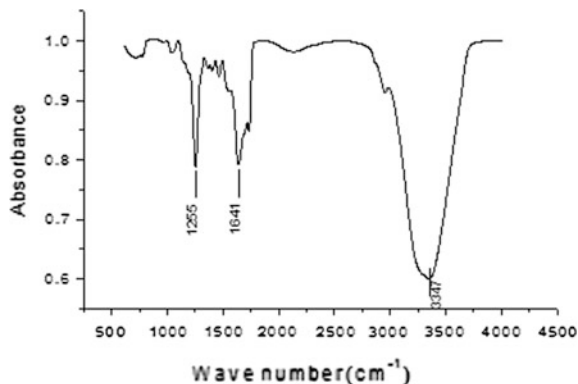
The films were prepared by casting the samples onto a poly (tetrafluoroethylene) at room temperature for 48 h, followed by drying at 80 °C for 3 h.

## ***2.4 Characterization***

Fourier transform infrared (FT-IR) spectroscopy measurement was used to identify the structure of the samples. The average particle size of the samples was determined by the dynamic light scattering (DLS) using a Zetasizer Series. Thermo gravimetric analysis (TGA) was made with a Netzsch TG209C instrument.

Referenced to GB/T1040-92 the tensile properties and elongation at break were measured at room temperature using a universal testing machine (WL2100, WITHLAB). Across-head speed of 10 mm/min was used to determine the ultimate tensile strength and the elongation at break.

**Fig. 1** FTIR spectra of the waterborne polyurethane dispersion



### 3 Results and Discussion

#### 3.1 Characterization of WPU Dispersion

Figure 1 showed the FT-IR spectra of the WPU. The spectra exhibited a strong absorption band at  $3347\text{ cm}^{-1}$ , which may be seen as the  $\text{-NH}$  groups. The absorption band at about  $1641\text{ cm}^{-1}$  reflected to the  $\text{-C=C-}$ , which was introduced by HEA. The disappearance of the  $\text{-NCO}$  band at  $2270\text{ cm}^{-1}$ , indicated the completion of the whole reaction and the formation of the predesigned WPU dispersions.

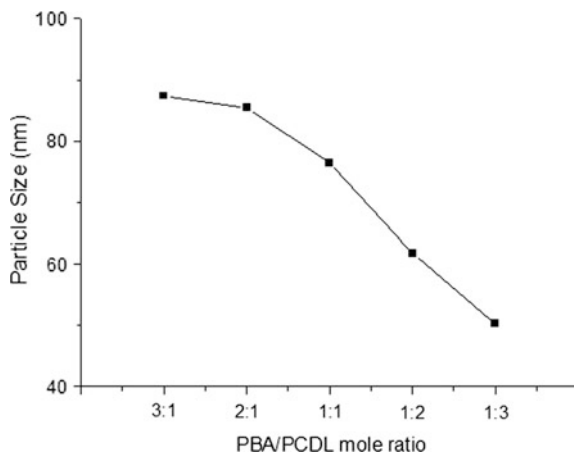
#### 3.2 Effect of Different Mole Ratio of PCDL/PBA on the WPU Emulsion Particle Size

The particle size can be controlled by emulsification conditions such as stirring speed or dispersing temperature, which has a great influence on the viscosity of the PU dispersion. Figure 2 showed the emulsion particle size was decreased from 87.41 to 50.30 nm when the molar ratio of PBA/PCDL changed from 3:1 to 1:3. The reason was that the molecules of PCDL were arranged in an order and easy to crystallize. When increased the content of PCDL, the strong hydrogen bonding interactions between urethane and carbonate groups were formed which increased the molecular cohesion. In this way, the emulsion particle size was decreased.

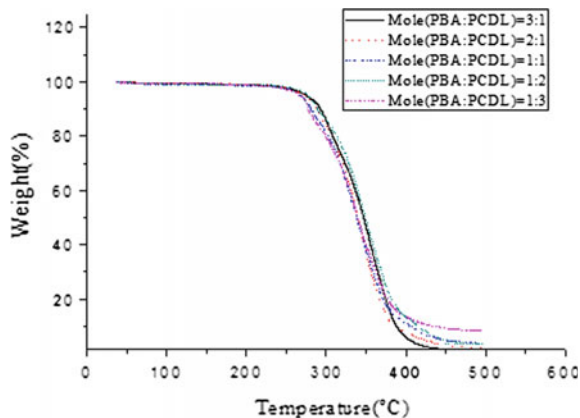
#### 3.3 Characterization of the Thermal Stability

The thermal stability of the WPU was showed in Fig. 3. There were two stages in the result. First when the temperature was descended to  $200\text{ }^{\circ}\text{C}$ , which was

**Fig. 2** The influence of PCDL/PBA mole ratio on particle size of WPU

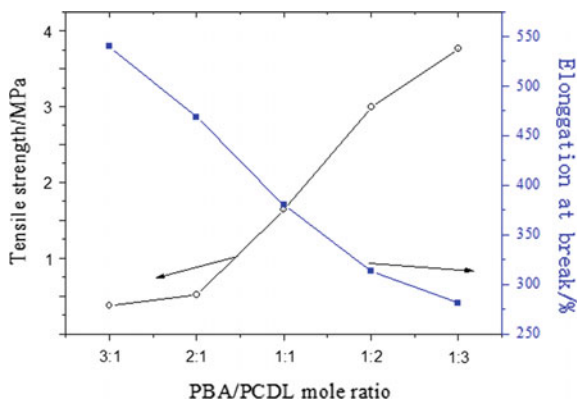


**Fig. 3** TGA curves of the polyurethane dispersion



attributed to decomposition of urethane bonds, the thermal stability of urethane bonds was the lowest in the PU and decomposed firstly. As for the WPU which contained more PCDL formed excessive hydrogen bonds between the soft segment and the hard segment, delayed the decomposition of the urethane bonds. Then the temperature was promoted, when the temperature exceeded 325 °C, which mainly correlated to the soft segment. The result showed that the thermal stability of the WPU which contained more PBA-2000 was better, and the PUA-4 was the lowest. With the increasing of PBA, the thermal stability became better. The reason was that the molecular weight of PBA was high. With the increasing molecular weight of the soft segment, the force between molecular chains was enhanced. In this way the thermal stability of prepolymer was enhanced.

**Fig. 4** Tensile strain–stress curves of the waterborne polyurethane films



### 3.4 Mechanical Properties of the Waterborne PU Films

As seen in Fig. 4, the tensile strength of the films was decreased with increasing PCDL content, but the elongation at break of the film sample was increased with increasing the PCDL content. The reason of the above results might be that increasing the molecular weight of polyol (PBA-2000) led to improvement of the soft segment content in the polymer. More and more hydrogen bond was formed which tidied the segments closely, limiting the freedom movement between segments. It was well known that the soft segment in PU mainly affected the flexibility. Therefore, increasing the molecular weight of segment resulted in higher tensile strength and lower elongation at break.

## 4 Conclusions

The waterborne polyurethane dispersion contain different mole ratio of PBA/PCDL was synthesized, and the effect of the polyol on the physical and mechanical properties was investigated. The result showed that the particle size and tensile strength were decreased with increasing the PCDL contain, because the PCDL contains lots of carbonyl groups which forms hydrogen bonds between hard segment and soft segment, the TAG results supported the above results. Increasing the molecular weight of polyol (PBA-2000) improved the soft segment content in the polymer. More and more hydrogen bond was formed which tidied the segments closely, limiting the freedom movement between segments, in this way, improved the thermal properties and tensile strength.

## References

1. M, M, Rahman. W, K, Lee. (2009). Properties of isocyanate-reactive waterborne polyurethane adhesives: Effect of cure reaction with various polyol and chain extender content. *Journal of Applied Polymer Science*, 144(6), 3767–3773.
2. B, Kim. J, Shin. (2002). Modification of waterborne polyurethane by forming latex interpenetrating polymer networks with acrylate rubber. *Colloid and Polymer Science*, 280 (8), 716–724.
3. X, Zhu. X, Jiang. Z, Zhang (2008). Influence of ingredients in water-based polyurethane-acrylic hybrid latexes on latex properties. *Progress in Organic Coatings*, 62(3), 251–257.
4. M, M, Rahman. E, Y, Kim. (2008). Cross-linking reaction of waterborne polyurethane adhesives containing different amount of ionic groups with hexamethoxymethyl melamine. 28 (1–2), 47–54.
5. Qiu, F, X. Zhang, J, L. Wu, D, M. (2010). Waterborne polyurethane and modified polyurethane acrylate composites. *Plastics, Rubber and Composites*, 39(10), 454–459.
6. Tielemans, M. Roose, P. Groote, P, D. (2006). Colloidal stability of surfactant-free radiation curable polyurethane dispersions. *Progress in Organic Coatings*, 55(2), 128–136.
7. Yildirima, E. Yurtsevera, M. (2016) Effect of intersegmental interactions on the morphology of segmented polyurethanes with mixed soft segments: A coarse-grained simulation study. *Polymer*, doi:[10.1016/j.polymer.2016.03.008](https://doi.org/10.1016/j.polymer.2016.03.008), 204–214.
8. Lili, Q. Jun, N. Yong, H. (2014). Synthesis and properties of polyurethane acrylate modified by different contents of stearyl alcohol. *Journal of Coatings Technology and Research*, 12(1), 197–204.



# Study of Dispersion of the Yellow UV-LED Inkjet Ink

Yiran Li, Xianfu Wei and Beiqing Huang

**Abstract** The dispersibility is one of the important physical properties of inkjet ink, it plays a crucial role on whether the ink can be sprayed smoothly and whether the nozzle will be clogged by the ink, it is the key performance indicator relating to the dispersion system's stability and uniformity of pigment particle. The study analyzed and compared the effects of monomer and dispersant on the dispersion of yellow UV-LED inkjet ink. Research shows that the particle size of different yellow color paste grinded by different monomer has difference; the dispersion of color paste of single monomer is better than that of composite monomer; the type and content of the dispersant have different effects on the particle size of yellow color paste, under this experimental condition, when the content of dispersant BYK9077 is 8%, its grind effect is the best; moreover, through the study, the formula of color paste of the yellow UV-LED inkjet ink is optimized and determined.

**Keywords** Yellow UV-LED inkjet ink · Dispersion · Monomer · Dispersant

## 1 Introduction

UV-LED printing curing system is the application emitting ultraviolet to cure the ink, compared to traditional UV curing system, UV-LED curing system has many advantages such as: power saving, ozone-free, low ink odor, reduce of thermal influence on the substrate, space saving, light preparation time saving, high environmental protection, durable etc [1].

There are many factors that influence the dispersion of the inkjet ink. Among them, it is the crucial factor that the matching of pigment and monomer, and the binder ratio's determine. Generally speaking, the better the pigment particles in the monomer wetted, the better dispersion of the ink has. The adding of the dispersant will contribute to the dispersion of pigment particle and prevent their aggregation at

---

Y. Li (✉) · X. Wei · B. Huang  
Beijing Institute of Graphic Communication, Beijing, China  
e-mail: 547673002@qq.com

the same time. UV-LED inkjet ink requires the dispersion is great and the size of pigment particles can reach to about 500 nm. It is very important to choose the appropriate monomer and dispersant for the pigment in the preparation of color paste.

## **2 Experiments**

### **2.1 *Experimental Materials***

Prepolymer: Viajet400 (Allnex LTD.); monomer: EOEOEA, HDDA, DPGDA, TPGDA, TMPTA, NPGDA (Tianjin tianjiao co.); wetting and dispersing agents: 9077, 111, 9151, 9150 (BYK Chemie); flattening agent: 432; pigment: yellow pigment (Ciba Specialty Chemicals).

### **2.2 *Equipments***

Isothermal magnetic agitator (Jiangsu Ronghua instrument CO.); JJ-I type mechanical agitator (Changzhou guohua electric appliance co., LTD); GJ-2S type high speed grinding machine (Qingdao haitong dedicated instrument co., LTD); microtrac S3500 laser particle sizer (US Microtrac Co.).

### **2.3 *Preparation of Yellow Color Paste***

We add the monomer and dispersant separately into the beaker, put the beaker onto the magnetic mixer and move it until the liquor is uniform, and then put yellow pigment added liquor under the JJ-I type mechanical agitator to pre-disperse for about 30 min. Then the pre-dispersed paste was poured into a grinder, and we added in the appropriate weight of zirconium beads, let the high speed grinder mill for 150 min, so that the pigment can be dispersed in the connection compound well, thus we can get the yellow color paste.

### **2.4 *Test Method of Ink's Dispersibility***

The dispersibility of ink can be tested by the laser particle sizer, the particle size and distribution of ink can be obtained from the particle size distribution graphs of the

ink. In this paper, the particle size of ink was expressed by 95% of the maximum particle size distribution of ink.

### 3 Experiment Results and Analysis

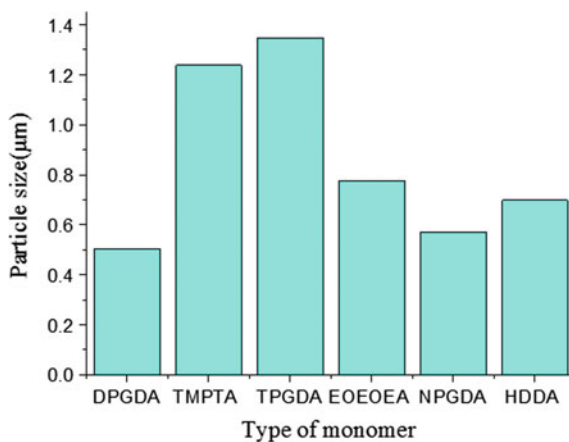
#### 3.1 Influence of Monomer on the Dispersion of Yellow Color Paste

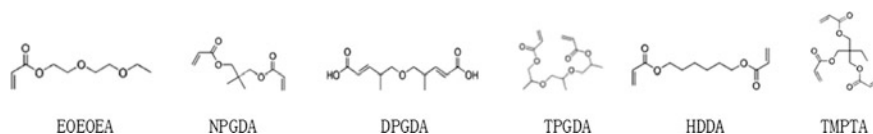
The dispersibility is one of the important physical properties of inkjet ink, it plays a crucial role on whether the ink can be sprayed smoothly and whether the nozzle will be clogged by the ink, it is the key performance indicator relating to the dispersion system's stability and uniformity of pigment particle [2]. The primary particle size of the pigment particles is generally small on nanometer level, however, due to the combined action of the external causes: transportation, storage and so on and the internal reasons: intermolecular force, the action of high-energy chemical bonds (hydrogen bonds), electrostatic interaction and so on, the agglomeration of pigment particle has occurred when in actual use, so the grind method should be used to make the agglomerated pigment particle disperse to uniform dispersed color paste. The binder ratio of the color paste and the matching ability of pigment and monomer are the key factors.

##### 3.1.1 Influence of the Type of Monomer on the Dispersion of Yellow Color Paste

In this study, the content of each components in yellow color paste is fixed, six kinds of monomer: HDDA, EOEOEA, DPGDA, NPGDA, TPGDA and TMPTA

**Fig. 1** The influence of the type of monomer on the dispersion of yellow color paste





**Fig. 2** Structures of monomer

were used to prepare yellow color paste respectively, after 150 min's grinding, the color paste was sampled and tested, the results are shown in Fig. 1.

As shown in Fig. 1, the particle size of different yellow color paste grinded by different monomer has difference. The particle size of DPGDA-grind color paste is the smallest, the particle size of HDDA-grind and NPGDA-grind color paste is relatively small. The particle size of TPGDA-grind color paste is the biggest. This is because that the essence of the grinding of color paste is to make the pigment particles well dispersed in the monomer medium. Structure, the physical and chemical properties of the monomer have a significant impact on its dispersion effect. The structure of monomers used in this study is shown in Fig. 2. As shown in Fig. 2, EOEOEA is mono-functional monomer. NPGDA, DPGDA, HDDA and TPGDA are bifunctional monomers. TMPTA monomer is trifunctional. Among the six monomers, DPGDA have less branched chain. In addition, the molecular chain of DPGDA is long, symmetrical and relatively structured. Its structure contributes to the wetting and dispersion of pigment particle. The dispersion of yellow color paste grinded by DPGDA is best. The molecule structures of bifunctional monomer TPGDA and trifunctional monomer TMPTA which has three-dimensional structure are irregular. Their large surface tension does not conduce to the dispersion of pigment. Besides, their viscosity is relatively large which is not conducive to the motion of pigment particles in the grinding system [3], all of this reason results in the TMPTA-grind and TPGDA-grind yellow color paste are not well dispersed. Bifunctional monomer NPGDA and HDDA have relatively short molecular chain, less branched chain and lower viscosity which in favor of the wetting and dispersion of the pigment particle so that the NPGDA-grind and HDDA-grind yellow color paste has relatively good dispersion. EOEOEA has less branched chain, relatively regular structure and moderate viscosity, so the particle size of EOEOEA-grind color paste is at an intermediate level.

### 3.1.2 Influence of Composite Monomer on the Dispersion of Yellow Color Paste

Considering the effect of different monomer to the dispersion of the color paste, and the nature of the different functional monomers, we selected 3 monomers which are NPGDA, DPGDA and HDDA to make the formulation and design experiments. The purpose is that the ratio of the compound monomer in which the yellow pigment has good dispersibility can be obtained. The study takes three factors and

**Table 1** Data of the formulation experiment of the dispersion of yellow color paste

Group	X1 (NPGDA)	X2 (DPGDA)	X3 (HDDA)	Particle size (150 min 95%)
1	1	0	0	0.572
2	0	1	0	0.503
3	0	0	1	0.698
4	1/2	1/2	0	1.034
5	1/2	0	1/2	1.875
6	0	1/2	1/2	1.704
7	1/3	1/3	1/3	1.011

three order simplex centroid to design experiment. We set the X1, X2, X3 that represent the mass percentage of NPGDA, DPGDA, HDDA, respectively in the color paste, and produced yellow color paste samples and tested their dispersion, the experimental results are shown in Table 1.

The particle sizes of the data in Table 1 are substituted into the formula to obtain the regression coefficients, and then we substitute the regression coefficients into the equation, the regression equation between the particle size and variate is as shown in Eq. 1.

$$y = 0.57x_1 + 0.5x_2 + 0.69x_3 + 1.98x_1x_2 + 4.96x_1x_3 + 0.52x_2x_3 - 22.74x_1x_2x_3 \quad (1)$$

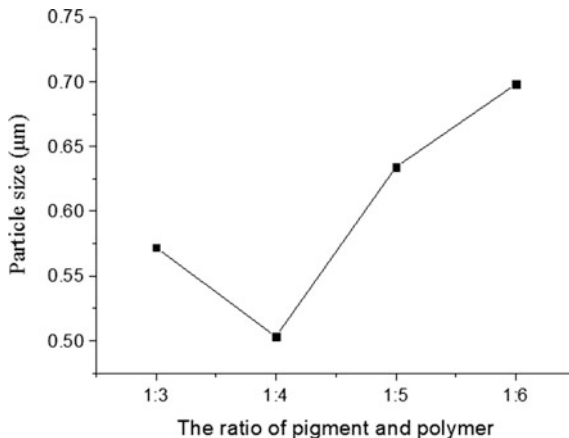
The smaller the value of the regression equation is, the better dispersibility the color paste has. According to the experimental data analysis, we know that, under this experimental condition, the color paste's dispersion of single monomer is better than the composite monomer's. According to the excel solver result, the best mass ratio of composite monomer is, NPGDA:DPGDA:HDDA = 0:1:0, that is, using monomer DPGDA alone can prepare the yellow color paste which has the best dispersion ability, its particle size is 0.503  $\mu\text{m}$  (95%, 150 min).

### 3.2 Influence of Binder Ratio on the Dispersion of Yellow Color Paste

In this study, the content of dispersant in yellow color paste is fixed, four gradients of the ratio of yellow pigment and monomer (referred as "binder ratio" below): 1:3, 1:4, 1:5 and 1:6 were used to prepare yellow color paste respectively, after 150 min's grinding, the color paste was sampled and tested, the results are shown in Fig. 3.

As shown in Fig. 3, with the decrease of the binder ratio, that is, the relative amount of the yellow pigment in the dispersion system is less, the particle size of paste firstly decreases and then gradually increases and reaches to a minimum when

**Fig. 3** The influence of binder ratio on the dispersion of yellow color paste



the binder ratio is 1:4. This is because that the purpose of preparing the color paste is making pigment particle well dispersed in the monomer. The nature of the dispersion of the pigment is flowing progress, and only achieves to the optimum flow point. The color paste can get effective shearing force, [4] in which way the dispersion is at the best status. The decrease of binder ratio means the increase of monomer in the grind system which results in the change of viscosity, and in the grind process, the shearing action is different because of the difference of the viscosity [5], because of the difference of viscosity of monomer and the flow degree of pigment caused by the adsorption of monomer, the binder ratio of different color paste is different. Therefore, in order to make the ink prepared have the best dispersion state, the binder ratio should be determined firstly, under this experimental condition, yellow color paste's best binder ratio is 1:4.

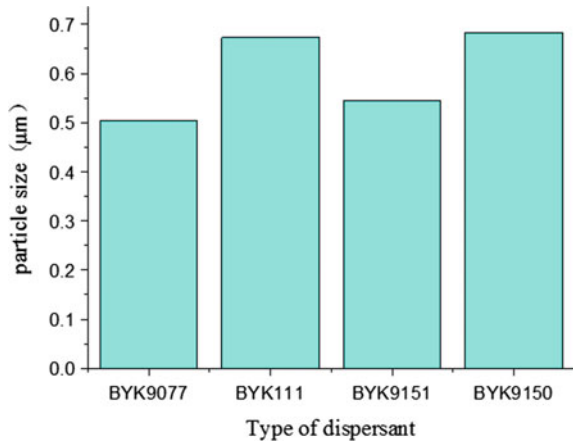
### ***3.3 Influence of Dispersant on the Dispersion of Yellow Color Paste***

The function of dispersant in color paste system is making the pigment particle have better dispersion and prevent the organic pigment particles sink to the bottom, the dispersant used in light curable ink is mainly the polymer containing pigment affinity groups.

#### **3.3.1 Influence of Dispersant on the Dispersion of Yellow Color Paste**

In this study, the content of each component in yellow color paste is fixed, four kinds of dispersant: BYK9077, BYK111, BYK9150 and BYK9151 were used to

**Fig. 4** The influence of the type of dispersant on the dispersion of yellow color paste



prepare yellow color paste respectively. After 150 min grinding, the color paste was sampled and tested, and the results are shown in Fig. 4.

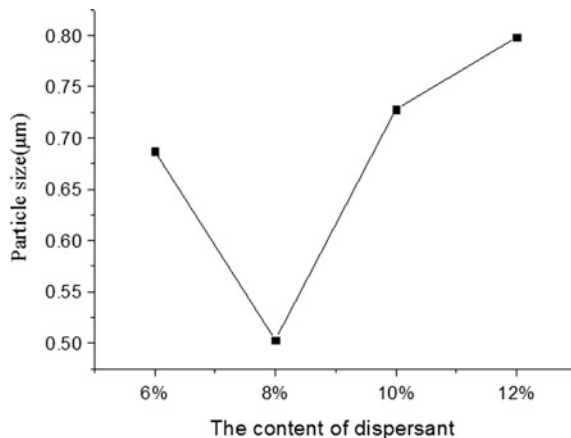
As shown in Fig. 4, the particle sizes of different yellow color paste grinded by different dispersant have difference. Among them, the particle size of color paste grinded by BYK9077 is the smallest, the particle size of the other three are relatively big. The common dispersant in the light curable ink is the polymer containing pigment affinity groups. The molecule structure of dispersant can be divided into two parts: (1) Anchoring groups, which can be tightly adsorbed on the pigment particle surface, prevent the dispersant molecules from desorbing. (2) Solvation chain which has a good compatibility with the dispersion medium can form a sufficiently thick protective layer [6]. When there are two pigment particles absorbed dispersant close to each other, steric effect of the protective layer can separate the two pigment particles apart to make the pigment disperse stably in the system [7]. The anchoring groups of BYK9077 can form a closer structure with yellow pigment. In addition, its solvation chain can dissolve into the monomer better to form stronger steric hindrance preventing the occurrence of agglomeration caused by pigment particles in contact with each other. So the BYK9077-grind yellow color paste has the smallest particle size.

### 3.3.2 Influence of the Dosage of Dispersant on the Dispersion of Yellow Color Paste

In this study, the content of other components in yellow color paste were fixed. Four gradients of the content of dispersant: 6, 8, 10 and 12% were used to prepare yellow color paste respectively. After 150 min's grinding, the color paste was sampled and tested, the results are shown in Fig. 5.

As shown in Fig. 5, when the content of the dispersant is increased from 6–8%, the particle size of the system is decreasing; when the content of the dispersant is 8%,

**Fig. 5** The influence of the dosage of the dispersant on the dispersion of yellow



the particle size of the system reach to a minimum. If we continue to increase the content of dispersant, the particle size of the system will also increase, that is because when the content of dispersant is less than 8%, the dispersant does not provide sufficient thick adsorption layer so that the agglomeration of many pigment particle still occur; when the content of the dispersant is 8%, the effect of the dispersant in the system is the most obvious. The system can achieve the best flow status in which the dispersion of the paste is the best; [8] When the content of the dispersant is more than 8%, due to the excessive content, the dispersant affects the structure of the stable system formed resulting in the reduce of the dispersity of the ink.

## 4 Conclusions

Through the research above, we get the following conclusions under this experimental condition:

1. The particle sizes of different yellow color paste grinded by different monomer have difference. The HDDA-grind color paste's particle size is the smallest.
2. The dispersion of the color paste grinded by single monomer is better than the composite monomer. Using monomer DPGDA alone can prepare the yellow color paste which has the best dispersity, its particle size is 0.503 μm (95%, 150 min).
3. The particle sizes of different yellow color paste grinded by different dispersant have difference. The particle size of BYK9077-grind color paste is the smallest. The anchoring groups of BYK9077 can form a closer structure with yellow pigment and its solvation chain can dissolve into the monomer better to form stronger steric hindrance preventing the occurrence of agglomeration caused by pigment particles in contact with each other.



4. The amount of dispersant is a factor that influences the dispersion of yellow color paste. With the increase of the amount of dispersant, the dispersion of ink will get better. But to a certain extent, the particle size will increase. In our experimental condition, the most appropriate content of BYK-9077 is 8%.

## References

1. Yangzhi Jin (2008). The progress of the market radiation curing technology [A]. (2008 the silver halide imaging conference on development and application of technology and materials [C], 2008).
2. Yunxing Lin, Liansheng Xue (2009). Ink technical manuals. Printing Industry Press, Beijing.
3. Jie Wei, Yangzhi Jin (2013). Photocurable coating. Chemical Industry Press, Beijing.
4. Jianwen Yang, Zhaozha Zeng, Yonglie Cheng (2006). Uv-curable coatings and application. Chemical Industry Press, Beijing.
5. Xianfu Wei (2009). Printing ink technology and development trend. Printing technique.
6. Xiaokun Qi, Wenhua Zhou, Yonggang Yang (2008). Printing materials and eligibility. Printing Industry Press, Beijing.
7. Xianfu Wei, Beiqing Huang, Pujun Deng (2014). The printing principle and process. China Light Industry Press, Beijing.
8. Xingrong Li (1986). Printing ink. Printing Industry Press, Beijing.

# Double-Layer Corrosion Protection of Aluminium Pigments Applied in Water-Based Silver Ink

Wenlong Zhao, Shisheng Zhou and Zhengneng Wu

**Abstract** In consideration of the active chemical property, rapid agglomeration in water-based silver ink application, poor compatibility with organic resin and poor adhesion to the substrate of aluminium pigment, double-layer corrosion protection of aluminium pigments were realized by combining sol/gel method in this paper. The optimum ratio was obtained via characterization of gloss, corrosion inhibition efficiency, scanning electron microscopy (SEM) and infrared spectroscopy (FTIR): 0.35 g of MMA, 0.005 g of BPO, 85 °C of polymerization temperature and 5 h of reaction time. Then water-based silver ink was formulated at the optimal mass ratio: 0.2 g of the modified aluminium pigments, 2.1 g of acrylic resin and 0.2 g of butyl acetate. The results showed that the dispersibility and compatibility with resin of aluminium pigments are significantly reinforced and can be widely applied in the actual production.

**Keywords** Aluminium pigment · Modification · Compatibility · Water-based silver ink

## 1 Introduction

Corrosion protection of aluminium pigment [1] is traditionally a high-profile issue as a result of its various excellent performances like special metallic luster, “flip-flop” effect, float, etc. For that reason water-based paint is a good choice [2, 3]. However, water-based paints are formulated mostly in alkaline condition which may initiate serious corrosion of aluminium pigment. The reactions seriously weaken the metallic luster of aluminium pigments, and hydrogen generation increase the pressure inside the storage container significantly which may induce insecurity in production as the risk of explosion. Furthermore, aluminium pigment

---

W. Zhao (✉) · S. Zhou · Z. Wu  
Faculty of Printing, Packing Engineering and Digital Media Technology,  
Xi'an University of Technology, Shaanxi, China  
e-mail: 1548298891@qq.com

© Springer Nature Singapore Pte Ltd. 2017  
P. Zhao et al. (eds.), *Advanced Graphic Communications  
and Media Technologies*, Lecture Notes in Electrical Engineering 417,  
DOI 10.1007/978-981-10-3530-2\_110

is a kind of inorganic ultrafine powder with large specific surface area and high surface energy, thus it's prone to agglomeration and is difficult to disperse in practical application. By the way, poor compatibility of inorganic particles and organic resin as a result of large nature difference between them makes it hard for aluminium pigment adhere to the substrate and is easy to drop from the surface under an external force [4–6]. Thus, surface corrosion protection of aluminium pigment by changing its surface properties, enhancing its corrosion resistance and improving its compatibility with the resin is a key issue that needs urgent solution to expand its application fields.

## 2 Experiments

### 2.1 *Materials and Equipments*

Aluminium pigment (average particle size 30  $\mu\text{m}$ ), Ethanol ( $\geq 99.7\%$ ), ammonia (25–28%), tetraethoxysilane (TEOS) ( $\geq 28\%$ ), vinyltriethoxysilane (VTES) ( $\geq 98.7\%$ ), methyl methacrylate (MMA) ( $\geq 99.0\%$ ), butyl acetate ( $\geq 99.0\%$ ), benzoyl peroxide (BPO) ( $\geq 96.0\%$ ), xylene ( $\geq 99.0\%$ ), acetone ( $\geq 99.5\%$ ), distilled water (homemade).

Four-necked round-bottomed flask, serpentine condenser, thermometer, nitrogen device, HH-2 electrothermal thermostatic water-bath pot, JJ-1 agitator (100 W), ZK vacuum drying oven, KH-600KDB high-power NC ultrasonic cleaning device.

### 2.2 *Sample Preparation*

2.0 g of aluminium pigments and 50 mL of anhydrous ethanol were added in a 250 mL four-necked flask which was equipped with condenser, thermometer and nitrogen in and outlet, the mixture was stirred at room temperature for 1 h.

Heat the temperature up to 50  $^{\circ}\text{C}$ , 2 ml of TEOS diluted with 30 ml of anhydrous ethanol, 3 ml of VTES, 3 ml of ammonia and 5 ml of water diluted with 30 ml of anhydrous ethanol were added into the mixture respectively by controlling 1 drop/sec for about 1 h. Continue stirring for 6 h, the solution was vacuum filtered and was washed three times with anhydrous ethanol. Then monolayer modified aluminium pigments (TV/Al) were acquired after vacuum drying for 6 h at 50  $^{\circ}\text{C}$ .

A certain amount of TV/Al, xylene and butyl acetate (Volume ratio of xylene and butyl acetate is 1:1) were added into a 250 mL four-necked flask simultaneously. The mixture was ultrasonic dispersed and under nitrogen protection for 2 h at room temperature.

Heat the temperature up to a certain value, butyl acetate solution containing monomers (mass ratio of MMA and MA is 1:1) and initiator BPO was added dropwise to the system at 1 drop/sec, continue stirring for several hours.

The mixture was filtered, and the product was washed several times with acetone, then double layer modified aluminium pigment (TVPA/Al) were obtained after vacuum drying for 24 h at 50 °C.

### 3 Sample Characterization (Modified Double-Coated Aluminum Pigments)

#### 3.1 Characterization of Gloss and the Inhibition Efficiency

$L_9$  ( $3^4$ ) orthogonal table was constructed as follows:

Remark: 1. Prepare water-based silver ink with aluminium, and measure the sample's gloss using Gloss KGZ-1C type. 2. The sample of 0.5 g aluminum pigment is dispersed a certain amount of hydrochloric acid solution of PH 1, using hydrogen gas gathering drainage collected product according to the following formula can obtain sustained efficiency [4, 5].

$$J = \frac{V_0 - V}{V_0} \times 100\%$$

$V_0$  represents hydrogen evolution of the original aluminum in hydrochloric acid solution and  $V$  is the hydrogen evolution of a modified aluminum in hydrochloric acid solution, the units are ml.

It is obvious that the gloss of TVPA/Al suffer most from the MMA content which is the main factor to be considered. Select the best level of each factor according to the principles of orthogonal test to obtain the optimum conditions: 0.35 g of MMA, 85 °C of polymerization temperature, 5 h of reaction time and 0.005 g of BPO. Optimizing experiments are made premised on subjective analysis and the results are shown in Table 2.

As Table 1 shows, reaction time has the most influence on the corrosion inhibition efficiency [6–8] of TVPA/Al. Select the best level of each factor according to the principles of orthogonal test to obtain the optimum conditions: 85 °C of polymerization temperature, 0.35 g of MMA, 5 h of reaction time and 0.005 g of BPO. Optimizing experiments were made premised on subjective analysis and the results are shown in Table 2.

The 10 groups of gloss and corrosion inhibition efficiency results are shown in Figs. 1 and 2, sample 5# shows the biggest gloss and it also shows a much higher corrosion inhibition efficiency; sample 6# has maximum corrosion inhibition efficiency but with an ordinary gloss. The gloss of sample 10# is smaller than sample 5# and is larger than sample 6#, its corrosion inhibition efficiency is slightly lower than sample 6#.

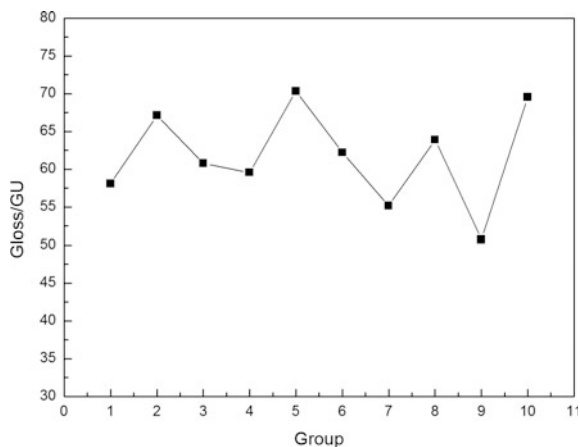
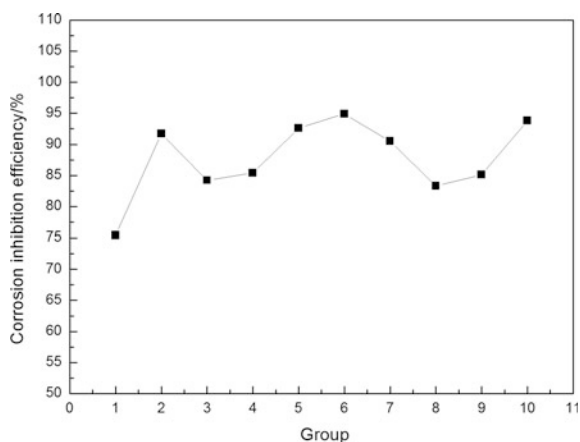
**Table 1** Results of TVPA/Al

Group	Factors					
	Temperature/°C	MMA/g	BPO/g	Time/h	Gloss/GU	Corrosion inhibition efficiency/%
1	80	0.20	0.001	4	58.08	75.4
2	80	0.35	0.003	5	67.14	91.7
3	80	0.50	0.005	6	60.80	84.2
4	85	0.20	0.003	6	59.57	85.4
5	85	0.35	0.005	4	70.35	92.6
6	85	0.50	0.001	5	62.22	94.9
7	90	0.20	0.005	5	55.16	90.5
8	90	0.35	0.001	6	63.90	83.3
9	90	0.50	0.003	4	50.74	85.1
Average1	186.02	172.81	184.20	179.17	Gloss 547.96	
Average2	192.14	201.39	177.45	184.52		
Average3	169.80	173.76	186.31	184.27		
Range1	22.34	28.58	8.86	5.35		
Average4	251.3	251.3	253.6	253.1	Corrosion inhibition efficiency 783.1	
Average5	272.9	267.6	262.2	277.1		
Average6	258.9	264.2	267.3	252.9		
Range2	21.6	16.3	13.7	24.2		

**Table 2** Optimized results of TVPA/Al

Factors	Temperature/°C	MMA/g	BPO/g	Time/h	Gloss/GU	Corrosion inhibition efficiency/%
Maximum gloss (5#)	85	0.35	0.005	4	70.35	92.6
Maximum corrosion inhibition efficiency (6#)	85	0.50	0.001	5	62.22	94.9
Optimizing experiment (10#)	85	0.35	0.005	5	69.53	93.8

According to the above comprehensive analysis, the optimized conditions of preparing TVPA/Al with good metallic luster and high corrosion inhibition efficiency are: 0.35 g of MMA, 0.005 g of BPO, 85 °C of polymerization temperature and 5 h of reaction time.

**Fig. 1** Gloss of each group**Fig. 2** Corrosion Inhibition efficiency of each group

### 3.2 Infrared Spectroscopy (FTIR) Analysis

The FTIR spectrums of the original aluminium pigments (a) and the modified aluminium pigments 5# (b), 6# (c), 10# (d) are shown in Fig. 3. A significant and strong broad absorption peak near  $1125\text{ cm}^{-1}$  appearing in samples (b), (c) and (d) show Si-O-Si anti-symmetric stretching vibration absorption peak; the appeared absorption peak near  $1724\text{ cm}^{-1}$  shows C=O characteristic peak; absorption peak appearing near  $3000\text{ cm}^{-1}$  shows methyl and methylene characteristic peaks; absorption peak at  $3434\text{ cm}^{-1}$  shows vibration absorption peak of Si-OH. These absorption peaks can't be traced in the original aluminium pigments FTIR spectrum which means that  $\text{SiO}_2$  is coated on the aluminium pigments surface successfully and the polymerization of MMA and MA also occurs.

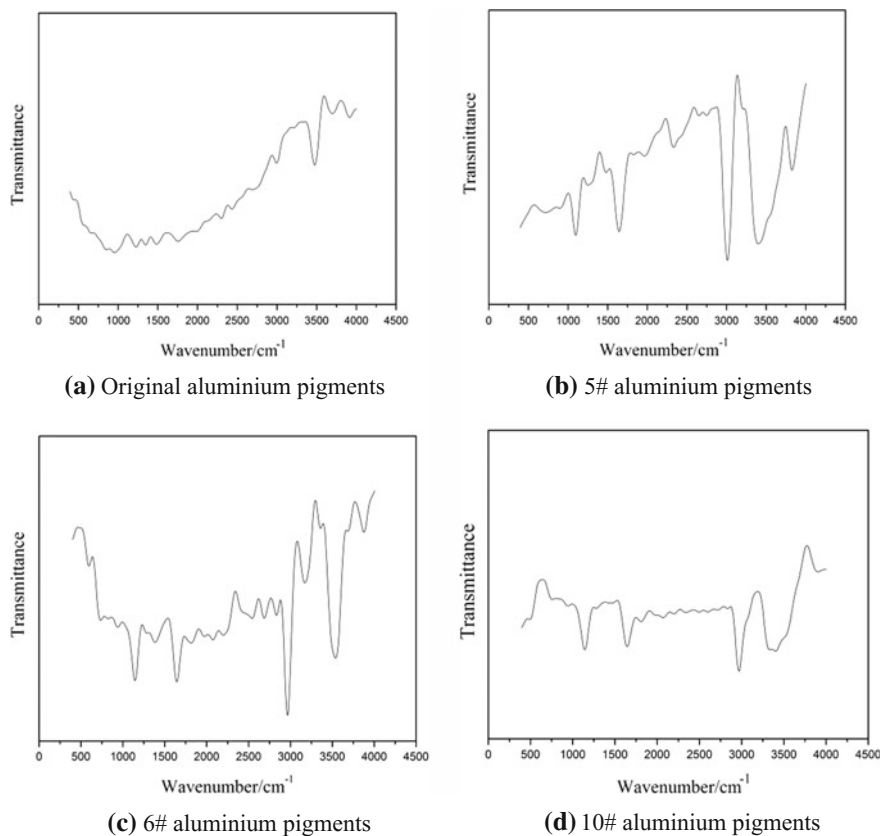
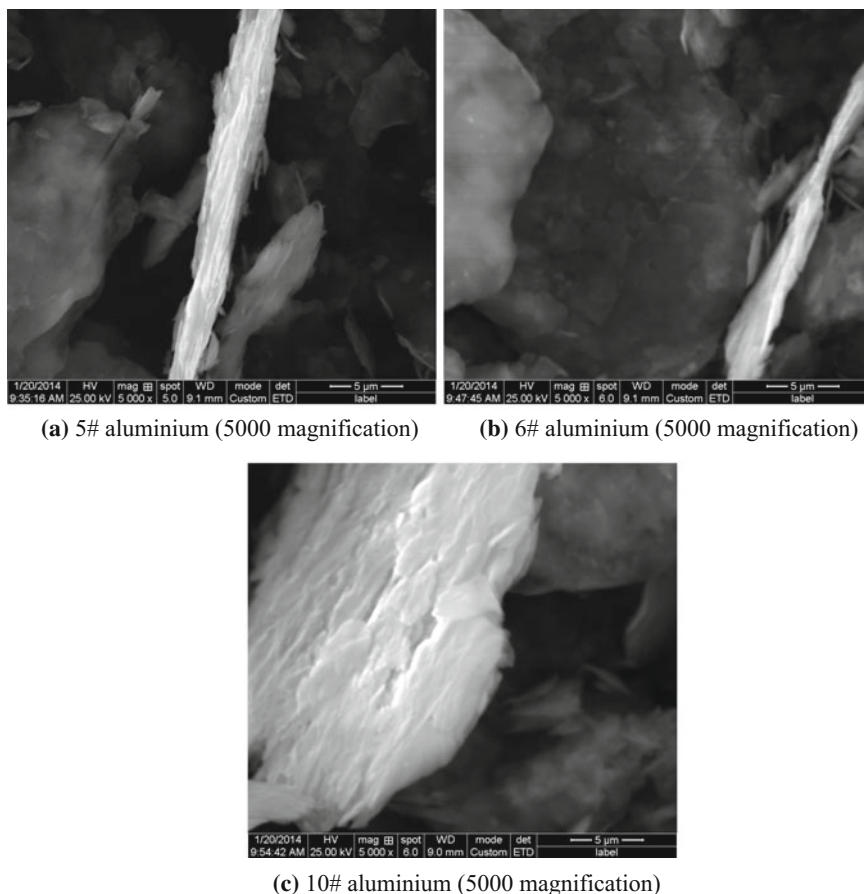


Fig. 3 FTIR spectra of different aluminium pigments

### 3.3 Scanning Electron Microscopy (SEM) Analysis

Figure 4 shows SEM images of the samples following modification in different conditions, including samples 5# (a), 6# (b) and 10# (c), at a magnification of 5000 respectively. It is notable that all the samples are covered with a layer of semi-transparent film, that is, polyacrylate (PA). From the microscopic point of view, the surface of sample (a) is not smooth and it has rough edges; the edge of sample (b) is relatively smooth, but the coating is not very dense; sample (c) shows smooth surface and is covered with dense coating.



**Fig. 4** SEM images of different modified aluminium pigments

#### 4 Preparation of Modified Water-Based Silver Ink

The above TVPA/Al is used as pigments, and acrylic resin is used as binders and butyl acetate (analytical reagent) is used as co-solvent in this paper. Taking the impacts towards the water-based silver ink properties of acrylic resin, aluminium pigments and co-solvent amount into account, an orthogonal experiment is devised as Table 3.

Gloss, viscosity and stability are used as evaluation indicators and we can see from Table 3 that acrylic resin content affects the ink gloss most, followed by aluminium pigments content. The gloss range shows that the optimal combination of three reagents is: 0.2 g of aluminium pigments, 0.20 g of co-solvent and 2.1 g of acrylic resin, namely experiment 5#; the ink viscosity suffers most by the aluminium pigments content. In consideration of the relationship between viscosity,



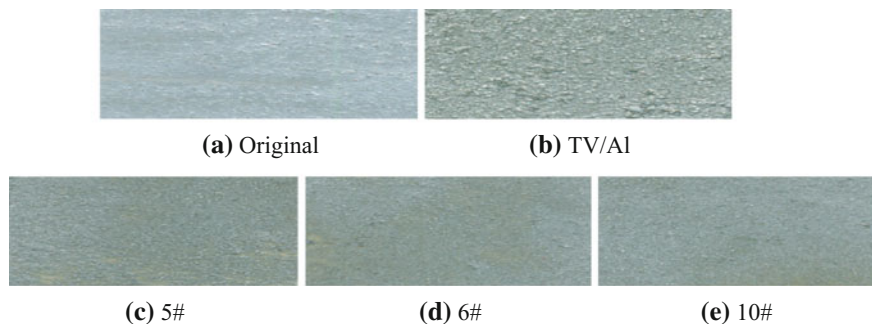
**Table 3** Results of formulated water-based silver ink

Group	Factors					
	Butyl acetate/g	Aluminum pigments/g	Acrylic resin/g	Gloss/GU	Viscosity/mPa·s	Stability
1	0.15	0.1	1.5	48.24	47	Level 2
2	0.15	0.2	1.8	43.12	65	Level 3
3	0.15	0.3	2.1	48.22	48	Level 2
4	0.20	0.1	1.8	40.00	39	Level 3
5	0.20	0.2	2.1	56.23	52	Level 1
6	0.20	0.3	1.5	49.76	56	Level 1
7	0.25	0.1	2.1	47.84	48	Level 2
8	0.25	0.2	1.5	52.48	41	Level 1
9	0.25	0.3	1.8	42.58	50	Level 3
Average1	139.58	136.08	150.48	Gloss 428.47		
Average2	145.99	151.83	125.70			
Average3	142.90	140.56	152.29			
Range1	6.41	15.75	26.59			
Average1	160	134	144	Viscosity 446		
Average2	147	158	154			
Average3	139	154	148			
Range2	21	24	10			

Remark: level 1 represents approximate; level 2 represents a little discoloration; level 3 represents discoloration

printing speed and printing material, the common viscosity of water-based silver ink is between 50 and 70 mPa·s according to production experience. It can be seen from the viscosity range that the optimal combination of three reagents is: 0.2 g of aluminium pigments, 0.15 g of co-solvent and 1.8 g of acrylic resin, namely experiment 2#; sample 5#, 6# and 8# reflect good stability, the stability of sample 1#, 3# and 7# is ordinary, while that of sample 2#, 4# and 9# is very poor.

As can be seen from Fig. 5, silver ink (a) prepared by the original aluminium pigments shows high gloss, but most of the aluminium pigments gather together and they are hard to disperse effectively. What's more, large area corrosion of the original aluminium pigment occurs in an aqueous environment makes it unsuited to the preparation of water-based silver ink and printing. Silver ink (b) prepared by monolayer modified aluminium pigments ensures the metal gloss and also improves the corrosion resistance, but a surge of particle size resulted from poor compatibility of aluminium pigments and resin will wear machines severely in the printing process. The other three samples 5#, 6# and 10# show small decline on gloss as a result of a dense layer formation on the surface of aluminium pigments. In addition, the dispersion of all the three samples have been greatly enhanced compared with the former ones, especially sample 10#, indicating that the modification experimental can assure the compatibility of aluminium pigments and resin as well as the



**Fig. 5** Samples of water-based silver ink

special metallic luster and corrosion resistance, thereby the produced water-based silver ink can be widely used in actual production and life [9, 10].

## 5 Conclusions

1. According to the combination of sol/gel method and in situ polymerization using orthogonal experiment with evaluation indicators gloss and corrosion inhibition efficiency, the optimal ratio of preparing double-layer modified aluminium pigments applied in water-based silver ink was confirmed as follows: 0.35 g of MMA, 0.005 g of BPO, 85 °C of polymerization temperature, 5 h of reaction time.
2. From the gloss and corrosion inhibition efficiency analysis, it can be seen that the double-layer encapsulated aluminium pigments gloss decline slightly compared with the original ones, while its corrosion resistance has been significantly improved which can satisfy the actual production of water-based silver ink.
3. FTIR analysis indicates that the polymerization of MMA and MA also occurs on the surface of the modified aluminium pigments apart from the SiO<sub>2</sub> film.
4. The comparison of SEM images of the samples following modification in different conditions tells that the modified aluminium pigments are covered with a semi-transparent film, that's to say the compatibility of aluminium pigments and resin can be increased by forming a dense polymer layer on the surface.
5. Taking consideration of the ink gloss, viscosity and stability, the optimal water-based silver ink ratio is: 0.2 g of aluminium pigments, 0.20 g of co-solvent 0.20 g and 2.1 g of acrylic resin. Through the double-layer corrosion protection of aluminium pigments, the compatibility of aluminium pigments and resin has been significantly reinforced and the special metallic luster and corrosion resistance have been ensured at the same time, thereby the produced water-based silver ink can be widely used in actual production and life [11, 12].

## References

1. Dinesh Balgude, Anagha Sabnis. Sol-gel derived hybrid coatings as an environment friendly. *Sol-gel Sci Technol*, 2012(64): 124–134.
2. Liu H., Ye H. Q., Zhang Y. C., et al. Preparation and characterization of Poly (trimethylolpropane triacrylate) / flaky aluminum composite particle by in situ polymerization. *Dyes and Pigments*, 2008, 79(3): 236–241.
3. Zuzanna Żotek-Tryznowska, Joanna Izdebska, Mariusz Tryznowski. Branched polyglycerols as performance additives for water-based flexographic printing inks. *Progress in Organic Coatings*, 2015, 78: 334–339.
4. H. Ashassi-Sorkhabi, Z. Ghasemi, D. Seifzadeh. The inhibition effect of some amino acids towards the corrosion of aluminum. *Applied Surface Science*, 2005(11): 408–418.
5. B. Müller. Citric acid as corrosion inhibitor for aluminum pigment. *Corrosion Science*, 2004, 46: 159–167.
6. Hamed R, Reza M, Akbar H N. Corrosion and wear resistance characterization of environmentally friendly sol-gel hybrid nanocomposite coating on AA5083. *J. Mater. Sci. Technol.*, 2013, 29(7): 603–608.
7. Zaafarany I. Corrosion Inhibition of aluminum in aqueous alkaline solutions by alginate and pectate water-soluble natural polymer anionic polyelectrolytes. *Portugaliae Electrochim Acta*, 2012, 30(6): 419–426.
8. Chris O A, Conrad K E, Cynthia E O, et al. Corrosion inhibition of aluminium pigments in aqueous alkaline medium using plant extracts. *Environ. Pollut.*, 2012, 1(2): 45–60.
9. Zhu H W, Chen Z X, Sheng Y, et al. Flaky polyacrylic acid/aluminium composite particles prepared using in-situ polymerization. *Dye. Pigment.*, 2010, 86: 155–160.
10. Emregül K. C., Aksüt A. A. The effect of sodium molybdate on the pitting corrosion of aluminum. *Corrosion Science*, 2003, 45(11): 2415–2433.
11. Kimura I, Yoshinari T, Haruyuki Y, et al. Encapsulation of aluminum flakes by dispersion polymerization of styrene in a nonaqueous system with reactive surfactants. *J. Appl. Polym. Sci.*, 2001, 81: 675–683.
12. Bin Du\*, Shisheng Zhou, Nali Li, et al. Optimization of SiO<sub>2</sub> coatings on the surface of aluminum pigments. *Energy Education Science and Technology Part A: Energy Science and Research*, 2013, 31(1): 469–472.

# Wettability and Dispersion of Phthalocyanine Blue Pigment and Evaluation of Its Effect on Printing Quality

Ruichun Cao, Xianfu Wei, Qi Wang and Hui Zhang

**Abstract** In this chapter, we investigated the wettability and dispersion of phthalocyanine blue pigment in water-based solution, and qualitatively evaluated its effect on printing quality. First, we measured the contact angle between the phthalocyanine blue pigment and water, determined the sizes and size distributions of the pigment particles, and then mixed the pigment with resin and additives to produce water-based ink and determine the dispersion of the ink. We then made a proof on coated paper and measured its printing density, glossiness and smoothness. We produced several ink samples by adding different amounts of dispersant, determined the dispersion of these ink samples again, and then made printing samples of these inks and measured the resulting printing density, glossiness, and smoothness properties of the samples. We found there was a large contact angle between the phthalocyanine blue pigment and water droplets ( $72.6^\circ$ ). Untreated phthalocyanine blue pigment has poor dispersion in aqueous ink, and the dispersion of the ink could be greatly improved by adding dispersant. The samples printed with inks containing different amounts of dispersant all had higher printing density than the untreated proof, and the glossiness and smoothness of these samples were also greatly improved. Thus, we consider that an organic pigment such as phthalocyanine blue pigment, which has poor wettability, cannot be used in aqueous ink directly unless it has been properly treated. Using a dispersant is an efficient way to improve dispersion, but the optimum dosage must be determined experimentally. Good wettability and dispersion improve the optical and other printing properties of ink.

**Keywords** Phthalocyanine blue pigment · Dispersion · Contact angle · Size distribution · Dispersant · Printing density · Glossiness · Smoothness

---

R. Cao · X. Wei · Q. Wang · H. Zhang (✉)  
Nanjing Forestry University, Nanjing, China  
e-mail: zhnjfu@163.com

X. Wei  
Beijing Institute of Graphic Communication, Beijing, China

## 1 Introduction

Water-based ink, recognized as the most environment-friendly ink and which mainly uses water as a solvent, is now widely used in the packaging of food, pharmaceuticals, cigarettes, children toys and other products. Although the performance of water-based ink has been greatly improved in recent years, compared with solvent-based ink some disadvantages remain, such as adhesion to non-absorbent materials and water resistance.

Organic pigments, an important ingredient in ink, have many excellent properties compared with inorganic pigments, including better color properties. The biggest problem associated with organic pigments is their poor wettability in aqueous dispersion. At the same time, the dispersion of water-based ink has a direct influence on printing adaptability, such as glossiness and smoothness [1, 2]. Good and stable dispersion is a necessary precondition of ink production. Hence, treatment to improve the hydrophilic properties of organic pigments is necessary when they are used in aqueous ink, and adding dispersant to facilitate dispersion of ink may be most convenient.

A suspension maintains its dispersion stability by two main mechanisms. The electrostatic mechanism is based on the electrostatic repulsion between double layers surrounding the particles (when adding electrolytes to the suspension) [3, 4]. The other mechanism is steric stabilization, in which large surfactant or polymer molecules adsorb onto the particle surfaces and act as a protective barrier against agglomeration [5, 6]. Thus far, every dispersant has been designed and produced based on these stable mechanisms.

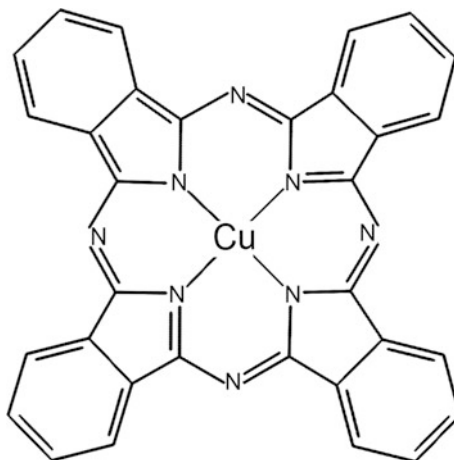
Phthalocyanine blue is a typical organic pigment with low hydrophilic properties. In this chapter, we selected phthalocyanine blue pigment for making aqueous ink, and used sodium dodecyl sulfate (SDS) as a dispersant. We then evaluated the performance of the phthalocyanine blue pigment and the effect of SDS on dispersion [7–9]. We also determined the influence of dispersion on printability.

## 2 Experimental

### 2.1 Materials

We obtained phthalocyanine blue pigment (YHB1531, C.I. name: Pigment Blue 15:3) from Shandong Yuhong New Pigment Co. Ltd (Dezhou, China), and Fig. 1 shows its chemical structure. We purchased liquid acrylic resin (BS-960), antifoaming agent (BYC-206), dispersant, ammonia, and ethanol from Wanyuan Chemical Store (Zhengzhou, China). All the chemicals used in this study were of reagent grade, and we used deionized water in all the experiments.

**Fig. 1** Chemical structure of phthalocyanine blue pigment



## 2.2 Performance of the Pigment

We used a laser particle size analyzer (MasterSizer2000, Malvern Instruments, England) to characterize the particle sizes and size distributions of the phthalocyanine blue particles. We used the pendant drop method and a contact angle meter (DSA20, Kruss, Germany) to determine the contact angle between the pigment particles and deionized water droplets.

## 2.3 Preparation of Ink Dispersion

We carried out the ink synthesis experiments in a flask and measured the pH at certain time intervals. Typically, we dispersed 25 g of phthalocyanine blue particles in deionized water with the same weight. We stirred the dispersion for 10 min before adding other chemicals. Then, we simultaneously mixed acrylic resin (40 g), antifoaming agent (1 mL), ammonia (14.79 mol/L) and ethanol (5 mL) into the pigment dispersion and stirred the mixture vigorously. We maintained the pH of the dispersion at about 8.5 by controlling the titration speed of the ammonia solution. Then, we milled the dispersion for 1.5 h with a grinder machine (HSYM-0.75A) and filtered it with a top-entry bag filter (DSG-A). We labeled this aqueous ink sample S1.

We made ink samples S2, S3, S4 in the same way, with the only difference between the samples being the amount of dispersant. The S1 sample contained no dispersant (sodium dodecyl sulfate) at all, while S2, S3, S4 contained 2, 3, 5wt%, respectively.

## 2.4 Characterization

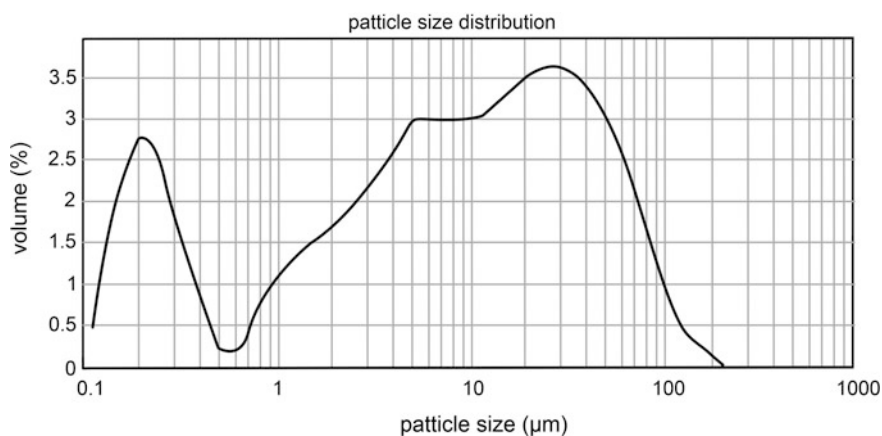
As stated above, we determined the particle sizes and size distributions of the ink samples with a laser particle size analyzer (MasterSizer2000, Malvern Instruments, England). We then made printing proofs from these ink samples, using gravure proofer (CB100-E, Zhongshan Nuobang Color Equipment, China) and two-side coated art printing paper ( $128 \text{ g/m}^2$ ). We used different inks in these proofers (S1, S2, S3 and S4), which we labeled P1, P2, P3 and P4, respectively. We measured the printing density, glossiness, and smoothness of each of these proofers using a density meter, glossiness meter and smoothness tester, respectively. The glossiness meter (PN-GM) and smoothness tester (PN-BST) were produced by Hangzhou Pnshar Technology Co. Ltd. (Hangzhou, China).

## 3 Results and Discussion

### 3.1 Hydrophilicity of Phthalocyanine Blue Pigment

Based on our measurements, the contact angle of phthalocyanine blue particles to deionized water is  $72.6^\circ$ , which is smaller than that reported in previous chapter. Obviously, the pigment had been treated in some way by the manufacturer to make it more suitable for water-based ink, but the wettability of the pigment is still not ideal, and the pigment particles showed poor hydrophilicity.

Figure 2 shows the particle sizes and size distributions. We can see that the particles sizes ranged from about  $0.1\text{--}200 \mu\text{m}$  with a wide range of distribution, which is unfavorable for ink dispersion. Based on these results, we can conclude



**Fig. 2** Particle sizes and size distributions of phthalocyanine *blue* pigment

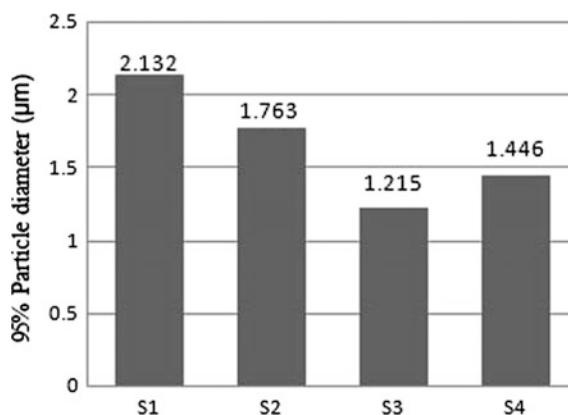
that phthalocyanine blue pigment must be treated to improve its hydrophilicity when used in aqueous ink. Dispersants facilitate ink dispersion and are also convenient to use.

### 3.2 Dispersion of Ink Samples

With respect to ink suspension, there are four methods commonly used to evaluate its dispersion and dispersion stability, including the settlement, granularity observation, zeta potential measurement, and light transmittance methods [10]. Here we used the granularity observation method to estimate the dispersion of the ink samples.

Figure 3 shows the 95% particle diameters of the four ink samples. The S1 sample containing no dispersant had the largest particle size, and S3 had the smallest. Samples S2 and S4 had particle sizes between those of S1 and S3. Obviously, the dispersant does indeed take an important role in pigment particle dispersion. The particles sizes can be effectively altered by the dispersant. The dispersant provides greater charge repulsion and steric hindrance—both key factors for ink dispersion. The 95% particle diameter decreased with an increase in the dispersant, from 2.132 to 1.215  $\mu\text{m}$ . When the dispersant increased from 3 to 5wt%, the ink particle size also increased from 1.215 to 1.446  $\mu\text{m}$ . S3, with a 3% weight ratio, yielded the smallest particle size. This may be due to the structure of the dispersant, which includes two parts: the attachment of individual dispersant monomers to the polymer chain, and their attachment to the ink particles. When the ratio was 3%, almost every ink particle was well separated, and the ink showed good dispersion stability. When the ratio increased to 5%, redundant dispersant in the ink tended to aggregate. Hence, we can conclude that a suitable amount of dispersant is beneficial to ink dispersion, but the dosage must be appropriate.

Fig. 3 95% particle diameter of ink samples





### 3.3 Effect of Dispersion on Printability

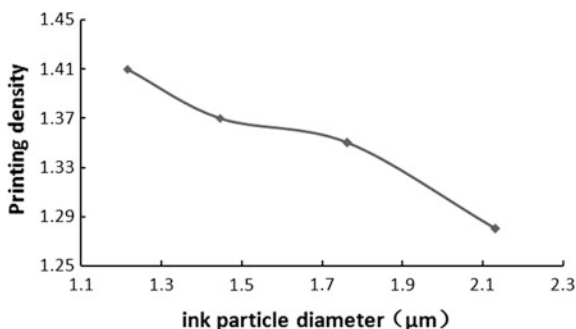
#### 3.3.1 Effect on Printing Density

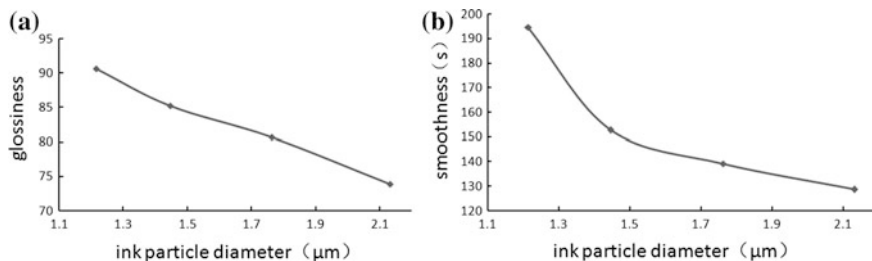
Next, we evaluated the effect of dispersion on printability, as measured by its density, glossiness, and smoothness. Figure 4 shows the effect of dispersion on printing density, which increased as the ink particle size decreased, from 1.28 to 1.41. The calculation method we used to measure printing density is based on reflectivity. When the light shines on the ink, most of the light is absorbed by colorful pigment particles, and the rest of the light is reflected and can be detected. With a decrease in the size of the pigment particles, the particles in the ink film tended to arrange more closely, so the light absorbed by the ink film increased gradually, and the reflected light decreased, resulting in an increase in the density value. This means that an ideal ink dispersion is conducive to the enhancement of printing density and color efficiency.

#### 3.3.2 Effect on Glossiness and Smoothness

Glossiness indicates the ability to reflect light incident upon the surface of the ink film. With a decrease in the ink particle size, the tiny ink particles are arranged more closely and form a flatter surface than the bigger particles. Figure 5 shows the effect on glossiness and smoothness, which increased with a decrease in ink particle size, from 73.9 to 90.6 and 128.7 s to 194.5 s, respectively. Proofer P3, printed with the ink sample S3 containing 3wt% dispersant, showed the highest glossiness and smoothness values. Compared with proofer P1, which contained no dispersant, the glossiness and smoothness improved about 23 and 51%, respectively. Obviously, good dispersion not only enhances printing density, but glossiness and smoothness as well.

**Fig. 4** Effect of dispersion on printing density





**Fig. 5** Effect of dispersion on glossiness **a** and smoothness **b**

## 4 Conclusions

In this chapter, we determined the performance of phthalocyanine blue pigment in two experiments. In the first, we measured the contact angle between the ink particles and deionized water ( $72.6^\circ$ ), and in the second, we determined the ink particle sizes and size distributions. The results indicate that phthalocyanine blue pigment has poor hydrophilicity, so hydrophilic treatment is necessary when being used in aqueous ink. A dispersant can facilitate ink dispersion and is also convenient to use. In this chapter, we produced four ink samples with different dispersant weight ratios. We then evaluated the effect of the dispersant on dispersion. Furthermore, the effect of dispersion on printing density, glossiness and smoothness were also determined. We can conclude that a suitable amount of dispersant is helpful in reducing ink particle size when milling ink dispersion, and the good dispersion can enhance the printability of ink, with respect to printing density, glossiness, and smoothness.

**Acknowledgements** This chapter was supported by Nanjing Forestry University, Jiangsu Provincial Key Lab of Pulp and Paper Science and Technology Open Foundation (201534).

## References

1. Jia, X. X, Huang, B. Q, Yan, Y. N, Wei, X. F, & Liu, J. (2011). Influence of pigment dispersion on the printability of UV flexo ink. *China printing and packaging study*, 3(2), 50–54.
2. Sun, J. Z, Wei, X. F, Huang, B. Q, & Zong, X. S. (2012). Influence of pigment dispersion on the performance of water-based plastic gravure ink. *China printing and packaging study*, 4(3), 47–51.
3. Verwey, E. J. W. (1947). Theory of the stability of lyophobic colloids. *The journal of physical and colloid chemistry*, 51(3), 631–636.
4. Noshchenko, O, Kuscer, D, Mocioiu, O. C, Zaharescu, M, Bele, M, et al. (2014). Effect of milling time and pH on the dispersibility of lead zirconate titanate in aqueous media for inkjet printing. *Journal of the European Ceramic Society*, 34(2), 297–305.

5. Yuan, J. J., Xing, W. T., Gu, G. X., & Wu, L. M. (2008). The properties of organic pigment encapsulated with nano-silica via layer-by-layer assembly technique. *Dyes and Pigments*, 76(2), 463–469.
6. Tian, A. L., Zhang, L. P., Wang, C. X., Fu, S. H., & Xu, C. H. (2015). Preparation of SiO<sub>2</sub>/PSSS dispersion for formulation of white inkjet ink. *Polymer Bulletin*, 72(5), 963–975.
7. Jadhav, S. A., Bongiovanni, R., Marchisio, D. L., Fontana, D., & Egger, C. (2014). Surface modification of iron oxide (Fe<sub>2</sub>O<sub>3</sub>) pigment particles with amino-functional polysiloxane for improved dispersion stability and hydrophobicity. *Pigment & Resin Technology*, 43(4), 219–227.
8. Sh, M. S., Golestani-Fard, F., & Sarpoolaky, H. (2009). Improvement of water/resin wettability of graphite using carbon black nano particles coating via ink media. *Journal of Alloys and Compounds*, 482(1–2), 361–365.
9. Fu, S., Zhang, K., Zhhang, M. J., & Tian, L. (2012). Encapsulated phthalocyanine blue pigment with polymerisable dispersant for inkjet printing inks. *Pigment & Resin Technology*, 41(1), 3–8.
10. Zhou, X. Y., Li, W. H., & He, L. (2006). Dispersion stability of nano particles and its evaluation methods. *Materials protection*, 39(6), 51–54 + 83.

# Preparation and Characterization of Nano Silver Applied in UV-Curing Conductive Ink

Ting Mi, Qifeng Chen and Guangxue Chen

**Abstract** Compared with ordinary conductive ink, the UV-curing conductive ink combines UV-curing technology and conductive ink technology, which gives the conductive ink good printability and broad application prospects. This chapter describes the main processes of generating UV-curing nano silver conductive ink, and analyses the results. The chapter includes two parts as follows: Firstly, using  $\text{AgNO}_3$  as the precursor, hydration hydrazine as reducing agent, PVP as protective agent, and controlling the reaction conditions, nano silver particles is generated by the liquid phase reduction method. And by using experimental methods such as Malvern Zetasizer, SEM, the nano silver particles is characterized. The results show that the size of nano silver particles is controllable, and it has good dispersion and appearance. Finally, using nano silver as UV-curing conductive filler, UV-curing nano silver conductive ink is generated, and its conductive properties are discussed. Results show that the content of conductive filler has an effect on the resistivity of conductive ink.

**Keywords** Conductive ink · Nano silver · UV-curing · Resistivity

## 1 Introduction

Nanotechnology is emerging as a cutting edge technology interdisciplinary with biology, chemistry and material science. Silver nanoparticles (AgNPs) are important materials that have been studied extensively [1]. Silver nanoparticles, due to their

---

T. Mi  
South China University of Technology, Guangzhou, China

Q. Chen (✉) · G. Chen (✉)  
State Key Lab of Pulp and Paper Engineering, National Engineering Research Center of Papermaking and Pollution Control, South China University of Technology, Guangzhou, China  
e-mail: chenqf@scut.edu.cn

G. Chen  
e-mail: chengx@scut.edu.cn

unique physical and chemical properties, have attracted increasing research interest in applications, such as optics, electrics, catalysis, sensors, anti-bacterium, and so on. Most of these applications require nanoparticles with a small particle size and a narrow size distribution [2]. A number of methods for the preparation of silver nanoparticles have been reported, such as chemistry reduction [3], photo-reduction, seed medium [4],  $\gamma$ -radiation [5], laser ablation, and supercritical liquid [6].

Development and innovation researches of conductive ink have practical significance because conductive ink is a key material for printed electronic technology. The main component of the conductive ink to have the conductive effect is electrically conductive filler, and conductive filler of UV-curing nano silver conductive ink is nano silver in this chapter.

## 2 Experimental Sections

### 2.1 *Preparation of Spherical Nano Silver and Sheet Nano Silver*

#### 2.1.1 Chemicals and Materials

Chemicals:  $\text{AgNO}_3$  (Sinopharm Chemical Reagent Co., LTD, AR grade), PVP (Shanghai Bio Science and Technology Co., LTD, K30), Hydration hydrazine (Guangzhou Chemical Reagent Factory, AR grade), Anhydrous ethanol (Sinopharm Chemical Reagent Co., LTD, AR grade), Glycerol (PEG, Guangdong Guanghua Science and Technology Co., Ltd.), Deionized water (Homemade).

Materials: JJ-1-type Precision Force electric mixer, HH-1-type Constant temperature water bath, 800-type Electric centrifuge, AL204-type Electronic balance, S-550-type Scanning electron microscopy, ZEN3690 Malvern nano-size and potential analyzer.

#### 2.1.2 Experimental Procedure

Preparation of nano-silver samples: In this chapter, two nano-silver samples, A and B, were prepared.

A: 1.275 g  $\text{AgNO}_3$  dissolved in 150 ml deionized water, Weigh 1.249 g PVP, and add it into the  $\text{AgNO}_3$  solution slowly, Use an electric mixer to stir at the speed of 300 r/min at 60 °C in 30 min. Then hydration hydrazine by drop method of 1 mL syringe injection dropwise. Wherein dropping no more than 0.5 mL/min of 2.5 mL 5% hydration hydrazine was added to the mixed solution slowly. After the dropwise, stir it for 30 min sequentially. Finally, use ethyl alcohol absolute to wash at the speed of 4000 r/min for 4times, and each time for 10 min. After the washing is complete, use anhydrous ethanol to save dispersedly, the spherical nano silver is prepared.

B: 2.55 g AgNO<sub>3</sub> dissolved in 50 ml deionized water. Weigh 3.663 g PVP, and add it into the AgNO<sub>3</sub> solution slowly. Use an electric mixer to stir at the speed of 1000 r/min at 50 °C in 80 min. Then the process is as above. Finally, use Glycerol to wash at the speed of 3800 r/min for 4 times (each time for 10 min). After the washing is complete, use Glycerol to save dispersedly. The sheet-shaped nano silver is prepared.

## 2.2 UV-Curing Conductive Ink Formulations

### 2.2.1 Chemicals and Materials

Chemicals: 621A-80-type epoxy acrylate (Changxing Chemical Materials Co., Ltd.), nano-cellulose (Guangzhou Silok Chemical Co.), neopentyl glycol diacrylate (Guangzhou Silok Chemical Co.), trimethylol propane triacrylate (Jiangmen Tianhengli ultraviolet light Materials Co., Ltd.), photo-initiator ITX (Tianjin Jiuri Chemical Co., Ltd.), spherical silver nanoparticles (Homemade), dispersing agents, leveling agents, defoamers (Guangzhou Silok Chemical Co.).

### 2.2.2 Experimental Procedure

#### UV-Curing Conductive Ink Formulations

The spherical nano silver is mixed with anhydrous ethanol; the sheet-shaped nano silver is mixed with glycerol completely. The solid content nano-silver was 44 wt%. Table 1 shows the formulation of UV-curing conductive ink.

#### The Formulation of Spherical Silver and Sheet-Shaped Silver

The morphology of nano silver particles has a great relationship with conductivity of conductive ink, because the contact manner among spherical particles is point to

**Table 1** The formulation of UV-curing conductive ink

Ingredients	Weight percentage (%)	Roles
Epoxy acrylate	11.2	Prepolymer
Nano-cellulose	16.8	Prepolymer
TMPTA	9.3	Dilution monomers
NPGDA	9.3	Dilution monomers
Spherical nano silver	13.2	Conductive filler
Sheet-shaped nano silver	30.8	Conductive filler
ITX	5.6	Photo-initiator
Dispersing agents, defoamers etc	3.8	Additives

point. While the contact among sheet-shaped nano silver is surface to surface, the contact area is significantly increased, and after printing and drying, it shows a state of scaly overlap. In this chapter, in order to improve the conductivity of the ink, the spherical nano-silver and the sheet-shaped nano silver are mixed as conductive fillers.

### 3 Results and Discussion

#### 3.1 Characterization of Nano-Silver Samples

##### 3.1.1 Malvern Zetasizer

Figure 1 notes that the prepared nano silver particles are concentrated in the vicinity of 30 nm, and with a small distribution range. The data in Fig. 1 shows that the average diameter of the nano silver is 30.15 nm, PDI value is 0.29. It hardly exist a particle whose size is larger than 60 nm or less than 20 nm.

##### 3.1.2 Sem

Figure 2 shows that prepared spherical silver nanoparticles have an average diameter of about 30 nm, and the dispersion property is very good, While prepared with sheet-shaped nano silver, the average particle size of about 180 nm, an average thickness of sheet-shaped nano silver is about 20 nm, the ratio of diameter and thickness about 9:1.

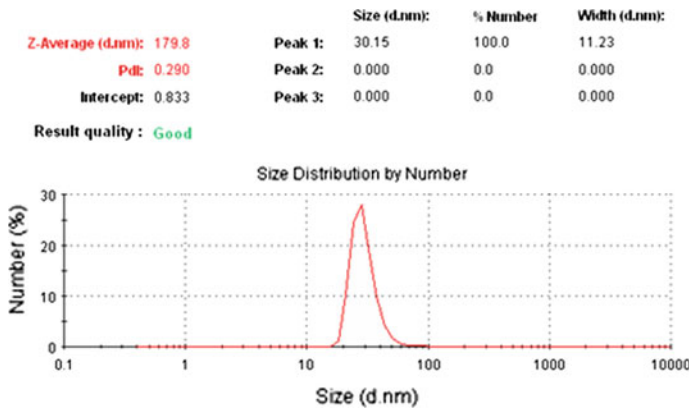


Fig. 1 The Malvin size distribution of nano silver particles

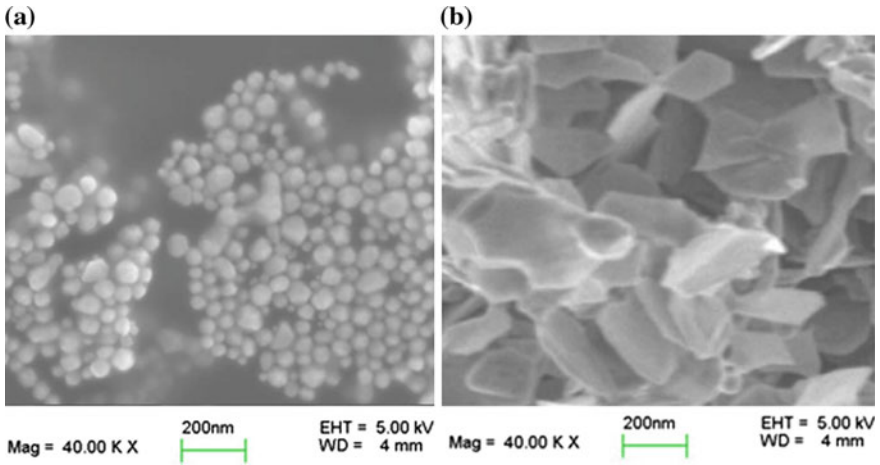


Fig. 2 SEM images of two samples: **a**–spherical nano silver, **b**–sheet nano silver

### 3.2 *Electrical Conductivity Characterization of Conductive Ink*

In this formulation, the proportion of epoxy acrylate and nano-cellulose is 2:3; the total content of prepolymer and dilution monomers is 1.5:1. The photo-initiator accounts 10% in the rest of conductive ink besides nano silver. When the ratio of spherical silver and sheet silver is 3:8, and nano silver accounts solids content of 44%, the resistivity of the conductive ink reach the magnitude of  $10^{-6} \Omega \cdot \text{m}$ .

## 4 Conclusions

After discussion of the above ratio experiments and the effect, when the ratio of spherical silver and sheet silver is 3:8, and nano silver accounts solids content of 44%, the resistivity of the conductive ink reach the magnitude of  $10^{-6} \Omega \cdot \text{m}$ . The best formulation to determine the conductive ink is as follows: 1. The prepolymer: epoxy acrylate-11.2%, Nano-cellulose-16.8%. 2. Dilution monomers: TMPTA-9.3%, NPGDA-9.3%. 3. The conductive filler: spherical silver nanoparticle-12%, sheet-shaped nano silver-32%. 4. Photo-initiator: ITX-5.6%. 5. Additives: 3.8%.

**Acknowledgements** This chapter is supported by the grants from the open fund of the key Laboratory of pulp and paper science and technology, ministry of education (No. KF201502), the Fundamental Research Funds for the Central Universities (No. D2154620), the Guangdong Provincial Science and Technology Project (No. 2013B010401007), the independent research project of state Key Lab of Pulp and Paper Engineering, South China University of Technology (No. 2016C02).



## References

1. Maqsood Ahamed, Mohd Javed Akhtar, Maqsood A. Siddiqui (2010). Oxidative stress mediated apoptosis induced by nickel ferrite nanoparticles in cultured A549 cells. *Clinica Chimica Acta*, 441: 1841.
2. Z.T. Chen, L. Gao (2007). A facile and novel way for the synthesis of nearly monodisperse silver nanoparticles, *Mater. Res. Bull.* 42, 1657–1661.
3. P.K. Khanna, N. Singh, S. Charan, V.V.V.S. Subbarao, R. Gokhale, U.P. Mulik (2005). Synthesis and characterization of Ag/PVA nano composite by chemical reduction method, *Mater. Chem. Phys.* 93, 117–121.
4. X.L. Tian, W.H. Wang, G.Y. Cao (2007). A facile aqueous-phase route for the synthesis of silver nanoplates, *Mater. Lett.* 61, 130–133.
5. P. Chen, L.Y. Song, Y.K. Liu (2007). Synthesis of silver nanoparticles by  $\gamma$ -ray irradiation in acetic water solution containing chitosan, *Radiat. Phys. Chem.* 76, 1165–1168.
6. J.Y. Chang, J.J. Chang, B. Lo, S.H. Tzing, Y.C. Ling (2003). Silver nanoparticles spontaneously organize into nano wires and nano banners in supercritical water, *Chem. Phys. Lett.* 379, 261–267.

# Effect of Ketone and Hydrazine Self-Crosslinking Reaction on Polyurethane Emulsion

Yunlong Huang, Zhigang Hu, Ying Chen, Xiaoyu Li  
and Haiqiao Wang

**Abstract** A kind of multiple amine chain extender which consists of (EDA-di (diacetone propionamido) (EDDP) and EDA-diacetone propionamido (EDP)), was synthesized firstly. Then the extender reacted with polyurethane prepolymer emulsion to form a polyurethane emulsion, containing carbonyl groups in the side chains of molecules. The resulting emulsion would increase room temperature self-crosslinking reaction between the carbonyl groups and added adipic dihydrazid (ADH) in the process of drying but not during the emulsion being stored, to improve the properties of the latex film. Effects of self-crosslinking reaction on performance of the polyurethane emulsion were systematically studied. The results showed that the water resistance of the latex film boosted greatly, and some other properties including elongation at break and tensile strength improved as well.

**Keywords** Polyurethane ink · Emulsion · Chain extender · Crosslink at RT

## 1 Introduction

Compared with other kinds of ink, polyurethane ink has many better properties such as heat resistance, high gloss, strong adhesion as well as rub resistance, so it's widely used in the printing of plastics, high-grade goods packing and food packing materials. Nowadays, more and more researchers attach great importance to the water-based ink, which has a low and even zero VOC, to meet the increasingly stringent environmental requirements [1]. The performance of the ink is mainly

---

Y. Huang · Z. Hu · Y. Chen  
Beijing University of Chemical Technology, Beijing, China

X. Li (✉) · H. Wang (✉)  
Key Laboratory of Carbon Fiber and Functional Polymers, Ministry of Education,  
Beijing University of Chemical Technology, Beijing, China  
e-mail: lixy@mail.buct.edu.cn

H. Wang  
e-mail: wanghaiqiao@mail.buct.edu.cn

determined by the polyurethane emulsion. However in contrast with external emulsification method, self-emulsifying method is more commonly used, because the emulsion synthesized in this way has better film-forming performance and mechanical performance. But as the hydrophilic groups still remain in the film, the water resistance of the coating is poor, which greatly limits the application of aqueous polyurethane ink. Thus improvement of the resistance to water and other solvent has been a crucial challenge for years.

The method of crosslinking is a most effective one. For example, Lai synthesized latent curing agents from the reaction of aziridine with hexandiol diacrylate and trimethylol propane triacrylate, respectively. Using the curing agents to cure two different polymers, they obtained new polymer hybrids with improving performance [2]. Luo [3] found that crosslinking of polycarbodiimide could improve the adhesion, flexibility and cold crack-resistance, as well as the thermal stability of the cured films. Yang synthesized water-borne blocked polyurethane curing agent with low VOC content and high blocked degree by using sodium bisulfite as blocking agent. The polyurethane can increase crosslink after the NCO groups unblocked, so that the water resistance of the film would get stronger [4]. There are plenty of literatures and patents reporting the study on curing agents in recent years, however those reported curing agents still have some defects such as leaving volatile toxic substances in printout, taking a long time to dry in high temperature or reducing the stability of the emulsion.

Ketone and hydrazine cross-linking reaction is widely used in the synthesis of polyacrylate emulsion. The cross-linking reaction arises between ketone carbonyl groups and hydrazine groups in the process of drying but not during the emulsion being stored [5]. In this chapter we synthesized a new extender containing ketone and amino groups. As the amino groups could react with the NCO groups very quickly, the extender could react with NCO after emulsification, which resulted in a polyurethane emulsion with carbonyl groups in the side chains of the resins. As a result, self-crosslinking reaction could take place in the presence of ADH, which would improve the performance of polyurethane emulsion, while not affect the stability of the emulsion.

## 2 Experimental

### 2.1 Materials

Diacetone acrylamide (DAAM), Ethanol (Et), Isophorone diisocyanate (IPDI), Polycarbonate-1000 (PC-1000), Adipic dihydrazid (ADH), Ethylenediamine (EDA), Polycarbonate-2000 (PC-2000), Acetone, 2,2-Bis (hydroxymethyl) butyric acid (DMBA), Dibutyltin dilaurate (DBTDL), Triethylamine (TEA).

## ***2.2 Synthesis of the Room Temperature Self-Crosslinking Chain Extender***

DAAM and EDA were solved in ethanol respectively, and then were added into a round-bottom flask with a reflux condenser. The mixture was allowed to react for 10 h at 75 °C. Then remove the solvent and the materials that didn't react by reduced pressure distillation, and EDA-di (diacetone propionamido) (EDDP) and EDA-(diacetone propionamido) (EDP) were obtained finally.

## ***2.3 Emulsion Preparation***

The polymerization was carried out in a 250-ml four-neck round flask equipped with a stirrer, a reflux condenser, a nitrogen inlet and a thermometer. A certain amount of IPDI, PC-1000, PC-2000, DMBA, DBTDL and acetone were added into the flask, and stirred for 3 h at 80 °C. Then the prepolymer was cooled down to 40 °C, the mixture of TEA and acetone was dropped in. After 30 min' neutralization reacting, put the flask into the ice-water bath. When the mixture was cooled down, water was fed in. Once the emulsion was formed, the compound aqueous solution was added. The mixture was allowed to react for another 1.5 h before the EDA aqueous solution was added. Then the emulsion was stirred for 2 h more and the pH of the emulsion was adjusted to 9–9.3 with AMP-95. At last, the emulsion was stirred for half an hour after ADH was added.

## ***2.4 Characterizations***

1. Fourier transform infrared (FTIR) spectra: The infrared spectra obtained by using a BRUKER129605 spectrometer.
2. Mass Spectrum (MS): The mass spectra were acquired by a VG70-SE mass spectrometer.
3. Particle size: The particle size was determined by dynamic light scattering using a zetasizer Nano-ZS. The reported results are average of 3 runs.
4. Water absorption: A certain amount of latex was cast into a container on the glass pane with an area of 6\*8 cm<sup>2</sup> and was dried under room temperature for 72 h to obtain films. Taking a part of the film which weighted  $m_1$ , and putting it into deionized water for 24 h, then taking out from water, absorbing the water of the surface, and weighted as  $m_2$ . The water absorption is defined as follows:

$$(a) \text{ water absorption} = \frac{m_2 - m_1}{m_1} * 100\% \tag{1}$$

5. Tensile test: After machining the film to a certain specification, the films were slowly loaded in a tensile testing machine, and load  $F$  and displacement (extension)  $\Delta L$  are recorded.

### 3 Results and Discussion

#### 3.1 Chemical Structure Analysis of the Extender

The chain extender is produced by Michael reaction. As it's shown in Fig. 1, EDA reacts with DAAM at 75 °C. Two compounds are supposed to produce. As both of the compounds can react as extender and cross-linker, so purifying is unnecessary.

Figure 2 illustrates the FTIR spectra of the compound and DAAM. In the FTIR spectrum of DAAM, the peak at 1625 is attributed to the C = C stretching vibrations. While the broad band centered near 650 and 960 corresponds to the C-H bonds in Olefins bending vibrations. Compared with the FTIR spectrum of DAAM, there are no characteristic absorption peaks of C = C in the FTIR spectra of the compound, which indicates that DAAM completely reacted with EDA.

Figure 3 shows the Mass spectrum of the compound. As one can see, the product was composed of relative molecular mass 230 and 400, which completely meet the expected result.

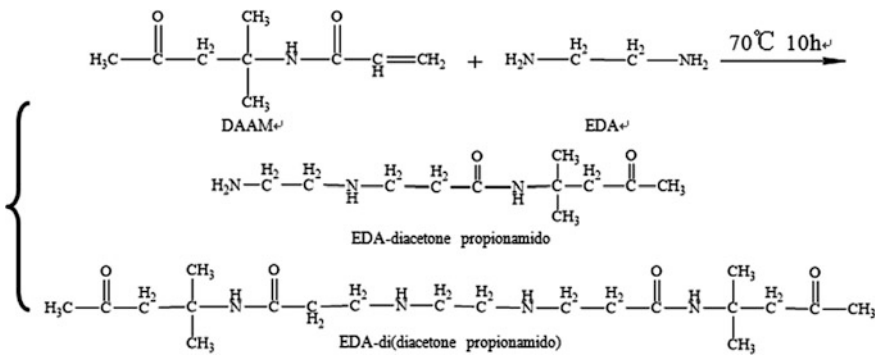


Fig. 1 Reaction between EDA and DAAM

Fig. 2 The FTIR spectra

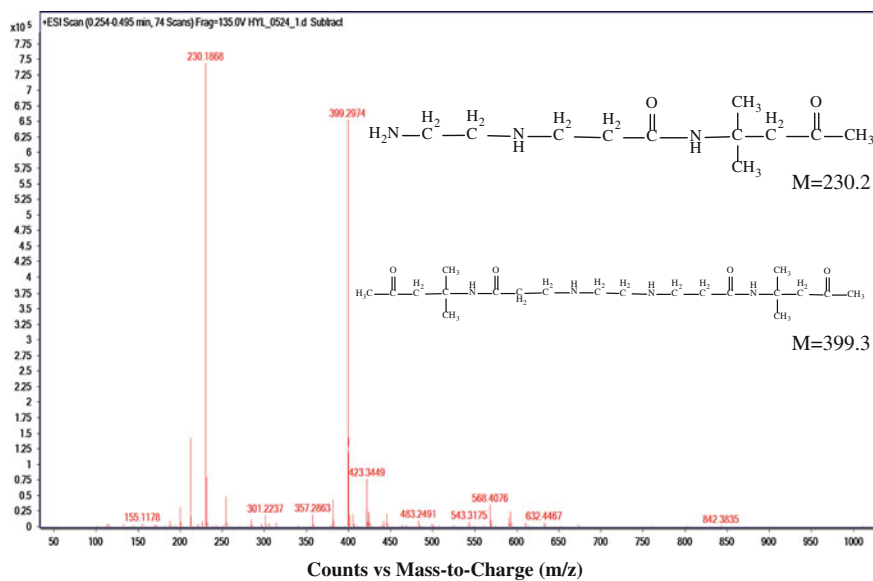
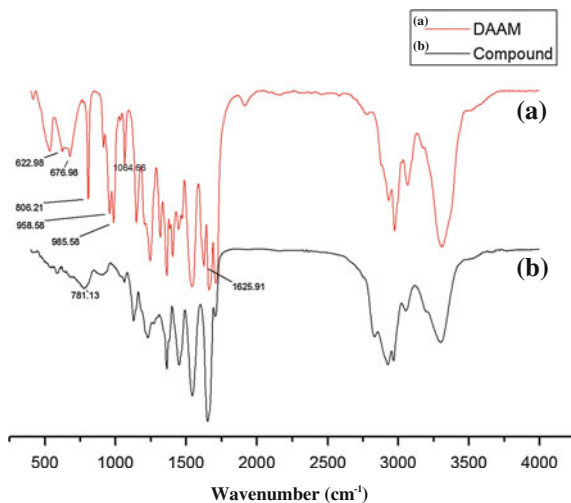


Fig. 3 The mass spectra of compound

### 3.2 The Impact of the Chain Extender's Dosage on the Properties of the Emulsions

We prepared the emulsion with different dosage of the chain extender based on five different formulations, and studied the effects of the chain extender on the emulsion performance. Table 1 depicted the fundamental properties of the obtained emulsions. The results demonstrated that introduction of the chain extender can not only improve the resistance to water, but also has great influence on the tensile strength and breaking length of the latex films.

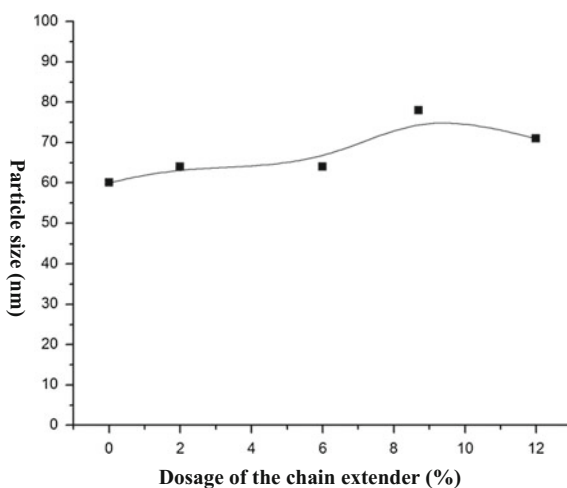
As it shown in Fig. 4, the dosage of the chain extender has little influence on the particle size of the emulsion. Figure 5 indicates that with the increasing of the dosage of the chain extender, the water absorption decreases obviously at first. While the dosage gets to 6%, the water absorption doesn't change with the dosage of the chain extender.

The curves in Fig. 6 displayed that the stress responses to the strain is to a large extent influenced by the dosage of the chain extender. With the chain extender's

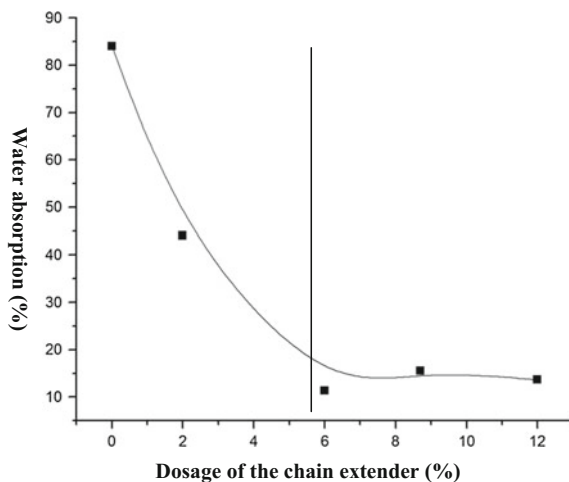
**Table 1** Impact of the chain extender's dosage

Self-crosslinking extender (%)	Particle size (nm)	PDI	Water absorption (%)	Tensile strength (MPa)	Breaking length (mm)
0	60	0.08	84		
2	64	0.04	44	7.1	305.6
6	64	0.08	11.3	28.4	317.8
8.7	78	0.06	15.5	31.9	259.6
12	71	0.09	13.7	21.3	154.3

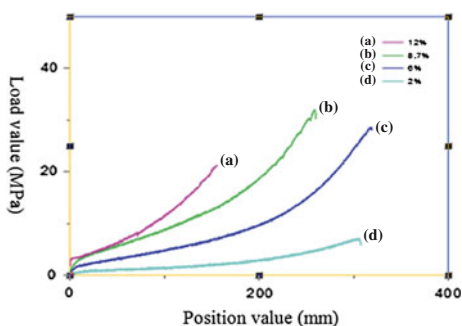
**Fig. 4** Connection between extender and particle size



**Fig. 5** Connection between extender and water absorption



**Fig. 6** Tensile test



content rising, the tensile modulus goes up, which indicates that the crosslinking density increases with the dosage of the chain extender.

## 4 Conclusions

A kind of self-crosslinking chain extender containing carbonyl groups was synthesized by Michael addition. Then the chain extender is used to react with a prepolymer containing NCO groups to prepare polyurethane emulsions. It shows that introduction of the chain extender has no influence on the particle size and PDI of the emulsion, but can greatly improve the films' resistance to water. What's more, the mechanical properties of the films are influenced in a certain degree. In all, the ketone and hydrazine cross-linking extender developed in this chapter are very effective for improving the performance of polyurethane.



## References

1. Shunji Sugano (2006). Aqueous Polyurethane Dispersions Using Aromatic Diisocyanate. *Macromol. Symp*, 239, 51–57.
2. Lai J Z, Ling H J, Chen GN (2003). Polymer Hybrids from Self-emulsifying PU Anionomer and Water-reducible Acrylate Copolymer via a Postcuring Reaction. *J Appl Polymer Sci*, 90 (4): 3578–3587.
3. Luo Chunhui, Qu Jinqing, CHEN Huanqin (2009). Crosslinking Modification of Aqueous Polyurethane Dispersions and its Properties. *Journal of Chemical Engineering of Chinese Universities*, 23(4): 650–654.
4. Yang Yongqiang, Chen Qi, Wang Gang, Huang Richu (2011). Preparation and Characterization of Low VOC Waterborne Sodium Bisulfite-Blocked Polyurethane Curing Agent. *Paint & Coatings Industry*, 41(7): 33–36.
5. Lv Xiaoli (2008). Research on Application of Ketone and Hydrazine Self Cross-linking Reaction by Emulsion polymer. Guangxi University, 2008: 1–7.

# Luminescent Properties of Rhodamine 6G Doped with DNA-CTMA and Its Application in Fluorescent Ink-Jet Ink

Hui Hao, Xia Li, XiaoYu Zhu, Huan Zheng, Beiqing Huang, Xianfu Wei and Lijuan Liang

**Abstract** In recent years, the research of molecular devices, fluorescent labels and fluorescent probes based on the interaction between biological molecules DNA and fluorescent dyes has aroused widespread concern and attention. This chapter discussed the luminescent properties of fluorescent dye Rhodamine 6G doped with DNA-CTMA lipid complexes. By testing the absorption spectrum and fluorescence spectrum, the effect of DNA-CTMA lipid complexes on the optical properties of dye Rhodamine has been studied, and the emitting mechanism based on the molecular structure has been analyzed. In addition, the luminance ink-jet ink was prepared through using the Rhodamine dye doped with DNA-CTMA as the fluorescent dye, and the ink sample showed good printability and security performance.

**Keywords** Rhodamine 6G · DNA-CTMA · Fluorescent ink-jet ink

## 1 Introduction

Rhodamine is a fluorescent dye based on xanthine and its most common dye is Rhodamine 6G [1]. Rh6G is the most commonly used fluorescent dye in biological medicine and other fields of analytical chemistry with good fluorescence stability, high fluorescence quantum efficiency, biological non-toxic and low cost. DNA is a double helix molecular structure, which possess genetic instructions could guide biological development and the operation of vital functions. There are four kinds of bases in double-helix structure, which is connected by hydrogen bonds and its structure is  $\pi$ - $\pi$  electronic overlap [2–4]. Additionally, the presence of some major grooves and narrow minor grooves in DNA provide the spaces so that many of the dyes such as rhodamine, rare earth ions can be easily embedded into the groove to achieve the purpose of strengthening the fluorescence emission intensity [5, 6].

---

H. Hao · X. Li · X. Zhu · H. Zheng · B. Huang · X. Wei · L. Liang (✉)  
Beijing Institute of Graphic Communication, Beijing, China  
e-mail: lianglijuan@bigc.edu.cn

DNA molecule has excellent optical and electrical properties, and has important application prospects in the fields of biological science, information science and optoelectronics. And with the development of the modern technology in chemical synthesis, compound separation means, the analytical technology of chemical molecular structure, the theory and research techniques of molecular recognition as well as the interactions between molecules, the research on the interaction between DNA and other molecules becomes a more active research field [7].

In this chapter, the luminescent properties of Rhodamine 6G are discussed by testing the absorption spectra and fluorescence spectra, and the effects DNA-CTMA lipid complexes on the luminescent properties of Rh6G dye have been studied. At the same time, the interaction between the fluorescent dye and DNA-CTMA lipid complexes has been analyzed based on the molecular structure. In addition, the fluorescent ink-jet ink was prepared by using rhodamine dye doped with DNA-CTMA as the luminous dye, the printability and security properties of the ink has been discussed.

## **2 Experimental**

### **2.1 Materials**

DNA, derived from salmon fish was purchased from Japan. Cexadecyltrimethyl-ammonium bromide (CTMA) was purchased from TCI. Rhodamine 6G were purchased from Sigma-Aldrich.

### **2.2 Instruments**

The solution was prepared through using the MS-H magnetic mixer. Vacuum oven was used to dry the DNA-CTMA complex. UV-Vis absorption was measured using 2501PC UV-Vis spectrophotometer. Emission spectral was measured using RF-5301PC fluorescence spectrometer.

### **2.3 Preparation of DNA-CTMA**

DNA and CTMA were dissolved in ultrapure water and stirred about 30 min through using magnetic stirrer, respectively. Then both the solutions were mixed and stirred for about 20–30 min, and the resulting solid was filtered and dried for at least 24 h to obtain the DNA-CTMA compound. The compound was dissolved in the n-butyl alcohol, and then the DNA-CTMA solution was obtained.

## 2.4 Preparation of Fluorescent Ink Jet Ink

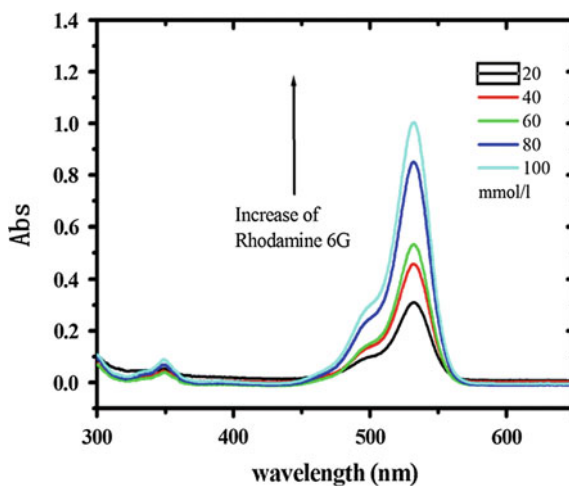
Firstly, the adhesive was pre-dispersed in solvent, and dissolved by stirring at room temperature completely. The fluorescent dye was added to the carrier until it is completely dissolved, and then the assistant was added. Then get the fluorescent ink-jet ink after filtered.

## 3 Results and Discussion

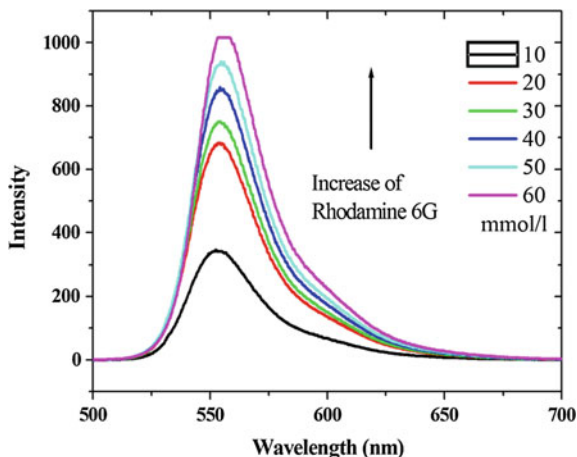
In order to study the luminescent properties of rhodamine dye, the ultraviolet absorption spectrum of Rhodamine 6G solution with different concentration from 10–200 mmol/L has been tested, as shown in Fig. 1. It is shown that there are two absorption bands at the wavelength of 350 and 532 nm, respectively. According to these two wavelengths, the possible excitation wavelength has been obtained. And with the increasing of the concentration, the absorption also increases.

Figure 2 shows the fluorescent spectrum of rhodamine 6G solution under different concentrations. Electrons jump from the first excited state of the lowest vibrational energy layer to the ground state when the fluorescence emits. Since rhodamine has rigid planar structure so that it could reduce the vibration of molecules and decreased the interaction with the solvent, thus it emits strong fluorescence. As can be seen from the Fig. 2, the emission wavelength of rhodamine 6G is 550 nm with the excited wavelength of 532 nm, so that rhodamine shows the bright red light. And with the increasing of the concentration of rhodamine 6G, the fluorescence intensity also increases.

**Fig. 1** The absorption spectrum of rhodamine 6G solution with different concentration



**Fig. 2** The Emission spectrum of Rhodamine 6G with different concentration (excitation wavelength: 532 nm)



**Fig. 3** Absorption spectrum of Rhodamine 6G solution doped with DNA-CTMA

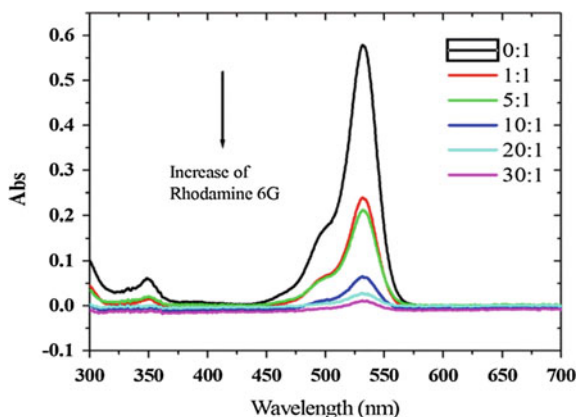
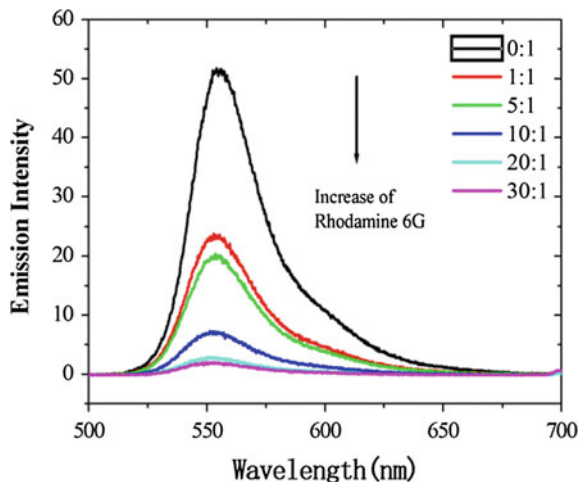


Figure 3 shows the absorption spectrum of Rhodamine 6G solution doped with DNA-CTMA under different concentration. As seen from the figure, the absorbance band at wavelength of 340 and 530 nm decreases with the increasing of the doped concentration of DNA-CTMA lipid complexes. In addition, when DNA-CTMA is not added to the Rhodamine 6G solution ([DNA-CTMA]: [Rhodamine 6G] = 0:1), the absorption maximum is 340 nm. With the increasing of the concentration of DNA-CTMA, the absorption maximum is slightly red shift, meaning that the maximum wavelength moves to the longer wavelength with the increasing of DNA-CTMA complex. These results indicate that the rhodamine 6G is intercalated or semi-intercalated into the DNA-CTMA complex.

Figure 4 shows the emission spectrum of rhodamine 6G which is doped with DNA-CTMA lipid complex at different concentration ratios, including 0:1, 1:1, 5:1, 10:1, 20:1, 30:1, respectively. As shown in the figure, in the solution state, with increasing of the concentration of DNA-CTMA complex, the fluorescence intensity

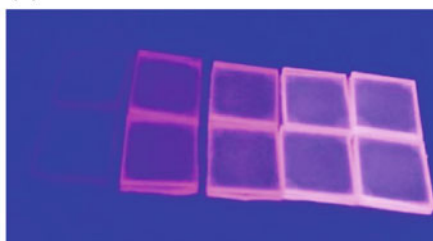
**Fig. 4** The Emission spectrum of Rhodamine 6G with different concentration (excitation wavelength: 532 nm)



(a)



(b)



**Fig. 5** The film under **a** ordinary light, **b** under UV light

of rhodamine decreases, this result is consistent with the absorption spectrum. Therefore, the decreased fluorescent intensity is attributed to the intercalation of the rhodamine 6G in the DNA-CTMA complex, which makes the electronic energy of the excited state of rhodamine changed. At the same time, the maximum wavelength has not shifted which also indicated that there is strong interaction between rhodamine 6G and DNA-CTMA complex. In order to make further study in the interaction between rhodamine 6G and DNA-CTMA complex, different films are prepared by spin coating with same concentration applied in the solution state, and the films are observed under ultraviolet light and ordinary light, the results are shown in Fig. 5.

As shown in the Fig. 5, in the film state, when the concentration of [DNA-CTMA]: [Rhodamine 6G] equal to 0:1, the fluorescent intensity is too weak to be observed. However, the emission intensity increased with the increasing of the concentration of DNA-CTMA complex. It is because that in the film state, with the drying of the film, the non-radiative transition of Rhodamine 6G is decreased effectively. So the intensity increases, and the film emits strong red light.

**Table 1** The comparison of the Epson ink and self-making ink

	Fluorescent intensity	Viscosity/mpa s	Surface tension (dyn/cm)	Conductivity/ ( $\mu\text{s/cm}$ )	pH value
Epson ink	–	3.9	31.0	3460	8.25
Ink sample	3960	4.8	29.6	49.4	8.28

In addition, according to the composition of the fluorescent dye, the ink sample is prepared through using the Rhodamine 6G doped with DNA-CTMA complex, as the concentration of DNA-CTMA and Rhodamine 6G is 30:1, and the performance of the inkjet ink sample is shown in Table 1.

As shown in the Table 1, the performance of the fluorescent ink jet ink which is prepared using the Rhodamine 6G doped with DNA-CTMA as the fluorescent dye has almost the same properties as the Epson original ink, which means that the self-making ink sample could print through using the Epson printer. According to the performance such as surface tension, viscosity, as well as the fluorescent intensity, the fluorescent ink-jet ink sample shows wonderful printability and good anti-counterfeit effect.

## 4 Conclusions

The luminescent properties of Rhodamine 6G itself and doped with DNA-CTMA with different concentration have been studied. From the absorption spectra, it can be seen that the absorption wavelengths of rhodamine are 350 and 532 nm, respectively. From the emission spectra, it is shown that the emission wavelength of Rhodamine 6G is 550 nm, which emits strong red light under the ultra-violet light. In addition, the interactions between rhodamine 6G and DNA-CTMA lipid complexes are studied both in the state of solution and film. Finally, the fluorescent ink-jet ink is prepared by applying Rhodamine 6G doped with DNA-CTMA complex as the fluorescent dye, and the sample shows the excellent printability and anti-counterfeit effect.

**Acknowledgements** This chapter is funded by the China postdoctoral science foundation, the Beijing Natural Science Foundation (2164061), general project of science and technology of Beijing Municipal Education Commission (SQKM201610015006), the scientific project of Beijing college student.

## References

1. Hartshorn R M, Barton J K. Novel Dipyridophenazine Complexes of Ruthenium (II): Exploring Luminescent Reporters of DNA. *J. Am. Chem. Soc.*, 1992, 114(15): 5919–5925. (No. 27170115005/017).

2. Friedman A E, Chambron J C, Sauvage J P, et al. Molecular "Light Switch" for DNA: Ru. *J. Am. Chem. Soc.*, 1990, 112(12): 4960–4962.
3. Olson E J C, Hu D, Hörmann A, et al. First Observation of the Key Intermediate in the "Light-Switch" Mechanism of  $[\text{Ru}(\text{phen})_2\text{dppz}]^{2+}$ . *J. Am. Chem. Soc.*, 1997, 119(47): 11458–11467.
4. Turro C, Bossmann S H, Jenkins Y, et al. Proton Transfer Quenching Solution and Bound to DNA. *J. Am. Chem. Soc.*, 1995, 117(35): 9026–9032.
5. Nair R B, Cullum B M, Murphy C J. Optical Properties of  $[\text{Ru}(\text{phen})_2\text{dppz}]^{2+}$  as a Function of Nonaqueous Environment. *Inorg. Chem.*, 1997, 36(6): 962–965.
6. Liu X W, Li J, Deng H, et al. Experimental and DFT studies on the DNA-binding trend and spectral properties of complexes  $[\text{Ru}(\text{bpy})_2\text{L}]^{2+}$  (L = dmdpq, dpq, and dcdpa). *Inorganica Chimica Acta.*, 2005, 358: 3311–3319.
7. Ji L N, Zhang Q L, Liu J G. DNA structure binding mechanism and biology functions of polypyridyl complexes in biomedicine. *Science in China (Series B)*. 2001, 44(3): 246–259.



# Luminescence Properties of Eu (TTA)<sub>3</sub>(H<sub>2</sub>O)<sub>2</sub> Doped with DNA-CTMA and Its Application in Fluorescent Inkjet Ink

Tong Zhao, Chunrui Lin, Xiaoyu Zhu, Huan Zheng, Lianfang Li, Beiqing Huang, Xianfu Wei and Lijuan Liang

**Abstract** In this chapter, the Eu(TTA)<sub>3</sub>(H<sub>2</sub>O)<sub>2</sub> complex was synthesized and the luminescence property was analyzed. The interaction between Eu(TTA)<sub>3</sub>(H<sub>2</sub>O)<sub>2</sub> and DNA-CTMA complex both in solution and films state were studied. In addition, the fluorescent inkjet ink sample was prepared using the Eu(TTA)<sub>3</sub>(H<sub>2</sub>O)<sub>2</sub> complex doped with DNA-CTMA as the fluorescent dye. The results showed that the main emission wavelength of Eu(TTA)<sub>3</sub>(H<sub>2</sub>O)<sub>2</sub> complex was 614 nm, and the emission intensity was the highest when the concentration reached 60%. In the film state, the fluorescence of the Eu(TTA)<sub>3</sub>(H<sub>2</sub>O)<sub>2</sub> complex doped with DNA-CTMA compound was enhanced greatly. Moreover, the prepared inkjet ink sample showed good printability and anti-false effect.

**Keywords** Eu(TTA)<sub>3</sub>(H<sub>2</sub>O)<sub>2</sub> · DNA-CTMA · Fluorescent inkjet ink

## 1 Introduction

In recent years, the Eu luminescent materials become one of the key materials for information display and high efficient lighting because of its narrow spectral bands, high purity, good conversion efficiency and stability [1]. Eu luminescent materials showed widely application in the fields of luminescence, optical information transmission, solar photovoltaic conversion, X-ray image and laser [2, 3].

---

T. Zhao · C. Lin · X. Zhu · H. Zheng · L. Li · B. Huang · X. Wei · L. Liang (✉)  
School of Printing and Packaging Engineering, Beijing Institute of  
Graphic Communication, Beijing, China  
e-mail: lianglijuan@bigc.com

T. Zhao  
College of Engineering, Qufu Normal University, Rizhao, Shandong, China  
e-mail: 751317633@qq.com

DNA, which has the stable double helix molecular chain structure is the genetic material of organism, carrying and expressing genetic information, which plays a decisive role in the life phenomenon [4]. In recent years, the research of molecular devices based on the interaction of fluorescent dyes with DNA has attracted wide attention. However, DNA is a negatively charged polyamine, and each nucleotide with a negative charge. Nowadays, a lot of research showed that, DNA with positively charged surfactants such as hexadecyltrimethyl-ammonium bromide, CTMA occurs ion exchange reaction, formation of DNA-CTMA cationic surfactants which insoluble in water but soluble in organic solvent such as butanol.

In this chapter, the preparation process of  $\text{Eu}(\text{TTA})_3(\text{H}_2\text{O})_2$  complex and DNA-CTMA compound was reported. The absorption and fluorescence properties of  $\text{Eu}(\text{TTA})_3(\text{H}_2\text{O})_2$  solution with different concentrations were studied, and the interaction between Eu complex and DNA-CTMA has been analyzed. And the inkjet ink sample was prepared through using  $\text{Eu}(\text{TTA})_3(\text{H}_2\text{O})_2$  complex doped with DNA-CTMA as the fluorescent dye.

## 2 Experimental

### 2.1 Materials

DNA, derived from salmon fish, purchased from Japan. CTMA and Hexadecyltrimethyl-ammonium bromide purchased from TCI Company. Europium (III) acetate hydrate, 2-Thenoyltrifluoroacetone and mineral spirits purchased from TCI Company.

### 2.2 Instruments

The solution was prepared through using the MS-H magnetic mixer. Vacuum drying oven used to dry the DNA-CTMA complex. UV-Vis absorption spectral was measured using 2501PC UV-Vis spectrophotometer. Emission spectral was measured using RF-5301PC fluorescence spectrometer.

### 2.3 Preparation of DNA-CTMA

DNA and CTMA dissolved in ultrapure water and stirred about 30 min through using magnetic stirrer, respectively. Then both the solution were mixed and stirred for about 20 min, the resulting solid was filtered and dried for 24 h to obtain the DNA-CTMA compound. The compound dissolved in the n-butyl alcohol, and then, with a magnetic mixer for about 5–6 h, until the DNA-CTMA compound completely dissolved.

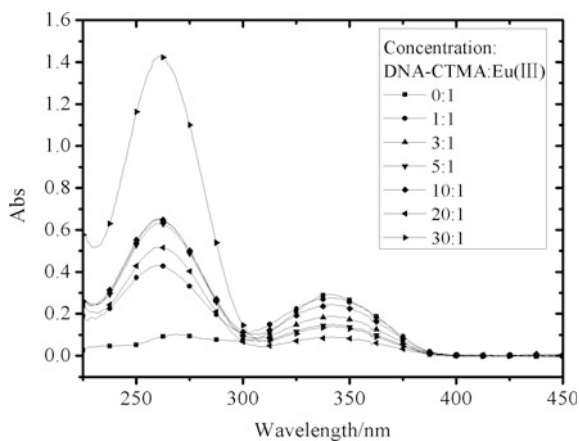




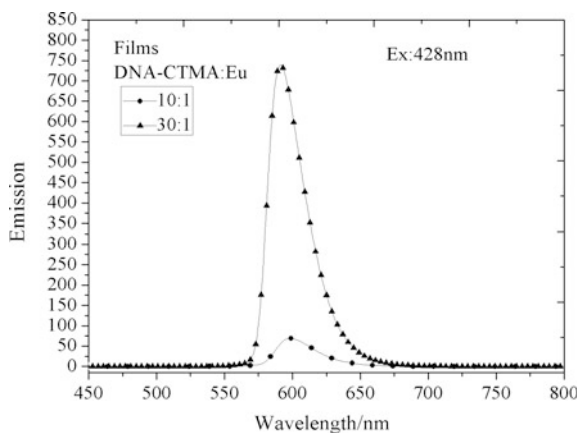
intercalation, and mean that the  $\text{Eu}(\text{TTA})_3(\text{H}_2\text{O})_2$  complex was intercalated into the based pairs of DNA-CTMA complex.

In order to further clarify the effect of DNA-CTMA complex on the luminescence properties of  $\text{Eu}(\text{TTA})_3(\text{H}_2\text{O})_2$  compound, the  $\text{Eu}(\text{TTA})_3(\text{H}_2\text{O})_2$  film doped with DNA-CTMA complex film with different concentration including 10:1, 30:1 had been prepared using the spin coating method, and the fluorescence spectrum of the films were tested, shown as Fig. 4. From the Fig. 4, the fluorescence intensity has been improved greatly when the DNA-CTMA are doped. According to the fluorescent spectra, with the increase in the proportion of DNA-CTMA compound, the fluorescence intensity of films enhanced, and the film emitted sharp red light. This was because that in the film state, the  $\text{Eu}(\text{TTA})_3(\text{H}_2\text{O})_2$  was intercalated into the groove gap of the DNA-CTMA complex, which decreased the non-radiative transition effectively, so the fluorescent intensity improved. In addition, because of the existing of the DNA-CTMA complex, the Eu(III) ion was effected by the steric hindrance and the obstruction of the double helix structure of the polymer, which

**Fig. 3** UV spectra of different proportion DNA-CTMA and Eu (III) ratios



**Fig. 4** Emission spectra of and Eu-complex films coped with DNA-CTMA thin at 614 nm



**Table 1** The performance of the fluorescent inkjet ink and Epson ink

Sample	Fluorescent intensity	Viscosity (mpa/s)	Surface tension (mN/m)	Conductivity (S/cm)	pH value
Fluorescent ink	4530	6.8	25.4	50.3	7.86
Epson ink	–	5.6	28.3	3290	8.15

made the emission ion could disperse in the groove of DNA-CTMA complex. So the Eu(III) ion was difficult to close to each other and gather together, as a result the emission intensity was improved greatly.

In order to make practical application of the  $\text{Eu}(\text{TTA})_3(\text{H}_2\text{O})_2$  doped with DNA-CTMA, the fluorescent inkjet ink sample was prepared, and the performance of the inkjet ink sample was tested, shown as in Table 1. As shown in the table, the performance of the fluorescent inkjet ink prepared has almost the same surface tension and viscosity as the Epson ink, which played an important role in the injection, this mean that the fluorescent inkjet ink could print through using the Epson printer. The high fluorescent intensity indicated that the ink sample showed the good anti-counterfeit effect: under the ordinary light, almost nothing could observe, but a clearly fluorescent image could observe under the ultraviolet light.

## 4 Conclusions

In this chapter, the  $\text{Eu}(\text{TTA})_3(\text{H}_2\text{O})_2$  compound has been prepared, and the absorption spectra and fluorescent spectra have been tested, respectively. And the interaction between the  $\text{Eu}(\text{TTA})_3(\text{H}_2\text{O})_2$  and DNA-CTMA complex have been analyzed, and the fluorescent intensity of the  $\text{Eu}(\text{TTA})_3(\text{H}_2\text{O})_2$  complex has been improved greatly when the DNA-CTMA is doped. In addition, the fluorescent inkjet ink has been prepared using the  $\text{Eu}(\text{TTA})_3(\text{H}_2\text{O})_2$  doped with DNA-CTMA as the luminous dye, and the inkjet ink sample shows the good anti-counterfeit effect.

**Acknowledgements** This chapter is funded by the China postdoctoral science foundation, the Beijing Natural Science Foundation (2164061), general project of science and technology of Beijing Municipal Education Commission (SQKM201610015006), the scientific research project of Beijing college student, and the initial funding for the Doctoral program of BIGC (NO. 27170115005/017).

## References

1. SU. W. B, GU. X. X, ZOU. H, & ZHU. R. H. (2001). Lumine science Characteristic and Their Utility of Rare-earth Elements. *Chemical Research*, 12(4), 55–59.
2. MA. J. L, NI. H. Q, & X. B. (2007). Study Progress of Lumine science of Rare Earth Polymer Complex. *Anhui Chemical Industry*, 33(1), 8–11.

3. Rosendo. A, Flores. M, & Cordoba. G. (2003). Synthesis, Characterization and Luminescence Properties of  $\text{Tb}^{3+}$  and  $\text{Eu}^{3+}$  Doped Poly. *Material Letter*, 57, 2885–2893.
4. Thockchom. B, Niyazi. S, & James. G. (2009). Bio-Organic Optoelectronic Devices Using DNA. *Advances in Polymer Science*, 223, 73–112.
5. GUO. D. C, SHU. W. L, & ZHOU. Y, etc. (2004). Synthesis and reflective study of reactive ternaryterbium complex. *Journal of the Chinese Rare Earth Society*, 22(2), 196–200.
6. WANG. L. H, WANG. Q.M, & XIAO. W. H. (2004). Preparation of photochromic functional films and investigation of their properties. *Jiang xi Chemical Industry*, 2, 115–118.
7. WANG. Z. M, CAO. J. R, & CHEN. Z. R, etc. (1998). Study on terbium doped polypropylene film. *Journal of the Chinese Rare Earth Society*, 16(4), 315–318.
8. TANG. C. W, & VANSLYKE. S. A. (1987). Organic electroluminescent diodes. *Applied Physics Letters*, 51, 913–915.

# Influence of Coalescent on the Gloss of Plastic Water-Based Flexographic Ink

Xue Gao, Zhiyong Sun, Yun Ouyang, Xiaofang Wang, Xiaoli Liu, Li Yang and Xiaojuan Feng

**Abstract** This article analyzed and studied the effects of different types of coalescing agent on gloss of plastic water-based flexographic ink. As one of the most important characters for plastic water-based flexographic ink, gloss determines the quality of the flexo-printing products. It is significant for plastic water-based flexographic ink to improve the film quality and reduce the dosage of coalescing agent. We mainly studied on the influence of mass fraction of alcohol coalescing agent (A1), esters coalescing agent (A2) and esters coalescing agent (A3) in plastic water-based flexographic ink. The results indicated that the best dosages of the three kinds of coalescing agents are 1.4, 1.0 and 1.0%. The gloss is increasing 5.2, 14.6 and 10.3% respectively. The esters coalescing agent (A2) have notable effect on the gloss of the ink.

**Keywords** Plastic water-based flexographic ink · Coalescent · Gloss

## 1 Introduction

As a new type of green printing and packaging material, plastic water-based flexographic ink has vast prospect applied to alcohol, food, beverage, medicine, children's toys and other printing products with strict health condition requirement [1, 2]. Gloss is a very important properties of plastic water-based flexographic ink, affects the appearance of the product. Gloss is refers to the ability of reflection of light from the ink layer in a certain angle. Lack of gloss is the main problem of plastic water-based flexographic ink, which hinders the application for printing and packaging fields seriously at present [3–5]. Therefore, it is urgent to find a kind of suitable coalescing agent to solve this problem.

---

X. Gao (✉) · Z. Sun · Y. Ouyang · X. Wang · X. Liu · L. Yang · X. Feng  
Beijing Key Laboratory of Packaging and Printing New Technology,  
China Academy of Printing Technology, Beijing, China  
e-mail: gaoxue@keyin.cn



There are three kinds of coalescent, including hydrophobic hydrocarbon coalescent, half-hydrophilic coalescent and hydrophilic coalescent [6]. The hydrophobic hydrocarbon coalescing agent will cause a decline in the adhesion. The third kind of coalescing agents are used to improve the freeze-thaw stability of ink as antifreeze.

In this chapter, we focus on the impact on plastic water-based flexographic ink with amounts of second kind of coalescing agents, such as alcohol coalescent (A1), esters coalescent (A2) and esters coalescent (A3). Prepared the ink with different amount of coalescent, the properties of overprinted biaxially-oriented polypropylene plastic film (BOPP) with those inks, i.e. and gloss, are compared.

## 2 Experiments

### 2.1 Materials

Base ink	Base ink (C3) (Beijing xin nuo an Co., Ltd.);
Resin	Acrylic resin R1 (BASF);
Additives	alcohol coalescent (A1), esters coalescent (A2), esters coalescent (A3), defoamer 810 (Deutsche Degussa), deionized water.
Printing substrate	BOPP film.

### 2.2 Equipments

Laboratory dispersers	SWFS-4000 (Shanghai Sower Mechanical and Electrical Equipment Co., Ltd.);
Printability Tester	IGT F1 Basic;
Gloss Meter	TC-108DP/A (Tokyo Denshoku Co., Ltd.);
Surface Roughometer	M590-PPS (Messmer Instruments Ltd.).

### 2.3 Preparation Method of Water-Based Ink

Weighing a certain quality of acrylic resin R1 in a beaker and adding C3 slowly while mixing for 20 min, and then dropping in 810 (0.7%) stirring for another 20 min. Finally, adding the coalescent in the plastic water-based flexographic ink with a certain mass fraction and high-speed of 1500 revolutions per minute stirring for 1 h, then water-based ink is obtained.

### 3 Test Methods

#### 3.1 Proofing Method

Use flexographic proofing device. Wherein, the printing pressure is 100 N, printing speed is 0.3 m/s, and the anilox line screen number is 480 dpi.

#### 3.2 Gloss Test

Gloss mainly depends on the angle of the lighting and observation, taking the angles of measurement is 20°, 45°, 60° or 85°. In our experiment, the angle of detect the ink film gloss is 60°, recorded data after test, take average of five points.

#### 3.3 Surface Roughness Test

Surface roughness refers to the ink layer surface with small spacing and small peak valley of roughness. The distance between the two peaks or two troughs (wave distance) is very small (under 0.1  $\mu\text{m}$ ), it belongs to the micro geometry shape error. The smaller the surface roughness, the smoother of the ink layer surface is. Put ink layer between the test head and the rubber bearing and recorded data after testing, take average of five points.

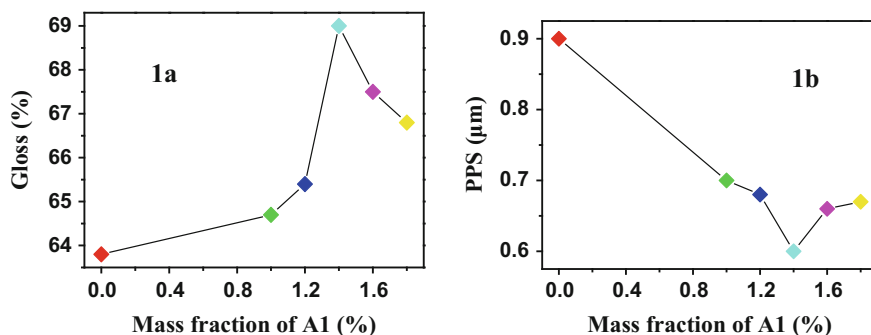
## 4 Results and Discussion

### 4.1 Effects of Alcohol Coalescent (A1) on Gloss

Fixed ink ratio of components, with the mass fraction of alcohol coalescent (A1) (0, 1.0, 1.2, 1.4, 1.6, 1.8%). Figure 1 demonstrates the surface roughness and gloss of water-based ink.

As shown in Fig. 1a, the gloss increases gradually and reaching its maximum percentage of 69%, which enhanced 10.3% to the original ink, and continued to decline. At the same time, surface roughness gets minimum value (0.6  $\mu\text{m}$ ) with the same proportion (Fig. 1b). The amounts of A1 give rise to a rising for gloss. Basic data onto experiment is shown as Table 1.

A tiny bump on the surface of ink layer will give the degree of light scatter increases, which causes the gloss decline. Alcohol agent (A1) is small molecular substances can reduce the surface tension of plastic water-based flexographic ink. Thought a small amount of Alcohol agent (A1) couldn't reduce the ink tension



**Fig. 1** Effects of the mass fraction of A1 on gloss and surface roughness of ink

**Table 1** The effect of different mass fraction of A1 on ink

Coalescent	Amount/%	0	1	1.2	1.4	1.6	1.8
A1	V4/s	41.68	49.79	49.23	47.35	46.06	45.59
	Size/ $\mu\text{m}$	25	30	30	30	30	35
	pH	7.73	7.74	7.75	7.74	7.74	7.74
	Dryness/mm	111	85.5	109	113.5	120	122
	Solid content/%	49	49	49	49	49	49
	PPS/ $\mu\text{m}$	0.9	0.7	0.68	0.6	0.66	0.67
	Gloss/%	63.8	64.7	65.4	69	67.5	66.8

obviously brings about the poor flowing property and gloss. What's more, an excess of A1 could cause a decrease of ink adhesion and reduce the layer thickness, then reduces the gloss [7]. So we found the best dosage of A1 in plastic water-based flexographic ink is 1.4%.

## 4.2 Effects of Ethers Coalescent (A2) and Esters Coalescent (A3) on Gloss

Fixed ink ratio of components, with the mass fraction of ethers coalescing agent (A2) at 0.5, 1.0, 1.5, 2.0 and 2.5%. Figure 2 demonstrates the surface roughness and gloss of water-based ink.

Figure 2a indicates that the gloss achieves maximum (78.4%) with the proportion of A2 is 1.0%, which enhanced 14.8% to the original ink. And gloss fall back slightly with the increase of A2. Surface roughness has sharp dropped to 0.6  $\mu\text{m}$  with the A2 at the same proportion. The effect of A2 on surface roughness and gloss just the opposite, which indicated in Fig. 2b. Basic data onto experiment is shown as Table 2.

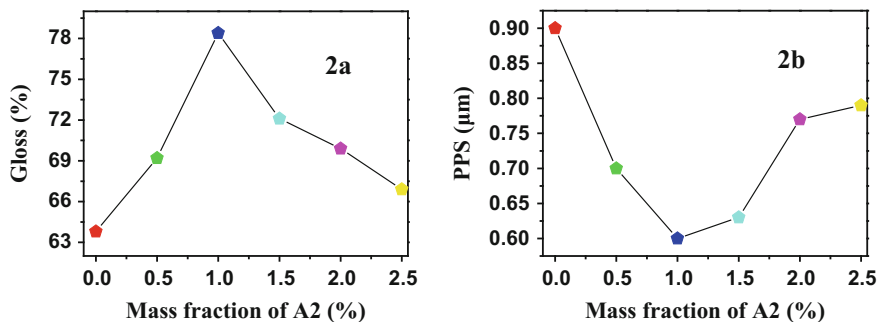


Fig. 2 Effects of the mass fraction of A2 on gloss and surface roughness of ink

Table 2 Effect of different mass fraction of A2 on ink

Coalescent	Amount/%	0	0.5	1	1.5	2	2.5
A2	V4/s	41.68	44.99	46.9	47.36	54.7	58.46
	Size/μm	25	35	35	35	40	35
	pH	7.73	7.84	7.84	7.84	7.84	7.83
	Dryness/mm	111	101	104	110	115	123
	Solid content/%	49	49	49	49	49	49
	PPS/μm	0.9	0.7	0.6	0.63	0.77	0.79
	Gloss/%	63.8	69.2	78.4	72.1	69.9	66.9

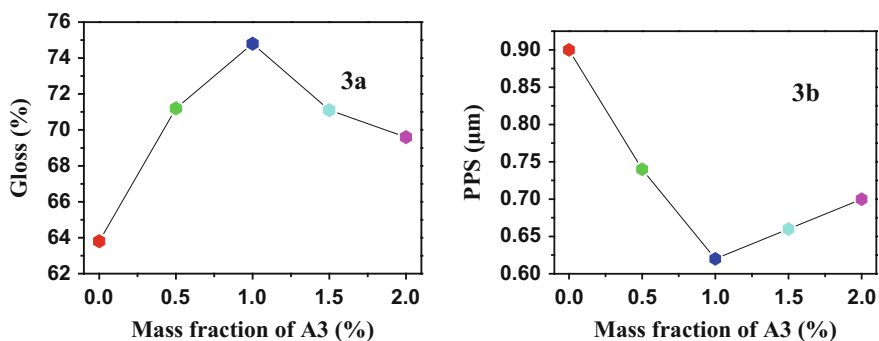


Fig. 3 Effects of the mass fraction of A3 on gloss and surface roughness of ink

The mass fraction of esters coalescing agent (A3) in water-based ink is at 0.5, 1.0, 1.5 and 2.0%. Figure 3 demonstrates the surface roughness and gloss of water-based ink. As shown in Fig. 3a, the gloss scratches maximum (74.8%) when the proportion of A3 is 1.0%, an increase of 10.3% compared to the original ink. Surface roughness has sharp drop with the addition of A3 (0.62 μm), which indicated in Fig. 3b. Basic data onto experiment is shown as Table 3.

**Table 3** The effect of different mass fraction of A3 on ink

Coalescent	Amount/%	0	0.5	1	1.5	2
A3	V4/s	41.68	43.82	45.76	47.38	50.14
	Size/ $\mu\text{m}$	25	40	45	40	40
	pH	7.73	7.85	7.85	7.85	7.85
	Dryness/mm	111	126	124	122	124
	Solid content/%	49	49	49	49	49
	PPS/ $\mu\text{m}$	0.9	0.74	0.62	0.66	0.7
	Gloss/%	63.8	71.2	74.8	71.1	69.6

From the data above, we could consider that there are no obviously difference between ethers coalescing agent (A2) and esters coalescing agent (A3) in acrylic resin system. Compare A2 and A3, the impact on water-based ink of A3 is relatively stable, but the gloss is higher when A2 in a suitable content.

As film coalescent can reduce the MFFT of resin effectively so that can help to form a smooth film [8], A2 and A3 can reduce the MFFT of acrylic resin effectively so that can help to form a smooth film. Besides, as glycol ether, the polarity of A2 and A3 is stronger that can reduce the surface tension notably then improve the gloss and reduce surface roughness. But an excess of film coalescing agents can bring adverse effect on dispersion of water-based ink. So we should pay a great attention to amount of coalescent when we use it in actual production.

## 5 Conclusions

Mass fraction of coalescent has great influenced on gloss of plastic water-based flexographic ink. The results indicated that the best dosages of the three kinds of coalescing agents are 1.4, 1.0 and 1.0. The gloss is increasing 5.2, 14.6 and 10.3% respectively. The esters coalescing agent (A2) have notable effect on the gloss of the ink.

As alcohol coalescent (A1) is small molecular substances can cause a decrease of ink adhesion and with an excess of A1 (>1.4%) reduce the layer thickness, then influence surface roughness and gloss seriously. Due to an excess of film coalescing agents contain the VOC, we should pay attention to the mass fraction of ether coalescent (A2) and ester coalescent (A3) when we use them in actual production. We found the best level in water-based ink is 1.0%, and the influence of A2 to gloss is better than A3 for plastic water-based flexographic ink at the same condition.

As the best content of coalescing agents for gloss are different, we should according to the different printing products to choose the best one for plastic water-based flexographic ink.

**Acknowledgements** This study is funded by Press and publication reform development project library (0020131646) and culture industry development foundation of China.

## References

1. Zuzanna Z, Joanna I. (2015). Branched polyglycerols as performance additives for water-based flexographic printing inks. *Progress in Organic Coatings*, 78, 334–339.
2. Wentao H. (2013). Study on the water-based ink for flexographic printing and synthesis of acrylic resin. *South China University of Technology, China*.
3. Chenghong Q, Yuanyuan N. (2008). The analysis of the ink to print gloss effect. *Printing Field*, 11, 68–69.
4. Xiaodong L, Chuanxiang Z. (2010). The glossiness influence factor analysis of flexographic printing water-based ink. *Packaging Journal*, 2, 25–27.
5. Fuzhong Z, Beiqing H. (2014). The study of effect factors on glossiness of water-based gravure ink. *Journal of Beijing Institute of Graphic Communication*, 22, 17–19.
6. Hongsen H, Jianyong L. (2006). Application and development of auxiliaries in water-borne coatings. *Fine and Specialty Chemicals*. 14, 4–6.
7. Yingjie X, Beiqing H. (2008). Influence of promoter on the color density and glossiness of water-based gravure ink. *Packaging Engineering*, 10, 43–44.
8. Yixuan L. (2012). Film-forming mechanism, performance and development trend of film-forming agent. *Chemical Materials for Construction*, 4, 14–19.

# Study on Properties of Magenta Water-Based Flexo Ink Used on BOPP Film

Yang Liu, Beiqing Huang, Xianfu Wei and Ying Shen

**Abstract** Alcohol-soluble or solvent-borne plastic flexo-printing ink is widely used by Current domestic industries. It is great harmful to the environment because of the harmful substances it contained. With today's increasing awareness of environmental protection, it is becoming the trend that green waterborne plastic flexo printing ink replaces solvent-based ink. By studying dispersion factors such as grinding resin, pigment/binder ratio and dispersant and testing print properties such as density, surface tension, glossiness and adhesion, water-based flexo ink formulation with good quality would obtain. Results showed that: by studying and testing print properties, water-based flexo ink formulates with good dispersion and adhesion, high color density and glossiness.

**Keywords** Water-based flexo ink · Dispersion · BOPP film

## 1 Introduction

In the printing and packaging industry, solvent-based ink was widely used due to its excellent printing properties. Due to large amounts of volatile organic compounds it contained and great harms to environment it created, environmental restrictions policy had launched from environmental protection agencies around the world. Thus, water-based ink came into being [1]. At present, domestic water-based flexo ink had a larger share of the market, but plastic flexo ink was dependent on

---

Y. Liu (✉) · B. Huang · X. Wei · Y. Shen  
Beijing Institute of Graphic Communication, Beijing, China  
e-mail: 960783212@qq.com

B. Huang  
e-mail: huangpeiqing@bigc.edu.cn

X. Wei  
e-mail: weixianfu@bigc.edu.cn

Y. Shen  
e-mail: 943854005@qq.com

alcohol-soluble ink. Compared with alcohol-soluble ink, water-based flexo ink had many problems such as poor adhesion when it printed on BOPP film, so its use was limited greatly. Poor print quality of water-based flexo ink used on BOPP film needed to settle. Solving these problems in print quality was enormous challenge that water-based flexo ink faced.

## **2 Experiments**

### **2.1 Materials**

Pigments: Red 6BW (Peng lai chemical Company); grinding resin: HPD96 (Germany BASF), AZR acrylic resin (Tianjin company), BT-20 (Tuo zi Fine Chemical Company); Film-forming resin: Joncryl<sup>®</sup>S-2919, Joncryl<sup>®</sup>S-2916, Joncryl<sup>®</sup>624 (BASF), 813, 503 (Shanghai TuiTu Chemical Company); Dispersant: 750, 760 (Degussa Corporation); defoamers: 810 (Deutsche Degussa); deionized water.

### **2.2 Equipments**

JG-2S high-speed stirring disperser (Shanghai Division Music Instrument Co., Ltd.), D2004 W electric Mixer (Shanghai Division Music Instrument Co., Ltd.), Microtrac S3500 series laser particle size analyzer (Microtrac US company), KRUSS surface tension meter K100 (Germany company), X-528 spectroscopic densitometer (X-Rite), IGT-F1-type printability tester (Netherlands), AR2000 rheometer (TA US company).

### **2.3 Preparation Method of Water-Based Ink**

Depending on the content of each component in the ink formulations, add the pigment, grind resin, dispersant, defoamer and deionized water into the beaker, and then dispersed for 30 min on a pre-D2004 W electric mixer. The mixture then dispersed into JG-2S digital high-speed mixer speed grinding 2 h, in the course of grinding to add to the grinding media (zirconia beads).

The base ink, film-forming resin in accordance with its content added to the ink, then HJ-6 A-type digital thermostat long magnetic stirrer for 30 min.



### 3 Test Methods

#### 3.1 Proofing Method

Use flexographic proofing device. Wherein the printing pressure is 85 N; printing speed is 0.5 m/s; the anilox line count is 200lpi.

#### 3.2 Dispersion Performance Test

Microtrac S3500 with the company's Zetasizer particle size of the ink test, the smaller the particle, the more uniform particle size distribution curve that is more narrow, indicating better dispersion to the ink particle size of 95% to be dispersible evaluation.

#### 3.3 Color Density Test

Taking into account the characteristics of the plastic substrate, the test performed by using a reflection densitometer. Specific test method: put a piece of coated paper below the spline. Firstly, we measure no ink color of density values for calibration, and then measure the colored portion of the ink density, and this measurement value is the color density of the ink.

#### 3.4 Surface Tension Test

At room temperature 25 °C conditions, surface tension measurement performed by using KRUSS Process Tensimeter K100.

#### 3.5 Apparent Performance Test

Apparent performance test is mainly in visual way. The apparent properties of the ink directly relate to leveling, leveling of the ink on a non-absorbent material is

**Table 1** Apparent performance grading standards

Performance	Chaotic	Irregular	General	Smooth	Flow completely
level	1	2	3	4	5

good, and the apparent performance is good. The apparent performance divides into five levels as follows (Table 1).

### 3.6 Adhesion Test

20 mm × 20 mm 3 M adhesive tape was adopted on the proofs, One hundred 1 mm<sup>2</sup> graph paper in 10 mm × 10 mm were placed behind samples, and then constant force in the direction of 90° was used to tear off 3 M tape, the remaining percentage of the graph paper with ink was calculated to evaluate adhesion.

## 4 Research on Dispersion of Water-Based Flexo Ink

### 4.1 The Impact on the Dispersion of Different Grinding Resin and Different Pigment/Binder Ratio

Dispersion is one of the printing performances for ink. Grinding resin and pigment/binder ratio are important factors that influenced on dispersion of ink. Pigment content is fixed, and the sample of water-based flexo ink formulates with different grinding resin and different pigment/binder ratio. Then particle size of ink is tested, and results are as shown in Fig. 1.

As shown in Fig. 1, ink has different dispersion due to different types of grinding resin, and because of different pigment/binder ratio, ink has different dispersion as well. There is a trend that particle size of ink become smaller firstly and then become larger with the changing of pigment/blinder ratio. When pigment/blinder ratio is large, the ink viscosity is very small, and the ink cannot obtain sufficient shear effect, so particle size is large. With the increasing amount of grinding resin,

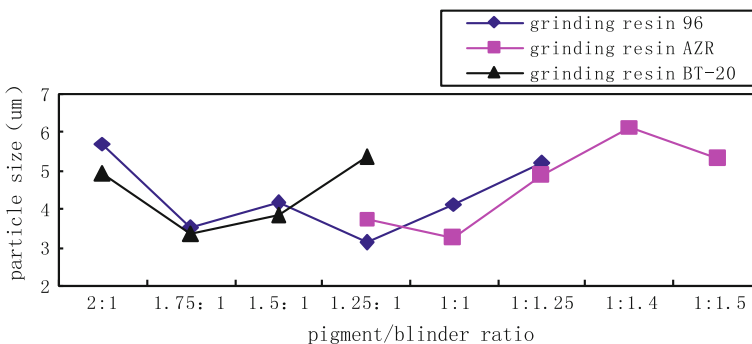


Fig. 1 Particle size of magenta ink

viscosity also increases. When the best flow point is reached, ink gets fully effective shear, and dispersing property shows the best [2, 3], so particle size is smallest. When viscosity is increased, the ink is not flowing and shearing is not sufficient, so the particle size increases.

Among three types of grinding resin, grinding resin 96 has the best dispersion with pigment/binder ratio 1.25:1. Three types of grinding resin are belonging to different kinds of waterborne resins. Its chemical structure and composition are not the same, so grinding resin 96 has strong affinity with the pigment surface modifier and it is easier to pigment wetting, so its dispersion effect is better [4].

## 4.2 The Impact on the Dispersion of Different Dispersant

Two types of dispersants are studied to explore the effect of dispersant on the dispersion in inks for pigment particles dispersing steadily in the ink; pigment content, grinding resin and pigment/binder ratio are fixed, and then 2 types of dispersants are added to ink respectively, and the test results are as shown in Fig. 2.

As shown in Fig. 2, the particle size of ink with dispersant 750 is significantly smaller than that with dispersant 760. Through charge repulsion effect or polymer steric effect, particles can steadily disperse in solution and bilayer structure can form on the surface of pigment particles by dispersant 750 and 760, but outer polar-side of dispersant 750 has a stronger affinity with water, increasing the degree of pigment particles wetted by water. Pigment particles get away from each other due to electrostatic repulsion.

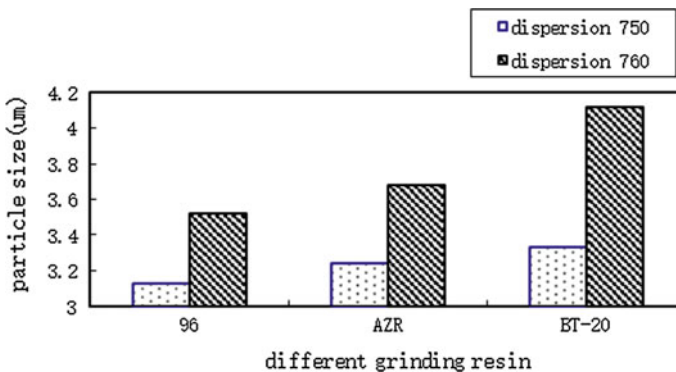


Fig. 2 Effect of different pigment/resin ratio on the dispersion property

## 5 Research on Printing Quality and Performance of Ink

### 5.1 Quality and Properties of the Film-Forming Resin for Printing Ink

Pigment content, grinding resin and pigment/Binder ratio are fixed. Film-forming resin is key factors influencing properties of ink printing. Different film-forming resin has different molecular structure, so ink with different film-forming resin has different ink printability. Water-based flexo ink with different film-forming resin will be studied, and test results are shown in Figs. 3, 4, 5, 6, 7.

As shown in Fig. 3, particle size of water-based flexo ink with film-forming resin 813, film-forming resin S-2916, film-forming resin S-2919 is smaller than that with film-forming resin 503, film-forming resin 624. Because pigment particles are sufficiently filled by film-forming resin 813, film-forming resin S-2916, film-forming resin S-2919. Film-forming resin impedes the mutual contact between the particles and prevents “aggregates” generates further, so the dispersion can be better [4].

As shown in Fig. 4, surface tension of ink with film-forming resin S-2916 is smaller than other four species. Because five film-forming resins has its own surface tension and are not the same with each other, so surface tension of ink with every film-forming resin is different.

As shown in Fig. 5, color density of ink with film-forming resin 624 is larger than other four species. Color density relates with ink transferability, rheological property of film-forming resin and resin compatibility. Because rheological property of film-forming resin 624 is better than remaining four species and film-forming resin 624 is better to compatible with three grinding resins, so color density of ink with film-forming resin 624 is larger.

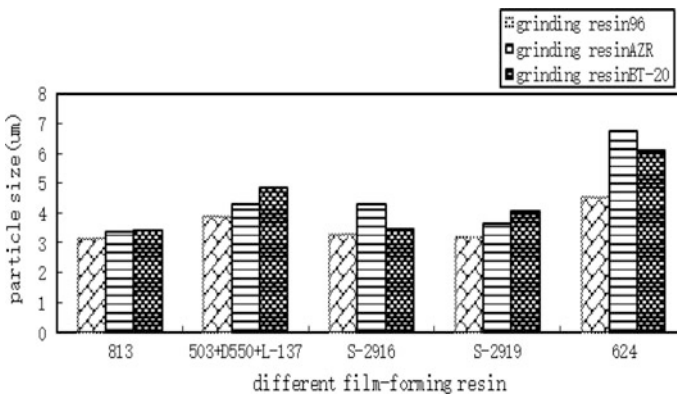


Fig. 3 Effect of different film-forming resin on the particle size

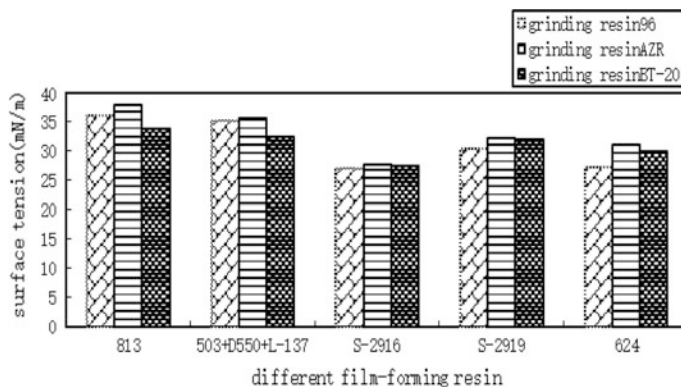


Fig. 4 Effect of different film-forming resin on the surface tension

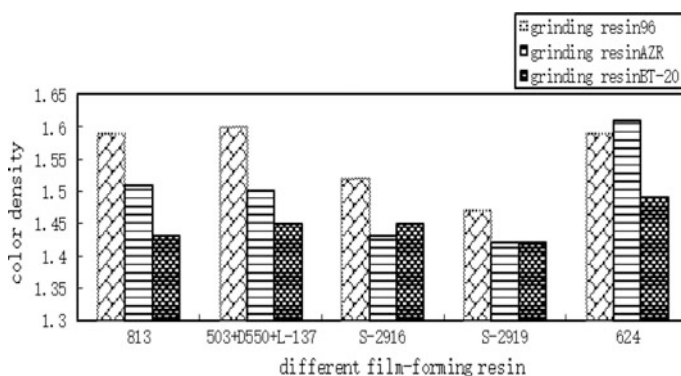


Fig. 5 Effect of different film-forming resin on the color density

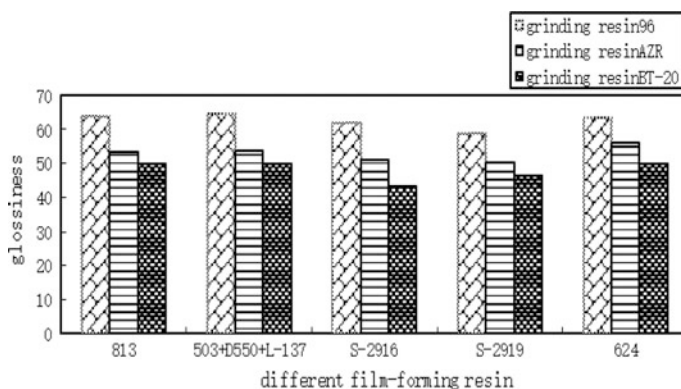
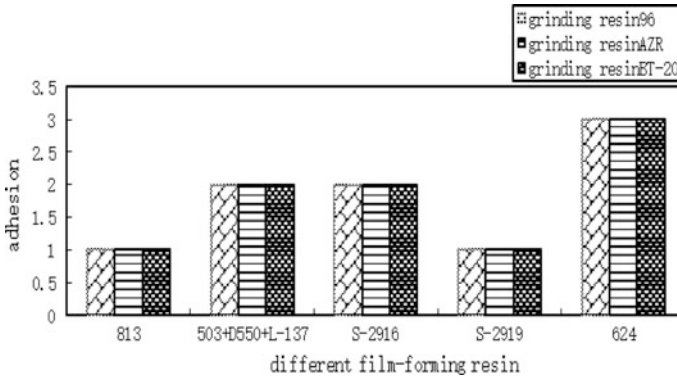


Fig. 6 Effect of different film-forming resin on the glossiness



**Fig. 7** Effect of different film-forming resin on the adhesion

As shown in Fig. 6, the difference of glossiness with five film-forming resins is not big, but glossiness of ink with grinding resin 96 is larger than glossiness of ink with grinding resin AZR and grinding resin BT-20. Because dispersion of ink with grinding resin 96 is the best, so rheological property of ink is better, and then glossiness is better.

As shown in Fig. 7, adhesion of ink with film-forming resin 813 or film-forming resin S-2919 is better than other three species. Although five film-forming resins are acrylic resins, molecules and molecular structures are different, and functional groups of adhesion are different, so adhesion of ink with every film-forming resin is different.

### 5.2 Film-Forming Resin Formulation Experiments

According to printing performance result of the ink with every film-forming resin: surface tension of ink with film-forming resin S-2916 is smallest; color density of ink with film-forming resin 624 is largest; adhesion and dispersion of ink with film-forming resin 813 and film-forming resin S-2919 is the best. Each film-forming resin has its own advantage, so composite resin of complex distribution experiment need to filter out printing performance optimal of ink formula. Film-forming resin 813, S-2919 and S-2916 select to complete complex distribution experiment. Test results as shown in Table 2.

Setting Weight: leveling 0.2, color density 0.1, gloss 0.2, surface tension 0.2, adhesion 0.3. The regression equation for calculating the ink of the experiment by a simple centroid design principles,  $x_1 = 0.63$ ,  $x_2 = 0$ ,  $x_3 = 0.37$ , the regression equation get the maximum extreme value 0.94. It can be drawn that 813: S-2916 = 63:37, the best print quality can be obtained (Table 3).

**Table 2** Formulation test results

813	S-2919	S-2916	Surface tension	Color density	Glossiness	Rheological property	Adhesion
1	0	0	36.13	1.59	64.0	1	1
0	1	0	30.28	1.47	58.9	3	1
0	0	1	27.05	1.52	62.0	2	2
1/2	1/2	0	32.97	1.54	63.3	1	2
0	1/2	1/2	29.69	1.58	63.4	3	1
1/2	0	1/2	29.39	1.57	64.5	1	1
1/3	1/3	1/3	28.78	1.61	62.4	2	2

**Table 3** Best print quality

Particle size	Glossiness	Color density	Surface tension	Adhesion
2.718 $\mu\text{m}$	64.7	1.65	32.53 mN/m	0

Under the experimental conditions, according to the optimum distribution ink printability is superior to others.

## 6 Conclusions

Through the study of the properties of Magenta water-based flexo ink and formulation design optimization experiments, the conclusions are as follows:

1. Due to different types of grinding resin, ink has different dispersion; dispersion of ink with grinding resin 96 is better than other two samples. Because of different pigment/binder ratio, ink also has different dispersion; it is a trend that particle size of ink becomes smaller firstly and then become larger with the changing of pigment/blinder ratio; particle size of ink with dispersant 750 is significantly smaller than that with dispersant 760. That obtains dispersion of ink when grinding resin 96, pigment/blinder ratio is 1.25:1, and select dispersant 750.
2. Surface tension of ink with film-forming resin S-2916 is smallest, color density of ink with film-forming resin 624 is largest, adhesion and dispersion of ink with film-forming resin 813 and film-forming resin S-2919 is the best. Combined with the overall printing performance, film-forming resin 813, film-forming resin S-2919 and film-forming resin S-2916 is selected to complete complex distribution experiment, and when 813: S-2916 = 63:37, the ink with best print quality can be obtained.

## References

1. Fang Changqing (2013). Zhou Xing. New Progress in the aqueous ink binder resin. Xi'an University of Technology.
2. Huang Beiqing, Wei Xianfu (2007). Effect of pigment to binder ratio of water-based gravure inks dispersion. Packaging Engineering.
3. Zhang Fuzhong (2014). Gravure ink technology and the pure water production Application. Beijing Institute of Graphic Communication.
4. Sun Baowei (2014). Development of low scratch resistance, high wear resistance of water-based flexo ink color. Qufu Normal University.



# Preparation of Acrylate Latex via RAFT Soap-Free Emulsion Polymerization

Weiwei Liu, Zhi Qiao, Jinqiang Tu, Xiaoyu Li and Haiqiao Wang

**Abstract** Without effects of residual surfactants, soap-free emulsion polymerization products could have better physical and chemical properties, mechanical properties and water resistance compared with those prepared via conventional emulsion polymerization. In this work, soap-free reversible addition-fragmentation chain transfer (RAFT) emulsion polymerization of methyl methacrylate and n-butyl acrylate was successfully accomplished in the presence of poly (acrylic acid-*b*-styrene)-*b*-trithiocarbonate as surfactant and RAFT agent. Effect of NaOH aqueous solution neutralizing agent on polymerization process and the properties of latex and film were studied. The results showed that the addition of NaOH aqueous solution affected the polymerization process and the particle size of polyacrylate latex. Moreover, the water contact angle and the water absorption ratio of the latex film could reach 90° and 3.9%, respectively, by controlling the dosage of NaOH.

**Keywords** RAFT polymerization · Soap-Free emulsion · Acrylate latex · Properties

## 1 Introduction

In conventional emulsion polymerization, small molecular surfactants didn't participate in the polymerization reaction. So after the polymerization, surfactants were attached to the latex particle surface in the form of physical adsorption. Therefore, the easy desorption influenced by the external environment could cause the

---

W. Liu · Z. Qiao · J. Tu  
Beijing University of Chemical Technology, Beijing, China

X. Li (✉) · H. Wang (✉)  
Key Laboratory of Carbon Fiber and Functional Polymers, Ministry of Education,  
Beijing University of Chemical Technology, Beijing, China  
e-mail: lixy@mail.buct.edu.cn

H. Wang  
e-mail: wanghaiqiao@mail.buct.edu.cn

condensation of latex particles, and make the stability of the latex poor. Furthermore, surfactants tended to migrate to the surface in the process of film forming, and affected adhesion, water resistance, wet rub resistance, and compactness, etc. [1]. In order to overcome the above shortcomings, many scholars had been committed to the development of soap-free emulsion polymerization technology.

As a research hotspot of controlled “living” radical polymerization (CRP), RAFT polymerization [2] not only had the advantages of wide applicable monomer range and mild polymerization conditions, but also could be performed by a variety of polymerization methods. RAFT soap-free emulsion polymerization can also eliminate the bad effects of small molecular surfactants. Latex with single distribution of colloidal particles, controlled molecular weight and well-defined structures can be prepared via RAFT soap-free emulsion polymerization [3–6].

In this work, poly (acrylic acid-*b*-styrene) macro-RAFT agent (AA<sub>50</sub>-St<sub>10</sub>-macro-RAFT agent) was prepared in the first step. Then polymerization of MMA and BA was carried out by using this macro-RAFT agent as chain transfer agent and surfactant, and stable latex having potential applications in waterborne ink was obtained.

## 2 Experimental

### 2.1 Materials

Methacrylate (MMA), *n*-butylacrylate (nBA) and styrene (St) were distilled under reduced pressure. Acrylic acid (AA, 99%), potassium persulfate (KPS, >99%), 4, 4'-azobis(4-cyano-valeric acid) (V501, >99%), sodium hydroxide (NaOH, >96%) and 1, 4-dioxane (>99%) were provided by Tianjin Fuchen Chemical Reagents Factory and used without further purification. Deionized water, which was used in all reaction, was prepared in the laboratory. The small RAFT agent, S-dodecyl-S'-(*a*, *a*'-dimethyl-*a*'-acetic acid) trithiocarbonate (DDMAT), was synthesized and purified as described in Ref. [5].

### 2.2 Synthesis

#### 2.2.1 Synthesis of AA<sub>50</sub>-St<sub>10</sub>-Macro-RAFT Agent

The AA<sub>50</sub>-St<sub>10</sub>-macro-RAFT agent was synthesized in dioxane. First, a solution containing 2.336 g ( $6.4 \times 10^{-3}$  mol) of DDMAT, 0.1792 g ( $6.4 \times 10^{-4}$  mol) of V501, 23.04 g (0.32 mol) of AA, and 75.16 g of dioxane in a flask was deoxygenated by nitrogen, and proceeded with stirring at 80 °C for 1.5 h, then 6.656 g (0.064 mol) of deoxygenated St was added to the system and reacted for further

2 h. The product (macro-RAFT agent) was collected by precipitation of the mixture in cyclohexane and dried under vacuum at 50 °C.

### 2.2.2 Soap-Free Emulsion Polymerization of Methyl Methacrylate and N-Butyl Acrylate Mediated by AA<sub>50</sub>-St<sub>10</sub>-Macro-RAFT Agent

The AA<sub>50</sub>-St<sub>10</sub>-macro-RAFT agent, monomers (MMA and BA) and deionized water were added into a four neck flask. The mixture was stirred and deoxygenated by nitrogen for 30 min. Then the system was heated to 70 °C and initialized by potassium persulfate (KPS, 1:5 [RAFT]). The reaction was taken for 2 h.

## 2.3 Characteristic

Latex size was determined by dynamic light scattering by using a zetasizer Nano-ZS (Malvern Instruments) at 25 °C. The reported results were average of 3 runs. FT-IR spectra recorded on a VECTOR 22 FT-IR spectrometer. Water contact angle (CA) was measured with the Dataphysics OCA 20 (German). Tg values were determined on second heating runs (typically 10 K/min) using a DSC-1 (Mettler-Toledo, Switzerland) differential scanning calorimeter under a dry nitrogen protection (40 mL/min).

Number-average molecular weight (Mn), weight-average molecular weight (Mw), and PDI (Mw/Mn) were measured by gel permeation chromatography (GPC515-2410, Waters Corporation, Milford, MA). Specimens were dried in a vacuum oven until constant weight, and then dissolved in THF solution. Hydrochloric acid was added to mask COOH group interactions with GPC columns according to Ref. [7]. Molecular weight and PDI were measured based on polystyrene standards.

## 3 Results and Discussion

### 3.1 Synthesis of AA<sub>50</sub>-St<sub>10</sub>-Macro-RAFT Agent

In the macro-RAFT agent polymerization step, AA<sub>50</sub>-St<sub>10</sub>-macro-RAFT agent was prepared by using V501 as initiator and DDMAT as chain transfer agent in dioxane. To make the macro-RAFT agent well dissolved in aqueous, an amphiphilic macro-RAFT agent with high AA/St ratio, as shown in Fig. 1, was designed. The results of GPC showed that Mn, exp was in good agreement with Mn, th and the

PDI was relatively narrow. Obviously, polymerization was successfully carried out under RAFT free-radical polymerization mechanism.

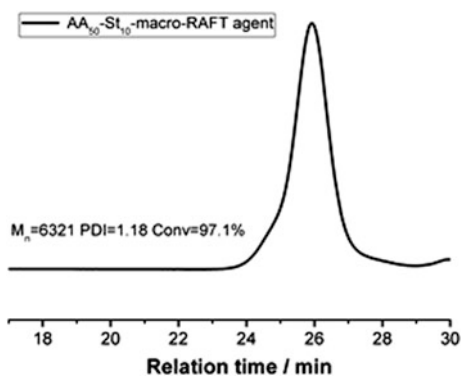
### 3.2 Soap-Free Emulsion Polymerization of NBA and MMA Mediated by the Macro-RAFT Agent

The synthetical condition was similar as the work reported by Wang X. G. et al. [6]. The final polymer with theoretical Mn (80,000 g/mol) was designed to study the soap-free RAFT polymerization process, and the results were shown in Table 1. Only one single peak could be observed on GPC chromatograms, suggesting the increase of MW and no inactivation of macro-RAFT agent during the polymerization process. The final MW distribution of E1 copolymer was acceptable (PDI 1.34) with Mn up to  $1.1 \times 10^5$  g/mol, and the coagulum content was up to 3.91%.

FT-IR spectrum of the products in different synthesis stages were shown in Fig. 2. The peaks on curve (a) were consistent with those in Ref. [5], proving the small RAFT agent was successfully synthesized. The peak at  $1710 \text{ cm}^{-1}$  ( $\nu\text{C}=\text{O}$ ) and  $3200\text{--}2500 \text{ cm}^{-1}$  ( $\nu\text{O-H}$ ) on curve (b) proved the polymerization of AA, and at  $699 \text{ cm}^{-1}$  ( $\gamma = \text{C-H}$ ) on curve (c) showed that styrene had polymerized. Only the infrared characteristic peaks of polyacrylate appeared on curve (d) because the AA<sub>50</sub>-St<sub>10</sub>-macro-RAFT agent had a rather small proportion in the final polymer.

In this work, the macro-RAFT agent could dissolve in aqueous phase without neutralization because of the high AA/St ratio. The coagulum in E1 was caused by the coalescence because of the high MMA and BA to macro-RAFT agent ratio. Post-addition of NaOH aqueous solution was employed to solve this problem. After the polymerization proceeded for 30 min and reached 20% conversion, that is to say, at the end of nucleation stage, the addition of NaOH aqueous solution to the system could increase the surface charge of particles [6]. Except the amount of NaOH, the polymerization conditions were same from E1 to E4, and NaOH was post-added after the polymerization started for 30 min. As shown in Table 1,

**Fig. 1** GPC curve of the AA<sub>50</sub>-St<sub>10</sub>-Macro-RAFT agent

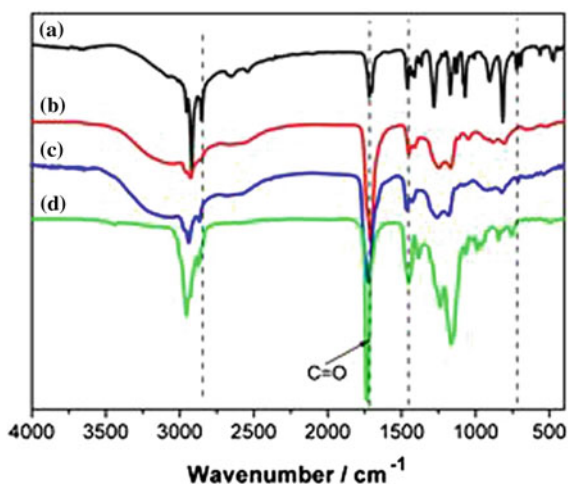


**Table 1** Soap-free emulsion polymerization mediated by AA<sub>50</sub>-St<sub>10</sub>-macro-RAFT agent without NaOH and with post-addition and pre-addition of NaOH solution

E <sup>a</sup>	NaOH: AA	<sup>b</sup> pH values	Conv (%)	Mn, exp (g/mol)	PDI (Mw/Mn)	Particle diameter (nm)	Particle diameter PDI	Coagulum (%)
1	0:50	2.5	90.4	114,861	1.34	107.6	0.042	3.91
2	10:50	3.3	80.8	100,040	1.92	101.1	0.020	0
3	25:50	3.8	98.4	119,369	1.76	124.9	0.057	0
4	50:50	7.0	90.5	81,905	1.36	113.4	1.002	0
5	25:50	4.4	98.0	12,2335	4.29	63.64	0.118	0

<sup>a</sup>The theoretical Mn of E1 was about 80000 g/mol. <sup>b</sup>pH values were measured with pH test paper after polymerization

**Fig. 2** FT-IR spectrum of **a** DDMAT, **b** AA<sub>50</sub>-Macro-RAFT agent, **c** AA<sub>50</sub>-St<sub>10</sub>-Macro-RAFT agent and **d** the product of E1



conversion, molecular weight and PDI changed very little, though pH values and latex particle size increased, along with the amount of NaOH increased. More hydrophilic head of the macro-RAFT molecule was ionized as the NaOH increased, so the latex particle was larger in size due to the better solubility of PAA. Good colloidal stability was achieved in E2-4 with controlled molecular weight and low PDI.

As shown in Table 1, with pre-addition of NaOH (E5), the molecular weight became higher than the designed Mn, th, PDI (4.29) was much higher than that without neutralization, and latex particle size (63.64 nm) was much smaller than those of the other four latexes. The reason for this phenomenon is that the surface area covered by the macro-RAFT agents increased greatly due to the strong static electronic repulsion with neutralization, so a low number of such amphiphilic surfactant molecules is required to form a micelle, and therefore a high number of micelles is generated, and the micelles could not be totally consumed in the polymerization, as in the case of micro-emulsion polymerization. This led to a very

broad molecular weight distribution and molecular weight higher than the theoretically predicted, as reported in the literature 5.

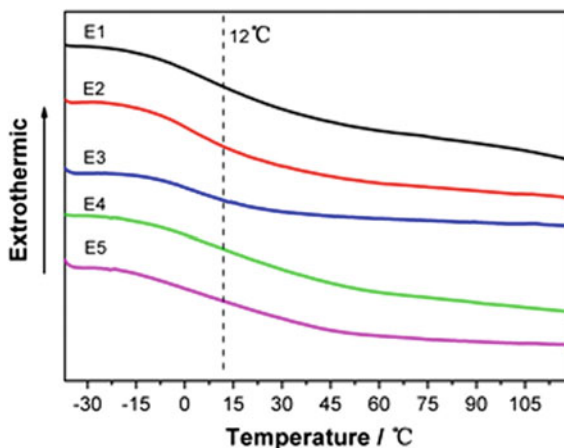
### 3.3 Properties of Latex and Film

Without considering contribution of T<sub>g</sub> of macro-RAFT agent, theoretical T<sub>g</sub> of the copolymer of MMA and BA was designed as 10 °C. The DSC curves of the final products are shown in Fig. 3. Almost all the polymers' T<sub>g</sub> was around 12 °C, so the emulsions could form films directly at room temperature.

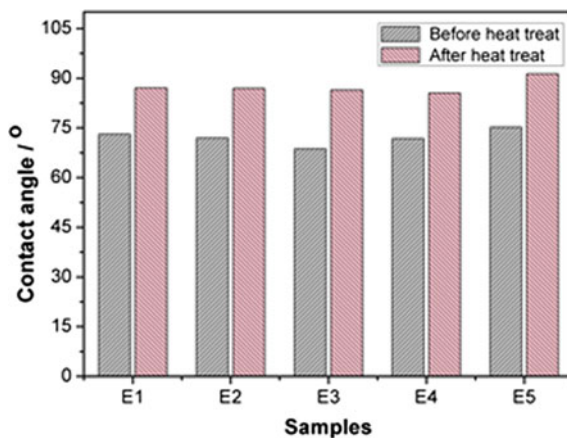
In our group's previous work, we have studied the mechanism of heat treatment on the water contact angle of films [8]. Because of the hydrophilic carboxylate group in PAA, the water contact angle of film surface was less than 75 °. After a treatment at 120 °C for 12 h, nearly all the CA value of the film increased to 90°. With the increase of NaOH addition, CA value decreased for sodium carboxylate is more hydrophilic than carboxylate group, as shown in Fig. 4. Comparing E1 with E5 in Fig. 4, we found that even the amount of NaOH addition was the same, CA value of film with NaOH pre-addition was higher than that of film with NaOH post-addition.

Water resistance is an important performance index of the films, and it can be characterized by water absorption ratio. Water absorption ratio can be obtained by the following method. First, the latex in a container with an area of 6 × 8 cm<sup>2</sup> was dried under 50 °C for 24 h to obtain films. A part of the film (weight m<sub>1</sub>) was putted into deionized water for 24 h, and then took out from water. The water on the film surface was absorbed, and then the film was weighted as m<sub>2</sub>. Water absorption ratio can be calculated from the two weighted results. Figure 5 showed that addition of NaOH increased the water absorption ratio and made the water resistance poor. The water absorption ratio of E3 was 3.9%.

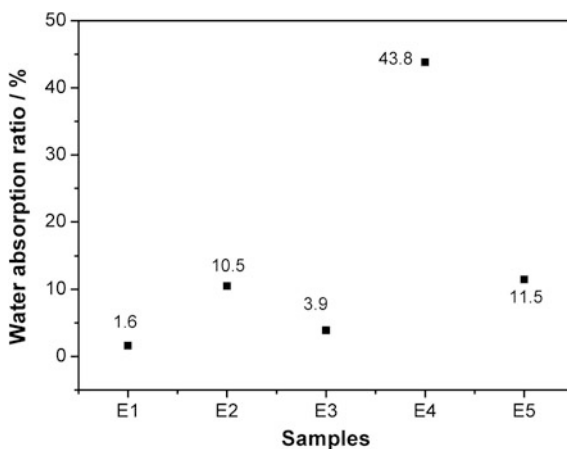
Fig. 3 DSC curves of different products



**Fig. 4** Water contact angle of different films



**Fig. 5** Water absorption ratio of different films



## 4 Conclusions

In this work, colloidal stable acrylate emulsion was obtained via RAFT soap-free emulsion polymerization of MMA and BA by using poly (acrylic acid-*b*-styrene) macro-RAFT agent as chain transfer agent and surfactant, and KPS as initiator. The effects of NaOH neutralization on the polymerization, and the properties of latex and film were investigated. The addition of NaOH aqueous solution could decrease the coagulum and improve stability of the latex. The latex could form films at room temperature. Furthermore, the CA value was high and the water absorption ratio was low. Application of the obtained latex in waterborne ink would be studied in the further research.

## References

1. Hu, J, Ma, J. Z, Deng, W. J. (2008). Properties of acrylic resin/nano-SiO<sub>2</sub> leather finishing agent prepared via emulsifier-free emulsion polymerization. *Materials Letters*, 62(17), 2931–2934.
2. Chiefari, J, Chong, Y. K, Ercole, F, et al. (1998). Living Free-Radical Polymerization by Reversible Addition-Fragmentation Chain Transfer: The RAFT Process. *Macromolecules*, 31(16), 5559–5562.
3. Guo, L. H, Jiang, Y. J, Qiu, T, et al. (2014). One-pot synthesis of poly (methacrylic acid)-b-poly (2, 2, 2-trifluoroethyl methacrylate) diblock copolymers via RAFT Polymerization. *Polymer*, 55(18), 4601–4610.
4. Guo, L. H, Jiang, Y. J, Chen, S. Y, et al. (2014). Self-Assembly of Poly (methacrylic acid)-b-poly (butyl acrylate) Amphiphilic Block Copolymers in Methanol via RAFT Polymerization and during Film Formation for Wrinkly Surface Pattern. *Macromolecules*, 47(1), 165–174.
5. Ferguson, C. J, Hughes, R. J, Nguyen, D, et al. (2005). Ab Initio Emulsion Polymerization by RAFT-Controlled Self-Assembly. *Macromolecules*, 38(6), 2191–2204.
6. Wang, X. G, Luo, Y. W, Li, B. G, et al. (2009). Ab Initio Batch Emulsion RAFT Polymerization of Styrene Mediated by Poly(acrylic acid-b-styrene) Trithiocarbonate. *Macromolecules*, 42(17), 6414–6421.
7. Isabelle, C, Muriel, L, Franck, D'Agosto, et al. (2012). RAFT Polymerization of Methacrylic Acid in Water. *Macromolecules*, 45(3), 1241–1247.
8. Qiao, Z, Qiu, T, Liu, W. W. (2016). Novel tri-block copolymers of poly (acrylic acid)-b-poly (2, 2, 3, 3, 4, 4-hexafluorobutyl acrylate)-b-poly(acrylic acid) prepared via two-step RAFT emulsion polymerization. *Polym. Chem.*, 24(7), 3993–3997.



# Effect of Defoamer on the Performance of Plastic Water-Based Flexographic Ink

Xiaoli Liu, Yun Ouyang, Xiaofang Wang, Zhiyong Sun, Xue Gao and Yanchao Yu

**Abstract** The formula of water-based ink is designed to study the performance of defoamers of water-based flexographic ink on plastic. Four kinds of defoamers which are mineral oil, silicone-free polymeric, polysiloxane and polyether modified polysiloxane. Effect of defoamer on the ink is discussed, such as defoaming of different kinds of defoamers, defoaming speed, defoaming persistence. Defoamer test methods are used stirring-in air by dissolver and gradient experiments. The results show that F6 which is polysiloxane and F8 which is polyether modified polysiloxane have good performance. Inks have best performance on the BOPP film when F6 and F8 are used 0.8 and 0.6wt% respectively.

**Keywords** Water-based flexographic ink on plastic · Defoamer · Defoaming speed · Defoaming persistence

## 1 Introduction

From October 2015 to June 2016, there are 11 provinces and cities who began to charge volatile organic solvents (VOCs) of some industries including ink in China. Facing the new challenge, printing enterprises accelerate the application and developments of environment-friendly printing technology and materials. Meanwhile flexographic water-based ink on plastic has become a big trend.

Water-based ink has higher surface tension, because water is dispersion medium and there are no VOCs in use. In order to make it have good spreading on non-polar plastic film, it is necessary to add wetting agent and leveling agent which are easily foaming to reduce the surface tension of the ink [1]. This makes ink produce

---

X. Liu (✉) · Y. Ouyang · X. Wang · Z. Sun · X. Gao  
Beijing Key Laboratory of Packaging and Printing New Technology,  
China Academy of Printing Technology, Beijing, China  
e-mail: liuxiaoli@keyin.cn

Y. Yu  
Food Science and Engineering College, Beijing University of Agriculture, Beijing, China

bubbles in the process of production and printing easily. Too many bubbles could affect ink dispersed and reduce the quality of print. Suitable defoamers can solve these problems, but improper use will also result in shrinkage, spot and other surface defects on the film. In this chapter, acrylic polymers are the binder of water-based flexographic ink on plastic; defoamers used in this formula are determined through series of experiments, and their optimum amounts are determined by tests.

## 2 Experiments

### 2.1 Raw Materials

Pigment	cyan color paste C3.
Resin	acrylic dispersion resins R1 and R2, acrylic film-forming resins R3 and R4.
Additives	leveling agent L5, wetting agent W7, wax emulsions WE1, defoamers DF-19, DF7015, TEGO845, BYK011, BYK024, BYK 093, TEGO810 and AFE-0013.
Printing substrate	BOPP film.

### 2.2 Experimental Method

1. Preliminary selection of defoamers. According to recommendations of defoamer companies and experience, suitable defoamers are selected. And the same amount of them is added in the ink. Defoamer test method is used stirring-in air by dissolver. Preliminary selection by factors such as compatibility, defoaming speed, influence to the ink.
2. Determine amount of the selected defoamers. Through the first step of tests, one or more defoamers are selected that are suitable for this formula. Through detailed experiment, the optimum amount of them is determined.

### 2.3 Test Methods

#### 2.3.1 Defoamer Test Method

Defoamer test method is used stirring-in air by dissolver. Firstly weight 10 g ink that is not added defoamer in the measuring cylinder, record its height " $H_0$ ". And then stir the ink added defoamer at the speed of 3000 revolutions per minute

(RPM) 3 min. Weight 10 g ink and record its height  $H_1$ ,  $H_2$ ,  $H_3$ ,  $H_4$ ,  $H_5$ ,  $H_6$ ,  $H_7$  at the time of 0, 5, 10, 15, 20, 25, 30 min respectively.

### 2.3.2 Defoamer Compatibility Test Method

Compatibility test is usually measured after 24 h, that could make defoaming, persistence and defects reach balance. Test method is that drops ink on the scraper fineness meter, and then observe film surface. If there are no defects, the defoamer is compatible; if not, the defoamer is incompatible.

### 2.3.3 Performance Tests

1. Adhesive test: use 3-M tape to stick the film, and then observe to evaluate the adherence of the remaining ink.
2. Gloss test: gloss is tested with glossmeter TC-108DPA.
3. Print-surf roughness (PPS) test: PPS is tested with M590-PPS.

## 3 Results and Discussion

### 3.1 Preliminary Screening of the Defoamers

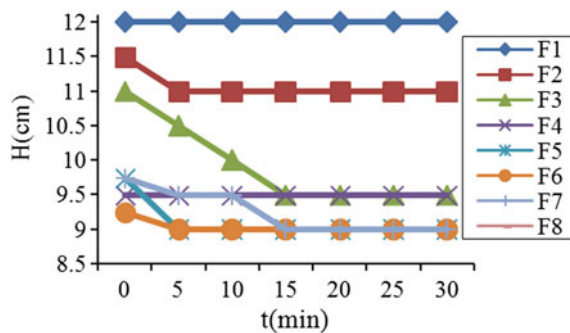
Four kinds of defoamers which are used in the water-based ink are mineral oil, silicone-free polymeric, polysiloxane and polyether modified polysiloxane respectively [2, 3]. Besides stronger defoaming speed, compatibility with the ink is more important. If the defoamer has poor compatibility, defects will happen; if not, defoaming may be diminished. So we should find the best balance between them [4].

Eight defoamers are selected that are suitable for water-based ink of polyacrylic acid system. Defoamers are replaced with the letter "F". 0.5% of defoamer is added in the ink that is no defoamer. Defoaming speed is detected according to the test method. Figure 1 is the change of the foam height with time. Type of defoamers, compatibility, recoatability and adhesion are shown in Table 1. Figure 2 shows the recoatability of F1 and F6, film proofed by ink adding F6 is exquisite, while film proofed by ink adding F1 has serious shrinkage cavity.

Integrated Fig. 1 and Table 1 data, we can draw the following conclusions.

1. Mineral oil defoamer: it can be seen from data of F1 and F2, this kind of defoamers has poor compatibility with system and slower defoaming speed, produces large amounts of bubbles while dispersed, and reduces the adhesion of film. Therefore, we can speculate that mineral oil defoamers are not applicable to this formula.

**Fig. 1** Foam height with time while amount of defoamers is 0.5%

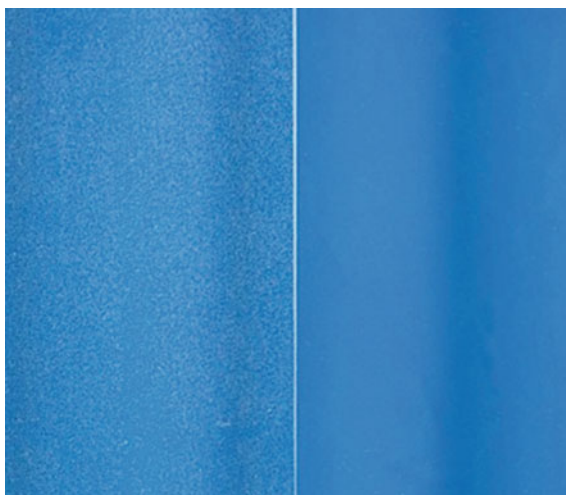


**Table 1** Effect of different kinds of defoamers on the performance of ink

Type	Code	Defoamer	Compatibility	Recoatibility	Adhesive
Mineral oil	F1	DF-19	Worst	Worst	2
	F2	DF7015	Worst	Worst	3
Silicone-free polymeric	F3	TEGO845	Good	Good	4
	F4	BYK011	Good	Good	4.5
Polysiloxane	F5	BYK024	Good	Good	4.5
	F6	BYK093	Good	Good	0
Polyether modified polysiloxane	F7	TEGO810	Worse	Worse	0.5
	F8	AFE-0013	Good	Good	0

Notes while adhesive is 0, it indicates the best; while 5, it indicates the worst

**Fig. 2** Recoatability of F1 (left) and F6 (right)



2. Silicone-free polymeric defoamer: inks adding this kind of defoamers have good compatibility with the ink. So it can be dispersed very well in a short time. It

may be that this kind of defoamers and resins are both polymers; but they have poor adhesion, poor stability and slower defoaming speed. So this kind of defoamers is also not applicable to this formula.

3. Polysiloxane defoamer: ink adding F6 has fast defoaming speed, good compatibility, good recoatability, stability and adhesion; but ink adding F5 has poor stability and adhesion.

4. Polyether modified polysiloxane defoamer: this kind of defoamers has fast defoaming speed. F7 has poor compatibility, leading to poor recoatability and worse adhesive of film; ink adding F8 has good performance.

Integrated above data, silicone-free polymeric defoamers have good compatibility with the ink; most of mineral oil defoamers and silicones defoamers are difficult to disperse. It may be that these defoamers contain hydrophobic particles [5]; mineral oil ones have the worst defoaming in four kinds of defoamers; F6 and F8 are better and selected.

### ***3.2 Effect of Different Amount of Defoamer on the Performance of Water-Based Ink***

Adding right amount of defoamer can make water-based ink have best defoaming and antifoaming [6]. Defoamer added not enough will reduce defoaming effect; too much of them could make printing quality decline. Gradient experiments of F6 and F8 are carried out. This paper mainly studies effect of different amount of defoamers that are 0.2, 0.4, 0.6, 0.8, 1 and 1.2wt% on the performance of water-based ink, and concludes the best amount.

#### **3.2.1 Effect of Different Amount of Defoamer on the Defoaming Speed**

As shown in Fig. 3, while F6 and F8 increase to 0.8 and 0.6% respectively, defoaming speed increases, and the speed has no obvious improvement while adding their amount.

#### **3.2.2 Effect of Different Shear Mode of F6 on Defoaming Persistence**

Effect of two kinds of defoamer's shear mode on defoaming and its persistence is compared. Method 1 is stirring-in air by dissolver, adding 0.8% of F6 in the ink at a speed of 1500 RPM, and stirring 1 h after adding. Method 2 is stirring-in air by dissolver, adding 0.8% of F6 in the ink at the speed of 1500 RPM, and stirring 20 min, and then using concussion instrument to shear 15 min with high-speed. Store two ink samples 24 h, and then shear them 3 min at the speed of 3000 RPM. Weight 10 g of the ink in measuring cylinder, record the foam height and

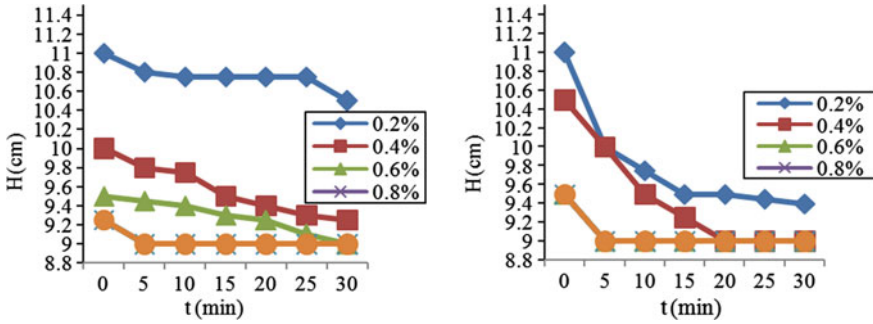


Fig. 3 Foam height of different mass proportion of F6 (left) and F8 (right) over time

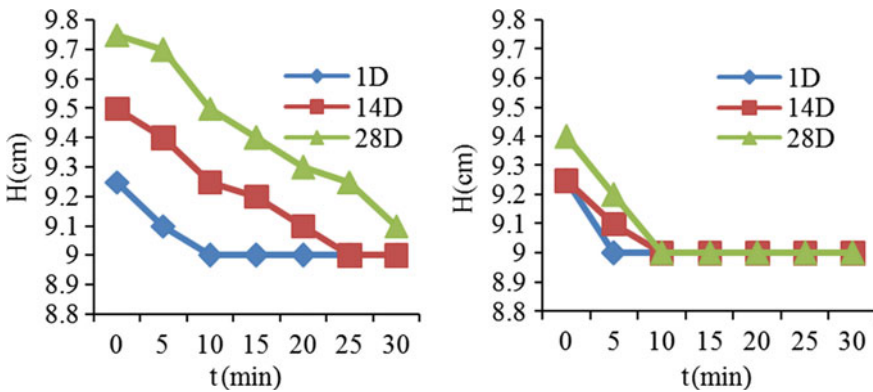


Fig. 4 Defoaming speed using shearing of method 1 (left) and method 2 (right)

defoaming time. In order to improve efficiency, the ink samples are put in the 50 °C oven for 2 and 4 days (equivalent to room temperature storage for 14 days and 28 days). Detect and compare defoaming with the ink sample of 24 h, the better defoaming, and the better persistence.

From Fig. 4, the instant defoaming of two methods is basically identical. But storing a period of time, defoaming of the ink made by method 1 gradually declines, while ink made by method 2 has good defoaming. It may be that after high speed shearing, particle size of defoamer becomes smaller, which improve the dispersion and stability of the defoamer in the ink, and not easy to reunite [7]. However, defoaming efficiency also falls slightly after a period of time, probably because defoamer interacts with surfactant of the ink.

**Table 2** Effect of different mass proportion of defoamers on the ink layer performance

Defoamer	Performance/Proportion (%)	0.2	0.4	0.6	0.8	1.0	1.2
F6	Gloss	70.6	71.4	71.2	72.4	70.9	70.5
	PPS	0.46	0.47	0.47	0.48	0.46	0.47
	Adhesion	0	0	0	0	0.5	1
F8	Gloss	71.4	70.6	72.2	69.4	67.7	68.4
	PPS	0.47	0.48	0.47	0.46	0.47	0.47
	Adhesion	0	0	0	0.5	1	1.5

### 3.2.3 Effect of Different Amount of Defoamer on Ink Layer Performance

According to the data of Table 2, F6 and F8 have little impact on gloss and PPS; when amount of F6 and F8 increase to 1 and 0.8%, the stability and adhesion of the ink decrease. Especially when F8 increases to 1.2%, the adhesion becomes worse.

## 4 Conclusions

1. According to defoaming speed, compatibility with the ink and effect on the performance of the ink, F6 and F8 are selected to do gradient experiments.
2. While amount of F6 and F8 is 0.8 and 0.6wt% of the formula respectively, inks have the best defoaming speed, persistence and best performance.
3. For water-based flexographic ink on plastic, the choice of defoamer is complex. It is also very necessary to adding suitable defoamer. It is only made the preliminary screening results in the lab. The finally formula only can be determined through the practical printing application and test.

**Acknowledgements** This study is funded by press and publication reform development project library (0020131646) and culture industry development foundation of China.

## References

1. Xiaokun Qi, Hua Fan (2000). Effect of defoamer agent on the performance of water-based ink. Journal of Beijing institute of graphic communication, DOI/8(4), 18–24.
2. Liming Wang (2009). The classification and application of defoamer. Surfactant soap and detergent, DIO/3, 70–73.
3. Xiaowei Huang (2012). The application of high-performance defoamer in the water-based ink. Guangdong chemical, DIO/39(6), 75–76.
4. Manna Li (2015). The mechanism and screening methods of defoamers in waterborne coatings. China coatings, DOI/30(8), 61–64.

5. Timothy N. Hunter, Robert J. Pugh, George V. Franks (2008). The role of particles in stabilising foams and emulsions. *Advances in colloid and interface science*, DIO/137, 57–81.
6. Yuecheng Wang (2011). The application and research of defoamer in the water-based ink. *Printing Field*, DOI/300(3), 70–72.
7. Zhiyong Huang, Yanqin Lu (2006). The application of wetting and defoamer in the water-based wood coatings. *China coatings*, DOI/10(13531), 40–41.



# Research on the Performance Optimization of Silver Water-Based Gravure Ink

Tengfei Zhou, Beiqing Huang, Xihao Li and Xianfu Wei

**Abstract** At present, with the increasing requirements of environmental protection and the printing quality, the development of water-based gravure ink has become a trend. And silver ink has been favored by people deeply because of its excellent and exquisite packaging effect. So the development of silver water-based gravure ink has become an inevitable. Factors affecting the performance of ink such as types of silver pigments, pigment/binder ratio, type and dosage of dispersant, the type of film-forming resin were discussed. And the ink properties such as dispersion, gloss, surface tension etc. were studied and tested. Finally, we obtained formulation of the silver water-based gravure ink with good quality. The experimental results showed that the PHY20 aluminum pigment is the most suitable pigment with the minimum particle size that meeting the requirement of the gravure printing ink, and its best pigment/binder ratio is 2:3. The ink added dispersant JL115A with 2% owns the best dispersion property. When using the compound film-forming resins that 813: S2919 is 16: 9, the comprehensive performance of the ink is the best.

**Keywords** Aluminum pigment · Gloss · Water-based gravure ink

## 1 Introduction

At present, although gravure ink has occupied a large share of the market in the printing and packaging industry, the gravure printing ink is mainly alcohol soluble ink that is not friendly to environment. Compared with solvent-based inks, water-based ink has the advantages of no VOC emission, non-combustible and so

---

T. Zhou (✉) · B. Huang · X. Li · X. Wei  
Beijing Institute of Graphic Communication, Beijing, China  
e-mail: 937328516@qq.com

B. Huang  
e-mail: huangpeiqing@bigc.edu.cn

X. Wei  
e-mail: weixianfu@bigc.edu.cn

on. It is a promising and environmental friendly printing ink. Aluminum pigment is one of the important metallic one, and it has been favored by consumers deeply because of its unique aesthetic effect and metal flash effect. Gravure printing ink has the features of thick ink layer, clear hierarchy, and it has more and more applications in food, beverages, tobacco, pharmaceutical and other industrial. Therefore, research and development of silver water-based gravure ink is a necessity under the double requirements of printing quality and environmental protection. Dispersion property is an important performance of ink, it not only affects the gloss, but also it has an influence on viscosity and ink transferring [1]. Different film-forming resins have different membrane effects. They have a certain effect on the gloss and smoothness of the ink, so this study mainly from the aspects of these to improve formulation and optimize performance.

## 2 Experiments

### 2.1 *Experimental Materials*

Aluminum powder pigment YYH15, aluminum powder pigment 1800#, aluminum powder pigment PHY20 (JINJIANG YAKUN PIGMENT CO.); aluminum paste pigment YY-10, aluminum paste pigment ZF8108 (Zhangqiu Metal Pigment Co.); water-based acrylic resin AZR (TianJin ATOZ Fine Chemicals Co.); dispersant 750, dispersant 760, defoamer 810 (Germany Degussa company); film-forming resin 813 (Shanghai RuiFig. Chemical Co.); film-forming resin s2919 (German BASF Inc); film-forming resin s2916 (German BASF Inc); copperplate paper; deionized water.

### 2.2 *Experimental Instruments*

Microtrac S3500 Laser particle size analyzer (America); D2004 W electric mixer (Shanghai Division Music Instrument Co.); Electronic balance UX2200H (Shimadzu); Multi-angle gloss meter (Shanghai International Trade Co.); Intaglio proofing press (Guangzhou, Keyu New material Technology Co.); KRUSS surface tension instrument k100 (Germany KRUSS company); 81-2 type constant temperature magnetic stirrer (Shanghai Shengke Instrument Equipment Co.); 400 ml beaker; glass rod; rotor.

## **2.3 Method of Ink Preparation**

### **2.3.1 Preparation of Primary Ink**

All materials were added into the breaker according to the formulation. Stir with a glass rod to make the pre-dispersed evenly. And then use a high speed mixer to stir for 100 min at the speed of 300 r/min. Finally we get the silver water-based primary ink.

### **2.3.2 Preparation of Ink**

Mix the primary ink and film-forming resin with the proportion of 1:1, then the magnetic stirring for 60 min. Finally we get the silver ink into ink.

## **2.4 Proofing Method and Performance Test**

### **2.4.1 Proofing Method**

The  $7.5 \times 24$  cm coated paper is fixed on the roller of gravure proofing press. Take a small amount of aqueous silver ink to drop on the proofing machine near the scraper, and proof it at the speed of 40 m/min.

### **2.4.2 Dispersion Performance Test**

Microtrac S3500 with the company's Zetasizer particle size of the ink test, the smaller the particle, the more uniform particle size distribution curve that is narrower, indicating better dispersion to the ink particle size of 95% to be dispersible evaluation.

### **2.4.3 Glossiness Test**

Under the condition of room temperature and  $75^\circ$ , test spline's gloss by multi-angle glossmeter. Each color lump was measured 5 times. We get the average glossiness by removing the highest value and the minimum value.

### 2.4.4 Surface Tension Test

At room temperature 25 °C conditions, surface tension measurement is performed by using KRUSS Process Tensimeter K100.

### 2.4.5 Apparent Performance Test

Apparent performance test is mainly in visual way. The apparent property of the ink is directly related to leveling, leveling of the ink on a non-absorbent material is good, and the apparent performance is good. The apparent performance is divided into five levels as follows: (Table 1).

## 3 Results and Discussion

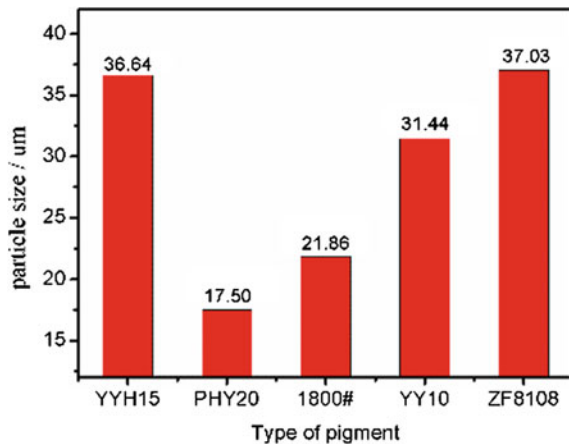
### 3.1 Influence of Silver Pigment’s Type on the Dispersion Properties

Different kinds of silver pigments have different particle sizes. For gravure printing, the pigment particle size plays a crucial role in the performance of ink. When the pigment particle diameter is close to or larger than the size of gravure mesh, it would have a bad influence on the ink transfer rate, and gloss properties. The ink

**Table 1** Apparent performance grading standards

Performance level	Chaotic	Irregular	General	Smooth	Flow completely
	1	2	3	4	5

**Fig. 1** Particle size of different pigments



samples were prepared with different kinds of silver pigments, and the particle size of the ink was tested and the results are showed by Fig. 1.

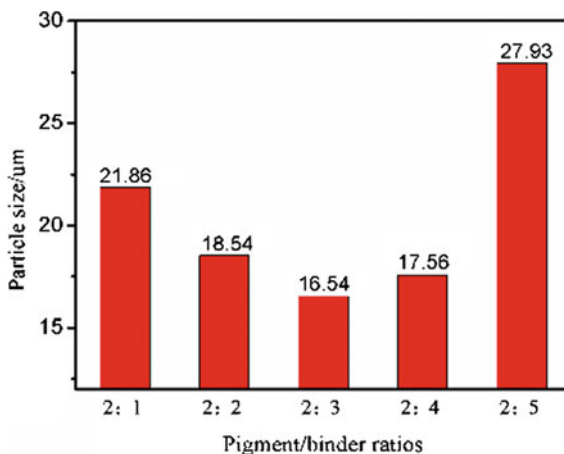
As shown in Fig. 1, different type of pigment has different particle size. Aluminum powder pigment PHY20 has the smallest particle size. In the actual production process of pigment, the production process is different, which makes the particle size of aluminum powder is different. The smaller the particle size is, the more easily the ink infiltrates a printing plate and the better the printing rate is. Comparing particle size of several kinds of pigment, the aluminum powder pigment PYH20 is the optimal choice for silver water-based gravure ink.

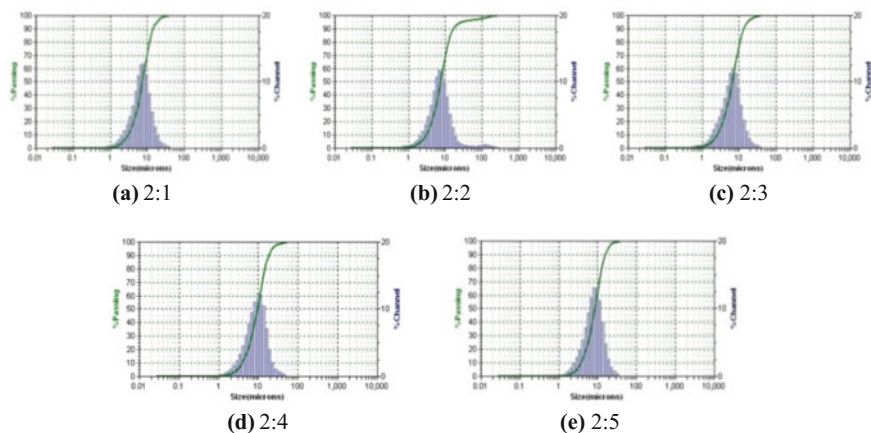
### 3.2 Influence of Pigment/Binder Ratio on the Dispersion Properties

The pigment/binder ratio is the ratio of pigment and resin in paint. It has a great influence on the dispersion of ink. Using the same amount of pigments, different sample inks were prepared with different pigment/binder ratio, and the particle size was tested. The test results were shown in Figs. 2 and 3. As can be seen from Fig. 2, with the increasing proportion of the grinding resin in the ink system, the overall particle size of the ink increases first and then decreases. Especially when the pigment/binder ratio is 2:3, the particle size of the aluminum powder pigment is the smallest.

Pigment/binder ratio has a great impact on the dispersion of ink. This is because the dispersion process is actually a flow process. Only to achieve the best flow point, ink can get effective shear effect and the dispersion can reach the best state. The shear action is different due to the different pigment/binder ratio. We should first determine the best pigment/binder ratio to make the ink get the best dispersing

Fig. 2 Particle size of different pigment/binder ratio





**Fig. 3** Particle size distribution of different pigment/binder ratio

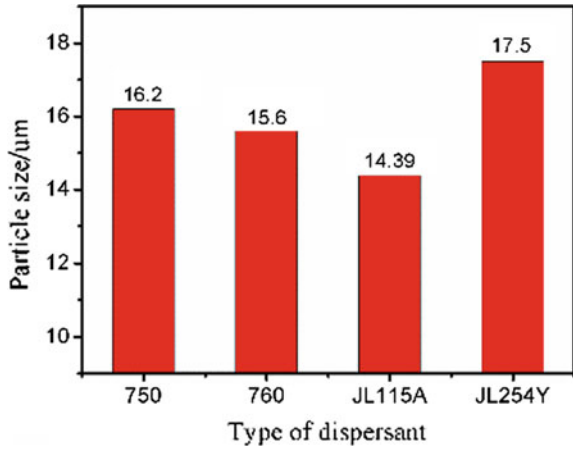
state, and then use the best ratio to prepare the ink sample [2–4]. Figure 3 that named by a, b, c, d, e, respectively, is the particle size distribution of different pigment/binder ratio. When the pigment/binder ratio is too large or too small, D95 (ink's particle size at 95%) is large and the size distribution is loose. Only when the pigment/binder ratio is 2:3, we can get the suitable ink with concentrate size distribution and suitable particle size.

### 3.3 Influence of the Dispersant' on the Dispersion Properties

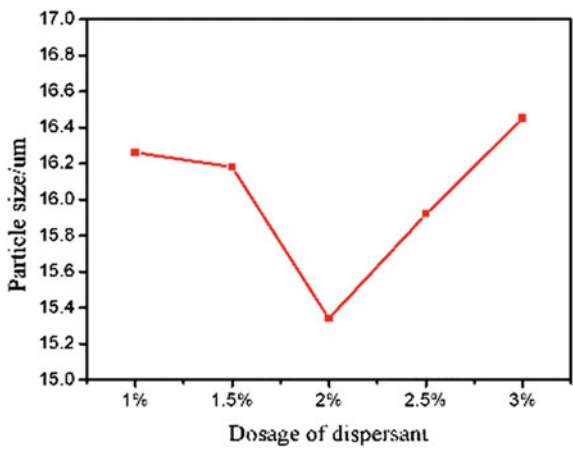
Dispersing agent has a certain effect on the dispersion of ink. In order to study the effect of dispersant on the dispersing properties of ink, the corresponding samples were prepared respectively by selecting four dispersing agents (750760, JL254Y, JL115A). The test results are shown in Fig. 4. Using dispersant JL115A, we prepared the sample ink with different dosage of dispersant JL115A, respectively. Test results as shown in Fig. 5.

As seen from Fig. 4, the ink added with dispersant JL115A has the best dispersing property, followed by the ink with dispersant 760, ink with dispersant 750, and ink with dispersant JL254Y. Different dispersing agents have different dispersing effects because they have different structure. Under this experimental condition, the dispersant JL115A is the most suitable for the system and the dispersing effect is best. As shown in Fig. 5, when the dosage of dispersant JL115A is 2%, the dispersing effect is the best. After the dispersing agent is added in the water, it is absorbed on the surface of the particles by the surface tension of the pigment particles and forms a protective film, which blocks the agglomeration of pigment

**Fig. 4** Effect of dispersant on dispersion



**Fig. 5** Effect of the dosage of JL115A on dispersion

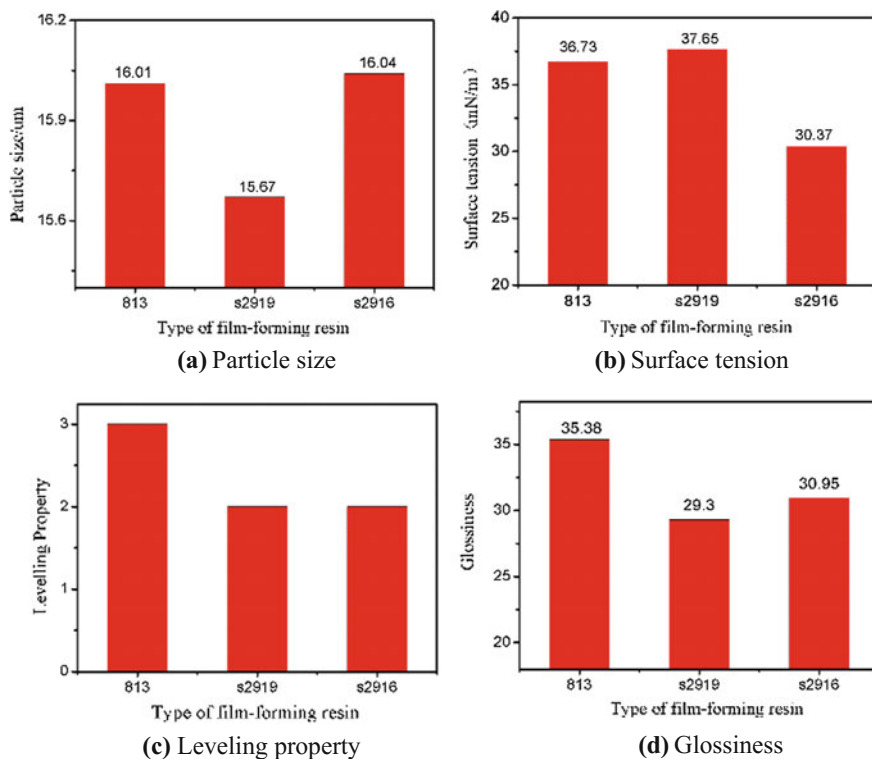


particles under the action of the steric effect and the electrostatic repulsion. When the adding amount of dispersant is too little, it can't form an effective protective film and make the dispersion become worse. When the amount is too much, the excess dispersant breaks the balance among the particles and makes the dispersion bad as well. Only adding proper amount of dispersant, the ink's dispersion performance can reach the best.

### 3.4 Influence of Film-Forming Resin's Type on Ink's Properties

When pigment content, grinding resin and the pigment/binder ratio are fixed, the film-forming resin is the key factor which affects the printing performance of the ink. Due to different film-forming resins have different molecular structures, and the printing performance of the ink is also different. Ensure the formulation of primary ink is fixed, using three kinds of film-forming resin respectively, printing ink sample was prepared according to the ratio that primary ink: film-forming resin is 1:1. The printing performance of 3 different kinds of film-forming resin was studied. The results are shown in Fig. 6.

Figure 6a shows the particle size of s2919 ink is the smallest during the three kinds of film-forming resins. Because the film-forming resin S2919 filled in the pigment particles fully and hindered the mutual contact between the particles, which prevent the generation of “aggregate”. So the particles can be dispersed better. Figure 6b shows that the surface tension of s2916 ink is minimal, because the s2916 film-forming resin has the minimum surface tension. Figure 6c shows



**Fig. 6** Effect of different film-forming resins on the properties of ink



that the levelling of the s2916 and s2919 is better. S2916 ink’s leveling is better, because the surface tension of s2916 is small and it is easy to spread. S2916 ink’s leveling is better because of small particle size and good dispersion. Seen from Fig. 6d, ink made of 813 has the best gloss. Three kinds of film-forming resins have different influence on the performance of ink because of their different molecular composition and molecular structure.

### 3.5 Formulation Experiment of Film-Forming Resin

According to printing performance results of ink with every film-forming resin, each film-forming resin has its own advantage. It is hard to choose the most suitable one. Therefore, formula experiment of composite resin is needed to filter out optimal formula of ink with good printing performance. Film-forming resin S-2916 is used to complete complex distribution experiment. Test results as shown in Table 2.

The weights are set as follows: gloss 0.4, leveling 0.2, particle size 0.2, surface tension 0.2. The solution can be obtained through the calculating with regression equation. When  $x_1 = 0.64$ ,  $x_2 = 0.36$ ,  $x_3 = 0$ , the equation obtained the maximum value of  $y = 0.6827$ . Therefore, when the ratio of resin 813 and s2919 is 16:9, the overall performance of the ink is the best. Specific performance is as shown in Table 3.

**Table 2** Formulation test results

Number	813	S2919	S2916	Surface tension	Gloss	Leveling	Particle size
1	1	0	0	36.73	35.38	3	16.01
2	0	1	0	37.65	29.3	2	15.67
3	0	0	1	30.37	30.95	2	16.04
4	1/2	1/2	0	31.58	34.17	4	15.13
5	1/2	0	1/2	33.85	33.48	3	16.21
6	0	1/2	1/2	32.33	29.92	2	16.10
7	1/3	1/3	1/3	29.25	30.53	2	16.01

**Table 3** Best print quality

Particle size	Glossiness	Leveling property	Surface tension
15.54 $\mu\text{m}$	35.32	1.65	30.10 mN/m

## 4 Conclusions

Through the study of silver water-based intaglio ink, we finally get the following conclusion:

1. For gravure printing, the pigment particle size plays a crucial role in the performance of ink. Under the experimental conditions, the aluminum powder pigment PYH20 is the optimal choice for silver water-based gravure ink.
2. The pigment/binder ratio has a great influence on dispersion. If we want to obtain the ink with good performance, we must prepare the ink at the best pigment/binder ratio. Under the condition of this experiment, the best pigment/binder ratio of the silver water-based intaglio ink is 2:3.
3. Dispersing agent has an important influence on the dispersion property of ink. The ink added dispersant JL115A with 2 percent owns the best dispersion property.
4. Different film-forming resin has different effects on the performance of the ink. During the three kinds of film-forming resin: glossiness of ink with resin 813 is best; surface tension of ink with film-forming resin S2916 is smallest; the ink with film-forming s2916 and the ink with film-forming s2919 have the best leveling; dispersion of ink with film-forming resin S-2919 is the best. Considering the overall printing performance, when using the composite resin that film-forming resin 813: film-forming resin S2919 is 16:9, the printing performance of ink is optimal.

## References

1. Zhang Fuzhong, Beiqing Huang, Wei Xianfu, Li Xin (2014). The influence factors on gloss of water-based gravure ink [J]. Journal of Beijing Institute of printing, 22 (2): 17–19.
2. Beiqing Huang, Xianfu Wei, Gao Jie, TaoChen Yue (2007). The influence of pigment/binder ratio on dispersion of water-based gravure ink. Packaging engineering, 28 (11): 65–67.
3. Xiang Yang, Jiexian Wang (2000). Printing materials and suitability, Beijing: Printing Industry Press.
4. Qian Junhao (2003). Application technology of printing ink, Beijing: Chemical Industry Press.

**Part VIII**  
**Paper and Related Technology**

# Revealing the Components at Work in Classical Liquid Imbibition Models: Inertial, Bosanquet and Viscous Lucas-Washburn Applied to Printing

Guodong Liu, Xinya Zhang, Meiyun Zhang and Patrick Gane

**Abstract** The classical imbibition models: inertial, Bosanquet and the later dominance of viscous flow, thus following the Lucas-Washburn regime, frequently are employed to characterise the imbibition behaviour of printing fluids in paper or paper-based materials. To explore the interaction relationship among these imbibition models, theoretical simulation regarding the imbibition process based on these three models is discussed and analysed in this paper under uniform physical parameters. Additionally, their mutual relationship also was displayed by means of analysis and simulation results with different radii of the equivalent capillary tube aiming at different papers or paper-based materials, with focus on coated grades. It is found that these classical imbibition models indeed have an interaction relationship in the whole imbibition process, which is that Bosanquet is a more general form to characterize imbibition behaviour both inertial and viscous, each of which describe the dominant imbibition stages during the absorption process and have an overlapping area at initial stages and times of geometrical change within the structure related to the inertial regime respectively. The overlapping point timescale changes, and is extended when the equivalent radius of capillary tube of print materials is relatively large or small. It means that the consistency of this circumstance between inertial and viscous behaviour would extend into longer periods when having a large equivalent radius of capillary tube. By contrast, if the equivalent radius is small, the inertial and viscous regimes would reach a parallel situation at an earlier point of imbibition time. It also indicates that inertial imbibition and the viscous imbibition model enable one solve the Bosanquet imbibition at the initial stage and later imbibition during some specific cases, but the

---

G. Liu (✉) · X. Zhang · M. Zhang  
College of Light Industry and Energy, Shaanxi University of Science  
and Technology, Xi'an, China  
e-mail: lgdmax587@aliyun.com

G. Liu · P. Gane  
Department of Forest Products Technology, School of Chemical Technology,  
Aalto University, Aalto, Finland

P. Gane  
Omya International AG, Oftringen, Switzerland

permeability and viscous flow dominate at the later bulk volume imbibition stage. In addition, Bosanquet takes care of transitions between the inertial model and the L-W model due to including both effects in its expression. Thus, when the whole imbibition process needs to be characterised, the Bosanquet would be the optimal choice if the complex network structure is well characterized and the computational model available.

**Keywords** Inertial imbibition · Bosanquet imbibition model · Lucas-Washburn imbibition model · Interaction relationship

## 1 Introduction

When liquid or paste pigmented printing inks interact with the surface layer of coated paper, the ink colorant pigments stay on the surface of the coating to form the desired print image, made fast (fixed) by cross-linking resin, while the ink vehicle, constituting the continuous liquid phase, is removed by either thermal evaporation or imbibition into the paper, or both. In the case of dye-based ink, the dye enters into the surface pore structure together with the ink vehicle and becomes adsorbed onto the internal pore surface of paper. The removal of ink vehicle and its component interaction with the internal pore surface in all cases is critical in determining the print setting, fastness (strength) and optical properties. It is, thus, a major focus area for the paper or coating technologist to control the liquid pore network interactions driving both the absorption and chromatographic separation of vehicle components. Therefore, the imbibition mechanism or absorption process for print fluids, and the factors affecting it, has been the topic of much in-depth study. Some classical imbibition models, such as Lucas-Washburn [1], inertial model [2] and, in combination, the Bosanquet model [3] can commonly be used to describe the specific imbibition process, but they were established in terms of different dynamic force-controlled systems. The Lucas-Washburn regime has been reported widely to describe the interaction role between paper and printing ink but there exist some major deviations from the observed experimental imbibition in some cases. Schoelkopf et al. [4] and Ridgway et al. [5] observed the experimental deviation from the specific imbibition into coating material for coated paper based on the Lucas-Washburn imbibition regime, which were attributed to omitting the inertial, mass-related, role during the imbibition process. The Bosanquet model was proposed to enhance the contributory role of the inertial force in the imbibition process, alternatively reflected in terms of the Gibbs' free energy parallel description [6], and has been employed more successfully to characterise imbibition behaviour as a function of time, bridging the short and long timescale phenomena. However, in the past decades, the Bosanquet equation has not been widely employed compared with the traditional Lucas-Washburn equation. This was partly due to Bosanquet's own application for the concept to a single capillary, himself explaining that the inertial effect was too short lived to be of importance. As a result, many researchers thought

the impact of inertia on imbibition to be negligible because of its influence only over very short time during initial imbibition. Though this is true in general for the single capillary case or when studying the imbibition process on a long timescale for some printing liquids, those who rejected the concept overlooked the ever-present acceleration and deceleration effects at the wetting front in a complex geometry network structure. Thus, the cumulative effect of inertia should not be ignored in an interconnected network structural paper-based material, and is required as an integral part of the physics when analysing the process of dynamic forces acting during imbibition at the wetting front, although the decay of imbibition rate from linear  $t$  to  $\sqrt{t}$  is intrinsic to the eventual dominance of viscous drag within the saturated medium behind the wetting front. Gane et al. [7] highlighted this aspect (cumulative effect of inertia), and established the expression of complexity of a porous network based on the coating material structure analysis of fine printing paper. Liu et al. [8] demonstrated the positive role of inertia during the initial imbibition phase when considering the whole timescale range of the imbibition process for the selected coating material, ground calcium carbonate (GCC).

Although the classical models described above have all been applied to characterise the imbibition process of printing fluid in paper or paper-based materials over a range of physical situations, the optimal choice for the printing imbibition process and the relationship between the models are still worth to be explored further. Therefore, in this paper we set out to analyse and discuss the relationship between inertia and viscous flow during the imbibition process employing constant physical parameters, which can help us understand the specific imbibition behaviour when printing fluid interacts with surface layer of coated paper, and thus provide some original imbibition data for the papermaking manufacturer to adjust the pore structure of paper and further enhance or modify the imbibition behaviour of paper or paper-based materials.

## 2 Classical Imbibition Models for Printing Fluid Absorption

### 2.1 *Inertial Imbibition Model*

When printing ink contacts the surface of paper at the initial phase, the mass of printing ink is small on the surface layer of paper, such that the action of gravity is very limited, and so can be omitted from the description of the proceeding imbibition. In the case of offset printing, the pressure of the printing nip is known not to create any direct impregnation into the coating layer due to the exceedingly high viscosity. Considering mass transport only once capillarity acts, the dynamic force system for imbibition behaviour under inertia alone just includes the capillary force and the inertial retardation force, such that the imbibition model in this situation can be written as

$$l = t \sqrt{\frac{2\gamma \cos \theta}{\rho R}} \quad (1)$$

where  $l$  is the distance travelled by the wetting front of the printing liquid with density,  $\rho$ , undergoing imbibition in a capillary of radius  $R$ , representing the equivalent hydraulic (hydrodynamic) capillary of the sample, with a wetting force given as the liquid surface tension,  $\gamma$ , in contact with the solid surface having a meniscus boundary contact angle of  $\theta$ . According to the inertial model, the imbibition length ( $l$ ) has a linear relationship with increasing time. This model assumes purely plug flow with a lubricated or slip boundary condition between the liquid and the capillary wall.

## 2.2 Bosanquet Imbibition Model

As the imbibition process continues, the absorbed amount of print liquid is increased, and the role of the corresponding liquid viscosity begins to manifest itself. Once again, considering the effect of gravity to be minor in this system, the positive driving force remains that of capillarity [9], and so the dynamic force system controlling imbibition consists of the initial inertial force plus the evolving viscous force, derived from laminar Poiseuille-flow. Therefore, the imbibition model in this stage is shown in Eq. (2), namely the Bosanquet imbibition model. The imbibition length no longer has a simple linear relation with imbibition time.

$$l^2 = \frac{\gamma \cos \theta \cdot R}{a} \left[ t - \frac{R^2 \rho}{8\eta} \left( 1 - e^{-\frac{8\eta}{R^2 \rho} t} \right) \right] \quad (2)$$

## 2.3 Lucas-Washburn Imbibition Model

Along with imbibition proceeding further, the viscous force increases its role greatly to resist the capillary force during the imbibition process, such that the inertial force becomes smaller since acceleration no longer plays a role under the steady state flow. This is the Lucas and Washburn proposal, and the long-accepted Lucas-Washburn imbibition regime ignoring the minor impact of inertia at long times in a single capillary and usually represented by

$$l = \sqrt{\frac{\gamma \cdot R \cos \theta}{2\eta}} t \quad (3)$$

From the expression of Lucas-Washburn imbibition, it is distinct that the imbibition length is in proportion to root time, not the direct proportionality with time shown in the inertial regime.

### 3 Simulation Analysis of the Classical Imbibition Models

In order to explore the interaction relationship and differences between these models, and to propose which one could describe the specific printing imbibition most effectively, a comprehensive comparison and analysis is undertaken using uniform physical parameters. As a hexadecane, typically found as a main ingredient in digital printing inks, also is frequently used as a non-reactive wetting liquid for imbibition experimentation. Hexadecane (Dow Chemical Company, Midland, Michigan 48674, USA), therefore, is employed as the example fluid in this study. The surface tension,  $\gamma$ , viscosity,  $\eta$ , and density,  $\rho$ , of the liquid are given in Table 1. The equivalent radius of capillary tube of coated material, GCC representing a coated layer of paper, was measured in terms of gravimetric experimental imbibition, and shown to be in the range of 200–300  $\mu\text{m}$  for a variety of GCCs [9]. The range of equivalent capillary was expanded further at the large scale to represent the different paper-based printing materials and to probe sufficient model data. Thus, the equivalent radius of capillary tube used in this study is set respectively as 3  $\mu\text{m}$ , 5  $\mu\text{m}$ , 200  $\mu\text{m}$ , 300  $\mu\text{m}$ , 500  $\mu\text{m}$ , 2 mm and 3 mm. The contact angle of hexadecane in general paper-based materials,  $\theta$ , is assumed to be effectively zero [10].

The imbibition performance under these uniform physical parameters based on each classical model was simulated using a Matlab. Other imbibition situations with different equivalent radius of capillary tube were summarized in the Table 2. In order to demonstrate the imbibition process clearly, the imbibition time axis is thus defined as short timescale and long timescale, the former can adequately show initial imbibition for these three models, and the latter is to display subsequently the imbibition changes. From Figs. 1 and 2, although these three imbibition models are set up by means of different dynamic force systems, they indeed have some clear relationships. At the initial imbibition phase, the inertial regime and Bosanquet complete model are overlapped, as marked with the ellipse in Fig. 1. This is to say, that at the initial imbibition stage, the inertial force plays a dominant role and controls the imbibition performance, and the viscous retardation force of the print fluid in Bosanquet at this stage has no practical role to play. The imbibition length

**Table 1** The physical properties of printing liquid-hexadecane [11]

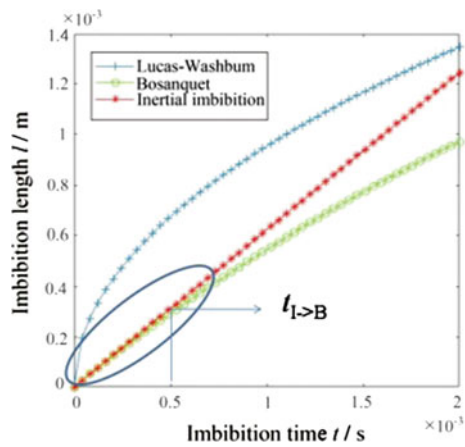
Printing liquid	Viscosity (Pa.s)	Density ( $\text{kgm}^{-3}$ )	Surface tension ( $\text{Nm}^{-1}$ )	Contact angle ( $^\circ$ )
Hexadecane	0.003	773	0.030	0



**Table 2** Imbibition transition area expressed as timescale with different equivalent radius of capillary tube ( $R$ )

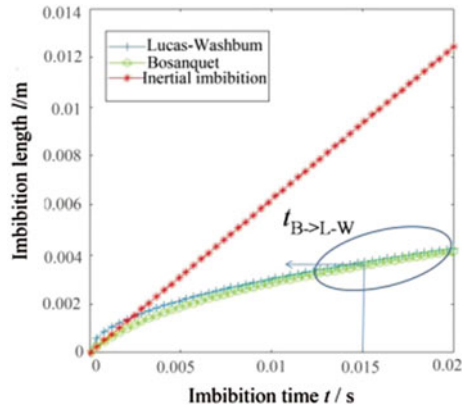
The equivalent radius ( $R$ )	3 $\mu\text{m}$	5 $\mu\text{m}$	200 $\mu\text{m}$	300 $\mu\text{m}$	500 $\mu\text{m}$	2 mm	3 mm
Transition between inertial and Bosanquet $t_{I \rightarrow B}/\text{s}$	$9 \times 10^{-8}$	$4 \times 10^{-7}$	$5 \times 10^{-4}$	$2 \times 10^{-3}$	$3.5 \times 10^{-3}$	0.08	0.12
Starting time of overlap between Bosanquet and Lucas-Washburn $t_{B \rightarrow L-W}/\text{s}$	$2.5 \times 10^{-6}$	$1 \times 10^{-5}$	0.015	0.025	0.1	0.7	2.5

**Fig. 1** The imbibition at short timescale ( $R = 200 \mu\text{m}$ )



has a linear relationship with imbibition time  $t$ . The overlap ends at a time  $t_{I \rightarrow B} = 5 \times 10^{-4}$  s. In the meanwhile, as the imbibition proceeds, the Bosanquet imbibition is in good agreement with the Lucas-Washburn regime, as marked with ellipse in Fig. 2. The start point of overlap is from  $t_{B \rightarrow L-W} = 0.015$  s onward during the subsequent imbibition, which signifies that the inertial force for Bosanquet imbibition is increasingly removed as the imbibition proceeds further and it eventually transforms the Lucas-Washburn regime controlled by capillary force and viscous force, i.e. the acceleration subsides and the laminar equilibrium flow takes over. Bosanquet imbibition is thus equivalent to Lucas-Washburn regime during the subsequent phase of imbibition. When  $R = 3 \mu\text{m}$ ,  $5 \mu\text{m}$ ,  $300 \mu\text{m}$ ,  $500 \mu\text{m}$ ,  $2 \text{ mm}$  and  $3 \text{ mm}$ , the imbibition behaviour based on these classical models is totally parallel with the situation  $R = 200 \mu\text{m}$ . Therefore, from the whole imbibition process, it can be concluded that the Bosanquet regime in its general form combining inertial and viscous flow consecutively is able to describe the whole imbibition behaviour. Thus, the inertial regime and Lucas-Washburn viscous regime are two important imbibition stages, which are expected to apply in practice and are combined conveniently in the Bosanquet expression.

**Fig. 2** The imbibition at long timescale ( $R = 200 \mu\text{m}$ )

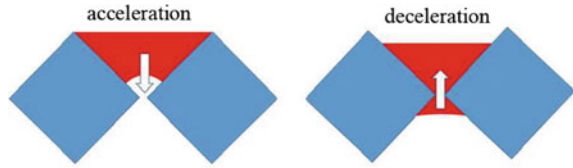


With different equivalent radius of the capillary tube, there is a different transition time between the initial and subsequent imbibition, respectively, as seen in Table 2. The increase of equivalent radius of capillary tube, the overlap area between inertial alone and Bosanquet is extended correspondingly, which means if the value of equivalent radius is big or sufficient for some papers or paper-based materials, the simple inertial imbibition regime characterises the initial imbibition. In contrast, as with the increase in equivalent radius of capillary tube the transition area between Bosanquet and Lucas-Washburn would be postponed the longer the imbibition time. It signifies that they would be overlapping at an earlier time stage if the equivalent radius becomes smaller, as shown in Table 2. Interestingly, large pore radii exhibit an inertial retardation in the longer timescale, but the finest pores deliver faster imbibition under the acceleration force at the short timescale because the viscous drag in these pores is too high to compete with the acceleration given to the tiny mass of liquid involved. In this way we can understand the fast ink setting on fine pore papers, recalling that there are many more fine pores per unit area than large ones, and slow ink setting on large pore papers due to the inertial retardation, essentially the opposite to what the Lucas-Washburn equation would predict based on viscosity only.

## 4 Reality-Complex Pore Network

These illustrations simply demonstrate visually what is clear from the mathematics of the models. Bosanquet combines inertia and viscous flow as two discrete terms and so once acceleration or deceleration have subsided, the laminar viscous flow model of Lucas-Washburn appears to be satisfactory in a single capillary. This is the point at which most workers in the field make a fatal error in assuming that the equivalent capillary is indeed realistic in itself. This is clearly not the case as a paper coating consists of a complex geometrical pore network. Take for example,

**Fig. 3** Liquid passing through a simple constriction—at first the liquid mass is accelerated, and then decelerated



the simple passage of liquid in the  $z$ -direction between two solid rectangular rods lying in the  $y$  direction. This can be mapped as a 2D problem in the  $x/z$  plane as shown in Fig. 3, where the rods form an edge to edge packing.

We see in Fig. 3 that the transition of size as the meniscus progresses through the geometry results in an at first decreasing meniscus radius, and then in an increasing one. The decrease in radius means that the Laplace pressure,  $|\Delta P|$ , of capillarity increases linearly as  $d(1/r(z))/dz$  until the liquid passes through the small gap and begins its passage on the other side, such that the meniscus capillary pressure on the other side now decreases as  $-d(1/r)/dz$ . For the bulk liquid of mass held above this geometry, the change in capillary force is first seen as acceleration followed by a deceleration. In both cases, inertia will thus play a significant role. This means that throughout the network structure, viscous flow will be disrupted by microscopic changes in acceleration of the order of the fine pore size. Therefore, despite the attraction of considering the Lucas-Washburn model simply because the function of imbibition experimentally decays to the square root of  $t$  at the long timescale, this only reflects the domination of viscous flow at these long timescales, but the network cannot be modelled adequately by the Lucas-Washburn derived equivalent hydrodynamic radius alone at short timescales.

## 5 Conclusions

In this paper, we discussed the transitions as a function of time amongst the classical imbibition models using uniform physical parameters. The different imbibition performances are thus simulated and displayed in respect to a range of equivalent capillary tube radii. We show that inertial and Lucas-Washburn have a transition in imbibition during the specific initial and later imbibition phases. This is to say that the Bosanquet equation, which expresses both factors is a more general form to characterise the imbibition behaviour compared with either the inertial or Lucas-Washburn models alone, which are actually simply the special imbibition cases describing plug flow versus laminar viscous flow. The inertial regime is consistent with the Bosanquet at shorter timescale, but for larger radii pores, the inertial regime remains active for longer than in small radii pores as a retarding effect, whereas in the finest pores, it is an accelerating effect. The Bosanquet could be replaced using a simple inertial regime when emphasising and exploring the initial process of imbibition. By contrast, if the equivalent radius is not very big but smaller one, Lucas-Washburn regime would have an overlap situation at an earlier point of

imbibition time, because the viscous drag begins to dominate. However, this interpretation only holds for a single capillary. Reality is that paper coatings are complex pore networks where the solution every time an acceleration or deceleration occurs is the inertial term, and only overall does the liquid supply follow a viscous controlled function and thus an observation close to the square root of time. Therefore, the Lucas-Washburn equation is able to substitute the Bosanquet equation when having a small equivalent radius only on respect to the imbibitions behaviour on the long timescale. When the whole imbibition process needs to be characterised, the Bosanquet equation is the optimal choice, as it contains a full dynamic force system: inertial force, capillary force and viscous force and could enable us to characterize the transitions between the inertial model and the L-W model well. The complexity of the pore network would need to be known to extract the power given to us through the simple mechanical expression Bosanquet provided.

**Acknowledgements** The authors acknowledge the Scientific Research Project (51402180) supported by NSFC. This work is also supported by Natural Science Basic Research Plan in Shaanxi Province of China (Program No. 2016JQ3033), the Collaborative innovation Research Plan in Shaanxi Province of China (Program No. 2015XT-64) and Doctor Initial Funding Program of Shaanxi University of Science and Technology (BJ15-11).

## References

1. Washburn, E.W. (1921). The dynamics of fluid flow. *J. Phys. Rev.*, 17, 273–283.
2. Quéré, D. (1997). Inertial capillarity. *Europhys. Lett.*, 39(5), 533–538.
3. Bosanquet, C.H. (1923). On the flow of liquids into capillary tubes. *Philos. Mag.*, 6 (45), 525–531.
4. Schoelkopf, J., Gane, P.A.C., Ridgway, C.J., & Matthews, G.P. (2000). Influence of inertia on liquid absorption into paper coating structures. *Nordic Pulp Paper Res. J.*, 15(5), 422–430.
5. Ridgway, C.J., Schoelkopf, J., Matthews, G.P., & Gane, P.A.C., James, P.W. (2001). The effects of void geometry and contact angle on the absorption of liquids into porous calcium carbonate structures. *J. Colloid Interface Sci.*, 239(2), 417–431.
6. Ma, D., Carter, R.D., Laine, J., & Stenius, P. (2008). Gibbs energy of imbibition of nonpolar and polar solutions into calcium carbonate and kaolin coatings. *Nordic Pulp Paper Res. J.*, 23(3), 333–338.
7. Gane, P.A.C., Ridgway, C.J., & Schoelkopf, J. (2004). Absorption rate and volume dependency on the complexity of porous network structures. *Transp. Porous Med.*, 54(1), 79–106.
8. Liu, G., Zhang, M., Ridgway, C., & Gane, P.A.C. (2014). Spontaneous inertial imbibition in porous media using a fractal representation of pore wall rugosity. *Transp. Porous Med.*, 104(1): 231–251.
9. Liu, G., Zhang, M., Ridgway, C., & Gane, P.A.C. (2014). Pore wall rugosity: the role of extended wetting contact line length during spontaneous liquid imbibition in porous media. *Colloid Surf. A. Physicochem. Eng. Asp.*, 443, 286–295.
10. Chibowski, E., & Holysz, L. (1997). On the use of Washburn's equation for contact angle determination. *Journal of Adhes. Sci. Technol.*, 11(10), 1289–1301.
11. Schoelkopf, J., Gane, P., Ridgway, C., & Matthews, G.P. (2002). Practical observation of deviation from Lucas-Washburn scaling in porous media. *Colloid Surf. A. Physicochem. Eng. Asp.*, 206, 445–454.

# Effect of Main Composition of Dissolving Pulp on Its Reactivity

Wei Liu, Guangxue Chen and Siwang Li

**Abstract** When dissolving pulp is used to prepare viscose or cellulose derivatives, the key property of the pulp is its reactivity which has great influence in printing process. There are four different dissolving pulps as materials to find the main factors which affect the reactivity. Fock's method was introduced to determine the reactivity of dissolving pulps in this paper. The results showed that the pulp with high reactivity has low hemicellulose content and low viscosity, alpha-cellulose content did not show obvious effect on reactivity when they are very high. Content of acetone extract and ash content did not show obvious influence to reactivity when they are very low.

**Keywords** Dissolving pulp · Chemical composition · Reactivity

## 1 Introduction

Dissolving pulp is one kind of chemical refined stock, which has mainly been used to produce viscose fiber, acetate fiber and cigarette filters in industry as a very important kind of biology material. Reactivity of dissolving pulp is an important indicator characterizing the quality dissolving pulp, and the paper made by high reactivity dissolving pulp usually have good printing ink absorbency and provide a good condition for printing process.

Reactivity of dissolving pulp refers to the amount of reacted cellulose when they reacted with right amount of NaOH and CS<sub>2</sub>. In factory, the filtration performance of cellulose sulfonate after the reaction usually used to characterize the reactivity in dissolving pulp [1, 2].

---

W. Liu · G. Chen (✉)  
State Key Laboratory of Pulp and Paper Engineering,  
South China University of Technology, Guangzhou, China  
e-mail: chengx@scut.edu.cn

S. Li  
South China University of Technology, Guangzhou, China

In my paper, amounts of the A-cellulose,  $S_{10}$ ,  $S_{18}$ , pentosan, acetone extract, ash content and *TAPPI* viscosity with different dissolving pulp samples has been measured. Then find out the correlation between among component content of the dissolving pulp and its reactivity. This is a good indicator to produce high quality dissolving pulp.

## 2 Experiment Section

### Chemicals and Materials:

Experimental medicine: Four kinds of industrial dissolving pulp samples: A, B, C which come from different dissolving pulp producers, and D is an unqualified sample which comes from another dissolving pulp producer.

Chemicals: Carbon disulfide (analytically pure), NaOH solution (9%), sulfuric acid solution (29%), sulfuric acid solution (68%), potassium dichromate solution (1/6 mol/L), sodium thiosulfate solution (0.1 mol/L), potassium iodide (analytically pure), starch (analytically pure).

Experimental apparatus and equipment: Vacuum drying oven, magnetic stirring apparatus, fuming cupboard, reflux unit (electric stove, condenser pipe, conical flask), titration apparatus.

The reactivity of cellulose was measured by modified Fock's method. the sample, sodium hydroxide and carbon disulfide were stirred together, cellulose sulfate was created of which a certain amount transformed to regenerated cellulose then, finally measured transformation rate of transformational cellulose. According to reactivity of Fock, it can not only have shown the percentage of residual cellulose, but also have expressed the transformation rate of transformational cellulose.

### 2.1 Regenerated Cellulose's Oxidation and Titrimetry

20 mL  $H_2SO_4$  (68%) was added in regenerated cellulose, stirred for 1 h by magnetic stirring apparatus, the solution after stirring were diluted to 50 mL, added 10 mL  $K_2Cr_2O_7$  (1/6 mol/L), heated reflux for a 1 h and the regenerated cellulose was fully oxidation, the solution became clear. Transferred the solution after cooling into volumetric flask (100 mL), then transferred 40 mL into beaker (250 mL), added 1 g *KI*, titrated by  $Na_2S_2O_3$  (0.1 mol/L), added 1.5 g starch when brown solution became shallow, then the solution became mazarine, kept titrating until the solution became nattier blue and noted the volume of  $Na_2S_2O_3$  used in experiment. The computational formula of reacting cellulose is as follow:

$$X = 100 \times 9.62^a \frac{M(V_1 C_1 - \frac{600V_2 C_2}{40^b})}{4Y} \quad (1)$$

- $X$  reacting cellulose (%)  
 $Y$  weight of sample  
 $V_1$  volume of  $K_2Cr_2O_7$  (mL)  
 $V_2$  volume of  $Na_2S_2O_3$  (mL);  
 $M$  molecular weight of  $C_6H_{10}O_5$  (162 g/mol)  
 $C_1$  concentration of  $K_2Cr_2O_7$  (mol/L)  
 $C_2$  concentration of  $K_2Cr_2O_7$  (mol/L)  
 $a$  the quality diluent of the first time is 100 g, took out 10 mL (10.4 g),  
 $100/10.4 = 9.62$ ;  
 $b$  the volume diluent of the second time is 100 mL, took out 10 mL,  
 $100/40 = 2.5$

Method of measuring content of alpha cellulose: referring to *GB/T5401*.

Methods of measuring content of alkali solubility,  $S_{10}$  and  $S_{18}$ : referring to *GB/T5401-2004*.

Method of measuring content of pentosan's content: referring to article "The comparison between the method of spectrophotometry and volumetric [3]".

Method of measuring content of acetone's extraction content: referring to soxhlet extraction method.

Method of measuring content of ash content: referring to *GB/T742-2008*.

Method of measuring content of TAPPI viscosity: referring to *TAPPI T30*.

### 3 Results and Discussion

#### 3.1 Pentosan Content of Dissolving Samples

Pentosan content in dissolving pulp reflects content of hemicellulose, in the production of dissolving pulp, it is better to keep pentosan content very low. Pentosan content is directly influence dissolving pulp's reactivity [4], and the increase of hemicellulose content will reduce alpha-cellulose content [5, 6]. The factory adopts the method of measuring pentosan content to reflect content of hemicellulose. The pentosan content of four kinds of dissolving samples is as follow:

From Table 1, pentosan contents of four dissolving samples are low, the highest of which is only 4.03%. The low pentosan contents of those four samples show that they are qualified for pentosan contents, most parts of hemicellulose had separated. Look at sample A, B, C only, sample A have the highest reactivity of which the pentosan content is 3.26% that is the lowest of all samples; sample B have the lowest reactivity of which the pentosan content is 4.03% that is the highest of all samples. Those experimental data show pentosan in dissolving pulp have negative effects to reactivity a certain extent, the higher pentosan contents of dissolving sample, the lower reactivity. At the same time, pentosan content of sample A, B, C have no big difference and all are qualified for pentosan contents, it is shows that pentosan content is not the main elements that effect reactivity of those four kinds dissolving pulp.

**Table 1** Pentosan,  $S_{10}$ ,  $S_{18}$  and  $S_{10}-S_{18}$  contents of four kinds of dissolving pulp samples

Type	Pentosan content (%)	$S_{10}$ (%)	$S_{18}$ (%)	$S_{10}-S_{18}$ (%)	Reactivity (%)
Sample A	3.26	11.95	5.30	6.65	79.41
Sample B	4.03	8.82	6.83	1.99	70.92
Sample C	3.66	7.77	5.76	2.01	74.56
Sample D	3.26	8.64	3.23	5.41	42.99

From sample D, its pentosan content is equal to sample A, but reactivity differs a lot, it can also show that pentosan content is not unique element that effect reactivity, there are other reasons for low reactivity of sample D.

### 3.2 Content of Alkali Solution Degree $S_{10}$ , $S_{18}$

Original alkali solution degree has crucial effect to hemicellulose yield of alkaline treatment in the production of artificial fiber pulp, to volume of carbon dioxide in sulfonation reaction. Therefore alkali solution degree in original pulp is an important technical indicator in factory.  $S_{10}$  and  $S_{18}$  refer to pulp's alkali solution degree in NaOH (10%) and NaOH (18%) respectively. Alkali solution degree  $S_{10}$  reflects content of short chain degradative cellulose and hemicellulose, alkali solution degree  $S_{18}$  reflects content of typical hemicellulose of gamma absorptiometry cellulose.

Form Table 1, the data of  $S_{18}$  content keep the same trend with pentosan content. Except sample D, other three samples display the trend that the higher  $S_{18}$  content, the lower reactivity, those prove that hemicellulose have negative effect to reactivity of dissolving pulp again.

The data of  $S_{10}-S_{18}$  content shows that sample A is higher than sample B and C a lot which means sample A have more tiny fiber components, size degradation of fiber is bigger. Compared  $S_{10}-S_{18}$  content of sample A, B and C, we also find that sample with higher  $S_{10}-S_{18}$  content have better Fock reactivity, this is because highly degraded fiber dissolves easily in alkaline solution in measurement of Fock method, so fiber residual volume is low and show high reactivity. In fact, highly degraded fiber will make the viscose yield decline.

According to the date of sample D, we can find that hemicellulose content is very low, and fiber degrades severely, but those data still not explain its low reactivity.

### 3.3 Alpha-Cellulose Content of Dissolving Samples

Alpha-cellulose is the main component of dissolving pulp and reacted with sulfur dioxide. From Table 2, alpha-cellulose contents of four kinds of dissolving samples



are all very high; the lowest content is sample A which is 88.10%, while the highest is sample C which is 92.15%. Compared alpha-cellulose contents of four samples, it finds that there is no obvious relationship between alpha-cellulose content and reactivity, and this is inconformity to our prospective result (the higher alpha-cellulose content, the higher reactivity). Those may be explained that when alpha-cellulose content is high to a certain extent, its content has not been the main effect on reactivity while pentosan content and cellulose supermolecule structure have more effect on reactivity.

### 3.4 Content of Acetone Extraction and Ash Content

Content of acetone extract shows organic matter content that can be extracted by acetone, including resin, fatty acid, oils, etc. There is records show that a certain amount of acetone extract is beneficial of improving reactivity. Ash is inorganic substance of dissolving pulp. Generally speaking, we think that mineral salt ions reacted with acid and generated insoluble compound which make viscose filter hard and block spinning jet. In addition, ash is harmful for strength of viscose fiber, luster and viscosity. It is better to extract out it as possible.

From Table 2, it cannot verify that acetone extract is benefit for reactivity. Four samples all have low acetone extract content which are below 0.2%. Form the data of Table 2, sample C which is 0.1975% is the highest compared with others, while its reactivity is in medium level; sample A of which the reactivity is the highest but have the lowest acetone extract content. Those may be explained by that it is too low of acetone extract content that have limited effect on reactivity, it needs more experiments.

According to Table 2, the data of ash content also cannot show that ash content have negative effect on reactivity, sample A with the highest reactivity has the highest ash content comparatively, but all four samples have very low ash content that are below 0.2% and they have little difference. Therefore ash content is too low to have big influence on reactivity, even though there is some change, the ash content is also very low.

**Table 2** Alpha-cellulose, acetone extract, ash content and viscosity of four kinds of dissolving pulp samples

Type	Alpha-cellulose content (%)	Content of acetone extract (%)	Ash content (%)	Viscosity (mPa s)	Reactivity (%)
Sample A	88.10	0.0520	0.175	3.852	79.41
Sample B	91.10	0.0676	0.082	4.910	70.92
Sample C	92.15	0.1975	0.057	4.749	74.56
Sample D	91.34	0.0545	0.093	4.742	42.99

### 3.5 TAPPI Viscosity

Viscosity of dissolving pulp shows degree of polymerization of cellulose in dissolving pulp, the higher viscosity, the higher degree of polymerization. In general, if viscosity is lower, cellulose cytoderm is damaged more severe and exposed active genes have more. Therefore the reactivity improved. From the Table 2, sample A which has the highest reactivity owns the lowest viscosity which is 3.852 Pa s; sample B which has the lowest reactivity in qualified samples owns the highest viscosity which is 4.910 mPa s. Those results show that reducing the viscosity is of benefit for higher reactivity. In addition, it is testified that cellulose of sample A have degraded severely combined the data of  $S_{10}$ – $S_{18}$  test with viscosity further, it keep high reactivity.

Come back to sample D, it can found that viscosity of sample D is 4.742 mPa s which is in similar level with sample C, while it has very low reactivity, those also proved that there is no distinct relationship between viscosity and reactivity of sample D which is unqualified dissolving pulp.

## 4 Conclusions

The main components of four kinds of different dissolving samples have been measured and the effects have been compared, the conclusions are as follows:

1. Hemicellulose of dissolving pulp has negative effect on reactivity, the higher the content of dissolving pulp, the better reactivity.
2. Alpha-cellulose content of dissolving samples is very high while having no distinctive effect on reactivity. Alpha-cellulose content is not the main factors effect reactivity.
3. Content of acetone extract and ash content of dissolving samples is very low, which has no distinctive effects on reactivity.
4. The degree of polymerization of cellulose in dissolving pulp plays a big role on reactivity, reducing the viscosity is of benefit for higher reactivity.
5. Reactivity of sample D which is unqualified sample is low, it is not because of the contents of main components. It may be because of supermolecule structure.

**Acknowledgements** This research was financially supported by the Guangdong Provincial Science and Technology Project (2013B010401007) and Guangzhou City Science and Technology Project (201607020045).

## References

1. Tan, L. H., Zhou K. P. (2013) the influencing factors and their controlling measures for reaction ability and ferrous content of dissolving pulp [J]. 34(6):75–77.
2. Strunk, P. (2012) Characterization of cellulose pulps and the influence of their properties on the process and production of viscose and cellulose ethers [Z]. Umea: Umefi University.
3. Lei, Y. C., Li S. W. (2013) The comparison between the method of spectrophotometry and volumetric [J]. 32:65–68.
4. Cao, Y., Tan, H. M. (2005) Study on crystal structures of enzyme-hydrolyzed cellulosic materials by X-ray diffraction [J]. Enzyme and Microbial Technology. (36): 314–317.
5. Ron J., Saake, B., Puls, J. (2008) Upgrading of paper grade pulps to dissolving pulps by nitren extraction: yields, molecular and supramolecular structures of nitren extracted pulp [J]. Cellulose. (15): 739–750.
6. Li, P. P. (2013) Preparation of pine dissolving pulp and study on the prehydrolysates [D]. South China University of Technology. Guangzhou.

# Study on the Antistatic Coating Technology and Coated Paperboard Performance

Qinghua Gao, Junyan Huang, Shangjie Jiang and Huizhong Zhang

**Abstract** In order to study various properties of the coated antistatic corrugated board, the effect of coating weight on the antistatic property of paper board was understood by pre-test, thus the optimal coating weight was selected. The three layers (S5S) and five layers (S545S) ordinary corrugated board, printed and coated antistatic corrugated board were produced by coated machine and corrugated board production line, and the edgewise crush resistance, flat crush resistance, compressive strength and antistatic property in the optimal coating weight were tested and analyzed. The results showed that the physical performance and antistatic property of the coated antistatic corrugated board are better than the printed antistatic corrugated board, and close to or slightly higher than ordinary corrugated board, and it is more specifically suitable for the electrostatic sensitive objects packaging and its long-term protection.

**Keywords** Coated · Antistatic · Corrugated board · Performance

## 1 Introduction

In recent years, the accident occurred frequently due to careless packing, storage and transportation of the electrostatic sensitive objects in China's electronics industry, petroleum industry, weapons industry, textile industry, rubber industry, aviation and military field, and its loss was also very serious [1, 2]. So research on the antistatic packaging quickly became one of the hot in package field. As one of the most promising packing materials, corrugated board can become timber substitute, plastic substitute, recyclable and environmentally-friendly [3, 4]. Therefore,

---

Q. Gao · J. Huang (✉) · S. Jiang  
Dalian Polytechnic University, Liaoning, China  
e-mail: huangjunyan@126.com

Q. Gao  
e-mail: 1138859496@qq.com

H. Zhang  
Tat Seng Packaging (Suzhou) Co.,Ltd, Jiangsu, China

the research and use of antistatic corrugated board to pack the sensitive electricity contents have a broad application market especially in electronic components, initiating explosive device, semiconductor, precision instruments and industrial products [5].

Antistatic board is the general term of board with antistatic property [6], it normally refers to coating antistatic coatings on inside paper board (on the inner surface of the corrugated carton) to make it have the antistatic property. In the current market, antistatic board is made by print method [7], which is made by printing antistatic coatings directly on the corrugated board paper surface. This method would lead to crushing of the corrugated shape and degradation of strength property to some extent, and board's wear resistance was also negative and its ink was easy to fall off. So in order to ensure board's antistatic property, varnish oil had been coated on corrugated board after printed to reduce the falling of ink, but greatly reducing antistatic property and increasing costs. We mainly focused on the pre-test which coated coatings on inside paper board in this experiment [8], and then elevated pressure, dried, molded, and produced antistatic corrugated board, so as to develop antistatic corrugated board and carton with better performances.

## 2 Experiments

### 2.1 Raw Materials

<sup>#</sup>S corrugated medium and case board were made by Long Chen paper Co., Ltd.

Antistatic coatings were purchased from Michelman Company.

The three (S5S/B) and five (S545S/BC) layers composite corrugated board or carton (herein after referred to as ordinary type); The three and five layers coated antistatic corrugated board or carton (herein after referred to as coated). The three and five layers printed antistatic corrugated board or carton (herein after referred to as printed), were made by Tat Seng Packaging (Suzhou) Co., Ltd.

### 2.2 Instrument

Edgewise crush resistance instrument, flat crush resistance instrument and measurement and control compression instrument were made by Sichuan Changjiang Papermaking Instrument co., Ltd. Electronic universal testing machine was made by Changchun Second Testing Machine Co., Ltd.

### 2.3 Method

In pre-test different weight of antistatic coatings were coated on inside paper board and board's antistatic property were tested, and then optimal coated weight was selected.

Under the optimal coating weight we performed two experiments. The first group was comparison of the strength of corrugated board which was the three layers (S5S/B) ordinary type, printed and coated. The second group was comparison of the strength of corrugated board which was the five layers (S545S/BC) ordinary type, printed and coated.

## 3 Results and Analysis

### 3.1 Result and Discussion of the Antistatic Property of Inside Paper Board with Different Coating Weight

The effect of different coating weight on the antistatic property of inside paper board was shown in Fig. 1. The resistance value decreased with the increment of coating weight, but conductive ability increased and antistatic property improved [9]. As the figure shown that when coated weight were from 4 to 12 g/m<sup>2</sup>, antistatic property changed quickly; from 12 to 14 g/m<sup>2</sup>, it changed relatively slow, but after 14 g/m<sup>2</sup>, the antistatic property remained the same. Considering cost, wear problem and suit for assembly line production, 12 g/m<sup>2</sup> was more appropriate.

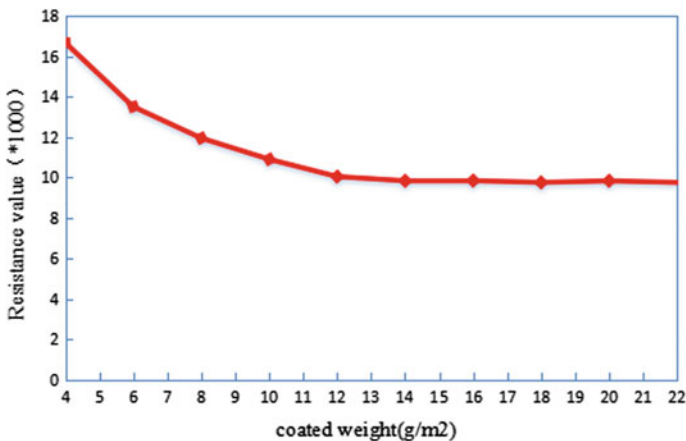


Fig. 1 The effect of different coating weight on the antistatic property of inside paper board

### 3.2 Comparison of the Edgewise Crush Resistance Test Results of the Corrugated Board Respectively with the Three and Five Layers Ordinary Type, Printed, Coated Corrugated Board

The edgewise crush resistance test results of the corrugated board respectively with the three and five layers ordinary type, printed, coated corrugated board were shown in Figs. 2 and 3. From the chart, we can conclude that the edgewise crush resistance of the coated reached the same or slowly higher than ordinary type but far better than printed. 8th dates of three layers coated peaked at 371 N/m, 3.4% over ordinary type. Also, 8th dates of five layers peaked at 605 N/m, 0.7% over ordinary type. Thus the edgewise crush resistance of the coated almost reached the same or slowly higher than ordinary type, but it was much higher than the printed.

### 3.3 Comparison of the Flat Crush Resistance Test Results of the Corrugated Board Respectively with the Three and Five Layers Ordinary Type, Printed, Coated Corrugated Board

The flat crush resistance test results of the corrugated board respectively with the three and five layers ordinary type, printed, coated corrugated board were shown in Figs. 4 and 5. The figures showed that ordinary type and coated were all relatively

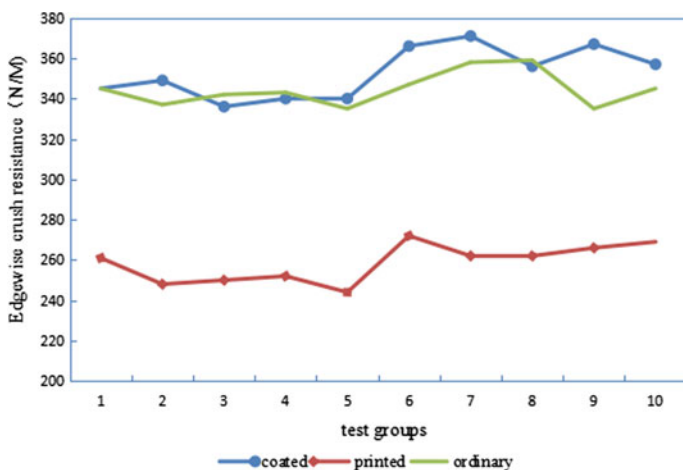
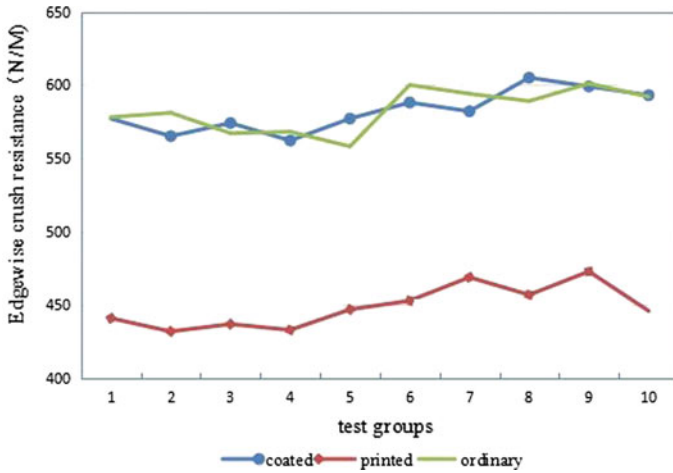


Fig. 2 The comparison of the edgewise crush resistance of the corrugated board with three layers ordinary type, printed, coated corrugated board



**Fig. 3** The comparison of the edgewise crush resistance of the corrugated board with five layers ordinary type, printed, coated corrugated board

close to each other, while printed was inferior to them. The fluctuating range of five layers printed flat crush resistance curve was higher, it may be due to machine commissioning in printing process. 6th dates of three layers coated reached the highest, was 383 N/32.2 cm<sup>2</sup>, it increased by 4.1% over ordinary type, 12.5% over printed. Because of slight fluctuating of five layers printed and ordinary type dates, so the experiment was adopted average number to analyze and explain, average numbers of coated, ordinary type, printed were 489.8 N/32.2 cm<sup>2</sup>, 483.9 N/32.2 cm<sup>2</sup>, 476.5 N/32.2 cm<sup>2</sup>, coated was up by 1.3 and 2.8% over the ordinary type and printed respectively.

### ***3.4 Comparison of the Compressive Strength Test Results of the Corrugated Carton Respectively with the Three and Five Layers Ordinary Type, Printed, Coated Carton***

The compressive strength test results of the corrugated carton respectively with the three and five layers ordinary type carton, printed carton, coated carton were shown in Figs. 6 and 7. From the chart, we can conclude that no matter what three or five layers corrugated carton, the whole tendency was that comprehensive strength of printed carton was lowest, coated carton's was close to ordinary type's. Average number of the three layers coated carton was 2390.9 N/m<sup>2</sup>, which increased by 4.5% over ordinary type carton and 25.3% over printed carton. In printing process, due to machine commissioning may result in corrugated crushing, so compressive strength was relatively low.



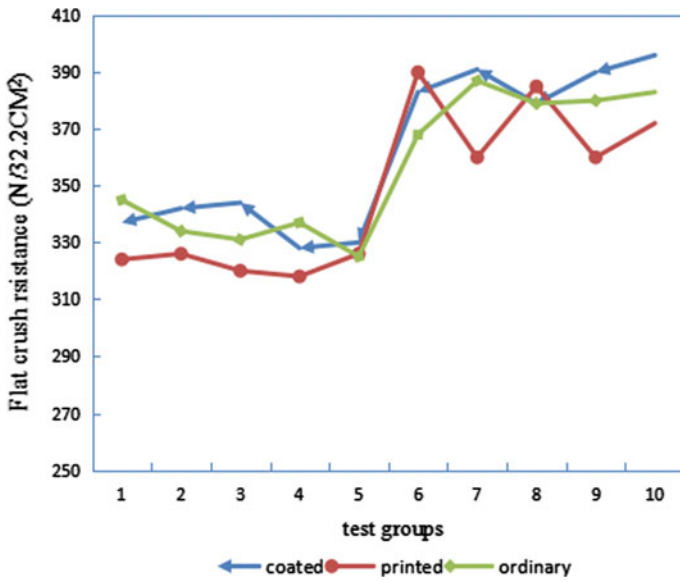


Fig. 4 The comparison of the flat crush resistance of the corrugated board with three layers ordinary type, printed, coated corrugated board

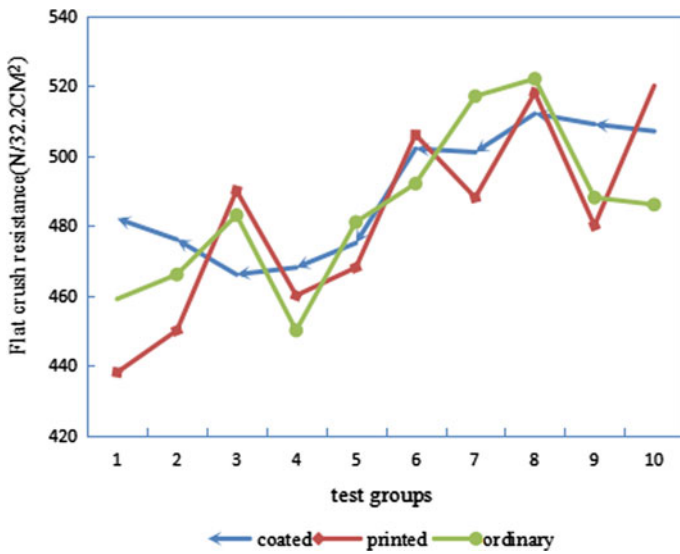


Fig. 5 The comparison of the flat crush resistance of the corrugated board with five layers ordinary type, printed, coated corrugated board

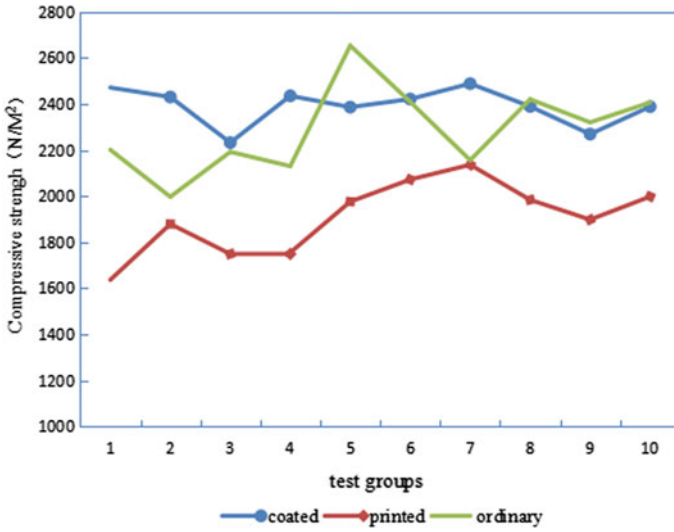


Fig. 6 The comparison of the compressive strength of the corrugated board with three layers ordinary type carton, printed carton, coated carton

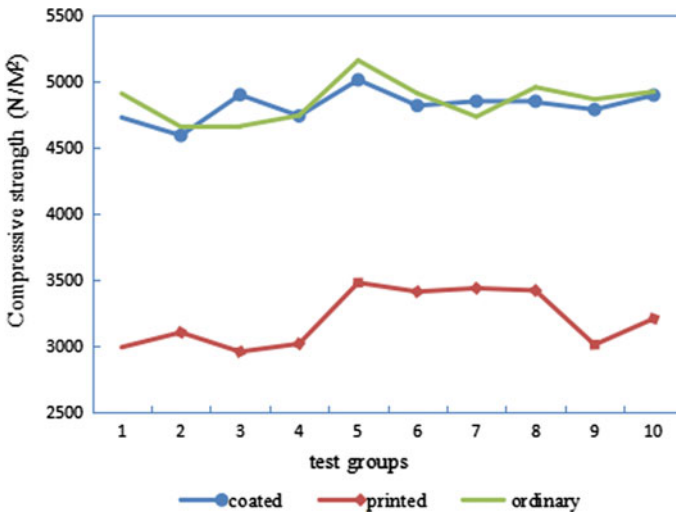
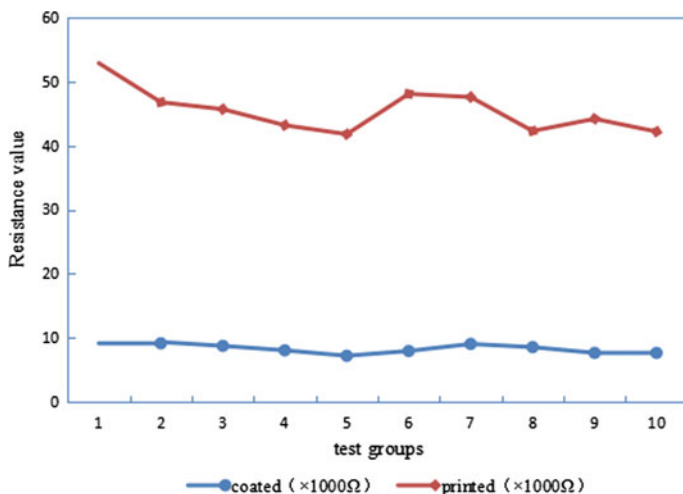


Fig. 7 The comparison of the compressive strength of the corrugated board with five layers ordinary type carton, printed carton, coated carton



**Fig. 8** The comparison of the antistatic property of the corrugated board with coated, printed corrugated board

### 3.5 Comparison of the Antistatic Property Test Results of Corrugated Board Respectively with the Printed, Coated Corrugated Board

The comparison of the antistatic property test results of corrugated board respectively with the printed, coated corrugated board were shown in Fig. 8. No matter what three and five layers corrugated board, conductive property and antistatic property enhanced with resistance value decreasing. The antistatic property of coated was much higher 5–6 times than the printed, its superior antistatic property can be obviously seen. Antistatic property of corrugated board had the very big enhancement after coating. Antistatic property raised with coating weight, and the strength property of corrugated board was close or slightly higher than ordinary type, which was concerned with coated antistatic corrugated board production process. From economic considerations, coating weight of  $12 \text{ g/m}^2$  antistatic corrugated board can be for mass production.

## 4 Conclusions

According to test results of the edgewise crush resistance, flat crush resistance, antistatic property of corrugated board and the compressive strength of the corrugated carton which was three and five layers coated, printed, ordinary type of corrugated board respectively, we can concluded that no matter what three or five layers corrugated board, the strength property of coated antistatic corrugated board

and its antistatic property were much outstanding than printed and ordinary type. It's easy to operate, recycle and conform to the requirements of the green packing. To some degree, it can replace the previous plastic or metal sealed packing and had a widely application foreground.

## References

1. Wenhui Zhang (2016). Harm and Protection Measures of Static Electricity in Electronic Components Screening. *Modern Industrial Economy and Informationization*, 6(4):52–54.
2. Bo Liang, Jianzheng Yi (2008). Protection of Electrostatic Hazards in Military Field. *Equipment Environmental Engineering*, 5(2):80–82.
3. He Li (2006). The Tendency and Development of Corrugated Carton at Home and Abroad, *Hunan Packaging*, 4:10–12.
4. De Gao, Zhuang Liu, Jing Dong, et al. (2005). The Property and Prospect of the Corrugated Paper Board. *Packaging Engineering*, 26(1):1–4.
5. Junhong Chang, Fei Wang (2014). Research on New Technology of Military Special Packaging. *New Technology & New Process*, 11:108–110.
6. Dezhi Zhou (2013). Water-based Antistatic Corrugated Board Coatings and its Preparation Method CN102392388A. *Technology and Market*, 7:364.
7. Mudong Zhao (2015). Introduction of the Static Electricity in Printing Process and its Control and Prevention. *China Print*, 8:76–78.
8. Apichaya Jianprasert, Pathavuth Monvisade, Masayuki Yamaguchi. (2016). Surface Improvement on Water and Oil Affinities and Absorption Rate of PVA/Tung Oil-Coated Paperboard and Fiberboard. *Journal of Coatings Technology and Research*, 2.
9. Xiaojun Zhang, Junran Li (2016). Research of Nano Fe<sub>3</sub>O<sub>4</sub>/Cellulose Antistatic Composite Packaging Film Science & Technology, 7:23–27, 44.

# Influence of Silica Pigments with Different Sizes on the Performances of Coated Ink-Jet Printing Paper

Xu Liu, Yunzhi Chen and Zhengjian Zhang

**Abstract** Coated ink-jet printing paper, with a porous coating layer on its surface, has a good performance of ink absorption, and its quality of printing is significantly higher than the ordinary ink-jet printing paper. Therefore, the problem about how to improve the performances of the coated ink-jet printing paper is attracting more attention. So, in this study, it used the self-made silica with different particle sizes of D90, including 5.9, 13.6, 21.1, 25.6, 35.4  $\mu\text{m}$  and the mixtures of two kinds of silica with different particle sizes, including 5.9 and 13.6  $\mu\text{m}$ , 5.9 and 21.1  $\mu\text{m}$ , 13.6 and 21.1  $\mu\text{m}$  to prepare the coated ink-jet printing paper as pigments. The performances of different paper were compared by measuring the contact angle, roughness, air permeability, solid density and print contrast. Results of the experiment showed that the smaller size of silica particle was, the better the wettability of coated paper surface was. The roughness and air permeability of coated paper added with the increase of particle size, and the speed of add was faster and faster. But the print contrast and solid density dropped with it, and the speed of decrease was slower and slower. When the smaller particles were mixed in the larger pigment particles, it could improve the performances of coated paper. In conclusion, the coated paper using 5.9  $\mu\text{m}$  silica particles as pigment had the best performances in the different coated paper prepared in the experiment.

**Keywords** Pigment · Particle size · Coated ink-jet printing paper · Silica

## 1 Introduction

With the popularization of microcomputer and ink-jet printer, the research and production of printing supplies are developing rapidly [1]. Coated ink-jet printing paper, with a porous coating layer on its surface, has a good performance of ink absorption, and its quality of printing is significantly higher than the ordinary

---

X. Liu · Y. Chen (✉) · Z. Zhang  
Tianjin University of Science and Technology, Tianjin, China  
e-mail: yzchen@tust.edu.cn

© Springer Nature Singapore Pte Ltd. 2017  
P. Zhao et al. (eds.), *Advanced Graphic Communications  
and Media Technologies*, Lecture Notes in Electrical Engineering 417,  
DOI 10.1007/978-981-10-3530-2\_124

1015

ink-jet printing paper. The structure of the coating layer is greatly influenced by the size of pigment particles in the coating [2]. And the silica particles have small particle size and large specific surface area. So the preparation of coated ink-jet printing paper usually uses silica particles as pigments to make the paper to absorb more ink. When it use the Sol-gel method to synthesize silica, the particle sizes of silica can be controlled by changing the temperatures, stirring speeds, drop speeds of silicon source and other experiment conditions [3]. But the sizes are difficultly controlled in the laboratory and the errors are about 2  $\mu\text{m}$ . For reducing the effect of errors, this study chose five kinds of silica particles with different particle sizes of D90, including 5.9, 13.6, 21.1, 25.6 and 35.4  $\mu\text{m}$ . And it used these silica particles as different kinds of pigments to prepare the paper. By comparing and analysing the contact angle, roughness, air permeability, solid density and print contrast of different paper, the effects of pigment particle sizes on performance of coated ink-jet printing paper could be observed. And the result of this study could provide guidances to the production.

## 2 Experimental

In the experiment, the Polyvinyl Alcohol was used as adhesive, and the silica with different particle sizes were used as pigments. The coatings were made of them and the mass ratio was 3:10 under the condition of absolute dry. And 8 kinds of paper were prepared with these coatings. The numbers of paper and the corresponding sizes of silica particles were showed in the Table 1.

Then the performances of different paper were compared by measuring the contact angle, roughness, air permeability, solid density and print contrast. The ink used in the print experiment was magenta water-based ink. And the calculation formula of the print contrast was showed in (1). The relevant detection equipments were video contact angle system (America, AST), SE115 roughness and air permeability tester (Sweden, Lorentzen & Wettre), and X-Rite 518 reflection type density meter (America, X-Rite).

$$K = 1 - \frac{D_T}{D_S} \quad (1)$$

$K$  The print contrast,

$D_T$  The density of 80% dots,

$D_S$  The solid density.

**Table 1** The numbers and silica particle sizes of different paper

Number	1	2	3	4	5	6	7	8
Particle size (µm)	5.9	13.6	21.1	25.6	35.4	5.9, 13.6	5.9, 21.1	13.6, 21.1
Rate of different silica	–	–	–	–	–	1:1	1:1	1:1

**Table 2** Initial values of contact angles of different paper

Numbers	1	2	3	4	5	6	7	8
Contact angles (°)	40.6	62.1	60.1	65.7	76.3	47.3	55.7	66.5

### 3 Results and Discussions

#### 3.1 Initial Values of Contact Angles of Different Paper

Table 2 showed the initial values of contact angles between water-based ink and different paper.

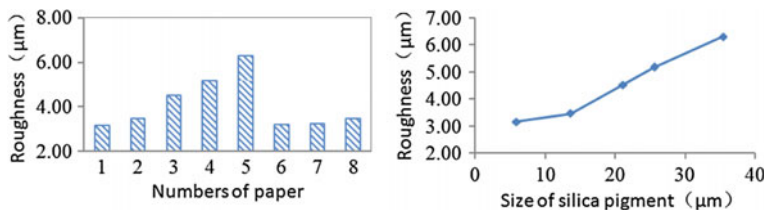
It showed that the initial contact angle changed from 40.6° to 76.3° with the increase of the pigment particle sizes, and the rate of increase was 87.9%. The initial contact angle declined 23.8% from No. 2 to No. 6. And the value declined 7.3% from No. 3 to No. 7. When the size of pigment particle was bigger, the specific surface area of it was smaller, and the surface energy of coated paper was lower too. That meant the surface of the paper was more difficult to be wetted. So the initial value of contact angle became larger. Under this condition, When the ink drops fell and touched the paper, they would spread and be absorbed very slowly. Therefore, the drying time was extended. But the wetting property of ink on paper surface was improved, when the pigment mixed with smaller silica particles with larger specific surface areas. And the smaller the mixed particles were, the more obvious the effect was.

But the initial contact angle of No. 8 was larger than the value of No. 3. The reason was that the coating on paper surface was not uniform, and the test areas lacked of pigment particles. So these areas had a low surface energy and could not be wetted easily.

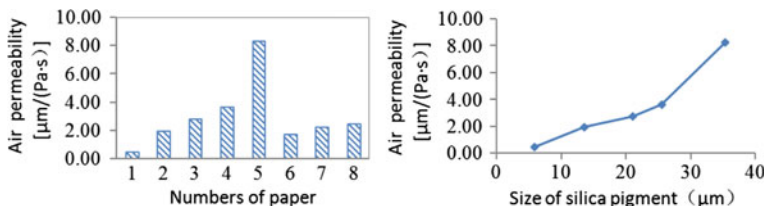
#### 3.2 Roughnesses of Different Paper

The roughnesses were showed in the Fig. 1.

The results showed that the roughness of paper increased with the raise of silica particle sizes, and the speed of increase was faster and faster. The base paper composed of reticular fibers and a small number of fillers had a very rough surface.



**Fig. 1** Roughnesses of different paper, and pigment sizes and roughnesses of No. 1 to No. 5



**Fig. 2** Air permeabilities of different paper, and pigment sizes and air permeabilities of No. 1 to No. 5

And the pigment particles in coating could fill the sunken places on base paper surface and improve the degree of flatness. So the silica with a smaller particle size was good able to fill minor defects and pores, and it could make the roughness of paper surface get a more obvious reduction. In addition, there were many silica particles in the coating layers. The smaller the particle size was, the smaller the height differences of surface were, and the lower the roughness was, and the obscurer the change of roughness was.

The roughness of No. 6 was smaller than the value of No. 2 by 8.07%. No. 7 was smaller than No. 3 by 28.26%. And No. 8 was smaller than No. 3 by 22.96%. It could be seen that the roughness of coated ink-jet printing paper was reduced by mixing smaller silica particles in the pigments. Because the coating made of larger pigment particles had a porous structure, and the differences of its microscopic surface were larger. The smaller particles could enter the recesses and the pores of the coating, then the structural differences would be reduced. So the overall smoothness of paper surface would be improved.

### 3.3 Air Permeabilities of Different Paper

The air permeabilities were showed in the Fig. 2.

It showed the air permeability of the coated ink-jet printing paper increased with the raise of pigment particle sizes, and the speed of increase was faster and faster. The air permeability of No. 1 was only 5.31% of the value of No. 5. Because the silica particles in coating could cover the surface of the fibers in base paper and fill



the spaces between them. Gases would be hindered when passed through the paper inside. The smaller the particle size was, the easier the silica filled the microscopic spaces, and the more difficultly the gases passed, and the obscurer the change of air permeability was.

And No. 6 was smaller than No. 2 by 13.47%. No. 7 was smaller than No. 3 by 18.98%. No. 8 was smaller than No. 3 by 10.95%. It showed that the air permeability of paper was reduced when the pigment mixed with smaller silica particles, and the smaller the mixed particles were, the more obvious the effect was. The reason was that the smaller particles could uniformly disperse around the larger ones and reduce the original spaces in the coating, therefore the air permeability came down.

### 3.4 Solid Densities of Different Paper

The solid densities of magenta were showed in the Fig. 3.

The solid density of the coated ink-jet printing paper decreased with the raise of pigment particle sizes, and the speed of decrease was slower and slower. In the process of printing the color blocks, smaller silica particle could adsorb more ink on its surface with a larger specific surface area. In addition, the pores between smaller particles were less, and the infiltration of ink could be hindered more effectively. So more ink would be fixed in the top layer of paper, and the value of the solid density would also be larger. That meant the paper had a wider print tone range, and the quality of printing was better. But when the pigments were big, the ink would infiltrate excessively, and the change of solid density would become obscure.

And No. 6 was larger than No. 2 by 17.98%. No. 7 was larger than No. 3 by 15.91%. No. 8 was larger than No. 3 by 10.23%. It showed that the solid density of paper was improved when the pigment mixed with smaller silica particles, and the smaller the mixed particles were, the more obvious the effect was. The reason is that smaller silica particles enhanced the ability of fixing ink of the paper surface and reduced the degree of the ink excessive infiltration. So the solid density of paper was larger.

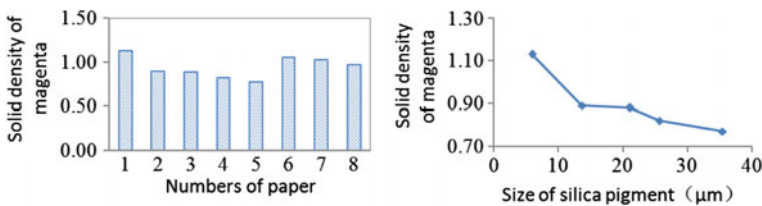


Fig. 3 Solid densities of different paper, and pigment sizes and solid densities of No. 1 to No. 5

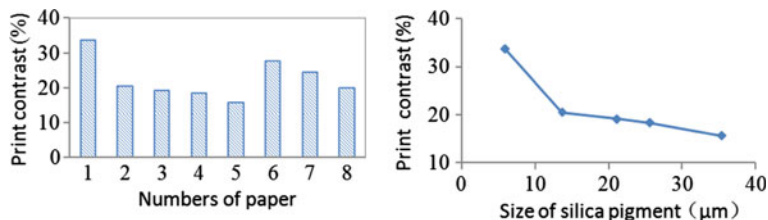


Fig. 4 Print contrasts of different paper, and pigment sizes and print contrasts of No. 1 to No. 5

### 3.5 Print Contrasts of Different Paper

The print contrasts of magenta of different paper were showed in the Fig. 4.

The results showed that the print contrast decreased with the raise of pigment particle sizes, and the speed of decrease was slower and slower. When the size of silica particles became larger, the excessive spread of ink would increase for the bigger specific surface area and pore. The colour densities of 80% dots and 100% dots were closer. So the print contrast and the change of its value became smaller. When the pigment mixed with smaller silica particles, the excessive spread was reduced. So the print contrast and print quality of paper were improved. And the smaller the mixed particles were, the larger the improvement was.

## 4 Conclusions

The results of the experiment showed that the smaller size of silica particle was, the better the wettability of coated paper surface was. The roughness and air permeability added with the increase of particle size, and the speed of add was faster and faster. But the print contrast and solid density dropped with it, and the speed of decrease was slower and slower. When the smaller particles were mixed in the larger pigment particles, it could improve the performances of coated paper. In this experiment, the paper prepared with 5.9 μm silica particles as pigment had the best performances.

## References

1. Chen Yunzhi. (2011). Coating technology of coated color ink jet printing paper. Research on printing and packaging in China, 2011, 03 (01): 6–14.
2. Wang Qiushuang. (2012). Effect of different particle sizes of silica on the microstructure of color ink-jet printing paper coating layer. Light industry science and technology, 2012, 03 (03): 32–34.
3. Jia Ningning, Gao Yanmin, Zhou Chao, et al. (2013). Effects of process factors on the particle size of SiO<sub>2</sub> microspheres prepared by sol-gel method. Journal of Wuhan University of Science and Technology, 2013, 36 (1): 36–40.

# Study on the Neutral Deinking Technology of Old Digital Printing Paper (ODP)

Longkang Cong, Xiaolin Zhang, Liu Shi and Xiangsheng Deng

**Abstract** With the rapid development of digital printing technology, old digital printing paper (ODP) become a new waste paper resource, which has triggered more and more attention on the wastepaper utilization industry. In this study, orthogonal experiment and single factor experiment was used to analyze the influence of deinking agent, addition agent, flotation time, curing time and curing temperature on the ODP neutral deinking technology. The results showed that the optimum neutral deinking conditions for ODP was deinking agent of 0.5%, emulsifying agent (OP-10) of 0.5%, sodium dodecylbenzene sulfonate (SDBS) of 0.1%, curing temperature of 70 °C, curing time of 15 min and flotation time of 6 min. At the same time, under the optimum neutral deinking conditions for ODP, the brightness of deinking pulp reached the maximum value of 99.3% SBD and the pulp yield of ODP reached to 76.8%.

**Keywords** Neutral deinking · ODP · Deinking agent · Brightness · Pulp yield

## 1 Introduction

Along with the decreasing of forest resources, the effective recycling utilization of secondary fiber, such as old digital printing paper (ODP), has triggered more and more attention the wastepaper utilization industry, because of enormous economic and social benefits [1]. Currently, the alkaline deinking technology is one of the most common deinking one. Alkaline can react with lignin and non-ferrous substance which may make the deinked pulp turn blackening [2]. Furthermore, Alkaline deinking technology not only decreases the strength of the pulp, but also increases the chemical oxygen consumption (COD) value of deinking waste water which do seriously harm to our environment and is difficult to treat [3]. However,

---

L. Cong · X. Zhang (✉) · L. Shi · X. Deng

Faculty of Printing, Packaging Engineering and Digital Media Technology, Xi'an University of Technology, Xi'an, Shaanxi, China

e-mail: zxlmmm@sina.com

© Springer Nature Singapore Pte Ltd. 2017

P. Zhao et al. (eds.), *Advanced Graphic Communications*

and *Media Technologies*, Lecture Notes in Electrical Engineering 417,

DOI 10.1007/978-981-10-3530-2\_125

1021

alkaline deinking technology has no remarkable influence on the deinking efficiency of digital printing ink and other non-contact printing ink, with the increasing of ODP. Neutral deinking is a new deinking technology under neutral or near-neutral conditions [4]. The surfactants of neutral deinking technology can weak the interfacial bonding force between ink and fiber by penetrating into the interface, and make ink particles separate from fibers under the mechanical shear force [2, 5]. The dissociative ink particles can be removed by floatation and washing in the pulp. Moreover, the utilization of neutral deinking technology can save cost by reducing the use of chemicals [6]. The low COD value of neutral deinking waste water is beneficial to the protection of the environment [7].

In this paper, the old digital printing paper for ink-jet printer (printing time more than one year) was chosen as the experimental materials for the study of neutral deinking technology. Orthogonal experiment and single factor experiment were used to obtain the optimum neutral deinking conditions for ODP.

## **2 Experiment**

### **2.1 Materials**

The ODP (EPSON semigloss photo paper (190 g)) for ink-jet printer was torn into size of  $2 \times 2$  cm, mixed uniformly, and put it into sealed plastic bags. The moisture of ODP was measured according to the National Standards of the People's Republic of China GB/T462-2003. The sodium dodecylbenzene sulfonate (SDBS) and OP-10 were all chemical purity. The self-compounded deinking agent consists of non-ionic and anionic surfactant. All the reagents were diluted into about 1% consistency.

### **2.2 Equipments**

The following equipments were used: electro-thermostatic water bath (model HH-2), multifunctional beater (model YK-250C), the air bubble generator, the sheet-making apparatus (model ZQJ1-B) and digital brightness detector (model PN-488).

### **2.3 Experimental Method**

Firstly taking the ODP into a 500 ml beaker, adding self-compounded neutral deinking agent and neutral additives, adding some deionized water, putting the beaker into electro-thermostatic water bath for 10 min at 50 °C. Secondly, using the

multifunctional beater to break the ODP into pulp paste for 60 s and diluting the pulp paste into about 1.0% consistency. The pulp was washed with deionized water through a 80 mesh screen after floatation for 9 min. Finally, the pulp was formed to a paper sheet by the sheet-making apparatus. The brightness was measured by digital brightness detector.

## 2.4 Analysis Method

The brightness was measured by digital brightness detector, and the arithmetic mean value was obtained from three samples. The brightness and pulp yield of the blank sample were 93.09 and 84.6% respectively.

The pulp yield of ODP was counted by the Eq. (1), and the arithmetic mean value was obtained from three samples.

$$M = m_1/m_0 \times 100 \quad (1)$$

where M is the yield of pulp,  $m_1$  is the mass of the paper sheet after deinking,  $m_0$  is the mass of ODP before deinking (in grams).

## 3 Results and Discussions

### 3.1 Orthogonal Experiment

The results of orthogonal experiment of neutral deinking is shown in Table 1. The self-compounded deinking agent has considerable impact on the efficiency of deinking. The factors of A, B, C Column have  $K_1 > K_2 > K_3$ , so the brightness of ODP decreased with increasing the concentration of SDBS, OP-10 and deinking agent. This was because deinking agent could weak the interfacial bonding force between ink and fiber. With the increasing of deinking agent, the strong emulsifying and dispersing ability of deinking agent could make ink particles decomposed too small, which was very difficult to be removed in the flotation process. The increments of brightness (IB) is main evaluating indicator in this experiment, so the optimum proportion for neutral deinking agent should choose the corresponding level of the maximum value of  $K_1$ ,  $K_2$  and  $K_3$ . The optimum proportion for neutral deinking agent is as follow: self-compounded deinking agent of 0.5%, OP-10 of 0.5% and SDBS of 0.1%. Table 1 shows the results of range analysis of neutral deinking. The addition of OP-10 has significant influence on the efficiency of neutral deinking, which is little better than those of deinking agent and SDBS. The OP-10 could facilitate the emulsification of ink, and then made ink particles separate from fibers.

**Table 1** The results of orthogonal experiment and range analysis

Number	A: Deinking agent (%)	B: OP-10 (%)	C: SDBS (%)	Brightness (%)	IB (%)	Pulp yield (%)
1	0.5	0.5	0.1	98.4	5.7	80.1
2	0.5	1.0	0.3	97.5	4.7	80.1
3	0.5	1.5	0.5	94.5	1.5	75.0
4	1.0	0.5	0.3	96.6	3.8	76.7
5	1.0	1.0	0.5	93.5	0.5	72.4
6	1.0	1.5	0.1	94.0	1.0	77.2
7	1.5	0.5	0.5	96.8	4.0	76.9
8	1.5	1.0	0.1	98.1	5.4	78.5
9	1.5	1.5	0.3	93.3	0.1	81.9
K <sub>1</sub>	11.9	13.5	12.1	R <sub>B</sub> > R <sub>A</sub> > R <sub>C</sub>		
K <sub>2</sub>	5.3	10.6	8.6			
K <sub>3</sub>	9.5	2.6	6.0			
R	6.6	10.9	6.1			
Optimum proportion	A <sub>1</sub>	B <sub>1</sub>	C <sub>1</sub>	Optimum proportion (A = 0.5%, B = 0.5%, C = 0.1%)		

**Table 2** Effect of curing temperature on the efficiency of neutral deinking

Curing temperature (°C)	40	50	60	70	80
Brightness (%)	92.6	95.4	96.1	97.3	87.1
Pulp yield (%)	73.7	80.1	73.6	76.8	78.4

Disposing conditions: deinking agent 0.5%, OP-10 0.5%, SDBS 0.1%, curing time 10 min, flotation time 9 min, pulping time 60 s

## 3.2 Single Factor Experiment

### 3.2.1 Influence of Curing Temperature

The brightness of ODP increased with the curing temperature up to 70 °C is shown in Table 2. However, The brightness of ODP begin to decrease when the curing temperature increased to 80 °C. So the optimum curing temperature is 70 °C, with the maximum brightness value of 97.3. The appropriate increasing of curing temperature can be beneficial to the soften of ink particles, and help to remove the ink particles from ODP [2]. However, too high curing temperature may change the properties of deinking agent, which can decline the brightness of ODP.

**Table 3** Effect of curing time on the efficiency of neutral deinking

Curing time (min)	5	10	15	20	25
Brightness (%)	93.7	94.6	98.0	96.3	95.2
Pulp yield (%)	73.3	77.8	76.8	71	69

Disposing conditions: deinking agent 0.5%, OP-10 0.5%, SDBS 0.1%, curing temperature 70 °C, flotation time 9 min, pulping time 60 s

**Table 4** Effect of flotation time on the efficiency of neutral deinking

Flotation time (min)	3	6	9	12	15
Brightness (%)	93.4	99.3	97.2	93.7	91.3
Pulp yield (%)	75.2	76.8	74.5	73.8	72.1

Disposing conditions: deinking agent 0.5%, OP-10 0.5%, SDBS 0.1%, curing temperature 70 °C, curing time 15 min, pulping time 60 s

### 3.2.2 Influence of Curing Time

Table 3 reveals that the curing time of neutral deinking has significant influence on the efficiency of deinking for ODP. The brightness of ODP increases firstly and then decreases, when the curing time increased from 5 to 25 min. The brightness of ODP increases with the curing time up to 15 min. However, The brightness of ODP begin to decrease when the curing time increased from 20 to 25 min. If the curing time was too long, more and more ink particles would redeposit on the pulp fiber, because of the bad foaming power of deinking agent and instability foaming, which could lead to the decline of brightness of ODP.

### 3.2.3 Influence of Flotation Time

As we can see from Table 4, the brightness of the ODP pulp reaches maximum value of 99.26%, with the flotation time up to 6 min. In the early flotation process, the foams could absorb more ink particles because of the big mass fraction of ink particles in the ODP pulp suspension. But with the increasing flotation time, the decline of the mass fraction of ink particles resulted in the low absorption of foams for ink particles in the pulp suspension. Moreover, The pulp yield of ODP increases firstly and then decreases. And the decrease of pulp yield of ODP was caused by the large number of small fiber mixed in the bubble. After comprehensive consideration, the optimum flotation time is 6 min with the brightness of 99.3% and pulp yield of 76.8%.

## 4 Conclusions

In this study, the mainly technical parameters of neutral deinking process on the domestic waste digital printing paper had been carried out. The orthogonal experiment of neutral deinking showed that the optimum proportion for neutral deinking agent was as follow: deinking agent of 0.5%, OP-10 of 0.5% and SDBS of 0.1%. And the single factor experiment illustrated that the suitable operation neutral deinking conditions for ODP as follow: curing temperature of 70 °C, curing time of 15 min and flotation time of 6 min. Under the optimum neutral deinking conditions for ODP, the brightness of deinking pulp of 99.3% SBD and the pulp yield of ODP of 76.8%.

**Acknowledgements** The authors appreciate the financial supported by Natural Science Foundation of Shanxi Province (2015JM3080), the Foundation of Xi'an urban and rural construction commission (104-221410).

## References

1. Meng, Q., Wan, J., Ma, Y. et al. (2013). Effect of different deinking processes on fiber morphology. *Bioresources* 8, (2):2398–2416.
2. Zhang, X. I., Wang R. m. (2011). OMG Neutral Deinking Technical Conditions and Mechanism. *Adv Mater Res* 236–238: 1351–1354.
3. Zhang, X., Renaud, S., Paice, M. (2008). Cellulase deinking of fresh and aged recycled newsprint/magazines (ONP/OMG). *Enzyme Microb Tech* 43, (2): 103–108.
4. Lapierre, L., Dorris, G., Merza, J. et al. (2004). Mill trials on near-neutral sulphite deinking Part II. *Pulp Pap-Canada* 105, (2):50–52.
5. Zhang X. I., Wang R. m. (2012). Effect of Deinking Process on Wastepaper Fiber Properties. *Transactions of China Pulp and Paper* 27, (1): 45–49.
6. Taylor, C., ALLEN, J., Hill, G. et al. (2006). A 10-day mill trial of near-neutral sulphite deinking, Part I: Deinked pulp optical and physical properties. *Pulp Pap-Canada* 107, (4): 54–57.
7. Lapierre, L., Castro, C., Kish, J. et al. (2006). A 10-day mill trial of near-neutral sulphite deinking Part III: Overall mill assessment. *Pulp Pap-Canada* 17, (5):39–43.



**Part IX**  
**Film and Related Material Technology**

# Preparation and Properties of Nano Zinc Oxide/Poly Lactic Acid Antibacterial Packaging Films

Xing Yin, Cheng Sun, Zhiqiang Gao and Li Xue

**Abstract** Nano zinc oxide (Nano-ZnO) has been a hotspot because of its excellent antibacterial properties. Nano-ZnO was added into the poly lactic acid (PLA) to form the antibacterial film, and then the properties were tested, including the antibacterial rate, mechanical property, light transmittance, haze, the water vapor permeability, surface and fracture morphology observed by SEM. It was showed that the packaging material had the antibacterial properties due to it was added with Nano-ZnO particles. The mass fraction of the Nano-ZnO was 6%, which could inhibit the growth of staphylococcus aureus and escherichia coli effectively. The mass fraction of the Nano-ZnO was 4%, the mechanical properties of the antibacterial film was the best. With the addition of Nano-ZnO, The light transmittance of the antibacterial film decreased, the haze increased. So it affected on visibility of product. Nano-ZnO/PLA antibacterial film as biodegradable functional material has a certain application prospects in the packaging.

**Keywords** Poly lactic acid · Nano zinc oxide (Nano-ZnO) · Antibacterial film · Composite packaging material

## 1 Introduction

Fruits and vegetables are vulnerable to the microorganism and lead to rot. Nano zinc oxide (Nano-ZnO) is a compound semiconductor material, which has a regular hexagonal wurtzite structure, and its form is white powder or red zinc ore. Its characteristics include good stability, wide antimicrobial spectrum, the effective

---

X. Yin (✉) · C. Sun · Z. Gao  
Packaging and Printing Engineering College, Tianjin University of Science and Technology,  
Tianjin, China  
e-mail: yvette8030@163.com

L. Xue  
Tianjin Vocational Institute, Packaging and Printing Engineering College, Tianjin, China

antimicrobial periods long, decomposition under the high temperature and low cost [1–3]. Therefore, it has been used increasingly in antibacterial materials [4–7].

Poly lactic acid (PLA) is a new type of biodegradable polymer materials which can be completely degraded in nature. And carbon dioxide and water are generated without pollution ultimately. It is recognized as environmentally friendly materials [8–10].

Nano-ZnO was added into the poly lactic acid (PLA) to form the antibacterial film, and then the properties of the packaging material were tested, including the antibacterial rate, mechanical property, light transmittance, haze, the water vapor permeability rate, and surface and fracture morphology observed by SEM. It provided a theoretical basis for developing the functional composite packaging materials.

## 2 Materials and the Method

### 2.1 Materials

Poly lactic acid (PLA), its shapes was granular, its relative molecular weight is 68,000, Dongguan City Zhangmutou Dafeng plastic materials management department. Methylene chloride ( $\text{CH}_2\text{Cl}_2$ ), absolute ethyl alcohol, sodium chloride, Tween 80, AR, Tianjin City air Chemical Reagent Co., Ltd. Nano Zinc Oxide (Nano-ZnO), model HQ-FL20, grain size 20 nm, sphere, Shanghai Pei Kun Industry Co. Ltd. *Escherichia coli*, *staphylococcus aureus*, College of Biological Engineering, Tianjin University of Science and Technology. Agar powder, beef extract, peptone, biological reagents, Beijing Star Biotechnology Co., Ltd. Obo.

### 2.2 Antibacterial Material Preparation

The PLA and Nano-ZnO were dried in an oven at 40 °C for 12 h before the experiment. The Nano-ZnO was stirred for 3 h in  $\text{CH}_2\text{Cl}_2$  at 25 °C by electric mixer, and the PLA was added until it completely dissolved. The concentration of PLA solution was 0.1 g/ml. The film was scratch by the automatic scraping film machine at a speed of 10 mm/s on a glass plate to ensure uniformity of the film thickness. After drying, the film was lifted and then it was dried in an oven at 50 °C for 24 h in order to the  $\text{CH}_2\text{Cl}_2$  was removed completely. The antibacterial rate was measured to find the best ratio of the Nano-ZnO. The mass fraction of the Nano-ZnO were 0, 2, 4, 6, 8, 10%, of which the mass fraction of Nano-ZnO = mass of the Nano-ZnO/(mass of the Nano-ZnO + mass of PLA).

## **2.3 Performance Measurement of Antibacterial Film**

### **2.3.1 Determination of Antibacterial Rate**

According to QB/T2591-2003, a series of antimicrobial films were cut at the  $(50 \pm 2) \text{ mm} \times (50 \pm 2) \text{ mm}$  standard size. PE film was as a cover film, and it was cut at the  $(40 \pm 2) \text{ mm} \times (40 \pm 2) \text{ mm}$  standard size. The 200  $\mu\text{L}$  bacterial liquid was extracted with pipette on the antibacterial film and then the cover film after sterilization was picked on the antimicrobial film by forceps. The bacteria were cultured at the temperature 37 °C, relative humidity greater than 90% for 24 h. The samples were cleaned by 20 mL eluent, and the 100  $\mu\text{L}$  bacterial liquid was inoculated on the nutrient agar under the same conditions. According to GB/T 4789.2, the number of viable cells was measured.

Each proportion was prepared for 5 parallel samples, then measured and averaged. The best mass fraction of the Nano-ZnO was found.

### **2.3.2 Determination of Mechanical Property**

According to GB/T1040-2006, the antibacterial film was cut into the size of 15 mm  $\times$  150 mm, clip distance was set to 50 mm, the tensile speed was set to 50 mm/min. The tensile strength and the breaking elongation of the antibacterial film were test. Each proportion was prepared for 10 parallel samples, then measured and averaged. The deviation value was  $\pm 5\%$ .

### **2.3.3 Determination of Light Transmittance and Haze**

According to GB/T2410-2008, the antibacterial film was cut into square pieces of 50 mm  $\times$  50 mm, and light transmittance and haze were tested. Each proportion was prepared for 5 parallel samples, then measured and averaged. The deviation value was  $\pm 5\%$ .

### **2.3.4 Determination of Water Vapor Permeability**

According to GB/T1037-1988, the antibacterial film was cut into area pieces of 33.18  $\text{cm}^2$ , and water vapor permeability was tested. The test condition was at RH 90% and 38 °C. Each proportion was prepared for 5 parallel samples, then measured and averaged. The deviation value was  $\pm 5\%$ .

### 2.3.5 Determination of Thickness

10 points of the antibacterial film were tested and then the results were averaged.

### 2.3.6 SEM of the Antibacterial Film

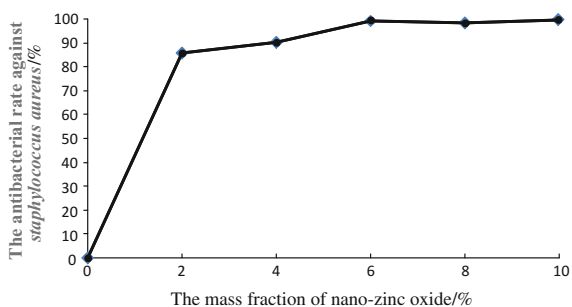
The surface and fracture of the antibacterial film were glue to the conductive glue, sprayed gold and tested by SEM, the scanning voltage was set at 10 kV.

## 3 Results and Discussion

### 3.1 Effect of Nano-ZnO Content of the Antibacterial Film on Antibacterial Rate

According to Figs. 1 and 2, the effect of Nano-ZnO/PLA antibacterial film against staphylococcus aureus and escherichia coli were significant. And the effect was more obvious as the content of Nano-ZnO increased.

**Fig. 1** Effect of Nano-ZnO content of the antibacterial film against staphylococcus aureus rate



**Fig. 2** Effect of Nano-ZnO content of the antibacterial film against escherichia coli rate

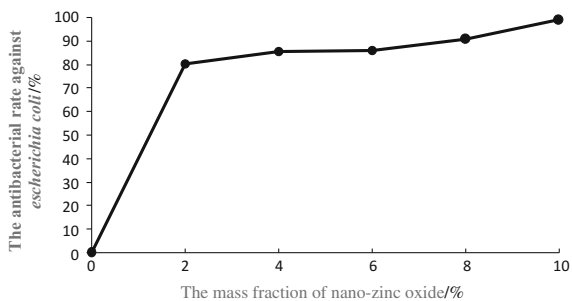


Figure 1 showed that the antibacterial rate against staphylococcus aureus reached 90.06% when the content of Nano-ZnO was 4%, and it was greater than II grade level of QB/T2591-2003 standard. And the antibacterial rate against staphylococcus aureus reached 99.18% when the content of Nano-ZnO was 6%, and it was greater than I grade level. Figure 2 showed that the antibacterial rate against escherichia coli reached 90.58% when the content of Nano-ZnO was 8%, and it was greater than II grade level of QB/T2591-2003 standard.

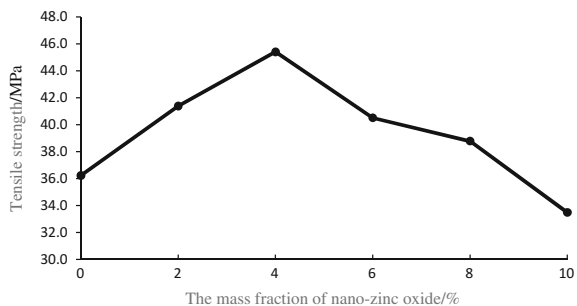
With the increase of the amount of Nano-ZnO, antibacterial affect had become increasingly significant. Because the amounts of nanoparticles were related to the antibacterial property, the more the amount of Nano-ZnO, the more release of the antibacterial metal ion, the more antibacterial property improving.

### 3.2 Effect of Nano-ZnO Content of the Antibacterial Film on Mechanical Property

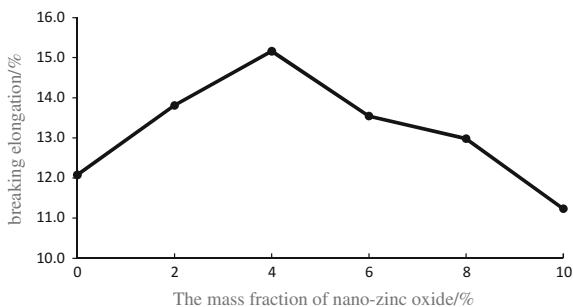
The Nano-ZnO content were 0, 2, 4, 6, 8, 10% respectively, and the average thickness of the antibacterial film were  $57.68 \pm 0.52$ ,  $58.75 \pm 0.7$ ,  $61.1 \pm 0.9$ ,  $67.42 \pm 0.2$ ,  $68 \pm 0.85$ ,  $75.05 \pm 0.92$   $\mu\text{m}$ .

Effect of Nano-ZnO content of the antibacterial film on tensile strength was shown in Fig. 3. With the increase of Nano-ZnO content, the tensile strength of the antibacterial film increased first and then decreased. When the content of Nano-ZnO was 4%, the highest tensile strength reached 45.40 MPa. When the mass fraction were 6, 8, 10%, the tensile strength were 40.51, 38.78, 33.50 MPa respectively. Because when the Nano-ZnO content was less than 4%, the Nano-ZnO particles uniformly dispersed among the PLA. Meanwhile nano particle was small particle size and large surface area, and interfacial interaction generated. Thus the tensile strength increased. When the Nano-ZnO content was higher than 4%, the nano particles reunited, the tensile strength decreased.

**Fig. 3** Effect of Nano-ZnO content of the antibacterial film on tensile strength



**Fig. 4** Effect of Nano-ZnO content of the antibacterial film on breaking elongation



**Fig. 5** Effect of Nano-ZnO content of the antibacterial film on light transmittance

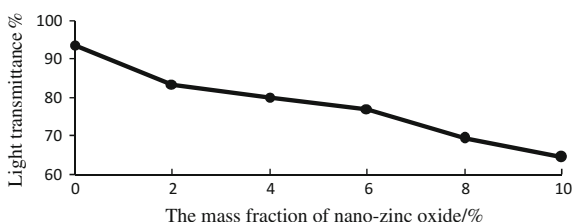
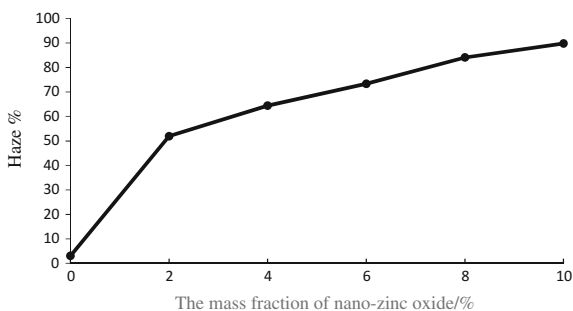


Figure 4 showed the effect of Nano-ZnO content of the antibacterial film on breaking elongation. When the content of Nano-ZnO was 4%, the breaking elongation reached a maximum of 15.16%. Due to the nanoscale particles was small particle size, large specific surface area and a large contact area with PLA, they could effectively disperse. The more the content of Nano-ZnO, the more the contact between particles, there may be reunion. Thus it could lead to a decline of tensile strength and breaking elongation [11].

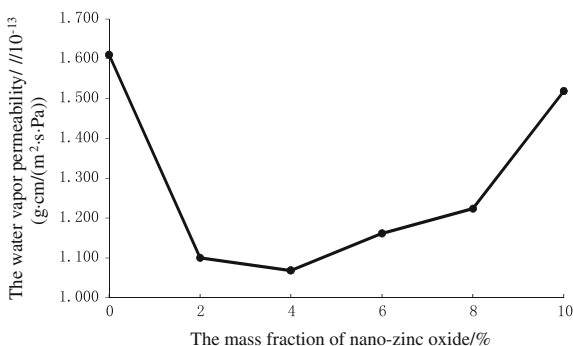
### 3.3 Effect of Nano-ZnO Content of the Antibacterial Film on Light Transmittance and Haze

Figure 5 showed the effects of Nano-ZnO content of the antibacterial film on light transmittance. The light transmittance of pure PLA was best. With the increase of Nano-ZnO content, the light transmittance of the antimicrobial film gradually decreased. The light transmittance of the 10% Nano-ZnO antibacterial film compared with pure PLA film declined by 29.25%. According to Fig. 6, the haze of pure PLA film was 3.095, and the haze of antibacterial film increased as the content of Nano-ZnO added more. Therefore, with the increase the content of Nano-ZnO film, light absorbed increased, transmitted light reduced and haze increased. Nano-ZnO/PLA antibacterial film had a certain effect on the degree of transparency and post-imaging products for packaging.

**Fig. 6** Effect of Nano-ZnO content of the antibacterial film on haze



**Fig. 7** Effect of Nano-ZnO content of the antibacterial film on the water vapor permeability coefficient



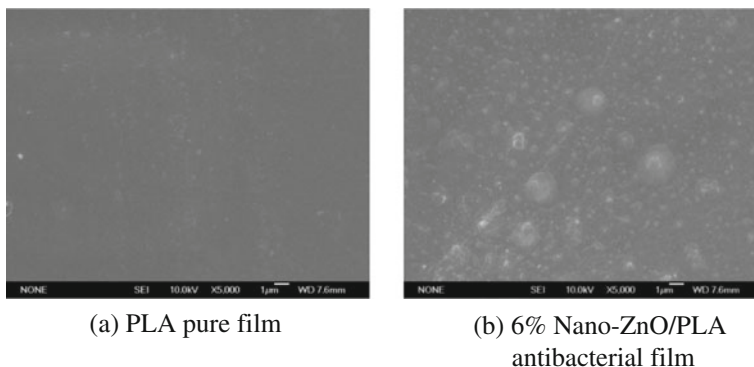
### 3.4 Effect of Nano-ZnO Content of the Antibacterial Film on the Water Vapor Permeability

Effect of Nano-ZnO content of the antibacterial film on the water vapor permeability coefficient was shown in Fig. 7. With the increase of Nano-ZnO content, the water vapor permeability of the antibacterial film decreased first and then increased. When the content of Nano-ZnO was 4%, the water vapor permeability coefficient was the minimum, to  $1.068 \times 10^{-13}$  g cm/(cm<sup>2</sup> s Pa), because a large number of Nano-ZnO particles penetrated into the amorphous regions of PLA, its structure was close and the porosity decreased, and it resulted the water vapor permeability decreased. When the content exceeded 4%, a lot of Nano-ZnO particles penetrated into PLA crystallization region, and it broke the film compact structure, and increased water vapor permeability coefficient.

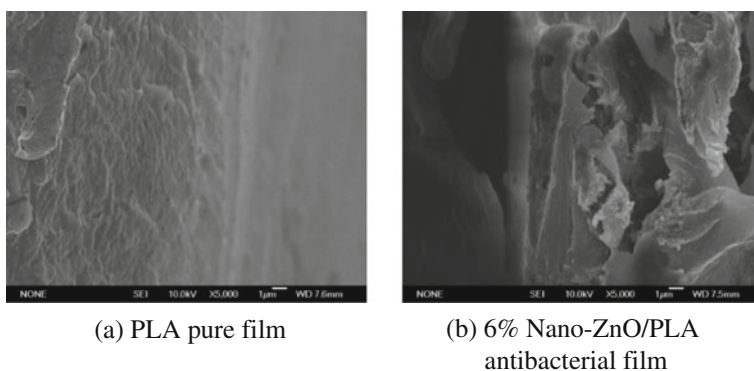
### 3.5 Morphology of Nano-ZnO/PLA Antibacterial Film

Figure 8a was SEM surface photo of PLA pure film. Its surface was relatively flat and smooth. Figure 8b was SEM plane photo of 6% Nano-ZnO/PLA antibacterial film. There were particles above the antibacterial film, which dispersed evenly. And the





**Fig. 8** SEM surface photo



**Fig. 9** SEM fracture photo

cracks or holes did not exist on the antibacterial film. From the SEM photo, the size of Nano-ZnO particle was uniform, dispersed good with local agglomeration [12–14].

Figures 9a, b showed the SEM fracture photo of PLA pure film and 6% of the mass fraction of Nano-ZnO/PLA antibacterial film respectively. The fracture of PLA pure film was a layered structure which was easy to brittle. The fracture of the antibacterial film was more rough, pores large, and it was consistent with the result of water vapor permeability.

## 4 Conclusions

(1) The effect of Nano-ZnO/PLA antibacterial film against staphylococcus aureus and escherichia coli was significant. When the content of Nano-ZnO was 4%, effect against staphylococcus aureus was obvious. When the content of Nano-ZnO was

6%, effect against *Escherichia coli* was obvious. (2) The Nano-ZnO added affected the mechanical properties of antibacterial films. When the mass fraction of the Nano-ZnO was 4%, the mechanical property of the antibacterial film was the best. More than 4% the value of tensile strength and breaking elongation decreased, the antibacterial film was easy to brittle fracture. (3) The light transmittance and haze were measured and analyzed, the light transmittance of pure PLA film was the best. With the increase of Nano-ZnO content, the transmittance of Nano-ZnO/PLA antibacterial film material reduced, the haze increased. (4) With the increase of Nano-ZnO content, the water vapor permeability of the antibacterial film decreased first and then increased. When the content of Nano-ZnO was 4%, the water vapor permeability coefficient was the minimum, to  $1.068 \times 10^{-13} \text{ g cm}^2 / (\text{cm}^2 \text{ s Pa})$ . (5) According to the SEM surface photo and fracture photo, there were particles above the antibacterial film which dispersed evenly, and the fracture of the antibacterial film was more rough, pores large than the PLA pure film.

## References

1. FengXia YANG, Qi-Li LIU, BI Lei. (2006). Research on the Application of Nano-Zinc Oxide. *Anhui Chemical Industry*, (1), 13–15.
2. Wenkui LIU. (2013). Characterization and properties of ZnO nanostructure. MA thesis, University of Hunan, Changsha, China.
3. Guangli WANG. (2011). Study on micro controlled synthesis and photocatalytic performance of nano-Zinc Oxide. MA thesis, Qufu Normal University, Rizhao, China.
4. Gang YU. (2007). Study on the Preparation and Characteristics of Nano-Zinc oxide Antibacterial Materials. MA thesis, Huazhong University of Science and Technology, Wuhan, China.
5. Meng LV. (2013). Study on preparation and properties of antibacterial film composed of fish gelatin, chitosan & nano-ZnO. MA thesis, Ocean University of China, Qingdao, China.
6. Ye LU, Fu-xin YANG, Heng-guang ZHANG. (2013) Preparation and Properties of Silver-loaded LDPE Antibacterial Films. *Packaging Engineering*, 11, 27–30.
7. Hui-juan KUANG, Lin Yang, Heng-yi XU etc. (2015). Antibacterial properties and mechanism of zinc oxide nanoparticles. *Chinese Journal of Pharmacology and Toxicology*, 2 (29): 153–154.
8. Qi ZHANG. (2012). Study on modification of poly lactic acid. MA thesis, Beijing University of Chemical Technology, Beijing, China.
9. Ning ZHANG, Jun-jie ZHANG. (2010). Recent progress in study of biomacromolecular material polylactide. *Journal of Hebei Polytechnic University(Natural Science Edition)*, 2010,32(3):116–120.
10. Qi ZHANG. (2012). Study on modification of poly lactic acid. MA thesis, University of Chemical Technology, Beijing, China.
11. Dutta RK, Nenavathu BP, Gangishetty MK. (2012). Studies on antibacterial activity of ZnO nanoparticles by ROS induced lipid peroxidation. *Colloids Surf B Biointerfaces*, 94: 143–150.
12. L Yang, Hyung-II K. (2012). Characterization and antibacterial properties of genipin-crosslinked chitosan/ poly (ethylene glycol)/ZnO/Ag nano composites. *Carbohydrate Polymers*, 89(1):111–116.
13. Jin-Fang CHEN. (2015). The preparation and characterization of compound nanometer ZnO and the application research on performance of photocatalyst. MA thesis, Dalian Ocean University, Dalian, China.
14. Hai-feng ZHANG. (2009). Surface Modification of Nano-ZnO and Effects on Properties of Acrylic Polyurethane. MA thesis, Jiangsu University of Science and Technology, Zhenjiang, China.

# Barrier Mechanism Analysis of Silicon Oxide Film by SEM

Lihua Zhu, Yan Li, Wensi Liang, Jun Wu, Yunjin Sun  
and Yun Ouyang

**Abstract** Since barrier packaging materials go through low barriers of polyethylene (PE) to middle barriers of polyester (PET) and even to high barriers of Polyvinyl Dichloride (PVDC), Ethylene vinyl alcohol copolymer (EVOH) and Aluminum foil, the rise of silicon oxide film represents the novel trend in the barrier packaging area due to super-barrier, transparent, micro-wave able, printing adaptability and high addition values, however, how to effectively test the barrier properties of silicon oxide film will become key point to realize the industrial application of its lamination packaging materials. Given that barrier characteristics of barrier materials is relate with all kinds of factors, based on the previous study, we compare different samples manufactured by different preparation methods and found that Scanning Electron Microscopy (SEM) is an effective and direct measurement tool to characterize the barrier properties. The interface variations of coating samples induced by electron beam evaporation, magnetron sputtering, ion assisted electron beam evaporation and plasma enhanced chemical vapor deposition were compared in this study, and it could be concluded that surface roughness and internal stress mainly contribute to coating quality and barrier properties, which could be used to determine the level of barrier performance.

**Keywords** Silicon oxide film · Barrier properties · SEM

## 1 Introduction

In the food packaging industry, more and more packaging materials appear with advanced requirements from the customers and manufacturers to further reduce the barrier coefficient against oxygen gas, special flavor and water vapor. Especially,

---

L. Zhu · Y. Li · W. Liang · J. Wu · Y. Sun (✉)  
Beijing Laboratory of Food Quality and Safety, Faculty of Food Science  
and Engineering, Beijing University of Agriculture, Beijing, China  
e-mail: aosdf2@163.com

Y. Ouyang  
China Academy of Printing Technology, Beijing, China

some ready-to-eat food in short shelf life will decay or deteriorate when exposed to gas, moisture and flavor if no barrier packaging process is performed. Otherwise, some food juice, beer or liquid beverage is also easy to be oxidized due to long transportation and storage period. Thus, barrier packaging technology has been strongly demanded to be widely used in food packaging application. Based on the barrier coefficients and related performance, barrier packaging material can be divided into three stages, take OTR for example, those include low barrier in more than  $200 \text{ cc/m}^2 \text{ day atm}$ , middle barrier from 10 to  $200 \text{ cc/m}^2 \text{ day atm}$  and high barrier levels in less than  $10 \text{ cc/m}^2 \text{ day atm}$ . Correspondingly, all the packaging polymer materials can be obviously classified into three groups from the viewpoint of packaging materials: First, normal organic polymers with no barrier functions are usually used as packing or to laminate with other films, such as low-density polyethylene (LDPE), high-density polyethylene (HDPE), cast polypropylene film (CPP), Polyamide (6); Second, normal barrier packaging polymers with middle barrier dominate the barrier market, such as PET, PVDC and EVOH; Third, high barrier packaging materials in development are gradually showing its faces in public, such as laminated aluminum foil, metal container and ceramic oxide compounds [1].

As one of representative ceramic oxides, silicon oxide film shows its outstanding characteristics, such as super-barrier, transparent, micro-waveable, excellent printing adaptability and high addition values. Theoretically, silicon oxide film has absolutely zero permeation against gas, moisture or flavor since barrier property can mainly be determined by diffused and transmitted coefficients, both of which can be reduced to zero for silicon oxide films. As for the optimized barrier depth for different preparation method is in the nanoscale of 50–300 nm [2], barrier performance of silicon oxide film is sincerely affected by surface topology and roughness. In fact, defect, pinhole and micro crack always exists inside [3] during various preparation processes, such as sol-gel methods [4], electron beam vapor deposition [5], magnetron sputtering [6] and plasma enhanced chemical vapor deposition [7]. Although more attention and efforts has been paid on the relationship between barrier properties and film components, discharge source, film structure for different preparation methods [8], barrier mechanism and dominant influence factors are seldom elucidated in detailed to distinguish and filter the most possible preparation methods for the future potential applications.

In this study, a novel and effective comparison method has been brought out to obviously elucidate barrier principle of silicon oxide film though different preparation methods.

## 2 Experiments

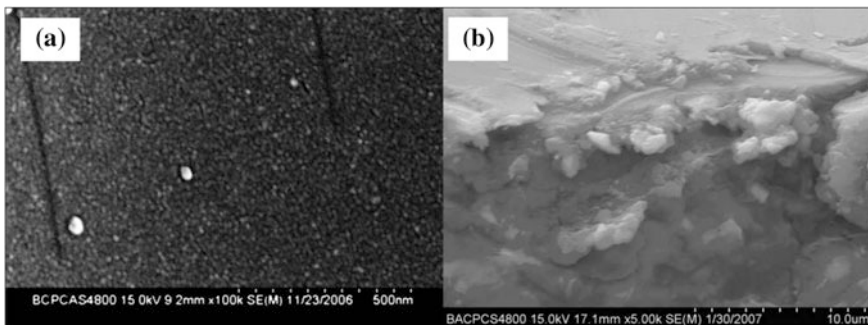
Testing samples, which are manufactured by four typical manufacturing methods including plasma enhanced chemical vapor deposition (PECVD), electron beam evaporation (EB), ion source assisted electron beam deposition (IAEB) and

magnetron sputtering deposition (MS), are analyzed by Scanning Electron Microscopy (Sirion, S-4800IIFE-SEM, Holland and Shimadzu, SEM-5500, Japan) to reveal the surface topology and thus indicate the barrier principle. In order to guarantee the consistency of experimental results, all the films are deposited on PET substrate with the depth of 12.5  $\mu\text{m}$ .

For PECVD, Hexamethyldisiloxane (HMDSO) is used as the precursor with addition of oxygen gas, which was deposited based on the magnetic field enhanced plasma technology [9]. The voltage for EB method is set as 6 kV with  $\text{SiO}_2$  as original evaporated source and Argon is chosen to be sputtering gas with oxygen as reactive gas to oxide sputtered grains from silicon target for MS.

### 3 Results and Discussions

Silicon oxide film can be deposited on various polymers to improve the barrier properties of matrix, and PET is one of most alternative substrates due to relative higher glass temperature and strong mechanical strength. Before deposition process, organic polymer substrate are usually pretreated by surface corona treatment, which indicate in our previous results that pretreated samples have a higher barrier performance and better interfacial adhesion due to surface cleaning and bond activation [9]. As for no pretreated samples, debris, micro grains and impurity usually exist on the surface and subsequently change subsequently coating surface, as shown in Fig. 1a. This micro impurity always leads to micro cracks or pinhole, which have a detrimental effect on the barrier properties since Grüniger et al. [7] found that the existence of persistent pores in the substrate is in direct relation with the success of a silicon oxide coating in terms of the reduction of the oxygen permeability. Meanwhile, cross section indicate that substrate is a lay-by-lay stacked in the three dimensional direction, and could not guarantee absolute barrier functions [5]. Therefore, the surface coatings of silicon oxide film will compensate this drawback by forming ceramic and dense barrier walls as will be elucidated later.



**Fig. 1** Surface (a) and Cross (b) section of blank PET for next deposition process

Generally, silicon oxide layer coated on PET substrate is less than several hundred nanometers to completely cover the whole surface while keep flexible properties in a certain degree for post laminated process. However, some preparation methods can not produce this kind of ideal barrier samples in a nanoscale depth. For example, coating topology through MS can be clearly seen in Fig. 2a, the whole coated film is not complete and continuous, which have a little positive effect on the barrier properties. Although electron beam evaporation method has a high deposition rate by direct solid grain evaporation [5], the deposited coating consists of various islands, leaving cracks and pinholes as shown in Fig. 2b. It can be deduced that barrier properties of samples manufactured by above two methods can not fit for modern enhanced barrier requirements, such as food and organic light emitting diode packing.

In comparison to EB and MS, PECVD has a low deposition rate but good adhesion to substrate by covalent binding to surface groups of substrate as shown in Fig. 3a. Interface line is not clearly figured out, indicating the coating is strongly combined to the substrate. Literatures indicate that PECVD coated film has a certain degree of carbon content originating from the organic silicon precursor, which

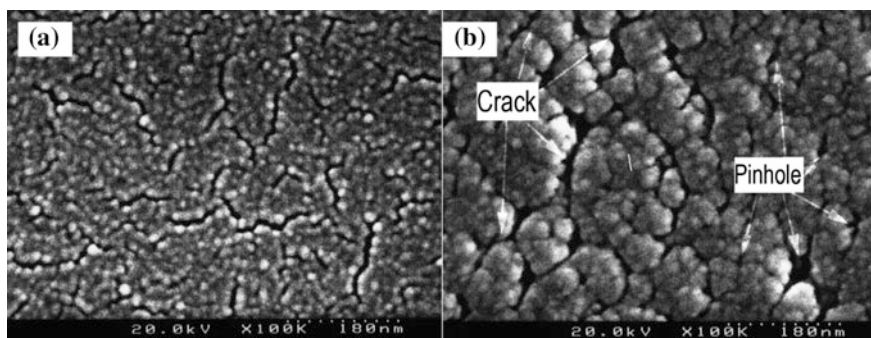


Fig. 2 Surface topology of silicon oxide films by MS (a) and EB (b)

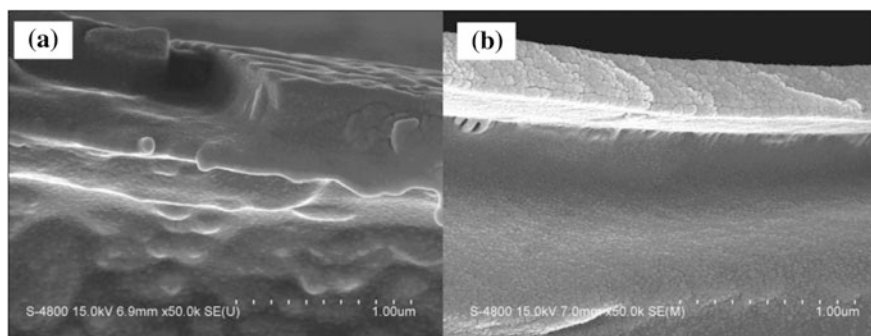


Fig. 3 Cross topology of silicon oxide films by PECVD (a) and IAEB (b)

**Table 1** OTR and WVTR scope of silicon oxide films as indicated by OTR and WVTR [2, 6, 11]

Items	MS	EB	IAEB	PECVD
OTR (cc/m <sup>2</sup> day atm)	>20	1–20	1–5	0.1–1
WVTR (g/m <sup>2</sup> day, RH 90%, 38 °C)	>20	–	1–5	0.1–1

breaks crystalline order of silicon oxide and form amorphous state [6, 9]. Therefore, the amorphous silicon oxide film shows a good barrier property against to gas or moisture. In contrast, EB coated film is assisted by ion source to gain a dense and homogenous silicon oxide layer as shown in Fig. 3b, but high crystalline degree will reduce the adhesion to substrate and increase the brittleness, leading to the gas permeation through grain boundary.

Barrier properties for silicon oxide coatings can be expressed as follows:

$$Q = \frac{K \times A \times t(p_1 - p_2)}{L} \quad (1)$$

where, Q is transmission rate, L is coating depth, K is the permeation coefficient, A is the effective surface area, P is the gas pressure.

It can be easily deduced that the key point for barrier function is the permeation coefficient, which can be indicated as  $K = D \cdot S$ , D is diffusion degree and S is solubility degree. For organic polymer films, it is difficult to avoid gaps between polymer chains due to high free volume of each atom, resulting in higher D and S since polymer films have low density and more flexibility [5]. However, the value of S for ceramic coating is nearing to zero and that of D is strong dependent on the surface topology since micro cracks and pinholes will give gas or moisture the channel to pass through [3], as can be diagnosed by surface topology. Therefore, it can be concluded that SEM is a directive and effective tool to assess the barrier properties of silicon oxide films. Meanwhile, OTR and WVTR results indicate that samples deposited by magnetron sputtering and electron beam evaporation are more than 20.0 cc/m<sup>2</sup> day atm while those by PECVD and IAEB are less than 5.0 cc/m<sup>2</sup> day atm as shown in Table 1, which is consistent with our SEM measurements from the viewpoint of defect barrier mechanisms [10], and the close relationship between the surface topology and barrier properties will need to be further studied in the future research, such as grain size, inert stress, adhesion force and coating density and so on.

## 4 Conclusions

Silicon oxide films are prepared on PET substrate to enhance the barrier properties of composite films in food packaging application by four typical deposition methods such as magnetron sputtering, electron beam evaporation, ion assisted electron beam evaporation and plasma enhanced chemical vapor deposition.

The surface topology indicate that micro crack and pinhole exist for samples from electron beam evaporation and magnetron sputtering while continuous and good adhesive to substrate is observed for plasma enhanced chemical vapor deposition and ion assisted electron vapor deposition. Finally, from the view point of barrier mechanism, our results indicate that SEM is directive and effective tool to assess the barrier properties of silicon oxide films, which is consistent with OTR and WVTR results.

**Acknowledgements** This article was financially supported by Key Construction Discipline Program of Beijing Municipal Commission of Education (PXM2014-014207-0000029), Youth Science Fund Project of Beijing University of Agriculture and Youth Teacher Foundation of Da Bei Nong Group of Beijing University of Agriculture (14ZK006).

## References

1. Czeremuskin, G., Latrèche, M., Wertheimer, M.R., Silva Sobrinho, A.S. (2001). Ultrathin silicon-compound barrier coatings for polymeric packaging materials: An industrial perspective. *Plasma And Polymers* 6: 107–120.
2. Howells, D.G., Henry, B.M., Madocks, J., Assender, H.E. (2008). High quality plasma enhanced chemical vapor deposited silicon oxide gas barrier coatings on polyester films. *Thin Solid Films* 516: 3081–3088.
3. Grüniger, A., Rudolf von Rohr, P. (2004). Influence of defects in SiO<sub>x</sub> thin films on their barrier properties. *Thin Solid Films* 459: 308–312.
4. Neiss, E., Flury, M., Gérard, P., Mager, L., et al. (2008). Multi-level relief structures in sol-gel and photoresist fabricated by laser ablation and analyzed with coherence probe microscopy. *Applied Surface Science* 254: 1986–1992.
5. Roberts, A.P., Henry, B.M., Sutton, A.P., et al. (2002). Gas permeation in silicon-oxide/polymer (SiO<sub>x</sub>/PET) barrier films: role of the oxide lattice, nano-defects and macro-defects. *Journal of Membrane Science* 208: 75–88.
6. Iwamori, S., Gotoh, Y., Moorthi, K. (2003) Characterization of silicon oxynitride gas barrier films. *Vacuum* 68:113–117.
7. Grüniger, A., Rudolf von Rohr, P., (2003). Deposition of SiO<sub>2</sub>-like diffusion barriers on PET and paper by PECVD, *Surface and Coating Technology* 174–175:1043–1047.
8. Liehr, M., Wieder, S., Dieguez-Campo, M. (2006). Large area microwave coating technology. *Thin Solid Films* 502:9–14.
9. Sun, Y.J., Fu, Y.B., Chen, Q., et al. (2008). Silicon dioxide coating deposited by PDPs on PET Films and influence on oxygen transmission rate. *Chin. Phys. Lett.* 25, 5: 1753–1756.
10. Rochat, G., Leterrier, Y., Garamszegi, L., Manson, J.AE., Fayet, P. (2003) Durability of hybrid PECVD-based coatings on semicrystalline polymers. *Surface and Coating Technology* 174–175:1029–1032.
11. Iwamori, S., Gotoh, Y., Moorthi, K. (2003). Silicon oxide gas barrier films deposited by reactive sputtering. *Surface and Coating Technology* 166: 24–30.



# Preparation and Characterization of Cellulose Gel Films

Junran Li, Xiaojun Ma, Yunfei Wang and Xuejiao Zhang

**Abstract** In this study, 7 wt% NaOH/12 wt% urea/81 wt% aqueous solvent was used to dissolve the cellulose in low temperature condition, and researched the cellulose content how to influence the cellulose gel films which were prepared by a casting method. The characterization methods involved mechanical properties, Scanning Electron Microscopy (SEM), Fourier Transform Infrared Spectroscopy (FTIR), and X-Ray Diffraction (XRD). The results showed that mechanical properties increased at first and then decreased with the cellulose content increased. The mechanical properties was best when cellulose content was 3.6 wt%; SEM pictures showed that the cellulose gel films surface was rough and had large holes or crack when the cellulose content below or above 3.6 wt%; XRD patterns revealed the crystallinity of cellulose gel films with 4.0 wt% cellulose was the biggest. The lattice planes and crystal grain growth of the cellulose film with 3.6 wt% cellulose was better. FTIR showed that the sensitive groups of cellulose films with different contents of cellulose were not essentially different.

**Keywords** Cellulose · Gel films · Preparation · Biodegradation

## 1 Introduction

In recent years, the growing environmental pollution which caused by polymer materials made the research began to focus on green materials. Cellulose is a renewable natural polymer, which becoming a hot spot of green material research because of its high strength, low price and bio-degradability [1]. Intramolecular and

---

J. Li (✉)

College of Packing and Printing Engineering, Tianjin University of Science and Technology, Tianjin, China  
e-mail: lijunran999@126.com

X. Ma · Y. Wang · X. Zhang

Tianjin Food Safety and Low Carbon Manufacturing Collaborative Innovation Center, Tianjin, China

© Springer Nature Singapore Pte Ltd. 2017

P. Zhao et al. (eds.), *Advanced Graphic Communications and Media Technologies*, Lecture Notes in Electrical Engineering 417, DOI 10.1007/978-981-10-3530-2\_128

1045

intermolecular hydrogen bond exist in cellulose, which makes it not only maintain high strength characteristics, but also difficult to dissolve in common solvents [2]. Therefore, it is the key to choose solvent with high cellulose dissolving rate for preparing a good performance cellulose film.

Cellulose solvents can be divided into derivatization system and under derivatization system [3, 4]. The main derivative solvent system includes  $\text{CS}_2/\text{NaOH}/\text{H}_2\text{O}$  system, paraformaldehyde/dimethyl sulfoxide (PF/DMSO) system, etc. The common under derivatization system comprises  $\text{NaOH}/\text{urea}/\text{water}$  system, the ionic liquid system, etc. [5, 6]. Advantageously, the  $\text{NaOH}/\text{urea}/\text{water}$  system can quickly dissolve cellulose, and has a low cost, non-toxic, recyclable, etc. [7]. Chen et al. [8], Dormanns et al. [9], utilized  $\text{NaOH}/\text{urea}/\text{water}$  system dissolve cellulose and research their relative performance.

Cellulose solution needs to be coagulated and regenerated by using the coagulant. Different coagulants and solidification conditions would be prepared different cellulose gel films with diverse forms and characteristics [10]. Water,  $\text{H}_2\text{SO}_4/\text{Na}_2\text{SO}_4$  solution and ethanol are commonly used coagulant [11–13]. Using different coagulant would form different density gel films, which can be applied in different areas. Cellulose gel films can be used in biological substrate composite materials, drug delivery, packing materials, etc. [14, 15], or as a substrate which can composite with other materials.

Cellulose could be used in the packaging fields, and it could effectively reduce the environmental pollution caused by white pollution. Cellulose gel films conformed to the requirements of green packaging. In this paper,  $\text{NaOH}/\text{urea}/\text{water}$  system was utilized to prepare the cellulose gel films with different content cellulose. The physical and mechanical properties of the cellulose gel films were characterized by mechanical properties testing, SEM, FTIR and XRD.

## 2 Experimental

### 2.1 Materials

Cotton pulp (degree of polymerization of 467);  $\text{NaOH}$ , urea, methanol, acetone and ethanol; Homemade deionized water.

### 2.2 Preparation of Cellulose Gel Films

#### 2.2.1 Cellulose Pretreatment

Cotton pulp was dried at  $110\text{ }^\circ\text{C}$  for 2 h, then smash with the grinder to obtain cottony cotton cellulose. The cellulose was soaked in deionized water, methanol and acetone for 24 h, respectively, filtered after each soaking then dried at  $110\text{ }^\circ\text{C}$ .

## 2.2.2 Preparation of Cellulose Gel Films

The different content of cellulose dissolved in 7 wt% NaOH/12 wt% urea/81 wt% aqueous system, it could get transparent cellulose solution by stirring in high speed after frozen for a period of time. Three kinds of 40 g clear solutions which contain 3.2, 3.6 and 4.0 wt% cellulose respectively were transferred to glass plate and got the cast films. Then the cellulose gel films were coagulated with 60% of ethanol for 40 min, the wet gel films were washed several times with deionized water and then dried.

## 2.3 Test

### 2.3.1 Mechanical Properties

The mechanical performance tests of cellulose films were according to the standard ASTM D882-2010. The tensile strength, elongation at break and modulus of elasticity of the materials were got by mechanical properties testing.

### 2.3.2 Scanning Electron Microscopy

The surface morphology of the cellulose films were examined by JSM-6360LV (JEOL, Japan). The specimen was sprayed gold treatment.

### 2.3.3 Fourier Transform Infrared Spectroscopy

The instrument was used by Nicolet 6700 (Thermo electron, US). The films were scanned 8 times in the range of 500–4000  $\text{cm}^{-1}$ .

### 2.3.4 X-Ray Diffraction Analysis

The X-ray diffraction instrument was used by D/max-2500 (Rigaku). The diffraction angle ranged from 5 to 80. Scanning rate was  $2^\circ/\text{min}$ .

## 3 Results and Discussion

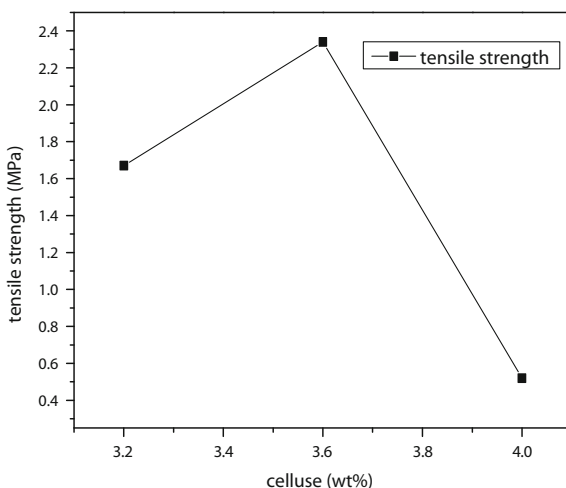
### 3.1 Mechanical Properties of the Cellulose Films

The experiments results showed that the cellulose solution couldn't be solidified to prepare film due to the low cellulose concentration which less than 3.2 wt%; when

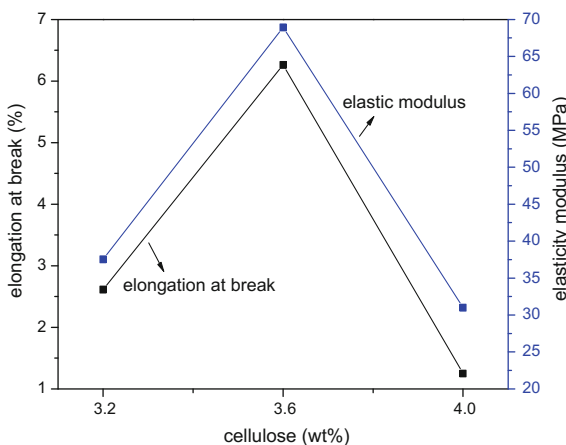
the cellulose content was higher than 4.0 wt%, the cellulose couldn't form a uniform transparent solution which contained a large amount of bulk fiber when stirred with homogenizer. Therefore, the cellulose films with 3.2, 3.6, 4.0 wt% were used to prepare test samples.

Figure 1 was tensile strength of the cellulose films. With the cellulose content increased, the tensile strength of the cellulose films increased at first and then decreased. The tensile strength of the cellulose films with 3.2, 3.6 and 4.0 wt% cellulose were 1.67, 2.34, 0.52 MPa, respectively, which increased by 40.1%, then decreased by 77.8%. It was because that solved cellulose restructured to form less hydrogen bonds when the concentration was low, while dissolved cellulose inhibited the rearrangement of hydrogen bonds when the concentration was too high, which caused the tensile strength of cellulose films with 3.2 and 4.0 wt% cellulose was lower than cellulose films with 3.6 wt% cellulose. Figure 2 were the

**Fig. 1** The tensile strength of the cellulose films with different content cellulose



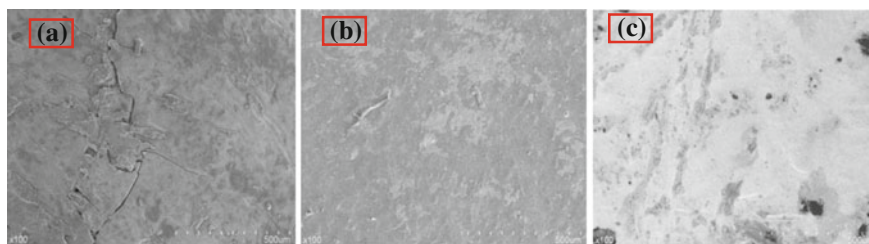
**Fig. 2** The elongation at break and modulus of elasticity of the cellulose films with different content cellulose



elongation at break and modulus of elasticity of cellulose films. The elongation at break of cellulose films with 3.2, 3.6 and 4.0 wt% cellulose was 2.613, 6.262 and 1.25%, and the modulus of elasticity was 37.54, 68.93, 30.99 MPa, respectively. The trend of the elongation at break and elastic modulus of the cellulose films was increasing at first and then decreasing with the increase of the cellulose content. Based on the above, we can draw a conclusion that the internal bond strength was the largest inside the cellulose films with 3.6 wt% cellulose, and it had the best mechanical properties.

### 3.2 Surface Morphology of the Cellulose Films

Generally, there were two forms of film surface which were prepared by flow casting method: one had some micellar aggregation pores formed by adjacent micellar aggregation, the pores' size was larger but fewer; the other was the small molecules restructuring to form new hydrogen bonds after decomposition, its surface was smooth and density. Figure 3 showed the SEM of the cellulose films with 3.2, 3.6 and 4.0 wt% cellulose, respectively, which magnify the surface morphology 100 times. There were obvious cracks on the surface in the figure a; in Fig. 3c, we could see apparent porosity and surface roughness, even urea precipitation. Differently, Fig. 3b showed smooth surface. After the dissolution of the cellulose, at the process of cellulose regeneration and solidification, hydrogen bonds between cellulose intramolecular and intermolecular chains restructured, cellulose solution gradually turned into cellulose gel state which contained solvent. Compared with the cellulose films with 3.6 wt% cellulose, the number of intramolecular hydrogen bonds restructured was less when the cellulose concentration was 3.2 wt%, so the strength was lower. When the content was 4.0 wt%, there was a lot of insoluble cellulose in the solvent, the relationship was not decomposed and restructured between cellulose, but partly dissolved cellulose acted as adhesives to bond the insoluble cellulose which resulted in the reduction of the hydrogen bond and emerged a large number of pores.



**Fig. 3** a–c are the scanning of electron microscope of the cellulose films with 3.2, 3.6 and 4.0 wt% cellulose, respectively

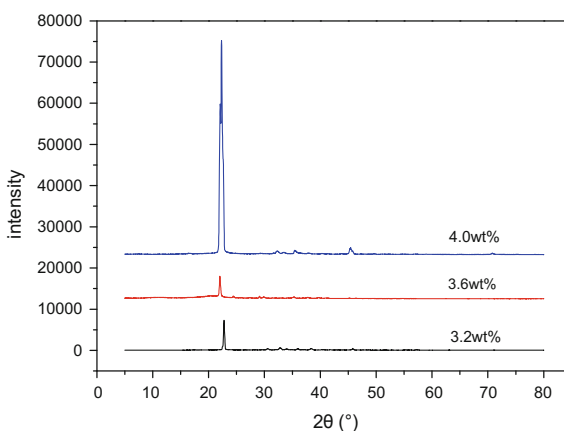
### 3.3 X-Ray Diffraction Analysis of the Cellulose Films

Figure 4 compared the XRD patterns of the cellulose films. XRD patterns revealed that all the cellulose had the diffraction peak which located at around  $22.5^\circ$  diffraction Angle, the  $22.5^\circ$  diffraction Angle represented the (002) lattice planes of cellulose I structure, The intensities of the diffraction peaks were quite different, the intensities of the cellulose films with 4.0 wt% cellulose was much greater than the cellulose films with 3.6 and 3.2 wt% cellulose, this showed that the crystallinity of cellulose films with 4.0 wt% cellulose was much larger. Because of the larger crystallinity, the brittleness of cellulose films with 4.0 wt% cellulose increased, for above reason, the mechanical properties were poor. Compared with the cellulose film with 3.2 wt% cellulose, the diffraction peak of the cellulose film with 3.6 wt% cellulose was broad and dispersive, this indicated that its' lattice planes and crystal growth was better, meanwhile, the degree of crystallinity was smaller. The lattice planes growth of the cellulose films with 3.2 wt% cellulose was poor, so its' mechanical properties was lower than the cellulose films with 3.6 wt% cellulose.

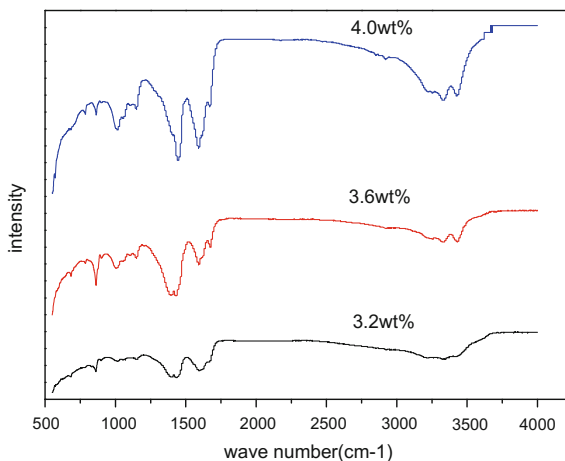
### 3.4 Fourier Transform Infrared Spectroscopy (FTIR) Analysis

Figure 5 compared the FTIR spectroscopy of the cellulose films. The sensitive groups of cellulose films with different content cellulose were not essentially different. With the cellulose content increased, FTIR spectrum of  $-OH$  stretching vibration showed a increment in the intensity of absorption band at  $3331\text{ cm}^{-1}$ , this indicated that the hydroxyl content increased. There was no sharp absorption peak at  $3600\text{--}3650\text{ cm}^{-1}$ , this because that it hadn't free hydroxyl groups in the cellulose films. A  $-CH_2$  shear vibration weak peak appeared around the band at  $1431\text{ cm}^{-1}$ , this was caused by

**Fig. 4** X-ray diffraction of the cellulose films with different content cellulose



**Fig. 5** FTIR of the cellulose films with different content cellulose



breakage of the hydrogen bonds in the  $-\text{CH}_2-\text{OH}$  groups at the process of dissolution, the hydrogen bonds fractured, then new intramolecular hydrogen bonds formed. The intensity of C–O stretching vibration peak at  $1013\text{ cm}^{-1}$  of the cellulose films with 4.0 wt% cellulose was much higher than the others, this indicated that the former cellulose dissolved uncompletely. The absorption band at  $897\text{ cm}^{-1}$  was assigned to the C–O–C stretching vibration at  $\beta$ -(1  $\rightarrow$  4)-glycosidic linkages, which was considered as amorphous band [16], the cellulose films with 3.6 wt% cellulose exhibited the very strong peak, indicated that the degree of crystallinity was minimum, as observed from the XRD analysis.

## 4 Conclusions

In this paper, cellulose was dissolved in the NaOH/urea/water system to prepare the cellulose gel films with different content cellulose and compared the properties. Mechanical properties test results showed that the tensile strength, elongation at break and elastic modulus of cellulose films with 3.6 wt% cellulose were the best, which values were 2.34 MPa, 6.262% and 68.93 MPa, respectively. SEM results showed that the film surface was smooth and defect-free of cellulose films with 3.6 wt% cellulose. XRD patterns revealed that the diffraction peak of the cellulose film with 3.6 wt% cellulose was broad and dispersive, and had the smallest crystallinity. FTIR showed the characteristic peak of cellulose, and provided an important basis to explain the mechanical properties of cellulose films.

**Acknowledgements** This work is supported by the national natural science fund project (31270607), and the national college students' innovative entrepreneurial training program (201510057007).

## References

1. Lee Ken Voon, Suh Cem Pang, Suk Fun Chin. (2016). Highly porous cellulose beads of controllable sizes derived from regenerated cellulose of printed paper wastes. *Materials Letters*, 164: 264–266.
2. Mukund Adsul, Sarvesh K. Soni, Suresh K. Bhargava, et al. (2012). Facile Approach for the Dispersion of Regenerated Cellulose in Aqueous System in the Form of Nanoparticles. *Biomacromolecules*, 13: 2890–2895.
3. Hongjuan Geng. (2014). Structures and Properties of Cellulose Films and Gels Prepared In Low Temperature Dissolution System. Shandong: Qilu University technology.
4. Bi Xiong. (2014). NMR Studies on the Mechanism of Cellulose Dissolution in Alkali/urea Solvent System. Wuhan: Wuhan University.
5. Xiaogang Luo, Lina Zhang. (2013). New solvents and functional materials prepared from cellulose solutions in alkali/urea aqueous system. *Food Research International*, 52: 387–400.
6. YuXia LV, XiaoYan LI, QinYong MI, et al. (2011). Cellulose aerogels prepared from cellulose/AmimCl solutions. *Science in China: Chemistry*, 41(8): 1331–1337.
7. Jianai He, Junlong Song. (2012). Cellulose dissolve in NaOH/urea. *Jiangsu Paper*, (2): 29–32.
8. Xiong Chen, Jinghuan Chen, Tingting You, et al. (2015). Effects of poly-morphs on dissolution of cellulose in NaOH/urea aqueous solution. *Carbohydrate Polymers*, 125: 85–91.
9. Jan W. Dormanns, Jeremias Schuermann, Jörg Müssig, et al. (2016). Solvent infusion processing of all-cellulose composite laminates using anaqueous NaOH/urea solvent system. *Composites: Part A*, 82: 130–140.
10. Yuan Mao. (2005). Studies on Coagulation Conditions of Cellulose Membrane and Fiber in NaOH/Urea Aqueous Solution. Wuhan: Wuhan University.
11. Yangcheng Lv, Yingxin WU. (2007). Influence of Coagulation Bath on Morphology of Cellulose Membranes Prepared by NMMO Method. *Journal of Chemical Engineering of Chinese Universities*, 21(3): 398–403.
12. Yun Lu. (2014). Research of aerogel-like functional materials via hierarchical assembly of biopolymer micro-/nano-building blocks. Herbin: Northeast Forestry University.
13. Xuan Zhong, XiantaoTong, Yue Zhang, et al. (2014). Effects of coagulation components on structures and properties of cellulose fibers from cellulose doped in NaOH/thiourea/urea aqueous solution. *Journal of Cellulose Science and Technology*, 22(1): 12–17.
14. Miikka Visankoa, Henrikki Liimatainenb, Juho Antti Sirviöc, et al. (2014). Porous thin film barrier layers from 2,3-dicarboxylic acid cellulose nano-fibrils for membrane structures. *Carbohydrate Polymers*, 102: 584–589.
15. Kathirvel Ganesan, Anne Dennstedt, Adam Barowski. (2016). Design of aerogels, cryogels and xerogels of cellulose with hierarchical porous structures. *Materials and Design* 92: 345–355.
16. Geng H.J., Yuan Z.W., Fan Q.R., et al. (2014). Characterization of cellulose films regenerated from acetone/water coagulants. *Carbohydrate Polymers*, 102: 438–444.



# Preparation and Research of POSS Modified PLLA Films: Mechanical Properties

Xiaohui Zhang and Feiyan Zheng

**Abstract** Octa ( $\gamma$ -chloroammoniumpropyl) octasilsesquioxane (POSS-NH<sub>3</sub>Cl) is used to improve the properties of PLLA by grafting in the paper. Star-shaped polymer that polylactic acid grafted with polyhedral oligomeric silsesquioxane (POSS-g-PLLA) is prepared, POSS-NH<sub>3</sub>Cl and L-lactic acid (L-LA) are used as reagents and stannous (II) octanoate (Sn(Otc)<sub>2</sub>) is used as catalyst. Meanwhile, a series of modified PLLA films are prepared by using star-shaped POSS-g-PLLA, the structure of the modified PLLA films is characterized by FTIR, and the mechanical properties of the modified PLLA films are also investigated. It is discovered that the mechanical properties of the modified PLLA films are enhanced evidently compared with that of blank PLLA film, and elongation at break and the tensile strength of the modified PLLA films are 4 times and 3.2 times respectively higher than those properties of blank PLLA film.

**Keywords** PLLA · POSS-NH<sub>3</sub>Cl · Modified PLLA films · Mechanical properties

## 1 Introduction

Poly(L-lactic acid) (PLLA), which is one of the simplest and fully biodegradable new synthetic polyesters produced from renewable resources [1–3], has received much interest for use in medical field, packaging industry, agriculture and general plastic field, and it has many excellent properties such as biodegradability, compatibility [4–6], recycle and so on. Though PLLA has some mechanical properties compared with polystyrene and poly (ethyleneterephthalate), its thermal property and brittle nature can limit its further commercial application. Recently, organic polymers, inorganic substances [6] and nanocomposites [7, 8] have been used to modify PLLA by copolymerization, blending, and reinforced composite methods.

---

X. Zhang (✉) · F. Zheng  
School of Media and Design, Hangzhou Dianzi University, Hangzhou, China  
e-mail: zhang\_xiao\_hui2014@126.com

Recently, POSS used as a new nano-filler has been widely to improve the properties of PLLA. By using POSS, the thermal, mechanical, oxidation resistance, gas permeability, pressure resistance properties of the material can be improved, and the flammability of the material can be reduced [9–13]. Up to present, researches which PLLA is blend with POSS have been studied a lot [12, 13]. However, researches that PLLA is grafted with POSS have rarely been reported [13]. In previous report [12], POSS-PLA (polylactide tethered with POSS) was synthesized by using the ring-opening polymerization of L-lactide with 3-hydroxypropyl hepta isobutyl POSS, and the properties of PLLA blended with POSS-PLA were studied. It is found that the mechanical properties of the materials could be amended by the method that PLLA is blended with POSS. However, the reinforced properties of the blends were limited since the simple blending of organic materials with inorganic materials is thermodynamically immiscible.

The paper is studied based on the previous research [14]. Firstly, POSS-g-PLLA is synthesized. Secondly, the modified PLLA films are prepared. Thirdly, the mechanical properties of modified PLLA films are studied.

## 2 Experimental Procedures

### 2.1 Materials

L-LA is bought from Shenzhen Brightchina Industry Co. Ltd. and pretreated by using the method described in the Ref. [14]. Ethanol (A.R) and Sn(Oct)<sub>2</sub> (A.R) are obtained from Chemical Reagent Co. Ltd. Chloroform (A.R) is purchased from Shanghai Experiment Reagent Co. Ltd. POSS-NH<sub>3</sub>Cl is prepared according to the method described in the Ref. [15]. Deionized water is prepared in the laboratories.

### 2.2 Preparations of PLLA, POSS-g-PLLA, Composites Films

PLLA and POSS-g-PLLA are prepared based on the method described in the Ref. [14]. The synthesis of modified PLLA films is shown in Fig. 1. Firstly, PLLA (or POSS-g-PLLA) and chloroform are poured into a flask equipped with a magnetic stirrer until the mixture is fully dissolved. Secondly, a certain percentage of TDI [14] and dibutyltin are added into the mixture, and the mixture is stirred at 80 °C for 5 h. Thirdly, PEG, TDI and dibutyltin are charged into the reaction mixture, which is stirred at 80 °C for 5 h. Finally, the mixture is poured into a Teflon mould subsequently, and retained for about 24 h at room temperature to give an about 0.5 mm thick sheet of films with smooth surface.

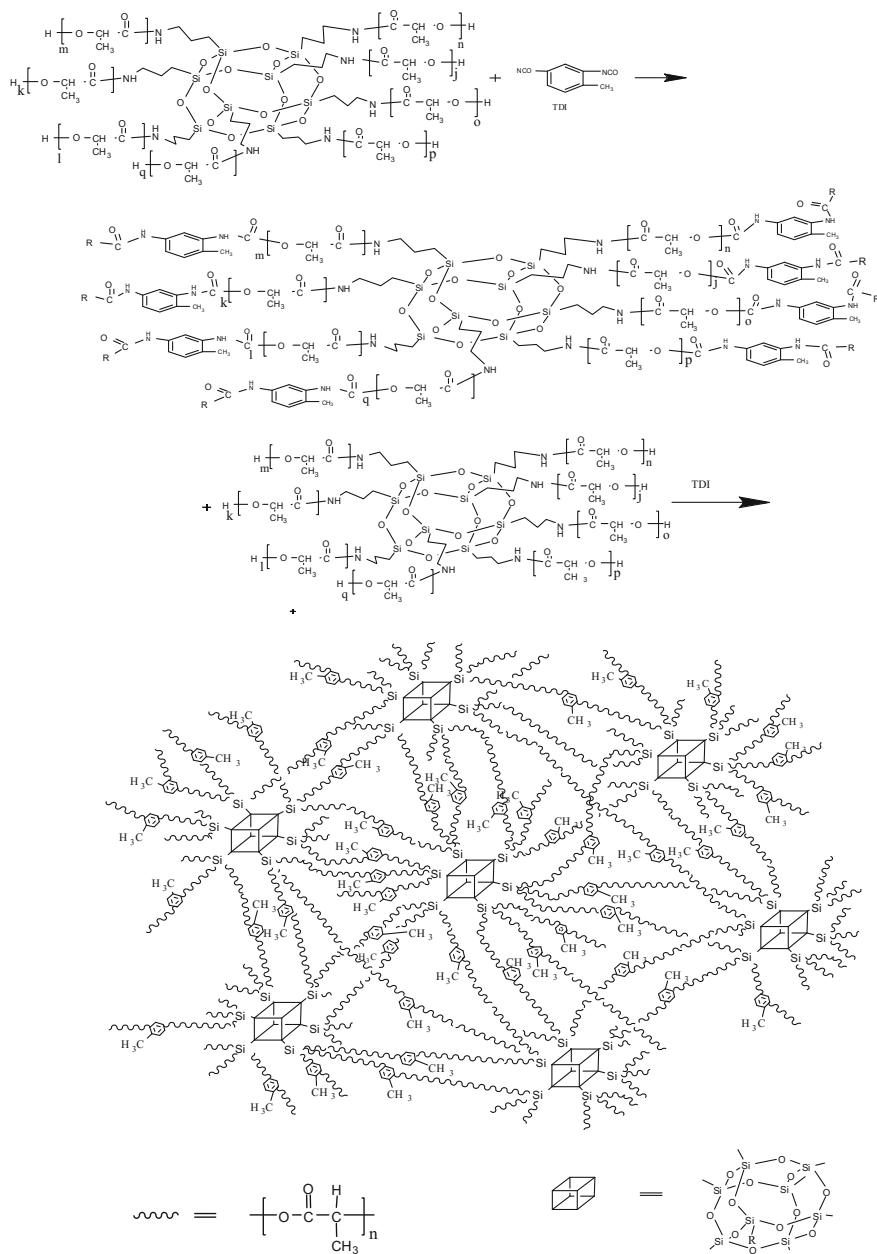


Fig. 1 Synthesis of modified PLLA films

### 3 Characterizations

FTIR are performed on Nicolet AVATAR 360FT infrared analyzer. KBr powder is used as a nonabsorbent medium. Firstly, sample is ground with KBr which is made a 0.5 wt% mixture and then the mixture is pressed into a disk. Secondly, the spectral analysis of sample is recorded and the recordation of FTIR is 4000 to 400  $\text{cm}^{-1}$ .

Mechanical tensile tests are performed on a computer control electronic universal testing machine (CMT 6503). The mechanical properties such as modulus, elongation at break and tensile strength are measured, and the cross-head speed is 20 mm/min. The dumbbell-shaped specimens are gained from cured sheet. Meanwhile, datum is recorded, and it is an average of five measurements for each sample.

## 4 Results and Discussion

### 4.1 Preparation of Modified PLLA Film

FTIR for the modified PLLA film is shown in Fig. 2. The peak at 1760  $\text{cm}^{-1}$  is the stretching vibration of carbonyl groups. 1647 and 1544  $\text{cm}^{-1}$  which are newly emerged peaks at could show the existence of NH-C=O, 1604  $\text{cm}^{-1}$  is the bending vibrations of N-H. 1460  $\text{cm}^{-1}$  is attributed to methyl. The peak at 1380  $\text{cm}^{-1}$  is assigned to the methane groups. The peak at 1090, 809 and 457  $\text{cm}^{-1}$  is caused by the Si-O-Si stretching vibration [16, 17], and the peak at 1090  $\text{cm}^{-1}$  is the LO and TO of Si-O-Si vibration [18], 1190 and 1090  $\text{cm}^{-1}$  are the C-O-C stretching bands. 3030, 1604, 1540, 1460 and 760  $\text{cm}^{-1}$  is the benzene and  $\text{CH}_2$ .

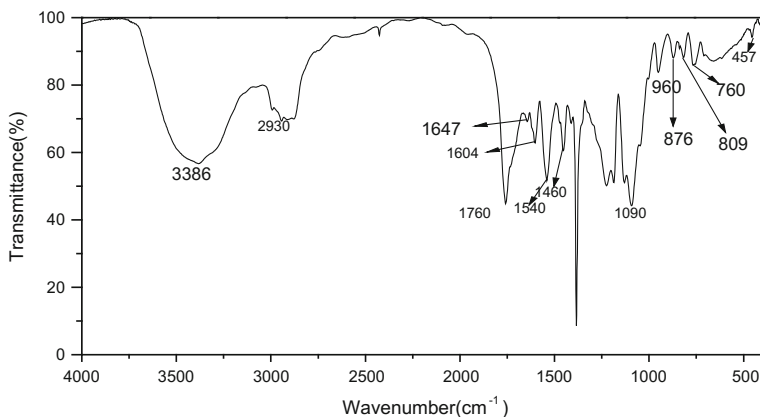


Fig. 2 FTIR spectrum of modified PLLA film

## 4.2 Mechanical Properties

The components of films are POSS-g-PLLA, chain extender, catalyst, plasticizer, in which every element can affect the properties of the films. POSS-g-PLLA network structure forms through chain extension reaction between POSS-g-PLLA and chain extender in the presence of catalyst. The process is very sensitive to changes in several factors such as the concentrations of catalysis, the proportion of chain extender and type of POSS-g-PLLA, temperature and moisture under circumstance. In the paper, one type of POSS-NH<sub>3</sub>Cl and catalyst are used, and the weight of chain extender, weight of catalyst and preparing condition are kept constant, only the weight of POSS-NH<sub>3</sub>Cl is changed in the films to investigate the effect on mechanical properties of modified PLLA films with the enhancement of POSS-NH<sub>3</sub>Cl. The modified films formulation with various weight percent of POSS-NH<sub>3</sub>Cl and the mechanical properties of the modified PLLA films are listed in Table 1.

It is obviously found that not only modulus, tensile strength but also elongation at break is changed from the Table 1. First, not only the modulus, tensile strength but also elongation at break is increased with the increase of POSS-NH<sub>3</sub>Cl content, and then they decrease gradually. The tensile strength of PP2 is 2.5 times as large as that of PP1. And the elongation at break is almost twice higher than that of PP1. The mechanical properties of PP4 are more excellent than that of others, in which, the tensile strength of PP4 is 3.2 times higher than that of PP1, and the elongation at break of PP4 is 4 times larger than that of PP1. And then, not only the tensile strength but also the elongation at break of films is decreased with the increase of POSS-NH<sub>3</sub>Cl content.

It is reasonable that the three-dimensional cage features resulting from POSS-NH<sub>3</sub>Cl is maintained after in situ polymerization, which could lead to good mechanical properties of modified PLLA films [12]. The obtained results are consistent with the previous literatures [13, 19–21] which are found that the mechanical properties of polymer can be amended with the nanostructure and cage type structural features of POSS. However, with the increase of POSS-NH<sub>3</sub>Cl, the branched-chain of Star-shaped POSS-g-PLLA becomes shorter. So the molecular

**Table 1** Mechanical properties of samples

Samples	$W_{\text{POSS-NH}_3\text{Cl}}/W_{\text{L-LA}}$	Modulus (MPa)	Tensile strength (MPa)	Elongation at break (%)
PP1	0/20	0.95	1.71	50
PP2	0.3/20	3.68	4.17	93
PP3	0.84/20	4.6	5.08	114
PP4	1/20	5.39	5.5	191
PP5	1.5/20	3.23	3.54	117
PP6	2/20	3.19	3.33	113

weight of POSS-g-PLLA is reduced, and the crystallinity of POSS-g-PLLA is reduced, which can induce that the mechanical properties of Modified PLLA films could not be further improved.

## 5 Conclusions

In this research, star-shaped POSS-g-PLLA is synthesized by using POSS-NH<sub>3</sub>Cl and L-LA as reagents. The mechanical properties of the modified PLLA films are enhanced. It is clearly shown that the elongation at break and the tensile strength of modified PLLA films are 4 times and 3.2 times higher than that of blank PLLA film.

**Acknowledgements** The work was supported by Zhejiang Provincial Education Department Research (Project No. Y201120780).

## References

1. Cinelli, P., & Chiellini, E. (2006). Foamed articles based on potato starch, corn fibers and poly (vinyl alcohol). *Polymer Degradation Stability*, 91, 1147–1155.
2. Holland, S. J., & Tighe, B. J. (1992). Biodegradable Polymers. *Advances in Pharmaceutical Science*, 101–164.
3. Gewin, V. (2003). Genetically modified corn-environmental benefits and risks, *PLoS Biology*, 1, 15–19.
4. Deplaine, H., Lebourg, M., & P. Ripalda. (2013). Biomimetic hydroxyapatite coating on pore walls improves osteointegration of poly(L-lactic acid) scaffolds, *Journal of Biomedical Materials Research Part B Applied Biomaterials*, 101(1), 173–186.
5. Jonnalagadda, S., & Robinson, D.H. (2004). Effect of the inclusion of peg on the solid-state properties and drug release from polylactic acid films and microcapsules, *Journal of Applied Polymer Science*, 93, 2025–2030.
6. Kondratowicz, F. Q., & Ukielski, R. (2009). Synthesis and hydrolytic degradation of poly (ethylene succinate) and poly(ethylene terephthalate) copolymers, *Polymer Degradation Stability*, 94, 375–382.
7. Chiang, M. F., & Wu, T. M. (2010). Synthesis and characterization of biodegradable poly (L-lactide)/layered double hydroxide nanocomposites, *Composites Science and Technology*, 70, 110–115.
8. Chen, H. M., Chen, J., & Shao, L. N. (2013). Comparative Study of Poly(L-lactide) Nanocomposites with Organic Montmorillonite and Carbon Nanotubes, *Journal of Polymer Science Part B: Polymer Physics*, 51, 183–196.
9. Markovic, E., & Matison, J. (2007). Poly(ethylene glycol) Octafunctionalized Polyhedral Oligomeric Silsesquioxane: WAXD and Rheological Studies, *Macromolecules*, 40(13): 4530–4534.
10. K. M. Lee & P. T. Knight. (2008). Polycaprolactone-POSS Chemical/Physical Double Networks, *Macromolecules*, 41, 4730–4738.
11. Kai, W. & Hua, L. (2008). Polyhedral oligomeric silsesquioxane and fullerene-end-capped poly ( $\epsilon$ -caprolactone), *Macromolecular Chemistry and Physics*, 209, 1191–1197.

12. Lee, J. H., & Jeong, Y. G. (2010). Preparation and Characterization of Nanocomposites Based on Poly lactides Tethered with Polyhedral Oligomeric Silsesquioxane, *Journal of Applied Polymer Science*, 115, 1039–1046.
13. Pan, H. & Qiu, Z. B. (2010). Biodegradable poly(L-lactide)/polyhedral oligomeric silsesquioxanes nanocomposites: enhanced crystallization, mechanical properties, and hydrolytic degradation, *Macromolecules*, 43, 1499–1506.
14. Zhang, X. H., Gu, W. J., & Li, H. B. (2012). Synthesis and Characterization of Star-shaped polylactic acid with polyhedral oligomeric silsesquioxanes, *Applied Mechanics and Materials*, 200, 397–400.
15. Gravel, M. C., Zhang, C., et al. (1999). Octa(3-chloroammoniumpropyl) octasilsesquioxane, *Applied Organometallic Chemistry*, 13, 329–336.
16. Koh-ichi, U., Satoshi, S., et al. (1999). Preparation and properties of silica films with higher-alkyl groups, *Journal of Non-Crystalline Solids*, 260 (2): 199–207.
17. Capozzi, C. A., Pye, L. D., et al. (1992). Vibrational spectral/structural changes from the hydrolysis/polycondensation of methyl-modified silicates. *Materials Letters*, 15(2): 130–136.
18. Que, W., & Hua, X. (2003). Sol-Gel Derived Titania/ $\gamma$ -Glycidoxypolytri-Methoxysilane and Methyltrimethoxy-silane Hybrid Materials for Optical Waveguides', *Journal of Sol-Gel Science and Technology*, 28(3): 319–325.
19. Mei, F., Zhong, J. S., & Yang, X. P. (2007). Improved Biological Characteristics of Poly (L-Lactic Acid) Electrospun Membrane by Incorporation of Multiwalled Carbon Nanotubes/Hydroxyapatite Nanoparticles, *Biomacromolecules*, 8, 3729–3735.
20. Kim, H. S., Choi, Y. S., & Kwon, H. (2009). Thermal degradation behaviour of multi-walled carbon nanotube-reinforced poly(L-lactide) nanocomposites, *Polymer International*, 58, 826–831.
21. Qiu, Z. B., & Pan, H. (2010). Preparation, crystallization and hydrolytic degradation of biodegradable poly(L-lactide)/polyhedral oligomeric silsesquioxanes nanocomposite, *Composites Science and Technology*, 70, 1089–1094.

# Preparation and DSC Analysis of $\gamma$ -Poly Glutamic Acid Ester

Wei Xiao, Zhihui Sun, Fengqing Wang and Jing Dong

**Abstract** With the increasing utilization of plastic in packaging industry, plastic waste caused great impact on the environment. So the research and development of new materials of biodegradable plastics could alleviate the deterioration of ecological environment and the shortage of resources which was strategic development significance. Chemical method was used to change the strong hydroscopic of  $-\text{COOH}$  of the  $\gamma$ -poly glutamic acid ( $\gamma$ -PGA) to hydrophobic by esterification reaction to meet the requirements of hydrophobic of packaging materials. The optimum reaction time, reaction temperature and reaction reagent, etc. of  $\gamma$ -PGA were decided through the experiments. And the melting point was tested by DSC technology to determine the resistance to heat which could provides the theory for the research of  $\gamma$ -PGA ester in the field of packaging in the future.

**Keywords** Biodegradable ·  $\gamma$ -PGA · Esterification · Packaging materials · DSC

## 1 Introduction

Plastic is a kind of polymer which was most widely used as packaging materials and most of the packing plastic is non-biodegradable material on the market. Although these additives maybe migration from packaging material to the packaged product, which polluted the product under certain conditions, additives were added in the productive process in order to improve the processing and usability of plastic products. In addition, the global plastics packaging castoff has reached nearly one

---

W. Xiao · Z. Sun (✉)

Engineering Technology Laboratory, College of Food Engineering  
and Packaging Science, Harbin Commercial University, Harbin, China  
e-mail: sunzhihui1962@163.com

F. Wang

College of Food Engineering, Harbin Commercial University, Harbin, China

J. Dong

School of Food Engineering, Harbin Commercial University, Harbin, China

© Springer Nature Singapore Pte Ltd. 2017

P. Zhao et al. (eds.), *Advanced Graphic Communications  
and Media Technologies*, Lecture Notes in Electrical Engineering 417,  
DOI 10.1007/978-981-10-3530-2\_130

1061



hundred million tons a year in recent years, and the plastic castoff landfill occupies lots of land resources what make the yields of crop down and incineration of plastic waste make the air severely contaminated which have already taken focus by the packaging industry. Therefore, in order to protect land resources and the environment, green biodegradable packaging materials should be developed in the future which is also the trend of the development of packaging industry.

Biodegradable materials refer to put the packaging film in the atmosphere or soil, and the film is broken down by the microorganisms under certain time and condition. The process makes the high molecular polymer fracture to low molecular weight. Biodegradation can be either the effect of fermentation in material internal catalyzed by bio-enzyme or the microbial decay something of the polymer to consumable material which make the polymer chain rupture and then degraded into  $\text{CO}_2$  and  $\text{H}_2\text{O}$  [1]. The advent of biodegradable material brought hope to reduce or eliminate the pollution, some of which can be used as the new packaging materials because they are safety, edible or all degradability. With the development of green chemical products become the new trend of world industrial, researchers found that amino acids polymer as a new type of material has great application prospect.  $\gamma$ -PGA has been found that it is a kind of good degradability poly amino acid [2], which is very suitable for development as packaging material. But there are a large number of  $-\text{COOH}$  in the molecular chain of  $\gamma$ -PGA which make  $\gamma$ -PGA has strong water absorption and can not meet the requirements of packaging materials for water resistance [3–5]. Therefore, the esterification reaction of  $\gamma$ -PGA needs to be performed which could change its hydrophilic to hydrophobic and give full play to the characteristics of the biodegradable used in packaging field which could reduce the environmental pollution caused by packaging castoff [6]. In addition, differential scanning calorimetry (DSC) test which is a kind of technology to measure the relation of power and temperature between material and reference by control the experiment temperature under the program was carried out on the modified materials. The heat resistance and process ability of the modified materials  $\gamma$ -PGA ester could be observed from the differential thermal analysis curve [6].

## 2 Experiments

### 2.1 *Materials and Methods*

#### 2.1.1 Experiment Reagent and Instrument

The experiment reagents:  $\gamma$ -PGA (homemade in college of food engineering of Harbin commercial university), DMSO, HCl, DMF, DBN,  $\text{NaHCO}_3$ , anhydrous ethanol, THF. All the reagents are analytically pure. The experimental apparatus: 250 ml boiling flask-3-neck, measuring cylinder, the evaporating dish, pipette, separatory funnel, centrifuge tube, etc. The experimental equipment: water bath pot,

magnetic stirrer, centrifuge, drying oven, airing chamber, electronic balance, DSC experimental apparatus, aluminum crucible, etc.

### 2.1.2 Methods

$\gamma$ -PGA, solvents,  $\text{NaHCO}_3$  and bromine ethane were added in boiling flask-3-neck. It was noteworthy that bromine ethane should be slowly dropped with separatory funnel and the whole process of the reaction was under heating and stirring. Cold HCl aqueous solution with pH was 2 was added after the reaction, and then centrifuged under 3000 r/min to get the deposits. After vacuum drying under 45 °C, the product was alternate soaked and washed repeatedly with anhydrous ethanol and distilled water, and then vacuum drying to get the high purity products [7, 8]. The modified equation of  $\gamma$ -PGA was shown in Fig. 1.

For study the influence of the reaction time, reaction temperature and reaction reagent on modification of  $\gamma$ -PGA, control variable method was used. The experiment was divided into 50 groups, and each group repeated three times. The average of receiving rate was taken in order to get the best reaction parameters. The 25 groups were taken DMSO as solvent and the other 25 groups were taken DMF as solvent. All the 50 groups make time and temperature as variable. After completely dry and adequate washing and dry again, the high purity white powder was gotten [9, 10].

The sample of  $\gamma$ -PGA ester which was grinded or cut into powder was evenly put into the crucible. Then the crucible was put into the DSC instrument with final temperature was 280 °C, the heating rate was 20 °C/min. The input pressure of nitrogen which was used as inert gas was regulated to 120 ml/min.

## 2.2 Results and Discussion

Through the average of receiving rate of each experiment, the curve of relationship between different reaction solvents, reaction temperature, reaction time and the receiving rate could be gotten as shown in Figs. 2 and 3. The calculation formula of receiving rate was seen in type (1):

$$\text{receiving rate} = \frac{\text{average quality}}{\text{quality of raw material}} \times 100\% \quad (1)$$

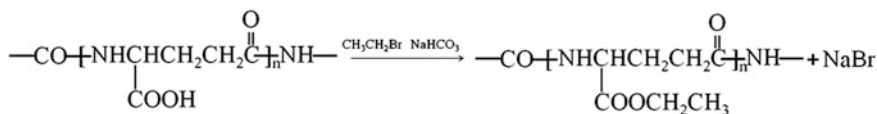
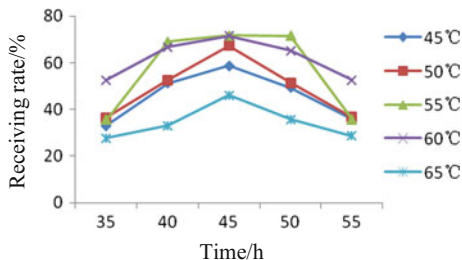
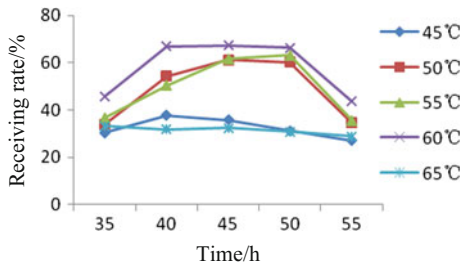


Fig. 1 Modified equation of  $\gamma$ -PGA

**Fig. 2** Receiving rate of product with the solvent as DMSO



**Fig. 3** Receiving rate of product with the solvent as DMF



The highest receiving rate of the product reached 71.75% in 50 group experiments which took DMSO as the solvent, 45 h as the reaction time, 55 °C as reaction temperature. When the reaction temperature above 60 °C or below 50 °C the product was less and the quality was inferior. It may be caused by the reaction temperature was too high to make product properties change and molecular weight drops or the reaction temperature was not enough to make reaction was not completely.

All of the 50 groups were tested by DSC in order to get the heat resistance of the  $\gamma$ -PGA ester. There were 6 groups with the higher receiving rate and excellent heat resistance in 50 groups, which reaction time was 45 h and other experimental parameters and the results were shown in Table 1.

It was seen that the 13th group has the highest melting point from Table 1. The best experiment parameters were 55 °C, 45 h and using DMSO as the solvent combined with receiving rate. The melting points of the commonly used packaging

**Table 1** Experiment parameters and results of 6 groups

Group	8	13	18	33	38	43
Temperature	50	55	60	50	55	60
Solvent	DMSO	DMSO	DMSO	DMF	DMF	DMF
Receiving rate (%)	67.25	71.75	71.5	67	66.3	67.42
Melting points (°C)	172.4	190.5	176.7	176.7	184.6	169.1

materials such as PP, LDPE or HDPE were inferior to  $\gamma$ -PGA ester which has the good heat resistance and can be used as packaging film under certain condition.

### 3 Conclusions

The biodegradable material  $\gamma$ -PGA was the research object in this study, and its hydrophilic was modified to make it meet the requirement as the water resistance of packaging materials. The best experiments parameters of modification were determined, and the excellent heat resistance was seen by DSC test results, which provide certain reference for related research. Although it is determined that  $\gamma$ -PGA ester can be used as a kind of biodegradable packaging materials, it is not widely used in the market at present due to the high prices of raw material, the long time of esterification reaction and the difficult of mass production of  $\gamma$ -PGA ester. The paucity of research on other properties such as mechanical properties, transparency, printability and formability also restricted the development to some extent. The study on industrialization production of raw material, improvement of preparation process of  $\gamma$ -PGA ester and cost control should strengthen in the future. In addition,  $\gamma$ -PGA ester could be grafted with chitosan, silver nitrate and levorotatory VC, etc. to prepare antibacterial or antioxidant packaging materials or through technology improvement to realize multi-layer co-extrusion with other material in order to improve the capacity and performance of the material and make  $\gamma$ -PGA ester replace the non-degradable packaging materials [11].

**Acknowledgements** This study is funded by graduate student innovation scientific research funds of Harbin commercial university (YJSCX2015-356HSD) awarded to the first author in 2015. This work is also supported by Natural Science Foundation of Heilongjiang Province, China (NO. E2016049).

### References

1. Yuichi Ohya. (2015). Encyclopedia of polymeric Nanomaterials: Biodegradable Materials: 139–145.
2. Lin W C, Yu D G, Yang M C. (2006). Blood compatibility of novel poly ( $\gamma$ -glutamic acid)/polyvinyl alcohol hydrogels. *Colloids and Surfaces B: Biointerfaces*, 47(1): 43–49.
3. Makoto Ashiuchi. (2013). Microbial production and chemical transformation of poly- $\gamma$ -glutamate. *Microbial Biotechnology*, 6(6): 664–674.
4. Alessandra de Cesaro, Suse Botelho da Silva, Vanessa Zimmer da Silva. (2014). Physico-chemical and rheological characterization of poly-gamma-glutamic acid produced by a new strain of *Bacillus subtilis*. *European Polymer*, (57): 91–98.
5. Xiulin Shu, Qingshan Shi, Yousheng Ouyang, Yiben Chen. (2011). Research advancements of modification of  $\gamma$ -polyglutamic acid and their highly added value applications. *Fine and Specialty Chemicals*, 19(10): 4–10.
6. Joerg M Buescher, Argyrios Margaritis. (2007). Microbial biosynthesis of polyglutamic acid biopolymer and applications in the biopharmaceutical, biomedical and food industries. *Critical reviews in biotechnology*, 27: 1–19.

7. Kubota H, Nambu Y, Takeshi Endo. (1995). Convenient esterification of poly( $\gamma$ -glutamic acid) produced by microorganism with alkyl halides and their thermal properties. *Polymer Science, Part A: Polymer Chemistry*, 33(1): 85–88.
8. Morillo M, Marinez de Ilarduya A, Mu oz-Guerra S. (2001). Comblike alkyl esters of biosynthetic poly ( $\gamma$ -glutamic acid) I. Synthesis and characterization. *Macromolecules*, 34 (22): 7868– 7875.
9. YingJun Wang, XiuMiao Zhou, Li Ren. (2008). Synthesis and characterization of Hydroxyl-Terminated Poly( $\gamma$ -benzy-L-glutamate). *Macromolecular science. Part A: Pure and Applied Chemistry*, (45): 381–386.
10. Hidetoshi Kubota, Yoko Nambu, Takshi Endo. (1933). Convenient and quantitative esterification of Poly( $\gamma$ -glutamic acid)produced by microorganism. *Polymer Science, Part A: Polymer Chemistry*, 31(11): 2877–2878.
11. Jari Vartiainen, Yingfeng Shen, Timo Kaljunen, et al. (2015). Bio-based multilayer barrier films by extrusion, dispersion coating and atomic layer deposition. *Journal of Applied Polymer Science*, 133(2): 1–6.

# Application of Anti-static Release Coating in Packaging Film

Jichao Huang, Shenghong Chen, Chengzhi Li, Chunxiu He and Yun Xiang

**Abstract** In order to improve the anti-static (AS) and release function of OPP film surface, the anti-static release coating of OPP film is developed. The coating can not only quickly dissipate the accumulated electronic on the surface of the material, but also reduce the surface energy of the material surface. And it does not affect the physical properties of OPP film. The results showed that the surface resistance of the protective film is reduced from  $10^{12}$  to  $10^8 \Omega$ . The peel strength of the film is reduced from 2980 g/25 mm to 20 g/25 mm after coated with anti-static release coating. The yield rate is reduced from 24.6 to 0.53%. The protective film products with coating can solve the problem in auto packaging process and improve production efficiency.

**Keywords** Anti-static (AS) · Release · Anti-blocking

## 1 Introduction

Most polymer materials are excellent electrical insulating materials. Electronic is easy to be accumulated on the surface of the polymer materials, which cause product quality problems, fire or explosion etc [1]. Anti-static coating can quickly dissipate the accumulated electronic on the material surface. According to the electrical conduction principle, anti-static coating could be divided into structural (intrinsic) and composite (doped) conducting coating [2]. Different kinds of film, contact type, contact time, contact area and separation speed of the films can influence time and voltage of electrostatic discharge. For example, the better the material electrical performance is, the higher the electrostatic voltage is. Friction between the same materials is also easy to accumulate electronic. When two close contact plastic materials are quickly separated, the transient static voltage will be up to ten thousand volts. In addition, liquid and gas without water are also easy to

---

J. Huang · S. Chen (✉) · C. Li · C. He · Y. Xiang  
CymMetrik (Shenzhen) Printing Co., Ltd, Guangdong, China  
e-mail: shenghong.chen@cymmetrik.com

accumulate electronic. The ability of different printing materials to accumulate electronic is not the same, such as paper, plastic, printing ink or printing plate. There is great pressure to keep them in close contact and high speed to separate them in printing process, which will be easy to accumulate electronic [3]. With the rapid development of the domestic packaging industry, packaging equipments have reached high-precision drive and high automation. Intelligent control is used in packaging process, thus greatly improving packaging efficiency [4].

## 2 Experimental

### 2.1 Materials and Equipment

50  $\mu\text{m}$  OPP film (Guangdong Weifu packaging material Co. Ltd.); ME-002 organic silicone (H. j. unkel Co. Ltd); CFS-333 anti-static agent and GS-X1 (Ling'an Dechang Hangzhou electrostatic science and Technology Co., Ltd.);  $\text{C}_2\text{H}_5\text{OH}$  (Huizhou Yongji Chemical Co. Ltd).

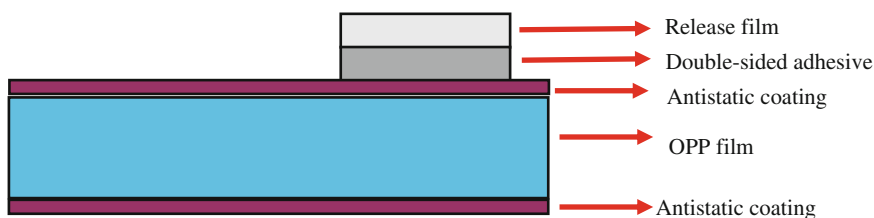
Coating machine (shunyi Machinery Co., Ltd.); Surface resistance tester (Mitsubishi Chemical); GH-951CS stripping test machine (guohong Detection Instrument Co., Ltd.); Hygrothermograph (Anymetre); Electronic scale (Chengdu PRIS Electronic Co., Ltd); IR (Thermo-Fisher Scientific); Dyne Test Pen (arcotest);

### 2.2 Experimental Method

Take 5.25% weight percent anti-static agent and 0.3% organic silicone to 94.45% ethanol, and then stir uniformly to get anti-static release coating.

The coating is applied to the positive and negative sides of OPP film with 200 anilox roller. Then they are placed in the 70  $^{\circ}\text{C}$  environment for one minute to get anti-static release OPP film.

Cut OPP film with die-cutting machine and stick double-sided adhesive to get protective film. As shown in Fig. 1.



**Fig. 1** Structure picture of protective film

### 2.3 Experiment Test

According to ANSI/ESD STM11.11-2006 criterion, place the samples on the insulation pad and keep them in the environment of  $23 \pm 1$  °C,  $50 \pm 5\%$  RH. Test the samples with surface resistance test instrument. Test voltage is set to 100 V and test time is set to 30 s.

According to the GB/T2792-2014 criterion, using GH-951CS stripping test machine to carry out 180° stripping test. Cut 25 mm × 300 mm size from the samples, stick them on Tesa 07475 tape, then stick the samples and tape on stainless steel. Roll on the samples two circles with 2 kg automatic wheel. Keep them in the environment of  $23 \pm 1$  °C,  $50 \pm 5\%$  RH for 20 min. Peel the samples from the tape with 180° angle by 300 mm/min.

Place the test sample on the test platform. Draw the lines on the sample surface with Dyne Test Pen. Finally observe whether the lines become droplets in three seconds [5].

### 2.4 DOE Experimental Design

The experimental design is carried out by using Taguchi Method. Choose the release film of double-sided adhesive, antistatic agent and organic silicone additive as the factors. Choose type of antistatic agent, type of release film of double-sided adhesive and addition of organic silicone additive as the factors (X). Choose the protective film yield rate as response value (Y). Test method: Simulated automatic adhesion test and statistical data (Test 200 PCS in each group). It is bad that more than 2 PCS protective films are stuck together.

### 2.5 Establish DOE Model

Establish DOE model as shown in Table 1. There are 3 factors type of antistatic agent, type of release film of double-sided adhesive and addition of organic silicone additive. All of them are controllable. Levels of factors are chosen shown in Table 1. Type of release film of double-sided adhesive has 2 levels. Type of antistatic agent has 2 levels. Addition of organic silicone additive has 3 levels.

**Table 1** Level model of factor

No.	Input variables (X's)	Level 1	Level 2	Level 3
A	Type of release film of double-sided adhesive	AS	NO AS	–
B	Type of antistatic agent	CFS-333	GS-X1	–
C	Addition of organic silicone additive	0.75%	0.30%	0



### 3 Results and Discussion

#### 3.1 DOE Model Analysis

The experiment is designed by Minitab. Enter data into Minitab to get the following graphics as Fig. 2.

From Fig. 2, we can see that type of antistatic agent and addition of organic silicone additive are the main reasons.  $A_1B_1C_2$  scheme is the best.

#### 3.2 Result Verification

Make protective film samples with  $A_1B_1C_2$  scheme and mark them as Sample 1. Test 10,000 PCS on the automatic packaging machine. Protective films without improvement are marked as Sample 2. Compare with 2 samples by each 10,000 PCS. The result of yield rate is listed in Table 2. From the Table 2, we can see that the performance of sample 1 is much better than sample 2. It is easy to accumulate charge in dry environment when plastics have friction. In order to solve this problem, the plastic surface is usually coated with a layer of anti-static coating [6].

#### 3.3 Property of Antistatic Release Coatings

From Fig. 3, we can see that surface resistance of film is decreased from  $10^{12}$  to  $10^8 \Omega$  and peel strength is decreased from 2980 g/25 mm to 20 g/25 mm after coated. The films with coating have good antistatic and release effect.

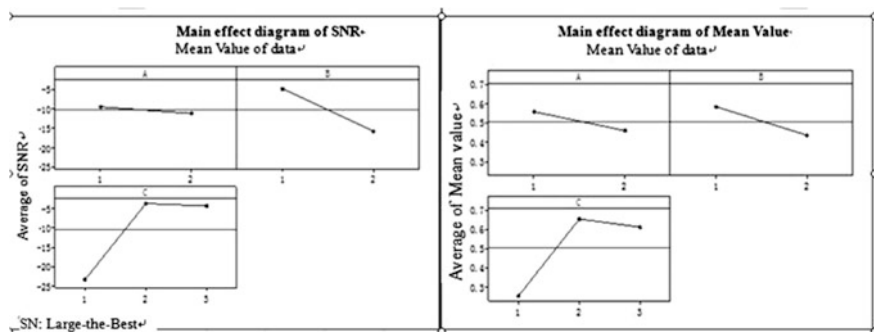
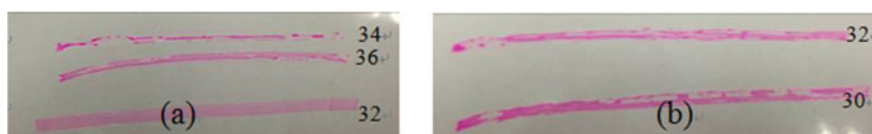
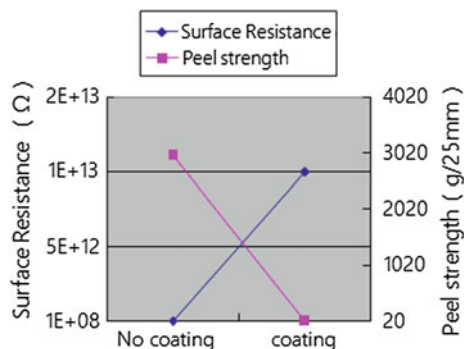


Fig. 2 Main effect diagram of SNR and mean value

**Table 2** Yield rate of two kinds of protective films

Type of sample	Total number of (PCS)	Number of adhesion (PCS)	Yield rate (%)
Sample 1	10,000	53	99.47
Sample 2	10,000	2460	75.4

**Fig. 3** Surface resistance and peel strength of coated and non-coated films**Fig. 4** Dyne graph of film sample: **a** film without coating; **b** film with coating

### 3.4 Dyne Analysis

From Fig. 4, we can see that dyne of film without coating is 32–34 dynes/cm and film with coating is below 30 dynes/cm. It shows that surface Gibbs free energy of the film after coated is decreased.

### 3.5 IR Analysis

From Fig. 5 we can see that the P=O peak of  $1258.53 \text{ mm}^{-1}$  and the P–O–C stretching vibration peak of  $1090 \text{ mm}^{-1}$  show that there is Hydrophilic Organic phosphate ( $-\text{OPO}_3\text{M}$ ) in the coating. It spreads to the coating surface, absorbs water in the air to form a layer of antistatic layer, which has affect of electrostatic dissipation. As shown in Fig. 6, the Si–O peak of  $804.35 \text{ mm}^{-1}$  can promote the coating's surface flow and significantly reduce the surface tension.

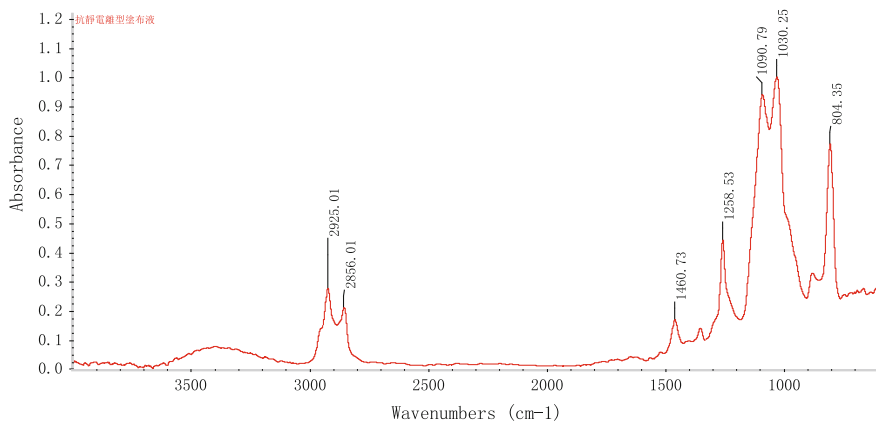


Fig. 5 Infrared spectrum of antistatic release coating

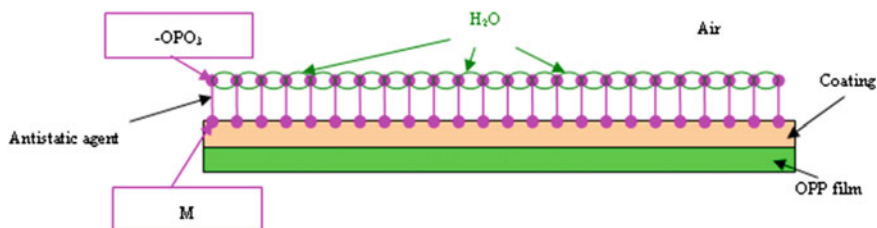


Fig. 6 Anti static principle of coating

## 4 Conclusions

The best formula is that the weight percent ratio of anti-static agent, organic silicone additive and alcohol solution is 5.25:0.3:94.45. Hydrophilic Organic phosphate (-OPO<sub>3</sub>M) on the coating surface absorbs water molecules in the air to form a layer of anti-static layer, which has effect of electrostatic dissipation. The Si-O can promote the coating's surface flow and significantly reduce the surface tension. Anti-static release coating for films is helpful to improve adhesion effect.

## References

1. Zhang, C. H., Zhao, X. (2008). Research in the synthesis of PBS. *Polyester Industry*, 21 (2): 8-11.
2. Liao, C. Z. (2010). Research progress on biodegradation of PBS. *Plastic Science and Technology*, 38 (7): 93-98.

3. Yang, H. L. (2005). Application of antistatic technology in packaging and printing industry. *China Packaging Newspaper*.
4. Xu, W. C. (2007). State and development trend of packaging industry. *Printing Industry*.
5. Sun, D. C., Sun, D. S. (2009). Synthesis and application in antistatic coatings of PEDOT/PSS. *Polymer Materials Science and Engineering*.
6. Yang, G. S., Wei, F., Dong, S. J., Liu, G., Bao, J. N. (2015). Research progress on PEDOT/PSS. *Dye stuff and Coloration*.

# Edible Coating Packaging and Its Preservation Effect to Cherry Tomatoes

Liya Zhou, Junyan Huang, Hao Xing, Qinghua Gao, Yaoqi Li and Xiaomin Li

**Abstract** In order to study the edible coating packaging and its preservation effect to cherry tomatoes, three edible coating materials including carrageenan, carboxymethyl cellulose, sodium alginate were respectively made into coating solution, and coating packaging for cherry tomatoes were performed by the dipping way, and then they were put in the photosynthetic gas preservation box for preservation experiment. The performance of coating packaging cherry tomatoes in different experimental group were tested and analyzed. The results showed that carrageenan coating packaging significantly can reduce the water loss rate of cherry tomatoes, decay rate and MDA during storage, and delay cherry tomatoes hardness, soluble solids content, vitamin C content and organic acid content decline, and also has a better sensory evaluation. Therefore, carrageenan coating material has better effects in the preservation of cherry tomatoes.

**Keywords** Edible coating materials · Cherry tomatoes · Coating packaging · Modified atmosphere packaging · Preservation effects

## 1 Introduction

The coating packaging technology and modified atmosphere preservation technology are new technology in the applicant of modern preservation packaging field, they will be a better preservation effect when both methods combined in packaging of fruit and vegetable. Three edible coating materials such as carrageenan, carboxymethyl cellulose and sodium alginate were prepared respectively coating

---

L. Zhou · J. Huang (✉) · H. Xing · Q. Gao · Y. Li · X. Li  
Dalian Polytechnic University, Dalian, Liaoning, China  
e-mail: huangjunyan@126.com

L. Zhou  
Petro China Dalian Lubricating Oil Research and Development Center,  
Dalian, Liaoning, China  
e-mail: 297315303@qq.com

solution [1], coated on cherry tomatoes and performed preservation packaging experiment combined with modified atmosphere preservation technology [2]. The sensory index and physiological index of cherry tomatoes were tested, and the preservation impact of edible coating packaging on cherry tomatoes was contrastively analyzed [3]. The aim is to provide useful refer to the research and application of edible coating for fruits and vegetables [4].

## **2 Experimental**

### **2.1 *Materials and Instruments***

The cherry tomatoes which purchased in the market were smooth, the same size, medium well, no pests and mechanical damage. The carrageenan, carboxy methyl cellulose and sodium alginate were provided by Dalian East China reagent factory.

The photosynthetic gas preservation boxes were provided by Jiang Shan Zhen (Shanghai) Co., Ltd.; The Gy series fruit hardness tester was provided by Cable Optical Technology (Shanghai) Co., Ltd; the handheld refractometer was provided by Samsung (Shanghai) Co., Ltd; The UV spectrophotometer was provided by Dalian Analysis Instrument General Factory.

### **2.2 *Experimental Method***

#### **2.2.1 Configuration of Coating Solution**

Through precoating experiment, the concentration and solution temperature of carrageenan, carboxymethyl cellulose and sodium alginate coating material which is better coating effect were chosen separately to carry on the experiment.

- (1) The configuration of carrageenan coating solution (group A): 6 g carrageenan in a beaker was weighed to configure carrageenan coating solution with the concentration of 0.6% and cool to room temperature [1].
- (2) The configuration of carboxymethyl cellulose (CMC) coating solution (group B): 10 g carboxymethyl cellulose in a beaker was weighed to configure carboxymethyl cellulose coating solution with the concentration of 1% and cool to room temperature [1].
- (3) The configuration of sodium alginate coating solution (Group C): 14 g sodium alginate in a beaker was weighed to configure sodium alginate coating solution with the concentration of 1.4% and cool to room temperature [1].
- (4) The group (Group D) was blank control group without coating treatment.

### 2.2.2 Method of Coating Packaging

Fresh cherry fruit were divided into four groups equally, each of them was about 1.5 kg washed with the detergent, dried and reserved for coating experiment.

By the dipping way [4], the cherry tomatoes were put into the three configured coating solution A, B and C, and the coating solution was covered on the cherry tomatoes. So a layer of uniform, transparent and shining edible film was formed in the surface of cherry tomatoes after dried.

### 2.2.3 Method of Modified Atmosphere Preservation

The covered group A, B, C and uncovered group D cherry tomatoes were put into the photosynthetic gas preservation box. Inside, the concentration of O<sub>2</sub> gradually decreased and the concentration of CO<sub>2</sub> gradually increased by the respiration of cherry tomatoes itself, and the respiration of cherry tomatoes can be suppressed. At the same time, the gas environment in the box was regulated by the photosynthesis through the stomata on the box, so as to create an ideal gas preservation environment. The box was placed in the light and stored at room temperature, and then they observed and tested.

### 2.2.4 Measuring Items and Methods

In the experiment, the changes of various physiological and biochemical indexes of cherry tomatoes were observed and tested after 1, 5, 10, 15 and 20 days.

- (1) Weight loss rate was measured using weighing method [4, 5]. 5 Cherry tomatoes were taken out from group A, B, C and D every time to weigh using electronic scales and its average value were calculated.
- (2) Hardness was measured using GY series fruit hardness tester. 4 cherry tomatoes were taken out randomly from each group every time to test and its average value was calculated.
- (3) Soluble solids were measured using handheld pocket refractometer. 4 cherry tomatoes were taken out randomly from each group every time to test and its average value was calculated.
- (4) Organic acid content was measured according to the method of GB/T 12456-2008 «Determination of total acid in food» [6]. 4 cherry tomatoes were taken out respectively from each group every time to test and repeated three times each group and its value was calculated.
- (5) Vitamin C content was measured using molybdenum blue colorimetric method [7, 8]. 5 cherry tomatoes were taken out respectively from each group every time to test and repeated three times each group and its value was calculated.
- (6) Malondialdehyde (MDA) content was measured using thiobarbituric acid colorimetric method [9]. The minced cherry tomatoes sample was taken out

respectively from each group to test and repeated three times each group and its value was calculated.

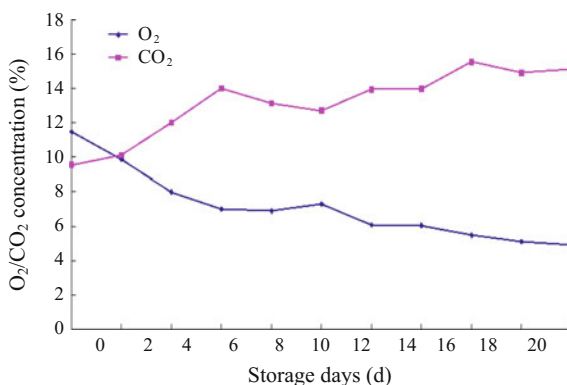
- (7) Decay rate was measured using observation method. 40 cherry tomatoes were taken out respectively from 4 group to test, the number of rotten cherry tomatoes which include the lesions, mildew, rot and the edible portion less than 4/5 during storage were recorded [10], and then decay rate value was calculated.
- (8) Sensory evaluation was measured using observation method. Through observing the color, smoothness in surface and the gloss of 4 group cherry tomatoes, make a sensory evaluation for the cherry tomatoes [4, 9].

### 3 Results and Discussion

#### 3.1 Changes of $O_2$ and $CO_2$ Concentration in the Photosynthetic Gas Preservation Box During Storage

The change of  $O_2$  and  $CO_2$  concentration in the photosynthetic gas preservation box during storage of cherry tomatoes is shown in Fig. 1. It appears that the concentration of  $O_2$  gradually decreased and the concentration of  $CO_2$  gradually increased with the storage duration. The concentration of  $O_2$  and  $CO_2$  reached a balance basically after six days, the concentration of  $O_2$  was maintained at around 6%, and the concentration of  $CO_2$  was maintained at about 14%. The respiration of cherry tomatoes can be suppressed basically and the goal of fruit preservation has been attained [11, 12].

**Fig. 1** Changes of  $O_2$  and  $CO_2$  concentration in the photosynthetic gas box during storage





### 3.2 *Effect of Coating Packaging on Cherry Tomatoes Water Loss Rate*

During storage, the effect of different coating packaging on cherry tomatoes water loss rate is shown in Fig. 2. It can be seen from Fig. 2, the water loss rate of cherry tomatoes gradually increased with the increase of storage time. The highest water loss rate was in group D, in the other three groups a layer of porous network film was formed on the surface of tomatoes with coating packing, so it can prevent the water exchange with the outside, reduce the transpiration of water, slow the water loss and reduce the loss of quality of cherry tomatoes [13].

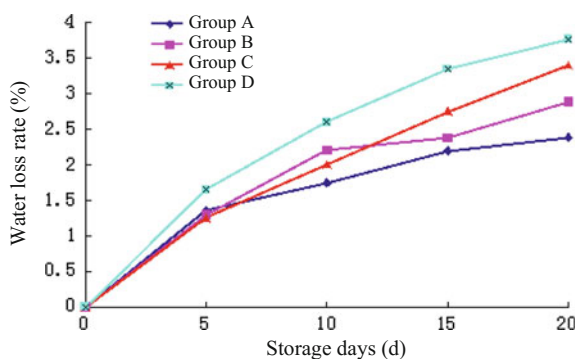
### 3.3 *Effect of Coating Packaging on Cherry Tomatoes Hardness*

During storage, the effect of different coating packaging on cherry tomatoes hardness is shown in Fig. 3. The water loss and the hardness of cherry tomatoes showed a declining trend gradually with the increase of storage time [14]. The slowest declining speed of the hardness was in group A, so it can be seen that the carrageenan coating packaging in group A significantly delayed the hardness drop of cherry tomatoes during storage.

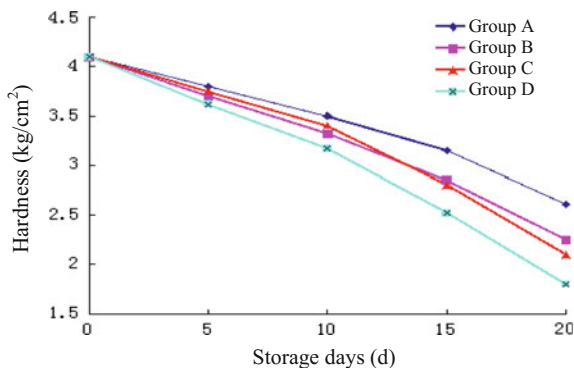
### 3.4 *Effect of Coating Packaging on Soluble Solids Content*

The effect of different coating packaging on the cherry tomatoes soluble solids content is shown in Fig. 4. It shows that the soluble solids content of cherry tomatoes with different coating packaging appeared a trend of first rise and then drop with the increasing of storage time [15]. After ten days, the soluble solids

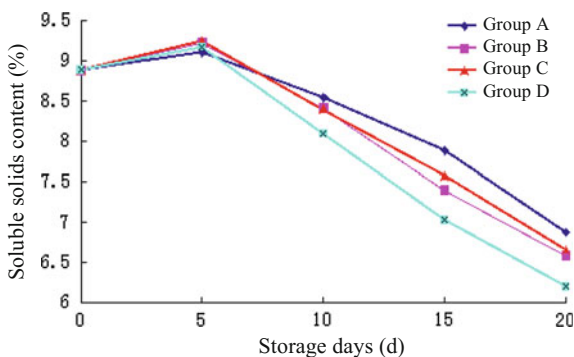
**Fig. 2** Effect of coating packaging on the cherry tomatoes water loss rate



**Fig. 3** Effect of coating packaging on the cherry tomatoes hardness



**Fig. 4** Effect of coating packaging on the cherry tomatoes soluble solids content

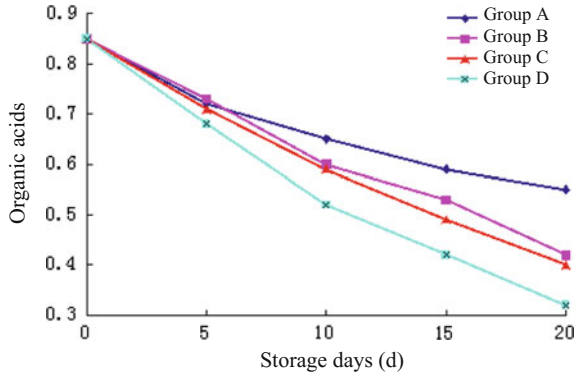


content of cherry tomatoes in group A was obviously higher than that in group B, C and D, so it can be seen that the carrageenan coating packaging in group A can obviously delay the declining of soluble solids content of cherry tomatoes during storage.

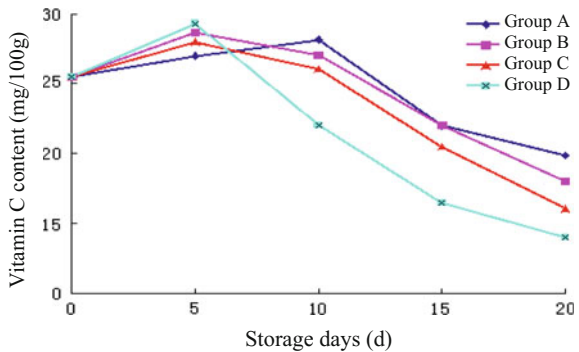
### 3.5 Effect of Coating Packaging on Organic Acid Content

The effect of different coating packaging on organic acid content of cherry tomatoes is shown in Fig. 5. The organic acids content gradually reduced with the increase of storage time in these four groups [16]. After five days, the content of organic acid of cherry tomatoes in group A was obviously higher than that in the other three groups. So it can be seen that the carrageenan coating packaging in group A can significantly delay the fall of the organic acid content of cherry tomatoes during storage.

**Fig. 5** Effect of coating packaging on the organic acid content of cherry tomatoes



**Fig. 6** Effect of coating packaging on the cherry tomatoes vitamin C content



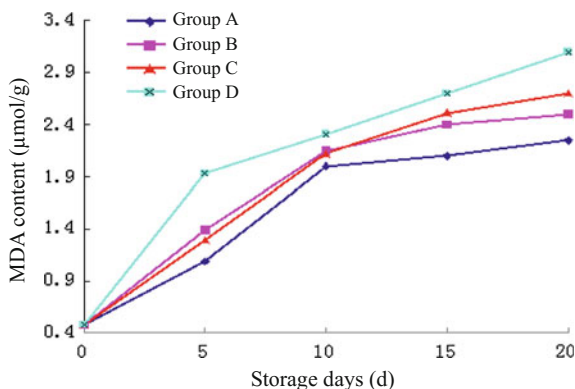
### 3.6 Effect of Coating Packaging on Cherry Tomatoes Vitamin C Content

The effect of different coating packaging on vitamin C content of cherry tomatoes is shown in Fig. 6. The vitamin C content in cherry tomatoes appeared a trend of first rise and then drop with the increasing storage time [17]. The carrageenan coating packaging in group A can significantly delay the fall of the vitamin C content of cherry tomatoes during storage, as shown in Fig. 6.

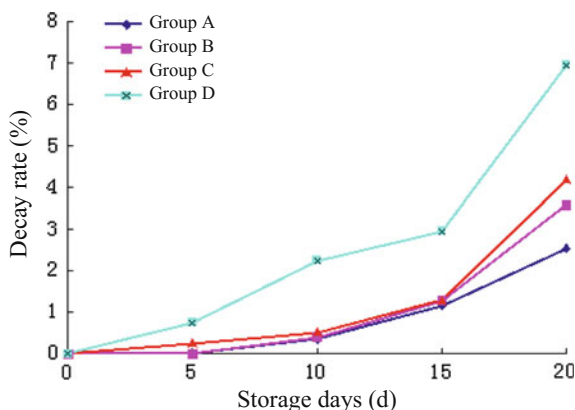
### 3.7 Effect of Coating Packaging on the Content of MDA

Malondialdehyde (MDA) is the sign of fruit senescence and the product of membrane lipid peroxidation [18]. The effect of different coating packaging on the content of MDA of cherry tomatoes is shown in Fig. 7. The content of MDA of cherry tomatoes with four kinds of different processing gradually increased with the increase of storage time. Among them, the content of MDA in group D sample

**Fig. 7** Effect of coating packaging on cherry tomatoes MDA content



**Fig. 8** Effect of coating packaging on cherry tomatoes decay rate



increased obviously, and the range of increase in the content of MDA of cherry tomatoes in group A was the smallest, so carrageenan coating packaging in group A during storage can significantly delay the increase of the content of MDA of cherry tomatoes.

### 3.8 Effect of Coating Packaging on the Decay Rate

The effect of different coating packaging on the decay rate of cherry tomatoes is shown in Fig. 8. The decay rate of samples in four groups gradually increased with the increase of storage time. The rising trend of cherry tomatoes decay rate in group D significantly was greater than that in the other three groups. After coating packaging a gas environment with low  $O_2$  content and high  $CO_2$  content was formed within membrane of cherry tomatoes in the other three groups, which delayed the senility and rot of tomatoes. The decay rate in group A was less than

**Table 1** The sensorial evaluative changes of cherry tomatoes

Experimental group	Color	Smoothness
Group A	Gradually changed from jacinth to red, with a small amount yellow	Slight fold individually
Group B	Gradually changed from jacinth to red	Fold individually
Group C	Gradually changed from jacinth to red	A large amount of fold
Group D	Changed from jacinth to dark red	All fold

that in the other three groups, as shown in Fig. 8. The carrageenan coating packaging in group A can significantly delay the increase of the decay rate in cherry tomatoes during storage.

### 3.9 Sensory Evaluation of Coating Packaging for Cherry Tomatoes

Sensory evaluative was made in the 15th day of storage. From Table 1, the color of cherry tomatoes with carrageenan coating materials in group A gradually changed from jacinth to red, had a small amount yellow and slight fold individually. It has a good appearance in color and smoothness than the other three groups. Therefore, the cherry tomatoes with carrageenan coating packing in group A can keep a good appearance.

## 4 Conclusions

In this experiment, three kinds of coating solution made from edible coating material carrageenan, carboxymethyl cellulose and sodium alginate were coated onto the surface of cherry tomatoes, then the preservation packaging experiment combined with modified atmosphere technology were made, the sensory index and physiological index of cherry tomatoes were tested to validate the effect of preservation on the cherry tomatoes with the edible coating packaging. The study shows that developed edible coating material carrageenan coating solution has an obvious preservation effect on cherry tomatoes, which can be used in preservation packaging for the cherry tomatoes and other fruits and vegetables.

## References

1. Le Yang, Hongxin Wang. (2011). Effect of different edible coatings preservative on the preservation of *Chimonobambusa busa utilis* shoots. *The Science and Technology of Food Industry*, 32(2): 306–308.

2. Baogang Wang, Wensheng Li, Xiaoyuan Feng, et al. (2011). Changes of qualities in sweet cherry stored with CA Box. *Chinese Agricultural Science Bulletin*, 27(30): 253–257.
3. Lingyun Pang, Yu Li, Meiyun Zhu, et al. (2009). Preservation effect of Soy Protein Isolate (SPI)—Chitosan composite film on Cherry Tomatoes. *Food Science*, 30(20): 426–429.
4. Yana Li, Ruiyong Li. (2011). Study of Cherry Tomato Preservation with Chitosan Coating. *Packaging and Food Machinery*, 29(3): 9–23.
5. Kaihua Liu, Yuhang Zhang, Shujie Xing. (2014). Study on the effect of tea Polyphenol-incorporated Chitosan Antibacterial films on fresh preservation of Cherry Tomatoes. *Food Research and Development*, 35(2): 109–112.
6. General Administration of Quality Supervision, Inspection and Quarantine of the People's Republic of China. (2009). GB/T 12456-2008 Determination of Total Acid in Food. Beijing: Standards Press of China.
7. Jun Li. (2000). Determining Reductive Ascorbic by Molybdenum Blue Colorimetry. *Food Science*, 21(8): 42–44.
8. Yanchun Xiao, Enchun Lei, Xiujie Guan, et al. (2011). Comparison of two methods of determining the content of reductive Vitamin C in Vegetable. *Hubei Agricultural Sciences*, 50(5): 1035–1037.
9. Zaibin Hao. (2004). Plant Physiology Experiment. Harbin: Harbin Institute of Technology Press.
10. Xianliang Song, Shengying Ye, Wei Huang, et al. (2010). Fresh-keeping effect of Nano-Titania/Corn starch compound coating on Cherry Tomato. *Food Science*, 31(12): 255–259.
11. Huayun Zhang, Deren Xiu Qiulian Kong, et al. (1999). Analysis on the factors affecting storage quality of ju-feng grape. *Sino-Overseas Grapevine & Wine*, (2): 8–11.
12. Kunming Zhang, Zhiqiang Zhu, Shaozhuang Nong, et al. (2011). Effects of controlled freezing point technology combined with modified atmosphere package on preservation for grape. *Food Research and Development*, 32(1): 126–130.
13. Wenbin Ye, Liang Fan, Hanbo Yuan. (2010). Preservation effect of Polysaccharide Coating and Refrigerated packing on Waxberry. *Hubei Agricultural Sciences*, 52(3): 650–654.
14. Wenhui Wang, Xisheng Sun, Zhiqiang Li, et al. (2004). Effects of 1-MCP on some Postharvest Physiological and Biochemical indexes of Pears. *Plant Physiology Communication*, 40(2): 175–177.
15. Snowdon A L. (1990). A colour Atlas of postharvest and Diseases Disorder of Fruits and vegetables. London: Dnolfe Scientific Ltd, 206–231.
16. Hui Wang, Dili A. (1992). The Relationship between the Metabolism of Organic Acid and the Browning of Grapes during Storage. *Study on Arid Area*, (4): 68–71.
17. Li Tong, Xin Wang, Qianmu Wen, et al. (2008). Relationship between the change of gross sugar content, Vitamin C content, respiration intensity, penetrability of cell membrane and storability. *Seed*. 27(10): 23–25.
18. Yiqiang Ge, Weiyi Zhang, Qiang Ye, et al. (1997). The Effect of Sulfur Dioxide on Some Enzyme Activities, Nutrient Compositions and Membrane Permeability of Table Grape. *Journal of Xinjiang Agricultural University*, 20(2): 48–52.

**Part X**  
**Novel Functional Material Technology**

# Highly Sensitive Flexible Pressure Sensor with Microstructural Dielectric Layer

Zhengbo Li, Lianfang Li, Lixin Mo, Zhenguo Wang, Wei Yang, Hui Zhou, Haichao Zhang and Luhai Li

**Abstract** Flexible pressure sensors have attracted increasing attention recently because of their high sensitive, flexible and widely applications in wearable electronics. In this paper, a flexible pressure sensor based on parallel plate capacitor mold was prepared. The high sensitivity of the prepared pressure sensor is achieves by fabricating the microstructural dielectric layer of polydimethylsiloxane (PDMS), which is more compressible compared to that of non-microstructural PDMS. The fabricating process of the microstructural dielectric, the effects of the microstructures, elastic modulus and thickness of the dielectric layer on the sensitivities of the flexible pressure sensor are investigating. The optimizing sensor exhibits high sensitivity of  $1.284 \text{ kPa}^{-1}$ , relatively low detection limits of 50 mg and superior physical robustness. The prepared flexible pressure sensor has the potential applications into the wearable electronics and health monitor devices such as breath, heartbeat and blood pressure detections.

**Keywords** Flexible pressure sensor · Microstructure · Highly sensitive · Wearable electronics

## 1 Introduction

Nowadays, the flexible pressure sensors have received significant attention for their high sensitivity and wide applications in the wearable electronics, environmental monitoring, human-machine interfaces and robotics [1, 2]. Especially monitoring human physiological signals with the newly flexible pressure sensor has considered

---

Z. Li · L. Li · L. Mo (✉) · Z. Wang · W. Yang · H. Zhou · H. Zhang · L. Li (✉)  
Beijing Engineering Research Center of Printed Electronics, Beijing Institute of Graphic Communication, Beijing, China  
e-mail: molixin@bigc.edu.cn

L. Li  
e-mail: liluhai@bigc.edu.cn



as an effective approach to evaluate human health [3, 4]. The reported pressure sensor was mainly based on four detection mechanism: the resistive mold [5, 9–14], triboelectric mold [8, 9], piezoelectric mold [15–17], and capacitive mold [6, 7, 18–22]. While the capacitive pressure sensor has received tremendous attention in recently years because of its advantage in tiny pressure detection and rapid response. For achieving high sensitivity, increasing researchers focus their attentions on fabricating microstructure layers of the sensor. Recently, Pang et al. [23] reported a highly sensitive, multiplex strain sensor based on the microstructure of the interlocked nanofiber arrays. Bao et al. [24] also used different microstructural elastomers as dielectric layer in capacitive pressure sensors and investigated the effects of the structure on the properties of the sensor. The results indicated that the optimal shapes could sharply increase the sensitivity of the pressure sensor. Zhang et al. [25] duplicated the microstructure of the silk with polydimethylsiloxane (PDMS) and used the microstructural PDMS as electrodes to increase the device's sensitivity.

In this paper, we present a highly sensitive and flexible capacitive pressure sensor with the microstructural dielectric layer. The fabrication process of the microstructural dielectric, the effects of the microstructures, elastic modulus and thickness of the dielectric layer on the sensitivity of the flexible pressure sensor are investigating. The prepared flexible pressure sensor has the potential applications into the wearable electronics and health monitor devices such as breath, heartbeat and blood pressure detections.

## 2 Experiment

### 2.1 *Preparation and Characterization of the Microstructural PDMS (Dielectric Layer)*

The microstructural PDMS used as the dielectric layer of the flexible pressure sensor was fabricating by duplicating the etched silicon template with pyramidal structure. First, the silicon template with pyramidal structure of 40  $\mu\text{m}$  base and 38  $\mu\text{m}$  high in the interval of 40  $\mu\text{m}$  was prepared by etching. Then the prepared silicon template was treating by tridecafluoro-1, 1, 2, 2-tetrahydrooctyl trichlorosilane (AR, Sigma-Aldrich) with the CVD method, which facilitate the peeling-off of the PDMS from the surface of the silicon template. The mixture of the PDMS and its curing agent (10:1 in volume, Sylgard 184, Dow Corning) was casting onto the surface of the silicon template, followed by degassing and 80  $^{\circ}\text{C}$  heating for 2 h in the vacuum oven. Finally, the cured and micro-structured PDMS is peeling off from the surface of the silicon template. The microstructure of the prepared PDMS was observed by Scanning Electron Microscope (SEM, S4800, Hitachi).

## 2.2 Preparation and Characterization of the Flexible Pressure Sensor

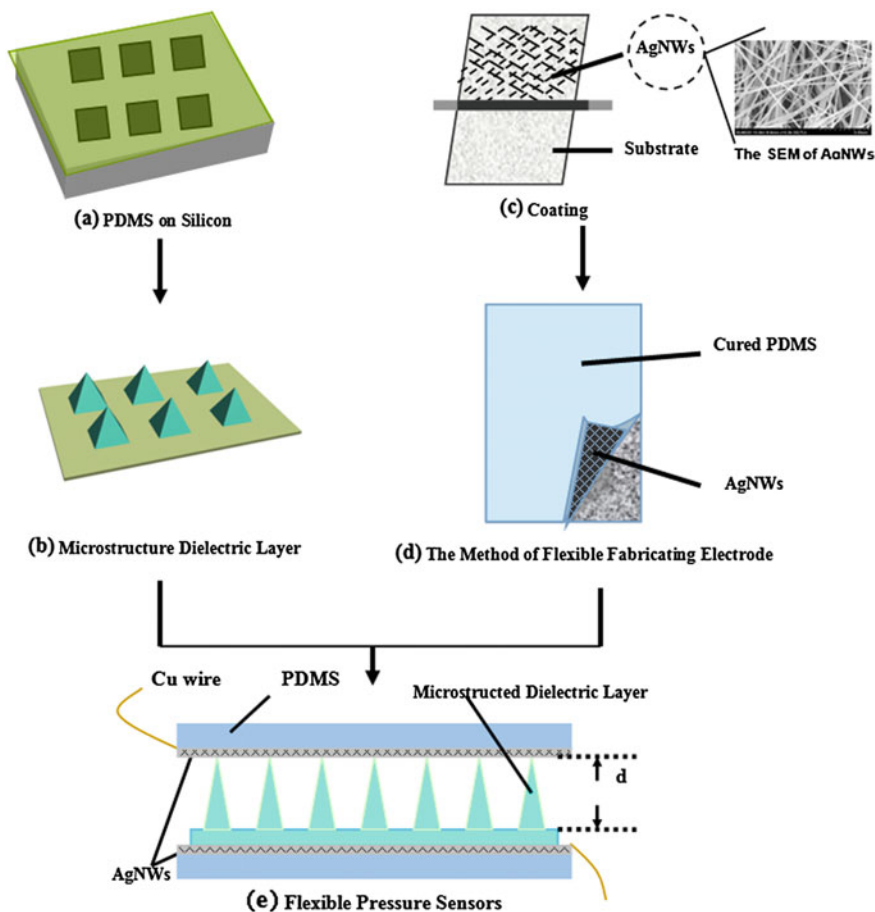
Figure 1 gives the preparation processes and the structure of the flexible pressure sensor. The flexible pressure sensor is a “sandwich” structure, which composes two opposite electrodes and a microstructural dielectric layer in the middle (Fig. 1e). The prepare process of dielectric layer described in Sect. 2.1 is shown in Fig. 1a–b. The prepare process of the electrodes was given in Fig. 1cd. The 7 wt% silver nanowires suspension was coated onto the surface of the substrate (photographic paper, Epson, S020) by 7# Mayer rod, followed by 80 °C heating for 10 min to increase its conductivity. Then the silver nanowires were transfer from photographic paper onto the surface of the PDMS by the method described in Sect. 2.1. The force gauge (HP-5, Handpi Digital) was using to apply the external pressure. The capacitances of the flexible sensor under various applied pressures were measure by digital capacitance multimeter (TH2617).

## 3 Results and Discussion

### 3.1 Effect of the Microstructures of Dielectric Layer on the Sensitivity of the Pressure Sensor

The cross section images of the prepared flexible pressure sensor are giving in Fig. 2a, b. As shown in Fig. 2a, the pyramidal structures are clearly observing on the top of the PDMS base. In addition, the pyramidal structures support and separate two opposite electrodes shown in Fig. 2b.

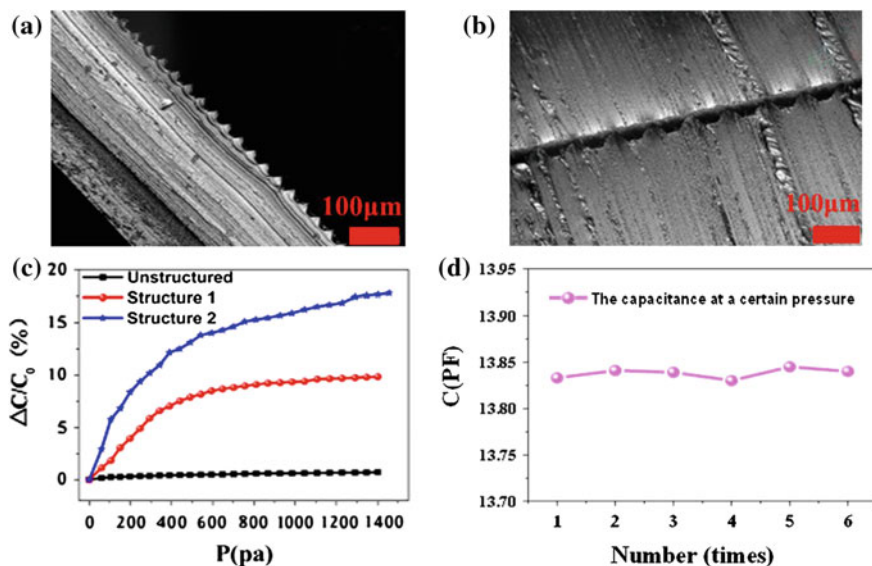
It is widely known that the capacitance change is inversely proportional to the distances change of the two opposite electrodes. Thus increasing the compressibility of the dielectric layer under pressure could improve the sensitivity of the sensor in theory. Figure 2c gives the pressure dependent capacitance change curves of the flexible sensors with and without the microstructural dielectric layer. The results indicate that the sensitivity of the sensor with the microstructural dielectric layer is significant higher than that of the sensor without the microstructural dielectric layer. The result suggests that the fabrication of the microstructure of the sensor could improve its sensitivity effectively. In addition, the stability of the flexible pressure sensor in the condition of loading-unloading cycles was also investigating shown in Fig. 2d. A certain weight was loaded and unloaded onto the pressure sensor in six times. The tested capacitances are almost the same (the variation is under 0.1 PF), which indicates that the prepared flexible pressure sensor demonstrates a relatively good stability.



**Fig. 1** Preparation processes of the flexible pressure sensor, **a–b** the fabrication of the microstructural dielectric layer, **c–d** the preparation of the electrodes based on silver nanowires and PDMS substrate, **e** the “sandwich” structure of the sensor

### 3.2 *Effects of Elastic Modulus of Dielectric Layer on the Sensitivity of Flexible Pressure Sensor*

As mentioned in Sect. 3.1, the compressibility of the dielectric layer has a significant influence on the sensitivity of the capacitance pressure sensor. Thus in this section, the Young’s modulus of PDMS was adjusted by changing the weight ratio between pre-polymer and curing agent and its effects on the sensitivity of the pressure sensor was investigated. Table 1 shows the Young’s modulus of the PDMS in different curing agents. It could see that as the decreasing of the curing agent, the Young’s modulus of the PDMS also decreases accordingly. This is

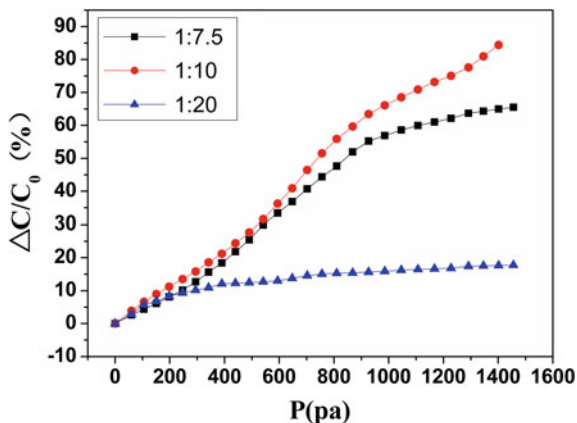


**Fig. 2** a–b is the cross section images of the sensor with pyramidal structural dielectric layer, c pressure dependent capacitances change of the sensors with and without microstructure, d the stability testing of the flexible pressure sensor

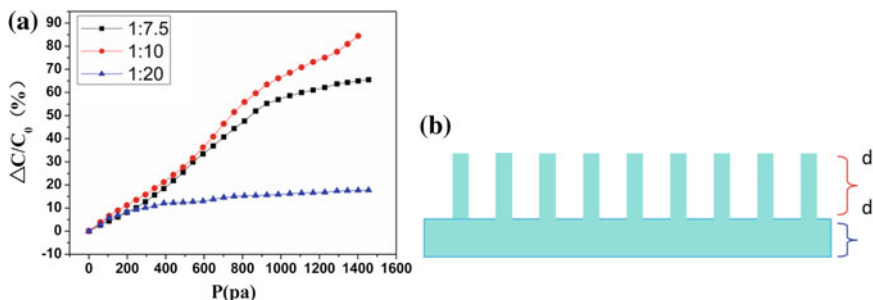
**Table 1** Young’s modulus of the PDMS prepared in different curing agent

Curing agent: PDMS	Young’s modulus (MPa)
1:7.5	3.01
1:10	2.03
1:20	0.55

attributing to the less formation of the cross-link structure of the PDMS when the curing agent is decrease. Figure 3 gives the pressure dependent capacitances change of the flexible pressure sensors with different Young’s modulus dielectric layers. The sensitivities of the sensors are almost the same in the very beginning (0–200 Pa). While the sensitivity of the sensor with relatively low Young’s modulus of 0.55 MPa decreases sharply when the applied pressure above 200 Pa. And the pressure sensor using the PDMS dielectric layer with Young’s modulus of 2.03 MPa (the weight ratio between curing agent and pre-polymer is 1:10) exhibits relatively large testing range from 0 to 1600 Pa. Above results indicate that the dielectric layer with large Young’s modulus has relatively small deformation, resulting in relatively low sensitivity. On the other hand, excessively low Young’s modulus makes the dielectric layer easy to reach the deformation limit under certain pressure, leading to the relatively small testing range.



**Fig. 3** Pressure dependent capacitances change of different sensors with various young's modulus dielectric layer



**Fig. 4** a Effects of the spin coating speed on the capacitances change of the sensors, b the schematic of the dielectric layer with base and microstructure

### 3.3 Effect of Dielectric Layer's Thickness on Sensors' Sensitivity

In this section, the effects of the dielectric layer's thickness on sensors' sensitivity are investigating. The thickness of the dielectric layer was adjusting by changing the speed of the spin coating. The capacitances change of the sensors with different thickness dielectric layer in various spin coating speed is showing in Fig. 4a. It is obviously that the sensitivity of the flexible pressure sensor increases as the spin coating speed increasing. When the spin coating speed is 3000 rpm, the sensitivity of the sensor is  $1.284 \text{ kPa}^{-1}$ , which is over 2 order magnify compared to that of the 500 rpm spin coating ( $0.008 \text{ kPa}^{-1}$ ). Above discussion has confirmed that the microstructure plays an important role in increasing the sensitivity of the flexible pressure sensor. In this section, the increasing spin coating speed could decrease

the thickness of the dielectric layer's base ( $d'$  in Fig. 4b), which enlarge the microstructural effects on the sensitivity of the sensor. However, when the spin coating speed was over 3000 rpm, the dielectric layer is too thin to be peeling off from the silicon wafer.

## 4 Conclusions

In conclusion, the highly sensitive flexible pressure sensor based on microstructural dielectric layer has been prepared in a low cost and easy way. The fabrication process of the microstructural dielectric layer, the effects of the microstructures, Young's modulus and thickness of the dielectric layer on the sensitivity of the flexible sensor have been investigate. The results show that the microstructures of the dielectric layer increase its compressibility, resulting in the increasing of the sensitivity. The optimized sensor with pyramidal structural dielectric layer of 2.03 MPa Young's modulus exhibits a high sensitivity of  $1.284 \text{ kPa}^{-1}$  and relatively low detection limits of 50 mg. The prepared flexible pressure sensor has the potential applications into the wearable electronics and health monitor. The relating work is ongoing.

**Acknowledgements** This work was supported by NSFC (61474144), Beijing Municipal Commission of Education (KZ201510015001), Beijing Institute of Graphic Communication talents selection & training project, Beijing Innovation Ability Improving Program (TJSHG201310015016), Beijing Municipal Commission of Education 2011 Collaborative innovation center, printed electronics technology & engineering discipline construction (III) and BIGC (23190414033).

## References

1. C. Wang, D. H. Wang, Z. Yu, K. Takei, J. Park, T. Chen, B. Ma and A. Javey, (2013). User-interactive electronic skin for instantaneous pressure visualization, *Nat. Mater.*, 12, 899–904.
2. D. J. Lipomi, M. Vosgueritchian, B. C. K. Tee, S. L. Hellstrom, J. A. Lee, C. H. Fox and Z. Bao, (2011), Skin-like pressure and strain sensors based on transparent elastic films of carbon nanotubes, *Nat. Nanotechnol.*, 6, 788–792.
3. L. Masia, H. I. Krebs, (2007), Design and characterization of hand module for whole-arm rehabilitation following stroke, *IEEE/ASME Trans. Mechatronics*, 12, 399–407.
4. M. Donati, N. Vitiello, (2013), Flexible sensor technology for the distributed measurement of interaction pressure, *Sensors*, 13, 1021–1045.
5. C. Pang, G.-Y. Lee, T.-I. Kim, S. M. Kim, H. N. Kim, S.-H. Ahn and K.-Y. Suh, (2012). A flexible and highly sensitive strain-gauge sensor using reversible interlocking of nanofibres, *Nat. Mater.*, 11, 795–801.
6. S. C. B. Mannsfeld, B. C.-K. Tee, R. M. Stoltenberg, S. Barman, B. V. O. Muir, A. N. Sokolov, C. Reese and Z. Bao, (2010), Highly sensitive flexible pressure sensors with microstructured rubber dielectric layers, *Nat. Mater.*, 9, 859–864.

7. S. Yao and Y. Zhu, (2014), Wearable multifunctional sensors using printed stretchable conductors made of silver nanowires, *Nanoscale*, 6, 2345–2352.
8. E. S. Dellon, R. Mourey and A. L. Dellon, (1992), Human pressure perception values for constant and moving one- and two-point discrimination, *J. Plast. Reconstr. Surg.*, 90, 112–117.
9. B. C.-K. Tee, C. Wang, R. Allen and Z. Bao, (2012), An electrically and mechanically self-healing composite with pressure- and flexion-sensitive properties for electronic skin applications, *Nat. Nanotechnol.*, 7, 825–832.
10. H.-B. Yao, J. Ge, C.-F. Wang, X. Wang, W. Hu, Z.-J. Zheng, Y. Ni and S.-H. Yu, (2013), a flexible and highly pressure-sensitive graphene-polyurethane sponge based on fractured microstructure design, *Adv. Mater.*, 25, 6692–6698.
11. L. Pan, A. Chortos, G. Yu, Y. Wang, S. Isaacson, R. Allen, Y. Shi, R. Dauskardt and Z. Bao, (2014), An ultra-sensitive resistive pressure sensor based on hollow-sphere microstructure induced elasticity in conducting polymer film, *Nat. Commun.*, 5, 3002.
12. B. Zhu, Z. Niu, H. Wang, W. R. Leow, H. Wang, Y. Li, L. Zheng, J. Wei, F. Huo and X. Chen, (2014), Microstructured graphene arrays for highly sensitive flexible tactile sensors, *Small*, 10, 3625.
13. J. Lee, S. Kim, J. Lee, D. Yang, B. C. Park, S. Ryu and I. Park, (2014), A stretchable strain sensor based on a metal nanoparticle thin film for human motion detection, *Nanoscale*, 6, 11932–11939.
14. Q. Shao, Z. Niu, M. Hirtz, L. Jiang, Y. Liu, Z. Wang and X. Chen, (2014), High-Performance and Tailorable Pressure Sensor Based on Ultrathin Conductive Polymer Film, *Small*, 10, 1466–1472.
15. J. Chen, K. Y. Lee, C.-Y. Kang, M. W. Kim, S.-W. Kim and J. M. Baik, (2014), Embossed Hollow Hemisphere Based Piezoelectric Nanogenerator and highly responsive pressure sensor, *Adv. Funct. Mater.*, 24, 2038–2043.
16. C. Hou, T. Huang, H. Wang, H. Yu, Q. Zhang and Y. Li, (2013), A strong and stretchable self-healing film with self-activated pressure sensitivity for potential artificial skin applications, *Sci. Rep.*, 3, 3138.
17. C. Pan, L. Dong, G. Zhu, S. Niu, R. Yu, Q. Yang, Y. Liu and Z. L. Wang, (2013), High-resolution electroluminescent imaging of pressure distribution using a piezoelectric nanowire LED array, *Nat. Photonics*, 7, 752–758.
18. W. Hu, Z. Niu, R. Zhao and Q. Pei, (2013), Elastomeric transparent capacitive sensors based on an interpenetrating composite of silver nanowires and polyurethane, *Appl. Phys. Lett.*, 102, 083303.
19. J. Kim, T. N. Ng and W. S. Kim, (2012), Highly sensitive tactile sensors integrated with organic transistors, *Appl. Phys. Lett.*, 101, 103308–103308-5.
20. D. J. Lipomi, M. Vosgueritchian, B. C.-K. Tee, S. L. Hellstrom, J. A. Lee, C. H. Fox and Z. Bao, (2011), Skin-like pressure and strain sensors based on transparent elastic films of carbon nanotubes, *Nat. Nanotechnol.*, 6, 788.
21. K.F. Lei, K.-F. Lee and M.-Y. Lee, (2012), Development of a flexible PDMS capacitive pressure sensor for plantar pressure measurement, *Microelectron. Eng.*, 99, 1–5.
22. H. Vandeparre, D. Watson and S. P. Lacour, (2013), Extremely robust and conformable capacitive pressure sensors based on flexible polyurethane foams and stretchable metallization, *Appl. Phys. Lett.*, 103, 204103–204103-4.
23. C. Pang, G. Y. Lee, T. I. Kim, S. M. Kim, H. N. Kim, S. H. Ahn, K. Y. Suh, (2012), A flexible and highly sensitive strain-gauge sensor using reversible interlocking of nanofibres, *Nat. Mater.*, 11, 795–801.
24. Benjamin C.-K. Tee, Alex Chortos, Roger R. Dunn, Gregory Schwartz, Eric Eason, and Z. Bao, (2014), Tunable Flexible Pressure Sensors using Microstructured Elastomer Geometries for Intuitive Electronics, *Adv. Funct. Mater.*, 24, 5427–5434.
25. X. W. Wang, Yang G., T. Zhang, (2014), Silk-molded flexible, ultrasensitive, and highly stable electronic skin for monitoring human physiological signals, *Adv. Mater.*, 26, 1336–1342.

# Hydrophilic Modification and Characterization of Bagasse Cellulose

Tingli Liu and Guangxue Chen

**Abstract** The presence of surface hydroxyl groups of the cellulose makes it have good hydrophilia. By means of alkali treatment, the fiber surface polarity could be lower, reducing the surface polarity of the fibers make it readily recombine with thermoplastic materials, therefore the composite material properties become better. With the experiments of different treatment time and concentration of alkali treatment, measuring the untreated and treated surface free energy of fibers. By means of analysis and comparison, the conclusions are as below: Polar surface free energy after the alkali treatment of bagasse fibers is reduced in varying degrees. The optimum time and concentration of alkali treatment are 48 h and 20%.

**Keywords** Plant fiber · Surface modification · Alkali treatment · Contact angle

## 1 Introduction

The characteristic of the fiber surface plays an important role in plant fiber/thermoplastic composite materials. Because the surface of the bagasse fiber has the strong hydroxyl groups, while the surface of the thermoplastic material mainly exist non-polar hydrocarbyl. Therefore, providing the surface polar of bagasse fiber is less small, its surface is more conducive to improve the strength of thermoplastic composite materials [1]. This paper is to analyze the surface property after the alkali treatment to find the approach that enables the surface polarity is the lowest.

---

T. Liu · G. Chen (✉)

State Key Laboratory of Pulp and Paper Engineering,  
South China University of Technology, Tianhe Qu, Guangdong, China  
e-mail: chengx@scut.edu.cn



## 2 Obtainment of the Surface Free Energy of the Bagasse Fibers Without Modification

### 2.1 Experimental Principle

The contact angle is the angle, conventionally measured through the liquid, where a liquid–vapor interface meets a solid surface and also represents the wetness degree. After the alkali and silanization treatment, the surface of the bagasse fiber powder has changed, which enables to reduce the hydrophilic property. Therefore, the modified bagasse fiber powder enables the contact angle to become larger, due to the reduced hydrophilic property so that the weaker the hydrophilic property the larger the contact angle becomes. Furthermore, whether the hydrophilic property of the modified bagasse fiber powder is strong or not that will be judged by measuring the contact angle of the modified bagasse fiber powder.

There are two approaches to measure the contact angle of the solid powder [2]: the permeating method (the permeating height method as well as the permeating speed measurement) and the thin-layer wicking technique [3]. This experiment mainly adopts permeating height method.

The specific steps are as follows: the bottom of the measuring pipe is inserted the specific gasket to prevent the powder leaking and make the liquid flow freely. Then the solid powder with the same quality is put in the sounding pipe in line with the same method as to make the liquid contact the bottle of the pipe by the opportune clamping and lifting tool. Therefore, the liquid is constantly rising under the capillary forces and the rising height  $A$  within  $t$  can be described by the Washburn equation:

$$h^2 = (\gamma R \cos \theta / 2\eta) \cdot t \quad (1)$$

which the surface tension of the liquid is  $\gamma$ , the valid capillary radius of the powder column  $R$ , the viscosity of the liquid  $\eta$ , the contract angle  $\theta$ , the time of the rising height  $t$ . And to draw the figure used  $h^2$  as well as  $t$  is to get the slope of the straight line

$$k = \gamma R \cos \theta / 2\eta \quad (2)$$

And then could get:

$$\cos \theta = 2k\eta / (\gamma R) \quad (3)$$

In the beginning, the experiment often performed with the liquid samples that have contract angle at zero degree as to find the effective:  $R$ , while other experiments are carried on with other liquid to derive the corresponding  $\theta$  so that the solid surface free energy can be estimated by Young equation [4].

## 2.2 *Experimental Methods and Steps*

### 2.2.1 **Treatment of the Bagasse Fiber**

The over dry stock of bagasse is smashed with the grinder and screen with the size of 80–100, ultimately, the screened fiber powder need proceed the alkali and silanization treatment [5].

### 2.2.2 **Preparation of the Measuring Tube**

Preparing several 2 ml pipettes and intercepting 60 mm of the scale and polishing the cut of the pipette with sandpaper.

### 2.2.3 **Putting the Sample**

The gasket is initially put on the head of the tube, then putting the fiber powder into the tube by the small funnel, whereas the weight of the measuring tube should be measured with scale before putting the sample, for the sake of the same weight. Next, peeling and measuring to control the addition after putting the sample, then the operation should keep same in putting the sample, for keeping the same tightness.

### 2.2.4 **Experiment**

The measuring tube which is loaded with the samples is nipped with the lifting shelf and contains its verticality. Then make the detective liquid filled in the 130 mm-diameter glassware and directly places it under the tube. Putting the tube under the detective liquid about 5 mm, when the liquid in the tube is up to the predetermined scale, timing and recording the rising distance  $h$  and the corresponding time:  $t$ .

The experimental data is obtained by measured powder contact angle, drawing with the rising height of capillary  $h^2$  and time  $t$  and obtain the slope  $k$ , then determining the effective capillary radius  $R$  of the bagasse fiber powder column in line with Washburn equation  $h^2 = (\gamma R \cos \theta / 2\eta) \cdot t$ ,  $\gamma_{LV}$  of selected standard liquid, and the formula  $\cos \theta = 2k\eta / (\gamma R)$ . In this experiment, methanol alcohol with the lowest surface tension is selected as the standard liquid. Therefore, after derived the radius  $R$  and taking back it into the formula:  $\cos \theta = 2k\eta / (\gamma R)$ , therefore, cosine value of the contract angle of ethylene glycol, methyl amide as well as distilled water in the bagasse fiber power surface are derived. After derived  $\cos \theta$  of the contract angle of the bagasse fiber power surface in various detective liquids, substituting the cosine value into the formula respectively:

$$\frac{\gamma_{LV}(1 + \cos \theta)}{2(\gamma_{LV}^d)^{\frac{1}{2}}} = (\gamma_S^d)^{\frac{1}{2}} + (\gamma_S^p)^{\frac{1}{2}} \left( \frac{\gamma_{LV}^p}{\gamma_{LV}^d} \right)^{\frac{1}{2}} \quad (4)$$

$\gamma_{LV}$  is the surface tension of the liquid,  $\gamma_{LV}^d$  is the non-polar surface free energy of the liquid,  $\gamma_{LV}^p$  is the polar surface free energy of the liquid. Using  $\left(\frac{\gamma_{LV}^p}{\gamma_{LV}^d}\right)^{\frac{1}{2}}$  as abscissa axis and  $\frac{\gamma_{LV}(1 + \cos \theta)}{2(\gamma_{LV}^d)^{\frac{1}{2}}}$  as vertical axis to draw a diagram and calculate the square of the slope, which is the value  $\gamma_S^p$  of the polar surface free energy and the intercept square is the value  $\gamma_S^d$  of the non-polar surface free energy of the bagasse fiber [6]. The  $\gamma_{LV}$ ,  $\gamma_{LV}^d$ ,  $\gamma_{LV}^p$  and viscosity  $\eta$  of the liquids are shown in Table 1. After multiple metering and linear regressions in the average  $k$  and  $\cos \theta$  of the bagasse fiber powder without modification could be obtained in line with the Formulas (2) and (3) as shown in Table 2.

The average  $\gamma_S^d$  and  $\gamma_S^p$  of the bagasse fiber powder without modification could be obtained in line with the formula (4), therefore the surface free energy  $\gamma_S$  could be obtained. The surface free energy  $\gamma_S$  of the bagasse fiber without modification is  $36.452 \text{ mJ m}^{-2}$ , the non-polar surface free energy  $\gamma_S^d$  is  $13.133 \text{ mJ m}^{-2}$ , the polar surface free energy  $\gamma_S^p$  is  $23.319 \text{ mJ m}^{-2}$ .

**Table 1** Data of the surface tension and viscosity of the detective liquid

Detective liquid	$\gamma_{LV}$ (mNm <sup>-1</sup> )	$\gamma_{LV}^d$ (mNm <sup>-1</sup> )	$\gamma_{LV}^p$ (mNm <sup>-1</sup> )	$\eta$ (mNs m <sup>-2</sup> )
Methyl alcohol	22.5	22.5	0	0.593 (20 °C)
Ethanediol	48.3	29.3	19	21 (20 °C)
Formamide	58.2	39.5	18.7	3.764 (20 °C)
Distilled water	72.8	21.8	51	1.002 (20 °C)

**Table 2** Value of the  $k$  and the  $\cos \theta$  of the contact angle of the bagasse fiber powder without modification in different detective liquid

Detective liquid	$k$	$\cos \theta$
Methyl alcohol	50.865	1.000
Ethanediol	1.740	0.564
Formamide	3.254	0.157
Distilled water	13.417	0.138

### 3 Effect of the Alkali Treatment on the Bagasse Fiber

#### 3.1 Process of the Alkali Treatment

##### 3.1.1 Different Time of the Alkali Treatment

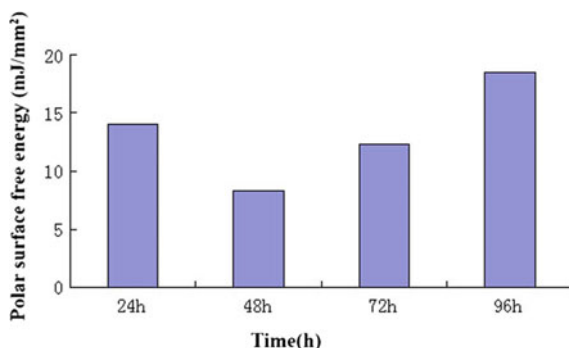
Weighing 2.5 g pre-treated bagasse fiber to put them into 4 dry 250 ml Erlenmeyer flask respectively, then adding 50 ml 20 wt% NaOH, quietly shaking it, stirring it with the magnetic stirrer in the same direction for 30 min as to scatter the bagasse fiber evenly in alkali liquid. Placing 24, 48, 72, 96 h under 20 °C. Up to the given time, filtering and cleaning the treated liquid until it neutral with a few drops of the acetic acid deionized water and dries below 60 °C. Therefore, the data diagram is drawn by measuring the witting contract angle of the bagasse fiber powder.

After multiple metering and linear regression, the average  $k$  and  $\cos \theta$  of the bagasse fiber powder with the alkali treatment could be obtained as shown in Table 3.

After collating and linear regression, the polar surface free energy of bagasse fiber after different times after the alkali treatment could be shown in the Fig. 1.

**Table 3** Value of the  $k$  and the  $\cos \theta$  of the contact angle of the alkali treated bagasse with 20% NaOH in liquid after 24, 48, 72 and 96 h

Detective liquid	$k$				$\cos \theta$			
	24 h	48 h	72 h	96 h	24 h	48 h	72 h	96 h
Methyl alcohol	33.069	32.175	14.003	28.451	1.000	1.000	1.000	1.000
Ethanediol	0.752	1.484	0.367	0.712	0.3682	0.761	0.4318	0.4122
Formamide	4.444	8.164	6.101	6.9625	0.3237	0.6227	1.000	0.6004
Distilled water	22.066	10.800	8.838	25.378	0.3421	0.1752	0.3296	0.4657



**Fig. 1** Polar surface free energy of the bagasse fiber under the different time after the alkali treatment

The above data illustrates that after alkali treatment 48 h, the polar surface free energy of the bagasse fiber is smaller in comparison of the treatment after 24 h. When the treatment time is over 48 h, the polar surface free energy is gradually increasing, which means the opportune treatment time of the bagasse fiber is 48 h of the treatment with 20 wt% NaOH, because the polarity of the bagasse fiber is minimum and the hydrophilia is weakest in this time.

### 3.1.2 Different Concentration of the Alkali Treatment

Weighing 2.5 g pre-treated bagasse fiber to put them into 4 dry 250 ml Erlenmeyer flask respectively, then adding 50 ml NaOH concentrated 10, 15, 20, 25 wt% respectively, shaking it quietly, stirring it with the magnetic stirrer in the same direction for 30 min as to scatter the bagasse fiber evenly in alkali liquid, and placing respectively below 20 °C in 48 h. Up to the given time, filtering and cleaning the treated liquid until it neutral with a few drops of the acetic acid deionized water and dries below 60 °C. After multiple metering of contract angle and linear regression, the average  $k$  and  $\cos \theta$  of the bagasse fiber powder with the alkali treatment could be obtained in line with the Formulas (2) and (3) as shown in Table 4.

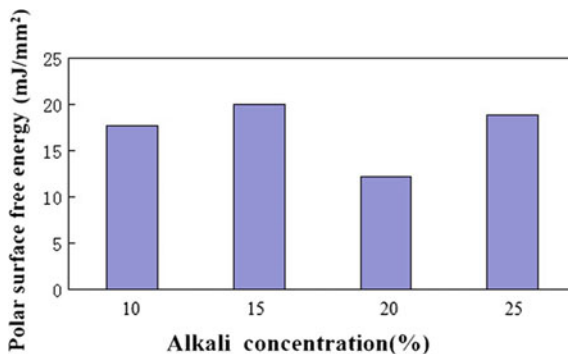
After collating and linear regression, the polar surface free energy of bagasse fiber under the different alkali concentration could be shown in the Fig. 2.

The experimental data illustrates that when the concentration of NaOH is up to 20 wt%, the polarity of the bagasse fiber is the minimum and the hydrophilia is weakest. While the concentration is increased to 25%, the polarity of the bagasse fiber becomes larger, which shows that the opportune concentration is 20 wt%.

**Table 4** Value of the  $k$  and the  $\cos \theta$  of the contact angle of the alkali treated bagasse with 10, 15, 20 and 25 wt% NaOH in liquid after 48 h

Detective liquid	k				cos $\theta$			
	10%	15%	20%	25%	10%	15%	20%	25%
Methyl alcohol	33.069	32.175	14.003	28.451	1.000	1.000	1.000	1.000
Ethanediol	0.752	1.484	0.367	0.712	0.3682	0.761	0.4318	0.4122
Formamide	4.444	8.164	6.101	6.9625	0.3237	0.6227	1.000	0.6004
Distilled water	22.066	10.800	8.838	25.378	0.3421	0.1752	0.3296	0.4657

**Fig. 2** Polar surface free energy of the bagasse fiber under the different alkali concentration of alkali treatment after 48 h



## 4 Conclusions

The above experiment shows that the alkali treatment could reduce the polar surface free energy of the bagasse fiber and enable the polarity of the fiber surface to become small and the reduce hydrophilia. While the opportune time of alkali treatment is in 48 h and the optimal concentration of alkali treatment is 20 wt%.

**Acknowledgements** This research was financially supported by the Guangdong Provincial Science and Technology Project (2013B010401007) and Science and Technology Program of Guangzhou (201607020045).

## References

1. CUI Yihua, ZHOU Yeqing, J. (2006). Interface Study on Wood Fiber Reinforced Thermoplastic Composites. *Fiber Composites*, (1), 53–57 + 36.
2. CHU Hong, Cui Zhenggang, J. (2004). Determination to the Contact Angle of the Small Particles. *Chemical Industry Times*, 18(10), 44–47.
3. CHU Hong, CUI Zhenggang, J. (2005). Determination of Contract Angle and Surface Free Energy Components of the Small Particles by Thin-Layer Wicking Technique. *Journal of Southern Yangtze University (Natural Science Edition)*, 4(3), 302–305.
4. LI Yali, GAO Mianhong, CAO Qiang, LIU Juan, J. (2014). Study on the Interfacial Compatibility of Modified Corn Stover Fibers. *Science Technology and Engineering*, 14(30), 221–224.
5. FANG Hongxia, WU Qianglin, JIANG Rong, LI Haiyun, ZHENG Yu, HAN Xin, J. (2014). Preparation and Carbonization Behavior of Bamboo Fiber Modified by Copolymerized Phenolic Resin. *Chinese Journal of Materials Research*, 28(11), 853–857.
6. REN Yiping, WANG Zheng, GAO Li, CHANG Liang, J. (2011). Effects of Coupling Agents on Bamboo Surface Wettability and Bonding Strength. *Adhesion* 32(7), 50–53.
7. WANG Yu, LIU Zhi-ming, J. (2015). Preparation and Silanization Modification of Nanofibrillated Cellulose. *Biomass Chemical Engineering*, 49(2), 17–20.

# Synthesis of 2-Allyloxy-3, 6, 7, 10, 11-Pentabutoxytriphenylene and Its Mesophases Study

Wanying Zhang, Xingtian Hao, Feng Hong, Jianchuang Wang, Shuaifeng Zhang, Chunxiu Zhang and Jialing Pu

**Abstract** A novel triphenylene-based discotic liquid crystal 2-Allyloxy-3, 6, 7, 10, 11-pentabutoxytriphenylene was synthesized. The chemical structure of this compound has determined by  $^1\text{H}$ NMR and FT-IR spectrum, and its mesophase was investigated by differential scanning calorimeter (DSC) and polarizing optical microscopy (POM) methods. This compound was expected to show classical texture of columnar phase in a wide mesophase temperature. Since this compound has an unsaturated bond, it also sets the foundation of designing liquid crystal polymer.

**Keywords** Liquid crystal · Columnar phase · Triphenylene

## 1 Introduction

Since the first discovery of discotic liquid crystals on the hexaesters of benzene in 1977 by Chandrasekhar [1], there has been an increasing interest in the synthesis and research of various new discotic liquid crystals. Among many different discotic molecules, discotic liquid crystals based on triphenylene core is the most widely synthesized and well-researched materials. Due to their pronounced photoconductivity and high charge carrier mobility, triphenylene-based columnar discotic liquid crystals show great potential as molecular organic materials for optoelectronic devices [2].

Triphenylene derivatives are easily to synthesis and purify. They have low melting point and good thermal stability, and they have already been excellent materials because of those great properties [3, 4]. In this paper, a novel triphenylene-based discotic liquid crystal 2-Allyloxy-3, 6, 7, 10, 11-pentabutoxytriphenylene was synthesized and analyzed. It's chemical structure

---

W. Zhang · X. Hao · F. Hong · J. Wang · S. Zhang · C. Zhang (✉) · J. Pu  
Beijing Institute of Graphic Communication, Beijing, China  
e-mail: zhangchunxiu@bigc.edu.cn

W. Zhang  
e-mail: zhangwanyingbigc@163.com

was determined by  $^1\text{H}$ NMR and FT-IR spectrum, and its mesophase was investigated by differential scanning calorimeter (DSC) and polarizing optical microscopy (POM) methods.

## 2 Experimental

Chemicals used in the synthesis if not specified were all analytic reagents (Beijing Chemical Reagents Co). The chemical structure was characterized by measuring on a Bruker DMX-300 300 MHz NMR spectrometer and FTIR-8400.

### 2.1 Synthesis of 2-Allyloxy-3, 6, 7, 10, 11-Pentabutoxytriphenylene

The target compound 4 was synthesized according to the route which was shown in Fig. 1.

The compound 1 was prepared according to the Williamson reaction. And then, 2, 3, 6, 7, 10, 11-hexabutoxytriphenylene was synthesized through the trimerization reaction catalysed by iron(III) chloride [5]. To get 2-hydroxyl-3, 6, 7, 10,

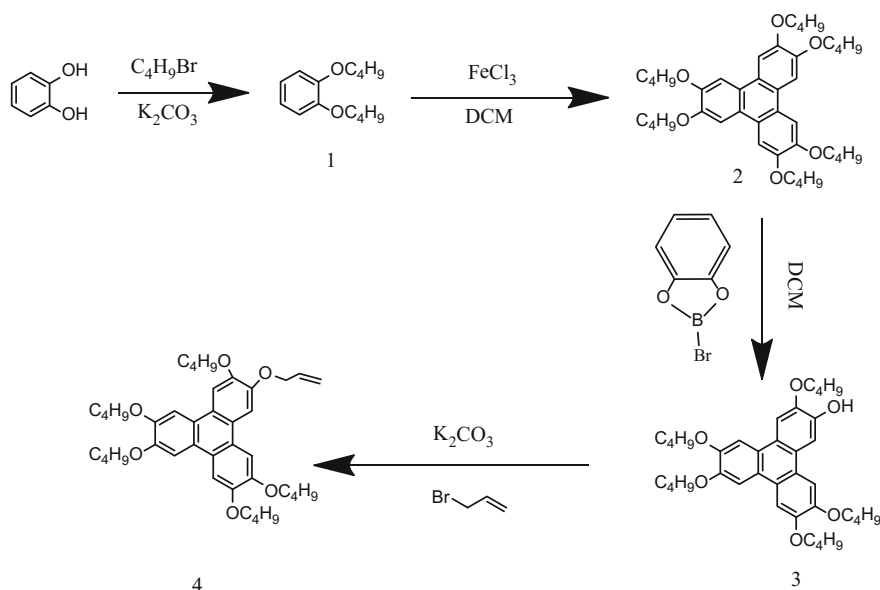


Fig. 1 Synthesized route of compound 4



11-pentabutoxytriphenylene (compound 3), I conducted a reaction on the basis of selective ether cleavages with B-bromocatecholborane [6]. I put 2-hydroxyl-3,6,7,10,11-pentabutoxytriphenylene (500 mg, 0.82 mmol), Potassium carbonate (334 mg, 2.42 mmol) and acetone (48 mg, 0.82 mmol) into a three-necked flask (100 ml) and stirred for 10–15 min, and then 3-Bromopropene (119 mg, 0.98 mmol) was added into it. This reaction was refluxed for 12 h on an oil bath with the protection of nitrogen at 60 °C. The product (compound 4) was purified by chromatography with the eluent of ethyl acetate-dichloromethane ether (1:8 v/v) and recrystallized in ethanol, the yield of compound 4 is 48.9%.

## 2.2 Characterization

Thermal and optical properties of the synthesized material were observed by using a Lecia polarizing optical microscope (POM) equipped with a Linkam LC600 hot stage and a Netzsch differential scanning calorimeter DSC (Thermal Analysis DSC 2010). The ramp rate in both POM and DSC was 10 °C min<sup>-1</sup>. The phase transition in the temperature range from 0 to 155 °C and related enthalpy was calculated by DSC.

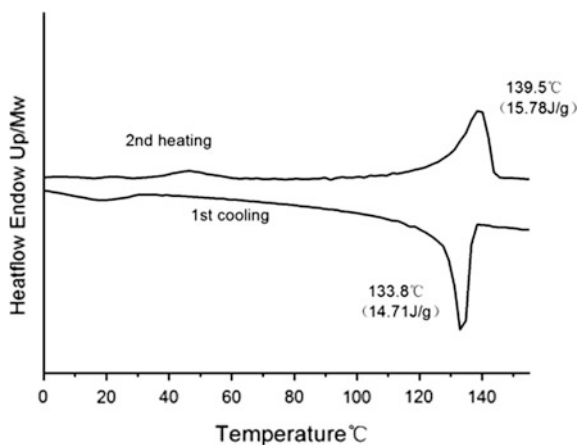
## 3 Results and Discussion

### 3.1 FT-IR and <sup>1</sup>HNMR

FT-IR (KBr):  $\nu_{\max}$  (cm<sup>-1</sup>): 1039, 917 (–CH=CH<sub>2</sub>), 2957, 2933, 2867 (–CH<sub>3</sub>/–CH), 3096, 3079 (–CH<sub>2</sub>), 1262, 1167 (–C–O–C–), 1616, 1523, 1436 (–C=C–).  
1H-NMR:  $\delta$ H (300 MHz, CDCl<sub>3</sub>): 7.80–7.89 (t, 6H), 6.17–6.26 (m, 1H), 5.34–5.57 (q, 2H), 4.82–4.83 (d, 2H), 4.24–4.26 (d, 10H), 1.54–1.67 (m, 20H), 1.02–1.07 (t, 15H).

### 3.2 Dsc

As we can see in the DSC thermogram (Fig. 2), the compound 4 has an endothermic transition (15.78 J/g) at 139.5 °C which is a clearing point during second heating run. This point shows us that the compound 4 transits into an isotropic phase and no other transitions detected during this process. During first cooling, there is an exothermic transition (14.71 J/g) at 133.8 °C, which shows the compound 4 transit from columnar phase into isotropic phase. Approximate enthalpies also prove this conclusion.



**Fig. 2** DSC thermogram of compound 4



**Fig. 3** Textures observed at 120 °C (*left*), 100 °C (*center*) and room temperature (*right*) during cooling process

### 3.3 Pom

Compound 4 is birefringent at room temperature and has no crystalline phase. As it is heated, it becomes a kind of mobile liquid, which becomes isotropic at 140 °C. When the liquid sample is cooled from 140 °C to the room temperature, it shows the texture as showed in Fig. 3. The POM revealed that it has the classical columnar phase textures.

## 4 Conclusions

A novel compound 2-allyloxy-3, 6, 7, 10, 11-pentabutoxytriphenylene was synthesized. Its structure was determined by  $^1\text{H}$ NMR and FT-IR spectrum, and its mesophase transition was characterized by differential scanning calorimeter (DSC) and polarizing optical microscopy (POM). This compound is shown

columnar phase at room temperature to 140 °C. Above all, this compound is determined as a typical columnar phase.

**Acknowledgements** This work is supported by the fund from the Beijing Municipal Education Commission Project (Grant No. 23190115024, Grant No. 25000115006, No. Byyc201316-007). The Importation and Development of High Caliber Talents Project of Beijing Municipal Institutions (CIT&TCD201304123), NSFC (21174016).

## References

1. Chandrasekhar S, Sadashiva BK, Suresh KA. (1977). Liquid crystals of disk-like molecules. *Pramana*, 7: 471–480.
2. Kumar, S., & Manickam, M. (1998). Synthesis of functionalized triphenylenes by selective ether cleavage with B-bromocatecholboane. *Synthesis*, 8, 1119–1122.
3. Bushby, R. J., & Lozman, O. R. (2002). Discotic liquid crystals 25 years on. *Current Opinion in Colloid & Interface Science*, 7: 342–354.
4. Kumar, S. (2004). Recent developments in the chemistry of triphenylene-based discotic liquid crystals. *Liquid Crystals*, 31(8): 1037–1059.
5. Boden, N., Borner, R. C., Bushby, R. J., Cammidge, A. N., & Jesudason, M. V. (1993). The synthesis of triphenylene-based discotic mesogens new and improved routes. *Liquid Crystals*, 15(6): 851–858.
6. Kumar, S., & Manickam, M. (1998). Synthesis of functionalized triphenylenes by selective ether cleavage with B-bromocatecholboane. *Synthesis*, 8:1119–1122.

# Research on the Preparation of Silver Nanoparticles by Chemical Reduction Method

Yanxiang Li and Fuqiang Chu

**Abstract** The synthesis of silver nanoparticles (AgNPs) by chemical reduction method was introduced in this chapter. The silver ammonia solution was taken as precursor, hydrazine hydrate was taken as reducing agent, and polyvinyl pyrrolidone (PVP) was taken as protective agent. This chapter mainly researched on ultra-fine silver powder prepared by chemical reduction method. The synthetic nano silver particle size was very small, which could be applied to conductive ink as the filler. The results showed that the comprehensive performance of AgNPs was optimal under the following synthetic conditions: the reaction temperatures was 50 °C, the mass fraction ammonia is 2%. The characterization was as follows: the average particle size was 157.1 nm, the surface of AgNPs was coated by PVP, and the UV-vis absorption spectra were measured at 427 nm.

**Keywords** Silver nanoparticles · Chemical reduction method · Particle size

## 1 Introduction

In the modern information society, the updating of electronic products is changing the way of people's life style and living environment. In recent years, the print electronic technology sets off at home and abroad, to accelerate the development of conductive paste. Because the conductive properties of ultrafine silver powder is optimal, coupled with the current level of technology does not make other base metals effectively replace the silver powder [1, 2], which has been widely used in the electronics industry, the basic functions of electronic materials for the conductor material.

Silver nanoparticles (AgNPs) are widely used in electronics, chemical industry, medicine, energy and other fields [3, 4]. As an important part of conductive paste,

---

Y. Li · F. Chu (✉)

College of Printing and Packaging Engineering,  
Qilu University of Technology, Jinan, China  
e-mail: fqchu@126.com

© Springer Nature Singapore Pte Ltd. 2017

P. Zhao et al. (eds.), *Advanced Graphic Communications*

and *Media Technologies*, Lecture Notes in Electrical Engineering 417,

DOI 10.1007/978-981-10-3530-2\_136

1109

AgNPs have significant influence on the performance of the silver paste. Currently, the synthetic methods of silver nanoparticles include microemulsion method, chemical reduction method, electrochemical reduction method, high-energy ball mill method, biological synthesis, plasma evaporation condensation method [5–7], as well as other synthetic method.

Among them, the chemical reduction method possesses simple process, convenient operation, low production cost etc. Chemical reduction method can effectively control the particle size and morphology [8] of AgNPs by changing the reaction conditions.

In this chapter, AgNPs were synthesized by the chemical reduction method. By means of measuring the performance, such as particle size, FTIR spectrum, and UV-vis spectrum, the results showed that the synthetic nano silver was suitable for the preparation of conductive ink.

## 2 Experimental

### 2.1 Materials and Equipment

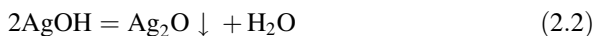
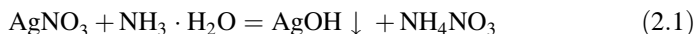
Silver nitrate ( $\text{AgNO}_3$ ), AR, was supplied by Tianjin Kemiou Chemical Reagent Co., Ltd. Hydrazine hydrate was produced by Tianjin Fuyu Fine Chemical Co., Ltd. Ammonium hydroxide and polyvinyl pyrrolidone K30 (PVP K30) were provided by Sinopharm Chemical Reagent Co., Ltd. Deionized water was made in the laboratory.

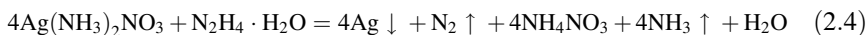
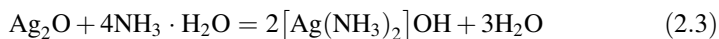
Nano particle and zeta potentiometer was used to measure the particle size of AgNPs. Fourier transform infrared spectrometer (FTIR) was used to character infrared spectra. Ultraviolet-visible spectrophotometer (UV-vis) was purchased from Shimadzu Enterprise Management (China) Co., Ltd. High-speed centrifuge was supplied by Hunan Xiangyi Instrument Centrifuge Co., Ltd.

### 2.2 Experiment Principle

In this experiment, the silver ammonium solution was taken as the precursor, PVP K30 was taken as the protective agent, and hydrazine hydrate [9] was taken as the reducing agent, to prepare nano silver.

Reaction principle was as follows:





### 2.3 Synthesis of Silver Nanoparticles

First of all, a certain amount of hydrazine hydrate was dissolved in deionized water, and the PVP K30 was added. The mixture was stirred well in thermostat water bath. Secondly, a certain amount of 28% wt ammonia water was diluted to 2 wt%. The silver nitrate was dissolved in the deionized water, and 2% wt ammonia water was added to the silver nitrate solution slowly, until that the precipitate was disappeared. The last solution was silver ammonia solution. Thirdly, the silver ammonia solution was added to the reducing solution at a uniform speed. Finally, the system turned brownish green turbid liquid, and the reaction terminated.

### 2.4 Characterization and Test

The particle size of the turbid liquid was tested by the Malvern nanoparticle and zeta potentiometer to characterize the influence of reaction temperature on the particle size of nano silver. The surface of AgNPs was measured by FTIR. The protective agent is determined by the infrared absorption spectrum. The turbid liquid was centrifuged by high-speed centrifuge at 8000 rpm, and washed by deionized water. UV-vis measured the absorption spectrum of nano silver.

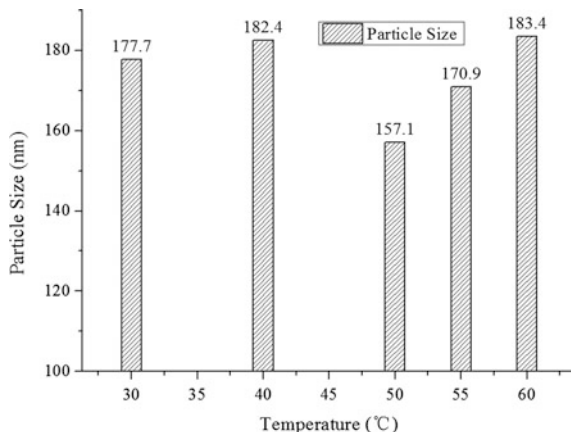
## 3 Results and Discussion

### 3.1 Influence of Reaction Temperature

The main factor affecting the particle's dissolution into the nucleus was the temperature. If the temperature was too high in reaction process, it was easy to reunite. The effect of the temperature on the synthesis of AgNPs was reflected by the average particle size.

As shown in Fig. 1, effects of temperature on the silver particle size could be seen that the particle size decreased first and then increased with the increase of the reaction temperature. With the increase of reaction temperature, the reaction rate was accelerated, the number of silver atoms was more and more, the silver atoms reached the degree of saturation, and the formation of the number of Argent Crystal increased in a short period of time.

**Fig. 1** Malvin particle size of the samples obtained at different temperatures



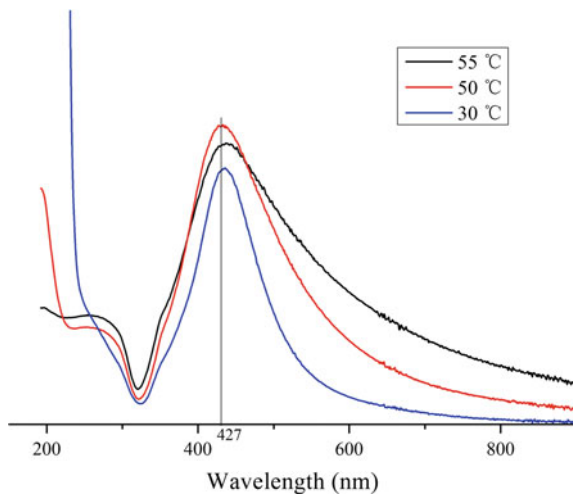
The samples obtained at different reaction temperatures were placed in a volumetric flask and diluted to a calibration line. Then, a certain amount of dilution of the liquid was taken into the sample pool, and measured. The measured results were shown in Fig. 1. The average particle size of nano silver obtained at a temperature of 50 °C is the smallest and relatively concentrated from Fig. 1. It is 157.1 nm.

### 3.2 UV-Vis Analysis

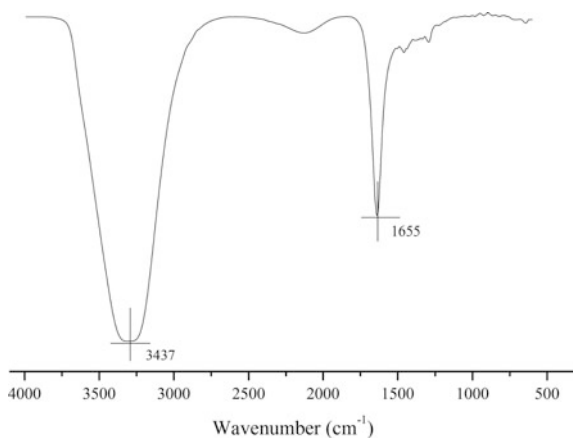
The absorption of light by a certain size of noble metal nanoparticles was a continuous vibration generated by the interaction between the electron and the magnetic field, namely surface plasmons resonance. It was the performance of a small particle size effect, and no existing in the block. The position of the plasma resonance absorption peak of metal nanoparticles has a great relationship with the shape and size, the dielectric and the adsorption of the metal nanoparticles. The silver nanoparticles in the preparation process, the reaction was not only can be judged from the color change of the reaction liquid, but also by the UV-vis spectrum proved. In Fig. 2, the absorption peak position change was not particularly obvious, but the total trend was red shift due to the change of the size and shape of nano silver particles.

The silver nanoparticles was centrifuged by high-speed centrifuge for 3–4 times at 8000 rpm for 30 min, and saved in the deionized water. A quantitative liquid was placed in the quartz sample cell, and then analyzed by UV-vis. The results were shown in Fig. 2. The UV-vis absorption spectra were measured at 427 nm. It indicated that the product was nano silver.

**Fig. 2** UV-vis spectrum of silver nanoparticles



**Fig. 3** FTIR spectrum of silver nanoparticles



### 3.3 FTIR Analysis of AgNPs

The surface of AgNPs was covered with PVP K30, which is the protective agent to prevent it from reuniting. A small amount of the nano silver turbid liquid was measured by FTIR, and the absorption spectrum was shown in Fig. 3. The peak at 3437 cm<sup>-1</sup> was due to the vibration of absorbed water in AgNPs. Notably, the AgNPs had a significant peak at 1655 cm<sup>-1</sup>, which was due to the vibration of carbonyl ( $\text{-C}=\text{O}$ ) transition band on the surface of AgNPs. This result indicated that the surface of silver nanoparticles was covered with the polyvinyl pyrrolidone.



## 4 Conclusions

In this experiment, with silver ammonia solution as precursor, hydrazine hydrate as reducing agent, the polyvinyl pyrrolidone k30 as protective agent, and the silver nanoparticles was prepared by chemical reduction method. The experimental results showed that the optimal temperature was 50 °C in the system. The average particle size was 157.1 nm in 50 °C. Through FTIR analysis, it could be obtained that the surface of AgNPs had PVP K30 protection, and it effectively prevented the nano silver from reuniting. By UV-vis analysis, the nano silver was achieved in the system. It can satisfy the requirement of conductive ink.

## References

1. S. D. Sathaye, K. P. Patil, D.V. Paranjape, et al. (2001). Nanocrystalline silver particulate films by liquid-liquid interface reaction technique (LLIRT). *Materials Research Bulletin*, 36, 1149–1155.
2. P. K. Khanna, V. V. V. S. Subbarao. (2003). Nanosized silver powder via reduction of silver nitrate by sodium formaldehydesulfoxylate in acidic pH medium. *Materials Letters*, 57, 2242–2245.
3. Kwon, S. Ma, R. Kim, U et al. (2014). Flexible electromagnetic interference shields made of silver flakes, carbon nanotubes and nitrile butadiene rubber. *Carbon*, 68, 118–124.
4. Lee C L. Yang H L. Chen C W et al. (2013). Silver nanoplates: Tetradecyltrimethylammonium ions as additives in seed-growth synthesis and their potential application as catalysts for glucose oxidation reaction. *Electrochimica Acta*, 106, 411–417.
5. Rad Shayani M, Kompany A, Zak Khorsand M et al. (2015). The effect of silver concentration and calcination temperature on structural and optical properties of ZnO: Ag nanoparticles. *Modern Physics Letters B*, 29(1), 1450254.
6. Kienskaya K I. Sigal K V. (2015). Synthesis of silver nanoparticles and their application in cosmetics. *Mikroelementy v Meditsine*, 12(2), 51–56.
7. Kahraman M. Daggumati P. Kurtulus O et al. (2013). Fabrication and characterization of flexible and tunable plasmonic nanostructure. *Sci Rap*, 3, 3396.
8. Kosmala A. Wright Q et al. (2011). Synthesis of silver nanoparticles and fabrication of aqueous Ag inks for inkjet printing. *Mater Chem Phys*, 129 (3), 1075–1080.
9. Patil, R. S. Kokate, M. R. Salvi, P. P et al. (2011). A novel one step synthesis of silver nanoparticles using room temperature ionic liquid and their biocidal activity. *C. R. Chim*, 14, 1122–1127.

# Optical Emission Spectroscopy Diagnostics of HMDSO/O<sub>2</sub> Magnetized Plasma

Zhonghua Bian, Xinyue Wang, Yunjin Sun and Qiang Chen

**Abstract** Based on general plasma enhanced chemical vapor deposition (PECVD), a novel plasma set-up equipped with horizontal electronic field and perpendicular magnetic field is built in this study for a purpose of obtaining a high density plasma source. In order to characterize plasma parameters, optical emission spectroscopy (OES) was used to diagnose the electron temperature and electron density in plasma. The electron temperature calculated through Stark broadening function is in the range of 1.0–5.0 eV while the electron density is in the range of 5.0–10.0 × 10<sup>15</sup> cm<sup>-3</sup>. The electron density is three orders of magnitude higher than that in normal plasma. OES results also indicate that oxygen concentration plays an essential role both on the dissociation of Hexamethyldisiloxane (HMDSO) molecule for Si precursor and on oxidation reactions of fragments, which supplies the theoretical research of plasma chemical reaction mechanism.

**Keywords** OES · Plasma parameters · Magnetically enhanced plasma source

## 1 Introduction

Due to excellent performances, such as chemical stability, excellent barrier diffusion against water vapor or gases, and good transparent, silicon oxide coating attracts a great interest in organic electronics and food packaging surfaces [1–3].

---

Z. Bian  
Jiangsu Chunshentang Pharmaceutical Co., Ltd, Jiangsu, China

X. Wang · Y. Sun (✉)  
Beijing Laboratory of Food Quality and Safety, Faculty of Food Science and Engineering, Beijing University of Agriculture, Beijing, China  
e-mail: aosdf2@163.com

Q. Chen (✉)  
Laboratory of Plasma Physics and Materials, Beijing Institute of Graphic Communication, Beijing, China  
e-mail: chenqiang@bigc.edu.cn

Comparing to many manufacturing methods of silicon oxide ( $\text{SiO}_x$ ) coating, PECVD exhibiting lots of advantages such as good adhesion, homogenous, pin hole free and convenience to mediate structural component [2, 4] becomes much popular method. However, the deposition rate for this technology is so low (less than 30 nm/min in practical [5]) that the application of silicon oxide products in industrial scale is seriously hampered.

Recently, the addition of magnetron field to the plasma discharge area was developed to increase ionized species density and thus to enhance the deposition rate [6]. In our previous study [7], the magnetic field confined plasma source was built where the magnetic field in electrode configuration generated the electron Hall current in an endless loop and thus decreases the diffusion rate of ions, electron, and charged species. Similarly, Rank et al. [6] has observed that addition of a magnetic field could not only enhance the properties of capacitive coupling RF discharge sources but also improve the pretreatment speed rate of plastic webs. So, it can be deduced that the power efficiency could be highly improved by magnetized plasma. Essentially, the existence of magnetic field in the plasma could effectively constraint the electron mobile path in the discharge area, resulting in speeding up the ion collision rate and thus enhancing ionization degree [8].

As for silicon dioxide film deposited by PECVD, discharge and deposition principles for normal plasma source were systematically investigated and various diagnosis technologies were developed [9], but the plasma parameters and reaction mechanisms of plasma sources coupled with magnetron field is seldom studied. This is because the confined electron mobility after the magnetron affiliation will have a significant influence on the trajectory of charged particles, which makes feedback current and voltage inaccurate. Although some diagnostics methods become invalid to effectively investigate plasma parameters, especially for Langmuir probe (LP) and mass spectroscopy (MS), OES could compensate above shortcomings and is verified to be an effectively way to perform diagnostic function of magnetron enhanced plasma [10]. Therefore, magnetron enhanced plasma parameters are investigated by OES to disclose the chemical reaction principle in this study.

## 2 Brief Theories for Stark Broadening Function

According to Gig-Card theory [6, 9], electron density can be generally calculated by Stark broaden function through the full width at half maximum (FWHM) that a globally neutral, homogeneous and isotropic system exists in thermal equilibrium. Herein, FWHM is determined by width of special line at a center of decisive wave number, which consists of all kinds of widths such as natural (or instrumental), Doppler, Zeeman, Stark, Lorenz, as consist into  $\Delta\lambda_0$  in the formula  $\lambda = \lambda_0 \pm \Delta\lambda_0$ . Stark broadening can be available through subtracting the factual spectral FWHM  $\Delta\lambda_{1/2}$  by all kinds of other broadening widths for the purpose of electron density  $N_e$ .

Consuming the existence of local heat dynamic equilibrium the optical relativity strength  $I_{nm}$  can be formulated as follows:

$$I_{nm} = \frac{1}{4\pi} h \gamma_{nm} N_n A_{nm} D \quad (1)$$

where  $n$ ,  $m$  correspond to up/down principal quantum number respectively;  $\gamma_{nm}$ ,  $A_{nm}$  are optical frequency and self-transition rate, respectively;  $D$  is the plasma depth at the observing direction,  $N_n$  is upper energy level of distribution density, and  $h$  is Planck constant. Given the same ionization species of different levels obeys to Boltzmann distribution, we get

$$\frac{N_n}{N_1} = \frac{g_n}{g_1} \exp\left(-\frac{x_{1n}}{KT_e}\right) \quad (2)$$

where  $N_1$  are the basic energy level of distribution density,  $g_1$ ,  $g_2$  are the basic or excited ionized statistics averaged equally, respectively;  $x_{1n}$  is excited potentials of  $n$  level (eV),  $KT_e$  is electron temperature (eV).

The similar other optical relative strength can also be written as:

$$I_{pq} = \frac{1}{4\pi} \frac{g_p}{g_1} h \gamma_{pq} A_{pq} D N_1 \exp\left(-\frac{x_{1p}}{KT_e}\right) \quad (3)$$

Comparing Formula (2) with Formula (3) we get the Formula (4) for electron temperature:

$$\frac{I_{nm}}{I_{pq}} = \frac{g_n \gamma_{nm} A_{nm}}{g_p \gamma_{pq} A_{pq}} \exp\left(\frac{x_{1p} - x_{1n}}{KT_e}\right) \quad (4)$$

In this Formula, parameters, except  $I_{nm}$  and  $I_{pq}$  through optical emission spectroscopy, can be obtained in Ref. [11], and then  $KT_e$  can be calculated.

### 3 Experimental

The experiment equipment used here can be traced back to our previous study [6]. The roll-to-roll electrodes are connected to 40 kHz pulsed discharge source (duty ratio is set at 50%). hexamethyldisiloxane (Arish, USA. 98+ %) is used as precursor of Si and oxygen gas of 99.9% purity is used as the dilution gas. The flow ratio of HMSDO and oxygen is set at 2:1, and the working pressure is kept constant at 1.5 Pa with the basic pressure of  $10^{-3}$  Pa. The optical emission spectroscopy (AvaSpec-ULS2048-8, AVANTES B.V., Netherlands) has a grating logarithm of 300 lines/mm and slim depth of 10  $\mu$ m to provide the resolution of 0.8 nm in the wavelength range of 300–900 nm.

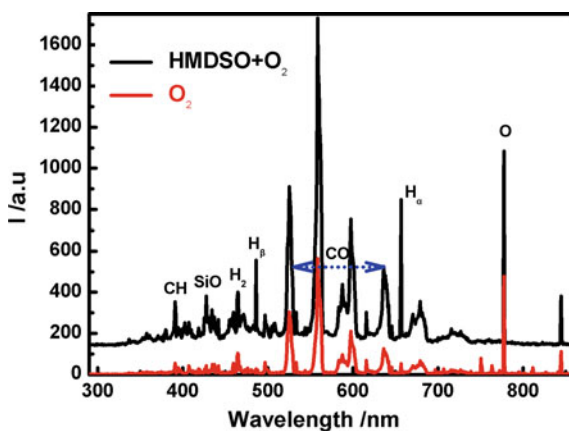
## 4 Results and Discussion

Figure 1 depicts OES results of plasma when the applied power, pressure and precursor and oxygen ratio were set at 300 W, 1.2 Pa and 2:1, respectively. One can see that when discharge was performed in pure oxygen, only several peaks for molecule CO in 525.31, 558.42, 597.18, 615.63 and 635.75 nm were detected in the range of 520–635 nm, although the strong oxygen signal appear at 777.44 and 844.75 nm. CO species could be traced to oxygen plasma etching effect of flexible substrate of polyethylene terephthalate (PET).

Once the precursor HMDSO was inputted, the strong lines appeared at 391.02, 427.57, 486.22 and 656.40 nm, which contribute to CH, SiO,  $H_{\alpha}$  and  $H_{\beta}$  species, respectively, as shown in Table 1. The dissociated fragmentations of HMDSO lead to generation of complex mixture of active species, such as SiC and  $CH_x$ , leading to organic component deposited in polymeric film. It is consistent with our previous results [7] that the stoichiometric value of silicon oxide was  $SiO_{1.32}$ , and carbon content was ca. 23.5% in complex mixture. Choudhury et al. [12] also observed the existence of CH, SiO, H and O radicals in HMDSO/ $O_2$  plasma, and found that the peak intensity of CH, SiO, H and O were almost equal, resulting in an organic character in the film structures. Saloum et al. [13] has studied the correlation between the plasma parameters and coating structures in remote RF hollow cathode technology and found the similar species.

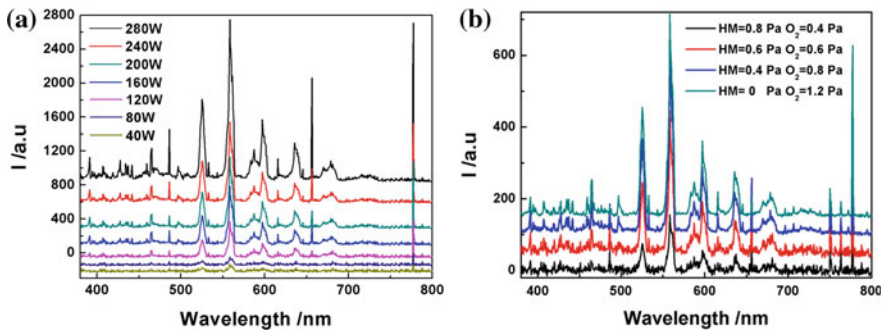
However, the absence of SiH species at 414.7 nm in our data inferred the strong oxidization reaction in our plasma source, which was favorable to the subsequent formation of SiO and  $H_2$  since SiH radical was always an essential transition state during the dissociation process of HMDSO [14]. It is notice that the intensities of  $H_{\alpha}$  and  $H_{\beta}$  were much higher than others like SiO and CH species, which confirm the strong ionization of  $CH_x$  in this plasmas source. The highest intensity of CO species further verifies the oxidization from CH and H fragments to avoid the formation of SiH through combination of Si and H radicals.

**Fig. 1** OES of discharge plasma with  $O_2$  and HMDSO +  $O_2$  mixtures

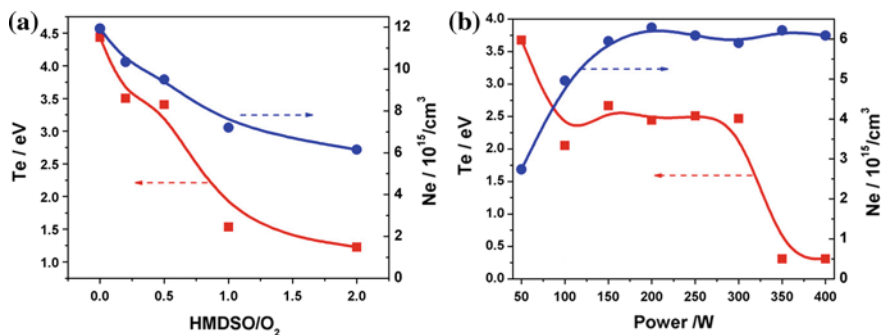


**Table 1** Species detected by OES in HMDSO/O<sub>2</sub> plasma [16]

Species	Transition	Wavelength (nm)
CH	$X^2\Pi - B^2\Sigma^-$	391
SiH		414.7
SiO		427.57
CO	$B^1\Sigma - A^1\Pi(v, v') (0, 0)$	451.1
	-id-(0, 1)	483.5
	-id-(0, 2)	519.8
	-id-(0, 3)	561.0
	-id-(0, 4)	608.0
	-id-(0, 5)	662.0
H	H $_{\beta}$ : H(n = 4) $\rightarrow$ H(n = 2)	486.22
	H $_{\alpha}$ : H(n = 3) $\rightarrow$ H(n = 2)	656.4
H <sub>2</sub>	Fulcher $\alpha$ : $d^3\Pi_u - a^3\Sigma_g^+$	453–464, 570–650
	$^5P - ^5S_0$	777.44
O	$^3P - ^3S_0$	844.75

**Fig. 2** OES of discharge plasma with HMDSO/O<sub>2</sub> mixtures as a function of discharge power (a) and HMDSO/O<sub>2</sub> ratios (b)

Regarding the oxidation rate and deposition rate related to the chemical reaction and subsequent coating structure, there are two factors needed to be further studied: applied power and HMDSO/O<sub>2</sub> ratio. Figure 2a shows the OES of HMDSO/O<sub>2</sub> plasma as function of applied power. One can see that the peak locations keep constant while their intensities are increased along with discharge power. Considering four typical species, O in 777.44 nm, H in 486.22 nm, CO in 451.1 nm and CH in 391.02 nm, one can find that although O in 777 nm increases much fast with discharge power, the relativity of O/H, CO and CH keep constant. On the contrary, the oxidation degree of HMDSO strongly depends on the O<sub>2</sub> concentration as shown in Fig. 2b, since O intensity decreased and H $_{\beta}$  intensity increased with the inputted HMDSO. Thus, it can be concluded that the high intensity



**Fig. 3** Electron temperature and intensity of mixture plasma with different HMDSO/O<sub>2</sub> ratios (a) and discharge power (b)

of O plays a positive contribution to the species oxidization, such as CH or H into CO or H<sub>2</sub>O, respectively while the decrease of CO intensity indicate further ionization of CH<sub>x</sub> fragment.

In comparison with the densities of species in their fundamental state, the emission intensity by the activated species is a function of the excited states. OES can be utilized to measure relative concentrations based on the actinometrical method [15]. Lasorsa et al. [16] has found that the competition between Si–O at the substrate and Si–C species in the plasma phase is sensitive to variations of electron temperature in PECVD. So, in our study, all intensities were calibrated by O in 777.42 nm in order to analyze the reaction principles. The lines of H<sub>β</sub> 486.2 nm, C=O 451.1 nm, C–H 391.02 nm were utilized to calculate the electron temperature and ionized density according to the Formula (4).

Figure 3a shows that both electron temperature and density were decreased from 4.5 to 1.2 eV and 12 to 6.0 × 10<sup>15</sup> cm<sup>-3</sup> respectively, with the precursor concentration. With the increase of precursor, the atomic oxygen species, which etches the polymeric surface under high initial density, was consumed by breaking CH or Si–C bonds to form H<sub>2</sub>O and CO, leaving Si–O species in deposition process, since electrons impact cause an increase of more than two or three orders than that in normal plasma phase. Compared with Fig. 2b, when the ratio varied from zero to 2, the high fragmented degree of precursor and relatively low oxidation counterpart of fragments will lead to more organic formation in finally deposited layer.

On the other hand, at the constant working pressure, the electron temperature decreases from 3.7 to 2.5 eV with increment of discharge power from 40 to 100 W, and keep a constant value until 300 W, finally dropped to a low level of 0.5 eV, as shown in Fig. 3b. At the same time, the electron density increases from 1.7 to 6.0 × 10<sup>15</sup> cm<sup>-3</sup> and then keep constant regardless of discharge power. Therefore, it can be concluded that discharge power has a positive effect on the decrement of electron temperature, and lead to electron impact and speeding up the chemical reaction rate for precursor/oxygen phase process to obtain a high stoichiometric ratio of SiO<sub>x</sub> as verified by species composition in plasma phase shown in Fig. 2a.

Furthermore, the relationship of composition structure of deposited film with plasma phase should be built, as will be investigated in the next process.

## 5 Conclusions

In this paper, OES was adapted to explore the principle mechanism of polymerization reaction in the magnetized plasma for purpose of explaining the essence of the magnetized plasma. OES results indicated that the species in plasma phase depended on the oxygen concentration. When the precursor was inputted, the electron temperature and density calculated through Stark broaden function, decreased from 5.0 to 1.0 eV and  $10.0\text{--}5.0 \times 10^{15} \text{ cm}^{-3}$ , respectively, indicating the O etching effect. On the other hand, the discharge power had a positive effect on the decrements of both electron temperature and acceleration of the chemical reaction for precursor/oxygen plasma phase.

**Acknowledgements** This article was financially supported by Key Construction Discipline Program of Beijing Municipal Commission of Education (PXM2014-014207-0000029), Youth Science Fund Project of Beijing University of Agriculture and Youth Teacher Foundation of Da Bei Nong Group of Beijing University of Agriculture (14ZK006).

## References

1. Czeremuskin, G., Latrèche, M., Wertheimer M. R., da Silva Sobrinho, A. S. (2001). Ultrathin silicon-compound barrier coatings for polymeric packaging materials: An industrial perspective. *Plasm. Poly.* 6(1):107–120.
2. Madocks, J., Rewinkle, J., Barton, L. (2005). Packaging barrier films deposited on PET by PECVD using a new high density plasma source. *Mater. Sci. Eng. B* 119:268–273.
3. Jang, W.S., Rawson, I., Grunlan, J.C. (2008). Layer-by-Layer assembly of thin film oxygen barrier. *Thin Solid films* 516:4819–4825.
4. Howwells, D.G., Henry, B.M., Leterrier, Y., Manson, J-A.E., Madocks, J., Assender, H.E. (2008). Mechanical properties of SiO<sub>x</sub> gas barrier coatings on polyester films. *Surf. & Coat. Tech.* 202:3529–3537.
5. Wu, D.S., Lo, bW.C., Chang, L.S., Horng, R.H. (2004). Properties of SiO<sub>2</sub>-like barrier layers on polyethersulfone substrates by low-temperature plasma-enhanced chemical vapor deposition. *Thin Solid Films* 468: 105–108.
6. Rank, R., Wünsche, T., Günther, S. (2003). Magnetically enhanced RF discharges for effective pre-treatment of plastic webs at high speed. *Surf. & Coat. Tech.* 174–175: 218–221.
7. Sun, Y.J., Fu, Y.B., Chen, Q., et al. (2008). Silicon dioxide coating deposited by PDPs on PET films and influence on oxygen transmission rate. *Chin. Phys. Lett* 25(5): 1753–1756.
8. Rank, R., Wünsche, T., Günther, S. (2003). Magnetically enhanced RF discharges for effectively pre-treatment of plastic webs at high speed. *Surf. & Coat. Tech.* 174–175: 218–221.
9. Saloum, S., Naddaf, M. (2008). Optical constants of silicone-like (Si:Ox:Cy:Hz) thin films deposited on quartz using hexamethyldisiloxane in a remote RF hollow cathode discharge plasma. *Vacuum* 82:50–55.



10. Torres, J., Sande, M.J., Mullen, J.J.A.M., Gamero, A., Sola, A. (2006). Stark broadening for simultaneous diagnostics of the electron density and temperature in atmospheric microwave discharges. *Spect. Acta Part B* 61:58–68.
11. Dong, L., Ran, J., Mao, Z. (2005). Direct measurement of electron density in microdischarge at atmospheric pressure by Stark broadening. *Appl. Phys. Lett.* 86: 161501–161503.
12. Choudhury, A.J., Barve, S.A., Chutia, J., Pal, A.R., Kishore, R., et al. (2011). RF-PACVD of water repellent and protective HMDSO coatings on bell metal surfaces: Correlation between discharge parameters and film properties. *App. Sur. Sci.* 257: 8469–8477.
13. Saloum, S., Naddaf, M. (2008). Optical constants of silicone-like (Si:Ox:Cy:Hz) thin films deposited on quartz using hexamethyldisiloxane in a remote RF hollow cathode discharge plasma. *Vacuum* 82: 50–55.
14. Li, K., Gabriel, O., Meichsner, J., (2004). Fourier transformation infrared spectroscopy study of molecular structure formation in thin films during hexamethyldisiloxane decomposition in low pressure rf discharge. *J. Phy. D: Appl. Phys.* 37: 588–594.
15. Lieberman, M.A., Lichtenberg, A.J. (1994). Principles of plasma discharges and materials processing. New York: Wiley.
16. Lasorsa, C., Morando, P.J., Rodrigo, A. (2005). Effects of the plasma oxygen concentration on the formation of SiO<sub>x</sub>C<sub>y</sub> films by low temperature PECVD. *Surf. & Coat. Tech.* 194: 42–47.

# Experimental Analysis of the Effect of Vacuum Degassing Technology on the Solventless Laminating Adhesive Performance

Hongwei Xu, Xusheng Wang, Ruining Lei, Xuhong Chen  
and Donghong Liu

**Abstract** Solventless laminating technology has advantages of energy saving and environmental protection, and is widely used in package printing industries now. For solventless laminating technology, the quality of solventless laminating adhesive has a big effect on the quality of laminating results. In this paper, some experiments have been done to analyze the effect of vacuum degassing technology on the performances of solventless laminating adhesive, such as fold endurance, adhesion force and peel strength. The analysis of experimental results shows that the vacuum degassing technology not only decreases the quantity of small air bubbles in the laminating adhesive which is mixed by A/B material, but also improves the performances of solventless laminating adhesive in the fold endurance, adhesion force and peel strength. This research shows that the vacuum degassing technology is helpful for improving the solventless laminating quality.

**Keywords** Solventless · Laminate · Vacuum degassing · Performance

---

H. Xu (✉) · X. Wang · R. Lei · X. Chen  
Xi'an University of Technology, Xi'an, China  
e-mail: xuhongwei@xaut.edu.cn

X. Wang  
e-mail: Xusheng.Wang@hotmail.com

R. Lei  
e-mail: 609677409@qq.com

X. Chen  
e-mail: 2271450046@qq.com

D. Liu  
Weinan Outai Printing Machinery Technology Co. LTD, Weinan, Shaanxi, China  
e-mail: ldh200588@126.com

## 1 Introduction

There is an increasing trend towards solventless laminating both on environmental and economic grounds. In order to approach the high level performance of laminating products, many investigations aimed at the development of solventless laminating adhesive in recent years [1].

After decades of development and application, the solventless laminating technology has been mature. Laminating without solvent is beneficial to environmental protection and clean production and ensures food and drug packing free from the compound contamination [2]. In recent years, with the improvement of Chinese product quality and food safety awareness, solventless laminating is increasingly gets the attention of laminating film packaging industries.

At present the performance and application of solventless adhesives have some defects in the scope of its limitation heat resistance and dielectric resistance. And it is limited adapt to the temperature, especially in high-temperature cooking bags. These defects make the application scope of solventless laminating adhesive is limited. For those who require high performance and complex packaging products, solventless laminating adhesive have to not to be choice [3].

Indeed, there are many factors which have effects on the performance of solventless laminating. Chen et al. [4, 5] study some materials which effect on the performance of solventless laminating adhesive. In some ways, the bubbles which hide in the laminating adhesive have a great effect on the quality of laminating. Now, the author study using the vacuum degassing technology in mixing process of A/B solventless laminating adhesives in order to decrease the quantity of foams in the adhesives.

## 2 Vacuum Degassing Technologies

Vacuum degassing technology is a process which can be used to eliminate the air bubbles which hide in liquid materials through stirring and vacuum. In this way, vacuum degassing machine which is used to make vacuum degassing technology into truth is improved, as shown in Fig. 1.

The vacuum degassing machine can be used to eliminate small air bubbles which hide in A/B solventless laminating adhesives by vacuuming and stirring. The A/B solventless laminating adhesives are placed into the vacuum degassing pots respectively, and stirred and removed the air bubbles. Then they can be used to be mixed and can be used to laminate the materials, such as PE, BOPP, PET.

Figure 2 shows two cups of mixed solventless adhesive. One is not processed by vacuum degassing technology, and the other is processed by vacuum degassing technology.

From Fig. 2, it can be seen that there are fewer air bubbles on the surface of the second cup in which the solventless adhesive is processed by vacuum degassing



**Fig. 1** Vacuum degassing machine



(a) Not be processed by vacuum degassing



(b) Processed by vacuum degassing technology

**Fig. 2** Mixed solventless adhesive

technology. Whether the new technology which is used in the mixing process of A/B solventless laminating adhesives can have an effect on the performance of solventless laminating adhesives is need to be studied. In this paper, some experiments are held to examine the effect of vacuum degassing technology on the performance of solventless laminating adhesive.

### 3 Experiment of Folding Endurance of Solventless Laminating Adhesives

In this experiment, the WD8118 A/B type solventless laminating adhesives which are produced by Shanghai Kangda New Materials Co., Ltd are used to examine the folding endurance with no vacuum degassing technology and with vacuum degassing technology. The mixed proportion of A/B is 100/70 according to the suggesting by Kangda Company. And the Sorbel type folding apparatus is used to test the folding endurance of these solvent-free laminating adhesives.

Folding endurance is refers to the specimen under a certain tension, reciprocating folding number. In these experiments, the paper is same. Therefore the folding degree will include the folding endurance of papers. As the member of specimen, the performance of solventless laminating adhesive influences the results deeply.

Table 1 showed that the vacuum degassing technology has effect on the folding endurance of solventless laminating adhesive. The folding endurance is improved obviously through the vacuum degassing technology.

### 4 Experiment of Adhesion Force of Solventless Laminating Adhesive Under Different Processing

Adhesion force is very important performance to adhesive [6]. According to the ISO standard, the adhesion force is divided into 0–5. The lower the series will be the stricter. In this experiment, the mixed proportion of A/B solventless laminating adhesives is 100:70. There are two sets of mixing solventless laminating adhesive for to be used in the experiment. One set is processed by vacuum degassing technology, and the other is not processed by vacuum degassing technology. These two sets adhesives are smeared evenly on three materials respectively, PET, BOPP, PE. And a Hundred Grid Knife is used to lattice the samples.

**Table 1** Results of experiments of folding endurance

Vacuum degassing	Folding degree (times)
No	11
Yes	17

**Table 2** Results of adhesion force experiment

Vacuum degassing	Back material	ISO degree
No	PET	1
	BOPP	3
	PE	4
Yes	PET	0
	BOPP	2
	PE	3

Six different samples are putted on the table, and the Hundred Grid Knife is use to cut out ten columns on the coating of the samples with lattice graphics. Self adhesive tapes are used to measure the peel strength of solventless laminating adhesive under different processing on the three materials. Using a magnifying glass to observe the grid area, and evaluate the adhesion in accordance with the ISO standard. The results of this experiment are shown in Table 2.

Table 2 shows that with the processing of vacuum degassing technology, the adhesion force of the solventless laminating adhesive is improved.

**Table 3** Peel strength under the adhesive with no vacuum degassing processing

Material	Dry time (s)	Peel strength (N)
BOPP	0	2.5
	10	3.5
	20	4.0
	30	4.0
	40	4.5
PE	0	1.0
	10	1.0
	20	1.0
	30	1.5
	40	2.0
PET	0	8.0
	10	9.0
	20	10.0
	30	10.5
	40	11.5
BOPP	0	6.0
	10	6.5
	20	7.0
	30	7.5
	40	7.5
PE	0	1.0
	10	1.0
	20	1.5
	30	2.0
	40	3.0
PET	0	10.0
	10	11.0
	20	11.5
	30	12.0
	40	13.0

## 5 Experiment of Peel Strength of Solventless Laminating Adhesive Under Different Processing

Samples are prepared by lamination of mixed solventless adhesives. One is processed by vacuum degassing technology; the other is not processed by vacuum degassing technology. There are three materials which are used for laminating, PET BOPP, PE. These materials are cut into strips with 25 mm width and 150 mm length. The two sets of mixed solventless adhesives are smeared evenly on the three materials respectively. Then they are dried in the air, and after 0, 10, 20, 30, 40 s, the same materials are laminated with each other. And the peel strengths are tested by using a portable torsion balance.

One side of the test specimen is fixed, and the other side is pulled by the portable torsion balance. When the laminated materials begin open apart, the value of the strength will be recorded as the peel strength. Table 3 showed the results of peel strength experiment.

From Table 3, it can be seen that the peel strength became higher when the dry time longer. And when the A/B solvent adhesives are processed by vacuum degassing technology, the peel strength is improved obviously.

## 6 Conclusions

Vacuum degassing technology can help to decrease the quantity of air bubbles in mixed solventless laminating adhesive. Through the experiments of the effect of vacuum degassing technology on the performance of solventless laminating adhesive, the results are analyzed and the conclusions are gotten as follows.

- (1) The vacuum degassing technology has effect on the folding endurance of solventless laminating adhesive. The folding endurance is improved when the A/B solventless laminating adhesive is processed by vacuum degassing technology.
- (2) The adhesion force and peel strength are also improved through the processing of vacuum degassing technology.

Therefore, for WD8118 A/B type solventless laminating adhesives, it is better for the laminating quality to process the A/B adhesives with vacuum degassing technology. Vacuum degassing technology not only decreases the quantity of air bubbles which hide in the mixing adhesive, but also improves the performance of the mixing adhesive.

**Acknowledgements** This work was financially supported by the Shaanxi Province Education Department Service Special Plan Project Foundation (14JF018).

## References

1. Lv ling, Xu Wencai, Zuo Guangshen (2010). Characteristics research about coating system of solventless laminator. *Proceedings of the 17<sup>th</sup> IAPRI World Conference on Packaging*
2. Zhao Zhongyou, Wang Guoliang, Lu Qiting et al. (2008). Opportunities and development for domestic solventless laminating. *Plastic Packaging*, 18: 23–26 (In Chinese)
3. Chen Changjie. (2008). Development trend of laminating adhesive for household paper. *Plastic Packaging*. 18: 27–31 (In Chinese)
4. Chen Shuanglian, Chen Guangxue, Liu Jiangwen (2013). Study on an apiphatic polyurethane laminating adhesive based on castor oil. *Applied Mechanics and Materials*. 262: 551–556
5. Qing Wanga, Chen Guangxue, Chen Shuanglian, et al. (2012). Research on synthesis and performance of solvent-free aluminum-plastic composite polyurethane adhesive *Advanced Materials Research*. 583, 9–13
6. N.M.M. Ramos, M.L. Simoes, J.M.P.Q. Delgado et al (2012). Reliability of the full-off test for in situ evaluation of adhesion strength. *Construction and Building Materials*, 31, 86–93



# Effect of Monomer and Promoter on UV-LED Varnish Performance

Xiaoli Li, Shiyong Luo and Wencai Xu

**Abstract** To study the effects of monomer and promoter on the UV-LED varnish performance and develop a kind of UV-LED varnish with excellent comprehensive performance. By controlling the other components unchanged, then changing the monomer species or the dosage of promoter, different varnish was prepared. The viscosity, surface tension and curing rate of varnish, flexibility and water contact angle of curing film were tested. After many experiments, it was concluded that the optimum dosage of leveling agent was 0.2%, viscosity of varnish was 120 s, surface tension was 23.28 m N/m and curing rate was 95 m/min, the flexibility of the curing film was 2 mm, water contact angle was 84.2. The UV-LED varnish with excellent comprehensive performance can be developed through selecting monomer and promoter rationally, considering various factors comprehensive and finding the best dosage of varnish components.

**Keywords** UV-LED varnish · Monomer · Promoter

## 1 Introduction

With the development of science and technology, UV-LED varnish has become the focus of research because of its more energy saving and environmental friendly [1]. However, due to the high price of UV-LED curing equipment and the lack of photo initiator matching with the UV-LED light source and other shortcomings, the UV-LED varnish has not been widely used. Monomer and promoter are important components of varnish and influence the varnish performance significantly. So this study can provide theoretical basis for further development and application of UV-LED varnish, and promote the growth of UV-LED varnish.

---

X. Li · S. Luo (✉) · W. Xu

Printing and Packaging Institute, Beijing Institute of Graphic Communication, Beijing, China  
e-mail: luoshiyong@bigc.edu.cn

© Springer Nature Singapore Pte Ltd. 2017

P. Zhao et al. (eds.), *Advanced Graphic Communications*

and *Media Technologies*, Lecture Notes in Electrical Engineering 417,

DOI 10.1007/978-981-10-3530-2\_139

## 2 Experiment

### 2.1 *Experimental Materials*

A polyurethane–acrylate oligomer and an epoxy acrylate oligomer (from Shanghai Gurease Chemical Co. Ltd.), which undergoes radical-type polymerization, were used as UV-LED curable resin. 1, 6-Hexanediol diacrylate (HDDA), Tripropylene glycol diacrylate (TPGDA) and Trimethylolpropane triacrylate (TMPTA) (from Sartomer-Chemie Co. Ltd.) were used as UV-LED curable monomer. 2, 4, 6-trimethyl benzoyl diphenylphosphine oxide (TPO) and phenyl bis (2,4,6-trimethylbenzoyl)-phosphine oxide (819) (from Shanghai Gurease Chemical Co. Ltd.) were used as photoinitiator. A polyether modified polydimethylsiloxane from BYK-Chemie used as a surfactant. A reactive amine was from Sartomer-Chemie.

### 2.2 *Laboratory Equipment*

DT-200B electronic counting scale (Changshu Golden Goat Balance Co. Ltd.); Iwata viscosity cup; American TA AR2000ex rheometer; K100 type surface tension instrument (Germany KRUSS); Magnetic heating stirrer; QTY-32 coating bending test instrument (Tianjin YONGLIDA); DSA100 video contact angle instrument (Kruss Company of Germany); UV-LED curing light source, wavelength radiation for 365 nm, uvata (Shanghai); Hand coated type wire rod.

### 2.3 *Experimental Methods*

#### 2.3.1 *Preparation of Varnish*

According to the basic formula of UV-LED varnish, experimental materials were weighed with electronic counting scale, then mixed in a beaker, and stirred to mix evenly using a magnetic stirrer at 25 °C. Finally the varnish was prepared.

#### 2.3.2 *Performance Test*

- (1) Rheological property and viscosity. Rheological property was tested with AR2000 rheometer. Viscosity was tested with Iwata viscosity cup.
- (2) Surface tension. It was tested with K100 type surface tension tester.
- (3) Curing speed. Varnish was coated on transfer paper (varnish thickness was about 24 μm). After irradiated one time under UV-LED lamp (irradiation

power was  $4 \text{ W/cm}^2$ ), varnish surface was pressed with a finger. Observing obvious fingerprints in the varnish surface or feeling sticky illustrated that varnish curing was incomplete. If the curing was not complete, the speed of the conveyor belt was reduced and varnish was radiated again until completely cured. The curing rate of UV-LED varnish is represented by conveyor speed. The greater the curing rate, the better the curing property of varnish.

- (4) Flexibility. Varnish sample was coated on white cardboard (varnish thickness was about  $24 \mu\text{m}$ ), after UV-LED lamp irradiating (irradiation power was  $4 \text{ W/cm}^2$ ), the flexibility of varnish curing film was tested using QTY-32 paint film bending test instrument. The diameter of the minimum bearing when film begins to bend and fracture represents flexibility.
- (5) Water contact angle test of UV-LED varnish curing film. It was tested using DSA100 video contact angle tester.

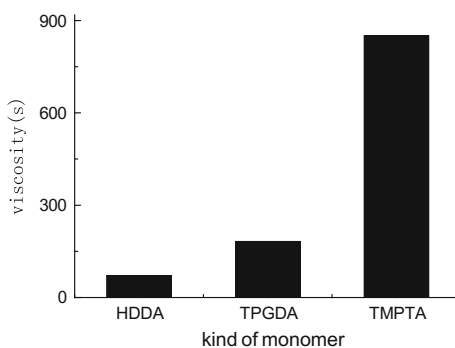
### 3 Results and Discussion

#### 3.1 Shear Viscosity Curve of UV-LED Varnish

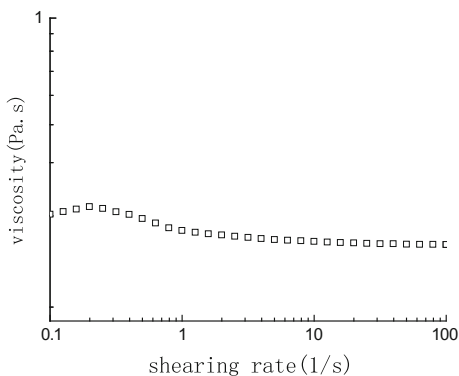
Viscosity is a nature to prevent the fluid to flow, namely the resistance of fluid flow [2]. Viscosity directly affects whether varnish can be successfully coated on the substrate, the appropriate viscosity is conducive to the smooth transfer of varnish. Different varnish was prepared through controlling the same other components and changing the kind of monomer.

As can be seen from Fig. 1, the viscosity of the varnish is not same due to different monomer. Generally speaking, the viscosity of varnish is affected by the number of monomer functionality, the more the monomer functionality, the greater the viscosity of the varnish [3]. TPGDA is more than HDDDA an ethoxy group and molecular chain is longer, so the viscosity is larger.

**Fig. 1** Effect of monomer on UV-LED varnish viscosity



**Fig. 2** Shear viscosity curve of UV-LED varnish



**Fig. 3** Effect of monomer on UV-LED surface tension

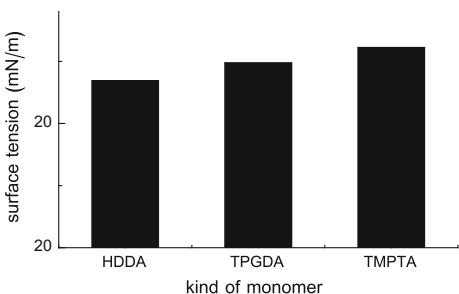


Figure 2 is the shear viscosity curve of UV-LED varnish. From Fig. 2 we can see that shear viscosity curve of UV-LED varnish does not conform to the Newton’s law. Viscosity decreases with shear rate increasing within a region then tends to equilibrium value, which reflects the characteristic of non-Newtonian fluid. The feature meets the technological requirements of varnish post-press processing.

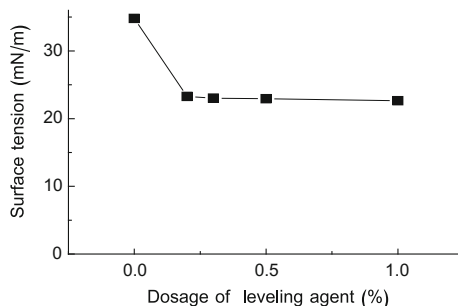
UV-LED varnish viscosity is 120 s tested by the Iwata viscosity cup.

### 3.2 Surface Tension of UV-LED Varnish

Surface tension represents mutual traction force between adjacent two parts of the liquid surface, which makes the liquid surface tend to the shrink state [4]. Surface tension affects the adhesion of varnish. Varnish is not easy to spread due to larger surface tension, which is not conducive to varnish drying, thus reduces varnish adhesion. All of these will affect the post-press processing quality.

Figure 3 tells us that the different structure of the monomer causes the different intermolecular force on the varnish surface, thus the surface tension is different. The surface tension of TMPTA with stereochemical structure is the largest, and the surface tension of HDDA with the straight chain is the least.

**Fig. 4** Relationship between the varnish amount of leveling agent and the surface tension of varnish



The surface tension of different varnish was measured by changing the dosage of leveling agent, and the data were as Fig. 4. From Fig. 4 we can see that with leveling agent dosage increasing, the surface tension becomes gradually stabilized. Organosilicone leveling agent is widely used in the coating industry with lower surface tension and good wetting property [5]. Leveling agent dosage should be appropriate, because the leveling agent dosage too little to form very thin single molecular layer on the film surface, which causes uneven surface. Film surface is easily caused defects such as wrinkle, shrink hole and pitting due to surface tension gradient problem, which affects the film gloss; however, too much leveling agent is easy to generate side effects such as film fogging and loss of light. In addition, more use of leveling agent can also cause adhesion decrease [6]. After the experiment, the optimum dosage of the leveling agent was 0.2%.

Surface tension of the UV-LED varnish measured by the ring method is 23.28 m N/m. In general, the surface tension of varnish between 20 and 30 m N/m can achieve better adhesion and stability.

### 3.3 Curing Rate of UV-LED Varnish

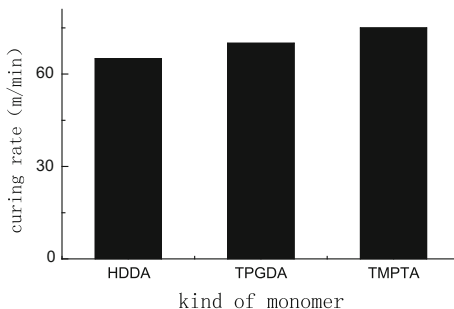
Curing rate is a very important characterization and critical index in the UV-LED varnish curing process. Higher curing rate of UV-LED varnish is very important to the film drying and prints can show a high quality of gloss and bright degree [2].

Fixing the other components, different varnish was developed by using different monomers. The curing rate of these varnish were respectively tested. The data were as follows.

From Fig. 5 we can see that the curing rate of varnish prepared by different monomers is different. The curing rate of the tri-functional group monomer TMPTA is the largest. The curing rate of varnish is increasing with the increase of the functional groups number. Although both TPGDA and HDDA are two functional monomers, TPGDA is more than HDDA an ethoxyl group, the molecular chain is longer, so the curing rate is slightly higher than HDDA.

After testing, the biggest curing rate of UV-LED varnish is 95 m/min.

**Fig. 5** Effect of monomer on UV-LED varnish curing rate



### 3.4 Flexibility of UV-LED Varnish

Flexibility is one of important indicators measuring the performance of varnish. It directly affects fineness of post-press processing and printing qualities [7]. The flexibility of film produced by varnish coated on white card paper was measured. The data were as follows:

Flexibility: the Zhenlong (traditional UV curing varnish): 14, self-made varnish: 2

The results show that the flexibility of the self-made UV-LED varnish is obviously superior to the traditional UV curing varnish.

### 3.5 Water Contact Angle Test of UV-LED Varnish Curing Film

Contact angle is defined as the angle  $\theta$  between the tangent lines of gas–liquid interface making at the gas, liquid and solid three-phase intersection place and the boundary of the liquid and solid–liquid,  $\theta$  is a measurement of wetness degree [8]. According to the principle of wetting, materials are defined as non-wetness when  $\theta > 90^\circ$  and wetness when  $\theta < 90^\circ$ . When the contact angle equal to zero, liquid spreads on the surface of the solid and solid is completely wet [9]. It is the most convenient method to measure the wetting performance of paper surface.

Varnish was prepared through mixing the raw materials of varnish according to a certain proportion. The varnish was evenly coated on transfer paper with hand coated type wire rod and cured under the UV-LED lamp completely. The contact angle data of transfer paper were as follows (Table 1).

Varnish A and B did not add leveling agent, varnish a and b added 0.2% of leveling agent, the ratio of the rest material were kept unchanged. We can see that water contact angle of not coated UV-LED varnish is obviously less than that of transfer paper coated UV-LED varnish. Leveling agent further enables water contact angle of varnish curing film to become larger, and the wetting property of that become smaller. Wetting performance has a significant impact on the various

**Table 1** Comparison of water contact angles of different UV-LED varnish curing films

Sample names	Water contact angles				
Not coating varnish	56.5	56.2	57.3	58.5	55.9
Varnish A	66.7	69.8	64.8	66.1	65.9
Varnish a	88.3	86.6	83.8	85.8	82.9
Varnish B	70.5	71.4	73.9	73.0	76.4
Varnish b	84.7	80.0	84.0	86.7	85.4

properties of the material surface, including waterproof, anti-frost, self-cleaning, anti-corrosion and so on [10].

## 4 Conclusions

- (1) The monomer has important influence on the performance of UV-LED varnish. Generally with the monomer functionality increasing, viscosity, surface tension, curing rate of UV-LED varnish will increase, flexibility of varnish curing film will reduce.
- (2) The effect of leveling agent on the surface tension of UV-LED varnish is great. Addition of a very small amount of leveling agent can greatly reduce the surface tension of UV-LED varnish and increase the water contact angle of curing film. The optimum adding amount of leveling agent is 0.2%.
- (3) After many experiments, the varnish with excellent comprehensive performance was produced. Viscosity of the varnish is 120 s, the surface tension is 23.28 m N/m, the curing rate is 95 m/min; the flexibility of varnish curing film is 2 (mm), water contact angle is: 84.2.

## References

1. Shifan Zhang, Yongsheng Ma, Weiwei Huang. (2015). Application of UV-LED technology in number ink. *Label Technology*, 05: 30–31.
2. Qing Yi. Research on UV-LED Inkjet Ink. Nanjing Forestry University, 2014.
3. Zhengjian Zhang, Ruquan Huang, Yunzhi Chen, Pengrui Yin. (2015). Development of UV varnish for printing samples of copper printing paper. *Packaging Engineering*, 36(09): 144–149.
4. Qing YI, Beiqing Huang, Xianfu Wei, Qi Wang. (2014). Effect of monomers on printing quality of UV-LED ink-jet ink. *China Printing and Packaging Study*, 6(01): 45–50.
5. Xiaofang Wang. Preparation of Water-base UV Varnish. Qufu Normal University, 2010.
6. Xiaofang Wang, Xianfu Wei, Beiqing Huang, Xiaomei Chen. (2009). Influence of promoter on the performance of water-base UV varnish. *Packing Engineering*, 30(11): 86–88+92.
7. Fengxian Sang, Beiqing Huang, Xianfu Wei, Zhenzhi Sun, Nianjun Zhu. (2008). Effect of monomers and oligomers on flexibility of UV varnish curing film. *Information Recording Material*, 9 (02): 3–6.

8. Xue Bao, Taijin Lu, Ran Wei, Yong Zhang, Haibo Li, Hua Chen, Jie Ke. (2014). Application of surface tension on gem and jade identification and measurement of surface contact angle. *Rock Testing*, 33 (05): 681–689.
9. Xia Li. Research on High Gloss aqueous coatings. Xi'an University of Technology, 2006.
10. Wenting Chen. (2013). Studies on Fabrication and Properties of Low-Adhesion Super hydrophobic Surface Coatings. Shanghai Jiao Tong University.



# Study of Printability of Hybrid Light Curable Material Used in 3D Printing—Product Flexographic Plate

Beiqing Huang, Xiaoyue Shang, Yiran Li, Xianfu Wei  
and Changlong Guo

**Abstract** Using 3D printing to make flexographic plate is an addition process, which avoids the environmental pollution and materials wasting in the subtraction process of exposure, development, etc. in traditional flexographic plate making. In order to make the 3DFP that has good printability, we focus on the hybrid UV curable material system having good adaptability, we studied the influence for prepolymer and monomer on the plate forming and ink transfer ability of 3D printing to make flexographic plate, and determined the best formula for the material of 3DFP. Research indicates that the 3D printing-product flexographic plate (referred to as 3DFP in following part) product by the hybrid light curable material we studied has good forming effect and good ink transfer ability.

**Keywords** 3D printing · Flexographic plate · Hybrid light curable material · Performance

## 1 Introduction

Flexographic printing is known as “green printing”, which has dominated the field of package printing in the United States and Europe. However, traditional flexo plate making process requires a plurality of processes, such as exposure, development and drying, the plate-making process requires the use of large amounts of developer, wash solution and other chemical substances [1], its plate making method is subtraction, which causes some pollution on for the environment. Using 3D printing to make flexographic plate is an addition process which is beneficial for environmental protection. It also simplifies the production process and reduces the cost of production.

---

B. Huang (✉) · X. Shang · Y. Li · X. Wei · C. Guo  
Beijing Institute of Graphic Communication, School of Printing  
and Packaging Engineering, Beijing, China  
e-mail: huangbeiqing@bigc.edu.cn

Three-dimensional printing is a mature printing technique [2], the material used is liquid light curable resin, the resin could be injected by the nozzles of 3D printer and cured by UV light layer by layer, this technique combines injection molding technology and light-curing technology which improve the molding accuracy and reduce costs [3]. Therefore, this method is suitable for the production of flexographic plate.

The radical-cationic hybrid light curable polymerization system contains radical and cationic photoinitiator, the two kinds of photoinitiator excited after absorbing light to generate active center, and make photocuring polymerization reaction [4] at the same time. This system combines the advantages of the two kinds of polymerization methods, and at the same time has compensation for the certain drawbacks of the two kinds of methods. Therefore, the radical-cationic hybrid light curable polymerization system can meet the property requirements of 3DFP material such as high curing speed, low shrinkage ratio and good mechanical properties and so on. In addition, the printability is one of the important properties of the flexographic plate determining the quality of the printing plate, as for 3DFP material, the prepolymer, monomer have big impact on the flexographic plate.

## 2 Experiments

### 2.1 *Experimental Materials*

Prepolymer: Viajet 400 (Allnex LTD.); E44 (Shandong Tian Mau New Materials Technology Co., Ltd.); DOX (Jiangsu Tai Teer New Material Technology Co., Ltd.); Epoxy polybutadiene (Gaomi City Zhongyuan Chemical Technology Co., Ltd.); Monomer: EOEOEA; HDDA (Tianjin Tianjiao Co.); TTA21, TTA26 (Jiangsu Tai Teer New Material Technology Co., Ltd.); Photoinitiator: 907 (Tianjin long day Chemical Co., Ltd.); PAG-201, PAG-202 (Changzhou Powerful Electronic New Materials Co.).

### 2.2 *Equipments*

81-2 type constant temperature magnetic stirrer (Shanghai Sile Instrument Co., Ltd.); Light Hammer 6 UV curing machine (American Fusion system company); AR2000ex type Rheometer (US TA Instruments); TY-32 type Film-type bending tester (Tianjin Wynn Laboratory Equipment Co., Ltd.); K100 type Automatic surface tension meter (Germany KRUSS Company); DSA100 type Video contact angle meter (Germany KRUSS Company); Flexographic proofer (UK RK Company); 3D printer (Beijing CaiYun Digital Technology Co., Ltd.); X-Rite 530 type Densitometer (Rite USA).

### **2.3 Preparation Method of 3DFP Material**

We add the raw materials: monomer, prepolymer and photoinitiator separately to the beaker, put a magneton into the beaker, and then put the beaker onto the magnetic mixer about 30 min and move it until the liquor is uniform and transparent, thus the preparation is done.

### **2.4 Performance Test Methods of 3DFP Material**

#### **2.4.1 Test Method of Viscosity**

Using rheometer to test the material's viscosity at constant temperature 25 °C, the rotor used is Al material and its diameter is 60 mm, the viscosity of the sample is the viscosity collected at the shear rate of 1 s<sup>-1</sup>.

#### **2.4.2 Test Method of Shrinkage Ratio**

The test method of shrinkage ratio is in accordance with the relevant provisions of the International Standard ISO 3521. The shrinkage ratio (SR) of 3D printing-product light-cured resin can be calculated by Eq. (1). Wherein,  $\rho_1$  is the density of the liquid material sample which measured by the QBB type pycnometer,  $\rho_2$  is the density of the material cured which measured by the precise density balance.

$$SR = \frac{\rho_2 - \rho_1}{\rho_2} \times 100\% \quad (1)$$

#### **2.4.3 Test Method of Flexibility**

Using a No. 4 bar to uniformly coat the prepared material on a PET film and cure it by UV curing machine. After curing, the PET films coated with cured films are fixed into film cylindrical bending tester, bent cured film on different diameter mandrels, and then use the ten times magnifying glass to check if the surface of cured film is textured, crack, peeling and so on. To produce these phenomena thickest shaft rod is the flexibility of the material. The diameter of the thickest bar making the cured film have the phenomenon above is the flexibility of the material, its unit is mm. The smaller the diameter is, the better the cured film's flexibility is.

#### **2.4.4 Test Method of Curing Speed**

Using a No. 3 bar to uniformly coat the prepared material on a offset paper and cured by UV curing machine, the power of UV curing machine is fixed at 100%, cured the material with the speed from fast to slow. Using finger touch method to determined the curing speed which is, the fast speed of pressing the film with pulp, if there is no sticky feeling and no liquid on pulp, the speed is the curing speed of this kind of material, its unit is m/min.

#### **2.4.5 Test Method of Surface Tension**

Using surface tension meter to test the surface tension of material, its unit is mN/m.

#### **2.4.6 Test Method of Contact Angle**

Using a No. 4 bar to uniformly coat the prepared material on a PET film and prepare a solution by water and surfactant (Rd2300) whose surface tension is similar to it of flexo ink: 34 mN/m, dropping the solution on the film, using a contact angle meter to observe the contact angle between the liquid and the cured film.

#### **2.4.7 Test Method of Plate Transfer Performance**

Using 3D printer to print the prepared material to flexographic plate, install it on the cylinder of flexographic printer, under the conditions that the printing pressure is 100 Pa and the speed is 40 m/s, use water-based flexo ink to proof, and then measure the density of proofing samples by density gauge, the bigger the density is, the better the plate transfer performance is.

### **3 Experiment Results and Analysis**

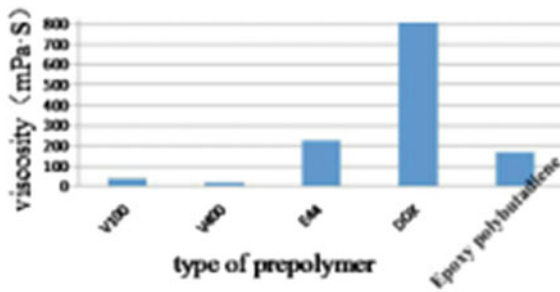
#### ***3.1 Polymer's Influence on the Properties of 3DFP Materials***

##### **3.1.1 Influence of the Type of Polymer on the Properties of 3DFP Material**

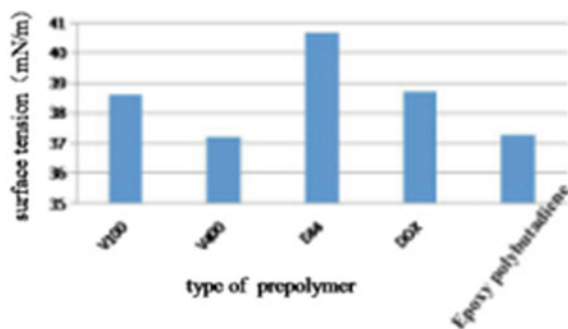
Prepolymer is the basic skeleton of the 3D printing light curable molding material, it has a major impact on the performance and usability of the prepared material. Different types of prepolymer have different molecular structures, so they have

different influence on the material's performance. We fixed other content of components, prepared the 3DFP material by different kinds of cationic type and free radical type prepolymer, measured each performance of material respectively, the results are shown in Table 1 and Figs. 1, 2, 3, 4, 5 and 6.

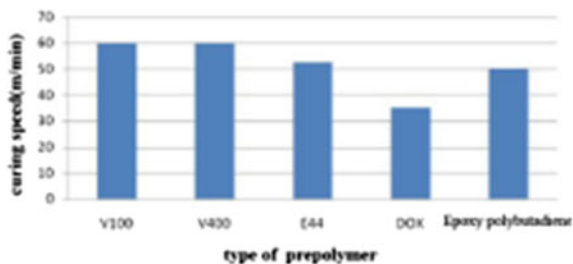
**Fig. 1** Influence of the type of prepolymer on the viscosity of the system



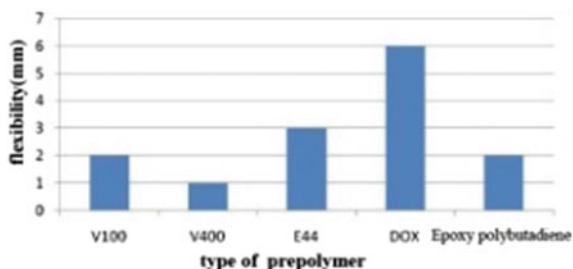
**Fig. 2** Influence of the type of prepolymer on the surface tension of the material



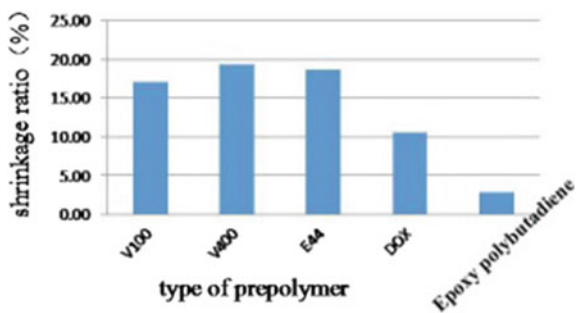
**Fig. 3** Influence of the type of prepolymer on the curing speed of the material



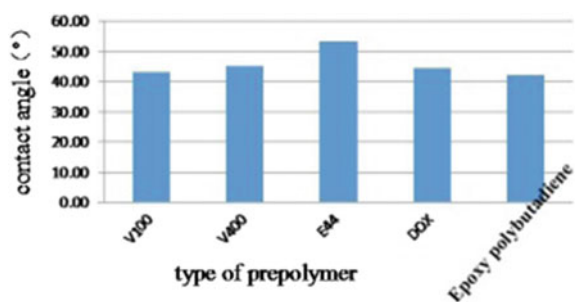
**Fig. 4** Influence of the type of prepolymer on the flexibility of the cured film



**Fig. 5** Influence of the type of prepolymer on the shrinkage ratio of the 3D printing-product flexographic plate material



**Fig. 6** Influence of the type of prepolymer on the contact angle of the 3DFP material



**Table 1** Performance of 3DFP material prepared by different kinds of prepolymer

Prepolymer	Viscosity (mPa s)	Surface tension (mN/m)	Curing speed (cm/s)	Flexibility (mm)	Shrinkage ratio (%)	Contact angle (°)
V400	38.86	38.63	60	2	17.14	43.30
V100	17.10	37.21	60	1	19.4	45.17
E44	226.00	40.68	52.5	3	18.66	53.43
DOX	806.90	38.71	35	6	10.54	44.47
Epoxy polybutadiene	169.80	37.26	50	2	2.87	42.27

As shown in Fig. 1, the viscosity of different prepolymer prepared 3DFP material have large difference. This is related to the structure and molecular weight of prepolymer. Wherein the viscosity of material prepared by the hyperbranched acrylic acid resin, as V400 and V100 are approximate and relatively low which caused by their hyperbranched structure. Moreover, because the molecular mass of V400 is slightly larger than the V100, so the viscosity of the V400 prepared material is slightly larger than the V100 prepared material; the viscosity of material prepared by oxetane DOX is the biggest caused by its cyclic structure. The viscosity of materials prepared by bisphenol an epoxy resin E44 and epoxy polybutadiene is relatively large, which is due to their large molecular weight and non-hyperbranch structure (Table 1).

As shown in Fig. 2, the surface tensions of different prepolymer prepared 3DFP material have little difference, substantially 38 mN/m or so, which is due to the little difference in the surface tension of the light curable prepolymer.

As shown in Fig. 3, the curing speed of different prepolymer prepared 3DFP material has difference, the curing speed of materials prepared by the hyper-branched acrylic acid resin: V400 and V100 are the fastest, this is due to that the acrylic resin has relatively high activity and they are not easy to occur chain transfer phenomenon, they can form network polymer in a short period of time [5]. The light curable materials prepared by bisphenol. A epoxy resin E44 and epoxy polybutadiene have relatively high curing speed, this is caused by their epoxy structure; The material prepared by oxetane has the slowest curing speed.

As shown in Fig. 4, the flexibility of different prepolymer prepared 3DFP material have difference, among them, the flexibility of the V100 prepared material is the best, the flexibility of the oxetanyl alkanes DOX prepared material is the worst. The differences between the flexibility of the resin are primarily caused by the difference of the molecular structure of the resin, the flexibility of polyester-structure resin is great, in addition, the molecular structure of the resin material is easy to form a network structure during the polymerization which makes the cured film exhibits rigidity and a poor flexibility.

As shown in Fig. 5, the shrinkage ratios of different prepolymer prepared materials are different, overall, the shrinkage ratios of materials prepared by radical prepolymer V400, V100 and E44 are relatively large, and the shrinkage ratios of materials prepared by cationic prepolymer DOX, epoxy polybutadiene are small, especially the shrinkage ratio of epoxy polybutadiene is just 2.87%. Which is due to the difference of the chemical bond change in distance in different resin during the light-curing reaction. In the radical type light curing reaction, the double bond in the prepolymer molecule open and change to single bond, the effective range of Van der Waals forces between the liquid molecules originally transform to the effective range of covalently bonded, which will produce volume shrinkage; as for cation type light curing reaction, it will also produce volume shrinkage because of the distance change of the Van der Waals forces, but the forming of carbon-oxygen bond in the cation type light curing reaction will greatly reduces the volume shrinkage of the light-curing reaction volume shrinkage.

The contact angle indicates the wettability of liquid to solid, the key property of the flexographic plate depends on if it can be well wetted by the ink which is a prerequisite to ensure the flexographic plate have a good ink transfer ability [6], and the ink flexographic printing used is mostly water-based ink. As shown in Fig. 6, the contact angles of aqueous liquid and the material prepared by different prepolymer are different, but they substantially between 40° and 50°, relatively speaking, the contact angles of aqueous liquid and the material prepared by epoxy polybutadiene is the smallest which means that the 3DFP made by this kind of material can be well wetted by the water-based ink. Whether the solid can be well wetted by the liquid depends on the solid surface energy and the interfacial energy of solid and liquid [6], because there is little difference in surface energy between 3DFP materials prepared by different prepolymer, so the wettability mostly depends

on the interfacial energy of liquid and this kind of material, the interfacial energy of aqueous liquid and the material prepared by epoxy polybutadiene is relatively small which ensure the material can be well wetted by water-based ink.

### 3.1.2 Formulation of Mixed Prepolymer

Through the study above we find that, different prepolymers have different excellent properties, there is no one kind of prepolymer that performances excellently in all aspects, in order to get a kind of material which has good overall performance, we should use mixed prepolymer to prepare it. Fixing the content of other ingredient, we choose 4 kinds of good performance prepolymer: V400, V100, E44 and epoxy polybutadiene to make formulation experiment, we use the four-component simplex centroid design, the performance of 3DFP material is shown in Table 2.

According to the experimental conditions and the different importance of the properties of the material which impact on the 3DFP material, we determined the weighting factors of viscosity, surface tension, curing speed, flexibility, shrinkage ratio and contact angle are 0.05, 0.05, 0.2, 0.2, 0.3 and 0.2 respectively, according to the excel solver, we can obtain that, when  $V400 = 0.49$ ;  $V100 = 0.10$ ;  $E44 = 0.41$ , the regression equation can reach to a maximum value of 0.90, that is using mixed prepolymer  $V400:V100:E44 = 5:1:4$  to prepare the 3DFP material, we can get the material with good comprehensive performance, the performance of 3DFP material prepared by this mixed prepolymer is shown in Table 3.

**Table 2** Property of material in the commixture prepolymer formulation experiments

Experiment no.	Viscosity (mPa s)	Surface tension (mN/m)	Curing speed (cm/s)	Flexibility (mm)	Shrinkage ratio (%)	Contact angle (°)
1	38.86	38.63	60	2	17.14	43.3
2	17.10	37.21	60	1	19.41	45.17
3	226.00	40.68	52.5	3	18.66	53.43
4	169.80	37.26	50	2	2.87	42.27
5	33.33	38.86	65	3	7.31	44.97
6	106.70	39.43	75	1	5.84	33.53
7	88.00	38.30	67.5	1	5.78	49.17
8	69.03	38.63	65	1	5.49	54.53
9	60.37	37.38	70	1	5.33	49.03
10	147.80	38.66	74.8	1	2.62	56.30
11	53.95	38.65	75.8	1	6.15	40.83
12	55.00	37.62	67.5	2	6.57	47.60
13	101.60	38.60	72	1	4.83	54.97
14	82.92	38.14	71.5	1	4.32	54.53
15	71.42	38.39	74.5	1	5.35	50.23



**Table 3** Properties of 3DFP material prepared by the best hybrid prepolymer

Viscosity (mPa s)	Surface tension (mN/m)	Curing speed (cm/s)	Flexibility (mm)	Shrinkage ratio (%)	Contact angle (°)
67.42	38.38	67.5	1	4.29	46.22

As shown in Table 3, material prepared for 3DFP has better overall performance.

## 3.2 *Monomer's Influence on the Properties of 3DFP Material*

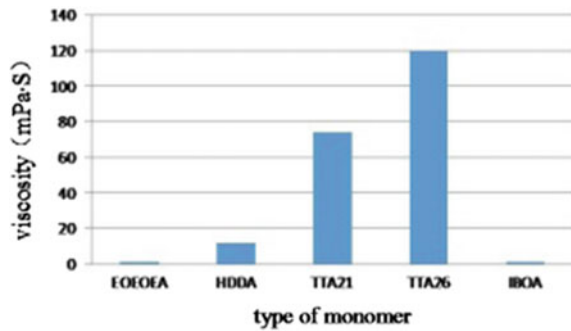
### 3.2.1 **Influence of the Type of Monomer on the Properties of 3DFP Material**

Monomer is also the basic component of the 3D printing light curable molding material, it can dilute the system and also can take part in the light curing reaction, has a relatively big impact on the curing speed and the performance of cured film. Different types of monomer have different molecular structures, so they have different influence on the performance of material. We fixed other content of components, prepared the 3DFP material by different kinds of cationic type and free radical type monomer, measured each performance of material respectively, the results are shown in Table 4 and Figs. 7, 8, 9, 10, 11 and 12.

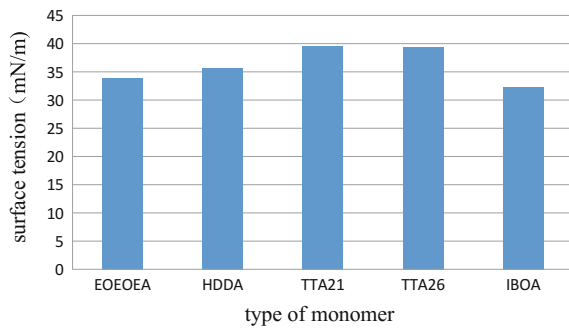
As shown in Fig. 7, the viscosity of different monomer prepared material has difference, the viscosity of the material prepared by cationic monomer TTA21 and TTA26 are relatively large, and the viscosity of the material prepared by bifunctional radical monomer is relatively small; the viscosity of the material prepared by monofunctional radical monomer EOEOEA and IBOA are the smallest. This is due to that with the functional groups in the acrylate active monomer increases, the flow friction between moleculars increases, and the viscosity of the material increases. As for epoxy active monomer, the molecular weight of it is relatively large, so the intermolecular resistance of it is large which causes to the viscosity of it is larger and then it of the acrylate active monomer (Table 4).

As shown in Fig. 8, the types of monomer have a certain influence on the surface tension of the material, the surface tension of materials prepared by cationic monomer TTA21, TTA26 are larger and then the surface tension of materials prepared by radical monomer, this is because that the polarity of cationic monomer is relatively big causing its surface tension is relatively big, as for radical monomer, the surface tension of materials prepared by bifunctional monomer HDDA is slightly larger than the surface tension of materials prepared by monofunctional monomer EOEOEA and IBOA, this difference in surface tension is also caused by the difference of the polarity of the monomer.

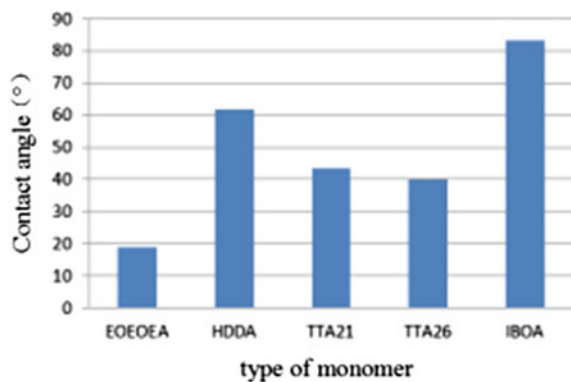
**Fig. 7** Influence of the type of monomer on the viscosity of the 3DFP material



**Fig. 8** Influence of the type of the monomer on the surface tension of the 3DFP material

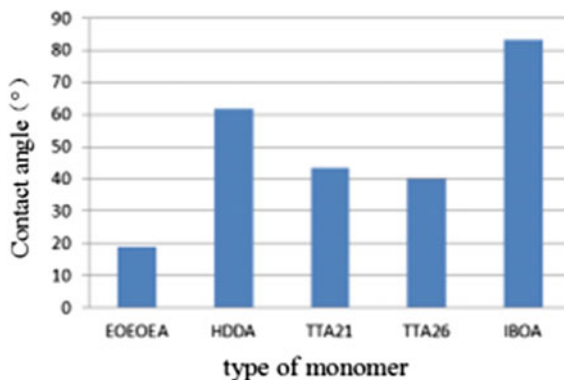


**Fig. 9** Influence of the type of the monomer on the contact angle of the 3DFP material

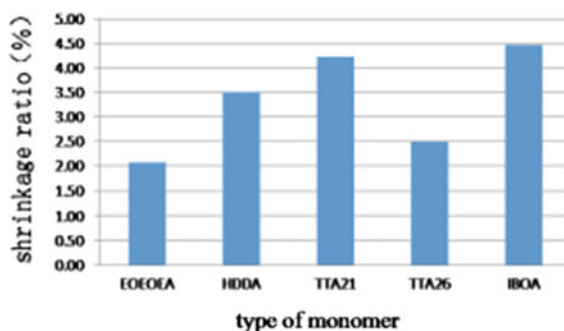


As shown in Fig. 9, the curing speed of different monomer prepared 3DFP material have difference, the curing speed of materials prepared by the cationic monomer TTA21 and TTA26 are the fastest, more than 70 m/min. However, the curing speed of materials prepared by the radical monomer is relatively slow, only 30–35 m/min, which due to the reactivity of cationic monomer is generally higher than the reactivity of radical monomer.

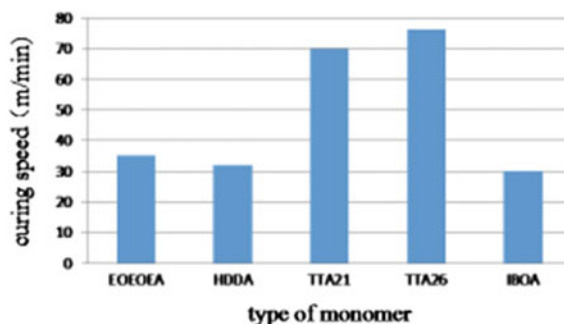
**Fig. 10** Influence of the type of monomer on the flexibility of the cured film



**Fig. 11** Influence of the type of monomer on the shrinkage ratio of the cured film



**Fig. 12** Influence of the type of the monomer on the contact angle of the 3D printing-product flexographic plate material



As shown in Fig. 10, the flexibility of different monomer prepared material has large difference, as for radical monomer, the flexibility of material prepared by straight-chain monofunctional monomer EOEOEA is great, this is due to that with the increase of the functionality of the reactive monomer, the degree of crosslinking of the molecular is bigger, and the rigidity of cured film is bigger. In addition, molecule formed a long chain structure in curing process, no more branched, its flexibility is good. This epoxy molecule has similar result, and due to the ring-opening polymerization of ethylene molecule, and single molecule has good

**Table 4** Performance of 3DFP material prepared by different kinds of monomer

Monomer	Viscosity (mPa s)	Surface tension (mN/m)	Curing speed (cm/s)	Flexibility (mm)	Shrinkage ratio (%)	Contact angle (°)
EOEOEA	0.54	33.91	35	1	2.09	18.8
HDDA	11.74	35.65	32	4	3.50	61.8
TTA21	73.86	39.64	70	2	4.22	43.5
TTA26	119.70	39.40	76.5	3	2.50	39.9
IBOA	0.48	32.27	30	4	4.48	83.3

chain structure, so the flexibility of material prepared by TTA21 and TTA26 is relatively good.

As shown in Fig. 11, the shrinkage ratios of different monomer prepared materials have no big difference, the shrinkage ratio of EOEOEA-prepare material is the smallest, about 2%; which is due to that the shrinkage ratio of light curable material is closely related to the prepolymer, its relationship with the monomer is relatively small. There is less covalent bond changed from van der Waals forces in the straight-chain monofunctional monomer EOEOEA during light-curing reaction, so the distance change of it is less.

As shown in Fig. 12, the contact angles of aqueous liquid and the material prepared by different monomer are different, the contact angles of aqueous liquid and the material prepared by EOEOEA is the smallest which means that the 3DFP made by this kind of monomer can be well wetted by the water-based ink. Contact angle depends on the solid surface energy and the interfacial energy of solid and liquid [7], because there is big difference in surface energy between 3DFP materials prepared by different monomer, additionally, there is big difference in the interfacial energy of solid and liquid, so there is big difference in their contact angle, It can be seen that the surface tension of the cured film prepared by TTA21, TTA26 are high, the contact angle with aqueous liquid of them are small; But the surface tension of the cured film prepared by IBOA, HDDA are low, their contact angles with aqueous liquid are big; Though the surface tension of the cured film prepared by EOEOEA is relatively small, its contact angle with aqueous liquid is also relatively low, so the contact angle is small.

### 3.2.2 Formulation of Mixed Monomer

Through the study above we find that, different monomers have different excellent properties, there is no one kind of monomer that performances excellently in all aspects, in order to get a kind of material which has good overall performance, we should use mixed monomer to prepare it. Fixing the content of other ingredient, we choose 4 kind of good performance monomer EOEOEA, HDDA, TTA21 and TTA26 to make formulation experiment, we use the four-component simplex centroid design, the performance of 3DFP material is shown in Table 5.

**Table 5** Properties of material in the commixture monomer formulation experiments

Experiment no.	Viscosity (mPa s)	Surface tension (mN/m)	Curing speed (cm/s)	Flexibility (mm)	Shrinkage ratio (%)	Contact angle (°)
1	0.54	33.91	35	1	2.09	18.8
2	11.74	35.65	32	4	3.50	61.8
3	73.86	39.64	70	2	4.22	43.5
4	119.70	39.40	76.5	3	2.50	39.9
5	8.21	34.85	34	2	5.24	42.0
6	15.88	36.38	72.5	1	3.55	50.0
7	20.47	36.02	75	1	4.59	41.6
8	23.03	37.38	75.8	2	4.71	42.6
9	30.39	37.08	76	2	6.02	45.6
10	91.02	39.36	76	1	3.12	38.7
11	13.52	35.81	76	1	6.92	33.0
12	16.36	35.85	75	1	5.72	38.8
13	29.61	36.94	76.5	1	2.82	36.1
14	37.05	37.90	76.5	1	5.59	40.4
15	22.88	36.52	76	1	3.33	41.0

**Table 6** Property of 3DFP material prepared by the best hybrid monomer

Viscosity (mPa s)	Surface tension (mN/m)	Curing speed (cm/s)	Flexibility (mm)	Shrinkage ratio (%)	Contact angle (°)
23.61	36.32	75	1	2.79	40.6

The weighting factors in this formulation is same with the prepolymer formulation, according to the excel solver, we can obtain that, When EOEOEA = 0.32; HDDA = 0.06; TTA21 = 0.30; TTA26 = 0.32, the regression equation can reach to a maximum value of 0.84, that is using mixed monomer EOEOEA:HDDA:TTA21:TTA26 = 16:3:15:16 to prepare the 3DFP material, we can get the material with good comprehensive the performance of 3DFP material prepared by this mixed monomer is shown in Table 6.

As shown in Table 6, material prepared for 3DFP has better overall performance.

### 3.3 Test of Material Forming Ability and Transfer Performance of 3DFP

#### 3.3.1 Test of Print the Flexographic Plate by the Material We Studied

Inject the 3DFP material we studied into 3D printer's nozzle, set the temperature is 44 °C, print out the flexographic plate whose size is 250 mm × 80 mm, print 20 layers, the thickness is about 1 mm, the result is shown in Figs. 13 and 14.

**Fig. 13** Full point flexographic plate



**Fig. 14** Graphic flexographic plate



**Fig. 15** *Left* 3DFP, proof; *right* traditional flexographic plate proof



As shown in Figs. 13 and 14, the 3DFP printed by the miscellaneous light curable material studied is a clear pattern with tidy edges, it has relatively good performance on the full point, graphics, text, etc., and also has good flexibility, and it has good printing plate forming ability which can basically meet the requirements.

### 3.3.2 Test of the Ink Transfer Ability of 3DFP

Using 3D printer to print the full point flexographic plate, install the plate on the cylinder of flexographic printer to proof, at the same time with the same conditions, using the traditional plate to proof and compare the two proof samples showing in Fig. 15, and then measure the color density of the samples, as shown in Table 7.

**Table 7** Color density of proofs

Plate type	Yellow	Cyan	Magenta
Traditional flexographic plate	1.12	1.48	1.29
3DFP	1.14	1.34	1.20

As shown in Fig. 15 and Table 7, the proof printed by 3DFP is similar to the proof printed by traditional plate, there is little difference in their color density, which means that the 3DFP has good ink transfer ability, it can meet the printing requirements.

## 4 Conclusions

Through the research above, we get the following conclusions under this experimental condition:

1. The structure of prepolymer has a major impact on the performance of 3DFP material, the material prepared by cation prepolymer has big viscosity and bad flexibility; the material prepared by hyperbranched radical prepolymer has low viscosity, good flexibility, high curing speed; the material prepared by epoxy polybutadiene has low shrinkage ratio, good flexibility; there is little difference in surface tension of materials prepared by every kind of prepolymer, they could be well wetted by the water-based ink, when the mass ratio of prepolymer is V400:V100:E44 = 5:1:4, the 3DFP material has good overall performance.
2. The structure of monomer has a major impact on the performance of 3DFP material, the material prepared by cation monomer has big viscosity and surface tension and high curing speed; the material prepared by the straight-chain monofunctional monomer EOEOEA has low viscosity, good flexibility, low shrinkage ratio, low surface tension, and it could be well wetted by the water-based ink; but monomer has little influence on the shrinkage ratio of the light curable material after film formation, when the mass ratio of monomer is EOEOEA:HDDA:TTA21:TTA26 = 16:3:15:16, the 3DFP material prepared has good overall performance.
3. The 3DFP printed by the mixed light curable material we studied has good forming effect and good ink transfer ability.

## References

1. Jiaping Gu. (2014). Direct flexo platemaking technology (Publishing and printing).
2. Min Wang, Hua Zhang. (2013). Analysis of combined Chinese patent application development in 3D printing (Jilin Engineering and Technical Teachers College).

3. Haitao Liu. (2009). Light-cured three dimensional printing research and application of the molding material. [PhD thesis], Huazhong University of Science and Technology.
4. Changlong Guo, Beiqing Huang. (2014). Research for 3D printing Hybrid UV curing system. Journal of Beijing Institute of Graphic Communication.
5. Yangzhi Jin. (2010). Light-cured material properties, application notes. Chemical Industry Press, Beijing.
6. Xianfu Wei, Beiqing Huang, Pujun Deng. (2011). The printing principle and process. China Light Industry Press, Beijing.
7. Zhitao Wang. (2011). Research of solvent-free epoxy coating volume shrinkage. *Coatings Industry*.



# Discussing the Preparation Conditions of Graphene

Xiaotong Xiong, Beiqing Huang and Xianfu Wei

**Abstract** The oxide reduction process of preparation graphene always accompanies the stirring process. The stirring speed affects the efficiency of sulfuric acid to access the graphite sheet, but also affects the efficiency of potassium permanganate to oxidize the graphite and affects the reducer to reduce graphene oxide. So the stirring speed has a non-negligible efficiency to control the synthesis of graphene. Focusing on this problem, this study uses oxidation reduction to compound the graphene, changing stirring speed in the process of synthetic experiment in order to prepare different graphene dispersions, then the samples are go through FT-IR, Raman spectrum, transmission electron microscopy (TEM) and resistivity test analysis. The experiment results express that graphene's conductivity is much better when stirring speed is 300 r/min than other speed (100 and 500 r/min) in preparation. In addition, the order degree and the flatness of graphene layers are more excellent. The graphene at 500 r/min stirring speed preparation contains less oxygen groups.

**Keywords** Graphene · Preparation conditions · Stirring speed · Test analysis

## 1 Introduction

Graphene is a two-dimensional (2D) crystalline material that consisted by a single atomic layer of carbon bonded all together in a honeycomb. Graphene has attracted a lot of attention and has been the subject of numerous theoretical and practical investigations owing to its extraordinary physical and chemical properties [1]. There are some methods for preparation of graphene, such as: mechanical peeling method, chemical vapor deposition method, liquid-phase stripping method, oxidation-reduction method and so on.

---

X. Xiong (✉) · B. Huang · X. Wei  
Beijing Institute of Graphic Communication, School of Printing  
and Packaging Engineering, Beijing, China  
e-mail: 521144884@qq.com

This paper uses oxidation reduction to prepare graphene, so far, there is some literatures report that reducing agent dosage and reaction time have an impact on reduction effect [2]. Not only that, reaction temperature and pH value have an impact on reaction rate, product range [3]. As a result, researching the influence of reaction conditions the graphene sheets is very significance.

The oxide reduction process of preparation graphene always accompanies the stirring process. The stirring speed affects the efficiency of sulfuric acid to access the graphite sheets, but also affects the efficiency of potassium permanganate to oxide the graphene and affects the reducer to reduce graphene oxide. In this paper, we used the oxidation reduction to compound the graphene, setting the stirring speed of the reaction course to: 100, 300, 500 r/min (rest of the experimental conditions without changing) to prepare different graphene dispersion. Then the samples went through FT-IR, Raman spectrum, transmission electron microscopy and resistivity test analysis, exploring the impact of the preparation's condition on graphene's functional group, morphology, lamella, degree of order and resistivity.

## **2 Experiment**

### **2.1 *Experimental Materials***

Graphite, 98% H<sub>2</sub>SO<sub>4</sub>, NaNO<sub>3</sub>, KMnO<sub>4</sub>, ionized water, H<sub>2</sub>O<sub>2</sub>, HCl, glucose, pH test paper.

### **2.2 *Experimental Instrument***

D2004 W electric mixer, HZ85-2 magnetic stirrer, RJ-TDL-60A low-speed large-capacity desktop centrifuge, BS244S electronic analysis The balance, KQ3200DE ultrasonic cleaner, DZF-6210 vacuum oven, RTS-9 four-probe tester, Renishaw in Via Raman spectrometer, Nicolet iS 50 infrared spectroscopy, CSPM5000 atomic force microscope, Tecnai G2 F20 S-TWIN transmission electron microscope, 200 ml beaker, 400 ml beaker, three-neck flask, glass rod.

### **2.3 *Oxidation-Reduction Preparation of Graphene***

#### **2.3.1 Preparation of Graphene Oxide**

Taking graphite powder 1, 0.5 g NaNO<sub>3</sub>, 23 ml 98% H<sub>2</sub>SO<sub>4</sub> at 0 °C mix, magnetic stirrer continue embrace mixing (respectively 100, 300, 500 r/min), and slowly add

6 g  $\text{KMnO}_4$  with stirring for 2 h at 0 °C, then stirring for 4 h at 35 °C (respectively 100, 300, 500 r/min). Adding 138 ml deionized water to the resulting solution slowly for dilution, and raise the temperature to 95 °C for 0.5 h with stirring. In this case we add 130 ml deionized water and 20 ml  $\text{H}_2\text{O}_2$  to the solution with stirring (respectively 100, 300, 500 r/min) 1 h and stand it overnight. After that we decant the upper clear liquid, then add 5% dilute HCl for dilution, and then stand it overnight again, decanting the upper clear liquid again, repeating three times. Finally, the solution is placed in dialysis bag until the pH gets to 6. Take some solution to place into an ultrasonic cleaner (45 W, 50 Hz), ultrasound 1 h, then the graphene oxide dispersion was obtained [4].

### **2.3.2 Reduce Graphene Oxide to Prepare Graphene**

Measuring 10 ml deionized water and oxide graphene formulated as 1 mg/ml solution of graphene oxide, adding ammonia so that the pH gets to 8–9 value. Adding 250 mg glucose to the reaction mixture with stirring (respectively 100, 300, 500 r/min). Furthermore, Stirring the solution at 95 °C in an oil bath (respectively 100, 300, 500 r/min), at the same time, making a reduction reaction reflux condenser for 12 h. Then using a centrifuge wash to the product (with deionized water washed six times) until pH value reaches 7. Finally, the product is washed and dried in a vacuum box for 48 h. At last, we get three groups of graphene which were prepared always at a stirring speed: 100, 300, and 500 r/min [4].

## **2.4 Sample Characterization and Test Methods**

### **2.4.1 Resistivity Characterization**

We press the graphene powder into a sheet, then using a four-probe resistivity tester to test each sample. To select three areas for measurement in each sample then calculate an average resistivity.

### **2.4.2 Infrared Spectroscopy Characterization**

Using KBr tablet method, we take a small amount of graphene sample with KBr grinding evenly and placed in a tableting machine to tablet, then put it into the infrared spectroscopy for test [4, 5].

### 2.4.3 Raman Spectroscopy Characterization

Raman spectroscopy analysis is based on light scattering by the Raman scattering effect. Putting the graphene into the sample bottle and kept in a dark environment [3], moving the probe tip keep the distance to 2 mm, scanning graphene at an excitation wavelength of 514 nm [5].

### 2.4.4 Transmission Electron Microscopy (TEM) Characterization

Mixing the graphene sample with deionized water and taken an ultrasonic dispersion, drop it in the copper sulfate medium using a transmission electron microscope to observe the graphene surface morphology and measure graphene's structure and detail [6].

## 3 Results and Analysis

### 3.1 Resistivity Analysis

The graphene's slice thickness and quality have a causal relationship with graphene resistivity [7], so we use the four-probe tester at different speeds to test three sets of graphene samples' resistivity, data are as follows (Table 1).

As can be seen in the table, the resistivity of the graphene at 100 r/min stirring speed preparation is the biggest, which means the conductivity is worse than the graphene at 300 and 500 r/min stirring speed preparation obtained, which hints the graphene prepared at a low stirring speed contained more oxygen species or more hetero groups and the opening degree of the graphite sheets during the preparation of graphene is not complete, the reaction efficiency of oxidant and reductant with the reactant are relatively low. The resistivity of graphene at 300 r/min stirring speed preparation is smallest, which means the conductivity is the most.

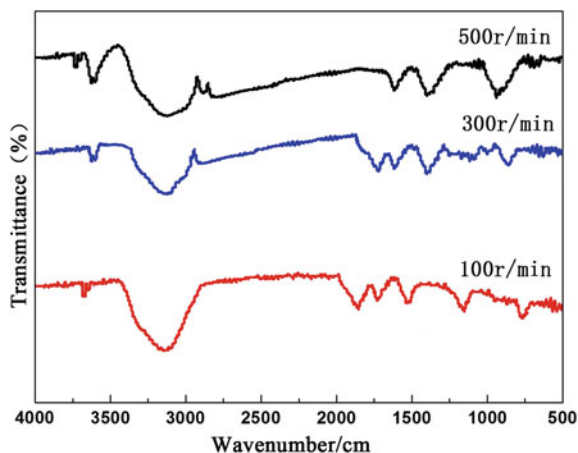
### 3.2 Infrared Spectroscopy Analysis

In order to accurately analyze the influence of stirring speed on graphene molecular structure, we through infrared spectroscopy to characterize the three groups of

**Table 1** Graphene resistivity prepared at different speeds

Rotate speed (r/min)	Resistivity ( $\Omega$ m)
100	53.2
300	47.8
500	48.1

**Fig. 1** IR spectra of graphene under different stirring speeds preparation



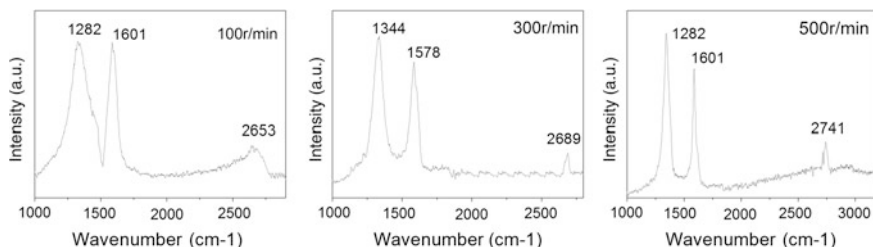
products and get Fig. 1 the IR spectra of graphene under different stirring speeds preparation, which is as follows.

Figure 1 can be seen that three curves all have the broad strong absorption peak and they appear in  $3000\text{--}3200\text{ cm}^{-1}$  which means the water molecule stretching vibration of  $\text{--O--H}$ ,  $2800\text{--}3000\text{ cm}^{-1}$  is  $\text{sp}^2$  hybridized C-H stretching vibration peak,  $1550\text{--}1650\text{ cm}^{-1}$  is graphene stretching vibration of the C=C,  $1300\text{ cm}^{-1}$  is C-O stretching vibration of the peak, in addition, there are smaller C=O ( $\sim 1720\text{ cm}^{-1}$ ) and the C-O-C ( $\sim 1068\text{ cm}^{-1}$ ) stretching vibration of three curves. The graphene at 500 r/min stirring speed preparation compare with the graphene at 100 and 300 r/min stirring speed preparation, the former contains less oxygen group peaks, while it has more C=C peak and  $\text{sp}^2$  hybrid C-H stretching vibration peak [10].

### 3.3 Raman Spectroscopy Analysis

In order to explore influence of the stirring speed on graphene sheets regularity furtherly, under excitation wavelength of 514 nm to characterize the three groups of products through Raman spectrometer. We get the Raman spectra of graphene under different stirring speed as Fig. 2, the position of G peak and D peak and ratio of them as Table 2.

As we know that: D peak is characteristic defect peaks of graphene structures, G peak and D peak relative intensity ratio is an important parameter to characterize the degree of disorder and defects of the carbon material, the ratio is larger, the defects content is more. 2D peak occurs in the vicinity of  $2700\text{ cm}^{-1}$ , and the peak 2D is stronger illustrates the graphene has fewer defects and fewer layers [9]. As can be seen from the above data, three groups of graphene have strong D peaks and weak 2D peaks, which describe the three groups of graphene were all flawed.



**Fig. 2** Raman spectra of graphene under different stirring speed

**Table 2** Position data of G peak, D peak and 2D peak; the  $I_D/I_G$

Rotate speed (r/min)	D-band peak/cm	G-band peak/cm	$I_D/I_G$	2D-band peak/cm
100	1282	1601	1.216	2653
300	1344	1578	0.959	2669
500	1337	1585	1.074	2741

The graphene at 300 r/min stirring speed preparation compare with the graphene at 100 and 500 r/min stirring speed preparation, the former's  $I_D/I_G$  are smaller, which shows the graphene at 300 r/min stirring speed preparation has the greater grain size and the lower degree of disorder and defects as well. The graphene at 500 r/min stirring speed preparation has a largest 2D peaks which transfers that the thickness of graphene layers is thinnest.

### 3.4 Transmission Electron Microscopy Characterization

In order to observe the layer and the appearance of three groups graphene, we use the transmission electron microscopy to characterize graphene, and get the TEM of graphene under different stirring speed, which is as follows (Fig. 3).

The dark area of picture represents a lot of graphene layers, and the light area represents a small number of graphene layers [7]. From the chart we can see clearly the edges of graphene. There is little difference in thickness of each portion, showing the graphene dispersed uniform in a solution of copper mesh. At the same time, we can see the fold surface of the graphene, and the figure on the left has the most obvious situation. That means a lot of groups of the graphene at 100 r/min stirring speed preparation have been destroyed the structure of the carbon ring. And graphene sheets superposed with each other to form the folds. Learning from the shades of figures, three groups of graphene have fewer layers, but their edge has some defects. Among this, the graphene at 500 and 300 r/min stirring speed preparation have not obvious wrinkles, and a little overlap portion, what's more, their surface texture is clear, smooth and orderly.

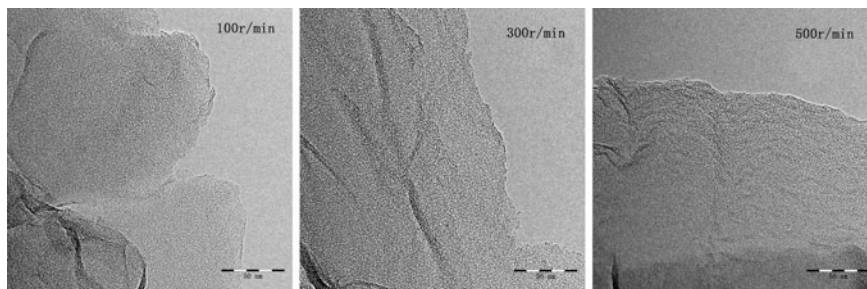


Fig. 3 TEM of graphene under different stirring speed

## 4 Conclusions

By comparison of the above experimental analysis, we find that the graphene at 300 r/min stirring speed preparation compare with that the graphene at 100 and 500 r/min stirring speed preparation, the former has the better conductivity, and the graphene has not obvious wrinkles, not too much overlap portion, the surface texture is clear, smooth and orderly state. The graphene at 500 r/min stirring speed preparation contains less oxygen groups.

## References

1. Hummers W, Offeman R. (1958). Preparation of graphene oxide. *Am Chem. Soc.*, 80: 1339–1339.
2. Zhu P Y, Shen M, Xiao S H, et al. (2011). Experimental study on the reducibility of graphene oxide by hydrazine hydrate[J]. *Physica B*, 406: 498–502.
3. Ge Hao, TIAN Hui, et al. (2014). Influence of Reaction Conditions on the eduction Efficiency of the Surface Function Groups of Graphene Oxide Reduced by Hydrazine Hydrate. *Science*, 4–5.
4. Stankovieh S, Dikin D A, Piner R D, et al. (2007). Synthesis of graphene-based nanosheets via chemical reduction of exfoliated graphene oxide. *Carbon*, 45(7): 1558–1565.
5. Gao W, Alemany L B, Ci L J, et al. (2009). New insights into the structure and reduction of graphite oxide. *Nat. Chem.*, 1(5): 403–408.
6. Pei S F, Zhao J P, Du J H. (2010). Direct reduction of graphene oxide films into highly conductive and flexible graphene films by hydrohalic acids. *Carbon*, 48: 4466–4474.
7. Taisuke O, Aaron B, Thomas S, et al. (2006). Controlling the electronic structure of bilayer grapheme. *Science*, 313: 951–954.

# Study on the UV Curing Molding Material in 3D Printing Modification of Expanding Monomer

Lu Zhang, Beiqing Huang and Xianfu Wei

**Abstract** Expanding monomer is a type of substance that would cause volumn expanding in the polymerization reaction. Expanding monomer is capable of ring-opening polymerization reaction under the action of a photoinitiator, and is accompanied by volume expansion, copolymerized with epoxy resin to reduce the volume shrinkage during curing process. To solve the problems of volume shrinkage in light-cured polymerization polymerization reaction, a spiro orthocarbonate expanding monomer 3, 9-diethyl-3, 9-dihydroxymethyl-1, 5, 7, 11-tetraoxa-spiro [5.5] undecane was synthesized by two steps in this paper. The construction of the monomer product was determined by the characterization of IR. The monomer is used in UV curing molding material of 3D printing. The shrinkage rate of expanding monomer was decreased from 5.665 to 4.387% when adding amount was 1%. Through the fully study of viscosity, surface tension, and the volume shrinkage to analysis the influence of expanding monomer in UV curing molding material.

**Keywords** Expanding monomer · Spiral original carbonate · 3D printing · Swelling

## 1 Introduction

UV-curing Three-dimensional Printing (3DP) is similar to UV ink-jet printing, which is the spray forming of UV resin droplets. In the forming process, two sets for printing heads simultaneously spray UV-curing building material and

---

L. Zhang (✉) · B. Huang · X. Wei  
Beijing Institute of Graphic Communication, Beijing, China  
e-mail: 634698575@qq.com

B. Huang  
e-mail: huangpeiqing@bigc.edu.cn

X. Wei  
e-mail: weixianfu@bigc.edu.cn



UV-curing support material respectively. Then the materials are cured by ultraviolet light. The materials accumulate layer by layer. Lastly, when the printing is completed, removing the support material by water gun, the prototyping part is achieved. UV-curing Three-dimensional Printing combines the advantages of UV-curing and spray forming, to improve the efficiency and accuracy of rapid prototyping and reduce costs. During the process of the resins, because the bond distance between molecular was changed so that result in volumn shrinkage. Slight shrinkage would lead to internal stress rapid then the model was destroyed, heavy shrinkage would lead the sample structural deformation, and then made the model failure [1].

Expanding monomer is a type of substance that would cause volumn expanding in the polymerization reaction [2]. Since 1972, Bailey discovered swelling monomer, there have been a variety of spiro carbonate (SOC), spiro orthoester (SOE), a bicyclic orthoester (BOE) are successively synthesized [3]. Expanding monomer is capable of ring-opening polymerization reaction under the action of a photoinitiator, and is accompanied by volume expansion, copolymerized with epoxy resin to reduce the volume shrinkage during curing, even a slight swelling.

In this paper, a synthetic monomer used in the expansion of 3D printing Hybrid UV curing system, study on the effect of the expansion in the 3D printing monomer mixed reaction mechanism of the light-curing system and the impact on the volume shrinkage. The other property of 3D printing Hybrid UV curing system was tested. The expanding monomer reduces the volume shrinkage, and achieved good results.

## 2 Experimental

### 2.1 *Materials and Reagents*

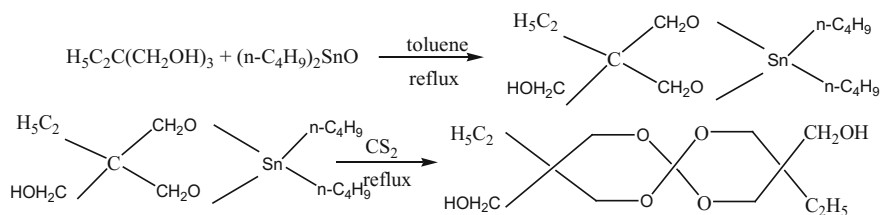
Trimethylolpropane (industrial) products for the Japanese company Mitsubishi; Di-n-butyl tin oxide (industrial grade) Zhangjiagang City for Health and Chemical Co., Ltd; Prepolymer: Bisphenol A epoxy resin (E44, Shandong Tianmao Chemical), Hyperbranched polyester acrylate prepolymer (V400, Cytec Industries), Hyperbranched polyester acrylate (V100, Cytec Industries); Reactive monomer: 3,4-Epoxycyclohexylmethyl 3,4-Epoxycyclohexane Carboxylate (TTA21, Jiangsu Tai Teer Chemical); Bis ((3,4-epoxycyclohexyl) methyl) adipate (TTA26, Jiangsu Tai Teer Chemical); hoxymethoxy acrylate (EOEOEA, Changxing chemical Taiwan); 1,6-hexanediol diacrylate (HDDA, Changxing chemical Taiwan); Photoinitiator: Thiophenyl—oxygen ring nitrogen acetone (907 Tianjin Long Day Chemistry); Mixed triarylsulfonium hexafluorophosphate sulfate (PAG 201, Changzhou powerful electronic); Mixed triarylsulfonium hexafluorophosphate (PAG202, Changzhou Powerful Electronic).

## 2.2 Equipment

81-2 constant temperature magnetic stirrer (Changzhou curing Ltd.); K100 automatic surface tension meter (Germany KRuSS); Viscolite 700 portable viscometer (Shanghai Hydramotion); Light Hammer 6 UV curing machine type (USA FUSION); iS50FT-IR (USA Thermo).

## 2.3 Synthesis of Expansion Monomers [4–6]

In a three necked 250 ml round bottom flask provided with hermocouple, reflux condenser and water separator were placed 13.4 g (0.1 mol) of Trimethylolpropane, 26.6 g (0.1 mol) of Di-n-butyl tin oxide and 100 ml toluene. The reaction was stirred at reflux temperature for 12 h or anhydrous generated. The reaction was cooled to room temperature, a certain amount of carbon disulfide was slowly added drop wise from the pressure-equalizing dropping funnel once that the addition is finished the temperature was raised to 110 °C and kept at this temperature for 12 h. The toluene was evaporated under reduced pressure, the resulting viscous solution was washed several times with n-hexane, the resulting solid (I) was recrystallized in toluene and dried in vacuum to give a white solid. The yield of the reaction was 83%. The synthesis of monomer is as follows:



## 2.4 Preparation of Light-Curing Materials Containing the Expanding Monomer

The mass fraction of 0.5, 1, 1.5, 2% expanding monomer is added to the light curing material basic formulation (see Table 1) respectively and stirred with a glass rod until the expansion monomer was completely dissolved. At the same time a blank test was prepared.

**Table 1** Formation of 3D printing light cured material

Ingredient name	Mass percentage (%)
V400	10
V100	2
E44	8
EOEOEA	31.5
HDDA	3.5
TTA21	17.5
TTA26	17.5
Photoinitiator	10

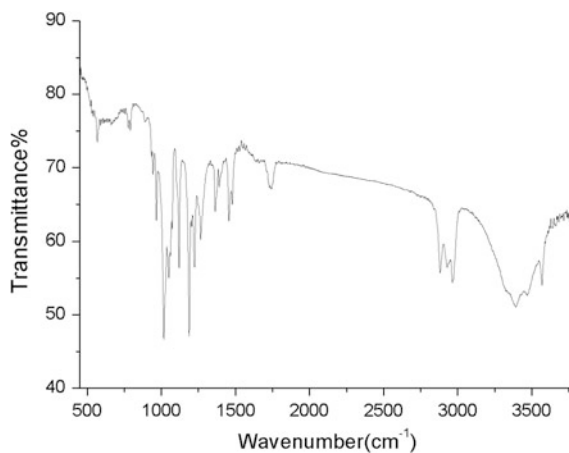
## 2.5 Characterization and Testing

### 2.5.1 Infrared Characterization

A wave number of  $1220\text{ cm}^{-1}$  can be seen in Fig. 1, the monomer having a obvious spiro ring group characteristic absorption peaks, In the wave number  $3400\text{ cm}^{-1}$  appears near the hydroxyl absorption peak width, It confirmed the synthesized monomers and reactive monomer structure consistent.

### 2.5.2 Viscosity Test

A certain amount of the sample was filled in a beaker, the viscosity was tested by Viscolite 700 portable viscometer, unit is mPa s.

**Fig. 1** IR spectrum of the expanding monomer

### 2.5.3 Volume Shrinkage Test

The shrinkage volume of liquid resin was compute according the following formula:

$$SR = \frac{\rho_2 - \rho_1}{\rho_2} \times 100\% \quad (1)$$

$\rho_1$  is the destiny of liquid resin measured by the type of QBB Pycnometer

$\rho_2$  is the destiny of resin after curing measured by precision density balance.

### 2.5.4 Surface Tension Test

The surface tension of molding material was tested by K100 automatic surface tension meter (Germany KRuSS), using the pull-off method for measuring surface tension, A known side pulled platinum sheet was immersed in a liquid, tension and edge length size is calculated by the following formula based on the surface tension:

$$F = \alpha \times 2D \quad (2)$$

In the formula, F is the tension when liquid film from the platinum; D is a platinum sheet side;  $\alpha$  is surface tension of the liquid.

## 3 Results and Discussion

### 3.1 Expansion Monomer Effect on Volume Shrinkage

Properties of the Cured Material Influenced by Expansion Monomers were shown in Fig. 2. As can be seen from Fig. 2, with the increasing content of expansion monomer, system volume shrinkage ration decreased, this might be in the curing reaction of the prepolymer, expansion monomer polymerization, on the one hand it reduces the volume shrinkage due to the double bond produced by the polymerization reaction in polymerization system, on the other hand, it do two different polymerization with bisphenol A epoxy resin (E44). Expansion monomer result in photoinitiator of cationic polymerization, Bisphenol A epoxy resin (E44) simultaneously do radical polymerization, both showed good synergy, two polymer network was formed, IPN structure may form. However, the shrinkage ration was increased when the mass fraction was 1%, which may due to the unreacted expanding monomer aggregation.

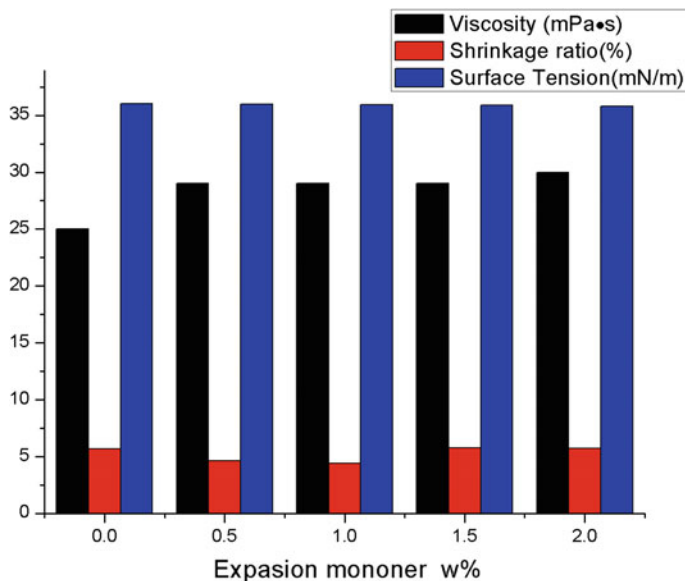


Fig. 2 Effect of expansion monomer content on of system performance

### 3.2 Expanding Monomer Effect on Viscosity and Surface Tension

As can be seen from Fig. 2, adding a small amount of expanding monomer has little effect on the viscosity and surface tension of systems, only a slight influence on the viscosity and surface tension of systems because added the different amounts of expanding monomer.

## 4 Conclusions

- (1) Synthesis of a spiro expansion carbonate monomer with two steps, the structure of the product was characterized by IR.
- (2) The expansion monomer was applied to the photo-curable material system, conclude that added the amount of expansion monomers can reduce the volume shrinkage of the UV curing system.

## References

1. CANELLIDIS V, GIANNATsIs J, DEDOUSSIS V. (2013). Efficient parts nesting schemes for improving stereolithography utilization. *Computer-Aided Design*, 45(5):875–886.
2. XU X Q, ZHOU L, LIANG B, et al. (2014). Synthesis of copolymers containing double spiro orthocarbonate and used as anti-shrinkage additives in epoxy resin composite *Polymer-Plastics Technology and Engineering*, 53(8): 753–759.
3. HAYAL BULBUI SONMEZ, FRED WUEL. (2003). Synthesis dpolymers based on spiro-orthocarbonates. *Polymer preprints*, 44(2): 803.
4. Shizuyoshi Sakai, Yoshihiro Kobayashi and Yoshio Ishii. (1971). Reaction of dialkyltin dialkoxides with carbon disulfide at higher temperature. *dialkoxi J. Org. Chem*, 36: 1176–1180.
5. Bailey W J, Sun R L, Katsuki T et al, (1977). Ring-opening polymerization with expansion in volume, in *Ring-Opening Polymerization*, ACS Symp. Ser., No. 59, Saegusa T and Goethals E., Eds., American Chemical Society, Washington, D.C., 53.
6. Bailey W J, Endo T. (1976). Synthesis of monomers that expand on polymerization: synthesis and polymerization of 3, 9-dimethylene-1, 5, 7, 11-tetraoxaspiro [5.5] undecane, *J. Polym. Chem. Ed.*, 14, 1735.

# Preparation of Branched Polymers Using a Polymerizable RAFT Agent

Guiyu Ma, Zhongxiao Li, Yingqun Qi and Ti Wu

**Abstract** A reversible addition-fragmentation chain transfer (RAFT) agent, 2-((2-(((dodecylthio)carbonothioyl)thio)propanoyl)oxy)ethyl acrylate (DTEA), was synthesized through the condensation reaction of 2-(dodecylthio-carbonothioylthio) propanoic acid with 2-hydroxyethyl acrylate. DTEA is a bifunctional molecule which is characterized by having one double bond and one thiocarbonylthio group. Branched poly(methyl acrylate)s (BPMAs) were prepared through one-step radical polymerization of methyl acrylate (MA) in the presence of DTEA.  $^1\text{H}$  NMR spectra of the polymers were used to study the degree of branching (DB). The DB values of the three prepared BPMAs were calculated to be 0.46, 0.18 and 0.087, respectively. It was found that the DB value could be adjusted by controlling the ratio of MA to DTEA.

**Keywords** Reversible addition fragmentation transfer (RAFT) · Bifunctional molecule · Branched polymer · Degree of branching

## 1 Introduction

Hyperbranched polymers have drawn much attention due to their ease of synthesis on a large scale, unique properties and potential applications in diverse fields such as coatings, additives, medicines, nano technology, supramolecular science and so on [1, 2]. Hyperbranched polymers can be prepared by self-polymerization (polycondensation) of  $\text{AB}_x$  monomers (or latent  $\text{AB}_x$ ) and direct polycondensation for two suitable monomers (such as polymerization of  $\text{A}_2$  and  $\text{B}_3$  monomers). The two methods usually yield highly branched polymers with a multitude of end groups [3].

---

G. Ma · Z. Li (✉) · Y. Qi · T. Wu  
Laboratory of Printing and Packaging Material and Technology,  
Beijing Institute of Graphic Communication,  
Xinghua Avenue (Band Two), Beijing, China  
e-mail: lizhongxiao@bigc.edu.cn

Free radical polymerization is a key synthetic route for obtaining a wide variety of different polymers and material composites. Fréchet and his coworkers reported a so-called self-condensing vinyl polymerization (SCVP) for generating hyperbranched polymers [4]. Smeets prepared by amphiphilic hyperbranched polymers through the copolymerization of vinyl and divinyl monomers in the presence of a chain transfer agent [5]. Additionally, hyperbranched polymers can also be prepared by RAFT polymerization, allowing end group control or control over the branching density [6]. Wei reported one-pot synthesis of hyperbranched polymers using small molecule and macro RAFT inimers [7]. Haldar reported a new polyhedral oligomeric silsesquioxane (POSS) containing “inimer” and employed in RAFT copolymerization with various vinyl monomers to develop novel hybrid hyperbranched copolymers [8].

In this paper, we report the synthesis of a RAFT agent bearing a polymerizable group (inimer) and its use in the polymerization of methyl acrylate to produce branched polymers.

## 2 Experimental

### 2.1 *Synthesis of the Polymerizable RAFT Agent of 2-((2-(((Dodecylthio) Carbonothioyl) Thio) Propanoyl) Oxy) Ethylacrylate (DTEA)*

2-(((Dodecylthio) carbonothioyl) thio) propanoic acid (DTPA) was synthesized in our laboratory [9]. DTPA (17.5 g), hydroxyethyl methacrylate (5.8 g) and dichloromethane (50 ml) were placed in a 200 ml three-necked flask equipped with a magnetic stirrer. The mixture was stirred to afford a clear solution which was cooled to 10 °C. Then, 0.5 g of DMAP and 10.3 g of DCC were added to the mixture under constant stirring. The mixture was stirred for at 10 °C for 2 h and then stirred at room temperature for additional 10 h. The reaction mixture was then vacuum filtered, and the filtrate was washed with two portions of 10 ml sodium hydroxide aqueous solution (5.0 wt%) and three portions of 10 ml water. The organic layer was dried over Na<sub>2</sub>SO<sub>4</sub>, and the solvents were evaporated to obtain a yellowish transparent viscous liquid. FTIR (KBr, cm<sup>-1</sup>): 2932, 2852, 1719, 1654, and 1077. <sup>1</sup>H NMR (300 MHz, CDCl<sub>3</sub>): 5.90–6.47 (3H, CH=CH<sub>2</sub>); 4.40 (4H, –OCH<sub>2</sub>CH<sub>2</sub>O–); 4.82–4.87 (1H, CH); 3.34–3.37 (2H, CH<sub>2</sub>); 3.34–3.37 (2H, CH<sub>2</sub>); 1.71–1.77 (2H, CH<sub>2</sub>), 1.50–1.71 (3H, CH<sub>3</sub>), 1.27–1.29 (18H, C<sub>9</sub>H<sub>18</sub>); 0.88–0.91 (3H, CH<sub>3</sub>). ESI (m/e, percentage of relative intensity): 448.



## **2.2 Preparation of Branched Poly (Methyl Acrylate)s (BPMA)s by the Polymerization of Methyl Acrylate in the Presence of DTEA**

In a typical experiment, MA, DTEA, AIBN (2.5 wt% of MA) and 1,4-dioxane were placed in a three-necked flask and stirred to obtain a clear solution. The solution was purged with gentle nitrogen flow and the polymerization was conducted at 70 °C for 8 h. After cooling to room temperature, the polymer solution was slowly poured into an excess of cold water (0–5 °C) to afford a yellowish solid. The solid was collected, washed repeatedly with cold water and dried at room temperature. Three polymers were prepared, and the molar ratios of MA to DTEA for the polymers were 5/1(BPMA-1), 10/1(BPMA-2) and 20/1(BPMA-3), respectively.

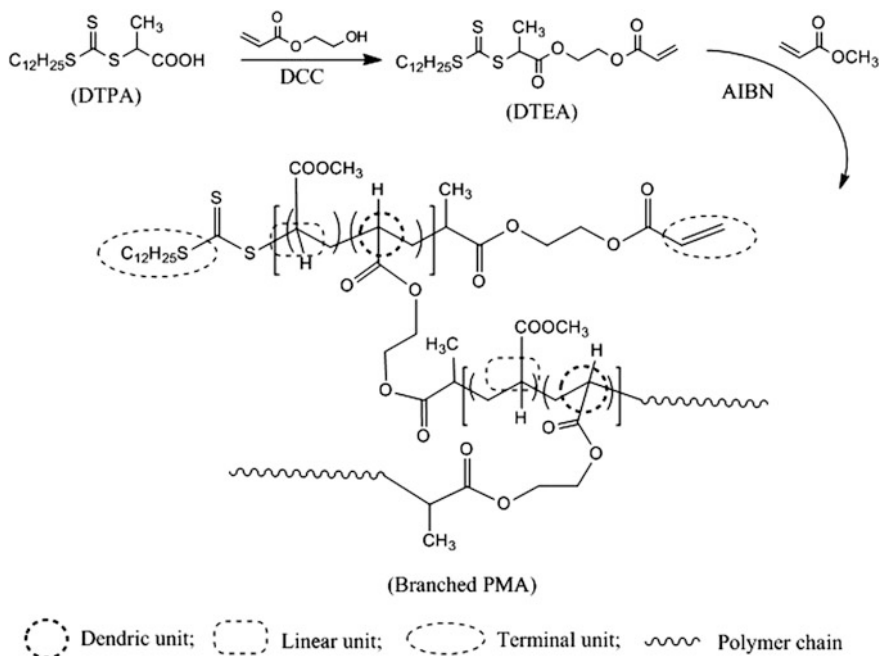
## **3 Results and Discussion**

### **3.1 Preparation of DTEA and BPMA**

As shown in Scheme 1, DTPA was firstly synthesized and then reacted with hydroxyethyl acrylate to obtain the RAFT agent, DTEA, which was characterized by IR, <sup>1</sup>H NMR and MS. DTEA contains one polymerizable double bond and one thiocarbonylthio group which can control the radical polymerization in a RAFT manner. During the polymerization process, the double bond of DTEA has the similar polymerization activity to that of methyl acrylate. With the progress of the polymerization, more than one RAFT active points (thiocarbonylthio groups) were incorporated into the polymer chain, giving a highly branched polymer. As a result, branched product will be obtained with the propagation of the polymer chain. It is noted that only low monomer conversion was found in the case of BPMA. This is because of the higher content of DTEA as well as its retardation effect on the radical polymerization of MA.

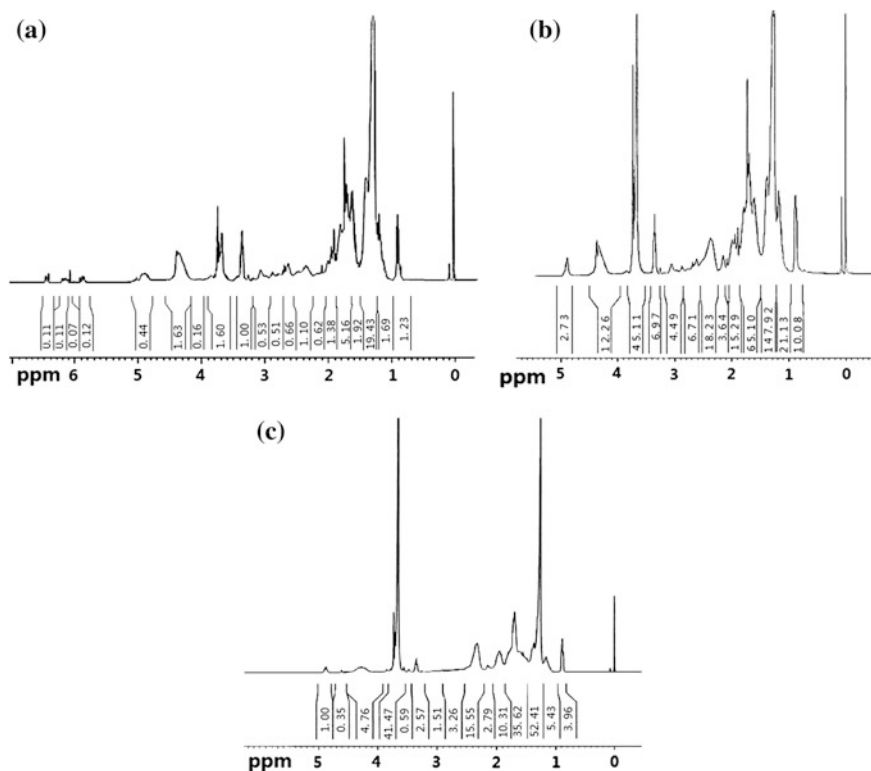
### **3.2 Estimation of Degree of Branching (DB)**

Branched polymers have three repeating units: the dendritic unit (D), the terminal unit (T) and the linear unit (L). The DB value can be calculated with the following equation:  $DB = (D + T)/(D + T + L)$ . As shown in Scheme 1, L of BPMA are attributed to the polymerization of MA, and the thiocarbonylthio groups and the



**Scheme 1** Preparation of branched PMA (BPMA) in the presence of DTEA

double bonds are transformed into D and T of BPMA. The integration values for L, D and T of BPMA can be calculated by the  $^1\text{H}$  NMR spectra (Fig. 1). According to Fig. 1, the resonance signals of the double bonds near 6.0 ppm are only found in Fig. 1a (BPMA-1), implying that quite a number of the terminal vinyl groups of DTEA were not involved in polymerization. The unpolymerized double bond of DTEA became the terminal group of BPMA-1. However, no signals of the double bonds are found in Fig. 1b, c, indicating high conversion of the double bonds of DTEA. The triplet peak in the range of 0.75–0.90 ppm is assigned to the terminal methyl group of the dodecyl substituent of DTEA, which represents the protons of T and D; the peak in the range of 3.50–3.90 ppm is assigned to the methyl group of MA, which represents the protons of L. The DB values are listed in Table 1. BPMA-3 prepared with a higher molar ratio of MA/DTEA has a lower DB value than BPMA-2 and BPMA-1. This is in accordance with the expected results.



**Fig. 1**  $^1\text{H}$  NMR spectra of BPMA-1 (a), BPMA-2 (b) and BPMA-3 (c)

**Table 1** Estimation of the DB value of BPMA

Samples	Molar ratio of MA/DTEA	Integral area		DB
		L	D + T	
BPMA-1 <sup>a</sup>	5	$1.60/3 = 0.53$	$0.41/3 + 1.23/3 = 0.46$	0.46
BPMA-2	10	$45.11/3 = 15.04$	$10.08/3 = 3.36$	0.18
BPMA-3	20	$41.47/3 = 13.82$	$3.96/3 = 1.32$	0.087

<sup>a</sup>The conversion rate of the monomer (MA) is relatively lower

## 4 Conclusions

A RAFT agent of DTEA was synthesized and characterized in this work. Branched poly(methyl acrylate)s were prepared through one-step radical polymerization in the presence of the RAFT agent. The DB values of the branched polymers could be calculated by  $^1\text{H}$  NMR spectra. Results showed that the DB value of the branched polymers was dependent on the molar ration of the monomer to the RAFT agent.

This is a simple method to prepare branched polymers via radical polymerization, and can be used as a platform to synthesize a range of other branched polymers.

**Acknowledgements** This work was supported by Beijing Municipal Education Commission (CIT&TCD20140320, TJSHG201310015017 and KM201410015002) the National Natural Science Foundation of China (21302012).

## References

1. Hult A, Johansson M, Malmström E. (1999). Hyperbranched Polymers, *Advances in Polymer Science*, 143, 1–34.
2. Jikei M, Kakimoto M. (2001). Hyperbranched polymers: a promising new class of materials. *Progress in Polymer Science*, 26, 1233–85.
3. Yan DY, Gao C, Frey H. (2011). Hyperbranched Polymers: Synthesis, Properties, and Applications. John Wiley & Sons, Inc., New York.
4. Fréchet JMJ, Henmi M, Gitsov I, Aoshima S, Leduc MR, Grubbs RB. (1995). Self-condensing vinyl polymerization: An approach to dendritic materials, *Science*, 269, 1080–1083.
5. Niels MB Smeets. (2013). Amphiphilic hyperbranched polymers from the copolymerization of a vinyl and divinyl monomer: The potential of catalytic chain transfer polymerization, *European Polymer Journal*, 49, 2528–2544.
6. Gregory A, Stenzel MH. (2012). Complex polymer architectures via RAFT polymerization: From fundamental process to extending the scope using click chemistry and nature's building blocks, *Progress in Polymer Science* 37, 38–105.
7. Wei ZK, Hao XJ, Kambouris PA. (2012). One-pot synthesis of hyperbranched polymers using small molecule and macro RAFT inimers, *Polymer*, 53, 1429–1436.
8. Haldar U, Roy SG, De P. (2016). POSS tethered hybrid “inimer” derived hyperbranched and starshaped polymers via SCVP-RAFT technique, *Polymer*, 97 113–121.
9. Li ZX, Zhang YJ, Li LH, Pu JL. (2007). Preparation and properties of thermo-sensitive latex films, The 23th International Conference on Digital Printing Technology, 591–594.